Isoprene Oxidation Mechanisms and Secondary Organic Aerosol Formation Under HO_2-Dominated Conditions

Thesis by
Kelvin Hamilton Bates

In Partial Fulfillment of the Requirements for the
degree of
Doctor of Philosophy

CALIFORNIA INSTITUTE OF TECHNOLOGY
Pasadena, California

2017
Defended 5 May 2017

Kelvin Hamilton Bates
ORCID: 0000-0001-7544-9580

ACKNOWLEDGEMENTS

I would like to thank the generous support of the National Science Foundation's Graduate Research Fellowship Program, which funded my last three years of graduate school; the Sharp Fellowship at Caltech, which funded my first year of study; and numerous other grants from the National Science Foundation, the Department of Energy, the Environmental Protection Agency, the Office of Naval Research, and the Electric Power Research Institute, which funded the research described herein.

The work represented in this thesis would not have been remotely possible without the assistance of an entire community of researchers and friends who guided me through graduate school, both in and out of the laboratory. While I cannot thank everyone by name, I would like to express my gratitude to everyone who made my experience at Caltech so productive and enjoyable; it was only with your support and your friendship that I made it this far.

To my advisors, Professors John Seinfeld, Brian Stoltz, and Paul Wennberg: thank you for encouraging my growth as a scientist by providing me with myriad opportunities for exciting research, by teaching me to ask the right questions, by offering guidance when I needed it and freedom when I didn't, and above all by fostering my passion for scientific enquiry. It has truly been a privilege to work with you and to learn from you throughout the past five years. I consider myself quite fortunate to have had the opportunity to work across three labs during my graduate studies, and I am grateful to each of you for your help in making this unique arrangement a success. I would also like to thank the other two members of my committee – Professors Michio Okumura and Robert Grubbs – for their helpful conversations and for providing a valuable external perspective on my work.

To my colleagues and coworkers in the Seinfeld, Stoltz, and Wennberg groups: thank you for all the hard work you put into our collaborative projects, for the helpful guidance and discussions you provided even when our projects didn't overlap, and for the camaraderie that made my time in the lab so fulfilling. I am especially appreciative of the spirit of cooperation and support that made each lab feel like a family. I owe a particular debt of gratitude to the senior members of each group who showed me the ropes, trained me in the techniques and facilities unique to each laboratory, and helped me to hit the ground running. Thanks to Nathan Bennett for teaching me organic synthesis; to John Crounse and Jason St. Clair for acquainting

me with atmospheric instrumentation; to Tran Nguyen for coaching me through every aspect of designing and carrying out a chamber study; to Becky Schwantes for her help with modeling and the chamber; to Matt Coggon for introducing me to fieldwork; and to the rest of my collaborators and labmates who offered guidance, assistance, and support throughout my graduate career.

To my friends at Caltech and beyond: thank you for making sure that my time here wasn't entirely spent in the lab, and even when it felt like it was, for making my experience at Caltech so enjoyable. I feel immensely lucky to have met so many wonderful people in this community, and to have found individuals and groups here that I could rely on to lift my spirits and enrich my life; you truly made the days fly by. Thanks to my EXPLiCIT and FD friends for sharing their love of theater and singing with me, to the fabulously supportive community of the Caltech Center for Diversity, to my fellow RA's and the undergrads of Page who helped me as much I hope I helped them, to my fellow graduate students for welcoming me into whatever department I pretended to be in, and of course to my main partners-in-crime, Christopher, Matt, and Giuliana.

Finally, I would like to thank those who motivated me to undertake this journey into research and academia, and those who have done the most to keep me inspired along the way. To my many incredible teachers and professors, at Evergreen, Lakeside, Davidson, and now Caltech: thank you for instilling in me an insatiable appetite for learning and a passion for research, reason, and the pursuit of knowledge. Though it was not always clear I would end up in chemistry, your dedication and encouragement throughout my education guaranteed that I would never stop learning. To my early mentors in atmospheric chemistry, particularly through the NOAA Hollings Scholarship and NASA Student Airborne Research Programs: thank you for introducing me to this fascinating field of study, and for your patience in initiating me into the world of scientific research. To my family, and especially my parents: thank you for your unwavering support and guidance, both in science and in life; for giving me the tools I needed to succeed throughout my education and beyond; and for the all the opportunities and encouragement that allowed me to forge my own path to a PhD. And of course, to Dylan: thank you for the joy you have brought me, for keeping me sane and grounded, and for always being by my side. Despite the difficulties of graduate schools and distance, I am grateful for our ability to share in each other's successes and stresses as we pursue our own aspirations. Your love and support mean the world to me.

ABSTRACT

Isoprene, a volatile hydrocarbon emitted by plants, represents the single most abundant source of non-methane organic carbon to the atmosphere. After its rapid oxidation by OH radicals in the troposphere, isoprene may follow any of a number of complex reaction mechanisms to form more highly functionalized products, depending in large part on the relative abundance of reactive radicals such as HO_2 and NO; some of these products can be sufficiently water-soluble, non-volatile, and/or reactive to partition into atmospheric particles and contribute to the creation of secondary organic aerosol (SOA). In this work, I explore the gas-phase oxidation mechanisms and SOA formation potential of second- and later-generation products formed in the HO_2-dominated reaction cascade, which predominates in remote regions and is estimated to account for >40% of isoprene oxidation. Pure standards of significant isoprene products, such as isoprene epoxydiols (IEPOX) and C_4 dihydroxycarbonyl compounds, are synthesized, and the rates and product yields of their gas-phase reactions with OH are measured by CF_3O^- chemical ionization mass spectrometry in environmental chamber experiments. Results are compared to field observations from the Southern Oxidant and Aerosol Study in the Southeastern United States, where significant concentrations of these compounds were detected, and are integrated into a global chemical transport model to investigate their effects throughout the atmosphere. Further, the results from these and other gas-phase kinetic and product studies are incorporated into an explicit isoprene oxidation mechanism, designed to simulate the effects of isoprene chemistry on oxidant concentrations and to produce accurate representations of products known to be involved in condensed phase processes, including IEPOX. Finally, additional chamber experiments with synthetic IEPOX and inorganic seed aerosol are performed to derive particle uptake coefficients and examine the effects of particle pH, liquid water content, and chemical composition on IEPOX-SOA formation, using aerosol mass spectrometry and differential mobility analysis. The gas- and particle-phase reaction rates and product yields reported herein, along with the explicit model, provide important constraints on the fate of isoprene-derived carbon in the atmosphere and on the influence the HO_2-dominated isoprene oxidation pathway exerts on SOA and oxidant budgets.

PUBLISHED CONTENT AND CONTRIBUTIONS

Bates, K. H., T. B. Nguyen, A. P. Teng, J. D. Crounse, H. G. Kjaergaard, B. M. Stoltz, J. H. Seinfeld, and P. O. Wennberg (2016). "Production and fate of C4 dihydroxycarbonyl compounds from isoprene oxidation". In: *J. Phys. Chem. A* 120.1, pp. 106–117. DOI: 10.1021/acs.jpca.5b10335.
K. H. B. conducted syntheses and experiments, analyzed data, performed GEOS-Chem modeling, and wrote the manuscript for this project.

Liu, Y., J. Brito, M. R. Dorris, J. C. Rivera-Rios, R. Seco, K. H. Bates, P. Artaxo, S. Duvoisin, F. N. Keutsch, S. Kim, A. H. Goldstein, A. B. Guenther, A. O. Manzi, R. A. F. Souza, S. R. Springston, T. B. Watson, K. A. McKinney, and S. T. Martin (2016). "Isoprene photochemistry over the Amazon rainforest". In: *Proc. Nat'l. Acad. Sci.* 113.22, pp. 6125–6130. DOI: 10.1073/pnas.1524136113.
K. H. B. performed GEOS-Chem modeling and assisted in the writing of relevant manuscript sections for this project.

Nguyen, T. B., G. S. Tyndall, J. D. Crounse, A. P. Teng, K. H. Bates, R. H. Schwantes, M. M. Coggon, L. Zhang, P. Feiner, D. O. Milller, K. M. Skog, J. C. Rivera-Rios, M. Dorris, K. F. Olson, A. Koss, R. J. Wild, S. S. Brown, A. H. Goldstein, J. A. de Gouw, W. H. Brune, F. N. Keutsch, J. H. Seinfeld, and P. O. Wennberg (2016). "Atmospheric fates of Criegee intermediates in the ozonolysis of isoprene". In: *Phys. Chem. Chem. Phys.* 18.15, pp. 10241–10254. DOI: 10.1039/C6CP00053C.
K. H. B. assisted in the chamber experiments for this project.

Wang, Z., M. Mora Ramirez, H. Dadashazar, A. B. MacDonald, E. Crosbie, K. H. Bates, M. M. Coggon, J. S. Craven, P. Lynch, J. R. Campbell, M. Azadi Aghdam, R. K. Woods, H. Jonsson, R. C. Flagan, J. H. Seinfeld, and A. Sorooshian (2016). "Contrasting cloud composition between coupled and decoupled marine boundary layer clouds". In: *J. Geophys. Res. - Atmos.* 121.19, pp. 11679–11691. DOI: 10.1002/2016JD025695.
K. H. B. collected and analyzed field data for this project.

Zhang, X., N. Dalleska, D. Huang, K. Bates, A. Sorooshian, R. Flagan, and J. Seinfeld (2016). "Time-resolved molecular characterization of organic aerosols by PILS + UPLC/ESI-Q-TOFMS". In: *Atmos. Environ.* 130, pp. 180–189. DOI: http://doi.org/10.1016/j.atmosenv.2015.08.049.
K. H. B. assisted in the chamber experiments for this project.

Nguyen, T. B., K. H. Bates, J. D. Crounse, R. H. Schwantes, X. Zhang, H. G. Kjaergaard, J. D. Surratt, P. Lin, A. Laskin, J. H. Seinfeld, and P. O. Wennberg (2015). "Mechanism of the hydroxyl radical oxidation of methacryloyl peroxynitrate (MPAN) and its pathway toward secondary organic aerosol formation in the atmosphere". In: *Phys. Chem. Chem. Phys.* 17.27, pp. 17914–17926. DOI: 10.1039/C5CP02001H.
K. H. B. assisted in the syntheses and chamber experiments for this project.

Praske, E., J. D. Crounse, K. H. Bates, T. Kurtén, H. G. Kjaergaard, and P. O. Wennberg (2015). "Atmospheric fate of methyl vinyl ketone: Peroxy radical reactions with NO and HO2". In: *J. Phys. Chem. A* 119.19, pp. 4562–4572. DOI: 10.1021/jp5107058.
K. H. B. performed GEOS-Chem modeling for this project.

St. Clair, J. M., J. C. Rivera-Rios, J. D. Crounse, H. C. Knap, K. H. Bates, A. P. Teng, S. Jorgensen, H. G. Kjaergaard, F. N. Keutsch, and P. O. Wennberg (2015). "Kinetics and products of the reaction of the first-generation isoprene hydroxy hydroperoxide (ISOPOOH) with OH". In: *J. Phys. Chem. A* 120.9, pp. 1441–1451. DOI: 10.1021/acs.jpca.5b06532.
K. H. B. performed GEOS-Chem modeling and assisted with gas-phase chamber experiments for this project.

Bates, K. H., J. D. Crounse, J. M. St Clair, N. B. Bennett, T. B. Nguyen, J. H. Seinfeld, B. M. Stoltz, and P. O. Wennberg (2014). "Gas phase production and loss of isoprene epoxydiols". In: *J. Phys. Chem. A* 118.7, pp. 1237–46. DOI: 10.1021/jp4107958.
K. H. B. conducted syntheses and experiments, analyzed data, and wrote the manuscript for this project.

Nguyen, T. B., M. M. Coggon, K. H. Bates, X. Zhang, R. H. Schwantes, K. A. Schilling, C. L. Loza, R. C. Flagan, P. O. Wennberg, and J. H. Seinfeld (2014a). "Organic aerosol formation from the reactive uptake of isoprene epoxydiols (IEPOX) onto non-acidified inorganic seeds". In: *Atmos. Chem. Phys.* 14, pp. 3497–3510. DOI: 10.5194/acp-14-3497-2014.
K. H. B. assisted in the syntheses, chamber experiments, and data analysis for this project.

Nguyen, T. B., J. D. Crounse, R. H. Schwantes, A. P. Teng, K. H. Bates, X. Zhang, J. M. St. Clair, W. H. Brune, G. S. Tyndall, F. N. Keutsch, J. H. Seinfeld, and P. O. Wennberg (2014b). "Overview of the Focused Isoprene eXperiment at the California Institute of Technology (FIXCIT): Mechanistic chamber studies on the oxidation of biogenic compounds". In: *Atmos. Chem. Phys.* 14.24, pp. 13531–13549. DOI: 10.5194/acp-14-13531-2014.
K. H. B. assisted in the chamber experiments for this project.

TABLE OF CONTENTS

LIST OF ILLUSTRATIONS

LIST OF TABLES

NOMENCLATURE AND ABBREVIATIONS

2MGA. 2-methylglyceric acid; an oxidation product of isoprene known to contribute to isoprene-derived SOA mass, with chemical formula $C_4H_8O_4$.

ABS. Ammonium bisulfate; $(NH_4)HSO_4$.

Aerosol. Fine solid or liquid particles suspended in a gas. The term aerosol can refer either to the particles themselves or the colloid of particles and gas.

AMS. Aerosol mass spectrometer; an instrument that measures the size and chemical composition of nonrefractory sub-micron particles in real time by coupling a particle time-of-flight separator, a filament to thermally vaporize particles and ionize their constituents *via* electron impact ionization, and a mass analyzer to determine the mass-to-charge ratios of the fragment ions.

APN. Acylperoxy nitrate; a class of compounds (including PAN and MPAN) containing the $C(=O)OONO_2$ moiety formed in the reaction of acylperoxy radicals with NO_2, which are often respiratory and eye irritants and a key component of photochemical smog. Also called peroxyacyl nitrate.

AS. Ammonium sulfate; $(NH_4)_2SO_4$.

BBOA. Biomass burning organic aerosol; primary or secondary organic particulate matter emitted from the combustion of living or dead vegetation.

BOAS. Biological and oceanic atmospheric study; an airborne atmospheric field campaign based in Marina, CA, that took place in July and August of 2015.

CCN. Cloud condensation nuclei; atmospheric particles onto which water vapor may condense to form cloud droplets.

CI*. Activated or excited Criegee intermediate; the energetic carbonyl oxide formed following the decomposition *via* retro 1,3 cycloaddition of a primary ozonide (POZ) during an ozonolysis reaction, which may have enough internal vibrational energy to rapidly isomerize or dissociate.

CIMS. Chemical ionization mass spectrometer; an instrument that ionizes analyte gases by colliding them with charged reagent gas molecules (*e.g* H_3O^+ in PTR-MS, or CF_3O^- in the Caltech CIMS) and then measures the mass-to-charge ratios of analyte ions.

CPC. Condensation particle counter; an instrument that counts particles by first growing them *via* supersaturated vapor condensation and then detecting them by laser scattering.

CTM. Chemical transport model; a numerical computer model used to simulated the stocks and fluxes of chemicals in the atmosphere.

DMA. Differential mobility analyzer; an instrument that separates charged particles based on their mobility in an electric field.

E-PEACE. Eastern Pacific Emitted Aerosol Cloud Experiment; an atmospheric field campaign based in Marina, CA, that took place in July and August of 2011, with airborne and ship-based measurements.

ELVOC. Extra low volatility organic compound; generally defined as any organic compound found in the atmosphere with a saturation vapor mass concentration $C^* \leq 10^{-3.5}$ μg m^{-3}.

ESI. Electrospray ionization; a soft ionization technique by which a solute is ionized in its passage through a charged capillary tip, then aerosolized into a spray of droplets that evaporate to form gaseous ions.

FIXCIT. Focused Isoprene eXperiment at the California Institute of Technology; an atmospheric chamber campaign that consisted of 26 environmental chamber experiments conducted over the course of January of 2014.

GC. Gas chromatography; an instrumental technique to separate gas-phase analytes by passing them through a column coated with a stationary phase with which the analytes interact, and generally increasing the column temperature to elute analytes.

GEOS-Chem. A 3-D chemical transport model that simulates atmospheric chemical composition using meteorological input from the Goddard Earth Observing System.

GLYC. Glycolaldehyde; a volatile organic compound with the chemical formula $C_2H_4O_2$, and a common oxidation product of larger VOCs, including isoprene.

GLYX. Glyoxal; a volatile organic compound with the chemical formula $C_2H_2O_2$, and a common oxidation product of larger VOCs, including isoprene.

GOAmazon. Green Ocean Amazon; an atmospheric field campaign based in various locations near Manaus, Brazil, that took place between January of 2014 and November of 2015, with airborne and ground-based measurements.

H/C. Hydrogen-to-carbon ratio, usually in reference to bulk organic aerosol as measured by aerosol mass spectrometry.

HAC. Hydroxyacetone; a volatile organic compound with the chemical formula $C_2H_4O_2$, and a common oxidation product of larger VOCs, including isoprene.

High-NO. Conditions under which organic peroxy radicals in the gas phase react primarily with nitric oxide. The exact NO concentration at which this occurs depends on a number of conditions, but is generally on the order of $\gtrsim$1 ppb in the troposphere.

HMML. Hydroxymethyl-methyl-α-lactone; a suspected product of MPAN photooxidation that may contribute to isoprene-derived SOA, with chemical formula $C_4H_6O_3$.

HO_2-dominated. Conditions under which organic peroxy radicals in the gas phase react primarily with the hydrogen dioxide radical.

HO_x. The hydrogen oxide radical family, defined as the sum of the hydroxyl (OH) and hydrogen dioxide (HO_2) radicals.

HPALD. Isoprene hydroperoxy aldehyde; a first-generation stable atmospheric product of isoprene photooxidation under low-NO conditions with chemical formula $C_5H_8O_3$. Two isomers of HPALD are known to form in the atmosphere from the isomerization of *Z*-δ-ISOPOO, while two others are expected to form as second-generation isoprene oxidation products from the reaction of ISOPOOH with OH.

HR. High resolution; in reference to mass spectrometry, refers to methods with mass resolving power $>10^4$ m/Δm.

ICN. Isoprene carbonylnitrate; a first-generation stable atmospheric product of isoprene's reaction with NO_3, followed by O_2 addition and reaction with NO or RO_2. Four isomers of ICN, with chemical formula $C_5H_7O_4N$, are known to form in the atmosphere.

IEPOX. Isoprene epoxydiol; a second-generation stable atmospheric product of isoprene photooxidation under HO_2-dominated conditions with chemical formula $C_5H_{10}O_3$, and a major SOA precursor in the low-NO isoprene reaction pathway. Four isomers of IEPOX can form in the atmosphere from the reaction of ISOPOOH or IHN with OH.

IHN. Isoprene hydroxynitrate; a first-generation stable atmospheric product of isoprene photooxidation under high-NO conditions with chemical formula $C_5H_9O_4N$, and a major contributor to NO_x transport and removal from isoprene oxidation. Eight isomers of IHN can form in the atmosphere from the reaction of ISOPOO with NO or the reaction of isoprene nitrooxy peroxy radicals with RO_2.

IHNE. Isoprene hydroxynitrooxyepoxide; a second-generation stable atmospheric product of isoprene's oxidation by NO_3 with chemical formula $C_5H_9O_5N$. Six isomers of IHNE can form in the atmosphere from the reaction of IPN with OH.

IPN. Isoprene hydroperoxynitrate; a first-generation stable atmospheric product of isoprene's reaction with NO_3, followed by O_2 addition and reaction with HO_2. Six isomers of IPN, with chemical formula $C_5H_9O_5N$, are known to form in the atmosphere.

ISOPN. Isoprene hydroxynitrate; see IHN.

ISOPOO. Isoprene hydroxyperoxy radical; a radical species formed following the addition of OH and O_2 to isoprene. Eight isomers of ISOPOO can form in the atmosphere, and their relative ambient abundance depends on the species' lifetime against isomerization and reaction with NO, HO_2, and RO_2.

ISOPOOH. Isoprene hydroxyhydroperoxide; a first-generation stable atmospheric product of isoprene photooxidation under HO_2-dominated conditions with chemical formula $C_5H_{10}O_3$. Eight isomers of ISOPOOH can form in the atmosphere from the reaction of ISOPOO with HO_2.

Isoprene. A volatile unsaturated hydrocarbon with chemical formula C_5H_8, emitted to the atmosphere primarily by deciduous trees in quantities exceeding 500 Tg y^{-1}.

IVOC. Intermediate volatility organic compound; generally defined as any organic compound found in the atmosphere with a saturation vapor mass concentration in the range of $10^{2.5}$ μg m^{-3} $\leq$ C* $\leq$ $10^{6.5}$ μg m^{-3}.

K_H. Henry's law constant; a measure of a compound's volatility, defined as the ratio of that compound's concentration in solution to its partial pressure in a parcel of air in equilibrium with that solution (mol L^{-1} atm^{-1}). Also commonly denoted H or H^{cp}.

Lifetime. The amount of time a chemical species lasts before being lost *via* such processes as reaction, deposition, or transport. The lifetime against a specific process refers only to the loss rate due to that process. Generally defined as the *e*-folding time, *i.e.*, the tame it takes to deplete a species to 1/*e* of its former amount.

LOD. Limit of detection; the analyte concentration below which a signal cannot be distinguished from noise.

Low-NO. Conditions under which organic peroxy radicals in the gas phase react primarily with compounds other than nitric oxide. The exact NO concentration at which this occurs depends on a number of conditions, but is generally on the order of $\lesssim$1 ppb in the troposphere.

LVOC. Low volatility organic compound; generally defined as any organic compound found in the atmosphere with a saturation vapor mass concentration in the range of $10^{-3.5}$ μg m^{-3} $\leq$ C* $\leq$ $10^{-0.5}$ μg m^{-3}.

***m/z*.** mass-to-charge ratio; usually in reference to an analyte ion detected by mass spectrometric methods.

MACR. Methacrolein; a volatile unsaturated aldehyde with chemical formula C_4H_6O, produced in the oxidation of isoprene by OH and O_3.

MAE. Methacrylic acid epoxide; a suspected product of MPAN photooxidation that may contribute to isoprene-derived SOA, with chemical formula $C_4H_6O_3$.

MGLY. Methylglyoxal; a volatile organic compound with the chemical formula $C_3H_4O_2$, and a common oxidation product of larger VOCs, including isoprene.

MPAN. Methacryloyl peroxynitrate; an acylperoxy nitrate with chemical formula $C_4H_5O_5N$ formed from the sequential reactions of methacrolein with OH, O_2, and NO_2, and an important SOA precursor in the high-NO oxidation pathway of isoprene.

MS. Mass spectrometry; an instrumental technique for measuring the mass-to-charge ratios of analyte ions.

MVK. Methyl vinyl ketone; a volatile unsaturated ketone with chemical formula C_4H_6O, produced in the oxidation of isoprene by OH and O_3.

MW. Molecular weight (g mol^{-1}).

NiCE. Nucleation in California Experiment; an airborne atmospheric field campaign based in Marina, CA, that took place in July and August of 2013.

NMHC. Non-methane hydrocarbons; volatile organic compounds found in the atmosphere that contain only hydrogen and carbon, excluding methane.

NMR. Nuclear magnetic resonance spectroscopy; an instrumental technique to determine the molecular structure and purity of a sample by measuring the effects of a strong magnetic field on the spin of atomic nuclei.

NO_3. Nitrate radical; the dominant oxidant in the troposphere at night, when NO_3 is typically present in concentrations on the order of 1-10 pptv.

NO_x. The nitrogen oxide radical family, defined as the sum of the nitric oxide (NO) and nitrogen dioxide (NO_2) radicals.

Nonrefractory. Used in conjunction with aerosol mass spectrometry to denote species that vaporize in 1 s or less at 600 °C under high vacuum, and can therefore be observed by AMS. This includes most secondary inorganic salts (*e.g* ammonium sulfate) and organic compounds. Also written non-refractory.

NSS. Non-sea-salt, referring to the portion of particle chemical constituents (*e.g* sulfate or chloride) that are not derived from primary emissions of sea salts.

O_3. Ozone; a major tropospheric oxidant, with typical concentrations on the order of 10 ppb. As a component of photochemical smog, tropospheric ozone also causes adverse health effects and contributes to greenhouse warming.

O/C. Oxygen-to-carbon ratio, usually in reference to bulk organic aerosol as measured by aerosol mass spectrometry.

OA. Organic aerosol, referring to the portion of particulate mass composed of organic compounds.

OC. Organic carbon, referring to the fraction of aerosol mass composed of carbon contained in organic molecules.

OH. Hydroxyl radical; the dominant oxidant in the troposphere, with typical daytime concentrations on the order of 1×10^6 molec cm^{-3}.

OM. Organic mass, used in reference to aerosol as a synonym for OA.

OOA. Oxidized organic aerosol; used in conjunction with aerosol mass spectrometry to refer to aerosol mass composed of oxygen-containing organic compounds.

PAN. Peroxyacetyl nitrate; the most abundant gaseous acylperoxy nitrate, with a chemical formula of $C_2H_3O_5N$, formed in the reaction of the peroxyacetyl radical with NO_2. PAN is a lachrymator and serves as a reservoir and transport mechamisn for NO_x.

PCASP. Passive cavity aerosol spectrometer probe; an instrument used to measure particle size distributions between 100 nm and 3 μm by light scattering.

PILS. Particle-into-liquid sampler; an aerosol sample acquisition method by which particles are grown *via* supersaturated water vapor condensation and collected by inertial impaction.

POA. Primary organic aerosol; particles emitted directly to the atmosphere.

POZ. Primary ozonide; the initial 5-member cyclic intermediate formed by the cycloaddition of ozone to a double bond during an ozonolysis reaction. Also called a molozonide or a 1,2,3-trioxolane.

PTR-MS. Proton transfer reaction mass spectrometry; a soft-ionization MS technique by which analyte gases are ionized by proton transfer from hydronium ions (H_3O^+).

RH. Relative humidity; water vapor concentration as a percentage of the concentration required for saturation at the same temperature.

RO_2. Any organic peroxy radical, where R represents an unspecified stable organic group.

SCI. Stabilized Criegee intermediate; the carbonyl oxide formed following the stabilization of an activated Criegee intermediate (CI*) *via* collisional energy transfer.

SEAC4RS. Studies of Emissions and Atmospheric Composition, Clouds and Climate Coupling by Regional Surveys; an airborne atmospheric field campaign based in Houston, TX, that took place in August and September of 2013.

SMPS. Scanning mobility particle sizer; an instrument consisting of a coupled differential mobility analyzer and condensation particle counter, used to measure particle size distributions.

SOA. Secondary organic aerosol; particle mass formed in the atmosphere from the condensation and reaction of gaseous species.

SOAS. Southern Oxidant and Aerosol Study; an atmospheric field campaign based in various locations throughout the Southeast United States that took place in June and July of 2013, with aiborne and ground-based measurements.

SVOC. Semi-volatile organic compound; generally defined as any organic compound found in the atmosphere with a saturation vapor mass concentration in the range of $10^{-0.5}$ μg m^{-3} $\leq$ C* $\leq$ $10^{2.5}$ μg m^{-3}.

ToF. Time-of-flight; a mass analysis technique in which an analyte ion's mass-to-charge ratio is measured by the time it takes to reach a detector after passing through an electric field.

UPLC. Ultra performance liquid chromatograph; a chemical separation technique utilizing a column with smaller beads (>2 μm in diameter) and higher flow rates and pressure to achieve greater resolution, speed, and sensitivity than other chromatographic techniques.

VOC. Volatile organic compound; generally defined as any organic compound found in the atmosphere with a saturation vapor mass concentration C* $\geq$ $10^{6.5}$ μg m^{-3}.

WSOC. Water-soluble organic carbon; particulate organic matter that dissolves into aqueous solution.

Chapter 1

INTRODUCTION

1.1 Background and Motivation

Earth's atmosphere can be roughly imagined as a slow-burning flame, gradually oxidizing its chemical constituents in a series of reactions driven largely by ozone (O_3) and families of oxide radicals. In the troposphere, two such families drive the ambient oxidative chemistry: HO_x (= OH + HO_2) and NO_x (= NO + NO_2). These radical pairs are described as families because of their rapid cycling; species within chemical families interconvert much more rapidly than they are produced or destroyed. The HO_x family typically initiates oxidation by the reaction of reduced compounds with OH, a highly reactive radical formed following the photolysis of ozone, while the NO_x family efficiently propagates radical chain reactions and leads to ozone formation. The abundance and cycling of these radical families together set the timescale of oxidation and determine the reactive fate of other chemicals in the troposphere (Seinfeld and Pandis, 2006).

Among the most abundant of the other chemicals with which radical families may react are volatile organic compounds (VOCs), which act as fuel for the atmosphere's slow-burning flame. VOCs are emitted from a variety of sources, both biogenic and anthropogenic, and their oxidation in the atmosphere can be initiated *via* two main pathways: the abstraction of a hydrogen atom by OH, or the addition of OH, O_3, NO_3, or Cl to a double bond. In each case, an alkyl radical species in formed, which then undergoes a series of radical-propagating reactions, illustrated for methane in Figure 1.1, ultimately resulting in the formation of stable oxidized species such as CO_2.

Alkyl radicals formed in the oxidation of VOCs typically add O_2 to form peroxy radicals, denoted RO_2 (*e.g.* $CH_3OO^{\cdot}$ in Figure 1.1). These peroxy radicals represent a branching point in the oxidative mechanism: depending on the ambient conditions, they may react with other peroxy radicals, NO, or HO_2, or isomerize before reacting. The relative prominence of these pathways frequently determines the chemical products of the overall VOC oxidation mechanism. For example, reaction with NO may lead to greater ozone production through the formation and photolysis of NO_2, while reaction with HO_2 may lead to the formation of hydroperoxides and

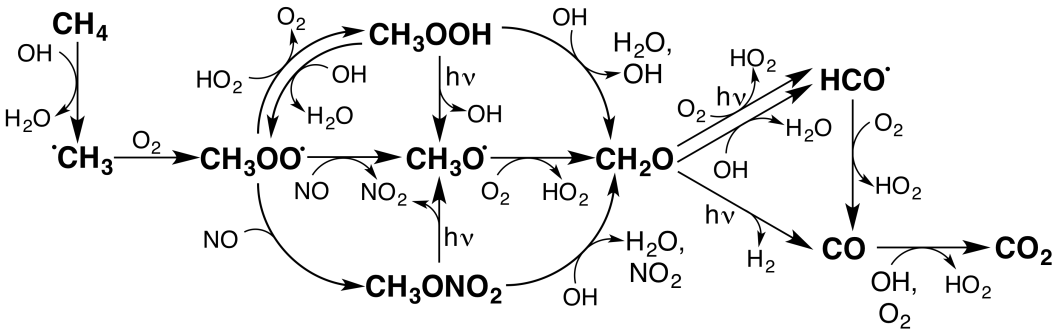

Figure 1.1: Steps in the atmospheric oxidation of methane. The relative abundance of NO_x and HO_x controls not just the fate of the $CH_3OO^{\cdot}$ radical, but also the total radical cycling and ozone formation from VOC oxidation. Thus, the overall net reaction under NO-dominant conditions, and including subsequent photolysis of NO_2 and other reactions, is $CH_4 + 10O_2 \rightarrow CO_2 + H_2O + 5O_3 + 2OH$, while the net reaction under HO_2-dominant conditions is $CH_4 + 2OH + 2O_2 \rightarrow CO_2 + 2H_2O + 2HO_2$, assuming CH_2O photolyzes to form HCO in either case (Jacob, 1999).

other less-volatile species. Under conditions of low anthropogenic influence (*i.e.* low NO_x), the reactive fate of peroxy radicals is dominated by HO_2, which is the primary focus of the work included in this thesis.

Whatever the fate of the peroxy radicals, the chemical products resulting from VOC oxidation include many species commonly referred to collectively as "smog," which can have a wide range of adverse effects when present even in trace quantities. Ozone, for example, is a commonly regulated pollutant around the world (EPA, 2015), known to cause premature mortality and a variety of disease responses in humans (Bell *et al.*, 2006; Jerrett *et al.*, 2009; Li *et al.*, 2016), negatively impact plant health (Chameides *et al.*, 1994; Fuhrer, 2002; Zinser *et al.*, 2000), and contribute to radiative climate forcing in the troposphere (Pachauri *et al.*, 2014; Worden *et al.*, 2008). VOC oxidation typically constitutes the dominant source of local ozone pollution (Jacob, 1999); a detailed understanding of VOC oxidation mechanisms is therefore imperative to accurately assess and forecast ozone formation.

When VOC oxidation produces compounds with sufficiently low volatility, such species can then condense onto suspended ambient particles (or nucleate new particles) to form secondary organic aerosol (SOA), another component of smog. Like ozone, tropospheric particulate matter is harmful to human health; epidemiological studies suggest that particulate pollution contributes annually to over 4.2 million premature deaths worldwide (Cohen *et al.*, 2017; Lelieveld *et al.*, 2015; Nel, 2005; Pope *et al.*, 2002; Pope *et al.*, 2009; Pope and Dockery, 2006), and targeted studies

have shown specific adverse effects of particles within the respiratory and circulatory systems (Gaschen *et al.*, 2010; Künzi *et al.*, 2015; Nelin *et al.*, 2012). Aerosols also affect visibility (Watson, 2002) and play a prominent but uncertain role in climate forcing through their direct radiative properties as well as their indirect impacts *via* cloud formation (Myhre *et al.*, 2013; Raes *et al.*, 2010). Globally, a large and highly variable portion (20-90%) of particulate mass below 2.5 μm in diameter consists of organic material (Murphy *et al.*, 2006; Zhang *et al.*, 2007), and a significant fraction (30-95%) of that organic aerosol is SOA (Jimenez *et al.*, 2009; Zhang *et al.*, 2007), implying that the oxidation of VOCs can exert a strong influence on particulate mass budgets.

Although over 10,000 unique organic compounds may exist in the atmosphere (Goldstein and Galbally, 2007), each with its own oxidation mechanism and smog formation potential, one particular VOC holds outsized significance for its sheer abundance: 2-methyl-1,3-butadiene, or isoprene. Isoprene is emitted primarily by deciduous plants in quantities exceeding 500 Tg y^{-1}, comprising approximately a third of the total VOC emissions to the atmosphere (Guenther *et al.*, 2012), and is oxidized rapidly in the troposphere ($\tau \sim 1$ h), primarily by the addition of OH to one of its double bonds (Atkinson and Arey, 2003b). The subsequent chemistry by which isoprene-derived radicals and VOCs react in the atmosphere forms a highly complex mechanism, with numerous distinct branching pathways and hundreds of stable products (Jenkin *et al.*, 2015). In recent years, a combination of field observations, chamber experiments, quantum calculations, and modeling – including some of studies contained in this thesis – has substantially improved our knowledge of these complex oxidation mechanisms, providing valuable insight into the effects of isoprene on HO_x and NO_x cycling, ozone production, SOA formation, and other important aspects of air quality and atmospheric chemistry.

In regions with abundant isoprene emissions, including the the Amazon, the southeast United States, and other highly productive tropical and temperate forests, the chemistry of isoprene oxidation alone can effectively determine the oxidative capacity of the atmosphere and contribute the majority of local O_3 and SOA production. Such areas are typically located away from major anthropogenic pollution sources, leading to relatively low levels of NO; as such, reaction with HO_2 represents the predominant fate of most peroxy radicals formed in the oxidation mechanism (although rapid isomerization has recently been shown to compete in some cases, *e.g.* Crounse *et al.*, 2011, Peeters *et al.*, 2014, and Teng *et al.*, 2017). In the

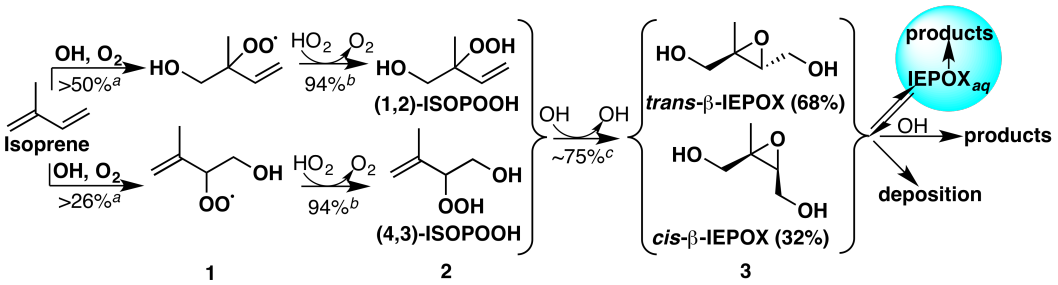

Figure 1.2: Dominant reaction channels in the oxidation of isoprene under HO_2-dominated conditions. Reported yields are from [a]Teng *et al.* (2017), [b]Liu *et al.* (2013), and [c]Appendix D. The reported isoprene peroxy radical yields are given at the kinetic limit of short RO_2 lifetimes, but under most ambient conditions, the dynamic equilibration between peroxy radicals will produce much higher yields of the β isomers shown. The isomers shown are therefore estimated to comprise >95% of the total ISOPOOH and IEPOX formed in the atmosphere (see Chapters 2 and 4).

HO_2-dominated isoprene oxidation mechanism (the major steps of which are shown in Figure 1.2), the initial isoprene hydroxy peroxy radicals (**1**) react with HO_2 to produce isoprene hydroxy hydroperoxides (ISOPOOH, **2**) in high yields (Liu *et al.*, 2013; Paulot *et al.*, 2009a). The predominant ISOPOOH isomers can then add another OH and rapidly react to form a dihydroxy epoxide (IEPOX, **3**), recycling one equivalent of OH in the process. This unique rearrangement was only recently discovered (Paulot *et al.*, 2009b) thanks to instrumental advances enabling the differentiation of isobaric ISOPOOH and IEPOX.

The subsequent fate of IEPOX in the atmosphere has been the subject of intense scrutiny, and is addressed in multiple chapters in this thesis. It is known to react with OH, deposit onto surfaces, or undergo reactive uptake onto particles, but the relative contributions of these pathways and their eventual consequences were, until recently, largely unknown. Because IEPOX is produced in ~70% overall yield (Liu *et al.* (2013) and Appendix D) from isoprene under HO_2-dominated conditions, and ~30% yield globally when non-HO_2 pathways are included (4, characterizing the fate of IEPOX is of vital importance for determining how the HO_2-dominated pathway affects oxidant cycling and contributes to the production of ozone and SOA. A better understanding of IEPOX will be an integral piece of the broader question: how does isoprene influence air quality and the oxidative chemistry of the troposphere, and what role does the HO_2-dominated pathway play in this effect?

1.2 Content

The work included in the chapters and appendices of this thesis represents my efforts to answer this question through a variety of research projects and methods. In the course of my work, I have employed three key tools of atmospheric chemical research: laboratory studies, generally in the form of environmental chamber experiments; fieldwork, or the measurement of ambient atmospheric chemical conditions; and modeling, using either idealized box models or global chemical transport models to simulate the chemistry in question. The interaction of these three methods in the field of atmospheric chemistry has enabled remarkable success in the identification, understanding, and mitigation of such important issues as urban air pollution and stratospheric ozone depletion (Abbatt *et al.*, 2014; Burkholder *et al.*, 2017; Melamed *et al.*, 2015). As each tool relies on the insights ascertained from the others to inform their own analysis and direction, it is through their application in tandem that meaningful conclusions are reached and the field advances. Some of the projects included in each chapter here focus on just one of these three pillars; most employ some elements of each. Detailed descriptions of experimental techniques can be found in each chapter, but a brief overview of the three key methods is presented here, followed by an outline of the rest of the thesis.

1.2.1 Laboratory Studies

Laboratory studies represent our primary means of characterizing the fundamental processes underlying the chemistry of the atmosphere. The most widely used laboratory method is the environmental chamber experiment, or the isolation of a volume of air inside a reaction vessel (*e.g.* a large Teflon bag); Chapters 2, 3, and 5 in this thesis all employ chamber studies, as do Appendices A-F. Chamber experiments are designed to pinpoint a specific chemical process in a regulated environment, without interference from the confounding factors present in ambient air. By controlling as many variables as possible, chamber studies allow researchers to identify and measure the process in question more accurately and precisely than they could in the field, and to systematically vary chamber conditions to the factors influencing that process.

In a typical experiment, reactants of interest are first introduced to the chamber and, following a brief stabilization and mixing period, exposed to the desired reactive chemical environment. These reactive conditions may include ultraviolet light for the study of photolysis; chemical oxidants, such as ozone or OH; or seed particles onto which a compound may condense. Air from the chamber is then drawn into

various instruments to measure relevant properties of the gas and particle phases. Specific instruments are described in greater detail in each chapter, but among the most commonly used instrumental methods in this thesis are gas chromatography (GC), chemical ionization mass spectrometry (CIMS), aerosol mass spectrometry (AMS), and scanning mobility particle sizing (SMPS). The GC and CIMS measure concentrations of gaseous species; our GC is primarily sensitive to hydrocarbons, while the CF_3O^- reagent ion in our time-of-flight and triple-quadrupole CIMS most efficiently ionizes compounds with strong dipoles or high polarizability (Crounse *et al.*, 2006; St. Clair *et al.*, 2010), making them complementary measurement techniques. The AMS (Jayne *et al.*, 2000) and SMPS (Wang and Flagan, 1990) detect the chemical composition and size distribution, respectively, of sub-micron particles suspended in the chamber.

Although chamber experiments have been a mainstay of atmospheric laboratory studies for many decades, recent advances have opened new avenues of study for this dependable method. Among those employed in this thesis are novel pathways for the synthesis of reactants previously unavailable for chamber experimentation, including IEPOX (Chapters 2 and 5) and other late-generation isoprene oxidation products (Chapter 3), and new instrumentation, including a coupled GC-CIMS capable of separating isobaric compounds that were previously indistinguishable (Chapters 2 and 3, and Appendices A, B, and D).

The ubiquity of chambers in atmospheric laboratories has spurred extensive characterization of their properties and the techniques employed in such experiments (see, *e.g.*, Schwantes, 2017 for the Caltech environmental chambers, and Cocker *et al.*, 2001, Carter *et al.*, 2005, and Wang *et al.*, 2011 for others). Still, chamber experiments have important limitations that can confound the interpretation of their data. Some such limitations, including the losses of particles to chamber walls (Crump and Seinfeld, 1981; McMurry and Rader, 1985), have been carefully parameterized (Hildebrandt *et al.*, 2009; Hildebrandt *et al.*, 2011; Loza *et al.*, 2014; Loza *et al.*, 2012; Weitkamp *et al.*, 2007), while others remain poorly understood, including the losses of gaseous species to surfaces in chambers and instruments (Bernhammer *et al.*, 2017; Matsunaga and Ziemann, 2010a; Rivera-Rios *et al.*, 2014; Zhang *et al.*, 2015). While chamber experiments remain our primary method for understanding the fundamental chemistry of the atmosphere, field measurements and modeling are necessary to ensure that the processes studied in the laboratory are well understood and atmospherically relevant.

1.2.2 Field Studies

Another longstanding cornerstone of atmospheric research is the *in situ* measurement of ambient gases, particles, and meteorological conditions. Fieldwork is vital for determining the relevance and significance of known chemical processes in the atmosphere, and for identifying new avenues of research. It is only by observing the actual atmosphere, and comparing those measurements to laboratory data and simulations, that we can establish how well we understand the chemistry that occurs in ambient conditions and what previously unexplored processes may be important. As an example relevant to the contents of this thesis, it was, in large part, observations of oxidant recycling and unexplained particulate organic matter (such as C_5 tetrols) in the Amazon and other isoprene-rich areas that spurred further research into the oxidative chemistry and potential SOA production of isoprene under low-NO conditions (Claeys *et al.*, 2004; Karl *et al.*, 2007; Kleindienst *et al.*, 2009; Kleindienst *et al.*, 2007; Kuhn *et al.*, 2007; Lelieveld *et al.*, 2008; Tan *et al.*, 2001).

Data from two primary types of field study – stationary and airborne measurements – are used in this thesis. Both employ a wide variety of instruments, including those described above in Section 1.2.1, assembled on some form of research platform. In stationary field campaigns, the research platform is usually a tower, on which instruments can sample air at one or more vertical levels of interest. This enables measurements of the variability at a single site caused by changing conditions through time – *e.g.* temperature, insolation, wind direction, humidity, etc. – but limits the breadth of the campaign to conditions experienced exclusively at that site. The stationary campaigns that feature in this thesis include Green Ocean Amazon (GOAmazon, Appendix G), which studied the interaction of remote Amazonian airmasses with the urban plume from the Brazilian city of Manaus between January 2014 and December 2015, and the Southern Oxidant and Aerosol Study (SOAS, Chapter 3 and Appendices A and E), which investigated similar biogenic-anthropogenic interactions from a smaller tower in Centreville, Alabama between June and July of 2013.

Airborne field campaigns, in which instruments are loaded into the body of an airplane and sample air through external ports in flight, enable the sampling of a wider variety of altitudes and conditions that can be accessed by plane, but at the expense of observing the temporal evolution of those conditions. This thesis uses data from airborne measurements collected as part of GOAmazon (Appendix G) and from a series of small campaigns investigating oceanic aerosol and cloud

composition in coastal California (Appendix H) during the summers of 2011 (Eastern Pacific Emitted Aerosol Cloud Experiment, E-PEACE; Russell *et al.*, 2013), 2013 (Nucleation in California Experiment, NiCE; Coggon *et al.*, 2014) and 2015 (Biological and Oceanic Atmospheric Study, BOAS).

1.2.3 Modeling

Finally, the advent of improved computing power has enabled researchers to carry out simulations that can quickly and effectively model the chemistry that occurs in laboratory studies and in the field. These modeling capabilities are a powerful tool for determining whether known chemical processes can accurately describe the results of chamber experiments or the observations of field campaigns, and if not, for potentially diagnosing the sources of those inaccuracies. The ease with which such complex simulations can be performed makes them attractive for a wide range of applications, but models have their own limitations; chiefly, they are only as good as the chemistry that goes into the them, and when they do not align with observations, it can be difficult (if not impossible) do determine what aspects of that chemistry are wrong. Additionally, when models encompass wider parameter spaces (*e.g.* increasing to a global scale, including meteorology and emissions, etc.), and when they employ simplified chemical mechanisms, their potential for error widens substantially (Knote *et al.*, 2015).

Two major varieties of simulations are employed in the work included in this thesis: box models and chemical transport models (CTMs), each with their own applications and limitations. Box modeling refers to the zero- or one-dimensional (time-dependent) simulation of chemical reactions of well-mixed constituents, and is particularly useful for comparison with chamber experiments to determine whether the measured or estimated rates and products of a given process align with observations. The complexity and scope of box models spans a wide range, from simple custom-made simulations for individual experiments to more sophisticated and widely available models, such as the Master Chemical Mechanism (MCM; Jenkin *et al.*, 2015), the Generator of Explicit Chemistry and Kinetics of Organics in the Atmosphere (GECKO-A; Aumont *et al.*, 2005), the Framework for 0-D Atmospheric Modeling (F0AM; Wolfe *et al.*, 2016), and the Gas-Aerosol Model for Mechanism Analysis (GAMMA; McNeill *et al.*, 2012 and Woo and McNeill, 2015), some of which contain thousands of chemical reactions. In this thesis, Chapter 4 discusses the compilation of an explicit isoprene oxidation box model, while Appendices D, E, and G make extensive use of subsets of the isoprene model to compare

against observations.

Chemical transport modeling takes a usually simplified version of the same chemical mechanism and expands the domain to four dimensions, taking into account the spatial distribution of the relevant chemicals by integrating meteorology and simulating their evolution through time and space, frequently on a regional or global scale. In so doing, CTMs give insight into how the chemistry measured in chambers and in field studies plays out in the broader context of the atmosphere at large, thus providing some idea of the overall importance of that chemistry. In this thesis, Chapter 3 and Appendices B, D, and G make use of this capacity with GEOS-Chem (Bey *et al.*, 2001; Mao *et al.*, 2013), a widely used CTM, while Chapter 4 discusses the development of a new isoprene mechanism for GEOS-Chem.

1.2.4 Outline

The following chapters and appendices of this thesis describe the individual research projects to which I have contributed toward the goal of identifying the chemical mechanisms by which isoprene can influence ambient oxidant cycling, particle formation, and the concentrations of various VOCs, especially *via* the IEPOX formation pathway that occurs under HO_2-dominated conditions. While the chapters relate in this overarching goal, they are written to stand alone as published manuscripts (or, in the case of Chapter 4, a manuscript in preparation). The projects most directly related to the HO_2-dominated oxidation of isoprene, and to which I most substantially contributed, are included as chapters, while the appendices, arranged chronologically, represent more tangentially related projects on which I served as a coauthor.

Chapters 2 and 3 describe experiments designed to investigate the fate of IEPOX in the gas phase. As described above, IEPOX is produced in high yields from the reaction of OH with ISOPOOH (described in Appendix D), which is itself a first-generation oxidation product of isoprene under HO_2-dominated conditions. IEPOX can either be oxidized (primarily by OH) in the gas phase, deposit onto surfaces, or undergo reactive uptake onto particles and contribute to SOA mass. Because of the ubiquity of IEPOX in remote forested areas, the branching between these pathways is of primary importance to local formation of SOA and small OVOCs. The experiments in Chapter 2 were designed to determine the relative importance of the gas phase oxidation pathway. Using synthetic standards of three IEPOX isomers, chamber experiments were performed to measure the isomers' rates of reaction with

OH, oxidation products, and relative abundances from isoprene oxidation. The use of GC-CIMS to separately quantify IEPOX isomers proved crucial in determining that two isomers – *cis*- and *trans*-β – comprise nearly all IEPOX formed in the atmosphere, and that they are consistently formed in a 1:2 ratio from isoprene oxidation.

Chapter 3 continues this same line of enquiry by following the oxidative chemistry of isoprene one generation further. Three putative products of the reactions of *cis*- and *trans*-β-IEPOX with OH, proposed in Chapter 2, were synthesized and oxidized in a series of chamber experiments. 3,4-dihydroxy-2-butanone (DHBO) was identified as the major product from both IEPOX isomers, and the rates and products of its own reaction with OH were measured. The results from these experiments were then compared against field measurements and used to assemble a multigenerational mechanism of IEPOX oxidation. Global simulations with this mechanism using GEOS-Chem showed that 54 Tg of DHBO and other C_4 dihydroxycarbonyl compounds are produced annually from IEPOX – roughly a 10% overall mass yield from isoprene.

Chapter 4 focuses further on the compilation of isoprene oxidation mechanisms for modeling purposes. The IEPOX mechanism in Chapter 3 is combined with those of other isoprene oxidation pathways from numerous additional studies (including those described in Appendices B-E regarding methyl vinyl ketone, methacryloyl peroxynitrate, ISOPOOH, and isoprene ozonolysis) to create a new state-of-the-science explicit isoprene oxidation mechanism. With particular emphasis on the initial peroxy radical dynamics, oxidant budgets, and compounds known or suspected to contribute to organic aerosol formation, the explicit mechanism is presented primarily for use in box modeling, although an accompanying reduced mechanism condenses the model down to a size more manageable for chemical transport models while retaining its most salient features. Future work will then incorporate this reduced mechanism into GEOS-Chem and, in a series of global simulations, examine its effects on oxidant budgets, aerosol precursors, and small OVOCs of interest. Preliminary results show that the updated mechanism enhances NO_x transport and reduces ozone formation compared to previous parameterizations, and substantially improves the model's ability to accurately capture the relative importance of each isoprene peroxy radical isomer and its subsequent chemistry.

Chapter 5 addresses another atmospheric fate of IEPOX: reactive uptake onto particles and formation of SOA. Using the same synthetic IEPOX isomers from

Chapter 2, additional chamber experiments were performed to examine the uptake of IEPOX onto seed aerosol composed of various inorganic salts with a range of particle liquid water contents. IEPOX was found to undergo kinetically limited partitioning onto hydrated ammonium sulfate and, to a lesser extent, ammonium chloride seeds, but not onto dry seeds or those with other cations, suggesting a role for ammonium in the reactive uptake of IEPOX into aqueous aerosol. The Henry's Law constants of *cis*- and *trans*-β-IEPOX were also measured, and the organic aerosol growth from the two isomers was not found to differ significantly.

Finally, Chapter 6 concludes with a brief summary of the atmospheric fate of IEPOX, the significance of the HO_2-dominated isoprene oxidation pathway, and directions for further research.

Chapter 2

GAS PHASE PRODUCTION AND LOSS OF ISOPRENE EPOXYDIOLS

Bates, K. H., J. D. Crounse, J. M. St Clair, N. B. Bennett, T. B. Nguyen, J. H. Seinfeld, B. M. Stoltz, and P. O. Wennberg (2014). "Gas phase production and loss of isoprene epoxydiols". In: *J. Phys. Chem. A* 118.7, pp. 1237–46. DOI: 10.1021/jp4107958.

Abstract

isoprene epoxydiols (IEPOX) form in high yields from the OH-initiated oxidation of isoprene under low-NO conditions. These compounds contribute significantly to secondary organic aerosol formation. Their gas-phase chemistry has, however, remained largely unexplored. In this study, we characterize the formation of IEPOX isomers from the oxidation of isoprene by OH. We find that *cis*- and *trans*-β-IEPOX are the dominant isomers produced, accounting respectively for 31 ± 5% and 66 ± 4 % of the IEPOX yield from low-NO oxidation of isoprene. Three isomers of IEPOX, including *cis*- and *trans*-β, were synthesized and oxidized by OH in environmental chambers under high- and low-NO conditions. We find that IEPOX reacts with OH at 299 K with rate coefficients of $(0.84 \pm 0.07) \times 10^{-11}$, $(1.52 \pm 0.07) \times 10^{-11}$, and $(0.98 \pm 0.05) \times 10^{-11}$ cm^3 molecule^{-1} s^{-1} for the δ1, *cis*-β, and *trans*-β isomers. Finally, yields of the first-generation products of IEPOX + OH oxidation were measured, and a new mechanism of IEPOX oxidation is proposed here to account for the observed products. The substantial yield of glyoxal and methylglyoxal from IEPOX oxidation may help explain elevated levels of those compounds observed in low-NO environments with high isoprene emissions.

2.1 Introduction

isoprene, a volatile organic compound (VOC) produced by deciduous plants, comprises the single most abundant atmospheric non-methane hydrocarbon by emission to the atmosphere, with estimates near 500 Tg C y^{-1} (Guenther *et al.*, 2006). The rapid oxidation of isoprene by OH radicals ($k = 1.0 \times 10^{-10}$ cm^3 molecule^{-1} s^{-1}) (Atkinson *et al.*, 2006) makes it an important driver in tropospheric chemistry, particularly in forested regions. When NO concentrations are sufficiently low, as is the

case in many areas with high isoprene emissions, isoprene oxidation can proceed by a HO_x-mediated (OH + HO_2) mechanism, which until recently was largely unexplored (Kuhlmann and Lawrence, 2004; Rosenstiel *et al.*, 2003; Wiedinmyer *et al.*, 2006). OH addition to isoprene, followed by O_2 addition and the peroxy radical + HO_2 reaction, leads to formation of isoprene hydroxyhydroperoxide (ISOPOOH) in yields exceeding 70% (Crutzen *et al.*, 2000; Lelieveld *et al.*, 2008; Ren *et al.*, 2008), with approximately 2.5% forming methacrolein (MACR) and 3.8% forming methylvinylketone (MVK) (Liu *et al.*, 2013; Navarro *et al.*, 2011).

Paulot *et al.* (2009b) showed that the reaction of ISOPOOH with OH forms isoprene epoxydiols (IEPOX) in yields exceeding 75% (Figure 2.1). The oxidation mechanism regenerates one equivalent of OH, partially accounting for the stability of HO_x levels observed in remote forested regions (Lelieveld *et al.*, 2008; Paulot *et al.*, 2009b; Ren *et al.*, 2008; Thornton *et al.*, 2002). IEPOX formation contributes to secondary organic aerosol (SOA) formation from low-NO_x isoprene oxidation, as its low volatility and high water solubility allow it to partition into the condensed phase (Lin *et al.*, 2012; Nguyen *et al.*, 2014a; Surratt *et al.*, 2010; Surratt *et al.*, 2006). Uptake of IEPOX onto acidic aerosol has been shown to contribute significantly to SOA in forested areas where anthropogenic pollutants (*e.g.* SO_2) are present (Zhang *et al.*, 2013). Estimates of global isoprene oxidation show that 95 ± 45 Tg C of IEPOX per year is formed globally, with the implication that the products of its subsequent reactions play a crucial role in tropospheric chemistry (Paulot *et al.*, 2009b).

Here, we report the relative yield of IEPOX isomers from isoprene oxidation, as well as the rate coefficients and products of their oxidation by OH. Using existing procedures with one significant novel enhancement, three isomers of IEPOX were synthesized. We then performed a series of individual experiments in which IEPOX isomers were oxidized by OH in an environmental chamber. Reaction rate coefficients of the IEPOX isomers were measured relative to propene. The lifetimes of δ1, *cis*-β, and *trans*-β-IEPOX against oxidation by OH (at 299 K and $[OH] = 1.0 \times 10^6$ molecule cm^{-3}, a typical atmospheric value) were found to be 33, 18, and 28 h, respectively. By comparing the isomers' retention times in a gas chromatograph (GC) connected to a chemical ionization mass spectrometer (CIMS) with that of IEPOX formed in situ by low-NO oxidation of isoprene, we show that *cis*- and *trans*-β-IEPOX account for the majority of IEPOX produced in the atmosphere, while the yield of δ1-IEPOX is small (<3%). These isomer ratios are consistent

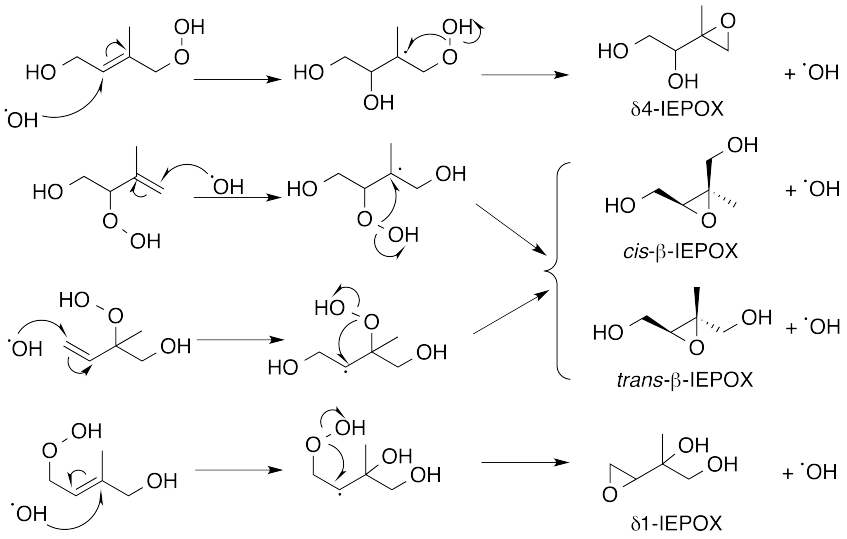

Figure 2.1: Mechanism for the formation of IEPOX from OH-initiated oxidation of ISOPOOH.

with the relative concentrations of their hydrolysis products (2-methylerythritol and 2-methylthreitol) observed in ambient aerosol (Claeys *et al.*, 2004; Ding *et al.*, 2008; Kourtchev *et al.*, 2005; Schkolnik *et al.*, 2005; Xia and Hopke, 2006; Zhang *et al.*, 2013). Additionally, experiments in the absence of propene were performed to determine the products of IEPOX oxidation by OH. Previous studies have inferred the products by a combination of theoretical models, observations of low-NO isoprene oxidation, and targeted chamber studies on IEPOX analogs (Paulot *et al.*, 2009a; Xie *et al.*, 2013). A more recent study measured the products of δ4 and *trans-*β-IEPOX oxidation by OH (Jacobs *et al.*, 2013). We observed a number of compound masses consistent with products predicted or detected in previous studies, for which we propose oxidative mechanisms. Differences in product yields between high- and low-NO conditions and between IEPOX isomers are described.

2.2 Experimental Methods

2.2.1 Synthesis

The IEPOX isomers used in these experiments were synthesized according to the procedures described by Zhang *et al.* (2012), with one significant change described below. All chemicals were purchased from Sigma Aldrich. The δ1- and *cis-*β-IEPOX used in photochemical oxidation experiments was 99% pure, as determined by NMR; the *trans-*β-IEPOX was >92% pure, and the impurity was not found to interfere with any part of the experiments.

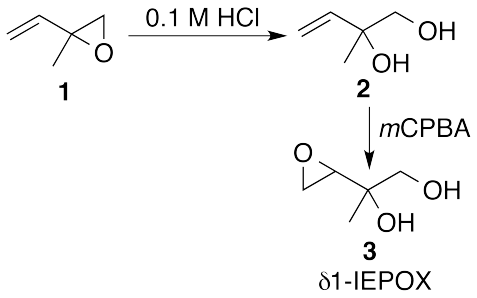

Figure 2.2: Reactions in the synthesis of δ1-IEPOX.

Briefly, δ1-IEPOX (2-(oxiran-2-yl)-propane-1,2-diol) was prepared from 2-methyl-2-vinyloxirane (**1**) as shown in Figure 2.2. The epoxide in compound 2 (0.98 g, 11.67 mmol) was first converted to the diol (**2**) by treatment with 0.1 M hydrochloric acid (10 mL), and the product was isolated by lyophilysis. The diol was then treated with *meta*-chloroperoxybenzoic acid (*m*CPBA, 4.25 g, 70%, 17.3 mmol) to afford δ1-IEPOX (**3**, 0.23 g, 1.9 mmol, 17% yield). The ^{1}H NMR spectrum (Figure 2.11 in the Supporting Information) matched previously published spectra (Zhang *et al.*, 2012).

Cis-β-IEPOX (*cis*-2-methyl-2,3-epoxy-1,4-butanediol) was prepared from 3-methylfuran-2(5H)-one, which in turn was prepared from citraconic anhydride (**4**) using procedures described by Nefkens *et al.* (1997) (Figure 2.3). Briefly, compound **4** (10 mL, 111.26 mmol) was treated with dicyclohexylamine (DCA, 25 mL, 122.4 mmol) in methanol to produce the DCA salt **5** (20.4 g, 62.7 mmol, 56% yield). Compound **5** was then treated with isobutyl chloroformate ($ClCO_2iBu$, 9 mL, 68.9 mmol) followed without purification by sodium borohydride ($NaBH_4$, 5 g, 132 mmol), to afford 3-methylfuran-2(5H)-one (**6**, 3.93 g, 40 mmol, 64% yield), which was purified by fractional distillation.

Conversion of compound **6** to 2-methyl-2-butene-1,4-diol (**7**) was adapted from procedures developed by Hoang *et al.* (2002), and was the only major change from the procedures of Zhang *et al.* (2012). The use of diisobutylaluminum hydride (DIBAL-H) instead of lithium aluminum hydride improved yields from 27% to 83%.

A flame-dried 100 mL round-bottom flask equipped with a stir bar was charged with compound **6** (1.63 g, 16.6 mmol, 1.00 equiv) and toluene (14 mL, 1.2 M) and lowered into a 0 °C bath (ice/water). DIBAL-H (neat, 4 mL, 22.4 mmol, 1.35 equiv) was added dropwise over several minutes. Once the addition was complete, the

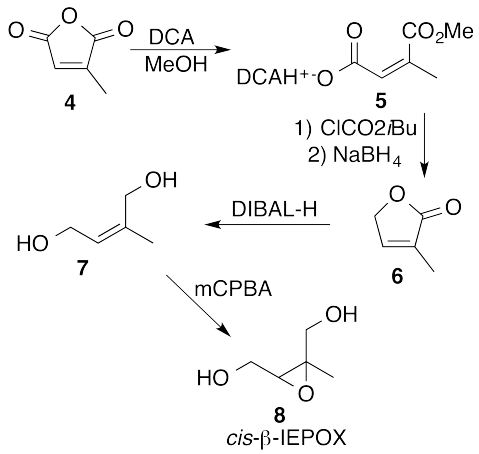

Figure 2.3: Reactions in the synthesis of *cis-β*-IEPOX.

bath was removed and the reaction was allowed to warm to room temperature. An additional portion of DIBAL-H (2.2 mL, 12.3 mmol, 0.74 equiv) was added after 1.5 h. TLC analysis at 3 h indicated no remaining starting material. Consequently, the reaction was lowered into a 0 °C bath and quenched with the dropwise addition of methanol (9 mL). The resulting mixture was diluted with toluene (14 mL) and water (3 mL), generating a large amount of solid that was broken up with a spatula. After 1.5 h of stirring, the reaction mixture developed into a biphasic suspension with no significant solids. $MgSO_4$ was added to the flask, and the reaction contents were filtered through a Celite/$MgSO_4$ column eluting with MeOH. The resulting organics were concentrated under reduced pressure, generating a white viscous oil. This oil was diluted with ethyl acetate (EtOAc) and again dried over $MgSO_4$, filtered, and concentrated under reduced pressure. The resulting crude oil was purified by flash column chromatography (SiO_2, 28 × 2 cm, 20% EtOAc in hexanes → 100% EtOAc) to afford compound **7** (1.40 g, 13.7 mmol, 83% yield) as a pale yellow oil. Compound **7** (0.33 g, 3.35 mmol) was treated with mCPBA (2.19 g, 77%, 9.8 mmol) according to the procedures of Zhang *et al.* (2012) to give *cis-β*-IEPOX (**8**, 0.16 g, 1.4 mmol, 42% yield). The ^{1}H NMR spectrum (Figure 2.12 in the Supporting Information) matched previously published spectra (Zhang *et al.*, 2012).

Trans-β-IEPOX (trans-2-methyl-2,3-epoxybutane-1,4-diol) was also prepared using procedures published by Zhang *et al.* (2012) (Figure 2.4). Briefly, 3-methyl-2-buten-1-ol (**9**, 4.7 g, 54.3 mmol) was treated with *tert*-butyldimethylchlorosilane (TBDMSCl, 9.9 g, 65.7 mmol) and diisopropylethylamine (Pr_2NEt, 10.5 mL, 60.3 mmol) to give compound **10** (7.92 g, 39.6 mmol, 73% yield). A hydroxyl group

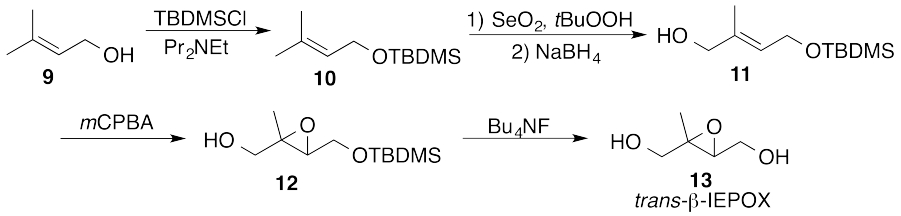

Figure 2.4: Reactions in the synthesis of *trans*-β-IEPOX.

was added to compound **10** in the *trans* position by treatment with selenium dioxide (SeO_2, 2.38 g, 21.5 mmol) and *tert*-butylhydroperoxide (*t*-BuOOH, 5.5 M in decanes, 8 mL, 44 mmol) followed without purification by reduction with sodium borohydride ($NaBH_4$, 1.36 g, 36 mmol) to give compound **11** (3.36 g, 15.5 mmol, 39% yield). Epoxidation with *m*CPBA (6.04 g, 77%, 27 mmol) yielded compound **12** (1.51 g, 6.5 mmol, 42% yield), and deprotection with tetrabutylammonium fluoride (Bu_4NF, 1 M in THF, 13.5 mmol) gave *trans*-β-IEPOX (**13**, 703 mg, 5.96 mmol, 92% yield). The ^{1}H NMR spectrum (Figure 2.13 in the Supporting Information) matched previously published spectra (Zhang *et al.*, 2012).

2.2.2 Gas Phase Experiments

Instruments and experimental procedures for gas-phase OH oxidation have been described in detail elsewhere (Paulot *et al.*, 2009b). Briefly, experiments were performed in a 0.85 m^3 fluorinated ethylene propylene copolymer (Teflon-FEP, Dupont) chamber at 299 K (± 2 K). Hydrogen peroxide (H_2O_2), at an initial mixing ratio of 2.5 ppm (± 10%), provided the source of HO_x for oxidation upon photolysis under UV lights. Each IEPOX isomer was oxidized in both high- and low-NO conditions (those in which the isoprene peroxy radicals react preferentially with NO or HO_2, respectively) with 570 ppb NO added for high-NO oxidation. Propene (125 ppb) provided the internal standard for OH concentration in experiments to determine the oxidation rate coefficient; in product studies, no propene was added.

The chamber was flushed with dry air and evacuated at least four times between successive experiments. In each experiment, IEPOX (30 ppb ± 50%, as measured by CIMS) was added to the chamber by spreading a single drop of the compound on the interior surface of a small glass cylinder and passing dry air through the cylinder into the chamber at 20 std L min^{-1}. Addition of δ1-IEPOX took 5 min per experiment; addition of *cis*- and *trans*-β-IEPOX took 30 min, and for *cis*-β-IEPOX the glass cylinder was heated to 60 °C in a water bath during addition to increase

volatility. H_2O_2 (~8.0 mg, 30% m/m in water) was added by the same method, for 10 min without heating. Propene gas was added by evacuating a 500 cm^3 glass bulb and filling it to ~11 Torr with propene, after which the bulb was back-flushed with N_2 to atmospheric pressure and pumped down to 11 Torr again. The contents were then flushed into the chamber by passing dry air through the bulb at 20 std L min^{-1} for 1 min. NO was added similarly, by filling the evacuated bulb to ~370 Torr with 1994 ± 20 ppm NO in N_2, and flushing the contents into the chamber for 1 min at 20 std L min^{-1}.

The chamber's contents were monitored throughout the experiment through a single sample line connected to five instruments: a time-of-flight chemical ionization mass spectrometer (ToF-CIMS, Tofwerk/Caltech); a triple quadrupole MS-MS CIMS (Varian/Caltech); a gas chromatograph with a flame-ionization detector (GC-FID Agilent 5890 II) to measure propene concentrations; a NO_x Monitor (Teledyne 200EU); and an O_3 monitor (Teledyne 400E). Both CIMS systems, which use CF_3O^- as the chemical ionization reagent gas, have been described in detail elsewhere (Crounse *et al.*, 2006; Paulot *et al.*, 2009b; St. Clair *et al.*, 2010).

Throughout the experiments, the ToF-CIMS monitored all *m/z* between 50 and 340 in negative-ion mode, while the MS-MS CIMS switched between scanning MS mode and tandem MS mode, to detect the fragmentation of IEPOX and its products and to resolve products of isobaric masses. All *m/z* signals are normalized to the reagent anion signal. IEPOX is monitored at *m/z* 203 (IEPOX+CF_3O^-) on both CIMS instruments and by *m/z* 203 → *m/z* 183 (IEPOX+CF_3O^-−HF) on the MS-MS CIMS in tandem MS mode. Photooxidation lasted approximately 3-7 h in each experiment. Nine gas-phase photooxidation experiments were performed, along with two experiments without oxidation to monitor loss of IEPOX to surfaces; details of the experiments are shown in Table 2.1.

Before and after photooxidation, monitoring by the five instruments described above was interrupted to separate compounds by gas chromatography before sampling by ToF-CIMS (GC-CIMS). One to three GC-CIMS runs were performed before and after each experiment. In each run, approximately 200 cm^3 of gas sample was cryo-collected on the head of an RPK 1701 column submerged in isopropanol chilled with liquid nitrogen (249 ± 3 K). The isopropanol bath was removed and the column was allowed to warm for 60 s before the GC temperature program was started (30 °C for 0.1 min, +3 °C/min to 60 °C, +10 °C/min to 130 °C, hold 3 min). Compounds eluted from the GC were ionized by CF_3O^- and monitored between *m/z* 50 and 340

expt #	IEPOX isomer	$[NO]_0$ (ppbv)	$[propene]_0$ (ppbv)	duration of photooxidation	experimental objective
1	*cis*-β	571	125	4:54:10	OH rate
2	*cis*-β	0	124	6:08:40	OH rate
3	*cis*-β	0	0	-	wall loss
4	δ1	0	126	5:58:30	OH rate
5	δ1	563	123	3:13:00	OH rate
6	*cis*-β	0	0	-	wall loss
7	*cis*-β	0	0	6:59:30	products
8	*cis*-β	570	0	7:01:30	products
9	*trans*-β	0	124	4:00:00	OH rate
10	*trans*-β	568	124	4:00:00	OH rate
11	*trans*-β	567	0	4:30:00	products

Table 2.1: Gas phase IEPOX experiments.

at a time resolution of 10 s^{-1}. Transmission through the GC varied between 60% and 70% for both IEPOX isomers, and was not statistically significantly different between the isomers. Further details regarding the GC-CIMS methodology will be provided in a forthcoming manuscript.

2.2.3 Determination of CIMS Sensitivity to IEPOX

The CIMS sensitivity to IEPOX was determined in four experiments, two each for *cis*- and *trans*-β-IEPOX, performed in the larger (24 m^3) Caltech environmental chamber. In each experiment, dilute (1-3 mM) aqueous solutions containing one IEPOX isomer and hydroxyacetone (as an internal standard) were atomized into the Teflon-FEP chamber for 2-8 h through a 15 cm perfluoroalkoxy Teflon transfer line. Temperature was ramped from 35 °C to 45 °C over the course of atomization to ensure minimal condensational losses. The measured weight of solution atomized allowed quantification of the moles in the chamber. During atomization, the mixing ratio of gas-phase IEPOX was monitored by negative-ion CIMS with a Varian triple quadrupole mass analyzer, described in greater detail elsewhere (St. Clair *et al.*, 2010). The instrument operated at 26.6 Torr and switched between scanning MS mode (*m/z* 50-250) and tandem MS mode, with unit mass resolution and 2-5 min time resolution. Dividing the CIMS normalized counts at *m/z* 203 (scanning MS mode) by the moles of IEPOX in the gas phase provided an estimate of the CIMS sensitivity. The dependence of IEPOX sensitivity on humidity was measured by adding various mixing ratios of water vapor to the CIMS during IEPOX detection.

No humidity dependence was detected. We find that the *cis*-β-IEPOX sensitivity is 1.8 times that of *trans*-β-IEPOX, consistent with the previously calculated ion-molecule collision rate ratio of 1.61 to 1 based on polarizability and dipole moments (Paulot *et al.*, 2009b).

2.2.4 Wall loss Experiments

Experiments were performed in both the 0.85 m^3 and 24 m^3 chambers to determine the extent to which the decay of IEPOX concentration with time could be attributed to loss to chamber walls. In both chambers, wall loss of IEPOX (~0.4% h^{-1}) was negligible compared to either loss by photooxidation or signal fluctuations due to temperature, except when nitric acid was injected to acidify the walls in the small chamber. The dramatic loss under acidic conditions is expected based on the sensitivity of the epoxide group in IEPOX to acid. Wall losses were accounted for in subsequent calculations of IEPOX photooxidation rates and products.

2.3 Results and Discussion

2.3.1 IEPOX + OH Rate Coefficients

Rate coefficients for the reaction of each IEPOX isomer with OH were calculated relative to that of propene with OH, for which the rate coefficient is well characterized; the value used in these calculations was 2.62×10^{-12} cm^3 $molecule^{-1}$ s^{-1} at 299 K (Atkinson and Arey, 2003a). A linear regression analysis of the natural log of the IEPOX concentration (normalized to the initial concentration) versus time over the course of photooxidation (Figure 2.5) gives a slope equal to the rate coefficient, k, multiplied by the concentration of OH. A similar regression can be performed for propene. The ratio of the two slopes is thus equal to the ratio of rate coefficients for oxidation of IEPOX and propene by OH, which allows for the calculation of the OH oxidation rate coefficient of IEPOX.

IEPOX + OH rate coefficients were calculated for each experiment with propene (Exp. 1, 2, 4, 5, 9, and 10), which included a high- and low-NO run for each of the three isomers. Propene concentrations were measured by GC-FID, and IEPOX concentrations by ToF-CIMS. Rate coefficients were then calculated using a linear regression method incorporating error in both dimensions, followed by an error-weighted mean (York *et al.*, 2004) of each isomer's runs. Rate coefficients determined in high- and low-NO experiments differed by no more than 19%, and the run-to-run differences did not correlate with NO level. Primary sources of error include fluctuations in temperature, which affect both oxidation rate coefficients and

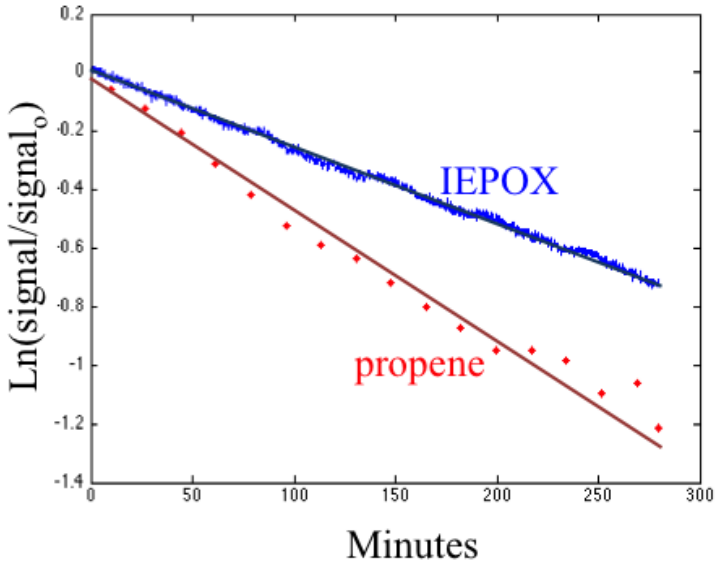

Figure 2.5: Decay of *cis*-β-IEPOX and propene in Expt. 1. The ratio of the slopes of propene and IEPOX concentrations over time (both on logarithmic scales) is equal to the ratio of the rate constants of each species' reaction with OH. Propene data are from GC-FID, while IEPOX data are from ToF-CIMS measured at *m/z* 203.

CIMS sensitivity to IEPOX, and the relative precision and frequency of GC-FID propene measurements.

Calculated OH oxidation rate coefficients and lifetimes for the three IEPOX isomers at ambient temperature are given in Table 2.2. *Cis*-β-IEPOX was found to react significantly faster than δ1 or *trans*-β-IEPOX with OH. The rate coefficients range from $(0.84 \pm 0.07) \times 10^{-11}$ cm^3 molecule^{-1} s^{-1} to $(1.52 \pm 0.07) \times 10^{-11}$ cm^3 molecule^{-1} s^{-1}, consistent with the value previously estimated as an upper limit by Paulot *et al.* (2009b) of 1.5×10^{-11} cm^3 molecule^{-1} s^{-1}. The only other study to have measured the OH oxidation rate coefficients of specific IEPOX isomers, by Jacobs *et al.* (2013), reported the rate coefficient of δ4-IEPOX + OH to be $(3.52 \pm 0.72) \times 10^{-11}$ cm^3 molecule^{-1} s^{-1} and that of *trans*-β-IEPOX + OH to be $(3.60 \pm 0.76) \times 10^{-11}$ cm^3 molecule^{-1} s^{-1}. These values are significantly higher than those reported here, and are inconsistent with the dynamics of the isoprene system studied by Paulot *et al.* (2009b) Clearly, further studies will be needed to resolve these differences.

isomer	rate (k)	$k_{low[NO]}$	$k_{high[NO]}$	lifetime (h)
δ1	0.84 ± 0.07	0.97	0.82	33.0 ± 2.8
cis-β	1.52 ± 0.07	1.40	1.62	18.3 ± 0.8
trans-β	0.98 ± 0.05	0.88	1.05	28.3 ± 1.4

Table 2.2: Rate coefficients for the reaction with OH of δ1, *cis*-β and *trans*-β-IEPOX. k is in units of cm^3 $molecule^{-1}$ s^{-1} $\times$ 10^{-11}, and lifetimes are for [OH] = 10^6 molecules cm^{-3}.

2.3.2 Relative Yields of IEPOX Isomers

Comparison of GC retention times of each IEPOX isomer to those of low-NO isoprene oxidation products reveals that *cis*- and *trans*-β-IEPOX are produced in much higher yield than δ1-IEPOX in the gas phase oxidation of isoprene by OH. These results are shown in Figure 2.6, in which *m/z* 203 (CF_3O^- plus IEPOX or ISOPOOH) normalized counts are plotted versus retention time for the three IEPOX isomers and for two time points in the low-NO oxidation of isoprene by OH, conducted under the same conditions as the low-NO IEPOX experiments detailed above. After 1 h, isoprene oxidation forms primarily two isomers of ISOPOOH, which appear on the GC-CIMS *m/z* 203 trace as two peaks centered at 12.5 and 13.3 min. After 10 h, some ISOPOOH remains, but two IEPOX peaks dominate, centered at 13.9 and 14.4 min. These correspond to *trans*- and *cis*-β-IEPOX, respectively. δ1-IEPOX also appears on the oxidized isoprene trace, but with a far smaller signal. The ratio of peak areas corresponding to δ1, *cis*-β, and *trans*-β-IEPOX is, respectively, 1 to 20.5 to 27.9.

While the CIMS sensitivity of δ1-IEPOX was not directly measured, previous calculations of molecular dipoles have determined that the sensitivity to δ1-IEPOX should be nearly equivalent to that of *cis*-β-IEPOX, and any deviation from this prediction is not expected to outweigh the large difference in peak areas between δ1-IEPOX and the other isomers. Thus, δ1-IEPOX is far less atmospherically relevant than the β-IEPOX isomers. δ4-IEPOX forms by a mechanism similar to that of the δ1 isomer, and likely has a similar retention time in the GC due to its analogous structure. No additional peaks were observed near the retention time of δ1-IEPOX that could have been assigned to δ4-IEPOX in the 10 h GC trace. Therefore, the δ4 isomer is expected either not to be formed or to co-elute with δ1-IEPOX, in which case the integrated peak area assigned to δ1-IEPOX accounts for the sum of the δ1 and δ4 isomers.

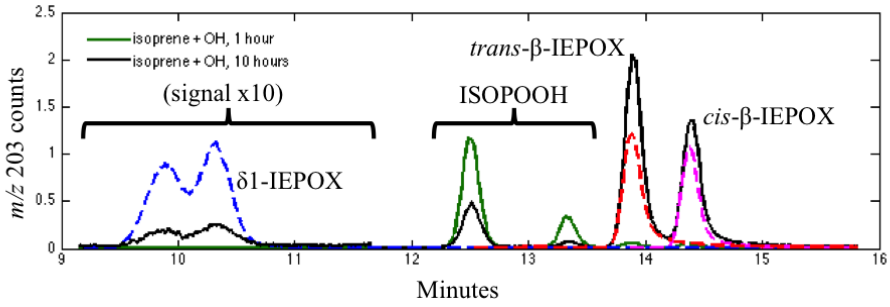

Figure 2.6: CIMS signals at *m/z* 203 from GC-CIMS chromatograms of δ1-IEPOX (blue), *cis*-β-IEPOX (pink), and *trans*-β-IEPOX (red) synthesized standards, as well as the *m/z* 203 products from OH-initiated low-NO_x oxidation of isoprene. The two major peaks seen after one hour of isoprene + OH oxidation (green) represent ISOPOOH, while the two major peaks seen after ten hours of oxidation (black) correspond with *cis*- and *trans*-β-IEPOX. The ten-hour signal is multiplied by a factor of ten between minutes 9.2 and 11.7, to show that a minor amount of δ1-IEPOX is formed. δ1-IEPOX appears as a double peak because the compound has two diastereomers.

Results from the sensitivity calibrations discussed above show that the single MS CIMS signal at *m/z* 203 is 1.83 times more sensitive to *cis*-β-IEPOX than *trans*-β-IEPOX. Scaling the signal areas by the sensitivity, we find that OH-initiated low-NO oxidation of isoprene produces concentrations of *cis*- and *trans*-β-IEPOX after 10 hours of oxidation in a ratio of 1 to 2.5 ($\pm$ 0.5). Part of this difference in concentrations can be explained by the faster reaction with OH of *cis*-β-IEPOX relative to *trans*-β-IEPOX. Using a simple kinetic model of isoprene, ISOPOOH, and IEPOX mixing ratios based on the signals observed in the low-NO oxidation of isoprene and the reaction rates calculated in the present study, we find the ratio of the yields of *cis*-β-IEPOX to *trans*-β-IEPOX produced from the reaction of isoprene with OH to be 1 to 2.13 ($\pm$ 0.30), and that *cis*-β and *trans*-β-IEPOX together account for >97% of observed IEPOX. The ratio of the *cis*- and *trans*- yields is similar to the ratio of 2-methyltetrol isomers found in SOA created by oxidation of isoprene by OH. Assuming that particle-phase hydrolysis of IEPOX proceeds by a typical acid-catalyzed mechanism as the evidence suggests (Eddingsaas *et al.*, 2010), in which protonation of the epoxide is followed by S_N2 attack by water, *cis*-β-IEPOX is expected to form 2-methylthreitol, while *trans*-β-IEPOX would form 2-methylerythritol. These 2-methyltetrol isomers have repeatedly been observed in isoprene-generated SOA in ratios of approximately 1 to 2, comparable to the ratio between *cis*- and *trans*-β-IEPOX we observe (Claeys *et al.*, 2004; Ding *et al.*, 2008;

Kourtchev *et al.*, 2005; Schkolnik *et al.*, 2005; Xia and Hopke, 2006; Zhang *et al.*, 2013).

2.3.3 Gas Phase Products of the Reaction of IEPOX with OH

Experiments performed in the 0.85 m^3 chamber in the absence of propene (Exp. 7, 8 and 11) were used to determine the products of gas-phase OH oxidation of *cis*- and *trans*-β-IEPOX. No product studies were performed on δ1-IEPOX due to its low atmospheric relevance. Mixing ratios of oxidation products were determined by multiplying the CIMS signal, normalized to the concentration of reagent ion in the chemical ionization region, by a calibration factor. For small, commercially available compounds, mixing ratio calibration factors were determined in previous experiments (Paulot *et al.*, 2009a). For larger products without authentic standards, instrumental sensitivities were assumed to be equal to those of their parent IEPOX isomer, as estimated in previous work based on polarizability and dipole moments (Paulot *et al.*, 2009a,b). Yields were then calculated by determining the slope of a simple linear regression between the mixing ratios of IEPOX and each product over the first 10-20 minutes of oxidation.

Time traces of oxidation products are shown in Figures 2.7 and 2.8, and first-generation product yields are given in Table 2.3. Reported uncertainties of yields account only for the standard deviations of the regressions, and do not include possible errors in calibration factors (estimated to be ± 30% for hydroxyacetone and glycolaldehyde and ± 20% for formic and acetic acid). Because these calibration factors have significant uncertainty and the CIMS sensitivity to IEPOX was not directly measured on the instruments used for these experiments, absolute yields cannot be accurately quantified, but yields can be compared between experiments. Additionally, because the yields reported in Table 2.3 are given as a percent of the IEPOX lost rather than as a percent of the total products observed, they do not necessarily add to 100%. Products lost to walls, products undetectable by our CIMS instruments, and uncertainty in sensitivity estimates all contribute to this deviation from carbon parity. We believe that uncertainties in the IEPOX and other large product sensitivity estimates account for the majority of error in the calculated yields, and for modeling purposes we suggest scaling the yields to a sum of 100%, knowing that significant uncertainties will persist until a more accurate determination of product yields can be measured.

The dominant small products of IEPOX oxidation detected by CIMS (Figure

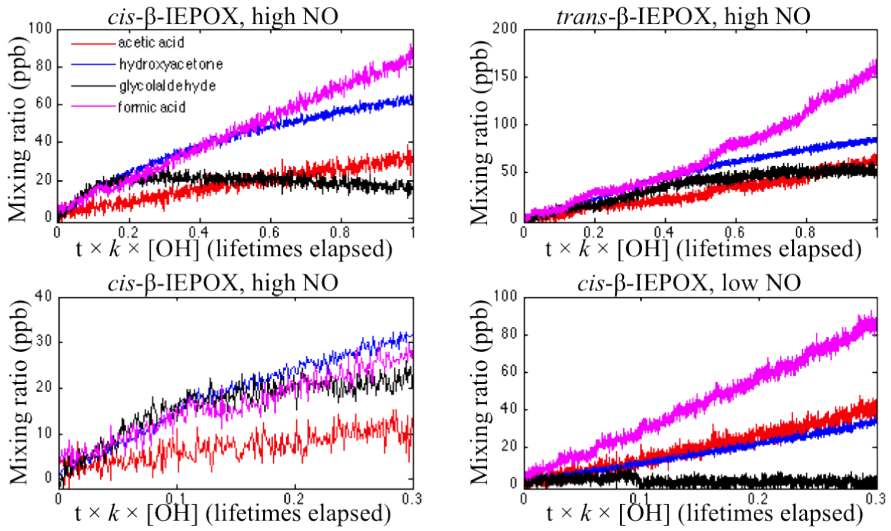

Figure 2.7: Time traces of dominant small products observed in the OH-initiated oxidation of *cis*- and *trans*-β-IEPOX: acetic acid (red), hydroxyacetone (blue), glycolaldehyde (black), and formic acid (magenta).

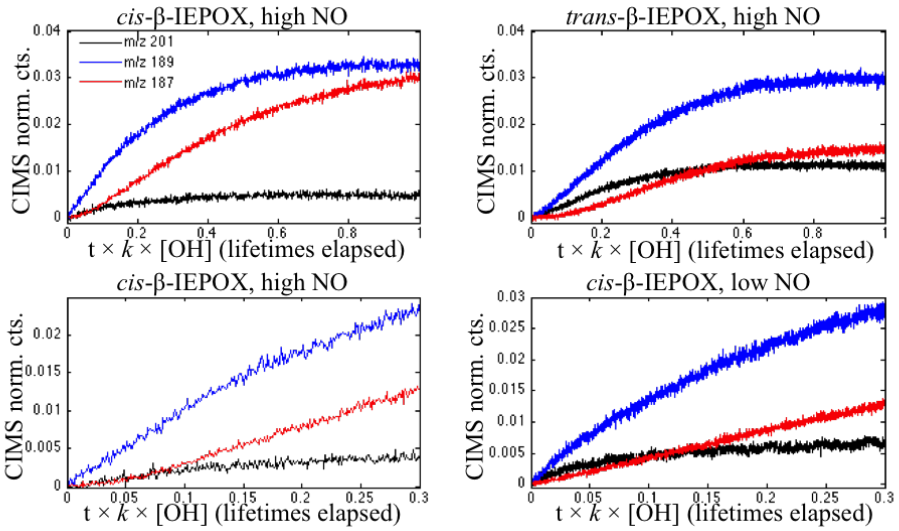

Figure 2.8: Time traces of dominant large products observed in the OH-initiated oxidation of *cis*- and *trans*-β-IEPOX as *m/z* 201 (black), 189 (blue), and 187 (red).

compound	sensitivity	yield (%)		
		cis-β-IEPOX high [NO]	*cis*-β-IEPOX low [NO]	*trans*-β-IEPOX high [NO]
m/z 201	variable	10.6 ± 0.7	12.9 ± 1.0	10.5 ± 0.27
m/z 189	variable	46.4 ± 1.7	37.1 ± 2.2	21.7 ± 0.5
m/z 187	variable	14.4 ± 0.6	10.4 ± 0.6	3.69 ± 0.15
glycolaldehyde	4.0×10^{-4}	11.8 ± 0.5	2.5 ± 0.6	4.55 ± 0.24
hydroxyacetone	3.8×10^{-4}	16.8 ± 0.3	8.5 ± 0.5	5.41 ± 0.17
acetic acid	2.3×10^{-4}	4.3 ± 0.3	7.8 ± 1.2	2.7 ± 0.3
formic acid	2.7×10^{-4}	15.8 ± 0.5	27.8 ± 2.1	8.8 ± 0.5

Table 2.3: First-generation yields of dominant products from the oxidation of *cis*- and *trans*-β-IEPOX. Sensitivities are in units of normalized counts per ppt in the CIMS flow tube, and the large products with "variable" sensitivities are assumed to have sensitivities equal to those of their parent IEPOX isomer (4.0×10^{-4} for *cis*-β-IEPOX and 2.2×10^{-4} for *trans*-β-IEPOX

2.7) were formic acid (FA, monitored at *m/z* 65 for FA·F^-), acetic acid (AA, *m/z* 79 for AA·F^-), glycolaldehyde (GLYC, *m/z* 145 for GLYC·CF_3O^-, corrected for AA·CF_3O^-), and hydroxyacetone (HAC, *m/z* 159 for HAC·CF_3O^-). Under high-NO conditions, both *cis*- and *trans*-β-IEPOX produced nearly equivalent first-generation yields of glycolaldehyde and hydroxyacetone. This matches previous speculation on the oxidation mechanism of IEPOX, such as those used in SAPRC-07 and MCM 3.2 (Carter, 2010; Saunders *et al.*, 2003). Both isomers also produced significant levels of formic and acetic acids, which had not been previously reported in IEPOX oxidation. Low-NO oxidation of *cis*-β-IEPOX resulted in diminished first-generation yields of glycolaldehyde and hydroxyacetone and elevated yields of acetic and formic acids relative to oxidation under high-NO conditions, suggesting a strongly NO-dependent mechanism for the formation of these small products.

The most prevalent C_4-C_5 products detected by CIMS (Figure 2.8) appeared at *m/z* 201, 189, and 187. Under high- and low-NO conditions, the two isomers gave nearly identical yields of the m/z 201 product. In contrast, *cis*-β-IEPOX produced over twice as much of the *m/z* 189 product as the *trans* isomer did, and nearly four times as much of the *m/z* 187 product. This evidence, along with differences in the yields of small products between the isomers, suggests a stark disparity between the oxidation pathways of the two isomers. We do not currently have an explanation for this difference, but ongoing computational studies are expected to shed light on this intriguing chemistry. Additionally, the appearance of significant amounts of large

products under high-NO conditions contrasts with the IEPOX oxidation mechanism used currently in photochemical models (*e.g.* MCM v3.2 and SAPRC07), in which IEPOX degrades quickly to form hydroxyacetone, glycolaldehyde, and other small products (Saunders *et al.*, 2003). Low-NO oxidation of *cis*-β-IEPOX produced slightly less of the *m/z* 189 and 187 products and slightly more of the *m/z* 201 product than under high-NO conditions, but the small magnitude of these changes suggests only a minor NO dependence of this oxidation pathway.

Proposed structures for the *m/z* 201, 189, and 187 compounds are shown in Figure 2.9. While many of these structures have been suggested previously as intermediates in the oxidative degradation of IEPOX, most have not yet been considered first-generation products, and their designation as such requires reconsideration of the mechanism for the first steps of IEPOX oxidation. We propose such a mechanism in Figure 2.10. We stress that this mechanism is neither complete nor certain, and it does not yet account for differing oxidation pathways between the two β-IEPOX isomers, nor for the formation of formic and acetic acids, but it improves upon existing mechanisms by incorporating both previous insights and the present results.

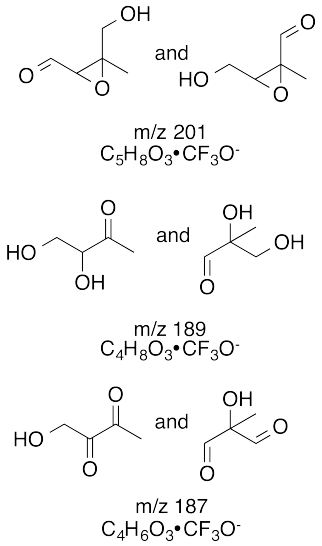

Figure 2.9: Proposed structures of the dominant large products observed in the OH-initiated oxidation of *cis*- and *trans*-β-IEPOX.

The mechanism begins with hydrogen abstraction by OH at the 1, 3, or 4 position. In the case of abstraction at positions 1 or 4, addition of O_2 and subsequent elimination of HO_2 gives the *m/z* 201 product, which accounts for ~10% of the first-generation pathway. Alternatively, a series of rearrangements can form a more

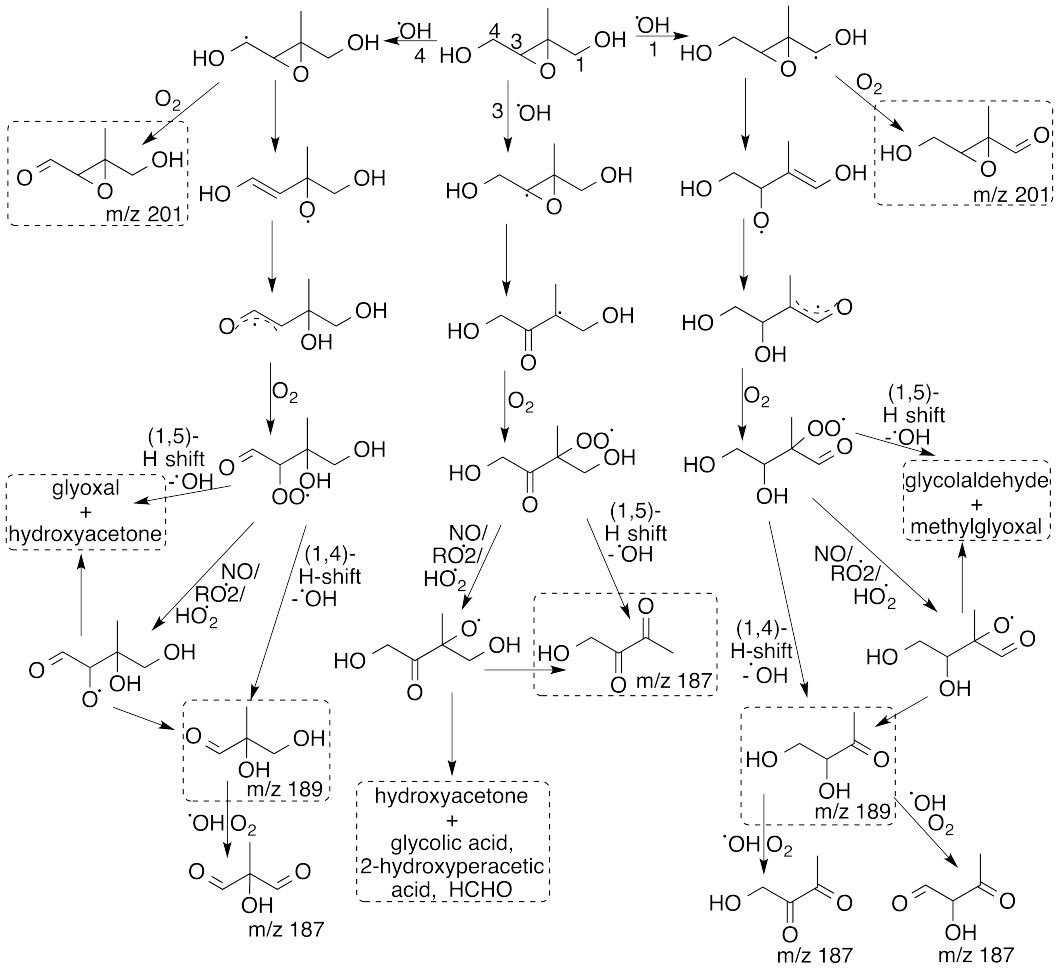

Figure 2.10: Proposed mechanism for the OH-initiated oxidation of β-IEPOX. Proposed first-generation products are outlined in dashed boxes.

stable alkyl radical prior to O_2 addition. The resulting peroxy radical can then undergo a variety of possible transformations. Reaction with HO_2, NO, or RO_2 to form the alkoxy radical results in fragmentation of the molecule, forming either a C_3 and a C_2 product or a C_4 product and CO. These pathways account for the formation of hydroxyacetone, glycolaldehyde, and the product detected at *m/z* 189. This mechanism also implies that glyoxal and methylglyoxal – neither of which can be detected by the CIMS instruments used here – are produced concurrently with hydroxyacetone and glycolaldehyde, respectively. Additionally, the peroxy radical can undergo unimolecular decomposition, *via* a 1,4-H shift from the α aldehyde or a 1,5-H shift from the α hydroxyl group, to form the same sets of products accessed by the alkoxy radical pathway. The product detected at *m/z* 189 can further react with OH and O_2 to form products detectable at *m/z* 187. Theoretically, the peroxy

radical could also react with HO_2 to form a hydroperoxide, or with NO to form a nitrate. Low product signal was observed at a mass consistent with the hydroperoxide (<5% under low-NO conditions), and almost no product was observed at a mass consistent with the nitrate (<1% under high-NO conditions), suggesting either that these reactions do not readily occur or that the non-volatile products are quickly lost to chamber walls.

In the case of hydrogen abstraction by OH at position 3, no product detectable at *m/z* 201 can be formed. Instead, isomerization and addition of O_2 leads directly to the peroxy radical, which can again undergo a 1,5-H shift with the α hydroxyl group and decompose to form a C_4 fragment. The C_4 fragment produced by the H-shift mechanism differs from those produced by abstraction at positions 1 and 4, and accounts for the first-generation yield of the product detected at *m/z* 187. Alternatively, the peroxy radical can react with HO_2, NO, or RO_2 to form the alkoxy radical, which decomposes to form either the same C_4 fragment or hydroxyacetone and a C_2 fragment. The C_2 fragment produced by this mechanism is expected to form glycolic or 2-hydroxyperacetic acids by reaction with HO_2 or decompose to formaldehyde (Saunders *et al.*, 2003). Low product signal was observed at masses consistent with the two acids (<2%). The sum of the yields of *m/z* 187 and hydroxyacetone provides an upper limit for the fraction of IEPOX + OH hydrogen abstraction that occurs at position 3, as hydroxyacetone can also be formed from other pathways. The yields reported in this study suggest that the first-generation formation of the *m/z* 189 products is the dominant pathway of IEPOX oxidation, and thus that hydrogen abstraction by OH occurs primarily at positions 1 and 4, but all pathways shown in Figure 2.10 contribute to the overall product breakdown of OH-initiated IEPOX degradation.

Many aspects of our proposed mechanism coincide with the one recently proposed by Jacobs *et al.* (2013) for *trans*-β-IEPOX, with the exception of our inclusion of the *m/z* 189 and 187 products, which they did not observe. Setting aside these compounds, the relative yields of hydroxyacetone, glycolaldehyde, and the *m/z* 201 product from *trans*-β-IEPOX oxidation are similar to those reported by Jacobs *et al.* (2013). Their study also shows products that our CIMS would observe at *m/z* 163, 217, and 235. With the exception of *m/z* 235, of which we detect small yields (<5%) with low statistical significance, these products are not observed in our experiments.

2.4 Conclusions

The recent discovery of IEPOX, and evidence of its importance as an isoprene oxidation product and SOA precursor, has led to widespread interest in its atmospheric fate. As IEPOX is estimated to account for a significant mass of global VOC (~100 Tg C y^{-1}), an understanding of its chemistry is critically important. The results presented here provide new insight into IEPOX behavior, which can be incorporated into chemical mechanisms of low-NO isoprene oxidation. The relative yields of IEPOX isomers as reported here, along with the OH oxidation rates of those isomers, serve to constrain the isomer distribution in the atmosphere, and explain the isomeric yields of 2-methyltetrols found in SOA. As differences in oxidation pathways between IEPOX isomers are elucidated, isomer abundances will further improve estimates of product yields.

The product studies conducted in this investigation largely corroborate existing predictions of the IEPOX oxidation pathway. Major products observed at *m/z* 189 and 187 fit with the existing MCM mechanism (Saunders *et al.*, 2003), although they notably appear as first-generation products rather than subsequent intermediates. Atmospheric observations of these products in high-isoprene, low-NO environments would test this finding. Yields of smaller products also generally match predictions, with the exception of formic acid, which has a much higher yield than currently predicted. However, differences in yields of most products between the two *beta*-IEPOX isomers suggest substantial divergence in the oxidation pathways for the two atmospherically dominant IEPOX isomers. Additionally, assuming glyoxal and methylglyoxal are co-products of hydroxyacetone and acetaldehyde in the oxidation of IEPOX, this chemistry is likely important in closing some of the disagreement between simulated and observed levels of these compounds in isoprene-rich environments (Myriokefalitakis *et al.*, 2008; Wittrock *et al.*, 2006). Although further studies incorporating measurements of glyoxal and methylglyoxal will be necessary to fully constrain the products of IEPOX oxidation, and to reconcile differences between our experiments and those of Jacobs *et al.* (2013), the products reported here provide a framework from which to improve existing models.

2.5 Supporting Information

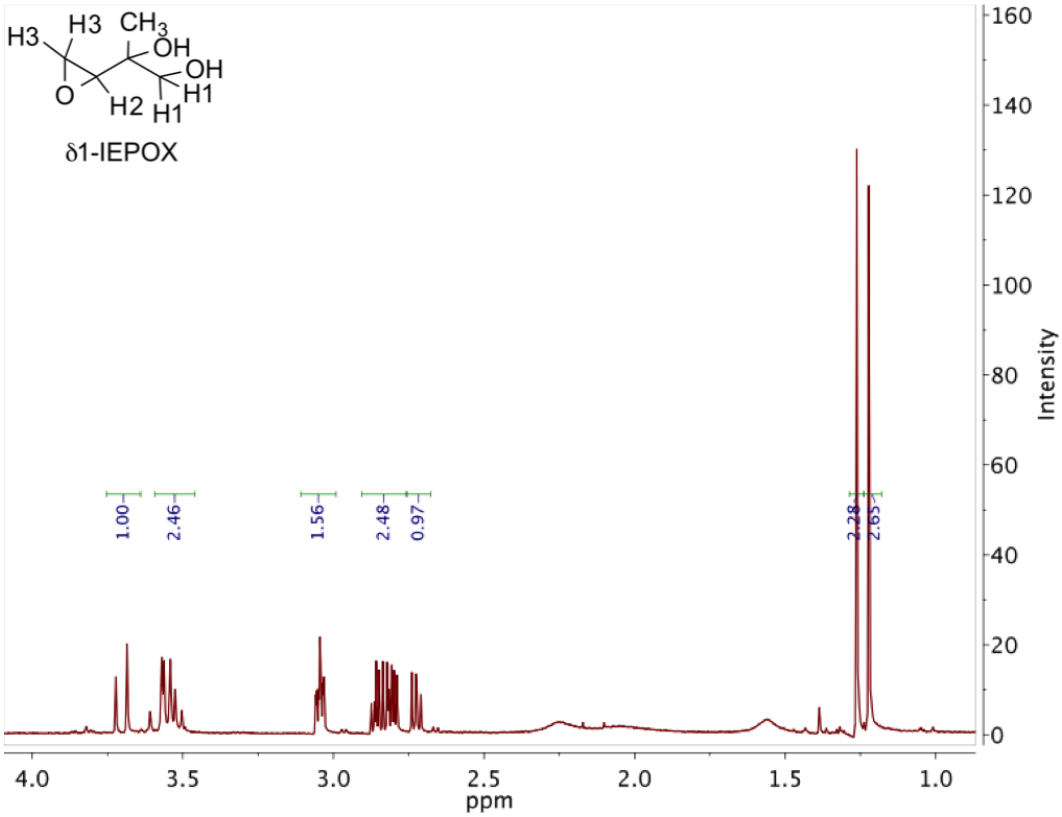

Figure 2.11: ^{1}H NMR (300 MHz, $CDCl_3$) of δ1-IEPOX.

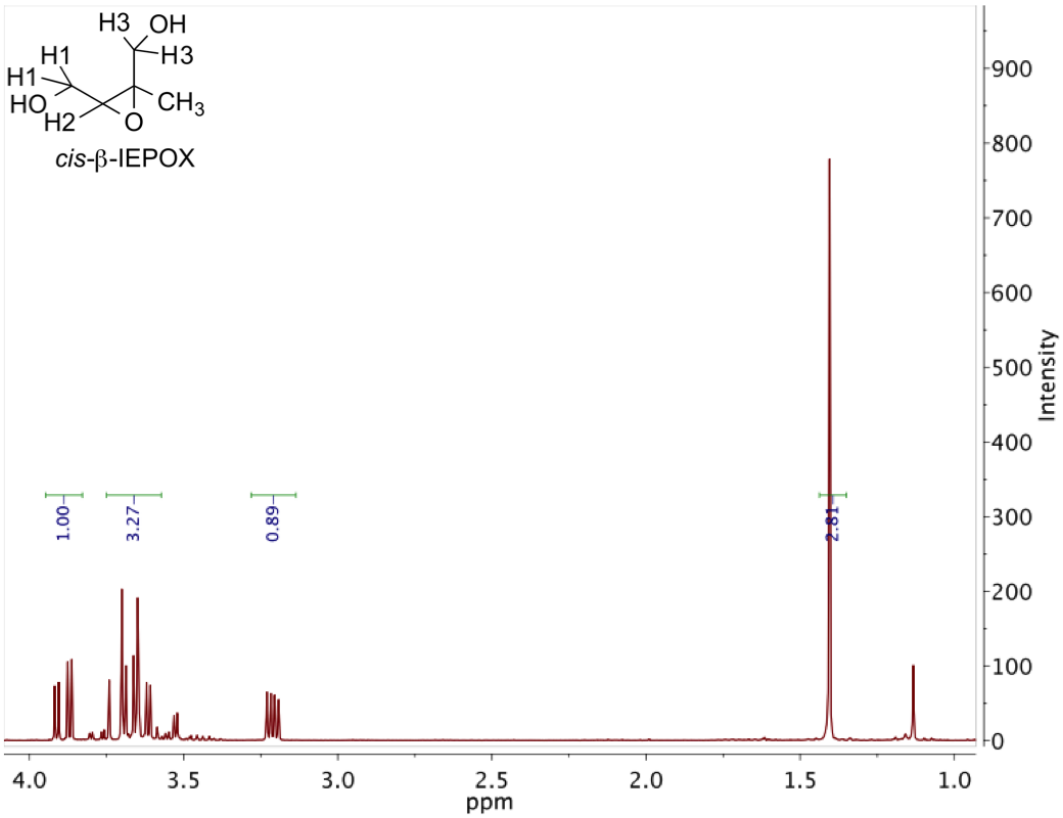

Figure 2.12: ^{1}H NMR (300 MHz, D_2O) of *cis-β*-IEPOX.

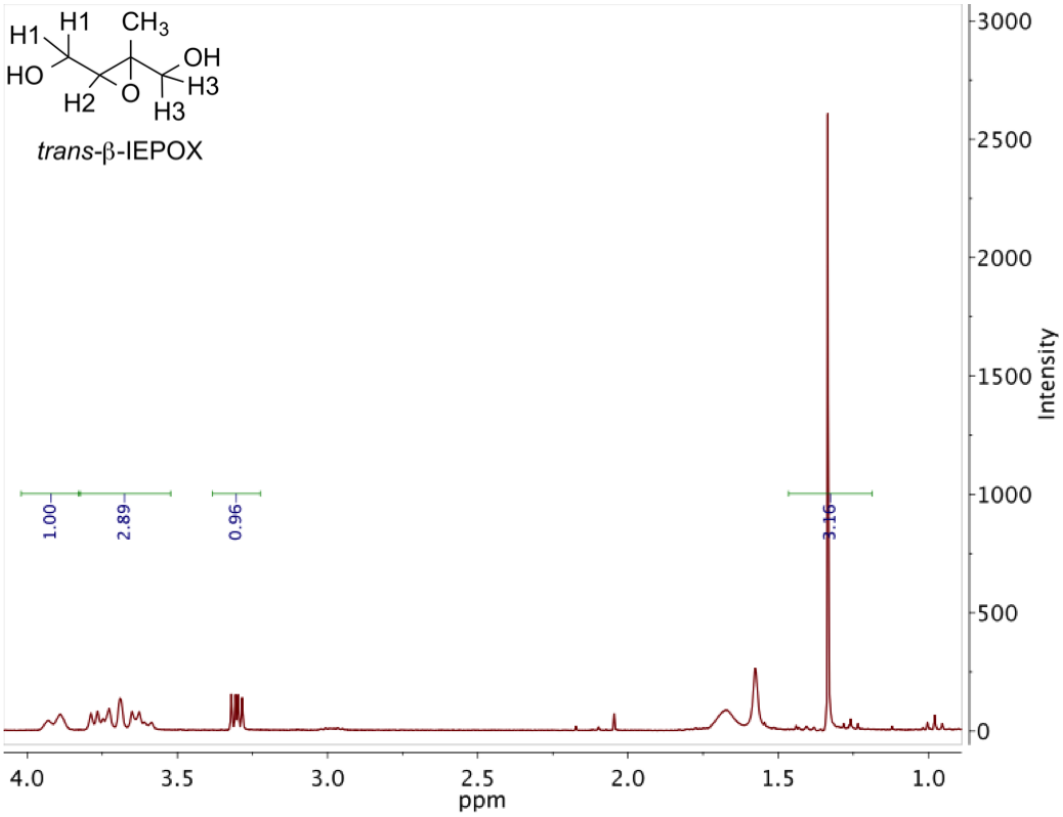

Figure 2.13: ^{1}H NMR (300 MHz, $CDCl_3$) of *trans-β*-IEPOX.

Chapter 3

PRODUCTION AND FATE OF C_4 DIHYDROXYCARBONYL COMPOUNDS FROM ISOPRENE OXIDATION

Bates, K. H., T. B. Nguyen, A. P. Teng, J. D. Crounse, H. G. Kjaergaard, B. M. Stoltz, J. H. Seinfeld, and P. O. Wennberg (2016). "Production and fate of C4 dihydroxycarbonyl compounds from isoprene oxidation". In: *J. Phys. Chem. A* 120.1, pp. 106–117. DOI: 10.1021/acs.jpca.5b10335.

Abstract

isoprene epoxydiols (IEPOX) are formed in high yield as second-generation products of atmospheric isoprene oxidation in pristine (low-NO) environments. IEPOX has received significant attention for its ability to form secondary organic aerosol, but the fate of IEPOX in the gas phase, and those of its oxidation products, remains largely unexplored. In this study, three dihydroxycarbonyl compounds with molecular formula of $C_4H_8O_3$ – putative products of IEPOX oxidation – are synthesized to determine their isomer-specific yields from IEPOX. We find that 3,4-dihydroxy-2-butanone (DHBO) comprises 43% and 36% of the products from *cis*- and *trans*-β-IEPOX respectively, and is by far the most abundant $C_4H_8O_3$ dihydroxycarbonyl compound produced by this mechanism. OH is found to react with DHBO with a rate coefficient of 1.10×10^{-11} cm^3 molecule^{-1} s^{-1} at 297 K, forming two hydroxydicarbonyl compounds that share the molecular formula $C_4H_6O_3$ with unitary yield. The results of this study are compared with field observations and used to propose a multigenerational mechanism of IEPOX oxidation. Finally, global simulations using GEOS-Chem, a chemical transport model, show that the $C_4H_8O_3$ dihydroxycarbonyl compounds and their oxidation products are widespread in the atmosphere, and estimate annual global production of $C_4H_8O_3$ dihydroxycarbonyls to be 54 Tg y^{-1}, primarily as DHBO.

3.1 Introduction

Atmospheric emissions of isoprene, derived primarily from deciduous plants, are estimated to exceed 500 Tg y^{-1} globally, making isoprene the most abundantly emitted non-methane hydrocarbon by mass (Guenther *et al.*, 2006; Guenther *et al.*, 2012). The rapid oxidation of both isoprene and its oxidation products in

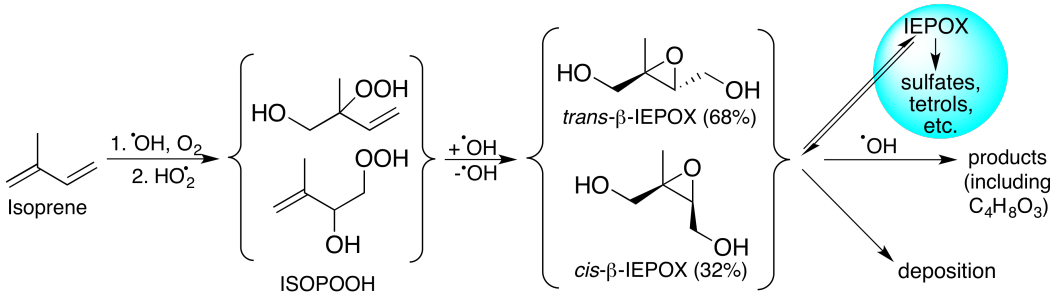

Figure 3.1: Steps and compounds in the HO_x-mediated (low-NO) oxidation of isoprene.

the gas phase, principally by OH radicals (Atkinson *et al.*, 2006), helps to set the atmosphere's oxidative capacity and leads to the formation of both highly oxygenated gaseous compounds and secondary organic aerosol (SOA) (Archibald *et al.*, 2010; Lelieveld *et al.*, 2008). These effects can exert a strong influence on climate, health, and tropospheric chemistry in areas with high biogenic emissions.

In regions of the atmosphere with low concentrations of NO, which typically occur in remote forests where isoprene emissions are high, the oxidation of isoprene proceeds predominantly by a HO_x-mediated (OH + HO_2) pathway shown in Figure 3.1 (Kuhlmann and Lawrence, 2004; Rosenstiel *et al.*, 2003; Wiedinmyer *et al.*, 2006). The addition of OH and O_2 is followed by reaction with HO_2 to form hydroxy hydroperoxides (ISOPOOH) in yields of >80% (Crutzen *et al.*, 2000; Paulot *et al.*, 2009b). A recent synthetic route to the dominant ISOPOOH isomers has facilitated measurements of the rates and products of their reactions with OH (St. Clair *et al.*, 2015), which previously relied on estimates from OH + isoprene experiments (Paulot *et al.*, 2009b). The dominant fate of ISOPOOH is reaction with OH to form isoprene epoxydiols (IEPOX) in yields of 70-80%, resulting in an isomeric ratio of 2:1 for *trans-* to *cis-β*-IEPOX (St. Clair *et al.*, 2015). This reaction recycles one equivalent of OH (Paulot *et al.*, 2009b), contributing to the stability of HO_x in remote forested regions (Lelieveld *et al.*, 2008; Ren *et al.*, 2008; Thornton *et al.*, 2002).

In the atmosphere, IEPOX can then follow a number of subsequent pathways. IEPOX has been shown to contribute substantially to biogenic SOA in the field (Budisulistiorini *et al.*, 2013; Froyd *et al.*, 2011; Worton *et al.*, 2013; Zhang *et al.*, 2013), where its aerosol uptake depends on a variety of factors such as particle liquid water content, total particulate surface area, anionic activity (*e.g.* sulfate

and other nucleophiles), cationic activity (primarily hydronium in many areas), and organic coating (Gaston *et al.*, 2014; Liao *et al.*, 2015; Nguyen *et al.*, 2014a; Surratt *et al.*, 2010; Xu *et al.*, 2015). The properties of its reactive uptake have been further examined in chamber experiments (Gaston *et al.*, 2014; Lin *et al.*, 2012; Liu *et al.*, 2015; Nguyen *et al.*, 2014a; Surratt *et al.*, 2010), facilitated by the development of synthetic routes to four IEPOX isomers (Zhang *et al.*, 2012). A laboratory study focusing on particle free acidity and surface area placed constraints on IEPOX aerosol uptake at <5 h (pH <1) to >25 h (pH >3), and noted that organic coatings on aerosols significantly suppress IEPOX uptake, suggesting that the aerosol uptake can be self-limiting (Gaston *et al.*, 2014). These results imply that particle uptake may be the dominant IEPOX loss process only when aerosol pH is less than 1 on freshly exposed aqueous sulfate particles.

Additional IEPOX loss processes include deposition and reaction with OH in the gas phase. Dry deposition of IEPOX and its gas phase oxidation products to a forested environment has also been measured in the field, with a typical lifetime of 13 h under daytime turbulent mixing conditions (Nguyen *et al.*, 2015a). Laboratory studies of the gas phase oxidation of IEPOX by OH measured lifetimes of 3-28 h, and identified a number of stable products (Bates *et al.*, 2014; Jacobs *et al.*, 2013). All together, previous work suggests that gas phase reaction with OH dominates IEPOX loss (~44%) under environmental conditions typical of IEPOX production (daytime, turbulent 1.5 km mixed layer, ~200 μm^2 cm^{-3} particle surface area with aerosol pH = 3), with deposition (~37%) and particle uptake (~19%) contributing smaller proportions (Bates *et al.*, 2014; Gaston *et al.*, 2014; Nguyen *et al.*, 2015a).

Bates *et al.* (2014) identified a dominant product from the gas phase oxidation of both the *cis*- and *trans*-β-IEPOX by OH as an unknown compound with a nominal mass of 104 a.m.u., with yields of 33 (±11) %. A likely formula of $C_4H_8O_3$ was assigned to the product, and two possible structures were proposed, but no further information on the compound(s) could be determined. Given the high measured yields and the atmospheric importance of IEPOX – with an estimated 226 Tg y^{-1} produced globally (St. Clair *et al.*, 2015) – the identity and subsequent fate of this unknown product may have profound impacts on oxidant budgets, SOA formation, and other important aspects of tropospheric chemistry in low-NO high-isoprene environments.

In the experiments detailed here, standards of IEPOX and three $C_4H_8O_3$ compounds, shown in Figure 3.2, were synthesized in order to identify these 104 a.m.u.

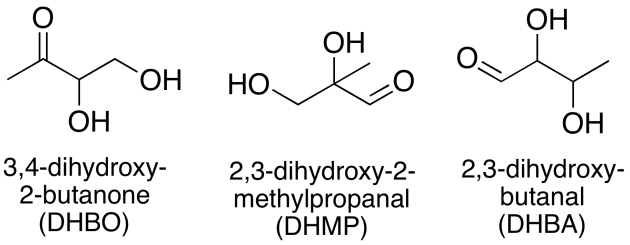

Figure 3.2: Dihydroxycarbonyl species synthesized and investigated in this study, collectively referred to as $C_4H_8O_3$.

products of IEPOX + OH and to measure their yields with greater precision, using an improved gas chromatography-chemical ionization mass spectrometry (GC-CIMS) technique. The rates and products of the reactions of the three synthetic $C_4H_8O_3$ compounds with OH were then determined in individual chamber experiments. Additionally, field measurements from the isoprene-rich Southeastern United States were analyzed *vis-à-vis* the newly elucidated reaction rates and product yields. Finally, the oxidation mechanism of IEPOX and the $C_4H_8O_3$ compounds was incorporated into GEOS-Chem, a global chemical transport model, to estimate their global production and potential impact on tropospheric chemistry.

3.2 Experimental Methods

3.2.1 Synthesis

Five compounds were synthesized for use in chamber experiments: *trans-β*-IEPOX, *cis-β*-IEPOX, DHBO, 2,3-dihydroxy-2-methylpropanal (DHMP), and 2,3-dihydroxybutanal (DHBA). All compounds were characterized by 300 MHz ^{1}H NMR. Reagents were purchased from Sigma-Aldrich unless otherwise noted.

Trans-β-IEPOX was prepared from 3-methyl-2-buten-1-ol by a method identical to that used by Bates *et al.* (2014) derived from the techniques of Zhang *et al.* (2012) *cis-β*-IEPOX was prepared in a method similar to that of Bates *et al.* (2014) except that two steps of the synthetic pathway were bypassed by reducing citraconic anhydride directly to 2-methyl-2-butene-1,4-diol using diisobutylaluminum hydride (DIBAL-H), as shown in Figure 3.3. The procedure for this reduction was identical to that described for the reduction of 3-methylfuran-2(5H)-one in the original synthesis (Bates *et al.*, 2014), except that 5 equivalents of DIBAL-H were necessary to achieve the desired reaction, and the yield was reduced to 28%, slightly below the combined yield of 30% for the three steps it replaced. ^{1}H NMR spectra of *cis-* and *trans-β*-IEPOX matched previously published characterization (Bates *et al.*, 2014).

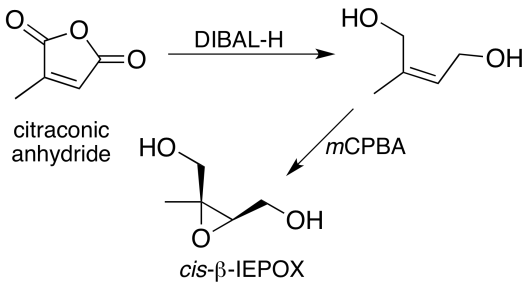

Figure 3.3: Steps in the synthesis of *cis*-β-IEPOX.

The three $C_4H_8O_3$ compounds were synthesized individually in two steps, using known procedures with slight adaptations, as shown in Figure 3.4 for the synthesis of DHBO from methyl vinyl ketone (MVK, ≥95%). DHMP and DHBA were synthesized with the same two steps, but using methacrolein (95%) and crotonaldehyde (≥99.5%, ~1:20 *cis*:*trans*) respectively as starting compounds. The starting material was first epoxidized under basic conditions (House and Ro, 1958; Payne, 1959; Wellman *et al.*, 1976) by addition to a solution of 17.5% hydrogen peroxide (H_2O_2) in water, brought to 0 °C and pH 8.5-9 by addition of NaOH. The reaction was allowed to warm to room temperature 10 min after addition; stirring continued for 2 h after addition, and during the entire reaction, pH was kept at 8.5-9 by slow addition of NaOH. After the reaction was complete, it was neutralized with HCl and the epoxide intermediate was isolated by extraction with dichloromethane (DCM), dried with Na_2SO_4, filtered, and concentrated under reduced pressure. The epoxide intermediates were then hydrolyzed (Long and Pritchard, 1956; Wang *et al.*, 2008b) in neutral aqueous solution by heating for 24 h to 65 °C (DHMP), 70 °C (DHBA), or 80 °C (DHBO). Unreacted starting material was removed by extraction with DCM; the $C_4H_8O_3$ dihydroxycarbonyl compounds remained in the aqueous phase, and were concentrated slightly under reduced pressure with minimal heating (<30 °C) and used without further purification. Where available, ^{1}H NMR spectra matched previously published characterization (Bischofberger *et al.*, 1988; Guérard-Hélaine *et al.*, 2011; Kholodar and Murkin, 2013; Wellman *et al.*, 1976).

3.2.2 Chamber experiments

Initial conditions for each of the chamber experiments conducted in this study are listed in Tables 3.1 and 3.2. The environmental chamber used for gas phase OH oxidation experiments, along with the associated techniques and instruments, has been described extensively in previous literature (Bates *et al.*, 2014; Crounse

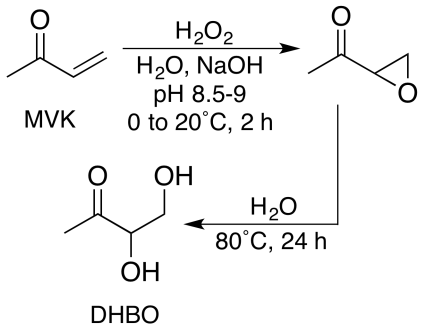

Figure 3.4: Steps in the synthesis of dihydroxybutanone (DHBO).

expt #	reactant	$[reactant]_0$ (ppbv)	$[H_2O_2]_0$ (ppbv)	$[propene]_0$ (ppbv)	$[NO]_0$ (ppbv)	reaction time (h)
1	DHBO	103.75	2.4	105	0	6.0
2	DHBO	104.61	2.9	117	580	6.0
3	DHMP	2.75	2.7	130	582	6.0
4	DHMP	5.17	2.6	166	0	6.0
5	DHMP	2.63	3.2	141	0	3.0, 3.0
6	DHBA	0.72	2.6	132	576	6.0
7	DHBA	1.60	2.6	130	576	3.0, 3.0
8	DHBA	0.34	2.9	142	0	3.0, 3.0

Table 3.1: Initial conditions for kinetic-focused chamber experiments.

et al., 2013; Lee *et al.*, 2014; St. Clair *et al.*, 2015), so only a cursory summary is provided herein, with particular detail for aspects unique to this study. Experiments were conducted in 0.85 m^3 environmental chambers made of fluorinated ethylene propylene (Teflon-FEP, DuPont) kept at 297 ± 5 K and 745 Torr, with separate chambers used for high- and low-NO experiments. The chamber was cleaned by flushing with dry air from a purge gas generator (Perkin, Model 75-52) and evacuating at least six times between experiments.

To prepare each experiment, the synthetic compound of interest was added to the chamber by flowing dry air at 20 L min^{-1} into the chamber's single sample port through a small glass vial containing ~50 μL of the target compound (pure IEPOX, or a dilute solution of $C_4H_8O_3$ in H_2O) for 30 min. For IEPOX injections, the vial was heated to 45 °C (*trans*) or 60 °C (*cis*) in a water bath. Hydrogen peroxide (50% w/w in H_2O, ~6 mg) was added by the same method for 10 min without heating, to achieve an initial mixing ratio of ~2.5 ppmv. For kinetic experiments, propene gas was added by flushing the contents of a dilute 500 cm^3 glass bulb into the chamber

expt \$	reactant	$[reactant]_0$ (ppbv)	$[H_2O_2]_0$ (ppbv)	$[NO]_0$ (ppbv)	reaction time (h)
9	*cis*-β-IEPOX	94.89	3.0	0	5.0
10	*cis*-β-IEPOX	53.28	2.8	0	8.4
11	*cis*-β-IEPOX	30.83	2.9	581	2.0, 2.0
12	*cis*-β-IEPOX	55.23	2.8	0	3.1
13	*cis*-β-IEPOX	83.82	3.2	346	1.6
14	*trans*-β-IEPOX	81.74	2.7	592	2.7
15	*trans*-β-IEPOX	131.41	3.6	0	6.2
16	*trans*-β-IEPOX	126.87	3.0	0	2.5, 3.5
17	DHBO	81.22	2.7	589	1.5
18	DHBO	74.21	2.9	0	3.0

Table 3.2: Initial conditions for product-focused chamber experiments.

with 20 L min^{-1} of dry air for 1 min. The bulb was prepared by serial dilution of propene (Sigma-Aldrich, ≥99%) to ~225 ppmv with N_2. For NO-dominated experiments, NO was added last by filling the same bulb to ~370 Torr with 1994 ± 20 ppm NO in N_2 (Matheson Gas Products) and flushing the bulb's contents into the chamber with 20 L min^{-1} of dry air for 1 min. Finally, the chamber was filled with dry air to a total volume of 850 L.

After preparing the environmental chamber, the injection port was reconnected to the sampling instruments, which measured the chamber's contents for at least 1.5 hours prior to photooxidation. Oxidation was performed using eight UV broadband lamps centered around 350 nm (Sylvania) to photolyze H_2O_2, forming OH and subsequently HO_2 by the reaction of OH with H_2O_2. Photooxidation lasted anywhere between 1.5 and 8.5 hours, and in some experiments two separate episodes of photooxidation were performed with a period of dark sampling in between, as listed in Tables 3.1 and 3.2.

Chemical species in the chamber were measured throughout the experiment through a single length of PFA tubing (6.35 mm OD, ~2 m long). A NO_x monitor (Teledyne 200 EU) and an O_3 monitor (Teledyne 400 E) sampled continuously, as did a gas chromatograph with flame ionization detection (GC-FID, Agilent 5890 II) to measure propene. IEPOX, $C_4H_8O_3$, and their oxidation products were measured with a time-of-flight chemical ionization mass spectrometer (ToF-CIMS, Tofwerk/Caltech), which has been described in detail previously (Crounse *et al.*, 2006; Paulot *et al.*, 2009a; Praske *et al.*, 2015; St. Clair *et al.*, 2010). The CIMS uses

CF_3O^- as its reagent gas, which is produced by flowing CF_3OOCF_3 in N_2 (1 ppmv) through a ^{210}Po ionizer, and provides measurements of all *m/z* between 19 and 396 at 1 Hz time resolution. CF_3O^- clusters with acids, alcohols, hydroperoxides, and other polar compounds to form ions with *m/z* equal to that of the analyte plus 85; thus, IEPOX is detected at *m/z* 203 and $C_4H_8O_3$ at *m/z* 189. All *m/z* signals are normalized to the reagent anion signal, characterized by the sum of CF_3O^-, $H_2O{\cdot}CF_3O^-$, and $H_2O_2{\cdot}CF_3O^-$, and scaled by a sensitivity factor. CIMS sensitivities were estimated from the target compound's polarizability and dipole moments, calculated using density functional theory (DFT) as described previously (Garden *et al.*, 2009; Paulot *et al.*, 2009a,b; Praske *et al.*, 2015; Su and Chesnavich, 1982). Estimated CIMS sensitivities for compounds of interest in this work are given in Table 3.7 in the Supporting Information.

Before and after photooxidation, and between photooxidation episodes in experiments 5, 7, 8, 11, and 16, the ToF-CIMS was disconnected from the chamber and connected to the outlet of a gas chromatography oven (GC-CIMS), to separate isobaric compounds in a technique described previously (Bates *et al.*, 2014; Lee *et al.*, 2014; Praske *et al.*, 2015; Teng *et al.*, 2015). 150-300 cm^3 of chamber air was cryogenically trapped on the head of a 4 m Restek RTX-1701 column for 4 – 8 min using a bath of isopropanol cooled with liquid nitrogen to -30 – -20 °C. Following the removal of the cold trap, the column temperature was ramped in the GC oven (30 °C for 0.1 min, +3 °C min^{-1} for 10 min, +10 °C min^{-1} for 7 min, hold for 3 min). Analytes were passed through the column directly into the ToF-CIMS for detection.

3.2.3 GEOS-Chem Simulations

The location and extent of production of $C_4H_8O_3$ compounds in the atmosphere was evaluated using GEOS-Chem, a global chemical transport model (Bey *et al.*, 2001). The simulations described in this study employed GEOS-Chem version 9.02 with GEOS5 meteorology and the Rosenbrock Rodas-3 solver, and were run on a 4° × 5° grid for the year 2012, following a 1.5 year spinup.

The standard isoprene mechanism included in GEOS-Chem v9.02 (Mao *et al.*, 2013) was updated to include a number of recently published results, including the separation of ISOPOOH and IEPOX isomers and revision of their reaction rates and yields (Bates *et al.*, 2014; St. Clair *et al.*, 2015); the inclusion of new deposition velocities based on recent field measurements (Nguyen *et al.*, 2015a); and revised rates and yields of photolysis and reaction with OH and O_3 for MVK (Praske *et*

al., 2015) and first- and second-generation isoprene nitrate products (Jacobs *et al.*, 2014; Jenkin *et al.*, 2012; Lee *et al.*, 2014; Müller *et al.*, 2014). Further revisions based on the results of experiments in this study, including the addition of $C_4H_8O_3$ compounds and their products, were then applied as described below and detailed in Table 3.8 in the Supporting Information.

3.2.4 Field Observations

Experimental and simulated results were compared with measurements of $C_4H_8O_3$ compounds, as well as IEPOX and other related species, taken as part of the Southern Oxidant and Aerosol Study (SOAS; SOAS2013.rutgers.edu). Observation occurred between June 1st and July 15th, 2013, at the Southeastern Aerosol Research and Characterization (SEARCH) site in Centreville, Alabama (32.903 °N, 87.250 °W). The sampling site, surrounded by predominantly deciduous forests and located >50 miles from large urban areas, provided an archetypal high-isoprene environment; isoprene comprised 82 mol% of biogenic volatile organic compounds at the site (Xu *et al.*, 2015). During the sampling period, temperatures ranged between a diurnal mean high of 28.6 °C and a mean low of 21.6 °C, while relative humidity averaged >50% during the day and >90% at night (Xu *et al.*, 2015).

The same CIMS described above was deployed at the site and operated with only minor adjustments, which have been described previously (Nguyen *et al.*, 2015a). The most significant change was the replacement of the chamber sampling line with a high-flow (2000 L min^{-1}) fluoropolymer-coated glass inlet (0.4 m long, 3.1 cm inner diameter) to minimize losses of semivolatile compounds. The CIMS was positioned atop a metal sampling tower with a measurement height of 22 m, surrounded on three sides by forest with a canopy height of 10 m, and was placed in an insulated enclosure to control the instrument's temperature.

As described above, the CIMS detected relevant compounds as clusters with CF_3O^-, adding 85 to the nominal mass. After normalization to the reagent anion signal, the CIMS counts were scaled by estimated sensitivity factors to derive mixing ratios. For any *m/z* at which a mixture of isobaric compounds was expected (*e.g.*, IEPOX and ISOPOOH at *m/z* 203, all $C_4H_8O_3$ compounds at *m/z* 189, and all $C_4H_6O_3$ compounds at *m/z* 187), an average sensitivity was computed by weighting each compound's sensitivity according to its relative abundance in a simple steady-state box model of ISOPOOH oxidation, employing the rates and product yields reported in this and previous studies (Bates *et al.*, 2014; St. Clair *et al.*, 2015).

3.3 Results and Discussion

3.3.1 $C_4H_8O_3$ + OH Rate Coefficients

Rate coefficients (k_{OH}) for the reactions of each $C_4H_8O_3$ isomer with OH were derived using data from experiments 1 – 8 (Table 3.1) and were calculated relative to that of propene ($k_{propene}$ = 2.59 × 10^{-11} cm^3 $molecule^{-1}$ s^{-1} at 298 K and 993 hPa) (Atkinson and Arey, 2003a; Atkinson *et al.*, 2006). For each experiment, a linear regression incorporating error in both dimensions (York *et al.*, 2004) was performed on the natural log of the propene mixing ratio (measured by GC-FID) versus time, giving a slope equal to $k_{propene}$ × [OH], from which [OH] was calculated. The slope derived from a similar regression performed on the $C_4H_8O_3$ mixing ratio was then divided by [OH] to provide $k_{analyte}$.

For DHBO, enough analyte could be introduced to the chamber (>100 ppbv) to provide a strong CIMS signal with high signal-to-noise, which the GC-CIMS confirmed was overwhelmingly composed of DHBO with little (<1%) isobaric impurity. This allowed the CIMS signal to be converted directly to mixing ratio, using ion-molecule collision rate-estimated sensitivity, with low risk of systematic error from background interference. The calculated mixing ratio was then used for the error-weighted linear regression described above, from which k_{DHBO} was calculated.

For DHMP and DHBA, only small amounts (0.3-5.2 ppbv) of analyte could be introduced to the chamber, and the GC-CIMS showed that isobaric impurities interfered with the raw signal at *m/z* 189. These impurities, along with background signals and low signal-to-noise, could cause appreciable systematic error in an estimation of their oxidation rates based solely on the raw CIMS signal. Therefore, the linear regressions were performed on the integrated areas of analyte peaks as measured by GC-CIMS before, after, and between photooxidation periods. This method provides less precision, because it uses far fewer data points for each linear regression, but it introduces less systematic error by isolating the CIMS signal exclusively from the analyte of interest and integrating that signal over the 4-8 min GC sample collection time.

Measured rate coefficients for the reactions of DHBO, DHMP, and DHBA with OH are reported in Table 3.3. The reported values are relative-inverse-variance-weighted averages of the individual experimentally derived coefficients. Reported uncertainties include those of the linear regressions and the propene rate coefficient, propagated through the weighted averaging. Differences between measured rate

	k_{OH} ($\times 10^{-11}$ cm^3 molec^{-1} s^{-1})		
compound	this work	MCM	SAR
DHBO	1.10 ± 0.16	1.88	1.07
DHMP	3.0 ± 0.65	3.42	2.52
DHBA	3.7 ± 0.63	7.01	3.58

Table 3.3: Rate coefficients for the reactions of DHBO, DHMP, and DHBA with OH as measured in this work, reported in MCM, and estimated by SAR.

coefficients for individual experiments performed on a given analyte did not correlate or differ appreciably with [NO].

The rate coefficients measured in these experiments are consistent with those estimated by structure-activity relationship (SAR), also reported in Table 3.3, to within one standard deviation (Kwok and Atkinson, 1995). The SAR rate coefficients for DHBO and DHBA differ by only 3% from the experimentally determined values, while that of DHMP differs by 16%. Table 3.3 also includes the rate coefficient values currently used in the Master Chemical Mechanism (MCM v3.2) (Saunders *et al.*, 2003), which show a larger deviation from experimentally determined values, but agree to within a factor of two.

3.3.2 IEPOX Product Studies

Experiments 9-16 (Table 3.2) were used to estimate product yields from the reactions of IEPOX isomers with OH. Each yield was estimated from the slope of a simple linear regression between the normalized CIMS counts at *m/z* 203 (IEPOX) and those of the observed product over the first 15-20 minutes of oxidation, during which 10% of the initial IEPOX was oxidized; in these early periods, yields were observed to be linear and the high [IEPOX]:[product] ratio minimized interference from subsequent reactions of products. The regression slope was then multiplied by the ratio between the CIMS sensitivities (Table 3.7 in the Supporting Information) of the product and IEPOX to provide fractional product yields. Yields were corrected for loss of products to reaction with OH with the methods introduced by Atkinson *et al.* (1982) Product yields calculated in high- and low-NO experiments for each isomer were not found to be statistically significantly different (using the errors of the slopes of the linear regressions); for this reason, yields from all experiments with each individual IEPOX isomer were combined with a relative-inverse-variance-weighted mean to give the values reported in Table 3.4. Additional discussion of NO dependence can be found in the mechanism description below.

	molar yields (%)		
product	*cis*-β-IEPOX	*trans*-β-IEPOX	presumed coproducts
m/z 201 ($C_5H_8O_3$)	21 ± 7	18 ± 2	HO_2
DHBO	41 ± 13	36 ± 4	CO + OH
DHMP	5 ± 2	9 ± 1	CO + OH
m/z 187 ($C_4H_6O_3$)	8 ± 2	7 ± 1	CH_2O + OH
hydroxyacetone	8 ± 1	16 ± 1	glyoxal + OH
glycolaldehyde	17 ± 5	14 ± 7	methylglyoxal + OH

Table 3.4: Experimentally determined product yields from *cis*- and *trans*-β-IEPOX + OH.

Five masses were observed to account for a near unity yield (100% for *cis*-β-IEPOX, 95% for *trans*-β-IEPOX). Reported uncertainties for all masses except *m/z* 189 include only the standard deviations of the linear regression slopes propagated through the inverse-variance averaging; additional uncertainties in CIMS sensitivities are estimated to be ±30%. Between these uncertainties and the potential for additional systematic errors (*e.g.* products rapidly lost to walls or undetectable by CIMS), carbon parity is not necessarily expected in the product yields measured herein. However, because unity yields are useful for simulations, and because the five observed product masses require little scaling to achieve that result, yields (and corresponding uncertainties) reported in Table 3.4 are scaled to achieve carbon parity. It should be noted that a number of products not observed in this study have previously been shown or proposed to form from IEPOX (Jacobs *et al.*, 2013; Saunders *et al.*, 2003); possible reasons for their lack of detection are discussed below. Should these unobserved products prove to account for a considerable yield from the reaction of IEPOX with OH, the product yields reported in this study and any conclusions drawn from them will need to be scaled accordingly.

To determine the isomeric yields of the $C_4H_8O_3$ products, the *m/z* 189 signals from GC-CIMS samples taken after and between photooxidation episodes were analyzed to determine which isomers were present. Figure 3.5 shows an example of the signals from a GC-CIMS sample taken after IEPOX oxidation, along with signals from GC-CIMS samples of the three synthetic $C_4H_8O_3$ standards. In addition to their characteristic retention times, the $C_4H_8O_3$ isomers can be distinguished by their unique ratios of coeluting fragments and alternate ion pairs (*e.g.* $C_4H_8O_3{\cdot}F^-$ at *m/z* 123), also shown in Figure 3.5. Only DHBO and DHMP were observed to form from both *cis*- and *trans*-β-IEPOX, and the integrated areas of their GC-CIMS peaks were

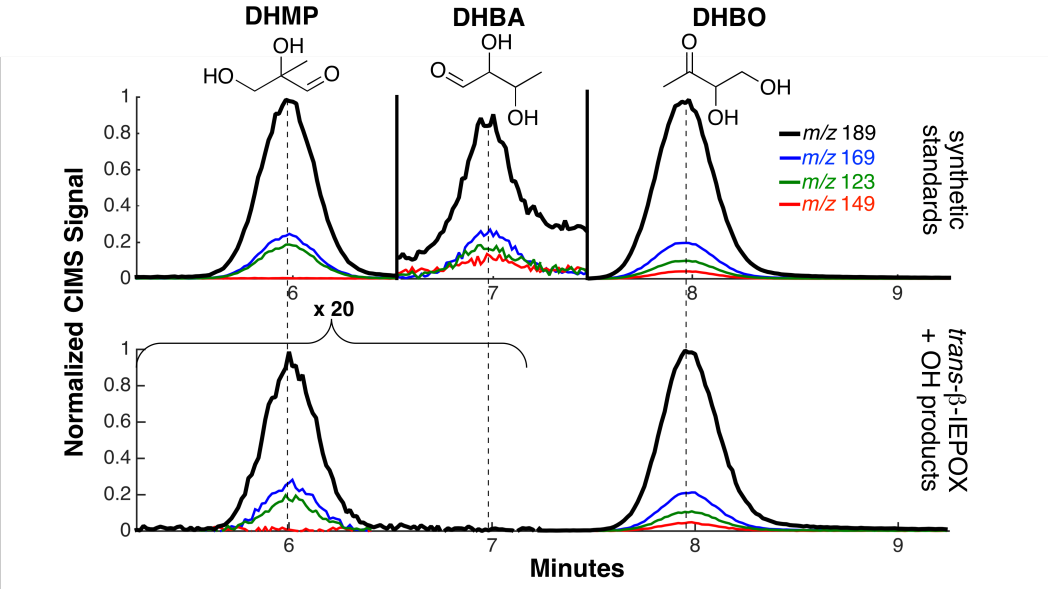

Figure 3.5: GC-CIMS chromatograms of the three synthetic $C_4H_8O_3$ standards (top) and of the products of *trans-β*-IEPOX + OH (bottom). Product signals are scaled up by 20× between 5.25 and 7.25 minutes for visibility. The products of *trans-β*-IEPOX + OH share the same retention times and coeluting masses as DHMP and DHBO.

scaled by their calculated CIMS sensitivities to provide estimated mixing ratios. A simple box model calculation was performed, incorporating IEPOX oxidation rates and the oxidation rates of the $C_4H_8O_3$ products; yields of the $C_4H_8O_3$ products were then adjusted to fit measured mixing ratios. DHBO was found to be the single highest yielding product, accounting for 43% and 36% of the products from *cis-* and *trans-β*-IEPOX respectively, while DHMP was produced in yields of 5% and 9%.

The six major products observed by CIMS in the oxidation of IEPOX by OH include hydroxyacetone, glycolaldehyde, DHBO, DHMP, and compounds observed at *m/z* 187 and 201. These products have all been observed in prior studies of IEPOX oxidation, and mechanisms to account for their formation have been previously published (Bates *et al.*, 2014; Jacobs *et al.*, 2013). An updated version of an IEPOX oxidation mechanism, originally proposed by Bates *et al.* (2014), is shown in Figure 3.6; this mechanism accounts for all six of the observed major products, and is described in detail in the following paragraph.

In the proposed mechanism, hydrogen abstraction by OH from IEPOX at carbons 1 and 4 (see numbering in Figure 3.6) can be followed immediately by reaction with O_2, forming the epoxide-retaining product at *m/z* 201 (herein labeled IEPOXO) and

generating an equivalent of HO_2. Alternatively, abstraction at carbons 1 and 4 can be followed by cleavage of the epoxide ring and an intramolecular hydrogen shift prior to O_2 addition, forming C_5 peroxy radicals. These peroxy radicals may undergo a (1,4)-H shift of the aldehydic hydrogen to the peroxy moiety, which precedent suggests will be rapid Crounse *et al.* (2012, 2013), followed by decomposition to form the $C_4H_8O_3$ dihydroxycarbonyls DHBO or DHMP along with CO and OH. Alternatively, the C_5 peroxy radicals may react with either HO_2 or NO to form alkoxy radicals, which would decompose to form either the same $C_4H_8O_3$ dihydroxycarbonyls or the hydroxyacetone and glycolaldehyde observed in these studies, along with their presumed respective coproducts of glyoxal and methylglyoxal. Yields of these C_2-C_3 products were found to increase slightly in high-NO experiments, with a minor corresponding decrease in $C_4H_8O_3$ yields, but the changes were not statistically significant. While the relative rates of isomerization and reaction with NO or HO_2 are not known for the C_5 peroxy radicals shown in Figure 3.6, the minor differences in product yields between high- and low-NO experiments suggest that formation of DHBO or DHMP may be insensitive to these rates. However, because the branching between these three reactive pathways affects radical recycling, further work should focus on determining these rates. Finally, the product at *m/z* 187 is thought to be the α-diketone 1-hydroxy-2,3-butadione (HBDO), which has also been observed as an oxidation product of MVK under low-NO conditions (Praske *et al.*, 2015). HBDO is predicted to form following hydrogen abstraction from carbon 3 of IEPOX, and would likely be accompanied by formaldehyde and OH as coproducts.

A number of products proposed in previous studies of *cis*- and *trans*-β-IEPOX do not appear in this mechanism, as they were not observed in the studies described herein. In particular, the products observed by Jacobs *et al.* (2013) at *m/z* 89, 133, and 151 ($M+H^+$) along with other C_5 compounds predicted to form in MCM (Saunders *et al.*, 2003) were not seen to form from IEPOX in these experiments. That these compounds were not observed by CIMS does not necessarily mean they were not produced; they may have been lost to chamber walls, been photolyzed, or be undetectable by CF_3O^- CIMS. However, because the observed products do achieve a result near carbon parity, unobserved products are not expected to account for a large yield, and were therefore not included in the mechanism. The formic and acetic acids observed by Bates *et al.* (2014) were also seen in the experiments conducted in the present study, but in low and highly variable yields. The organic acids were also observed in blank experiments performed without any IEPOX added to chamber, and are thought to result in part from wall reactions; furthermore, they

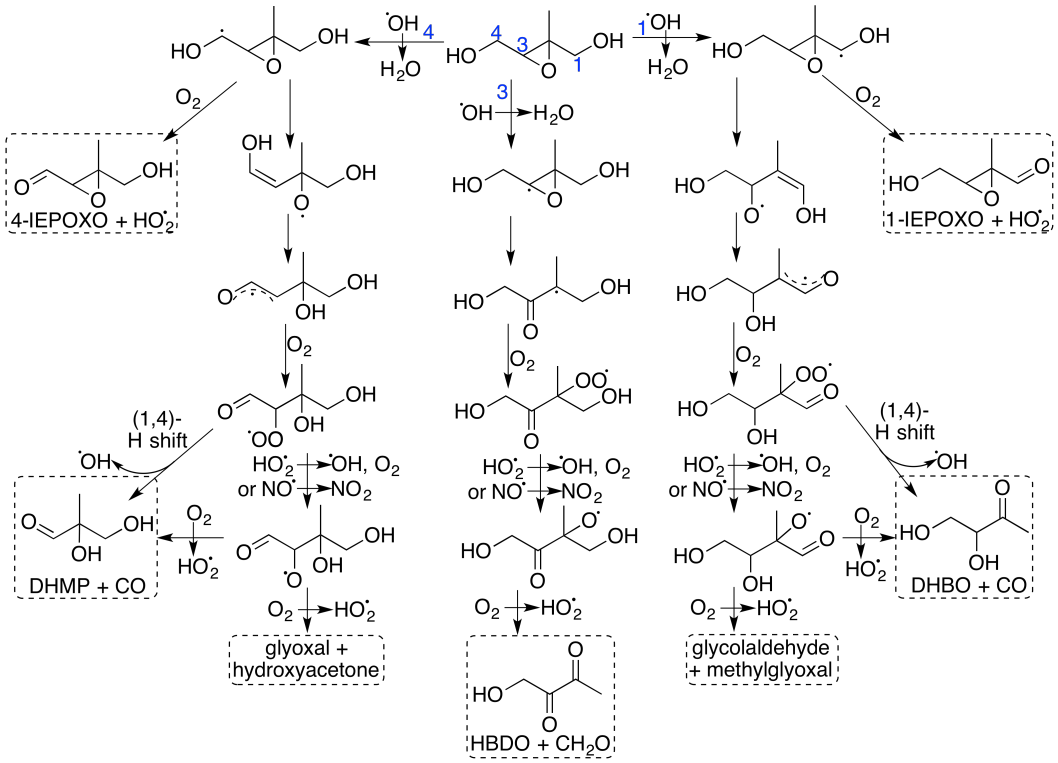

Figure 3.6: Steps in the OH-initiated oxidation of IEPOX. Stable products observed in this study are boxed. It is possible that HBDO may result from a slow (1,5)-H shift, forming HO_2 in addition to the boxed products, rather than from reaction with HO_2 or NO; similarly, though the aldehydic (1,4)-H shifts are predicted to occur quickly, the same products (CO, OH, and DHMP or DHBO) could be formed by reaction of the peroxy radicals with HO_2 or NO.

are not expected to form from IEPOX + OH by any known direct mechanism. Therefore, they were not included as products in this analysis.

Notably, five of the six major products of IEPOX + OH, accounting for ≥80% of the yield, are expected to recycle OH as a coproduct; only IEPOXO is not, though its coproduct of HO_2 still propagates the radical chain. This high recycling rate results from the intramolecular hydrogen shifts that allow for fragmentation of the IEPOX-peroxy radical before it can react with NO, HO_2, or other species present. While it is possible that the observed products could result from the reaction of IEPOX-peroxy radicals with other radical species, which would not cause such high OH recycling rates, the lack of dependence of product yields on [NO] suggests that intramolecular hydrogen shifts dominate the reaction pathways. If this is true, the first generation of IEPOX oxidation should not be considered oxidant-consuming, and may contribute to sustained high OH concentrations over remote forests.

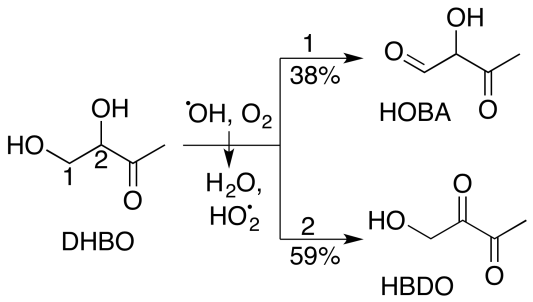

Figure 3.7: Anticipated products of DHBO + OH. Yields are calculated by SAR.

3.3.3 $C_4H_8O_3$ Oxidation Product Studies

Since DHBO was observed to be the highest yielding product from IEPOX + OH, and because it could be introduced in high quantity and purity to the chamber, experiments 17-18 were performed to examine the products of its oxidation by OH. The two experiments – one with and one without NO – were executed and analyzed in a manner identical to that of the IEPOX product yield experiments.

Because the α-hydroxy hydrogens of DHBO are expected to be most labile, the anticipated mechanism of DHBO + OH would involve H abstraction at carbons 1 or 2 (see numbering in Figure 3.7), followed by addition of O_2 and loss of HO_2 to convert one of the alcohols into a carbonyl group, as illustrated in Figure 3.7. The resulting $C_4H_6O_3$ compound would be detected by CIMS at *m/z* 187. By SAR (Kwok and Atkinson, 1995), abstraction at carbon 2 is estimated to account for 59% of OH reactivity, which would form the α-diketone HBDO, itself a direct product of IEPOX + OH as discussed above. Abstraction at carbon 1, accounting for 38% of OH reactivity, would form 2-hydroxy-3-oxobutanal (HOBA). CIMS sensitivities to these compounds, along with the analogous 2-hydroxy-2-methylpropanedial (HMPD) that would form from α-hydroxy hydrogen abstraction of DHMP, were estimated by the method described above, and are shown in Table 3.7 in the Supporting Information.

As expected, in experiments 17 and 18, compounds detected by CIMS at *m/z* 187 were the only major products observed from DHBO + OH. The combined yield of these compounds was estimated by taking a simple linear regression between the normalized CIMS counts at *m/z* 189 and *m/z* 187 over the first 15-30 minutes of oxidation, during which 5% of the DHBO was consumed. The resulting slope was scaled by a ratio of the compounds' estimated CIMS sensitivities; the CIMS sensitivity to the *m/z* 187 products was calculated as an average of the two products predicted above by SAR, weighted by their expected yields. Computed yields from

the two experiments were then averaged in a relative-inverse-variance-weighted mean to give a combined $C_4H_6O_3$ yield of (96 ±14)%, which is statistically indistinguishable from both the SAR results and a unity yield. Unfortunately, the $C_4H_6O_3$ products did not separate reliably on the GC-CIMS column, and a lack of synthetic standards prevented their identification, but the agreement of the combined yield with the SAR predictions suggests that the isomeric breakdown from SAR provides a reasonable estimate of individual HBDO and HOBA yields from DHBO.

Although the chain of gas phase IEPOX oxidation products could not be extended further in these experiments, some degree of conjecture on subsequent reactions may provide a useful framework for chemical models such as MCM and GEOS-Chem. A speculative oxidation mechanism, extending from the $C_4H_8O_3$ products of IEPOX to molecules already appearing in GEOS-Chem, can be found in Figure 3.8. This mechanism was compiled from SAR calculations, reactions already in the MCM, and analogy to previous work on similar pathways.

Due to the speculative nature of the proposed mechanism in Figure 3.8, it will only be considered briefly here. As discussed above, DHBO reacts with OH to form HBDO and HOBA. These two $C_4H_6O_3$ compounds can then react with OH as well, with rate coefficients estimated by SAR in Table 3.9 in the Supporting Information. HOBA + OH is expected to form an acylperoxy radical, which would then decompose or react with NO or HO_2 to form methylglyoxal and CO (perhaps through a peracid intermediate when reacting with HO_2). HBDO would most likely photolyze, as has been previously reported for α-diketones (Bouzidi *et al.*, 2014). Praske *et al.* (2015) measured a "loosely constrained" photolysis rate for HBDO of 1×10^{-5} s^{-1} (for laboratory J_{NO_2} of 2.5×10^{-3} s^{-1}). Photolysis of HBDO and subsequent reaction with O_2 would produce a peroxyacetyl radical (denoted MCO_3 in GEOS-Chem) and a hydroxyperacetyl radical, the latter of which is predicted in MCM to react with other radical species and fragment to form CO_2 and CH_2O. Both HOBA and HBDO could also react with OH to form a C_4 tricarbonyl, which would then rapidly photolyze or react with OH; the most likely products of this fragmentation would be CO and the peroxyacetyl radical. DHMP, the other $C_4H_8O_3$ product of IEPOX, is also expected to react with OH, forming either 2-hydroxy-2-methylpropanedial (HMPD) or a DHMP-acylperoxy radical. HMPD – the third $C_4H_6O_3$ compound in this mechanism, along with HBDO and HOBA – is itself expected to react with OH, with a rate coefficient estimated by SAR (Table 3.9 in the Supporting Information), eventually fragmenting to form methylglyoxal. The

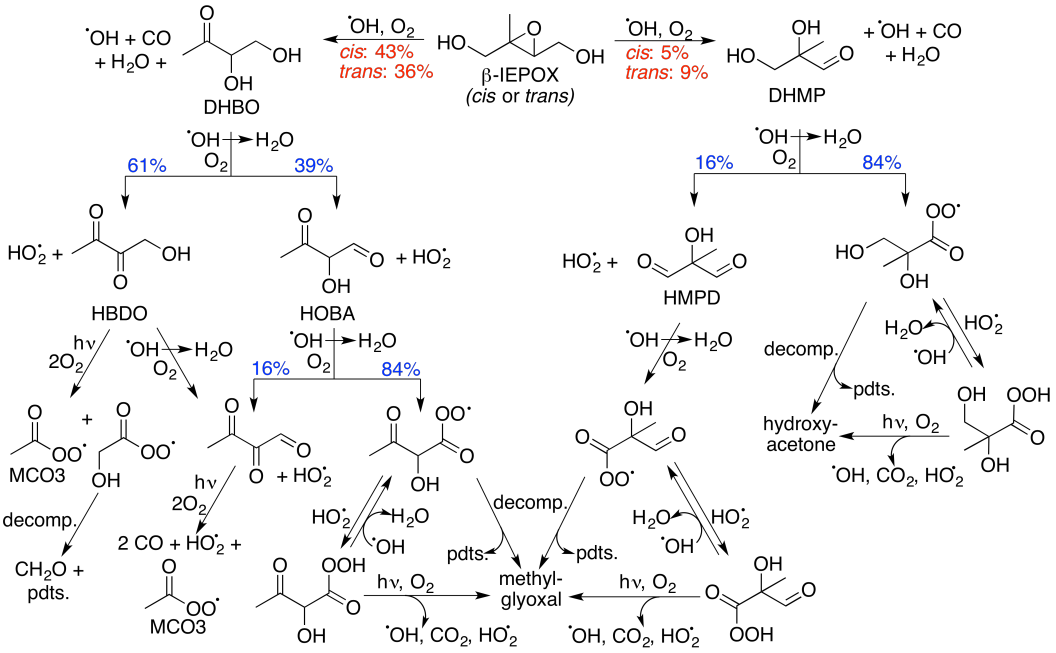

Figure 3.8: Anticipated steps in the OH-initiated of oxidation of DHBO and DHMP. Product yields in blue are calculated by SAR; those in red are measured in the present study. Reaction pathways of acylperoxy radicals labeled "decomp." may occur by a number of pathways (leading to various differing coproducts, labeled "pdts.") including: internal H shifts, producing OH and CO_2; fragmentation prior to O_2 addition to the alkyl radical, followed by reaction with O_2 to produce CO and HO_2; reaction with NO and O_2, producing NO_2, CO_2, and HO_2; reaction with RO_2 and O_2, producing RO, CO_2, and HO_2; or reaction with HO_2 and O_2, producing OH, O_2, CO_2, and HO_2. Stable products of reactions between organic radicals and NO_x (*e.g.*, peroxyacyl nitrates), while possible, are not shown in this mechanism.

DHMP-acylperoxy radical can decompose or react with NO or HO_2, eventually fragmenting to form hydroxyacetone.

A simplification of the mechanism in Figure 3.8 was incorporated into GEOS-Chem using the reactions in Table 3.8 in the Supporting Information for this study. While the mechanism may offer reasonable assumptions for chemical models of IEPOX oxidation, it should be stressed that the majority of reactions shown in Figure 3.8 are speculative. Further work is required to connect the observed first- and second-generation gas phase products of IEPOX + OH to the smaller compounds already incorporated into models, and to better constrain the radical recycling in these pathways.

3.3.4 GEOS-Chem Simulations

GEOS-Chem simulations were used to estimate the global effects of the chemistry explored in this work and to investigate where in the atmosphere it occurs. To the updated GEOS-Chem isoprene mechanism described above were added a number of new chemical species, including the two $C_4H_8O_3$ compounds observed to form from IEPOX + OH, the three $C_4H_6O_3$ isomers they produce, and the $C_5H_8O_3$ product of IEPOX + OH. Chemical reactions added to the GEOS-Chem model can be found in Table 3.8 in the Supporting Information. Wherever possible, these new reactions incorporated the measured rates and yields found in this work; for reactions lacking experimental verification, rates were estimated by SAR. Temperature dependences of rate coefficients were extrapolated from those of similar compounds existing in the GEOS-Chem mechanism. An additional simulation was run in which HBDO was allowed to photolyze, using the loosely constrained rate suggested by Praske *et al.* (2015); results unique to this simulation, which differs appreciably from the primary simulation only in its modeled concentrations of $C_4H_6O_3$ compounds, are shown in Figure 3.11 in the Supporting Information.

Simulated annual average mixing ratios of IEPOX, IEPOXO, $C_4H_8O_3$ compounds, and $C_4H_6O_3$ compounds in the lowest 1 km of the atmosphere are shown in Figure 3.9. As expected, simulated concentrations of IEPOX and its products are highly correlated. Maximum mixing ratios of $C_4H_8O_3$ compounds are seen in remote and heavily forested equatorial regions, including the Amazon and Congo Basins; in the latter, the $C_4H_8O_3$ mixing ratio reaches an annually averaged peak of 420 pptv in the lowest 1 km of the atmosphere. Mixing ratios of $C_4H_6O_3$ and IEPOXO are collocated with those of $C_4H_8O_3$, reaching maxima of 460 pptv and 70 pptv respectively in the Congo Basin. Seasonal average mixing ratios can be found in Figure 3.12 in the Supporting Information; as expected, simulated concentrations of IEPOX and its products increase over forests during the summer months. The inclusion of the $C_4H_8O_3$ and $C_4H_6O_3$ compounds and their coproducts and products in these simulations caused only minor (<3%) changes in tropospheric oxidant levels, as shown in Figure 3.13 in the Supporting Information, but the oxidant recycling in these and later steps of the mechanism is still largely unknown.

In addition to mixing ratios, GEOS-Chem can provide estimates of total annual production of selected compounds, which are listed in Table 3.5. From isoprene emissions of 515 Tg y^{-1}, the simulations performed here estimate that 352 Tg y^{-1} of ISOPOOH are produced, which go on to form 230 Tg y^{-1} of IEPOX. Further gen-

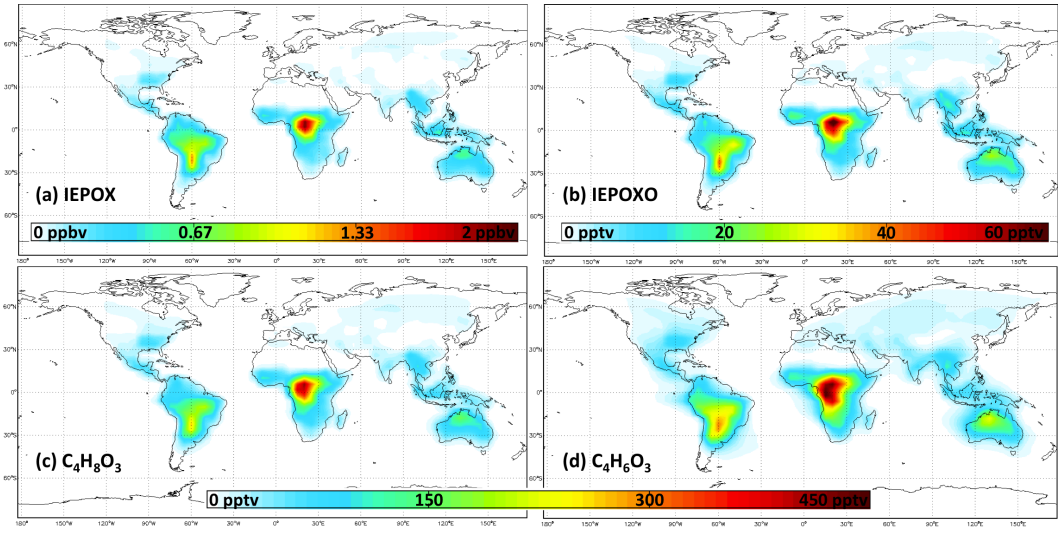

Figure 3.9: Annual average mixing ratios of IEPOX, IEPOXO, $C_4H_8O_3$ dihydroxycarbonyl compounds, and their $C_4H_6O_3$ products in the lowest 1 km of the atmosphere, as simulated using GEOS-Chem.

erations of oxidation from IEPOX then produce 54 Tg y^{-1} of $C_4H_8O_3$ compounds (84% DHBO, 16% DHMP), 51 Tg y^{-1} of $C_4H_6O_3$ compounds (49% HBDO, 31% HOBA, 20% HMPA), and 25 Tg y^{-1} of IEPOXO. Of the $C_4H_8O_3$ dihydroxycarbonyl compounds produced, 7% are estimated to be lost to deposition using the rates estimated by Nguyen *et al.* (2015a) and the rest to oxidation by OH. For all species investigated, approximately 80% of production occurs in the tropics (24 °S – 24 °N). While the low spatial resolution and simplification of certain reactions and processes in these GEOS-Chem simulations necessarily render estimated production and mixing ratios imprecise, the results shown here indicate that an appreciable fraction of isoprene reacts to form $C_4H_8O_3$ and $C_4H_6O_3$ compounds, and therefore imply that the subsequent chemistry of these compounds will impact local tropospheric oxidant and carbon budgets.

3.3.5 Field Observations

To evaluate the new IEPOX oxidation mechanism in an isoprene-rich environment, CIMS measurements obtained in Alabama during the summer of 2013 as part of the SOAS field campaign were analyzed. Figure 3.10 shows CIMS measurements at *m/z* 203 (ISOPOOH/IEPOX·CF_3O^-), *m/z* 189 ($C_4H_8O_3$·CF_3O^-), and *m/z* 187 ($C_4H_6O_3$·CF_3O^- or $C_5H_8O_2$·CF_3O^-) for a representative two weeks during the summer. While the CIMS was able to detect IEPOXO at *m/z* 201 ($C_5H_8O_3$·CF_3O^-) as well, isobaric interferences from isoprene hydroperoxy aldehydes, formed by a

	production (Tg y^{-1})					
compound(s)	total	northern hemisphere	southern hemisphere	tropics	northern extratropics	southern extratropics
ISOPOOH	351.8	147.9	203.9	295.7	30.7	25.5
IEPOX	230.0	100.1	129.9	187.6	23.4	19.1
$C_4H_8O_3$	53.5	23.0	30.5	41.9	6.1	5.5
$C_4H_6O_3$	51.4	22.0	29.5	39.7	6.0	5.7
IEPOXO	25.3	10.9	14.4	19.8	2.9	2.6

Table 3.5: Annual global production of compounds in the low-NO oxidation mechanism of isoprene, as simulated with GEOS-Chem.

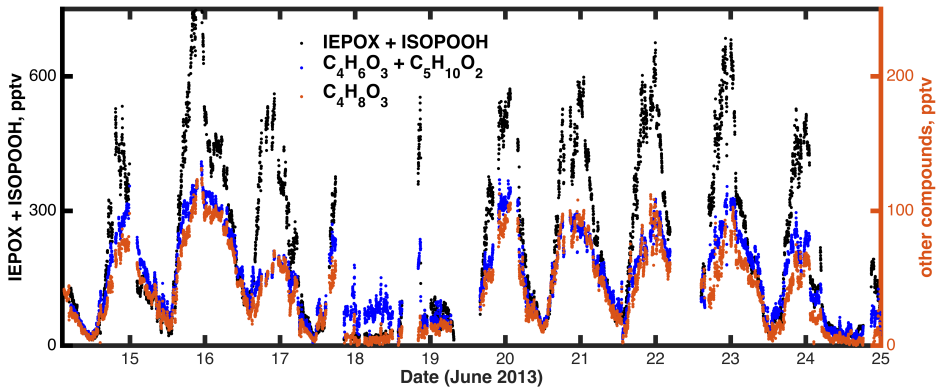

Figure 3.10: CIMS measurements of selected compounds in the low-NO oxidation pathway of isoprene during a section of the SOAS field campaign in Centreville, Alabama.

different oxidation mechanism, prevented the detailed analysis of IEPOXO in these field measurements (Crounse *et al.*, 2011).

All three masses displayed in Figure 3.10 show appreciable atmospheric loading throughout the summer, peaking at daytime averages of ~600 pptv of ISOPOOH + IEPOX and ~100 pptv apiece of $C_4H_8O_3$ and $C_4H_6O_3$. Furthermore, signals at the three masses have a remarkably high correlation, indicative either of coemission from a single source or of coproduction as part of the same mechanism. The results of both simple and error-weighted (York *et al.*, 2004) linear regressions between product masses and those of their putative progenitors are shown in Table 3.6. $C_4H_8O_3$ and $C_4H_6O_3$ show high correlations with ISOPOOH + IEPOX (r^2 = 0.83 and 0.81 respectively) and no indication of separate slopes from interfering isobaric species. While methylbutene diols ($C_5H_8O_2$) produced from isoprene nitrates might be expected to interfere with the signal of isobaric $C_4H_6O_3$ compounds, the low

	ratios			goodness of fit	
ratio	error-weighted regression	simple linear regression	GEOS-Chem	σ_{slope}, error-weighted regression	r^2, simple linear regression
$C_4H_8O_3/C_5H_{10}O_3$	0.16	0.15	0.18	0.006	0.83
$C_4H_6O_3/C_5H_{10}O_3$	0.16	0.16	0.121	0.006	0.81
$C_4H_6O_3/C_4H_8O_3$	1.04	1.00	1.20	0.006	0.92

Table 3.6: Ratios between concentrations of compounds in the low-NO oxidation mechanism of isoprene, as measured during SOAS and simulated using GEOS-Chem.

correlation between isoprene nitrates and *m/z* 187 (r^2 = 0.42; see Figure 3.14 in the Supporting Information) suggests that $C_4H_6O_3$ dominates the *m/z* 187 signal. $C_4H_8O_3$ and $C_4H_6O_3$ also correlate exceptionally well with each other (r^2 = 0.92), as shown in Figure 3.15 in the Supporting Information. That the slope between the two compounds' concentrations is so nearly unity may simply be an impressive coincidence, considering that it conflates both their respective yields and their oxidation and photolysis rates, which are unlikely to be equal.

To further explore the relationships between the low-NO products of isoprene oxidation, the product ratios measured during SOAS were compared to the results of the GEOS-Chem simulations discussed above. The relevant GEOS-Chem results were selected as the average summertime (June 21 – September 22, 2012) mixing ratios in the lowest 1 km of the atmosphere over the grid box containing the Alabama field site; the relevant ratios of these concentrations are listed in column five of Table 3.6. The newly implemented GEOS-Chem mechanism effectively captures the ratios of $C_4H_8O_3$ and $C_4H_6O_3$ to ISOPOOH + IEPOX, overpredicting them by only 13% and 31% respectively. The GEOS-Chem simulation including HBDO photolysis underpredicts the ratio of $C_4H_6O_3$ to ISOPOOH + IEPOX by 56%; however, because of the isobaric interference of $C_5H_8O_2$ with $C_4H_6O_3$ in the SOAS data, this underprediction may not be as severe as it seems. The general agreement between GEOS-Chem results and field observations implies that, despite the gaps remaining in our understanding of the low-NO gas phase oxidation pathways of isoprene, the mechanism presented herein can adequately represent the $C_4H_8O_3$ and $C_4H_6O_3$ generations of products.

3.4 Conclusions

Despite the importance of IEPOX as a product of isoprene oxidation, as evidenced by its simulated annual production of 230 Tg y^{-1} and observed daytime mixing ratios of ~600 pptv, its fate in the atmosphere remains poorly constrained. Many studies have focused on its reactive partitioning into particles, identifying a number of factors influencing its rate of uptake, but when active sites on particles are low in isoprene-rich environments, IEPOX loss is likely dominated by reaction with OH in the gas phase, with deposition and particle uptake contributing to a lesser extent. While the rates of reactions between OH and IEPOX isomers have been described previously, disagreement persists as to the reactions' products, and the lack of authentic standards in prior product studies precluded the differentiation of isobaric species.

This study has significantly reduced uncertainties in the gas phase oxidation mechanism of IEPOX, both in the first and second generations. Using synthetic standards, DHBO was conclusively identified as the major product of both *cis*- and *trans*-β-IEPOX + OH, while the isobaric DHMP was found to be a relatively minor coproduct. Both DHBO and DHMP were then reacted with OH, along with a third $C_4H_8O_3$ isomer, to examine their rates of oxidation, and the products of DHBO + OH were discussed. Finally, GEOS-Chem modeling and field observations revealed that the $C_4H_8O_3$ isomers and their $C_4H_6O_3$ products contribute substantially to total concentrations of volatile organic compounds (VOCs) in isoprene-rich, low-NO environments.

While this study marks the first laboratory investigation of $C_4H_8O_3$ dihydroxycarbonyls in the gas phase, and their first conclusive isomeric identification from atmospheric precursors, it should not be the last; considering their noted importance as oxidation products of isoprene, continued study of the $C_4H_8O_3$ isomers is warranted to further elucidate their oxidation pathways and determine whether they or their products contribute to SOA creation, tropospheric oxidant budgets, or the formation of other important VOCs. Deposition rates of the $C_4H_8O_3$ and $C_4H_6O_3$ compounds have already been measured at SOAS (Nguyen *et al.*, 2015a), but additional observation of $C_4H_8O_3$ dihydroxycarbonyls in the ambient atmosphere will help to constrain the fate of IEPOX and quantify the relative rates of its reaction with OH versus uptake to particles. Finally, incorporation of the $C_4H_8O_3$ compounds, their products, and the updated mechanisms proposed in this study into chemical models such as MCM and GEOS-Chem may improve the models' ability

to replicate VOC and oxidant budgets in isoprene-rich environments, particularly once further work has been done to solidify the $C_4H_8O_3$ compounds' complete oxidative mechanisms.

3.5 Supporting Information

compound	dipole (D)	polarizability (Å^3)	sensitivity
trans-β-IEPOX	2.47	8.98	0.371
cis-β-IEPOX	1.00	9.01	0.231
IEPOXO	1.93	8.57	0.303
DHBO	2.35	7.49	0.358
DHMP	2.09	7.52	0.331
DHBA	2.22	8.69	0.353
HBDO	2.14	7.22	0.335
HMPD	1.00	8.35	0.233
HOBA	1.08	7.27	0.228

Table 3.7: Estimated CIMS sensitivities (in normalized counts per ppbv in the inlet flow), along with their constituent parameters, for species relevant to this study.

The dipole and polarizability of the molecules are calculated with use of density functional theory at the B3LYP level, with the basis sets: 6-31G(d), 6-31+G(d) or ccpVTZ. The sensitivity is related to the relative collision rate and depends mostly on the dipole moment of the molecule colliding with the ion. The dipole moments listed in Table 3.7 are the dipole moment averaged over the possible conformers with a Boltzmann abundance larger than 0.1%. The polarizability is similar for different conformers, and the collision rate has a weak dependence on the polarizability, and is thus only calculated for the lowest energy conformer. The calculated sensitivities are estimated to have an error of less than 10%.

reactants	products	rate coefficient $k = A \times e^{r/T}$		reference
		A	r	
$RIO_2 + HO_2$	$0.629\times$(1,2)-ISOPOOH + $0.272\times$(4,3)-ISOPOOH + $0.037\times\delta$-ISOPOOH + $0.063\times(OH + HO_2 + CH_2O) + 0.025\times$MACR + $0.038\times$MVK	2.06×10^{-13}	1300	1
(1,2)-ISOPOOH + OH	$0.75\times RIO_2 + 0.25\times HC_5OO + 0.125\times(OH + HO_2)$	6.13×10^{-12}	200	1
(1,2)-ISOPOOH + OH	$0.85\times OH + 0.15\times HC_5OO + 0.578\times$*trans*-$\beta$-IEPOX + $0.272\times$*cis*-β-IEPOX	1.70×10^{-11}	390	1
(4,3)-ISOPOOH + OH	$0.48\times RIO_2 + 0.52\times HC_5OO + 0.26\times(OH + HO_2)$	4.14×10^{-12}	200	1
(4,3)-ISOPOOH + OH	$OH + 0.68\times$*trans*-β-IEPOX + $0.32\times$*cis*-β-IEPOX	2.97×10^{-11}	390	1
δ-ISOPOOH + OH	$0.25\times RIO_2 + 0.75\times HC_5OO + 0.375\times(OH + HO_2)$	5.11×10^{-12}	200	1
δ-ISOPOOH + OH	$0.5\times(OH + \delta$-IEPOX + $HC_5OO)$	2.92×10^{-11}	390	1
trans-β-IEPOX + OH	$0.83\times OH + 0.45\times CO + 0.36\times$DHBO + $0.09\times$DHMP + $0.08\times(HBDO + CH_2O) + 0.17\times(IEPOXO + HO_2) + 0.16\times(HAC + GLYX) + 0.14\times(GLYC + MGLY)$	3.73×10^{-11}	-400	2
cis-β-IEPOX + OH	$0.8\times OH + 0.48\times CO + 0.43\times$DHBO + $0.05\times$DHMP + $0.08\times(HBDO + CH_2O) + 0.2\times(IEPOXO + HO_2) + 0.08\times(HAC + GLYX) + 0.16\times(GLYC + MGLY)$	5.79×10^{-11}	-400	2
δ-IEPOX + OH	$0.6\times$IEPOXDOO + $0.4\times(IEPOXO + HO_2)$	3.20×10^{-11}	-400	2, 3, 4
IEPOXO + OH	$OH + 1.5\times CO + 0.5\times(CH_2O + MGLY + HAC)$	9.85×10^{-12}	410	3, 4, 5
IEPOXDOO + HO_2	$HAC + GLYC + HO_2 + OH$	2.06×10^{-13}	1300	3, 4
IEPOXDOO + NO	$HAC + GLYC + HO_2 + NO_2$	2.70×10^{-12}	350	3, 4
DHBO + OH	$HO_2 + 0.609\times$HBDO + $0.391\times$HOBA	8.70×10^{-12}	70	this work
DHMP + OH	$0.838\times(HAC + CO_2 + OH) + 0.162\times(HMPD + HO_2)$	7.49×10^{-12}	410	this work
DHBA + OH	$1.528\times CO_2 + 0.764\times(ALD_2 + OH) + 0.236\times(HOBA + HO_2)$	9.38×10^{-12}	410	this work
HBDO + OH	$2\times CO + MCO_3 + HO_2$	2.13×10^{-12}	70	4, 5
HMPD + OH	$MGLY + CO_2 + OH$	1.06×10^{-11}	410	4, 5
HOBA + OH	$MGLY + CO_2 + OH$	6.27×10^{-12}	410	4, 5

Table 3.8: Reactions in the low-NO isoprene oxidation pathway edited or added to GEOS-Chem for the simulations performed in this study. Standard GEOS-Chem notation is used for product abbreviations. References listed include [1](St. Clair *et al.*, 2015), [2](Bates *et al.*, 2014), [3](Jacobs *et al.*, 2013), [4](Saunders *et al.*, 2003), and [5](Kwok and Atkinson, 1995).

	k_{OH} (10^{-11} cm^3 molec^{-1} s^{-1})	
compound	MCM	SAR
HBDO	0.27	0.27
HMPD	13.2	4.18
HOBA	2.45	2.48

Table 3.9: Rate coefficients for the reactions of $C_4H_6O_3$ hydroxydicarbonyl compounds with OH, as used in the Master Chemical Mechanism v3.2 (MCM) (Saunders *et al.*, 2003) and calculated by structure-activity relationship (SAR) (Kwok and Atkinson, 1995).

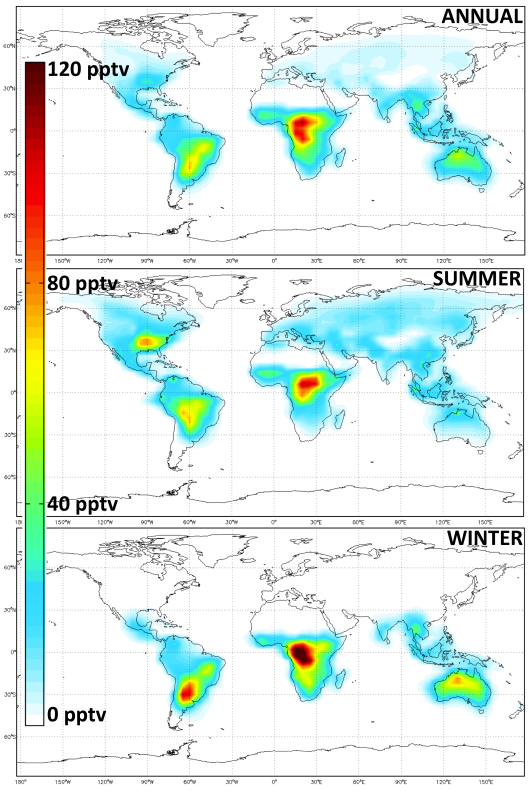

Figure 3.11: Annual and seasonal average mixing ratios of $C_4H_6O_3$ dihydroxycarbonyl compounds in the lowest 1 km of the atmosphere, as simulated using GEOS-Chem and including photolysis of HBDO.

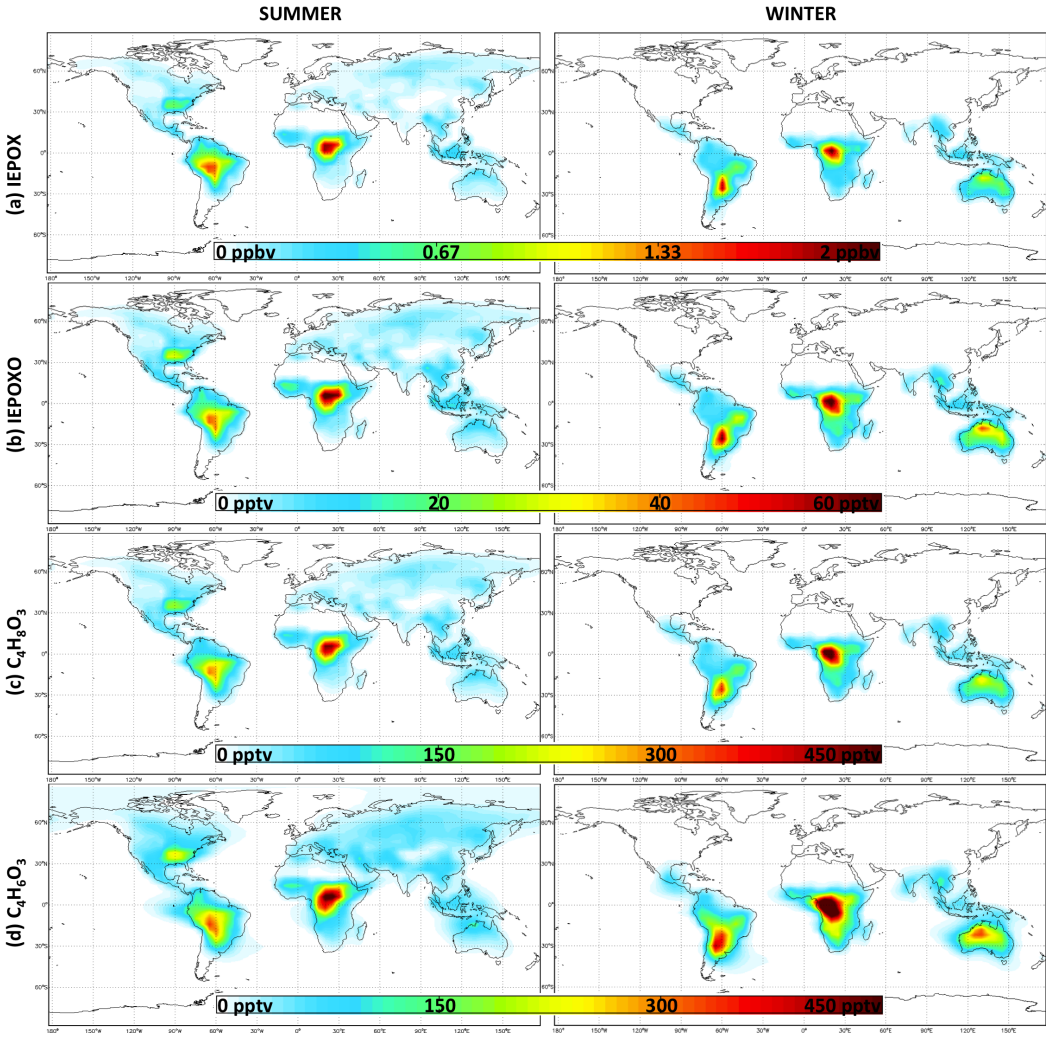

Figure 3.12: Seasonal average mixing ratios of IEPOX, IEPOXO, $C_4H_8O_3$ dihydroxycarbonyl compounds, and their $C_4H_6O_3$ products in the lowest 1 km of the atmosphere, as simulated using GEOS-Chem.

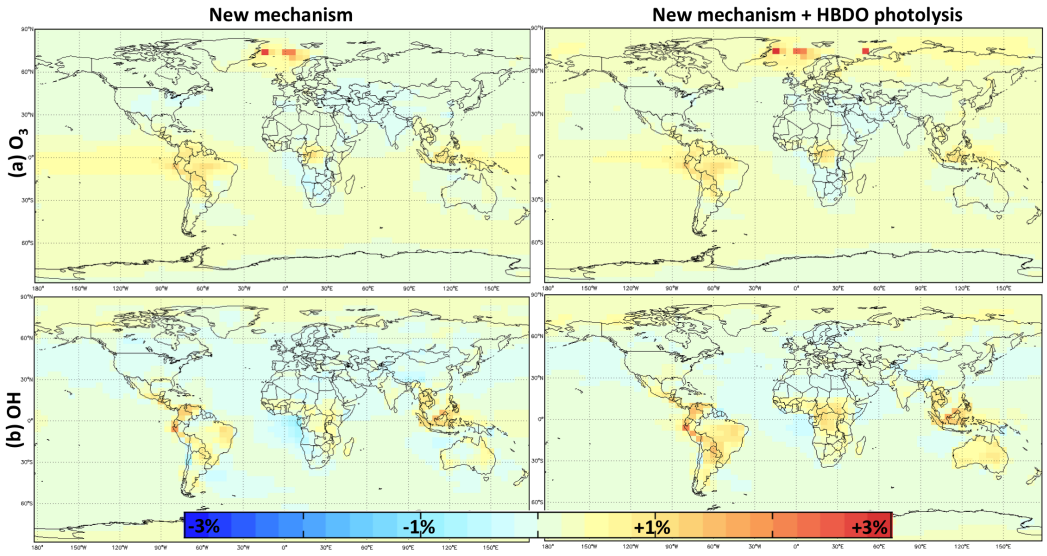

Figure 3.13: Percent changes in annual average OH and O_3 mixing ratios in the lowest 1 km of the atmosphere caused by the inclusion of the $C_4H_8O_3$ and $C_4H_6O_3$ compounds and their coproducts and products, as compared with a mechanism using the products of IEPOX + OH originally included in GEOS-Chem v.9-02 (Paulot *et al.*, 2009b).

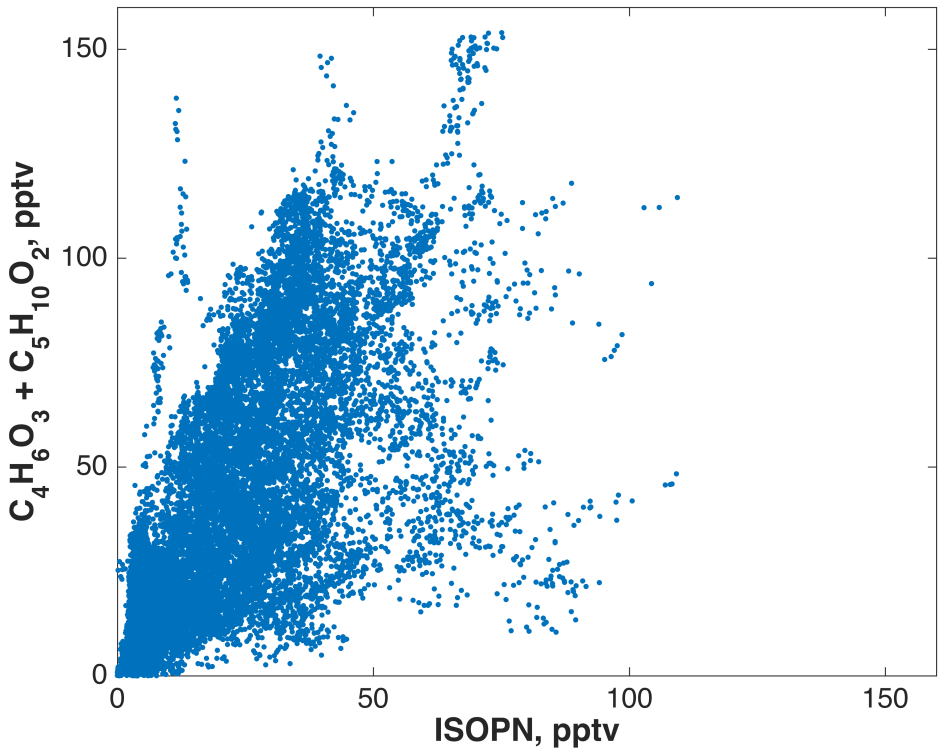

Figure 3.14: Correlation between isoprene nitrates and $C_4H_6O_3$ + $C_5H_{10}O_2$ during the entire SOAS campaign.

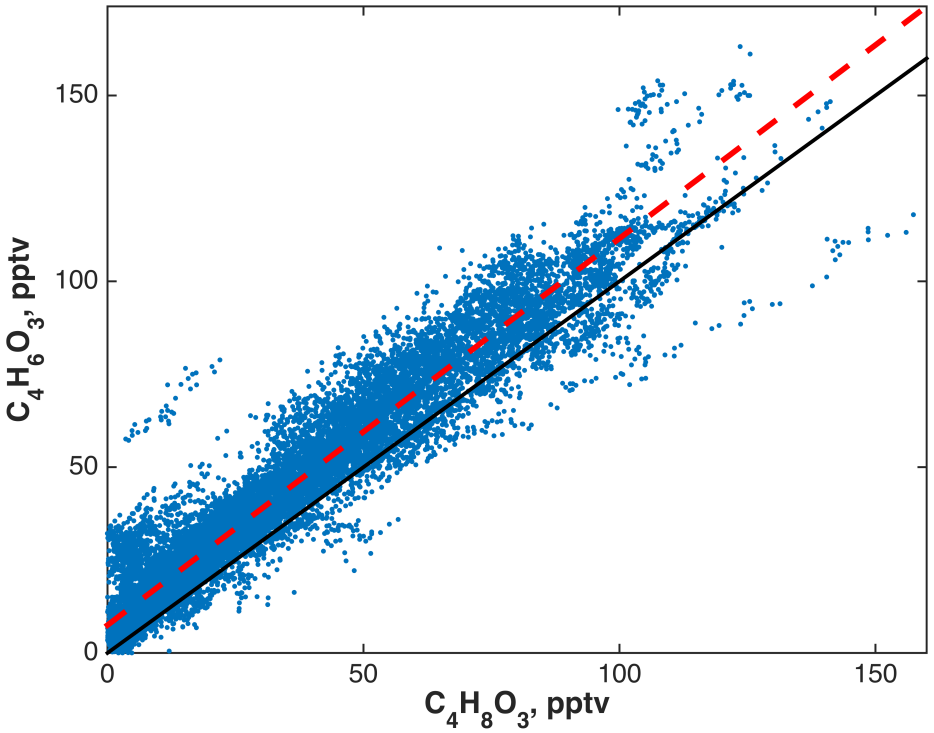

Figure 3.15: Correlation between $C_4H_8O_3$ and $C_4H_6O_3$ during the entire SOAS campaign, overlaid with a line of best fit (red, dashed; r^2 = 0.92) and a 1:1 line (black, solid).

Chapter 4

THE GAS-PHASE OXIDATION OF ISOPRENE AND ITS FIRST-GENERATION PRODUCTS

Abstract

The gas-phase oxidation of isoprene and its major oxidation products are described in detail. The mechanism is developed with the aim of both providing accurate simulations of the impact of isoprene emissions on HO_x and NO_x free radical concentrations and to produce realistic representation of the yields of products known to be involved in condensed phase processes. The schemes presented represent a synthesis of recent laboratory studies at the California Institute of Technology and elsewhere that have provided a new wealth of detail on the mechanisms at play. Insights from new theoretical approaches are also incorporated. Finally, we present a reduced mechanism appropriate for implementation in chemical transport models that retains the essential chemistry required to accurately simulate this chemistry under the typical conditions where isoprene is emitted and oxidized in the atmosphere.

4.1 Introduction

Volatile organic compounds (VOCs) emitted from vegetation significantly impact atmospheric photochemistry. This biogenic carbon flux is dominated by a single compound, isoprene (C_5H_8, 2-methyl-1,3-butadiene). The global budget of isoprene has been estimated by several approaches (Müller *et al.*, 2008; Wang and Shallcross, 2000), typically constrained using surface flux measurements (Guenther and Hills, 1998; Wiedinmyer *et al.*, 2004) and/or satellite observations (Shim *et al.*, 2005). Estimates do not significantly vary between different approaches. The most up-to-date modeling framework suggests that, at roughly 500 Tg y^{-1}, the emissions of isoprene alone comprise about half the total biogenic emissions of non-methane VOCs worldwide (Guenther *et al.*, 2012). This emission originates from a broad taxonomic distribution of plants (*e.g.*, mosses, ferns, and trees).

The majority of isoprene's massive flux originates from a light-dependent *de novo* synthesis in plants using carbon from the Calvin cycle; dark production from microorganisms, plants, and animals is only a minor contribution (Sharkey, 1996). The question of why leaves emit isoprene is more complex. A recent unified hypothesis

suggests that isoprene is synthesized in plant tissue to mitigate the compounded effects from several environmental stress factors that produce reactive oxygen species *in vivo* (Vickers *et al.*, 2009), *e.g.*, extreme temperatures, high light, water deficiency, soil salinity, air pollution, and mechanical damage.

Following biosynthesis, isoprene is lost to the atmosphere through stomata and does not significantly accumulate in the leaves (Fall and Monson, 1992). As a result, nearly the entire flux of isoprene occurs during daytime (Loreto and Sharkey, 1990; Monson and Fall, 1989). Further information on the biogenesis of isoprene and historical context of studies is provided by a number of reviews (Kuzuyama and Seto, 2003; Monson *et al.*, 2012; Sanadze, 2004; Sharkey *et al.*, 2008; Sharkey and Yeh, 2001). Here, we focus on isoprene's atmospheric reactions and those of its immediate oxidation products.

As a five carbon conjugated diene, isoprene reacts rapidly with atmospheric oxidants. The high reactivity of isoprene limits its accumulation in the atmosphere, such that despite its large flux, only moderate mixing ratios are observed (0 - 10 ppbv) (Kuhlmann *et al.*, 2004). Under typical atmospheric daytime conditions, the reactive conversion of isoprene into more oxidized VOCs (OVOCs) occurs with a time constant of approximately 1 - 2 h (Atkinson and Arey, 2003b). Reaction with the hydroxyl radical (OH) is the dominant sink (τ_{OH} = 1.25 h, [OH]= 2×10^6 molec cm^{-3}), followed by ozone (O_3) (τ_{O_3} = 17 h, [O_3] = 50 ppbv), the nitrate radical (NO_3) (τ_{NO_3} = 16 h, [NO_3] = 1 pptv), and the chlorine radical (Cl) (τ_{Cl} = 29 d, [Cl] = 1×10^3 molec cm^{-3}). Because isoprene emissions peak in the daytime, and NO_3 radical concentrations peak in the nighttime, oxidation by ozone is generally a larger sink for isoprene than by the nitrate radical. Nevertheless, nitrate radical chemistry is an important source of organic nitrates and formation of these nitrates can represent a major pathway for loss of NO_x from the atmosphere (Horowitz *et al.*, 2007; Paulot *et al.*, 2012) with significant impacts on [OH] and O_3 formation (Dunker *et al.*, 2016; Squire *et al.*, 2015; Travis *et al.*, 2016).

The large flux and rapid oxidation of isoprene conspire to make its chemistry, and the chemistry of the associated products, of high global importance. The reactions have broad implications for regional air quality (Chameides *et al.*, 1988; Squire *et al.*, 2015; Trainer *et al.*, 1987) and global climate (Kanakidou *et al.*, 2005). For example, isoprene chemistry significantly affects tropospheric ozone production by perturbing the NO_x cycle (NO + NO_2; Atkinson, 2000), the rate of oxidation of many compounds by impacting HO_x (OH + HO_2; Lelieveld *et al.*, 2008; Peeters *et al.*,

2009), and the Earth's radiative balance and human health through the production of secondary organic aerosols (SOA; Carlton *et al.*, 2009; Claeys *et al.*, 2004). In addition, the precise impact of isoprene chemistry depends on the environment in which it is oxidized. In particular, the levels of anthropogenically emitted pollutants such as NO_x and SO_x will affect the oxidation pathways of isoprene and its oxidation products.

Quantification of isoprene's global impacts by atmospheric chemical transport models (CTMs) requires, at minimum, an accurate description of oxidation mechanisms and VOC emission fields (Carter, 1996; Dodge, 2000; Mao *et al.*, 2013; Paulot *et al.*, 2012; Zimmermann and Poppe, 1996). Over the past ten years, renewed experimental and theoretical efforts in elucidating the detailed photochemical and dark oxidation mechanisms of isoprene have advanced our understanding of the chemistry substantially (references herein). However, there are still large gaps in our knowledge that preclude the inclusion of an accurate description of isoprene chemistry into CTMs. These lingering kinetic and mechanistic uncertainties translate to uncertainties in the simulations of global air quality and climate feedbacks. In the spirit of past reviews on the isoprene oxidation mechanism (Fan and Zhang, 2004; Jenkin *et al.*, 2015; Paulson and Seinfeld, 1992; Pöschl *et al.*, 2000; Saunders *et al.*, 2003), this work seeks to allay such uncertainties by compiling a state-of-the-science mechanism from recent experimental work, with a particular focus on recent results from the Caltech laboratories.

4.2 Mechanism development

This work has three primary goals: (1) to organize the results of recent mechanistic studies undertaken at the California Institute of Technology (hereafter "Caltech") and other laboratories and to place them within the context of current knowledge on the dark and photochemical reactions of isoprene; (2) to provide a recommendation for an explicit and comprehensive mechanism describing the atmospheric reactions of isoprene for use in detailed chemical models; and (3) to synthesize a condensed mechanism that adequately captures the primary features of the isoprene chemistry but with a footprint small enough to be implemented in global CTMs. In order to make our mechanisms widely relevant to CTMs and other broad applications within atmospheric chemistry, we prioritize retaining carbon balance and providing accurate representations of isoprene's impact on HO_x and NO_x free radical concentrations, as well as the formation of products that may contribute to organic aerosol formation.

The following sections proceed systematically through the steps of isoprene oxidation, detailing recent advances in the measurements of reaction rates and product yields. As oxidation by OH accounts for ~90% of isoprene's atmospheric fate and has been the focus of most recent experimental studies at Caltech and elsewhere, we provide the greatest detail on the first (Section 4.3) and second (Section 4.7) generations of this chemistry. In our mechanism, we attempt to provide reaction recommendations for all products formed in >1% overall yield from isoprene in typical atmospheric conditions, with the exception of ubiquitous fragmentation products (*e.g.* hydroxyacetone, glyoxal, CH_2O), for which we defer to previous recommendations. We also provide a detailed description and mechanism for the chemistry following isoprene's oxidation by NO_3 (Sections 4.5 and 4.7.5), which has recently been elucidated in multiple studies. While we include descriptions of isoprene's oxidation by ozone (Section 4.4) and chlorine (Section 4.6), we only provide a cursory treatment of the ozone chemistry in our explicit mechanism, and we omit chlorine chemistry altogether.

Our full mechanism recommendations are illustrated in each section's corresponding figures, with yields reported at 298 K and 1 atm, and recommendations for the condensed mechanism are described in the figure captions. More detailed treatments of the reactions can be found in the Supplemental Information, where the full and reduced mechanisms are made available as computer-readable codes for communal use and development. Further description of the codes and the model formulation can be found in Section 4.8. To denote the positions of isoprene's reactions and substituents in the figures and text, we assign numbers to the carbons of isoprene as follows: carbons 1-4 comprise the conjugated butadiene backbone, with the methyl substituent (carbon 5) connected to carbon 2 of the backbone. Throughout the text, we refer to these carbons as "C#" without subscripts (*e.g.* "C2"); subscripted numbers (*e.g.* "C_2") are used instead to refer to fragmentation products containing a specific number of carbon atoms.

Generally, while the full mechanism treats all isomers of isoprene's oxidation products separately if they are known to have different subsequent reaction rates and products, the condensed mechanism makes use of isomer grouping (*e.g.* "δ-hydroxynitrate" to represent *E*-1-OH,4-ONO_2-, *Z*-1-OH,4-ONO_2-, *E*-1-ONO_2,4-OH-, and *Z*-1-ONO_2,4-OH-hydroxynitrates) to minimize the number of species and reactions included in the mechanism while retaining an accurate description of the oxidative fate of those grouped species. The condensed mechanism also

uses a steady-state approximation for the initial isoprene-hydroxy-peroxy radical distribution, enabling the removal of many intermediate species and reactions. The mechanism is further reduced by ignoring some particularly minor pathways (<2% branching ratio) of later-generation reactions. The condensed mechanism thus includes 105 compounds and 285 reactions, compared to the 330 compounds and 812 reactions included in the full mechanism.

Our recommended reaction rate coefficients, including their temperature dependences, and product yields are described in the following sections. Those that are not directly addressed are either taken from IUPAC recommendations or MCM v.3.3.1 (Jenkin *et al.*, 2015), or, when no experimental data have previously been reported in the literature, extrapolated from analogous reactions. For some classes of reactions we use a single generic rate parameterization. For example, the overall rates of reactions between NO and RO_2 (excluding acyl peroxy radicals) have been shown not to vary significantly with the structure of the peroxy radical (Miller *et al.*, 2004); we therefore use a single temperature-dependent rate coefficient formula for all non-acyl peroxy radical + NO reactions in our mechanism:

$$k_{RO_2+NO} = 2.7 \times 10^{-12} \times exp(350/T) cm^3 molec^{-1} s^{-1} \quad (4.1)$$

Accurate simulation of organic nitrate formation in these reactions is essential for properly describing the influence of isoprene chemistry on NO_x, and therefore ozone formation as well (Dunker *et al.*, 2016; Squire *et al.*, 2015). These nitrates are produced *via* the reaction of RO_2 with NO and *via* nitrate radical addition to alkenes. Because different isomers of the same compound have significantly different subsequent chemistry, it is also necessary to capture the distribution of isomers formed correctly.

The yields of organic nitrates from reaction of NO with individual peroxy radicals are complicated functions of pressure, temperature, molecular size and structure. While it is not possible to encompass this diversity in a simple set of rules, we take as a starting point the parameterization developed by Arey *et al.* (2001) for the temperature, pressure, and molecular size dependent yields of organic nitrates, which is derived from earlier formulations by Carter and Atkinson (1985) and Carter and Atkinson (1989). Arey *et al.* (2001) constrained their parameterization with data only for simple alkanes. As with the HO_2 chemistry, we modify their approach to use the sum of all heavy atoms rather than just carbon, consistent with the recommendation of Teng *et al.* (2015), who measured the hydroxynitrate yields

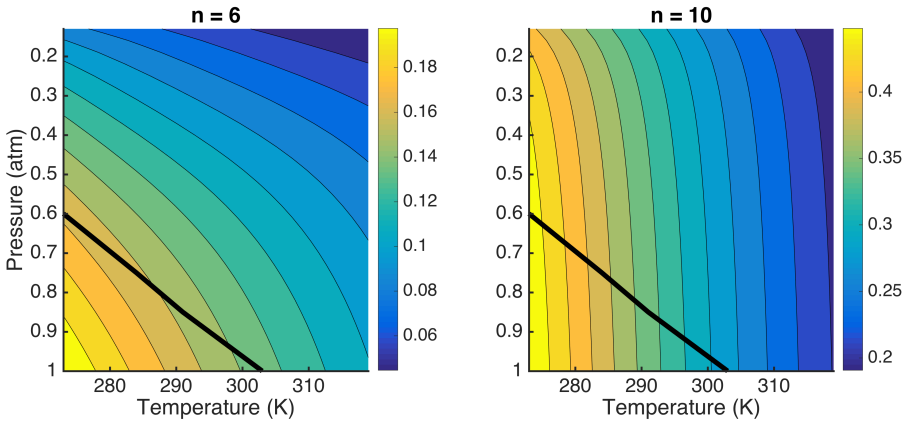

Figure 4.1: Nitrate yield (α, on color scales) as a function of temperature and pressure for a peroxy radical with n (= the number of non-hydrogen atoms, not including the peroxy moiety) = 6 (left) and n = 10 (right), using the parameterization in Equations 4.2-4.4. The thick black lines show typical altitude profiles of temperature and pressure over a tropical continent.

(α) from a variety of alkenes at 293 K and 993 hPa to derive the formula:

$$\alpha_{RONO_2}(n) = \frac{k_{RO_2+NO\rightarrow RONO_2}}{k_{RO_2+NO,total}} = (0.045 \pm 0.016) \times n - (0.11 \pm 0.05) \qquad (4.2)$$

where n again represents the number of heavy atoms excluding the peroxy moiety. Taking this formula as a baseline yield (α_0), we add the temperature and pressure dependence from Arey *et al.* (2001) to derive the following parameterization:

$$\alpha_{RONO_2}(T, P, n) = \frac{A(T, P, n)}{A(T, P, n) + A_0(n) \times \frac{1-\alpha_0}{\alpha_0}} \qquad (4.3)$$

where $A_0(n) = A$(293 K, 993 hPa, n), and A(T,P,n) is given by the Arey *et al.* (2001) formula:

$$A = \frac{\gamma \times e^n \times [M]}{1 + \frac{\gamma \times e^n \times [M]}{0.43 \times (T/298)^{-8}}} \times 0.41^{(1+[log(\frac{\gamma \times e^n \times [M]}{0.43 \times (T/298)^{-8}})]^2)^{-1}} \qquad (4.4)$$

where $\gamma = 2 \times 10^{-22}$ cm^3 molec^{-1}, [M] is the number density of air (molec cm^{-3}), and n is again the number of heavy atoms excluding the peroxy moiety. The pressure and temperature dependences of the nitrate yield resulting from this parameterization are shown in Figure 4.1 for n = 6 and n = 10.

Laboratory measurements of the nitrate yields for multifunctional compounds often fall below this recommendation, likely reflecting a shorter lifetime for the OONO group. In our mechanism, we use insight gleaned from these studies to modify Equation 4.3 to account for molecular structure. For example, we reduce

nitrate yields from primary peroxy radicals by 50%, following substantial experimental evidence (Arey *et al.*, 2001; Carter and Atkinson, 1985, 1989; Teng *et al.*, 2015), and increase those from tertiary peroxy radicals by 50%, following studies by Teng *et al.* (2015). Additionally, we reduce by 90% the nitrate yields from reactions of β-carbonyl peroxy radicals + NO, following insights from observed nitrate yields of MVK and MACR (Praske *et al.*, 2015); we similarly reduce nitrate yields from β-hydroxy, β-hydroperoxy, and β-nitrooxy peroxy radicals by 30%, 60%, and 90%, although we note that these adjustments are poorly constrained, and further experimental evidence could substantially improve this parameterization.

Where laboratory measurements of nitrate yields have been made, these are explicitly noted, and are used in place of the formula described above. Finally, for many of the larger peroxy radicals considered here, the pressure and temperature dependence of the yields largely compensate so that the yield calculated using the modified Arey approach at conditions throughout the lower atmosphere is not significantly different than the yield at the surface (Figure 4.1).

Reactions of RO_2 with HO_2 have been shown to follow a simple pattern that depends both on temperature and the number of carbon atoms in the peroxy radical (Jenkin *et al.*, 1997; Saunders *et al.*, 2003):

$$k_{RO_2+HO_2} = 2.91 \times 10^{-13} \times exp(1300/T) \times [1 - exp(-0.245 \times n)] cm^3 molec^{-1} s^{-1} \quad (4.5)$$

where n represents the number of carbon atoms in the peroxy radical molecule. We suggest, similarly to the organic nitrate yield parameterization, that n should be the number of heavy (non-hydrogen) atoms other than the peroxy moiety – not just carbon. Refitting the HO_2 + RO_2 data, using IUPAC recommended rates where available and rates from Boyd *et al.* (2003) for additional species, with n=C+O+N-2 (subtracting off the peroxy moiety) gives an improved fit to the experimental data, with a slightly different formula:

$$k_{RO_2+HO_2} = 2.82 \times 10^{-13} \times exp(1300/T) \times [1 - exp(-0.231 \times n)] cm^3 molec^{-1} s^{-1} \quad (4.6)$$

We therefore use this new rate coefficient formula for all peroxy radical + HO_2 reactions in our mechanism.

While reactions of organic peroxy radicals with HO_2 are generally expected to form hydroperoxides, terminating the radical chain, they may also result in radical propagation *via* a channel that forms an alkoxy radical and OH (see Orlando and

Tyndall, 2012). This channel was initially identified for acylperoxy radicals (Dillon and Crowley, 2008; Hasson *et al.*, 2004, 2012; Hurley *et al.*, 2006; Jenkin *et al.*, 2007), but has recently been shown to occur in other peroxy radical species as well, with higher yields for α-carbonyl and more highly substituted species (Hasson *et al.*, 2012; Jenkin *et al.*, 2008, 2010). Insight from theoretical studies suggests that the radical recycling pathway proceeds through a singlet tetroxide intermediate (ROOOOH), which, when stabilized by hydrogen bonding between the -OOH hydrogen and other functional groups on the RO_2 radical, may decompose to RO, O_2, and OH (Hasson *et al.*, 2005; Hou *et al.*, 2005a,b; Hou and Wang, 2005). Here, we use measured hydroperoxide yields wherever possible to constrain the branching between radical terminating and recycling pathways; where such data do not exist, we extrapolate from related compounds using the observations compiled in Orlando and Tyndall (2012) – namely, that increased functionalization of the peroxy radical (particularly α-carbonyl and β-nitrate substituents, and other functional groups enabling intramolecular hydrogen bonding of the tetroxide intermediate) tends to increase the yield of OH + RO.

Additional details regarding rate coefficient formulas, photolysis parameterizations, and the naming scheme used in the explicit model can be found in Section 4.8.

4.3 The reaction of OH with isoprene

Reaction with OH represents the largest loss pathway for isoprene in the atmosphere, owing both to the two species' synchronous diurnal cycles of production and their fast reaction rate. Globally, oxidation by OH is estimated to account for ~85% of the reactive fate of isoprene (Paulot *et al.*, 2012).

The rate coefficient for the reaction of OH with isoprene has been measured numerous times and the JPL Burkholder *et al.* (2015) and IUPAC (Atkinson *et al.*, 2006) reviews provide consistent recommendations:
$k_{OH+ISOP} = 3.0 \times 10^{-11} \times e^{(360/T)}$ cm^3 molec^{-1} s^{-1} [JPL]
$k_{OH+ISOP} = 2.7 \times 10^{-11} \times e^{(390/T)}$ cm^3 molec^{-1} s^{-1} [IUPAC]
As isoprene is oxidized in the atmosphere over a rather small temperature range (*e.g.* 280-315 K), either expression can be used (these parameterizations are within 1%). The estimated uncertainty in this rate coefficient (T = 300 K) is less than 10% (Atkinson *et al.*, 2006; Burkholder *et al.*, 2015). Here, we use the IUPAC expression.

Our recommendation for the complex peroxy radical chemistry that follows addition of OH to isoprene follows the structure described by Peeters *et al.* (2014, 2009). The dynamic nature of the isomer-specific chemistry results in variable product yields that depend on atmospheric conditions. In particular, the pathways followed change depending on the bimolecular lifetime of the hydroxy peroxy radicals and temperature. The recommended reaction rate coefficients, thermochemistry, and product yields needed to capture this chemistry are those determined by Teng *et al.* (2017). One essential aspect of our recommendation is that the chemistry following addition of OH to either C1 or C4 (see numbering in Figure 4.2) is sufficiently distinct that these systems must be treated separately. Finally, in addition to the explicit rates and yields as detailed in Teng *et al.* (2017), we provide a recommendation for parameterizations that capture this highly complex chemistry for most atmospheric conditions.

4.3.1 Location of OH addition to isoprene

The reaction of OH with isoprene at temperatures relevant for atmospheric chemistry goes *via* addition to the unsaturated backbone. Despite the allylic resonance, abstraction of the methyl hydrogen is likely less than 1% of the total reaction (see recent calculations on propene, Zador *et al.*, 2009).

OH can add at any of four positions on the conjugated carbon chain (Figure 4.2). Consistent with both theory and experiments, the majority of the addition occurs at the terminal (primary) carbons. On the basis of theoretical calculations by Greenwald *et al.* (2007), IUPAC recommends a ratio of 0.67:0.02:0.02:0.29 for isomers 1,2,3,4. Work in Simon North's laboratory has suggested that following internal addition, isomerization *via* a cyclopropane-like structure leads to the formation of an unsaturated ketone (*via* C2 addition) or aldehyde (*via* C3 addition), as shown in Figure 4.2 (Greenwald *et al.*, 2010; Park *et al.*, 2003). Recent laboratory studies at Caltech suggest that formation of β hydroxyperoxy radicals *via* OH addition at C2 and C3 is less than 1% of the total (Teng *et al.*, 2017).

Given the lack of experimental evidence and the need to simplify the mechanism, we suggest that the internal channels be ignored in atmospheric modeling for now, though their importance should be revisited with an additional focus on potential for aerosol formation *via* H-shift autoxidation (Crounse *et al.*, 2013).

Here, we recommend yields of: 0.635:0.00:0.00:0.365 for OH addition to C1-C4 Teng *et al.* (2017). It is essential to treat the C1 and C4 addition channels separately

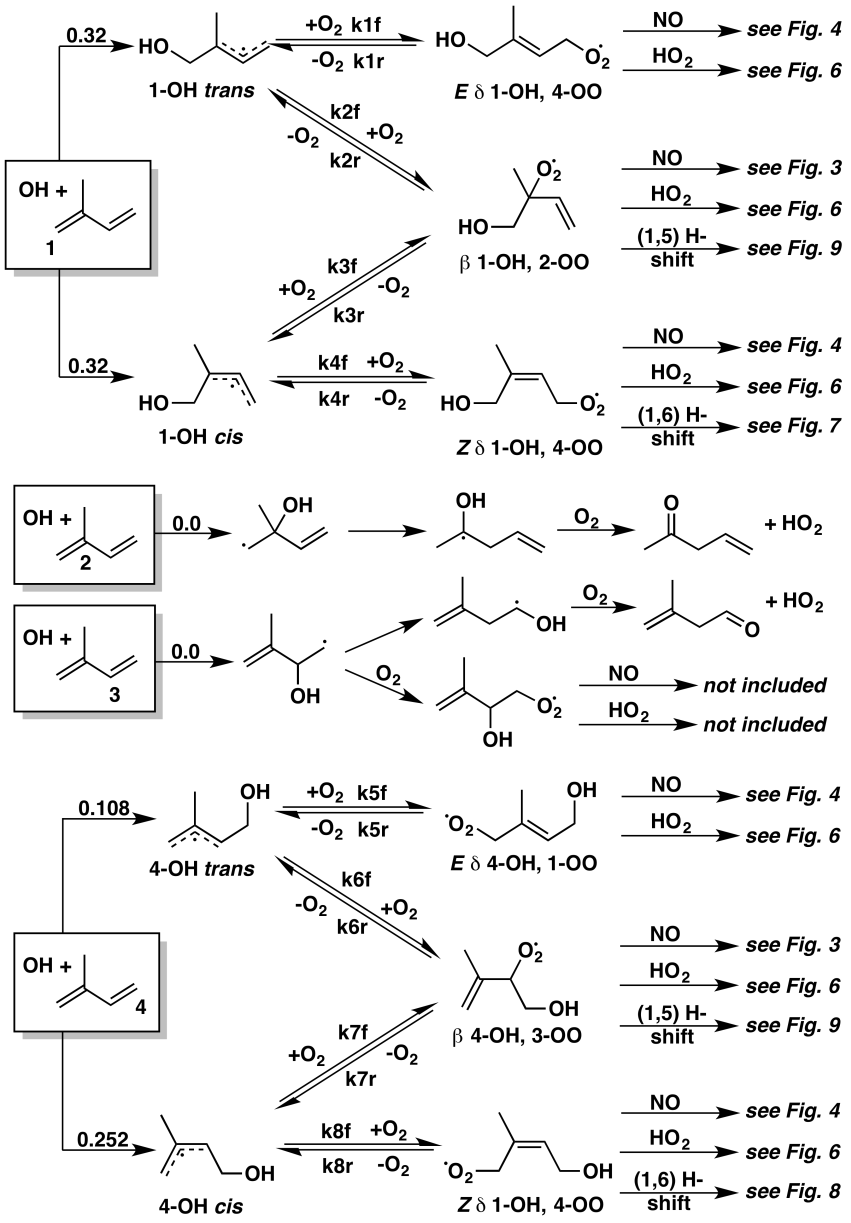

Figure 4.2: Dynamics of the isoprene + OH + O_2 system; 1-OH addition (top) accounts for 64% of isoprene + OH reactivity, while the 4-OH addition system accounts for the remaining 36%. For the full mechanism, we explicitly treat all forward and backward reaction rates. For the reduced mechanism, we treat the peroxy radical pool as a steady-state distribution, using bimolecular chemistry only for the β and E-δ isomers, and parameterizing the isomerization loss of the Z-δ isomers, as described in Section 4.3.2. These reductions are appropriate for atmospheric conditions where $k_{bimolecular}$ <1 s^{-1}, at >280 K and 0.5-1 atm.

as the subsequent product yields and mechanisms are not sufficiently similar to allow traditional lumping.

4.3.2 Addition of O_2 to the hydroxy allylic radicals

4.3.2.1 *Cis/trans* allylic radical distribution

Following addition of OH to the unsaturated backbone, two separate pools of allylic radicals are established – one each for the 1-OH and 4-OH adducts (Figure 4.2). In each pool, the rotation of the internal carbon bond between *cis* and *trans* OH-isoprene adducts is rapid upon OH addition but slows upon thermalization (Peeters *et al.*, 2009). The initial distribution of *cis* to *trans* adducts is therefore set by the steady-state distribution upon collisional thermalization. Without any experimentally available constraints, we recommend the Peeters *et al.* (2014) computational estimate for the distribution of *cis*:*trans* allylic radicals of 0.5:0.5 for the 1-OH adducts and 0.7:0.3 for the 4-OH adducts. In the atmosphere, where the peroxy radical pools generally live for longer than 1 s, this choice does not substantially impact the final product distribution.

4.3.2.2 Initial (kinetic) distribution of isoprene hydroxy peroxy radicals (ISOPOO)

Following collisional thermalization, each OH- isoprene allylic radical will add oxygen at either the β or δ position to form three distinct hydroxy peroxy radicals (Figure 4.2). The overall distribution of ISOPOO is therefore initially set by both the *trans/cis* allylic distribution and the oxygen forward addition rates for the β and δ positions. Isomer-specific O_2 addition rates are not experimentally constrained, and therefore provide little insight into the initial ISOPOO distribution. Previous estimates for the initial distribution of peroxy radicals have been based on computational estimates (Lei *et al.*, 2001) or bulk product analysis (Paulot *et al.*, 2009a). Using speciated distribution of isoprene nitrates measured at very short RO_2 lifetime (<10 ms, ~2 ppmv NO), Teng *et al.* (2017) constrain the product of the thermalized radical isomer distribution (*cis/trans*) and the ratios of the forward O_2 addition rates to form either β or δ ISOPOO (Tables 4.1 and 4.2). Table 4.3 provides a summary of the recommendations for the initial (kinetic) RO_2 distribution resulting from OH + isoprene + O_2 system at 296K, as well as the MCM 3.3.1 recommendations for reference. Our recommendation is slighly modified by that presented in Teng *et al.* (2017) as we adopt isomer-dependent yields for the hydroxy nitrates yields as

reaction - see labeling in Figure 4.2	relative rate
k_1: 1-OH *trans* + O_2 $\rightarrow$ *E*-δ 1-OH,4-OO	0.48
k_2: 1-OH *trans* + O_2 $\rightarrow$ β 1-OH,2-OO	1
k_3: 1-OH *cis* + O_2 $\rightarrow$ β 1-OH,2-OO	1
k_4: 1-OH *cis* + O_2 $\rightarrow$ *Z*-δ 1-OH,4-OO	0.18

Table 4.1: O_2 addition rates for 1-OH isoprene adducts, relative to that of 1-OH-*cis* + O_2 $\rightarrow$ β 1-OH,2-OO.

reaction - see labeling in Figure 4.2	relative rate
k_5: 4-OH *trans* + O_2 $\rightarrow$ *E*-δ 4-OH,1-OO	0.75
k_6: 4-OH *trans* + O_2 $\rightarrow$ β 4-OH,3-OO	1
k_7: 4-OH *cis* + O_2 $\rightarrow$ β 4-OH,3-OO	1
k_8: 4-OH *cis* + O_2 $\rightarrow$ *Z*-δ 4-OH,1-OO	0.33

Table 4.2: O_2 addition rates for 4-OH isoprene adducts, relative to that of 4-OH-*cis* + O_2 $\rightarrow$ β 4-OH,3-OO.

	distribution	
peroxy radical	our recommendations	MCM 3.3.1
1-OH 2-OO	0.46	0.415
E 1-OH 4-OO	0.10	0.045
Z 1-OH 4-OO	0.05	0.169
4-OH 3-OO	0.26	0.262
E 4-OH 1-OO	0.06	0.014
Z 4-OH 1-OO	0.07	0.095

Table 4.3: Kinetic RO_2 isomer distributions at 297 K from Teng *et al.* (2017), adjusted slightly to account for our recommended nitrate yields from each isomer (Section 4.3.3.1) along with the kinetic distribution inferred from MCM 3.3.1 (Jenkin *et al.*, 2015). The MCM values are reported only as a fraction of the total RO_2 arising from external addition of OH; MCM 3.3.1 apportions 8.4% of total OH reactivity to internal addition.

discussed below.

Assuming the ratio of *cis:trans* allylic radicals calculated by Peeters *et al.* (2014) is accurate, the isomer distribution of the organic nitrates produced from ISOPOO implies a similar oxygen addition ratio at the δ position in the *cis* and *trans* OH-isoprene allylic radicals (Teng *et al.*, 2017). There exists, however, significant disagreement between the experimentally-derived O_2 addition rate coefficient recommendations here and recent theoretical calculations. Peeters *et al.* (2014), for example, suggest

that the O_2 addition rate to the *cis* δ position is significantly faster than to the *trans* δ position in both 1-OH and 4-OH systems. For both the theory and experiments, the absolute recommendations for individual isomer O_2 addition rates are constrained only by the assumed bulk O_2 addition rates. Here, we recommend an overall O_2 addition rate constant of $2.3 \pm 2.0 \times 10^{-12}$ cm^3 s^{-1} at 298K (Park *et al.*, 2004) though, within the framework for our recommendation, this choice has little impact on the product yields.

4.3.2.3 The reversibility of O_2 addition

Peroxy radicals formed β to olefinic carbon centers, such that electronic resonance is established upon loss of molecular O_2, have relatively small R-OO bond dissociation energy (BDE) (<20 kcal mol^{-1}; *e.g.*, Benson and Shaw, 1968; Howard, 1972; Pratt *et al.*, 2003, and references therein). For such RO_2, the addition of O_2 is reversible at 300 K for typical peroxy radical lifetimes in the atmosphere. Using theoretical calculations, Peeters *et al.* (2009) suggested that this reversibility is essential to capture for ISOPOO, as it is fast relative to the timescale of the peroxy radicals' lifetime in the atmosphere. This proposal has subsequently been confirmed experimentally (Crounse *et al.*, 2011; Teng *et al.*, 2017). The importance of this reversibility is that the six major RO_2 radicals formed from OH + isoprene + O_2 interconvert (two subgroups of three defined by a common OH position can interconvert with the subgroup, but not between the subgroups – see Figure 4.2). The interconversion has significance in that the subsequent chemistry of the individual RO_2 isomers is distinct, both in terms rates of reaction and product distribution. In addition, there is now strong evidence (Teng *et al.*, 2017) that the kinetic RO_2 distribution from OH + isoprene + O_2 is substantially different than the equilibrated thermal RO_2 distribution. From estimated daytime RO_2 lifetimes in the atmosphere (20-120 s, equivalent to 200-40 pptv NO at pressure of 1 atm), the average isoprene RO_2 distribution is close to the thermal equilibrium distribution (Teng *et al.*, 2017). In contrast, most laboratory studies of the product distribution from OH + isoprene have been at or near the initial (or kinetically-determined) RO_2 distribution.

In addition to constraining the kinetic RO_2 distribution from isoprene + OH, Teng *et al.* (2017) use the observed change in the isomeric distribution of isoprene nitrates as a function of RO_2 lifetime to constrain the equilibrium constants which describe the interconversion of the RO_2 isomers. We recommend these equilibrium constants here (Table 4.4).

equilibrium formula	K (10^{-14} cm^3 molec^{-1})
K_1 = [*E*-1-OH,4-OO-ISOP]/([*trans*-1-OH-ISOP][O_2])	2
K_2 = [1-OH,2-OO-ISOP]/([*trans*-1-OH-ISOP][O_2])	49
K_3 = [1-OH,2-OO-ISOP]/([*cis*-1-OH-ISOP][O_2])	269
K_4 = [*Z*-1-OH,4-OO-ISOP]/([*cis*-1-OH-ISOP][O_2])	0.5
K_5 = [*E*-4-OH,1-OO-ISOP]/([*trans*-4-OH-ISOP][O_2])	13
K_6 = [4-OH,3-OO-ISOP]/([*trans*-4-OH-ISOP][O_2])	237
K_7 = [4-OH,3-OO-ISOP]/([*cis*-4-OH-ISOP][O_2])	507
K_8 = [*Z*-4-OH,1-OO-ISOP]/([*cis*-4-OH-ISOP][O_2])	2.1

Table 4.4: Equilibrium constants describing the RO_2 distribution from isoprene + OH at 297 K.

4.3.2.4 Constraint on the absolute rates of O_2 loss from β-ISOPOO

Synthesis of isoprene hydroxy hydroperoxide (ISOPOOH) isomers in pure form (Rivera-Rios *et al.*, 2014; St. Clair *et al.*, 2015) enabled an estimate of the absolute rate of O_2 loss from the β-hydroxy peroxy radical isomers (Teng *et al.*, 2017). As discussed in Section 4.7.3, OH reacts with (1-OH,2-OO) ISOPOOH (St. Clair *et al.*, 2015) to form (at ~10% yield) β RO_2 radicals *via* abstraction of the ROO-H hydrogen. This chemistry yields an isomerically pure source of a single isoprene RO_2 radical. By studying the nitrate distribution as a function of RO_2 lifetime, Teng *et al.* (2017) constrained the rate of O_2 loss from the (1-OH,2-OO) ISOPOO peroxy radicals to be ~2 s^{-1} at 297 K. This finding is consistent with an O_2 loss rate derived from the assumed bulk addition rate coefficient and the measured equilibrium constant Teng *et al.*, 2017.

4.3.2.5 Modeling of ISOPOO isomer distribution

The complete list of reactions for the addition of OH to isoprene, the addition of O_2 to the isoprene-OH adduct, and the loss of oxygen from the resulting peroxy radicals can be found in the supplement. Incorporation of the complete RO_2 interconversion processes into a global chemical transport model requires the addition of a number of chemical species and reactions, and increases the computational load substantially. However, it has been shown theoretically by Peeters *et al.* (2014), and experimentally by Teng *et al.* (2017) that the RO_2 distribution can be approximately described using the equilibration constants, the forward O_2 + alkyl radical reaction rates, and the bimolecular RO_2 lifetime ($k_{bimolecular} = k_{NO} \times [NO] + k_{HO_2} \times [HO_2] + k_{RO_2} \times [RO_2]$). To reduce the mechanism, we simplify the ten-species isoprene alkoxy and

peroxy radical system to two species, representing the steady-state peroxy radical distributions from the 1-OH and 4-OH additions. The full list of reactions used in the simplified model can be found in the Supplement. Isomer-specific bimolecular reactions and the isomerization of the β isomers can then be treated as second- and first-order processes of these peroxy radicals, scaled by the relative contributions of each isomer in steady state, while the isomerization of the Z-δ isomers requires a more complicated parameterization combining a first-order process from the peroxy radicals with a zeroth-order initial yield from isoprene + OH. These simplifications, which substantially reduce the numbers of species and reactions required to model the isomer distributions of isoprene's first-generation oxidation products, provide isomer and reaction pathway branching ratios within 5% of the full model for atmospheric conditions (*i.e.* $k_{bimolecular}$ <1 s^{-1}, T >280 K and P = 0.5-1 atm).

4.3.3 Reactions of ISOPOO

The peroxy radicals formed following addition of OH and O_2 to isoprene will react with NO (Figures 4.3-4.5), HO_2 (Figure 4.6), or other peroxy radicals. The Z-δ and β isomers also undergo intramolecular H-shift chemistry leading to hydroperoxy aldehydes and other products (Figures 4.7-4.9).

4.3.3.1 Reaction of ISOPOO with NO

Kinetics (Table 4.5) - There have been many studies of the room temperature rate constant for the reaction of ISOPOO with NO (Chuong and Stevens, 2002; Ghosh *et al.*, 2010; Miller *et al.*, 2004; Park *et al.*, 2004; Reitz *et al.*, 2002; Stevens *et al.*, 1999; Zhang *et al.*, 2003b). Ghosh *et al.* (2010), Chuong and Stevens (2002), Reitz *et al.* (2002), Stevens *et al.* (1999), and Park *et al.* (2004) used LIF to detect the OH radical. Since OH is not produced in the nitrate pathway, this method measures only the rate of the alkoxy pathway, and the total rate includes errors in the nitrate branching ratios (Chuong and Stevens, 2002; Ghosh *et al.*, 2010; Park *et al.*, 2004; Reitz *et al.*, 2002; Stevens *et al.*, 1999). Zhang *et al.* (2003b) and Miller *et al.* (2004) found rates by measuring the decay of the isoprene peroxy radical with CIMS. Currently, IUPAC recommends a value of $(8.8 \pm 1.2) \times 10^{-12}$ cm^3 $molec^{-1}$ s^{-1} (Atkinson *et al.*, 2006), which is equal to the value determined experimentally by Miller *et al.* (2004).

Only Ghosh *et al.* (2010) has measured an isomer-specific rate constant for the reaction of ISOPOO with NO. They synthesized a precursor whose photolysis forms

k_{NO} ($\times 10^{-12}$ cm^3 molec^{-1} s^{-1})	T (K)	technique	citation
9(+9, −4.5)	298	DF-LIF	Stevens *et al.* (1999)
25 ± 5	295	PLP-LIF	Reitz *et al.* (2002)
11 ± 8	300	DF-LIF	Chuong and Stevens (2002)
9 ± 3	298	DF-CIMS	Zhang *et al.* (2003b)
8.8 ± 1.2	298	DF-CIMS	Miller *et al.* (2004)
9.0 ± 3.0	298	PLP-LIF	Park *et al.* (2004)
8.1(+3.4, −2.1)	298	PLP-LIF	Ghosh *et al.* (2010)
8.8 ± 1.25	298	-	IUPAC recommendation
$2.7 \times 10^{-12} \times e^{(350/T)}$	**-**	**-**	**our recommendation**

Table 4.5: Chronological measurements of rates of reaction of ISOPOO with NO.

only isomers with OH on carbon 1. Their value, 8.1(+3.4, −2.1)$\times 10^{-12}$ cm^3 molec^{-1} s^{-1}, is indistinguishable from the other studies. Miller *et al.* (2004) found k_{NO} for a large variety of simple alkenes, and all rate constants were within error of k_{NO} of isoprene, suggesting that small changes in the structure of the peroxy radical do not significantly affect k_{NO}. Thus, for all isomers of isoprene hydroxy peroxy radicals, we recommend the standard RO_2+NO temperature dependent rate coefficient of $k = 2.7 \times 10^{-12} \times exp(350/T)$ cm^3 molec^{-1} s^{-1}.

Mechanism (Figures 4.3-4.5; Tables 4.6 and 4.7) - The reaction of ISOPOO with NO leads to the formation of organic nitrates (IHN) and alkoxy radicals (ISOPO).

Mechanism - isoprene hydroxy nitrate (IHN) formation (Figures 4.3 and 4.4; Table 4.6) - Formation of IHN represents a radical chain-terminating step and, therefore, acts as a significant local sink for both HO_x and NO_x (Ito *et al.*, 2007; Paulot *et al.*, 2012; Wu *et al.*, 2007). Laboratory estimates of the room temperature yield of IHN, Y_{IHN} vary from 0.04 (Chen *et al.*, 1998) to 0.15 (Chuong and Stevens, 2002). Table 4.6 lists laboratory studies and their methodology. Currently, the extent to which individual ISOPOO isomers have different branching ratios to form IHN is poorly constrained. Studies on saturated and monoalkenes show conflicting results (Arey *et al.*, 2001; Cassanelli *et al.*, 2007; Espada *et al.*, 2005; Teng *et al.*, 2015). Teng *et al.* (2017), however, suggest that the difference in yields between the β and δ isomers is less than ± 20%. Paulot *et al.* (2009a) had suggested much larger differences based on the ratio of delta IHN to HC_5. As discussed above, we now know that the HC_5 yield is much lower than assumed by Paulot *et al.* (2009a).

Recent results from Caltech suggest a branching fraction for hydroxynitrate for-

α	T (K)	P (Torr)	technique	citation
~0.08-0.14	298	740	chamber, FT-IR	Tuazon and Atkinson (1990)
0.044 (± 0.008)	298	743	chamber, GC-Pyrolysis-NO_2 detection	Chen *et al.* (1998)
0.12 (± 0.07)	297	750	flowtube, FT-IR	Sprengnether *et al.* (2002)
0.08 (± 0.06)	297	445	flowtube, FT-IR	Sprengnether *et al.* (2002)
0.15 (± 0.10)	300	150	flowtube, LIF-OH radical cycling	Chuong and Stevens (2002)
0.086	298	~760	Structure Activity Relationship	Giacopelli *et al.* (2005)
0.07	298	100	flowtube, PTRMS/CIMS	Patchen *et al.* (2007)
0.117 (± 0.03)	296.5	~750	chamber, CIMS and modeling	Paulot *et al.* (2009a)
0.07 (+0.025/-0.015)	295	~760	chamber, GC-ECD with standards	Lockwood *et al.* (2010)
0.1 (± 0.05)	298	760	-	IUPAC recommendation
0.09 (+0.04/-0.03)	~297	~760	chamber, I^- CIMS	Xiong *et al.* (2015)
0.13 (± 0.02)	297	745	chamber, CF_3O^- CIMS	Teng *et al.* (2017)
0.13	**297**	**745**	**-**	**our recommendation**[a]

Table 4.6: Chronological estimates for α of ISOPOO + NO to form IHN at 298 K and 1 atm (unless otherwise noted). [a]bulk yield at 297 K and 745 torr; for isomer-specific yields and T/P dependence, see Sections 4.3.3.1 and 4.2, respectively.

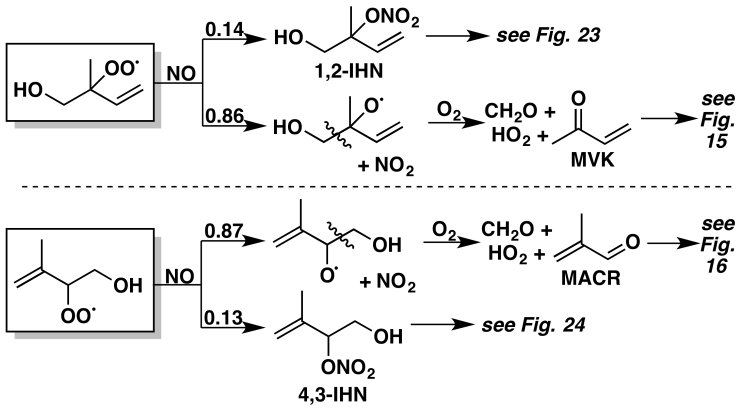

Figure 4.3: Reactions of the β-isoprene-OH-OO isomers with NO. Yields are for 298 K and 1 atm; the relative contributions of the nitrate and alkoxy pathways vary with both temperature and pressure.

mation of 0.13 at 297K, nearly independent of peroxy radical isomer (Teng *et al.*, 2017). Teng *et al.* (2017) note, however, that the ratio of 1-OH,2-ONO_2-IHN to 4-OH,3-ONO_2-IHN exceeded that of 1-OH,2-OOH-ISOPOOH to 4-OH,3-OOH-ISOPOOH by ~10%, and that nitrate yields from δ-ISOPOO may be slightly lower than those from the β-ISOPOO. Based on these findings, we recommend yields of 14%, 13%, and 12% for 1,2-IHN, 4,3-IHN, and the δ-IHNs, respectively, at 297 K.

We recognize that our recommended IHN yield is at the high end of the laboratory studies (Table 4.6). As discussed by Xiong *et al.* (2015), the relatively low yield determinations made at Purdue before 2015 (Chen *et al.*, 1998; Lockwood *et al.*, 2010) were likely impacted by significant heterogenous losses of the most abundant nitrate, the 1,2 β isomer (Teng *et al.*, 2017). Lower yields were also reported by Sprengnether *et al.* (2002) (0.08) and Patchen *et al.* (2007) (0.07), but these were obtained at lower pressure (590 and 133 hPa, respectively). The yield reported by Xiong *et al.* (2015) (0.09 +0.04/-0.03) based on I^- CIMS measurements is also somewhat lower. As discussed by Xiong *et al.* (2015), however, this yield estimate is sensitive to assumptions about the distribution of the IHN isomers and their rate of subsequent loss *via* OH chemistry. To estimate the isomer distribution, Xiong *et al.* (2015) used a model developed from the theoretical calculations of (Peeters *et al.*, 2014). Using the measured IHN distribution from Teng *et al.* (2017) for the conditions of the Purdue study, we calculate an updated yield for the Xiong *et al.* (2015) experiments of 0.115. Additionally, the recently measured rate constant for the reaction of OH with 1,2 IHN Xiong *et al.* (2015) is 50% faster than assumed (Teng *et al.*, 2017) – also leading to an underestimate of the reported yield in this

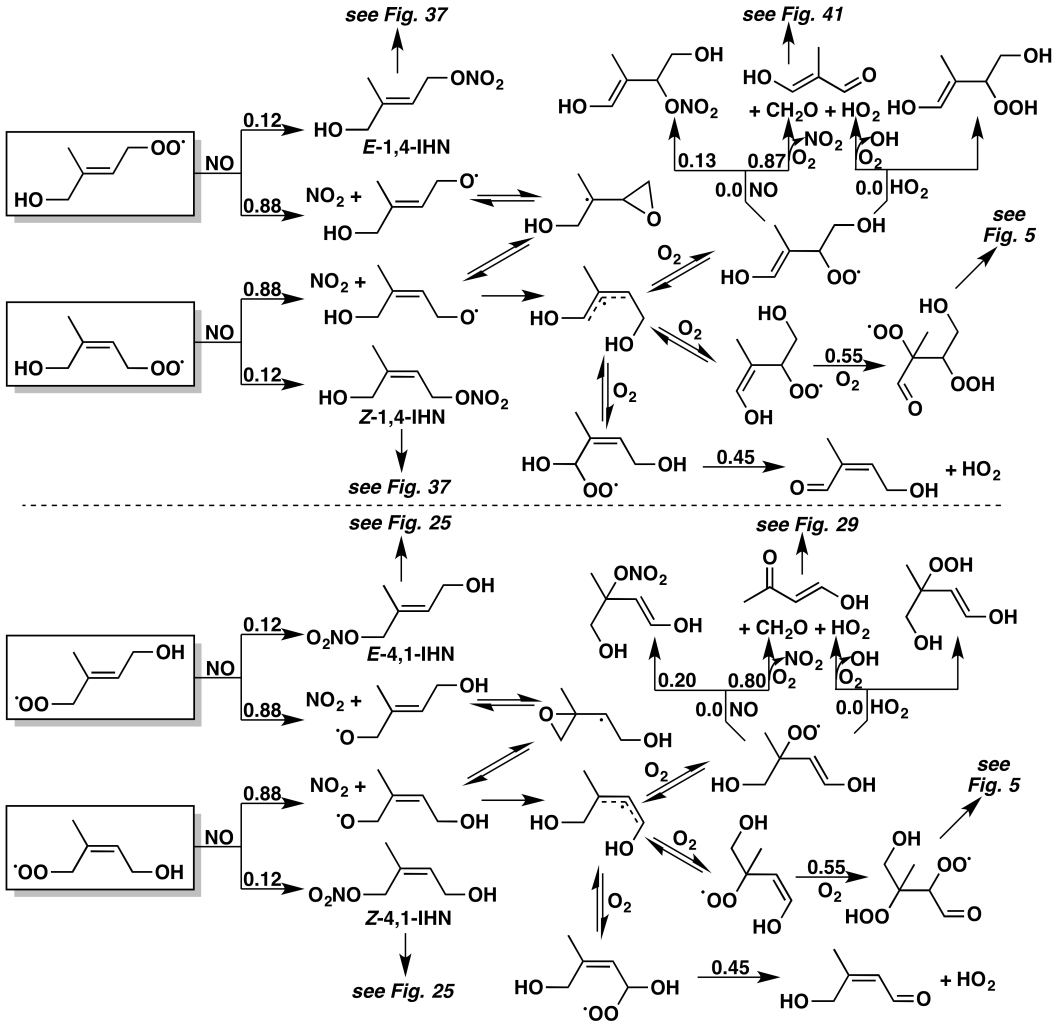

Figure 4.4: Reactions of the δ-isoprene-OH-OO isomers with NO. Yields are for 298 K and 1 atm; the relative contributions of the nitrate and alkoxy pathways vary with both temperature and pressure. For the reduced mechanism, we ignore the Z-δ isomers.

study. We conclude that there is more consensus on the yield of IHN than the diversity of results listed in Table 4.6 would imply.

Finally, we recommend a temperature and pressure dependence of the isomer-specific IHN yields based on studies of Carter and Atkinson (1989) and Teng *et al.* (2017). Crounse *et al.* (2011) find that the temperature dependent parameterization is consistent with the change in the hydroxy nitrate yield with temperature. Error in the yield is estimated to be ±20%.

Mechanism - decomposition of ISOPO (Figures 4.3-4.5; Table 4.7) - Methyl vinyl ketone (MVK), methacrolein (MACR), (and, following reaction with O_2, formaldehyde (CH_2O) and HO_2) are believed to be the sole fate of the β-ISOPO radicals produced from the reaction of NO with the β ISOPOO (Figure 4.3). The –OH group β to the nascent alkoxy group lowers the barrier to decomposition substantially. In the structure activity relationship, Peeters *et al.* (2004) predict that the –OH group lowers the barrier to decomposition by a full 8 kcal mol^{-1}, making decomposition much more favorable relative to the competing reaction with O_2 (Aschmann *et al.*, 2000; Dibble, 2001; Orlando *et al.*, 1998; Peeters *et al.*, 2004; Vereecken and Peeters, 1999). As detailed in Table 4.7) Yields determined experimentally under NO dominated conditions range from 30-45% for MVK and 20-30% for MACR. In the presence of oxygen, formaldehyde is produced in a yield equal to the combined yield of MVK and MACR (Miyoshi *et al.*, 1994; Sprengnether *et al.*, 2002; Tuazon and Atkinson, 1990).

Because the fraction of ISOPOO that are β isomers varies with peroxy radical lifetime, the yield of MVK and MACR from isoprene oxidation is not fixed. As shown in Table 4.7, the NO concentrations in many of the chamber experiments (except for those of Karl *et al.* (2006) and Liu *et al.* (2013)) are much higher than those typically found in the troposphere. As discussed in Section 4.3.2, in the atmosphere the ISOPOO isomer distribution favors the thermodynamically more stable β-substituted isomers. Since these isomers (that lead to MVK and MACR) are typically present at a lower fraction in chamber experiments than in the atmosphere, these experiments systematically underpredict MACR and, especially, MVK yields in the atmosphere. Liu *et al.* (2013) and Karl *et al.* (2006),who used NO concentrations comparable to the urban troposphere (2×10^{10} and 5×10^{9} molec cm^{-3}, respectively), found MVK and MACR yields higher than many other studies that employed higher NO concentrations (Table 4.7). The estimated MACR yield by

MVK yield	MACR yield	[NO] (molec cm^{-3})	citation
33 ± 7^a	24 ± 5^a	$1.9 - 3.8 \times 10^{14}$	Tuazon and Atkinson (1990)
35.5 ± 4	25 ± 3	$1.4 - 2.4 \times 10^{14}$	Paulson and Seinfeld (1992)
32 ± 5	22 ± 2	2×10^{14}	Miyoshi *et al.* (1994)
31 ± 3	20 ± 2	$1.5 - 15 \times 10^{13}$	Ruppert and Heinz Becker (2000)
44 ± 6	28 ± 4	7.8×10^{14}	Sprengnether *et al.* (2002)
41 ± 3	27 ± 3^b	5×10^{9}	Karl *et al.* (2006)
30.4 ± 1.3	22.01 ± 0.62	$6 - 12 \times 10^{12}$	Galloway *et al.* (2011)
44.5 ± 5.5^c	31.8 ± 4.2^c	2×10^{10}	Liu *et al.* (2013)
40	**23**	**-**	**our recommendation**^{d}

Table 4.7: MVK and MACR yields (%) from isoprene *via* RO_2 + NO. ^{a}corrected for O^3P reaction as communicated to Paulson and Seinfeld (1992). ^{b}Karl *et al.* (2006) did not account for isomerization; at [NO] $\approx$ 0.2 ppb (RO_2 lifetime 25 s), isomerization would account for ~10% of peroxy radical reactivity, which would imply a corrected yield of MACR from NO + RO_2 of 35%. ^{c}assumes that 93% of the peroxy radicals react with NO (Liu *et al.*, 2013). ^{d}at the kinetic limit RO_2 distribution, as in Table 4.3.

Karl *et al.* (2006) is likely a lower limit as they were unaware that a significant fraction of the hydroxy peroxy radicals from the 4-OH system were undergoing 1,6 H-shift isomerization. In addition, subsequent studies have illustrated that MVK and MACR measurements can often be impacted by analytical challenges when ISOPOOH is present (Rivera-Rios *et al.*, 2014). Here, for the β-ISOPOO + NO reactions, we take the yield of MACR/MVK to be (1-Y_{IHN}).

1,4- and 4,1-δ ISOPOO react with NO to form δ-ISOPO radicals (Figure 4.4). The *Z*-δ-ISOPO radicals will undergo 1,5 hydrogen shift (Dibble, 2002). This isomerization is faster than that of simple alkanes due activation of the H-shift hydrogen by the –OH group (Atkinson, 2007; Orlando *et al.*, 2003b). While the *E* 4-1 ISOPO cannot undergo such chemistry due to the lack of an abstractable hydrogen, Peeters and Nguyen (2012) calculate that rapid isomerization between the *E* and *Z* isomers *via* an epoxide intermediate results in both alkoxy radicals exiting *via* 1,5 H-shift from the *Z* isomer. Indeed, they calculate that similar epoxide-isomerization and the much faster 1,5 H-shift from the hydrogen α to the OH group vis-a-vis H-shift from the methyl group leads to both 1,4 isomers following similar chemistry. Here, we follow this recommendation.

Following the 1,5 H-shift, O_2 adds to the allylic radical either β or γ to C1 (C4). Addition β yields two 5-carbon hydroxy carbonyl species (HC_5). Teng *et al.* (2017) determine the yield to be 45 ± 10% in both the 1-OH and 4-OH systems

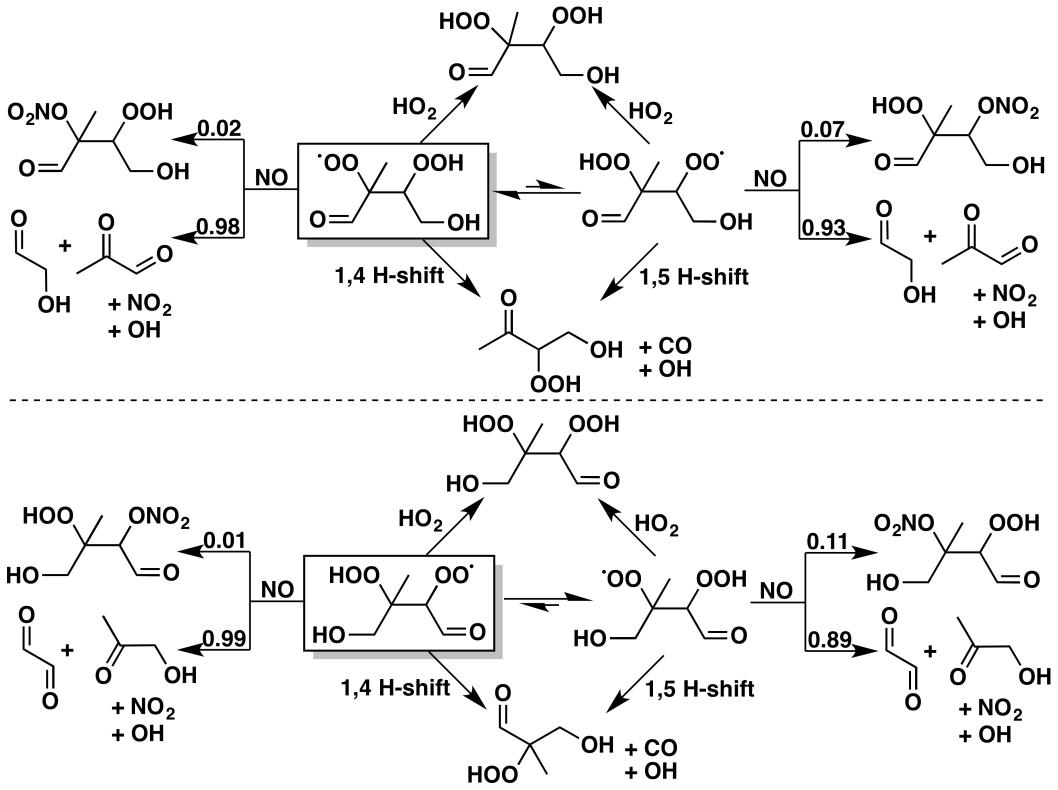

Figure 4.5: Reactions of the isoprene-CO-OH-OOH-OO isomers produced by δ-isoprene-OH-OO + NO. Yields are for 298 K and 1 atm; the relative contributions of the nitrate and alkoxy pathways vary with both temperature and pressure. For the reduced mechanism, we assume that the 1,5 and 1,6 H-shift from the aldehyde outcompetes all bimolecular chemistry.

suggesting that approximately 55% undergoes O_2 addition γ leading to formation of a ketene peroxy radical. The subsequent fate of these peroxy radicals is unknown, but based on studies by Galloway *et al.* (2011), Sprengnether *et al.* (2002) and Paulot *et al.* (2009a), we suggest that the products are likely hydroxyacetone, glyoxal, and glycoaldehyde (Figures 4.4 and 4.5).

4.3.3.2 Reaction of ISOPOO with HO_2

ISOPOOH has long been considered the likely product of isoprene RO_2 + HO_2 reactions (Atkinson, 1997; Jenkin *et al.*, 1998; Madronich and Calvert, 1990). The first reported field measurements of ISOPOOH were over the Amazon basin in Suriname in 1998 (Crutzen *et al.*, 2000; Warneke *et al.*, 2001; Williams *et al.*, 2001) and over savannahs in Venezuela in 1999-2000 (Holzinger *et al.*, 2002) by proton transfer mass spectrometry, though recent laboratory investigations of PTR ion chemistry

with synthetic standards suggests that the *m/z* 101 signal identified as ISOPOOH may instead be isoprene dihydroxy epoxides (IEPOX). Shortly thereafter, as its importance in the tropospheric chemistry of low-NO high-isoprene regions became clear, ISOPOOH began to receive attention in computational studies (Vereecken *et al.*, 2004), atmospheric chemical models (Kuhlmann *et al.*, 2004; Pfister *et al.*, 2008), and chamber studies (Paulot *et al.*, 2009b), where chemical ionization mass spectrometry (CIMS) demonstrated successful measurement of ISOPOOH (Paulot *et al.*, 2009b; St. Clair *et al.*, 2015).

Kinetics - The rate constant for the reaction of HO_2 + RO_2 for the isoprene hydroxy peroxy radical has been measured only once, with $k = 1.74 \pm 0.25 \times 10^{-11}$ cm^3 molec^{-1} s^{-1} at 298 K (Boyd *et al.*, 2003). Most chemical mechanisms implement the parameterized recommendation of MCM (Equation 4.5), which varies with the number of carbons in the molecule (Jenkin *et al.*, 1997; Saunders *et al.*, 2003); for isoprene hydroxy peroxy + HO_2, this gives $k = 2.06 \times 10^{-13} \times e^{(1300/T)}$ or $k = 1.61 \times 10^{-11}$ cm^3 molec^{-1} s^{-1} at 298 K. Using our alternate parameterization (Equation 4.6), which depends instead on the number of heavy atoms in the molecule (excluding the peroxy moiety), gives an improved fit and a value of $k = 1.66 \times 10^{-11}$ cm^3 molec^{-1} s^{-1} for isoprene hydroxy peroxy + HO_2 at 298 K. To match the measured rate coefficient of (Boyd *et al.*, 2003), We scale our standard recommendation:

$$k = 2.12 \times 10^{-13} \times e^{(1300/T)} \text{ cm}^3 \text{ molec}^{-1} \text{ s}^{-1}$$

with an uncertainty of ±20% from the experimental rate. Further measurements of this rate would be welcome.

Mechanism - (Figure 4.6; Table 4.8) - The main product of the reaction is the unsaturated hydroxy hydroperoxide, ISOPOOH, in yields estimated to be 88 ± 12% (Paulot *et al.*, 2009b) or 93.7 ± 2.1% (Liu *et al.*, 2013). Six possible isomers of ISOPOOH can be formed from this series of reactions, as shown in Figure 4.6, with their relative abundances determined by the distribution of their precursor RO_2. Under most atmospherically relevant conditions, the two β isomers – (1,2)- and (4,3)-ISOPOOH – comprise the majority (~95%) of the total, with only ~5% in the E δ isomers (4,1) and (1,4). MVK and MACR have been suggested as minor products from isoprene RO_2 + HO_2 for the (1,2)-RO_2 and (4,3)-RO_2, respectively (Liu *et al.*, 2013; Paulot *et al.*, 2009b) (Dillon and Crowley, 2008; Hasson *et al.*, 2005). The 93.7% ISOPOOH yield was determined as (1-MVK-MACR) (Liu *et al.*, 2013). Liu *et al.* (2013) determined the yields of MVK (3.8 ± 1.3%) and MACR

	% yields			
	Liu *et al.* (2013)[a]	our recommendations		
products	ISOPOO	1,2-ISOPOO	4,3-ISOPOO	δ-ISOPOO
ISOPOOH	93.7 ± 2.1	93.7	93.7	100
MVK + OH + HO_2 + CH_2O	3.8 ± 1.3	6.3	0	0
MACR + OH + HO_2 + CH_2O	2.5 ± 0.9	0	6.3	0

Table 4.8: Products of isoprene hydroxy peroxy RO_2 + HO_2. [a]at RO_2 lifetime of ~4 s ([HO_2 = 1000 ppt]). MVK and MACR yields may be lower to the extent that the laboratory results may have been impacted by RO_2 + RO_2 chemistry.

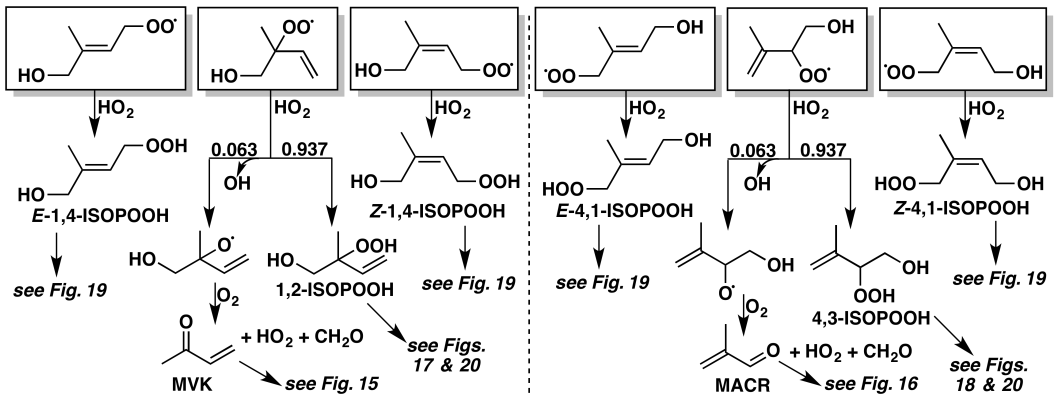

Figure 4.6: Reactions of the isoprene-OH-OO isomers with HO_2. For the reduced mechanism, we ignore the *Z*-δ isomers, as they contribute less than 1% of the bimolecular chemistry for atmospheric conditions.

(2.5 ± 0.9%) separately at RO_2 lifetime of ~4s (*e.g.* [HO_2] = 1000 ppt). At this lifetime, Teng *et al.* (2017) find that the ~93% of the RO_2 are β-isomers. This result suggests that the MACR yield from 4,3-ISOPOO is slightly higher than MVK yield from 1,2-ISOPOO. This seems unlikely and suggests, perhaps, that some fraction of the MVK and MACR observed in the study may have been produced *via* RO_2 + RO_2. Here, we recommend 1,2-ISOPOO + HO_2 → MVK + OH + HO_2 + CH_2O with a yield of 6.3% and, equivalently, 4,3-ISOPOO + HO_2 → MACR + OH + HO_2 + CH_2O with the same yield, 6.3%. The balance yields ISOPOOH.

4.3.3.3 Reaction of ISOPOO with RO_2

Peroxy radical self- and cross-reactions are important in low-NO_x environments. A large body of work exists for the kinetics of prototypical organic peroxy radicals; these reactions have been the subject of several review papers (Kirchner and Stockwell, 1996; Lightfoot *et al.*, 1992; Orlando and Tyndall, 2012; Tyndall *et al.*, 2001;

Wallington *et al.*, 1992).

Kinetics (Tables 4.9 and 4.10) - Very few direct experimental measurements have been completed on the self- and cross-reactions for ISOPOO. Overall rate constants, as well as the accessible product channels, vary widely with the type of peroxy radical involved. The cocktail of ISOPOO formed during OH-initiated oxidation of isoprene makes deconvolution of the individual isomer-specific rates and branching ratios complex. Jenkin and Hayman (1995) used a structure-activity relationship (SAR) method to infer the self- and cross-reaction rates and branching fractions for ISOPOO radicals. The SAR results were improved later with OH-initiated oxidation experiments on 1,3-butadiene and 2,3-dimethyl-1,3-butadiene, which differ from isoprene only by the presence or absence of a methyl group on the carbon backbone, conducted at high radical concentrations (2.0-6.8 $\times$ 10^{13} molec cm^{-3} of OH) in a small ($\sim$175 cm^3) quartz reaction cell (Jenkin *et al.*, 1998). The resulting experimental rate constants are much faster than those proposed with SAR arguments using smaller peroxy radicals, but appear to adequately describe the kinetics observed in isoprene oxidation experiments. MCM combines all peroxy radical rate constants into one value for each isomer by using a rate constant which is twice the geometric mean of the self-reaction rate constant for that isomer and the methyl peroxy self-reaction.

The overall reaction rate constants for all isomers are based on their structure (primary > secondary > tertiary peroxy radicals) and functionality (β-hydroxy peroxy radicals are significantly activated; allylic peroxy radicals are slightly activated). Here, we consider only the reactions of the two β peroxy radicals, as they comprise the large majority of the RO_2 radical pool from isoprene. Table 4.9 compares the self-reaction rate constants inferred from SAR arguments for smaller peroxy radicals (Jenkin and Hayman, 1995) with those derived from 1,3-butadiene and 2,3-dimethyl-1,3-butadiene (Jenkin *et al.*, 1998) as well as our recommended rate constants. With the exception of the β 4-OH 3-OO isomer, that we believe is mistakenly associated with a peroxy radical that is not allylic, our recommendations match those of MCM v3.3.1.

Mechanism (Tables 4.10 and 4.11) - Peroxy radicals (RO_2) react *via* three channels:

$RO_2 + RO_2 \rightarrow RO + RO + O_2$ (R1a)

$RO_2 + RO_2 \rightarrow ROH + R'HO + O_2$ (R1b)

isomer	Jenkin and Hayman (1995)	Jenkin *et al.* (1998)	our recommendations
β 1-OH,2-OO	1.65	6.92 ± 1.38	6.92
β 4-OH,3-OO	139	574 ± 57	574

Table 4.9: Self-reaction rate constants ($\times 10^{-14}$ cm^3 molec^{-1} s^{-1}) for the two β isomers of isoprene hydroxy peroxy radicals.

$$RO_2 + RO_2 \rightarrow ROOR + O_2 \quad \text{(R1c)}$$

The branching between these channels controls the contributions of each reaction to the formation of additional radical species, or in some cases low-volatility products. The alkoxy radicals (RO) formed in R1a undergo further reactions described in the "decomposition of ISOPO" subsection of Section 4.3.3.1, propagating the radical chain. R1b is a chain-terminating reaction that forms alcohol and aldehyde products through a hydrogen-bonded transition state involving a hydrogen atom α- to the peroxy radical. This product channel does not occur for tertiary peroxy radicals. R1c has never been directly observed, but the ROOR product would likely have a low vapor pressure and would be important to the particle phase.

Similarly, the cross-reactions have been shown to undergo three channels (exclusive of the analogous ROOR channel) where $R1O_2$ and $R2O_2$ are different peroxy radicals:

$$R1O_2 + R2O_2 \rightarrow R1O + R2O + O_2 \quad \text{(R2a)}$$

$$R1O_2 + R2O_2 \rightarrow R1OH + R2'HO + O_2 \quad \text{(R2b)}$$

$$R1O_2 + R2O_2 \rightarrow R1'HO + R2OH + O_2 \quad \text{(R2c)}$$

Like the self-reaction, if either $R1O_2$ or $R2O_2$ are tertiary peroxy radicals, the corresponding aldehyde product channel is not accessible. Given the potential influence of R1a and R2a on radical propagation in low-NO environments, the chain branching of the self- and cross-reactions must be considered when developing an overall mechanism for ISOPOO.

In Table 4.11, we compare the findings of Jenkin and Hayman (1995) and Jenkin *et al.* (1998) for the branching fraction to form alkoxy radicals by Reaction R1a. The yield of R1c (formation of ROOR) is assumed to be zero and the branching fraction for channel R1b is the remainder of the rate constant. The tertiary peroxy radical β 1-OH 2-OO cannot undergo reaction R1b, so the branching fraction is 1, by definition. As discussed previously, the alkoxy radicals will likely instantaneously decompose to either MVK or MACR.

The treatment of cross-reactions is complex in the case of ISOPOO. Individual

reaction	parameter	Jenkin and Hayman (1995)	Jenkin *et al.* (1998)	our recommendation
β 1-OH,2-OO	Rate ($\times 10^{-14}$ cm^3 $molec^{-1}$ s^{-1})	15.1	308	308
$+\beta$ 4-OH,3-OO	Yield: MVK + MACR + $2HO_2$ + $2CH_2O$	0.875	0.9	0.9
	Yield: ISOP3CO4OH + ISOP1OH2OH	0.125	0.1	0.1
All isomers + CH_3O_2	Rate ($\times 10^{-14}$ cm^3 $molec^{-1}$ s^{-1})		200	200
β 1-OH,2-OO	Yield: MVK + CH_3O + HO_2 + CH_2O		0.5	0.5
+ CH_3O_2	Yield: ISOP1OH2OH + CH_2O		0.5	0.5
β 4-OH,3-OO	Yield: MACR + CH_3O + HO_2 + CH_2O		0.5	0.5
+ CH_3O_2	Yield: ISOP3OH4OH + CH_2O		0.25	0.25
	Yield: ISOP3CO4OH + CH_3OH		0.25	0.25

Table 4.10: RO_2-RO_2 cross-reaction rate constants and branching fractions. Individual rate constants and expected product branching rates are indicated for each radical pair ($\times 10^{-14}$ cm^3 $molec^{-1}$ s^{-1}).

isomer	Jenkin and Hayman (1995)	Jenkin *et al.* (1998)	our recommendations	products
β 1-OH,2-OO	1	1	1	2MVK + 2HO_2 + 2CH_2O
β 4-OH,3-OO	0.75	0.8	0.8	2MACR + 2HO_2 + 2CH_2O
	0.25	0.2	0.2	ISOP3CO4OH + ISOP3OH4OH

Table 4.11: Product yields from the self-reactions of the two β isomers of isoprene hydroxy peroxy radicals.

isomers are expected to react with any available peroxy radical, including the methyl peroxy radical. We have again presented the rate constants and branching fractions for only the β isomers in Table 4.10; a more detailed treatment of the cross-reactions can be found in the Supplement. In the case of primary or secondary peroxy radicals, channels R2a and R2b are assumed to make up equal portions of the remaining rate constant. We also list the rate constant for ISOPOO reactions with CH_3O_2, which is assumed to be the same for all isomers.

4.3.3.4 H-Shift Isomerization of ISOPOO

Based on theoretical calculations, two novel HO_x recycling pathways involving H-shift isomerizations of the ISOPOO radicals have been proposed (Peeters *et al.*, 2014, 2009; Silva *et al.*, 2010).

1,6 H-shift - Following a 1,6 H-shift to the *Z*-δ hydroxy peroxy radicals of isoprene, reaction with O_2 and elimination of HO_2 to form unsaturated hydroperoxy aldehydes (HPALDs) can occur. Peeters *et al.* (2009) suggested that these HPALD compounds photolyze rapidly to reform OH, sustaining HO_x, even in the face of high levels of isoprene and low levels of NO_x.

Kinetics - Laboratory studies by Crounse *et al.* (2011) determined that the bulk HPALD formation rate is substantially slower than predicted by Peeters *et al.* (2009), but still fast enough to have importance for atmospheric isoprene chemistry. Improved calculations of the isoprene RO_2 equilibrium constants (Section 4.3.2) and H-shift rates (Peeters *et al.*, 2014), along with the recognition that the HPALD yield following the 1,6 H-shift is likely not unity (Crounse *et al.*, 2011; Teng *et al.*, 2017), bring the laboratory and theoretical determinations for the individual peroxy radical isomerization rates well within their combined uncertainties.

Here, we recommend the 1,6 H-shift rates of the *Z*-δ isoprene peroxy radicals calculated by Teng *et al.* (2017). These calculations assumed 1,5 H-shift rates of β hydroxy peroxy radicals (see below) and tunneling temperature dependences

($e^{1\times10^8/T^3}$) reported in Peeters *et al.* (2014).

$$k_{(1,6-H),z-1-OH-4-OO} = 5.47 \times 10^{15} \times e^{(-12200/T)} \times e^{(1\times10^8/T^3)} s^{-1} \quad (4.7)$$

$$k_{(1,6-H),z-4-OH-1-OO} = 2.40 \times 10^{9} \times e^{(-7160/T)} \times e^{(1\times10^8/T^3)} s^{-1} \quad (4.8)$$

Teng *et al.* (2017) estimate that these rates are only certain within a factor of 3.5, which puts their values at ambient temperatures (0.36 s^{-1} and 3.7 s^{-1}, respectively, at 297 K) well within the range of those calculated by Peeters *et al.* (2014) (0.49 ± 0.32 s^{-1} and 5.4 ± 3.3 s^{-1}, respectively). Although the absolute rate for 1,6 H-shift to the *Z*-δ hydroxy peroxy radicals is highly uncertain due to large uncertainty in the fraction of ISOPOO present in this isomer, uncertainty in the bulk rate coefficient within each system (OH addition at C1 or C4) is much smaller (see Teng *et al.*, 2017) provided self-consistent application of the thermochemistry is employed.

Mechanism (Figures 4.7 and 4.8) - Teng *et al.* (2017) also estimated the yields of HPALDs and other products from the 1,6 H-shifts of the *Z*-δ isoprene peroxy radicals, and proposed a tentative mechanism for the formation of the observed products, which we modify slightly for our own recommendations. There remains considerable uncertainty in the yields of HPALDs and other products from the 1,6 H-shifts. Currently, from experimental (Crounse *et al.*, 2011; Teng *et al.*, 2017) and theoretical (Peeters *et al.*, 2014) work we recommend that the HPALD yield from each 1,6 H-shift channel is 0.33. We arrive at this estimate by combining the measurement of HPALD with an additional isomerization product identified by Teng *et al.* (2017) with the same mass. The balance of the isomerization products remain uncertain. (Crounse *et al.*, 2011; Teng *et al.*, 2017) observed approximately half of the non-HPALD products produced *via* the 1,6 H-shift chemistry at masses consistent with products of hydroperoxy acetone and hydroperoxy ethanal. Here, we recommend that these products are formed *via* bimolecular chemistry and accompanied by HO_x recycling. The remainder of the carbon is routed to the C_4 dihydroperoxy carbonyls (3-OOH,4-OOH MVK and 2-OOH,3-OOH MACR) proposed by Peeters *et al.* (2014). These products may be rapidly lost to walls of chambers or tubing, and/or too fragile to detect at specific product masses with the CF_3O^- ion chemistry used in the Teng *et al.* (2017) study. In the atmosphere, they may undergo rapid photolysis (Peeters *et al.*, 2014; Praske *et al.*, 2015), leading to further HO_x regeneration. Other experimental evidence for HO_x recycling (Fuchs *et al.*, 2013) and HPALD formation (Berndt, 2012; Crounse *et al.*, 2011) is consis-

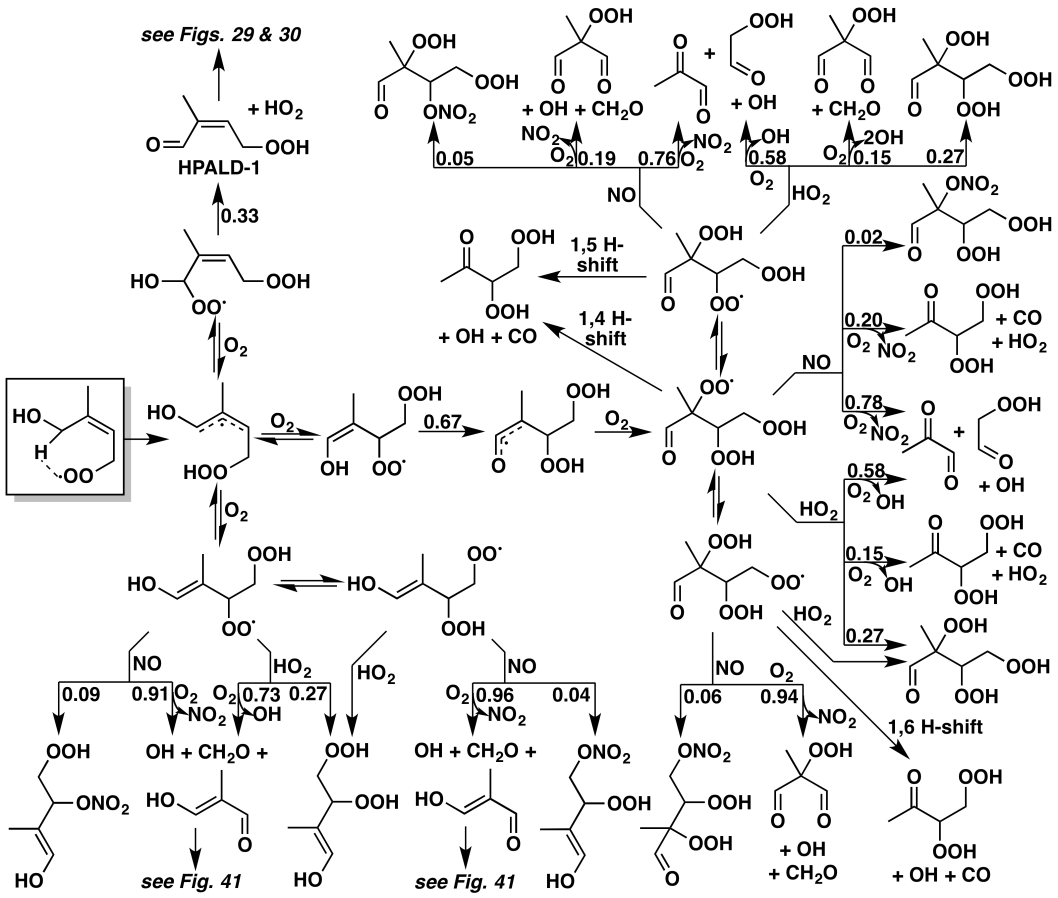

Figure 4.7: Reactions and products following the 1,6 H-shift of the *Z*-1-OO,4-OH-isoprene-hydroxy-peroxy radical. Yields are for 298 K and 1 atm; in reactions of peroxy radicals with NO, the relative contributions of the nitrate and alkoxy pathways vary with both temperature and pressure. Although we show the possible bimolecular reactions of the *E*-enol peroxy radicals (lower left) for completeness, we assume the initial addition and removal of oxygen occurs quickly enough to route all the non-HPALD products *via* the *Z*-enol peroxy radical (center). For the reduced mechanism, we represent the pool of hydroperoxy-peroxy radicals as a single species, and we assume the C_4 dihydroperoxycarbonyl compounds decompose immediately to form 2×OH + methylglyoxal + CH_2O.

tent with the determinations of Teng *et al.* (2017), though they do not reduce the uncertainty in the isomerization rates or product yields.

1,5-H-shift (Figure 4.9) - The 1,5-H-shift of the O-H hydrogen in the major β hydroxy peroxy radicals has been calculated by several groups (Peeters *et al.*, 2014, 2009; Silva *et al.*, 2010) to have only minor importance in the atmospheric oxidation of isoprene. The products include MVK, MACR, HCHO, and OH. Here, we use the

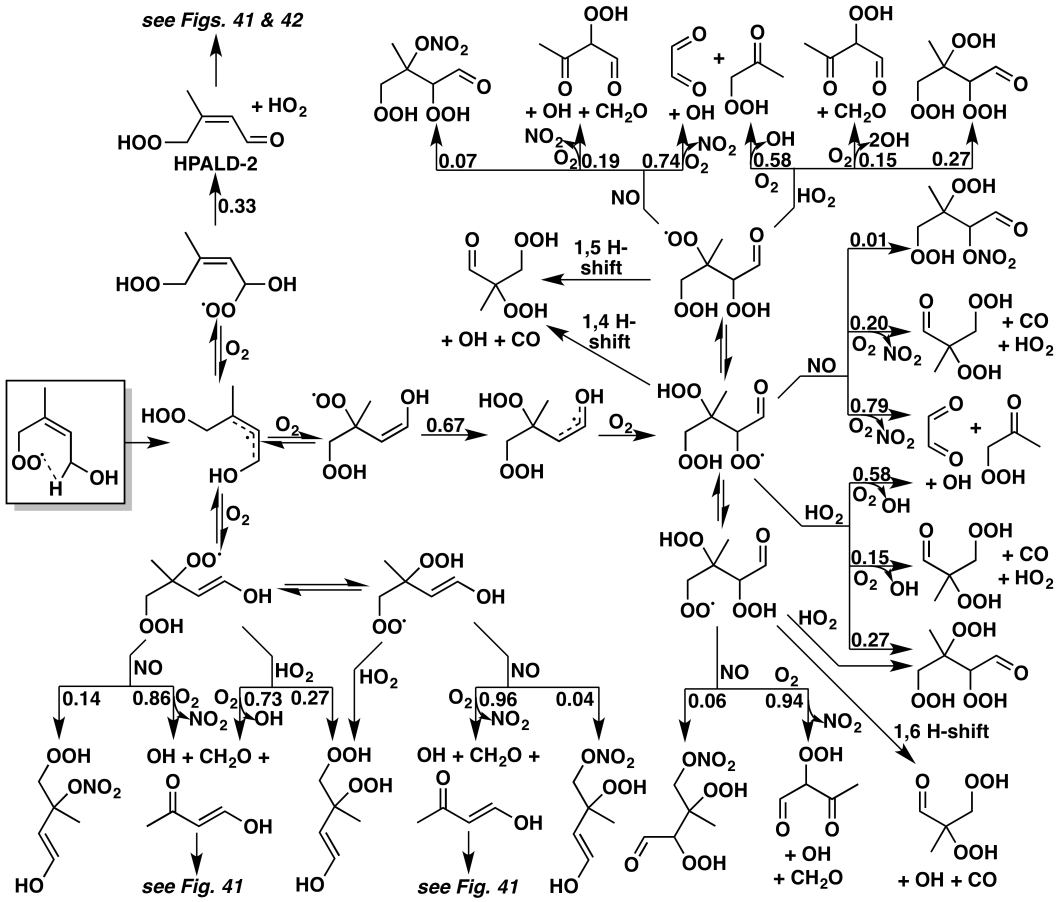

Figure 4.8: Reactions and products following the 1,6 H-shift of the *Z*-1-OH,4-OO-isoprene-hydroxy-peroxy radical. Yields are for 298 K and 1 atm; in reactions of peroxy radicals with NO, the relative contributions of the nitrate and alkoxy pathways vary with both temperature and pressure. Although we show the possible bimolecular reactions of the *E*-enol peroxy radicals (lower left) for completeness, we assume the initial addition and removal of oxygen occurs quickly enough to route all the non-HPALD products *via* the *Z*-enol peroxy radical (center). For the reduced mechanism, we represent the pool of hydroperoxy-peroxy radicals as a single species, and we assume the C_4 dihydroperoxycarbonyl compounds decompose immediately to form 2×OH + methylglyoxal + CH_2O.

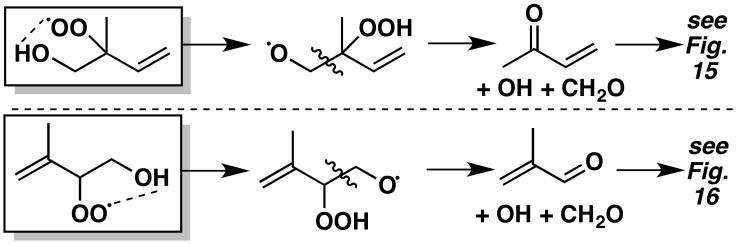

Figure 4.9: Reactions and products following the 1,5 H-shift of the β-isoprene-OH-OO isomers.

rates coefficients reported in Peeters *et al.* (2014), consistent with the experimental constraints of Crounse *et al.* (2011):

$$k_{(1,5-H),1-OH-2-OO} = 1.04 \times 10^{-11} \times e^{(-9746/T)} \text{ s}^{-1}$$

$$k_{(1,5-H),4-OH-3-OO} = 1.88 \times 10^{-11} \times e^{(-9752/T)} \text{ s}^{-1}$$

4.4 isoprene + O_3

Although reaction with OH constitutes the dominant isoprene loss process, reaction with ozone is estimated to account for approximately 10% of isoprene removal in the atmosphere (Atkinson *et al.*, 2006; Isidorov, 1990). Through a complex series of reactions and intermediates, ozonolysis of isoprene provides a source of OH radicals, organic peroxy radicals, and secondary organic aerosols (SOA) precursors to the atmosphere (*e.g.*, Biesenthal *et al.*, 1998; Kamens *et al.*, 1982; Nguyen *et al.*, 2010). In isoprene-rich regions, ozonolysis of isoprene can also represent an important ozone loss mechanism (Fiore *et al.*, 2005).

Kinetics (Table 4.12) - A number of studies have reported the rate coefficients for the reaction of ozone with isoprene. Most (Table 4.12) utilized environmental chambers and included addition of compounds such as cyclohexane, *n*-octane or carbon monoxide to remove the OH generated from ozonolysis. The measured reaction rate constants are generally in good agreement. Adeniji *et al.* (1981) reported an abnormally high value, likely because they did not use any OH scavenger (Klawatsch-Carrasco *et al.*, 2004). The causes of other smaller discrepancies are unclear. The IUPAC preferred value of $k_{isop+O_3} = 1.1 \times 10^{-14} \times e^{-2000/T}$ cm^3 molec^{-1} s^{-1} is adopted here.

Mechanism (Figure 4.10) - The mechanism of isoprene ozonolysis has also been the subject of numerous investigations, with more widely varying results. Here, we outline a reaction scheme developed from that compiled in Nguyen *et al.* (2016).

methodology	T (K)	rate constant ($\times 10^{-17}$ cm^3 $molec^{-1}$ s^{-1})	citation
chamber, excess reactant, no scavenger	295 ± 1	1.27	Arnts and Jr (1979)
chamber, excess reactant, no scavenger	294 ± 2	1.65	Adeniji *et al.* (1981)
chamber, excess reactant, no scavenger	296 ± 2	1.17 ± 0.19	Atkinson *et al.* (1982)
outdoor chamber, no scavenger	291	1.1	Kamens *et al.* (1982)
relative rate technique, n-octane scavenger	296 ± 2	1.16 ± 0.02	Greene and Atkinson (1992)
chamber, excess reactant, no scavenger	298	1.28 ± 0.12	Treacy *et al.* (1992)
chamber, cyclohexane scavenger	293 ± 2	0.895 ± 0.025	Grosjean *et al.* (1993b)
chamber, cyclohexane scavenger	291 ± 2	1.13 ± 0.32	Grosjean and Grosjean (1996)
relative rate technique, He diluent gas	298	1.3 ± 0.08	Khamaganov and Hites (2001)
theoretical study	300	1.58	Zhang and Zhang (2002)
relative rate technique, trimethylbenzene scavenger	298	1.22 ± 0.03	Avzianova and Ariya (2002)
chamber, CO scavenger	293 ± 2 K	1.19 ± 0.09	Klawatsch-Carrasco *et al.* (2004)
chamber, no scavenger	286 K	0.96 ± 0.07	Karl *et al.* (2004)
IUPAC / our recommendation	**240-360**	$1030 \times e^{(-1995/T)}$	**Atkinson *et al.* (2006)**

Table 4.12: Chronological estimates of isoprene + O_3 reaction rate constants.

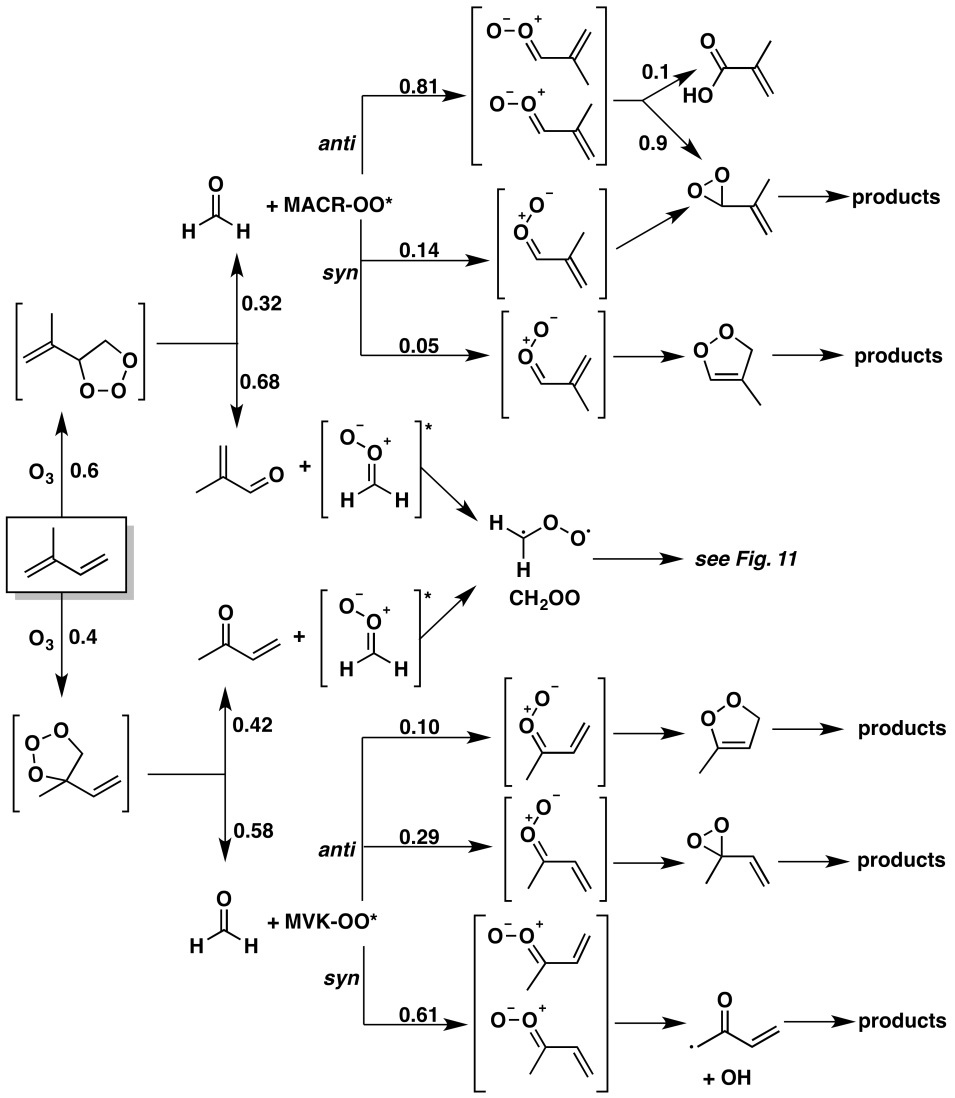

Figure 4.10: Reactions and products following the ozonolysis of isoprene. Many of the Criegee decomposition products remain unidentified; we therefore generally assume that they decompose to small, stable products. Our full and reduced recommended mechanisms can be found in the supplemental tables. For a more detailed treatment of the complete ozonolysis mechanism, see Nguyen *et al.* (2016).

Because of their uncertainty and minor yields, a number of C_3-C_4 stable products of the C_4 Criegee intermediates are not treated discretely here; instead, to ensure mass balance, they are assumed to decompose to smaller products.

The generally accepted first step of ozonolysis involves the cycloaddition of ozone at either double bond in isoprene to form one of two possible primary ozonides (POZ) (*e.g.*, Zhang and Zhang, 2002). In our mechanism, we use the POZ branching ratio from Aschmann and Atkinson (1994), which suggests that the electron donating

effects of the methyl group are outweighed by its steric hindrance, leading to a 60% yield of the 3,4-addition POZ and a 40% yield of the 1,2-addition POZ.

Decomposition of the POZ yields MACR or formaldehyde in the major branch and MVK or formaldehyde for 1,2-addition. Both branches also yield a highly reactive C_1 or C_4 carbonyl oxide, also known as the activated Criegee intermediate (CI*, where the asterisk denotes the unstable, activated state) (Criegee, 1975; Criegee and Wenner, 1949).

The zwitterionic C_4 CI* has a number of distinct conformations – four each for MVK-OO* and MACR-OO*, either *syn* or *anti* to their methyl or vinyl groups – for which the barriers to interconversion are expected to be large (Anglada *et al.*, 1996; Hull, 1978; Taatjes *et al.*, 2013). We recommend the isomer branching ratios in Nguyen *et al.* (2016), derived in turn from Kuwata and Valin (2008) and Kuwata *et al.* (2010). The CI* undergoes unimolecular decomposition, forming OH and a β-oxy alkyl radical (Kroll *et al.*, 2001), or is thermally stabilized to form a stabilized Criegee intermediate (SCI).

4.4.1 Reactions of the stabilized Criegee intermediate

The C_1 SCI (CH_2OO) is formed from the ozonolysis of all terminal alkenes, and has therefore been studied in much greater detail than the C_4 SCIs. Because CH_2OO lacks substituents and cannot have a *syn* conformation, it has low unimolecular reactivity (Anglada *et al.*, 2011). Instead, CH_2OO reacts with a number of gaseous molecules, the most relevant of which are shown in Figure 4.11.

Kinetics - We recommend reaction rate constants for the SCIs from Nguyen *et al.* (2016). The principal reaction partners of CH_2OO in the atmosphere are water and its dimer, $(H_2O)_2$. At relative humidity below 60%, reaction with the water monomer dominates, with a rate constant of $k_{H_2O} = 9 \times 10^{-16}$ cm^3 molec^{-1} s^{-1}, consistent with previous estimates (Welz *et al.*, 2012). At RH > 60%, reaction of CH_2OO with the water dimer dominates, with a rate constant of $k_{(H_2O)_2} = 8 \times 10^{-13}$ cm^3 molec^{-1} s^{-1} – much faster than that with the water monomer, and consistent with some (Leather *et al.*, 2012; Newland *et al.*, 2015) but slower than other estimates (Berndt *et al.*, 2014; Chao *et al.*, 2015; Lewis *et al.*, 2015).

Despite the dominance of reaction with water and its dimer in determining the fate of the C_1 SCI, other pathways may be important. In our mechanism, we include the reactions of CH_2OO with SO_2 and formic acid, that while minor, can contribute to the local loss of those reactants. For reaction with SO_2, we suggest a relative

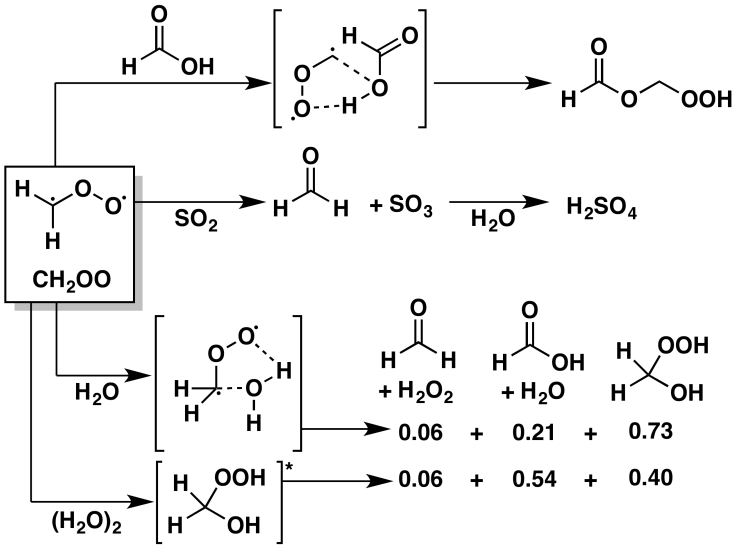

Figure 4.11: Reactions and products of the stabilized C_1 Criegee produced in the ozonolysis of isoprene. For the reduced mechanism, we remove the reactions with SO_2 and HCOOH.

rate constant of $k_{SO_2}/(k_{H_2O} + k_{(H_2O)_2}) = 2.2(\pm 0.3) \times 10^4$ (Nguyen *et al.*, 2016), consistent with previous estimates (Atkinson and Lloyd, 1984; Newland *et al.*, 2015; Welz *et al.*, 2012). For reaction with formic acid, we use a relative rate constant of $k_{HCOOH}/k_{SO_2} = 2.8$ (Sipilä *et al.*, 2014). Reactions of CH_2OO with isoprene and RO_2 radicals ($k_{isop} = 1.78 \times 10^{-13}$ cm^3 molec^{-1} s^{-1} and $k_{RO_2} = 5 \times 10^{-12}$ cm^3 molec^{-1} s^{-1} respectively; Vereecken *et al.*, 2012) are not included in our mechanism. These may be relevant in chamber experiments performed with high isoprene loadings.

Mechanism (Figure 4.11) - We use recommendations from Nguyen *et al.* (2016) for products of the various reactions of the C_1 SCI. The reactions of CH_2OO with water and the water dimer both follow three product channels – forming hydroxymethyl hydroperoxide (HMHP), formic acid and water, or formaldehyde and hydrogen peroxide – with differing branching ratios, shown in Figure 4.11. The subsequent chemistry of HMHP is described in Section 4.7.8. The reaction of CH_2OO with SO_2 produces formaldehyde and SO_3, which goes on to form sulfuric acid, while its reactions with formic acid produces hydroperoxy methylformate (HPMF).

The fates of the C_4 CI* and SCI products are significantly less certain. Unlike CH_2OO, the C_4 Criegees are most likely to undergo unimolecular decomposition

(either before or after stabilization), the rate and products of which depend on the conformation of the CI (Gutbrod *et al.*, 1997; Nguyen *et al.*, 2016); proposed pathways are shown in Figure 4.10. *Syn*-MVK-OO* Criegees are expected to form a vinyl hydroperoxide, which will subsequently decompose to form OH and a β-oxy alkyl radical (Aschmann and Atkinson, 1994; Donahue *et al.*, 2011; Gutbrod *et al.*, 1997; Kuwata *et al.*, 2010; Paulson *et al.*, 1992). The other C_4 Criegees are presumed to decompose primarily *via* 5-member dioxole or 3-member dioxirane intermediates (Kuwata *et al.*, 2010; Kuwata and Valin, 2008; Vereecken *et al.*, 2012). As stated previously, our mechanism does not treat their stable products individually; for a more detailed treatment of the decomposition products of C_4 Criegee intermediates, see Nguyen *et al.* (2016).

4.5 The reaction of NO_3 with isoprene

NO_3 represents a minor sink for isoprene in the atmosphere. As NO_3 readily photolyzes during the day, this chemistry is generally important only at night. When photolysis rates are reduced, however, such as below dense forest canopies or clouds, NO_3 oxidation can also be important during the day. Although isoprene emissions are typically low at night, many field studies demonstrate that isoprene can accumulate in the early evening. Sharp declines in isoprene concentration after sunset have been credited to NO_3 oxidation (Brown *et al.*, 2009; Starn *et al.*, 1998; Stroud *et al.*, 2002). Formation of isoprene NO_3 oxidation products (*e.g.*, organic nitrates) have been observed at night (Beaver *et al.*, 2012; Grossenbacher *et al.*, 2004). Horowitz *et al.* (2007) and Xie *et al.* (2013) using global chemical transport models predicted a considerable proportion (~40-50%) of isoprene derived nitrates are produced from NO_3 oxidation even though this chemistry represents a rather minor sink for isoprene (~5-6%; Horowitz *et al.*, 2007; Ng *et al.*, 2008).

Kinetics (Table 4.13) - NO_3 reacts with isoprene much like OH, by adding to a double bond. A number of studies have reported rate constants for the reaction of isoprene with NO_3; a summary of measured rate coefficients from kinetic studies can be found in Table 4.13, along with the rates used in various models and those recommended by IUPAC (Atkinson *et al.*, 2006) and JPL (Burkholder *et al.*, 2015). Our mechanism uses the IUPAC value of $2.95 \times 10^{-12} \times e^{(-450/T)}$ cm^3 molec^{-1} s^{-1}.

Mechanism (Figure 4.12; Tables 4.14 and 4.15) - C1 addition of NO_3 is favored over C4 addition (Berndt and Boge, 1997; Schwantes *et al.*, 2015; Skov *et al.*, 1992), and a *cis:trans* ratio of 1:1 is assumed as calculated by Peeters *et al.* (2009) for OH

methodology[a]	T (K)	rate constant (cm^3 $molec^{-1}$ s^{-1})	citation
relative rate, GC-FID, $N_2O_5 \rightleftharpoons NO_2 + NO_3$	295 ± 1	$(5.94 \pm 0.16) \times 10^{-13}$	Atkinson *et al.* (1984)
flow tube, DF-MS, $F + HNO_3 \rightarrow HF + NO_3$	298	$(1.3 \pm 0.14) \times 10^{-12}$	Benter and Schindler (1988)
flow tube, LIF, $N_2O_5 \rightleftharpoons NO_2 + NO_3$	297	$(6.52 \pm 0.78) \times 10^{-13}$	Dlugokencky and Howard (1989)
relative rate, FTIR, $N_2O_5 \rightleftharpoons NO_2 + NO_3$	298 ± 2	$(1.21 \pm 0.20) \times 10^{-12}$	Barnes *et al.* (1990)
flow tube, DF-MS, $F + HNO_3 \rightarrow HF + NO_3$	298	$(7.30 \pm 0.44) \times 10^{-13}$	Wille *et al.* (1991)
flow tube, DF-MS, $F + HNO_3 \rightarrow HF + NO_3$	298	$(8.26 \pm 0.60) \times 10^{-13}$	Lancar *et al.* (1991)
UV-VIS, $F + HNO_3 \rightarrow HF + NO_3$	295 ± 2	$(1.07 \pm 0.20) \times 10^{-12}$	Ellermann *et al.* (1992)
relative rate, FTIR, $N_2O_5 \rightleftharpoons NO_2 + NO_3$	298	$(6.86 \pm 0.55) \times 10^{-13}$	Berndt and Boge (1997)
flow tube, CIMS, $N_2O_5 \rightleftharpoons NO_2 + NO_3$	298 ± 2	$(7.3 \pm 0.2) \times 10^{-13}$	Suh *et al.* (2001)
relative rate, FTIR, $N_2O_5 \rightleftharpoons NO_2 + NO_3$	296 ± 2	$(7.0 \pm 0.6) \times 10^{-13}$	Stabel *et al.* (2005)
relative rate, CIMS, $N_2O_5 \rightleftharpoons NO_2 + NO_3$	295 ± 2	$(6.13 \pm 0.12) \times 10^{-13}$	Zhao *et al.* (2011)
model: CMAQ	-	$3.03 \times 10^{-12} \times e^{(-448/T)}$	Xie *et al.* (2013)
model: GEOS-Chem	-	$3.3 \times 10^{-12} \times e^{(-450/T)}$	Mao *et al.* (2013)
model: MCM v3.3.1	-	$3.15 \times 10^{-12} \times e^{(-450/T)}$	Jenkin *et al.* (2015)
JPL recommendation	251-381	$3.5 \times 10^{-12} \times e^{(-450/T)}$	Burkholder *et al.* (2015)
IUPAC / our recommendation	**250-390**	$2.95 \times 10^{-12} \times e^{(-450/T)}$	Atkinson *et al.* (2006)

Table 4.13: Chronological estimates of isoprene + NO_3 reaction rate constants, and those used in models. [a]studies employed a chamber technique unless otherwise noted.

nitrate yield	instrument for detection	chamber method	citation
~ 80%	In situ FTIR[a]	$N_2O_5 \rightleftharpoons NO_2 + NO_3$	Barnes *et al.* (1990)
~ 90%	In situ FTIR[a]	$N_2O_5 \rightleftharpoons NO_2 + NO_3$	Berndt and Boge (1997)
70 ± 8%	TD-LIF[b]	$NO_2 + O_3 \rightarrow NO_3 + O_2$	Rollins *et al.* (2009)
65 ± 12%	TD-LIF[b] and PTRMS[c]	$NO_2 + O_3 \rightarrow NO_3 + O_2$	Perring *et al.* (2009)
~ 80%	CF_3O^- CIMS[d]	$N_2O_5 \rightleftharpoons NO_2 + NO_3$	Kwan *et al.* (2012)
76 ± 15%[e]	CF_3O^- CIMS[d]	$NO_2 + O_3 \rightarrow NO_3 + O_2$, $NO_3 + CH_2O \rightarrow HO_2 + HNO_3$	Schwantes *et al.* (2015)

Table 4.14: Chronological estimates of overall molar nitrate yield from isoprene NO_3 oxidation. Abbreviations: [a]Fourier transform infrared spectrometer; [b]thermal dissociation-laser induced fluorescence; [c]proton transfer reaction mass spectrometer; [d]chemical ionization mass spectrometer. [e]Reported nitrate yield is a lower bound. Isoprene also reacts to some extent with O_3, which is unlikely to form nitrates.

addition to C1 of isoprene.

Following addition of NO_3, nitrooxy peroxy radicals are formed *via* addition of oxygen. The nitrooxy peroxy radical (INO_2) isomers and subsequent chemistry are displayed in Figure 4.12. The δ-INO_2 exist in either the *Z*- or *E*-isomers. In our mechanism, these are combined with the exception of the *Z* and *E* isomers of IHN that are considered separately to be consistent with the OH-generated counterparts.

The INO_2 distribution used here (Table 4.15) is not as well characterized as the ISOPOO distribution presented in Section 4.3.2. This distribution is the average distribution estimated by Schwantes *et al.* (2015) at an RO_2 lifetime of ~30 s based on products detected from the INO_2 + HO_2 reaction including IPN isomers. To estimate this distribution, a number of assumptions were made, including that all isomers of INO_2 react with HO_2 at the same rate (see Schwantes *et al.* (2015) for more details). The δ-INO_2 abundance is slightly higher than that of β-INO_2 - opposite to the ISOPOO isomer ratio in the OH oxidation at similar RO_2 lifetimes (Section 4.3.2). This suggests that peroxy radicals produced from NO_3 oxidation have different thermodynamic and kinetic properties. Future experimental and theoretical studies are recommended to better understand how the RO_2 lifetime influences the INO_2 isomer distribution.

4.5.1 INO_2 reaction with HO_2

Kinetics - As discussed in Section 4.2, we use a relationship between the number of heavy atoms in INO_2 to estimate the rate coefficient for the reaction of INO_2 with HO_2; this parameterization gives a rate coefficient of $2.47 \times 10^{-13} \times exp(1300/T)$

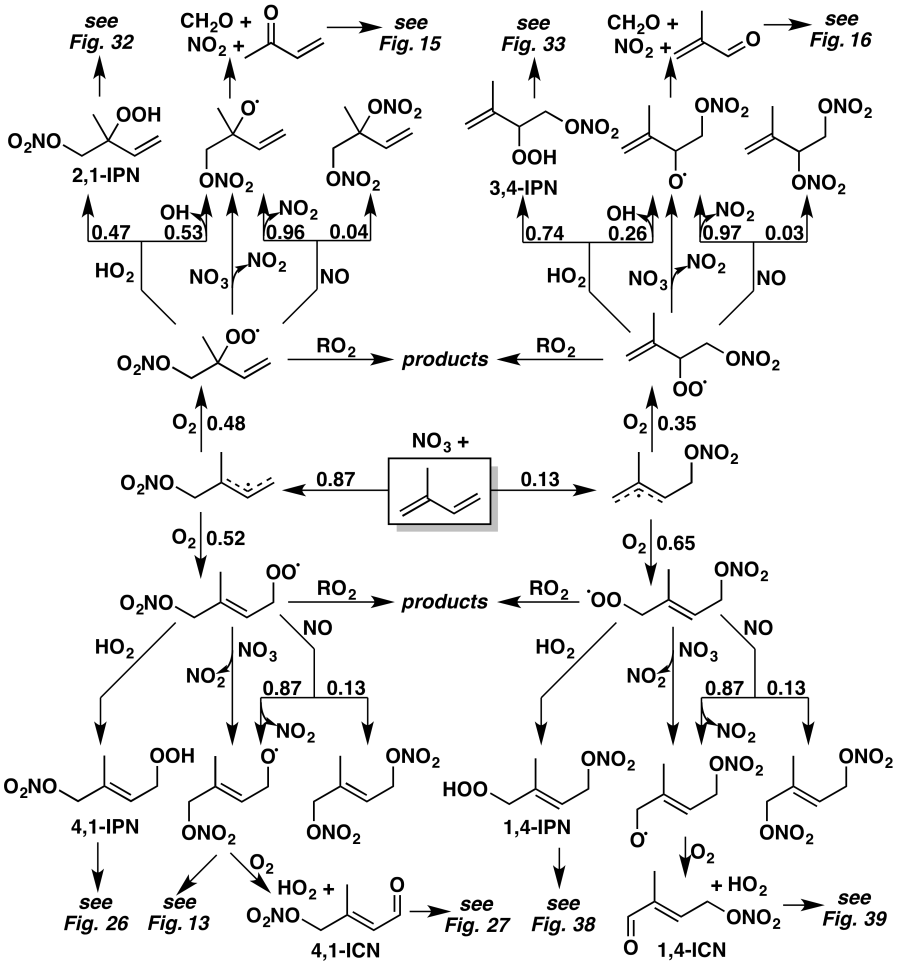

Figure 4.12: Reactions and products following the addition of NO_3 to isoprene. While δ -nitrates are presumed to form as equal mixtures of E and Z isomers, the subsequent chemistry of those stereoisomers is expected to be largely the same; we therefore show only E-δ nitrate products for brevity (bottom half). Yields are for 298 K and 1 atm; in reactions of peroxy radicals with NO, the relative contributions of the nitrate and alkoxy pathways vary with both temperature and pressure. RO_2 + RO_2 reactions may be important peroxy radical sinks at night; for a discussion of the expected products, see Section 4.5.3. For the reduced mechanism, we combine the two β isomers, with their subsequent product yields scaled to the ratio of their contributions, and doing the same with the two δ isomers, as shown in the supplemental tables.

isomer	fraction [a]
β-(1-ONO_2,2-OO)-INO_2	0.42
β-(4-ONO_2,3-OO)-INO_2	0.045 ±0.015 [b]
δ-(1-ONO_2,4-OO)-INO_2	0.45 ± 0.01 [b]
δ-(4-ONO_2,1-OO)-INO_2	0.085 ± 0.005 [b]

Table 4.15: Nitrooxy peroxy radical distribution at RO_2 lifetime of ~30 s. [a]Fraction reported by (Schwantes *et al.*, 2015). [b]Only a range of fractions was reported by (Schwantes *et al.*, 2015). The average is used in the mechanism, and the range is included above for reference.

isomer	products	yield, % [a]
β-(1-ONO_2,2-OO)-INO_2	MVK, CH_2O, OH, NO_2	53
	β-(1-ONO_2,2-OOH)-IPN	47
β-(4-ONO_2,3-OO)-INO_2	MACR, CH_2O, OH, NO_2	26.5 ± 26.5 [b]
	β-(4-ONO_2,3-OOH)-IPN	73.5 ± 26.5 [b]
δ-(1-ONO_2,4-OO)-INO_2	δ-(1-ONO_2,4-OOH)-IPN	100
δ-(4-ONO_2,1-OO)-INO_2	δ-(4-ONO_2,1-OOH)-IPN	100

Table 4.16: Estimated products from the reaction of INO_2 + HO_2. [a]Yield reported by (Schwantes *et al.*, 2015). [b]Only a range of yields was reported by (Schwantes *et al.*, 2015). The average is used in the mechanism, and the range is included above for reference.

cm^3 $molec^{-1}$ s^{-1}.

Mechanism (Table 4.16) - Traditionally, peroxy radicals are assumed to react with HO_2 to produce a hydroperoxide (in this case, IPN) in near unity yield. Recent studies have shown, however, that other pathways are important (Orlando and Tyndall, 2012, and references therein). Rollins *et al.* (2009) first proposed that INO_2 + HO_2 reactions yields OH. Kwan *et al.* (2012) constrained the OH producing pathway to 38-58%, somewhat higher than Schwantes *et al.* (2015), who estimated the yield of OH to be 22-25% at RO_2 lifetimes of ~30 s. The OH yield of the INO_2 + HO_2 reaction is expected to be isomer specific and so will depend on this lifetime (Schwantes *et al.*, 2015). The recommended products from the INO_2 + HO_2 reaction for each INO_2 isomer as estimated by Schwantes *et al.* (2015) are shown in Table 4.16.

4.5.2 INO_2 reaction with NO/NO_3

Kinetics - The reaction rate coefficients of INO_2 with NO and NO_3 are assumed to be $2.7 \times 10^{-12} \times e^{(350/T)}$ and 2.3×10^{-12} cm^3 $molec^{-1}$ s^{-1}, respectively. These are generic RO_2 + NO and RO_2 + NO_3 rate coefficients used by MCM v3.3.1 (Jenkin *et al.*, 2015).

Mechanism - The nitrate yield from INO_2 + NO has not been measured, but chamber studies have detected the formation of a dinitrate (Ng *et al.*, 2008; Schwantes *et al.*, 2015). We use the formula presented in Equation 4.3 to calculate individual dinitrate yields for each INO_2 isomer, shown in Figure 4.12. The remaining products are assumed to be NO_2 and an alkoxy radical, the fate of which is discussed in Section 4.5.4. INO_2 + NO_3 reactions are assumed to only form an alkoxy radical and NO_2.

4.5.3 INO_2 reaction with RO_2

Kinetics - RO_2 + RO_2 reaction rate constants for RO_2 radicals containing a nitrate functional group have not been well constrained. MCM v3.3.1 recommends the rate constant for RO_2 reactions with INO_2 to be 1.3×10^{-12} cm^3 $molec^{-1}$ s^{-1}. Experiments suggest, however, that the RO_2 + RO_2 reaction rate constants for INO_2 are actually much faster (Kwan *et al.*, 2012; Schwantes *et al.*, 2015). The faster INO_2 + INO_2 reaction rate constants estimated by Kwan *et al.* (2012) and Schwantes *et al.* (2015) are consistent with estimates for other electron withdrawing groups such as β-chloro, β-bromo, and β-hydroxy groups (Crowley and Moortgat, 1992; Jenkin and Hayman, 1995; Murrells *et al.*, 1991). Although Schwantes *et al.* (2015) estimated the self-reaction rate constants, they did not address potential cross-reactions as has been done for the OH system by Jenkin *et al.* (1998). Thus, the hydroxy peroxy radical reaction rate constants measured by Jenkin *et al.* (1998) are recommended to be used for the nitrooxy peroxy radical self- and cross-reactions (Table 4.10). The reaction rate constants for cross-reactions between nitrooxy peroxy radicals with methyl peroxy radicals are estimated by calculating the geometric mean of the individual self-reaction rate constants. Additional experimental studies are recommended to determine how nitrate groups influence RO_2 + RO_2 reactions.

Mechanism - Kwan *et al.* (2012) proposed that INO_2 + INO_2 leads to the following products: IHN + ICN (59-77%), ROOR (3-4%), and 2 INO (19-38%). Somewhat different yields - IHN + ICN (77%), ROOR (3.5%), and 2 INO (19.5%) - are

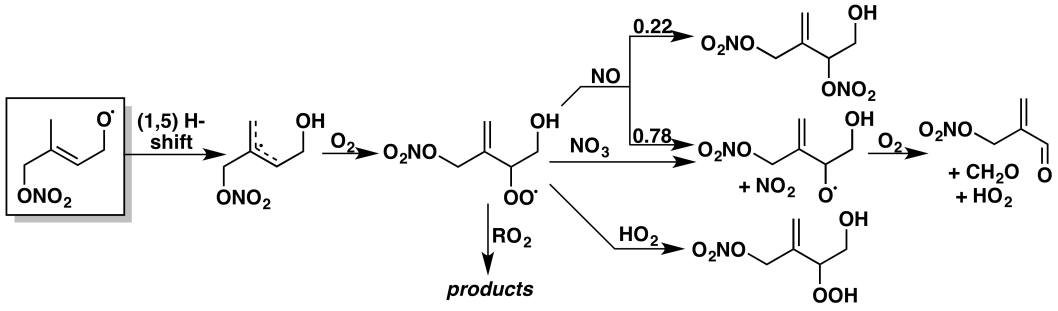

Figure 4.13: Reactions and products following the 1,5 H-shift of [1,4]-*E*-δ-INO, based on the mechanism proposed by Kwan *et al.* (2012). Yields are for 298 K and 1 atm; in reactions of peroxy radicals with NO, the relative contributions of the nitrate and alkoxy pathways vary with both temperature and pressure. RO_2 + RO_2 reactions may be important peroxy radical sinks at night; for a discussion of the expected products, see Section 4.5.3.

recommended here, as these best matched experimental results for individual IHN isomers in the study of Schwantes *et al.* (2015). All cross-reactions are assumed to have the same product yields as the self-reactions. The ROOR product is assumed to only form from INO_2 + INO_2 reactions.

4.5.4 INO radical fate

The alkoxy radical isomers are assumed to decompose or react with O_2 to form MVK, MACR, or ICN. [4,3]-β-INO is assumed to form only MACR as no [4,3]-β-ICN was detected in the work by Schwantes *et al.* (2015). In our mechanism, these reactions are generally included with the previous steps, except in the case of [1,4]-δ-*E*-INO, for which reaction with O_2 competes with isomerization.

4.5.4.1 H-shift isomerization reactions of INO and INO_2

Kwan *et al.* (2012) proposed that [1,4]-δ-*E*-INO would undergo a 1,5 H-shift to form the products shown in Figure 4.13. Schwantes *et al.* (2015) estimated this rate constant to be 3×10^5 s^{-1}. Following Peeters and Nguyen (2012), it is expected that the *E* and *Z* isomers will interconvert; deactivation by ONO_2 suggests that the H abstraction will be primarily from the *E* isomer as shown. This is in contrast to the OH system, in which the OH group is activating, leading most of the H-shift to occur from the Z isomer (Peeters and Nguyen, 2012).

The INO_2 isomers, similar to the peroxy radicals produced from isoprene + OH oxidation (Section 4.3.3.4), may also undergo 1,6 H-shift isomerization but *via* the

E rather than the Z isomer. For example, Schwantes *et al.* (2015) detected products that suggest that the E-[1,4]-δ-INO_2 isomer undergoes a 1,6 H-shift. The lifetime of the INO_2 radical is particularly long at night suggesting this chemistry may be important in the atmosphere. Too little information is known about this pathway to incorporate it into the chemical mechanism at this time. Future theoretical and experimental studies addressing the potential isomerization of INO_2 isomers are needed.

4.6 isoprene + Cl

Oxidation by chlorine radicals serves as a minor sink of isoprene. While the globally averaged concentration of Cl is estimated to have an upper limit of 10^3 atoms cm^{-3} (Rudolph *et al.*, 1996), concentrations peaking at 10^5 atoms cm^{-3} have been inferred for the marine boundary layer (Singh *et al.*, 1996). Recent observations of chlorine precursors in Boulder, Colorado have further suggested the importance of chlorine chemistry in mid-continental urban regions (Thornton *et al.*, 2010). Chlorine chemistry is thus expected to have the greatest impact on isoprene in coastal urban areas. In particular, unique products predicted in the oxidation of isoprene by Cl have been observed in Houston, Texas (Riemer *et al.*, 2008). Assuming [OH] $\sim 10^6$ molec cm^{-3} and a peak [Cl] $\sim 10^5$ atoms cm^{-3}, we estimate a relative reaction rate of k_{Cl}[Cl]/k_{OH}[OH] ~0.43 to represent an upper bound on the importance of Cl oxidation in isoprene chemistry.

Sources of Cl atoms in the troposphere include photochemical degradation of gaseous halocarbons emitted both naturally and anthropogenically (Seinfeld and Pandis, 2006). In the marine boundary layer, multiphase and heterogeneous reactions of sea salt spray are known to yield photolabile precursors (Behnke *et al.*, 1997; Finlayson-Pitts *et al.*, 1989; Roberts *et al.*, 2008; Schroeder and Urone, 1974). Recent laboratory work has also shown the potential for chlorine activation through surface catalyzed chemistry of HCl with nitrogen oxides (Raff *et al.*, 2009). Many of these reactions do not require sunlight, suggesting the nighttime buildup of precursors which rapidly photolyze in the morning to yield reactive Cl (Ravishankara, 2009).

Kinetics - There have been many experimental and theoretical studies on the rate constant for the reaction of Cl with isoprene. The NASA JPL data evaluation recommends a rate constant of 4.1×10^{-10} cm^3 $molec^{-1}$ s^{-1} at 298 K, which is an average of the values found in experimental studies (Burkholder *et al.*, 2015).

The recommended temperature-dependent rate constant is $7.6 \times 10^{-11} \times \exp(500/T)$ cm^3 $molec^{-1}$ s^{-1}, which is scaled from the value reported in the sole temperature-dependent study to match the recommended value at 298 K (Bedjanian *et al.*, 1998). The reaction of isoprene with Cl is approximately four times faster than its reaction with OH at 298 K.

Mechanism (Figure 4.14) - Our recommended mechanism for Cl oxidation of isoprene, carried out to first generation products, is presented in Figure 4.14. While we expect both *E* and *Z* stereoisomers of δ-chloro peroxy radicals to form, we only show the *E* isomers for brevity (the chemistry of the *Z* isomers is expected to be similar). Isoprene reacts with Cl predominantly through an addition mechanism. The branching fractions for the Cl-isoprene adducts formed from the addition channel have been determined in a theoretical study as 0.40:0.02:0.08:0.50 for 1:2:3:4-addition at 300 K (Lei *et al.*, 2002b). Unlike OH addition, 4-addition of Cl is predicted to exceed 1-addition. Experimental measurements have shown that abstraction of a methyl hydrogen to yield HCl and an allylic radical also occurs at atmospheric temperatures, with measured branching fractions in the range of 0.13 – 0.17 (Bedjanian *et al.*, 1998; Fantechi *et al.*, 1998; Ragains and Finlayson-Pitts, 1997; Suh and Zhang, 2000; Xing *et al.*, 2009). No pressure dependence is observed despite the range of pressures used in the various experiments. The NASA JPL data evaluation recommends a branching fraction to form HCl of 0.15 at 298 K, which is an average of the values found in those studies (Burkholder *et al.*, 2015). The recommended temperature-dependent branching fraction is $1.1 \times \exp(-595/T)$, which is scaled from the value reported in the sole temperature-dependent study to match the recommended value at 298 K (Bedjanian *et al.*, 1998). Comparison of Cl oxidation rate constants for isoprene and isoprene-d_8 at low pressures has suggested that the abstraction pathway is not concerted, but instead occurs through an addition mechanism with subsequent elimination of HCl (Ragains and Finlayson-Pitts, 1997). Indeed, theoretical work has predicted the formation of a weakly bound complex between chlorine and isoprene, resembling a long-range interaction between HCl and the allylic C_5H_7 radical, which undergoes elimination (Braña and Sordo, 2001). The existence of this complex may influence branching between the four Cl-isoprene adducts. Our recommended branching fractions for the reaction of Cl with isoprene are 0.15:0.38:0.47 for abstraction:1-addition:4-addition at 298 K. These values are derived by scaling the outer addition branching fractions to assume the inner addition branching fractions are negligible, and then scaling the result to

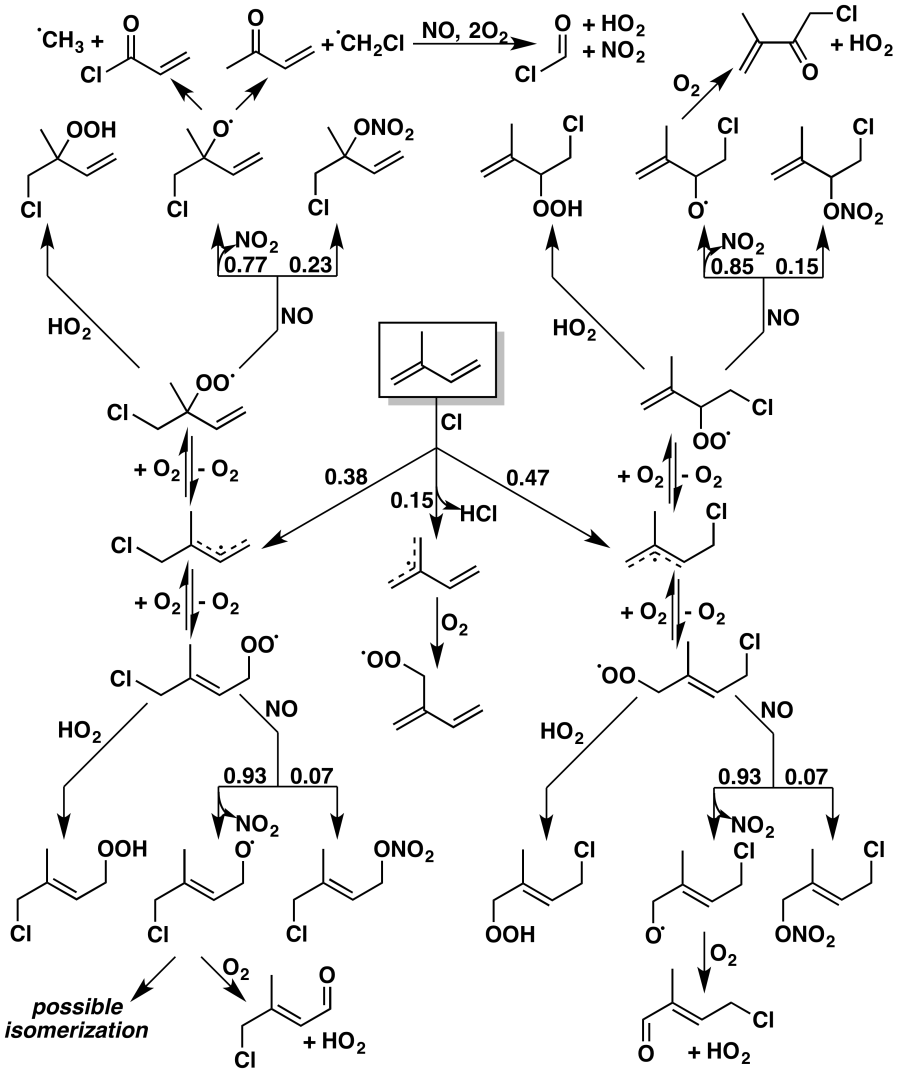

Figure 4.14: Reactions and products following the Cl-initiated oxidation of isoprene. While δ-chloro peroxy radicals are assumed to form as equal mixtures of E and Z isomers, we only show the E isomers for brevity (bottom half). The chemistry of the Z isomers is expected to be similar. Branching fraction recommendations are for 298 K and 1 atm. As discussed in the text, the possibility that certain stereoisomers of the δ-chloro alkoxy radicals could isomerize has not been previously studied.

account for the abstraction channel.

The carbon-centered radicals formed from Cl oxidation will immediately add O_2 to form peroxy radicals (ICl$\dot{O}$O). No work has been done on the distribution of peroxy radicals from the abstraction channel. For the Cl-addition channel, rates of O_2 addition have been computed in one theoretical study (Lei *et al.*, 2002a), which determined branching fractions of 0.44:0.56 for the [1,2]:[1,4] isomers and 0.60:0.40

for the [4,3]:[4,1] isomers at the kinetic limit. While the calculated energy difference between the β-chloro-peroxy radicals and *E*-δ-chloro-peroxy radicals from Lei *et al.* (2002a) are broadly consistent with those measured in the OH system by Teng *et al.* (2017), we note that the *Z*-δ-chloro-peroxy radicals were not considered in (Lei *et al.*, 2002a), and that even higher-level theoretical calculations were unable to provide an accurate assessment of the kinetic distribution in the OH system. We recommend, therefore, that the reversible O_2 addition kinetics from the OH system be used in the Cl system until such time that isomer specific data is available.

4.6.1 Reactions of IClOO

Kinetics - We do not present a recommendation for the fates of the dialkenlyperoxy radicals due to a lack of studies on the organic products from the abstraction channel. Nevertheless, 2-methylene-3-butenal, which is a possible product, has been tentatively identified (Nordmeyer *et al.*, 1997). Even for the major Cl addition products, rate constants for the subsequent reactions of the chloroalkenylperoxy radicals remain largely unexplored. A bulk rate constant (with no isomer specificity) has been measured for the reaction between the chloroalkenylperoxy radicals and NO using a turbulent flow reactor and chemical ionization mass spectrometry (Patchen *et al.*, 2005). This study directly measured the loss of chloroalkenylperoxy radicals under pseudo-first-order conditions to determine a rate constant of $(11.5 \pm 1.1) \times 10^{-12}$ cm^3 molec^{-1} s^{-1} for 298 K, which we adopt as our recommended value. A rate constant for the reaction of hydroxyalkenylperoxy radicals with NO of $(8.8 \pm 1.2) \times 10^{-12}$ cm^3 molec^{-1} s^{-1} was measured in a separate study using the same apparatus (Miller *et al.*, 2004). Cl-substitution is slightly activating for this reaction relative to OH-substitution. To our knowledge, no measurements of the reaction between these chloroalkenylperoxy radicals with RO_2 or HO_2 have been reported in the literature. Such studies would provide further information on how the reactivity of atmospherically relevant peroxy radicals is influenced by substituents. We do not include RO_2 chemistry due to its minor importance in the atmosphere.

Mechanism - We assume the only product of the reaction with HO_2 is the corresponding hydroperoxide. We expect that the reaction with NO will produce both alkoxy radicals and organic nitrates, and use the nitrate yield parameterization in Equation 4.3 to calculate branching ratios; we note that the electron-withdrawing effect might serve to decrease the nitrate yield from β-chloro peroxy radicals, akin to the effect of a β-carbonyl peroxy radical (Praske *et al.*, 2015), but do not account

for this due to lack of experimental evidence.

Our recommended fates for the alkoxy radicals are guided by several theoretical and product studies. Observed products include methyl vinyl ketone (MVK), chloromethyl vinyl ketone (Cl-MVK), formyl chloride, several chloromethylbutenal (CMBA) isomers, and a chloromethylbutenone (CMBO). Product studies using a variety of techniques (FTIR, GC-MS, API-MS) have consistently measured small yields of MVK (~9% or less) and negligible yields of methacrolein (MACR) (Fantechi *et al.*, 1998; Nordmeyer *et al.*, 1997; Orlando *et al.*, 2003a; Ragains and Finlayson-Pitts, 1997). The observation of Cl-MVK and small yields of MVK suggests that there are two competing decomposition pathways for the [1,2] isomer. The lack of MACR suggests that decomposition is unimportant for the [4,3] isomer. The small measured yields of formyl chloride, a coproduct of both MVK and MACR production, range 4.7–8% (Fantechi *et al.*, 1998; Orlando *et al.*, 2003a; Ragains and Finlayson-Pitts, 1997) and agree with the MVK yield to further indicate that MACR is not a significant product of Cl oxidation. Instead, it is believed that reaction of primary and secondary alkoxy radicals with O_2 dominates to form the CMBA and CMBO isomers as the principal products. A chamber study using GC-MS and API-MS indeed detected at least four CMBA and CMBO isomers as products of Cl-initiated isoprene oxidation (Nordmeyer *et al.*, 1997). However, absolute yields were unable to be quantified. Theoretical calculations on C-C bond decomposition of the chloroalkenylalkoxy radicals predict that decomposition proceeds slowly with a high barrier, and that reaction with O_2 is the major channel under atmospheric conditions (Zhang *et al.*, 2003a). This work is consistent with findings of the experimental studies, further suggesting that CMBA and CMBO are the dominant products. CMBA and CMBO act as useful tracers of chlorine chemistry since they have no known direct anthropogenic or natural emissions (Nordmeyer *et al.*, 1997). Field observations of these compounds have successfully been used to identify episodes of chlorine chemistry in Houston, Texas (Riemer *et al.*, 2008). Nevertheless, the utility of these species as tracers is limited by the lack of absolute yield measurements.

We recommend that future product studies on the Cl-initiated oxidation of isoprene focus on determining absolute yields of CMBA and CMBO. This would directly validate the current evidence that the dominant fate of the primary and secondary alkoxy radicals is reaction with O_2. These measurements should also be performed at a variety of NO_x concentrations. The aforementioned product studies

(Fantechi *et al.*, 1998; Nordmeyer *et al.*, 1997; Orlando *et al.*, 2003a; Ragains and Finlayson-Pitts, 1997) were all performed under NO-free or low-NO conditions, and relied on RO_2 chemistry to produce the alkoxy radicals. Alkoxy radicals produced from NO chemistry typically possess greater amounts of vibrational energy than alkoxy radical produced from RO_2 chemistry. While the decomposition barriers of the alkoxy radicals are predicted to be greater than the exothermicity of the RO_2 + NO reaction (Zhang *et al.*, 2003a), experimental evidence that CMBA and CMBO are the dominant products in the presence of NO_x is desirable. Finally, to our knowledge, the possibility that certain stereoisomers of the δ-chloro alkoxy radicals could isomerize has not been previously considered. Alkoxy radical isomerization occurs in OH and NO_3 oxidation of isoprene and could also be occurring in Cl oxidation. Both theoretical and experimental studies to address this possibility would be useful.

4.7 Photochemistry of Major Oxidation Products of isoprene

4.7.1 Methyl Vinyl Ketone (MVK)

Methyl vinyl ketone (MVK) is a major first-generation product from OH-, O_3-, and NO_3-initiated oxidation of isoprene. The dominant fate of MVK is loss *via* reaction with OH (Gierczak *et al.*, 1997; Tuazon and Atkinson, 1990). For typical ambient concentrations of OH and O_3, *i.e.*, 2×10^6 molec cm^{-3} (12 h average) and 30 ppb (24 h average), respectively, the lifetimes of MVK with respect to oxidation by OH and O_3 at room temperature are approximately 7 and 80 h, respectively. The reaction of MVK with NO_3 reaction is not competitive (Canosa-Mas *et al.*, 1999a; Kwok *et al.*, 1996; Rudich *et al.*, 1996).

Kinetics (Table 4.17) - A number of studies have measured the effective bimolecular reaction rate constant, k_{MVK+OH}, over a wide range of pressure and temperature (Atkinson *et al.*, 1983; Chuong and Stevens, 2003, 2004; Edney *et al.*, 1986; Gierczak *et al.*, 1997; Grosjean *et al.*, 1993b; Holloway *et al.*, 2005; Kleindienst *et al.*, 1982). A negative temperature dependence of k_{MVK+OH} was widely observed over a pressure range of 5 to 300 Torr (Chuong and Stevens, 2003; Gierczak *et al.*, 1997; Kleindienst *et al.*, 1982). Dependence of k_{MVK+OH} on pressure at 2 – 5 Torr was both observed and predicted in the temperature range of 300 – 425 K (Chuong and Stevens, 2003; Ochando-Pardo *et al.*, 2007). The reported values of k_{MVK+OH} at room temperature are in good agreement, falling into the range of $(1-2)\times10^{-11}$ cm^3 molec^{-1} s^{-1}, regardless of the pressure at which the measurements were conducted. Here, we use the IUPAC recommendation of $2.6\times10^{-12}\times e^{(610/T)}$ cm^3 molec^{-1} s^{-1}.

oxidant	k (cm^3 molec^{-1} s^{-1})	T (K)	citation
OH	1.48×10^{-11}	300	Cox *et al.* (1980)
OH	$3.85 \times 10^{-12} \times e^{[(456\pm73)/T]}$	298-424	Kleindienst *et al.* (1982)
OH	$(1.96 \pm 0.15) \times 10^{-11}$	299 ± 2	Atkinson *et al.* (1983)
OH	$(2.67 \pm 0.45) \times 10^{-12} \times e^{[(612\pm49)/T]}$	232-378	Gierczak *et al.* (1997)
OH	$(1.73 \pm 0.21) \times 10^{-11}$	300	Chuong and Stevens (2003)
OH	$(1.78 \pm 0.08) \times 10^{-11}$	300	Chuong and Stevens (2004)
OH	$(1.86 \pm 0.12) \times 10^{-11}$	298 ± 2	Holloway *et al.* (2005)
OH	$2.6 \times 10^{-12} \times e^{(610/T)}$	**230-380**	**IUPAC / our recommendation**
O_3	$(4.77 \pm 0.59) \times 10^{-18}$	296 ± 2	Atkinson *et al.* (1981)
O_3	4.0×10^{-18}	~ 294	Kamens *et al.* (1982)
O_3	$6.9 \times 10^{-16} \times e^{[(-1521\pm78)/T]}$	240-324	Treacy *et al.* (1992)
O_3	$(4.72 \pm 0.09) \times 10^{-18}$	291 ± 2	Grosjean *et al.* (1993b)
O_3	$(5.84 \pm 0.39) \times 10^{-18}$	291 ± 1	Grosjean and Grosjean (1998)
O_3	$(5.4 \pm 0.6) \times 10^{-18}$	296 ± 2	Neeb *et al.* (1998)
O_3	$8.5 \times 10^{-16} \times e^{(-1520/T)}$	240-330	IUPAC recommendation
NO_3	$< 6 \times 10^{-16}$	296 ± 2	Kwok *et al.* (1996)
NO_3	$\leq 1.2 \times 10^{-16}$	298	Rudich *et al.* (1996)
NO_3	$(5.0 \pm 1.2) \times 10^{-16}$	296 ± 2	Canosa-Mas *et al.* (1999a)
NO_3	$< 6 \times 10^{-16}$	298	IUPAC recommendation

Table 4.17: Chronological estimates of the reaction rate constants for OH-, O_3-, and NO_3-initiated oxidation of MVK.

MVK reacts slowly with O_3 - $k_{MVK+O_3} = (4-6) \times 10^{-18}$ cm^3 molec^{-1} s^{-1} at room temperature (Atkinson *et al.*, 1981; Cox *et al.*, 1980; Grosjean *et al.*, 1993b; Neeb *et al.*, 1998; Treacy *et al.*, 1992). A positive temperature dependence of k_{MVK+O_3} was observed by Treacy *et al.* (1992). Due to its minor importance, we do not include the reaction of MVK with O_3 in our mechanism.

Mechanism (Figure 4.15; Tables 4.18 and 4.19) - The OH-initiated oxidation of MVK occurs *via* OH addition to the double bond, forming two distinct RO_2. The branching ratio, as shown in Table 4.18, has been reported (Praske *et al.*, 2015; Tuazon and Atkinson, 1989). The reaction of MVK-derived RO_2 and NO has been studied extensively (Galloway *et al.*, 2011; Paulot *et al.*, 2009b; Praske *et al.*, 2015; Tuazon and Atkinson, 1989). Glycolaldehyde, methylglyoxal, formaldehyde, and organic nitrates have been quantified as the primary first generation products. The organic nitrates, hereafter denoted MVKN and MVKN' for the internal and external nitrate, have respective atmospheric lifetimes of 4.3 and 6.6 h due to photolysis (Müller *et al.*, 2014). A comprehensive overview of the product yields reported in the literature is shown in Table 4.19. Reactions arising from the HO_2-dominated regime, however, have only recently been reported (Praske *et al.*, 2015). Reaction of

citation	internal OH addition (%)	external OH addition (%)
Tuazon and Atkinson (1989)	28 ± 9	72 ± 21
Praske *et al.* (2015)	24 ± 14	76 ± 14

Table 4.18: OH addition branching for MVK.

citation	glycolaldehyde	methylglyoxal	MVKN	MVKN'
Tuazon and Atkinson (1989)	64 ± 8	25 ± 4		
Paulot *et al.* (2009a)	62.5			
Galloway *et al.* (2011)	67.4 ± 3	24.12 ± 0.14		
Praske *et al.* (2015)	74 ± 6		2.4 ± 0.4	1.6 ± 0.4
our recommendation	**74**	**22**	**2.3**	**1.7**

Table 4.19: Measured product yields (%) for the high-NO oxidation of MVK.

the internal RO_2 with HO_2 has been shown to follow three reaction channels, shown with their respective yields in Figure 4.15. Both the fragmentation and dicarbonyl pathways were found to be very efficient in the recycling of HO_x. The fragmentation route is analogous to the reactions of acetonyl RO_2 previously reported (Dillon and Crowley, 2008; Hasson *et al.*, 2005, 2004; Jenkin *et al.*, 2008). Formation of the dicarbonyl, however, was previously thought to occur only in halogenated peroxy systems (Hou *et al.*, 2005a,b; Hou and Wang, 2005). The hydroperoxide pathway, although radical terminating, promptly photolyzes with an atmospheric lifetime on the order of a few hours (Praske *et al.*, 2015). Assuming photolytic cleavage of the O-OH bond, this channel also serves to propagate the radical chain. Overall, the low NO chemistry of MVK was found to be much less HO_x consuming than previously thought. Future work should identify the reaction routes arising from HO_2 reaction with the external RO_2, as the current literature is largely speculative (Praske *et al.*, 2015). In this channel, a modest yield of methylglyoxal has been observed with the remaining assumed to form a hydroperoxide.

4.7.2 Methacrolein

Methacrolein (MACR) is a major first-generation product from both OH- and O_3-initiated oxidation of isoprene. The dominant fate of MACR is loss *via* reaction with OH (Gierczak *et al.*, 1997; Tuazon and Atkinson, 1990), but oxidation by O_3 and NO_3 is also considered.

Kinetics (Table 4.20) - OH: The reaction rate constant of MACR with OH has been closely studied, (Atkinson *et al.*, 1983; Chuong and Stevens, 2003, 2004;

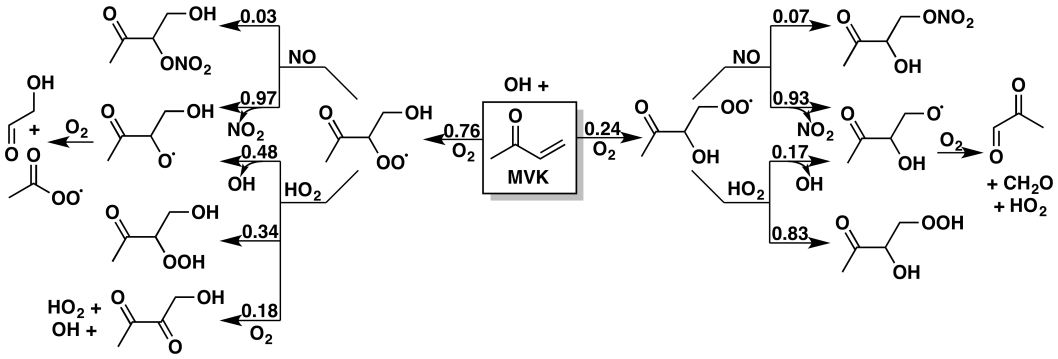

Figure 4.15: Reactions and products following the addition of OH to methyl vinyl ketone (MVK). Yields are for 298 K and 1 atm; in reactions of peroxy radicals with NO, the relative contributions of the nitrate and alkoxy pathways vary with both temperature and pressure. For the reduced mechanism, we treat (3-OO,4-OH)- and (3-OH,4-OO)-MVK as a single peroxy radical species, and scale the product yields of its reactions with NO and HO_2 according to the relative contributions of the two isomers.

Edney *et al.*, 1986; Gierczak *et al.*, 1997; Grosjean *et al.*, 1993b; Kleindienst *et al.*, 1982). The MACR + OH reaction exhibits an negative temperature dependence at pressure of 5 to 300 Torr (Chuong and Stevens, 2003; Gierczak *et al.*, 1997; Kleindienst *et al.*, 1982). Unlike the MVK + OH reaction, no strong pressure dependence is observed over a temperature range of 300 to 425 K, indicating the importance of the pressure-independent hydrogen abstraction reaction. The reported values of $k_{MACR+OH}$ at room temperature are in good agreement, in the range of $(3-4) \times 10^{-11}$ cm^3 molec^{-1} s^{-1}. Here, we recommend separate addition and abstraction rate coefficients, as shown in Table 4.20.

O_3: The ozonolysis of MACR proceeds *via* the O_3 addition to the C=C double bond to produce a primary ozonide which rapidly decomposes to methyoglyoxal or formaldehyde. The reaction rate constants, k_{MACR+O_3}, at room temperature have been measured within a range of $(1.0-1.5) \times 10^{-18}$ cm^3 molec^{-1} s^{-1} (Atkinson *et al.*, 1981; Grosjean *et al.*, 1993b; Neeb *et al.*, 1998; Treacy *et al.*, 1992).

NO_3: The rate constant of the NO_3 reaction with MACR has only been measured at room temperature (Canosa-Mas *et al.*, 1999a; Kwok *et al.*, 1996; Rudich *et al.*, 1996). We therefore estimate the temperature dependence based on acrolein, a chemical proxy. The temperature dependence of the OH kinetics for these two α,β-unsaturated aldehydes has been observed to be similar (Atkinson *et al.*, 2006; Magneron *et al.*, 2002; Vega-Rodriguez and Alvarez-Idaboy, 2009).

oxidant	k (cm^3 molec^{-1} s^{-1})	T (K)	citation
OH	$1.77 \times 10^{-11} \times e^{[(175\pm52)/T]}$	300-423	Kleindienst *et al.* (1982)
OH	$(2.96 \pm 0.24) \times 10^{-11}$	299 ± 2	Atkinson *et al.* (1983)
OH	$(3.90 \pm 0.31) \times 10^{-11}$	298 ± 2	Edney *et al.* (1986)
OH	$(7.73 \pm 0.65) \times 10^{-12} \times e^{[(379\pm46)/T]}$	234-273	Gierczak *et al.* (1997)
OH	$(9.8 \pm 3.8) \times 10^{-13} \times e^{[(1050\pm120)/T]}$	300-422	Chuong and Stevens (2003)
OH	$(3.22 \pm 0.10) \times 10^{-11}$	300	Chuong and Stevens (2003)
OH	$8.0 \times 10^{-12} \times e^{(380/T)}$	230-380	IUPAC recommendation
OH	$4.4 \times 10^{-12} \times e^{(380/T)}$	**-**	**our recommendation: addition**[a]
OH	$2.7 \times 10^{-12} \times e^{(470/T)}$	**-**	**our recommendation: abstraction**[b]
O_3	$(1.12 \pm 0.13) \times 10^{-18}$	296 ± 2	Atkinson *et al.* (1981)
O_3	1.1×10^{-18}	~ 294	Kamens *et al.* (1982)
O_3	$1.3 \times 10^{-15} \times e^{[(-2112\pm131)/T]}$	240-324	Treacy *et al.* (1992)
O_3	$(1.02 \pm 0.05) \times 10^{-18}$	291 ± 2	Grosjean *et al.* (1993b)
O_3	$(1.08 \pm 0.20) \times 10^{-18}$	290 ± 1	Grosjean and Grosjean (1998)
O_3	$(1.3 \pm 0.14) \times 10^{-18}$	296 ± 2	Neeb *et al.* (1998)
O_3	$1.4 \times 10^{-15} \times e^{(-2100/T)}$	**240-330**	**IUPAC / our recommendation**
NO_3	$(4.46 \pm 0.58) \times 10^{-15}$	296 ± 2	Kwok *et al.* (1996)
NO_3	$\leq 8 \times 10^{-15}$	298	Rudich *et al.* (1996)
NO_3	3.08 ± 0.18	298 ± 2	Chew *et al.* (1998)
NO_3	$(3.7 \pm 0.47) \times 10^{-15}$	296 ± 2	Canosa-Mas *et al.* (1999a)
NO_3	3.4×10^{-15}	298	IUPAC recommendation
NO_3	$1.85 \times 10^{-13} \times e^{(-1190/T)}$	**-**	**our recommendation**[c]

Table 4.20: Chronological estimates of the reaction rate constants for OH-, O_3-, and NO_3-initiated oxidation of MACR. [a]overall rate from Atkinson *et al.* (2006); scaling for addition from Orlando *et al.* (1999) and Tuazon and Atkinson (1990); [b]Ochando-Pardo *et al.* (2007); [c]overall rate from Atkinson *et al.* (2006);temperature dependence by analogy with acrolein (Salgado *et al.*, 2008).

Mechanism (Figure 4.16; Table 4.21) - OH addition: The addition of OH to the double bond occurs primarily at the external olefinic carbon, with a molar ratio estimated as ~85% under the assumption that all the observed methylglyoxal (8%, see Table 4.21 (Galloway *et al.*, 2011; Tuazon and Atkinson, 1990)) is produced from the internal OH addition. Crounse *et al.* (2012) suggested that this ratio can be up to 96.5% based on the measured yields of ^{18}O labeled hydroperoxyacetone (HPAC-^{18}O) and hydroxyacetone (HAC-^{18}O).

The MACR-derived RO_2 radicals can react with NO or HO_2 but, under typical atmospheric conditions, most of the RO_2 radicals from external OH addition will undergo a fast 1,4-H-shift isomerization process (Crounse *et al.*, 2012). The product of this isomerization process, a hydroxy hydroperoxy carbonyl radical, decomposes rapidly, producing hydroxyacetone and re-forming OH. Similarly, RO_2 radicals from internal OH addition undergo a rapid 1,5-H-shift isomerization followed by decomposition and reaction with O_2 to form hydroperoxyacetone (HPAC), CO, and

	products (%)				experimental conditions (ppb)			
citation	CH_2O	HAC	GLYX	MPAN	$[NO]_0$	$[NO_2]_0$	$[MACR]_0$	OH source
Tuazon and Atkinson (1990)	28-67	41 ± 3	8.4 ± 1.6	10-24	6000-8000	-	10000	C_2H_5ONO
Orlando *et al.* (1999)	40-70	47 ± 5	<12	4-30	1970-2630		1316-3950	CH_3ONO
Galloway *et al.* (2011)		39.5 ± 1.7	8.09 ± 0.45		231	437	42	HONO

Table 4.21: Molar yields of key products from OH-initiated oxidation of MACR in the presence of NO.

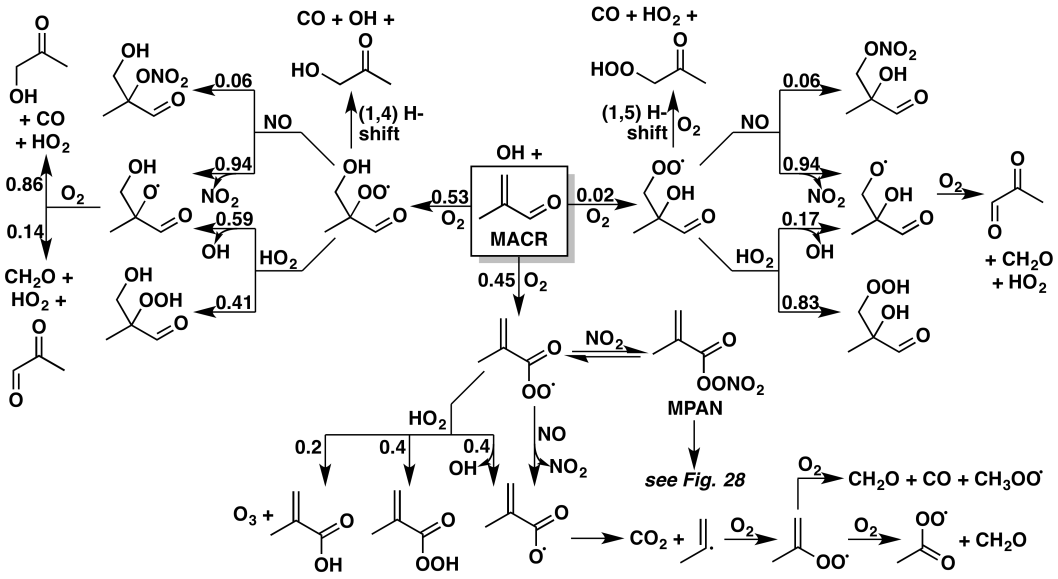

Figure 4.16: Reactions and products in the OH + methacrolein (MACR) system. Yields are for 298 K and 1 atm; the OH-abstraction and OH-addition pathways have different temperature dependences, and in reactions of peroxy radicals with NO, the relative contributions of the nitrate and alkoxy pathways vary with both temperature and pressure. For the reduced mechanism, we ignore the minor internal OH addition channel (combining it with the major addition channel and scaling the subsequent yields, as with MVK). We also assume that the peroxy radical formed from the external addition of OH proceeds entirely through the 1,4 H-shift isomerization channel.

HO_2.

The MACR-derived RO_2 radicals will react with NO yielding alkoxy radicals (RO) and organic nitrates, with a branching ratio of 94% and 6%, respectively (Unpublished, Caltech). The resulting RO radicals can undergo decomposition, isomerization and reaction with O_2, although the last two reaction pathways are not considered to be important in the RO degradation (Park *et al.*, 2003). Decomposition of the RO radicals produces hydroxyacetone (HAC), methylglyoxal, formaldehyde, CO, and HO_2 (Orlando *et al.*, 1999). The reaction of MACR-derived RO_2 with HO_2 is not well constrained. Here we assume that the MACR-derived RO_2 radicals behave similar to the MVK-derived RO_2 radicals, producing both RO radicals and peroxides upon reaction with HO_2 (Praske *et al.*, 2015). The MACR-derived RO_2 self/cross reactions are not considered as a major pathway in the MACR photochemistry, based on the measured reaction rate constants for β-hydroxy peroxy radicals, which are at least an order of magnitude less than those measured for RO_2 + HO_2 and RO_2 + NO

reactions (Jenkin and Hayman, 1995).

Mechanism (Figure 4.16) - H abstraction: The abstraction of the aldehydic hydrogen atom followed by O_2 addition leads to the peroxymethacryl radical (C=C(CH_3) C(O)O_2, MACR1OO), which subsequently reacts with NO, NO_2, and HO_2.

4.7.2.1 MACR1OO

Kinetics - The direct measurement of the rate constant for the MACR1OO + NO reaction was conducted by Gouw and Howard (1997) over the temperature range 240 – 360 K and at pressures of 1.3 – 3.9 Torr. Their measured value at 298 K is very close to the results from the analogous acetylperoxy radical ($CH_3C(O)O_2$) + NO reaction (Maricq and Szente, 1996; Sehested *et al.*, 1998; Villalta and Howard, 1996), indicating that the rate constant for $RC(O)O_2$ + NO reactions may not be sensitive to the structure of the R group.

Mechanism - The C=C(CH_3)C(O)O radical produced from MACR1OO + NO reaction decomposes to CO_2 and the methyl vinyl radical (CH_2=CCH_3), which ultimately yields formaldehyde, CO, and CO_2 (Orlando *et al.*, 1999). We recommend that the MACR1OO + NO reaction proceeds exclusively to the products of C=C(CH_3)C(O)O and NO_2, by analogy with measured product yields from the $CH_3C(O)O_2$ + NO reaction (Maricq and Szente, 1996).

The reaction of peroxymethacryl radical with NO_2 produces methacryloyl peroxynitrate (MPAN), which was directly observed by Orlando *et al.* (1999) *via* IR absorption spectroscopy. Kinetic data for this reaction are not available. Here we refer to the rate coefficients for the $CH_3C(O)O_2$ + NO_2 + M reaction reviewed by Atkinson *et al.* (2006). At 298 K and 1 bar, the rate constant for MPAN formation is 1×10^{-11} cm^3 $molec^{-1}$ s^{-1}, while the decomposition occurs with a rate constant of 3.3×10^{-4} s^{-1} at the same conditions. Subsequent chemistry of MPAN is described in Section 4.7.6. The chemical mechanism and kinetic data for the reaction of peroxymethacryl radical with HO_2 are evaluated based on the $CH_3C(O)O_2$ + HO_2 reaction, which yields peroxyacetic acid *via* channel R3a, acetic acid and ozone *via* channel R3b, and propagates OH radical *via* channel R3c:

$CH_3C(O)O_2 + HO_2 \rightarrow CH_3C(O)OOH + O_2$ (R3a)

$CH_3C(O)O_2 + HO_2 \rightarrow CH_3C(O)OH + O_3$ (R3b)

$CH_3C(O)O_2 + HO_2 \rightarrow CH_3C(O)O + OH + O_2$ (R3c)

The measured yield of OH radical from Reaction R3c is highly uncertain, ranging

from < 10% to 40%. (Hasson *et al.*, 2004; Horie and Moortgat, 1992; Jenkin *et al.*, 2007; Le Crane *et al.*, 2006; Niki *et al.*, 1985; Tomas *et al.*, 2001). Here we recommend an overall branching ratio of 0.4/0.2/0.4 obtained from the two most recent studies, Hasson *et al.* (2004) and Jenkin *et al.* (2007).

4.7.3 ISOPOOH

isoprene hydroxyhydroperoxide (ISOPOOH) is the major first-generation product of OH-initiated isoprene oxidation in regions with low NO concentrations, particularly remote forests, where HO_2 dominates the peroxy radical reactivity. The dominant sink of ISOPOOH in the atmosphere is reaction with OH, which leads primarily to the production of isoprene epoxydiols (IEPOX). Reaction with O_3 and NO_3 are not expected to contribute significantly to the fate of ISOPOOH. Photolysis is unlikely to be important given the very fast rate coefficient of OH with ISOPOOH.

Kinetics (Table 4.22) - The rate constants for ISOPOOH oxidation by OH were first inferred by Paulot *et al.* (2009b) from isoprene + OH chamber experiments. These experimental procedures precluded the separation of the individual isomer kinetic rates and reaction products. Recently, a synthetic route to the production of various ISOPOOH isomers has been developed that enables chamber experiments to achieve greater accuracy in measuring the rates of the specific isomers' oxidation, summarized in Table 4.22. St. Clair *et al.* (2015) performed chamber experiments at 297 K with (1,2)- and (4,3)-ISOPOOH, using both tandem-MS CF_3O^- CIMS and gas chromatography coupled to CF_3O^- CIMS to detect both ISOPOOH and its products (Crounse *et al.*, 2006; Paulot *et al.*, 2009b; St. Clair *et al.*, 2010). Experiments performed under high NO conditions were used to measure overall OH + ISOPOOH reaction rates, as well as to infer hydroperoxy-H-abstraction rates (by yields of isoprene hydroxynitrates) and the branching between non-IEPOX forming OH-addition (assumed only to yield hydroxyacetone, glycolaldehyde, hydroperoxyacetone, and hydroperoxyethanal) and IEPOX formation (by difference from unity). Experiments under HO_2-dominated conditions were used to measure non-hydroperoxy H-abstraction rates and further product yields. St. Clair *et al.* (2015) found that (1,2)-ISOPOOH reacts with OH with an overall rate constant of $7.5 \pm 1.2 \times 10^{-11}$ cm^3 molec^{-1} s^{-1}, while (4,3)-ISOPOOH proceeds with a rate constant of $1.18 \pm 0.19 \times 10^{-10}$ cm^3 molec^{-1} s^{-1}.

Mechanism (Figures 4.17-4.20; Table 4.23) - Paulot *et al.* (2009b) were also the

k	(1,2)-ISOPOOH (cm^3 $molec^{-1}$ s^{-1})	(4,3)-ISOPOOH (cm^3 $molec^{-1}$ s^{-1})
k_{total}	$7.5 \pm 1.2 \times 10^{-11}$	$1.18 \pm 0.19 \times 10^{-10}$
k_{OO-H}	$9.0 \pm 1.4 \times 10^{-12}$	$4.2 \pm 0.7 \times 10^{-12}$
$k_{total-H}$	1.2×10^{-11}	8×10^{-12}

Table 4.22: Rate coefficients for ISOPOOH + OH (St. Clair *et al.*, 2015).

first to report product yields from the oxidation of ISOPOOH by OH, estimating that isoprene dihydroxy epoxides (IEPOX) comprised >75% of the products, with the remainder assumed to form ISOPOO radicals or C_5 hydroxycarbonyl compounds following H-abstraction. The isomer-specific studies of St. Clair *et al.* (2015) largely corroborated these estimates while providing greater precision of yields and identification of some minor products. Product yields measured by St. Clair *et al.* (2015) are shown in Table 4.23; we adopt similar yields, with slight modifications for potentially undetected highly functionalized products (*e.g.* hydroperoxynitrates and dihydroxydihydroperoxides), in our recommendations, shown in Figures 4.17-4.20.

OH addition to (1,2)- and (4,3)-ISOPOOH (Figures 4.17 and 4.18) occurs predominantly at the external position, and proceeds primarily by rapid fragmentation of the hydroperoxide and cyclization to form IEPOX. The two isomers of β-IEPOX (in a ratio of approximately 2:1 *trans*:*cis*) were found to account for 71% of products from (1,2)-ISOPOOH and 79% of products from (4,3)-ISOPOOH, in line with the estimate of 75% from Paulot *et al.* (2009b). This leaves 13% and 14% of the total ISOPOOH + OH reaction pathway (for (1,2)- and (4,3)-ISOPOOH, respective) that proceeds by addition but does not produce IEPOX; this fraction is assumed to add oxygen, forming a peroxy radical that can react with HO_2 to form a dihydroxydihydroperoxide or with NO, forming hydroperoxynitrates or fragmenting to glycolaldehyde, hydroxyacetone, and their hydroperoxide analogs.

Hydrogen abstraction from ISOPOOH (Figure 4.19) represents only a small fraction of its reactivity, but accounts for some of the minor products observed by St. Clair *et al.* (2015) at *m/z* 185 and 201 using CF_3O^- CIMS. Abstraction of the hydroperoxy hydrogen represents 12% of overall (1,2)-ISOPOOH + OH reactivity and 4% of (4,3)-ISOPOOH + OH at 297 K and 745 Torr; this pathway regenerates the precursor ISOPOO, which will then follow the many reaction pathways discussed in Section 4.3.3. Abstraction of the α-hydroxy hydrogen from (1,2)-ISOPOOH (4% of overall reactivity at the same conditions) forms an alkyl radical

pathway/product	% yield from 1,2-ISOPOOH	% yield from 4,3-ISOPOOH
H-addition → IEPOX	*71*	*79*
of which, *trans*	67 ± 1	68 ± 2
of which, *cis*	33 ± 1	32 ± 2
H-addition → non-IEPOX[a]	*13*	*14*
high-NO: glycolaldehyde	9 ± 1	14 ± 2
high-NO: hydroxyacetone	13 ± 2	13 ± 2
high-NO: hydroperoxyacetone	-	~2
high-NO: hydroperoxyethanal	3 ± 1	-
OOH H-abstraction	*12*	*4*
other H-abstraction	*4*	*3*
low-NO: *m/z* 201[b]	2.0	2.3
low-NO: *m/z* 185[c]	2.0	1.1
unspecified		
low-NO: *m/z* 189	3.4	3.2
low-NO: hydroxyacetone	1.3	4.4
low-NO: glycolic acid	<1	1.4
low-NO: *m/z* 93	1.4	<1
low-NO: *m/z* 161	1.1	<1
low-NO: glycolaldehyde	0.9	<1
low-NO: unidentified[d]	16.9	8.6

Table 4.23: Oxidation products of ISOPOOH + OH, as measured and inferred by (St. Clair *et al.*, 2015). [a]Inferred by difference from unity of high-NO products; [b]presumed to be a C_5 unsaturated hydroperoxy aldehyde; [c]presumed to be either a C_5 unsaturated hydroxy epoxide or, in the case of 4,3-ISOPOOH, a C_5 unsaturated hydroxy carbonyl; [d]inferred by difference from unity of low-NO products.

that can either isomerize to form a hydroxyepoxide or react with O_2 to form a hydroperoxycarbonyl, the masses of which were observed by St. Clair *et al.* (2015) in ~2% overall yield from (1,2)-ISOPOOH. Similarly, abstraction of the α-hydroxy and α-hydroperoxy hydrogens from (4,3)-ISOPOOH (3% of overall reactivity at the same conditions) can yield hydroperoxycarbonyl and hydroxycarbonyl species, respectively, the masses of which were observed by St. Clair *et al.* (2015) in ~2.3% and ~1.1% overall yields.

A few unresolved mechanistic details remain for the OH + ISOPOOH reaction. The rates and products of the δ-ISOPOOH isomers have not yet been directly measured, though these isomers are likely only ~5% in total of the ISOPOOH formed from OH + isoprene in nature. Our recommendations for the δ-ISOPOOH oxidation

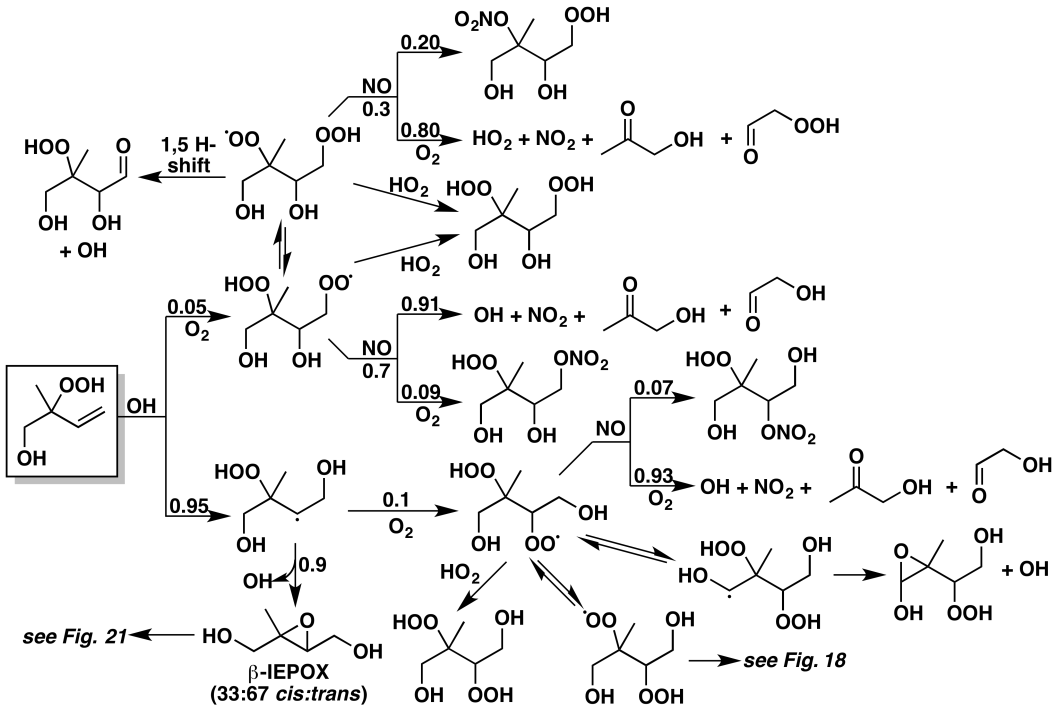

Figure 4.17: Reactions and products following the addition of OH to (1,2)-β-ISOPOOH. Yields are for 298 K and 1 atm; in reactions of peroxy radicals with NO, the relative contributions of the nitrate and alkoxy pathways vary with both temperature and pressure, and the branching ratios between IEPOX formation and O_2 addition also vary with pressure. For the simplified mechanism, we combine all six dihydroxy-hydroperoxy-peroxy radicals into a single species, which isomerize or react with NO or HO_2 with product yields scaled by the relative contributions of each isomer.

channels are shown in Figure 4.20. While the internal addition of OH to the double bond of (4,3)-ISOPOOH is likely very small, the OH internal addition to (1,2)-ISOPOOH may be more important (St. Clair *et al.*, 2015). St. Clair *et al.* (2015) did not observe any products other than IEPOX with a yield above 4%, suggesting that either the reaction has multiple product channels, CF_3O^- CIMS is not sensitive to the product(s), or the product is lost to the chamber walls. One potential product from internal OH addition to (1,2)-ISOPOOH is a diperoxydiol (D'Ambro *et al.*, 2017a; Krechmer *et al.*, 2015; Liu *et al.*, 2016; Riva *et al.*, 2016b), which can also be formed from external addition; another recent study suggests that external addition followed by intramolecular hydrogen shifts can result in the prompt formation of dihydroxy-hydroperoxy-epoxide (D'Ambro *et al.*, 2017b). These functionalization pathways, shown with our recommendations in Figure 4.17, and other potential autoxidation products from the internal addition are likely to produce secondary

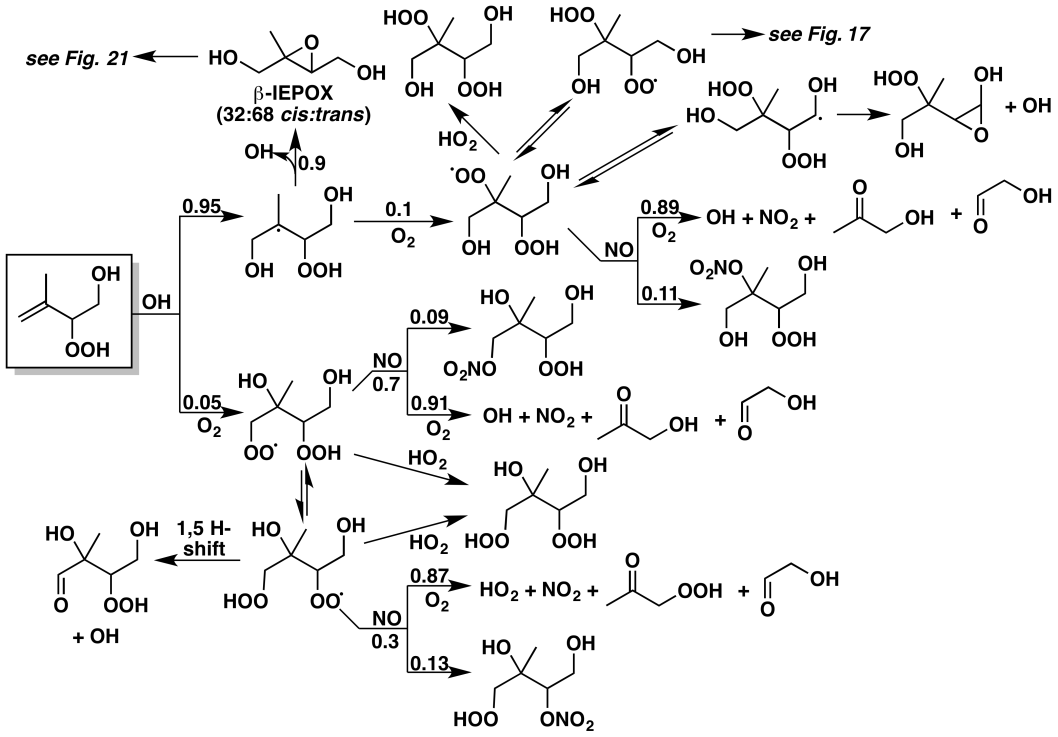

Figure 4.18: Reactions and products following the addition of OH to (4,3)-β-ISOPOOH. Yields are for 298 K and 1 atm; in reactions of peroxy radicals with NO, the relative contributions of the nitrate and alkoxy pathways vary with both temperature and pressure, and the branching ratios between IEPOX formation and O_2 addition also vary with pressure. For the simplified mechanism, we combine all six dihydroxy-hydroperoxy-peroxy radicals into a single species, which isomerize or react with NO or HO_2 with product yields scaled by the relative contributions of each isomer.

organic aerosol (SOA). The O_3 and NO_3 chemistry of ISOPOOH has yet to be investigated but is expected to play only a small role in the atmospheric fate.

4.7.4 IEPOX

isoprene expoxydiols (IEPOX) are the major product of the oxidation of ISOPOOH by OH (Paulot *et al.*, 2009b). Although four isomers of IEPOX can form following the addition of OH to the six ISOPOOH isomers, only two - *cis*- and *trans*-β-IEPOX - account for nearly all (>97%) IEPOX formed from isoprene. Due to the high global abundance, along with the high reactivity and low volatility of IEPOX, a number of studies have focused on its reactive uptake onto particles and contribution to SOA formation (Budisulistiorini *et al.*, 2013; Chan *et al.*, 2010b; Eddingsaas *et al.*, 2010; Froyd *et al.*, 2011; Hatch *et al.*, 2011; Lin *et al.*, 2013a; McNeill *et al.*, 2012;

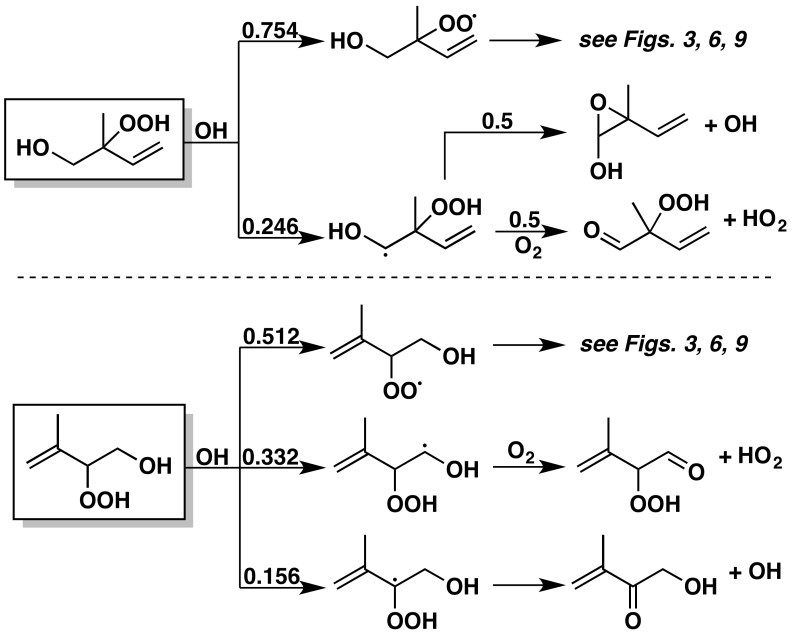

Figure 4.19: Reactions and products following the abstraction of a hydrogen from the two β-ISOPOOH isomers by OH. Branching ratios are for 298 K and 1 atm; the branching ratio between epoxide and hydroperoxy-aldehyde formation from (1-OH,2-OOH)-ISOPOOH varies with pressure.

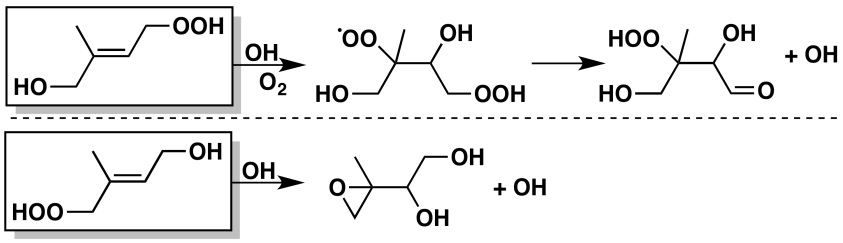

Figure 4.20: Reactions and products following the addition of OH to the δ-ISOPOOH isomers. *E*-δ isomers are shown for the reduced mechanism, but for the full mechanism their *Z*-δ counterparts are suggested to follow the same mechanisms.

isomer	Jacobs *et al.* (2013)	Bates *et al.* (2014)[a]	our recommendations
cis-β	-	1.52 ± 0.07	$5.82 \times e^{(-400/T)}$
trans-β	3.60 ± 0.76	0.98 ± 0.05	$3.75 \times e^{(-400/T)}$
$\delta 1$	-	0.84 ± 0.07	$3.22 \times e^{(-400/T)}$
$\delta 4$	3.52 ± 0.72	-	$3.22 \times e^{(-400/T)}$

Table 4.24: Rate coefficients for IEPOX oxidation by OH ($\times 10^{-11}$ cm^3 molec^{-1} s^{-1}). [a]Error bounds do not include 15% error in propene standard rate.

Minerath *et al.*, 2008; Nguyen *et al.*, 2014a; Surratt *et al.*, 2007a), aided by the development of synthetic pathways to produce pure IEPOX standards (Zhang *et al.*, 2012). The compound's gas-phase chemistry, on the other hand, has received less attention. Only three studies have investigated rates and product yields of IEPOX oxidation by OH and the discrepancies in their results suggest that additional studies will be required (Bates *et al.*, 2014, 2016; Jacobs *et al.*, 2013).

Kinetics (Table 4.24) - Both Jacobs *et al.* (2013) and Bates *et al.* (2014) determined the rate coefficients of IEPOX oxidation by OH, with widely differing results (Table 4.24). Jacobs *et al.* (2013) obtained the rate coefficients using a flow tube by comparing the rate of IEPOX oxidative loss to that of competitor molecules (pentenols and butenols) as measured by CIMS. IEPOX rate coefficient values from Jacobs *et al.* (2013) imply an atmospheric lifetime of only 4 h under standard conditions ($[OH] = 2 \times 10^6$ molec cm^{-3}). Bates *et al.* (2014) found the rate coefficients to be lower than those measured by Jacobs *et al.* (2013) by factors of two to four (Table 4.24). The Bates *et al.* (2014) rate coefficient values were determined by CIMS detection of IEPOX loss to reaction with OH in an environmental chamber, measured relative to propene oxidative loss at 299 K. These smaller rate coefficients imply atmospheric lifetimes of 18 – 33 h under standard conditions, and are more consistent with those inferred by Paulot *et al.* (2009b), which used IEPOX generated from isoprene in chamber experiments at 298 K to estimate an upper limit of 1.5×10^{-11} cm^3 molec^{-1} s^{-1} for the rate constant of IEPOX oxidation by OH. Further experiments are needed to resolve the discrepancies in measured reaction rate constants; at present, we recommend use of the rate coefficients from Bates *et al.* (2014), and suggest extrapolation of the $\delta 1$-IEPOX coefficient for the $\delta 4$ isomer.

Mechanism (Figures 4.21-4.22; Table 4.25) - Jacobs *et al.* (2013) and Bates *et al.* (2014) also measured the products of IEPOX oxidation by OH, and estimated the

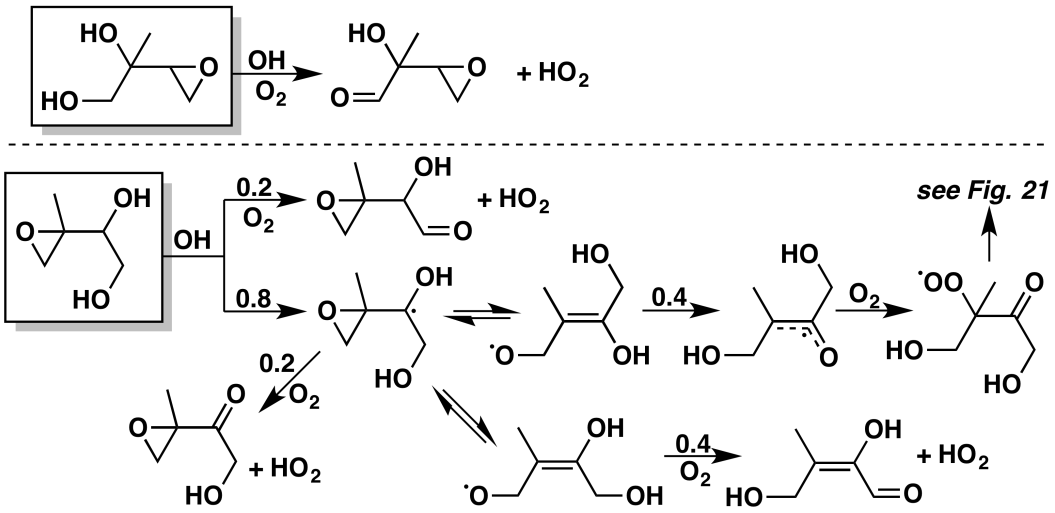

Figure 4.21: Reactions and products following the abstraction of a hydrogen from δ-IEPOX. Due to a lack of experimental data, these mechanisms remain highly speculative. Yields are for 298 K and 1 atm; branching between isomerization reactions and reaction with O_2 will vary with pressure. For the reduced mechanism, we ignore the δ-IEPOX isomers.

first-generation yields of a number of these products, shown in Table 4.25 (Bates *et al.*, 2014; Jacobs *et al.*, 2013). Only Jacobs *et al.* (2013) investigated the products of δ4-IEPOX oxidation, and proposed that OH exclusively abstracted the α-hydroxy hydrogens, leading either to formation of a C_5 hydroxycarbonyl epoxide or fragmentation to form hydroxyacetone and glyoxal. We propose that the fragmentation occurs in a slightly different pattern, leading to higher yields of C_5 hydroxycarbonyl epoxide, an isomeric C_5 dihydroxy aldehyde, or a C_4 hydroxydicarbonyl. Extrapolating this mechanism to δ1-IEPOX suggests that only the C_5 hydroxycarbonyl epoxide can form, because the molecule has no α-hydroxy β-epoxy hydrogen. These mechanisms for the δ-IEPOX isomers are included in our recommendations at the bottom of Table 4.25, and in Figure 4.21.

Both Jacobs *et al.* (2013) and Bates *et al.* (2014) investigated the products of β-IEPOX oxidation by OH, which are shown in a combined format in Figure 4.22. These mechanisms share a number of pathways, and both suggest little dependence on NO concentrations. In each reaction scheme, the abstraction of a hydrogen in a position α to a hydroxyl group can result in conversion of the hydroxyl substituent to a carbonyl. Both Jacobs *et al.* (2013) and Bates *et al.* (2014) found the resulting C_5 hydroxyepoxycarbonyl to account for 10-20% of the first-generation products of every IEPOX isomer studied. Both mechanisms also show a substantial amount

citation	isomer	NO	hydroxy-acetone[a,c]	glycolal-dehyde[b,c]	$C_5H_8O_3$[d]	$C_4H_8O_3$[c] + CO	$C_4H_6O_3$[c] + CH_2O	other
Bates *et al.* (2014)	*cis*-β	high	16.8 ± 0.3	11.8 ± 0.5	10.6 ± 0.7	46.4 ± 1.7	14.4 ± 0.6	20.1 ± 0.8
		low	8.5 ± 0.5	2.5 ± 0.6	12.9 ± 1.0	37.1 ± 2.2	10.4 ± 0.6	35.6 ± 3.3
	trans-β	low	5.41 ± 0.17	4.55 ± 0.24	10.5 ± 0.27	21.7 ± 0.5	3.69 ± 0.15	11.5 ± 0.8
Jacobs *et al.* (2013)	*trans*-β	high	25	14	22			39
		low	24	12	16			48
	δ4	high	81		19			
		low	78		22			
Our recommendations (including Bates *et al.* (2016))	*cis*-β		8	17	21	46	8	
	trans-β		16	14	18	45	7	
	δ1				100			
	δ4				68		32	

Table 4.25: Product yields (%) from IEPOX. Coproducts: [a]glyoxal; [b]methylglyoxal; [c]OH; [d]HO_2. [e]In Bates *et al.* (2014), other includes formic and acetic acids; in Jacobs *et al.* (2013), other includes products observed at *m/z* (MH^+) = 89 ($C_4H_8O_2$ or $C_3H_4O_3$), 133 ($C_5H_8O_4$), and 151 ($C_5H_{10}O_5$).

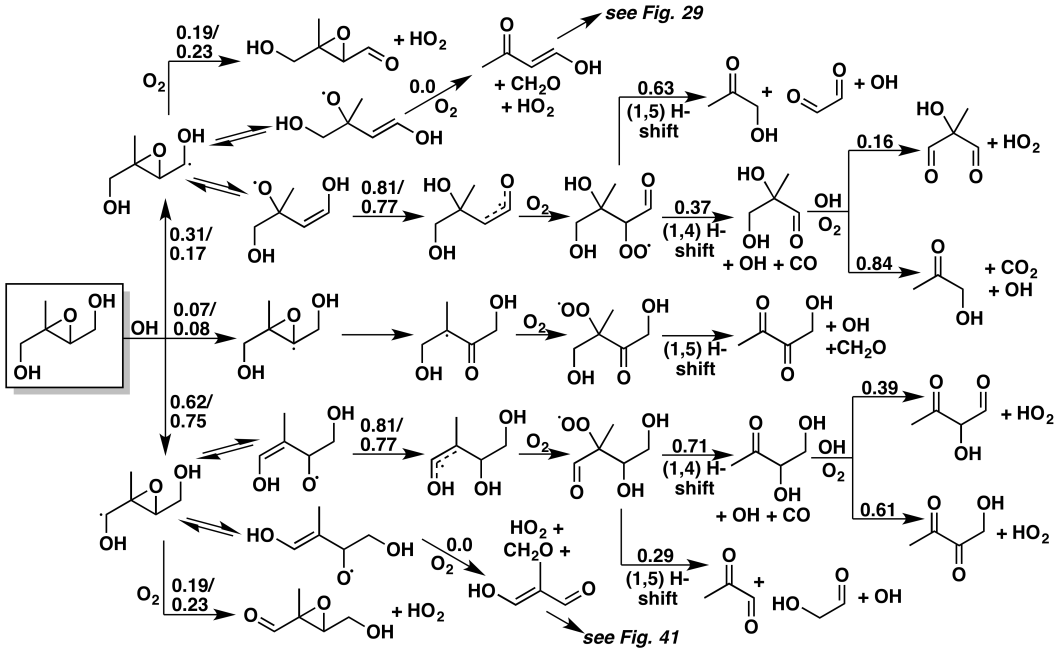

Figure 4.22: Reactions and products following the abstraction of a hydrogen from β-IEPOX. The oxidation mechanisms of the *cis* and *trans* isomers diverge only slightly in their branching ratios, which are denoted as "*trans*/*cis*" where they differ. Reactions labeled as 1,5 H-shifts could also proceed by reaction of the peroxy radical with NO, HO_2, or RO_2 to form an alkoxy radical, which would subsequently decompose to the identical products (along with NO_2, OH, or RO respectively).

of IEPOX fragmenting to a C_2 and a C_3 product, concurrently forming either hydroxyacetone and glyoxal or methylglyoxal and glycolaldehyde.

The remaining first-generation products differ between the two mechanisms, suggesting that further experimentation will be needed to constrain the products of IEPOX oxidation. Jacobs *et al.* (2013) detected large amounts of C_5 dihydroxy dicarbonyls and dihydroxy hydroperoxycarbonyls, in addition to an unidentified product postulated to be $C_4H_8O_2$ or $C_3H_4O_3$, none of which were detected by Bates *et al.* (2014). In contrast, Bates *et al.* (2014) determined that C_4 dihydroxycarbonyls and hydroxydicarbonyls are the most abundant first-generation products in the OH-initiated oxidation of both *cis*- and *trans*-β-IEPOX. In a subsequent study, Bates *et al.* (2016) refined the product yields from their 2014 study, and determined that the previously unidentified C_4 dihydroxycarbonyls consisted primarily of a single $C_4H_8O_3$ isomer, 1,2-dihydroxy-3-butanone, along with a minor contribution from 2,3-dihydroxy-2-methylpropanal. Our preliminary recommendations for product branching ratios can be found in Table 4.25, but additional efforts to identify and

quantify the products of IEPOX + OH oxidation and field measurements of these postulated products may be needed to reconcile the differences between the two postulated mechanisms and arrive at a more unified and comprehensive mechanism.

4.7.5 isoprene Nitrates: IHN, ICN, and IPN

First generation isoprene-derived organonitrates are produced from two main channels: the reaction of isoprene-peroxy radicals with NO (section 4.3.3.1) and the reaction of isoprene directly with NO_3 (Section 4.5). The former mechanism produces primarily β-hydroxynitrates, with a small yield of δ-hydroxynitrates, while the latter mechanism produces hydroxy-, carbonyl-, and hydroperoxy-nitrates depending on the fate of the peroxy radicals formed. Despite the importance of these products to local HO_x and NO_x budgets, their subsequent reactivities remain poorly constrained, and most estimates of their reaction rates and mechanisms have relied primarily on chemical intuition (Giacopelli *et al.*, 2005; Paulot *et al.*, 2009a; Rollins *et al.*, 2009). The recent development of synthetic routes to IHN has facilitated an improved understanding of their fates in the gas phase (Jacobs *et al.*, 2014; Lee *et al.*, 2014; Lockwood *et al.*, 2010; Teng *et al.*, 2017). Here, we recommend rate constants and products for the reactions of hydroxynitrate isomers with OH; we use these recommendations to provide guidance for the equivalent photochemistry of the other functionalized nitrates. Finally, we discuss other fates of the isoprene nitrates, including ozonolysis, photolysis, and reaction with NO_3.

4.7.5.1 Reactions of IHN, ICN, and IPN with OH

Kinetics (Tables 4.26 and 4.27) - Synthetic standards have enabled measurements of the rate constants for reactions of OH with all six isoprene hydroxynitrate (IHN) isomers produced following the reaction of isoprene with OH. Recommended values for these rate constants can be found in Table 4.26. The two main β-hydroxynitrates, which dominate the isomer distribution, exhibit similar rate constants; Teng *et al.* (2017) measured that of 1-OH,2-ONO_2 to be $3.0 \pm 0.9 \times 10^{-11}$ cm^3 molec^{-1} s^{-1}, while Lee *et al.* (2014) and Jacobs *et al.* (2014) report a slightly higher value for the 4-OH,3-ONO_2 isomer (4.2 ± 0.7 and $3.6 \pm 0.8 \times 10^{-11}$ cm^3 molec^{-1} s^{-1}). The δ-hydroxynitrates react faster with OH; Lee *et al.* (2014) measured the rate constant of 1-OH,4-ONO_2 + OH to be $1.1 \pm 0.2 \times 10^{-10}$ cm^3 molec^{-1} s^{-1}, and Teng *et al.* (2017) measured the rate constant of 4-OH,1-ONO_2-IHN + OH to be $8.0 \pm 2.4 \times 10^{-11}$ cm^3 molec^{-1} s^{-1}. No differences were reported between reaction rates of *E* and *Z* isomers for the two δ-hydroxynitrates.

isomer	$k_{OH} \times 10^{11}$	$k_{O_3} \times 10^{19}$	$k_{NO_3} \times 10^{14}$
1-OH, 2-ONO_2	3.0 ± 0.9	2.8	5
4-OH, 3-ONO_2	4.2 ± 0.7	5	5
E 1-OH, 4-ONO_2	11 ± 2	270	80
Z 1-OH, 4-ONO_2	11 ± 2	290	80
E 4-OH, 1-ONO_2	8 ± 2.4	270	80
Z 4-OH, 1-ONO_2	8 ± 2.4	280	80

Table 4.26: Recommended rate constants (cm^3 $molec^{-1}$ s^{-1}) at ~298 K for the reactions of OH, O_3, and NO_3 with isoprene hydroxynitrates formed following the reaction of isoprene with OH.

isomer	$k_{OH} \times 10^{11}$	$k_{O_3} \times 10^{19}$	$k_{NO_3} \times 10^{14}$
1-ONO_2, 2-OH IHN	3.0	2.8	5
4-ONO_2, 3-OH IHN	4.2	5	5
1-ONO_2, 2-OOH IPN	3.7	2.8	5
1-ONO_2, 4-OOH IPN	8.7	280	80
4-ONO_2, 1-OOH IPN	11.7	280	80
4-ONO_2, 3-OOH IPN	4.9	5	5
1-ONO_2, 4-CO ICN	3.4	44	80
4-ONO_2, 1-CO ICN	4.1	44	80
4-ONO_2, 3-CO ICN	1.0	0.8	5

Table 4.27: Proposed rate constants (cm^3 $molec^{-1}$ s^{-1}) at ~298 K for the reactions of OH, O_3, and NO_3 with isoprene hydroxynitrates, hydroperoxynitrates, and carbonyl nitrates formed following the reaction of isoprene with NO_3. *E* and *Z* isomers of the δ reactants are treated together.

For most of the organic nitrates produced in the reaction of isoprene with NO_3, no synthetic standards are available; we therefore use IHN as a model. Suggested rate constants are listed in Table 4.27. Briefly, we recommend the same rates of OH addition for 2-OH,1-ONO_2 as for 1-OH,2-ONO_2, and the same for 4-OH,3-ONO_2 as for 3-OH,4-ONO_2. For the isoprene hydroperoxynitrates (IPN), we recommend the same OH-addition rates as for their respective IHN isomers, but we also add a channel for abstraction of the hydroperoxy hydrogen, for which we use an average of the abstraction rate constants measured by St. Clair *et al.* (2015) for [1,2]- and [4,3]-ISOPOOH. Finally, for the carbonyl nitrates (ICN), we also recommend the same OH-addition rates as for their respective IHN isomers, but we include a channel for abstraction of the aldehydic hydrogen, as estimated from the SAR developed by Kwok and Atkinson (1995).

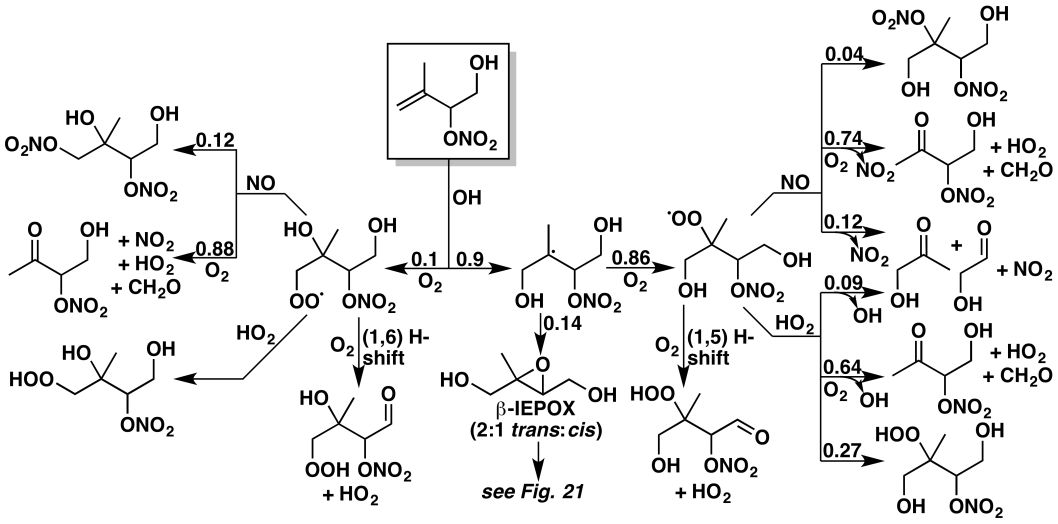

Figure 4.23: Reactions and products following the addition of OH to (4-OH,3-ONO_2)-IHN. Yields are for 298 K and 1 atm; in reactions of peroxy radicals with NO, the relative contributions of the nitrate and alkoxy pathways vary with both temperature and pressure, and the branching ratio between IEPOX formation and O_2 addition also varies with pressure. For the reduced mechanism, we combine the various isomers of stable C_5 tetrafunctionalized products.

Mechanism: OH + β-nitrates (Figures 4.23, 4.24, 4.31-4.33) - The most comprehensively studied isoprene nitrate is the (4-OH,3-ONO_2)-IHN, for which product studies have been carried out in bulk (Paulot *et al.*, 2009a) and with authentic standards (Jacobs *et al.*, 2014; Lee *et al.*, 2014), though only under NO-dominated conditions. Product yields from many other β-nitrates are inferred from these results. Our recommended OH + 4-OH,3-ONO_2-IHN mechanism is shown in Figure 4.23. We suggest OH reaction branching ratios of 90% 1-addition and 10% 2-addition, although this ratio is poorly constrained due to the similarity of products between the two channels (Jacobs *et al.*, 2014; Lee *et al.*, 2014).

Following OH and O_2 addition, the resulting peroxy radicals are expected to react predominantly with HO_2 and NO. Reactions of the peroxy radicals with both HO_2 and NO are expected to produce mainly alkoxy radicals, which then go on to fragment, except in the case of external peroxy radicals reacting with HO_2, which are expected to produce hydroperoxides in high yields. At atmospheric pressure, the main products of the fragmentation are formaldehyde and MVKN, although β-scission of the C2-C3 bond to yield NO_2, glycolaldehyde, and hydroxacetone is also a minor channel (Jacobs *et al.*, 2014; Lee *et al.*, 2014; Paulot *et al.*, 2009a).

In addition to the fragmentation reactions, a number of functionalization channels

have been observed or proposed. OH addition at the outer carbons can result in prompt IEPOX formation, the yield of which is pressure-dependent (Jacobs *et al.*, 2014). Yields of IEPOX reported by Jacobs *et al.* (2014) at 50 Torr were as high as 71%, with an extrapolated yield (based on pressure dependence measurements up to 450 Torr) of 16% at atmospheric pressure, consistent with the yield reported by St. Clair *et al.* (2015) of 12%. Alternatively, the peroxy radicals can undergo 1,5 and 1,6 H-shifts with external α-hydroxy hydrogens, which is followed rapidly by reaction with O_2 to form hydroxy-hydroperoxy-carbonyl-nitrates. Other functionalizations include reaction of the peroxy radicals with HO_2 and NO to produce dihydroxy-hydroperoxy-nitrates and dihydroxy-dinitrates respectively. Wall loss and/or aerosol formation make the measurement of these products difficult, but Lee *et al.* (2014) report a 3% dinitrate yield. The low yield requires a smaller branching ratio to form nitrates from RO_2 + NO when there are two electron withdrawing groups beta to RO_2, as in the case of the branching ratios to yield organic nitrates from methacrolein and methyl vinyl ketone (Crounse *et al.*, 2012; Praske *et al.*, 2015), which our formula in Equation 4.3 provides. For the dihydroxy-hydroperoxy-nitrate formation from reaction of peroxy radicals with HO_2, we assume a unity yield for primary peroxy radicals, and use yields for analogous hydroxynitrates assumed in Schwantes *et al.* (2015).

The recommended mechanism of the reaction of 1-OH,2-ONO_2-IHN with OH is shown in Figure 4.24, and is similar to that of 4-OH,3-ONO_2-IHN, with the main difference being the recommended branching ratios of 25% 3-OH-addition and 75% 4-OH-addition. Again, reactions of the resulting peroxy radicals with NO and HO_2 produce predominantly alkoxy radicals, which can then fragment to form either formaldehyde and MACRN or NO_2, glycolaldehyde and hydroxyacetone. The estimated IEPOX yield from 1-OH,2-ONO_2-IHN is inferred to be similar to that of 4-OH,3-ONO_2-IHN (St. Clair *et al.*, 2015), as are the dinitrate yields Lee *et al.* (2014). However, the overall hydroperoxide yield from the reaction of the peroxy radicals with HO_2 is predicted to be substantially higher than that of 4-OH,3-ONO_2-IHN, due to the larger fraction of primary peroxy radicals formed.

The oxidation mechanisms of β-functional nitrate isomers formed in the reaction of isoprene with NO_3 (Figure 4.31) are less well constrained; here, we apply a mechanism similar to that described in Schwantes *et al.* (2015), which draws upon both bulk chamber studies of isoprene + NO_3 and extrapolation from Lee *et al.* (2014) and Jacobs *et al.* (2014). Briefly, the positions of OH addition to the

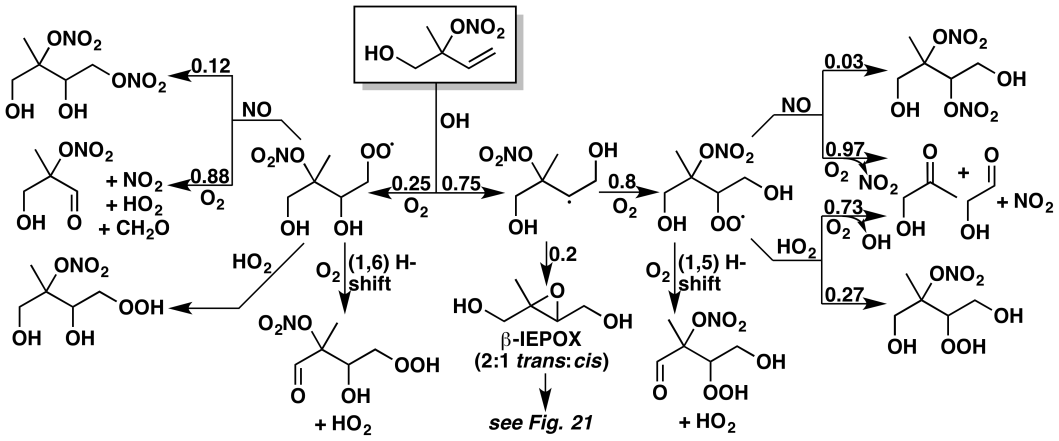

Figure 4.24: Reactions and products following the addition of OH to 1-OH,2-ONO_2-IHN. Yields are for 298 K and 1 atm; in reactions of peroxy radicals with NO, the relative contributions of the nitrate and alkoxy pathways vary with both temperature and pressure, and the branching ratio between IEPOX formation and O_2 addition also varies with pressure. For the reduced mechanism, we combine the various isomers of stable C_5 tetrafunctionalized products.

1-ONO_2 and 4-ONO_2 β nitrates are assumed to match those of MVK (Praske *et al.*, 2015) and MACR (Crounse *et al.*, 2012), respectively. The positions of the nitrate moieties preclude IEPOX formation, so all 1-ONO_2 and 4-ONO_2 β-IHNs form peroxy radicals in 100% yield. The fates of these peroxy radicals are similar to those of the 4-OH,3-ONO_2 and 1-OH,2-ONO_2-IHNs; reaction with NO can produce dinitrates, reaction with HO_2 can produce hydroperoxides, and reaction with either can cause fragmentation, forming smaller nitrates and carbonyl-containing compounds (PROPNN + GLYC or MACRN + CH_2O for 1-ONO_2,2-OH-IHN; ETHLN + HAC or MVKN + CH_2O for 3-ONO_2,4-OH-IHN). Recommended yields of these channels are calculated from Equation 4.3 or taken from Schwantes *et al.* (2015).

The 1-ONO_2 and 4-ONO_2 β-IPNs (Figures 4.32 and 4.33) follow the same OH oxidation mechanism as their corresponding IHNs, with two important exceptions. First, OH can abstract the hydroperoxy hydrogen, reforming the isoprene-nitrate-peroxy radical described in Section 4.5. Second, when OH adds at the terminal carbon, the hydroperoxide moieties on the IPNs can unimolecularly react in high yields (~50%) to form a nitrooxy-hydroxy-epoxide (INHE) similar to IEPOX (Schwantes *et al.*, 2015). The recommended subsequent chemistry of INHE (Figures 4.34 - 4.36) is extrapolated from the IEPOX chemistry described in Section 4.7.4, using averages of the *cis*- and *trans*-β-IEPOX isomers' branching ratios for the β-INHE

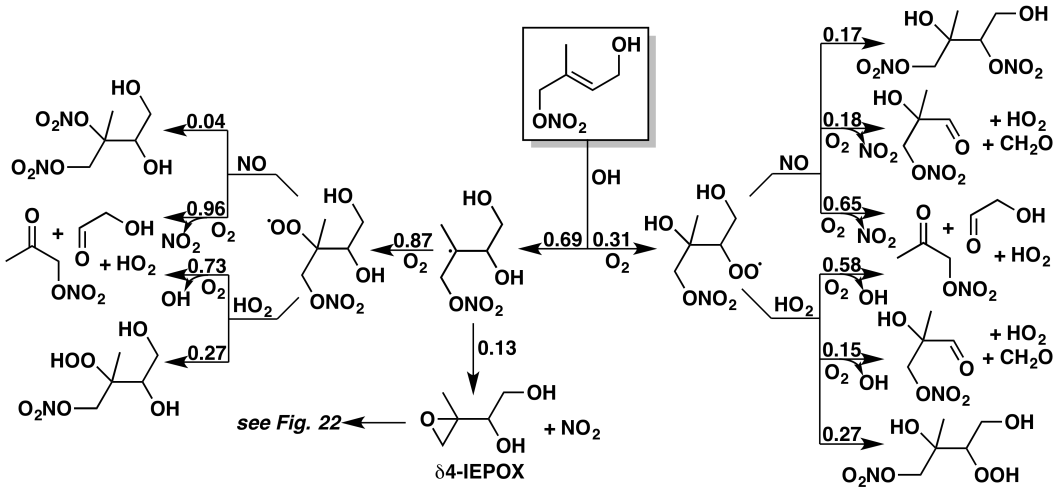

Figure 4.25: Reactions and products following the addition of OH to *E*-(1-ONO_2,4-OH)-IHN. *Z*-(1-ONO_2,4-OH)-IHN is expected to react identically. Yields are for 298 K and 1 atm; in reactions of peroxy radicals with NO, the relative contributions of the nitrate and alkoxy pathways vary with both temperature and pressure, and the branching ratio between IEPOX formation and O_2 addition also varies with pressure. For the reduced mechanism, we combine the δ-IHN isomers into a single species, and scale the product yields of its subsequent reactions according to the relative contributions of the isomers. We also combine the various isomers of stable C_5 tetrafunctionalized products.

isomers.

Mechanism: OH + δ-nitrates (Figures 4.25-4.27, 4.37-4.40) - Authentic standards for *E*- and *Z*-1-OH,4-ONO_2-IHN have been studied by Lee *et al.* (2014) and Jacobs *et al.* (2014). Schwantes *et al.* (2015) built upon their findings and additional bulk isoprene + NO_3 experiments to postulate complete mechanisms for δ-IHN, IPN, and ICN isomers. We draw heavily from Schwantes *et al.* (2015) for our recommendations. For all δ-nitrates, we assume OH adds to the C2 and C3 positions in a 30:70 ratio, as estimated by Teng *et al.* (2015) for 2-methyl-2-butene. The subsequent reactions of the dominant IHN, IPN, and ICN isomers are shown in Figures 4.25, 4.26, and 4.27, respectively, while those of the minor 4-ONO_2 isomers are shown in Figures 4.37, 4.38, and 4.39.

For the δ-IHNs, OH addition is followed either by O_2 addition or by decomposition of the nitrate moiety to form IEPOX + NO_2 in a 13% yield (Jacobs *et al.*, 2014; St. Clair *et al.*, 2015) for those isomers in the correct orientation. Subsequent reaction of the peroxy radicals with NO or HO_2 can result in formation of an

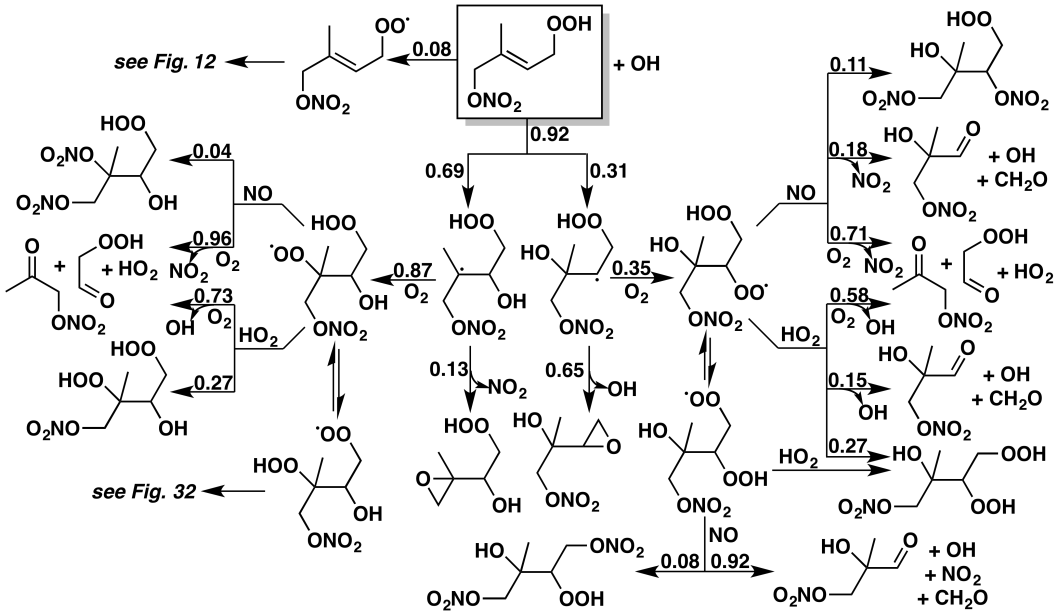

Figure 4.26: Mechanism of the reaction of OH with *E*-(1-ONO_2,4-OOH)-IPN. *Z*-(1-ONO_2,4-OOH)-IPN is expected to react identically. Yields are for 298 K and 1 atm; branching ratios between OH-addition and -abstraction, epoxide formation and O_2 addition, and nitrate and alkoxy formation all vary with temperature and/or pressure. For the reduced mechanism, we combine the δ-IPN isomers into a single species, and scale the product yields of its subsequent reactions according to the relative contributions of the isomers. We also combine the various isomers of stable C_5 tetrafunctionalized products.

alkoxy radical, which, as with the β isomers, fragments to form smaller nitrates and carbonyl-containing compounds (PROPNN + GLYC or MACRN' + CH_2O for 4-OH,1-ONO_2; ETHLN + HAC or MVKN' + CH_2O for 1-OH,4-ONO_2). Additionally, reaction of the peroxy radicals with NO can form dinitrates in small yields, while reaction of the peroxy radicals with HO_2 forms hydroperoxides in only moderate (~27%) yields, as assumed in Schwantes *et al.* (2015).

The reactions of δ-IPNs with OH follow similar channels to the δ-IHNs, with two exceptions. First, OH can abstract the hydroperoxy hydrogen, reforming the isoprene-nitrate-peroxy radical described in Section 4.5. Second, OH addition at the α-nitrooxy position allows the hydroperoxide moiety to unimolecularly form OH + the epoxide INHE, for which we recommend yields from Schwantes *et al.* (2015). The remaining OH reaction products of δ-IPNs are assumed to be similar to those formed from δ-IHNs.

The δ-ICNs also have unique channels in their reaction with OH, for which we use

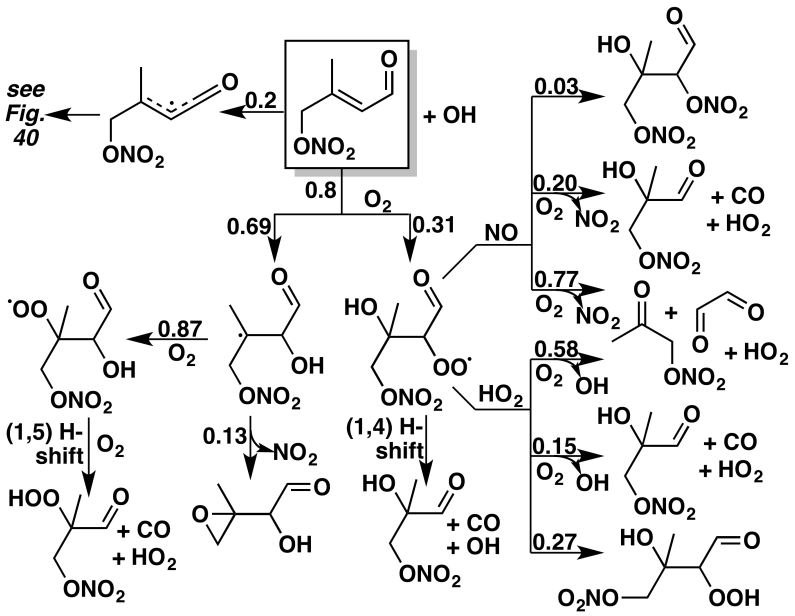

Figure 4.27: Mechanism of the reaction of OH with *E*-(1-ONO_2,4-CO)-ICN. *Z*-(1-ONO_2,4-CO)-ICN is expected to react identically. Yields are for 298 K and 1 atm; branching ratios between OH-addition and -abstraction, epoxide formation and O_2 addition, and nitrate and alkoxy formation all vary with temperature and/or pressure. For the reduced mechanism, we combine the four isomers of peroxy radicals derived from the addition of OH and O_2 to the δ-ICN isomers, and scale the product yields of its subsequent reactions with NO and HO_2 according to the relative contributions of the isomers. We also combine the various isomers of stable C_5 tetrafunctionalized products.

branching ratios from Schwantes *et al.* (2015). Peroxy radicals formed following OH addition can undergo [1,4]- and [1,5]-H-shifts, similar to those described by Crounse *et al.* (2012) for MACR. Under high NO conditions, Xiong *et al.* (2016) measured 27% and 9% yields of MVKN and ETHLN, respectively, from the reaction of (4-ONO_2,1-CO)-ICN with OH. This distribution suggests that the C-CHO bond on ICN is weaker than the C-CH_2OH bond on IHN. Thus, based on the product distribution measured by Xiong *et al.* (2016), for δ-ICN OH-addition products, we recommend that 75% of the alkyl radicals formed from RO_2 + NO and RO_2 + HO_2 reactions breaks at the C-CHO bond to form MVKN and MACRN. Additionally, products from OH hydrogen abstraction from the aldehyde group of ICN are estimated and included in the mechanism (Figure 4.40).

4.7.5.2 Reactions of IHN, ICN, and IPN with O_3 and NO_3

Published rate constants for the reactions of IHNs with O_3 based on authentic standards show significant disagreement. Lockwood *et al.* (2010) report ozone rates constants for the 1-OH,2-ONO_2, 2-OH,1-ONO_2, and *E*-1-OH,4-ONO_2 isomers that are two to three orders of magnitude faster than those reported by Lee *et al.* (2014) for the 4-OH,3-ONO_2 and *E*- and *Z*-1-OH,4-ONO_2. Based on ambient measurements which show significant isoprene hydroxy nitrates at night (Beaver *et al.*, 2012), it is unlikely that the ozone rate constants are as large as reported by Lockwood *et al.* (2010) and therefore we recommend the Lee *et al.* (2014) ozone rate constants. Unpublished measurements at Caltech of the 1-OH,2-ONO_2 ozonolysis rate constant show similar order of magnitude rate constant to 4-OH,3-ONO_2. Recommended rate constants for the reaction of ozone with the IHNs produced from isoprene + OH are listed in Table 4.26. Recommended rate constants for the reaction of ozone with the ICNs, IPNs, and IHNs produced from isoprene + NO_3 are listed in Table 4.27. Xiong *et al.* (2016) measured the ozone reaction rate constant for (4-ONO_2,1-CO)-ICN to be $4.4 \pm 0.3 \times 10^{-18}$ cm^3 molec^{-1} s^{-1}. As with the OH oxidation of ICN, all other ICN isomer rate constants were directly extrapolated using the rate measured by Xiong *et al.* (2016) and the isomer-specific rate constants from IHN. Ozonolysis rate constants for IPNs and IHNs are directly extrapolated from those of the IHNs produced by isoprene + OH.

There is currently little measured data on NO_3 rate constants with isoprene nitrates. Lee *et al.* (2014) discuss various SAR estimates for the potential importance of loss by NO_3 radical and finds that this process is probably negligible (lifetime of 13 h at 10 pptv NO_3, using a SAR estimate proposed by Pfrang *et al.*, 2008 and scaled by results for 1-hydroxy-2-butene by Zhao *et al.*, 2011) to completely negligible (lifetime of 130 h at similar conditions by Kerdouci *et al.* (2010)). In the absence of experimental data to provide guidance, we recommend a rate constant which is an average of the two revised SAR estimates from Lee *et al.* (2014) for the IHNs, and extend this directly to the ICNs and IPNs (see Tables 4.26 and 4.27).

4.7.5.3 Photolysis of organic nitrates

The photolysis of organic nitrates is still poorly understood, with few measured cross-sections. Several recent studies suggest, however, that photolysis may be a dominant loss process for some of these compounds under typical ambient conditions. Previously compiled mechanisms have usually assumed slow photolysis

of nitrates, and in particular, have assigned low quantum yields for the carbonyl nitrates (Saunders *et al.*, 2003; Xie *et al.*, 2013), with some making an exception for α-nitrooxy ketones, for which the neighboring functional groups demonstrably increase absorption cross-sections (Barnes *et al.*, 1993; Robert and Fajer, 1989). However, recent measurements of carbonyl nitrate photolysis by Suarez-Bertoa *et al.* (2012), along with analysis by Müller *et al.* (2014), suggest much faster photolysis for second-generation isoprene-derived nitrates, including PROPNN, ETHLN, MVKN, and MACRN. We include these increased photolysis rates in our mechanism.

In light of the recent studies on carbonyl nitrates, we recommend further research on the role of photolysis as a sink for the more complex organic nitrates formed in the isoprene oxidation mechanism. The photolysis of (4-ONO_2,1-CO)-ICN has been measured (4.6×10^{-4} s^{-1} at solar zenith angle = 0°) to be quite fast (Xiong *et al.*, 2016). All ICN are assumed to photolyze at this same rate. Xiong *et al.* (2016) detected a number of products from the dissociation of both the C-CHO and O-NO_2 bonds, but unfortunately no yields were reported. Future studies should focus on identifying product yields from ICN photolysis, as photolysis represents an important atmospheric sink for ICN (Xiong *et al.*, 2016). Additionally, hydroperoxy nitrates formed in the reaction of isoprene with NO_3 may have significant photolysis rates, and should be investigated. There has also been some suggestion of higher photolysis rates of non-carbonyl nitrates, including the first-generation hydroxy isoprene nitrates themselves (Xiong *et al.*, 2015). Further study is suggested.

4.7.6 MPAN

MPAN is formed from the reaction of methacryloyl peroxy radical (MACR1OO) with NO_2. The amount of MPAN in the atmosphere is extremely sensitive to the NO_2 to NO ratio. At high NO to NO_2 ratio, MACR1OO is channeled toward irreversible reaction with NO. The lifetime of MPAN is also highly dependent on temperature as this compound (and other acylperoxynitrates) is labile to thermal decomposition. At 298 K, the thermal loss of MPAN occurs with an *e*-folding time of 4.5 h. Oxidation with OH is also competitive within the thermal timescale (τ_{OH} = 4.8 h at 2×10^6 molec cm^{-3}), and is considered below. The reactions of MPAN with O_3 and NO_3 are likely too slow to be competitive with thermal decomposition and OH reaction (see Table 4.28).

Kinetics (Table 4.28) - IUPAC recommends a rate constant for the reaction of MPAN with OH of 2.9×10^{-11} cm^3 $molec^{-1}$ (at 298 K, adjusted based on OH +

oxidant	T (K)	k (cm^3 molec^{-1})	citation
OH	298 ± 2	$3.6 \pm 0.4 \times 10^{-12}$	Grosjean *et al.* (1993c)
OH	275 ± 3	$3.2 \pm 0.8 \times 10^{-11}$	Orlando *et al.* (2002)
OH	298	3.0×10^{-11}	our recommendation
O_3	291-297	$8.2 \pm 2 \times 10^{-18}$	Grosjean *et al.* (1993a)
NO_3	296 ± 2	$1.45 \pm 0.45 \times 10^{-16}$	Canosa-Mas *et al.* (1999b)

Table 4.28: Reaction rate constants for the oxidation of MPAN by OH, O_3, and NO_3.

propene temperature dependence). The rate constant determined by Grosjean *et al.* (1993c) is inexplicably 10 times lower than that determined by Orlando *et al.* (2002) (see Table 4.28), both by competitive rate techniques. The Orlando *et al.* (2002) rate constant is preferred by IUPAC based on analogy with the OH reaction of CH_2=C(CH_3)C(O)ONO_2 at 298 K (Saunders *et al.*, 1994). Recent determinations by Nguyen *et al.* (2015b) are also consistent with Orlando *et al.* (2002). The reaction of OH + MPAN may have a small (probably negative) temperature dependence by analogy with CH_2=C(CH_3)C(O)ONO_2, but for our mechanism, we follow the recommendation of Orlando *et al.* (2002) and assume no temperature dependence.

Mechanism (Figure 4.28) - The mechanism of the OH reaction with MPAN, which is remarkable due to its propensity to produce secondary organic aerosol (*e.g.*, Surratt *et al.*, 2010), has been subject of debate. Experimental studies of MACR photooxidation in the presence of NO_2 suggested the formation of an epoxide stable product, called methacrylic acid epoxide (MAE), and NO_3 (Lin *et al.*, 2013b) or an unstable dioxo-ketone product and NO_2 (Chan *et al.*, 2010a). A theoretical study (Kjaergaard *et al.*, 2012) suggested the formation of an unstable product, a hydroxy methyl methyl-α-lactone (HMML) and NO_3. The Kjaergaard *et al.* (2012) study proposes that 36% of HMML promptly decomposes to hydroxyacetone, while Lin *et al.* (2013b) proposes very low (~3%) hydroxyacetone formation. Compared to 60 ± 10% hydroxyacetone yield observations of Grosjean *et al.* (1993c), the suggestion of Kjaergaard *et al.* (2012) appears more favorable.

Recent laboratory work using synthesized and purified MPAN (Nguyen *et al.*, 2015b) confirms the formation of NO_3 in high yields. Yields of hydroxyacetone of approximately 30 ± 10% are in good agreement with theoretical predictions by Kjaergaard *et al.* (2012) but in poor agreement with experimental observations of Grosjean *et al.* (1993c). Further, the secondary organic aerosol yield was roughly equal to (1 – Y_{HAC}) and Y_{NO_3}. Notably, Nguyen *et al.* (2015b) did not observe MAE

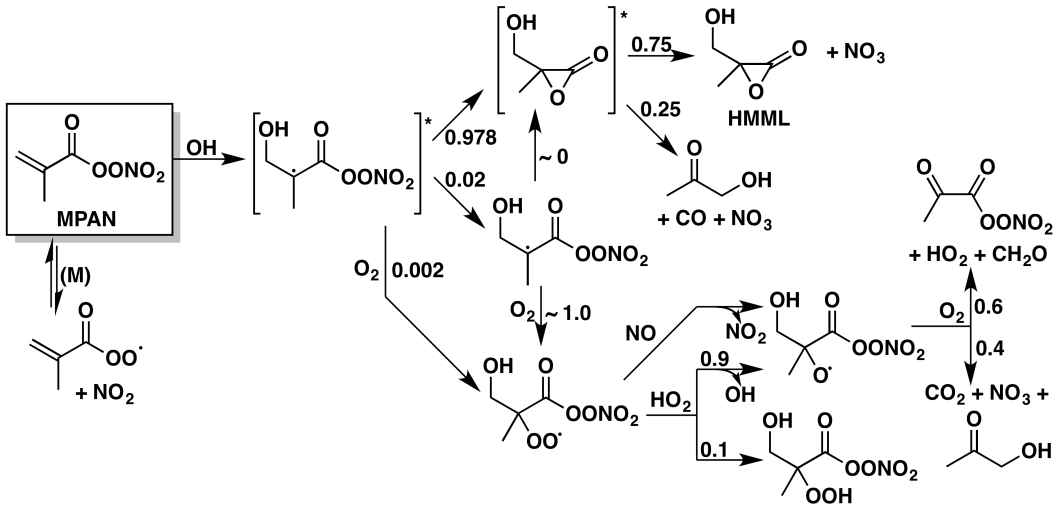

Figure 4.28: Reactions and products following the addition of OH to MPAN. Yields are for 298 K and 1 atm; in reactions of peroxy radicals with NO, the relative contributions of the nitrate and alkoxy pathways vary with both temperature and pressure. For the reduced mechanism, we ignore the low-yielding O_2-addition channel, and instead recommend the prompt formation of 1.0×NO_3 + 0.25×(hydroxyacetone + CO) + 0.75×HMML.

formation from MPAN + OH, but did observe what appears to be MAE formation (~3%) from MACR + OH + NO_2. Thus, based on experimental results from MPAN, we recommend the HMML formation mechanism and yields in Figure 4.28.

4.7.7 HPALDs

Two isomers of isoprene hydroperoxy aldehydes (HPALDs) can be formed from the 1,6 H-shift isomerization of the *Z*-δ isoprene hydroxy peroxy radicals: (1-CO, 4-OOH)-HPALD (HPALD1) from the *Z*-1-OH-4-OO radical, and (1-OOH, 4-CO)-HPALD (HPALD2) from the *Z*-1-OO-4-OH radical. Both remain in the *Z* configuration through the formation process. While other hydroperoxy-carbonyl compounds may be formed at other stages of the isoprene oxidation mechanism, these two represent major first-generation products, and their subsequent chemistry is therefore of primary importance. However, few experimental constraints exist on the oxidation of HPALD; our recommendations here should therefore be updated liberally as new evidence is published.

Kinetics - photolysis: Loss of HPALDs was originally predicted to occur mainly by fast photolysis on the order of J = 10^{-4} to 10^{-3} s^{-1} by Peeters and Muller (2010) and Peeters *et al.* (2009). The weak hydroperoxide O–OH bond has a low

cross section, while the α,β-enone has a high cross section in the 290–370 nm range and a stronger C–C bond. Fast internal conversion after absorption of a photon changes the molecule to a lower electronic but higher vibrational state which results in dissociation of the O–OH bond, resulting in a photolysis rate estimated to be some 2 orders of magnitude faster than for the chromophore moieties –O–OH or O=C–C=C– alone (Peeters and Muller, 2010). Experimental work using a synthetic C_6-HPALD corroborated these hypotheses, demonstrating a near-unity (±0.4) quantum yield over the range 300-400 nm, and thus estimating an HPALD atmospheric lifetime of 30–180 minutes (Wolfe *et al.*, 2012). However, recent theoretical calculations place the quantum yields much lower, at 0.58 for HPALD1 and 0.55 for HPALD2 (Liu *et al.*, 2017). This would result in a near-doubling of the HPALD lifetime against photolysis, potentially bringing modeled mixing ratios into closer alignment with aircraft measurements (Travis *et al.*, 2016). Based on the primary O=C–C=C– chromophore in HPALDs, we suggest a cross-section equivalent to that of methacrolein (MACR), along with the quantum yields from Liu *et al.* (2017).

Mechanism - photolysis (Figures 4.29 and 4.41): Peeters *et al.* (2009) predicted that initial photolysis of the O–OH bond is followed by a 1,5-H-shift, O_2 addition, a 1,6-H-shift and abstraction of a hydrogen atom by O_2 to yield an HO_2 and a peroxy-acid-aldehyde (PACALD). However, PACALDs were not detected in experiments (Wolfe *et al.*, 2012), and a subsequent theoretical study identified a faster photolysis route that bypassed the PACALD mechanism (Peeters *et al.*, 2014). The latest calculations from this fast photolysis channel (Liu *et al.*, 2017) are in reasonable agreement with what little experimental data exist, and we therefore recommend the product yields from that computational study, as shown in Figures 4.29 and 4.41 for HPALD 1 and 2 respectively. Of particular note is the high radical recycling from the photolysis of HPALDS, which produces ∼1.65 equivalents of OH.

Briefly, for both HPALDs, photolysis of the aldehyde π-bond can either be followed by a rapid 1,5-H shift of an α-hydroperoxy hydrogen and lose OH to form a resonance-stabilized carbonyl doublet radical (22% for HPALD1, 36% for HPALD2), or by a series of internal rearrangements and a loss of OH to form an alkoxy radical (78% for HPALD1, 64% for HPALD2). The carbonyl doublet radical intermediate is then expected to add oxygen; if it does so at the α-hydroxy position, it will undergo a 1,4 H-shift and lose HO_2 to form 2-methylbut-2-ene-1,4-dial (50%), while oxygen addition at an internal carbon is followed by a series of re-

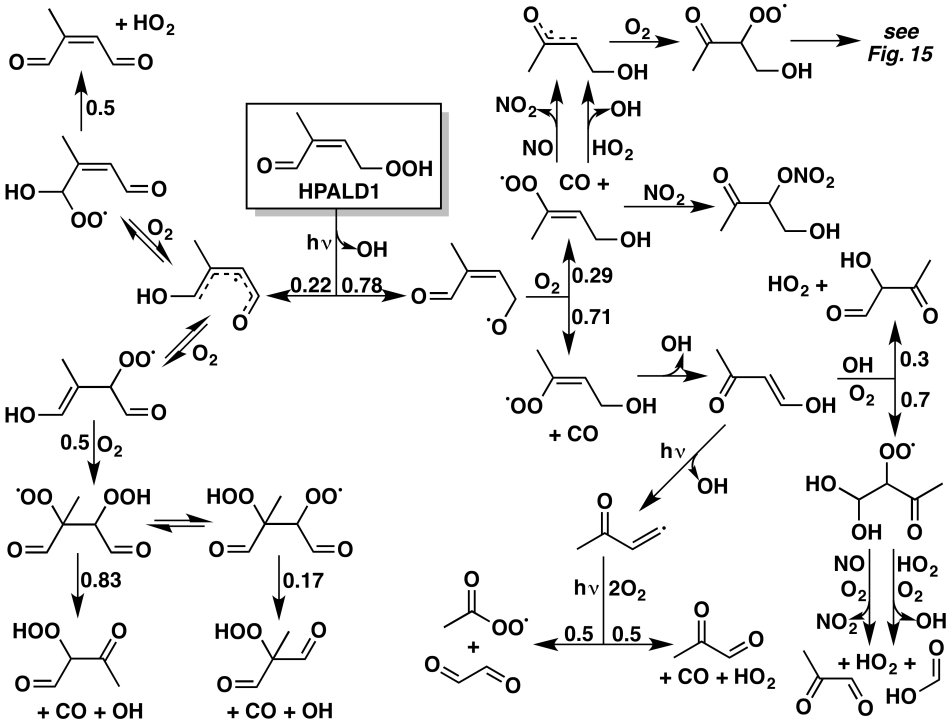

Figure 4.29: Reactions and products following the photolysis of the HPALD1.

arrangements, fragmentation, and further oxygen addition to form CO, OH, and a C_4-hydroperoxy-dicarbonyl (50%). The major product (71%) of the alkoxy radical is a C_4 enol (hydroxy-MVK for HPALD1 and hydroxy-methacrolein for HPALD2), which is coproduced with CO and OH. The minor channel (29%) from the alkoxy radical produces CO and a C_4 vinyl peroxy radical, which can then react with NO or HO_2. Liu *et al.* (2017) point out that another non-traditional but energetically favorable pathway for this peroxy radical is reaction with NO_2 followed by rearrangement to form (3-ONO_2, 4-OH)-MVK (HPALD1) or 2-ONO_2, 3-OH)-MACR (HPALD2). Some subsequent chemistry for the aforementioned products of HPALD photolysis is provided in the figures and the explicit mechanism (see Supporting Information), including the photolysis and reaction with OH of the enol products by extrapolation from Zhou *et al.* (2008), although we caution that these pathways are highly speculative.

Kinetics - reaction with OH: Loss of HPALDs also occurs by reaction with OH, though this is expected to be slower than photodissociation under most conditions (Wolfe *et al.*, 2012). Few direct constraints exist on the overall rate of reaction between OH and HPALD, let alone the rates of the individual reaction pathways.

Peeters and Muller (2010) estimated $k_{OH+HPALD} = 5.2 \times 10^{-11}$ cm^3 molec^{-1} s^{-1}, and Wolfe *et al.* (2012) measured the rate of reaction between OH and a C_6-HPALD to be $k_{OH+HPALD} = (5.1 \pm 1.8) \times 10^{-11}$ cm^3 molec^{-1} s^{-1}. Based on this evidence, we recommend an overall rate coefficient of $k_{OH+HPALD} = 5 \times 10^{-11}$ cm^3 molec^{-1} s^{-1} for both HPALD isomers at 298 K, although we note that this is surprisingly low compared to rate coefficients of similarly structured molecules.

To apportion this recommended rate between the likely reaction pathways, we extrapolate H-abstraction rates from similar molecules, and assign the remaining fraction of the overall rate to OH addition, divided between the C2 and C3 positions based on the 2:1 relative stability of their resulting alkyl radicals. We assign rate coefficients for H-abstraction of the α-carbonyl, α-hydroperoxy, and ROO-H hydrogens to be $k_{H_CO} = 3.8 \times 10^{-12} \times e^{400/T}$, $k_{H-ROOH} = 7.5 \times 10^{-12} \times e^{20/T}$, and $k_{H-OOR} = 2 \times 10^{-12} \times e^{200/T}$ cm^3 molec^{-1} s^{-1} for both HPALD isomers. These are derived, respectively, from H-abstraction rates of methacrolein (with temperature dependence from acetaldehyde), ethanol (increased by 4× due to the hydroperoxy moiety and the allylic stability of the alkyl radical), and ISOPOOH. By subtracting these abstraction rates from the overall rate, we derive OH addition rates at the C2 and C3 positions of $k_{C2} = 1 \times 10^{-12} \times e^{650/T}$ and $k_{C3} = 2 \times 10^{-12} \times e^{650/T}$ cm^3 molec^{-1} s^{-1}, respectively, for both HPALD isomers.

Mechanism - reaction with OH (Figures 4.30 and 4.42): The products of the reactions of HPALDs with OH are even more poorly understood than the rates. Peeters and Muller (2010) predicted that photolabile peroxy-acid-aldehydes (PACALDs) would be a major product, but no PACALDs were detected by Wolfe *et al.* (2012). Without strong experimental or theoretical constraints, we formulate our recommended mechanisms – shown in Figure 4.30 for HPALD1 and Figure 4.42 for HPALD2 – based largely on extrapolation from similar compounds found elsewhere in the isoprene mechanism.

Addition of OH to either HPALD isomer - which accounts for 50% of the OH reaction channels at 298 K - can occur either at the β-hydroperoxy or β-aldehydic positions. Addition at the β-hydroperoxy position is followed by O_2 addition and an intramolecular H-shift, which leads to fragmentation, forming CO, OH, and a C_4-hydroperoxy-hydroxy-carbonyl. Addition at the β-aldehydic position can follow a similar route, fragmenting instead to form CO, HO_2, and a C_4-dihydroperoxycarbonyl, but also enables the fragmentation of the hydroperoxide

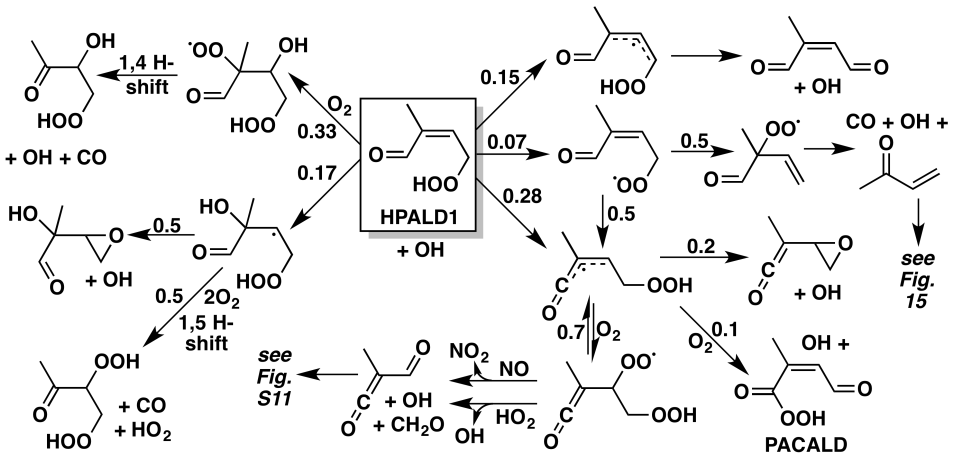

Figure 4.30: Reactions and products following the oxidation of HPALD1 by OH. Yields are for 298 K and 1 atm; the relative contributions of the H-abstraction and OH-addition pathways vary with both temperature, and the branching ratio between epoxide formation and O_2 addition varies with pressure.

followed by cyclization to form an epoxide and OH. We estimate that these two pathways each comprise 50% of the β-aldehydic OH addition mechanism.

Abstraction of the α-aldehydic hydrogen is both the dominant and most complex abstraction pathway, as it forms a vinyllic radical with ketene properties. We estimate that this radical will form an epoxy-ketene in 20% yield from the fragmentation and cyclization of the hydroperoxide; a C_5 PACALD in 10% yield from O_2 addition at the α-aldehydic position, followed by a 1,6 H-shift; and a hydroperoxy-ketene-peroxy radical in 70% yield from O_2 addition at the β-hydroperoxy position, which can then react either with HO_2 or NO and fragment to form CH_2O and a C_4 carbonyl-ketene. In each of the three pathways, OH is recycled as a coproduct of the stable organic products.

Abstraction of the hydroperoxy hydrogen (H-OOR) yields a peroxy radical that can follow two channels: an intramolecular 1,6 H-shift, forming the same vinyllic radical discussed in the preceding paragraph, or loss of O_2 and re-addition at the β-aldehydic position. The latter pathway is likely followed by a rapid 1,4 H-shift, producing CO, OH, and either MVK (from HPALD1) or MACR (from HPALD2). We recommend that each channel represent 50% of the total hydroperoxy H-abstraction. Finally, abstraction of the α-hydroperoxy hydrogen yields an alkyl radical that rapidly fragments to form OH and an unsaturated dialdehyde, which presumably photolyzes readily.

4.7.8 HMHP

HMHP is explicitly produced in our mechanism in contrast to most current atmospheric chemistry models. Thus, we also propose a reduced mechanism for its loss *via* OH chemistry and photolysis. We recommend an OH rate coefficient of $k_{HMHP+OH} = 4.3 \times 10^{-12} \times e^{190/T}$ cm^3 molec^{-1} s^{-1} with equal yields of CH_2O + HO_2 and formic acid + OH (Allen, et al., in prep.). Recommended photolysis rates, based on cross sections from Roehl *et al.* (2007) are also included. Products of the photolysis are 2OH and formaldehyde (Roehl *et al.*, 2007).

4.8 Model

A semi-explicit mechanism for isoprene is included in the Supplement comprising the reactions described in this paper along with rate constants and product distributions. The mechanism is in a format suitable for use with the Kinetic Preprocessor (KPP) tool. Table I.2 in Appendix I gives the names of the species in the mechanism according to our naming convention along with the corresponding MCM name (where available). Terminal species with no subsequent chemistry are shown in bold font, while radical species are shown in italic font.

4.8.1 Naming Scheme

Names of most species are based on precursor names (ISOP for isoprene, MVK for methyl vinyl ketone, MACR for methacrolein, etc.) that have the same carbon structure. Attached to the precursor name are any additional functional groups, each functional group immediately preceded by the carbon number that the functional group is attached to, in order of ascending location (*i.e.* functional groups attached to C1 precede functional groups attached to C2). Carbon numbers are those assigned to isoprene. E or Z or c (*cis*) or t (*trans*) are attached to the end of the name when appropriate to designate stereoisomers. A Stabilized Criegee Intermediate (SCI) is designated by "ci" before the precursor name and “OO” following. An energetically hot radical is designated by a lowercase "x" at the end of the name, and an alkyl radical is denoted by an "r" at the radical position. Any functional groups included within the precursor molecule (*e.g.*, ISOP) are not included within the name. Abbreviations for different functional groups are shown in Table I.1 in Appendix I.

Abbreviations for common species that do not follow this naming convention (such as GLYX for glyoxal) are also given in Table I.2 in Appendix I.

As an example of the naming scheme, an isoprene hydroxyhydroperoxide with

the peroxide group attached to C3 and the alcohol group attached to C4 would be named ISOP3OOH4OH. The double bond is not included in the name because this double bond is present in isoprene (the precursor molecule).

4.8.2 Temperature and pressure dependence of rate coefficients

Most rate coefficients in our mechanism are formulated with the traditional Arrhenius exponential parameterization for temperature dependence ($k = A \times e^{-r/T}$). However, our mechanism also includes four alternative forms of rate coefficients: (1) the 1,6 H-shift isomerizations with an extra tunneling factor, (2) the pressure- and temperature-dependent Troe modification of a Lindemann-Hinshelwood rate expression (Troe, 1983), (3) the pressure-dependent expression for epoxide formation rates formulated by Jacobs *et al.* (2014), and (4) the temperature- and pressure-dependent nitrate yields from RO_2 + NO reactions formulated by Arey *et al.* (2001) (and earlier by Carter and Atkinson (1985) and Carter and Atkinson (1989)), as described in Section 4.2. These parameterizations are described in greater detail below.

The 1,6 H-shift isomerization reactions described in Section 4.3.3.4 are modeled with a strongly negative T-dependent tunneling factor, best expressed as an Arrhenius rate parameterization with an additional exponential term that includes T^{-3} in the argument. We denote these rates with "k_tunneling[A,B,C]" in place of a typical rate coefficient formula, where A, B, and C can then be applied in the following formula:

$$k_{tunneling} = A \times e^{B/T} \times e^{C/T^3} \tag{4.9}$$

The modified Lindemann-Hinshelwood rate coefficient (Troe, 1983) is only applied in two reactions within our mechanism: the formation and decomposition of MPAN. These rates are denoted with "k_troe[A,B,C]", where A, B, and C, respectively, signify k_0, k_∞, and F_c in the equation:

$$k_{troe} = \frac{k_0 \times [M]}{1 + \frac{k_0 \times [M]}{k_\infty}} \times F_c^{(1+[log_{10}(\frac{k_0 \times [M]}{k_\infty})]^2)^{-1}} \tag{4.10}$$

The pressure dependence of epoxide yields can simply be understood as a means of including the O_2 concentration in the rate coefficient to skip a step and remove an intermediate compound from the mechanism. In the full explicit mechanism, OH addition to a double bond forms an alkyl radical, which can then either add O_2 or form an epoxide from an α-hydroperoxy or -nitrooxy group. Thus, the branching ratios

of O_2 addition and epoxide formation are dependent upon the O_2 concentration. Alternatively, the reaction can be written in a single step (OH addition to directly form an epoxide) if the O_2 concentration is included in the rate coefficient, in the form $k = k_0 \times 1/(A \times [O_2] + 1)$. This parameterization allows for the removal of a species from the mechanism (the intermediate alkyl radical), which may benefit models limited by computational capacity, but at the cost of making the rate formulations more complicated. We provide both parameterizations, such that either can be used depending on the priorities and limitations of the modeling platform. The primary explicit mechanism in the Supplement includes the intermediate alkoxy species and their relevant reactions for every epoxide-forming step in the mechanism (including those of ISOPOOH, isoprene hydroxynitrates, and other functionalized nitrates formed from NO_3 chemistry). A separate table is also included in the Supplement with the reactions required for the $[O_2]$-dependent rate coefficient parameterization, as well as a list of reactions to remove from the full mechanism.

Finally, the temperature- and pressure-dependent yields of organic nitrates from reactions of peroxy radicals with NO are described in Section 4.2, and we incorporate these dependences into the rate coefficients of all RO_2 + NO reactions in the explicit and reduced mechanism. We denote the rate coefficients of nitrate-forming reactions with "k_nitrate[X,Y,Z,n]", where X and Y are the preexponential and exponential factors in the Arrhenius equation for the overall reaction rate, Z is the normalization term for the nitrate yield (equal to $A_0(n) \times (1 - \alpha_0)/\alpha_0$ in Equation 4.3, and n is the number of heavy atoms excluding the peroxy moiety. Thus, as in Equation 4.3, the nitrate formation rate coefficient is given by the equation:

$$k_{nitrate} = \left(X \times e^{-Y/T}\right) \times \left(\frac{A(T, [M], n)}{A(T, [M], n) + Z}\right) \tag{4.11}$$

where A refers to the Arey *et al.* (2001) parameterization in Equation 4.4. Similarly, we denote non-nitrate-forming RO_2 + NO reactions with "k_alkoxy[X,Y,Z,n]", where the same parameters are used with only a minor adjustment:

$$k_{alkoxy} = \left(X \times e^{-Y/T}\right) \times \left(\frac{Z}{Z + A(T, [M], n)}\right) \tag{4.12}$$

While this parameterization is significantly more complex than other rate coefficients in the model, the yield dependence on temperature and pressure is necessary to accurately describe radical cycling through organic nitrates in the atmosphere. However, for some applications of the model, the full parameterization may not be necessary; in these cases, we recommend calculating branching ratios at the desired

temperature and pressure before running the simulation, and scaling the Arrhenius parameterization for the rate coefficients by the relative yields of each pathway.

4.8.3 Photolysis rates

Photolysis rates coefficients for photolytic reactions included in the mechanism are the rates calculated when the sun is directly overhead. When input into a box model, this rate can then be scaled with the sunlight intensity at a particular time of day. These rates are multiplied in the mechanism by the variable "SUN" to denote this.

4.9 Supporting Information

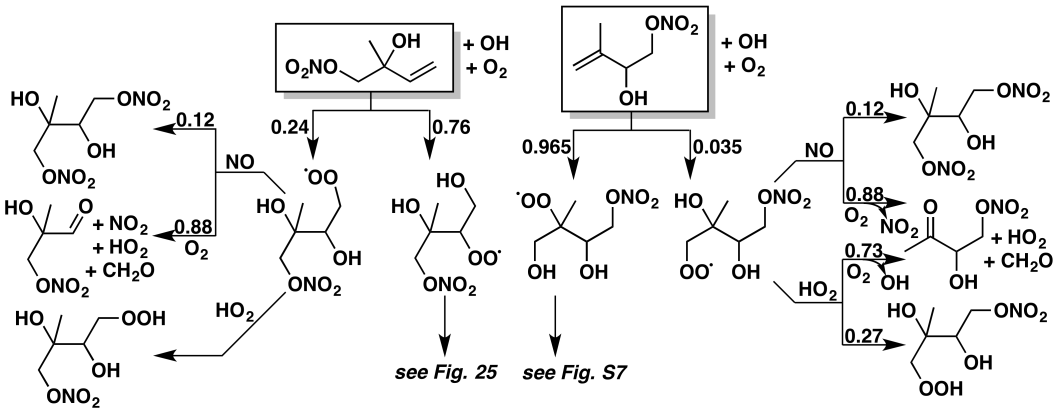

Figure 4.31: Mechanisms of the reactions of OH with (1-ONO_2,2-OH)-IHN and (3-OH,4-ONO_2)-IHN. Yields are for 298 K and 1 atm; in reactions of peroxy radicals with NO, the relative contributions of the nitrate and alkoxy pathways vary with both temperature and pressure. For the reduced mechanism, we combine the β-IHN isomers into a single species, and scale the product yields of its subsequent reactions according to the relative contributions of the isomers. We also combine the various isomers of stable C_5 tetrafunctionalized products.

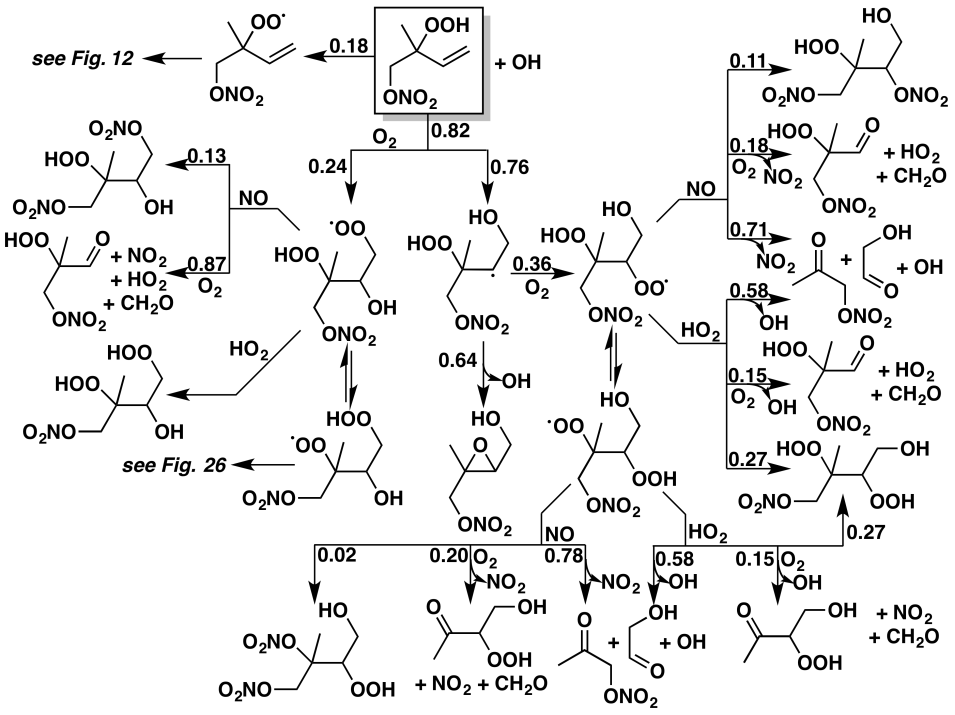

Figure 4.32: Mechanism of the reaction of OH with (1-ONO_2,2-OOH)-IPN. Yields are for 298 K and 1 atm; branching ratios between OH-addition and -abstraction, epoxide formation and O_2 addition, and nitrate and alkoxy formation all vary with temperature and/or pressure. For the reduced mechanism, we combine the β-IPN isomers into a single species, and scale the product yields of its subsequent reactions according to the relative contributions of the isomers. We also combine the various isomers of stable C_5 tetrafunctionalized products.

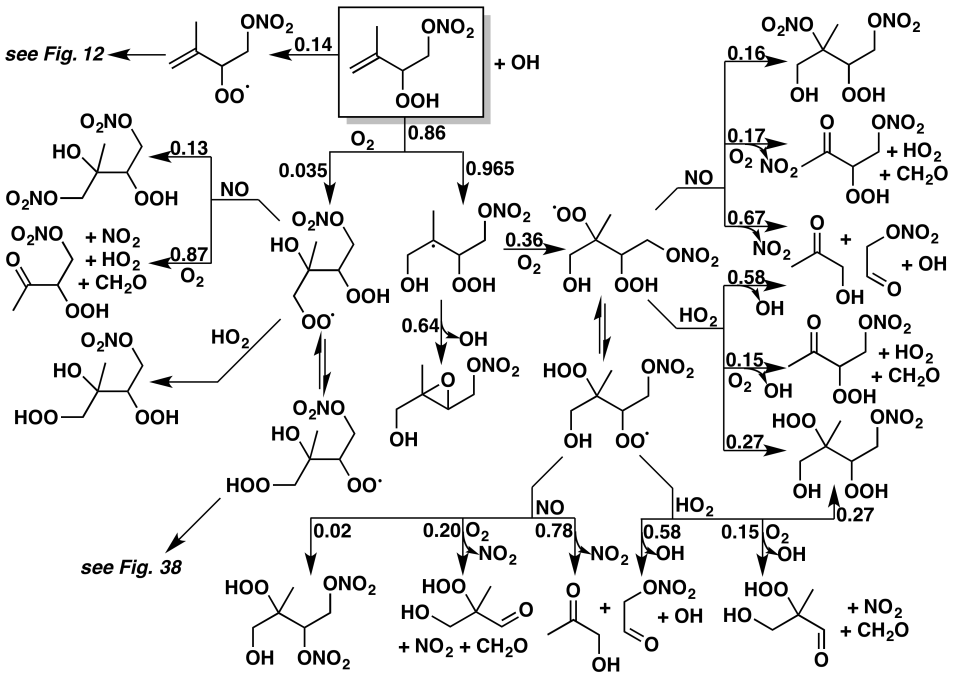

Figure 4.33: Mechanism of the reaction of OH with (3-OOH,4-ONO_2)-IPN. Yields are for 298 K and 1 atm; branching ratios between OH-addition and -abstraction, epoxide formation and O_2 addition, and nitrate and alkoxy formation all vary with temperature and/or pressure. For the reduced mechanism, we combine the β-IPN isomers into a single species, and scale the product yields of its subsequent reactions according to the relative contributions of the isomers. We also combine the various isomers of stable C_5 tetrafunctionalized products.

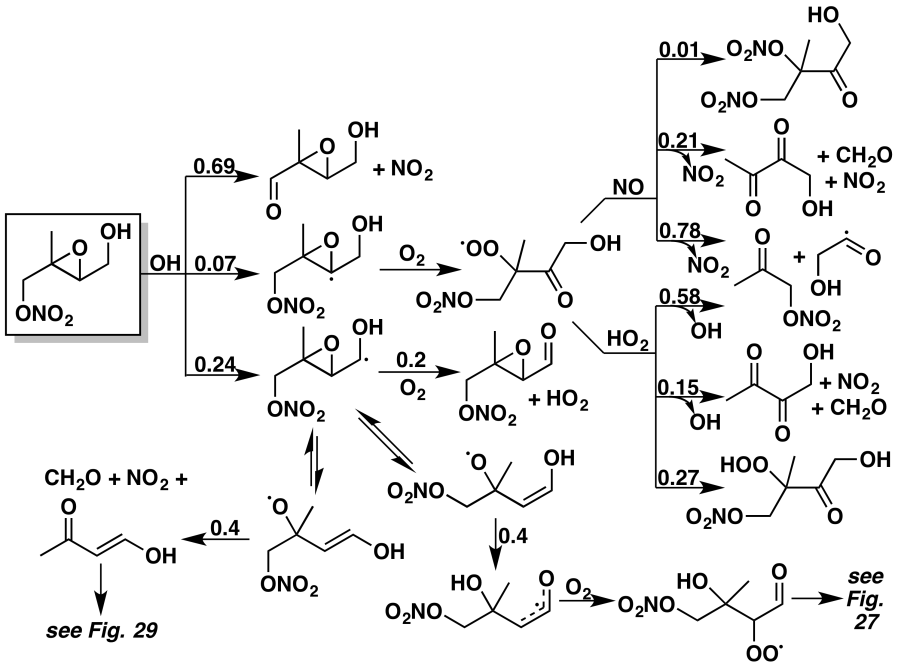

Figure 4.34: Mechanism of the reaction of OH with (1-ONO_2,2,3-O,4-OH)-INHE. The *cis* and *trans* isomers are not treated separately, as they are expected to react identically. Yields are for 298 K and 1 atm; branching ratios between nitrate and alkoxy formation in reactions with NO vary with both temperature and pressure. For both the full and reduced mechanisms, we simplify the INHE and ICN systems by combining some intermediate peroxy radicals and distributing their products according to the relative contributions of the isomers. For the reduced mechanism, we also combine the β-INHE isomers into a single species, and scale their product yields similarly. We further combine the various isomers of stable C_5 tetrafunctionalized products.

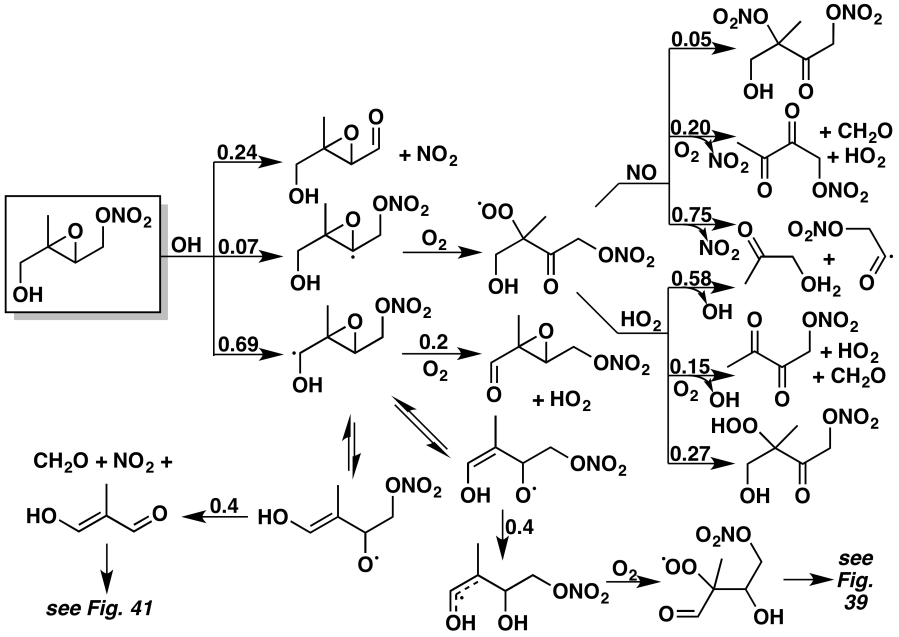

Figure 4.35: Mechanism of the reaction of OH with (1-OH,2,3-O,4-ONO_2)-INHE. The *cis* and *trans* isomers are not treated separately, as they are expected to react identically. Yields are for 298 K and 1 atm; branching ratios between nitrate and alkoxy formation in reactions with NO vary with both temperature and pressure. For both the full and reduced mechanisms, we simplify the INHE and ICN systems by combining some intermediate peroxy radicals and distributing their products according to the relative contributions of the isomers. For the reduced mechanism, we also combine the β-INHE isomers into a single species, and scale their product yields similarly. We further combine the various isomers of stable C_5 tetrafunctionalized products.

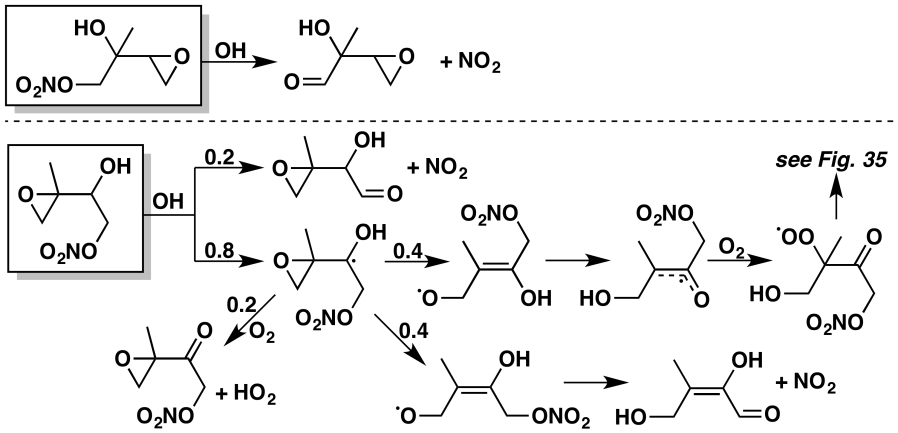

Figure 4.36: Mechanisms of the reactions of OH with (1,2-O,3-OH,4-ONO_2)- and (1-ONO_2,2-OH,3,4-O)-INHE. For both the full and reduced mechanisms, we simplify the INHE and ICN systems by combining some intermediate peroxy radicals and distributing their products according to the relative contributions of the isomers. For the reduced mechanism, we also combine the δ-INHE isomers into a single species, and scale their product yields similarly. We further combine the various isomers of stable C_5 tetrafunctionalized products.

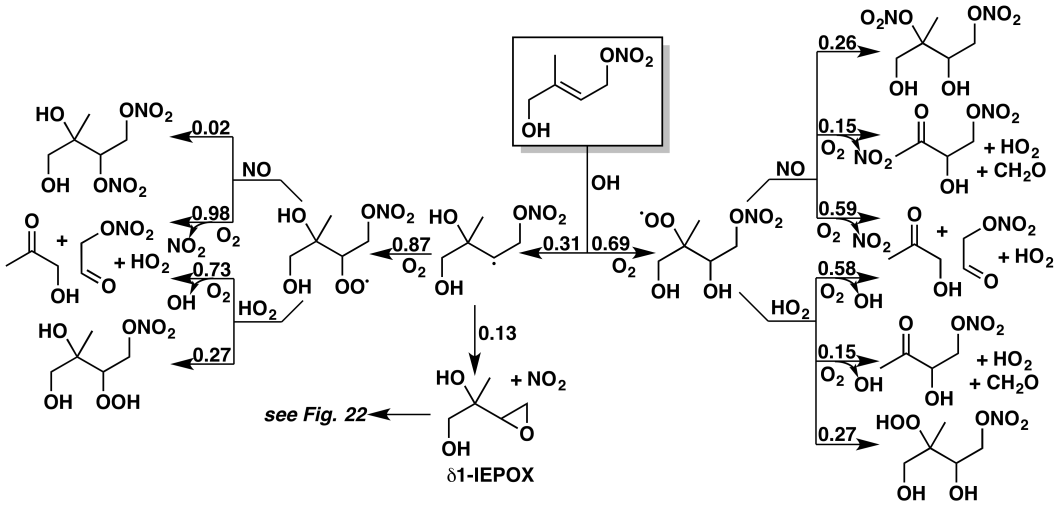

Figure 4.37: Mechanism of the reaction of OH with *E*-(1-OH,4-ONO_2)-IHN. *Z*-(1-OH,4-ONO_2)-IHN is expected to react identically. Yields are for 298 K and 1 atm; in reactions of peroxy radicals with NO, the relative contributions of the nitrate and alkoxy pathways vary with both temperature and pressure, and the branching ratio between IEPOX formation and O_2 addition also varies with pressure. For the reduced mechanism, we combine the δ-IHN isomers into a single species, and scale the product yields of its subsequent reactions according to the relative contributions of the isomers. We also combine the various isomers of stable C_5 tetrafunctionalized products.

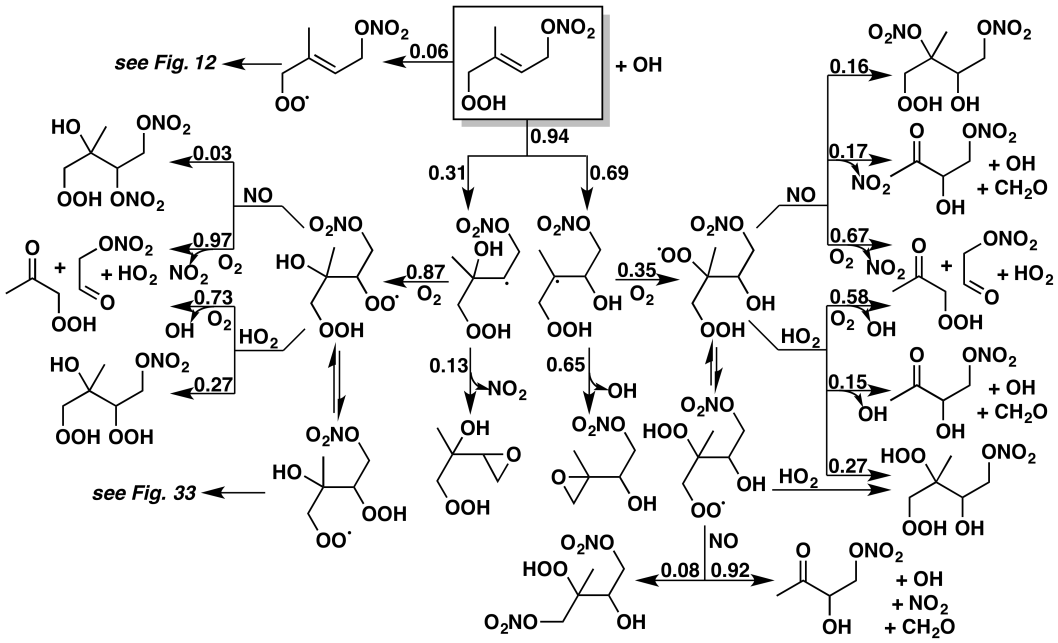

Figure 4.38: Mechanism of the reaction of OH with *E*-(1-OOH,4-ONO_2)-IPN. *Z*-(1-OOH, 4-ONO_2)-IPN is expected to react identically. Yields are for 298 K and 1 atm; branching ratios between OH-addition and -abstraction, epoxide formation and O_2 addition, and nitrate and alkoxy formation all vary with temperature and/or pressure. For the reduced mechanism, we combine the δ-IPN isomers into a single species, and scale the product yields of its subsequent reactions according to the relative contributions of the isomers. We also combine the various isomers of stable C_5 tetrafunctionalized products.

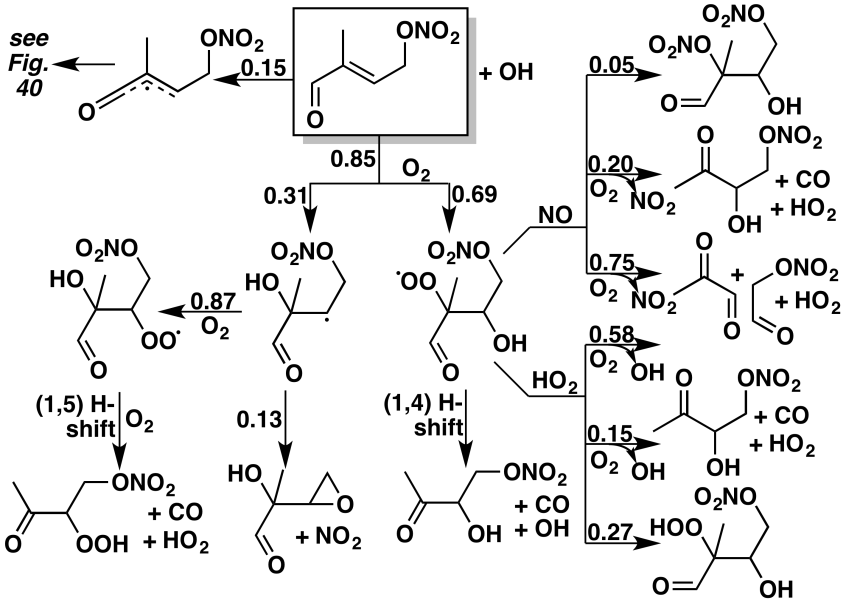

Figure 4.39: Mechanism of the reaction of OH with *E*-(1-CO,4-ONO_2)-ICN. *Z*-(1-CO,4-ONO_2)-ICN is expected to react identically. The terminal radical formed by H-abstraction (upper left) is presumed to add oxygen and react further like the analogous (though not identical) acyl peroxy radical in Figure 13. Yields are for 298 K and 1 atm; branching ratios between OH-addition and -abstraction, epoxide formation and O_2 addition, and nitrate and alkoxy formation all vary with temperature and/or pressure. For the reduced mechanism, we combine the four isomers of peroxy radicals derived from the addition of OH and O_2 to the δ-ICN isomers, and scale the product yields of its subsequent reactions with NO and HO_2 according to the relative contributions of the isomers. We also combine the various isomers of stable C_5 tetrafunctionalized products.

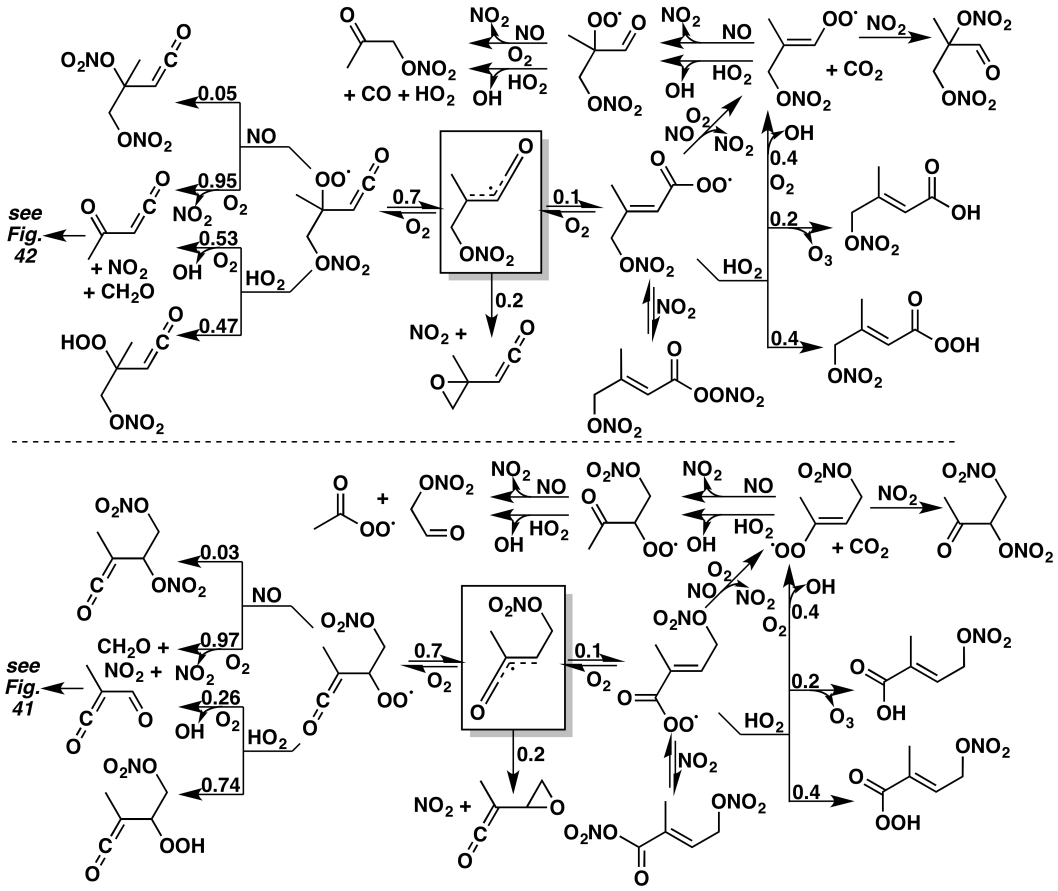

Figure 4.40: Mechanisms following the abstraction of an aldehydic hydrogen from the δ-ICNs that form from the reaction of isoprene with NO_3. Yields are for 298 K and 1 atm; branching ratios between epoxide formation and O_2 addition, as well as nitrate and alkoxy formation, vary with temperature and/or pressure. For the reduced mechanism, we group the ICN isomers together, and simplify the H-abstraction scheme to represent its effects on HO_x and NO_x budgets.

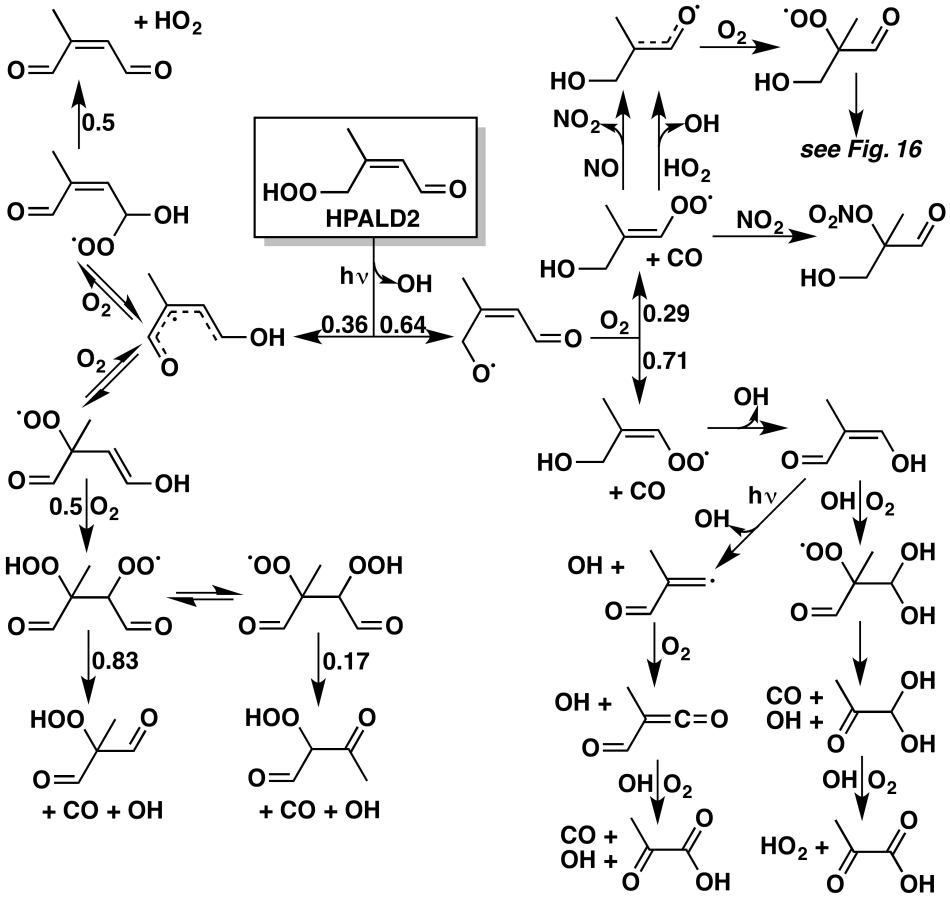

Figure 4.41: Reactions and products following the photolysis of the HPALD2.

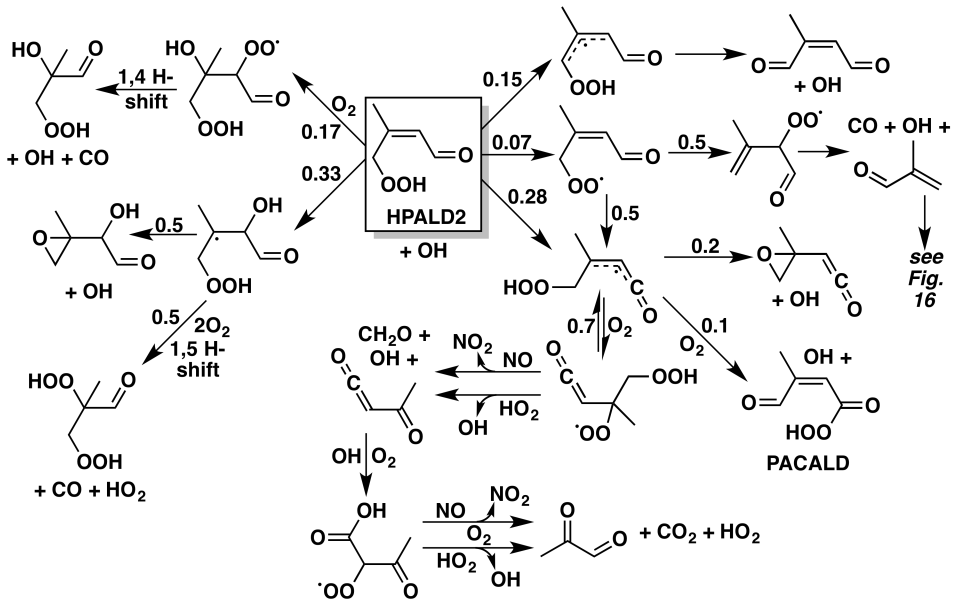

Figure 4.42: Reactions and products following oxidation of HPALD2 by OH. Yields are for 298 K and 1 atm; the relative contributions of the H-abstraction and OH-addition pathways vary with both temperature, and the branching ratio between epoxide formation and O_2 addition varies with pressure.

Chapter 5

ORGANIC AEROSOL FORMATION FROM THE REACTIVE UPTAKE OF ISOPRENE EPOXYDIOLS (IEPOX) ONTO NON-ACIDIFIED INORGANIC SEEDS

Nguyen, T. B., M. M. Coggon, K. H. Bates, X. Zhang, R. H. Schwantes, K. A. Schilling, C. L. Loza, R. C. Flagan, P. O. Wennberg, and J. H. Seinfeld (2014). "Organic aerosol formation from the reactive uptake of isoprene epoxydiols (IEPOX) onto non-acidified inorganic seeds". In: *Atmos. Chem. Phys.* 14, pp. 3497–3510. DOI: 10.5194/acp-14-3497-2014.

Abstract

The reactive partitioning of *cis*- and *trans*-β-IEPOX was investigated on hydrated inorganic seed particles, without the addition of acids. No organic aerosol (OA) formation was observed on dry ammonium sulfate (AS); however, prompt and efficient OA growth was observed for the *cis*- and *trans*-β-IEPOX on AS seeds at liquid water contents of 40–75% of the total particle mass. OA formation from IEPOX is a kinetically limited process, thus the OA growth continues if there is a reservoir of gas-phase IEPOX. There appears to be no differences, within error, in the OA growth or composition attributable to the *cis*/*trans* isomeric structures. Reactive uptake of IEPOX onto hydrated AS seeds with added base (NaOH) also produced high OA loadings, suggesting the pH dependence for OA formation from IEPOX is weak for AS particles. No OA formation, after particle drying, was observed on seed particles where Na^+ was substituted for NH_4^+. The Henry's Law partitioning of IEPOX was measured on NaCl particles (ionic strength ~9 M) to be 3×10^7 M atm^{-1} (-50%/+100%). A small quantity of OA was produced when NH_4^+ was present in the particles, but the chloride (Cl^-) anion was substituted for sulfate (SO_4^{2-}), possibly suggesting differences in nucleophilic strength of the anions. Online time-of-flight aerosol mass spectrometry and offline filter analysis provide evidence of oxygenated hydrocarbons, organosulfates, and amines in the particle organic composition. The results are consistent with weak correlations between IEPOX-derived OA and particle acidity or liquid water observed in field studies, as the chemical system is nucleophile-limited and not limited in water or catalyst activity.

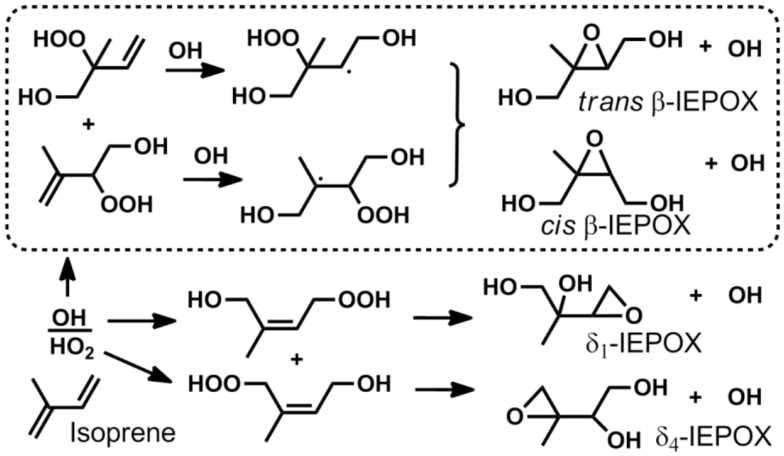

Figure 5.1: Formation of IEPOX isomers from relevant isoprene hydroxy hydroperoxide precursors in the low-NO photooxidation of isoprene. The expected dominant pathway is shown inside the box. The naming convention is based on Paulot *et al.* (2009b).

5.1 Introduction

A significant portion of the organic aerosol (OA) production from isoprene, a non-methane hydrocarbon emitted to the atmosphere in vast amounts, is attributed to the heterogeneous chemistry of isoprene epoxydiols (IEPOX) (Budisulistiorini *et al.*, 2013; Chan *et al.*, 2010b; Froyd *et al.*, 2011; Hatch *et al.*, 2011; McNeill *et al.*, 2012; Pye *et al.*, 2013; Surratt *et al.*, 2010). IEPOX, of which there are four isomeric forms (Fig. 5.1), is a second-generation low nitric oxide (NO) isoprene photooxidation product formed from the OH-oxidation of particular isomers of isoprene hydroxy hydroperoxides (Paulot *et al.*, 2009b). The mechanism for OA production from IEPOX has been proposed as ring-opening of the epoxide group, activated by proton transfer from a strong acid such as sulfuric acid (H_2SO_4), followed by nucleophilic addition of available nucleophiles in the condensed phase, *e.g.* addition of water to produce tetrols, sulfate to produce organosulfates, and so on (Eddingsaas *et al.*, 2010; Minerath *et al.*, 2008; Surratt *et al.*, 2010). This proposed mechanism has been corroborated by chamber investigations of particle acidity effects on OA formation (Lin *et al.*, 2012; Surratt *et al.*, 2007a), wherein dry acidic seeds ($MgSO_4$:$H_2SO_4 \approx 1$:1) prompted strong reactive uptake behavior from epoxides (Paulot *et al.*, 2009b), compared to negligible uptake for dry, non-acidified seeds.

Recent field data suggest that the story might be more complex than described above, as weak correlations between particle acidity and the abundance of IEPOX

particle-phase tracer products were observed in Southeastern USA sites (Budisulistiorini *et al.*, 2013; Lin *et al.*, 2013a). It should be noted that the indirect definition of "particle acidity," which relies on charge balance of cations and anions, have several limitations and may not effectively represent the activity of H^+ in the aqueous phase of particles in some cases (Gregoire, 2013). Nevertheless, from the field observations, Lin *et al.* (2013a) and coworkers proposed that other factors may possibly modulate OA formation from IEPOX in conjunction with particle $[H^+]$. One important distinction between previous chamber investigations, which have all been conducted under dry conditions (relative humidity, RH <5%), and the Southeastern USA location is the prevalence of particle liquid water on the ammonium sulfate seeds. Water is a ubiquitous and abundant component of the atmosphere, therefore the effect of liquid water on the uptake of OA precursors has important implications for much of the globe. The crystalline ammonium sulfate seeds used in dry chamber experiments may not have adequate liquid water for IEPOX to partition into the aqueous phase, nor sufficient H^+, NH_4^+, and SO_4^{2-} activities to promote reactive uptake. Similarly, a particle with a large weight percent of H_2SO_4 may have a sizable liquid water component, even at RH <5%, due to the strong hygroscopicity of H_2SO_4 (Xiong *et al.*, 1998), and the difference in reactive uptake of IEPOX may be due either to the differences in particle liquid water or the particle free acidity. In contrast, high concentrations of liquid water may cause dilution of aqueous ions, *i.e.* changing the acidity or ionic strength, which has been demonstrated to change the effective Henry's Law partitioning coefficient of glyoxal (Kampf *et al.*, 2013). Despite these important interactions, the effect of liquid water on OA formation from IEPOX has not been systematically explored in the laboratory.

We report here the reactive uptake of two isomers of IEPOX, the *cis*- and *trans*-β-IEPOX (Paulot *et al.*, 2009b), which together comprise more than 97% of the isomer distribution (Bates *et al.*, 2014). We synthesized authentic standards and observed the dark OA growth onto non-acidified and hydrated inorganic seeds at several particle liquid water concentrations. In the atmosphere, ammonium ions (NH_4^+) are one of the most abundant components of aerosols and considerable IEPOX-derived OA are observed, even when a dominant portion of the aerosols are charge-balanced, *e.g.* $2 \times [NH_4^+]/[SO_4^{2-}]$ or $[NH_4^+]/[NO_3^-] \approx 1$ (Lin *et al.*, 2013a). The aqueous NH_4^+ may possibly act as a catalyst for OA formation, as has been shown for a number of atmospherically important reactions (Ervens and Volkamer, 2010; Noziere *et al.*, 2009; Sareen *et al.*, 2010; Yu *et al.*, 2011). We study reaction with NH_4^+ as a potential rate-limiting mechanism for the IEPOX reaction. The role of cation and

anion compositions in the seed for OA formation is studied by using ammonium sulfate, ammonium chloride, sodium sulfate, and sodium chloride seeds.

5.2 Materials and Methods

5.2.1 Experimental Procedures

This work utilized a newly constructed 24 m^3 FEP Teflon environmental chamber specifically reserved for low-NO_x applications. The walls have not been in contact with strong acids and the chamber was operated in batch mode. Experiments were performed at room temperature (23-24 °C) and in the dark. Prior to the start of experiments, the chamber was thoroughly flushed with dry, purified air until particle concentrations are <0.01 μg m^{-3}. For humid experiments, water vapor was injected until the desired relative humidity (RH) was achieved in the chamber by flowing dry purified air over a Nafion membrane humidifier (FC200, Permapure LLC), which is kept moist by recirculating 27 °C ultrapurified (18 MΩ) water (Milli-Q, Millipore Corp). Temperature and RH were measured by a Vaisala HMM211 probe, calibrated with saturated salt solutions in the RH range of 11-95%. For RH <11%, the water vapor content was quantified by chemical ionization mass spectrometry (CIMS, Section 5.2.2.1).

Seed particles were injected by atomizing aqueous solutions (0.06 M) of ammonium sulfate ($(NH_4)_2SO_4$, AS), sodium chloride (NaCl), ammonium chloride (NH_4Cl), or sodium sulfate (Na_2SO_4) at 2100 hPa of air into the chamber through a ^{210}Po neutralizer and water trap. All inorganic seeds were injected through a 30 cm custom-built wet-wall denuder kept at 90 °C, such that the seed particles enter the chamber hydrated. Liquid water is expected to evaporate from the seed particles according to the salt's efflorescence behavior (Lee and Hsu, 2000) at the RH of the chamber; *e.g.*, in a dry chamber it is expected that the hydrated particles will enter the chamber fully dried. Particles were allowed to equilibrate until their volume concentrations are stable prior to organic injections.

Two isomers of isoprene epoxydiols (*cis*- and *trans*-β-IEPOX) are synthesized *via* procedures adapted from Zhang *et al.* (2012) and purified with normal-phase column chromatography until the estimated purity based on nuclear magnetic resonance (NMR) of the *cis*- and *trans*-β-IEPOX isomers are 99% and >92%, respectively. Details of the synthesis and NMR spectra are reported in Bates *et al.* (2014). Although the mole fractions of the impurities are low, their high volatility may lead to an over-represented abundance in the gas phase. For the *cis* isomer, we de-

tected experimental interference from the volatile 1,4-dihydroxy-2-methyl-2-butene (a precursor used in the synthesis), comprising ~50% of the vapor phase measured directly above a bulb of IEPOX droplets by CIMS (Section 5.2.2.1). In order to further purify before experiments were conducted, *cis*-β-IEPOX droplets were purged with dry N_2, and combined with 60 °C heating for >8 h until the measured impurity fraction dropped below 2% (Figure 5.9 in the Supporting Information). After the additional purification, IEPOX was injected into the chamber by flowing a 5–8 L min^{-1} stream of dry purified air past several droplets in a clean glass bulb heated to 60 °C for 2-4 h. The mixtures of IEPOX and seed aerosols were allowed to equilibrate for >1 h. Most of the experimental conditions were repeated and were found to be reproducible within 15%. We expect systematic error to dominate over the error of precision in this work.

5.2.2 Analytical Methods

5.2.2.1 Chemical ionization mass Spectrometry (CIMS)

Gas-phase IEPOX was measured with negative-ion chemical ionization mass spectrometry (CIMS) using CF_3O^- as the reagent ion, described in more detail previously (Crounse *et al.*, 2006; Paulot *et al.*, 2009a; St. Clair *et al.*, 2010). The mass analyzer is a Varian triple-quadrupole spectrometer with unit mass resolution. Air is brought from the chamber using a 3 mm inner diameter perfluoroalkoxy (PFA) Teflon line with flow rate of 2.5 L min^{-1}. Of the total chamber flow, a 145 mL min^{-1} analyte flow was sampled orthogonally through a glass critical orifice into the CIMS. The analyte flow was further diluted by a factor of 12 with dry N_2 to minimize the interaction of water vapor from the chamber with the reagent ion in the ion-molecule flow region. The subsequent data analysis corrects for the dilution factor. The operational pressure and temperature were kept at 35.5 hPa and 35 °C, respectively. The CIMS operated in a scanning MS mode (*m/z* 50–250) and tandem MS mode (MSMS). In MSMS mode, collisionally induced dissociation (CID) with 2.6 hPa of N_2 fragments analyte ions into product ions in the second quadrupole, following the ejection of neutral species. The MS cluster ion $C_5H_{10}O_3{\cdot}CF_3O^-$ (*m/z* 203) of IEPOX was used for quantification, due to the higher signal-to-noise (S/N) of this ion compared to MSMS ions. The MSMS product ion $C_5H_9O_3{\cdot}CF_2O^-$ (*m/z* 203 → *m/z* 183), found to be unique to IEPOX in the isoprene OH-oxidation system, was used to differentiate IEPOX from the isobaric isoprene hydroperoxide (ISOPOOH), which has been documented to yield mainly *m/z* 63 and a negligible amount of *m/z* 183 upon CID (Paulot *et al.*, 2009b). ISOPOOH (*m/z* 203 → *m/z* 63)

was not expected, nor observed, during IEPOX injections.

CIMS calibrations of *cis*- and *trans*-β-IEPOX were performed by separately atomizing dilute (1–3 mM) solutions of each isomer with equimolar concentrations of hydroxyacetone, used as an internal standard, into the chamber through a 15 cm PFA Teflon transfer line for a few hours. During synthesis, NMR analysis showed that IEPOX was stable in water solution for many hours if no acid was present, so decay of IEPOX in the atomizer solution was not expected over the course of the calibration experiment. Toluene was used as a tracer to obtain the exact volume of the Teflon bag for each calibration experiment. A measured volume of toluene (6 μL) was injected into a clean glass bulb with a microliter syringe (Hamilton) and quantitatively transferred into the chamber with a 5 L min^{-1} stream of dry purified air. The gas-phase toluene was monitored by commercial gas chromatograph with flame-ionization detector (GC-FID, Hewlett-Packard 6890N) using a calibrated HP-5 column (15 m, 0.53 mm i.d.). The initial chamber temperature was 35 °C, and the temperature was ramped until 45 °C or until no increase of IEPOX signal was observed in the CIMS. The atomized solution was weighed before and after atomization. Each sensitivity determination was repeated at least twice. The sensitivities of the IEPOX isomers were calculated from the ratio of the normalized ion counts (with respect to the reagent ion signal) to the number of atomized moles. Small amounts of nucleated organic aerosols were observed in the chamber from the atomization, as measured by a scanning mobility particle sizer (Section 5.2.2.3) and that volume concentration was subtracted from the theoretical moles of IEPOX (corrections of <1%). Based on their calculated dipole moments and average polarizability, the *cis* isomer was expected to have a sensitivity of ~1.6 times greater than the *trans* isomer (Paulot *et al.*, 2009b), and we found the sensitivity of the *cis* isomer to be a factor of 1.8 greater than the *trans* isomer in the MS mode. The difference between the two ratios is within the error of the sensitivity determination.

Additionally, several mixing ratios of water vapor were introduced into the CIMS ion-molecule region to measure the water dependence of the IEPOX detection. Water vapor was quantified by Fourier-transform infrared spectroscopy (FTIR, Nicolet Magna-IR 560) with a 19 cm pathlength quartz cell. Spectral fitting was performed using the HITRAN spectral database (Rothman *et al.*, 2009) and the nonlinear fitting software NLM4 developed by Griffith (1996). In the low RH range, outside the calibration limit of the membrane RH probe, the CIMS water ions $H_2O{\cdot}^{13}CF_3O^-$ (*m/z* 104) and $(H_2O)_2{\cdot}CF_3O^-$ (*m/z* 121) were used to quantify water vapor concentration

in the chamber after calibration of water vapor with FT-IR. These ions provide excellent sensitivity to water and linearity in the 20–3500 ppm range in the CIMS ion molecule flow region (corresponding to 1–100% RH in the chamber at 24 °C, before CIMS dilution). No water dependence in the detection of the IEPOX ions was observed within the range of water vapor observed by CIMS.

In order to quantify the gas-phase concentrations of IEPOX, the CIMS signal was corrected to account for the RH-dependent wall losses of IEPOX. The interactions of IEPOX with chamber walls have not been previously characterized, although those of its C_4 analog have been reported (Loza *et al.*, 2010). IEPOX wall loss experiments were conducted at RH = 3%, 46%, and 69%, as described in Section 5.2.1, continuously for 5–10 h. Figure 5.10 in the Supporting Information shows that the wall losses of IEPOX on non-acidic walls were negligibly small (~0.4% h^{-1} at RH 69%), within the error of CIMS measurements.

5.2.2.2 Aerosol Mass Spectrometry (AMS)

Online particle composition was measured with a highresolution time-of-flight aerosol mass spectrometer (ToF-AMS, Aerodyne Research Inc.). The ToF-AMS was operated in V mode (R≈2000 at *m/z* 200) and W mode (R≈3000-4000 at *m/z* 200). Prior to experiments, the ToF-AMS ionization efficiency was calibrated using size-selected 350 nm ammonium nitrate particles. The ToF-AMS monitored the content of ammonium (NH_4^+), sulfate (SO_4^{2-}) and other nonrefractory ions throughout the course of the experiment. The ammonium to sulfate ratio did not change over the course of the experiment. Gas interferences and elemental ratios were calculated using the fragmentation tables developed by Allan *et al.* (2004) and Aiken *et al.* (2008). Data were analyzed in IGOR Pro 6.31 (WaveMetrics, Inc.) using the SQUIRREL v 1.51H and PIKA v 1.10H analysis toolkits. Total concentration of organics (μg m^{-3}) was calculated by summing the nitrate-equivalent masses of each high-resolution ion correlated with the organic fraction from the V-mode data.

Particles were sampled through a 130 cm Nafion membrane diffusion drier (MD-110, Permapure LLC) to avoid flow obstructions from wet particles over time, at a flow rate of 0.084 L min^{-1}. It is expected that drying the particles may introduce particle or organic line losses in the drier tube and change the particle bounce characteristics on the AMS vaporizer plate. These perturbations may be corrected by applying a collection-efficiency (CE) factor. It was demonstrated that organic aerosol particles with higher water content have very low bounce probability,

which corresponds to a CE of unity (Docherty *et al.*, 2013; Matthew *et al.*, 2008). Comparatively, dry particles have much lower CE (~0.25 for pure, dry AS) due to the high bounce rate. The CE of IEPOX-derived organic aerosol-coated particles was calculated by measuring the mass concentrations of organics, sulfate, and ammonium of the wet particles without a drier, wherein CE was assumed to be unity and line losses assumed to be negligible, and comparing with measurements made through a drier. We observe a CE of 0.75 for all conditions in this work, which is consistent with the collection efficiency of organic aerosols measured previously (Docherty *et al.*, 2013). Further, it is expected that drying particles, relevant to the hydration/evaporation cycles of aerosols in nature, may lead to enhanced interactions between organic and inorganic compounds (De Haan *et al.*, 2011; Nguyen *et al.*, 2012), irreversibly forming OA.

5.2.2.3 Particle Size and Number Concentration

Particle size and number concentrations were measured with a scanning mobility particle sizer (SMPS), comprised of a custom-built differential mobility analyzer (DMA) coupled to a commercial butanol-based condensation particle counter (CPC, TSI Inc.). The SMPS particle size measurement was calibrated with polystyrene latex (PSL) spheres. The particles entering the chamber have a static polydisperse distribution, with peak dry particle diameter distributions in the range of 50–100 nm. The sample air flow was not dried in humid experiments. Particle mass concentrations were corrected for RH- and size-dependent wall losses. The mass concentration of particles typically ranged from 65–90 μg m^{-3} for all experiments, using a particle density of 1.2 g cm^{-3}.

For AS-based experiments, the particle liquid water content was calculated based on the size-dependent hygroscopicity of AS (Biskos *et al.*, 2006; Hu *et al.*, 2010). For each particle diameter bin measured by SMPS, a theoretical dry diameter was calculated based on size-dependent literature growth factor data at the RH of the experiment. The difference in the wet (measured) and dry (calculated) integrated area of the mass distribution yielded the liquid water concentration in g m^{-3}. Similarly, the percent of liquid water content is calculated as % LWC = 100% $\times$ (V_{wet}–V_{dry})/V_{wet}, using the predicted wet and dry diameters.

Particle wall loss characterizations were performed for AS seeds at RH = 3%, 20%, 50%, and 80% prior to the start of the experimental series to correctly quantify the mass concentrations of particles as a function of time. It was assumed that the

loss rates of AS were representative for particles of different composition. Seed aerosols were atomized into the dry or humid chambers in the dark, allowed to stabilize, and particle size and number concentrations were measured for >12 h. The particle correction method that accounts for wall loss has been discussed in detail previously (Loza *et al.*, 2012).

5.2.2.4 Filter Collection and Analysis

Offline OA composition analysis was performed by ultrahigh performance liquid chromatography time-of-flight electrospray ionization mass spectrometry (UPLC/ESI-ToFMS). Aerosol samples were collected onto Teflon membrane filters (Millipore, 1 μm pore), pulled at a 20 L min^{-1} flow through an activated charcoal denuder to remove the volatile and semivolatile components. Each filter was extracted with methanol (Fisher, Optima grade, ≥99.9%) by ultrasonication for 15 min in a 20 mL scintillation vial. The filtered extracts were blown dry under a gentle stream of ultra-highpurity N_2. The residue was reconstituted with 150 μL of 50:50 v/v acetonitrile (Fisher Optima grade, ≥99.9%) and water (Milli-Q).

Extracts were analyzed by a Waters Xevo G2-S UPLC/ESI-ToF-MS equipped with an Acquity CSH C_{18} column (1.7 μm, 2.1×100 mm). The solvents used for gradient elution were acetonitrile (Fisher Optima grade, ≥99.9%) and water with a 0.1% formic acid spike (solvent "A"). The flow rate was held at 0.5 mL min^{-1}. Accurate mass correction was completed by a lock spray of leucine enkephalin (0.61 ng μL^{-1} in 50:50 v/v acetonitrile / water with 0.1% formic acid). The ESI source was operated in negative mode, where most analytes are ionized by deprotonation and measured as [M-H]$^-$. Ionic molecular formulas were determined from accurate masses (mass resolution of 60,000 at *m/z* 400) using the elemental composition tool in Mass Lynx. Control filters (no particles) and laboratory controls (seeds only) were analyzed in the same manner.

5.3 Results and Discussion

5.3.1 Reactive Uptake of *cis*- and *trans*-β-IEPOX onto Ammonium Sulfate Seeds

5.3.1.1 Liquid Water Content of Seeds

Figure 5.2 shows the time profile for the organic aerosol (OA) growth corresponding to reactive uptake of the *trans*-β-IEPOX onto ammonium sulfate (AS) seeds at two RH conditions, dry (LWC ~0%) and RH 57% (LWC ~55%). The

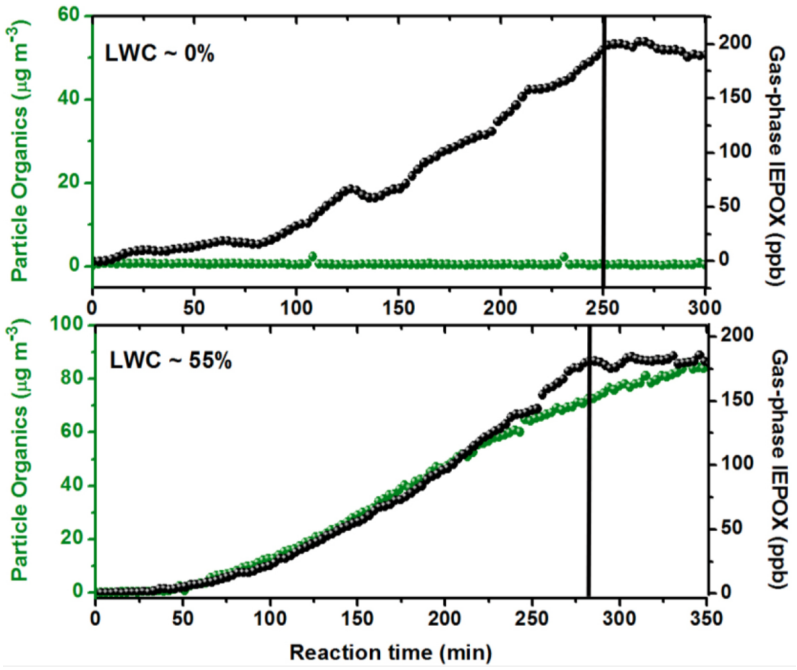

Figure 5.2: Typical uptake experiment results as a function of time, shown for the *trans* isomer, at dry (top) and humid (bottom) conditions with the corresponding percent of liquid water content (LWC). The solid black line indicates when IEPOX injection stopped and the mixture was allowed to equilibrate. Double y axes correspond to traces of the same color.

traces shown in Figure 5.2 are representative of uptake behavior for both isomers on the experimental timescale. For RH conditions above the ammonium sulfate (AS) efflorescence point tested in this work (E_{RH} ~35%; Biskos *et al.*, 2006), prompt and efficient OA growth onto AS seeds was observed for both IEPOX isomers. No OA growth was observed when the AS seeds were dry, in good agreement with other reports (Lin *et al.*, 2012; Surratt *et al.*, 2010).

The OA growth from IEPOX did not halt after the end of the gas-phase injection period (Figure 5.2, solid black line), even after periods of >2 h (Figure 5.11 in the Supporting Information, top panel). This behavior is indicative of a non-equilibrium process, as the addition of nucleophiles is not reversible after the rate-limiting step of IEPOX activation (Eddingsaas *et al.*, 2010). The formation of low-volatility compounds should continue as long as a reservoir of gas-phase IEPOX is available. The series of expected reactions leading to the formation of ring-opening products (ROP) is shown below, illustrated using a general proton donor (AH) and nucleophile (Nu).

$$\text{IEPOX}_{(g)} \rightleftarrows \text{IEPOX}_{(aq)},\ K_H \qquad \text{(R1)}$$

$IEPOX_{(aq)} + AH \rightleftarrows IEPOX\text{-}H^+ + A_{-H}$, k_{AH} (R2)

$IEPOX\text{-}H^+ + Nu \rightarrow ROP\text{-}H^+$, k_{Nu} (R3)

$ROP\text{-}H^+ + A_{-H} \rightarrow ROP + AH$, $k_{neutral}$ (R4)

For a solution with low AH and Nu activity, the equilibrium accommodation of IEPOX into the aqueous phase, described by the Henry's Law coefficient of IEPOX (K_H), can be measured in isolation. Henry's Law may not be an appropriate description of the IEPOX reactive uptake experiments performed on the liquid water of suspended aerosols, as the aerosol water layers represent highly non-ideal solutions and the OA formation is kinetically limited. The OA formation mechanism may include contributions from reactions other than Reactions R1–R4. To a first-order approximation, total OA mass formed from gas-phase reactive uptake of IEPOX will be a function of aqueous IEPOX concentration, nucleophile activity, and catalyst activity.

For the sake of comparison between experiments, it is useful to have a metric that includes the ratio of OA formed to gas-phase IEPOX injected and accounts for the variability in the size and number of injected seeds between experiments, which is reflected by the calculated aerosol water at different RH. We define here a reactive partitioning coefficient ($\Phi_{OA/IEPOX}$), calculated similarly to an effective Henry's Law coefficient, and thus having the same units (Seinfeld and Pandis, 2006):

$$\Phi_{OA/IEPOX} = (C_{OA}/C_{IEPOX})/[10^{-6} \cdot R \cdot T \cdot P_{LWC}] \tag{5.1}$$

where (C_{OA}/C_{IEPOX}) is the mass concentration ratio of the IEPOX-derived organic aerosol (dried), measured by ToF-AMS, and the gas-phase IEPOX, measured by negative-ion CIMS, P_{LWC} is the liquid water content of the inorganic aerosols prior to IEPOX introduction (g m^{-3}), R is the ideal gas constant (atm L mol^{-1} K^{-1}), T is the temperature (K), and 10^{-6} is a conversion factor (m^3 cm^{-3}). $\Phi_{OA/IEPOX}$ includes the contribution from Henry's Law equilibrium partitioning of IEPOX (Reaction R1), and thus is an upper limit for the effective Henry's Law constant.

We observe that $\Phi_{OA/IEPOX}$ was not time-dependent when both IEPOX and OA were increasing, as the ratio (C_{OA}/C_{IEPOX}) stabilized when OA grew in response to gasphase IEPOX (Figure 5.11 in the Supporting Information) but increased after IEPOX injection stopped. The stabilized ratio is used for $\Phi_{OA/IEPOX}$ calculations to compare between experiments. P_{LWC} did not have a significant time dependence due to a stable particle volume distribution before IEPOX gas-phase injections. The uncertainties in the accuracy of the $\Phi_{OA/IEPOX}$ and K_H measurements were estimated to be -50% and +100%, compounded from the uncertainties in the calculated

CIMS sensitivities, liquid water fraction, AMS organic mass determinations, and other measurements.

A summary of $\Phi_{OA/IEPOX}$ and other values is given in Table 5.1 for all AS-based uptake experiments. Figure 5.3 shows $\Phi_{OA/IEPOX}$, as a function of particle liquid water, for the *cis*- and *trans*-β-IEPOX uptake onto hydrated AS. A trend of decreasing $\Phi_{OA/IEPOX}$ with increasing LWC was reproducibly observed, despite the uncertainty range in the $\Phi_{OA/IEPOX}$ determinations. The suppression of $\Phi_{OA/IEPOX}$ as a function of added water is likely due to dilution. For example, high aerosol sulfate concentrations may cause a "salting-in" effect for IEPOX, or other water-soluble organic compounds (Kampf *et al.*, 2013), which is inversely proportional to water content. Higher water may also reduce the $[H^+]$, although the dependence of the reaction on catalyst concentrations is not expected to be high. Additionally, higher P_{LWC} dilutes the aqueous IEPOX and nucleophile concentrations in the aerosol liquid water, which reduce the rate of the chemical reaction as these species are direct reagents. The dilution effect from increasing the pure water fraction at a fixed ion content (moles of NH_4^+ and SO_4^{2-}) is in contrast to a modeled increase in OA mass in areas with high "anthropogenic water", in other words, mixtures of water-soluble compounds found in urban regions (Carlton and Turpin, 2013). In the atmosphere, the partitioning of anthropogenic gases like NH_3 and SO_2 will simultaneously impact aqueous acidity and inorganic concentration and thus may lead to enhanced OA formation in areas with higher P_{LWC}.

5.3.1.2 Particle Acidity

As the decrease of $\Phi_{OA/IEPOX}$ with increasing liquid water content may be due to more than one factor, an experiment was carried out to isolate the effect of pH. In experiment 9 (Table 5.1), the AS solution was neutralized with a strong base (NaOH) until the atomizer solution reached pH = 7. Solutions of AS without additives had pH ~5.5 before atomization because, although no strong acid was present, H^+ is expected to be present in small quantities based on the dissociation equilibria of inorganics, such as the bisulfate/sulfate dissociation, and dissolution of CO_2. An enhancement in the acidity of the particle may result from a smaller volume of water in the particle and/or through loss of NH_3 upon atomization. In the case of a fully hydrated AS particle, the pH in the particle is predicted to be pH ~4 using the E-AIM Model (Clegg *et al.*, 1998), and modeled pH values in the particle for all AS-based experiments are shown in Table 5.1. As the pH values of the particles in this work are

expt #	IEPOX isomer	seed composition	RH (%)	particle pH[a]	seed (μg m^{-3})	P_{LWC} (g m^{-3})	C_{OA}/C_{IEPOX}	$\Phi_{OA/IEPOX}$ (M atm^{-1})
1	*cis*	$(NH_4)_2SO_4$	3	-	70	$<1\times10^{-6}$	5.04×10^{-4}	-
2	*cis*	$(NH_4)_2SO_4$	42	3.67	91	3.74×10^{-5}	0.102	1.15×10^{8}
3	*cis*	$(NH_4)_2SO_4$	50	3.74	92	4.79×10^{-5}	0.118	1.01×10^{8}
4	*cis*	$(NH_4)_2SO_4$	86	3.90	81	5.68×10^{-5}	0.179	4.00×10^{7}
5	*trans*	$(NH_4)_2SO_4$	2	-	65	$<1\times10^{-6}$	4.74×10^{-4}	-
6	*trans*	$(NH_4)_2SO_4$	39	3.65	82	3.44×10^{-5}	0.090	1.06×10^{8}
7	*trans*	$(NH_4)_2SO_4$	57	3.77	89	4.64×10^{-5}	0.095	8.44×10^{7}
8	*trans*	$(NH_4)_2SO_4$	81	3.88	88	6.14×10^{-5}	0.115	7.66×10^{7}
9	*trans*	$(NH_4)_2SO_4$+NaOH, pH=7	70	~5.5	84	5.33×10^{-5}	0.090	6.89×10^{7}
N/A[b]	*cis*	$MgSO_4$+H_2SO_4 (1:1)	<5	~-10	48	1.62×10^{-5} [c]	0.058	1.47×10^{8}

[a] Modeled pH using E-AIM and AIOMFAC models (the value from Lin *et al.* (2012) is $a_{molality}$-based pH), see text (Section 5.3.1.2).

[b] Mean results from Lin *et al.* (2012)

[c] Based on hygroscopicity of H_2SO_4 at RH 5%, assumed growth factor 1.15 (Xiong *et al.*, 1998).

Table 5.1: Summary of results from representative reactive uptake experiments onto ammonium sulfate seeds. Mean results from Lin *et al.* (2012) are shown for comparison.

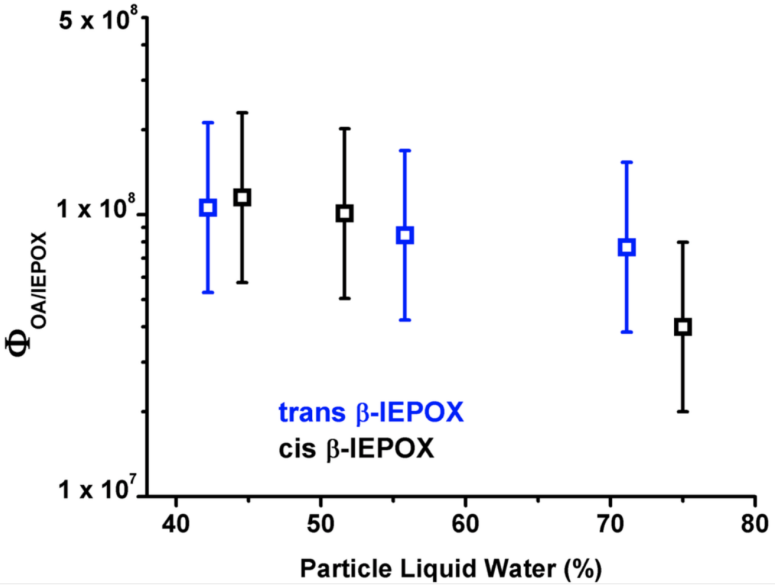

Figure 5.3: Reactive partitioning coefficients ($\Phi_{OA/IEPOX}$) during the gas-phase IEPOX injection for the *trans* and *cis* isomers as a function of particle liquid water concentration. Error bars indicate experimental uncertainty as described in the text.

derived using inorganic models, the values obtained may include any uncertainties inherent in the models, including uncertainties in the gas/particle partitioning of NH_3, hygroscopicity of salts, and/or acid dissociation equilibria. When the RH is below the deliquescence point of AS, the pH was estimated by calculating a concentration factor from the P_{LWC} at the lower RH. It is expected that atomization will also lead to slightly lower pH for the base-neutralized atomizer solution, so the particle may have pH <7. However, adding NaOH above neutralization to counter this effect may induce side reactions such as base-catalyzed epoxide opening and OH- nucleophilic addition (Solomons and Fryhle, 2004). NaOH is not explicitly treated in the E-AIM and AIOMFAC inorganic models (Zuend *et al.*, 2008); therefore, it was assumed that atomization of the AS + NaOH solution may lead to, at most, the same enhancement factor that occurred for the pH of the pure AS solutions.

Figure 5.4 shows that $\Phi_{OA/IEPOX}$ for the *trans*-β-IEPOX + AS system decreases slightly as pH is increased, reaching a plateau above pH ~4. We note that any perceived change is within the error of the measurement; however, it is clear that the trend of $\Phi_{OA/IEPOX}$ with pH is minor. These results differ from those of Eddingsaas *et al.* (2010), who observed a linear increase of epoxide reaction rate with H^+ activity. Eddingsaas *et al.* (2010) used H_2SO_4/Na_2SO_4 solutions, and thus the differences in observations may be entirely due to the high NH_4^+ activity in the

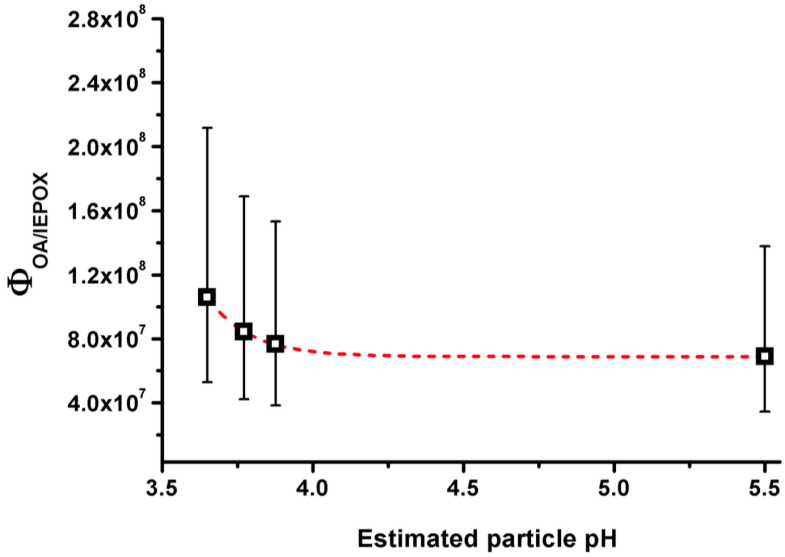

Figure 5.4: $\Phi_{OA/IEPOX}$ for the *trans*-β-IEPOX isomer as a function of modeled particle pH.

AS particles employed in this work. The data suggest that when $[H^+]$ is small, NH_4^+ may activate reactions leading to OA formation, similarly to its catalytic activity toward glyoxal (Noziere *et al.*, 2009), methylglyoxal (Sareen *et al.*, 2010), and other carbonyls (Bones *et al.*, 2010; Nguyen *et al.*, 2013). Interestingly, pH >4 is the range where NH_4^+ catalysis is most efficient. This is demonstrated by a stable reactivity of the NH_4^+ -catalyzed reaction to generate brown carbon from limonene SOA at pH 4–9, but a sharp decline of reactivity below pH 4 (Nguyen *et al.*, 2012). As the H^+ and NH_4^+ ions are reactive toward organics in low-moderate and moderate-high pH ranges, respectively, the resulting pH dependence may appear to be weak in AS-containing seeds. The dual reactivities of H^+ and NH_4^+ toward IEPOX is expected to be important in nature, as NH_4^+-based seeds are abundant.

In comparison, the $MgSO_4$:H_2SO_4 particles at RH <5% in the work of Lin *et al.* (2012) are strongly acidic. These particles are predicted to have a non-negligible amount of water due to the large hygroscopicity of H_2SO_4 – and indeed, acidity in particles is not a useful concept if water is not present. At RH = 0–5%, pure H_2SO_4 particles have a growth factor of 1.1–1.2 (Xiong *et al.*, 1998). Assuming a growth factor of 1.15, and taking into consideration the inorganic seed mass concentration, we calculated P_{LWC} for the mean results in Lin *et al.* (2012), shown in Table 5.1. The AIOMFAC Model (Zuend *et al.*, 2011, 2008) was used to estimate the pH based on the molal activity of H^+ in the $MgSO_4$:H_2SO_4 (1:1) particle. The calculated pH

is ~ -10 and the corresponding mean $\Phi_{OA/IEPOX}$ is ~1.5×10^8 M atm^{-1} for *cis* β-IEPOX (the *trans* isomer was not studied). $\Phi_{OA/IEPOX}$ for the acidic $MgSO_4$ seeds is slightly higher than, but within the error of, the $\Phi_{OA/IEPOX}$ values for non-acidified AS seeds when a small amount of water is present (RH ~40%). This comparison is meant to be qualitative and subject to uncertainty because the experiments were not performed under the same conditions. Nevertheless, the comparison shows that a solution of high H^+ activity and a solution of high NH_4^+ activity may both lead to a relatively similar reactive uptake coefficient. As $[NH_4^+] \gg [H^+]$ in the particles in this work, a similar $\Phi_{OA/IEPOX}$ would also suggest that $k_{NH_4^+} \ll k_{H^+}$ if the observed rate coefficient for Reaction R2 is defined as $k_{obs} = k_{AH} \cdot [AH]$. Eddingsaas *et al.* (2010) estimated $k_{H^+} \approx 5 \times 10^{-2}$ M^{-1} s^{-1} and (Cole-Filipiak *et al.*, 2010) determined $k_{H^+} = 3.6 \times 10^{-2}$ M^{-1} s^{-1} for IEPOX.

5.3.2 Molecular Picture of OA Formation from IEPOX

5.3.2.1 Cation and Anion Substitutions

To further investigate the role of NH_4^+ in IEPOX ring-opening reactions at near-neutral conditions, NH_4^+ was replaced by a cation that cannot act as a proton donor (Na^+). As isomer structure appears to be unimportant for uptake, only the *trans* isomer was used for this portion of the study. Further, many nucleophiles present in the atmosphere are known to add to the protonated epoxide to give the β-hydroxy ring-opening product, for example: H_2O (Solomons and Fryhle, 2004), SO_4^{2-} ions (Cavdar and Saracoglu, 2009), NH_3 or amines (Clayden *et al.*, 2001), and halide ions (Clayden *et al.*, 2001). Thus, SO_4^{2-} was substituted by Cl^- to study the anion (or nucleophile) effect.

Hydrated particles of AS ($(NH_4)_2SO_4$), sodium sulfate (Na_2SO_4), ammonium chloride (NH_4Cl), and sodium chloride (NaCl) were introduced into the chamber in separate experiments, followed by the introduction of *trans*-β-IEPOX. The mixtures were allowed to equilibrate for 3.5–6 h. The RH range for these reactions is 60–85%, chosen at a point well above their respective efflorescence RH (Martin, 2000), so that each seed would contain a considerable fraction of liquid water. The particle size distributions for each seed type were polydisperse and unimodal, with hydrated mobility diameters in the range of 15–600 nm and with 60–120 nm peak diameters. It is expected that the hydrated particles were spherical. The size-dependent hygroscopicities of AS and NaCl are well-studied; however, the calculations of liquid water content for other seed types are subject to error based

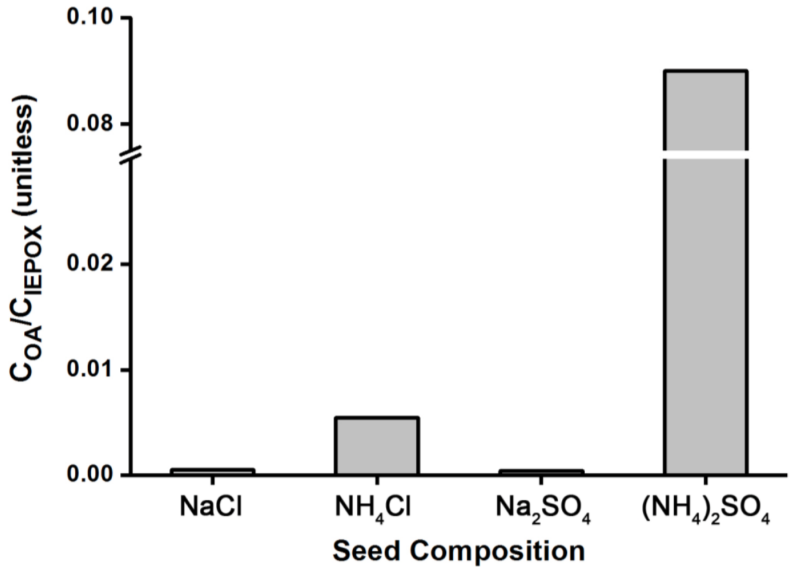

Figure 5.5: Ratio of organic aerosol produced to gas-phase *trans*-β-IEPOX injected for seeds of various compositions (RH 60–85%).

on the method we described due to limited literature data. Therefore, we opt to present results based only on the COA/CIEPOX for the comparison of inorganic seed compositions.

OA formation after particle drying, as detected by ToF-AMS, is negligible for both sodium salts (NaCl and Na_2SO_4). The OA mass did not grow in response to the addition of IEPOX for the Na^+-based particles (Figure 5.12 in the Supporting Information). Figure 5.5 shows the average stabilized ratios of OA formed with respect to *trans*-β-IEPOX injected for the four inorganic salts used in this work. The atomizer solution pH for Na^+-based seeds was also ~5.5, a typical pH for a water solution in equilibrium with CO_2 (Reuss, 1977). The large difference in reactivity of IEPOX on Na_2SO_4 vs. $(NH_4)_2SO_4$ seeds may be attributed primarily to NH_4^+ activity, although there will be some differences in $[H^+]$ for the NH_4^+-based and Na^+-based seeds due to the slight dissociation of $NH_4^+ \rightleftarrows NH_3 + H^+$. Additionally, in light of the weak pH dependence for AS solutions, it appears likely that NH_4^+ activity is an important factor in suppressing OA formation on Na_2SO_4 seed particles. The results show that equilibrium partitioning of IEPOX, *i.e.* any condensed-phase mass formed from unreacted IEPOX, onto salty solutions is not competitive with reactive partitioning for OA formation.

For the ammonium salts, NH_4Cl produced an order of magnitude lower mean C_{OA}/C_{IEPOX} ratio than $(NH_4)_2SO_4$, after an approximate 2 h delay (Figure 5.12 in

the Supporting Information). The modeled pH, using E-AIM, for both ammonium salt systems is similar (pH ~4-4.5), and thus, the difference in reactivity may be attributed to the nucleophilic activity of Cl^- compared to SO_4^{2-}. Interestingly, Minerath *et al.* (2009) showed that acid-catalyzed ring-opening products of an epoxide with Cl^- may be more efficient than SO_4^{2-}. In that study, sulfuric acid was added to the NaCl + epoxide aqueous solution, which provide sulfate and bisulfate ions to the solution. Therefore, the results may not be directly comparable to this work. If Cl^- can be a good nucleophile in aqueous solutions of IEPOX when coupled with NH_4^+ catalysis, we may expect to observe organochloride products. There was no evidence of organochloride-derived accurate mass fragments in ToF-AMS data for the NH_4Cl reactive uptake organics. Further, gas-phase organochlorides were not observed by the CIMS. It is possible that organochlorides are produced but are easily hydrolyzed in the aerosol liquid water due to the relatively good leaving group ability of Cl^-, *i.e.* that the hydrolysis behavior of organochlorides is more similar to that of tertiary organonitrates than that of organosulfates (Darer *et al.*, 2011). It is also possible that organochlorides are preferentially evaporated in the diffusion drier because they might be more volatile than organosulfates or polyols. In both situations, but more so the latter, the total organic mass from the NH_4Cl experiments would be underestimated by ToF-AMS. Although we did not quantify tetrols and other polyols in this work, it is expected that they are present in substantial quantities because they are the thermodynamically preferred products in the epoxide ring-opening reactions.

5.3.2.2 Henry's Law Constant

Although ToF-AMS did not observe OA formation for experiments using sodium salts (NaCl and Na_2SO_4) after particle drying, the wall-loss-corrected SMPS data (not dried) showed a minor and stable change in particle volume upon injection of IEPOX into the chamber with hydrated NaCl or Na_2SO_4 seeds (Figure 5.13a in the Supporting Information, shown for NaCl). It is likely that the dissolved but unreacted IEPOX was removed from the condensed phase upon particle drying, which would lead to no observed OA mass in the ToF-AMS data throughout the duration of the experiment. The reversibility of OA formation on the hydrated seeds indicates equilibrium-partitioning of IEPOX into the aerosol liquid water. The ratio of dissolved OA to injected IEPOX (Figure 5.13b in the Supporting Information) reached a steady-state value at the end of the IEPOX injection period. Because NH_4^+ is not present, and $[H^+]$ is not expected to be considerable in the aqueous phase,

Reactions R2 and R4 are unimportant for this system. Further, in experiments using NaCl seeds, where the nucleophilicity of the solution is weaker, we are able to neglect the contribution of Reaction R3, thereby isolating the equilibrium partitioning of IEPOX (Reaction R1).

We estimate the Henry's Law coefficient (K_H) for the equilibrium partitioning of IEPOX into a briny liquid (NaCl ~9 M ionic strength) representative of atmospheric aerosol to be 3×10^7 (-50%/+100%) M atm^{-1}. The K_H in a solution of NaCl may be different than the value in pure water, due to complex aqueous interactions of Cl^- and Na^+ with water-soluble organics. As an example, the Henry's Law constant for glyoxal was measured to be $K_H = (4.19 \pm 0.87) \times 10^5$ M atm^{-1} in pure water, 1.90×10^6 M atm^{-1} in a 0.05 M NaCl solution, and 8.50×10^5 M atm^{-1} in a 4.0 M NaCl solution at 298 K (Ip *et al.*, 2009). Ip *et al.* (2009) attributed the increase in K_H for NaCl solutions at low ionic strengths (compared to water) to hydrogen bonding interactions of Cl^- and OH groups and the decrease at high ionic strength to a "salting-out" effect. The K_H value for IEPOX has not been experimentally determined in the past; however, the range of K_H has been estimated using the HENRYWIN model (EPA, 2008) by several studies. For example, Eddingsaas *et al.* (2010) estimated $K_H = 2.7 \times 10^6$ M atm^{-1} using a bond contribution method, and $K_H = 2.9 \times 10^{10}$ M atm^{-1} using a group contribution method in version 4.0 of the model. The empirical K_H value reported here is within range of both estimations – closer to the bond contribution method estimate. These results provide a critical constraint in the partitioning coefficient, significantly decreasing the error associated with using K_H in a quantitative manner (from four orders of magnitude to a factor of two).

5.3.2.3 Organic Composition

A full analysis of the OA composition is outside the scope of this work. The reader is referred elsewhere for a discussion of the formation of oxygenated hydrocarbons, for example, tetrols and alkenetriols and organosulfates in the aqueous reaction of IEPOX catalyzed by acidic sulfate (Eddingsaas *et al.*, 2010; Surratt *et al.*, 2010). Although strong acid is absent in the systems studied in this work, we observe many similarities in the IEPOX-derived OA composition compared to the existing chamber and field results. For example, organosulfate products are abundant when hydrated AS seeds are used. The dominant ion observed in negative ion mode UPLC/ESI-ToF-MS for AS uptake was $C_5H_{11}SO_7^-$ (Figure 5.14 in the Supporting Information),

corresponding to the ring-opening trihydroxy organosulfate product of IEPOX. Derivatization was not performed in this work to detect tetrols. Organosulfate fragments were also observed in ToF-AMS (CSO family of fragments, not shown).

IEPOX-derived OA formed under near-neutral conditions in this work have ToF-AMS spectra similar to those of OA observed in the field. The suggested tracers for IEPOX-derived organics, *m/z* 53 (mostly $C_4H_5^+$) and *m/z* 82 (mostly $C_5H_6O^+$) (Budisulistiorini *et al.*, 2013; Lin *et al.*, 2012; Robinson *et al.*, 2011), were observed in uptake experiments using both isomers. These mass fragments were proposed to originate from the electron-impact (EI) ionization of furan-derived molecules that were suggested to be formed from the acid-catalyzed rearrangement of IEPOX (Lin *et al.*, 2013a). Although mass fragments produced by EI may have multiple sources, in the pure system used in this study, *m/z* 82 was found to be a good tracer for IEPOX-derived OA. Figure 5.6 shows the difference between mass spectra at the end of the experiment and those at the time period prior to organic injection, corresponding to the organic fraction of the OA formed from the uptake of both isomers. The spectral ion distributions are very similar to each other and *m/z* 53 and *m/z* 82 constituted a substantial fraction of the total ion intensity. The ion abundance of tracer fragments increased in accordance with the growth of OA mass (Figure 5.15 in the Supporting Information). As *m/z* 53 ($C_4H_5^+$) is a reduced fragment, it is also linked to hydrocarbon-like organics in chamber studies and may not be unique to IEPOX-derived OA. *m/z* 53 was observed in all experiments, including those that used Na^+-based seeds. However, *m/z* 82 is abundant only when NH_4^+-based seeds were used, supporting the suggestion that it can be formed though the EI fragmentation of an IEPOX-derived ring-opening product in ToF-AMS.

A unique aspect of the NH_4^+-catalyzed ring-opening reaction of IEPOX is the minor possibility of nucleophilic addition by NH_3, instead of reforming NH_4^+ after neutralizing the addition of another nucleophile. Figure 5.7 shows ion peaks for organic fragments containing C-N bonds observed in ToF-AMS data from the uptake of *trans*-β-IEPOX onto AS vs. Na_2SO_4 seeds. The same C-N fragments were observed in *cis*-β-IEPOX experiments using AS. These C-N fragments were not initially present in the AS seeds, and grow linearly following the introduction of IEPOX. Individual C-N fragments correlate well (Figure 5.16 in the Supporting Information, linear fit R^2 = 0.69–0.88) with the *m/z* 82 IEPOX-derived OA tracer fragment ($C_5H_6O^+$), suggesting that the reaction of IEPOX is responsible for the presence of these amines. Comparatively, C-N type fragments were negligible or

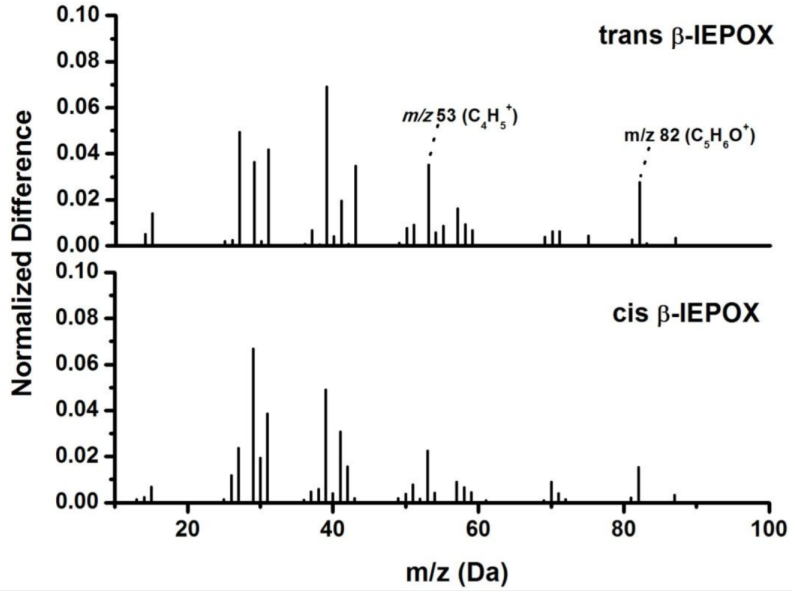

Figure 5.6: ToF-AMS normalized difference spectra (composition at peak OA growth minus composition during seed injection), showing the organic composition of the OA produced by reactive uptake of the *trans* and *cis* isomers. Select nominal mass ions previously suggested to be IEPOX-derived OA tracers are labeled.

non-existent in uptake experiments from Na^+-based seeds. The identification of amines is tentative; however, to the best of our knowledge, this is the first suggestion of amine formation from IEPOX. As organic nitrogen compounds also give rise to non-nitrogenous mass fragments in ToF-AMS, it is not possible to estimate a mass concentration for the amines in this work. However, the CN family of fragments comprised approximately 10% of the $C_5H_6O^+$ signal, an indication that amine formation may not be negligible. The formation of organic nitrogen from the IEPOX + NH_4^+ reaction has important implications in the atmosphere as the ring-opening reaction of epoxides with amines should be more efficient than with NH_3 (Azizi and Saidi, 2005). Further investigations may provide more insight on the source of organic nitrogen from the atmospheric reactions of epoxides.

5.4 Summary and Atmospheric Implications

It was demonstrated here that the conversion of IEPOX to organic aerosol (OA) depends on the coupled relationship between the inorganic composition and (P_{LWC}). The inorganic composition governs the catalyst and nucleophile characteristics, and P_{LWC} provides a reaction medium for the partitioning of IEPOX and controls the activities of all the aqueous components. The weak dependence on pH and the strong dependence on nucleophile activity and particle liquid water suggest that the

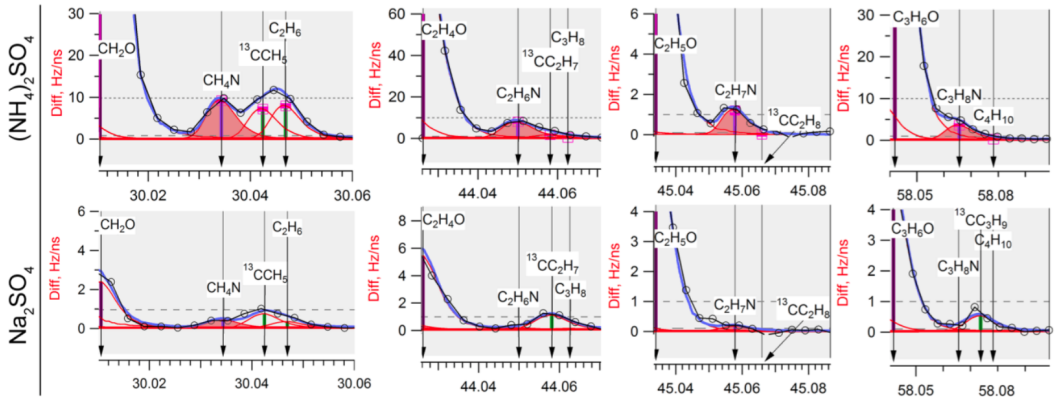

Figure 5.7: ToF-AMS difference spectra (open minus closed chopper) showing organic nitrogen (amine) fragments from the reactive uptake of *trans*-β-IEPOX onto AS vs. Na_2SO_4 seeds. Similar fragments were observed for *cis*-β-IEPOX using NH_4^+-based seeds and not observed in Na^+-based seeds.

IEPOX reactions in hydrated ammonium salts are nucleophile-limited, rather than catalyst-limited.

We showed that the equilibrium partitioning (Reaction R1) and the rate-limiting step of IEPOX activation (Reaction R2) do not proceed in the absence of liquid water; however, increasing the pure water content does not necessarily increase the reactive partitioning coefficient due to various dilution effects. When the inorganic particle is hydrated, the OA conversion is then determined by the catalyst and nucleophile activities. The rate of OA formation incorporates both Reactions R2 and R3, as illustrated by the cation and anion substitution case studies. In the hydrated Na_2SO_4 experiment, there was high activity of a relatively good nucleophile, but a good catalyst was absent. Therefore, the formation of OA, *i.e.*, the ring-opening product, was not observed because the equilibrium of Reaction R2 favors $IEPOX_{(aq)}$. The aqueous IEPOX mass that partitioned from the gas phase (K_H) onto the hydrated Na^+-based seeds was removed from the condensed phase following the evaporation of water. In the hydrated NH_4Cl experiment, there was high activity of a good catalyst but possibly a poorer nucleophile than sulfate ion. A smaller quantity of OA formed because the rate of Reaction R3 was slow, which was further supported by the observed 2 h delay in OA formation. Only when P_{LWC}, NH_4^+ activity, and SO_4^{2-} activity are all significant, as in the case of hydrated $(NH_4)_2SO_4$ seeds, is the OA formation efficient and prompt. The OA mass formed from IEPOX uptake onto 1:1 $MgSO_4$:H_2SO_4 seeds (RH <5%) from previous studies may also be explained in terms of these conditions, as P_{LWC} (~30%), catalyst (H^+) activity and nucleophile

(SO_4^{2-}) activity were all sufficiently high in the particle.

In the atmosphere, relationships of water-soluble OA with P_{LWC} may be different and more difficult to interpret compared to laboratory studies because an increase in the P_{LWC} of atmospheric particles is often accompanied by the copartitioning of water-soluble organic and inorganic compounds. The abundance of water-soluble organic compounds in the Southeast USA has been observed to be proportional to the liquid water contents of particles (Carlton and Turpin, 2013; Hennigan *et al.*, 2009; Hennigan *et al.*, 2008). In contrast, a weak correlation of modeled P_{LWC} with the abundance of IEPOX-derived OA tracers has also been observed, in the same geographical region (Budisulistiorini *et al.*, 2013). The results of this work may not be directly comparable to field observations, however, they do not necessarily conflict. Particles may experience multiple hydration/evaporation cycles in the atmosphere, and the majority of particles likely contain liquid water at some point during their long lifetimes. The OA produced from IEPOX reactive uptake onto AS is irreversible (not removed from particle drying in this work), and depending on whether it had been sampled in the atmosphere before or after an evaporation cycle, the apparent correlation of IEPOX-derived OA with P_{LWC} would be different. Consequently, systematic studies in the laboratory are important for elucidating observations from the field.

Our results offer an alternate explanation to the abundance of IEPOX-derived OA tracers when the free H^+ acidity in particles is modeled to be low (Lin *et al.*, 2013a). It has been suggested that the reason for the weak correlation with acidity is the reaction of an acidic seed particle with IEPOX to form organosulfates, which affects the particle acidity over time (Budisulistiorini *et al.*, 2013). We show here that particle acidity does not appear to be important for the IEPOX + AS system if particle liquid water is present, in that highly acidic seeds and weakly acidic AS seeds both have high potential to form OA from IEPOX reactive partitioning. The apparent correlation between OA mass from IEPOX and P_{LWC}, ammonium or acidity may be weak whenever water or catalyst concentrations are not limited; thus, in regions with high AS loading and RH, there should be a higher correlation with sulfate. This result would suggest that the OA formation process from IEPOX is insensitive to changes in the degree of neutralization of the particles in many AS dominated areas, including the Southeast USA. The typical $[NH_4^+]$ is several orders of magnitude larger than $[H^+]$ in atmospheric particles, making it very likely to activate the IEPOX ring-opening reaction. Current models consider only H^+ and

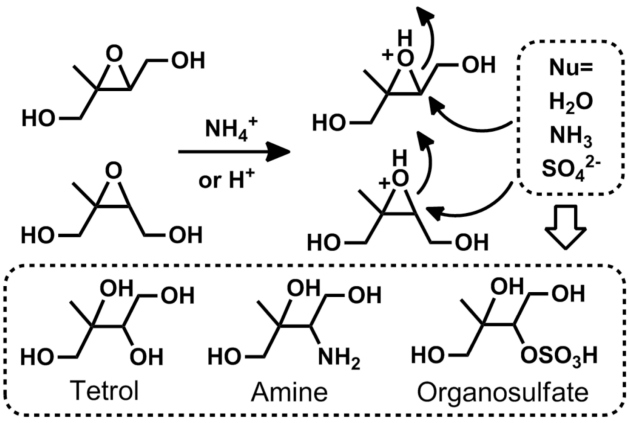

Figure 5.8: Addition of weak nucleophiles in the aqueous NH_4^+- and H^+-catalyzed ring opening of IEPOX to form low-volatility organic compounds.

HSO_4^- activity (McNeill *et al.*, 2012; Pye *et al.*, 2013), likely owing to the lack of experimental data describing the NH_4^+-initiated reaction with IEPOX, for example, kinetic coefficients like $k_{NH_4^+}$. Future experimental and modeling studies should consider the NH_4^+ activity of a particle, in addition to the H^+ and HSO_4^- activity, for a more-accurate representation of OA formation from IEPOX.

An updated reaction mechanism appears in Figure 5.8, in which NH_4^+ and H^+ are shown to donate a proton to the epoxide oxygen, followed by nucleophilic addition to form oxygenated hydrocarbons, ammonia (or amines), and organosulfates. The ability of NH_4^+ to catalyze a nucleophilic addition reaction is not unprecedented, as NH_4^+ can protonate aldehydes to facilitate nucleophilic addition (Noziere *et al.*, 2009), and the high ring strain of an epoxide should provide an even greater thermodynamic motivation for the reaction. Indeed, due to the strain of epoxides, ring opening is chemically facile and may be promoted by a wide range of aqueous chemical species and conditions common in atmospheric aerosols, in addition to H^+ and NH_4^+. For example, Lewis acids such as iron (Fe^{3+}) (Iranpoor and Salehi, 1994) and copper (Cu^{2+}) (Muzart and Riahi, 1992) ions may be even stronger catalysts. Furthermore, the reaction may proceed with no added catalyst, for example, in the presence of amines (Azizi and Saidi, 2005) or even hot water (60 °C) (Wang *et al.*, 2008b). The nucleophiles for these reactions may be water, amines or ammonia, thiols, sulfate ions, nitrate ion, halide ions, carboxylic acids, and alcohols (Clayden *et al.*, 2001; Iranpoor *et al.*, 1996; Jacobsen *et al.*, 1997). Because of the diversity in the composition of atmospheric aerosols and fog/cloud droplets (Graedel and Weschler, 1981), the distribution of IEPOX-derived products in nature may be more

complex and varied than currently believed.

5.5 Supporting Information

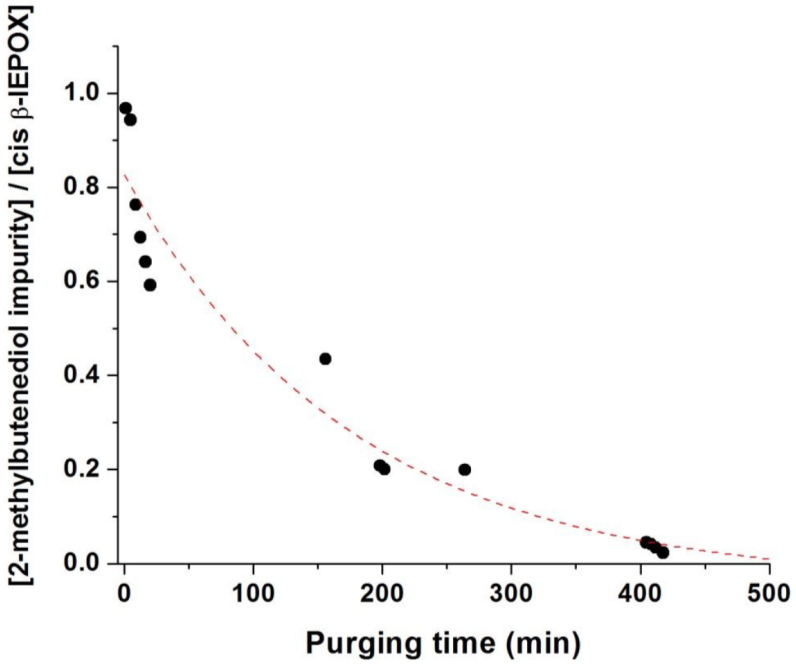

Figure 5.9: Purging the volatile 1,4-dihydroxy-2-methyl-2-butene impurity from *cis*-β-IEPOX droplets with dry N_2 over a heated bulb (60 °C) for several hours. The fraction of impurity to IEPOX, as measured by CIMS, was allowed to decay to <2% before use for experiments.

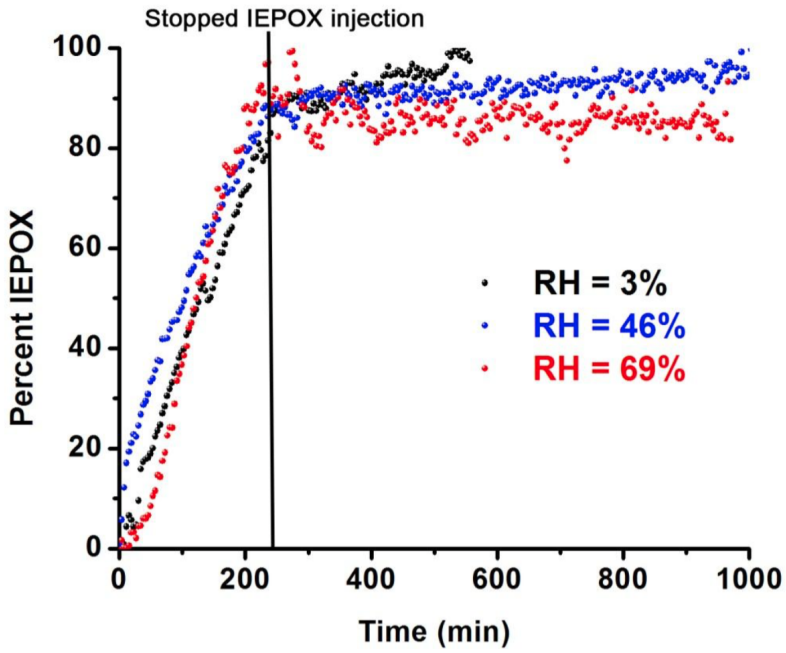

Figure 5.10: Vapor wall loss of *cis*-β-IEPOX to the chamber walls.

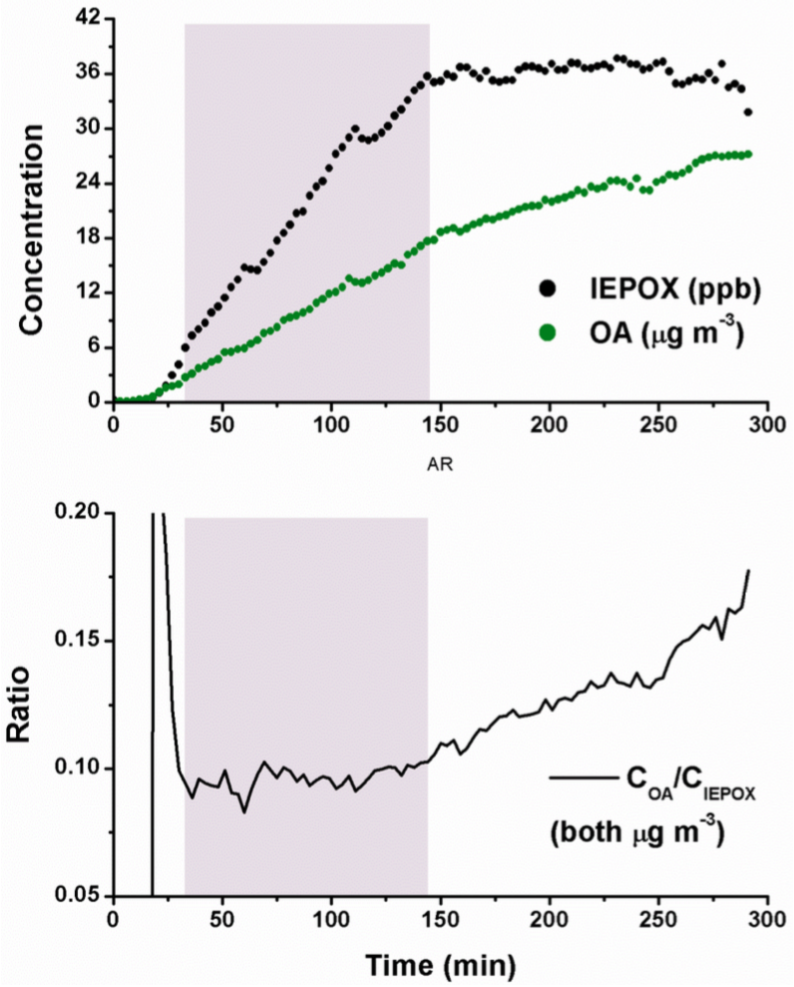

Figure 5.11: Top panel: OA grows in response to IEPOX gas-phase injection, but continues to grow after halting IEPOX injection, an indication that the system is not at equilibrium. Bottom panel: the ratio of the OA to gas-phase IEPOX starts off noisy and levels out as IEPOX is injected. The ratio continues to grow as gas-phase IEPOX stabilizes and OA continues to grow. The shaded panel where the ratio levels out is used in $\Phi_{OA/IEPOX}$ calculations.

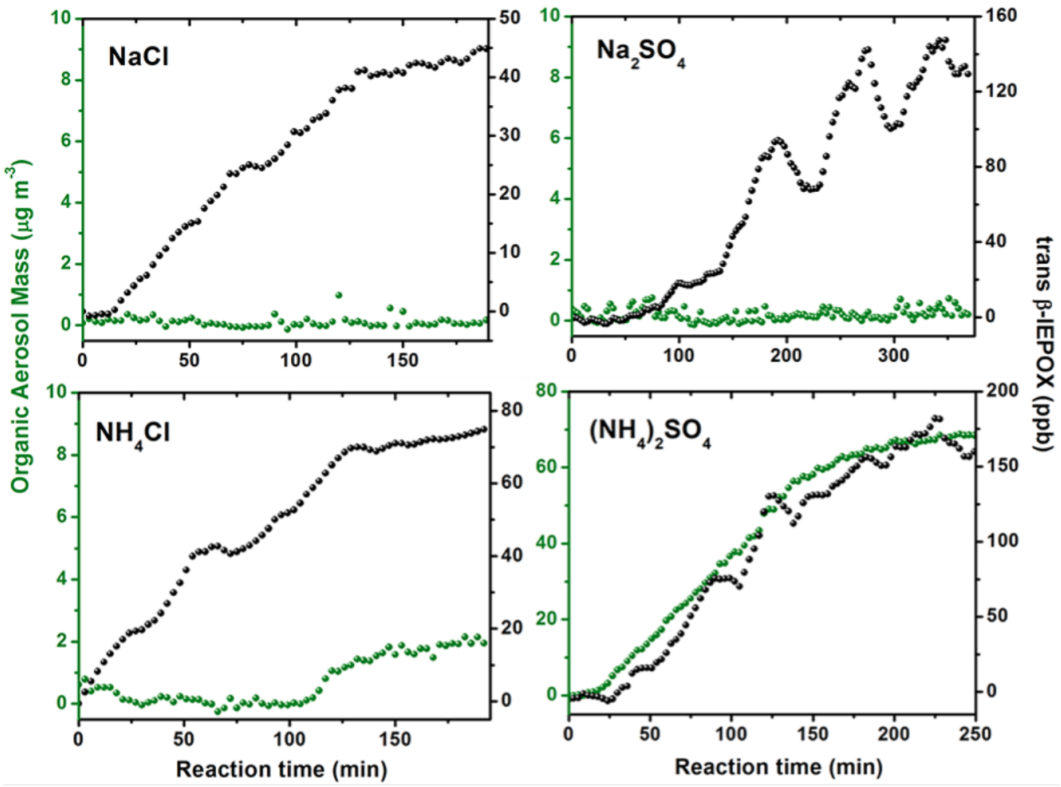

Figure 5.12: Typical behavior of the ratio of organic aerosol formed (detected by AMS) to gas-phase IEPOX (detected by CIMS) during the course of an experiment.

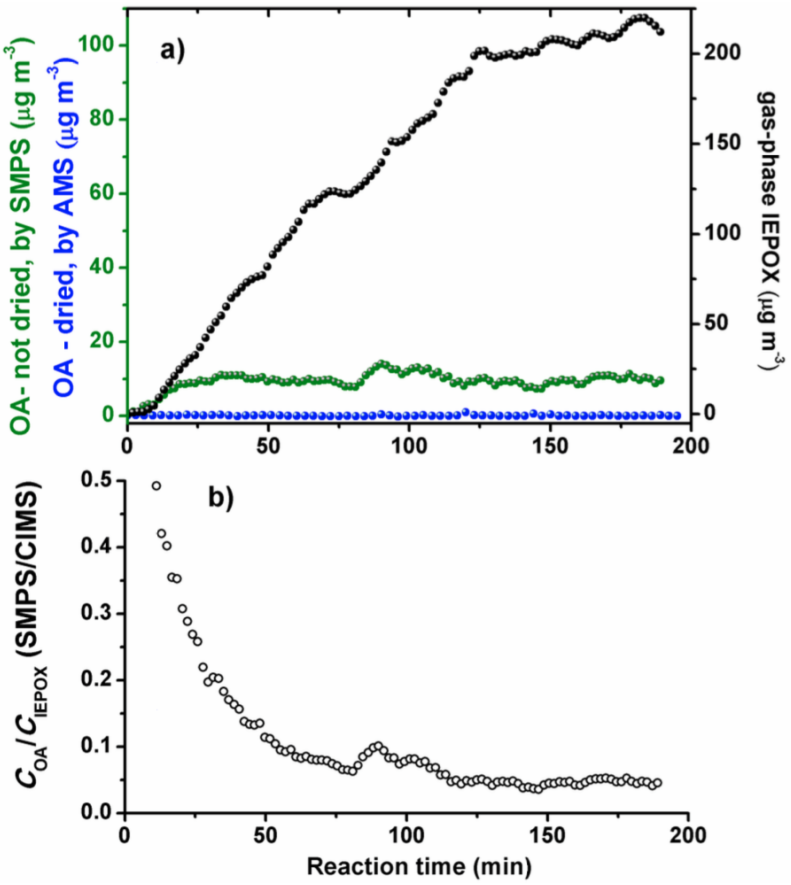

Figure 5.13: SMPS data showing an increase in particle volume when gas-phase IEPOX was injected with wet NaCl seeds, which stabilized over the course of the experiment. The ToF-AMS, which sampled dried particles, did not observe OA formation – an indication that the OA is reversibly formed in the liquid water of NaCl seeds (equilibrium partitioning) and that the unreacted IEPOX is removed from the particle phase upon drying.

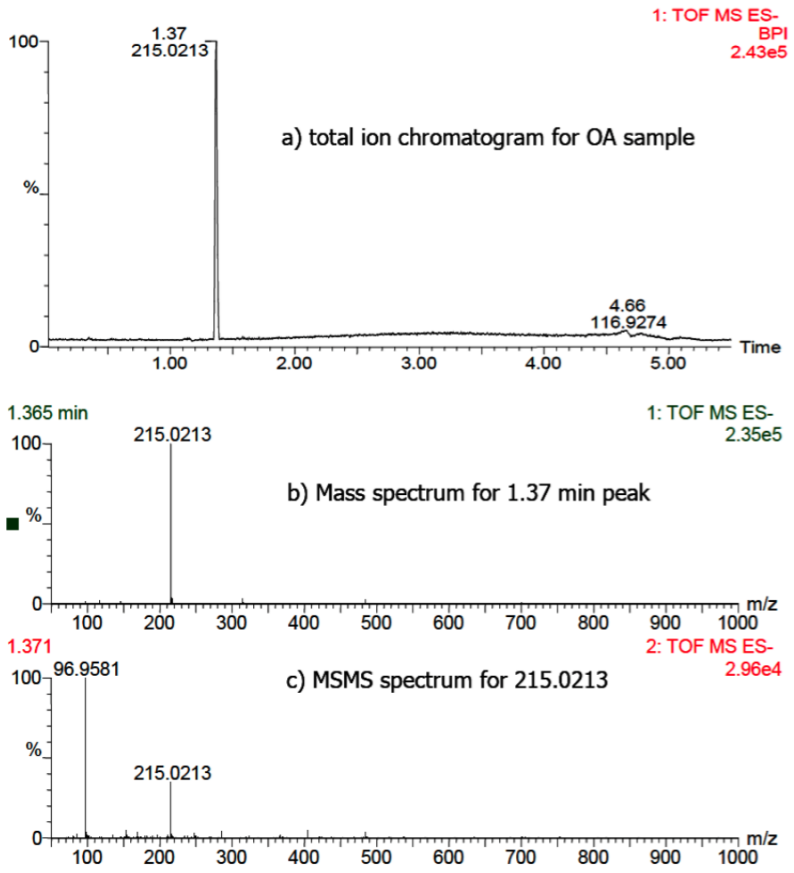

Figure 5.14: (a) Total ion chromatogram for the IEPOX-derived OA collected onto a filter. The sharp peak at 1.36 minutes corresponds to the elution of the IEPOX-derived organosulfate. (b) The mass spectrum corresponding to the 1.36 minute peak, showing that one peak ($C_5H_{11}SO_7^-$) dominates the spectrum. MSMS fragmentation (c) confirms organosulfates with the *m/z* 96.9581 (HSO_4^-) product ion.

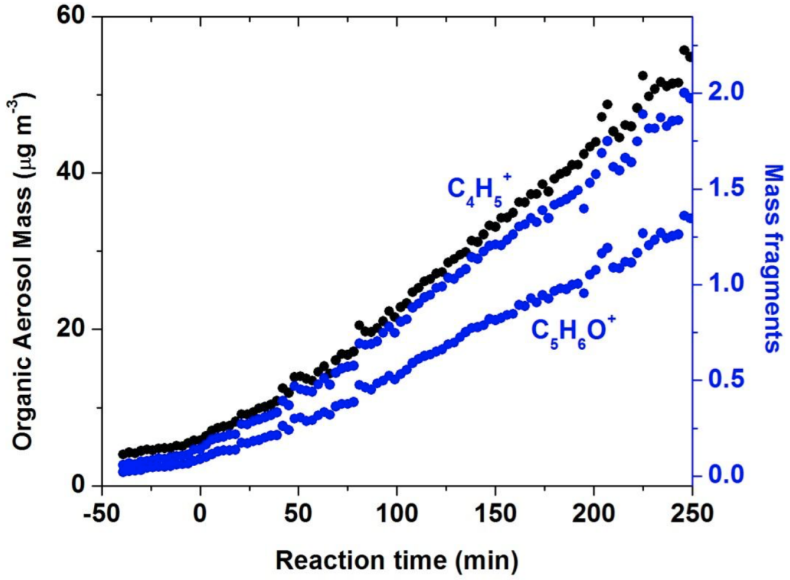

Figure 5.15: Proposed tracer mass fragments for IEPOX-derived OA correlate well (R^2>0.99) with the formation of OA mass.

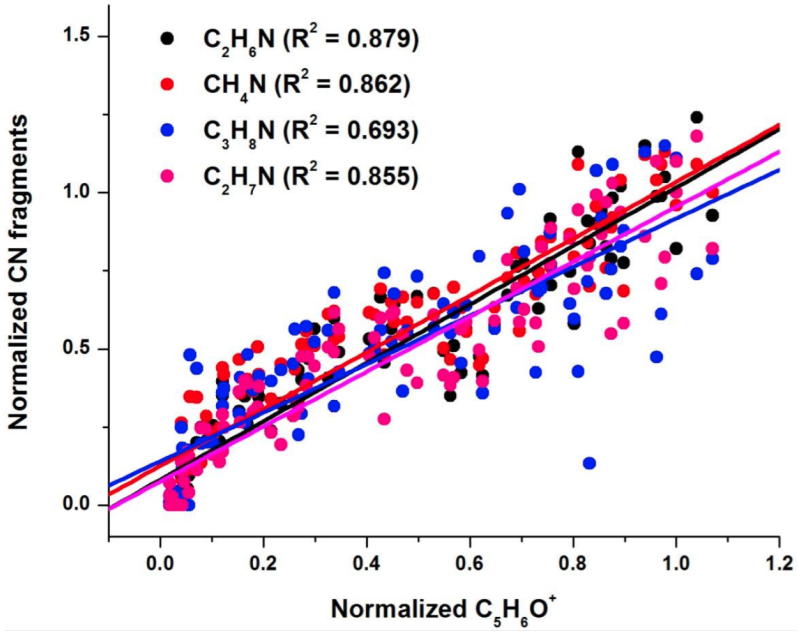

Figure 5.16: Correlation of four amine (C-N) fragments with the IEPOX tracer fragment ($C_5H_6O^+$) observed in ToF-AMS data for reactive uptake onto AS seeds.

Chapter 6

CONCLUSIONS

The preceding chapters of this thesis, along with the following appendices, contribute to the substantial recent progress in our understanding of the HO_2-dominated pathway of isoprene oxidation, and how that sub-mechanism fits into the broader contexts of both isoprene oxidation in general and the chemistry of the atmosphere as a whole. In the eight years since the publication of IEPOX's discovery (Paulot *et al.*, 2009b), a wealth of research has been conducted into its possible fates and reactive pathways, aided by the development of synthetic pathways for the production of four IEPOX isomers (Zhang *et al.*, 2012). The rates and products of its reaction with OH have been quantified, first by Jacobs *et al.* (2013) and then in the studies described in Chapters 2 and 3; subsequent experiments detailed in Chapter 3 also explored the chemistry of those products. Its contribution to SOA was first investigated in the laboratory by Lin *et al.* (2012) and Nguyen *et al.* (2014a) (Chapter 5), and many ensuing studies have contributed to this line of enquiry by examining particle phase reaction probabilities (Riedel *et al.*, 2015), the effects of aerosol acidity (Gaston *et al.*, 2014; Liu *et al.*, 2015; Wong *et al.*, 2015) and organic coatings (Riva *et al.*, 2016a) on IEPOX uptake, and the chemical composition (D'Ambro *et al.*, 2017a; Riva *et al.*, 2016b) and light-absorbing properties (Lin *et al.*, 2014) of that IEPOX-derived SOA. Additional studies of minor chemical pathways, such as dry deposition (Nguyen *et al.*, 2015a) and low-yield products of ISOPOOH chemistry (Berndt *et al.*, 2016; D'Ambro *et al.*, 2017b; Krechmer *et al.*, 2015; Liu *et al.*, 2016) have further amplified our understanding of isoprene's HO_2-dominated oxidation mechanism. Finally, as described briefly in Chapter 4, the results of these studies and others are now being incorporated into chemical models and used to investigate the importance of these newly explored oxidation pathways, as well as their effects on oxidant budgets, SOA formation, and other variables of interest in regional and global contexts (Marais *et al.*, 2016; Travis *et al.*, 2016).

As a result of the work in this thesis and the related studies mentioned above, the sinks of IEPOX have largely been constrained. Despite its myriad dependences on OH concentrations, the turbulence and depth of the mixing layer, and particle surface area and composition, the initial atmospheric fate of IEPOX can now be parameterized and modeled. Results from a number of such simple models are

listed in Table 6.1, including some based on measured ambient conditions. Further validation of IEPOX oxidation, uptake, and deposition parameterizations with field measurements will enable their implementation in more complex and broad-scale models.

Despite this recent progress, some aspects of the HO_2 dominated isoprene mechanism remain poorly constrained, which present promising avenues for further research. First, although many initial particle-phase products from the reactive uptake of IEPOX have been characterized, the potential reactivity and atmospheric fate of IEPOX-derived SOA is largely unknown. Aerosol aging encompasses a complex set of processes (including condensed-phase reactions, heterogeneous chemistry, photolysis, cloud processing, and others) that can cause changes in SOA chemical composition (George *et al.*, 2007; Molina *et al.*, 2004) and optical properties (Sareen *et al.*, 2013) and can even form volatile products that return to the gas phase (D'Ambro *et al.*, 2017a; Malecha and Nizkorodov, 2016; McNeill *et al.*, 2008). Preliminary results from the Seinfeld and McNeill laboratories suggest that exposure of IEPOX-derived SOA to gas-phase OH can cause rapid fragmentation of particle-phase organic species, leading to the volatilization of small acids and other compounds. If, as would thus be expected, these aging processes and their gas-phase products affect the lifetime of IEPOX-derived SOA and its overall loading, ozone formation, or oxidant cycling, then quantifying their effects they would be of vital importance to accurately describing the role of the HO_2-dominated isoprene oxidation pathway in the atmosphere.

Another auspicious field of future research regards unexplored product channels of the HO_2-dominated oxidation mechanism, including both later-generation chemistry and minor products from early generations that may have previously escaped detection. Chapter 3 identified stable oxidation products up to the fourth generation beyond isoprene, and observed that most compounds at that stage had fragmented to contain four or fewer carbon atoms, making them less likely to contribute to SOA; still, the dominant products are formed in such high abudnance (*e.g.*, the fourth-generation C_4 hydroxydicarbonyls are produced in excess of 50 Tg y^{-1} from isoprene oxidation) that their subsequent chemistry could have significant effects on local oxidant levels, radical cycling, and ozone formation. Additionally, new classes of highly oxidized compounds have recently been identified as potential minor products from the oxidation of ISOPOOH, including dihydroxy-dihydroperoxides and dihydroxy-hydroperoxy-epoxides (Berndt *et al.*, 2016; D'Ambro *et al.*, 2017b; Krechmer *et al.*,

citation	conditions	pathway contributions (%)		
		+ OH (gas phase)	particle uptake	dry deposition
Worton *et al.* (2013)	ambient: Sierra Nevada, CA, summer	52	<1	48
Gaston *et al.* (2014)	[OH]~10^6 molec cm^{-3}, ~100 $\mu m^2 cm^{-3}$ $(NH_4)_2SO_4$ particles	57	1	42
Gaston *et al.* (2014)	[OH]~10^6 molec cm^{-3}, ~100 $\mu m^2 cm^{-3}$ $(NH_4)HSO_4$ particles	30	48	22
Nguyen *et al.* (2015a)	low or non-acidic particle limit	-	-	≤45
Bates *et al.* (2016)	[OH]~2.5×10^6 molec cm^{-3}, ~200 $\mu m^2 cm^{-3}$ pH 3 particles	44	37	19
Hu *et al.* (2016)	ambient: Centreville, AL, summer	9	75	16

Table 6.1: Estimates of the relative contributions of reaction with OH, particle uptake, and deposition as pathways for the loss of gas phase IEPOX under various atmospheric conditions.

2015; Liu *et al.*, 2016). Despite their low yields, these products could contribute a substantial portion of isoprene-derived SOA under HO_2-dominated conditions due to their low volatility. These compounds are difficult to measure because of their rapid losses to chamber walls and instrumental surfaces, but new methods are now being employed to detect them directly or through their contribution to SOA. Further constraining the yields and uptake of these highly oxidized products is necessary to better understand and model SOA formation from the HO_2-dominated isoprene oxidation pathway.

Finally, the improved representation of isoprene reaction mechanisms in chemical transport models, for the sake of both comparison with field measurements and investigating the broader effects of isoprene oxidation, presents another promising avenue for further research. Notwithstanding from the comprehensive treatment of isoprene oxidation in Chapter 4, recent developments in isoprene chemistry have only been incorporated into global models on an *ad hoc* basis (*e.g.* in Chapter 3 and Appendices B, D, and G). Despite many recent improvements, chemical transport models still fail to accurately represent regional and global concentrations of isoprene-derived VOCs (Travis *et al.* (2016) and Appendix 7) as well as trace gases of broader importance such as OH (Turner *et al.*, 2017; Voulgarakis *et al.*, 2013) and ozone (Apel *et al.*, 2012; Parrish *et al.*, 2014; Whalley *et al.*, 2010). This thesis has demonstrated the importance of HO_2-dominated isoprene chemistry to such trace gas budgets across wide swaths of the globe; it is imperative that models incorporate accurate representations of this chemistry in order to determine isoprene's effects on air quality and climate, and to look at how those effects may change in the future. SOA, in particular, is currently only given cursory treatment in most chemical transport models. Given its high and uncertain importance to climate forcing (Pachauri *et al.*, 2014), the potential for significant changes in future SOA loading (Lin *et al.*, 2016), and the major contribution of HO_2-dominated isoprene chemistry to global SOA budgets, improving parameterizations of SOA and the chemistry of its precursors in models will be a prominent direction for further research.

The importance of isoprene to the chemistry of the troposphere can hardly be overstated; its high emissions and reactivity mean that even minor channels in its oxidation mechanism can play outsized roles in local atmospheric chemistry, and major oxidation channels, such as the HO_2-dominated pathway, can effectively set oxidant cycling, ozone production, and SOA formation rates across broad swaths

of the globe. Comprehending this mechanism is thus crucial to determining the role isoprene plays in affecting air quality and climate, and how that role may change over time. This thesis has presented a small but important step toward that comprehension, and will hopefully inform future studies that can bring us even closer to that goal.

BIBLIOGRAPHY

Abbatt, J., C. George, M. Melamed, P. Monks, S. Pandis, and Y. Rudich (2014). "New directions: Fundamentals of atmospheric chemistry: Keeping a three-legged stool balanced". In: *Atmos. Environ.* 84, pp. 390–391. DOI: http://doi.org/10.1016/j.atmosenv.2013.10.025.

Adeniji, S. A., J. A. Kerr, and M. R. Williams (1981). "Rate constants for ozone–alkene reactions under atmospheric conditions". In: *Int. J. Chem. Kinetics* 13.2, pp. 209–217. DOI: 10.1002/kin.550130210.

Adler, T. B., G. Knizia, and H.-J. Werner (2007). "A simple and efficient CCSD(T)-F12 approximation". In: *J. Chem. Phys.* 127.22, p. 221106. DOI: 10.1063/1.2817618.

Aiken, A. C., P. F. DeCarlo, and J. L. Jimenez (2007). "Elemental analysis of organic species with electron ionization high-resolution mass spectrometry." In: *Anal. Chem.* 79, pp. 8350–8. DOI: 10.1021/ac071150w.

Aiken, A. C., P. F. DeCarlo, J. H. Kroll, D. R. Worsnop, J. A. Huffman, K. S. Docherty, I. M. Ulbrich, C. Mohr, J. R. Kimmel, D. Sueper, Y. Sun, Q. Zhang, A. Trimborn, M. Northway, P. J. Ziemann, M. R. Canagaratna, T. B. Onasch, M. R. Alfarra, A. S. H. Prevot, J. Dommen, J. Duplissy, A. Metzger, U. Baltensperger, and J. L. Jimenez (2008). "O/C and OM/OC ratios of primary, secondary, and ambient organic aerosols with high-resolution time-of-flight aerosol mass spectrometry". In: *Environ. Sci. Technol.* 42.12, pp. 4478–4485. DOI: 10.1021/es703009q.

Aljawhary, D., A. K. Y. Lee, and J. P. D. Abbatt (2013). "High-resolution chemical ionization mass spectrometry (ToF-CIMS): Application to study SOA composition and processing". In: *Atmos. Meas. Tech.* 6.11, pp. 3211–3224. DOI: 10.5194/amt-6-3211-2013.

Allan, J. D., A. E. Delia, H. Coe, K. N. Bower, M. R. Alfarra, J. L. Jimenez, A. M. Middlebrook, F. Drewnick, T. B. Onasch, and M. R. Canagaratna (2004). "A generalised method for the extraction of chemically resolved mass spectra from Aerodyne aerosol mass spectrometer data". In: *J. Aerosol Sci.* 35, pp. 909–922.

An, Z.-W., R. D'Aloisio, and C. Venturello (1992). "A new, facile synthesis of methyltartronic acid". In: *Synthesis*, pp. 273–275.

Anglada, J. M., J. Gonzalez, and M. Torrent-Sucarrat (2011). "Effects of the substituents on the reactivity of carbonyl oxides. A theoretical study on the reaction of substituted carbonyl oxides with water". In: *Phys. Chem. Chem. Phys.* 13 (28), pp. 13034–13045. DOI: 10.1039/C1CP20872A.

Anglada, J. M., J. M. Bofill, S. Olivella, and A. Solé (1996). "Unimolecular isomerizations and oxygen atom loss in formaldehyde and acetaldehyde carbonyl oxides:

A theoretical investigation". In: *J. Am. Chem. Soc.* 118.19, pp. 4636–4647. DOI: 10.1021/ja953858a.

Apel, E. C., J. R. Olson, J. H. Crawford, R. S. Hornbrook, A. J. Hills, C. A. Cantrell, L. K. Emmons, D. J. Knapp, S. Hall, R. L. Mauldin Iii, A. J. Weinheimer, A. Fried, D. R. Blake, J. D. Crounse, J. M. S. Clair, P. O. Wennberg, G. S. Diskin, H. E. Fuelberg, A. Wisthaler, T. Mikoviny, W. Brune, and D. D. Riemer (2012). "Impact of the deep convection of isoprene and other reactive trace species on radicals and ozone in the upper troposphere". In: *Atmos. Chem. Phys.* 12.2, pp. 1135–1150. DOI: 10.5194/acp-12-1135-2012.

Archibald, A. T., M. C. Cooke, S. R. Utembe, D. E. Shallcross, R. G. Derwent, and M. E. Jenkin (2010). "Impacts of mechanistic changes on HOx formation and recycling in the oxidation of isoprene". In: *Atmos. Chem. Phys.* 10.17, pp. 8097–8118.

Arey, J., S. M. Aschmann, E. S. Kwok, and R. Atkinson (2001). "Alkyl nitrate, hydroxyalkyl nitrate, and hydroxycarbonyl formation from the NOx-air photooxidations of C5-C8 n-alkanes". In: *J. Phys. Chem. A* 105.6, pp. 1020–1027.

Arnts, R. R. and B. W. G. Jr (1979). *Photochemistry of some naturally emitted hydrocarbons*. Tech. rep. EPA-600/3-79-081. Research Triangle Park, NC: U. S. Environmental Protection Agency.

Asatryan, R., G. d. Silva, and J. W. Bozzelli (2010). "Quantum chemical study of the acrolein (CH2CHCHO) + OH + O2 reactions". In: *J. Phys. Chem. A* 114.32, pp. 8302–8311. DOI: 10.1021/jp104828a.

Aschmann, S. M., J. Arey, and R. Atkinson (2000). "Formation of beta-hydroxycarbonyls from the OH radical-initiated reactions of selected alkenes". In: *Environ. Sci. Technol.* 34.9, pp. 1702–1706. DOI: 10.1021/es991125a.

Aschmann, S. M. and R. Atkinson (1994). "Formation yields of methyl vinyl ketone and methacrolein from the gas-phase reaction of O3 with isoprene". In: *Environ. Sci. Technol.* 28.8, pp. 1539–1542. DOI: 10.1021/es00057a025.

Atkinson, R. (1997). "Gas-phase tropospheric chemistry of volatile organic compounds: 1. Alkanes and alkenes". In: *J. Phys. Chem. Ref. Data* 26.2, pp. 215–290.

– (2000). "Atmospheric chemistry of VOCs and NOx". In: *Atmos. Environ.* 34.12–14, pp. 2063–2101. DOI: http://dx.doi.org/10.1016/S1352-2310(99)00460-4.

– (2007). "Rate constants for the atmospheric reactions of alkoxy radicals: An updated estimation method". In: *Atmos. Environ.* 41.38, pp. 8468–8485. DOI: 10.1016/j.atmosenv.2007.07.002.

Atkinson, R. and J. Arey (2003a). "Atmospheric degradation of volatile organic compounds". In: *Chem. Rev.* 103.12, pp. 4605–4638.

– (2003b). "Gas-phase tropospheric chemistry of biogenic volatile organic compounds: A review". In: *Atmos. Environ.* 37, pp. 197–219.

Atkinson, R. and S. M. Aschmann (1993). "Hydroxyl radical production from the gas-phase reactions of ozone with a series of alkenes under atmospheric conditions". In: *Environ. Sci. Technol.* 27.7, pp. 1357–1363. DOI: 10.1021/es00044a010.

Atkinson, R., S. M. Aschmann, J. Arey, and B. Shorees (1992). "Formation of OH radicals in the gas phase reactions of O3 with a series of terpenes". In: *J. Geophys. Res. - Atmos.* 97.D5, pp. 6065–6073. DOI: 10.1029/92JD00062.

Atkinson, R., S. M. Aschmann, and J. N. Pitts (1983). "Kinetics of the gas-phase reactions of OH radicals with a series of alpha,beta-unsaturated carbonyls at 299 +/- 2 K". In: *Int. J. Chem. Kinetics* 15.1, pp. 75–81. DOI: 10.1002/kin.550150108.

Atkinson, R., S. M. Aschmann, A. M. Winer, and J. N. Pitts (1981). "Rate constants for the gas-phase reactions of O3 with a series of carbonyls at 296 K". In: *Int. J. Chem. Kinetics* 13.11, pp. 1133–1142. DOI: 10.1002/kin.550131104.

– (1984). "Kinetics of the gas-phase reactions of nitrate radicals with a series of dialkenes, cycloalkenes, and monoterpenes at 295 +/- 1 K". In: *Environ. Sci. Technol.* 18.5, pp. 370–375. DOI: 10.1021/es00123a016.

Atkinson, R., D. L. Baulch, R. A. Cox, J. N. Crowley, R. F. Hampson, R. G. Hynes, M. E. Jenkin, M. J. Rossi, and J. Troe (2006). "Evaluated kinetic and photochemical data for atmospheric chemistry: Volume 2: Reactions of organic species". In: *Atmos. Chem. Phys.* 6, pp. 3625–4055.

Atkinson, R. and A. C. Lloyd (1984). "Evaluation of kinetic and mechanistic data for modeling of photochemical smog". In: *J. Phys. Chem. Ref. Data* 13.2, pp. 315–444. DOI: http://dx.doi.org/10.1063/1.555710.

Atkinson, R., E. C. Tuazon, and S. M. Aschmann (1995). "Products of the gas-phase reactions of O3 with alkenes". In: *Environ. Sci. Technol.* 29.7, pp. 1860–1866. DOI: 10.1021/es00007a025.

Atkinson, R., A. Winer, and J. Pitts (1982). "Rate constants for the gas phase reactions of O3 with the natural hydrocarbons isoprene and alpha- and beta-pinene". In: *Atmos. Environ.* 16.5, pp. 1017–1020. DOI: http://dx.doi.org/10.1016/0004-6981(82)90187-1.

Aumont, B., S. Szopa, and S. Madronich (2005). "Modelling the evolution of organic carbon during its gas-phase tropospheric oxidation: Development of an explicit model based on a self generating approach". In: *Atmos. Chem. Phys.* 5.9, pp. 2497–2517. DOI: 10.5194/acp-5-2497-2005.

Avzianova, E. V. and P. A. Ariya (2002). "Temperature-dependent kinetic study for ozonolysis of selected tropospheric alkenes". In: *Int. J. Chem. Kinetics* 34.12, pp. 678–684. DOI: 10.1002/kin.10093.

Azizi, N. and M. R. Saidi (2005). "Highly chemoselective addition of amines to epoxides in water". In: *Org. Lett.* 7.17, pp. 3649–3651. DOI: 10.1021/ol051220q.

Bakwin, P. S., S. C. Wofsy, and S.-M. Fan (1990a). "Measurements of reactive nitrogen oxides (NOy) within and above a tropical forest canopy in the wet season". In: *J. Geophys. Res. - Atmos.* 95.D10, pp. 16765–16772. DOI: 10.1029/JD095iD10p16765.

Bakwin, P. S., S. C. Wofsy, S.-M. Fan, M. Keller, S. E. Trumbore, and J. M. Da Costa (1990b). "Emission of nitric oxide (NO) from tropical forest soils and exchange of NO between the forest canopy and atmospheric boundary layers". In: *J. Geophys. Res. - Atmos.* 95.D10, pp. 16755–16764. DOI: 10.1029/JD095iD10p16755.

Barket, D. J., J. W. Grossenbacher, J. M. Hurst, P. B. Shepson, K. Olszyna, T. Thornberry, M. A. Carroll, J. Roberts, C. Stroud, J. Bottenheim, and T. Biesenthal (2004). "A study of the NOx dependence of isoprene oxidation". In: *J. Geophys. Res. - Atmos.* 109.D11. DOI: 10.1029/2003JD003965.

Barnes, I., K. H. Becker, and T. Zhu (1993). "Near UV absorption spectra and photolysis products of difunctional organic nitrates: Possible importance as NOx reservoirs". In: *Atmos. Chem.* 17, pp. 353–373. DOI: 10.1007/BF00696854.

Barnes, I., V. Bastian, K. H. Becker, and Z. Tong (1990). "Kinetics and products of the reactions of nitrate radical with monoalkenes, dialkenes, and monoterpenes". In: *J. Phys. Chem.* 94.6, pp. 2413–2419.

Bateman, A. P., S. A. Nizkorodov, J. Laskin, and A. Laskin (2010). "High-resolution electrospray ionization mass spectrometry analysis of water-soluble organic aerosols collected with a particle into liquid sampler". In: *Anal. Chem.* 82.19, pp. 8010–8016. DOI: 10.1021/ac1014386.

Bates, K. H., J. D. Crounse, J. M. St Clair, N. B. Bennett, T. B. Nguyen, J. H. Seinfeld, B. M. Stoltz, and P. O. Wennberg (2014). "Gas phase production and loss of isoprene epoxydiols". In: *J. Phys. Chem. A* 118.7, pp. 1237–46. DOI: 10.1021/jp4107958.

Bates, K. H., T. B. Nguyen, A. P. Teng, J. D. Crounse, H. G. Kjaergaard, B. M. Stoltz, J. H. Seinfeld, and P. O. Wennberg (2016). "Production and fate of C4 dihydroxycarbonyl compounds from isoprene oxidation". In: *J. Phys. Chem. A* 120.1, pp. 106–117. DOI: 10.1021/acs.jpca.5b10335.

Beaver, M., J. St Clair, F. Paulot, K. Spencer, J. Crounse, B. LaFranchi, K. Min, S. Pusede, P. Wooldridge, G. Schade, *et al.* (2012). "Importance of biogenic precursors to the budget of organic nitrates: Observations of multifunctional organic nitrates by CIMS and TD-LIF during BEARPEX 2009". In: *Atmos. Chem. Phys.* 12.13, pp. 5773–5785.

Becker, K. H., J. Bechara, and K. J. Brockmann (1993). "Studies on the formation of H2O2 in the ozonolysis of alkenes". In: *Atmos. Environ.* 27.1, pp. 57–61. DOI: http://dx.doi.org/10.1016/0960-1686(93)90070-F.

Becker, K. H., K. J. Brockmann, and J. Bechara (1990). "Production of hydrogen peroxide in forest air by reaction of ozone with terpenes". In: *Nature* 346.6281, pp. 256–258.

Bedjanian, Y., L. Gerard, and B. Georges Le (1998). “Low-pressure study of the reaction of Cl atoms with isoprene”. In: *J. Phys. Chem. A* 102.6, pp. 953–959. DOI: 10.1021/jp973336c.

Behnke, W., C. George, V. Scheer, and C. Zetzsch (1997). “Production and decay of ClNO2 from the reaction of gaseous N2O5 with NaCl solution: Bulk and aerosol experiments”. In: *J. Geophys. Res. - Atmos.* 102.D3, pp. 3795–3804. DOI: 10.1029/96JD03057.

Bell, M. L., R. D. Peng, and F. Dominici (2006). “The exposure–response curve for ozone and risk of mortality and the adequacy of current ozone regulations”. In: *Environ. Health Perspectives* 114.4, pp. 532–536. DOI: 10.1289/ehp.8816.

Benson, S. W. and R. Shaw (1968). “Thermochemistry of Oxidation Reactions”. In: *Oxidation of Organic Compounds*. Ed. by F. R. Mayo. American Chemical Society, pp. 288–294. DOI: 10.1021/ba-1968-0075.ch022.

Benter, T. and R. N. Schindler (1988). “Absolute rate coefficients for the reaction of NO3 radicals with simple dienes”. In: *Chem. Phys. Lett.* 145.1, pp. 67–70. DOI: http://dx.doi.org/10.1016/0009-2614(88)85134-0.

Berndt, T. (2012). “Formation of carbonyls and hydroperoxyenals (HPALDs) from the OH radical reaction of isoprene for low-NOx conditions: Influence of temperature and water vapour content”. In: *J. Atmos. Chem.* 69.4, pp. 253–272. DOI: 10.1007/s10874-012-9245-2.

Berndt, T. and O. Boge (1997). “Gas-phase reaction of NO3 radicals With isoprene: A kinetic and mechanistic study”. In: *Int. J. Chem. Kinetics* 29, pp. 755–765.

Berndt, T., H. Herrmann, M. Sipilä, and M. Kulmala (2016). “Highly oxidized second-generation products from the gas-phase reaction of OH radicals with isoprene”. In: *J. Phys. Chem. A*. DOI: 10.1021/acs.jpca.6b10987.

Berndt, T., J. Voigtlander, F. Stratmann, H. Junninen, R. L. Mauldin III, M. Sipila, M. Kulmala, and H. Herrmann (2014). “Competing atmospheric reactions of CH2OO with SO2 and water vapour”. In: *Phys. Chem. Chem. Phys.* 16 (36), pp. 19130–19136. DOI: 10.1039/C4CP02345E.

Berner, A. H., C. S. Bretherton, and R. Wood (2011). “Large-eddy simulation of mesoscale dynamics and entrainment around a pocket of open cells observed in VOCALS-REx RF06”. In: *Atmos. Chem. Phys.* 11.20, pp. 10525–10540. DOI: 10.5194/acp-11-10525-2011.

Bernhammer, A. K., M. Breitenlechner, F. N. Keutsch, and A. Hansel (2017). “Technical note: Conversion of isoprene hydroxy hydroperoxides (ISOPOOHs) on metal environmental simulation chamber walls”. In: *Atmos. Chem. Phys.* 17.6, pp. 4053–4062. DOI: 10.5194/acp-17-4053-2017.

Bertman, S. B. and J. M. Roberts (1991). “A PAN analog from isoprene photooxidation”. In: *Geophys. Res. Lett.* 18.8, pp. 1461–1464. DOI: 10.1029/91GL01852.

Bertram, A. K., S. T. Martin, S. J. Hanna, M. L. Smith, A. Bodsworth, Q. Chen, M. Kuwata, A. Liu, Y. You, and S. R. Zorn (2011). "Predicting the relative humidities of liquid-liquid phase separation, efflorescence, and deliquescence of mixed particles of ammonium sulfate, organic material, and water using the organic-to-sulfate mass ratio of the particle and the oxygen-to-carbon elemental ratio of the organic component". In: *Atmos. Chem. Phys.* 11.21, pp. 10995–11006. DOI: 10.5194/acp-11-10995-2011.

Bey, I., D. J. Jacob, R. M. Yantosca, J. A. Logan, B. Field, A. M. Fiore, Q. Li, H. Liu, L. J. Mickley, and M. Schultz (2001). "Global modeling of tropospheric chemistry with assimilated meteorology: Model description and evaluation". In: *J. Geophys. Res.* 106, pp. 23073–23096.

Biesenthal, T. A., J. W. Bottenheim, P. B. Shepson, S.-M. Li, and P. C. Brickell (1998). "The chemistry of biogenic hydrocarbons at a rural site in eastern Canada". In: *J. Geophys. Res. - Atmos.* 103.D19, pp. 25487–25498. DOI: 10.1029/98JD01848.

Biesenthal, T. A. and P. B. Shepson (1997). "Observations of anthropogenic inputs of the isoprene oxidation products methyl vinyl ketone and methacrolein to the atmosphere". In: *Geophys. Res. Lett.* 24.11, pp. 1375–1378. DOI: 10.1029/97GL01337.

Birdsall, A. W., C. A. Zentner, and M. J. Elrod (2013). "Study of the kinetics and equilibria of the oligomerization reactions of 2-methylglyceric acid". In: *Atmos. Chem. Phys.* 13.6, pp. 3097–3109. DOI: 10.5194/acp-13-3097-2013.

Bischofberger, N., H. Waldmann, T. Saito, E. S. Simon, W. Lees, M. D. Bednarski, and G. M. Whitesides (1988). "Synthesis of analogues of 1,3-dihydroxyacetone phosphate and glyceraldehyde 3-phosphate for use in studies of fructose-1,6-diphosphate aldolase". In: *J. Org. Chem.* 53, pp. 3457–3465.

Biskos, G., D. Paulsen, L. M. Russell, P. R. Buseck, and S. T. Martin (2006). "Prompt deliquescence and efflorescence of aerosol nanoparticles". In: *Atmos. Chem. Phys.* 6.12, pp. 4633–4642. DOI: 10.5194/acp-6-4633-2006.

Bones, D. L., D. K. Henricksen, S. A. Mang, M. Gonsior, A. P. Bateman, T. B. Nguyen, W. J. Cooper, and S. A. Nizkorodov (2010). "Appearance of strong absorbers and fluorophores in limonene-O3 secondary organic aerosol due to NH4+-mediated chemical aging over long time scales". In: *J. Geophys. Res.* 115, p. D05203.

Bouzidi, H., C. Fittschen, P. Coddeville, and A. Tomas (2014). "Photolysis of 2,3-pentanedione and 2,3-hexanedione: Kinetics, quantum yields, and product study in a simulation chamber". In: *Atmos. Environ.* 82, pp. 250–257.

Boyd, A. A., P.-M. Flaud, N. Daugey, and R. Lesclaux (2003). "Rate constants for RO2 + HO2 reactions measured under a large excess of HO2". In: *J. Phys. Chem. A* 107.6, pp. 818–821. DOI: 10.1021/jp026581r.

Braña, P. and J. A. Sordo (2001). "Mechanistic aspects of the abstraction of an allylic hydrogen in the chlorine atom reaction with 2-methyl-1,3-butadiene (isoprene)". In: *J. Am. Chem. Soc.* 123.42, pp. 10348–10353. DOI: 10.1021/ja011302j.

Bretherton, C. S., R. Wood, R. C. George, D. Leon, G. Allen, and X. Zheng (2010a). "Southeast Pacific stratocumulus clouds, precipitation and boundary layer structure sampled along 20° S during VOCALS-REx". In: *Atmos. Chem. Phys.* 10.21, pp. 10639–10654. DOI: 10.5194/acp-10-10639-2010.

Bretherton, C. S. and M. C. Wyant (1997). "Moisture transport, lower-tropospheric stability, and decoupling of cloud-topped boundary layers". In: *J. Atmos. Sci.* 54.1, pp. 148–167. DOI: 10.1175/1520-0469(1997)054<0148:mtltsa>2.0.co;2.

Bretherton, C. S., J. Uchida, and P. N. Blossey (2010b). "Slow manifolds and multiple equilibria in stratocumulus-capped boundary layers". In: *J. Adv. Modeling Earth Systems* 2.4. DOI: 10.3894/JAMES.2010.2.14.

Brown, S. S., J. A. deGouw, C. Warneke, T. B. Ryerson, W. P. Dubé, E. Atlas, R. J. Weber, R. E. Peltier, J. A. Neuman, J. M. Roberts, A. Swanson, F. Flocke, S. A. McKeen, J. Brioude, R. Sommariva, M. Trainer, F. C. Fehsenfeld, and A. R. Ravishankara (2009). "Nocturnal isoprene oxidation over the Northeast United States in summer and its impact on reactive nitrogen partitioning and secondary organic aerosol". In: *Atmos. Chem. Phys.* 9.9, pp. 3027–3042. DOI: 10.5194/acp-9-3027-2009.

Browne, E. C. and R. C. Cohen (2012). "Effects of biogenic nitrate chemistry on the NOx lifetime in remote continental regions". In: *Atmos. Chem. Phys.* 12.24, pp. 11917–11932. DOI: 10.5194/acp-12-11917-2012.

Brune, W. H., P. S. Stevens, and J. H. Mather (1995). "Measuring OH and HO2 in the troposphere by laser-induced fluorescence at low pressure". In: *J. Atmos. Sci.* 52.19, pp. 3328–3336. DOI: 10.1175/1520-0469(1995)052<3328:MOAHIT>2.0.CO;2.

Budisulistiorini, S. H., M. R. Canagaratna, P. L. Croteau, W. J. Marth, K. Baumann, E. S. Edgerton, S. L. Shaw, E. M. Knipping, D. R. Worsnop, J. T. Jayne, A. Gold, and J. D. Surratt (2013). "Real-time continuous characterization of secondary organic aerosol derived from isoprene epoxydiols in downtown Atlanta, Georgia, using the Aerodyne Aerosol Chemical Speciation Monitor". In: *Environ. Sci. Technol.* 47.11, pp. 5686–5694. DOI: 10.1021/es400023n.

Burkholder, J. B., S. P. Sander, J. Abbatt, J. R. Barker, R. E. Huie, C. E. Kolb, M. J. Kurylo, V. L. Orkin, D. M. Wilmouth, and P. H. Wine (2015). *Chemical Kinetics and Photochemical Data for Use in Atmospheric Studies, Evaluation No. 18*. Report JPL Publication 15-10. Pasadena: Jet Propulsion Laboratory. URL: http://jpldataeval.jpl.nasa.gov.

Burkholder, J. B., J. P. D. Abbatt, I. Barnes, J. M. Roberts, M. L. Melamed, M. Ammann, A. K. Bertram, C. D. Cappa, A. G. Carlton, L. J. Carpenter, J. N. Crowley, Y. Dubowski, C. George, D. E. Heard, H. Herrmann, F. N. Keutsch, J. H.

Kroll, V. F. McNeill, N. L. Ng, S. A. Nizkorodov, J. J. Orlando, C. J. Percival, B. Picquet-Varrault, Y. Rudich, P. W. Seakins, J. D. Surratt, H. Tanimoto, J. A. Thornton, Z. Tong, G. S. Tyndall, A. Wahner, C. J. Weschler, K. R. Wilson, and P. J. Ziemann (2017). "The essential role for laboratory studies in atmospheric chemistry". In: *Environ. Sci. Technol.* 51.5, pp. 2519–2528. DOI: 10.1021/acs.est.6b04947.

Burleyson, C. D., S. P. de Szoeke, S. E. Yuter, M. Wilbanks, and W. A. Brewer (2013). "Ship-based observations of the diurnal cycle of southeast Pacific marine stratocumulus clouds and precipitation". In: *J. Atmos. Sci.* 70.12, pp. 3876–3894. DOI: 10.1175/JAS-D-13-01.1.

Butkovskaya, N. I., A. Kukui, G. Le Bras, M. T. Rayez, and J. C. Rayez (2015). "Pressure dependence of butyl nitrate formation in the reaction of butylperoxy radicals with nitrogen oxide". In: *J. Phys. Chem. A* 119.19, pp. 4408–4417. DOI: 10.1021/jp509427x.

Campbell, J. R., J. L. Tackett, J. S. Reid, J. Zhang, C. A. Curtis, E. J. Hyer, W. R. Sessions, D. L. Westphal, J. M. Prospero, E. J. Welton, A. H. Omar, M. A. Vaughan, and D. M. Winker (2012). "Evaluating nighttime CALIOP 0.532 um aerosol optical depth and extinction coefficient retrievals". In: *Atmos. Meas. Tech.* 5.9, pp. 2143–2160. DOI: 10.5194/amt-5-2143-2012.

Canagaratna, M., J. Jayne, J. Jimenez, J. Allan, M. Alfarra, Q. Zhang, T. Onasch, F. Drewnick, H. Coe, A. Middlebrook, A. Delia, L. Williams, A. Trimborn, M. Northway, P. DeCarlo, C. Kolb, P. Davidovits, and D. Worsnop (2007). "Chemical and microphysical characterization of ambient aerosols with the aerodyne aerosol mass spectrometer". In: *Mass Spec. Rev.* 26.2, pp. 185–222. DOI: 10.1002/mas.20115.

Canosa-Mas, C. E., S. Carr, M. D. King, D. E. Shallcross, K. C. Thompson, and R. P. Wayne (1999a). "A kinetic study of the reactions of NO3 with methyl vinyl ketone, methacrolein, acrolein, methyl acrylate and methyl methacrylate". In: *Phys. Chem. Chem. Phys.* 1 (18), pp. 4195–4202. DOI: 10.1039/A904613E.

Canosa-Mas, C. E., M. D. King, D. E. Shallcross, and R. P. Wayne (1999b). "Kinetic investigation of the reaction between the NO3 radical and peroxymethacrylic nitric anhydride (MPAN)". In: *Phys. Chem. Chem. Phys.* 1.10, pp. 2411–2414. DOI: 10.1039/A901576K.

Carlton, A. G. and B. J. Turpin (2013). "Particle partitioning potential of organic compounds is highest in the Eastern US and driven by anthropogenic water". In: *Atmos. Chem. Phys.* 13.20, pp. 10203–10214. DOI: 10.5194/acp-13-10203-2013.

Carlton, A. G., C. Wiedinmyer, and J. H. Kroll (2009). "A review of secondary organic aerosol (SOA) formation from isoprene". In: *Atmos. Chem. Phys.* 9.14, pp. 4987–5005. DOI: 10.5194/acp-9-4987-2009.

Carlton, A. G., B. J. Turpin, H.-J. Lim, K. E. Altieri, and S. Seitzinger (2006). "Link between isoprene and secondary organic aerosol (SOA): Pyruvic acid oxidation yields low volatility organic acids in clouds". In: *Geophys. Res. Lett.* 33.6. DOI: 10.1029/2005GL025374.

Carter, W. P. L. (1996). "Condensed atmospheric photooxidation mechanisms For isoprene". In: *Atmos. Environ.* 30, pp. 4275–4290.

– (2010). "Development of the SAPRC-07 chemical mechanism". In: *Atmos. Environ.* 44, pp. 5324–5335.

Carter, W. P. L. and R. Atkinson (1985). "Atmospheric chemistry of alkanes". In: *J. Atmos. Chem.* 3.3, pp. 377–405. DOI: 10.1007/BF00122525.

– (1989). "Alkyl nitrate formation from the atmospheric photoxidation of alkanes: A revised estimation method". In: *J. Atmos. Chem.* 8 (2), pp. 165–173.

Carter, W. P. L., D. R. Cocker Iii, D. R. Fitz, I. L. Malkina, K. Bumiller, C. G. Sauer, J. T. Pisano, C. Bufalino, and C. Song (2005). "A new environmental chamber for evaluation of gas-phase chemical mechanisms and secondary aerosol formation". In: *Atmos. Environ.* 39.40, pp. 7768–7788. DOI: http://doi.org/10.1016/j.atmosenv.2005.08.040.

Cassanelli, P., D. J. Fox, and R. A. Cox (2007). "Temperature dependence of pentyl nitrate formation from the reaction of pentyl peroxy radicals with NO". In: *Phys. Chem. Chem. Phys.* 9 (31), pp. 4332–4337. DOI: 10.1039/B700285H.

Chai, J.-D. and M. Head-Gordon (2008). "Long-range corrected hybrid density functionals with damped atom-atom dispersion corrections". In: *Phys. Chem. Chem. Phys.* 10.44, pp. 6615–6620. DOI: 10.1039/B810189B.

Chameides, W. L., P. S. Kasibhatla, J. Yienger, and H. Levy (1994). "Growth of continental-scale metro-agro-plexes, regional ozone pollution, and world food production". In: *Science* 264.5155, p. 74.

Chameides, W. L., R. W. Lindsay, J. Richardson, and C. S. Kiang (1988). "The role of biogenic hydrocarbons in urban photochemical smog: Atlanta as a case study". In: *Science* 241.4872, pp. 1473–1475.

Chan, A. W. H., M. N. Chan, J. D. Surratt, P. S. Chhabra, C. L. Loza, J. D. Crounse, L. D. Yee, R. C. Flagan, P. O. Wennberg, and J. H. Seinfeld (2010a). "Role of aldehyde chemistry and NOx concentrations in secondary organic aerosol formation". In: *Atmos. Chem. Phys.* 10.15, pp. 7169–7188. DOI: 10.5194/acp-10-7169-2010.

Chan, M. N., J. D. Surratt, A. W. H. Chan, K. Schilling, J. H. Offenberg, M. Lewandowski, E. O. Edney, T. E. Kleindienst, M. Jaoui, E. S. Edgerton, R. L. Tanner, S. L. Shaw, M. Zheng, E. M. Knipping, and J. H. Seinfeld (2011). "Influence of aerosol acidity on the chemical composition of secondary organic aerosol from beta-caryophyllene". In: *Atmos. Chem. Phys.* 11.4, pp. 1735–1751. DOI: 10.5194/acp-11-1735-2011.

Chan, M. N., J. D. Surratt, M. Claeys, E. S. Edgerton, R. L. Tanner, S. L. Shaw, M. Zheng, E. M. Knipping, N. C. Eddingsaas, P. O. Wennberg, and J. H. Seinfeld (2010b). "Characterization and quantification of isoprene-derived epoxydiols in ambient aerosol in the southeastern United States". In: *Environ. Sci. Technol.* 44, pp. 4590–4596.

Chao, W., J.-T. Hsieh, C.-H. Chang, and J. J.-M. Lin (2015). "Direct kinetic measurement of the reaction of the simplest Criegee intermediate with water vapor". In: *Science* 347.6223, pp. 751–754. DOI: 10.1126/science.1261549.

Chen, Q., D. K. Farmer, L. V. Rizzo, T. Pauliquevis, M. Kuwata, T. G. Karl, A. Guenther, J. D. Allan, H. Coe, M. O. Andreae, U. Pöschl, J. L. Jimenez, P. Artaxo, and S. T. Martin (2015). "Submicron particle mass concentrations and sources in the Amazonian wet season (AMAZE-08)". In: *Atmos. Chem. Phys.* 15.7, pp. 3687–3701. DOI: 10.5194/acp-15-3687-2015.

Chen, Q., D. K. Farmer, J. Schneider, S. R. Zorn, C. L. Heald, T. G. Karl, A. Guenther, J. D. Allan, N. Robinson, H. Coe, J. R. Kimmel, T. Pauliquevis, S. Borrmann, U. Pöschl, M. O. Andreae, P. Artaxo, J. L. Jimenez, and S. T. Martin (2009). "Mass spectral characterization of submicron biogenic organic particles in the Amazon Basin". In: *Geophys. Res. Lett.* 36.20. DOI: 10.1029/2009GL039880.

Chen, X., D. Hulbert, and P. B. Shepson (1998). "Measurement of the organic nitrate yield from OH reaction with isoprene". In: *J. Geophys. Res. - Atmos.* 103.D19, pp. 25563–25568.

Chew, A. A., R. Atkinson, and S. M. Aschmann (1998). "Kinetics of the gas-phase reactions of NO3 radicals with a series of alcohols, glycol ethers, ethers and chloroalkenes". In: *J. Chem. Soc. Faraday Trans.* 94 (8), pp. 1083–1089. DOI: 10.1039/A708183I.

Chew, A. A. and R. Atkinson (1996). "OH radical formation yields from the gas-phase reactions of O3 with alkenes and monoterpenes". In: *J. Geophys. Res. - Atmos.* 101.D22, pp. 28649–28653. DOI: 10.1029/96JD02722.

Chhabra, P. S., R. C. Flagan, and J. H. Seinfeld (2010). "Elemental analysis of chamber organic aerosol using an aerodyne high-resolution aerosol mass spectrometer". In: *Atmos. Chem. Phys.* 10.9, pp. 4111–4131. DOI: 10.5194/acp-10-4111-2010.

Chhabra, P. S., N. L. Ng, M. R. Canagaratna, A. L. Corrigan, L. M. Russell, D. R. Worsnop, R. C. Flagan, and J. H. Seinfeld (2011). "Elemental composition and oxidation of chamber organic aerosol". In: *Atmos. Chem. Phys.* 11.17, pp. 8827–8845. DOI: 10.5194/acp-11-8827-2011.

Christoffersen, T. S., J. Hjorth, O. Horie, N. R. Jensen, D. Kotzias, L. L. Molander, P. Neeb, L. Ruppert, R. Winterhalter, A. Virkkula, K. Wirtz, and B. R. Larsen (1998). "cis-pinic acid, a possible precursor for organic aerosol formation from ozonolysis of alpha-pinene". In: *Atmos. Environ.* 32.10, pp. 1657–1661. DOI: http://dx.doi.org/10.1016/S1352-2310(97)00448-2.

Chuong, B. and P. S. Stevens (2002). "Measurements of the kinetics of the OH-initiated oxidation of isoprene". In: *J. Geophys. Res. - Atmos.* 107.D13. DOI: 10.1029/2001JD000865.

– (2003). "Kinetics of the OH + methyl vinyl ketone and OH + methacrolein reactions at low pressure". In: *J. Phys. Chem. A* 107.13, pp. 2185–2191. DOI: 10.1021/jp026036q.

– (2004). "Measurements of the kinetics of the OH-initiated oxidation of methyl vinyl ketone and methacrolein". In: *Int. J. Chem. Kinetics* 36.1, pp. 12–25. DOI: 10.1002/kin.10167.

Claeys, M., B. Graham, G. Vas, W. Wang, R. Vermeylen, V. Pashynska, J. Cafmeyer, P. Guyon, M. O. Andreae, P. Artaxo, and W. Maenhaut (2004). "Formation of secondary organic aerosols through photooxidation of isoprene." In: *Science* 303, pp. 1173–6. DOI: 10.1126/science.1092805.

Clark, C. H., S. Nakao, A. Asa-Awuku, K. Sato, and D. R. Cocker (2013). "Real-time study of particle-phase products from alpha-pinene ozonolysis and isoprene photooxidation using particle into liquid sampling directly coupled to a time-of-flight mass spectrometer (PILS-ToF)". In: *Aerosol Sci. Technol.* 47.12, pp. 1374–1382. DOI: 10.1080/02786826.2013.844333.

Clayden, J., N. Greeves, S. G. Warren, and P. Wothers (2001). *Organic Chemistry*. Oxford, UK: Oxford University Press, p. 386.

Clegg, S. L., P. Brimblecombe, and A. S. Wexler (1998). "Thermodynamic model of the system H+-NH4+-SO42–NO3–H2O at tropospheric temperatures". In: *J. Phys. Chem. A* 102.12, pp. 2137–2154. DOI: 10.1021/jp973042r.

Coakley, J. A., P. A. Durkee, K. Nielsen, J. P. Taylor, S. Platnick, B. A. Albrecht, D. Babb, F. L. Chang, W. R. Tahnk, C. S. Bretherton, and P. V. Hobbs (2000). "The appearance and disappearance of ship tracks on large spatial scales". In: *J. Atmos. Sci.* 57.16, pp. 2765–2778. DOI: 10.1175/1520-0469(2000)057<2765:TAADOS>2.0.CO;2.

Cocker, D. R., R. C. Flagan, and J. H. Seinfeld (2001). "State-of-the-art chamber facility for studying atmospheric aerosol chemistry". In: *Environ. Sci. Technol.* 35.12, pp. 2594–2601. DOI: 10.1021/es0019169.

Coggon, M. M., A. Sorooshian, Z. Wang, J. S. Craven, A. R. Metcalf, J. J. Lin, A. Nenes, H. H. Jonsson, R. C. Flagan, and J. H. Seinfeld (2014). "Observations of continental biogenic impacts on marine aerosol and clouds off the coast of California". In: *J. Geophys. Res. - Atmos.* 119.11, pp. 6724–6748. DOI: 10.1002/2013JD021228.

Coggon, M. M., A. Sorooshian, Z. Wang, A. R. Metcalf, A. A. Frossard, J. J. Lin, J. S. Craven, A. Nenes, H. H. Jonsson, L. M. Russell, R. C. Flagan, and J. H. Seinfeld (2012). "Ship impacts on the marine atmosphere: insights into the contribution of shipping emissions to the properties of marine aerosol and clouds". In: *Atmos. Chem. Phys.* 12.18, pp. 8439–8458. DOI: 10.5194/acp-12-8439-2012.

Cohen, A. J., M. Brauer, R. Burnett, H. R. Anderson, J. Frostad, K. Estep, K. Balakrishnan, B. Brunekreef, L. Dandona, R. Dandona, V. Feigin, G. Freedman, B. Hubbell, A. Jobling, H. Kan, L. Knibbs, Y. Liu, R. Martin, L. Morawska, I. Pope C. Arden, H. Shin, K. Straif, G. Shaddick, M. Thomas, R. van Dingenen, A. van Donkelaar, T. Vos, C. J. L. Murray, and M. H. Forouzanfar (2017). "Estimates and 25-year trends of the global burden of disease attributable to ambient air pollution: An analysis of data from the Global Burden of Diseases Study 2015". In: *The Lancet*. DOI: 10.1016/S0140-6736(17)30505-6.

Cole-Filipiak, N. C., A. E. O'Connor, and M. J. Elrod (2010). "Kinetics of the hydrolysis of atmospherically relevant isoprene-derived hydroxy epoxides". In: *Environ. Sci. Technol.* 44, pp. 6718–6723.

Collett, J. L., A. Bator, X. Rao, and B. B. Demoz (1994). "Acidity variations across the cloud drop size spectrum and their influence on rates of atmospheric sulfate production". In: *Geophys. Res. Lett.* 21.22, pp. 2393–2396. DOI: 10.1029/94GL02480.

Cometto, P. M., P. R. Dalmasso, R. A. Taccone, S. I. Lane, F. Oussar, V. Daële, A. Mellouki, and G. L. Bras (2008). "Rate coefficients for the reaction of OH with a series of unsaturated alcohols between 263 and 371 K". In: *J. Phys. Chem. A* 112.19, pp. 4444–4450. DOI: 10.1021/jp7111186.

Compernolle, S., K. Ceulemans, and J. F. Müller (2011). "EVAPORATION: a new vapour pressure estimation methodfor organic molecules including non-additivity and intramolecular interactions". In: *Atmos. Chem. Phys.* 11.18, pp. 9431–9450. DOI: 10.5194/acp-11-9431-2011.

Considine, G. D. (1997). "Modeling the diurnal variability in cloud microphysics in boundary layer clouds". In: *J. Geophys. Res. - Atmos.* 102.D2, pp. 1717–1726. DOI: 10.1029/96JD02997.

Cox, R. A., R. G. Derwent, and M. R. Williams (1980). "Atmospheric photooxidation reactions: Rates, reactivity, and mechanism for reaction of organic compounds with hydroxyl radicals". In: *Environ. Sci. Technol.* 14.1, pp. 57–61. DOI: 10.1021/es60161a007.

Crawford, M. A., T. J. Wallington, J. J. Szente, M. M. Maricq, and J. S. Francisco (1999). "Kinetics and mechanism of the acetylperoxy + HO2 reaction". In: *J. Phys. Chem. A* 103.3, pp. 365–378. DOI: 10.1021/jp983150t.

Cremer, D., E. Kraka, and P. G. Szalay (1998). "Decomposition modes of dioxirane, methyldioxirane and dimethyldioxirane — a CCSD(T), MR-AQCC and DFT investigation". In: *Chem. Phys. Lett.* 292.1–2, pp. 97–109. DOI: http://dx.doi.org/10.1016/S0009-2614(98)00678-2.

Criegee, R. (1975). "Mechanismus der Ozonolyse". In: *Angewandte Chemie* 87.21, pp. 765–771. DOI: 10.1002/ange.19750872104.

Criegee, R. and G. Wenner (1949). "Die Ozonisierung des 9,10-Oktalins". In: *Justus Liebigs Annalen der Chemie* 564.1, pp. 9–15. DOI: 10.1002/jlac.19495640103.

Crosbie, E., Z. Wang, A. Sorooshian, P. Y. Chuang, J. S. Craven, M. M. Coggon, M. Brunke, X. Zeng, H. Jonsson, R. K. Woods, R. C. Flagan, and J. H. Seinfeld (2015). "Stratocumulus cloud clearings and notable thermodynamic and aerosol contrasts across the clear–cloudy interface". In: *J. Atmos. Sci.* 73.3, pp. 1083–1099. DOI: 10.1175/JAS-D-15-0137.1.

Crounse, J. D., H. C. Knap, K. B. Ørnsø, S. Jørgensen, F. Paulot, H. G. Kjaergaard, and P. O. Wennberg (2012). "Atmospheric fate of methacrolein. 1. Peroxy radical isomerization following adition of OH and O2". In: *J. Phys. Chem. A* 116, pp. 5756–5762.

Crounse, J. D., K. A. McKinney, A. J. Kwan, and P. O. Wennberg (2006). "Measurement of gas-phase hydroperoxides by chemical ionization mass spectrometry". In: *Anal. Chem.* 78.19, pp. 6726–6732.

Crounse, J. D., L. B. Nielsen, S. Jorgensen, H. G. Kjaergaard, and P. O. Wennberg (2013). "Autoxidation of organic compounds in the atmosphere". In: *J. Phys. Chem. Lett.* 4, pp. 3513–3520.

Crounse, J. D., F. Paulot, H. G. Kjaergaard, and P. O. Wennberg (2011). "Peroxy radical isomerization in the oxidation of isoprene". In: *Phys. Chem. Chem. Phys.* 13, pp. 13607–13613.

Crowley, J. N. and G. K. Moortgat (1992). "2-Bromoethylperoxy and 2-bromo-1-methylpropylperoxy radicals: Ultraviolet absorption spectra and self-reaction rate constants at 298 K". In: *J. Chem. Soc. Faraday Trans.* 88 (17), pp. 2437–2444. DOI: 10.1039/FT9928802437.

Crump, J. G. and J. H. Seinfeld (1981). "Turbulent deposition and gravitational sedimentation of an aerosol in a vessel of arbitrary shape". In: *J. Aerosol Sci.* 12.5, pp. 405–415. DOI: 10.1016/0021-8502(81)90036-7.

Crutzen, P. J., J. Williams, U. Po, P. Hoor, H. Fischer, C. Warneke, R. Holzinger, A. Hansel, W. Lindinger, B. Scheeren, and J. Lelieveld (2000). "High spatial and temporal resolution measurements of primary organics and their oxidation products over the tropical forests of Surinam". In: *Atmos. Environ.* 34, pp. 1161–1165.

Cuadros, F., I. Cachadiña, and W. Ahumada (1996). "Determination of Lennard-Jones interaction parameters using a new procedure". In: *Molecular Engineering* 6.3, pp. 319–325. DOI: 10.1007/bf01886380.

D'Ambro, E. L., B. H. Lee, J. Liu, J. E. Shilling, C. J. Gaston, F. D. Lopez-Hilfiker, S. Schobesberger, R. A. Zaveri, C. Mohr, A. Lutz, Z. Zhang, A. Gold, J. D. Surratt, J. C. Rivera-Rios, F. N. Keutsch, and J. A. Thornton (2017a). "Molecular composition and volatility of isoprene photochemical oxidation secondary organic aerosol under low- and high-NOx conditions". In: *Atmos. Chem. Phys.* 17.1, pp. 159–174. DOI: 10.5194/acp-17-159-2017.

D'Ambro, E. L., K. H. Moller, F. D. Lopez-Hilfiker, S. Schobesberger, J. Liu, J. E. Shilling, B. H. Lee, H. G. Kjaergaard, and J. A. Thornton (2017b). "Isomerization of second generation isoprene peroxy radicals: Epoxide formation and implications for secondary organic aerosol yields". In: *Environ. Sci. Technol.* submitted.

Darer, A. I., N. C. Cole-Filipiak, A. E. O'Connor, and M. J. Elrod (2011). "Formation and stability of atmospherically relevant isoprene-derived organosulfates and organonitrates". In: *Environ. Sci. Technol.* 45.5, pp. 1895–1902. DOI: 10.1021/es103797z.

Davidson, E. A., A. C. de Araujo, P. Artaxo, J. K. Balch, I. F. Brown, M. M. C. Bustamante, M. T. Coe, R. S. DeFries, M. Keller, M. Longo, J. W. Munger, W. Schroeder, B. S. Soares-Filho, C. M. Souza, and S. C. Wofsy (2012). "The Amazon basin in transition". In: *Nature* 481.7381, pp. 321–328.

Day, D. A., P. J. Wooldridge, M. B. Dillon, J. A. Thornton, and R. C. Cohen (2002). "A thermal dissociation laser-induced fluorescence instrument for in situ detection of NO2, peroxy nitrates, alkyl nitrates, and HNO3". In: *J. Geophys Res. - Atmos.* 107.D6. DOI: 10.1029/2001JD000779.

De Haan, D. O., L. N. Hawkins, J. A. Kononenko, J. J. Turley, A. L. Corrigan, M. A. Tolbert, and J. L. Jimenez (2011). "Formation of nitrogen-containing oligomers by methylglyoxal and amines in simulated evaporating cloud droplets". In: *Environ. Sci. Technol.* 45.3, pp. 984–991. DOI: 10.1021/es102933x.

DeCarlo, P. F., J. R. Kimmel, A. Trimborn, M. J. Northway, J. T. Jayne, A. C. Aiken, M. Gonin, K. Fuhrer, T. Horvath, K. S. Docherty, D. R. Worsnop, and J. L. Jimenez (2006). "Field-Deployable, High-Resolution, Time-of-Flight Aerosol Mass Spectrometer". In: *Anal. Chem.* 78.24, pp. 8281–8289. DOI: 10.1021/ac061249n.

Dibble, T. S. (2001). "Reactions of the alkoxy radicals formed following OH-addition to alpha-pinene and beta-pinene. C-C bond scission reactions". In: *J. Am. Chem. Soc.* 123.18, pp. 4228–4234. DOI: 10.1021/ja003553i.

– (2002). "Isomerization of OH-isoprene adducts and hydroxyalkoxy isoprene radicals". In: *J. Phys. Chem. A* 106.28, pp. 6643–6650. DOI: 10.1021/jp025682m.

– (2008). "Failures and limitations of quantum chemistry for two key problems in the atmospheric chemistry of peroxy radicals". In: *Atmos. Environ.* 42.23, pp. 5837–5848. DOI: http://dx.doi.org/10.1016/j.atmosenv.2007.11.005.

DiGangi, J. P., E. S. Boyle, T. Karl, P. Harley, A. Turnipseed, S. Kim, C. Cantrell, R. L. Maudlin Iii, W. Zheng, F. Flocke, S. R. Hall, K. Ullmann, Y. Nakashima, J. B. Paul, G. M. Wolfe, A. R. Desai, Y. Kajii, A. Guenther, and F. N. Keutsch (2011). "First direct measurements of formaldehyde flux via eddy covariance: Implications for missing in-canopy formaldehyde sources". In: *Atmos. Chem. Phys.* 11.20, pp. 10565–10578. DOI: 10.5194/acp-11-10565-2011.

Dillon, T. J. and J. N. Crowley (2008). "Direct detection of OH formation in the reactions of HO2 with CH3C(O)O2 and other substituted peroxy radicals". In: *Atmos. Chem. Phys.* 8.16, pp. 4877–4889. DOI: 10.5194/acp-8-4877-2008.

Ding, X., M. Zheng, L. Yu, X. Zhang, R. J. Weber, B. Yan, A. G. Russell, E. S. Edgerton, and X. Wang (2008). "Spatial and seasonal trends in biogenic secondary organic aerosol tracers and water-soluble organic carbon in the southeastern United States". In: *Environ. Sci. Technol.* 42.14, pp. 5171–5176.

Dlugokencky, E. J. and C. J. Howard (1989). "Studies of nitrate radical reactions with some atmospheric organic compounds at low pressures". In: *J. Phys. Chem.* 93.3, pp. 1091–1096. DOI: 10.1021/j100340a015.

Docherty, K. S., M. Jaoui, E. Corse, J. L. Jimenez, J. H. Offenberg, M. Lewandowski, and T. E. Kleindienst (2013). "Collection efficiency of the aerosol mass spectrometer for chamber-generated secondary organic aerosols". In: *Aerosol Sci. Technol.* 47.3, pp. 294–309. DOI: 10.1080/02786826.2012.752572.

Dodge, M. C. (2000). "Chemical oxidant mechanisms for air quality modeling: Critical review". In: *Atmos. Environ.* 34, pp. 2103–2130.

Donahue, N. M., G. T. Drozd, S. A. Epstein, A. A. Presto, and J. H. Kroll (2011). "Adventures in ozoneland: Down the rabbit-hole". In: *Phys. Chem. Chem. Phys.* 13.23, pp. 10848–10857. DOI: 10.1039/C0CP02564J.

Dong, X., A. C. Schwantes, B. Xi, and P. Wu (2015). "Investigation of the marine boundary layer cloud and CCN properties under coupled and decoupled conditions over the Azores". In: *J. Geophys. Res. - Atmos.* 120.12, pp. 6179–6191. DOI: 10.1002/2014JD022939.

Drewnick, F., S. S. Hings, P. DeCarlo, J. T. Jayne, M. Gonin, K. Fuhrer, S. Weimer, J. L. Jimenez, K. L. Demerjian, S. Borrmann, and D. R. Worsnop (2005). "A New Time-of-Flight Aerosol Mass Spectrometer (TOF-AMS)—Instrument Description and First Field Deployment". In: *Aerosol Science and Technology* 39, pp. 637–658. DOI: 10.1080/02786820500182040.

Drozd, G. T. and N. M. Donahue (2011). "Pressure dependence of stabilized Criegee intermediate formation from a sequence of alkenes". In: *J. Phys. Chem. A* 115.17, pp. 4381–4387. DOI: 10.1021/jp2001089.

Dunker, A. M., B. Koo, and G. Yarwood (2016). "Ozone sensitivity to isoprene chemistry and emissions and anthropogenic emissions in central California". In: *Atmospheric Environment* 145, pp. 326–337. DOI: http://doi.org/10.1016/j.atmosenv.2016.09.048.

Durkee, P. A., K. J. Noone, R. J. Ferek, D. W. Johnson, J. P. Taylor, T. J. Garrett, P. V. Hobbs, J. G. Hudson, C. S. Bretherton, G. Innis, G. M. Frick, W. A. Hoppel, C. D. O'Dowd, L. M. Russell, R. Gasparovic, K. E. Nielsen, S. A. Tessmer, E. Öström, S. R. Osborne, R. C. Flagan, J. H. Seinfeld, and H. Rand (2000). "The impact of ship-produced aerosols on the microstructure and albedo of warm marine stratocumulus clouds: A test of MAST hypotheses 1i and 1ii". In: *J. Atmos. Sci.* 57.16, pp. 2554–2569. DOI: 10.1175/1520-0469(2000)057<2554:tiospa>2.0.co;2.

Dye, C. and K. E. Yttri (2005). "Determination of monosaccharide anhydrides in atmospheric aerosols by use of high-performance liquid chromatography combined with high-resolution mass spectrometry". In: *Anal. Chem.* 77.6, pp. 1853–1858. DOI: 10.1021/ac049461j.

Dzepina, K., J. Arey, L. C. Marr, D. R. Worsnop, D. Salcedo, Q. Zhang, T. B. Onasch, L. T. Molina, M. J. Molina, and J. L. Jimenez (2007). "Detection of particle-phase polycyclic aromatic hydrocarbons in Mexico City using an aerosol mass spectrometer". In: *Int. J. Mass Spec.* 263.2–3, pp. 152–170. DOI: http://doi.org/10.1016/j.ijms.2007.01.010.

Eckart, C. (1930). "The penetration of a potential barrier by electrons". In: *Phys. Rev.* 35.11, pp. 1303–1309.

Eddingsaas, N. C., D. G. VanderVelde, and P. O. Wennberg (2010). "Kinetics and products of the acid-catalyzed ring-opening of atmospherically relevant butyl epoxy alcohols". In: *J. Phys. Chem. A* 114, pp. 8106–8113.

Edney, E. O., T. E. Kleindienst, and E. W. Corse (1986). "Room temperature rate constants for the reaction of OH with selected chlorinated and oxygenated hydrocarbons". In: *Int. J. Chem. Kinetics* 18.12, pp. 1355–1371. DOI: 10.1002/kin.550181207.

Edney, E. O., T. E. Kleindienst, M. Jaoui, M. Lewandowski, J. H. Offenberg, W. Wang, and M. Claeys (2005). "Formation of 2-methyl tetrols and 2-methylglyceric acid in secondary organic aerosol from laboratory irradiated isoprene/NOX/SO2/air mixtures and their detection in ambient PM2.5 samples collected in the eastern United States". In: *Atmos. Environ.* 39.29, pp. 5281–5289. DOI: http://dx.doi.org/10.1016/j.atmosenv.2005.05.031.

Ehn, M., J. A. Thornton, E. Kleist, M. Sipila, H. Junninen, I. Pullinen, M. Springer, F. Rubach, R. Tillmann, B. Lee, F. Lopez-Hilfiker, S. Andres, I.-H. Acir, M. Rissanen, T. Jokinen, S. Schobesberger, J. Kangasluoma, J. Kontkanen, T. Nieminen, T. Kurten, L. B. Nielsen, S. Jorgensen, H. G. Kjaergaard, M. Canagaratna, M. D. Maso, T. Berndt, T. Petaja, A. Wahner, V.-M. Kerminen, M. Kulmala, D. R. Worsnop, J. Wildt, and T. F. Mentel (2014). "A large source of low-volatility secondary organic aerosol". In: *Nature* 506.7489, pp. 476–479. DOI: 10.1038/nature13032.

Ellermann, T., O. J. Nielsen, and H. Skov (1992). "Absolute rate constants for the reaction of NO3 radicals with a series of dienes at 295 K". In: *Chem. Phys. Lett.* 200.3, pp. 224–229. DOI: http://dx.doi.org/10.1016/0009-2614(92)80002-S.

EPA, U. (2015). *National Ambient Air Quality Standards for Ozone*. Tech. rep. 206. Washington, DC: U. S. Environmental Protection Agency, pp. 65292–65468.

Ervens, B. and R. Volkamer (2010). "Glyoxal processing by aerosol multiphase chemistry: Towards a kinetic modeling framework of secondary organic aerosol formation in aqueous particles". In: *Atmos. Chem. Phys.* 10.17, pp. 8219–8244. DOI: 10.5194/acp-10-8219-2010.

Espada, C., J. Grossenbacher, K. Ford, T. Couch, and P. B. Shepson (2005). "The production of organic nitrates from various anthropogenic volatile organic compounds". In: *Int. J. Chem. Kinetics* 37.11, pp. 675–685. DOI: 10.1002/kin.20122.

Fall, R. and R. K. Monson (1992). "Isoprene emission rate and intercellular isoprene concentration as influenced by stomatal distribution and conductance". In: *Plant Physiology* 100, pp. 987–992.

Fan, J. and R. Zhang (2004). "Atmospheric oxidation mechanism of isoprene". In: *Environ. Chem.* 1.3, pp. 140–149.

Fan, S.-M., S. C. Wofsy, P. S. Bakwin, D. J. Jacob, and D. R. Fitzjarrald (1990). "Atmosphere-biosphere exchange of CO2 and O3 in the central Amazon Forest". In: *J. Geophys. Res. - Atmos.* 95.D10, pp. 16851–16864. DOI: 10.1029/JD095iD10p16851.

Fantechi, G., N. Jensen, O. Saastad, J. Hjorth, and J. Peeters (1998). "Reactions of Cl atoms with selected VOCs: Kinetics, products and mechanisms". In: *J. Atmos. Chem.* 31.3, pp. 247–267. DOI: 10.1023/A:1006033910014.

Fenske, J. D., A. S. Hasson, A. W. Ho, and S. E. Paulson (2000). "Measurement of absolute unimolecular and bimolecular rate constants for CH3CHOO generated by the trans-2-butene reaction with ozone in the gas phase". In: *J. Phys. Chem. A* 104.44, pp. 9921–9932. DOI: 10.1021/jp0016636.

Ferek, R. J., T. Garrett, P. V. Hobbs, S. Strader, D. Johnson, J. P. Taylor, K. Nielsen, A. S. Ackerman, Y. Kogan, Q. Liu, B. A. Albrecht, and D. Babb (2000). "Drizzle suppression in ship tracks". In: *J. Atmos. Sci.* 57.16, pp. 2707–2728. DOI: 10.1175/1520-0469(2000)057<2707:DSIST>2.0.CO;2.

Ferge, T., F. Mühlberger, and R. Zimmermann (2005). "Application of infrared laser desorption vacuum-UV single-photon ionization mass spectrometry for analysis of organic compounds from particulate matter filter samples". In: *Anal. Chem.* 77.14, pp. 4528–4538. DOI: 10.1021/ac050296x.

Finlayson-Pitts, B. J., M. J. Ezell, and J. N. Pitts (1989). "Formation of chemically active chlorine compounds by reactions of atmospheric NaCl particles with gaseous N2O5 and ClONO2". In: *Nature* 337.6204, pp. 241–244. DOI: 10.1038/337241a0.

Fiore, A. M., L. W. Horowitz, D. W. Purves, H. Levy, M. J. Evans, Y. Wang, Q. Li, and R. M. Yantosca (2005). "Evaluating the contribution of changes in isoprene emissions to surface ozone trends over the eastern United States". In: *J. Geophys. Res. - Atmos.* 110.D12. D12303. DOI: 10.1029/2004JD005485.

Fleming, Z. L., P. S. Monks, A. R. Rickard, D. E. Heard, W. J. Bloss, P. W. Seakins, T. J. Still, R. Sommariva, M. J. Pilling, R. Morgan, T. J. Green, N. Brough, G. P. Mills, S. A. Penkett, A. C. Lewis, J. D. Lee, A. Saiz-Lopez, and J. M. C. Plane (2006). "Peroxy radical chemistry and the control of ozone photochemistry at Mace Head, Ireland during the summer of 2002". In: *Atmos. Chem. Phys.* 6.8, pp. 2193–2214. DOI: 10.5194/acp-6-2193-2006.

Frisch, M. J., G. W. Trucks, H. B. Schlegel, G. E. Scuseria, M. A. Robb, J. R. Cheeseman, G. Scalmani, V. Barone, B. Mennucci, and G. A. Petersson (2009). *Gaussian 09*. Report. Gaussian, Inc.

Froyd, K. D., S. M. Murphy, D. M. Murphy, J. A. de Gouw, N. C. Eddingsaas, and P. O. Wennberg (2011). "Contribution of isoprene-derives organosulfates to free tropospheric aerosol mass". In: *Proc. Nat'l. Acad. Sci.* 107, pp. 21360–21365.

Fry, J. L., D. C. Draper, K. C. Barsanti, J. N. Smith, J. Ortega, P. M. Winkler, M. J. Lawler, S. S. Brown, P. M. Edwards, R. C. Cohen, and L. Lee (2014). "Secondary organic aerosol formation and organic nitrate yield from NO3 oxidation of biogenic hydrocarbons". In: *Environ. Sci. Technol.* 48.20, pp. 11944–11953. DOI: 10.1021/es502204x.

Fuchs, H., B. Bohn, A. Hofzumahaus, F. Holland, K. D. Lu, S. Nehr, F. Rohrer, and A. Wahner (2011). "Detection of H2 by laser-induced fluorescence: calibration and interferences from RO2 radicals". In: *Atmos. Meas. Tech.* 4.6, pp. 1209–1225. DOI: 10.5194/amt-4-1209-2011.

Fuchs, H., A. Hofzumahaus, F. Rohrer, B. Bohn, T. Brauers, H. P. Dorn, R. Haseler, F. Holland, M. Kaminski, X. Li, K. Lu, S. Nehr, R. Tillmann, R. Wegener, and A. Wahner (2013). "Experimental evidence for efficient hydroxyl radical regeneration in isoprene oxidation". In: *Nature Geosci.* 6.12, pp. 1023–1026. DOI: 10.1038/ngeo1964http://www.nature.com/ngeo/journal/v6/n12/abs/ngeo1964.html#supplementary-information.

Fuentes, J. D., L. Gu, M. Lerdau, R. Atkinson, D. Baldocchi, J. W. Bottenheim, P. Ciccioli, B. Lamb, C. Geron, A. Guenther, T. D. Sharkey, and W. Stockwell (2000). "Biogenic hydrocarbons in the atmospheric boundary layer: A review". In: *Bull. Am. Met. Soc.* 81.7, pp. 1537–1575. DOI: 10.1175/1520-0477(2000)081<1537:BHITAB>2.3.CO;2.

Fuhrer, J. (2002). "Ozone impacts on vegetation". In: *Ozone: Science and Engineering* 24.1, pp. 69–74. DOI: 10.1080/01919510208901597.

Gab, S., E. Hellpointner, W. V. Turner, and F. Korte (1985). "Hydroxymethyl hydroperoxide and bis(hydroxymethyl) peroxide from gas-phase ozonolysis of naturally occurring alkenes". In: *Nature* 316.6028, pp. 535–536.

Gäb, S., W. V. Turner, S. Wolff, K. H. Becker, L. Ruppert, and K. J. Brockmann (1995). "Formation of alkyl and hydroxyalkyl hydroperoxides on ozonolysis in water and in air". In: *Atmos. Environ.* 29.18, pp. 2401–2407. DOI: http://dx.doi.org/10.1016/1352-2310(95)00166-V.

Gaffney, J. S., R. M. Bornick, Y. H. Chen, and N. A. Marley (1998). "Capillary gas chromatographic analysis of nitrogen dioxide and pans with luminol chemiluminescent detection". In: *Atmos. Environ.* 32.8, pp. 1445–1454. DOI: http://dx.doi.org/10.1016/S1352-2310(97)00098-8.

Galloway, M. M., A. J. Huisman, L. D. Yee, A. W. H. Chan, C. L. Loza, J. H. Seinfeld, and F. N. Keutsch (2011). "Yields of oxidized volatile organic compounds during the OH radical initiated oxidation of isoprene, methyl vinyl ketone, and methacrolein under high-NOx conditions". In: *Atmos. Chem. Phys.* 11.21, pp. 10779–10790. DOI: 10.5194/acp-11-10779-2011.

Ganzeveld, L. N., J. Lelieveld, F. J. Dentener, M. C. Krol, A. J. Bouwman, and G.-J. Roelofs (2002). "Global soil-biogenic NOx emissions and the role of canopy processes". In: *J. Geophys. Res.* 107.D16. DOI: 10.1029/2001JD001289.

Gao, S., M. Keywood, N. L. Ng, J. Surratt, V. Varutbangkul, R. Bahreini, R. C. Flagan, and J. H. Seinfeld (2004). "Low-molecular-weight and oligomeric components in secondary organic aerosol from the ozonolysis of cycloalkenes and alpha-pinene". In: *J. Phys. Chem. A* 108.46, pp. 10147–10164. DOI: 10.1021/jp047466e.

Garcia-Montiel, D. C., P. A. Steudler, M. C. Piccolo, J. M. Melillo, C. Neill, and C. C. Cerri (2001). "Controls on soil nitrogen oxide emissions from forest and pastures in the Brazilian Amazon". In: *Global Biogeochemical Cycles* 15.4, pp. 1021–1030. DOI: 10.1029/2000GB001349.

Garden, A. L., F. Paulot, J. D. Crounse, I. J. Maxwell-Cameron, P. O. Wennberg, and H. G. Kjaergaard (2009). "Calculation of conformationally weighted dipole moments useful in ion-molecule collision rate estimates". In: *Chem. Phys. Lett.* 474, pp. 45–50.

Garreaud, R., J. Rutllant, J. Quintana, J. Carrasco, and P. Minnis (2001). "CIMAR–5: A snapshot of the lower troposphere over the subtropical southeast Pacific". In: *Bull. Am. Met. Soc.* 82.10, pp. 2193–2207. DOI: 10.1175/1520-0477(2001)082<2193:CASOTL>2.3.CO;2.

Gaschen, A., D. Lang, M. Kalberer, M. Savi, T. Geiser, A. Gazdhar, C.-M. Lehr, M. Bur, J. Dommen, U. Baltensperger, and M. Geiser (2010). "Cellular responses after exposure of lung cell cultures to secondary organic aerosol particles". In: *Environ. Sci. Technol.* 44.4, pp. 1424–1430. DOI: 10.1021/es902261m.

Gaston, C. J., T. P. Riedel, Z. Zhang, A. Gold, J. D. Surratt, and J. A. Thornton (2014). "Reactive uptake of an isoprene-derived epoxydiol to submicron aerosol particles". In: *Environ. Sci. Technol.* 48, pp. 11178–11186.

Gelencser, A., A. Hoffer, Z. Krivacsy, G. Kiss, A. Molnar, and E. Meszaros (2002). "On the possible origin of humic matter in fine continental aerosol". In: *J. Geophys. Res. - Atmos.* 107.D12. DOI: 10.1029/2001JD001299.

George, I. J., A. Vlasenko, J. G. Slowik, K. Broekhuizen, and J. P. D. Abbatt (2007). "Heterogeneous oxidation of saturated organic aerosols by hydroxyl radicals: Uptake kinetics, condensed-phase products, and particle size change". In: *Atmos. Chem. Phys.* 7.16, pp. 4187–4201. DOI: 10.5194/acp-7-4187-2007.

Gerber, H., B. G. Arends, and A. S. Ackerman (1994). "New microphysics sensor for aircraft use". In: *Atmos. Res.* 31.4, pp. 235–252. DOI: http://dx.doi.org/10.1016/0169-8095(94)90001-9.

Gerber, H., G. Frick, S. P. Malinowski, J. L. Brenguier, and F. Burnet (2005). "Holes and entrainment in stratocumulus". In: *J. Atmos. Sci.* 62.2, pp. 443–459. DOI: 10.1175/JAS-3399.1.

Ghosh, B., A. Bugarin, B. T. Connell, and S. W. North (2010). "Isomer-selective study of the OH-initiated oxidation of isoprene in the presence of O(2) and NO: 2. The major OH addition channel". In: *J. Phys. Chem. A* 114.7, pp. 2553–2560.

Giacopelli, P., K. Ford, C. Espada, and P. B. Shepson (2005). "Comparison of the measured and simulated isoprene nitrate distributions above a forest canopy". In: *J. Geophys. Res. - Atmos.* 110.D1. D01304. DOI: 10.1029/2004JD005123.

Gierczak, T., J. B. Burkholder, R. K. Talukdar, A. Mellouki, S. B. Barone, and A. R. Ravishankara (1997). "Atmospheric fate of methyl vinyl ketone and methacrolein". In: *Journal of Photochemistry and Photobiology* 110, pp. 1–10.

Glantz, P., K. J. Noone, and S. R. Osborne (2003). "Scavenging efficiencies of aerosol particles in marine stratocumulus and cumulus clouds". In: *Quart. J. Royal Met. Soc.* 129.590, pp. 1329–1350. DOI: 10.1256/qj.02.73.

Glowacki, D. R., C.-H. Liang, C. Morley, M. J. Pilling, and S. H. Robertson (2012). "MESMER: An open-source master equation solver for multi-energy well reactions". In: *J. Phys. Chem. A* 116.38, pp. 9545–9560. DOI: 10.1021/jp3051033.

Goldstein, A. H. and I. E. Galbally (2007). "Known and unexplored organic constituents in the Earth's atmosphere". In: *Environ. Sci. Technol.* 41.5, pp. 1514–1521. DOI: 10.1021/es072476p.

Goldstein, A. H., C. D. Koven, C. L. Heald, and I. Y. Fung (2009). "Biogenic carbon and anthropogenic pollutants combine to form a cooling haze over the southeastern United States". In: *Proc. Nat'l. Acad. Sci.* 106.22, pp. 8835–8840. DOI: 10.1073/pnas.0904128106.

Gonzalez, C. and H. B. Schlegel (1989). "An improved algorithm for reaction path following". In: *J. Chem. Phys.* 90.4, pp. 2154–2161. DOI: 10.1063/1.456010.

– (1990). "Reaction path following in mass-weighted internal coordinates". In: *J. Phys. Chem.* 94.14, pp. 5523–5527. DOI: 10.1021/j100377a021.

Gouw, J. A. de and C. J. Howard (1997). "Direct measurement of the rate coefficient for the CH2C(CH3)C(O)O2 + NO reaction using chemical ionization mass spectrometry". In: *J. Phys. Chem. A* 101.46, pp. 8662–8667. DOI: 10.1021/jp972107n.

Gouw, J. de and C. Warneke (2007). "Measurements of volatile organic compounds in the earth's atmosphere using proton-transfer-reaction mass spectrometry". In: *Mass Spec. Rev.* 26.2, pp. 223–257. DOI: 10.1002/mas.20119.

Graedel, T. E. and C. J. Weschler (1981). "Chemistry within aqueous atmospheric aerosols and raindrops". In: *Reviews of Geophysics* 19.4, pp. 505–539. DOI: 10.1029/RG019i004p00505.

Graham, B., O. L. Mayol-Bracero, P. Guyon, G. C. Roberts, S. Decesari, M. C. Facchini, P. Artaxo, W. Maenhaut, P. Köll, and M. O. Andreae (2002). "Water-soluble organic compounds in biomass burning aerosols over Amazonia 1. Characterization by NMR and GC-MS". In: *J. Geophys. Res. - Atmos.* 107.D20. DOI: 10.1029/2001JD000336.

Greenberg, A. and J. F. Liebman (1978). "Kinetic and Thermodynamic Stability". In: *Organic Chemistry: A Series of Monographs*. Vol. 38. Academic Press. Chap. 5, pp. 225–341.

Greene, C. R. and R. Atkinson (1992). "Rate constants for the gas-phase reactions of O3 with a series of alkenes at 296 +/- 2 K". In: *Int. J. Chem. Kinetics* 24.9, pp. 803–811. DOI: 10.1002/kin.550240905.

Greenwald, E. E., B. Ghosh, K. C. Anderson, K. S. Dooley, P. Zou, T. Selby, D. L. Osborn, G. Meloni, C. A. Taatjes, F. Goulay, and S. W. North (2010). "Isomer-selective study of the OH initiated oxidation of isoprene in the presence of O2 and NO. I. The minor inner OH-addition channel". In: *J. Phys. Chem. A* 114.2, pp. 904–912. DOI: 10.1021/jp908543a.

Greenwald, E. E., S. W. North, Y. Georgievskii, and S. J. Klippenstein (2007). "A two transition state model for radical-molecule reactions: Applications to isomeric branching in the OH-isoprene reaction". In: *J. Phys. Chem. A* 111.25, pp. 5582–5592. DOI: 10.1021/jp071412y.

Gregoire, P. (2013). "Implications of ambient ammonia on aerosol acidity and reactive nitrogen measurements". Thesis.

Griesbaum, K., Y. Dong, and K. J. McCullough (1997). "Ozonolyses of Acetylenes: Trapping of alpha-Oxo Carbonyl Oxides by Carbonyl Compounds and Stabilization of alpha-Oxo Ozonides by Derivatizations". In: *J. Org. Chem.* 62.18, pp. 6129–6136. DOI: 10.1021/jo9701795.

Griffin, R. J., D. R. Cocker, R. C. Flagan, and J. H. Seinfeld (1999). "Organic aerosol formation from the oxidation of biogenic hydrocarbons". In: *J. Geophys. Res. - Atmos.* 104.D3, pp. 3555–3567. DOI: 10.1029/1998JD100049.

Griffith, D. W. T. (1996). "Synthetic calibration and quantitative analysis of gas-phase FT-IR spectra". In: *Applied Spectroscopy* 50.1, pp. 59–70.

Grosjean, D., E. Grosjean, and E. L. Williams (1993a). "The reaction of ozone with MPAN, CH2=C(CH3)C(O)OONO2". In: *Environ. Sci. Technol.* 27.12, pp. 2548–2552. DOI: 10.1021/es00048a036.

Grosjean, D., E. L. W. II, and E. Grosjean (1993b). "Atmospheric chemistry of isoprene and of its carbonyl products". In: *Environ. Sci. Technol.* 27.5, pp. 830–840. DOI: 10.1021/es00042a004.

Grosjean, D., E. L. Williams, and E. Grosjean (1993c). "Gas phase reaction of the hydroxyl radical with the unsaturated peroxyacyl nitrate CH2C(CH3)C(O)OONO2". In: *Int. J. Chem. Kinetics* 25.11, pp. 921–929. DOI: 10.1002/kin.550251106.

Grosjean, E. and D. Grosjean (1996). "Rate constants for the gas-phase reaction of ozone with 1,1-disubstituted alkenes". In: *Int. J. Chem. Kinetics* 28.12, pp. 911–918. DOI: 10.1002/(SICI)1097-4601(1996).

– (1998). "Rate constants for the gas-phase reaction of ozone with unsaturated oxygenates". In: *Int. J. Chem. Kinetics* 30.1, pp. 21–29. DOI: 10.1002/(SICI)1097-4601(1998)30:1<21::AID-KIN3>3.0.CO;2-W.

Gross, C. B. M., T. J. Dillon, G. Schuster, J. Lelieveld, and J. N. Crowley (2014). "Direct kinetic study of OH and O3 formation in the reaction of CH3C(O)O2 with HO2". In: *J. Phys. Chem. A* 118.6, pp. 974–985. DOI: 10.1021/jp412380z.

Grossenbacher, J. W., D. J. Barket Jr., P. B. Shepson, M. A. Carroll, K. Olszyna, and E. Apel (2004). "A comparison of isoprene nitrate concentrations at two forest-impacted sites". In: *J. Geophys. Res. - Atmos.* 109.D11. D11311. DOI: 10.1029/2003JD003966.

Guenther, A. B., T. Karl, P. Harley, C. Wiedinmyer, P. I. Palmer, and C. Geron (2006). "Estimates of global terrestrial isoprene emissions using MEGAN (Model of Emissions of Gases and Aerosols from Nature)". In: *Atmos. Chem. Phys.* 6, pp. 3181–3210. DOI: 10.5194/acpd-6-107-2006.

Guenther, A., X. Jiang, C. L. Heald, T. Sakulyanontvittaya, T. Duhl, L. K. Emmons, and X. Wang (2012). "The Model of Emissions of Gases and Aerosols from Nature version 2.1 (MEGAN 2.1): an extended and updated framework for modeling biogenic emissions". In: *Geosci. Model Dev.* 5.6, pp. 1471–1492.

Guenther, A. B. and A. J. Hills (1998). "Eddy covariance measurement of isoprene fluxes". In: *J. Geophys. Res. - Atmos.* 103.D11, pp. 13145–13152. DOI: 10.1029/97JD03283.

Guenther, A., C. N. Hewitt, D. Erickson, R. Fall, C. Geron, T. Graedel, P. Harley, L. Klinger, M. Lerdau, W. A. McKay, T. Pierce, B. Scholes, R. Steinbrecher, R. Tallamraju, J. Taylor, and P. Zimmerman (1995). "A global model of natural volatile organic compound emissions". In: *J. Geophys. Res. - Atmos.* 100.D5, pp. 8873–8892. DOI: 10.1029/94JD02950.

Guérard-Hélaine, C., B. Légeret, C. Fernandes, V. Prévot, C. Forano, and M. Lemaire (2011). "Efficient immobilization of fructose-6-phosphate aldolase in layered double hydroxide: Improved stereoselective synthesis of sugar analogues". In: *New J. Chem.* 35, pp. 776–779.

Guo, H., L. Xu, A. Bougiatioti, K. M. Cerully, S. L. Capps, J. R. Hite Jr, A. G. Carlton, S. H. Lee, M. H. Bergin, N. L. Ng, A. Nenes, and R. J. Weber (2015). "Fine-particle water and pH in the southeastern United States". In: *Atmos. Chem. Phys.* 15.9, pp. 5211–5228. DOI: 10.5194/acp-15-5211-2015.

Gutbrod, R., E. Kraka, R. N. Schindler, and D. Cremer (1997). "Kinetic and theoretical investigation of the gas-phase ozonolysis of isoprene. Carbonyl oxides as an important source for OH radicals in the atmosphere". In: *J. Am. Chem. Soc.* 119.31, pp. 7330–7342. DOI: 10.1021/ja970050c.

Hallquist, M., I. Wängberg, E. Ljungström, I. Barnes, and K.-H. Becker (1999). "Aerosol and product yields from NO3 radical-initiated oxidation of selected monoterpenes". In: *Environ. Sci. Technol.* 33.4, pp. 553–559. DOI: 10.1021/es980292s.

Hansel, A., A. Jordan, R. Holzinger, P. Prazeller, W. Vogel, and W. Lindinger (1995). "Proton transfer reaction mass spectrometry: on-line trace gas analysis at the ppb level". In: *Int. J. Mass Spec. and Ion Processes* 149, pp. 609–619. DOI: http://dx.doi.org/10.1016/0168-1176(95)04294-U.

Hara, K., M. Hayashi, M. Yabuki, M. Shiobara, and C. Nishita-Hara (2014). "Simultaneous aerosol measurements of unusual aerosol enhancement in the troposphere over Syowa Station, Antarctica". In: *Atmos. Chem. Phys.* 14.8, pp. 4169–4183. DOI: 10.5194/acp-14-4169-2014.

Hart, A. B. (1949). "Thermal decomposition of hydrogen peroxide in the vapour phase". In: *Nature* 163, pp. 876–877. DOI: 10.1038/163876b0.

Hasson, A. S., M. Y. Chung, K. T. Kuwata, A. D. Converse, D. Krohn, and S. E. Paulson (2003). "Reaction of Criegee intermediates with water vapor an additional source of OH radicals in alkene ozonolysis?" In: *J. Phys. Chem. A* 107.32, pp. 6176–6182. DOI: 10.1021/jp0346007.

Hasson, A. S., A. W. Ho, K. T. Kuwata, and S. E. Paulson (2001a). "Production of stabilized Criegee intermediates and peroxides in the gas phase ozonolysis of alkenes: 2. Asymmetric and biogenic alkenes". In: *J. Geophys. Res. - Atmos.* 106.D24, pp. 34143–34153. DOI: 10.1029/2001JD000598.

Hasson, A. S., K. T. Kuwata, M. C. Arroyo, and E. B. Petersen (2005). "Theoretical studies of the reaction of hydroperoxy radicals (HO2) with ethyl peroxy (CH3CH2O2), acetyl peroxy (CH3C(O)O2), and acetonyl peroxy (CH3C(O)CH2O2) radicals". In: *Journal of Photochemistry and Photobiology A: Chemistry* 176, pp. 218–230. DOI: 10.1016/j.jphotochem.2005.08.012.

Hasson, A. S., G. Orzechowska, and S. E. Paulson (2001b). "Production of stabilized Criegee intermediates and peroxides in the gas phase ozonolysis of alkenes: 1. Ethene, trans-2-butene, and 2,3-dimethyl-2-butene". In: *J. Geophys. Res. - Atmos.* 106.D24, pp. 34131–34142. DOI: 10.1029/2001JD000597.

Hasson, A. S., G. S. Tyndall, and J. J. Orlando (2004). "A product yield study of the reaction of HO2 radicals with ethyl peroxy (C2H5O2), acetyl peroxy (CH3C(O)O2), and acetonyl peroxy (CH3C(O)CH2O2) radicals". In: *J. Phys. Chem. A* 108.28, pp. 5979–5989. DOI: 10.1021/jp048873t.

Hasson, A. S., G. S. Tyndall, J. J. Orlando, S. Singh, S. Q. Hernandez, S. Campbell, and Y. Ibarra (2012). "Branching ratios for the reaction of selected carbonyl-containing peroxy radicals with hydroperoxy radicals". In: *J. Phys. Chem. A* 116.24, pp. 6264–6281. DOI: 10.1021/jp211799c.

Hatakeyama, S. and H. Akimoto (1994). "Reactions of criegee intermediates in the gas phase". In: *Research on Chemical Intermediates* 20.3, pp. 503–524. DOI: 10.1163/156856794X00432.

Hatakeyama, S., H. Kobayashi, and H. Akimoto (1984). "Gas-phase oxidation of sulfur dioxide in the ozone-olefin reactions". In: *J. Phys. Chem.* 88.20, pp. 4736–4739. DOI: 10.1021/j150664a058.

Hatch, L. E., J. M. Creamean, A. P. Ault, J. D. Surratt, M. N. Chan, J. H. Seinfeld, E. S. Edgerton, Y. Su, and K. A. Prather (2011). "Measurements of isoprene-derived organosulfates in ambient aerosols by aerosol time-of-flight mass spectrometry-part 2: Temporal variability and formation mechanisms". In: *Environ. Sci. Technol.* 45.20, pp. 8648–8655. DOI: 10.1021/es2011836.

Hearn, J. D. and G. D. Smith (2004). "A chemical ionization mass spectrometry method for the online analysis of organic aerosols". In: *Anal. Chem.* 76.10, pp. 2820–2826. DOI: 10.1021/ac049948s.

Hegg, D. and P. Hobbs (1987). *Studies of the mechanisms and rates with which nitrogen species are incorporated into cloud water and precipitation. Final report*.

Hegg, D. A., D. S. Covert, H. Jonsson, and P. A. Covert (2005). "Determination of the transmission efficiency of an aircraft aerosol inlet". In: *Aerosol. Sci. Technol.* 39.10, pp. 966–971. DOI: 10.1080/02786820500377814.

Hellen, H., J. Dommen, A. Metzger, A. Gascho, J. Duplissy, T. Tritscher, A. S. H. Prevot, and U. Baltensperger (2008). "Using proton transfer reaction mass spectrometry for online analysis of secondary organic aerosols". In: *Environ. Sci. Technol.* 42.19, pp. 7347–7353. DOI: 10.1021/es801279m.

Hennigan, C. J., M. H. Bergin, A. G. Russell, A. Nenes, and R. J. Weber (2009). "Gas/particle partitioning of water-soluble organic aerosol in Atlanta". In: *Atmos. Chem. Phys.* 9.11, pp. 3613–3628. DOI: 10.5194/acp-9-3613-2009.

Hennigan, C. J., M. H. Bergin, J. E. Dibb, and R. J. Weber (2008). "Enhanced secondary organic aerosol formation due to water uptake by fine particles". In: *Geophys. Res. Let.* 35.18. DOI: 10.1029/2008GL035046.

Henriksen, N. E. and F. Y. Hansen (2008). *Theories of Molecular Reaction Dynamics: The Microscopic Foundation of Chemical Kinetics*. New York: Oxford University Press.

Henze, D. K., J. H. Seinfeld, N. L. Ng, J. H. Kroll, T. M. Fu, D. J. Jacob, and C. L. Heald (2008). "Global modeling of secondary organic aerosol formation from aromatic hydrocarbons: high- vs. low-yield pathways". In: *Atmos. Chem. Phys.* 8.9, pp. 2405–2420. DOI: 10.5194/acp-8-2405-2008.

Herath, N. and A. G. Suits (2011). "Roaming radical reactions". In: *J. Phys. Chem. Lett.* 2.6, pp. 642–647. DOI: 10.1021/jz101731q.

Herron, J. T. and R. E. Huie (1977). "Stopped-flow studies of the mechanisms of ozone-alkene reactions in the gas phase. Ethylene". In: *J. Am. Chem. Soc.* 99.16, pp. 5430–5435. DOI: 10.1021/ja00458a033.

Herron, J. T., R. I. Martinez, and R. E. Huie (1982). "Kinetics and energetics of the criegee intermediate in the gas phase. I. The criegee intermediate in ozone–alkene reactions". In: *Int. J. Chem. Kinetics* 14.3, pp. 201–224. DOI: 10.1002/kin.550140302.

Hersey, S. P., A. Sorooshian, S. M. Murphy, R. C. Flagan, and J. H. Seinfeld (2009). "Aerosol hygroscopicity in the marine atmosphere: a closure study using high-time-resolution, multiple-RH DASH-SP and size-resolved C-ToF-AMS data". In: *Atmos. Chem. Phys.* 9.7, pp. 2543–2554. DOI: 10.5194/acp-9-2543-2009.

Hewitt, C. N., J. D. Lee, A. R. MacKenzie, M. P. Barkley, N. Carslaw, G. D. Carver, N. A. Chappell, H. Coe, C. Collier, R. Commane, F. Davies, B. Davison, P. DiCarlo, C. F. Di Marco, J. R. Dorsey, P. M. Edwards, M. J. Evans, D. Fowler, K. L. Furneaux, M. Gallagher, A. Guenther, D. E. Heard, C. Helfter, J. Hopkins, T. Ingham, M. Irwin, C. Jones, A. Karunaharan, B. Langford, A. C. Lewis, S. F. Lim, S. M. MacDonald, A. S. Mahajan, S. Malpass, G. McFiggans, G. Mills, P. Misztal, S. Moller, P. S. Monks, E. Nemitz, V. Nicolas-Perea, H. Oetjen, D. E. Oram, P. I. Palmer, G. J. Phillips, R. Pike, J. M. C. Plane, T. Pugh, J. A. Pyle, C. E. Reeves, N. H. Robinson, D. Stewart, D. Stone, L. K. Whalley, and X. Yin (2010). "Overview: oxidant and particle photochemical processes above a south-east Asian tropical rainforest (the OP3 project): introduction, rationale, location characteristics and tools". In: *Atmos. Chem. Phys.* 10.1, pp. 169–199. DOI: 10.5194/acp-10-169-2010.

Hewitt, C. N., A. R. MacKenzie, P. Di Carlo, C. F. Di Marco, J. R. Dorsey, M. Evans, D. Fowler, M. W. Gallagher, J. R. Hopkins, C. E. Jones, B. Langford, J. D. Lee, A. C. Lewis, S. F. Lim, J. McQuaid, P. Misztal, S. J. Moller, P. S. Monks, E. Nemitz, D. E. Oram, S. M. Owen, G. J. Phillips, T. A. M. Pugh, J. A. Pyle, C. E. Reeves, J. Ryder, J. Siong, U. Skiba, and D. J. Stewart (2009). "Nitrogen management is essential to prevent tropical oil palm plantations from causing ground-level ozone pollution". In: *Proc. Nat'l. Acad. Sci.* 106.44, pp. 18447–18451. DOI: 10.1073/pnas.0907541106.

Hildebrandt, L., N. M. Donahue, and S. N. Pandis (2009). "High formation of secondary organic aerosol from the photo-oxidation of toluene". In: *Atmos. Chem. Phys.* 9.9, pp. 2973–2986. DOI: 10.5194/acp-9-2973-2009.

Hildebrandt, L., K. M. Henry, J. H. Kroll, D. R. Worsnop, S. N. Pandis, and N. M. Donahue (2011). "Evaluating the mixing of organic aerosol components using high-resolution aerosol mass spectrometry". In: *Environ. Sci. Technol.* 45.15, pp. 6329–6335. DOI: 10.1021/es200825g.

Hoang, T., J. W. Lauher, and F. W. Fowler (2002). "The topochemical 1,6-polymerization of a trieme". In: *J. Am. Chem. Soc.* 124, pp. 10656–10657.

Hoell, J. M., G. L. Gregory, D. S. McDougal, A. L. Torres, D. D. Davis, J. Bradshaw, M. O. Rodgers, B. A. Ridley, and M. A. Carroll (1987). "Airborne intercomparison of nitric oxide measurement techniques". In: *J. Geophys. Res. - Atmos.* 92.D2, pp. 1995–2008. DOI: 10.1029/JD092iD02p01995.

Hoffmann, T., J. R. Odum, F. Bowman, D. Collines, D. Klockow, R. C. Flagan, and J. H. Seinfeld (1997). "Formation of organic aerosols from the oxidation of biogenic hydrocarbons". In: *J. Atmos. Chem.* 26.2, pp. 189–222. DOI: 10.1023/a:1005734301837.

Hoffmann, T., R. Bandur, U. Marggraf, and M. Linscheid (1998). "Molecular composition of organic aerosols formed in the alpha-pinene/O3 reaction: Implications for new particle formation processes". In: *J. Geophys. Res. - Atmos.* 103.D19, pp. 25569–25578. DOI: 10.1029/98JD01816.

Holben, B. N., T. F. Eck, I. Slutsker, D. Tanré, J. P. Buis, A. Setzer, E. Vermote, J. A. Reagan, Y. J. Kaufman, T. Nakajima, F. Lavenu, I. Jankowiak, and A. Smirnov (1998). "AERONET—A federated instrument network and data archive for aerosol characterization". In: *Remote Sensing of Environment* 66.1, pp. 1–16. DOI: http://dx.doi.org/10.1016/S0034-4257(98)00031-5.

Holloway, A.-L., J. Treacy, H. Sidebottom, A. Mellouki, V. Daële, G. L. Bras, and I. Barnes (2005). "Rate coefficients for the reactions of OH radicals with the keto/enol tautomers of 2,4-pentanedione and 3-methyl-2,4-pentanedione, allyl alcohol and methyl vinyl ketone using the enols and methyl nitrite as photolytic sources of OH". In: *Journal of Photochemistry and Photobiology A: Chemistry* 176.1–3, pp. 183–190. DOI: http://dx.doi.org/10.1016/j.jphotochem.2005.08.031.

Holzinger, R., E. Sanhueza, R. von Kuhlmann, B. Kleiss, L. Donoso, and P. J. Crutzen (2002). "Diurnal cycles and seasonal variation of isoprene and its oxidation products in the tropical savannah atmosphere". In: *Global Biogeochemical Cycles* 16.4. DOI: 10.1029/2001GB001421.

Horie, O. and G. K. Moortgat (1992). "Reactions of CH3C(O)O2 radicals with CH3O2 and HO2 between 263 and 333 K. A product study". In: *J. Chem. Soc. Faraday Trans.* 88 (22), pp. 3305–3312. DOI: 10.1039/FT9928803305.

Horie, O., P. Neeb, S. Limbach, and G. K. Moortgat (1994a). "Formation of formic acid and organic peroxides in the ozonolysis of ethene with added water vapour". In: *Geophys. Res. Lett.* 21.14, pp. 1523–1526. DOI: 10.1029/94GL01174.

Horie, O., P. Neeb, and G. K. Moortgat (1994b). "Ozonolysis of trans- and cis-2-butenes in low parts-per-million concentration ranges". In: *Int. J. Chem. Kinetics* 26.11, pp. 1075–1094. DOI: 10.1002/kin.550261104.

Horowitz, L. W., A. M. Fiore, G. P. Milly, R. C. Cohen, A. Perring, P. J. Wooldridge, P. G. Hess, L. K. Emmons, and J.-F. Lamarque (2007). "Observational constraints on the chemistry of isoprene nitrates over the eastern United States". In: *J. Geophys. Res. - Atmos.* 112.D12. D12S08. DOI: 10.1029/2006JD007747.

Hottle, J. R., A. J. Huisman, J. P. DiGangi, A. Kammrath, M. M. Galloway, K. L. Coens, and F. N. Keutsch (2009). "A laser induced fluorescence-based instrument for in-situ measurements of atmospheric formaldehyde". In: *Environ. Sci. Technol.* 43.3, pp. 790–795. DOI: 10.1021/es801621f.

Hou, H., L. Deng, J. Li, and B. Wang (2005a). "A systematic computational study of the reactions of HO2 with RO2: The HO2 + CH2ClO2, CHCl2O2, and CCl3O2 reactions". In: *J. Phys. Chem. A* 109.41, pp. 9299–9309. DOI: 10.1021/jp052718c.

Hou, H., J. Li, X. Song, and B. Wang (2005b). "A systematic computational study of the reactions of HO2 with RO2: The HO2 + C2H5O2 reaction". In: *J. Phys. Chem. A* 109.49, pp. 11206–11212. DOI: 10.1021/jp0550098.

Hou, H. and B. Wang (2005). "A systematic computational study on the reactions of HO2 with RO2: The HO2 + CH3O2(CD3O2) and HO2 + CH2FO2 reactions". In: *J. Phys. Chem. A* 109.3, pp. 451–460. DOI: 10.1021/jp046329e.

House, H. O. and R. S. Ro (1958). "The stereochemistry of base-catalyzed epoxidation". In: *J. Am. Chem. Soc.* 80.10, pp. 2428–2433.

Howard, J. A. (1972). "Absolute Rate Constants for Reactions of Oxyl Radicals". In: *Advances in Free-Radical Chemistry*. Ed. by G. H. Williams. Vol. IV. London, UK: Logos Press, p. 49.

Hu, D., L. Qiao, J. Chen, X. Ye, X. Yang, T. Cheng, and W. Fang (2010). "Hygroscopicity of inorganic aerosols: Size and relative humidity effects on the growth factor". In: *Aerosol Air Qual. Res.* 10, pp. 255–264.

Hu, K. S., A. I. Darer, and M. J. Elrod (2011). "Thermodynamics and kinetics of the hydrolysis of atmospherically relevant organonitrates and organosulfates". In: *Atmos. Chem. Phys.* 11.16, pp. 8307–8320. DOI: 10.5194/acp-11-8307-2011.

Hu, W., B. B. Palm, D. A. Day, P. Campuzano-Jost, J. E. Krechmer, Z. Peng, S. S. de Sá, S. T. Martin, M. L. Alexander, K. Baumann, L. Hacker, A. Kiendler-Scharr, A. R. Koss, J. A. de Gouw, A. H. Goldstein, R. Seco, S. J. Sjostedt, J. H. Park, A. B. Guenther, S. Kim, F. Canonaco, A. S. H. Prévôt, W. H. Brune, and J. L. Jimenez (2016). "Volatility and lifetime against OH heterogeneous reaction of ambient isoprene-epoxydiols-derived secondary organic aerosol (IEPOX-SOA)". In: *Atmos. Chem. Phys.* 16.18, pp. 11563–11580. DOI: 10.5194/acp-16-11563-2016.

Huang, D., Z. M. Chen, Y. Zhao, and H. Liang (2013). "Newly observed peroxides and the water effect on the formation and removal of hydroxyalkyl hydroperoxides in the ozonolysis of isoprene". In: *Atmos. Chem. Phys.* 13.11, pp. 5671–5683. DOI: 10.5194/acp-13-5671-2013.

Huang, H.-L., W. Chao, and J. J.-M. Lin (2015). "Kinetics of a Criegee intermediate that would survive high humidity and may oxidize atmospheric SO2". In: *Proc. Nat'l. Acad. Sci.* 112.35, pp. 10857–10862. DOI: 10.1073/pnas.1513149112.

Hudman, R. C., N. E. Moore, A. K. Mebust, R. V. Martin, A. R. Russell, L. C. Valin, and R. C. Cohen (2012). "Steps towards a mechanistic model of global soil nitric oxide emissions: implementation and space based-constraints". In: *Atmos. Chem. Phys.* 12.16, pp. 7779–7795. DOI: 10.5194/acp-12-7779-2012.

Huisman, A. J., J. R. Hottle, K. L. Coens, J. P. DiGangi, M. M. Galloway, A. Kammrath, and F. N. Keutsch (2008). "Laser-Induced Phosphorescence for the in Situ Detection of Glyoxal at Part per Trillion Mixing Ratios". In: *Anal. Chem.* 80.15, pp. 5884–5891. DOI: 10.1021/ac800407b.

Hull, L. A. (1978). "MINDO/3 calculations on the stability of Criegee carbonyl oxides". In: *J. Org. Chem.* 43.14, pp. 2780–2785. DOI: 10.1021/jo00408a008.

Hurley, M. D., J. C. Ball, T. J. Wallington, M. P. Sulbaek Andersen, O. J. Nielsen, D. A. Ellis, J. W. Martin, and S. A. Mabury (2006). "Atmospheric chemistry of n-CxF2x+1CHO (x = 1, 2, 3, 4): Fate of n-CxF2x+1C(O) radicals". In: *J. Phys. Chem. A* 110.45, pp. 12443–12447. DOI: 10.1021/jp064029m.

Hyer, E. J., J. S. Reid, and J. Zhang (2011). "An over-land aerosol optical depth data set for data assimilation by filtering, correction, and aggregation of MODIS Collection 5 optical depth retrievals". In: *Atmos. Meas. Tech.* 4.3, pp. 379–408. DOI: 10.5194/amt-4-379-2011.

Iinuma, Y., C. Müller, T. Berndt, O. Böge, M. Claeys, and H. Herrmann (2007). "Evidence for the existence of organosulfates from beta-pinene ozonolysis in ambient secondary organic aerosol". In: *Environ. Sci. Technol.* 41.19, pp. 6678–6683. DOI: 10.1021/es070938t.

Ion, A. C., R. Vermeylen, I. Kourtchev, J. Cafmeyer, X. Chi, A. Gelencsér, W. Maenhaut, and M. Claeys (2005). "Polar organic compounds in rural PM2.5 aerosols from K-puszta, Hungary, during a 2003 summer field campaign: Sources and diel variations". In: *Atmos. Chem. Phys.* 5.7, pp. 1805–1814. DOI: 10.5194/acp-5-1805-2005.

Ip, H. S. S., X. H. H. Huang, and J. Z. Yu (2009). "Effective Henry's law constants of glyoxal, glyoxylic acid, and glycolic acid". In: *Geophys. Res. Let.* 36.1. DOI: 10.1029/2008GL036212.

Iranpoor, N. and P. Salehi (1994). "Highly efficient, regio- and stereoselective alcoholysis of epoxides catalyzed with iron(III) chloride". In: *Synthesis* 1994.11, pp. 1152–1154. DOI: 10.1055/s-1994-25661.

Iranpoor, N., T. Tarrian, and Z. Movahedi (1996). "FeCl3-6H2O supported on SiO2 catalysed ring opening of epoxides with alcohols, acetic acid, water, chloride, bromide and nitrate ions". In: *Synthesis* 1996.12, pp. 1473–1476. DOI: 10.1055/s-1996-4416.

Isaacman, G., K. R. Wilson, A. W. H. Chan, D. R. Worton, J. R. Kimmel, T. Nah, T. Hohaus, M. Gonin, J. H. Kroll, D. R. Worsnop, and A. H. Goldstein (2012). "Improved resolution of hydrocarbon structures and constitutional isomers in complex

mixtures using gas chromatography-vacuum ultraviolet-mass spectrometry". In: *Anal. Chem.* 84.5, pp. 2335–2342. DOI: 10.1021/ac2030464.

Isaacman-VanWertz, G. (2014). Thesis.

Isidorov, V. A. (1990). *Organic Chemistry of the Earth's Atmosphere*. Springer-Verlag. ISBN: 978-3-642-75096-0.

Ito, A., S. Sillman, and J. E. Penner (2007). "Effects of additional nonmethane volatile organic compounds, organic nitrates, and direct emissions of oxygenated organic species on global tropospheric chemistry". In: *J. Geophys. Res. - Atmos.* 112.D6.

Jacob, D. (1999). *Introduction to Atmospheric Chemistry*. Princeton University Press. ISBN: 9780691001852. URL: https://books.google.com/books?id=14whM9fEOzsC.

Jacob, D. J. and P. S. Bakwin (1991). "Cycling of NOx in Tropical Forest Canopies". In: *Microbial Production and Consumption of Greenhouse Gases: Methane, Nitrogen Oxides, and Halomethanes*. Ed. by J. E. Rogers and W. B. Whitman. Washington, D. C.: American Society for Microbiology, pp. 237–253.

Jacob, D. J. and S. C. Wofsy (1988). "Photochemistry of biogenic emissions over the Amazon forest". In: *J. Geophys. Res. - Atmos.* 93.D2, pp. 1477–1486. DOI: 10.1029/JD093iD02p01477.

Jacobs, M. I., W. J. Burke, and M. J. Elrod (2014). "Kinetics of the reactions of isoprene-derived hydroxynitrates: Gas phase epoxide formation and solution phase hydrolysis". In: *Atmos. Chem. Phys.* 14.17, pp. 8933–8946. DOI: 10.5194/acp-14-8933-2014.

Jacobs, M. I., A. D. Darer, and M. J. Elrod (2013). "Rate constants and products of the OH reaction with isoprene-derived epoxides". In: *Environ. Sci. Technol.* 47.22, pp. 12868–12876. DOI: 10.1021/es403340g.

Jacobsen, E. N., F. Kakiuchi, R. G. Konsler, J. F. Larrow, and M. Tokunaga (1997). "Enantioselective catalytic ring opening of epoxides with carboxylic acids". In: *Tetrahedron Letters* 38.5, pp. 773–776. DOI: http://dx.doi.org/10.1016/S0040-4039(96)02414-8.

Jang, M., N. M. Czoschke, S. Lee, and R. M. Kamens (2002). "Heterogeneous atmospheric aerosol production by acid-catalyzed particle-phase reactions". In: *Science* 298, pp. 814–817.

Jayne, J. T., D. C. Leard, X. Zhang, P. Davidovits, K. A. Smith, C. E. Kolb, and D. R. Worsnop (2000). "Development of an aerosol mass spectrometer for size and composition analysis of submicron particles". In: *Aerosol Sci. Technol.* 33.1-2, pp. 49–70. DOI: 10.1080/027868200410840.

Jenkin, M. E., A. A. Boyd, and R. Lesclaux (1998). "Peroxy radical kinetics resulting from the OH-initiated oxidation of 1,3-butadiene, 2,3-dimethyl-1,3-butadiene and isoprene". In: *J. Atmos. Chem.* 29, pp. 267–298.

Jenkin, M. E., M. D. Hurley, and T. J. Wallington (2007). "Investigation of the radical product channel of the CH3C(O)O2 + HO2 reaction in the gas phase". In: *Phys. Chem. Chem. Phys.* 9 (24), pp. 3149–3162. DOI: 10.1039/B702757E.

– (2008). "Investigation of the radical product channel of the CH3C(O)CH2O2 + HO2 reaction in the gas phase". In: *Phys. Chem. Chem. Phys.* 10.29, pp. 4274–4280. DOI: 10.1039/B802898B.

– (2010). "Investigation of the radical product channel of the CH3OCH2O2 + HO2 reaction in the gas phase". In: *J. Phys. Chem. A* 114.1, pp. 408–416. DOI: 10.1021/jp908158w.

Jenkin, M. E., S. M. Saunders, and M. J. Pilling (1997). "The tropospheric degradation of volatile organic compounds: A protocol for mechanism development". In: *Atmos. Environ.* 31, pp. 81–104.

Jenkin, M. E., K. P. Wyche, C. J. Evans, T. Carr, P. S. Monks, M. R. Alfarra, M. H. Barley, G. B. McFiggans, J. C. Young, and A. R. Rickard (2012). "Development and chamber evaluation of the MCM v3.2 degradation scheme for b-caryophyllene". In: *Atmos. Chem. Phys.* 12, pp. 5275–5308.

Jenkin, M. E., J. C. Young, and A. R. Rickard (2015). "The MCM v3.3.1 degradation scheme for isoprene". In: *Atmos. Chem. Phys.* 15.20, pp. 11433–11459. DOI: 10.5194/acp-15-11433-2015.

Jenkin, M. E. and G. D. Hayman (1995). "Kinetics of reactions of primary, secondary and tertiary beta-hydroxy peroxyl radicals". In: *J. Chem. Soc. Faraday Trans.* 91.13, p. 1911. DOI: 10.1039/ft9959101911.

Jerrett, M., R. T. Burnett, C. A. Pope, K. Ito, G. Thurston, D. Krewski, Y. Shi, E. Calle, and M. Thun (2009). "Long-term ozone exposure and mortality". In: *New England J. Med.* 360.11, pp. 1085–1095. DOI: 10.1056/NEJMoa0803894.

Jimenez, J. L., M. R. Canagaratna, N. M. Donahue, A. S. H. Prevot, Q. Zhang, J. H. Kroll, P. F. DeCarlo, J. D. Allan, H. Coe, N. L. Ng, A. C. Aiken, K. S. Docherty, I. M. Ulbrich, A. P. Grieshop, A. L. Robinson, J. Duplissy, J. D. Smith, K. R. Wilson, V. A. Lanz, C. Hueglin, Y. L. Sun, J. Tian, A. Laaksonen, T. Raatikainen, J. Rautiainen, P. Vaattovaara, M. Ehn, M. Kulmala, J. M. Tomlinson, D. R. Collins, M. J. Cubison, J. Dunlea, J. A. Huffman, T. B. Onasch, M. R. Alfarra, P. I. Williams, K. Bower, Y. Kondo, J. Schneider, F. Drewnick, S. Borrmann, S. Weimer, K. Demerjian, D. Salcedo, L. Cottrell, R. Griffin, A. Takami, T. Miyoshi, S. Hatakeyama, A. Shimono, J. Y. Sun, Y. M. Zhang, K. Dzepina, J. R. Kimmel, D. Sueper, J. T. Jayne, S. C. Herndon, A. M. Trimborn, L. R. Williams, E. C. Wood, A. M. Middlebrook, C. E. Kolb, U. Baltensperger, and D. R. Worsnop (2009). "Evolution of organic aerosols in the atmosphere". In: *Science* 326, pp. 1525–1529.

Jimenez, J. L., J. T. Jayne, Q. Shi, C. E. Kolb, D. R. Worsnop, I. Yourshaw, J. H. Seinfeld, R. C. Flagan, X. Zhang, K. A. Smith, J. W. Morris, and P. Davidovits (2003).

"Ambient aerosol sampling using the Aerodyne Aerosol Mass Spectrometer". In: *J. Geophys. Res. - Atmos.* 108.D7. DOI: 10.1029/2001JD001213.

Johnson, D. and G. Marston (2008). "The gas-phase ozonolysis of unsaturated volatile organic compounds in the troposphere". In: *Chem. Soc. Rev.* 37.4, pp. 699–716. DOI: 10.1039/B704260B.

Johnson, T. J., R. L. Sams, T. A. Blake, S. W. Sharpe, and P. M. Chu (2002). "Removing aperture-induced artifacts from fourier transform infrared intensity values". In: *Applied Optics* 41.15, pp. 2831–2839. DOI: 10.1364/AO.41.002831.

Jokinen, T., M. Sipilä, S. Richters, V.-M. Kerminen, P. Paasonen, F. Stratmann, D. Worsnop, M. Kulmala, M. Ehn, H. Herrmann, and T. Berndt (2014). "Rapid autoxidation forms highly oxidized RO2 radicals in the atmosphere". In: *Angewandte Chemie Int. Ed.* 53.52, pp. 14596–14600. DOI: 10.1002/anie.201408566.

Jones, C. R., C. S. Bretherton, and D. Leon (2011). "Coupled vs. decoupled boundary layers in VOCALS-REx". In: *Atmos. Chem. Phys.* 11.14, pp. 7143–7153. DOI: 10.5194/acp-11-7143-2011.

Jordan, A., S. Haidacher, G. Hanel, E. Hartungen, J. Herbig, L. Märk, R. Schottkowsky, H. Seehauser, P. Sulzer, and T. D. Märk (2009). "An online ultra-high sensitivity Proton-transfer-reaction mass-spectrometer combined with switchable reagent ion capability (PTR + SRI - MS)". In: *Int. J. Mass Spec.* 286.1, pp. 32–38. DOI: http://dx.doi.org/10.1016/j.ijms.2009.06.006.

Jørgensen, S., H. C. Knap, R. V. Otkjær, A. M. Jensen, M. L. H. Kjeldsen, P. O. Wennberg, and H. G. Kjaergaard (2016). "Rapid hydrogen shift scrambling in hydroperoxy-substituted organic peroxy radicals". In: *J. Phys. Chem. A* 120.2, pp. 266–275. DOI: 10.1021/acs.jpca.5b06768.

Junninen, H., M. Ehn, T. Petäjä, L. Luosujärvi, T. Kotiaho, R. Kostiainen, U. Rohner, M. Gonin, K. Fuhrer, M. Kulmala, and D. R. Worsnop (2010). "A high-resolution mass spectrometer to measure atmospheric ion composition". In: *Atmos. Meas. Tech.* 3.4, pp. 1039–1053. DOI: 10.5194/amt-3-1039-2010.

Kalberer, M., D. Paulsen, M. Sax, M. Steinbacher, J. Dommen, A. S. H. Prevot, R. Fisseha, E. Weingartner, V. Frankevich, R. Zenobi, and U. Baltensperger (2004). "Identification of polymers as major components of atmospheric organic aerosols". In: *Science* 303, pp. 1659–1662.

Kamens, R. M., M. W. Gery, H. E. Jeffries, M. Jackson, and E. I. Cole (1982). "Ozone–isoprene reactions: Product formation and aerosol potential". In: *Int. J. Chem. Kinetics* 14.9, pp. 955–975. DOI: 10.1002/kin.550140902.

Kampf, C. J., E. M. Waxman, J. G. Slowik, J. Dommen, L. Pfaffenberger, A. P. Praplan, A. S. H. Prevot, U. Baltensperger, T. Hoffmann, and R. Volkamer (2013). "Effective Henry's Law partitioning and the salting constant of glyoxal in aerosols containing sulfate". In: *Environ. Sci. Technol.* 47, pp. 4236–4244.

Kanakidou, M., J. H. Seinfeld, S. N. Pandis, I. Barnes, F. J. Dentener, M. C. Facchini, R. Van Dingenen, B. Ervens, A. Nenes, C. J. Nielsen, E. Swietlicki, J. P. Putaud, Y. Balkanski, S. Fuzzi, J. Horth, G. K. Moortgat, R. Winterhalter, C. E. L. Myhre, K. Tsigaridis, E. Vignati, E. G. Stephanou, and J. Wilson (2005). "Organic aerosol and global climate modelling: A review". In: *Atmos. Chem. Phys.* 5.4, pp. 1053–1123. DOI: 10.5194/acp-5-1053-2005.

Kaplan, W. A., S. C. Wofsy, M. Keller, and J. M. Da Costa (1988). "Emission of NO and deposition of O3 in a tropical forest system". In: *J. Geophys. Res. - Atmos.* 93.D2, pp. 1389–1395. DOI: 10.1029/JD093iD02p01389.

Karl, M., T. Brauers, H.-P. Dorn, F. Holland, M. Komenda, D. Poppe, F. Rohrer, L. Rupp, A. Schaub, and A. Wahner (2004). "Kinetic study of the OH-isoprene and O3-isoprene reaction in the atmosphere simulation chamber, SAPHIR". In: *Geophys. Res. Lett.* 31.5. L05117. DOI: 10.1029/2003GL019189.

Karl, M., H. P. Dorn, F. Holland, R. Koppmann, D. Poppe, L. Rupp, A. Schaub, and A. Wahner (2006). "Product study of the reaction of OH radicals with isoprene in the atmosphere simulation chamber SAPHIR". In: *J. Atmos. Chem.* 55.2, pp. 167–187. DOI: 10.1007/s10874-006-9034-x.

Karl, T., A. Guenther, A. Turnipseed, G. Tyndall, P. Artaxo, and S. Martin (2009). "Rapid formation of isoprene photo-oxidation products observed in Amazonia". In: *Atmos. Chem. Phys.* 9.20, pp. 7753–7767. DOI: 10.5194/acp-9-7753-2009.

Karl, T., A. Guenther, R. J. Yokelson, J. Greenberg, M. Potosnak, D. R. Blake, and P. Artaxo (2007). "The tropical forest and fire emissions experiment: Emission, chemistry, and transport of biogenic volatile organic compounds in the lower atmosphere over Amazonia". In: *J. Geophys. Res. - Atmos.* 112.D18. DOI: 10.1029/2007JD008539.

Karl, T., P. K. Misztal, H. H. Jonsson, S. Shertz, A. H. Goldstein, and A. B. Guenther (2013). "Airborne flux measurements of BVOCs above Californian oak forests: Experimental investigation of surface and entrainment fluxes, OH densities, and Damköhler numbers". In: *J. Atmos. Sci.* 70.10, pp. 3277–3287. DOI: 10.1175/jas-d-13-054.1.

Kerdouci, J., B. Picquet-Varrault, and J.-F. Doussin (2010). "Prediction of rate constants for gas-phase reactions of nitrate radical with organic compounds: A new structure–activity relationship". In: *ChemPhysChem* 11.18, pp. 3909–3920. DOI: 10.1002/cphc.201000673.

Khamaganov, V. G. and R. A. Hites (2001). "Rate constants for the gas-phase reactions of ozone with isoprene, alpha- and beta-pinene, and limonene as a function of temperature". In: *J. Phys. Chem. A* 105.5, pp. 815–822. DOI: 10.1021/jp002730z.

Kholodar, S. A. and A. S. Murkin (2013). "DXP reductoisomerase: Reaction of the substrate in pieces reveals a catalytic role for the nonreacting phosphodianion group". In: *Biochemistry* 52, pp. 2302–2308.

Kiendler-Scharr, A., J. Wildt, M. D. Maso, T. Hohaus, E. Kleist, T. F. Mentel, R. Tillmann, R. Uerlings, U. Schurr, and A. Wahner (2009). "New particle formation in forests inhibited by isoprene emissions". In: *Nature* 461.7262, pp. 381–384. DOI: http://www.nature.com/nature/journal/v461/n7262/suppinfo/nature08292_S1.html.

Kim, S., G. M. Wolfe, L. Mauldin, C. Cantrell, A. Guenther, T. Karl, A. Turnipseed, J. Greenberg, S. R. Hall, K. Ullmann, E. Apel, R. Hornbrook, Y. Kajii, Y. Nakashima, F. N. Keutsch, J. P. DiGangi, S. B. Henry, L. Kaser, R. Schnitzhofer, M. Graus, A. Hansel, W. Zheng, and F. F. Flocke (2013). "Evaluation of HOx sources and cycling using measurement-constrained model calculations in a 2-methyl-3-butene-2-ol (MBO) and monoterpene (MT) dominated ecosystem". In: *Atmos. Chem. Phys.* 13.4, pp. 2031–2044. DOI: 10.5194/acp-13-2031-2013.

Kirchner, F. and W. R. Stockwell (1996). "Effect of peroxy radical reactions on the predicted concentrations of ozone, nitrogenous compounds, and radicals". In: *J. Geophys. Res. - Atmos.* 101.D15, pp. 21007–21022. DOI: 10.1029/96JD01519.

Kjaergaard, H. G., H. C. Knap, K. B. Ornso, S. Jorgensen, J. D. Crounse, F. Paulot, and P. O. Wennberg (2012). "Atmospheric fate of methacrolein. 2. Formation of lactone and implications for organic aerosol production". In: *J. Phys. Chem. A* 116, pp. 5763–5768.

Kjaergaard, H. G., T. Kurtén, L. B. Nielsen, S. Jørgensen, and P. O. Wennberg (2013). "Criegee intermediates react with ozone". In: *J. Phys. Chem. Lett.* 4.15, pp. 2525–2529. DOI: 10.1021/jz401205m.

Klawatsch-Carrasco, N., J. F. Doussin, and P. Carlier (2004). "Absolute rate constants for the gas-phase ozonolysis of isoprene and methylbutenol". In: *Int. J. Chem. Kinetics* 36.3, pp. 152–156. DOI: 10.1002/kin.10175.

Kleindienst, T. E., M. Lewandowski, J. H. Offenberg, M. Jaoui, and E. O. Edney (2009). "The formation of secondary organic aerosol from the isoprene + OH reaction in the absence of NOx". In: *Atmos. Chem. Phys.* 9.17, pp. 6541–6558. DOI: 10.5194/acp-9-6541-2009.

Kleindienst, T. E., G. W. Harris, and J. N. Pitts (1982). "Rates and temperature dependences of the reaction of hydroxyl radical with isoprene, its oxidation products, and selected terpenes". In: *Environ. Sci. Technol.* 16.12, pp. 844–846. DOI: 10.1021/es00106a004.

Kleindienst, T. E., M. Jaoui, M. Lewandowski, J. H. Offenberg, C. W. Lewis, P. V. Bhave, and E. O. Edney (2007). "Estimates of the contributions of biogenic and anthropogenic hydrocarbons to secondary organic aerosol at a southeastern US location". In: *Atmos. Environ.* 41.37, pp. 8288–8300. DOI: http://doi.org/10.1016/j.atmosenv.2007.06.045.

Knap, H. C., S. Jørgensen, and H. G. Kjaergaard (2015). "Theoretical investigation of the hydrogen shift reactions in peroxy radicals derived from the atmospheric

decomposition of 3-methyl-3-buten-1-ol (MBO331)". In: *Chem. Phys. Lett.* 619, pp. 236–240. DOI: http://dx.doi.org/10.1016/j.cplett.2014.11.056.

Knizia, G., T. B. Adler, and H. J. Werner (2009). "Simplified CCSD(T)-F12 methods: Theory and benchmarks". In: *J. Chem. Phys.* 130.5, p. 054104. DOI: 10.1063/1.3054300.

Knote, C., P. Tuccella, G. Curci, L. Emmons, J. J. Orlando, S. Madronich, R. Baro, P. Jimenez-Guerrero, D. Luecken, C. Hogrefe, R. Forkel, J. Werhahn, M. Hirtl, J. L. Perez, R. S. Jose, L. Giordano, D. Brunner, K. Yahya, and Y. Zhang (2015). "Influence of the choice of gas-phase mechanism on predictions of key gaseous pollutants during the AQMEII phase-2 intercomparison". In: *Atmos. Environ.* 115, pp. 553–568. DOI: http://doi.org/10.1016/j.atmosenv.2014.11.066.

Knyazev, V. D. and I. R. Slagle (1995). "Kinetics of the reaction of vinyl radical With molecular oxygen". In: *J. Phys. Chem.* 99.8, pp. 2247–2249. DOI: 10.1021/j100008a002.

Koch, S., R. Winterhalter, E. Uherek, A. Kolloff, P. Neeb, and G. K. Moortgat (2000). "Formation of new particles in the gas-phase ozonolysis of monoterpenes". In: *Atmos. Environ.* 34.23, pp. 4031–4042. DOI: http://dx.doi.org/10.1016/S1352-2310(00)00133-3.

Kourtchev, I., T. Ruuskanen, W. Maenhaut, M. Kulmala, and M. Claeys (2005). "Observation of 2-methyltetrols and related photo-oxidation products of isoprene in boreal forest aerosols from Hyytiälä, Finland". In: *Atmos. Chem. Phys.* 5, pp. 2761–2770.

Krechmer, J. E., M. M. Coggon, P. Massoli, T. B. Nguyen, J. D. Crounse, W. Hu, D. A. Day, G. S. Tyndall, D. K. Henze, J. C. Rivera-Rios, J. B. Nowak, J. R. Kimmel, R. L. Mauldin, H. Stark, J. T. Jayne, M. Sipilä, H. Junninen, J. M. S. Clair, X. Zhang, P. A. Feiner, L. Zhang, D. O. Miller, W. H. Brune, F. N. Keutsch, P. O. Wennberg, J. H. Seinfeld, D. R. Worsnop, J. L. Jimenez, and M. R. Canagaratna (2015). "Formation hydroxyhydroperoxide low-NO oxidation". In: *Environ. Sci. Technol.* 49.17, pp. 10330–10339. DOI: 10.1021/acs.est.5b02031.

Kroll, J. H., J. S. Clarke, N. M. Donahue, and J. G. Anderson (2001). "Mechanism of HOx formation in the gas-phase ozone-alkene reaction. 1. Direct, pressure-dependent Mmasurements of prompt OH yields". In: *J. Phys. Chem. A* 105.9, pp. 1554–1560. DOI: 10.1021/jp002121r.

Kroll, J. H., N. M. Donahue, V. J. Cee, K. L. Demerjian, and J. G. Anderson (2002). "Gas-phase ozonolysis of alkenes: Formation of OH from anti carbonyl oxides". In: *J. Am. Chem. Soc.* 124.29, pp. 8518–8519. DOI: 10.1021/ja0266060.

Kuhlmann, R. V. and M. G. Lawrence (2004). "Sensitivities in global scale modeling of isoprene". In: *Atmos. Chem. Phys.* 4, pp. 1–17.

Kuhlmann, R. von, M. G. Lawrence, U. Pöschl, and P. J. Crutzen (2004). "Sensitivities in global scale modeling of isoprene". In: *Atmos. Chem. Phys.* 4.1, pp. 1–17. DOI: 10.5194/acp-4-1-2004.

Kuhn, U., M. O. Andreae, C. Ammann, A. C. Araújo, E. Brancaleoni, P. Ciccioli, T. Dindorf, M. Frattoni, L. V. Gatti, L. Ganzeveld, B. Kruijt, J. Lelieveld, J. Lloyd, F. X. Meixner, A. D. Nobre, U. Pöschl, C. Spirig, P. Stefani, A. Thielmann, R. Valentini, and J. Kesselmeier (2007). "Isoprene and monoterpene fluxes from Central Amazonian rainforest inferred from tower-based and airborne measurements, and implications on the atmospheric chemistry and the local carbon budget". In: *Atmos. Chem. Phys.* 7.11, pp. 2855–2879. DOI: 10.5194/acp-7-2855-2007.

Künzi, L., M. Krapf, N. Daher, J. Dommen, N. Jeannet, S. Schneider, S. Platt, J. G. Slowik, N. Baumlin, M. Salathe, A. S. H. Prévôt, M. Kalberer, C. Strähl, L. Dümbgen, C. Sioutas, U. Baltensperger, and M. Geiser (2015). "Toxicity of aged gasoline exhaust particles to normal and diseased airway epithelia". In: *Scientific Reports* 5, p. 11801. DOI: 10.1038/srep11801http://www.nature.com/articles/srep11801#supplementary-information.

Kurtén, T., J. R. Lane, S. Jørgensen, and H. G. Kjaergaard (2011). "A computational study of the oxidation of SO2 to SO3 by gas-phase organic oxidants". In: *J. Phys. Chem. A* 115.31, pp. 8669–8681. DOI: 10.1021/jp203907d.

Kuwata, K. T., M. R. Hermes, M. J. Carlson, and C. K. Zogg (2010). "Computational studies of the isomerization and hydration reactions of acetaldehyde oxide and methyl vinyl carbonyl oxide". In: *J. Phys. Chem. A* 114.34, pp. 9192–9204. DOI: 10.1021/jp105358v.

Kuwata, K. T. and L. C. Valin (2008). "Quantum chemical and RRKM/master equation studies of isoprene ozonolysis: Methacrolein and methacrolein oxide". In: *Chem. Phys. Lett.* 451.4–6, pp. 186–191. DOI: http://dx.doi.org/10.1016/j.cplett.2007.11.092.

Kuwata, M., S. R. Zorn, and S. T. Martin (2012). "Using elemental ratios to predict the density of organic material composed of carbon, hydrogen, and oxygen". In: *Environ. Sci. Technol.* 46.2, pp. 787–794. DOI: 10.1021/es202525q.

Kuzuyama, T. and H. Seto (2003). "Diversity of the biosynthesis of the isoprene units". In: *Natural Product Reports* 20.2, pp. 171–183. DOI: 10.1039/B109860H.

Kwan, A. J., A. W. H. Chan, N. L. Ng, H. G. Kjaergaard, J. H. Seinfeld, and P. O. Wennberg (2012). "Peroxy radical chemistry and OH radical production during the NO3-initiated oxidation of isoprene". In: *Atmos. Chem. Phys.* 12.16, pp. 7499–7515. DOI: 10.5194/acp-12-7499-2012.

Kwok, E. S. C. and R. Atkinson (1995). "Estimation of hydroxyl radical reaction rate constants for gas-phase organic compounds using a structure-reactivity relationship: An update." In: *Atmos. Environ.* 29, pp. 1685–1695.

Kwok, E. S. C., S. M. Aschmann, J. Arey, and R. Atkinson (1996). "Product formation from the reaction of the NO3 radical with isoprene and rate constants for the reactions of methacrolein and methyl vinyl ketone with the NO3 radical". In:

Int. J. Chem. Kinetics 28.12, pp. 925–934. DOI: 10.1002/(SICI)1097-4601(1996)28:12<925::AID-KIN10>3.0.CO;2-B.

LaFranchi, B. W. and G. A. Petrucci (2006). "A comprehensive characterization of photoelectron resonance capture ionization aerosol mass spectrometry for the quantitative and qualitative analysis of organic particulate matter". In: *Int. J. Mass Spec.* 258.1–3, pp. 120–133. DOI: http://doi.org/10.1016/j.ijms.2006.06.013.

Lancar, I. T., V. Daele, G. Lebras, and G. Poulet (1991). "Reaction of NO3 radicals with 2,3-dimethylbut-2-ene, buta-1,3-diene and 2,3-dimethylbuta-1,3-diene". In: *J. Chim. Phys. Pcb* 88.9, pp. 1777–1792.

Laskin, A., R. C. Moffet, M. K. Gilles, J. D. Fast, R. A. Zaveri, B. Wang, P. Nigge, and J. Shutthanandan (2012). "Tropospheric chemistry of internally mixed sea salt and organic particles: Surprising reactivity of NaCl with weak organic acids". In: *J. Geophys. Res. - Atmos.* 117.D15. DOI: 10.1029/2012JD017743.

Lavrich, R. J. and M. D. Hays (2007). "Validation studies of thermal extraction-GC/MS applied to source emissions aerosols. 1. Semivolatile analyte-nonvolatile matrix interactions". In: *Anal. Chem.* 79.10, pp. 3635–3645. DOI: 10.1021/ac0623282.

Le Crane, J.-P., J.-C. Rayez, E. Villenave, and M.-T. Rayez (2006). "A reinvestigation of the kinetics and the mechanism of the CH3C(O)O-2+HO2 reaction using both experimental and theoretical approaches". In: *Phys. Chem. Chem. Phys.* 8, pp. 2163–2171. DOI: 10.1039/b518321a.

Leather, K. E., M. R. McGillen, M. C. Cooke, S. R. Utembe, A. T. Archibald, M. E. Jenkin, R. G. Derwent, D. E. Shallcross, and C. J. Percival (2012). "Acid-yield measurements of the gas-phase ozonolysis of ethene as a function of humidity using Chemical Ionisation Mass Spectrometry (CIMS)". In: *Atmos. Chem. Phys.* 12.1, pp. 469–479. DOI: 10.5194/acp-12-469-2012.

Lee, C.-T. and W.-C. Hsu (2000). "The measurement of liquid water mass associated with collected hygroscopic particles". In: *J. Aerosol Sci.* 31.2, pp. 189–197. DOI: http://dx.doi.org/10.1016/S0021-8502(99)00048-8.

Lee, J. H., D. F. Leahy, I. N. Tang, and L. Newman (1993a). "Measurement and speciation of gas phase peroxides in the atmosphere". In: *J. Geophys. Res. - Atmos.* 98.D2, pp. 2911–2915. DOI: 10.1029/92JD02514.

– (1993b). "Measurement and speciation of gas phase peroxides in the atmosphere". In: *Journal of Geophysical Research: Atmospheres* 98.D2, pp. 2911–2915. DOI: 10.1029/92JD02514.

Lee, L., A. P. Teng, P. O. Wennberg, J. D. Crounse, and R. C. Cohen (2014). "On rates and mechanisms of OH and O3 reactions with isoprene-derived hydroxy nitrates". In: *J. Phys. Chem. A*.

Lei, W., D. Zhang, R. Zhang, L. T. Molina, and M. J. Molina (2002a). "Rate constants and isomeric branching of the Cl–isoprene reaction". In: *Chem. Phys. Lett.* 357.1–2, pp. 45–50. DOI: http://dx.doi.org/10.1016/S0009-2614(02)00437-2.

Lei, W., R. Zhang, W. S. McGivern, A. Derecskei-Kovacs, and S. W. North (2001). "Theoretical study of OH-O2-isoprene peroxy radicals". In: *J. Phys. Chem. A* 105.2, pp. 471–477. DOI: 10.1021/jp0027039.

Lei, W., R. Zhang, L. T. Molina, and M. J. Molina (2002b). "Theoretical study of chloroalkenylperoxy radicals". In: *J. Phys. Chem. A* 106.26, pp. 6415–6420. DOI: 10.1021/jp025799a.

Lelieveld, J., T. M. Butler, J. N. Crowley, T. J. Dillon, H. Fischer, L. Ganzeveld, H. Harder, M. G. Lawrence, M. Martinez, D. Taraborrelli, and J. Williams (2008). "Atmospheric oxidation capacity sustained by a tropical forest". In: *Nature* 452, pp. 737–40. DOI: 10.1038/nature06870.

Lelieveld, J., J. S. Evans, M. Fnais, D. Giannadaki, and A. Pozzer (2015). "The contribution of outdoor air pollution sources to premature mortality on a global scale". In: *Nature* 525.7569, pp. 367–371. DOI: 10.1038/nature15371.

Levine, J. G., A. R. MacKenzie, O. J. Squire, A. T. Archibald, P. T. Griffiths, N. L. Abraham, J. A. Pyle, D. E. Oram, G. Forster, J. F. Brito, J. D. Lee, J. R. Hopkins, A. C. Lewis, S. J. B. Bauguitte, C. F. Demarco, P. Artaxo, P. Messina, J. Lathière, D. A. Hauglustaine, E. House, C. N. Hewitt, and E. Nemitz (2015). "Isoprene chemistry in pristine and polluted Amazon environments: Eulerian and Lagrangian model frameworks and the strong bearing they have on our understanding of surface ozone and predictions of rainforest exposure to this priority pollutant". In: *Atmos. Chem. Phys. Discuss.* 2015, pp. 24251–24310. DOI: 10.5194/acpd-15-24251-2015.

Lewis, E. R. and S. E. Schwartz (2004). *Sea Salt Aerosol Production: MEchanisms, Methods, Measurements and Models - A Critical Review*. Vol. 152. Geophys. Monograph. Washington, D. C.: Amer. Geophys. Union.

Lewis, T. R., M. A. Blitz, D. E. Heard, and P. W. Seakins (2015). "Direct evidence for a substantive reaction between the Criegee intermediate, CH2OO, and the water vapour dimer". In: *Phys. Chem. Chem. Phys.* 17 (7), pp. 4859–4863. DOI: 10.1039/C4CP04750H.

Li, C., L. S. Balluz, A. Vaidyanathan, X.-J. Wen, Y. Hao, and J. R. Qualters (2016). "Long-term exposure to ozone and life expectancy in the United States, 2002 to 2008". In: *Medicine* 95.7, e2474. DOI: 10.1097/MD.0000000000002474.

Liao, J., K. D. Froyd, D. M. Murphy, F. N. Keutsch, G. Yu, P. O. Wennberg, J. M. St. Clair, J. D. Crounse, A. Wisthaler, T. Mikoviny, J.-L. Jimenez, P. Campuzano-Jost, D. A. Day, W. Hu, T. B. Ryerson, I. B. Pollack, J. Peischl, B. E. Anderson, L. D. Ziemba, D. R. Blake, S. Meinardi, and G. Diskin (2015). "Airborne mea-

surements of organosulfates over the continental U.S." In: *J. Geophys. Res. - Atmos.* 120.7, pp. 2990–3005.

Liebman, J. F. and A. Greenberg (1974). "Estimation by bond-additivity schemes of the relative thermodynamic stabilities of three-membered-ring systems and their open dipolar forms". In: *J. Org. Chem.* 39.2, pp. 123–130. DOI: 10.1021/jo00916a001.

Lightfoot, P. D., R. A. Cox, J. N. Crowley, M. Destriau, G. D. Hayman, M. E. Jenkin, G. K. Moortgat, and F. Zabel (1992). "Organic peroxy radicals: Kinetics, spectroscopy and tropospheric chemistry". In: *Atmos. Environ.* 26.10, pp. 1805–1961. DOI: http://dx.doi.org/10.1016/0960-1686(92)90423-I.

Limbeck, A., M. Kulmala, and H. Puxbaum (2003). "Secondary organic aerosol formation in the atmosphere via heterogeneous reaction of gaseous isoprene on acidic particles". In: *Geophys. Res. Let.* 30.19. DOI: 10.1029/2003GL017738.

Lin, G., J. E. Penner, and C. Zhou (2016). "How will SOA change in the future?" In: *Geophys. Res. Lett.* 43.4, pp. 1718–1726. DOI: 10.1002/2015GL067137.

Lin, Y.-H., S. H. Budisulistiorini, K. Chu, R. A. Siejack, H. Zhang, M. Riva, Z. Zhang, A. Gold, K. E. Kautzman, and J. D. Surratt (2014). "Light-absorbing oligomer formation in secondary organic aerosol from reactive uptake of isoprene epoxydiols". In: *Environ. Sci. Technol.* 48.20, pp. 12012–12021. DOI: 10.1021/es503142b.

Lin, Y.-H., E. M. Knipping, E. S. Edgerton, S. L. Shaw, and J. D. Surratt (2013a). "Investigating the influences of SO2 and NH3 levels on isoprene-derived secondary organic aerosol formation using conditional sampling approaches". In: *Atmos. Chem. Phys.* 13.16, pp. 8457–8470. DOI: 10.5194/acp-13-8457-2013.

Lin, Y.-H., H. Zhang, H. O. Pye, Z. Zhang, W. J. Marth, S. Park, M. Arashiro, T. Cui, S. H. Budisulistiorini, K. G. Sexton, W. Vizuete, Y. Xie, D. J. Luecken, I. R. Piletic, E. O. Edney, L. J. Bartolotti, A. Gold, and J. D. Surratt (2013b). "Epoxide as a precursor to secondary organic aerosol formation from isoprene photooxidation in the presence of nitrogen oxides". In: *Proc. Nat'l. Acad. Sci.* 110, pp. 6718–6723.

Lin, Y.-H., Z. Zhang, K. S. Docherty, H. Zhang, S. H. Budisulistiorini, C. L. Rubitschun, S. L. Shaw, E. M. Knipping, E. S. Edgerton, T. E. Kleindienst, A. Gold, and J. D. Surratt (2012). "Isoprene epoxydiols as precursors to secondary organic aerosol formation: Acid-catalyzed reactive uptake studies with authentic compounds". In: *Environ. Sci. Technol.* 46, pp. 250–258.

Lindinger, W. and A. Jordan (1998). "Proton-transfer-reaction mass spectrometry (PTR-MS): on-line monitoring of volatile organic compounds at pptv levels". In: *Chem. Soc. Rev.* 27.5, pp. 347–375. DOI: 10.1039/A827347Z.

Liu, J., E. L. D'Ambro, B. H. Lee, F. D. Lopez-Hilfiker, R. A. Zaveri, J. C. Rivera-Rios, F. N. Keutsch, S. Iyer, T. Kurten, Z. Zhang, A. Gold, J. D. Surratt, J. E. Shilling, and J. A. Thornton (2016). "Efficient isoprene secondary organic aerosol formation from a non-IEPOX pathway". In: *Environ. Sci. Technol.* 50.18, pp. 9872–9880. DOI: 10.1021/acs.est.6b01872.

Liu, Y. J., I. Herdlinger-Blatt, K. A. McKinney, and S. T. Martin (2013). "Production of methyl vinyl ketone and methacrolein via the hydroperoxyl pathway of isoprene oxidation". In: *Atmos. Chem. Phys.* 13, pp. 5715–5730. DOI: 10.5194/acp-13-5715-2013.

Liu, Y., M. Kuwata, B. F. Strick, R. J. Thomson, F. M. Geiger, K. a. McKinney, and S. T. Martin (2015). "Uptake of epoxydiol isomers accounts for half of the particle-phase material produced from isoprene photooxidation via the HO2 pathway". In: *Environ. Sci. Technol.* 49.1, pp. 250–258.

Liu, Z., V. S. Nguyen, J. Harvey, J.-F. Muller, and J. Peeters (2017). "Theoretically derived mechanisms of HPALD photolysis in isoprene oxidation". In: *Phys. Chem. Chem. Phys.* 19 (13), pp. 9096–9106. DOI: 10.1039/C7CP00288B.

Lockwood, A., P. Shepson, M. Fiddler, and M. Alaghmand (2010). "Isoprene nitrates: Preparation, separation, identification, yields, and atmospheric chemistry". In: *Atmos. Chem. Phys.* 10.13, pp. 6169–6178.

Löfgren, A., A.-C. Albertsson, P. Dubois, and R. Jérôme (1995). "Recent advances in ring-opening polymerization of lactones and related compounds". In: *J. Macromolecular Sci. C* 35.3, pp. 379–418. DOI: 10.1080/15321799508014594.

Long, F. A. and J. G. Pritchard (1956). "Hydrolysis of substituted ethylene oxides in H2O solutions". In: *J. Am. Chem. Soc.* 78.12, pp. 2663–2667.

Lopez-Hilfiker, F. D., C. Mohr, M. Ehn, F. Rubach, E. Kleist, J. Wildt, T. F. Mentel, A. Lutz, M. Hallquist, D. Worsnop, and J. A. Thornton (2014). "A novel method for online analysis of gas and particle composition: description and evaluation of a Filter Inlet for Gases and AEROsols (FIGAERO)". In: *Atmos. Meas. Tech.* 7.4, pp. 983–1001. DOI: 10.5194/amt-7-983-2014.

Loreto, F. and T. D. Sharkey (1990). "A gas-exchange study of photosynthesis and isoprene emission in Quercus rubra L." In: *Planta* 182.4, pp. 523–531. DOI: 10.1007/BF02341027.

Loza, C. L., J. S. Craven, L. D. Yee, M. M. Coggon, R. H. Schwantes, M. Shiraiwa, X. Zhang, K. A. Schilling, N. L. Ng, M. R. Canagaratna, P. J. Ziemann, R. C. Flagan, and J. H. Seinfeld (2014). "Secondary organic aerosol yields of 12-carbon alkanes". In: *Atmos. Chem. Phys.* 14.3, pp. 1423–1439. DOI: 10.5194/acp-14-1423-2014.

Loza, C. L., A. W. H. Chan, M. M. Galloway, F. N. Keutsch, R. C. Flagan, and J. H. Seinfeld (2010). "Characterization of vapor wall loss in laboratory chambers". In: *Environ. Sci. Technol.* 44.13, pp. 5074–5078. DOI: 10.1021/es100727v.

Loza, C. L., P. S. Chhabra, L. D. Yee, J. S. Craven, R. C. Flagan, and J. H. Seinfeld (2012). "Chemical aging of m-xylene secondary organic aerosol: Laboratory chamber study". In: *Atmos. Chem. Phys.* 12, pp. 151–167.

Lu, M.-L., A. Sorooshian, H. H. Jonsson, G. Feingold, R. C. Flagan, and J. H. Seinfeld (2009). "Marine stratocumulus aerosol-cloud relationships in the MASE-II experiment: Precipitation susceptibility in eastern Pacific marine stratocumulus". In: *J. Geophys. Res. - Atmos.* 114.D24. DOI: 10.1029/2009JD012774.

Lynch, P., J. S. Reid, D. L. Westphal, J. Zhang, T. F. Hogan, E. J. Hyer, C. A. Curtis, D. A. Hegg, Y. Shi, J. R. Campbell, J. I. Rubin, W. R. Sessions, F. J. Turk, and A. L. Walker (2016). "An 11-year global gridded aerosol optical thickness reanalysis (v1.0) for atmospheric and climate sciences". In: *Geosci. Model Dev.* 9.4, pp. 1489–1522. DOI: 10.5194/gmd-9-1489-2016.

Ma, Y., R. J. Weber, K. Maxwell-Meier, D. A. Orsini, Y. N. Lee, B. J. Huebert, S. G. Howell, T. Bertram, R. W. Talbot, J. E. Dibb, and E. Scheuer (2004). "Intercomparisons of airborne measurements of aerosol ionic chemical composition during TRACE-P and ACE-Asia". In: *J. Geophys. Res. - Atmos.* 109.D15. DOI: 10.1029/2003JD003673.

Madronich, S. and J. G. Calvert (1990). "Permutation reactions of organic peroxy radicals in the troposphere". In: *J. Geophys. Res.* 95.D5, pp. 5697–5715.

Magneron, I., R. Thévenet, A. Mellouki, G. L. Bras, G. K. Moortgat, and K. Wirtz (2002). "A study of the photolysis and OH-initiated oxidation of acrolein and trans-crotonaldehyde". In: *J. Phys. Chem. A* 106.11, pp. 2526–2537. DOI: 10.1021/jp013413a.

Mäkelä, J. M., P. Aalto, V. Jokinen, T. Pohja, A. Nissinen, S. Palmroth, T. Markkanen, K. Seitsonen, H. Lihavainen, and M. Kulmala (1997). "Observations of ultrafine aerosol particle formation and growth in boreal forest". In: *Geophys. Res. Lett.* 24.10, pp. 1219–1222. DOI: 10.1029/97GL00920.

Makino, K., M. M. Mossoba, and P. Riesz (1982). "Chemical effects of ultrasound on aqueous solutions. Evidence for hydroxyl and hydrogen free radicals (OH and H) by spin trapping". In: *J. Am. Chem. Soc.* 104.12, pp. 3537–3539. DOI: 10.1021/ja00376a064.

Malecha, K. T. and S. A. Nizkorodov (2016). "Photodegradation of secondary organic aerosol particles as a source of small, oxygenated volatile organic compounds". In: *Environ. Sci. Technol.* 50.18, pp. 9990–9997. DOI: 10.1021/acs.est.6b02313.

Mao, J., F. Paulot, D. J. Jacob, R. C. Cohen, J. D. Crounse, P. O. Wennberg, C. A. Keller, R. C. Hudman, M. P. Barkley, and L. W. Horowitz (2013). "Ozone and organic nitrates over the eastern United States: Sensitivity to isoprene chemistry". In: *J. Geophys. Res.* 118, pp. 11256–11268.

Mao, J., X. Ren, W. H. Brune, J. R. Olson, J. H. Crawford, A. Fried, L. G. Huey, R. C. Cohen, B. Heikes, H. B. Singh, D. R. Blake, G. W. Sachse, G. S. Diskin, S. R. Hall, and R. E. Shetter (2009). "Airborne measurement of OH reactivity during INTEX-B". In: *Atmos. Chem. Phys.* 9.1, pp. 163–173. DOI: 10.5194/acp-9-163-2009.

Mao, J., X. Ren, L. Zhang, D. M. Van Duin, R. C. Cohen, J. H. Park, A. H. Goldstein, F. Paulot, M. R. Beaver, J. D. Crounse, P. O. Wennberg, J. P. DiGangi, S. B. Henry, F. N. Keutsch, C. Park, G. W. Schade, G. M. Wolfe, J. A. Thornton, and W. H. Brune (2012). "Insights into hydroxyl measurements and atmospheric oxidation in a California forest". In: *Atmos. Chem. Phys.* 12.17, pp. 8009–8020. DOI: 10.5194/acp-12-8009-2012.

Marais, E. A., D. J. Jacob, J. L. Jimenez, P. Campuzano-Jost, D. A. Day, W. Hu, J. Krechmer, L. Zhu, P. S. Kim, C. C. Miller, J. A. Fisher, K. Travis, K. Yu, T. F. Hanisco, G. M. Wolfe, H. L. Arkinson, H. O. T. Pye, K. D. Froyd, J. Liao, and V. F. McNeill (2016). "Aqueous-phase mechanism for secondary organic aerosol formation from isoprene: application to the southeast United States and co-benefit of SO2 emission controls". In: *Atmos. Chem. Phys.* 16.3, pp. 1603–1618. DOI: 10.5194/acp-16-1603-2016.

Maricq, M. M. and J. J. Szente (1996). "Temperature-dependent study of the CH3C(O)O2 + NO reaction". In: *J. Phys. Chem.* 100.30, pp. 12380–12385. DOI: 10.1021/jp960792c.

Martin, S. T., P. Artaxo, L. A. T. Machado, A. O. Manzi, R. A. F. Souza, C. Schumacher, J. Wang, M. O. Andreae, H. M. J. Barbosa, J. Fan, G. Fisch, A. H. Goldstein, A. Guenther, J. L. Jimenez, U. Pöschl, M. A. SilvaDias, J. N. Smith, and M. Wendisch (2016). "Introduction: Observations and Modeling of the Green Ocean Amazon (GoAmazon2014/5)". In: *Atmos. Chem. Phys.* 16.8, pp. 4785–4797. DOI: 10.5194/acp-16-4785-2016.

Martin, S. T. (2000). "Phase transitions of aqueous atmospheric particles". In: *Chem. Rev.* 100.9, pp. 3403–3454. DOI: 10.1021/cr990034t.

Martin, S. T., M. O. Andreae, P. Artaxo, D. Baumgardner, Q. Chen, A. H. Goldstein, A. Guenther, C. L. Heald, O. L. Mayol-Bracero, P. H. McMurry, T. Pauliquevis, U. Pöschl, K. A. Prather, G. C. Roberts, S. R. Saleska, M. A. S. Dias, D. V. Spracklen, E. Swietlicki, and I. Trebs (2010). "Sources and properties of Amazonian aerosol particles". In: *Rev. Geophys.* 48.

Matsunaga, A. and P. J. Ziemann (2009). "Yields of beta-hydroxynitrates and dihydroxynitrates in aerosol formed from OH radical-initiated reactions of linear alkenes in the presence of NOx". In: *J. Phys. Chem. A* 113.3, pp. 599–606. DOI: 10.1021/jp807764d.

– (2010a). "Gas-wall partitioning of organic compounds in a Teflon film chamber and potential effects on reaction product and aerosol yield measurements". In: *Aerosol Sci. Technol.* 44.10, pp. 881–892. DOI: 10.1080/02786826.2010.501044.

Matsunaga, A. and P. J. Ziemann (2010b). "Yields of beta-hydroxynitrates, dihydroxynitrates, and trihydroxynitrates formed from OH radical-initiated reactions of 2-methyl-1-alkenes". In: *Proc. Nat'l. Acad. Sci.* 107.15, pp. 6664–6669. DOI: 10.1073/pnas.0910585107.

Matthew, B. M., A. M. Middlebrook, and T. B. Onasch (2008). "Collection efficiencies in an aerodyne aerosol mass spectrometer as a function of particle phase for laboratory generated aerosols". In: *Aerosol Sci. Technol.* 42.11, pp. 884–898. DOI: 10.1080/02786820802356797.

Maudlin, L. C., Z. Wang, H. H. Jonsson, and A. Sorooshian (2015). "Impact of wildfires on size-resolved aerosol composition at a coastal California site". In: *Atmos. Environ.* 119, pp. 59–68. DOI: http://dx.doi.org/10.1016/j.atmosenv.2015.08.039.

Mauldin, R. L., T. Berndt, M. Sipila, P. Paasonen, T. Petaja, S. Kim, T. Kurten, F. Stratmann, V. M. Kerminen, and M. Kulmala (2012). "A new atmospherically relevant oxidant of sulphur dioxide". In: *Nature* 488.7410, pp. 193–196. DOI: http://www.nature.com/nature/journal/v488/n7410/abs/nature11278.html#supplementary-information.

McMurry, P. H. and D. J. Rader (1985). "Aerosol wall losses in electrically charged chambers". In: *Aerosol Sci. Technol.* 4.3, pp. 249–268. DOI: 10.1080/02786828508959054.

McNeill, V. F., J. L. Woo, D. D. Kim, A. N. Schwier, N. J. Wannell, A. J. Sumner, and J. M. Barakat (2012). "Aqueous-phase secondary organic aerosol and organosulfate formation in atmospheric aerosols: A modeling study". In: *Environ. Sci. Technol.* 46.15, pp. 8075–8081. DOI: 10.1021/es3002986.

McNeill, V. F., R. L. N. Yatavelli, J. A. Thornton, C. B. Stipe, and O. Landgrebe (2008). "Heterogeneous OH oxidation of palmitic acid in single component and internally mixed aerosol particles: vaporization and the role of particle phase". In: *Atmos. Chem. Phys.* 8.17, pp. 5465–5476. DOI: 10.5194/acp-8-5465-2008.

Mechem, D. B. and Y. L. Kogan (2003). "Simulating the transition from drizzling marine stratocumulus to boundary layer cumulus with a mesoscale model". In: *Monthly Weather Rev.* 131.10, pp. 2342–2360. DOI: 10.1175/1520-0493(2003)131<2342:STTFDM>2.0.CO;2.

Melamed, M. L., P. S. Monks, A. H. Goldstein, M. G. Lawrence, and J. Jennings (2015). "The international global atmospheric chemistry (IGAC) project: Facilitating atmospheric chemistry research for 25 years". In: *Anthropocene* 12, pp. 17–28. DOI: http://doi.org/10.1016/j.ancene.2015.10.001.

Miller, A. M., L. Y. Yeung, A. C. Kiep, and M. J. Elrod (2004). "Overall rate constant measurements of the reactions of alkene-derived hydroxyalkylperoxy radicals with nitric oxide". In: *Phys. Chem. Chem. Phys.* 6.13, pp. 3402–3407. DOI: 10.1039/B402110J.

Minerath, E. C., M. T. Casale, and M. J. Elrod (2008). "Kinetics feasibility study of alcohol sulfate esterification reactions in tropospheric aerosols". In: *Environ. Sci. Technol.* 42, pp. 4410–4415.

Minerath, E. C., M. P. Schultz, and M. J. Elrod (2009). "Kinetics of the reactions of isoprene-derived epoxides in model tropospheric aerosol solutions". In: *Environ. Sci. Technol.* 43, pp. 8133–8139. DOI: 10.1021/es902304p.

Miyoshi, A., S. Hatakeyama, and N. Washida (1994). "OH radical-initiated photooxidation of isoprene: An estimate of global CO production". In: *J. Geophys. Res. - Atmos.* 99.D9, pp. 18779–18787. DOI: 10.1029/94JD01334.

Modini, R. L., A. A. Frossard, L. Ahlm, L. M. Russell, C. E. Corrigan, G. C. Roberts, L. N. Hawkins, J. C. Schroder, A. K. Bertram, R. Zhao, A. K. Y. Lee, J. P. D. Abbatt, J. Lin, A. Nenes, Z. Wang, A. Wonaschütz, A. Sorooshian, K. J. Noone, H. Jonsson, J. H. Seinfeld, D. Toom-Sauntry, A. M. Macdonald, and W. R. Leaitch (2015). "Primary marine aerosol-cloud interactions off the coast of California". In: *J. Geophys. Res. - Atmos.* 120.9, pp. 4282–4303. DOI: 10.1002/2014JD022963.

Molina, M. J., A. V. Ivanov, S. Trakhtenberg, and L. T. Molina (2004). "Atmospheric evolution of organic aerosol". In: *Geophys. Res. Lett.* 31.22. DOI: 10.1029/2004GL020910.

Monson, R. K. and R. Fall (1989). "Isoprene emission from aspen leaves: influence of environment and relation to photosynthesis and Photorespiration". In: *Plant Physiology* 90.1, pp. 267–274. DOI: 10.1104/pp.90.1.267.

Monson, R. K., R. Grote, U. Niinemets, and J.-P. Schnitzler (2012). "Modeling the isoprene emission rate from leaves". In: *New Phytologist* 195.3, pp. 541–559. DOI: 10.1111/j.1469-8137.2012.04204.x.

Moortgat, G. K., R. A. Cox, G. Schuster, J. P. Burrows, and G. S. Tyndall (1989). "Peroxy radical reactions in the photo-oxidation of CH3CHO". In: *J. Chem. Soc., Faraday Trans. 2: Molec. Chem. Phys.* 85.7, pp. 809–829. DOI: 10.1039/F29898500809.

Müller, J. F., T. Stavrakou, S. Wallens, I. De Smedt, M. Van Roozendael, M. J. Potosnak, J. Rinne, B. Munger, A. Goldstein, and A. B. Guenther (2008). "Global isoprene emissions estimated using MEGAN, ECMWF analyses and a detailed canopy environment model". In: *Atmos. Chem. Phys.* 8.5, pp. 1329–1341. DOI: 10.5194/acp-8-1329-2008.

Müller, J.-F., J. Peeters, and T. Stavrakou (2014). "Fast photolysis of carbonyl nitrates from isoprene". In: *Atmos. Chem. Phys.* 14.5, pp. 2497–2508. DOI: 10.5194/acp-14-2497-2014.

Murphy, D. M., D. J. Cziczo, K. D. Froyd, P. K. Hudson, B. M. Matthew, A. M. Middlebrook, R. E. Peltier, A. Sullivan, D. S. Thomson, and R. J. Weber (2006). "Single-particle mass spectrometry of tropospheric aerosol particles". In: *J. Geophys. Res. - Atmos.* 111.D23. DOI: 10.1029/2006JD007340.

Murrells, T. P., M. E. Jenkin, S. J. Shalliker, and G. D. Hayman (1991). "Laser flash photolysis study of the UV spectrum and kinetics of reactions of HOCH2CH2O2 radicals". In: *J. Chem. Soc. Faraday Trans.* 87 (15), pp. 2351–2360. DOI: 10.1039/FT9918702351.

Muzart, J. and A. Riahi (1992). "Palladium- and light-enhanced ring-opening of oxiranes by copper chloride". In: *J. Organometallic Chem.* 433.3, pp. 323–336. DOI: http://dx.doi.org/10.1016/0022-328X(92)80158-T.

Myhre, G., D. Shindell, F.-M. Bréon, W. Collins, J. Fuglestvedt, J. Huang, D. Koch, J.-F. Lamarque, D. Lee, B. Mendoza, T. Nakajima, A. Robock, G. Stephens, T. Takemura, and H. Zhang (2013). "Anthropogenic and Natural Radiative Forcing". In: *Climate Change 2013: The Physical Science Basis. Contribution of Working Group I to the Fifth Assessment Report of the Intergovernmental Panel on Climate Change*. Ed. by T. F. Stocker, D. Qin, G.-K. Plattner, M. Tignor, S. K. Allen, J. Boschung, A. Nauels, Y. Xia, V. Bex, and P. M. Midgley. Cambridge, UK: Cambridge University Press, pp. 659–740.

Myriokefalitakis, S., M. Vrekoussis, K. Tsirigaridis, F. Wittrock, A. Richter, C. Brühl, R. Volkamer, J. P. Burrows, and M. Kanakidou (2008). "The influence of natural and anthropogenic secondary sources on the glyoxal global distribution". In: *Atmos. Chem. Phys.* 8, pp. 4965–4981.

Navarro, M. A., S. Dusanter, R. A. Hites, and P. S. Stevens (2011). "Radical dependence of the yields of methacrolein and methyl vinyl ketone from the OH-initiated oxidation of isoprene under NO(x)-free conditions." In: *Environ. Sci. Technol.* 45, pp. 923–929. DOI: 10.1021/es103147w.

Neeb, P., O. Horie, and G. K. Moortgat (1995). "The nature of the transitory product in the gas-phase ozonolysis of ethene". In: *Chem. Phys. Lett.* 246.1, pp. 150–156. DOI: http://dx.doi.org/10.1016/0009-2614(95)01073-I.

Neeb, P., A. Kolloff, S. Koch, and G. K. Moortgat (1998). "Rate constants for the reactions of methylvinyl ketone, methacrolein, methacrylic acid, and acrylic acid with ozone". In: *Int. J. Chem. Kinetics* 30.10, pp. 769–776.

Neeb, P., F. Sauer, O. Horie, and G. K. Moortgat (1997). "Formation of hydroxymethyl hydroperoxide and formic acid in alkene ozonolysis in the presence of water vapour". In: *Atmos. Environ.* 31.10, pp. 1417–1423. DOI: http://dx.doi.org/10.1016/S1352-2310(96)00322-6.

Nefkens, G., J. W. Thuring, and B. Zwanenburg (1997). "A novel and convenient synthesis of 3-methylfuran-2(5H)-one". In: *Synthesis* 3, pp. 290–292. DOI: 10.1055/s-1997-1180.

Nel, A. (2005). "Air pollution-related illness: Effects of particles". In: *Science* 308.5723, pp. 804–806. DOI: 10.1126/science.1108752.

Nelin, T. D., A. M. Joseph, M. W. Gorr, and L. E. Wold (2012). "Direct and indirect effects of PM on the cardiovascular system". In: *Toxicology Lett.* 208.3, pp. 293–299. DOI: 10.1016/j.toxlet.2011.11.008.

Newland, M. J., A. R. Rickard, M. S. Alam, L. Vereecken, A. Munoz, M. Rodenas, and W. J. Bloss (2015). "Kinetics of stabilised Criegee intermediates derived from alkene ozonolysis: reactions with SO2, H2O and decomposition under boundary layer conditions". In: *Phys. Chem. Chem. Phys.* 17 (6), pp. 4076–4088. DOI: 10.1039/C4CP04186K.

Ng, N., A. Kwan, J. Surratt, A. Chan, P. Chhabra, A. Sorooshian, H. Pye, J. Crounse, P. Wennberg, R. Flagan, *et al.* (2008). "Secondary organic aerosol (SOA) formation from reaction of isoprene with nitrate radicals (NO3)". In: *Atmos. Chem. Phys.* 8.14, pp. 4117–4140.

Nguyen, T. B., A. P. Bateman, D. L. Bones, S. A. Nizkorodov, J. Laskin, and A. Laskin (2010). "High-resolution mass spectrometry analysis of secondary organic aerosol generated by ozonolysis of isoprene". In: *Atmos. Environ.* 44.8, pp. 1032–1042. DOI: 10.1016/j.atmosenv.2009.12.019.

Nguyen, T. B., M. M. Coggon, K. H. Bates, X. Zhang, R. H. Schwantes, K. A. Schilling, C. L. Loza, R. C. Flagan, P. O. Wennberg, and J. H. Seinfeld (2014a). "Organic aerosol formation from the reactive uptake of isoprene epoxydiols (IEPOX) onto non-acidified inorganic seeds". In: *Atmos. Chem. Phys.* 14, pp. 3497–3510.

Nguyen, T. B., J. D. Crounse, R. H. Schwantes, A. P. Teng, K. H. Bates, X. Zhang, J. M. St. Clair, W. H. Brune, G. S. Tyndall, F. N. Keutsch, J. H. Seinfeld, and P. O. Wennberg (2014b). "Overview of the Focused Isoprene eXperiment at the California Institute of Technology (FIXCIT): mechanistic chamber studies on the oxidation of biogenic compounds". In: *Atmos. Chem. Phys.* 14.24, pp. 13531–13549. DOI: 10.5194/acp-14-13531-2014.

Nguyen, T. B., J. D. Crounse, A. P. Teng, J. M. St. Clair, F. Paulot, G. M. Wolfe, and P. O. Wennberg (2015a). "Rapid deposition of oxidized biogenic compounds to a temperate forest". In: *Proc. Nat'l. Acad. Sci.* 112.5, E392–E401.

Nguyen, T. B., A. Laskin, J. Laskin, and S. A. Nizkorodov (2013). "Brown carbon formation from ketoaldehydes of biogenic monoterpenes". In: *Faraday Discussions* 165.

Nguyen, T. B., P. J. Roach, J. Laskin, A. Laskin, and S. A. Nizkorodov (2011a). "Effect of humidity on the composition of isoprene photooxidation secondary organic aerosol". In: *Atmos. Chem. Phys.* 11.14, pp. 6931–6944. DOI: 10.5194/acp-11-6931-2011.

Nguyen, T. K. V., M. D. Petters, S. R. Suda, H. Guo, R. J. Weber, and A. G. Carlton (2014c). "Trends in particle-phase liquid water during the Southern Oxidant and Aerosol Study". In: *Atmos. Chem. Phys.* 14.20, pp. 10911–10930. DOI: 10.5194/acp-14-10911-2014.

Nguyen, T. L., J. Peeters, and L. Vereecken (2009a). "Theoretical study of the gas-phase ozonolysis of beta-pinene (C10H16)". In: *Phys. Chem. Chem. Phys.* 11.27, pp. 5643–5656. DOI: 10.1039/B822984H.

Nguyen, T. L., R. Winterhalter, G. Moortgat, B. Kanawati, J. Peeters, and L. Vereecken (2009b). "The gas-phase ozonolysis of [small beta]-caryophyllene (C15H24). Part II: A theoretical study". In: *Phys. Chem. Chem. Phys.* 11.21, pp. 4173–4183. DOI: 10.1039/B817913A.

Nguyen, T. B., K. H. Bates, J. D. Crounse, R. H. Schwantes, X. Zhang, H. G. Kjaergaard, J. D. Surratt, P. Lin, A. Laskin, J. H. Seinfeld, and P. O. Wennberg (2015b). "Mechanism of the hydroxyl radical oxidation of methacryloyl peroxynitrate (MPAN) and its pathway toward secondary organic aerosol formation in the atmosphere". In: *Phys. Chem. Chem. Phys.* 17.27, pp. 17914–17926. DOI: 10.1039/C5CP02001H.

Nguyen, T. B., J. Laskin, A. Laskin, and S. A. Nizkorodov (2011b). "Nitrogen-containing organic compounds and oligomers in secondary organic aerosol formed by photooxidation of isoprene". In: *Environ. Sci. Technol.* 45.16, pp. 6908–6918. DOI: 10.1021/es201611n.

Nguyen, T. B., P. B. Lee, K. M. Updyke, D. L. Bones, J. Laskin, A. Laskin, and S. A. Nizkorodov (2012). "Formation of nitrogen- and sulfur-containing light-absorbing compounds accelerated by evaporation of water from secondary organic aerosols". In: *J. Geophys. Res. - Atmos.* 117.D1. DOI: 10.1029/2011JD016944.

Nguyen, T. B., G. S. Tyndall, J. D. Crounse, A. P. Teng, K. H. Bates, R. H. Schwantes, M. M. Coggon, L. Zhang, P. Feiner, D. O. Milller, K. M. Skog, J. C. Rivera-Rios, M. Dorris, K. F. Olson, A. Koss, R. J. Wild, S. S. Brown, A. H. Goldstein, J. A. de Gouw, W. H. Brune, F. N. Keutsch, J. H. Seinfeld, and P. O. Wennberg (2016). "Atmospheric fates of Criegee intermediates in the ozonolysis of isoprene". In: *Phys. Chem. Chem. Phys.* 18 (15), pp. 10241–10254. DOI: 10.1039/C6CP00053C.

Nicholls, S. (1984). "The dynamics of stratocumulus: Aircraft observations and comparisons with a mixed layer model". In: *Quart. J. Royal Met. Soc.* 110.466, pp. 783–820. DOI: 10.1002/qj.49711046603.

Nicholls, S. and J. Leighton (1986). "An observational study of the structure of stratiform cloud sheets: Part I. Structure". In: *Quart. J. Royal Met. Soc.* 112.472, pp. 431–460. DOI: 10.1002/qj.49711247209.

Niki, H., P. D. Maker, C. M. Savage, and L. P. Breitenbach (1980). "Further IR spectroscopic evidence for the formation of CH2(OH)OOH in the gas-phase reaction of HO2 with CH2O". In: *Chem. Phys. Lett.* 75.3, pp. 533–535. DOI: http://dx.doi.org/10.1016/0009-2614(80)80571-9.

– (1985). "FTIR study of the kinetics and mechanism for chlorine-atom-initiated reactions of acetaldehyde". In: *J. Phys. Chem.* 89.4, pp. 588–591. DOI: 10.1021/j100250a008.

Noone, K. J., D. W. Johnson, J. P. Taylor, R. J. Ferek, T. Garrett, P. V. Hobbs, P. A. Durkee, K. Nielsen, E. Öström, C. O'Dowd, M. H. Smith, L. M. Russell, R. C. Flagan, J. H. Seinfeld, L. De Bock, R. E. Van Grieken, J. G. Hudson, I. Brooks, R. F. Gasparovic, and R. A. Pockalny (2000). "A case study of ship

track formation in a polluted marine boundary layer". In: *J. Atmos. Sci.* 57.16, pp. 2748–2764. DOI: 10.1175/1520-0469(2000)057<2748:ACSOST>2.0.CO;2.

Nordmeyer, T., W. Wang, M. L. Ragains, B. J. Finlayson-Pitts, C. W. Spicer, and R. A. Plastridge (1997). "Unique products of the reaction of isoprene with atomic chlorine: Potential markers of chlorine atom chemistry". In: *Geophys. Res. Lett.* 24.13, pp. 1615–1618. DOI: 10.1029/97GL01547.

Northway, M. J., J. T. Jayne, D. W. Toohey, M. R. Canagaratna, A. Trimborn, K. I. Akiyama, A. Shimono, J. L. Jimenez, P. F. DeCarlo, K. R. Wilson, and D. R. Worsnop (2007). "Demonstration of a VUV lamp photoionization source for improved organic speciation in an aerosol mass spectrometer". In: *Aerosol. Sci. Technol.* 41.9, pp. 828–839. DOI: 10.1080/02786820701496587.

Nouaime, G., S. B. Bertman, C. Seaver, D. Elyea, H. Huang, P. B. Shepson, T. K. Starn, D. D. Riemer, R. G. Zika, and K. Olszyna (1998). "Sequential oxidation products from tropospheric isoprene chemistry: MACR and MPAN at a NOx -rich forest environment in the southeastern United States". In: *J. Geophys. Res. - Atmos.* 103.D17, pp. 22463–22471. DOI: 10.1029/98JD00320.

Novelli, A., L. Vereecken, J. Lelieveld, and H. Harder (2014). "Direct observation of OH formation from stabilised Criegee intermediates". In: *Phys. Chem. Chem. Phys.* 16.37, pp. 19941–19951. DOI: 10.1039/C4CP02719A.

Noziere, B., P. Dziedzic, and A. Cordova (2009). "Products and kinetics of the liquid-phase reaction of glyoxal catalyzed by ammonium ions (NH4+)". In: *J. Phys. Chem. A* 113, pp. 231–237.

Nozière, B. and I. Barnes (1998). "Evidence for formation of a PAN analogue of pinonic structure and investigation of its thermal stability". In: *J. Geophys. Res. - Atmos.* 103.D19, pp. 25587–25597. DOI: 10.1029/98JD01677.

Oakes, M., N. Rastogi, B. J. Majestic, M. Shafer, J. J. Schauer, E. S. Edgerton, and R. J. Weber (2010). "Characterization of soluble iron in urban aerosols using near-real time data". In: *J. Geophys. Res. - Atmos.* 115.D15. DOI: 10.1029/2009JD012532.

O'Brien, J. M., E. Czuba, D. R. Hastie, J. S. Francisco, and P. B. Shepson (1998). "Determination of the hydroxy nitrate yields from the reaction of C2-C6 alkenes with OH in the presence of NO". In: *J. Phys. Chem. A* 102.45, pp. 8903–8908. DOI: 10.1021/jp982320z.

O'Brien, R. E., B. Wang, S. T. Kelly, N. Lundt, Y. You, A. K. Bertram, S. R. Leone, A. Laskin, and M. K. Gilles (2015). "Liquid–liquid phase separation in aerosol particles: Imaging at the nanometer scale". In: *Environ. Sci. Technol.* 49.8, pp. 4995–5002. DOI: 10.1021/acs.est.5b00062.

Ochando-Pardo, M., I. Nebot-Gil, A. Gonzalez-Lafont, and J. M. Lluch (2007). "Methyl vinyl ketone + OH and methacrolein + OH oxidation reactions: A master equation analysis of the pressure- and temperature-dependent rate constants". In: *Chem. Eur. J.* 13, pp. 1180–1190.

O'Dowd, C. D., J. A. Lowe, and M. H. Smith (2000). "The effect of clouds on aerosol growth in the rural atmosphere". In: *Atmos. Res.* 54.4, pp. 201–221. DOI: http://dx.doi.org/10.1016/S0169-8095(00)00046-6.

Oktem, B., M. P. Tolocka, and M. V. Johnston (2004). "On-line Analysis of organic components in fine and ultrafine particles by photoionization aerosol mass spectrometry". In: *Anal. Chem.* 76.2, pp. 253–261. DOI: 10.1021/ac0350559.

Olzmann, M., E. Kraka, D. Cremer, R. Gutbrod, and S. Andersson (1997). "Energetics, kinetics, and product distributions of the reactions of ozone with ethene and 2,3-dimethyl-2-butene". In: *J. Phys. Chem. A* 101.49, pp. 9421–9429. DOI: 10.1021/jp971663e.

Omar, A. H., J.-G. Won, D. M. Winker, S.-C. Yoon, O. Dubovik, and M. P. McCormick (2005). "Development of global aerosol models using cluster analysis of Aerosol Robotic Network (AERONET) measurements". In: *J. Geophys. Res. - Atmos.* 110.D10. DOI: 10.1029/2004JD004874.

Orlando, J. J. and G. S. Tyndall (2012). "Laboratory studies of organic peroxy radical chemistry: an overview with emphasis on recent issues of atmospheric significance". In: *Chem. Soc. Rev.* 41, pp. 6294–6317.

Orlando, J. J., G. S. Tyndall, E. C. Apel, D. D. Riemer, and S. E. Paulson (2003a). "Rate coefficients and mechanisms of the reaction of cl atoms with a series of unsaturated hydrocarbons under atmospheric conditions". In: *Int. J. Chem. Kinetics* 35.8, pp. 334–353. DOI: 10.1002/kin.10135.

Orlando, J. J., G. S. Tyndall, S. B. Bertman, W. Chen, and J. B. Burkholder (2002). "Rate coefficient for the reaction of OH with CH2=C(CH3)C(O)OONO2 (MPAN)". In: *Atmos. Environ.* 36.11, pp. 1895–1900. DOI: http://dx.doi.org/10.1016/S1352-2310(02)00090-0.

Orlando, J. J., G. S. Tyndall, M. Bilde, C. Ferronato, T. J. Wallington, L. Vereecken, and J. Peeters (1998). "Laboratory and theoretical study of the oxy radicals in the OH- and Cl-initiated oxidation of ethene". In: *J. Phys. Chem. A* 102.42, pp. 8116–8123. DOI: 10.1021/jp981937d.

Orlando, J. J., G. S. Tyndall, and S. E. Paulson (1999). "Mechanism of the OH-initiated oxidation of methacrolein". In: *Geophys. Res. Lett.* 26.14, pp. 2191–2194.

Orlando, J. J., G. S. Tyndall, and T. J. Wallington (2003b). "The atmospheric chemistry of alkoxy radicals". In: *Chem. Rev.* 103.12, pp. 4657–4690. DOI: 10.1021/cr020527p.

Orsini, D. A., Y. Ma, A. Sullivan, B. Sierau, K. Baumann, and R. J. Weber (2003). "Refinements to the particle-into-liquid sampler (PILS) for ground and airborne measurements of water soluble aerosol composition". In: *Atmos. Environ.* 37.9–10, pp. 1243–1259. DOI: http://doi.org/10.1016/S1352-2310(02)01015-4.

Owicki, J. C., L. L. Shipman, and H. A. Scheraga (1975). "Structure, energetics, and dynamics of small water clusters". In: *J. Phys. Chem.* 79.17, pp. 1794–1811. DOI: 10.1021/j100584a010.

Pachauri, R. K., M. R. Allen, V. Barros, J. Broome, W. Cramer, R. Christ, J. Church, L. Clarke, Q. Dahe, and P. Dasgupta (2014). *Climate change 2014: Synthesis report. Contribution of working groups I, II and III to the fifth assessment report of the intergovernmental panel on climate change*. IPCC. ISBN: 9291691437.

Painemal, D. and P. Minnis (2012). "On the dependence of albedo on cloud microphysics over marine stratocumulus clouds regimes determined from Clouds and the Earth's Radiant Energy System (CERES) data". In: *J. Geophys. Res. - Atmos.* 117.D6. DOI: 10.1029/2011JD017120.

Pankow, J. F. and W. E. Asher (2008). "SIMPOL.1: a simple group contribution method for predicting vapor pressures and enthalpies of vaporization of multifunctional organic compounds". In: *Atmos. Chem. Phys.* 8.10, pp. 2773–2796. DOI: 10.5194/acp-8-2773-2008.

Park, J., C. G. Jongsma, R. Zhang, and S. W. North (2004). "OH/OD initiated oxidation of isoprene in the presence of O2 and NO". In: *J. Phys. Chem. A* 108.48, pp. 10688–10697. DOI: 10.1021/jp040421t.

Park, J., J. C. Stephens, R. Zhang, and S. W. North (2003). "Theoretical study of the alkoxy radicals derived from isoprene: Pressure- and temperature-dependent decomposition rates". In: *J. Phys. Chem. A* 107.33, pp. 6408–6414. DOI: 10.1021/jp0303321.

Parrish, D. D., J. F. Lamarque, V. Naik, L. Horowitz, D. T. Shindell, J. Staehelin, R. Derwent, O. R. Cooper, H. Tanimoto, A. Volz-Thomas, S. Gilge, H. E. Scheel, M. Steinbacher, and M. Fröhlich (2014). "Long-term changes in lower tropospheric baseline ozone concentrations: Comparing chemistry-climate models and observations at northern midlatitudes". In: *J. Geophys. Res. - Atmos.* 119.9, pp. 5719–5736. DOI: 10.1002/2013JD021435.

Parshintsev, J., M. Kivilompolo, J. Ruiz-Jimenez, K. Hartonen, M. Kulmala, and M.-L. Riekkola (2010). "Particle-into-liquid sampler on-line coupled with solid-phase extraction-liquid chromatography–mass spectrometry for the determination of organic acids in atmospheric aerosols". In: *J. Chromatography A* 1217.33, pp. 5427–5433. DOI: http://doi.org/10.1016/j.chroma.2010.06.026.

Patchen, A. K., M. J. Pennino, and M. J. Elrod (2005). "Overall rate constant measurements of the reaction of chloroalkylperoxy radicals with nitric oxide". In: *J. Phys. Chem. A* 109.26, pp. 5865–5871. DOI: 10.1021/jp050388q.

Patchen, A. K., M. J. Pennino, A. C. Kiep, and M. J. Elrod (2007). "Direct kinetics study of the product-forming channels of the reaction of isoprene-derived hydroxyperoxy radicals with NO". In: *Int. J. Chem. Kinetics* 39.6, pp. 353–361. DOI: 10.1002/kin.20248.

Paulot, F., J. D. Crounse, H. G. Kjaergaard, J. H. Kroll, J. H. Seinfeld, and P. O. Wennberg (2009a). "Isoprene photooxidation: new insights into the production of acids and organic nitrates". In: *Atmos. Chem. Phys.* 9, pp. 1479–1501.

Paulot, F., J. D. Crounse, H. G. Kjaergaard, A. Kurten, J. St Clair, J. H. Seinfeld, and P. O. Wennberg (2009b). "Unexpected epoxide formation in the gas-phase photooxidation of isoprene". In: *Science* 325.5941, pp. 730–3. DOI: 10.1126/science.1172910.

Paulot, F., D. K. Henze, and P. O. Wennberg (2012). "Impact of the isoprene photochemical cascade on tropical ozone". In: *Atmos. Chem. Phys.* 12.3, pp. 1307–1325. DOI: 10.5194/acp-12-1307-2012.

Paulson, S. E., M. Chung, A. D. Sen, and G. Orzechowska (1998). "Measurement of OH radical formation from the reaction of ozone with several biogenic alkenes". In: *J. Geophys. Res. - Atmos.* 103.D19, pp. 25533–25539. DOI: 10.1029/98JD01951.

Paulson, S. E., R. C. Flagan, and J. H. Seinfeld (1992). "Atmospheric photooxidation of isoprene part II: The ozone-isoprene reaction". In: *Int. J. Chem. Kinetics* 24.1, pp. 103–125. DOI: 10.1002/kin.550240110.

Paulson, S. E. and J. H. Seinfeld (1992). "Development and evaluation of a photooxidation mechanism for isoprene". In: *J. Geophys. Res. - Atmos.* 97.D18, pp. 20703–20715. DOI: 10.1029/92JD01914.

Payne, G. B. (1959). "Reactions of hydrogen peroxide. V. Alkaline epoxidation of acrolein and methacrolein". In: *J. Am. Chem. Soc.* 81.18, pp. 4901–4904.

Peeters, J. and J. F. Muller (2010). "HO(x) radical regeneration in isoprene oxidation via peroxy radical isomerisations. II: Experimental evidence and global impact". In: *Phys. Chem. Chem. Phys.* 12.42, pp. 14227–35. DOI: 10.1039/c0cp00811g.

Peeters, J., J. F. Muller, T. Stavrakou, and V. S. Nguyen (2014). "Hydroxyl radical recycling in isoprene oxidation driven by hydrogen bonding and hydrogen tunneling: The upgraded LIM1 mechanism". In: *J Phys. Chem. A*, Just Accepted. DOI: 10.1021/jp5033146.

Peeters, J. and T. L. Nguyen (2012). "Unusually fast 1,6-H shifts of enolic hydrogens in peroxy radicals: formation of the first-generation C2 and C3 carbonyls in the oxidation of isoprene". In: *J. Phys. Chem. A* 116.24, pp. 6134–6141. DOI: 10.1021/jp211447q.

Peeters, J., T. L. Nguyen, and L. Vereecken (2009). "HOx radical regeneration in the oxidation of isoprene". In: *Phys. Chem. Chem. Phys.* 11.28, pp. 5935–9. DOI: 10.1039/b908511d.

Peeters, J., G. Fantechi, and L. Vereecken (2004). "A generalized structure-activity relationship for the decomposition of (substituted) alkoxy radicals". In: *J. Atmos. Chem.* 48.1, pp. 59–80. DOI: 10.1023/B:JOCH.0000034510.07694.ce.

Peltier, R. E., R. J. Weber, and A. P. Sullivan (2007). "Investigating a liquid-based method for online organic carbon detection in atmospheric particles". In: *Aerosol Sci. Technol.* 41.12, pp. 1117–1127. DOI: 10.1080/02786820701777465.

Perring, A. E., S. E. Pusede, and R. C. Cohen (2013). "An observational perspective on the atmospheric impacts of alkyl and multifunctional nitrates on ozone and secondary organic aerosol". In: *Chem. Rev.* 113.8, pp. 5848–5870. DOI: 10.1021/cr300520x.

Perring, A., A. Wisthaler, M. Graus, P. Wooldridge, A. Lockwood, L. Mielke, P. Shepson, A. Hansel, and R. Cohen (2009). "A product study of the isoprene + NO3 reaction". In: *Atmos. Chem. Phys.* 9.14, pp. 4945–4956.

Peterson, K. A., T. B. Adler, and H.-J. Werner (2008). "Systematically convergent basis sets for explicitly correlated wavefunctions: The atoms H, He, B–Ne, and Al–Ar". In: *J. Chem. Phys.* 128.8, p. 084102. DOI: 10.1063/1.2831537.

Pfister, G. G., L. K. Emmons, P. G. Hess, J.-F. Lamarque, J. J. Orlando, S. Walters, A. Guenther, P. I. Palmer, and P. J. Lawrence (2008). "Contribution of isoprene to chemical budgets: A model tracer study with the NCAR CTM MOZART-4". In: *J. Geophys. Res.* 113. DOI: 10.1029/2007JD008948.

Pfrang, C., M. D. King, M. Braeckevelt, C. E. Canosa-Mas, and R. P. Wayne (2008). "Gas-phase rate coefficients for reactions of NO3, OH, O3 and O(3P) with unsaturated alcohols and ethers: Correlations and structure–activity relations (SARs)". In: *Atmos. Environ.* 42.13, pp. 3018–3034. DOI: http://dx.doi.org/10.1016/j.atmosenv.2007.12.046.

Pike, R. C., J. D. Lee, P. J. Young, G. D. Carver, X. Yang, N. Warwick, S. Moller, P. Misztal, B. Langford, D. Stewart, C. E. Reeves, C. N. Hewitt, and J. A. Pyle (2010). "NOx and O3 above a tropical rainforest: an analysis with a global and box model". In: *Atmos. Chem. Phys.* 10.21, pp. 10607–10620. DOI: 10.5194/acp-10-10607-2010.

Pope, C. A., R. T. Burnett, M. J. Thun, and et al. (2002). "Lung cancer, cardiopulmonary mortality, and long-term exposure to fine particulate air pollution". In: *J. Am. Med. Assoc.* 287.9, pp. 1132–1141. DOI: 10.1001/jama.287.9.1132.

Pope, C. A. I., M. Ezzati, and D. W. Dockery (2009). "Fine-particulate air pollution and life expectancy in the United States". In: *New England J. Med.* 360.4, pp. 376–386. DOI: doi:10.1056/NEJMsa0805646.

Pope, C. A. and D. W. Dockery (2006). "Health effects of fine particulate air pollution: Lines that connect". In: *J. Air Waste Management Assoc.* 56.6, pp. 709–742. DOI: 10.1080/10473289.2006.10464485.

Pöschl, U., S. T. Martin, B. Sinha, Q. Chen, S. S. Gunthe, J. A. Huffman, S. Borrmann, D. K. Farmer, R. M. Garland, G. Helas, J. L. Jimenez, S. M. King, A. Manzi, E. Mikhailov, T. Pauliquevis, M. D. Petters, A. J. Prenni, P. Roldin, D. Rose, J. Schneider, H. Su, S. R. Zorn, P. Artaxo, and M. O. Andreae (2010). "Rain-

forest aerosols as biogenic nuclei of clouds and precipitation in the Amazon". In: *Science* 329, pp. 1513–1516.

Pöschl, U., R. von Kuhlmann, N. Poisson, and P. J. Crutzen (2000). "Development and intercomparison of condensed isoprene oxidation mechanisms for global atmospheric modeling". In: *J. Atmos. Chem.* 37.1, pp. 29–52. DOI: 10.1023/A:1006391009798.

Prabhakar, G., B. Ervens, Z. Wang, L. C. Maudlin, M. M. Coggon, H. H. Jonsson, J. H. Seinfeld, and A. Sorooshian (2014). "Sources of nitrate in stratocumulus cloud water: Airborne measurements during the 2011 E-PEACE and 2013 NiCE studies". In: *Atmos. Environ.* 97, pp. 166–173. DOI: http://dx.doi.org/10.1016/j.atmosenv.2014.08.019.

Praske, E., J. D. Crounse, K. H. Bates, T. Kurtén, H. G. Kjaergaard, and P. O. Wennberg (2015). "Atmospheric fate of methyl vinyl ketone: Peroxy radical reactions with NO and HO2". In: *J. Phys. Chem. A* 119.19, pp. 4562–4572.

Pratt, D. A., J. H. Mills, and N. A. Porter (2003). "Theoretical calculations of carbon-oxygen bond dissociation enthalpies of peroxyl radicals formed in the autoxidation of lipids". In: *J. Am. Chem. Soc.* 125.19, pp. 5801–5810. DOI: 10.1021/ja034182j.

Pusede, S. E. and R. C. Cohen (2012). "On the observed response of ozone to NOx and VOC reactivity reductions in San Joaquin Valley California 1995-present". In: *Atmos. Chem. Phys.* 12.18, pp. 8323–8339. DOI: 10.5194/acp-12-8323-2012.

Pye, H. O., R. W. Pinder, I. R. Piletic, Y. Xie, S. L. Capps, Y. H. Lin, J. D. Surratt, Z. Zhang, A. Gold, D. J. Luecken, W. T. Hutzell, M. Jaoui, J. H. Offenberg, T. E. Kleindienst, M. Lewandowski, and E. O. Edney (2013). "Epoxide pathways improve model predictions of isoprene markers and reveal key role of acidity in aerosol formation". In: *Environ. Sci. Technol.* 47.19, pp. 11056–11064. DOI: 10.1021/es402106h.

Raes, F., H. Liao, W.-T. Chen, and J. H. Seinfeld (2010). "Atmospheric chemistry-climate feedbacks". In: *J. Geophys Res. - Atmos.* 115.D12. DOI: 10.1029/2009JD013300.

Raff, J. D., B. Njegic, W. L. Chang, M. S. Gordon, D. Dabdub, R. B. Gerber, and B. J. Finlayson-Pitts (2009). "Chlorine activation indoors and outdoors via surface-mediated reactions of nitrogen oxides with hydrogen chloride". In: *Proc. Nat'l. Acad. Sci.* 106.33, pp. 13647–13654. DOI: 10.1073/pnas.0904195106.

Ragains, M. L. and B. J. Finlayson-Pitts (1997). "Kinetics and mechanism of the reaction of Cl atoms with 2-methyl-1,3-butadiene (isoprene) at 298 K". In: *J. Phys. Chem. A* 101.8, pp. 1509–1517. DOI: 10.1021/jp962786m.

Rastogi, N., M. M. Oakes, J. J. Schauer, M. M. Shafer, B. J. Majestic, and R. J. Weber (2009). "New technique for online measurement of water-soluble Fe(II) in atmospheric aerosols". In: *Environ. Sci. Technol.* 43.7, pp. 2425–2430. DOI: 10.1021/es8031902.

Ravishankara, A. R. (2009). "Are chlorine atoms significant tropospheric free radicals?" In: *Proc. Nat'l. Acad. Sci.* 106.33, pp. 13639–13640. DOI: 10.1073/pnas.0907089106.

Reitz, J. E., W. S. McGivern, M. C. Church, M. D. Wilson, and S. W. North (2002). "The fate of the hydroxyalkoxy radical in the OH-initiated oxidation of isoprene". In: *Int. J. Chem. Kinetics* 34, pp. 255–261.

Ren, X., J. R. Olson, J. H. Crawford, W. H. Brune, J. Mao, R. B. Long, Z. Chen, G. Chen, M. a. Avery, G. W. Sachse, J. D. Barrick, G. S. Diskin, L. G. Huey, A. Fried, R. C. Cohen, B. Heikes, P. O. Wennberg, H. B. Singh, D. R. Blake, and R. E. Shetter (2008). "HOx chemistry during INTEX-A 2004: Observation, model calculation, and comparison with previous studies". In: *J. Geophys. Res.* 113, p. D05310. DOI: 10.1029/2007JD009166.

Rickard, A. R., D. Johnson, C. D. McGill, and G. Marston (1999). "OH yields in the gas-phase reactions of ozone with alkenes". In: *J. Phys. Chem. A* 103.38, pp. 7656–7664. DOI: 10.1021/jp9916992.

Ridley, B. and F. Grahek (1990). "A Small, Low Flow, High Sensitivity Reaction Vessel for NO Chemiluminescence Detectors". In: *J. Atmos. Ocean. Tech.* 7.2, pp. 307–311. DOI: 10.1175/1520-0426(1990)007<0307:ASLFHS>2.0.CO;2.

Riedel, T. P., Y.-H. Lin, S. H. Budisulistiorini, C. J. Gaston, J. A. Thornton, Z. Zhang, W. Vizuete, A. Gold, and J. D. Surratt (2015). "Heterogeneous reactions of isoprene-derived epoxides: Reaction probabilities and molar secondary organic aerosol yield estimates". In: *Environ. Sci. Technol. Lett.* 2.2, pp. 38–42. DOI: 10.1021/ez500406f.

Riemer, D., E. Apel, J. Orlando, G. Tyndall, W. Brune, E. Williams, W. Lonneman, and J. Neece (2008). "Unique isoprene oxidation products demonstrate chlorine atom chemistry occurs in the Houston, Texas urban area". In: *J. Atmos. Chem.* 61.3, pp. 227–242. DOI: 10.1007/s10874-009-9134-5.

Riva, M., D. M. Bell, A.-M. K. Hansen, G. T. Drozd, Z. Zhang, A. Gold, D. Imre, J. D. Surratt, M. Glasius, and A. Zelenyuk (2016a). "Effect of organic coatings, humidity and aerosol acidity on multiphase chemistry of isoprene epoxydiols". In: *Environ. Sci. Technol.* 50.11, pp. 5580–5588. DOI: 10.1021/acs.est.5b06050.

Riva, M., S. H. Budisulistiorini, Y. Chen, Z. Zhang, E. L. D'Ambro, X. Zhang, A. Gold, B. J. Turpin, J. A. Thornton, M. R. Canagaratna, and J. D. Surratt (2016b). "Chemical characterization of secondary organic aerosol from oxidation of isoprene hydroxyhydroperoxides". In: *Environ. Sci. Technol.* 50.18, pp. 9889–9899. DOI: 10.1021/acs.est.6b02511.

Rivera-Rios, J. C., T. B. Nguyen, J. D. Crounse, W. Jud, J. M. St. Clair, T. Mikoviny, J. B. Gilman, B. M. Lerner, J. B. Kaiser, J. de Gouw, A. Wisthaler, A. Hansel, P. O. Wennberg, J. H. Seinfeld, and F. N. Keutsch (2014). "Conversion of hydroperoxides to carbonyls in field and laboratory instrumentation: Observational bias in diagnosing pristine versus anthropogenically controlled atmospheric chemistry".

In: *Geophys. Res. Lett.* 41.23. 2014GL061919, pp. 8645–8651. DOI: 10.1002/2014GL061919.

Robert, J. M. and R. W. Fajer (1989). "UV absorption cross sections of organic nitrates of potential atmospheric importance and estimation of atmospheric lifetimes". In: *Environ. Sci. Technol.* 23.8, pp. 945–951. DOI: 10.1021/es00066a003.

Roberts, J. M. and S. B. Bertman (1992). "The thermal decomposition of peroxyacetic nitric anhydride (PAN) and peroxymethacrylic nitric anhydride (MPAN)". In: *Int. J. Chem. Kinetics* 24.3, pp. 297–307. DOI: 10.1002/kin.550240307.

Roberts, J. M., H. D. Osthoff, S. S. Brown, and A. R. Ravishankara (2008). "N2O5 oxidizes chloride to Cl2 in acidic atmospheric aerosol". In: *Science*. DOI: 10.1126/science.1158777. eprint: http://science.sciencemag.org/content/early/2008/07/03/science.1158777.full.pdf.

Roberts, J. M., J. Williams, K. Baumann, M. P. Buhr, P. D. Goldan, J. Holloway, G. Hübler, W. C. Kuster, S. A. McKeen, T. B. Ryerson, M. Trainer, E. J. Williams, F. C. Fehsenfeld, S. B. Bertman, G. Nouaime, C. Seaver, G. Grodzinsky, M. Rodgers, and V. L. Young (1998). "Measurements of PAN, PPN, and MPAN made during the 1994 and 1995 Nashville Intensives of the Southern Oxidant Study: Implications for regional ozone production from biogenic hydrocarbons". In: *J. Geophys. Res. - Atmos.* 103.D17, pp. 22473–22490. DOI: 10.1029/98JD01637.

Robinson, N. H., J. F. Hamilton, J. D. Allan, B. Langford, D. E. Oram, Q. Chen, K. Docherty, D. K. Farmer, J. L. Jimenez, M. W. Ward, C. N. Hewitt, M. H. Barley, M. E. Jenkin, A. R. Rickard, S. T. Martin, G. McFiggans, and H. Coe (2011). "Evidence for a significant proportion of secondary organic aerosol from isoprene above a maritime tropical forest". In: *Atmos. Chem. Phys.* 11.3, pp. 1039–1050. DOI: 10.5194/acp-11-1039-2011.

Roehl, C. M., Z. Marka, J. L. Fry, and P. O. Wennberg (2007). "Near-UV photolysis cross sections of CH3OOH and HOCH2OOH determined via action spectroscopy". In: *Atmos. Chem. Phys.* 7.3, pp. 713–720. DOI: 10.5194/acp-7-713-2007.

Rogge, W. F., M. A. Mazurek, L. M. Hildemann, G. R. Cass, and B. R. T. Simoneit (1993). "Quantification of urban organic aerosols at a molecular level: Identification, abundance and seasonal variation". In: *Atmos. Environ.* 27.8, pp. 1309–1330. DOI: http://dx.doi.org/10.1016/0960-1686(93)90257-Y.

Rollins, A. W., E. C. Browne, K.-E. Min, S. E. Pusede, P. J. Wooldridge, D. R. Gentner, A. H. Goldstein, S. Liu, D. A. Day, L. M. Russell, and R. C. Cohen (2012). "Evidence for NOx control over nighttime SOA formation". In: *Science* 337, pp. 1210–1212.

Rollins, A. W., A. Kiendler-Scharr, J. Fry, T. Brauers, S. S. Brown, H.-P. Dorn, W. P. Dubé, H. Fuchs, A. Mensah, T. Mentel, *et al.* (2009). "Isoprene oxidation by nitrate radical alkyl nitrate and secondary organic aerosol yields". In: *Atmos. Chem. Phys.* 9.18, pp. 6685–6703.

Rosenstiel, T., M. Potosnak, K. Griffin, R. Fall, and R. Monson (2003). "Increased CO2 uncouples growth from isoprene emission in an agriforest ecosystem". In: *Nature* 421, pp. 256–259. DOI: 10.1038/nature01351.1..

Rothman, L. S., I. E. Gordon, A. Barbe, D. C. Benner, P. F. Bernath, M. Birk, V. Boudon, L. R. Brown, A. Campargue, J. P. Champion, K. Chance, L. H. Coudert, V. Dana, V. M. Devi, S. Fally, J. M. Flaud, R. R. Gamache, A. Goldman, D. Jacquemart, I. Kleiner, N. Lacome, W. J. Lafferty, J. Y. Mandin, S. T. Massie, S. N. Mikhailenko, C. E. Miller, N. Moazzen-Ahmadi, O. V. Naumenko, A. V. Nikitin, J. Orphal, V. I. Perevalov, A. Perrin, A. Predoi-Cross, C. P. Rinsland, M. Rotger, M. Šimečková, M. A. H. Smith, K. Sung, S. A. Tashkun, J. Tennyson, R. A. Toth, A. C. Vandaele, and J. Vander Auwera (2009). "The HITRAN 2008 molecular spectroscopic database". In: *Journal of Quantitative Spectroscopy and Radiative Transfer* 110.9–10, pp. 533–572. DOI: http://dx.doi.org/10.1016/j.jqsrt.2009.02.013.

Rudich, Y., R. K. Talukdar, R. W. Fox, and A. R. Ravishankara (1996). "Rate coefficients for reactions of NO3 with a few olefins and oxygenated olefins". In: *J. Phys. Chem.* 100.13, pp. 5374–5381. DOI: 10.1021/jp953079g.

Rudolph, J., R. Koppmann, and C. Plass-Dülmer (1996). "The budgets of ethane and tetrachloroethene: Is there evidence for an impact of reactions with chlorine atoms in the troposphere?" In: *Atmos. Environ.* 30.10–11, pp. 1887–1894. DOI: http://dx.doi.org/10.1016/1352-2310(95)00385-1.

Ruppert, L. and K. Heinz Becker (2000). "A product study of the OH radical-initiated oxidation of isoprene: formation of C5-unsaturated diols". In: *Atmos. Environ.* 34.10, pp. 1529–1542. DOI: http://dx.doi.org/10.1016/S1352-2310(99)00408-2.

Russell, L. M., A. Sorooshian, J. H. Seinfeld, B. A. Albrecht, A. Nenes, L. Ahlm, Y.-C. Chen, M. Coggon, J. S. Craven, R. C. Flagan, A. A. Frossard, H. Jonsson, E. Jung, J. J. Lin, A. R. Metcalf, R. Modini, J. Mülmenstädt, G. Roberts, T. Shingler, S. Song, Z. Wang, and A. Wonaschütz (2013). "Eastern Pacific emitted aerosol cloud experiment". In: *Bull. Am. Met. Soc.* 94.5, pp. 709–729. DOI: 10.1175/BAMS-D-12-00015.1.

Ryzhkov, A. B. and P. A. Ariya (2003). "A theoretical study of the reactions of carbonyl oxide with water in atmosphere: the role of water dimer". In: *Chem. Phys. Lett.* 367.3–4, pp. 423–429. DOI: http://dx.doi.org/10.1016/S0009-2614(02)01685-8.

– (2004). "A theoretical study of the reactions of parent and substituted Criegee intermediates with water and the water dimer". In: *Phys. Chem. Chem. Phys.* 6.21, pp. 5042–5050. DOI: 10.1039/B408414D.

– (2006). "The importance of water clusters (H2O)n (n = 2,..., 4) in the reaction of Criegee intermediate with water in the atmosphere". In: *Chem. Phys. Lett.* 419.4–6, pp. 479–485. DOI: http://dx.doi.org/10.1016/j.cplett.2005.12.016.

Salgado, M. S., E. Monedero, F. Villanueva, P. Martín, A. Tapia, and B. Cabañas (2008). "Night-time atmospheric fate of acrolein and crotonaldehyde". In: *Environ. Sci. Technol.* 42.7, pp. 2394–2400. DOI: 10.1021/es702533u.

Sanadze, G. A. (2004). "Biogenic isoprene (a review)". In: *Russian Journal of Plant Physiology* 51.6, pp. 729–741. DOI: 10.1023/B:RUPP.0000047821.63354.a4.

Sanchez, K. J., L. M. Russell, R. L. Modini, A. A. Frossard, L. Ahlm, C. E. Corrigan, G. C. Roberts, L. N. Hawkins, J. C. Schroder, A. K. Bertram, R. Zhao, A. K. Y. Lee, J. J. Lin, A. Nenes, Z. Wang, A. Wonaschütz, A. Sorooshian, K. J. Noone, H. Jonsson, D. Toom, A. M. Macdonald, W. R. Leaitch, and J. H. Seinfeld (2016). "Meteorological and aerosol effects on marine cloud microphysical properties". In: *J. Geophys. Res. - Atmos.* 121.8, pp. 4142–4161. DOI: 10.1002/2015JD024595.

Sander, S. P., J. Abbatt, J. R. Barker, J. B. Burkholder, R. R. Friedl, D. M. Golden, R. E. Huie, C. E. Kolb, M. J. Kurylo, G. K. Moortgat, V. L. Orkin, and P. H. Wine (2011). *Chemical Kinetics and Photochemical Data for Use in Atmospheric Studies, Evaluation No. 17*. Report. Jet Propulsion Laboratory. URL: http://jpldataeval.jpl.nasa.gov.

Sareen, N., A. N. Schwier, E. L. Shapiro, D. Mitroo, and V. F. McNeill (2010). "Secondary organic material formed by methylglyoxal in aqueous aerosol mimics". In: *Atmos. Chem. Phys.* 10, pp. 997–1016.

Sareen, N., S. G. Moussa, and V. F. McNeill (2013). "Photochemical aging of light-absorbing secondary organic aerosol material". In: *J. Phys. Chem. A* 117.14, pp. 2987–2996. DOI: 10.1021/jp309413j.

Sauer, F., C. Schäfer, P. Neeb, O. Horie, and G. K. Moortgat (1999). "Formation of hydrogen peroxide in the ozonolysis of isoprene and simple alkenes under humid conditions". In: *Atmos. Environ.* 33.2, pp. 229–241. DOI: http://dx.doi.org/10.1016/S1352-2310(98)00152-6.

Saunders, S. M., D. L. Baulch, K. M. Cooke, M. J. Pilling, and P. I. Smurthwaite (1994). "Kinetics and mechanisms of the reactions of OH with some oxygenated compounds of importance in tropospheric chemistry". In: *Int. J. Chem. Kinetics* 26.1, pp. 113–130. DOI: 10.1002/kin.550260112.

Saunders, S. M., M. E. Jenkin, R. G. Derwent, and M. J. Pilling (2003). "Protocol for the development of the Master Chemical Mechanism, MCM v3 (Part A): tropospheric degradation of non-aromatic volatile organic compounds". In: *Atmos. Chem. Phys.* 3, pp. 161–180.

Schauer, J. J., B. T. Mader, J. T. DeMinter, G. Heidemann, M. S. Bae, J. H. Seinfeld, R. C. Flagan, R. A. Cary, D. Smith, B. J. Huebert, T. Bertram, S. Howell, J. T. Kline, P. Quinn, T. Bates, B. Turpin, H. J. Lim, J. Z. Yu, H. Yang, and M. D. Keywood (2003). "ACE-Asia intercomparison of a thermal-optical method for the determination of particle-phase organic and elemental carbon". In: *Environ. Sci. Technol.* 37.5, pp. 993–1001. DOI: 10.1021/es020622f.

Schilling Fahnestock, K. A., L. D. Yee, C. L. Loza, M. M. Coggon, R. Schwantes, X. Zhang, N. F. Dalleska, and J. H. Seinfeld (2015). "Secondary organic aerosol composition from C12 alkanes". In: *J. Phys. Chem. A* 119.19, pp. 4281–4297. DOI: 10.1021/jp501779w.

Schkolnik, G., A. H. Falkovich, Y. Rudich, W. Maenhaut, and P. Artaxo (2005). "A new method for the determination of levoglucosan, methyl-erythritol and related compounds and its application for rainwater and smoke samples". In: *Environ. Sci. Technol.* 39.8, pp. 2744–2752.

Schroeder, W. H. and P. Urone (1974). "Formation of nitrosyl chloride from salt particles in air". In: *Environ. Sci. Technol.* 8.8, pp. 756–758. DOI: 10.1021/es60093a015.

Schwantes, R. H. (2017). "Identifying isoprene and toluene gas-phase oxidation products to better constrain ozone and secondary organic aerosol formation in the atmosphere". Thesis.

Schwantes, R. H., A. P. Teng, T. B. Nguyen, M. M. Coggon, J. D. Crounse, J. M. S. Clair, X. Zhang, K. A. Schilling, J. H. Seinfeld, and P. O. Wennberg (2015). "Isoprene NO3 oxidation products from the RO2 + HO2 pathway". In: *J. Phys. Chem. A* 119.40, pp. 10158–10171. DOI: 10.1021/acs.jpca.5b06355.

Sehested, J., L. K. Christensen, O. J. Nielsen, M. Bilde, T. J. Wallington, W. F. Schneider, J. J. Orlando, and G. S. Tyndall (1998). "Atmospheric chemistry of acetone: Kinetic study of the CH3C(O)CH2O2+NO/NO2 reactions and decomposition of CH3C(O)CH2O2NO2". In: *Int. J. Chem. Kinetics* 30.7, pp. 475–489. DOI: 10.1002/(SICI)1097-4601(1998).

Seinfeld, J. H. and S. N. Pandis (2006). *Atmospheric Chemistry and Physics: From Air Pollution to Climate Change*. 2nd ed. Wiley.

Serjeant, E. P. and B. Dempsey (1979). *Ionisation Constants of Organic Acids in Aqueous Solution*. Vol. 23. IUPAC Chemical Data Series. Oxford; New York: Pergamon Press.

Sharkey, T. D. (1996). "Isoprene synthesis by plants and animals". In: *Endeavour* 20.2, pp. 74–78. DOI: http://dx.doi.org/10.1016/0160-9327(96)10014-4.

Sharkey, T. D., A. E. Wiberley, and A. R. Donohue (2008). "Isoprene emission from plants: Why and how". In: *Annals of Botany* 101.1, pp. 5–18. DOI: 10.1093/aob/mcm240.

Sharkey, T. D. and S. Yeh (2001). "Isoprene emission from plants". In: *Annual Review of Plant Physiology and Plant Molecular Biology* 52.1, pp. 407–436. DOI: 10.1146/annurev.arplant.52.1.407.

Sharon, T. M., B. A. Albrecht, H. H. Jonsson, P. Minnis, M. M. Khaiyer, T. M. van Reken, J. Seinfeld, and R. Flagan (2006). "Aerosol and cloud microphysical characteristics of rifts and gradients in maritime stratocumulus clouds". In: *J. Atmos. Sci.* 63.3, pp. 983–997. DOI: 10.1175/JAS3667.1.

Sharpe, S. W., R. L. Sams, and T. J. Johnson (2002). "The PNNL quantitative IR database for infrared remote sensing and hyperspectral imaging". In: *Applied Imagery Pattern Recognition Workshop, 2002. Proceedings.* Pp. 45–48. DOI: 10.1109/AIPR.2002.1182253.

Sharpe, S. W., T. J. Johnson, R. L. Sams, P. M. Chu, G. C. Rhoderick, and P. A. Johnson (2004). "Gas-phase databases for quantitative infrared spectroscopy". In: *Applied Spectroscopy* 58.12, pp. 1452–1461. DOI: 10.1366/0003702042641281.

Sheps, L., A. M. Scully, and K. Au (2014). "UV absorption probing of the conformer-dependent reactivity of a Criegee intermediate CH3CHOO". In: *Phys. Chem. Chem. Phys.* 16.48, pp. 26701–26706. DOI: 10.1039/C4CP04408H.

Shi, Y., J. Zhang, J. S. Reid, B. Liu, and E. J. Hyer (2014). "Critical evaluation of cloud contamination in the MISR aerosol products using MODIS cloud mask products". In: *Atmos. Meas. Tech.* 7.6, pp. 1791–1801. DOI: 10.5194/amt-7-1791-2014.

Shim, C., Y. H. Wang, Y. Choi, P. Palmer, D. S. Abbot, and K. Chance (2005). "Constraining global isoprene emissions with Global Ozone Monitoring Experiment (GOME) formaldehyde column measurements". In: *J. Geophys. Res.* 110.D24.

Shingler, T., S. Dey, A. Sorooshian, F. J. Brechtel, Z. Wang, A. Metcalf, M. Coggon, J. Mülmenstädt, L. M. Russell, H. H. Jonsson, and J. H. Seinfeld (2012). "Characterisation and airborne deployment of a new counterflow virtual impactor inlet". In: *Atmos. Meas. Tech.* 5.6, pp. 1259–1269. DOI: 10.5194/amt-5-1259-2012.

Siese, M., K. H. Becker, K. J. Brockmann, H. Geiger, A. Hofzumahaus, F. Holland, D. Mihelcic, and K. Wirtz (2001). "Direct measurement of OH radicals from ozonolysis of selected alkenes: A EUPHORE simulation chamber study". In: *Environ. Sci. Technol.* 35.23, pp. 4660–4667. DOI: 10.1021/es010150p.

Silva, G. d., C. Graham, and Z.-F. Wang (2010). "Unimolecular beta-hydroxyperoxy radical decomposition with OH recycling in the photochemical oxidation of isoprene". In: *Environ. Sci. Technol.* 44.1, pp. 250–256. DOI: 10.1021/es900924d.

Simonaitis, R., K. J. Olszyna, and J. F. Meagher (1991). "Production of hydrogen peroxide and organic peroxides in the gas phase reactions of ozone with natural alkenes". In: *Geophys. Res. Lett.* 18.1, pp. 9–12. DOI: 10.1029/90GL02602.

Simpson, C. D., M. Paulsen, R. L. Dills, L. J. S. Liu, and D. A. Kalman (2005). "Determination of methoxyphenols in ambient atmospheric particulate matter: Tracers for wood combustion". In: *Environ. Sci. Technol.* 39.2, pp. 631–637. DOI: 10.1021/es0486871.

Singh, H. B., G. L. Gregory, B. Anderson, E. Browell, G. W. Sachse, D. D. Davis, J. Crawford, J. D. Bradshaw, R. Talbot, D. R. Blake, D. Thornton, R. Newell, and J. Merrill (1996). "Low ozone in the marine boundary layer of the tropical Pacific Ocean: Photochemical loss, chlorine atoms, and entrainment". In: *J. Geophys. Res. - Atmos.* 101.D1, pp. 1907–1917. DOI: 10.1029/95JD01028.

Sinha, V., J. Williams, J. N. Crowley, and J. Lelieveld (2008). "The Comparative Reactivity Method - a new tool to measure total OH Reactivity in ambient air". In: *Atmos. Chem. Phys.* 8.8, pp. 2213–2227. DOI: 10.5194/acp-8-2213-2008.

Sipilä, M., T. Jokinen, T. Berndt, S. Richters, R. Makkonen, N. M. Donahue, R. L. Mauldin III, T. Kurtén, P. Paasonen, N. Sarnela, M. Ehn, H. Junninen, M. P. Rissanen, J. Thornton, F. Stratmann, H. Herrmann, D. R. Worsnop, M. Kulmala, V.-M. Kerminen, and T. Petäjä (2014). "Reactivity of stabilized Criegee intermediates (sCIs) from isoprene and monoterpene ozonolysis toward SO2 and organic acids". In: *Atmos. Chem. Phys.* 14.22, pp. 12143–12153. DOI: 10.5194/acp-14-12143-2014.

Skov, H., J. Hjorth, C. Lohse, N. R. Jensen, and G. Restelli (1992). "Products and mechanisms of the reactions of the nitrate radical (NO3) with isoprene, 1,3-butadiene and 2,3-dimethyl-1,3-butadiene in air". In: *Atmos. Environ.* 26.15, pp. 2771–2783. DOI: 10.1016/0960-1686(92)90015-D.

Smith, J. N., K. F. Moore, F. L. Eisele, D. Voisin, A. K. Ghimire, H. Sakurai, and P. H. McMurry (2005). "Chemical composition of atmospheric nanoparticles during nucleation events in Atlanta". In: *J. Geophys. Res. - Atmos.* 110.D22. DOI: 10.1029/2005JD005912.

Solomons, T. W. G. and C. B. Fryhle (2004). *Organic Chemistry*. 8th ed. Hoboken, NJ: John Wiley and Sons, Ing., p. 1255.

Sorooshian, A., S. M. Murphy, S. Hersey, H. Gates, L. T. Padro, A. Nenes, F. J. Brechtel, H. Jonsson, R. C. Flagan, and J. H. Seinfeld (2008). "Comprehensive airborne characterization of aerosol from a major bovine source". In: *Atmos. Chem. Phys.* 8.17, pp. 5489–5520. DOI: 10.5194/acp-8-5489-2008.

Sorooshian, A., Z. Wang, M. M. Coggon, H. H. Jonsson, and B. Ervens (2013). "Observations of sharp oxalate reductions in stratocumulus clouds at variable altitudes: Organic acid and metal measurements during the 2011 E-PEACE campaign". In: *Environ. Sci. Technol.* 47.14, pp. 7747–7756. DOI: 10.1021/es4012383.

Sorooshian, A., F. J. Brechtel, Y. Ma, R. J. Weber, A. Corless, R. C. Flagan, and J. H. Seinfeld (2006). "Modeling and characterization of a Particle-into-Liquid Sampler (PILS)". In: *Aerosol. Sci. Technol.* 40.6, pp. 396–409. DOI: 10.1080/02786820600632282.

Sorooshian, A., E. Crosbie, L. C. Maudlin, J.-S. Youn, Z. Wang, T. Shingler, A. M. Ortega, S. Hersey, and R. K. Woods (2015). "Surface and airborne measurements of organosulfur and methanesulfonate over the western United States and coastal areas". In: *J. Geophys. Res. - Atmos.* 120.16, pp. 8535–8548. DOI: 10.1002/2015JD023822.

Sorooshian, A., M.-L. Lu, F. J. Brechtel, H. Jonsson, G. Feingold, R. C. Flagan, and J. H. Seinfeld (2007). "On the source of organic acid aerosol layers above clouds". In: *Environ. Sci. Technol.* 41.13, pp. 4647–4654. DOI: 10.1021/es0630442.

Spittler, M., I. Barnes, I. Bejan, K. J. Brockmann, T. Benter, and K. Wirtz (2006). "Reactions of NO3 radicals with limonene and alpha-pinene: Product and SOA formation". In: *Atmos. Environ.* 40, Supplement 1, pp. 116–127. DOI: http://dx.doi.org/10.1016/j.atmosenv.2005.09.093.

Sprengnether, M., K. L. Demerjian, N. M. Donahue, and J. G. Anderson (2002). "Product analysis of the OH oxidation of isoprene and 1,3-butadiene in the presence of NO". In: *J. Geophys. Res. - Atmos.* 107.D15. DOI: 10.1029/2001JD000716.

Squire, O. J., A. T. Archibald, P. T. Griffiths, M. E. Jenkin, D. Smith, and J. A. Pyle (2015). "Influence of isoprene chemical mechanism on modeled changes in tropospheric ozone due to climate and land use over the 21st century". In: *Atmos. Chem. Phys.* 15.9, pp. 5123–5143. DOI: 10.5194/acp-15-5123-2015.

St. Clair, J. M., J. C. Rivera-Rios, J. D. Crounse, H. C. Knap, K. H. Bates, A. P. Teng, S. Jorgensen, H. G. Kjaergaard, F. N. Keutsch, and P. O. Wennberg (2015). "Kinetics and products of the reaction of the first-generation isoprene hydroxy hydroperoxide (ISOPOOH) with OH". In: *J. Phys. Chem. A*, just accepted. DOI: 10.1021/acs.jpca.5b06532.

St. Clair, J. M., K. M. Spencer, M. R. Beaver, J. D. Crounse, F. Paulot, and P. O. Wennberg (2014). "Quantification of hydroxyacetone and glycolaldehyde using chemical ionization mass spectrometry". In: *Atmos. Chem. Phys.* 14.8, pp. 4251–4262. DOI: 10.5194/acp-14-4251-2014.

St. Clair, J. M., D. C. McCabe, J. D. Crounse, U. Steiner, and P. O. Wennberg (2010). "Chemical ionization tandem mass spectrometer for the in situ measurement of methyl hydrogen peroxide". In: *Review of Scientific Instruments* 81.9. DOI: http://dx.doi.org/10.1063/1.3480552.

Stabel, J. R., M. S. Johnson, and S. Langer (2005). "Rate coefficients for the gas-phase reaction of isoprene with NO3 and NO2". In: *Int. J. Chem. Kinetics* 37.2, pp. 57–65. DOI: 10.1002/kin.20050.

Starn, T. K., P. B. Shepson, S. B. Bertman, D. D. Riemer, R. G. Zika, and K. Olszyna (1998). "Nighttime isoprene chemistry at an urban-impacted forest site". In: *J. Geophys. Res. - Atmos.* 103.D17, pp. 22437–22447. DOI: 10.1029/98JD01201.

Stavrakou, T., J. F. Muller, J. Peeters, A. Razavi, L. Clarisse, C. Clerbaux, P. F. Coheur, D. Hurtmans, M. De Maziere, C. Vigouroux, N. M. Deutscher, D. W. T. Griffith, N. Jones, and C. Paton-Walsh (2012). "Satellite evidence for a large source of formic acid from boreal and tropical forests". In: *Nature Geosci.* 5.1, pp. 26–30. DOI: http://www.nature.com/ngeo/journal/v5/n1/abs/ngeo1354.html#supplementary-information.

Stein, A. F., R. R. Draxler, G. D. Rolph, B. J. B. Stunder, M. D. Cohen, and F. Ngan (2015). "NOAA's HYSPLIT atmospheric rransport and dispersion modeling system". In: *Bull. Am. Met. Soc.* 96.12, pp. 2059–2077. DOI: 10.1175/BAMS-D-14-00110.1.

Stephens, E. R. (1969). "The formation, reactions, and properties of peroxyacyl nitrates (PANs) in photochemical air pollution". In: *Advances in Environmental Science and Technology*. Ed. by J. N. Pitts and R. L. Metcalf. Vol. 1. New York, NY: Wiley-Interscience.

Stephens, G. L. and T. J. Greenwald (1991). "The Earth's radiation budget and its relation to atmospheric hydrology: 2. Observations of cloud effects". In: *J. Geophys. Res. - Atmos.* 96.D8, pp. 15325–15340. DOI: 10.1029/91JD00972.

Stevens, B., D. H. Lenschow, G. Vali, H. Gerber, A. Bandy, B. Blomquist, J. L. Brenguier, C. S. Bretherton, F. Burnet, T. Campos, S. Chai, I. Faloona, D. Friesen, S. Haimov, K. Laursen, D. K. Lilly, S. M. Loehrer, S. P. Malinowski, B. Morley, M. D. Petters, D. C. Rogers, L. Russell, V. Savic-Jovcic, J. R. Snider, D. Straub, M. J. Szumowski, H. Takagi, D. C. Thornton, M. Tschudi, C. Twohy, M. Wetzel, and M. C. van Zanten (2003). "Dynamics and chemistry of marine stratocumulus—DYCOMS-II". In: *Bull. Am. Met. Soc.* 84.5, pp. 579–593. DOI: 10.1175/BAMS-84-5-579.

Stevens, P., D. L'Esperance, B. Chuong, and G. Martin (1999). "Measurements of the kinetics of the OH-initiated oxidation of isoprene: Radical propagation in the OH + isoprene + O2 + NO reaction system". In: *Int. J. Chem. Kinetics* 31.9, pp. 637–643. DOI: 10.1002/(SICI)1097-4601(1999)31:9<637::AID-KIN5>3.0.CO;2-O.

Stone, D., M. Blitz, L. Daubney, N. U. M. Howes, and P. Seakins (2014). "Kinetics of CH2OO reactions with SO2, NO2, NO, H2O and CH3CHO as a function of pressure". In: *Phys. Chem. Chem. Phys.* 16.3, pp. 1139–1149. DOI: 10.1039/C3CP54391A.

Stone, D. and D. M. Rowley (2005). "Kinetics of the gas phase HO2 self-reaction: Effects of temperature, pressure, water and methanol vapours". In: *Phys. Chem. Chem. Phys.* 7.10, pp. 2156–2163. DOI: 10.1039/B502673C.

Stroud, C. A., J. M. Roberts, E. J. Williams, D. Hereid, W. M. Angevine, F. C. Fehsenfeld, A. Wisthaler, A. Hansel, M. Martinez-Harder, H. Harder, W. H. Brune, G. Hoenninger, J. Stutz, and A. B. White (2002). "Nighttime isoprene trends at an urban forested site during the 1999 Southern Oxidant Study". In: *J. Geophys. Res. - Atmos.* 107.D16, ACH 7-1–ACH 7-14. DOI: 10.1029/2001JD000959.

Su, F., J. G. Calvert, and J. H. Shaw (1980). "A FT IR spectroscopic study of the ozone-ethene reaction mechanism in oxygen-rich mixtures". In: *J. Phys. Chem.* 84.3, pp. 239–246. DOI: 10.1021/j100440a003.

Su, T. and W. J. Chesnavich (1982). "Parameterization of the ion-polar molecule collision rate constant by trajectory calculations". In: *J. Chem. Phys.* 76.10, pp. 5183–5185.

Su, Y.-T., H.-Y. Lin, R. Putikam, H. Matsui, M. C. Lin, and Y.-P. Lee (2014). "Extremely rapid self-reaction of the simplest Criegee intermediate CH2OO and its implications in atmospheric chemistry". In: *Nat. Chem.* 6.6, pp. 477–483. DOI:

10.1038/nchem.1890http://www.nature.com/nchem/journal/v6/n6/abs/nchem.1890.html#supplementary-information.

Suarez-Bertoa, R., B. Picquet-Varrault, W. Tamas, E. Pangui, and J.-F. Doussin (2012). "Atmospheric fate of a series of carbonyl nitrates: photolysis frequencies and OH-oxidation rate constants". In: *Environ. Sci. Technol.* 46.22, pp. 12502–12509. DOI: 10.1021/es302613x.

Suh, I., W. Lei, and R. Zhang (2001). "Experimental and theoretical studies of isoprene reaction with NO3". In: *J. Phys. Chem. A* 105.26, pp. 6471–6478. DOI: 10.1021/jp0105950.

Suh, I. and R. Zhang (2000). "Kinetic studies of isoprene reactions initiated by chlorine atom". In: *J. Phys. Chem. A* 104.28, pp. 6590–6596. DOI: 10.1021/jp000605h.

Sullivan, A. P., R. E. Peltier, C. A. Brock, J. A. de Gouw, J. S. Holloway, C. Warneke, A. G. Wollny, and R. J. Weber (2006). "Airborne measurements of carbonaceous aerosol soluble in water over northeastern United States: Method development and an investigation into water-soluble organic carbon sources". In: *J. Geophys. Res. - Atmos.* 111.D23. DOI: 10.1029/2006JD007072.

Sullivan, R. C. and K. A. Prather (2005). "Recent advances in our understanding of atmospheric chemistry and climate made possible by on-line aerosol analysis instrumentation". In: *Anal. Chem.* 77.12, pp. 3861–3886. DOI: 10.1021/ac050716i.

Surratt, J. D., M. Lewandowski, J. H. Offenberg, M. Jaoui, T. E. Kleindienst, E. O. Edney, and J. H. Seinfeld (2007a). "Effect of acidity on secondary organic aerosol formation from isoprene". In: *Environ. Sci. Technol.* 41, pp. 5363–5369.

Surratt, J. D. (2013). "Atmospheric chemistry: Radical regeneration from isoprene". In: *Nature Geosci* 6.12, pp. 995–996. DOI: 10.1038/ngeo2022.

Surratt, J. D., A. W. H. Chan, N. C. Eddingsaas, M. Chan, C. L. Loza, A. J. Kwan, S. P. Hersey, R. C. Flagan, P. O. Wennberg, and J. H. Seinfeld (2010). "Reactive intermediates revealed in secondary organic aerosol formation from isoprene." In: *Proc. Nat'l. Acad. Sci.* 107, pp. 6640–6645. DOI: 10.1073/pnas.0911114107.

Surratt, J. D., Y. Gómez-González, A. W. H. Chan, R. Vermeylen, M. Shahgholi, T. E. Kleindienst, E. O. Edney, J. H. Offenberg, M. Lewandowski, M. Jaoui, W. Maenhaut, M. Claeys, R. C. Flagan, and J. H. Seinfeld (2008). "Organosulfate formation in biogenic secondary organic aerosol". In: *J. Phys. Chem. A* 112.36, pp. 8345–8378. DOI: 10.1021/jp802310p.

Surratt, J. D., J. H. Kroll, T. E. Kleindienst, E. O. Edney, M. Claeys, A. Sorooshian, N. L. Ng, J. H. Offenberg, M. Lewandowski, M. Jaoui, R. C. Flagan, and J. H. Seinfeld (2007b). "Evidence for organosulfates in secondary organic aerosol". In: *Environ. Sci. Technol.* 41.2, pp. 517–527. DOI: 10.1021/es062081q.

Surratt, J. D., S. M. Murphy, J. H. Kroll, N. L. Ng, L. Hildebrandt, A. Sorooshian, R. Szmigielski, R. Vermeylen, W. Maenhaut, M. Claeys, R. C. Flagan, and J. H. Seinfeld (2006). "Chemical composition of secondary organic aerosol formed from the photooxidation of isoprene." In: *J. Phys. Chem. A* 110, pp. 9665–90. DOI: 10.1021/jp061734m.

Szmigielski, R., J. D. Surratt, R. Vermeylen, K. Szmigielska, J. H. Kroll, N. L. Ng, S. M. Murphy, A. Sorooshian, J. H. Seinfeld, and M. Claeys (2007). "Characterization of 2-methylglyceric acid oligomers in secondary organic aerosol formed from the photooxidation of isoprene using trimethylsilylation and gas chromatography/ion trap mass spectrometry". In: *J. Mass Spectrometry* 42.1, pp. 101–116. DOI: 10.1002/jms.1146.

Taatjes, C. A., G. Meloni, T. M. Selby, A. J. Trevitt, D. L. Osborn, C. J. Percival, and D. E. Shallcross (2008). "Direct observation of the gas-phase Criegee intermediate (CH2OO)". In: *J. Am. Chem. Soc.* 130.36, pp. 11883–11885. DOI: 10.1021/ja804165q.

Taatjes, C. A., O. Welz, A. J. Eskola, J. D. Savee, A. M. Scheer, D. E. Shallcross, B. Rotavera, E. P. F. Lee, J. M. Dyke, D. K. W. Mok, D. L. Osborn, and C. J. Percival (2013). "Direct measurements of conformer-dependent reactivity of the Criegee intermediate CH3CHOO". In: *Science* 340.6129, pp. 177–180. DOI: 10.1126/science.1234689. eprint: http://science.sciencemag.org/content/340/6129/177.full.pdf.

Tan, D., I. Faloona, J. B. Simpas, W. Brune, P. B. Shepson, T. L. Couch, A. L. Sumner, M. A. Carroll, T. Thornberry, E. Apel, D. Riemer, and W. Stockwell (2001). "HOx budgets in a deciduous forest: Results from the PROPHET summer 1998 campaign". In: *J. Geophys. Res. - Atmos.* 106.D20, pp. 24407–24427. DOI: 10.1029/2001JD900016.

Taylor, W. D., T. D. Allston, M. J. Moscato, G. B. Fazekas, R. Kozlowski, and G. A. Takacs (1980). "Atmospheric photodissociation lifetimes for nitromethane, methyl nitrite, and methyl nitrate". In: *Int. J. Chem. Kinetics* 12.4, pp. 231–240. DOI: 10.1002/kin.550120404.

Teng, A. P., J. D. Crounse, L. Lee, J. M. St. Clair, R. C. Cohen, and P. O. Wennberg (2015). "Hydroxy nitrate production in the OH-initiated oxidation of alkenes". In: *Atmos. Chem. Phys.* 15, pp. 4297–4316.

Teng, A. P., J. D. Crounse, and P. O. Wennberg (2017). "Isoprene Peroxy Radical Dynamics". In: *J. Am. Chem. Soc.* 139.15, pp. 5367–5377.

Terai, C. R., C. S. Bretherton, R. Wood, and G. Painter (2014). "Aircraft observations of aerosol, cloud, precipitation, and boundary layer properties in pockets of open cells over the southeast Pacific". In: *Atmos. Chem. Phys.* 14.15, pp. 8071–8088. DOI: 10.5194/acp-14-8071-2014.

Thamm, J., S. Wolff, W. V. Turner, S. Gäb, W. Thomas, F. Zabel, E. H. Fink, and K. H. Becker (1996). "Proof of the formation of hydroperoxymethyl formate in the ozonolysis of ethene: synthesis and FT-IR spectra of the authentic compound". In: *Chem. Phys. Lett.* 258.1, pp. 155–158. DOI: http://dx.doi.org/10.1016/0009-2614(96)00625-2.

Thornton, J. A., P. J. Wooldridge, R. C. Cohen, M. Martinez, H. Harder, W. H. Brune, E. J. Williams, J. M. Roberts, F. C. Fehsenfeld, S. R. Hall, R. E. Shetter, B. P. Wert, and A. Fried (2002). "Ozone production rates as a function of NOx abundances and HOx production rates in the Nashville urban plume". In: *J. Geophys. Res.* 107.D12. DOI: 10.1029/2001jd000932.

Thornton, J. A., J. P. Kercher, T. P. Riedel, N. L. Wagner, J. Cozic, J. S. Holloway, W. P. Dubé, G. M. Wolfe, P. K. Quinn, A. M. Middlebrook, B. Alexander, and S. S. Brown (2010). "A large atomic chlorine source inferred from mid-continental reactive nitrogen chemistry". In: *Nature* 464.7286, pp. 271–274. DOI: http://www.nature.com/nature/journal/v464/n7286/suppinfo/nature08905_S1.html.

Tomas, A., E. Villenave, and R. Lesclaux (2001). "Reactions of the HO2 radical with CH3CHO and CH3C(O)O2 in the gas phase". In: *J. Phys. Chem. A* 105.14, pp. 3505–3514. DOI: 10.1021/jp003762p.

Torres, A. L. and H. Buchan (1988). "Tropospheric nitric oxide measurements over the Amazon Basin". In: *J. Geophys. Res. - Atmos.* 93.D2, pp. 1396–1406. DOI: 10.1029/JD093iD02p01396.

Trainer, M., E. J. Williams, D. D. Parrish, M. P. Buhr, E. J. Allwine, H. H. Westberg, F. C. Fehsenfeld, and S. C. Liu (1987). "Models and observations of the impact of natural hydrocarbons on rural ozone". In: *Nature* 329.6141, pp. 705–707.

Travis, K. R., D. J. Jacob, J. A. Fisher, P. S. Kim, E. A. Marais, L. Zhu, K. Yu, C. C. Miller, R. M. Yantosca, M. P. Sulprizio, A. M. Thompson, P. O. Wennberg, J. D. Crounse, J. M. St. Clair, R. C. Cohen, J. L. Laughner, J. E. Dibb, S. R. Hall, K. Ullmann, G. M. Wolfe, I. B. Pollack, J. Peischl, J. A. Neuman, and X. Zhou (2016). "Why do models overestimate surface ozone in the Southeast United States?" In: *Atmos. Chem. Phys.* 16.21, pp. 13561–13577. DOI: 10.5194/acp-16-13561-2016.

Treacy, J., M. E. Hag, D. O'Farrell, and H. Sidebottom (1992). "Reactions of ozone with unsaturated organic compounds". In: *Berichte der Bunsengesellschaft für physikalische Chemie* 96.3, pp. 422–427. DOI: 10.1002/bbpc.19920960337.

Troe, J. (1983). "Theory of thermal unimolecular reactions in the fall-off range. I. Strong collision rate constants". In: *Berichte der Bunsengesellschaft für physikalische Chemie* 87.2, pp. 161–169. DOI: 10.1002/bbpc.19830870217.

Tuazon, E. C. and R. Atkinson (1989). "A product study of the gas-phase reaction of methyl vinyl ketone with the OH radical in the presence of NOx". In: *Int. J. Chem. Kinetics* 21.12, pp. 1141–1152. DOI: 10.1002/kin.550211207.

Tuazon, E. C. and R. Atkinson (1990). "A product study of the gas-phase reaction of methacrolein with the OH radical in the presence of NOx". In: *Int. J. Chem. Kinetics* 22.6, pp. 591–602. DOI: 10.1002/kin.550220604.

Turner, A. J., C. Frankenberg, P. O. Wennberg, and D. J. Jacob (2017). "Ambiguity in the causes for decadal trends in atmospheric methane and hydroxyl". In: *Proc. Natl. Acad. Sci.* in press.

Turpin, B. J., P. Saxena, and E. Andrews (2000). "Measuring and simulating particulate organics in the atmosphere: Problems and prospects". In: *Atmos. Environ.* 34.18, pp. 2983–3013. DOI: http://doi.org/10.1016/S1352-2310(99)00501-4.

Tyndall, G. S., R. A. Cox, C. Granier, R. Lesclaux, G. K. Moortgat, M. J. Pilling, A. R. Ravishankara, and T. J. Wallington (2001). "Atmospheric chemistry of small organic peroxy radicals". In: *J. Geophys. Res. - Atmos.* 106.D11, pp. 12157–12182. DOI: 10.1029/2000JD900746.

Vakhtin, A. B., J. E. Murphy, and S. R. Leone (2003). "Low-temperature kinetics of reactions of OH radical with ethene, propene, and 1-butene". In: *J. Phys. Chem. A* 107.47, pp. 10055–10062. DOI: 10.1021/jp030230a.

Valin, L. C., A. R. Russell, and R. C. Cohen (2013). "Variations of OH radical in an urban plume inferred from NO2 column measurements". In: *Geophys. Res. Lett.* 40.9, pp. 1856–1860. DOI: 10.1002/grl.50267.

Valverde-Canossa, J., L. Ganzeveld, B. Rappenglück, R. Steinbrecher, O. Klemm, G. Schuster, and G. K. Moortgat (2006). "First measurements of H2O2 and organic peroxides surface fluxes by the relaxed eddy-accumulation technique". In: *Atmos. Environ.* 40, Supplement 1, pp. 55–67. DOI: http://dx.doi.org/10.1016/j.atmosenv.2006.03.038.

Varandas, A. J. C. (2012). "Ab initio treatment of bond-breaking reactions: Accurate course of HO3 dissociation and revisit to isomerization". In: *J. Chem. Theory and Comp.* 8.2, pp. 428–441. DOI: 10.1021/ct200773b.

Vega-Rodriguez, A. and J. R. Alvarez-Idaboy (2009). "Quantum chemistry and TST study of the mechanisms and branching ratios for the reactions of OH with unsaturated aldehydes". In: *Phys. Chem. Chem. Phys.* 11 (35), pp. 7649–7658. DOI: 10.1039/B906692F.

Verchot, L. V., E. A. Davidson, H. Cattânio, I. L. Ackerman, H. E. Erickson, and M. Keller (1999). "Land use change and biogeochemical controls of nitrogen oxide emissions from soils in eastern Amazonia". In: *Global Biogeochemical Cycles* 13.1, pp. 31–46. DOI: 10.1029/1998GB900019.

Vereecken, L., H. Harder, and A. Novelli (2012). "The reaction of Criegee intermediates with NO, RO2, and SO2, and their fate in the atmosphere". In: *Phys. Chem. Chem. Phys.* 14 (42), pp. 14682–14695. DOI: 10.1039/C2CP42300F.

Vereecken, L., H. Harder, and A. Novelli (2014). "The reactions of Criegee intermediates with alkenes, ozone, and carbonyl oxides". In: *Phys. Chem. Chem. Phys.* 16.9, pp. 4039–4049. DOI: 10.1039/C3CP54514H.

Vereecken, L., J. F. Muller, and J. Peeters (2007). "Low-volatility poly-oxygenates in the OH-initiated atmospheric oxidation of alpha-pinene: impact of non-traditional peroxyl radical chemistry". In: *Phys. Chem. Chem. Phys.* 9.38, pp. 5241–5248. DOI: 10.1039/B708023A.

Vereecken, L., T. L. Nguyen, I. Hermans, and J. Peeters (2004). "Computational study of the stability of alpha- hydroperoxyl-alpha-alkylperoxyl substituted alkyl radicals". In: *Chem. Phys. Lett.* 393, pp. 432–436.

Vereecken, L. and J. Peeters (2009). "Decomposition of substituted alkoxy radicals-part I: A generalized structure-activity relationship for reaction barrier heights". In: *Phys. Chem. Chem. Phys.* 11.40, pp. 9062–9074. DOI: 10.1039/B909712K.

Vereecken, L. and J. Peeters (1999). "Theoretical investigation of the role of intramolecular hydrogen bonding in beta-hydroxyethoxy and beta-hydroxyethylperoxy radicals in the tropospheric oxidation of ethene". In: *J. Phys. Chem. A* 103.12, pp. 1768–1775. DOI: 10.1021/jp9826930.

Vickers, C. E., J. Gershenzon, M. T. Lerdau, and F. Loreto (2009). "A unified mechanism of action for volatile isoprenoids in plant abiotic stress". In: *Nature Chem. Biol.* 5.5, pp. 283–291.

Vilà-Guerau de Arellano, J., K. van den Dries, and D. Pino (2009). "On inferring isoprene emission surface flux from atmospheric boundary layer concentration measurements". In: *Atmos. Chem. Phys.* 9.11, pp. 3629–3640. DOI: 10.5194/acp-9-3629-2009.

Villalta, P. W. and C. J. Howard (1996). "Direct kinetics study of the CH3C(O)O2 + NO reaction using chemical ionization mass spectrometry". In: *J. Phys. Chem.* 100.32, pp. 13624–13628. DOI: 10.1021/jp9614153.

Voulgarakis, A., V. Naik, J. F. Lamarque, D. T. Shindell, P. J. Young, M. J. Prather, O. Wild, R. D. Field, D. Bergmann, P. Cameron-Smith, I. Cionni, W. J. Collins, S. B. Dalsøren, R. M. Doherty, V. Eyring, G. Faluvegi, G. A. Folberth, L. W. Horowitz, B. Josse, I. A. MacKenzie, T. Nagashima, D. A. Plummer, M. Righi, S. T. Rumbold, D. S. Stevenson, S. A. Strode, K. Sudo, S. Szopa, and G. Zeng (2013). "Analysis of present day and future OH and methane lifetime in the ACCMIP simulations". In: *Atmos. Chem. Phys.* 13.5, pp. 2563–2587. DOI: 10.5194/acp-13-2563-2013.

Wallington, T. J., P. Dagaut, and M. J. Kurylo (1992). "UV absorption cross sections and reaction kinetics and mechanisms for peroxy radicals in the gas phase". In: *Chem. Rev.* 92.4, pp. 667–710. DOI: 10.1021/cr00012a008.

Wallington, T. J., M. D. Hurley, W. F. Schneider, J. Sehested, and O. J. Nielsen (1994). "Mechanistic study of the gas-phase reaction of CH2FO2 radicals with HO2". In: *Chem. Phys. Lett.* 218.1, pp. 34–42. DOI: http://dx.doi.org/10.1016/0009-2614(93)E1466-T.

Wang, B. and A. Laskin (2014). "Reactions between water-soluble organic acids and nitrates in atmospheric aerosols: Recycling of nitric acid and formation of organic salts". In: *J. Geophys. Res. - Atmos.* 119.6, pp. 3335–3351. DOI: 10.1002/2013JD021169.

Wang, J., J. F. Doussin, S. Perrier, E. Perraudin, Y. Katrib, E. Pangui, and B. Picquet-Varrault (2011). "Design of a new multi-phase experimental simulation chamber for atmospheric photosmog, aerosol and cloud chemistry research". In: *Atmos. Meas. Tech.* 4.11, pp. 2465–2494. DOI: 10.5194/amt-4-2465-2011.

Wang, J., Y. N. Lee, P. H. Daum, J. Jayne, and M. L. Alexander (2008a). "Effects of aerosol organics on cloud condensation nucleus (CCN) concentration and first indirect aerosol effect". In: *Atmos. Chem. Phys.* 8.21, pp. 6325–6339. DOI: 10.5194/acp-8-6325-2008.

Wang, K. Y. and D. E. Shallcross (2000). "Modelling terrestrial biogenic isoprene fluxes and their potential impact on global chemical species using a coupled sim-ctm model". In: *Atmos. Environ.* 34, pp. 2909–2925.

Wang, S. C. and R. C. Flagan (1990). "Scanning electrical mobility spectrometer". In: *Aerosol Sci. Technol.* 13.2, pp. 230–240. DOI: 10.1080/02786829008959441.

Wang, Z., A. Sorooshian, G. Prabhakar, M. M. Coggon, and H. H. Jonsson (2014). "Impact of emissions from shipping, land, and the ocean on stratocumulus cloud water elemental composition during the 2011 E-PEACE field campaign". In: *Atmos. Environ.* 89, pp. 570–580. DOI: http://dx.doi.org/10.1016/j.atmosenv.2014.01.020.

Wang, Z., C. Y.-T., Z.-B. Xu, and J. Qu (2008b). "Hot water-promoted ring-opening of epoxides and aziridines by water and other nucleophiles". In: *J. Org. Chem.* 73.6, pp. 2270–2274.

Wängberg, I., I. Barnes, and K. H. Becker (1997). "Product and mechanistic study of the reaction of NO3 radicals with alpha-pinene". In: *Environ. Sci. Technol.* 31.7, pp. 2130–2135. DOI: 10.1021/es960958n.

Warneke, C., R. Holzinger, A. Hansel, A. Jordan, W. Lindinger, U. Poschl, J. Williams, P. Hoor, H. Fischer, P. J. Crutzen, H. A. Scheeren, and J. Lelieveld (2001). "Isoprene and its oxidation products methyl vinyl ketone, methacrolein, and isoprene related peroxides measure online over the tropical rain forest of suriname in march 1998". In: *J. Atmos. Chem.* 38, pp. 167–185.

Warren, S., C. Hahn, J. London, R. Chervin, and R. Jenne (1986). "Global distribution of total cloud cover and cloud type over land". In: *NCAR Tech. Note NCAR/TN-273+ STR* 200.

Watson, J. G. (2002). “Visibility: Science and regulation”. In: *J. Air Waste Management Assoc.* 52.6, pp. 628–713. DOI: 10.1080/10473289.2002.10470813.

Weber, R. J., D. Orsini, Y. Daun, Y. N. Lee, P. J. Klotz, and F. Brechtel (2001). “A particle-into-liquid collector for rapid measurement of aerosol bulk chemical composition”. In: *Aerosol Sci. Technol.* 35.3, pp. 718–727. DOI: 10.1080/02786820152546761.

Wei, W.-m., R.-h. Zheng, Y.-l. Pan, Y.-k. Wu, F. Yang, and S. Hong (2014). “Ozone dissociation to oxygen affected by Criegee intermediate”. In: *J. Phys. Chem. A* 118.9, pp. 1644–1650. DOI: 10.1021/jp4121047.

Weitkamp, E. A., A. M. Sage, J. R. Pierce, N. M. Donahue, and A. L. Robinson (2007). “Organic aerosol formation from photochemical oxidation of diesel exhaust in a smog chamber”. In: *Environ. Sci. Technol.* 41.20, pp. 6969–6975. DOI: 10.1021/es070193r.

Wellman, G. R., B. Lam, E. L. Anderson, and E. V. White (1976). “A facile synthesis of 3,4-epoxybutanone”. In: *Synthesis* 8, pp. 547–548.

Welz, O., J. D. Savee, D. L. Osborn, S. S. Vasu, C. J. Percival, D. E. Shallcross, and C. A. Taatjes (2012). “Direct kinetic measurements of Criegee intermediate (CH2OO) formed by reaction of CH2I with O2”. In: *Science* 335.6065, pp. 204–207.

Wennberg, P. O. (2013). “Let’s abandon the "high-NOx" and "low-NOx" terminology”. In: *IGAC*. Ed. by M. L. Melamed.

Werner, H.-J., P. J. Knowles, G. Knizia, F. R. Manby, and M. Schütz (2012). “Molpro: A general-purpose quantum chemistry program package”. In: *Wiley Interdisciplinary Reviews: Computational Molecular Science* 2.2, pp. 242–253. DOI: 10.1002/wcms.82.

Whalley, L. K., K. L. Furneaux, A. Goddard, J. D. Lee, A. Mahajan, H. Oetjen, K. A. Read, N. Kaaden, L. J. Carpenter, A. C. Lewis, J. M. C. Plane, E. S. Saltzman, A. Wiedensohler, and D. E. Heard (2010). “The chemistry of OH and HO2 radicals in the boundary layer over the tropical Atlantic Ocean”. In: *Atmos. Chem. Phys.* 10.4, pp. 1555–1576. DOI: 10.5194/acp-10-1555-2010.

Wiedinmyer, C., A. Guenther, P. Harley, N. Hewitt, C. Geron, P. Artaxo, R. Steinbrecher, and R. Rasmussen (2004). “Global Organic Emissions from Vegetation”. In: *Emissions of Atmospheric Trace Compounds*. Ed. by C. Granier, P. Artaxo, and C. E. Reeves. Dordrecht: Springer Netherlands, pp. 115–170. ISBN: 978-1-4020-2167-1. DOI: 10.1007/978-1-4020-2167-1_4. URL: http://dx.doi.org/10.1007/978-1-4020-2167-1_4.

Wiedinmyer, C., X. Tie, A. Guenther, R. Neilson, and C. Granier (2006). “Future changes in biogenic isoprene emissions: how might they affect regional and global atmospheric chemistry?” In: *Earth Interactions* 10, pp. 1–19. DOI: 10.1175/EI174.1.

Wille, U., E. Becker, R. N. Schindler, I. T. Lancar, G. Poulet, and G. Le Bras (1991). "A discharge flow mass-spectrometric study of the reaction between the NO3 radical and isoprene". In: *J. Atmos. Chem.* 13.2, pp. 183–193. DOI: 10.1007/bf00115972.

Williams, J., U. Poschl, P. J. Crutzen, A. Hansel, R. Holzinger, C. Warneke, W. Lindinger, and J. Lelieveld (2001). "An atmospheric chemistry interpretation of mass scans obtained from a proton transfer mass spectrometer flown over the tropical rainforest of Surinam". In: *J. Atmos. Chem.* 38, pp. 133–166.

Wisthaler, A., N. Jensen, R. Winterhalter, W. Lindinger, and J. Hjorth (2001). "Measurements of acetone and other gas phase product yields from the OH-initiated oxidation of terpenes by proton-transfer-reaction mass spectrometry (PTR-MS)". In: *Atmos. Environ.* 35.35, pp. 6181–6191. DOI: http://dx.doi.org/10.1016/S1352-2310(01)00385-5.

Wittrock, F., A. Richter, H. Oetjen, J. P. Burrows, M. Kanakidou, S. Myriokefalitakis, R. Volkamer, S. Beirle, U. Platt, and T. Wagner (2006). "Simultaneous global observations of glyoxal and formaldehyde from space". In: *Geophys. Res. Lett.* 33. DOI: 10.1029/2006GL026310.

Wolfe, G. M., M. R. Marvin, S. J. Roberts, K. R. Travis, and J. Liao (2016). "The Framework for 0-D Atmospheric Modeling (F0AM) v3.1". In: *Geosci. Model Dev.* 9.9, pp. 3309–3319. DOI: 10.5194/gmd-9-3309-2016.

Wolfe, G. M., J. D. Crounse, J. D. Parrish, J. M. St. Clair, M. R. Beaver, F. Paulot, T. P. Yoon, P. O. Wennberg, and F. N. Keutsch (2012). "Photolysis, OH reactivity and ozone reactivity of a proxy for isoprene-derived hydroperoxyenals (HPALDs)". In: *Phys. Chem. Chem. Phys.* 14.20, pp. 7276–7286. DOI: 10.1039/C2CP40388A.

Wolfs, I. and H. O. Desseyn (1996). "Characteristic vibrational pattern for the cyclic dimer carboxylic acid function in the solid state". In: *Applied Spectroscopy* 50.8, pp. 1000–1006. DOI: 10.1366/0003702963905394.

Wong, J. P. S., A. K. Y. Lee, and J. P. D. Abbatt (2015). "Impacts of sulfate seed acidity and water content on isoprene secondary organic aerosol formation". In: *Environ. Sci. Technol.* 49.22, pp. 13215–13221. DOI: 10.1021/acs.est.5b02686.

Woo, J. L. and V. F. McNeill (2015). "simpleGAMMA v1.0 – a reduced model of secondary organic aerosol formation in the aqueous aerosol phase (aaSOA)". In: *Geosci. Model Dev.* 8.6, pp. 1821–1829. DOI: 10.5194/gmd-8-1821-2015.

Wood, R. (2012). "Stratocumulus clouds". In: *Monthly Weather Rev.* 140.8, pp. 2373–2423. DOI: 10.1175/MWR-D-11-00121.1.

Worden, H. M., K. W. Bowman, J. R. Worden, A. Eldering, and R. Beer (2008). "Satellite measurements of the clear-sky greenhouse effect from tropospheric ozone". In: *Nature Geosci.* 1.5, pp. 305–308. DOI: http://www.nature.com/ngeo/journal/v1/n5/suppinfo/ngeo182_S1.html.

Worton, D. R., J. D. Surratt, B. W. LaFranchi, A. W. H. Chan, Y. Zhao, R. J. Weber, J.-H. Park, J. B. Gilman, J. de Gouw, C. Park, G. Schade, M. Beaver, J. M. S. Clair, J. Crounse, P. Wennberg, G. M. Wolfe, S. Harrold, J. A. Thornton, D. K. Farmer, K. S. Docherty, M. J. Cubison, J.-L. Jimenez, A. A. Frossard, L. M. Russell, K. Kristensen, M. Glasius, J. Mao, X. Ren, W. Brune, E. C. Browne, S. E. Pusede, R. C. Cohen, J. H. Seinfeld, and A. H. Goldstein (2013). "Observational insights into aerosol formation from isoprene". In: *Environ. Sci. Technol.* 47.11, pp. 5686–5694.

Wu, S., L. J. Mickley, D. J. Jacob, J. A. Logan, R. M. Yantosca, and D. Rind (2007). "Why are there large differences between models in global budgets of tropospheric ozone?" In: *J. Geophys. Res. - Atmos.* 112.D5.

Xia, X. and P. K. Hopke (2006). "Seasonal variation of 2-methyltetrols in ambient air samples". In: *Environ. Sci. Technol.* 40.22, pp. 6934–6937.

Xie, Y., F. Paulot, W. P. L. Carter, C. G. Nolte, D. J. Luecken, W. T. Hutzell, P. O. Wennberg, R. C. Cohen, and R. W. Pinder (2013). "Understanding the impact of recent advances in isoprene photooxidation on simulations of regional air quality". In: *Atmos. Chem. Phys.* 13, pp. 8439–8455. DOI: 10.5194/acp-13-8439-2013.

Xing, J.-H., K. Takahashi, M. D. Hurley, and T. J. Wallington (2009). "Kinetics of the reaction of chlorine atoms with isoprene (2-methyl 1,3-butadiene, CH2C(CH3)CHCH2) at 297 +/- 2 K". In: *Chem. Phys. Lett.* 472.1–3, pp. 39–43. DOI: http://dx.doi.org/10.1016/j.cplett.2009.03.002.

Xiong, F., C. H. Borca, L. V. Slipchenko, and P. B. Shepson (2016). "Photochemical degradation of isoprene-derived 4,1-nitrooxy enal". In: *Atmos. Chem. Phys.* 16.9, pp. 5595–5610. DOI: 10.5194/acp-16-5595-2016.

Xiong, F., K. M. McAvey, K. A. Pratt, C. J. Groff, M. A. Hostetler, M. A. Lipton, T. K. Starn, J. V. Seeley, S. B. Bertman, A. P. Teng, J. D. Crounse, T. B. Nguyen, P. O. Wennberg, P. K. Misztal, A. H. Goldstein, A. B. Guenther, A. R. Koss, K. F. Olson, J. A. de Gouw, K. Baumann, E. S. Edgerton, P. A. Feiner, L. Zhang, D. O. Miller, W. H. Brune, and P. B. Shepson (2015). "Observation of isoprene hydroxynitrates in the southeastern United States and implications for the fate of NOx". In: *Atmos. Chem. Phys.* 15, pp. 11257–11272. DOI: 10.5194/acp-15-11257-2015.

Xiong, J. Q., M. Zhong, C. Fang, L. C. Chen, and M. Lippmann (1998). "Influence of organic films on the hygroscopicity of ultrafine sulfuric acid aerosol". In: *Environ. Sci. Technol.* 32.22, pp. 3536–3541. DOI: 10.1021/es980019q.

Xu, L., H. Guo, C. M. Boyd, M. Klein, A. Bougiatioti, K. M. Cerully, J. R. Hite, G. Isaacman-VanWertz, N. M. Kreisberg, C. Knote, K. Olson, A. Koss, A. H. Goldstein, S. V. Hering, J. de Gouw, K. Baumann, S.-H. Lee, A. Nenes, R. J. Weber, and N. L. Ng (2015). "Effect of anthropogenic emissions on aerosol formation from isoprene and monoterpenes in the southeastern United States". In: *Proc. Nat'l. Acad. Sci.* 112.1, pp. 37–42.

Yamashita, M. and J. B. Fenn (1984). "Negative ion production with the electrospray ion source". In: *J. Phys. Chem.* 88.20, pp. 4671–4675. DOI: 10.1021/j150664a046.

Yatavelli, R. L. N. and J. A. Thornton (2010). "Particulate organic matter detection using a Micro-Orifice Volatilization Impactor coupled to a Chemical Ionization Mass Spectrometer (MOVI-CIMS)". In: *Aerosol Sci. Technol.* 44.1, pp. 61–74. DOI: 10.1080/02786820903380233.

Yaws, C. L. (2003). *Handbook of Thermodynamic and Physical Properties of Chemical Compounds*. Norwich, NY: Knovel. ISBN: 1591244447.

York, D., N. Evensen, M. Martinez, and J. Delgado (2004). "Unified equations for the slope, intercept, and standard errors of the best straight line". In: *Am. J. Phys.* 72.3, pp. 367–375.

Youn, J. S., E. Crosbie, L. C. Maudlin, Z. Wang, and A. Sorooshian (2015). "Dimethylamine as a major alkyl amine species in particles and cloud water: Observations in semi-arid and coastal regions". In: *Atmos. Environ.* 122, pp. 250–258. DOI: http://dx.doi.org/10.1016/j.atmosenv.2015.09.061.

Yu, G., A. R. Bayer, M. M. Galloway, K. J. Korshavn, C. G. Fry, and F. N. Keutsch (2011). "Glyoxal in aqueous ammonium sulfate solutions: Products, kinetics and hydration effects". In: *Environ. Sci. Technol.* 45.15, pp. 6336–6342. DOI: 10.1021/es200989n.

Zador, J., A. W. Jasper, and J. A. Miller (2009). "The reaction between propene and hydroxyl". In: *Phys. Chem. Chem. Phys.* 11.46, pp. 11040–11053. DOI: 10.1039/B915707G.

Zahardis, J., B. W. LaFranchi, and G. A. Petrucci (2006). "The heterogeneous reaction of particle-phase methyl esters and ozone elucidated by photoelectron resonance capture ionization: Direct products of ozonolysis and secondary reactions leading to the formation of ketones". In: *Int. J. Mass Spec.* 253.1–2, pp. 38–47. DOI: http://doi.org/10.1016/j.ijms.2006.02.010.

Zhang, D. and R. Zhang (2002). "Mechanism of OH formation from ozonolysis of isoprene: A quantum-chemical study". In: *J. Am. Chem. Soc.* 124.11, pp. 2692–2703. DOI: 10.1021/ja011518l.

Zhang, D., R. Zhang, and D. T. Allen (2003a). "C–C bond fission pathways of chloroalkenyl alkoxy radicals". In: *J. Chem. Phys.* 118.4, pp. 1794–1801. DOI: http://dx.doi.org/10.1063/1.1531660.

Zhang, D., R. Zhang, and S. W. North (2003b). "Experimental study of NO reaction with isoprene hydroxyalkyl peroxy radicals". In: *J. Phys. Chem. A* 107.50, pp. 11013–11019. DOI: 10.1021/jp0360016.

Zhang, H., J. D. Surratt, Y. H. Lin, J. Bapat, and R. M. Kamens (2011). "Effect of relative humidity on SOA formation from isoprene/NO photooxidation: enhancement of 2-methylglyceric acid and its corresponding oligoesters under dry conditions". In: *Atmos. Chem. Phys.* 11.13, pp. 6411–6424. DOI: 10.5194/acp-11-6411-2011.

Zhang, J. and J. S. Reid (2006). "MODIS aerosol product analysis for data assimilation: Assessment of over-ocean level 2 aerosol optical thickness retrievals". In: *J. Geophys. Res. - Atmos.* 111.D22. DOI: 10.1029/2005JD006898.

Zhang, Q., J. L. Jimenez, M. R. Canagaratna, J. D. Allan, H. Coe, I. Ulbrich, M. R. Alfarra, A. Takami, A. M. Middlebrook, Y. L. Sun, K. Dzepina, E. Dunlea, K. Docherty, P. F. DeCarlo, D. Salcedo, T. Onasch, J. T. Jayne, T. Miyoshi, A. Shimono, S. Hatakeyama, N. Takegawa, Y. Kondo, J. Schneider, F. Drewnick, S. Borrmann, S. Weimer, K. Demerjian, P. Williams, K. Bower, R. Bahreini, L. Cottrell, R. J. Griffin, J. Rautiainen, J. Y. Sun, Y. M. Zhang, and D. R. Worsnop (2007). "Ubiquity and dominance of oxygenated species in organic aerosols in anthropogenically-influenced Northern Hemisphere midlatitudes". In: *Geophys. Res. Let.* 34.13. DOI: 10.1029/2007GL029979.

Zhang, X., R. H. Schwantes, M. M. Coggon, C. L. Loza, K. A. Schilling, R. C. Flagan, and J. H. Seinfeld (2014a). "Role of ozone in SOA formation from alkane photooxidation". In: *Atmos. Chem. Phys.* 14.3, pp. 1733–1753. DOI: 10.5194/acp-14-1733-2014.

Zhang, X., R. H. Schwantes, R. C. McVay, H. Lignell, M. M. Coggon, R. C. Flagan, and J. H. Seinfeld (2015). "Vapor wall deposition in Teflon chambers". In: *Atmos. Chem. Phys.* 15.8, pp. 4197–4214. DOI: 10.5194/acp-15-4197-2015.

Zhang, X. and J. H. Seinfeld (2013). "A functional group oxidation model (FGOM) for SOA formation and aging". In: *Atmos. Chem. Phys.* 13.12, pp. 5907–5926. DOI: 10.5194/acp-13-5907-2013.

Zhang, X., C. D. Cappa, S. H. Jathar, R. C. McVay, J. J. Ensberg, M. J. Kleeman, and J. H. Seinfeld (2014b). "Influence of vapor wall loss in laboratory chambers on yields of secondary organic aerosol". In: *Proc. Nat'l. Acad. Sci.* 111.16, pp. 5802–5807. DOI: 10.1073/pnas.1404727111.

Zhang, Z., Y.-H. Lin, H. Zhang, J. D. Surratt, L. M. Ball, and A. Gold (2012). "Technical Note: Synthesis of isoprene atmospheric oxidation products: isomeric epoxydiols and the rearrangement products cis- and trans-3-methyl-3,4-dihydroxytetrahydrofuran". In: *Atmos. Chem. Phys.* 12, pp. 8529–8535. DOI: 10.5194/acp-12-8529-2012.

Zhang, Z.-S., G. Engling, C.-Y. Chan, Y.-H. Yang, M. Lin, S. Shi, J. He, Y.-D. Li, and X.-M. Wang (2013). "Determination of isoprene-derived secondary organic aerosol tracers (2-methyltetrols) by HPAEC-PAD: Results from size-resolved aerosols in a tropical rainforest". In: *Atmos. Environ.* 70, pp. 468–476. DOI: 10.1016/j.atmosenv.2013.01.020.

Zhao, Z., S. Husainy, and G. D. Smith (2011). "Kinetics studies of the gas-phase reactions of NO3 radicals with series of 1-alkenes, dienes, cycloalkenes, alkenols, and alkenals". In: *J. Phys. Chem. A* 115.44. PMID: 21995489, pp. 12161–12172. DOI: 10.1021/jp206899w.

Zhou, S., I. Barnes, T. Zhu, I. Bejan, M. Albu, and T. Benter (2008). "Atmospheric chemistry of acetylacetone". In: *Environ. Sci. Technol.* 42.21, pp. 7905–7910. DOI: 10.1021/es8010282.

Zhou, Y., H. Hu, L. Li, H. Hou, and B. Wang (2013). "Ab initio study of the elusive HO3(X2A") radical and the reaction". In: *Computational and Theoretical Chem.* 1026, pp. 24–30. DOI: http://dx.doi.org/10.1016/j.comptc.2013.10.010.

Zimmermann, J. and D. Poppe (1996). "A supplement for the radm2 chemical mechanism: The photooxidation of isoprene". In: *Atmos. Environ.* 30, pp. 1255–1269.

Zinser, C., T. Jungblut, W. Heller, H. K. Seidlitz, J.-P. Schnitzler, D. Ernst, and H. S. Jr (2000). "The effect of ozone in Scots pine (Pinus sylvestris L.): Gene expression, biochemical changes and interactions with UV-B radiation". In: *Plant, Cell and Environment* 23.9, pp. 975–982. DOI: 10.1046/j.1365-3040.2000.00613.x.

Zuend, A., C. Marcolli, A. M. Booth, D. M. Lienhard, V. Soonsin, U. K. Krieger, D. O. Topping, G. McFiggans, T. Peter, and J. H. Seinfeld (2011). "New and extended parameterization of the thermodynamic model AIOMFAC: calculation of activity coefficients for organic-inorganic mixtures containing carboxyl, hydroxyl, carbonyl, ether, ester, alkenyl, alkyl, and aromatic functional groups". In: *Atmos. Chem. Phys.* 11.17, pp. 9155–9206. DOI: 10.5194/acp-11-9155-2011.

Zuend, A., C. Marcolli, B. P. Luo, and T. Peter (2008). "A thermodynamic model of mixed organic-inorganic aerosols to predict activity coefficients". In: *Atmos. Chem. Phys.* 8.16, pp. 4559–4593. DOI: 10.5194/acp-8-4559-2008.

Zuend, A., C. Marcolli, T. Peter, and J. H. Seinfeld (2010). "Computation of liquid-liquid equilibria and phase stabilities: implications for RH-dependent gas/particle partitioning of organic-inorganic aerosols". In: *Atmos. Chem. Phys.* 10.16, pp. 7795–7820. DOI: 10.5194/acp-10-7795-2010.

Appendix A

OVERVIEW OF THE FOCUSED ISOPRENE EXPERIMENT AT THE CALIFORNIA INSTITUTE OF TECHNOLOGY (FIXCIT): MECHANISTIC CHAMBER STUDIES ON THE OXIDATION OF BIOGENIC COMPOUNDS

Nguyen, T. B., J. D. Crounse, R. H. Schwantes, A. P. Teng, K. H. Bates, X. Zhang, J. M. St. Clair, W. H. Brune, G. S. Tyndall, F. N. Keutsch, J. H. Seinfeld, and P. O. Wennberg (2014). "Overview of the Focused Isoprene eXperiment at the California Institute of Technology (FIXCIT): Mechanistic chamber studies on the oxidation of biogenic compounds". In: *Atmos. Chem. Phys.* 14.24, pp. 13531–13549. DOI: 10.5194/acp-14-13531-2014.

Abstract

The Focused isoprene eXperiment at the California Institute of Technology (FIXCIT) was a collaborative atmospheric chamber campaign that occurred during January 2014. FIXCIT is the laboratory component of a synergistic field and laboratory effort aimed toward (1) better understanding the chemical details behind ambient observations relevant to the southeastern United States, (2) advancing the knowledge of atmospheric oxidation mechanisms of important biogenic hydrocarbons, and (3) characterizing the behavior of field instrumentation using authentic standards. Approximately 20 principal scientists from 14 academic and government institutions performed parallel measurements at a forested site in Alabama and at the atmospheric chambers at Caltech. During the 4 week campaign period, a series of chamber experiments was conducted to investigate the dark- and photo-induced oxidation of isoprene, α-pinene, methacrolein, pinonaldehyde, acylperoxy nitrates, isoprene hydroxy nitrates (ISOPN), isoprene hydroxy hydroperoxides (ISOPOOH), and isoprene epoxydiols (IEPOX) in a highly controlled and atmospherically relevant manner. Pinonaldehyde and isomer-specific standards of ISOPN, ISOPOOH, and IEPOX were synthesized and contributed by campaign participants, which enabled explicit exploration into the oxidation mechanisms and instrument responses for these important atmospheric compounds. The present overview describes the goals, experimental design, instrumental techniques, and preliminary observations from the campaign. This work provides context for forthcoming publications affiliated with the FIXCIT campaign. Insights from FIXCIT are anticipated to aid

significantly in interpretation of field data and the revision of mechanisms currently implemented in regional and global atmospheric models.

A.1 Introduction

A.1.1 Background

Biogenically produced isoprenoids (hydrocarbons comprised of C_5H_8 units) have global emission rates into the atmosphere surpassing those of anthropogenic hydrocarbons and methane (Guenther *et al.*, 2012; Guenther *et al.*, 1995). The biogenic carbon emission flux is dominated by isoprene (C_5H_8) and monoterpenes ($C_{10}H_{16}$), which account for approximately 50% and 30% of the OH reactivity over land, respectively (Fuentes *et al.*, 2000). Furthermore, it has been suggested that the atmospheric oxidation of isoprene, in particular, can buffer the oxidative capacity of forested regions by maintaining levels of the hydroxyl radical (OH) under lower nitric oxide (NO) conditions (Lelieveld *et al.*, 2008). Due to their large abundances, isoprene and monoterpenes also dominate the global budget of secondary organic aerosol (SOA) (Henze *et al.*, 2008). Thus, the accurate representation of detailed chemistry for isoprene and monoterpene is necessary for meaningful simulations of atmospheric HO_x (OH + HO_2), NO_x (NO + NO_2), surface ozone (O_3), trace gas lifetimes, and SOA.

Unsaturated hydrocarbons like isoprene and monoterpenes are primarily oxidized by OH, O_3, and the nitrate (NO_3) radical in the atmosphere. OH oxidation is the dominant fate for isoprene, but O_3 and NO_3 oxidation can dominate reactivity for monoterpenes and sesquiterpenes. Our understanding of the OH-initiated isoprene oxidation mechanism has significantly improved during the last decade, following the first suggestion of the capacity of isoprene to produce SOA (Claeys *et al.*, 2004). The mechanistic developments have been propelled by technological advancements in instrumentation (Crounse *et al.*, 2006; Hansel *et al.*, 1995; Jordan *et al.*, 2009; Junninen *et al.*, 2010), enabling the detection of more complex oxidation products derived from isoprene and other biogenic hydrocarbons. However, the scientific understanding of these biogenic oxidation mechanisms is far from complete. It is outside the scope of this overview to describe comprehensively the isoprene and monoterpene oxidation mechanisms. Rather, we provide a brief background of the oxidation of biogenic hydrocarbons, which includes "state-of-the-science" knowledge, to motivate the study. The mechanisms described here are illustrated in Figure A.1.

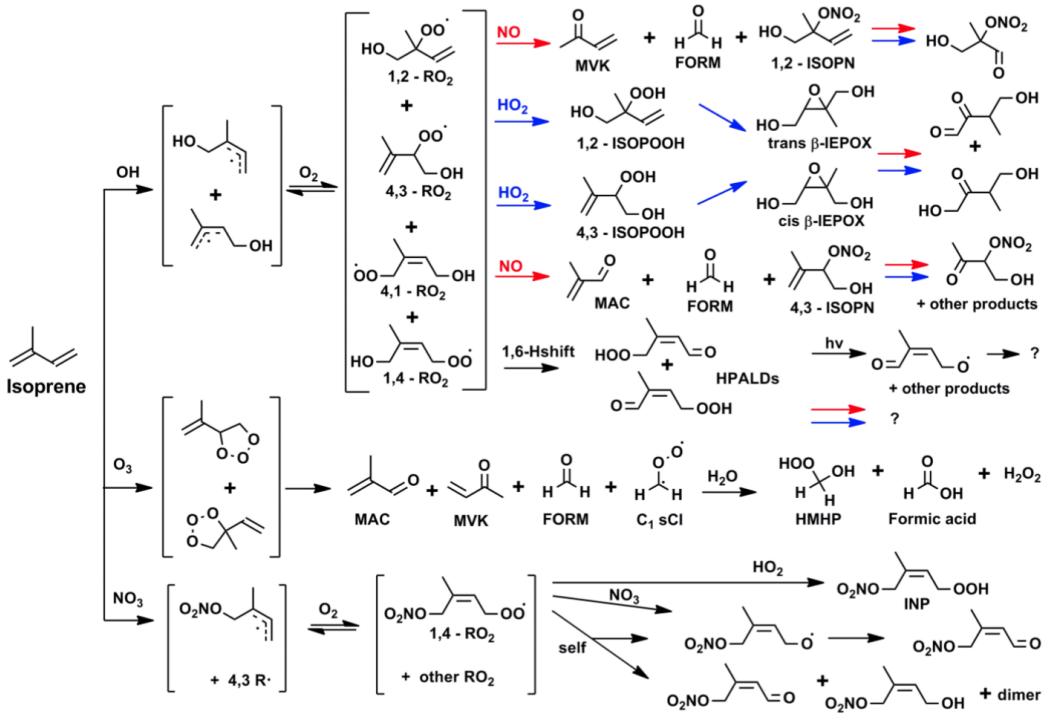

Figure A.1: Representative mechanism from the OH-, O_3- and NO_3-initated oxidation of isoprene. The most abundant isomers of a particular pathway are shown. Red and blue arrows in the OH-oxidation scheme denote the NO-dominated and HO_2-dominated RO_2 reactions, respectively. For the ozonolysis reaction, only the C_1 SCI and its reaction with water are shown as further-generation chemistry. For the NO_3-oxidation pathway, only one isomer each of R and RO_2 radicals is shown for brevity. Abbreviations are defined in the text.

A.1.1.1 OH Oxidation

OH predominantly adds to either of the double bonds of isoprene, followed by the reversible addition of O_2 (Peeters *et al.*, 2009) to produce several isomers of alkylperoxyl radicals (RO_2). In the atmosphere, these RO_2 react mainly with HO_2 and NO to form stable products, although self-reaction can be non-negligible under certain conditions. The stable products are often termed oxidized volatile organic compounds (OVOCs). In urban-influenced areas, the "high-NO" pathway is more important and in more pristine environments, the "low-NO" or HO_2-dominated pathway is more important. The high-NO pathway generates isoprene hydroxy nitrates (ISOPN) that act as reservoirs for NO_x, as well as other products such as methyl vinyl ketone (MVK), methacrolein (MAC), and hydroxyacetone (HAC) (Paulot *et al.*, 2009a). For conditions with sufficiently high NO_2-to-NO ratios, as is mainly the case in the atmospheric boundary layer outside of cities, methacryloyl

peroxynitrate (MPAN) is formed from the photooxidation of MAC. Further oxidation of MPAN can generate SOA (Chan *et al.*, 2010a; Surratt *et al.*, 2010). The low-NO pathway generates isoprene hydroxy hydroperoxides (ISOPOOH) in almost quantitative yields, and further OH oxidation of ISOPOOH produces the epoxydiols in an OH-conserving mechanism (Paulot *et al.*, 2009b). In unpolluted atmospheres, when the RO_2 lifetimes are sufficiently long (~100 s in a forest), isomerization of the RO_2 followed by reaction with O_2 becomes an important fate, producing the isoprene hydroperoxy aldehydes (HPALDs) and other products (Crounse *et al.*, 2011; Peeters *et al.*, 2009). These RO_2 isomerization reactions are a type of rapid oxygen incorporation chemistry (Crounse *et al.*, 2013; Ehn *et al.*, 2014; Vereecken *et al.*, 2007) that is thought to be responsible for the prompt generation of low-volatility SOA components. Further generations of OH oxidation in isoprene are currently being explored owing to recent success with chemical syntheses of important OVOCs (Bates *et al.*, 2014; Jacobs *et al.*, 2013; Lee *et al.*, 2014; Wolfe *et al.*, 2012). It has been found that the OH oxidation of IEPOX and ISOPN, surprisingly under both low-NO and high-NO conditions, results primarily in fragmentation of the C_5 skeleton.

Despite extensive work on the isoprene + OH mechanism, large uncertainties persist, some of which directly translate into uncertainties in atmospheric model predictions. These uncertainties stem from, for example, the large range in reported yields for isoprene nitrates (4–15%) (Paulot *et al.*, 2009a), disagreements up to 90% in reported MAC and MVK yields from the low-NO pathway (Liu *et al.* (2013), and references therein), various proposed sources of SOA from the high-NO pathway (Chan *et al.*, 2010a; Kjaergaard *et al.*, 2012; Lin *et al.*, 2013b), missing contributions to SOA mass from the low-NO pathway (Surratt *et al.*, 2010), uncharacterized fates of oxidized species like HPALDs (which may have isomer dependence), incomplete understanding of oxygen incorporation (Crounse *et al.*, 2013; Peeters *et al.*, 2009), and under-characterized impact of RO_2 lifetimes on chamber results (Wolfe *et al.*, 2012). The OH oxidation of α-pinene (Eddingsaas *et al.*, 2010) and other monoterpenes is less well characterized than that of isoprene, but, in general, proceeds through analogous steps.

A.1.1.2 Ozone Oxidation

Ozonolysis is a significant sink for unsaturated hydrocarbons and a large night-time source of OH, particularly in urban-influenced areas. Reaction with ozone is

more important for monoterpenes than isoprene, due to the faster rate coefficients (Atkinson and Lloyd, 1984) and the nighttime emission profile for the monoterpenes. Furthermore, monoterpene ozonolysis is highly efficient at converting VOC mass to SOA (Griffin *et al.*, 1999; Hoffmann *et al.*, 1997). There is a general consensus that ozonolysis occurs *via* the Criegee mechanism (Criegee, 1975), wherein ozone adds to a hydrocarbon double bond to form a five-member primary ozonide that quickly decomposes to a stable carbonyl product and an energy-rich Criegee intermediate (CI). In α-pinene oxidation, ozonolysis, NO_3-initiated, and OH-initiated reactions all produce pinonaldehyde ($C_{10}H_{16}O_2$) as a major product (Atkinson and Arey, 2003b; Wängberg *et al.*, 1997), whereas major first-generation products from isoprene ozonolysis include MAC, MVK, and formaldehyde. The "hot" Criegee can promptly lose OH (Kroll *et al.*, 2001) while ejecting an alkyl radical, or become stabilized by collision with atmospheric gases to form a stabilized Criegee intermediate (sCI) with long enough lifetimes to react bimolecularly. The subsequent reactions of sCIs produce both carbonyl products and non-carbonyl products such as hydroperoxides. The *syn* and *anti* conformers of CIs and SCI can have substantially different reactivities (Anglada *et al.*, 2011; Kuwata *et al.*, 2010), with syn conformers more likely to decompose unimolecularly, possibly through a vinyl hydroperoxide intermediate (Donahue *et al.*, 2011).

It has been suggested that reaction with water molecules is a major (if not dominant) bimolecular fate of SCI in the atmosphere due to the overwhelming abundance of atmospheric water (Fenske *et al.*, 2000). This suggestion is supported by observations of high mixing ratios (up to 5 ppbv) of hydroxymethyl hydroperoxide (HMHP), a characteristic product of reactions of the smallest SCI (CH_2OO) with water (Neeb *et al.*, 1997), over forested regions and in biomass burning plumes (Gab *et al.*, 1985; Lee and Hsu, 2000; Lee *et al.*, 1993a; Valverde-Canossa *et al.*, 2006). Although HMHP and other hydroperoxides produced from ozonolysis are important atmospheric compounds, their yield estimates are highly uncertain (Becker *et al.*, 1990; Hasson *et al.*, 2001a; Huang *et al.*, 2013; Neeb *et al.*, 1997; Sauer *et al.*, 1999). This may be attributable to the fact that hydroperoxide yields have mainly been determined by offline methods or under conditions with highly elevated hydrocarbon loadings. Furthermore, few empirical data exist on the humidity dependence of product branching in this reaction. Lastly, the rate coefficients for the SCI + H_2O reaction, and other SCI reactions, are still uncertain by several orders of magnitude (Johnson and Marston, 2008; Welz *et al.*, 2012), precluding the assessment of their atmospheric importance.

A.1.1.3 Nitrate Oxidation

NO_3 oxidation also produces RO_2 radicals by addition to alkenes in the presence of O_2. Owing to its high reaction rate coefficient coupled to atmospheric abundance, α-pinene is expected to be an important sink for NO_3 in many areas. The NO_3-derived RO_2 radicals react with (a) NO_3 to form alkoxy radicals (RO) that lead primarily to the production of nitrooxy carbonyls (b); with other RO_2 radicals to form RO radicals, nitrooxy carbonyls, hydroxy nitrates, and nitrooxy peroxy dimers; and (c) with HO_2 to form nitrooxy hydroperoxides. Further generation NO_3-oxidation produces dinitrates, amongst other products. As the NO_3 addition initiates the reaction, the thermodynamically preferred organic hydroxy nitrates produced through nighttime oxidation may be structurally different than those produced in the daytime through OH oxidation. During nighttime oxidation, tropospheric HO_2 mixing ratios often surpass those of NO_3 (Mao *et al.*, 2012), implying HO_2 reaction to be a common fate for NO_3-derived RO_2. However, previous studies of this reaction have maintained conditions where minimal HO_2 + RO_2 chemistry occurs and the dominant fate of RO_2 is reaction with NO_3 and RO_2 (Kwan *et al.*, 2012; Ng *et al.*, 2008; Perring *et al.*, 2009; Rollins *et al.*, 2009). This may be one of the reasons why nitrooxy hydroperoxides (the RO_2 + HO_2 product) are observed with much higher relative abundances in ambient air (Beaver *et al.*, 2012) than in chamber studies.

A.1.2 Scientific Goals

The 2014 Focused isoprene eXperiment at the California Institute of Technology (FIXCIT) is a collaborative atmospheric chamber campaign focused on advancing the understanding of biogenic hydrocarbon oxidation in the atmosphere. The campaign was motivated by the communal need for a tight coupling of field and laboratory efforts toward understanding the mechanistic details responsible for ambient observations, exploring explicit chemistry as driven by the fate of RO_2 radicals through well-controlled experiments, and fully characterizing instrumental response to important trace gases using authentic standards to guide data interpretation. To accomplish these goals, a suite of instruments typically deployed for field missions was used to perform parallel measurements at a forested site in Alabama and then in the atmospheric chambers at Caltech. This overview provides an account of the goals and conditions for the experiments performed during the campaign. A key component of FIXCIT is the re-design of "typical chamber experiments" to recreate the ambient atmosphere with higher fidelity so that results from laboratory studies can be implemented in models and used to interpret ambient observations with

higher confidence.

A.1.2.1 Understanding Ambient Observations

FIXCIT was designed as a sister investigation to the 2013 Southern Oxidant and Aerosol Study (SOAS). During SOAS (June-July 2013), a select sub-suite of instruments recorded ambient observations above the forest canopy on top of a metal walk-up tower 20 m in height. The sampling site, located in Brent, Alabama at the Centreville (CTR) SEARCH location managed by the Electric Power Research Institute (CTR: 32.90289 ° N, 87.24968° W), was surrounded by a temperate mixed forest (part of the Talladega National Forest) that was occasionally impacted by anthropogenic emission. CTR was characterized by high atmospheric water content (2.4–3 vol.% typically), elevated temperatures (28–30 °C during the day), high SOA loadings (particulate organics ~4-10 μg m^{-3}; sulfate ~2 μg m^{-3}), high isoprene mixing ratios (4-10 ppbv), high ozone (40-60 ppbv), low-to-moderate nitrogen oxides ([NO] ~0.3-1.5 ppbv, [NO_2] ~1-5 ppbv), occasional plumes of SO_2 from nearby power plants, and occasional biomass burning events during the SOAS campaign.

The first goal of the chamber campaign was to further investigate the more interesting observations at SOAS. Due to the ability of laboratory experiments to study the chemistry of a single reactive hydrocarbon in a controlled setting, it was possible to test hypotheses during FIXCIT in a systematic manner. Below we list some relevant questions from the SOAS campaign that were explored during FIXCIT.

1. Which reactions or environmental conditions control the formation and destruction of OVOCs in the southeastern US?

2. Are RO_2 isomerization and other rapid oxygen incorporation mechanisms of key hydrocarbons important during SOAS?

3. How do anthropogenic influences, *e.g.* NO_x, O_3, and $(NH_4)_2SO_4$, impact atmospheric chemistry over the forest?

4. How much does the NO_3-initiated reaction control nighttime chemistry during SOAS?

5. How do environmental conditions in the southeastern US affect ozonolysis end products, which are known to be water sensitive?

6. Which reactions or environmental conditions most significantly impact SOA mass and composition?

A.1.2.2 Updating the isoprene and Monoterpene Mechanisms

Several experiments were designed to "fill in the gaps" of the isoprene oxidation mechanisms by leveraging the comprehensive collection of sophisticated instrumentation at FIXCIT. We targeted the following acknowledged open questions.

7. What are the products of the photochemical reactions stemming from OVOCs like ISOPOOH, IEPOX, ISOPN, and pinonaldehyde?

8. What is the impact of photolysis vs. photooxidation for photolabile compounds?

9. What is the true yield of isoprene nitrates from the high NO photooxidation pathway?

10. What is the product distribution and true yield of nitrooxy hydroperoxides from the NO_3 oxidation reaction of isoprene and monoterpenes under typical atmospheric conditions?

11. How do products and yields change as RO_2 lifetimes in chamber studies approach values estimated to be prevalent in the troposphere?

A.1.2.3 Instrument Characterization

A final goal of FIXCIT was to evaluate, compare, and identify biases in field instrumentation by isolating one variable at a time. We focused on the following objectives.

12. Identify the causal factor(s) producing the "OH interference" (Mao *et al.*, 2012) that has been observed in various biogenically impacted regions by some gas-expansion laser-induced fluorescence (LIF) techniques.

13. Characterize the performance of newly commercially available CIMS instrumentation with respect to the detection of OVOCs by using authentic standards.

14. Compare similar measurements (*e.g.* OH reactivity, hydrocarbons, OVOCs) made with different techniques.

A.2 Scope of the Campaign

A.2.1 Facilities

Experiments were performed in the Caltech Atmospheric Chamber Facility within a 1 month period in January 2014. The facility contains several in-house gas- and aerosol-phase instruments and an 8×5 m insulated enclosure, housing two side-by-side Teflon atmospheric chambers that are suspended from the ceiling. The chambers were manufactured from fluorinated ethylene propylene (FEP) Teflon. The chamber volume was measured regularly by quantitative transfer of highly volatile organics such as isoprene by an externally calibrated GC-FID. Quantitative transfer was checked *via* injections of a measured quantity of isoprene (checked by gravimetric, volumetric, and FT-IR methods) into a pillow bag with known volume by timing a calibrated mass flow of air into the pillow bag. For most experiments, the chamber volume was between 23 and 24 m^3. The spatial configuration of instruments in the chamber facility during FIXCIT is shown in Figure A.2. The instruments, contributors, and identifying abbreviations used in this work are described in Table A.1. A total of 320 UV black lamps (broadband λ_{max} ~350 nm) are mounted on the walls of the enclosure. The lamps are located behind Teflon films so that the heat produced from the operation of the lamps can be removed by recirculating cool air. The interior of the enclosure is covered with reflective aluminum sheets. Light intensities can be tuned to 100, 50, 10, and 1%. J_{NO_2} was measured to be 7×10^{-3} s^{-1} at 100% light intensity. Light fluxes at several locations within the chamber (*e.g.* center, corner, right, left, high, low) did not vary more than 15%. Temperature controls in the chamber enclosure are tunable from 10 to 50 °C (typically set at 25 °C) and did not fluctuate more than 1 °C, except during periods when the temperature was explicitly changed or during a 30 min period immediately following a change in the light intensities (up to 2 °C increase was observed from switching on 100% lights.)

The chamber experiments were operated in batch mode throughout the campaign. Temperature and RH were monitored continuously inside the chamber by a Vaisala HMM211 probe calibrated with saturated salt solutions in the RH range of 11–95%. In the range RH <11%, water vapor measurements were provided by the TripCIMS. The chambers were flushed at least 24 h before each use with ultra-purified air (purified in-house *via* a series of molecular sieves, activated carbon, Purafil^{TM} media, and particulate filters), at elevated temperature when needed (~40 °C), so that the backgrounds on gas- and particle-phase instrumentation are at baseline levels. As a reference, NO levels before each run were typically less than 100

instrument	instr. ID	PI(s)	institutions	measurements	ref.
Ground-based hydrogen oxide sensor	GTHOS	W. H. Brune	PA State Univ. (PSU)	OH, HO_2, RO_2	a
LIF OH reactivity monitor	LIF-OHR	W. H. Brune	PSU	OH reactivity by decay of OH	b
Thermal dissociation LIF NO_2 monitor	TDLIF	R. C. Cohen	Univ. of CA, Berkeley (UCB)	NO_2, sum of org. nitrates (ΣANs), sum of peroxy nitrates (ΣPNs), particulate org. nitrates (pANs)	c
Switchable iodide and acetate ion HRToF-CIMS	IACIMS	D. K. Farmer	CO State Univ. (CSU)	Oxidized VOCs (organic nitrates, acids, *etc.*)	d
NO_3^- HRToF-CIMS	NO_3CIMS	M. R. Canagaratna, D. R. Worsnop, J. L. Jimenez	Aerodyne Research, Inc. (ARI) and Univ. of CO, Boulder (CUB)	Low-volatility organic compounds	e
LIP glyoxal monitor	GlyLIP	F. N. Keutsch	Univ. of WI, Madison (UWM)	glyoxal	f
LIF formaldehyde monitor	FormLIF	F. N. Keutsch	UWM	Formaldehyde	g
Comparative rate method OH reactivity monitor	CRM-OHR	S. Kim, A. B. Guenther	Univ. of CA, Irvine (UCI) and Pacific NW National Lab (PNNL)	OH reactivity by decay of hydrocarbons	h
Switchable reagent ion ($H_3O^+/NO^+/O_2^+$) HRToF-MS	SRI-ToFMS	A. B. Guenther, J. E. Mak, A. H. Goldstein	PNNL, SUNY Stonybrook (SUNY), and UCB	Hydrocarbons, carbonyls, alcohols, *etc.*	i
Chemical luminescence NO monitor	NO–CL	G. S. Tyndall, D. D. Montzka, A. J. Weinheimer	National Center for Atmospheric Research (NCAR)	NO (> 25 pptv)	j
CF_3O^- triple quadrupole CIMS	TripCIMS	P. O. Wennberg	CA Institute of Technology (Caltech)	ISOPOOH, IEPOX, glycolaldehyde, acetic acid, methyl hydroperoxide	k
CF_3O^- CToF-CIMS	ToFCIMS	P. O. Wennberg	Caltech	Oxygenated VOCs (hydroperoxides, organic nitrates, multifunctional compounds)	l
Gas chromatograph with ToFCIMS	GC-ToFCIMS	P. O. Wennberg	Caltech	Isomers for oxygenated VOCs	m
HRToF-aerosol mass spectrometer	ToF-AMS	J. H. Seinfeld	Caltech	Aerosol composition and size distribution	n
Gas chromatograph with flame-ionization detector	GCFID	J. H. Seinfeld	Caltech	isoprene, methacrolein, MVK, cyclohexane	N/A
Thermocouple and membrane probe	T /RH probe	J. H. Seinfeld	Caltech	Temperature and relative humidity	N/A
UV-absorption ozone monitor	O_3 monitor	J. H. Seinfeld	Caltech	O_3 (> 1000 pptv)	N/A
Chemical luminescence NO_x detector	NO_x monitor	J. H. Seinfeld	Caltech	NO (> 500 pptv), and NO_2 (catalytic conversion to NO)	N/A

Table A.1: List of participating instruments, principle investigators (PIs), and institutions. Key acronyms: laser-induced fluorescence (LIF), laser-induced phosphorescence (LIP), high-resolution time-of-flight (HRToF), compact time-of-flight (CToF), MS (mass spectrometer), and CIMS (chemical ionization mass spectrometer). References listed are: [a]Brune *et al.* (1995), [b]Mao *et al.* (2009), [c]Day *et al.* (2002), [d]Lee *et al.* (1993b), [e]Junninen *et al.* (2010), [f]Huisman *et al.* (2008), [g]DiGangi *et al.* (2011) and Hottle *et al.* (2009), [h]Sinha *et al.* (2008), [i]Jordan *et al.* (2009), [j]Ridley and Grahek (1990), [k]St. Clair *et al.* (2010), [l]Crounse *et al.* (2006), [m]Bates *et al.* (2014), and [n]Canagaratna *et al.* (2007) and DeCarlo *et al.* (2006).

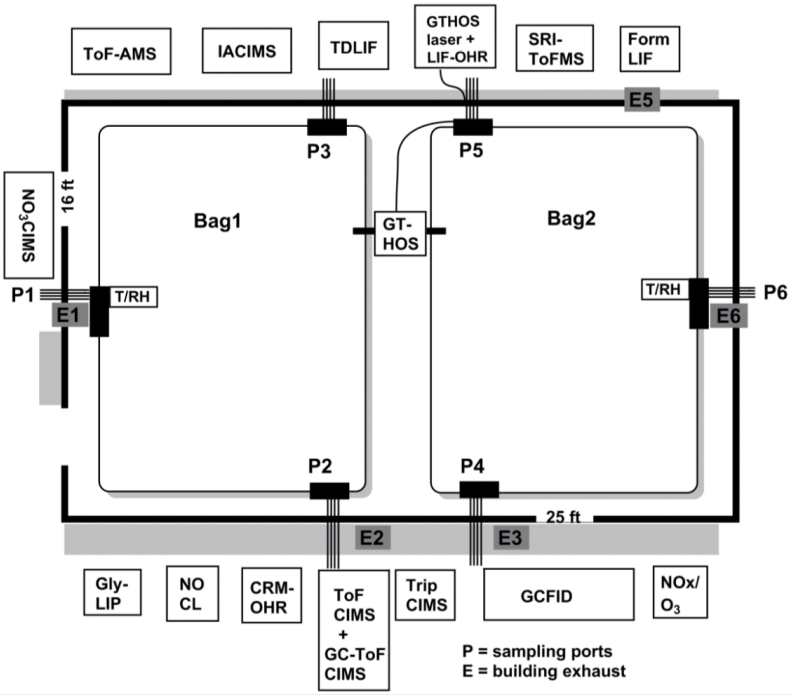

Figure A.2: Arrangement of instruments at the Caltech Atmospheric Chamber Facility during the campaign. Instrument IDs are in Table A.1.

pptv (from NO–CL measurements) and particle concentrations were less than 0.01 μg m^{-3}. Flushing rates, as balanced by exhaust rates, were typically 250 SD L min^{-1} (SLM) or ~0.6 chamber volumes per hour. Chambers were mixed on the timescale of minutes by injecting high-pressure pulses of air during the beginning of experiments.

Chamber 1 was reserved for low-NO experiments, so that the walls did not contact elevated levels of nitric acid and organic nitrates during the lifetime of the chamber, while Chamber 2 was reserved for moderate- to high-NO experiments. Experiments were carried out daily in alternating chambers to allow for the full flushing period of the previously used chamber. Each chamber was characterized separately prior to the campaign for vapor and particle wall loss rates. Typically, wall loss rates for gas-phase species are slightly higher in the high-NO chamber than the low-NO chamber due to the greater acidity of the walls. Particle wall loss rates were not significantly different between chambers. Measurements of the particle wall loss rates were performed by injecting ammonium sulfate (AS) seed aerosols into the chamber and monitoring the decay over the course of 10–24 h. Particles were injected *via* atomization of dilute salt solutions (*e.g.* AS 0.06 M) through a ^{210}Po neutralizer and water trap. Measurements of vapor wall loss rates were performed by injecting

OVOC standards (*e.g.* IEPOX, HMHP, *etc.*) into the chamber. Both particle and vapor wall loss characterizations were performed at several RH conditions (4–85% RH). These characterizations have been described in more detail previously (Loza *et al.*, 2010; Nguyen *et al.*, 2014a).

Organic compounds were injected into the chamber by two methods. (1) For volatile compounds, a measured volume was injected with a micro-syringe through a septum into a clean glass bulb, and the evaporated standard was quantitatively transferred into the chamber by dry purified air. Gas introduction of VOCs (done for isoprene and methacrolein) by filling an evacuated bulb with the chemical vapor, backfilling with nitrogen gas, and characterizing with Fourier transform infrared spectrometry before injecting did not produce significantly different results than volume injection. (2) For semivolatile compounds, the solid or liquid standard was placed inside a two-neck flask, which was heated by a water bath (35–65 °C), and the headspace was carried into the chamber by dry purified air. The ToFCIMS or TripCIMS instruments measured the gas-phase mixing ratio of the semi-volatiles in real time as the compounds entered the chamber, and injection was halted when a satisfactory quantity was introduced. OVOCs were calibrated by the ToFCIMS and TripCIMS by methods described earlier (Paulot *et al.*, 2009a). The desired RH inside the chamber was achieved by flowing dry purified air through a water-permeable (Nafion) membrane humidifier (FC200, Permapure LLC), kept moist by recirculating 27 °C ultra-purified (18 MΩ, 3 ppb TOC) water (Milli-Q, Millipore Corp). Particles were atomized into the chamber as described for particle wall loss experiments. When hydrated particles were needed for experiments, particles were injected *via* an in-line, heated, wet-wall denuder into a chamber that has RH above the efflorescence point of the particular salt (Martin, 2000).

A.2.2 Instrumentation and Sampling Modifications

Instruments were connected *via* sampling lines to both chambers through port holes in the enclosure as shown in Figure A.2. Sampling lines were capped when not in use. Inlet and tubing material were instrument specific, and included stainless steel (GTHOS and ToF-AMS), heated stainless steel and quartz (TDLIF), electro-polished steel and FEP Teflon (NO_3CIMS), polyetheretherketone (PEEK) and Teflon (SRIToFMS), and perfluoroalkoxy polymer (PFA) Teflon (other instruments).

The duration of each experiment (*i.e.*, the level of oxidation that can be probed) was critically dependent on the net sampling flow rates at which air was withdrawn

from the chamber. Sampling strategies were developed to minimize the effective sampling flow rate from each instrument, in such a way that instrument responses were not significantly different than during field campaigns. In many cases, a common high-flow Teflon sampling line was used to minimize the residence time of gases through tubing, and smaller flows were sampled orthogonally by each instrument. In some cases, a duty cycle was used as needed.

Several modifications from field designs were utilized for chamber sampling. The modifications were that (1) the GTHOS detection system was located between the chambers inside of the enclosure to minimize the residence time of HO_x inside the instrument (Figure A.2). The detection system was connected to the laser on the outside of the enclosure *via* a 3 m fiber optic cable fed through the side port hole. The sampling flow rate was similar to field flows (6 SLM); however, the fast-flow inlet was situated horizontally (~2 m in height) instead of vertically. The inlet was adapted to each bag directly, by attaching it to a Teflon plate that was in turn secured to the chamber walls *via* a large o-ring. The GTHOS inlet switched from Chamber 1 to Chamber 2 as needed. Chemical zeroing was performed by releasing hexafluoropropene (C_3F_6) into the inlet as an OH scrubber, and dark zeroing by measuring the difference between online and offline signals. Chemical and dark zeroing methods were used to distinguish between OH present in the chamber or atmosphere (chemical OH) and OH that may have been produced after the gas stream enters the instrument, which is additional to the chemical OH signal; (2) LIF-OHR was diluted a factor of 10 with nitrogen gas (effective flow 6 SLM); (3) NO_3CIMS was diluted a factor of 5 with scrubbed zero air (effective flow 2 SLM); (4) GlyLIP and FormLIF both operated at 5 SLM instead of the usual 17 and 10 SLM, respectively; and (5) SRIToFMS (1.5 SLM) and GCFID (0.1 SLM) occasionally sampled through a 0.125–0.2500 OD PFA Teflon tube that was submerged in a cold bath kept at -40 °C in order to remove interferences from certain OVOC (see Section A.2.3).

GC-ToFCIMS, first described in Bates *et al.* (2014), is an extension of the ToFCIMS. Analyte gas samples were focused with a cold trap onto the head of a RTX 1701 column (Restek) and eluted with a temperature ramping program (30–130 °C) in the oven before reaching the ToFCIMS for mass spectrometry detection. GC-ToFCIMS recorded data only when isomer separation was needed, because its operation took the standard scanning mode of the ToFCIMS offline. All other instruments operated normally with the following sampling flows: TDLIF

(4 SLM), ToFCIMS and TripCIMS (2 SLM), CRM-OHR (0.5 SLM), NO-CL (1 SLM), and IACIMS (2 SLM). Frequencies of zeroing (with dry N_2 or ultrazero air) and calibration (various methods) were instrument specific, with some instruments zeroing once per hour and calibrating once every few hours and others performing zeroing/calibration between experiments.

A.2.3 Experimental Design

The experiments performed at FIXCIT can be divided into several categories, each probing one or more specific science questions outlined in Section A.1.2. Every experiment included successful elements from past studies, but with a special focus on extending to atmospheric conditions. One example is reducing the occurrence of RO_2 + RO_2 side reactions in chamber experiments, which can lead to yields of atmospherically relevant products that are biased low. Enabled by the high sensitivity of field instruments, photooxidation was performed with precursor mixing ratios as low as 12 ppbv. Certain instruments that required extensive dilution in a chamber setting, *e.g.* LIF-OHR, had poorer-quality data for low loading experiments. Experimental durations were typically 4–6 h, with the exception of overnight runs where the majority of instruments sampled briefly to establish starting conditions, then were taken offline during the nighttime and resumed sampling in the morning. The typical reaction time for an overnight experiment was ~15 h. Experimental details are reported in Table A.2. OH concentrations were derived from hydrocarbon decay data from GCFID, SRI-ToFMS, or ToFCIMS, when available, using published rate coefficients (Atkinson *et al.*, 2006; Bates *et al.*, 2014; Lee *et al.*, 2014). Otherwise, preliminary GTHOS chemical-zeroing data were used. The following types of experiments were included in the study:

A. Blank (Expts. 4b and 5b): blank experiments were designed to investigate background signals present in experiments that may have sources other than gas-phase chemistry of the injected hydrocarbon, *e.g.* from heterogeneous oxidation of residual organics on the chamber walls. OH precursors, such as hydrogen peroxide, were added to each chamber, the UV lamps were turned on, and sampling occurred as usual. Furthermore, the temperatures inside the chambers were ramped from 25 to 35 °C to explore the extent to which elevated temperatures change the chamber background signals due to increased volatilization of organics. Blank experiments were performed under dry conditions. Common background compounds produced from heterogeneous wall reactions are formic acid and acetic acid.

expt. #	expt. type	HC pre-cursor	$[HC]_i$ (ppb)	Ox	Ox source	$[OH]_{ss}$ (# cm^{-3})	$[O_3]_i$ (ppb)	$[NO]_i$ (ppb)	$[NO_2]_i$ (ppb)	[NO]/ $[HO_2]$	Add'l inj.	Rxn T (°C)	RH (%)
2	b	ISOP	45	OH	HP + hν	1.5×10^6	<5	<0.04	<2	1/7	–	27	<5
3	c	ISOP	100	OH	HP + hν	2.4×10^6	<5	500	15	>100	–	26	<5
4a	i	ISOPOOHs	250	–	–	–	–	–	–	–	–	24	<3
4b	a	Blank C1	0	OH	HP + hν	2.0×10^6	<5	<0.04	<3	1/6	–	27–33	<5
5a	i	ISOPNs	<13	–	–	–	–	–	–	–	–	24	<3
5b	a	Blank C2	0	OH	HP + hν	2.0×10^6	<5	<0.04	<2	1/5	–	27	<5
6	e	ISOP	91	O_3	O_3 rxn	$[OH]_i \sim 1 \times 10^6$	615	<0.04	<3	–	–	25	<5
7*	d	ISOP	30	OH	MN + hν	4.1×10^4, 4.8×10^6	<5	0.08	45	2, 6	–	40, 40	<5
9	f	ISOP	18	NO_3	NO_2/O_3	3.8×10^8	55	0.10	100	2–3	HCHO	26	<5
10	b	α-PIN	30	OH	HP + hν	2.0×10^6	<5	<0.04	<2	1/10	–	27	<5
11	c	α-PIN	30	OH	HP + hν	2.5×10^6	<5	85	10	>100	–	26	<5
13	f	α-PIN	30	NO_3	NO_2/O_3	4×10^8	75	0.17	150	1.5–8	HCHO	25	<5
14	e	ISOP	100	O_3	O_3 rxn	[OH] ~0	605	<0.04	<3	–	CHX	25	<5
16*	d	α-PIN	30	OH	MN + hν	6×10^4, 4×10^6	<5	0.08	<3	2–3, 10	–	40, 40	<5
17	b, i	4,3-ISOPOOH	60	OH	HP + hν	1.2×10^6	<5	<0.04	<3	1/5	–	26	<5
18*	d	ISOP	28	OH	MN + hν	1.0×10^5, 4.3×10^6	<5	0.08	<3	2–3, >100	–	25, 26	<5
19	b, h	ISOP	60	OH	HP + hν	1.0×10^6	<5	<0.04	<4	1/5	wet AS	28	51
21	b	ISOP	22	OH	HP + hν	2.0×10^6	<5	<0.04	<2	1/10	–	27	<5
22	c	ISOP	100	OH	HP + hν	2.3×10^6	<5	430	15	>100	–	27	<5
23	e	ISOP	90	O_3	O_3 rxn	$[OH]_i \sim 1 \times 10^6$	600	<0.04	<3	–	–	25	50
24	c, h, i	4,3-ISOPN	12	OH	HP + hν	3×10^6	7	115	55	>100	wet AS	26	52
25	b	MAC	43	OH	HP + hν	3×10^6	<5	<0.03	<3	1/10	–	28	<5
26	g, h	MAC	45	OH	MN + hν	2×10^7	<5	3.5	50	10–20	MAE, wet AS	26	<5, 40
27	d, i	*trans*-β-IEPOX	60	OH	MN + hν	7.3×10^6	<5	0.25	<3	2–5	–	25	<5
29	e	ISOP	91	O_3	O_3 rxn	[OH] ~0	610	<0.04	<4	–	CHX	25	38
30	g, h, i	Pinonald.	15	OH	MN + hν	3.5×10^6	<5	0.50	<3	4–8	–	26	<5

Table A.2: Formal experiments and reaction conditions during the FIXCIT campaign. Chemical abbreviations are defined in Table A.3. Other abbreviations are C1 = Chamber 1, C2 = Chamber 2, ISOP = isoprene, α-PIN = α-pinene, HP = hydrogen peroxide, MN = methyl nitrite, CHX = cyclohexane, HCHO = formaldehyde, AS = ammonium sulfate seeds. Expt. types are defined in the text. Expt. no. corresponds to the date in January 2014 when the experiment was performed. * = 1% lights, 20% lights, then 100% lights.

synthesized standard	PI(s)	institutions	atmos. relevance	ref.
isoprene 1-hydroxy-2-hydro-peroxide (1,2-ISOPOOH)	F. N. Keutsch	UWM	major 1st-gen. low-NO isoprene + OH product	a
isoprene 3-hydroxy-4-hydro-peroxide (3,4-ISOPOOH)	F. N. Keutsch	UWM	major 1st-gen. low-NO isoprene + OH product	a
trans isoprene 2-epoxy-1,4-diol (*trans*-β-IEPOX)	P. O. Wennberg, J. H. Seinfeld	Caltech	major 2nd-gen. low-NO isoprene + OH product	b
cis isoprene 2-epoxy-1,4-diol (*cis*-β-IEPOX)	P. O. Wennberg, J. H. Seinfeld	Caltech	major 2nd-gen. low-NO isoprene + OH product	b
isoprene 4-hydroxy -3-nitrate (4,3-ISOPN)	R. C. Cohen, P. B. Shepson, A. S. Hasson, P. O. Wennberg	UCB, Purdue Univ., CSU Fresno (CSUF), and Caltech	major 1st-gen. high-NO isoprene + OH product	c
isoprene 2-hydroxy -1-nitrate (1,2-ISOPN)	A. S. Hasson	CSUF	major 1st-gen. high-NO isoprene + OH product	N/A
pinonaldehyde	P. O. Wennberg, J. H. Seinfeld	Caltech	major 1st-gen. α-pinene + OH/O_3 product	d
methacrylic acid epoxide (MAE)	J. D. Surratt, A. Gold	Univ. of NC Chapel Hill	minor product, possible SOA precursor from MAC + OH + NO_2	e

Table A.3: List of contributed synthesized chemical standards for experiments and calibration. Synthesis references are [(a)]Rivera-Rios *et al.* (2014), [(b)]Bates *et al.* (2014), [(c)]Lee *et al.* (2014), [(d)]Griesbaum *et al.* (1997), and [(e)]Lin *et al.* (2013b).

B. Low-NO photooxidation (Expts. 2, 10, 17, 19, and 25): the low-NO experiments that have been extensively investigated in atmospheric chamber studies were designed to be relevant to the pristine troposphere, and certain conditions at SOAS, where HO_2 reactions dominate the RO_2 fate. Experiments were initiated by H_2O_2 photolysis as a NO_x-free source of OH and HO_2:

$H_2O_2 + h\nu \rightarrow OH + OH$

$OH + H_2O_2 \rightarrow HO_2 + H_2O$

The execution of these experiments requires precise engineering to simulate the troposphere closely. One outstanding challenge of low-NO experiments is the variation in initial NO levels across different chamber settings and on different days. Because typical HO_2 levels in a chamber environment do not typically exceed ~200 pptv from the self-limiting HO_2 recombination, NO should be ~40 pptv during the reaction (a factor of 5 less abundant) in order for the C_5 RO_2 reactions to be dominated by HO_2 by a factor of 10 ($k_{RO_2+HO_2}$ ~1.6×10^{-11} and k_{RO_2+NO} ~8.5×10^{-12} cm^3 $molec^{-1}$ s^{-1} at 298K (Atkinson *et al.*, 2006). Thus, experimental variations in NO that can lead to discrepancies in low-NO kinetics typically elude quantification by commercially available NO chemiluminesence instruments, owing to their high limits of detection (~500 pptv).

NO levels in the Caltech chambers were suppressed by continually flushing with filtered air on the inside and outside the chamber walls. Initial NO levels of <40 pptv were typically achieved during experiments. The NO–CL instrument available during FIXCIT (Table A.1) has a limit of detection better than 25 pptv, and the GTHOS instrument provided online HO_2 quantification at the pptv level. Another common challenge for low NO experiments (even when [NO] is less than [HO_2]) is that homogeneous or cross RO_2 + RO_2 reactions may dominate the RO_2 reactivity ($k_{RO_2+RO_2}$ ~10^{-15}–10^{-11} cm^3 $molec^{-1}$ s^{-1} at 298 K; Atkinson *et al.*, 2006). These experiments may be more correctly characterized as "low-NO, high-RO_2". For experiments using [H_2O_2] as an OH precursor, RO_2 + RO_2 reactions were largely minimized by using reaction conditions that ensure [HO_2] greater than [RO_2] (*e.g.* $[H_2O_2]_0/[ISOP]_0$ ~10^2 and $J_{H_2O_2}$ ~$4–5 \times 10^{-6}$ s^{-1}). Thus, the peroxy radical self reaction channels are minor compared to RO_2 + HO_2 chemistry. We estimate that the low-NO experiments were HO_2-dominated by at least a factor of 10 in RO_2 reactivity by monitoring tracers of chemistry stemming from high-NO (isoprene nitrates), high-RO_2 (C_5 diols and other products), and low-NO (ISOPOOH and IEPOX) pathways. The molar yield of the low-NO products ISOPOOH + IEPOX (measured

within the first 15 min of reaction) was estimated at 95%, supporting the dominance of RO_2 + HO_2 chemistry over other channels. The structurally isomeric ISOPOOH and IEPOX that were formed from the HO_2-dominated isoprene photooxidation were distinguished by TripCIMS, and the sum was measured by ToFCIMS, IACIMS, and NO_3CIMS. These experiments were performed with isoprene, α-pinene, 4,3-ISOPOOH and MAC precursors.

C. High-NO photooxidation (Expts. 3, 11, 22, and 24): high-NO experiments are also commonly performed in chamber studies. These experiments were designed to be relevant to the urban-influenced troposphere, such as some cases at SOAS, where NO can dominate RO_2 reactions. Experiments were typically initiated by H_2O_2 with added NO during FIXCIT, but have been performed using HONO or other precursors elsewhere. It is easier to ensure that reaction with NO is the main fate of RO_2, even with higher hydrocarbon loadings, because NO mixing ratios are typically in excess of both HO_2 and RO_2 by hundreds of ppbv. Hydroxy nitrate products were measured by TDLIF, IACIMS, ToFCIMS, and GC-ToFCIMS. Functionalized carbonyl products were measured by SRI-ToFMS and ToFCIMS. glyoxal and formaldehyde, also important high-NO products, were measured by the GlyLIP and FormLIF, respectively. This well-studied experiment was important for multiple reasons, including calibration, diagnostics, and for determining the hydroxy nitrate yields from alkenes within the first few minutes of photooxidation. However, it should be noted that the experimental result represents a boundary condition that may not fully represent NO-influenced reactions in the atmosphere due to the extremely short RO_2 lifetimes (<0.01 s at 500 ppbv NO). These experiments were performed with isoprene, α-pinene, and the 4,3-ISOPN standard synthesized by the Caltech group.

D. Slow chemistry photooxidation (Expts. 7, 16, 18, and 27): the slow chemistry experiment is designed to extend RO_2 lifetimes closer to atmospheric values when both NO and HO_2 impact RO_2 reactivity (~3–30 s, assuming 1500–100 pptv NO and 40 pptv HO_2). This was achieved by employing low radical mixing ratios. With relevant RO_2 lifetimes, the RO_2 isomers may be closer to their equilibrium distribution because of the reversible addition of oxygen (Peeters *et al.*, 2009). Figure A.3 shows the progress of a representative slow chemistry experiment. The "slow" portion of experiments was performed under a low light flux (J_{NO_2} ~4×10^{-5} s^{-1}) with methyl nitrite as the OH precursor (Atkinson *et al.*, 1981):

$CH_3ONO + h\nu + O_2 \rightarrow HO_2 + NO + HCHO$

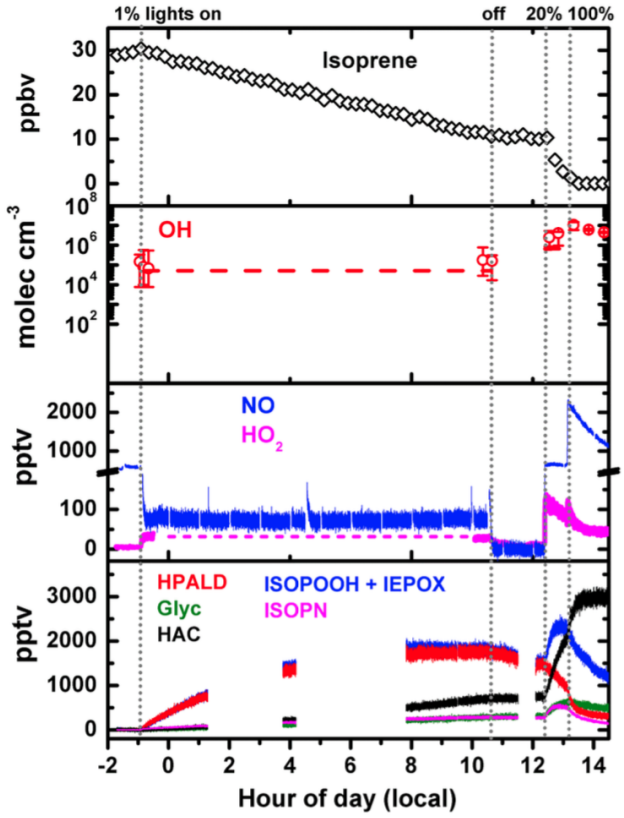

Figure A.3: Progress of the slow chemistry experiment performed on 01/07/2014. Isoprene data were provided by GCFID. The red dashed line in the OH plot is the steady-state OH concentration derived from the decay of isoprene as monitored by GCFID. OH and HO_2 preliminary data were provided by GTHOS, using chemical zeroing, although the steady-state value of (0.4–1) $\times 10^5$ molec cm^{-3} was below the detection limit of GTHOS. OH preliminary data were averaged to reduce noise. NO data were provided by NO–CL and OVOC data were provided by ToFCIMS.

$HO_2 + NO \rightarrow OH + NO_2$

These reactions produce a steady-state OH concentration of $[OH]_{ss}$ ~0.4–1 $\times 10^5$ molec cm^{-3} and an atmospherically relevant ratio of NO / HO_2 (2–3) that is stable throughout the majority of the experiment. Furthermore, we aimed to simulate the summer conditions at SOAS, where RO_2 isomerization is competitive with RO_2 + HO_2 and RO_2 + NO chemistry. Thus, most experiments of this type were performed at elevated temperatures (T ~40–45 °C) to facilitate the isoprene RO_2 isomerization to HPALDs (Crounse *et al.*, 2011), as measured by ToFCIMS. The atmospheric RO_2 fates were qualitatively deduced by observations of their respective products during SOAS (forthcoming papers) and during other campaigns (Beaver *et al.*, 2012; Paulot *et al.*, 2009b; Wolfe *et al.*, 2012).

The fate of HPALDs is not known, but has been suggested as being strongly influenced by photolysis based on reactions of chemical analogs (Wolfe *et al.*, 2012). After the slow chemistry period, 20–100% lights were turned on in order to diagnose the effects of direct photolysis and OH oxidation on the product compounds, which is especially instructive when coupled with photochemical modeling. Table A.2 reports conditions only for the ≤1% light period and the 20% light period due to availability of hydrocarbon decay data. When CH_3ONO experiments were performed with higher light flux from the start, the NO-to-HO_2 reactivities were still competitive, but the OH mixing ratios were higher. These experiments were performed with isoprene, α-pinene, and *trans*-β-IEPOX precursors.

E. Ozonolysis (Expts. 6, 14, 23, and 29): ozonolysis reactions were performed in the dark, with and without the use of excess cyclohexane (50 ppmv) as a scavenger for OH (Atkinson *et al.*, 1995). Ozone reacts with isoprene and α-pinene with rate coefficients of $k_{ISO+O_3} = 1.3 \times 10^{-17}$ molec cm^{-3} and $k_{\alpha-PIN+O_3} = 9.0 \times 10^{-17}$ molec cm^{-3} at 298 K, respectively (Atkinson *et al.*, 2006). After the first few steps of the reaction, however, little agreement exists in the literature for product yields, product distribution, or rate coefficients stemming from reactions of stabilized Criegee intermediates (sCI). This may be due to the large differences among studies in the hydrocarbon loadings ($[ISO]_i$ = 40–10 000 ppbv), ozone-to-isoprene ratios (<0.5 to >100), water vapor content (<10–20000 ppmv), reaction pressures (4–760 torr), analytical methods used for product analysis (GC, HPLC, FTIR, direct OH vs. scavenging, *etc.*), and methods used to generate SCI (CH_2I_2 + hν vs. gas-phase ozonolysis) (Drozd and Donahue, 2011; Hasson *et al.*, 2001a; Huang *et al.*, 2013; Johnson and Marston, 2008; Kroll *et al.*, 2002; Neeb *et al.*, 1997; Sauer *et al.*, 1999; Simonaitis *et al.*, 1991; Welz *et al.*, 2012).

We designed the ozonolysis experiments to have similar ozone-to-isoprene ratios to those observed during SOAS (~5–7), and performed the experiments under dry (RH ~4%) and moderately humid (RH ~50%) conditions. The ozonolysis experiments at FIXCIT primarily focused on studying unimolecular and bimolecular chemistry of SCI that affects the yields of OH, hydroperoxides, organic acids, aldehydes and ketones under humid vs. dry conditions. These experiments represent the first coupling between direct OH observations from GTHOS, aldehyde/ketone measurements from GCFID and SRI-ToFMS, online formaldehyde measurements from FormLIF, and online hydroperoxide measurements from the various CIMS instruments present to provide the most comprehensive picture thus far on the

humidity-dependent ozonolysis of isoprene.

F. Competitive HO_2 nitrate (NO_3) oxidation (Expts. 9 and 13): the NO_3-initiated experiments during the campaign were performed in the dark, under dry conditions. Excess formaldehyde ($[HCHO]_i$ ~4–8 ppmv) was used as a dark HO_2 precursor in order to elevate the contributions of RO_2 + HO_2 reactions in the NO_3 chemistry:

$O_3 + NO_2 \rightarrow NO_3 + O_2$

$HCHO + NO_3 \rightarrow HNO_3 + HCO$

$HCO + O_2 \rightarrow CO + HO_2$

$HO_2 + NO_2 \rightleftarrows HO_2NO_2$

$NO_2 + NO_3 \rightleftarrows N_2O_5$

This process produces an HO_2 / NO_3 ratio of approximately 2 (determined by photochemical modeling from the mechanism described in Paulot *et al.*, 2009a), a ratio more relevant to the troposphere during nighttime oxidation. As α-pinene has a higher NO_3 loss rate compared to isoprene, a factor of 2 greater mixing ratio of initial formaldehyde was used. The consequence of the experimental design is that the isoprene nitrooxy hydroperoxide (INP) and monoterpene nitrooxy hydroperoxide (MTNP) are major products, in contrast to experiments performed under RO_2 + RO_2 or RO_2 + NO_3 dominated conditions (Kwan *et al.*, 2012; Ng *et al.*, 2008; Perring *et al.*, 2009). The focus of these experiments was the quantification of INP and MTNP with the various CIMS and with TDLIF, and further exploration of their loss channels to OH oxidation (simulating sunrise) or to dry AS seed particles by measuring organic aerosol growth on the ToF-AMS. These experiments were performed with isoprene and α-pinene precursors.

G. High NO_2/NO photooxidation (Expts. 26 and 30): the high NO_2-to-NO ratios in the lower troposphere in most regions of the globe favor the production of acylperoxy nitrates (APNs) from the OH-initiated reaction of aldehydes like methacrolein and pinonaldehyde (Bertman and Roberts, 1991; Nozière and Barnes, 1998). Unlike the APN from methacrolein (MPAN), the APN from pinonaldehyde has never been measured in the atmosphere (Nouaime *et al.*, 1998; Roberts *et al.*, 1998; Wolfe *et al.*, 2012). The OH oxidations of aldehydes were performed with an NO_2 / NO ratio greater than 10, and NO_2 was replenished as it was reacted away. These reactions were initiated by CH_3ONO photolysis under higher light flux, producing [OH] greater than 3×10^6 molec cm^{-3}. Certain APNs were monitored with ToFCIMS, and total peroxy nitrates (ΣPNs) were monitored with TDLIF. A

major focus of the high NO_2 experiments was to investigate the SOA-formation potential and mechanisms from atmospherically relevant APNs, which is expanded in H.

H. SOA-formation chemistry (Expts. 19, 24, 26, and 30): experiments aimed specifically at studying chemistry leading to SOA formation have overlapping goals with those described above. One focus was the evaluation of the SOA-formation route from APNs by the proposed dioxo ketone, lactone, and epoxide mechanisms (Chan *et al.*, 2010a; Kjaergaard *et al.*, 2012; Lin *et al.*, 2013b), none of which has yet been validated by independent studies. However, the proposed epoxide chemistry has been integrated into some studies published soon after the proposal by Lin *et al.* (2013b) (Pye *et al.*, 2013; Worton *et al.*, 2013). After MPAN was formed from the high-NO_2 reaction of MAC + OH, a synthesized standard of methacrylic acid epoxide (MAE, provided by the UNC group), the proposed epoxide intermediate, was added to discern the SOA-forming potential of MAE vs. other reactive intermediates in the MPAN reaction. Following the injection and stabilization of MAE, water vapor was added until the reaction mixture reached ~40% RH. Then wet AS seeds were injected to investigate any SOA mass growth, as quantified by ToF-AMS.

SOA formation from ISOPN high-NO photooxidation and isoprene low-NO photooxidation products were investigated in the presence of wet AS seeds (40–50% particle liquid water by volume), meant to simulate the high particle liquid water and sulfate quantities during SOAS. For these experiments, the chambers were humidified to 40–50% RH, and hydrated AS particles were injected through a wet-wall denuder so that the seed particles retain liquid water above the efflorescence point of AS (Biskos *et al.*, 2006). In the ISOPN high-NO photooxidation, the potential for forming organics that will likely condense onto seed particles, *e.g.* dinitrates and IEPOX, was recently suggested (Jacobs *et al.*, 2014; Lee *et al.*, 2014). The dinitrate pathway was investigated as a potential source of particle-phase organic nitrogen. In the low-NO isoprene photooxidation, IEPOX reactive uptake onto acidic Mg_2SO_4 particles (Lin *et al.*, 2012) and non-acidified AS particles (Nguyen *et al.*, 2014a), both with non-zero liquid water content, were recently demonstrated. We focused on AS particles with no added acid. The impact of the partitioning of IEPOX on the gas-phase mixing ratios was examined as a potential reason for the differences in observed IEPOX in dry and humid regions.

I. Cross-calibrations (Expts. 4a, 5a, 24, 27, and 30): newly commercially available negative-ion CIMS (Junninen *et al.*, 2010; Lee *et al.*, 1993b) may become

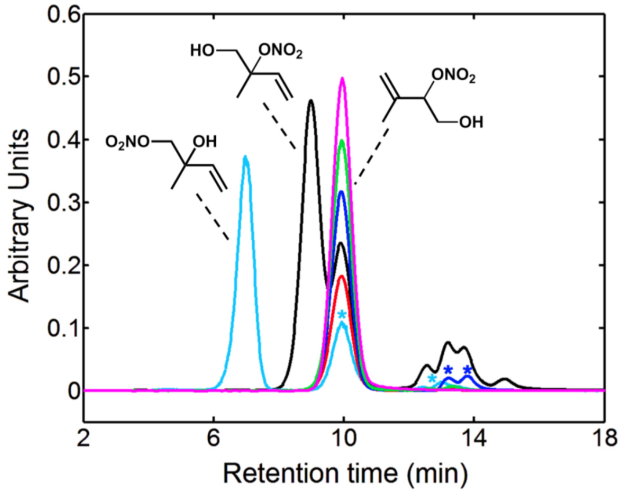

Figure A.4: GC-ToFCIMS chromatogram of ISOPNs from an isoprene high-NO photooxidation experiment (black), and from the introduction of 2,1-ISOPN standard synthesized by CSUF (cyan) and 4,3-ISOPN standards synthesized by Caltech (magenta), CSUF (green), UCB (blue), and Purdue (red). The rightmost four peaks apparent in the photooxidation chromatogram are preliminarily identified as the cis and trans 1,4-ISOPN and *cis* and *trans*-4,1-ISOPN, although the elution order is not clear. Asterisks (*) denote impurities in synthesized samples of corresponding color.

common tools for monitoring complex OVOCs in the atmosphere, similarly to the widespread adoption of positive ion CIMS (PTR-MS-based instruments). Some of the new negative ion CIMS instruments were deployed for the first time in field campaigns occurring in recent years. During FIXCIT, synthesized standards of eight isomer-specific compounds were available for cross calibrations with different CIMS in order to better understand the chemical sources of ambient signals during SOAS and in other field campaigns. Table A.3 shows the structures, abbreviations, and contributors of the synthesized chemicals. The TripCIMS and the GC-ToFCIMS separated structural isomers through collision-induced dissociation (CID) and through chromatography, respectively. Figure A.4 shows a GC-ToFCIMS separation of isomers of the ISOPN synthesized standards, as well as ISOPNs present in a complex photooxidation mixture. SRI-ToFMS and IACIMS tested the switchable reagent ion sources for preferential detection of one or more isomers of compounds with the same molecular formula.

For certain cross-calibration experiments, standards were injected into an inflatable pillow bag (~0.2–0.3 m^3) that was filled with dry N_2 to a known volume. The purities of the standards were quantified by nuclear magnetic resonance (NMR) or

Fourier transform infrared spectrometry (FT-IR). The injected material was measured by vapor pressure, quantitative volume transfer, or by ToFCIMS and TripCIMS that were calibrated using techniques described elsewhere (Bates *et al.*, 2014; Garden *et al.*, 2009; Lee *et al.*, 2014; Paulot *et al.*, 2009a). Some experiments, such as the IEPOX photooxidation experiment, also served a dual purpose for cross-calibration. For example, *trans*-β-IEPOX was injected into a clean chamber and instruments were allowed to sample for ~1 h to cross-calibrate before an oxidant precursor was injected. Both LIF-OHR and CRM-OHR were able to measure the OH reactivity of these OVOC compounds individually, which aids in determining the known and unknown OH reactivity in ambient environments.

J. GTHOS test experiments: the OH interference in GTHOS, and possibly other gas-expansion LIF techniques, has been shown to bias OH measurements systematically high in some biogenically influenced areas unless chemical zeroing was performed (Mao *et al.*, 2012). The excess OH was demonstrated not to be produced by the GTHOS laser itself (308 nm), but rather, more likely, in the low-pressure flow zone within the nozzle of the instrument. During FIXCIT, several hypotheses proposed by Mao *et al.* (2012), and some original proposals based on field observations, were tested. The interference precursor candidates were: (i) ozonolysis intermediates – tested with ozonolysis experiments and with ozone injection into the GTHOS inlet; (ii) biogenic peroxides like ISOPOOH or HMHP – tested with synthesized standards; (iii) background chemistry such as NO_2 + O_3 – tested by the nitrate-oxidation experiment and by sequential injection of NO_2 and O_3 separately; (iv) dry and humid HO_2 + O_3 reaction – tested by formaldehyde photolysis with ozone injection during a separate experiment (01/02/2014, not shown in Table A.2); (v) β-hydroxy RO_2 radicals formed from OH + alkene – tested with the photooxidation of 2-methyl-2-butanol and compared with 2,2-dimethylbutane (02/02/2014 and 31/01/2014, not shown in Table A.2); and (vi) heat-mediated decomposition of thermally unstable species – tested by temperature ramping to 35–40 °C inside the chamber. Often, single variables (like ozone or heat) were isolated by incremental additions toward the end of an experiment.

The experiments not described in Table A.2 (to test iv and v) were performed after the formal experiments; thus, not all investigators were present. Only GTHOS, ToFCIMS, TripCIMS, ToF-AMS, GCFID, O_3 monitor and NO_x monitor were collecting data. The HO_2 + O_3 test experiment (01/02/2014) was performed by injecting ~600 ppbv of ozone, then ~50 ppbv of cyclohexane as an OH tracer for CIMS (mon-

itored by the formation of cyclohexyl hydroperoxide). UV lights were turned on and then 4 ppmv of formaldehyde was injected, which photolyzed to produce 550 pptv of HO_2. The HO_2 reaction with formaldehyde produced a small yield of HMHP (Niki *et al.*, 1980). Water vapor was injected to diagnose the effect of humidity. Experiments to test the effects of RO_2 structure utilized CH_3ONO to oxidize ~50 ppbv of either 2-methyl-2-butanol and 2,2-dimethylbutane with OH. Ozone (~ 600 ppbv), water vapor (until RH ~30–40%), and NO_2 (400 ppbv) were added sequentially at toward the end of the photooxidation. Finally severally hundred ppb of NO was added to titrate away the ozone.

A.2.4 Analytical Challenges

Throughout the campaign, several sources of analytical interferences or systematic biases were discovered. Some challenges resulted from the integration of field instruments to a chamber setting, where high concentrations of certain chemicals were used to engineer extremely specific conditions. Thus, these issues do not affect ambient sampling. For example, (1) high NO_2 levels in some experiments affected the normal operation of TDLIF because the ΣANs and ΣPNs measurements were determined by subtraction of NO_2. When NO_2 is much higher than ΣANs and ΣPNs, the measurement by difference contains large uncertainties; (2) high H_2O_2 for low-NO conditions affected the operation of some CIMS instruments because the ppmv mixing ratios of H_2O_2 depleted a non-negligible quantity of reagent ions. In order to correct for this, the CIMS instruments needed to calibrate as a function of H_2O_2 in addition to traditional methods, or account for the true reagent ion signal (which was anti-correlated with H_2O_2 concentration). High H_2O_2 also affected GTHOS due to photolysis-derived OH production by the laser. GTHOS corrected for this effect by removing the OH background that was determined by sampling when only H_2O_2 was present; (3) High formaldehyde, cyclohexane, or H_2O_2 dominated the OH reactivity for certain experiments. In experiments where ppmv levels of volatile compounds were used, LIF-OHR and CRM-OHR did not operate. In contrast, high ozone and NO levels did not appear to affect the operation of any instruments. Temperature and humidity effects on ion sensitivities have been corrected for by ToFCIMS and TripCIMS as standard procedure. Other CIMS are actively characterizing these effects for analytes of interest.

However, other analytical challenges were not unique to laboratory studies. It was found that chemical artifacts were produced from the decomposition of multifunctional OVOC (*e.g.* ISOPN, ISOPOOH, IEPOX, and pinonaldehyde) under normal

operating conditions in some instruments; thus, possibly affecting ambient sampling and field data interpretation. Figure A.5 shows the proposed decomposition pathways of certain isomers of isoprene-derived OVOC to form MAC and MVK. We are aware of MAC and MVK interference only from the 1,2- and 4,3- isomers of ISOPOOH, the 1,2- and 4,3- isomers and ISOPN, and the β isomers of IEPOX (*i.e.*, the peroxide, nitrate, and epoxide groups are secondary or tertiary). Unfortunately, these isomers are expected to be the most abundant in the atmosphere, *e.g.* the β-IEPOXs are estimated to represent more than 97% of atmospheric IEPOX (Bates *et al.*, 2014). The extent of decomposition and product distribution may also vary based on the operating conditions of the particular analytical method. In general, the decomposition was exacerbated by instruments with harsher sampling conditions, *i.e.*, high ionization energy (*e.g.* the standard H_3O^+ mode of SRI-ToFMS), high temperatures, and/or materials incompatible with organics (*e.g.* the hot stainless steel sample loop and inlet of GCFID). OVOCs from the low-NO isoprene photooxidation have been shown to decompose to MAC and MVK in commercial PTRMS instruments (Liu *et al.*, 2013), but the exact identities of the compounds were unclear. During FIXCIT, it was observed that ISOPOOH, IEPOX, and pinonaldehyde were detected at *m/z* 71.050 in the SRI-ToFMS in PTR mode (the sum of MAC + MVK). Switchable reagent ions show promise for removing certain biases, but more work is needed to characterize the chemistry that forms interfering ions. Furthermore, we observed that the decomposition interference also affected GCFID, the other commonly used detection method for MAC and MVK in ambient samples. ISOPOOH, IEPOX, and ISOPN were detected as either MAC or MVK in the GCFID, depending on the specific isomer. The interferences may not be localized to this particular GCFID, and a more detailed account can be found in Rivera-Rios *et al.* (2014). Conversion efficiencies of OVOCs to the C_4 carbonyls in the Caltech GCFID range in order of ISOPOOH > IEPOX > ISOPN, and can be almost quantitative for ISOPOOH because of the facile cleavage of the weak O–O bond. Lastly, ISOPN were found to be converted to NO with a small yield in the NO–CL and a larger yield in commercial NO_x analyzers.

All decomposition-derived artifacts can be avoided by collecting the air sample through a length of tubing submerged in a cold bath (-40 °C), which trapped OVOCs that are less volatile than authentic MAC and MVK. Liu *et al.* (2013) implemented this technique successfully in their laboratory study using SRI-ToFMS, resulting in a lower yield than previously reported for MAC and MVK in the low-NO oxidation of isoprene. Field application may prove more challenging, however, as the trapping

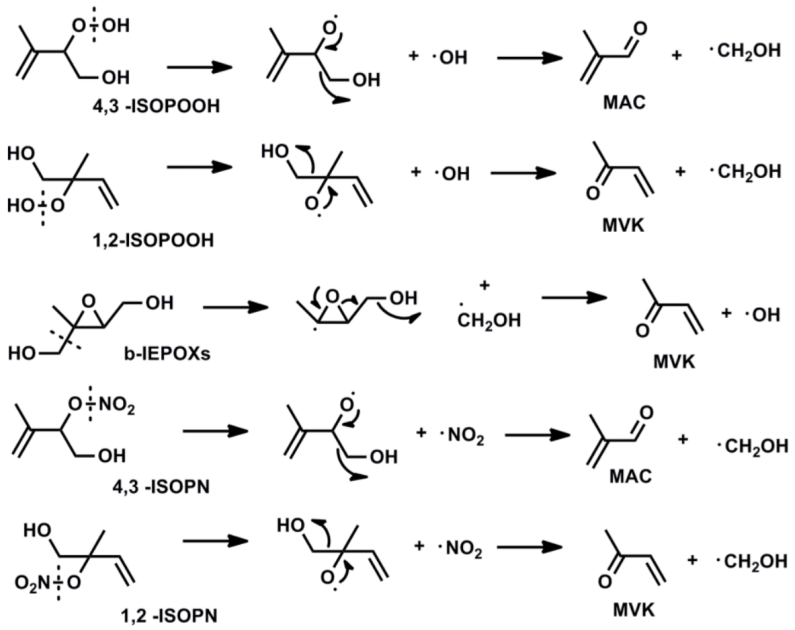

Figure A.5: Select proposed mechanism for the decomposition of OVOCs to carbonyls on contact with metal surfaces or high ionization energies within instrumentation. Other decomposition pathways likely exist and the branching ratios are dependent on instrument operation conditions. Cleavage sites are indicated by dashed lines.

is labor intensive and requires careful humidity control to avoid ice buildup and blockage. During FIXCIT, both GCFID and SRI-ToFMS employed trapping techniques at various times to avoid biases in the detection and interpretation of MAC and MVK data.

A.3 Preliminary Results and Atmospheric Implications

Forthcoming papers will discuss campaign results in detail. Here, we summarize a few interesting observations that appeared to be robust, based on preliminary data analysis of the laboratory and field work.

– Nighttime chemistry of alkenes, as controlled by the NO_3 radical, leads to several organic nitrates that are unique compared to daytime high-NO photooxidation. A significant product is the nitrooxy hydroperoxide, the atmospheric importance of which has likely been significantly underestimated in past chamber studies. The nitrooxy hydroperoxide reacts further in the daytime through a currently unknown mechanism.

– The high-NO hydroxy nitrate yield from isoprene is closer to the high end of the

spectrum (range 4–15%), important for the accurate simulations of volatile nitrogen in the atmosphere.

– Observed mixing ratios of isoprene low-NO photooxidation products are impacted by heterogeneous chemistry that appears to be mediated by aqueous processes, which has implications for the interpretation of IEPOX observations in dry vs. humid areas of the world.

– Environmental conditions in many locations, including within a biomass burning plume, are favorable for the H-shift RO_2 isomerization chemistry that produces compounds like HPALDs and very low-volatility oxygenates. The atmospheric fate of HPALDs is highly impacted by direct photolysis that recycles OH, as well as other complex chemistry and physical processes.

– The ozonolysis reaction of isoprene produces a high yield of C_1 compounds that are also observed with considerable abundance during ambient sampling. The hydroperoxide and acid yields appear to be underestimated by previous studies that detected these compounds *via* offline techniques. The OH yield may not follow the same trend with RH as the hydroperoxide and acid yields.

– APNs are efficient SOA precursors. SOA formation was prompt, and organic mass growth occurred quickly without the addition of inorganic seeds, *i.e.*, the SOA intermediate(s) from APN + OH condensed onto predominantly organic SOA material. Injections of the MAE standard did not increase the SOA mass growth.

– Several experiments produced significant amounts of excess OH, as measured by the GTHOS instrument, providing further avenues for investigation. These experiments also ruled out several candidates for the OH interference. More work is underway to characterize the phenomenon comprehensively.

– Calibrations with several synthesized standards of OVOC (Table A.3) significantly aid in data interpretation from OHR and new CIMS instruments. Sampling these OVOC through standard instrumentation may interfere with some routine field and chamber measurements (depends on the run conditions and instrument setup), but may be mediated by cold-trapping methods. This is likely a contributing factor in the high discrepancies in MAC and MVK yields from low-NO isoprene photooxidation previously reported. For example, we find the preliminary low-NO yields of MVK (6 ± 3%) and MAC (4 ± 2%), determined by GC-FID, from photooxidation of isoprene are consistent with Liu *et al.* (2013) when cold-trapping methods were employed (Expt. 21). However, the low-NO "yields" of MVK and MAC are each

greater than 40% when sampled directly by the GC-FID from the chamber (Expt. 2) due to interferences by isomers of ISOPOOH (Rivera-Rios *et al.*, 2014) and possibly other OVOCs.

Final data from the FIXCIT campaign will be made publicly available on archives hosted by the US National Oceanic and Atmospheric Administration (NOAA, http://esrl.noaa.gov) in January 2016. Data will be submitted in the ICARTT format, standardized by the US National Aeronautics and Space Administration (NASA, http://www-air.larc.nasa.gov/missions/etc/IcarttDataFormat.htm).

A.4 Summary

Although data analysis is ongoing, the goals of the FIXCIT campaign appear to have been met during the campaign period. The insights gained from experimental observations under well-controlled laboratory conditions have already proved valuable for understanding ambient observations from SOAS. The community effort to pursue atmospherically important chemistry with sensitive ambient techniques and custom-synthesized chemicals has elevated our understanding of atmospheric oxidation for a number of biogenic compounds. Novel mechanistic information obtained during FIXCIT will be helpful to update chemical mechanisms currently implemented in large-scale chemistry-coupled transport models. Instrumental intercomparisons, an important aspect of the campaign, have demonstrated that a thorough characterization of new and standard ambient sampling techniques using authentic standards is necessary for accurate data interpretation.

Chamber experiments are clearly invaluable to the field of atmospheric chemistry, as the results feed directly into models that are used to ascertain regional and global climate and chemistry feedbacks. Furthermore, chamber data aid in the interpretation of complex results obtained from field studies. However, it can be difficult to decipher the conditions under which chamber experiments are most relevant, and a standard protocol for data reporting may be needed. For example, best estimates of oxidation conditions in chambers (*i.e.*, if reactions are HO_2-dominated, low-NO but RO_2-dominated, high-NO, high-NO_x but low-NO, and so on) would greatly aid in comparisons of these experiments and others. The experiments in this campaign were fundamentally focused on the fate of the RO_2 radical as a delineation between chemical regimes. FIXCIT experiments (Table A.2) can be further improved or tailored to the specific needs of the scientist. It has been demonstrated, here and elsewhere, that chamber studies that include chemistry

representative of the atmosphere and well-characterized instrumental methods can accurately reproduce observations in the ambient environment. The results from FIXCIT make a case for future synergistic integration of laboratory studies with field campaigns, which maximizes the level of mechanistic understanding and data confidence obtained from the combination of both types of studies.

Appendix B

ATMOSPHERIC FATE OF METHYL VINYL KETONE: PEROXY RADICAL REACTIONS WITH NO AND HO_2

Praske, E., J. D. Crounse, K. H. Bates, T. Kurtén, H. G. Kjaergaard, and P. O. Wennberg (2015). "Atmospheric fate of methyl vinyl ketone: Peroxy radical reactions with NO and HO2". In: *J. Phys. Chem. A* 119.19, pp. 4562–4572. DOI: 10.1021/jp5107058.

Abstract

First generation product yields from the OH-initiated oxidation of methyl vinyl ketone (3-buten-2-one, MVK) under both low and high NO conditions are reported. In the low NO chemistry, three distinct reaction channels are identified leading to the formation of (1) OH, glycolaldehyde, and acetyl peroxy R2a, (2) a hydroperoxide R2b, and (3) an α-diketone R2c. The α-diketone likely results from HO_x-neutral chemistry previously only known to occur in reactions of HO_2 with halogenated peroxy radicals. Quantum chemical calculations demonstrate that all channels are kinetically accessible at 298 K. In the high NO chemistry, glycolaldehyde is produced with a yield of 74 ± 6.0%. Two alkyl nitrates are formed with a combined yield of 4.0 ± 0.6%. We revise a three-dimensional chemical transport model to assess what impact these modifications in the MVK mechanism have on simulations of atmospheric oxidative chemistry. The calculated OH mixing ratio over the Amazon increases by 6%, suggesting that the low NO chemistry makes a non-negligible contribution toward sustaining the atmospheric radical pool.

B.1 Introduction

MVK is one of the most abundant oxygenated volatile organic compounds in the Earth's atmosphere. It is a major product of the gas-phase oxidation of isoprene, a compound emitted by terrestrial vegetation to the atmosphere at a rate of approximately 500 Tg y^{-1} (Guenther *et al.*, 2012). Oxidation of isoprene by the hydroxyl radical (OH) produces MVK with a yield that depends on the concentrations of NO and HO_2 and temperature. MVK is also produced during the oxidation of isoprene by ozone and has been quantified in car exhaust (Biesenthal and Shepson, 1997; Zhang and Zhang, 2002). Globally, approximately 100 Tg of MVK are produced

annually from isoprene according to the GEOS-Chem simulations described here (Bey *et al.*, 2001).

MVK has an atmospheric lifetime of approximately 10 h with respect to oxidation by OH ([OH] = 1.5×10^6 molecules cm^{-3}), which constitutes its principal atmospheric loss process (Atkinson *et al.*, 2006). OH adds to either of the two olefinic carbon atoms forming distinct alkyl radicals. In the atmosphere, these alkyl radicals rapidly react with O_2 forming peroxy radicals (RO_2):

$CH_3C(=O)CH=CH_2 + OH + O_2 \rightarrow CH_3C(=O)CH(OO\cdot)CH_2OH$ (R1a)

$CH_3C(=O)CH=CH_2 + OH + O_2 \rightarrow CH_3C(=O)CH(OH)CH_2OO\cdot$ (R1b)

Tuazon and Atkinson (1989) studied the OH-initiated MVK oxidation in the gas phase and determined that R1a accounts for 72 ± 21% of the OH reactivity with the remaining following pathway R1b. The dominant fate of RO_2 radicals in the atmosphere is reaction with either HO_2 or NO. The reaction of MVK-derived RO_2 and NO to produce NO_2, HO_2, and carbonyl products has been previously characterized. Glycolaldehyde, methylglyoxal, formaldehyde, and peroxyacetyl nitrate have all been quantified as the primary first generation products of MVK oxidation under conditions where reaction with NO dominates the RO_2 fate (Galloway *et al.*, 2011; Tuazon and Atkinson, 1989). The yields of glycolaldehyde and methylglyoxal through NO-mediated chemistry were determined to be 64 ± 8% and 25 ± 4%, respectively (Tuazon and Atkinson, 1989). The yield of organic nitrates has been estimated to be 10 ± 10% (Chuong and Stevens, 2004). Alkyl nitrates are of interest due to their interactions with aerosol as well as their ability to act as temporary reservoirs of NO_x, which can be transported and lead to ozone formation downwind (Perring *et al.*, 2013).

The primary focus of this study is the chemistry of the reaction of the RO_2 radicals formed in R1a and R1b with HO_2. This chemistry is notably distinct, given the diverse set of reactions that RO_2 + HO_2 may undergo (Orlando and Tyndall, 2012). Traditionally, these reactions have been viewed as sinks for atmospheric radicals through the formation of organic hydroperoxides (Seinfeld and Pandis, 2006). As demonstrated here, however, this chemistry is largely HO_x neutral in the case of MVK. Two reaction channels R2a-R2b, previously described for the reaction of acetonyl RO_2 and HO_2 (Dillon and Crowley, 2008; Hasson *et al.*, 2005, 2004; Jenkin *et al.*, 2008), are observed to occur for MVK RO_2 with substantial yields. We have also identified a carbonyl forming channel R2c, which has only been reported in the reactions of halogenated RO_2 with HO_2 (Hou *et al.*, 2005a,b; Hou and Wang,

expt #	objective	$[MVK]_0$ (ppbv)	oxidant (ppmv)	$[NO]_0$ (ppmv)	temp. (±2 K)	UV (%)
1	$RO_2 + HO_2$	85	H_2O_2, 2.5	-	296	100
2	$RO_2 + HO_2$	79	H_2O_2, 2.5	-	296	100
3	$RO_2 + HO_2$	62	H_2O_2, 2.5	-	296	100
4	$RO_2 + HO_2$, hot	95	H_2O_2, 2.5	-	323	100
5	$RO_2 + HO_2$, slow, hot	60	CH_3ONO, 0.050	-	323	12.5
6	$RO_2 + HO_2$, slow, hot	28	H_2O_2, 1.6	-	323	12.5
7	$RO_2 + NO$	75	CH_3ONO, 0.100	1.3	296	25
8	$RO_2 + NO$	440	H_2O_2, 2.5	1.2	296	100
9	$RO_2 + NO$, hot	75	CH_3ONO, 0.100	1.2	323	25
10	$RO_2 + NO$, hot	78	CH_3ONO, 0.100	1.2	323	25

Table B.1: List of photo-oxidation experiments performed. For the UV lights, J_{NO_2} = 2.5×10^{-3} s^{-1} at 100% illumination.

2005). The reaction pathways are shown below:

$$CH_3C(=O)CH(OO\cdot)CH_2OH \rightarrow CH(=O)CH_2OH + CH_3C=O + OH + O_2 \quad \text{(R2a)}$$

$$CH_3C(=O)CH(OO\cdot)CH_2OH \rightarrow CH_3C(=O)CH(OOH)CH_2OH + O_2 \quad \text{(R2b)}$$

$$CH_3C(=O)CH(OO\cdot)CH_2OH \rightarrow CH_3C(=O)C(=O)CH_2OH + OH + HO_2 \quad \text{(R2c)}$$

The discovery of efficient HO_x recycling in MVK chemistry adds to the growing number of new findings that the oxidation of isoprene and other biogenic alkenes in low NO environments is less HO_x consuming than previously understood (Crounse *et al.*, 2012, 2011; Peeters *et al.*, 2009; Surratt, 2013). Here, we use the GEOS-Chem atmospheric chemical transport model to evaluate the impact of this chemistry on simulated OH levels within the lower atmosphere.

B.2 Experimental Methods

We performed a series of photo-oxidation experiments in a small Teflon-walled chamber (Table B.1). Experiments were designed to evaluate the products of reactions of the peroxy radicals formed in R1a and R1b with both NO and HO_2. To evaluate the importance of unimolecular reactions of these peroxy radicals, we also investigated the dependence of the product distribution on peroxy radical lifetime and temperature.

B.2.1 Chemicals

Methyl vinyl ketone (99%, Sigma-Aldrich), 3-hydroxy-2-butanone (≥96%, Sigma-Aldrich), 4-hydroxy-2-butanone (95%, Sigma-Alrich), glycolaldehyde dimer (Sigma-Aldrich), H_2O_2 (30% w/w, Macron), nitric oxide (1993 ± 20 ppmv NO in N_2,

Matheson), and isopropanol (≥99%, Macron) were all used as purchased.

B.2.2 Chamber and Instruments

Experiments were carried out in a 1 m^3 fluorinated ethylene propylene copolymer (Teflon-FEP, DuPont) environmental chamber at ambient laboratory pressure (~993 hPa), as previously described (Crounse *et al.*, 2011). The chamber was connected to instrumentation *via* ~2 m of 6.35 mm OD PFA tubing. Instrumentation included a Time of Flight Chemical ionization mass Spectrometer (ToF-CIMS), a triple quadrupole MS-MS CIMS, and a gas chromatograph with a flame ionization detector (GC-FID).

MVK was monitored by GC-FID, with product determination *via* CIMS. The GC-FID (Agilent 5890 II) had a run cycle of approximately 30 min and was equipped with a 30 m megabore 0.53 μm PLOT-Q column (JW Chemicals).

B.2.3 CIMS

The CIMS techniques have been previously described in detail (Crounse *et al.*, 2006; Paulot *et al.*, 2009b; St. Clair *et al.*, 2010). Reaction products were quantified using the CF_3O^- reagent ion (*m/z* = 85) at temporal resolution of 10 Hz. CF_3O^- was formed by passing 1 ppm of CF_3OOCF_3 in N_2 through a ^{210}Po radioactive source. The reagent ion was then introduced to a flow tube where the chamber sample was diluted (dry N_2, 1675 standard cubic centimeters per minute). Due to clustering with the reagent ion, most masses reported here are represented as the sum of the nominal compound mass and *m/z* 85. Fluoride transfer can occur for acidic analytes. For example, nitric and acetic acids were detected primarily at *m/z* 82 and *m/z* 79, respectively. Observed ion signals were normalized to that of the reagent ion to account for variations in CF_3O^- fluence. The reagent ion was represented as the sum of *m/z* = 86, 104, and 120, which corresponds to $^{13}CF_3O^-$ and its cluster with water and H_2O_2, respectively. Detection limits are typically ~10 pptv.

B.2.4 GC-CIMS

The CIMS was periodically connected to a GC column to enable the separation and quantification of isomers. The GC-CIMS technique has been previously described (Bates *et al.*, 2014; Lee *et al.*, 2014; Teng *et al.*, 2015). Briefly, both prior to and after photo-oxidation, samples of chamber air were analyzed using a gas chromatograph with the output of a 4 m Restek RTX-1701 column connected to the ToF-CIMS. The analytes were cryogenically trapped on the head of the column using an isopropanol

bath at approximately -20 °C. Sample collection lasted 4 min to yield a total sample volume of about 150 cm^3, after which a temperature ramp program was initiated (30 °C for 0.1 min, +3 °C/min until 60 °C, and +10 °C/min to 130 °C).

B.2.5 Calibration

Where available, synthetic standards were used to determine the sensitivity of the CIMS. For several of the products where standards were not available, we estimated the sensitivity using reagent ion-molecule collision rates, calculated using dipole moments and polarizabilities (see Section B.5) (Garden *et al.*, 2009; Su and Chesnavich, 1982). Isomer-specific sensitivities for the MVK-derived alkyl nitrates were previously determined by thermal dissociation LED-induced fluorescence coupled to the output of a GC column (Lee *et al.*, 2014). Glycolaldehyde, the principal MVK oxidation product upon which other yields are based, was calibrated using an authentic standard. Gas phase standards were prepared by methods involving either the evaporation of a solution containing glycolaldehyde or by decomposition of crystalline glycolaldehyde dimer. In the first method, a gravimetric standard of glycolaldehyde dimer was dissolved in methanol to yield a 2.8% w/w glycolaldehyde solution. A known quantity of this solution was injected *via* syringe into a sealed glass three-way vial, which was then transferred to the chamber by flushing with a known volume of dry zero air. In a second method, crystalline glycolaldehyde dimer was placed into a vial and heated to 100 °C and vacuum purged to remove high volatility species as well as water and air. After 10 min, the vial was cooled to room temperature. A steady flow of dry N_2 transferred the headspace over the remaining glycolaldehyde dimer into a 50 L Teflon bag. Between the vial and the bag, a cold trap (-15 °C) was used to reduce the transmission of dimer and other low volatility impurities. After the bag was filled, an aliquot was transferred into a glass sample cell and the absolute concentration of glycolaldehyde was determined by FTIR (Nicolet 560 Magna-IR) using tabulated absorption cross sections.(31) The referenced Pacific Northwest National Laboratory glycolaldehyde cross sections agree with those determined by Tuazon and Atkinson (1989) to better than 10%. A 500 cm^3 bulb was filled with the mixture and then flushed into the chamber with a known volume of air. The reproducibility of the calibration was verified twice for each technique, which confirmed that systematic and random error were below 7%. During each calibration, the signal on the chamber was monitored for 2-3 h in order to constrain wall loss processes and determine the effect of increasing relative humidity in the chamber. Over the time frame in which the sensitivity was derived,

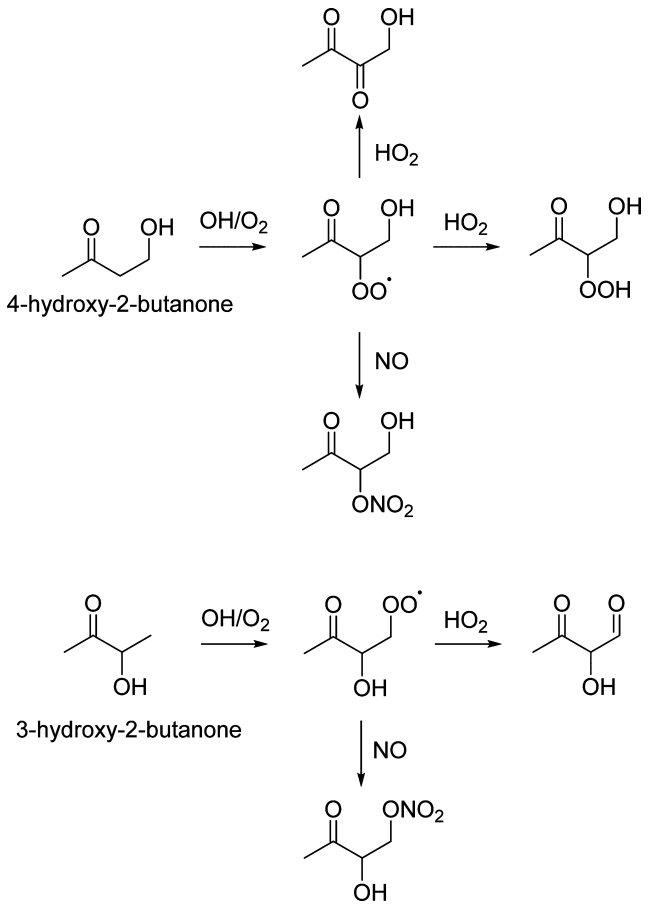

Figure B.1: Diagnostic experiments using commercially available precursors were conducted to identify structures associated with mass signals in MVK oxidation. The detected products resulting from NO/HO_2 reaction are shown.

the signal was stable to within ±0.1%.

Standards for several of the proposed products of the oxidation of MVK are not commercially available. To identify these products, we synthesized several of the proposed compounds in the gas phase from commercially available precursors. 3-Hydroxy-2-butanone and 4-hydroxy-2-butanone were oxidized in the presence of H_2O_2. Both compounds were first diluted in water to yield ∼10% w/w solutions that were then volatized into the chamber using the three-way glass vial addition method described above. The experiments (see Table B.2) were performed in both the HO_2- and NO-dominated regimes. The oxidation products (see Figure B.1) were analyzed by GC-CIMS to compare retention times with those of the products of MVK oxidation.

expt #	objective	hydrocarbon	oxidant	NO added (ppmv)	OH scavenger
11	RO_2 (R1a) + HO_2	4-hydroxy-2-butanone	H_2O_2	-	no
12	RO_2 (R1a) + NO	4-hydroxy-2-butanone	H_2O_2	0.8	no
13	RO_2 (R1b) + HO_2	3-hydroxy-2-butanone	H_2O_2	-	no
14	RO_2 (R1b) + NO	3-hydroxy-2-butanone	H_2O_2	0.8	no
15	Photolysis	MVK	H_2O_2	-	no
16	Photolysis	MVK	H_2O_2	-	yes

Table B.2: List of diagnostic experiments performed. Parentheses are used to indicate the isolation of peroxy radicals produced by reactions R1a or R1b.

B.2.6 MVK Photooxidation Experiments

The experiments performed are listed in Table B.1. Experiments were conducted at 296 ± 2 K, with the exception of experiments 4, 5, 6, 9, and 10 in which the chamber enclosure was heated and maintained at 323 K. Additions of MVK and oxidant were introduced sequentially to the chamber. MVK standards were prepared by serial dilution. First, a vapor pressure of ~13 hPa of MVK was siphoned into an evacuated 500 cm^3 glass bulb. An atmosphere of nitrogen was added to the bulb, which was subsequently pumped to ~13 hPa before being refilled with N_2. All pressures were measured by an MKS Baratron. The resulting MVK mixing ratio (~100 ppm) was verified by FTIR using tabulated absorption cross sections (Sharpe *et al.*, 2004). The sample was then introduced to the chamber and diluted with a regulated flow (20 L min^{-1}, MKS mass flow controller) of dry zero air.

H_2O_2 was used as a HO_x precursor in some experiments, while CH_3ONO was used in others. A known amount (~8 mg) of H_2O_2 (30% w/w in water) was transferred into a three-way glass vial and evaporated into the chamber using a stream of dry zero air for about 20 min to yield 2.50 ± 0.25 ppm of H_2O_2. The residual mass of the vial was measured to ensure complete transfer of the contents to the chamber.

OH and HO_2 are produced *via* the photolysis of H_2O_2 under full chamber UV lights (8 Sylvania 350 blacklights with $J_{H_2O_2} \sim 1.7 \times 10^{-6}$ s^{-1}, $J_{NO_2} \sim 2.5 \times 10^{-3}$ s^{-1}, and $J_{glycolaldehyde} \sim 1.5 \times 10^{-6}$ s^{-1}):

$H_2O_2 + h\nu \rightarrow 2OH$

$OH + H_2O_2 \rightarrow HO_2 + H_2O$

CH_3ONO was used as a radical precursor to create conditions where the peroxy radicals react at approximately equal rates with HO_2 and NO. Methyl nitrite was synthesized using a procedure similar to that outlined in Taylor *et al.* (1980). A

known pressure of CH_3ONO was added to a 500 cm^3 glass bulb, following a method similar to the addition of MVK. Only 2 UV lights were used in these experiments because the photolysis rate of CH_3ONO is much greater than that of H_2O_2 for the radiation emitted by our chamber lights. Radical generation proceeds by

$CH_3ONO + h\nu + O_2 \rightarrow HO_2 + NO + HCHO$

$HO_2 + NO \rightarrow OH + NO_2$

For experiments designed to measure the alkyl nitrate yield (7, 8, 9, and 10), ~1 ppm of NO was added to the chamber at the start of the experiments using the primary standard described above.

After filling the chamber with all reactants and diluting to the desired volume, background signals were quantified *via* direct (without chromatographic separation) and GC-CIMS sampling. UV lights were then switched on until the mixing ratio of MVK had decayed ~10%. This amount was chosen to minimize the influence of secondary reactions and other loss processes while producing quantifiable yields of products. The product yields reported here are derived from this initial oxidation period.

Experiments 5 and 6 were performed to probe unimolecular pathways in the mechanism. Similar to previous experiments detailing the oxidation of methacrolein described by Crounse *et al.* (2012) the peroxy radical lifetimes were extended by halving the concentration of both MVK and oxidant and employing very low light flux conditions. Additionally, the chamber was heated to 50 °C to increase the rate of any RO_2 isomerization processes.

Finally, experiments 15 and 16 were performed to measure the photolysis of the products of MVK oxidation. MVK was oxidized in the presence of H_2O_2 until a sufficient signal level was attained for the product compounds of interest. At this point, oxidation was halted by switching the lights off. Isopropanol, an OH scrubber, was added to the chamber *via* a 500 cm^3 glass bulb to yield a ~50 ppm mixing ratio. According to evaluated gas phase kinetic data (Atkinson *et al.*, 2006), >99% of OH present or subsequently produced preferentially reacted with the scrubber under these conditions. The chamber was fully illuminated once again for ~10 h. Photolysis experiments were conducted both with (experiment 16) and without (experiment 15) the presence of the OH scavenger.

B.2.7 Quantum Chemical Methods

We employed theoretical calculations to evaluate the thermodynamics of the three proposed reaction pathways for the reaction of MVK-derived RO_2 and HO_2 R2a-R2c. The lowest energy conformer for each of the stationary points along the reaction was found using the systematic search in Spartan14 except for the transitions states (TS) where the structures were inferred based on previous calculations in the literature (Hasson *et al.*, 2005; Hou *et al.*, 2005a,b; Hou and Wang, 2005). The B3LYP hybrid density functional with the standard 6-31+G(d) double-ζ basis set was used in these initial calculations. The optimized structure of each stationary point was subsequently refined with the the wB97XD functional (Chai and Head-Gordon, 2008) and the aug-cc-pVDZ and aug-cc-pVTZ, double and triple-ζ basis set, respectively (wB97XD/aVDZ and wB97XD/aVTZ). Only minor differences in structures are found between the wB97XD/aVDZ and wB97XD/aVTZ optimized structures. Harmonic vibrational frequencies are calculated for both wB97XD methods to confirm that each structure is either a minimum or a transition state (one imaginary frequency). The transition state (TS) structures are shown to connect the reactant or reactant intermediate and product on either side *via* intrinsic reaction coordinate (IRC) calculations with the wB97XD/aVDZ method. For all calculations, we used the unrestricted Kohn-Sham formalism with the spin symmetry of the initial guess wave function broken (Guess = Mix). The wB97XD DFT calculations are calculated using the Gaussian09 program suite with the default convergence criteria (Frisch *et al.*, 2009).

We improved the accuracy of the thermochemistry by calculating single-point energies with the explicitly correlated CCSD(T)-F12a/VDZ-F12 method (F12) at the wB97XD/aug-cc-pVTZ optimized structures (Knizia *et al.*, 2009). The F12 calculations on open-shell species are restricted open coupled cluster [ROCCSD(T)-F12] calculations based on a restricted-open Hartree-Fock (ROHF) determinant. The T1 diagnostic is less than 0.034 in all F12 calculations, which indicates that multiconfiguration effects are limited. All the F12 coupled cluster calculations are performed using the MOLPRO$_2$010 program suite with the default convergence criteria (Werner *et al.*, 2012).

We obtain ΔG for each structure with the F12 energies and the thermal contribution from the wB97XD/aug-cc-pVTZ calculation.

regime	RO_2 + NO	RO_2 + HO_2
Y_{GLYC}	74 ± 6.0%	38 ± 4.6%
Y_{MGLY}	24.12 ± 0.14%[a]	4 ± 1%[b]
$Y_{\alpha-DK}$	-	14 ± 5.3%
Y_{HHP}	-	27 ± 9.7%
Y_{MVKN}	2.4 ± 0.4%	-
$Y_{MVKN'}$	1.6 ± 0.4%	-

Table B.3: Measured yields (Y) based on experiments 7 and 8 for the high-NO regime and experiments 1-3 for the RO_2 + HO_2 regime. Abbreviations are: GLYC = glycolaldehyde, MGLY = methylglyoxal, α-DK = C_4 α-diketone, HHP = C_4 4,3 hydroxy hydroperoxide, MVKN = 3-ONO_2,4-OH-MVK, and MVKN' = 3-OH,4-ONO_2-MVK. Methylglyoxal was not measured in these experiments; values come from [a]Galloway *et al.* (2011) or [b]Personal communication from F. N. Keutsch.

B.3 Results and Discussion

B.3.1 Product Yields

The product yields from the reaction of the hydroxy peroxy radicals formed *via* R1a and R1b with NO or HO_2 are shown in Table B.3. Example time traces of the decay of MVK and the growth of these products are shown in Figure B.2.

The yield of glycolaldehyde is computed from the rate of its formation divided by the loss rate of MVK. The yields of the other products are determined relative to glycolaldehyde. The tabulated uncertainty in the yield of glycolaldehyde includes error in its measurement and from error in the amount of MVK oxidized (due to uncertainty in the GC-FID measurements and in the initial concentration of MVK resulting from uncertainty in the infrared cross sections). The uncertainty in the yields of the other products includes error in the absolute yield of glycolaldehyde in addition to error in the slope of the linear regression of the relative rate of product formation. Uncertainty in the calibration of glycolaldehyde is ∼7%, and for the hydroxy nitrates is ∼12%. Calibration of the remaining compounds is significantly more uncertain (30%) due to the lack of authentic standards (see Table B.6 of the Supporting Information). The error bounds in Table B.3 also include uncertainty in both measured and calculated calibration factors. Due to uncertainty in the calibrations, the yields do not necessarily achieve carbon parity.

In direct sampling from the chamber, the signal from both hydroxy nitrate isomers produced from MVK, 4-hydroxy-3-nitrooxy-2-butanone (MVKN), and 4-nitrooxy-3-hydroxy-2-butanone (MVKN'), is measured as the cluster with CF_3O^- (*m/z* 234).

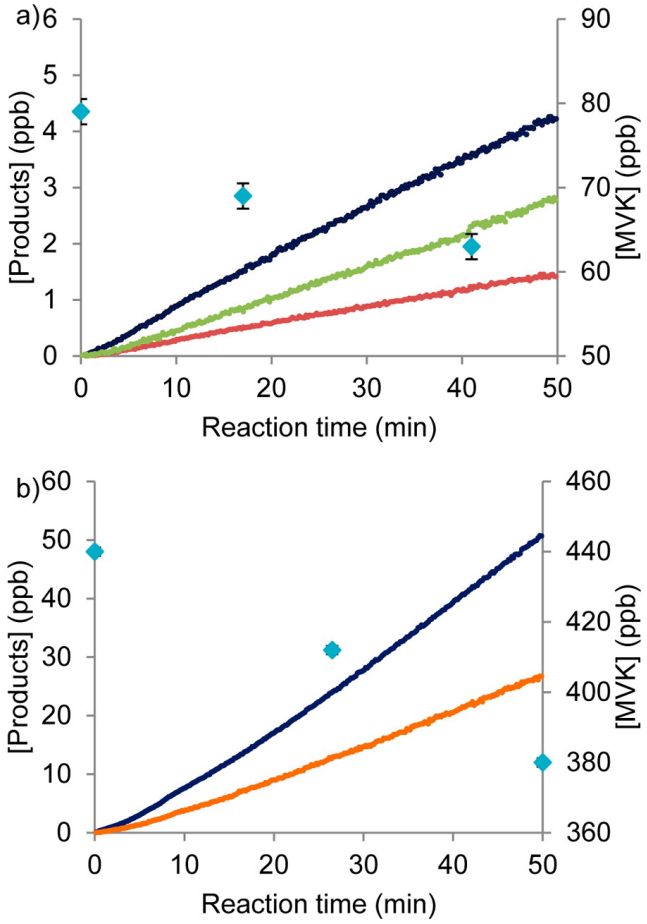

Figure B.2: Reaction profiles demonstrating the HO_2 and NO dependence of the chemistry. Species shown are glycolaldehyde (dark blue), a 4,3-hydroxy hydroperoxide (green), an α-diketone (red), organic nitrates ($\times$10, orange), and MVK (light blue diamonds). Data are derived from (a) experiment 2 in the low NO regime and (b) experiment 8 in the high NO regime. Error bounds reflect the uncertainty in the GC-FID quantification of MVK.

The isomer-specific yields were determined using GC-CIMS. We assigned the chromatographic peaks by comparing the individual retention times with those of the hydroxy nitrate carbonyls produced in experiments 12 and 14 (Figure B.10 of the Supporting Information).

The yield and identification of the dicarbonyl compound was based on analysis of experiments 11, 13, 15, and 16. As discussed below, there are two possible compounds detected as a CF_3O^- cluster with $C_4O_3H_6$ at *m/z* 187: an α-diketone (1-hydroxy-2,3-butanedione) or an aldehyde (2-hydroxy-3-oxobutanal). However, the oxidation of 4-hydroxy-2-butanone in experiment 11 produced a yield of the *m/z* 187 compound relative to glycolaldehyde identical to that shown in Table B.3. On

the other hand, the *m/z* 187 signal observed from 3-hydroxy-2-butanone oxidation in experiment 13 was produced as a second-generation product and was not accompanied by coproduction of glycolaldehyde. Thus, we conclude that the observed *m/z* 187 signal primarily arises from the α-diketone and that the contribution of the aldehyde is likely small (<2%).

Only a single hydroxy hydroperoxide was observed in GC-CIMS chromatograms obtained following the low NO oxidation of MVK (experiments 1-3). The elution time of this compound matched that of the hydroperoxide formed in experiment 11. The hydroxy hydroperoxides produced in experiments 1-3 and 11 also share identical and characteristic ion chemistry. Three major product ions are observed: *m/z* 205 results from the cluster of CF_3O^-; *m/z* 139 ($F{\cdot}C_4H_8O_4^-$) results from fluoride transfer; *m/z* 101 ($C_4H_5O_3^-$) likely results from loss of water and HF; and FCO_2^- (*m/z* 63) is a fragment of *m/z* 205 characteristic of CF_3O^- chemical ionization of hydroxy hydroperoxides (Paulot *et al.*, 2009b). The product ions (*m/z* 205:139:101:63) are produced in a ratio of 5:10:6.5:1. This analysis is further detailed in Figure B.10 of the Supporting Information. Given the identical elution time and similar product ion distribution between the MVK hydroperoxide and those derived from the oxidation of 4-hydroxy-2-butanone, we identify this hydroperoxide as 3-hydroperoxy-4-hydroxybutan-2-one (4,3-hydroxy hydroperoxide).

B.3.2 Reaction of RO_2 with NO: Constraining the Ratio R1a:R1b

In the reaction of the two peroxy radicals produced in R1a and R1b with NO, two alkoxy radicals and two alkyl nitrates are produced (see Figure B.3). Tuazon and Atkinson (1989) and Galloway *et al.* (2011) suggested that the internal and external alkoxy radicals decompose to glycolaldehyde and methylglyoxal with 100% yield, respectively. Consistent with this hypothesis, we have calculated the energy barriers associated with decomposition of the alkoxy formed from the reaction of the peroxy radical produced in R1a with NO. We find that fragmentation to methylglyoxal is likely uncompetitive with fragmentation to acetyl peroxy (PA) and glycolaldehyde (8.2 vs 1.5 kcal mol^{-1} in electronic energy, see the Supporting Information). This is consistent with the structure-activity relationship of Vereecken and Peeters (2009), which suggests these barriers to be 8.1 versus 3.7 kcal mol^{-1}, respectively. Thus, the product yields shown in Table B.3 suggest that the branching to R1a, derived by adding the glycolaldehyde yield and that of the corresponding hydroxy nitrate, is 76 ± 14%, while that to R1b is 24 ± 14%. The branching of R1b is defined as the difference between unity and the branching to R1a. Our estimation of the

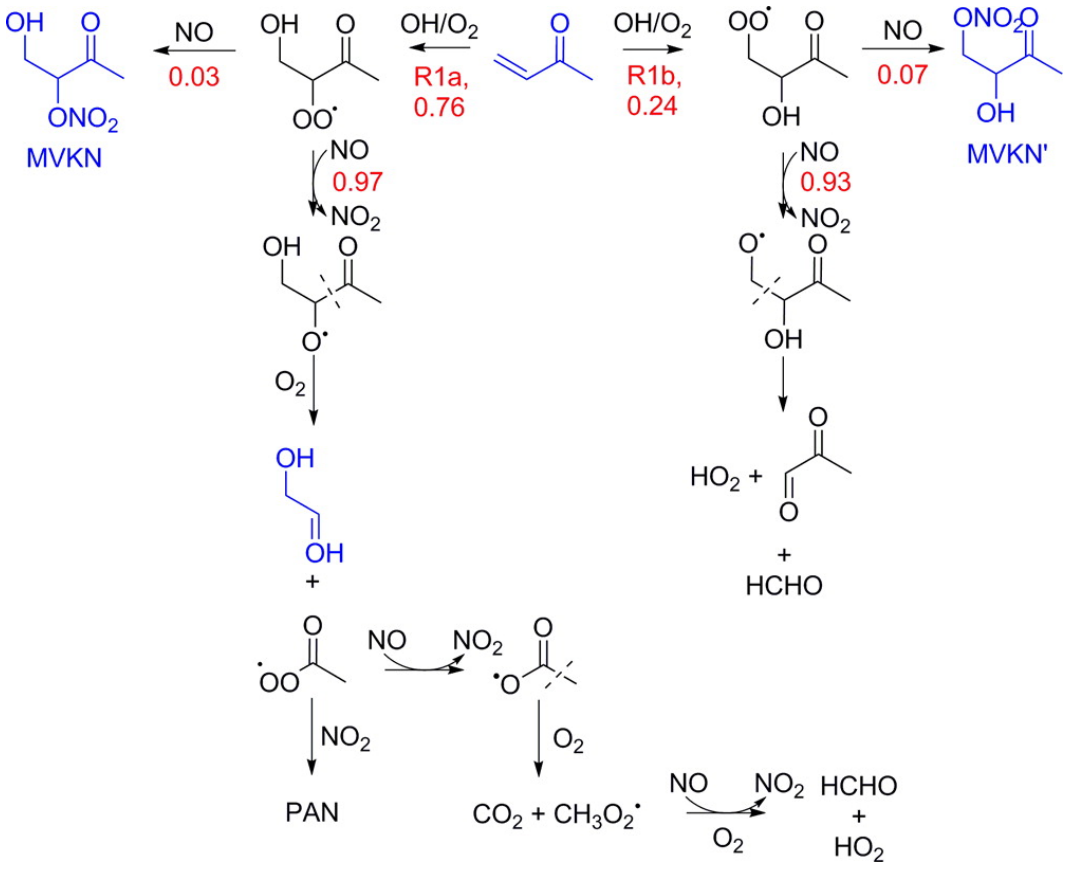

Figure B.3: Proposed mechanism for the high-NO regime (after Tuazon and Atkinson (1989)). Observed species are indicated in blue. Branching and yields (T = 296 K, P = 993 hPa) are in red.

branching ratio is consistent with previous estimates (Galloway *et al.*, 2011; Tuazon and Atkinson, 1989).

B.3.3 Reaction of RO_2 with NO: Formation of Alkyl Nitrates

The alkyl nitrate branching ratio from the reaction of the RO_2 produced in R1a with NO is 3.2 ± 0.6% at 296 K, while the branching ratio from the RO_2 produced in R1b is more than a factor of 2 larger (6.6 ± 1.5%). The combined yield at 296 K is 4.0 ± 0.6%, much lower than previously suggested (Chuong and Stevens, 2004; Tuazon and Atkinson, 1989). Comparing the yields from experiments 7 and 8 with those of 9 and 10, we find that the combined yield is a factor of ~1.8 times lower at 323 K than at 296 K. Furthermore, at 323 K, the production ratio of MVKN to MVKN' is 1.10 ± 0.05.

Alkyl nitrates likely form in a roaming radical mechanism. This mechanism

proceeds following destabilization of the ROONO moiety. In some cases, the nascent radicals do not separate but rather reform an activated $RONO_2$ complex, which then undergoes collisional stabilization to form the nitrate (Butkovskaya *et al.*, 2015; Dibble, 2008; Herath and Suits, 2011; O'Brien *et al.*, 1998). As such, the yield will depend on the lifetime of the complex. This general mechanism is consistent with findings that alkyl nitrate yields tend to increase with the size of molecule (Carter and Atkinson, 1989) and decrease with increasing temperature (Atkinson *et al.*, 1983). In addition, several studies have suggested that the formation of nitrates becomes less favorable when neighboring groups weaken the RO-ONO bond, enhancing the rate of decomposition (Matsunaga and Ziemann, 2009, 2010b; O'Brien *et al.*, 1998). Using the β-hydroxy nitrate yields quantified in our recent study of nitrates formed in the oxidation of alkenes (Teng *et al.*, 2015), we expect, based on the molecular size alone, that the alkyl nitrate yield from MVK would be ~14%. The much lower yield measured likely reflects destabilization of the RO-ONO moiety by the electron-withdrawing characteristics of the ketone group. Additionally, the lower yield and stronger temperature dependence of the nitrate formed from the RO_2 produced in R1a suggests that a β-ketone is more destabilizing than a γ-ketone.

The atmospheric fate of these nitrates remains unclear. A recent theoretical study has reported that the atmospheric lifetime of MVKN and MVKN' will be limited by photolysis (~5 h) (Müller *et al.*, 2014). Upon further oxidation by OH, the nitrates have been proposed to generate formic and pyruvic acid (Paulot *et al.*, 2009a).

B.3.4 Reaction of RO_2 with HO_2: New Chemistry and Radical Recycling

Reaction of the peroxy radicals with HO_2 is remarkably efficient in the recycling of radicals. We identified R2a-R2c for the reaction of HO_2 with the MVK RO_2 arising from R1a (see Figure B.4).

The large yield of glycolaldehyde (~40%) suggests that the OH radical is recycled efficiently *via* R2a. This chemistry is not unprecedented. Recent studies have demonstrated that OH generation occurs in several similar systems (Dillon and Crowley, 2008; Hasson *et al.*, 2005, 2004). For example, reaction of HO_2 with PA radical, produced in R2a upon addition of O_2 to the $CH_3C(O)$ radical, has been shown to follow three pathways. The dominant channel (R3a, yield = 0.61 ± 0.09 (Gross *et al.*, 2014)) produces OH and acetoxy radicals, while peracetic acid (R3b) and acetic acid and O_3 (R3c) are produced in smaller yields (Dillon and Crowley, 2008; Hasson *et al.*, 2005, 2004, 2012; Jenkin *et al.*, 2007):

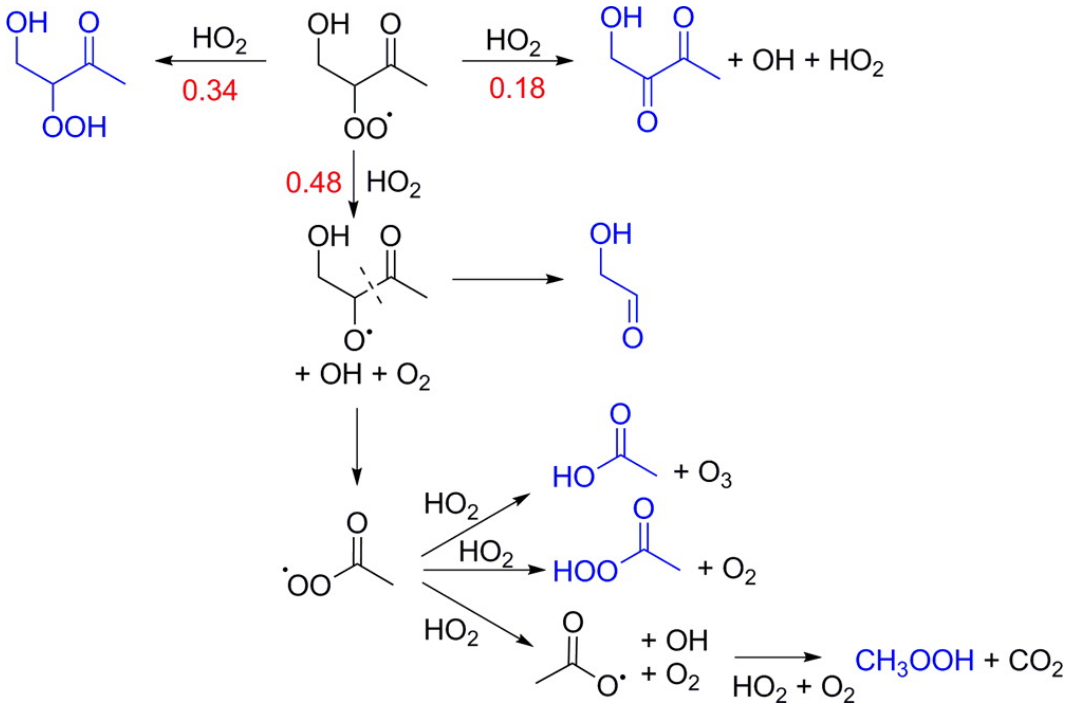

Figure B.4: Proposed mechanism for the OH-initiated oxidation of MVK following R1a in the HO_2-dominated regime. Observed products are indicated in blue. Yields (T = 296 K, P = 993 hPa) are in red.

$$CH_3C(=O)OO\cdot + HO_2 \rightarrow CH_3C(=O)O\cdot + OH + O_2 \quad \text{(R3a)}$$

$$CH_3C(=O)OO\cdot + HO_2 \rightarrow CH_3C(=O)OOH + O_2 \quad \text{(R3b)}$$

$$CH_3C(=O)OO\cdot + HO_2 \rightarrow CH_3C(=O)OH + O_3 \quad \text{(R3c)}$$

In the presence of HO_2, the radical produced in R3a leads to formation of methyl hydroperoxide (MHP):

$$CH_3C(=O)O\cdot \rightarrow CH_3\cdot + CO_2 \quad \text{(R4)}$$

$$CH_3\cdot + O_2 + M \rightarrow CH_3OO\cdot + M \quad \text{(R5)}$$

$$CH_3OO\cdot + HO_2 \rightarrow CH_3OOH + O_2 \quad \text{(R6)}$$

All stable organic end products identified in R3-R6 were detected in the HO_2-mediated reaction of MVK RO_2 and suggest greater radical recycling occurring beyond the initial OH reformation in R2a.

The 4,3-hydroxy hydroperoxide produced *via* R2b was found to promptly photolyze (Figure B.5). Independent of whether an OH scrubber was added (experiments 15 and 16), the hydroperoxide decayed with a first-order loss rate of 3.0 $\pm$ 0.1 $\times$ 10^{-5} s^{-1}. Scaling the J_{NO_2} in our chamber (2.5 $\times$ 10^{-3} s^{-1}) to that of a typical noontime atmosphere (0.01 s^{-1}) suggests that the atmospheric lifetime of

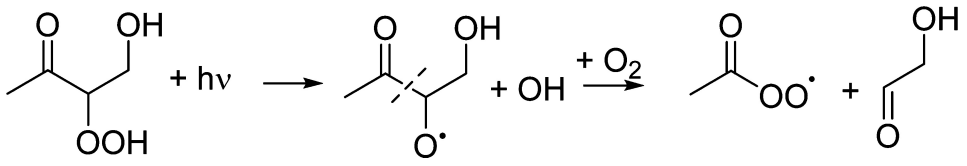

Figure B.5: Photolysis of the 4,3-hydroxy hydroperoxide, assuming cleavage of the O-OH bond, is expected to form PA and glycoladehyde, and recycle OH. Rapid photolysis of this species was observed.

this hydroxy hydroperoxide is short ($\ll$1 day). Assuming cleavage of the O-OH bond as the primary photolytic decomposition pathway, R2b will also recycle OH radicals efficiently.

The α-diketone produced *via* R2c likely results from a mechanism previously thought to be exclusive to halogenated RO_2. As we show below, this route likely produces OH + HO_2 in addition to the carbonyl. Similar chemistry was originally proposed by Wallington *et al.* (1994) to explain the formation of HC(=O)F in the reaction of CH_2FO_2 and HO_2. More recent theoretical studies have demonstrated that the energetic barrier to formation of OH and HO_2 from single-carbon fluorinated and chlorinated RO_2 is lower than the pathway to formation of H_2O and O_2, as originally proposed (Hou *et al.*, 2005a,b; Hou and Wang, 2005). To our knowledge, the MVK system provides the first evidence for this chemistry in nonhalogenated peroxy species.

Rapid photolysis has been previously reported for α-diketones (Bouzidi *et al.*, 2014). We designed experiments 15 and 16 to measure the rate of photolysis for the hydroxy diketone (*m/z* 187). Both prior to and after the initiation of photolysis, the signal was monitored for a period of 2 h to measure the wall loss rates. These were determined to be 2×10^{-7} s^{-1} and 2×10^{-6} s^{-1} before and after photolysis, respectively. Upon illumination by UV light, the *m/z* 187 signal decayed ~20% at a consistent rate. After 4 h, however, the loss ended such that an exponential decay no longer fit the data. This is likely due to the formation of a third-generation isobaric compound. Whether production of this compound existed during the initial period, although at a lower rate, is uncertain. Thus, we can only determine a loosely constrained value of $\sim 1 \times 10^{-5}$ s^{-1}, which includes corrections for wall loss and reaction with OH (<1% due to the presence of an OH scrubber). This rate is lower than the calculated photolysis rate of a similar α-diketone, methylglyoxal, under similar conditions (4.1×10^{-5} s^{-1}).

B.3.5 Internal OH Addition

We are unable to identify the majority of the products of the reaction of HO_2 with the terminal RO_2 (formed *via* R1b). By reference to the reactions arising from external OH addition (R1a), the products are likely methylgloxal, a hydroperoxide, and an aldehyde. The instruments employed in this study are insensitive to methylglyoxal, and thus we turn to unpublished data collected in the HO_2-dominated regime during the same set of experiments reported by Galloway *et al.* (2011). Preliminary analysis of this data *via* personal communication from the authors suggests an overall methylglyoxal yield of ~4%. In the current study, only a single *m/z* 205 peak, identified as the 4,3-hydroxy hydroperoxide, was observed in GC-CIMS analysis. No other peaks resembling a fragmentation pattern characteristic to hydroperoxide functionality were located in the vicinity of the elution time of the observed *m/z* 205 compound. It is possible that ionization of the 3,4-hydroxy hydroperoxide results in fragmentation to undetectable products. Alternatively, the hydroperoxide may decompose rapidly on the chamber walls. The C_4 aldehyde, as explained earlier, appears to be produced in, at most, a small yield. It may also be possible to form other products which are not observed by our CIMS.

B.3.6 Unimolecular RO_2 Channels

Functionalized peroxy radicals are known to undergo unimolecular hydrogen shifts from neighboring substituents (Crounse *et al.*, 2013; Orlando and Tyndall, 2012). Recent theoretical studies have suggested that a unimolecular pathway involving a 1,5 H-shift from the terminal hydroxy group to the RO_2 (R1a) could be of significance in the production of methylglyoxal and formaldehyde (see Figure B.6) (Asatryan *et al.*, 2010; Peeters *et al.*, 2009). While this mechanism proceeds through different intermediates, the end products are likely identical to the pathway involving HO_2 reaction with the terminal RO_2 to produce RO. Thus, the detection of this mechanism is complicated. Experiments 5 and 6 were designed to promote isomerization processes through active heating of the chamber to 50 °C and extension of RO_2 lifetimes. The product distributions and yields observed in these experiments were very similar to those seen in experiments 1-3. While the majority of products arising from R1b are poorly characterized, the ratio of MVKN to MVKN' in experiment 5 was consistent with those obtained in experiments 9 and 10. This suggests that neither of the RO_2 radicals had a significant unimolecular channel under the experimental conditions probed here.

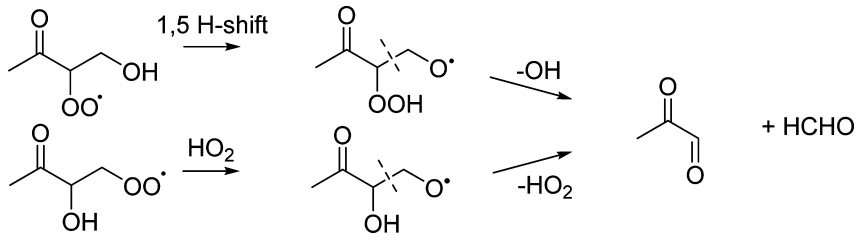

Figure B.6: A 1,5 H-shift, as suggested by Peeters *et al.* (2009) and Asatryan *et al.* (2010), is difficult to detect by the end products alone, as two pathways exist to their formation.

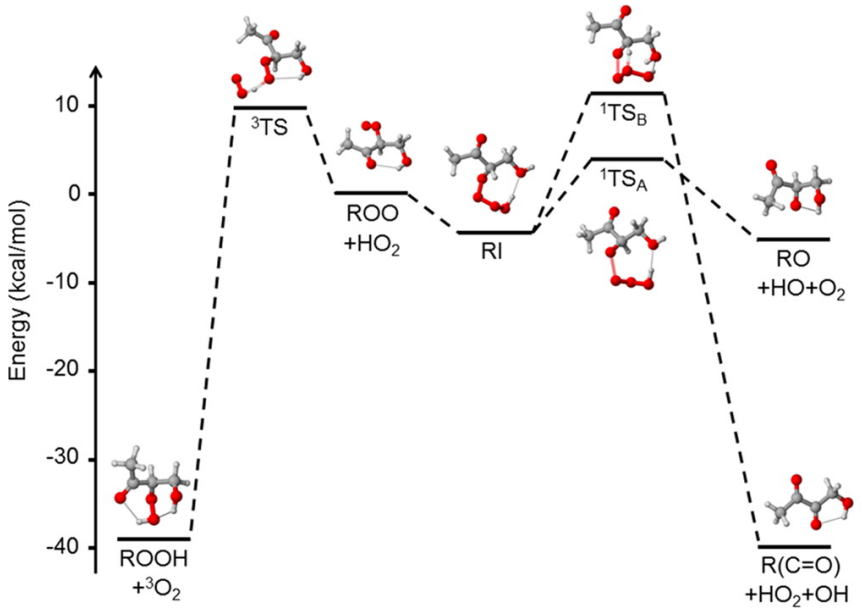

Figure B.7: Relative energies (ΔG_{298K}) for the three RO_2 + HO_2 channels. We have used wB97XD/aug-cc-pVTZ thermochemistry with ROHF-ROCCSD(T)-F12/VDZ-F12 energies. The wB97XD/aug-cc-pVTZ geometries for each of the stationary points are shown.

B.3.7 Quantum Chemical Calculations

Figure B.7 and Table B.4 show that all three postulated reaction pathways R2a-R2c in the reaction of HO_2 with RO_2 R1a are kinetically accessible at 298 K. Transition states for the reactions leading to the hydroperoxide (ROOH) and the alkoxy (RO) corresponded to those found for acetonyl RO_2 in the literature (Hasson *et al.*, 2005). In addition, a new channel leading to a diketone [R(C=O)] has been found. For all but TS_A of the reaction leading to RO, there is no significant spin contamination observed, with $<S^2>$ being within 0.02 of the expected values for singlet (0), doublet (3/4), and triplet (2), respectively (see Table B.9 of the Supporting Information).

	ΔE^a	ΔE^b	ΔG^c	TS (imaginary frequency, cm^{-1})
ROO + HO_2	0.0	0.0	0.0	-
^{3}TS	-3.2	+0.7	+10.2	934i
ROOH + O_2	-39.2	-43.1	-38.9	-
RI	-12.2	-20.4	-4.1	-
^1TS_A	2.5	-8.3	+4.1	212i
RO + OH + O_2	+5.7	+8.1	-5.0	-
^1TS_B	11.2	-0.7	+12.0	905i
R(C=O) + OH + HO_2	-22.3	-26.2	-40.0	-

Table B.4: Energetics of the different RO_2 + HO_2 channels. Energies are in units of kcal mol^{-1} and are calculated with ^{a}wB97XD/aug-cc-pVTZ, ^{b}ROHF-ROCCSD(T)-F12/VDZ-F12//wB97XD/aug-cc-pVTZ, and ^{c}the wB97XD/aug-cc-pVTZ thermochemistry with CCSD(T)-F12/VDZ-F12 single-point energy correction.

The ROOH reaction producing ground state O_2 takes place on the triplet surface *via* the transition state ^{3}TS (almost iso-energetic with the reactants) with a moderate free-energy barrier of about 10 kcal mol^{-1}. Tunneling will slightly enhance the reaction rate along this surface by a factor similar to that of the R(C=O) channel.

The RO reaction occurs *via* a tetroxide intermediate (labeled RI) and a low-energy, open-shell singlet transition state TS_A with a free-energy barrier of about 4 kcal mol^{-1}. The immediate products of TS_A are RO and an HO_3 radical, which further decomposes to OH and O_2. The structure and stability of HO_3 is a challenging problem for quantum chemical methods. Even high level methods such as CCSD(T)-F12 do not describe it accurately (see Zhou *et al.* (2013), Varandas (2012), and references therein).

We have also identified a reaction path leading to the α-diketone [R(C=O)]. This channel also proceeds *via* the tetroxide intermediate RI but to TS_B with a free-energy barrier of about 12 kcal mol^{-1} and leads to the diketone and an H_2O_3 radical; the latter decomposes to OH + HO_2. Decomposition to H_2O and triplet O_2 would be even more energetically favorable but is spin-forbidden as the reaction takes place along the singlet potential energy surface.

We have also found an alternative tetroxide structure about 2 kcal mol^{-1} below RI in electronic and free energy. This tetroxide can also decompose to both RO and R(C=O) products, although through a higher energy TS than the ones shown in Figure B.7. The two tetroxides differ only in their H-bonding pattern (see the Supporting Information).

We were unable to locate a transition state between the free reactants and either of the tetroxides, and we thus assume they form without a significant energy barrier.

The free-energy barriers computed for the three reaction routes, as shown in Table B.4, are within a few kcal mol^{-1} of each other. The electronic energy of all the transition states is around or below the electronic energy of the reactants. Furthermore, the routes with the largest free-energy barrier (leading to R(C=O) and ROOH) are slightly assisted by tunneling. The effect of tunneling with the Eckart tunneling correction was calculated to be a factor of 3 for the diketone channel and insignificant for the RO channel (Eckart, 1930).

The uncertainty of the computed energy barriers is possibly higher than the usual few kcal mol^{-1} for CCSD(T)-F12/VDZ-F12 energies due to the spin issues in particular for TS_A and multireference issues (see the discussion of the HO_3 intermediate product above; see also Section B.5). Thus, quantitative predictions of product yields are not reliable. Qualitatively, however, the calculations are consistent with the experimental observations, with the highest yields observed for the RO channel, followed by the ROOH and R(C=O) channels.

B.3.8 Atmospheric Implications

To assess the importance of the chemistry described here, we employed GEOS-Chem, a widely used chemical transport model (Bey *et al.*, 2001). A 1 year simulation (January to December 2012) of the model was conducted on a global 4° latitude × 5° longitude grid. The alkyl nitrate yield reported in this work was incorporated into the base chemistry to isolate the impact of HO_2 chemistry. Changes to the mechanism were applied separately to the base model to evaluate the impact of each modification of the chemistry. We began by implementing the yields of first generation products described by R2a-R2c (MVK scenario). An additional scenario (MVK + RCO_3) was created to assess the impact of PA radical production through R2a. The default GEOS-Chem 2012 mechanism does not treat PA according to recent findings. Thus, the most recent measurement of the OH yield from the reaction of PA + HO_2 was incorporated into both the base and the revised mechanism so as not to bias the results (Gross *et al.*, 2014). Given the considerable yield of PA in R2a, we believe this scenario to be most representative of the findings reported in this work. In order to provide an external benchmark, the OH production resulting from methacrolein (MACR) isomerization was included in a separate run (Crounse *et al.*, 2012). The final simulation incorporated all revisions

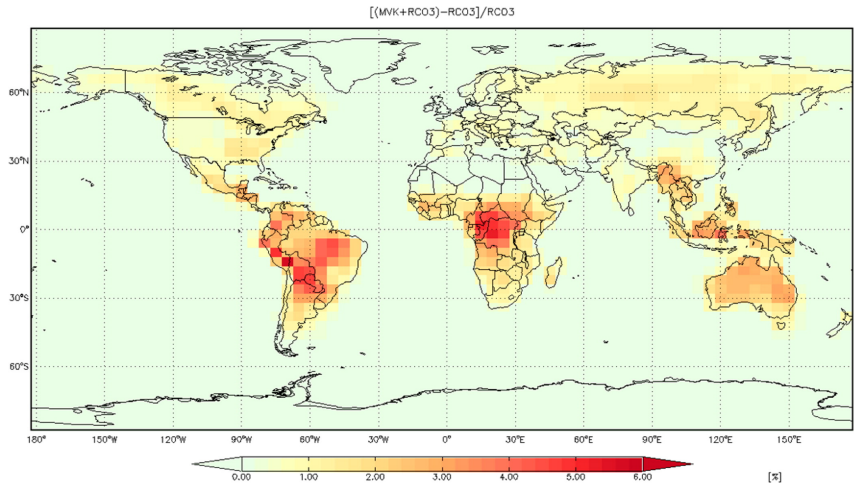

Figure B.8: Annual-averaged OH mixing ratio difference for 2012 resulting from the revised MVK mechanism (MVK + RCO_3). Results are reported for 0-1 km above the surface.

scenario	OH (ppt)	increase over base (%)
base	0.0539	0.00
MVK	0.0541	0.30
MVK + RCO_3	0.0544	0.89
MACR	0.0541	0.35
all + J_{ROOH}	0.0547	1.33

Table B.5: Comparison of various model scenarios with the increase determined relative to the base chemistry (see Section B.5 for scenario definitions). Global annual mean OH values were determined by averaging over all space between 0 and 1 km above the surface.

of the previous scenarios and the fast photolysis of MVK ROOH. We find these changes result in a greater than 1% increase in the global mean boundary layer concentration of OH (Table B.5). Locally, the impact is larger. In the forested tropical boundary layer, simulated OH concentrations are up to 6% larger (Figure B.8).

B.4 Conclusions

HO_x recycling channels have been proposed to explain first generation products arising from the oxidation of isoprene in pristine environments (Crounse *et al.*, 2011; Peeters *et al.*, 2009), as well as the production of hydroxyacetone from MVK's atmospheric sister compound, methacrolein (Crounse *et al.*, 2012). Yet the atmospheric chemistry of MVK, particularly in environments with low concentrations of NO, has

been largely unexplored. Here we demonstrate a number of new radical recycling channels that contribute to sustaining the oxidizing capacity of the atmosphere. We further illustrate dicarbonyl formation in a novel mechanism previously identified only for halogenated peroxy species. This finding suggests that carbonyl products may arise from reaction of HO_2 with other substituted peroxy radicals in an overall HO_x neutral process.

B.5 Supporting Information

B.5.1 Instrumental Calibration

CIMS sensitivity factors are determined by the specific molecule-ion collision rates and the binding energy of the resulting clusters. The rate of collision can be estimated from the dipole moment and polarizability of the analyte (Su and Chesnavich, 1982). These properties were calculated using DFT for the C_4 compounds produced in the oxidation of MVK. Because the dipole moment depends on the structural conformation of the molecule, we calculate the population density and dipole of all conformers with a relative population of >5% at 298 K to estimate the conformationally-weighted property. The polarizability was not found to exhibit significant conformational dependence and the calculation was therefore based on the lowest energy structure. Further detail of similar calculations is provided by Garden *et al.* (2009) A summary of these properties along with calibration factors for MVK systems is shown in Table B.6 in the Supporting Information.

B.5.2 Chemical Transport Model

Tables B.7 and B.8 in the Supporting Information describe changes made to the GEOS-Chem mechanism (Bey *et al.*, 2001). The maps (Figures B.11, B.12, and B.13 in the Supporting Information) illustrate the output of the model resulting from the changes. These simulations employ GEOS-Chem v9-02 using GEOS5 meteorology and initialize the model with a 1.5 year spinup before the January-December 2012 final simulation. The Rosenbrock Rodas-3 with Kinetic PreProcessing software was used as the solver.

B.5.3 Quantum Chemical Calculations

To test whether using a UHF reference wave function would lower the coupled-cluster energies for the spin-contaminated transition state TS_A, we performed qualitative RHF-RCCSD(T)/6-31+G(d) and UHF-UCCSD(T)/6-31+G(d) single-point energy calculations with the Gaussian 09 program on the wB97xd/aug-ccpVTZ - optimized geometry. While the UHF energy was 60.5 kcal mol^{-1} below the RHF energy, the UHF-UCCSD energy was 344.0 kcal mol^{-1} and the UHF-UCCSD(T) energy 272.9 kcal mol^{-1} above the RHF-RCCSD and RHF-RCCSD(T) energies, respectively. Inspection of the CCSD iterations (over 300 were required for convergence) indicates that the UCCSD probably converged to the wrong state. A similar comparison for the alternative TS_A isomer, for which CCSD convergence problems did not occur, yielded more modest energy differences, but the UHF-UCCSD(T)

energy was still 5.3 kcal mol^{-1} above the RHF-RCCSD(T) energy. Spin contamination at the UHF level was extreme for both of the TS_A isomers; $<S^2>$ = 0.93...0.95 before and 0.19...0.20 after annihilation. This indicates that using a UHF reference in the coupled cluster calculations would neither lower the barrier, nor improve the reliability of the results and suggests that multireference calculations are required to attain better accuracy. These problems are likely related to the difficulties of even advanced methods like CCSD(T) or even MRCISD in describing the structure and stability of the HO_3 intermediate product. Varandas (2012) has suggested that a quantitative prediction of the dissociation energy of HO_3 would require FCI calculations.

The DFT relative energies for reactant and products are within 4 kcal mol^{-1} of the ROHFROCCSD(T)-F12/VDZ-F12//wB97XD/aug-cc-pVTZ energies and give an idea of the uncertainty expected in these calculations. For the RI and the TS's the difference is higher than usual and, in conjunction with the spin and T1 values, an indication that multireference calculations are needed to obtain accurate values. The DFT barrier values for the ROOH and R(C=O) channels are such that these products would not be observed. The F12 barriers for these channels are lower and thus in better agreement with experiment.

The formation of intermediate product complexes of energies comparable to that of the reactants allow for back reactions that further complicate determination of yields.

B.5.4 Second Tetroxide

We have found a second tetroxide that also leads to both RO and R(C=O). It is lower in energy than the one in Figure B.6, however the TS leading to the products are higher in energy. These pathways are shown in Figure B.14 in the Supporting Information.

B.5.5 Decomposition of Alkoxy Radical Formed from External OH Addition to MVK (R1a)

The decomposition of the alkoxy radical formed in the reaction of NO with the peroxy radical produced in R1a can lead to either methylglyoxal (CH_3(C=O)CHO) and the CH_2OH radical or glycolaldehyde (CH_2OHCHO) and the CH_3C=O radical. The calculated energies and stationary points are shown in Figure B.15 and Table B.12 in the Supporting Information. The barrier of the internal alkoxy decomposition will likely be dominated by glycolaldehyde formation.

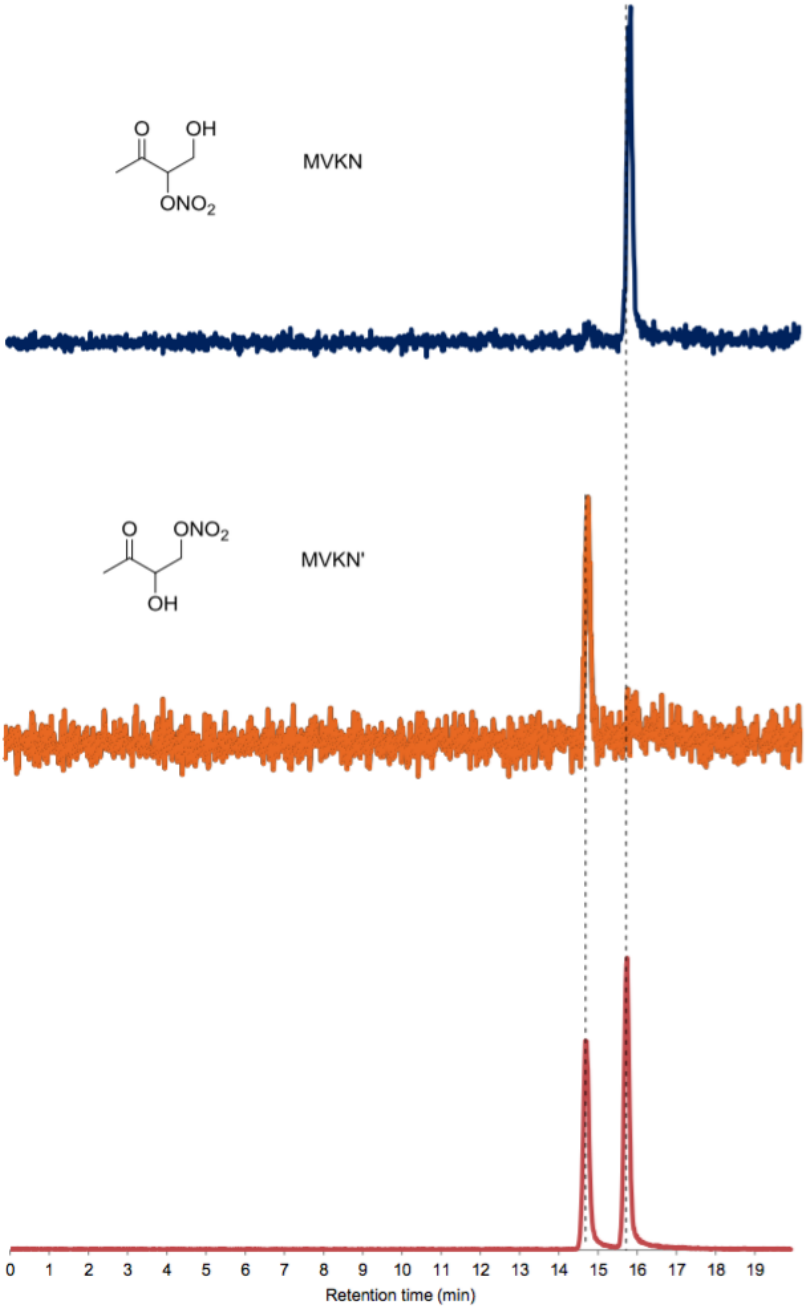

Figure B.9: Chromatographic analysis used for the identification of MVKN and MVKN'. Data are derived from experiments 8 (bottom panel), 14 (mid panel), and 12 (top panel). The latter two experiments isolated the chemistry of individual RO_2, enabling the structures and retention times of the individual organic nitrates to be discerned. This assignment also matches the elution order previously reported using a similar column (Lee *et al.*, 2014).

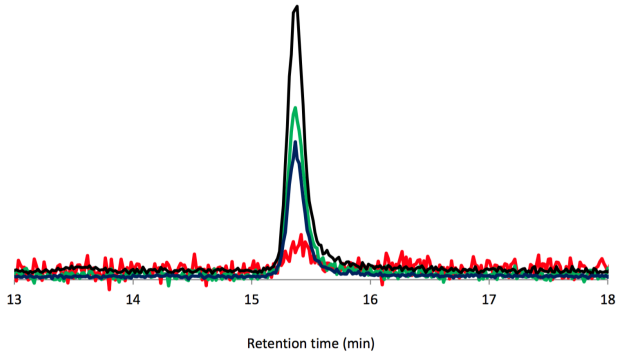

Figure B.10: Chromatographic analysis of the 4,3 hydroxy hydroperoxide derived from experiment 1. Shown are the major product ions in order of descending area: *m/z* 139 (black), *m/z* 101 (green), *m/z* 205 (blue), *m/z* 63 (red).

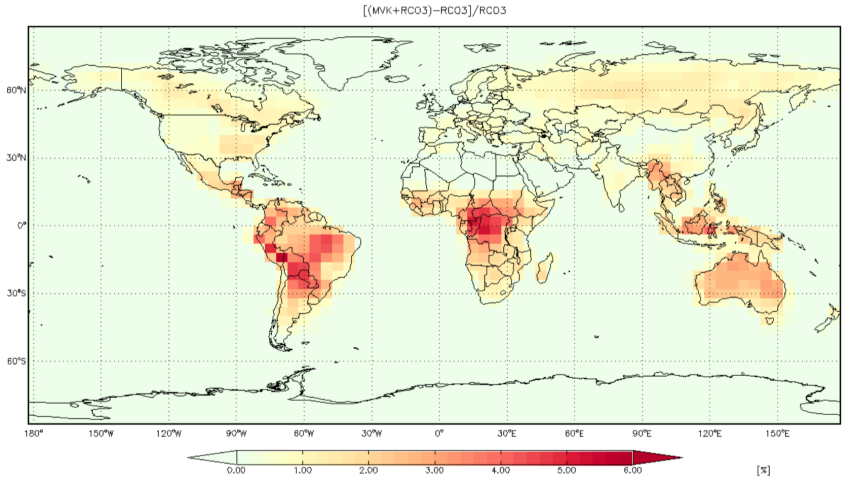

Figure B.11: Relative difference in the OH mixing ratio for MVK + RCO_3 in the boundary layer (0-1 km).

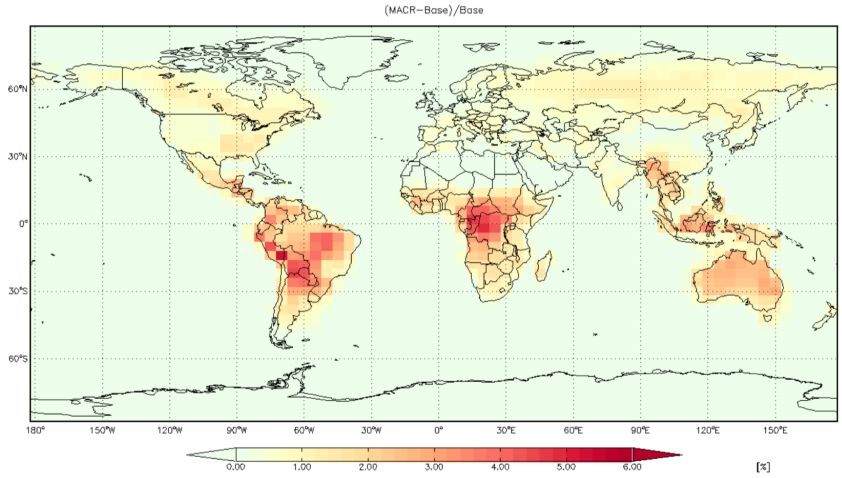

Figure B.12: Relative difference in the OH mixing ratio for MACR in the boundary layer (0-1 km).

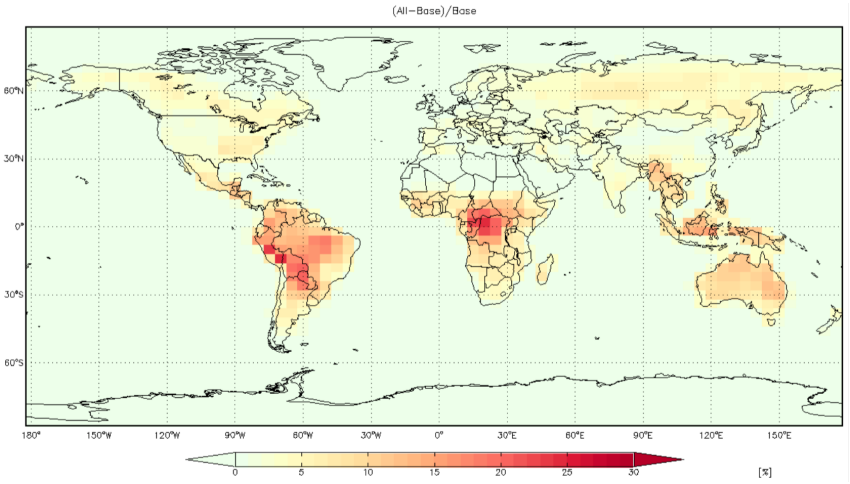

Figure B.13: All inclusive: MVK, MACR isomerization, RCO_3, J_{ROOH}; relative difference in the boundary layer (0-1 km).

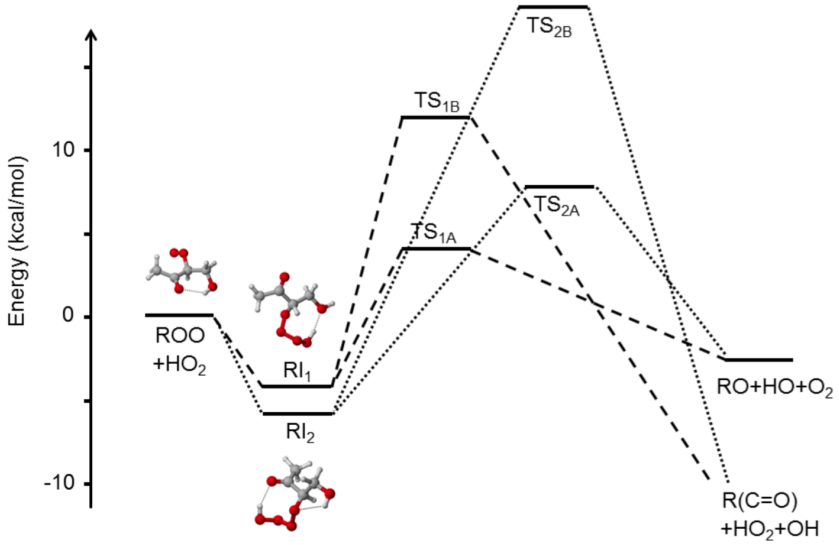

Figure B.14: Relative energies (ΔG_{298K}) for the two singlet RO_2 + HO_2 channels, including the second tetroxide (RI_2). RI_1 is identical to RI in the manuscript. We have used wB97XD/aug-ccpVTZ thermochemistry with ROHF-ROCCSD(T)-F12/VDZ-F12 energies. The wB97XD/auGCc-pVTZ geometries for each of the stationary points are shown.

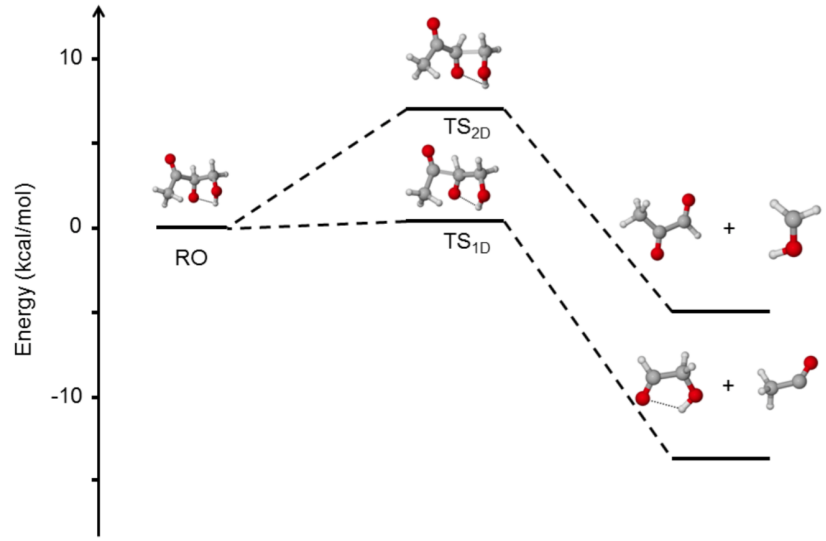

Figure B.15: Relative energies (ΔG_{298K}) for the two decomposition channels of the alkoxy formed from external OH addition to MVK. We have used wB97XD/aug-cc-pVTZ thermochemistry with ROHF-ROCCSD(T)-F12/VDZ-F12 energies. The wB97XD/aug-cc-pVTZ geometries for each of the stationary points are shown.

molecule	*m/z*	μ (D)	α (Å^3)	k_x (10^{-9} cm^3 molecule^{-1} s^{-1})	calculated sensitivity ($\times 10^{-4}$)	experimental sensitivity ($\times 10^{-4}$)
ISOPN-4,3	232	2.5	11	1.9	3.1	3.7
glycolaldehyde	145	2.3	4.5	2.0	3.1	3.0 ± 0.2
hydroxy diketone	187	2.1	7.2	1.8	2.7	-
4,3-hydroxyhydroperoxide	205+139+101+63	2.6	8.1	2.0	3.1	-
MVKN	234	2.3	9.9	1.8	2.8	2.6 ± 0.3
MVKN'	234	2.2	9.7	1.8	2.7	3.0 ± 0.3

Table B.6: Calculated conformer-weighted dipole moments (μ) and polarizabilites (α) served as the basis for sensitivity determination (see Paulot *et al.* (2009a) calculations for the hydroxy diketone and 4,3-hydroxy-hydroperoxide were performed in support of this work by HGK at the B3LYP/6-31G(d) level). k_x is the weighted average of the calculated collision rates (Su and Chesnavich, 1982) for conformers having an abundance greater than 5%. These are normalized to the average of the calculated collision rates for CF_3O^- with MVKN and MVKN' at 298 K (k = 1.8×10^{-9} cm^3 molecule^{-1} s^{-1}) and the mean of the experimentally determined MVKN and MVKN' sensitivities was used to infer the sensitivity for compounds for which no standards were available. Masses (*m/z*) represent the cluster mass with CF_3O^-. For compounds reacting with CF_3O^- to form multiple product ions, the sum of all known product ions have been used for quantification. Isoprene nitrate (1-hydroxy-3-methylbut-3-en-2-yl nitrate, ISOPN-4,3) has been included for additional comparison between theory and experiment. Calculated and experimental sensitivities are in units of normalized counts pptv^{-1} for the CF_3O^- CIMS. Hydroxy nitrate sensitivities were determined using thermal dissociation LED-induced fluorescence (Teng *et al.*, 2015) and glycolaldehyde was calibrated as described in the current work. Uncertainties are indicated for measured sensitivities.

scenario	base model	revised model
Base: $VRO_2 + NO \rightarrow$	$0.88NO_2 + 0.35HO_2 + 0.35CH_2O$ $+ 0.53MCO_3 + 0.53GLYC$ $+ 0.35MGLY + 0.12MVKN$: $k=2.7 \times 10^{-12} \times e^{(350/T)}$	$0.965NO_2 + 0.249HO_2 + 0.249CH_2O$ $+ 0.716MCO_3 + 0.716GLYC$ $+ 0.249MGLY + 0.035MVKN$: $k=2.7 \times 10^{-12} \times e^{(350/T)}$
MVK: $VRO_2 + HO_2 \rightarrow$	1.000 VRP: $k=1.82 \times 10^{-13} \times e^{(1300/T)}$	$0.38VRP + 0.62OH + 0.37GLYC + 0.13MEK$ $+ 0.37MCO_3 + 0.25HO_2 + 0.12MGLY + 0.12CH_2O$: $k=1.82 \times 10^{-13} \times e^{(1300/T)}$
MVK + RCO_3: $MCO_3 + HO_2 \rightarrow$	$0.16ACTA + 0.16O_3 + 0.61OH$ $+ 0.61MO_2 + 0.23MAP$: $k=5.2 \times 10^{-13} \times e^{(980/T)}$;	$0.16ACTA + 0.16O_3 + 0.61OH$ $+ 0.61MO_2 + 0.23MAP$: $k=5.2 \times 10^{-13} \times e^{(980/T)}$;
$RCO_3 + HO_2 \rightarrow$	$0.16RCOOH + 0.16O_3 + 0.61OH$ $+ 0.61ETO_2 + 0.23PP$: $k=4.3 \times 10^{-13} \times e^{(1040/T)}$;	$0.16RCOOH + 0.16O_3 + 0.61OH$ $+ 0.61ETO_2 + 0.23PP$: $k=4.3 \times 10^{-13} \times e^{(1040/T)}$;
$MAO_3 + HO_2 \rightarrow$	$0.16O_3 + 0.61OH + 0.61CO_2$ $+ 0.61CH_2O + 0.40MO_2 + 0.4CO$ $+ 0.21MCO_3 + 0.23MAOP$: $k=4.3 \times 10^{-13} \times e(1040/T)$;	$0.16O_3 + 0.61OH + 0.61CO_2$ $+ 0.61CH_2O + 0.40MO_2 + 0.4CO$ $+ 0.21MCO_3 + 0.23MAOP$: $k=4.3 \times 10^{-13} \times e^{(1040/T)}$;
$VRO_2 + HO_2 \rightarrow$	1.000VRP: $k=1.82 \times 10^{-13} \times e^{(1300/T)}$	$0.38VRP + 0.62OH + 0.37GLYC + 0.13MEK$ $+ 0.37MCO_3 + 0.25HO_2 + 0.12MGLY + 0.12CH_2O$: $k=1.82 \times 10^{-13} \times e^{(1300/T)}$
MACR $MRO_2 \rightarrow$	1.000CO + 1.000HAC + 1.000OH: k=0	1.000CO + 1.000HAC + 1.000OH: $k=2.90 \times 10^{7} \times e^{(-5297/T)}$

Table B.7: Revisions incorporated into the GEOS-Chem mechanism. The scenarios are consistent with those described in Table B.5. The base scenario includes the alkyl nitrate branching determined in this work. Naming conventions used below can be found at http://wiki.seas.harvard.edu/GEOS-Chem.

lower-bound wavelength (nm)	upper-bound wavelength (nm)	base cross section (cm^2)	new cross section (cm^2)
289	298.25	5.621×10^{-21}	5.665×10^{-20}
298.25	307.45	3.573×10^{-21}	4.000×10^{-20}
307.45	312.45	2.441×10^{-21}	2.740×10^{-20}
312.45	320.30	1.755×10^{-21}	2.140×10^{-20}
320.30	345	7.405×10^{-22}	7.085×10^{-21}
345	412.45	4.261×10^{-23}	5.634×10^{-22}
412.45	850	0	0

Table B.8: Revised wavelength bins utilized to define the photolysis frequency of the MVK hydroperoxide in the model.

	$<S^2>$ before annihilation	$<S^2>$ after annihilation	T1
ROO	0.7546	0.7500	0.023
OOH	0.7543	0.7500	0.034
^{3}TS	2.0124	2.0001	0.032
ROOH	0.0	0.0	0.013
O_2	2.0101	2.0001	0.008
RI	0.0	0.0	0.016
^1TS_A	0.5729	0.0167	0.020
RO	0.7577	0.7500	0.028
OH	0.7529	0.7500	0.007
^1TS_B	0.0	0.0	0.021
R(C=O)	0.0	0.0	0.014

Table B.9: Spin contamination and T1 diagnostic in the calculations from the different RO_2 + HO_2 channels. $<S^2>$ are from the UwB97XD/aug-cc-pVTZ calculation, and T1 is from the ROHF-ROCCSD(T)-F12/VDZ-F12//wB97XD/aug-cc-pVTZ calculation.

	ΔE^a	ΔE^b	$\Delta G298K^c$	TS (imaginary frequency, cm^{-1})
ROO + HO_2	0.0	0.0	0.0	-
RI≡RI_1	-12.2	-20.4	-4.1	-
RI_2	-13.7	-21.7	-6.0	-
TS_{1A} ≡TS_A	+2.5	-8.3	+4.1	212i
TS_{2A}	+3.9	-5.1	+7.8	169i
TS_{1B} ≡TS_B	+11.2	-0.7	+12.0	905i
TS_{2B}	+18.1	+6.7	+18.9	1011i

Table B.10: Comparison of the energetics of the channels associated with the two different tetroxides. Energies are in units of kcal mol^{-1} and are calculated with [a]wB97XD/aug-cc-pVTZ, [b]ROHF-ROCCSD(T)-F12/VDZ-F12//wB97XD/aug-cc-pVTZ, or [c]the wB97XD/aug-cc-pVTZ thermochemistry with CCSD(T)-F12/VDZ-F12 single point energy correction.

	$<S^2>$ before annihilation	$<S^2>$ after annihilation	T1b
RI_2	0.0	0.0	0.016
TS_{2A}	0.6813	0.0250	0.021
TS_{2B}	0.0	0.0	0.022

Table B.11: Spin contamination and T1 diagnostic associated with the second tetroxide RI_2 and its TS. $<S^2>$ are from the UwB97XD/aug-cc-pVTZ calculation, and T1 is from the ROHF-ROCCSD(T)-F12/VDZ-F12//wB97XD/aug-cc-pVTZ calculation.

	ΔE^a	ΔE^b	$\Delta G298K^c$	TS (imaginary freq., cm^{-1})
RO	0.0	0.0	0.0	-
TS_{1D}	+3.3	+1.5	+0.4	199.4i
GLYC + CH_3(C=O)	+14.2	+10.5	-5.1	-
TS_{2D}	+9.0	+8.2	+6.9	237.6i
MGLY + CH_2OH	+3.9	+0.2	-14.2	-

Table B.12: Energetics of the different RO decomposition channels. Energies are in units of kcal mol^{-1} and are calculated with [a]wB97XD/aug-cc-pVTZ, [b]ROHF-ROCCSD(T)-F12/VDZ-F12//wB97XD/aug-cc-pVTZ, or [c]the wB97XD/aug-cc-pVTZ thermochemistry with CCSD(T)-F12/VDZ-F12 single point energy correction. For TS1D, the structure is optimized and frequencies and thermal contributions to ΔG298K calculated using tight optimization criteria and an ultrafine integration grid in order to remove a spurious near-zero imaginary frequency. For consistency, the DFT energy has been computed with a single-point energy evaluation using the normal integration grid.

	$<S^2>$ before annihilation	$<S^2>$ after annihilation	T1b
TS_{1D}	0.7617	0.7500	0.018
$CH_3(C{=}O)CHO$	0.0	0.0	0.014
CH_2OH	0.7534	0.7500	0.020
TS_{2D}	0.7650	0.7501	0.018
CH_2OHCHO	0.0	0.0	0.015
$CH_3(C{=}O)$	0.7542	0.7500	0.016

Table B.13: Spin contamination and T1 diagnostic associated with the second RI and its TS. $<S^2>$ are from the UwB97XD/aug-cc-pVTZ calculation, and T1 is from the ROHF-ROCCSD(T)-F12/VDZ-F12//wB97XD/aug-cc-pVTZ calculation.

Appendix C

MECHANISM OF THE HYDROXYL RADICAL OXIDATION OF METHACRYLOYL PEROXYNITRATE (MPAN) AND ITS PATHWAY TOWARD SECONDARY ORGANIC AEROSOL FORMATION IN THE ATMOSPHERE

Nguyen, T. B., K. H. Bates, J. D. Crounse, R. H. Schwantes, X. Zhang, H. G. Kjaergaard, J. D. Surratt, P. Lin, A. Laskin, J. H. Seinfeld, and P. O. Wennberg (2015). "Mechanism of the hydroxyl radical oxidation of methacryloyl peroxynitrate (MPAN) and its pathway toward secondary organic aerosol formation in the atmosphere". In: *Phys. Chem. Chem. Phys.* 17.27, pp. 17914–17926. DOI: 10.1039/C5CP02001H.

Abstract

Methacryloyl peroxynitrate (MPAN), the acyl peroxynitrate of methacrolein, has been suggested to be an important secondary organic aerosol (SOA) precursor from isoprene oxidation, but the mechanism by which MPAN produces SOA through reaction with the hydroxyl radical (OH) remains unclear. We systematically evaluate three proposed mechanisms in controlled chamber experiments and provide the first experimental support for the theoretically-predicted lactone formation pathway from the MPAN + OH reaction, producing hydroxymethyl-methyl-α-lactone (HMML). The decomposition of the MPAN-OH adduct yields HMML + NO_3 (~75%) and hydroxyacetone + CO + NO_3 (~25%), out-competing its reaction with atmospheric oxygen. The production of other proposed SOA precursors, *e.g.* methacrylic acid epoxide (MAE), from MPAN and methacrolein are negligible (<2%). Furthermore, we show that the β-alkenyl moiety of MPAN is critical for lactone formation. Alkyl radicals formed cold *via* H-abstraction by OH do not decompose to HMML, even if they are structurally identical to the MPAN-OH adduct. The SOA formation from HMML, from polyaddition of the lactone to organic compounds at the particle interface or in the condensed phase, is close to unity under dry conditions. However, the SOA yield is sensitive to particle liquid water and solvated ions. In hydrated inorganic particles, HMML reacts primarily with H_2O to produce the monomeric 2-methylglyceric acid (2MGA) or with aqueous sulfate and nitrate to produce the associated organosulfate and organonitrate, respectively. 2MGA, a tracer for isoprene SOA, is semivolatile and its accommodation in aerosol water decreases with

decreasing pH. Conditions that enhance the production of neutral 2MGA suppress SOA mass from the HMML channel. Considering the liquid water content and pH ranges of ambient particles, 2MGA will exist largely as a gaseous compound in some parts of the atmosphere.

C.1 Introduction

Anthropogenic emissions of nitrogen oxides (NO_x = NO + NO_2) strongly influence the oxidative pathways of gaseous hydrocarbons from both natural and anthropogenic origins. In particular, the oxidation of isoprene (C_5H_8), arguably the most important non-methane hydrocarbon emitted to the atmosphere, has a significant sensitivity to the NO_x conditions under which it is oxidized. This NO_x sensitivity translates to regional environmental impacts. For example, the high-NO_x oxidation of isoprene controls the production of tropospheric ozone in regions rich with biogenic hydrocarbons (Browne and Cohen, 2012; Mao *et al.*, 2013; Pusede and Cohen, 2012) by accelerating the cycling of NO_x and producing NO_x reservoir species (*e.g.* organic nitrates and peroxynitrates). Isoprene chemistry also affects global climate primarily through the formation of secondary organic aerosol (SOA) (Carlton and Turpin, 2013; Goldstein *et al.*, 2009; Rollins *et al.*, 2012; Xu *et al.*, 2015). However, lingering uncertainties regarding SOA formation in various anthropogenically impacted but biogenically influenced systems preclude accurate simulations of human-induced climate and air quality feedbacks in atmospheric chemical transport models.

A common approach to identify the source of SOA is through tracer compounds, *e.g.* 2-methylglyceric acid (2MGA) in isoprene-derived ambient aerosols (Edney *et al.*, 2005; Ion *et al.*, 2005; Kourtchev *et al.*, 2005). 2MGA and its oligomers are thought to be enhanced under high-NO_x conditions, and can be uniquely traced to the oxidation of methacrolein, a first-generation isoprene oxidation product (Chan *et al.*, 2010a; Claeys *et al.*, 2004; Nguyen *et al.*, 2011b; Surratt *et al.*, 2006). Chan *et al.* (2010a) showed that high-NO_2 chemistry (as opposed to "high-NO_x", where most of the NO_x can be represented by NO) favours the production of SOA *via* the acyl peroxynitrate channel (APN, Figure C.1). Essentially all of the SOA generated in the laboratory studies of the isoprene high-NO_x route was shown to be derived from methacrolein photochemistry, suggesting a major role of the APN from methacrolein, methacryloyl peroxynitrate (MPAN). The suggestion by Chan *et al.* (2010a) was confirmed by the synthesis of MPAN and the measurement of its SOA formation through photochemistry (tested under high-NO conditions) (Surratt

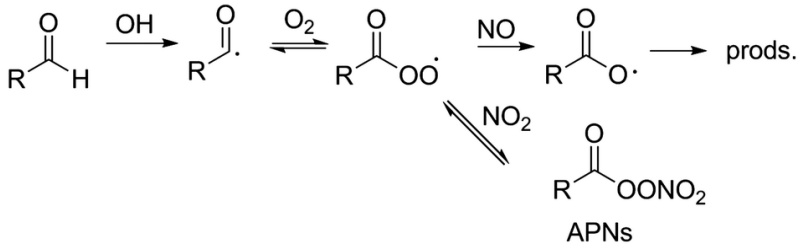

Figure C.1: The formation of acyl peroxynitrates (APNs) from the OH-initiated oxidation of aldehydes is favored under high NO_2/NO conditions. For methacrolein, the abstraction of the aldehydic H occurs roughly half of the time in the OH oxidation reaction at room temperature (Orlando *et al.*, 1999).

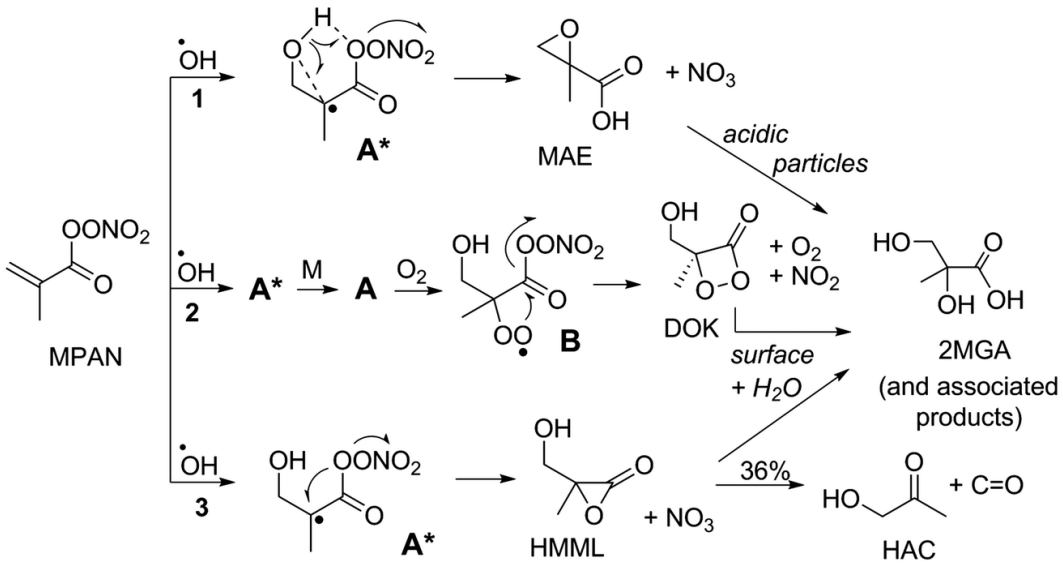

Figure C.2: The three proposed pathways to the formation of 2-methylglyceric acid (2MGA), a tracer for isoprene-derived ambient SOA. Mechanisms 1-3 and acronyms are discussed in the text.

et al., 2010).

Although the potential of MPAN + OH chemistry to produce SOA is relatively well established, the chemical mechanism leading to SOA from MPAN photooxidation has been subject of debate. It is also not clear whether the MPAN photooxidation is sensitive to NO_x, although past studies have all been performed in the presence of NO. Figure C.2 shows three possible pathways leading to SOA production that have been proposed by independent works (Chan *et al.*, 2010a; Kjaergaard *et al.*, 2012; Lin *et al.*, 2013b).

The initial step of the MPAN photooxidation is OH addition to the double bond,

primarily generating the energetically hot tertiary alkyl radical of MPAN (A*, Figure C.2). Chan *et al.* (2010a) in a series of photochemical chamber experiments, proposed that the main fate of A* is collisional stabilization (producing A) followed by reaction with molecular oxygen to form an alkylperoxyl radical (B), where the β-peroxyl moiety attacks at the carbonyl carbon to form a dioxoketone (DOK) and NO_2 as a coproduct (Figure C.2, mechanism 2). The suggestion by Chan *et al.* (2010a) was derived by performing methacrolein high-NO_2 photooxidation experiments at low O_2 content (~2%). The authors did not observe an increase in SOA yield and concluded that either O_2 addition is required for SOA formation or is non-competitive at those levels.

From a combined suite of density functional theory and coupled cluster calculations, Kjaergaard *et al.* (2012) proposed a rapid ring closure from an acylperoxyl oxygen of A* to form a 3-member lactone, hydroxymethyl-methyl-α-lactone (HMML), and NO_3 as a coproduct (Figure C.2, mechanism 3). Furthermore, the authors hypothesize that a significant fraction of the HMML product (36%) is generated with sufficient energy to further decompose to hydroxyacetone (HAC) and CO. Lin *et al.* (2013b) also identified the formation of HMML *via* density functional theory calculations; however, they hypothesized that HMML may be too unstable to form in the atmosphere.

Lin *et al.* (2013b) proposed a rapid H-migration induced ring closure at the hydroxyl oxygen, *via* a 6-member intermediate, to an epoxide product called methacrylic acid epoxide (MAE, Figure C.2, mechanism 1). This suggestion was formulated by comparing the composition of SOA (*e.g.* 2MGA and other products) from the photooxidation of methacrolein and the reactive uptake of laboratory-synthesized MAE onto highly-acidic particles, as well as through quantum chemistry calculations. The mechanism of the uptake was suggested to be nucleophilic ring opening of the epoxide in an analogous reaction to the isoprene epoxydiols (Paulot *et al.*, 2009b).

Notable differences between the proposed pathways include: (1) the fate of A* – whether cyclization/decomposition occurs more rapidly than thermalization and, thus, bimolecular reaction with O_2, (2) the stability of the products – MAE is the only product stable enough to be detected by current analytical instrumentation, and (3) the subsequent SOA formation mechanism under low humidity conditions – MAE requires highly-acidic seed aerosols to open the epoxide ring, while the ring opening of the more unstable compounds, DOK and HMML, would likely require

only collisions with a surface.

The uncertainties in the MPAN + OH mechanism persist due to ambiguities from previous work. For example, earlier studies of the MPAN + OH system did not measure SOA formation and were conducted with high mixing ratios of NO_x (blind to the formation of nitrogen products) (Grosjean *et al.*, 1993c; Orlando *et al.*, 2002). More recent laboratory studies of Chan *et al.* (2010a) and Lin *et al.* (2013b) were performed with methacrolein, such that products from MPAN oxidation and from the OH addition route of methacrolein (~55% probability) were formed simultaneously, complicating the analysis (Orlando *et al.*, 1999). The theoretical study of Kjaergaard *et al.* (2012) has yet to be experimentally validated. In this work, we elucidate the chemical mechanism governing the MPAN photooxidation (and the photooxidation of its chemical analogues) through a series of targeted chamber experiments using laboratory-synthesized MPAN under low humidity and low-NO conditions. We further study the chemical pathway with which the MPAN produces SOA under simulated ambient conditions with higher relative humidity and seed particle concentrations.

C.2 Experimental

C.2.1 Chamber Studies

The atmospheric chamber facility used for this work has been described in detail (Nguyen *et al.*, 2014b). A portion of the present work, namely, control experiments with α-pinene and exploratory experiments with methacrolein, were performed as part of the Focused isoprene eXperiment at the California Institute of Technology (FIXCIT) chamber campaign (Nguyen *et al.*, 2014b). Briefly, experiments were conducted in a large (24 m^3) Teflon chamber using purified dry air (<5% relative humidity (RH) at 298 K) such that initial NO mixing ratios were lower than 100 pptv (measured by G. S. Tyndall, D. D. Montzka, and A. J. Weinheimer at FIXCIT) and initial particle mass concentrations were much lower than 0.01 μg m^{-3} (measured by SMPS). For the experiments that were performed under humid conditions, water vapor was added to the chamber using a Nafion membrane humidifier (Perma Pure LLC) and recirculating ultrapure water (18 MΩ, Millipore Milli-Q). Particles were injected (mean particle diameter ~70 nm) by atomizing dilute solutions of ammonium sulfate (0.1 M) through a heated wet-wall denuder to deliquesce the particles prior to entering the chamber held at RH 40% or 85%. Corrections for the wall deposition of particles, using ammonium sulfate seed aerosols, were derived from control experiments performed at several water vapor mixing ratios in the

chamber. Volatile organics, excluding MPAN, were injected by microliter syringe into a clean glass bulb and quantitatively transferred with dry nitrogen gas into the chamber through a short section of tubing, optionally with gentle heating for the larger hydrocarbons such as α-pinene (<80 °C). The temperature in the chamber enclosure was adjusted to 15-25 °C for experiments as needed. MPAN experiments were performed at 15 °C to minimize the thermal decomposition of MPAN (thermal lifetime ~26 h at 15 °C, compared to ~5 h at 25 °C, for an NO_2/NO ratio of 10 that is representative of areas outside of urban centers) (Roberts and Bertman, 1992).

Table C.1 lists the laboratory conditions for the main experiments in this work, *e.g.* the gas-phase oxidation of MPAN (synthesized standard), methacrolein (MACR, Aldrich, 95%), isobutyraldehyde (ISOBUT, Aldrich, >99%), and 2-methylbut-3-ene-1-ol (231MBO, Aldrich, 98%). Photochemistry under low-NO conditions (HO_2 > NO) was initiated by the near-UV (300-400 nm, λ_{max} ~ 350 nm) photolysis of gas-phase hydrogen peroxide that has been evaporated into the chamber (Aldrich, 50 wt% in water):

$H_2O_2 + h\nu \rightarrow OH + OH$

$OH + H_2O_2 \rightarrow HO_2 + H_2O$

Photochemistry under high NO_2 (and typically lower in NO) conditions were initiated by the photolysis of gas-phase methyl nitrite (synthesized standard, stored in liquid N_2) in the presence of various mixing ratios of additional NO_2 (standard mixture in N_2):

$CH_3ONO + h\nu + O_2 \rightarrow HO_2 + NO + HCHO$

$HO_2 + NO \rightarrow OH + NO_2$

Methyl nitrite was introduced into the chamber by filling a clean, evacuated, 500 mL glass bulb with the desired pressure of the standard, backfilling with N_2, and transferring the contents of the bulb into the chamber with a stream of N_2. In high-NO_2 experiments, the added NO_2 and that formed from CH_3ONO photochemistry conspire to maintain the NO_2/NO ratio >10 throughout the experiment. Importantly, the near-UV broadband radiation used in this work does not efficiently photolyze NO_3 *via* mechanisms that yield a net destruction of NO_3 (J_{NO_2} ~5.5×10^{-4} s^{-1}, $J_{NO_3 \rightarrow NO+O_2}$ ~ 4.5×10^{-6} s^{-1}) (Sander *et al.*, 2011).

C.2.2 Analytical Measurements

MACR and isobutyraldehyde were quantified with a commercial gas chromatograph with a flame-ionization detector (GC-FID, HP 6890N) and calibrated by

expt.	HC precursor		oxidant		$[OH]_{ss}$	rxn	temp.	RH	$[NO]_0$	$[NO_2]_0$	additional
#	name	$[HC]_0$ (ppb)	source	$[Ox]_0$ (ppb)	(cm^{-3})	time (h)	(°C)	(%)	(ppb)	(ppb)	injections
1	MPAN	30	H_2O_2 + hν	2000	1.5×10^6	2.5	15	<5	<0.1	1	α-Pin (50 ppb)
2	MPAN	13	H_2O_2 + hν	2000	1.5×10^6	5	15	<5	<0.1	1	-
3	MPAN	23	H_2O_2 + hν	2000	1.5×10^6	4.5	15	<5	<0.1	1	-
4	MPAN	30	H_2O_2 + hν	2000	1.5×10^6	4.5	15	<5	<0.1	1	α-Pin (30 ppb), MAE (15 ppb)
5	MPAN	17	H_2O_2 + hν	2000	1.5×10^6	3.2	15	<5	<0.1	1	α-Pin (30 ppb), MAE (15 ppb)
6	MACR	100	H_2O_2 + hν	2000	1.5×10^6	5	15	<5	10	230	-
7	MACR	50	MN + hν	140	2×10^7	2.5	25	<5	<0.1	50	-
8	MACR	80	MN + hν	130	1×10^7	2.5	15	<5	<0.1	110	-
9	MACR	100	MN + hν	200	2×10^7	2.5	25	<5	10	100	-
10	ISOBUT	80	MN + hν	220	2×10^7	5.5	25	<5	10	50	-
11	231MBO	200	O_3, then MN + hν	~600 [O_3], 200 [MN]	2×10^7	24	25	<5	10	100	-
12	MACR	200	MN + hν	200	2×10^7	3.5	25	40	10	100	AS seeds
13	MACR	100	MN + hν	200	2×10^7	2.5	25	85	10	100	AS seeds

Table C.1: Experimental conditions for the laboratory photooxidation of hydrocarbons (HC) used in this work: MPAN, methacrolein (MACR), isobutyraldehyde (ISOBUT) and 2-methylbut-3-ene-1-ol (231MBO). The light intensity was 100% (J_{NO_2} ~7×10^{-3} s^{-1}) for hydrogen peroxide (HP) experiments and 10-20% for methyl nitrite (MN) experiments. Steady state OH is estimated from hydrocarbon decay (GC) data. α-pinene (α-Pin) and methacrylic acid epoxide (MAE) were added in select experiments to capture NO_3 and observe SOA formation, respectively. Control experiments of HP + hν, tridecane + HP + hν, and wall losses (described in Experimental section) are not included in table. Experiments were performed at various temperature and relative humidity (RH). Select experiments were performed with ~80 μg m^{-3} of ammonium sulfate (AS) seed particles.

volumetric injections of commercial standards. Particle size and number were measured by a scanning mobility particle sizer (SMPS), *i.e.* a custom-built differential mobility analyzer coupled to a commercial condensation particle counter (TSI Inc.). Aerosol speciation was measured using a high resolution time-of-flight aerosol mass spectrometer (AMS, Aerodyne) (Drewnick *et al.*, 2005). Bulk aerosol species (organic, sulfate, ammonium, nitrate) were calculated using AMS data analysis modules (Pika 1.14D). The instrument's ionization efficiency was calibrated with 350 nm ammonium nitrate particles.

Volatile acids and select polar organic compounds were quantified with a custom-built triple-quadrupole chemical ionization mass spectrometer (CIMS, Agilent/ Caltech) (St. Clair *et al.*, 2010). The CIMS operated in three modes: scanning negative ion mode using CF_3O^- as the reagent (*m/z* 50-250), scanning positive ion mode using primarily H_3O^+ as the reagent ion (*m/z* 50-200), and tandem mass negative ion mode (monitoring select precursor-product ion pairs). The ion chemistry (*e.g.* detection as $[M+F]^-$ and $[M+CF_3O]^-$ ions) and tandem mass determinations of the CF_3O^- CIMS have been described previously (Crounse *et al.*, 2006; St. Clair *et al.*, 2010).

Sensitivities of the triple-quadrupole CF_3O^- CIMS used in this work were determined based on a calibrated time-of-flight CF_3O^- CIMS instrument during the FIX-CIT campaign (Nguyen *et al.*, 2014b). The absolute calibration for commercially-available and synthesized standards in the time-of-flight CIMS, using gravimetric, optical, and thermal-dissociation + laser-induced fluorescence methods are described elsewhere (Nguyen *et al.*, 2015a). Uncertainty is estimated to be ± 30%. Synthesized standards of organic nitrates were found to have water-dependent sensitivities similar to HNO_3 (Lee *et al.*, 2014); thus the CIMS sensitivity of the pinene nitrooxyhydroperoxide (PNP), for which there are no authentic standards, is assumed to be similar to HNO_3 (estimated uncertainty ± 50%). For other compounds discussed in this work, theoretical calculations were used to estimate the sensitivity (estimated uncertainty ± 50%) (Garden *et al.*, 2009; Su and Chesnavich, 1982).

The observed ion of methacrylic acid epoxide (MAE, synthesized standard, detected as $[MAE{\cdot}F]^-$) was isobaric with a water cluster $[(H_2O)_2{\cdot}CF_3O]^-$ (*m/z* 121) in the single-ion analysis (Lin *et al.*, 2013b). Thus, MAE quantification is performed with collision-induced dissociation into its main precursor → product ion (*m/z* 121 → *m/z* 101). When experiments are performed at higher relative humidity, the water signal (*m/z* 121 → *m/z* 103) may have an extensive tail that would lead to an over-

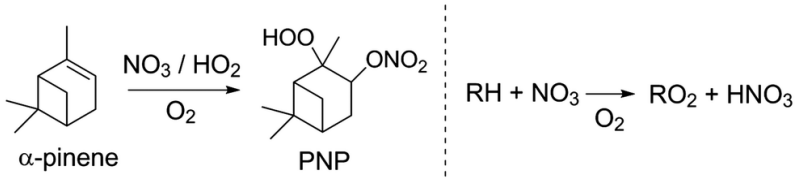

Figure C.3: The experimental scavenging of NO_3 into stable products detectable by CIMS: PNP (one of several isomers shown) and HNO_3.

estimation of MAE. The tandem signal that we measure must then be considered as an upper limit to the MAE concentration. The ion chemistry in the positive ion mode is similar to proton transfer reaction mass spectrometry (quantification mainly with $[M+H]^+$ ions in this work) (Lindinger and Jordan, 1998). Calibrations for select species in the positive ion mode (*e.g.* α-pinene and 231MBO) were performed immediately prior to experiments using commercial standards under dry conditions.

CIMS was also used to indirectly monitor nitrogen oxide chemistry (Figure C.3). For example, the reaction of NO_2 with HO_2 generates peroxynitric acid (HO_2NO_2, PNA), which was used as a sensitive tracer for NO_2. α-pinene was used in a subset of experiments to capture NO_3 as the pinene nitrooxy hydroperoxide (PNP), which is detectable by CIMS, under the condition where the HO_2/NO ratio is high (Figure C.3, left). α-pinene was chosen as an NO_3 scavenger because its reaction rate coefficient with OH is the lowest for a monoterpene that reacts rapidly with NO_3 (*i.e.* k_{NO_3}/k_{OH} ~0.12) (Atkinson *et al.*, 2006), and its reaction rate with NO_3 is at least four orders of magnitude larger than the MPAN reaction with NO_3 (Canosa-Mas *et al.*, 1999b). There are varying reports of SOA yield from the α-pinene + NO_3 reaction (0-16%), possibly decreasing with higher RH (Fry *et al.*, 2014; Hallquist *et al.*, 1999; Spittler *et al.*, 2006). Thus, experiments involving α-pinene were not included in the yield calculations from MPAN due to the possibility of interference from the α-pinene + OH or + NO_3 reaction. HNO_3, produced from H-abstraction chemistry of hydrocarbons (Figure C.3, right) when NO_2 is low (and thus NO_2 + OH is not a significant source of HNO_3), was also used as tracer for NO_3-initiated chemistry.

MPAN, peroxyacetyl nitrate (PAN), and NO_2 were measured with a commercial NO_2 and acyl peroxynitrate (NO_2/APN) analyzer (Fitz Aerometric Technologies). In the NO_2/APN instrument, NO_2, PAN, and MPAN were chromatographically separated, in that order, with a room-temperature deactivated DB-5 column, and detected by monitoring chemiluminescence from their reactions with luminol (Figure

C.11 in the Supporting Information). NO_2 was calibrated with a diluted standard mixture (488 ppmv NO_2 in N_2, Scott Specialty Gases). The sensitivity of PAN in the instrument was inferred from its relationship to NO_2 (Gaffney *et al.*, 1998). MPAN, in isolation, was calibrated using a commercial NO_x analyzer (Teledyne model T200) due to its quantitative decomposition to NO_2 when exposed to the heated (310 °C) molybdenum catalyst. A similar calibration was obtained by thermally decomposing MPAN to NO_2 in a heated stainless steel tube before the NO_2/APN analyzer. Sampling MPAN from the chamber (before adding other compounds) through room-temperature Teflon tubing leads to a small decomposition yield of NO_2 from MPAN (~4%, Figure C.11 in the Supporting Information). The NO_2 signal was corrected in the NO_2/APN data as a fraction of the MPAN integrated peak.

C.2.3 MPAN

The synthesis of MPAN from the peroxidation of methacrylic anhydride (Aldrich, 94%) and nitration of the methacrylic peracid (MPAA) was performed as suggested by Bertman and Roberts (1991) with the following revisions: we used 50 wt% H_2O_2 (Aldrich) instead of 30 wt% H_2O_2 and methanesulfonic acid (Aldrich, 99.5%) instead of concentrated H_2SO_4. The crude MPAN mixture in water-tridecane was stored frozen and separated in small fractions with tridecane on a silica gel column deactivated by successive solvent washes of methanol, acetone, ethyl acetate, hexanes, and tridecane. Signs of known impurities were checked by CIMS (*i.e.* methacrylic acid and MPAA) and the NO_2/APN instrument (PAN). MPAN is thought to be explosive when pure (Stephens, 1969) and no attempt was made to remove the solvent. The separated MPAN fraction in tridecane was stored at 0 °C or below and used promptly.

MPAN was injected by gently bubbling air through the tridecane-solvated mixture (submerged in an ice bath) placed inside the 15 °C chamber enclosure over the course of roughly 30 min to achieve 15-30 ppbv in the chamber. Tridecane was chosen as the storage solvent due to its low volatility, and thus, lower extent of co-evaporation into the chamber. To correct for any SOA originating from photooxidation of the solvent, we performed a control photooxidation experiment with tridecane + OH similarly to Expt. 2-3. The CIMS signals of tridecane (positive mode) and tridecane hydroperoxide (negative mode) were used to normalize the 10-50% correction of tridecane-derived SOA in MPAN experiments.

C.2.4 2MGA

2-Methylglyceric acid (2MGA) was synthesized and purified according to An *et al.* (1992) *via* oxidation of the C=C bond of methacrylic acid (Aldrich, 99%) using H_2WO_4 (Aldrich, 99%) and 50 wt% H_2O_2 (Aldrich). Proton NMR (in DMSO-d_6) was used to verify the isolated 2MGA with residual CH_3CN (93% 2MGA, Figure C.12a in the Supporting Information). The semi-pure 2MGA (viscous liquid) was then crystallized upon cooling, filtered with CH_3CN, and washed with Et_2O to afford the pure (99%) 2MGA crystalline solid. The CIMS observes 2MGA at the fluoride transfer ion ($C_4H_7O_4 \cdot HF^-$) and collision-induced dissociation leads primarily to the deprotonated 2MGA ion ($C_4H_7O_4^-$, Figure C.12b in the Supporting Information). The gas-phase signal of a 2MGA aqueous solution was measured at various solution pH values in a custom 10 mL glass vial fitted with 3 mm O.D. PTFE sampling tubes. A 0.075 M solution of 2MGA had similar pH to glyceric acid (pKa 3.5 (Serjeant and Dempsey, 1979)) at the same concentration. The 2MGA solution was further acidified incrementally by adding droplets of 1-10 wt% H_2SO_4 and the pH of the solution was measured with a digital pH meter (VWR, Model 8015) that had been calibrated with commercial buffer solutions. The headspace of the vial (at 24 °C) was sampled with CIMS at a flow rate of 147 std cm^3 s^{-1} for each solution pH.

C.2.5 High-Resolution Mass Spectrometry

At the end of photooxidation experiments, SOA samples were collected on hydrophilic PTFE-based membrane filters (Millipore, Omnipore, 0.2 μm diameter pores) by pulling chamber air through an activated charcoal denuder, vacuum-sealed, and frozen for further analysis. The SOA material on the filters was gently extracted by wetting with 100-300 μL of acetonitrile and water mixture (2:5 v/v, HPLC grades) for roughly 5 min. The filters were not exposed to heat or ultra-sonication conditions (which may produce free radicals such as OH through cavitation (Makino *et al.*, 1982)) in order to preserve organic species. The extracts were analyzed with high-performance liquid chromatography (HPLC) coupled to electrospray ionization mass spectrometry (ESI-MS). The separation was performed with a polar embedded C_{18} column with TMS endcapping (Phenomenex, Synergi^{TM} 4 μm Fusion-RP 80 Å, 150 × 2.0 mm) and an eluent mixture of acetonitrile and water (HPLC grades, Aldrich) with 0.5% of formic acid. Generally, the organic constituents eluted together (*e.g.* the entire oligomer family of 2-methylglyceric acid in the MPAN + OH samples) but are satisfactorily separated from the inorganics. Additionally, an ammonium sulfate solution was analyzed with HPLC-ESIMS as an inorganic blank.

HSO_4^-, $HSO_4(H_2SO_4)^-$, and $HSO_4(H_2SO_4)_2^-$ were the dominant ions observed from the ammonium sulfate solution. These ion signals were subtracted from the SOA mass spectra to remove the remaining inorganic contribution. The mass analyzer was a high-resolution (100,000 m/Δm at *m/z* 300) linear-ion-trap (LTQ) Orbitrap^{TM} mass spectrometer (Thermo Corp.) operated in the negative ion mode with a mass range of 80-2000 *m/z*. The LTQ-Orbitrap was calibrated with commercial standard (LTQ ESI Negative Ion Calibration Solution, Thermo Scientific, Inc.) prior to mass spectral analyzes (mass accuracy up to 0.5 ppm at *m/z* 500).

C.3 Results and Discussion

C.3.1 Photooxidation of MPAN

Figure C.4a shows the reaction progress for a representative low-NO MPAN experiment under dry conditions. Reagents were equilibrated in the chamber prior to the initiation of photochemistry (yellow shaded region). Figure C.4b shows a representative low-NO MPAN experiment where α-pinene was added at the beginning of the reaction to scavenge NO_3, and MAE was added at the end (after the reaction mixture has stabilized with lights off) to observe its effects on SOA formation.

A low yield of NO_2 (7 ± 3%) is observed by the NO_2/APN instrument and confirmed by the negligible CIMS PNA signal. This NO_2 formation is likely due to thermal decomposition of MPAN (τ_{288K} ~35 h at the NO_x conditions in Expt. 2-3 Nouaime *et al.*, 1998; Roberts and Bertman, 1992) because a 10 ± 5% yield of PAN was also observed. The MPAN decomposition produces NO_2 and acylperoxyl radical, which is subsequently converted to the acyloxyl radical from reaction with either NO or HO_2 (Orlando *et al.*, 1999). The acyloxyl radical decarboxylates to the vinyl radical that ultimately forms PAN and other products through subsequent reactions (Chuong and Stevens, 2004). The thermal decomposition is calculated to be 10-25% of the total MPAN loss, qualitatively consistent with observed yields. The uncertainty is due to difficulty in determining the NO_2/NO ratio when NO_x is low. Neither PAN nor the NO_2 yield was enhanced in the presence of α-pinene (Figure C.4b), suggesting they both originate from MPAN. The lower bound (10%) of the MPAN decomposition is used to correct gaseous molar yields.

In contrast to NO_2, the experiments performed with α-pinene conclusively demonstrate high yields of an NO_3 coproduct, as suggested by mechanisms 1 and 3 (Figure C.2). Figure C.5 shows that upon photooxidation of MPAN in the presence of α-pinene, PNP is formed in ~(35 ± 17)% yields with respect to α-pinene loss and

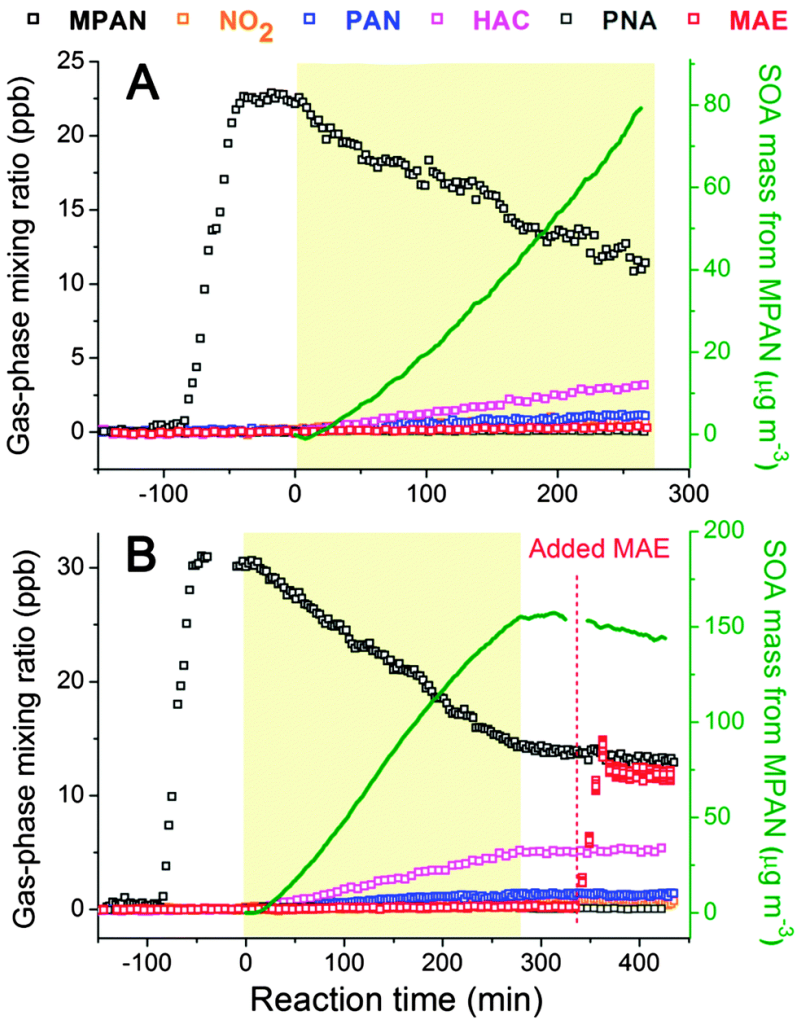

Figure C.4: Representative MPAN photooxidation experiments (A) performed with MPAN and H_2O_2 (Expt. 3, base experiment) and (B) the base experiment with the initial addition of α-pinene and subsequent injection of MAE standard (Expt. 4). The yellow shaded areas designate the time period when photochemistry occurs in each experiment. The right mass axis corresponds only to the SOA trace (green line).

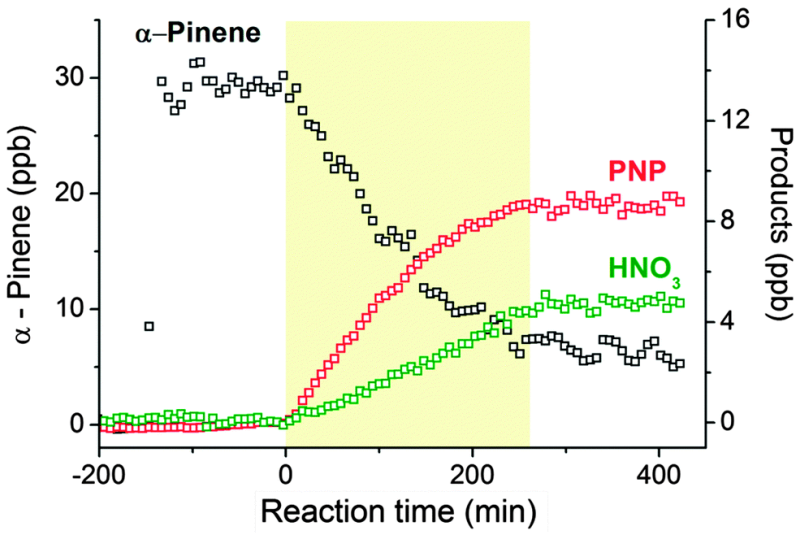

Figure C.5: Representative results from NO_3 scavenging experiment using α-pinene (Expt. 4). The yellow shaded area designates the time period when photochemistry occurs. Note the double-vertical scales.

~(70 ± 35)% yield with respect MPAN loss. Experiments without α-pinene did not produce interfering species at the mass used for quantification of PNP. Furthermore, experiments performed during the FIXCIT campaign (Expt. 10, 13 in Table 2 of that work (Nguyen *et al.*, 2014b)) with 30 ppbv of α-pinene demonstrate that PNP is not formed under low-NO photooxidation conditions, similar to those used to oxidize MPAN here (Figure C.13a in the Supporting Information). However, PNP is an abundant product when NO_3 is used as an oxidant while HO_2 is present in the chamber (Figure C.13b in the Supporting Information). Using known rate coefficients of α-pinene with NO_3 and OH (Atkinson *et al.*, 2006), we estimate the steady state NO_3 concentration in Expt. 4 (Table C.1) to be 6.5×10^6 mol cm^{-3}. The steady state OH concentration (~1.5×10^6 mol cm^{-3}), which is reproducible within 25% under identical oxidant precursor and light conditions, is derived from separate low-NO photolysis experiments using isoprene as a reference hydrocarbon (Nguyen *et al.*, 2014b). Thus, we estimate that the loss of α-pinene is ~40% by NO_3 and ~60% by OH. This is in relatively good agreement with the PNP yield from α-pinene assuming most of the pinene nitrooxy alkylperoxyl radical reacts with HO_2 to form PNP.

HNO_3 formation in MPAN experiments (Figure C.5) occurs likely from the NO_3-initiated H-abstraction of alkanes (*e.g.* tridecane from the introduction of MPAN) or other saturated compounds, as the reaction of NO_3 with α-pinene and MPAN

will result largely in addition rather than abstraction. Using the steady-state radical concentrations derived above and reaction rate coefficients from the literature (Canosa-Mas *et al.*, 1999b), we estimate <0.1% of the MPAN loss was due to reaction with NO_3 radicals. HNO_3 is observed in all MPAN photooxidation experiments due to the ubiquitous presence of the tridecane solvent, and no enhancement is observed in the presence of α-pinene. HNO_3 provides evidence of another 30 ± 9% NO_3 yield from MPAN, which taken together with PNP, suggests that MPAN efficiently yields NO_3 and a coproduct upon reaction with OH. The high NO_3 yield confirms one shared aspect of mechanisms 1 and 3 (Figure C.2) and, in combination with the low NO_2 observations, allows us to rule out mechanism 2 as a significant contributor to the MPAN photooxidation chemistry.

We observe a large mass yield of SOA from the dry MPAN + OH experiments (Figure C.4, green traces), suggesting that the MPAN photooxidation chemistry is efficient at forming SOA in the absence of NO_x. Approximately (125-145)% SOA by mass (with respect to MPAN mass reacted) is formed, and assuming an average molecular weight of 340 g mol^{-1} (the intensity-weighted average of the MPAN + OH high-resolution mass spectrometry data, assuming similar ESIMS sensitivities for observed analytes), approximately ~(60 +15/-5)% by mole. The uncertainty is derived from corrections (*e.g.* for tridecane-derived SOA, particle wall loss, and MPAN thermal decomposition) and analysis of the average molecular weight of the SOA. The observation that SOA formation from MPAN + OH is not NO-dependent is consistent with the suggestion in mechanisms 1 and 3 (Figure C.2) that the traditional RO_2 chemistry of the thermalized radical A does not come into play. However, we note the data do not eliminate the possibility that an RO_2 formed after O_2 addition also rapidly decomposes to the same products.

Importantly, the SOA formation from MPAN + OH is prompt and occurs without the injection of inorganic seed aerosols. It is possible the SOA forms *via* nucleation (*e.g.* from the chemistry of larger VOC like tridecane) or growth in the presence of pre-existing seed particles that are under the size detection limit of the SMPS and AMS. Even if SOA growth occurs on dry, pre-existing, nanoparticles, most of the SOA formation occurs on primarily-organic particles after the first few condensation cycles. This observation favors the proposed mechanism 3 over mechanism 1 due to the need for MAE to undergo reactive uptake partitioning, which is a slow process for this compound even in the presence of hydrated, acidic sulfate particles that would accelerate ring-opening of the epoxide ($\gamma \sim 5 \times 10^{-4}$ when seed aerosols are

50% H_2SO_4 by mass) (Riedel *et al.*, 2015).

Of the putative SOA precursors, MAE is the only compound that has been detected by mass spectrometry due to its chemical stability. Throughout all experiments, we observed small to negligible yields of MAE in the gas phase (2 ± 1%, upper limit, see Experimental), whether the precursor was MPAN or MACR. FIXCIT experiments of MACR under low-NO conditions also did not observe any appreciable MAE production (Nguyen *et al.*, 2014b). Lin *et al.* (2013b) similarly observed a small gas-phase yield of MAE (~1% from MACR, Figure S1 of that work), but suggested that MAE is so rapidly converted to SOA mass that most of it is observed in the condensed phase. Under the assumption that (50-80)% of MAE is observed as SOA, they estimated MAE yields are 18-32% from MPAN. We demonstrate that MAE is not well-converted to SOA and, in particular, not *via* the mechanism that forms the dominantly-organic particles in the MPAN experiments. It instead appears that MAE is a remarkably stable and volatile gas-phase species, with similar volatility to MPAN, which by itself does not form SOA through equilibrium partitioning. Notably, when ~(12 ± 50)% ppbv of MAE is injected into the chamber following the reaction period (Figure C.4b), no change to particle size or mass concentration can be observed.

To further evaluate the inertness of MAE, we injected a few hundred ppbv of MAE into a clean 1000 L Teflon bag alongside 500 ppbv of HNO_3 (~300 ppbv of which remained in the gas phase, and the rest, presumably, coated the chamber walls). No observable wall loss of MAE occurred over the course of 2.5 h (Figure C.14 in the Supporting Information); this is identical to its behavior in the absence of acid. It appears that the small quantity of MAE formed from MACR oxidation is not an eager participant in the surface- and/or water-induced partitioning that often leads to SOA formation. The inertness we observe provides insight into why 300 ppbv (~1250 μg m^{-3}) of MAE produced only ~10 μg m^{-3} of SOA through reactive uptake in the Lin *et al.* (2013b) work, even when using seed particles that are exceptionally acidic (~50 wt% H_2SO_4 at RH < 10%). The evidence suggests that the low (<2%) gas-phase mixing ratios observed in this work and by Lin *et al.* (2013b) (from MACR) indeed represent a measure of the entire yield of MAE. Thus, it appears that the disagreement between this work and that of Lin *et al.* (2013b) lies in the assumption of MAE's ability to form SOA, and not in the observations of MAE itself. As MAE formation is negligible both from MPAN and MACR, mechanism 1 is ruled out as a significant contributor to MPAN-derived SOA.

A key element to understanding the MPAN + OH reaction lies in the measurement of hydroxyacetone (HAC). The HAC yield determined here (~25 ± 7%) is consistent with the upper limit determined by Orlando *et al.* (2002) (<40%), but more than a factor of two lower than the yield determined by Grosjean *et al.* (1993c) (~60%). Both of the previous works were performed under high-NO conditions using ethyl nitrite as an OH precursor. The source of discrepancy with regards to the Grosjean work is not clear; however, a similar trend in data agreement can be observed in the determination of rate coefficients of OH + MPAN. We measured k_{288K} ~3 (±1) × 10^{-11} cm^3 mol^{-1} s^{-1}, which compares well with Orlando *et al.* (2002) (k_{277K} ~3.2 (±0.8) × 10^{-11} cm^3 mol^{-1} s^{-1}), but is an order of magnitude higher than the value reported by Grosjean *et al.* (1993c) (k_{298K} ~3.6 (±0.4) × 10^{-12} cm^3 mol^{-1} s^{-1}). The coefficient by Orlando *et al.* (2002) is preferred by IUPAC due to its consistency with the OH reaction with structurally similar APNs, and our data is in agreement with this recommendation (Atkinson *et al.*, 2006; Saunders *et al.*, 1994). Thus, we only consider the comparison between this work and that of Orlando *et al.* (2002).

If the production of HAC occurs *via* the lactone-production pathway (as the data seem to indicate) then the yield would be independent of NO mixing ratio. The agreement in the HAC yield obtained under low-NO conditions (this work) and high-NO conditions (Orlando *et al.*, 2002) suggests that HAC is not formed from the alkylperoxyl radical B in the MPAN + OH reaction. Finally, the experimentally-determined HAC yield (and, consequently the remainder HMML yield) is comparable to those theoretically predicted by Kjaergaard *et al.* (2012) (~36% of HAC). In contrast, Lin *et al.* (2013b) suggest a low HAC yield (~3%). The current work cannot differentiate the 2% of thermalized radical A that is predicted to form (Kjaergaard *et al.*, 2012), ultimately generating the alkoxyl radical under high NO_x conditions, because the products would likely include HAC and NO_3. Together, the experimental data support the HMML mechanism from the MPAN + OH reaction. We estimate approximately 25% of the reaction yields HAC + CO + NO_3 and 75% of the reaction yields HMML + NO_3, with 75-100% of HMML leading to the formation of SOA under dry conditions.

To investigate whether there is a route to HMML from thermalized alkyl radicals, we performed experiments with saturated APNs that are analogous to MPAN. The photooxidation of the saturated analogues occurs *via* H-abstraction instead of OH-addition, which generates lower-energy alkyl radicals. For example, we synthesized A in the chamber *via* the OH-initiated photochemistry of 3-hydroxy-

2-methylpropanoyl peroxynitrate (HMPPN). HMPPN is a major product of the high-NO_2 OH-initiated oxidation of hydroxymethyl propanal (HMP), which was produced by dark ozonolysis of 231MBO (Section C.5 and Figures C.15 and C.16a in the Supporting Information). Expected gas-phase products arising from RO_2 and RO radicals were observed from the chemistry of A but not A* (Figure C.17 in the Supporting Information), *e.g.* the hydroxynitrate, the hydroxyhydroperoxide, hydroxyacetone, and 2-oxopropanoyl peroxynitrate (Orlando *et al.*, 2002). Qualitatively compared to MACR, the SOA formation from the photochemistry of HMP (Expt. 11, Figure C.16b in the Supporting Information) and isobutyraldehyde (Expt. 10, not shown) is negligible ($\ll$1%). Chan *et al.* (2010a) first suggested the importance of the β-unsaturation in MPAN, following the observation that α,β-unsaturated aldehydes produced the largest SOA yields. Our results are consistent with their explanation.

Additionally, we use the potential energy surfaces from the Kjaergaard *et al.* (2012) work to calculate the relative fates of A. Compared to a typical effective rate for the reaction of alkyl radicals with O_2 at 1 atm air (O_2 = 21%) and 298 K (k_{eff} $\sim 1 \times 10^7$ s^{-1}), the thermalized unimolecular decomposition of A to HMML is much slower ($k_{A \rightarrow HMML} < 10^3$ s^{-1}). This translates to a calculated 0% yield of HMML in the HMPPN + OH reaction (100% reacts with O_2). In comparison, Kjaergaard *et al.* (2012) estimated the decomposition of A* to HMML is fast under the conditions they studied ($k_{A^* \rightarrow HMML}$ $\sim 4 \times 10^9$ s^{-1}), translating to a 61-74% HMML yield from MPAN (2% is stabilized to A). The theoretical-derived kinetic results are consistent with observations for these C_4 APN-derived alkyl radicals.

Figure C.6 summarizes the chemical mechanisms in the OH-initiated oxidation of MPAN and HMPPN to reflect the current scientific knowledge. It is also possible that larger APNs behave differently than the C_4 APNs discussed here. For example, it is not clear if APNs from the monoterpene aldehydes such as pinonaldehyde (saturated) and limonaldehyde (unsaturated, in the gamma position) are able to produce SOA or undergo a different photochemical fate. These larger APN systems are intriguing because they can be produced in the laboratory but have not been observed in the ambient atmosphere (Nguyen *et al.*, 2014b).

C.3.2 Atmospheric Fate of HMML

To study the SOA formation from HMML under conditions more relevant to the atmosphere, we performed MACR high-NO_2 photooxidation experiments with

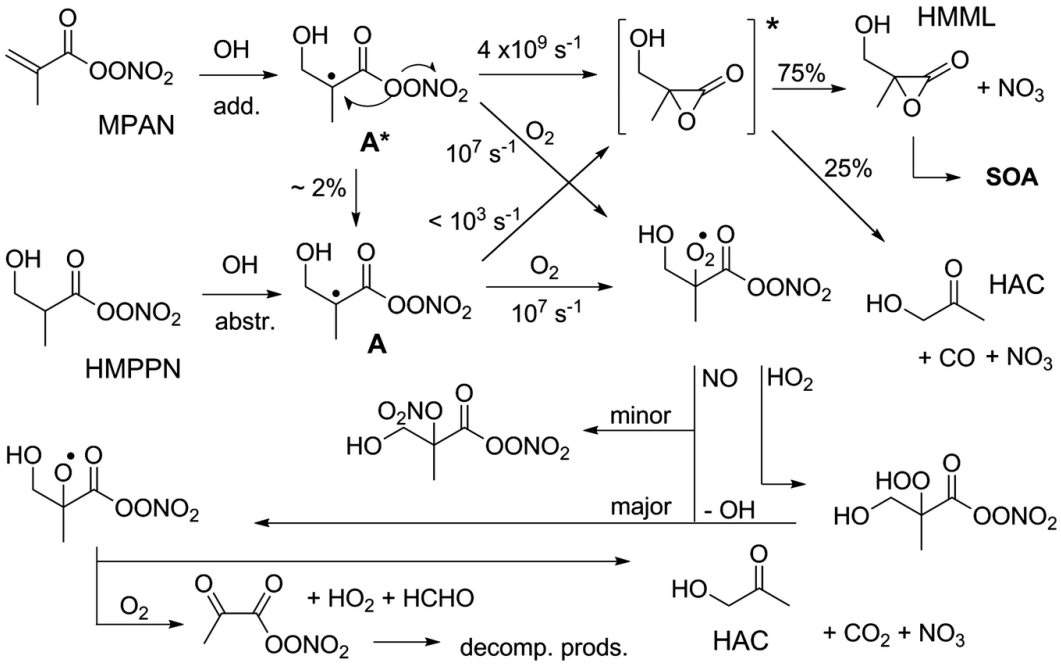

Figure C.6: The OH-initiated oxidation mechanism of MPAN and HMPPN derived from the low-RH experiments conducted in this work. The HMML formation from MPAN arises from a chemically-activated mechanism while the product formation from HMPPN arises from a thermalized alkyl radical + O_2 reaction.

hydrated ammonium sulfate (AS) seed particles at 40% and 85% RH (efflorescence and deliquescence RH of AS are ~30% and ~80%, respectively) (Biskos *et al.*, 2006). Figure C.7 shows that the SOA production is lower and gas-phase 2MGA yields are higher when the reaction occurs in deliquesced AS particles (Expt. 13, liquid water ~75 vol%) compared to primarily organic particles (under dry conditions, Expt. 9). The small MAE signal did not increase under humid conditions, suggesting that the formation of this compound is likely not important in the ambient environment. The production of HAC is observed to slightly increase toward the end of the experiment. However, this change is within the uncertainty of the HAC determination (±30%). If the difference in HAC signal between dry and humid is real, the underlying mechanism is unclear. The systematic uncertainty in calculating mixing ratio for 2MGA is approximately ±50%. However, if all of the ~12-13 ppb of 2MGA in the gas phase is converted to particle mass, the volatilization of 2MGA may explain almost 100% of the ~60 μg m^{-3} SOA mass discrepancy between the two experiments. 2MGA is typically used as a tracer for isoprene SOA; however, it appears that its accommodation in the condensed phase is low at typical aerosol-phase pH. Recent observations in the Southeast U.S. and Amazon forests support the

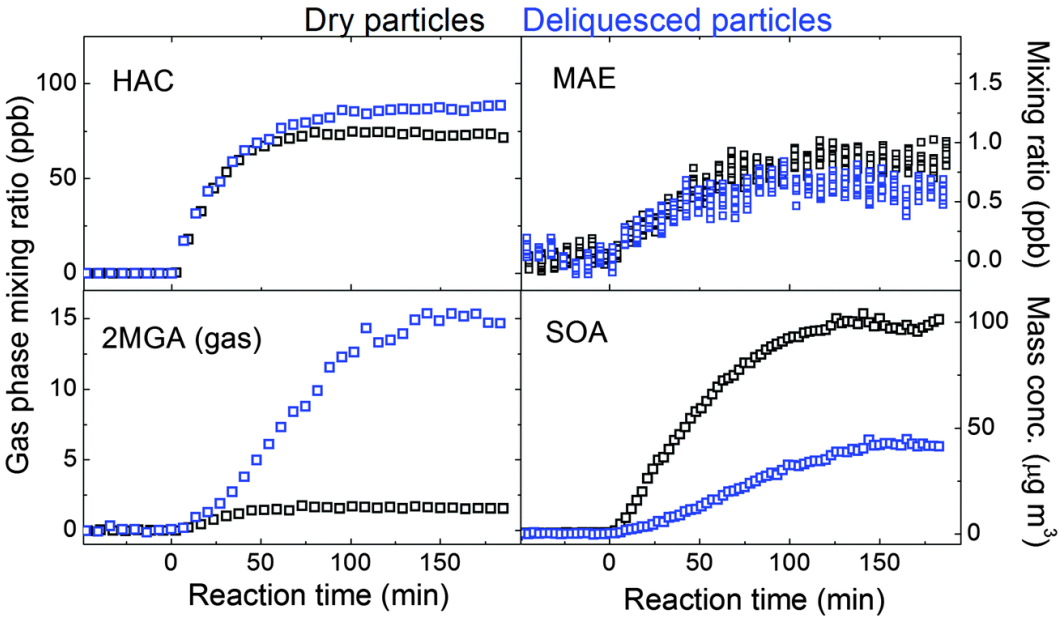

Figure C.7: The formation of gas-phase species and secondary organic aerosols under dry conditions (black markers) and under humid conditions (85% RH) with deliquesced ammonium sulfate seeds (blue markers).

idea that 2MGA may exist primarily in the gas phase in humid biogenic environments (Isaacman-VanWertz, 2014).

Figure C.8a shows the CIMS gas-phase measurement of 2MGA (from a 0.075 M solution of the synthesized standard) as the solution is increasingly acidified. 2MGA behaves similarly to a semivolatile compound such as isoprene epoxydiol in the CIMS instrument, *i.e.* it takes approximately 10 minutes to equilibrate with Teflon tubing compared to a more-volatile compound such as hydroxyacetone (<1 min). The gas-phase mixing ratio linearly increases with decreasing solution pH (Figure C.8b) in the measurement range, as expected for a semi-volatile organic acid. This pH-dependent volatilization is likely to be important for understanding the SOA formation from not only MPAN oxidation, but other types of atmospheric reactions that produce organic acids in the condensed phase, *e.g.* cloud-processing oxidation (Carlton *et al.*, 2006; Sorooshian *et al.*, 2007), ozonolysis of alkenes (Christoffersen *et al.*, 1998; Koch *et al.*, 2000), and other reactions.

Interestingly, gas-phase 2MGA is not significantly enhanced and aerosol mass is not significantly decreased in the 40% RH experiment (Expt. 12) compared to the dry experiments. It is possible that the liquid water content under these conditions (~30 vol%) is not high enough to dominate the reaction with HMML

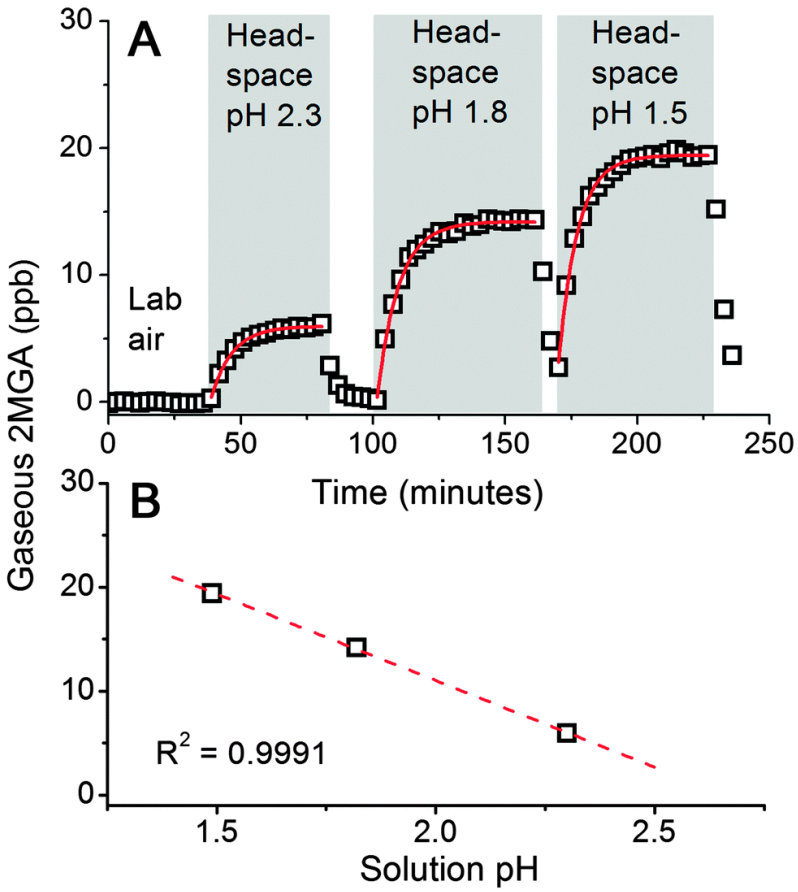

Figure C.8: CIMS measurements of the headspace air above a 0.075 M 2-methylglyceric acid (2MGA) solution: (A) the gaseous 2MGA signal when switching from lab air to solutions with different pH and (B) the headspace 2MGA mixing ratio (obtained through exponential fitting) is a linear function of pH in the measurement range.

or there is a barrier to 2MGA volatilization. For example, if organic-inorganic phase separation occurs at RH between efflorescence and deliquescence (Bertram *et al.*, 2011; O'Brien *et al.*, 2015), the reaction of gas-phase HMML with water and solvated ions and the volatilization of aqueous 2MGA may be hindered by an organic shell. Additionally, when liquid water content is lower (and thus, ionic strength is higher), organic acids such as 2MGA may form involatile salts with NH_4^+ and other cations (Wang and Laskin, 2014). Salt formation is not expected to be significant for deliquesced particles, but can be considerably enhanced for drier metastable particles at 30-50% RH (Laskin *et al.*, 2012).

Figure C.9 shows the results of high-resolution mass spectrometry (HR-MS) analyzes of SOA collected from MPAN and MACR photooxidation. When the

photooxidation of MACR is performed without inorganic seeds and under dry conditions, long oligomer families of 2MGA that are separated by 102.0317 Da (the exact mass of HMML) are observed, consistent with earlier mass spectrometry observations (Nguyen *et al.*, 2011b; Surratt *et al.*, 2006; Szmigielski *et al.*, 2007). The SOA composition from MPAN + OH appears almost identical to that of MACR + OH + NO_2. In addition to the 2MGA + HMML oligomers, the MACR high-NO_x photooxidation produces an organic nitrogen oligomer family (Figure C.9, blue peaks). The organic nitrogen family of 2MGA-nitrate + HMML elutes primarily at later retention times (8-20 min), likely due to their lower polarity compared to organic sulfates and acids, but is absent in other chemical systems, including the MPAN + OH low-NO_x reaction. These N-containing SOA compounds are likely formed from the reaction of HNO_3 (from NO_2 + OH reaction in the MACR high-NO_x experiments) with HMML in the condensed phase or interfacial region, which generate the nitrate ester of 2MGA through nucleophilic ring opening.

When aqueous sulfate is present, the sulfate ester of 2MGA is produced (Figure C.9, magenta peaks), which react with HMML similarly to 2MGA and 2MGA-nitrate. In ammonium sulfate particles at 40% RH, the oligomer families of 2MGA-sulfate + n(HMML) and 2MGA + n(HMML) are observed up to the trimer and dimer, respectively. In the deliquesced AS seeds at 85% RH, the monomer compounds 2MGA, 2MGA-sulfate, and the sulfate nitrate ($C_4H_6O_9NS^-$ ion) dominate the mass spectra. An exception is the dimer 2MGA-nitrate + HMML that has higher signal than the monomer. This may be attributed to the fact that nitrate ion is a poor nucleophile and nucleophilic substitution with water and sulfate may readily occur, so the monomer nitrate has a short condensed-phase lifetime. Thus, the organonitrate may be more stable in the dimer form. However, it is also possible the nitrate dimer is more ionizable in negative mode ESI compared to the monomer. We do not expect a large ionization difference between 2MGA-nitrate and 2MGA as the carboxyl moiety is believed to be the charge carrier for this compound in negative mode ESI with aqueous-based solvents (Yamashita and Fenn, 1984). The combined mass of the SOA from these organic acid and hetero-atom compounds in the 85% RH experiment, however, is lower than the mass of 2MGA in the gas phase (Figure C.7).

These aerosol phase HR-MS observations are consistent with earlier suggestions that relative humidity plays a role in modifying the composition and yield of isoprene-derived high-NO_x SOA (Nguyen *et al.*, 2011a; Zhang *et al.*, 2011). However, previous works did not study 2MGA particle/gas partitioning and discussions were

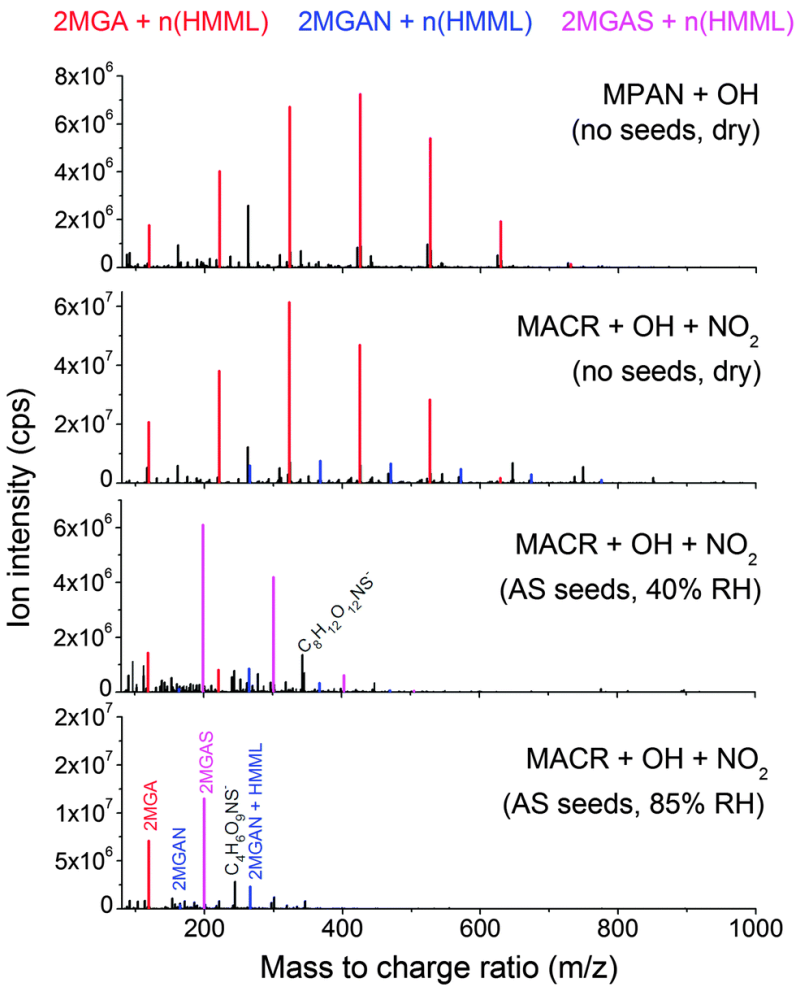

Figure C.9: Negative mode ESI-HRMS analysis of select SOA samples, integrated for retention times 2.5-3.5 min. The inorganic constituents have been separated by HPLC. Oligomer families comprised of HMML units are color-coded based on the monomer compounds (2MGA = 2-methylglyceric acid, 2MGAN = 2-methylglyceric acid nitrate, and 2MGAS = 2-methylglyceric acid sulfate).

framed with respect to poly-condensation reactions (*e.g.* a Fisher type esterification) – a hypothesis that is not consistent with the present data. Furthermore, it has been recently shown that Fisher type esterification is too slow to form 2MGA oligomers under standard conditions (Birdsall *et al.*, 2013). This does not, however, preclude condensation reactions from occurring when aerosol particles or cloud/fog droplets are evaporated (De Haan *et al.*, 2011; Nguyen *et al.*, 2012). In light of the gas-phase mechanism of MPAN + OH presented here, the molecular driving force behind the effect of RH on MPAN aerosol composition and yield can now be understood in terms of lactone polymerization.

Figure C.10 shows the proposed mechanism with which HMML is converted to SOA and gas-phase 2MGA. Lactones are well-known to produce polyesters *via* polyaddition (Löfgren *et al.*, 1995). We suspect that, in nature, the anionic ring opening polymerization scheme is the active mechanism. Nucleophilic attack at the sp^3 carbon is dominant for α-lactones (Greenberg and Liebman, 1978), partly due to the stability of the carboxylate (estimated to be only $\sim$10 kcal mol^{-1} higher in energy than the α-lactone) (Liebman and Greenberg, 1974). The propagated carboxylate can repeatedly add HMML under low RH conditions, where its main fate is reaction with organics that coat the particle. In ambient SOA, ring-opening initiators may be aqueous inorganic anions or myriad carboxylates that are present in the condensed phase. When liquid water is in excess (as is mainly the case in the lower troposphere), it appears the main fate of HMML is reaction with H_2O, aqueous sulfate, or aqueous nitrate, and not with organics. Because the organonitrate is more easily hydrolyzed, the major product of the reaction under typical atmospheric conditions is expected to be monomeric 2MGA and 2MGA sulfate. The 2MGA may re-partition into the gas phase, leading to significantly reduced SOA mass yields.

C.4 Atmospheric Implications

The representation of MPAN oxidation in atmospheric models has important ramifications. Thus far, only the proposed MAE mechanism (*i.e.* reactive uptake) has been considered for modelling SOA formation and framing field observations (Pye *et al.*, 2013; Worton *et al.*, 2013). Previously modelled SOA formation from MAE increases with particle acidity, while simulations based on HMML are expected to exhibit a different temporal and spatial variability. Pye *et al.* (2013) used the HMML and MAE yields suggested by Lin *et al.* (2013b) (57% and 21%, respectively); however, both compounds were assigned to have the acid-catalysed heterogeneous fate of MAE (*i.e.* essentially converting HMML mass to MAE). The observed and

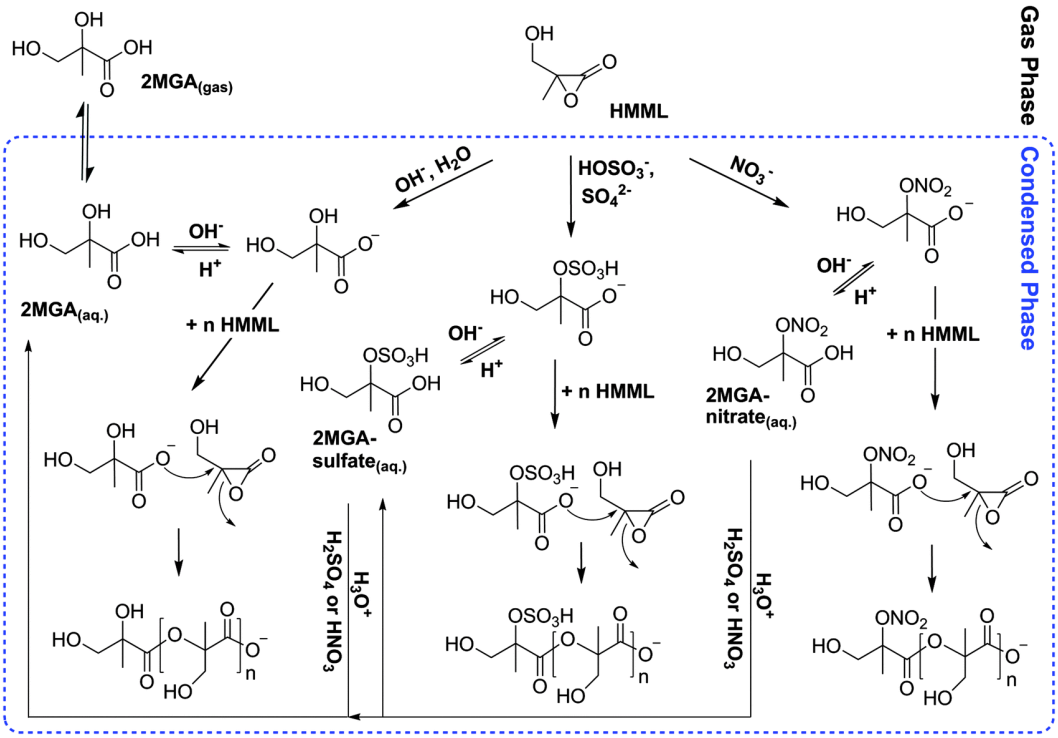

Figure C.10: Mechanism of SOA production from HMML (the blue dashed area represents the condensed phase). When particle liquid water is high, the main fate of HMML is reaction with water to produce monomeric 2MGA or sulfate and nitrate ions to produce 2MGA-sulfate and 2MGA-nitrate, respectively. The 2MGA monomer is volatile enough to re-partition to the gas phase. When the SOA composition is higher in organics than water, the main fate of HMML is reaction with its condensed-phase derivatives, producing low-volatility polyesters that increase SOA mass. Hydrated particles with higher free acidity may favour the monomeric form of 2MGA by neutralizing the carboxylate and hydrolyzing the sulfate and nitrate esters, possibly suppressing SOA growth.

predicted SOA from MPAN deviates from the 1:1 relationship in that work, likely a result of the assumed SOA mechanism. Figure C.8 and the mechanisms in Figure C.10 suggest a more complex impact of particle free acidity. For example, in conditions when particle free acidity is high, the neutral form of 2MGA will be favored and the organosulfate/organonitrate may hydrolyze more rapidly (Hu *et al.*, 2011). Both situations will enhance the abundance of 2MGA in the gas phase at the expense of lower-volatility derivatives that are important for SOA formation and growth.

The regional atmospheric importance of MPAN will vary with NO_2/NO ratio and isoprene emissions. Kjaergaard *et al.* (2012) estimated that approximately 4 Tg of HMML is produced per year (up to 0.8 μg m^{-3} day^{-1} in the Southeast

U.S.). However, whether the carbon from HMML is directed toward the formation of gaseous 2MGA or SOA will depend on atmospheric conditions and particulate matter characteristics. Typically, oligomers are not observed in ambient SOA and the mass concentrations of 2MGA and 2MGA-sulfate are low (*e.g.* 7-9 ng m^{-3} and 12 ng m^{-3} in Southeast U.S., respectively) (Lin *et al.*, 2013a). The low ambient observations in the Southeast US, a region characterized by higher particle liquid water and lower particle pH (Guo *et al.*, 2015; Nguyen *et al.*, 2014c), are consistent with the HMML-derived SOA formation mechanism (Figure C.10). This work demonstrates that certain "SOA tracers" have more complex fates in nature than previously recognized. Interpreting the abundance of aqueous 2MGA and 2MGA-sulfate will require knowledge of physical parameters that may not be available for these compounds (*e.g.* Henry's Law coefficients, reaction coefficients, temperature and pH-dependent accommodation). We expect that integrating the lactone mechanism into atmospheric models will produce a more accurate representation of the magnitude, temporal variation, and spatial distribution of isoprene-derived organic compounds (whether in the gas or condensed phase) near anthropogenically influenced regions.

C.5 Supporting Information

C.5.1 Photooxidation of Saturated Analogues of MPAN

Lactone formation has been suggested only for APNs of aldehydes with a β-alkenyl moiety, MACR and acrolein (Kjaergaard *et al.*, 2012). Here, we investigate the extent to which saturated APNs may access a similar reaction pathway. The OH-initiated oxidation of saturated and unsaturated compounds proceeds predominantly through abstraction and addition channels, respectively, illustrated here for ethylene and ethane:

$H_2C{=}CH_2 + OH \rightarrow CH_2(OH)^{-}{\cdot}CH_2$

$H_3C\text{-}CH_3 + OH \rightarrow H_3C^{-}{\cdot}CH_2 + H_2O$

The abstraction-generated alkyl radical is less energetic than the alkyl radical formed *via* addition of OH. It is unclear whether most of the abstraction radicals would be collisionally stabilized or if the -C(O)OONO$_2$ neighboring group enhances its decomposition. To investigate the effects of alkyl radical energetics, we conducted additional experiments using radicals A and C (Figure C.6) that are analogous to A*. The radical A (produced in Expt. 11) is the thermalized version of A*, given its formation mechanism; and C (produced in Expt. 10) is structurally similar to A, but missing the hydroxyl group. As the results of both experiments are consistent, we limit the discussion only to the chemistry of A, a third-generation oxidation intermediate of 2-methylbut-3-ene-1-ol (231MBO).

Figure C.16a in the Supporting Information shows the formation of the 3-hydroxy-2-methylpropanoyl peroxynitrate (HMPPN) from a chamber experiment. HMPPN is the precursor of A from 231MBO, formed in a synthetic scheme that involves ~21 h of dark ozonolysis chemistry (to react away most of the C=C bonds of 231MBO) followed by a shorter phase of high-NO$_2$ photooxidation. Ozonolysis of 231MBO produces the aldehyde hydroxymethyl propanal (HMP) in high yield alongside the simplest Criegee (CH$_2$OO), which is observed by CIMS as its bimolecular product with water, hydroxymethylhydroperoxide (not shown) (Neeb *et al.*, 1997). The ozonolysis period (performed without an OH scavenger) produced a small yield of SOA (<3%) that has the same temporal behavior as HMP. After the stabilization of the dark gas-phase mixture, NO$_2$ and methyl nitrite were injected and the near-UV lamps were switched on to initiate the OH-oxidation chemistry in the presence of NO$_2$. The slight decay of HMP prior to initiation of photochemistry (*e.g.* starting at -20 min, Figure C.7b) is due to reaction with NO$_3$, formed after the injection of NO$_2$ through its reaction with O$_3$; however, this slower chemistry is promptly overtaken by the OH oxidation that occurred in the photolytic period.

The photochemistry of HMP (and that of HMPPN) does not produce additional SOA (Figure C.16b in the Supporting Information, $\ll$1% SOA yield from HMP). In comparison, when MACR is oxidized in a similar manner (Figure C.16c in the Supporting Information), SOA is observed to grow after a ~15 min delay. A delay in observing SOA is fairly typical when seed particles are not used (Figure C.4) because the lower threshold for particle diameter in this work is 20 nm. Additionally, the SOA should be second-generation so the observed delay may encompass a chemical delay. As HMP and MACR both produce the APNs, which upon oxidation form structurally identical alkyl radicals, the results suggest that the difference in excess energy of A and A* is responsible for the disparate SOA formation behaviour.

Experimental evidence for HMPPN reaction and A + O_2 reaction can be provided by the CIMS observations of alkylperoxyl radical (RO_2) and alkoxyl radical (RO) reaction products (Figure C.17 in the Supporting Information; see Figure C.6 in the main text for the mechanism). During the photolytic period, we observed the minor products of the RO_2 + NO reaction channel, the hydroxynitrates (RO_2 + NO $\rightarrow$ $RONO_2$) and the major product of the RO_2 + HO_2 reaction channel, the hydroxyhydroperoxides (RO_2 + HO_2 $\rightarrow$ ROOH + O_2) from the HMPPN + OH reaction. These radical termination products have low volatility (*e.g.* the hydroperoxide has a molecular formula of $C_4H_7NO_8$) in addition to low yields, resulting in low analyte signals in the CIMS. We also observed the major products from the high-NO reaction (RO_2 + NO $\rightarrow$ RO + NO_2 $\rightarrow$ decomposition products), which include HAC (~25% from HMP) and the APN of pyruvaldehyde (2-oxopropanoyl peroxynitrate (2OPN), <1% from HMP, green trace in Figure C.17 in the Supporting Information) (Orlando *et al.*, 2002). The relative yields of HAC is 3 - 30 times higher compared to the 2OPN when estimated from HMPPN; however the absolute yields are not available as the amount of HMPPN reacted is unknown. The disparity in relative yields may be due to the expected propensity for 2OPN to decompose (*via* the NO_2 and NO_3 channels) compared to the high stability of HAC (Orlando *et al.*, 2002). The formation of RO_2 radical termination products and RO decomposition products in the MPAN + OH reaction was negligible (Figure C.17a in the Supporting Information). The HAC formation in the MPAN + OH reaction is *via* HMML decomposition. Together with SOA data and HMPPN-derived product observations, the RO_2 reaction products provides a consistent picture of predominantly HMML formation from MPAN + OH and RO_2 formation from HMPPN + OH.

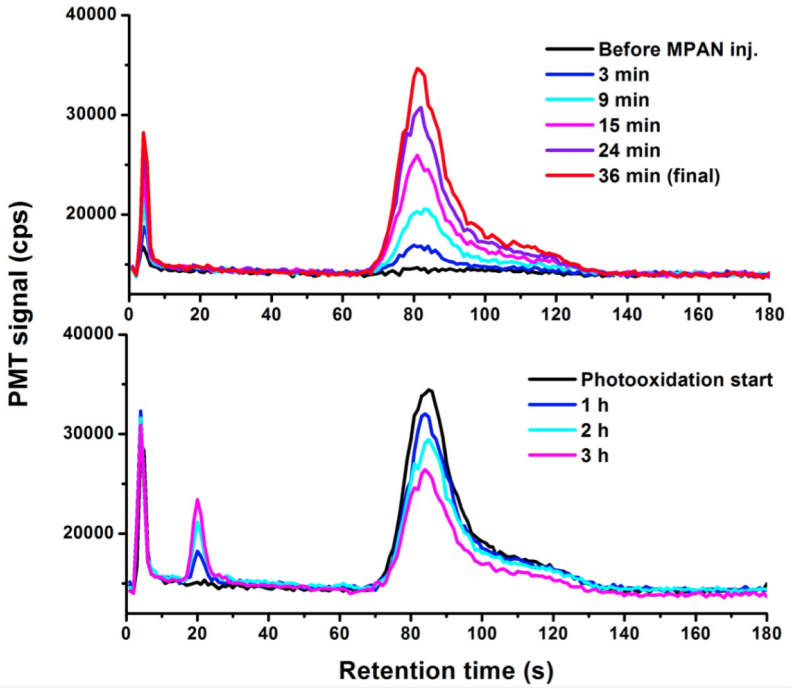

Figure C.11: Chromatograms of NO_2, PAN, and MPAN in the NO_2/APN analyzer (retention times 10, 20, and 80 s, respectively). Top panel: signals from NO_2 and MPAN are observed when introducing MPAN into the chamber due to a small decomposition yield of MPAN in room-temperature Teflon lines. This decomposition is not observed in the headspace of pure MPAN in tridecane when the standard is kept cold and the sampling line is short (< 0.3 m). Bottom panel: photooxidation of MPAN over the course of 3 h, when the MPAN signal decreases and PAN is observed to form. The NO_2 signal does not change significantly, possibly due to the compensating effects of decreasing signal from MPAN and increasing signal from other sources.

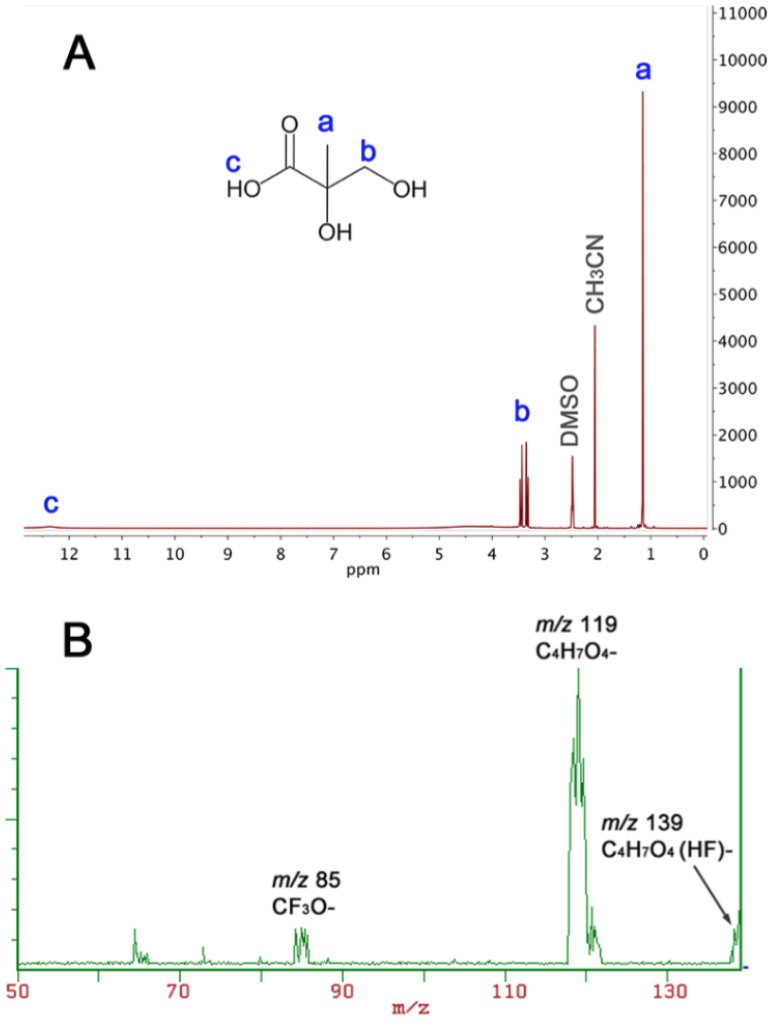

Figure C.12: Characterization of 2-methylglyceric acid with proton NMR using DMSO solvent, the semi-pure mixture (containing 7% acetonitrile) was further purified through crystallization and B: tandem mass spectrometry (MS/MS) with triple quadrupole CIMS, the 2-methylglyceric acid is observed only as its fluoride transfer ion with CF_3O^- and collision-induced dissociation leads primarily to the deprotonated compound ($C_4H_7O_4^-$).

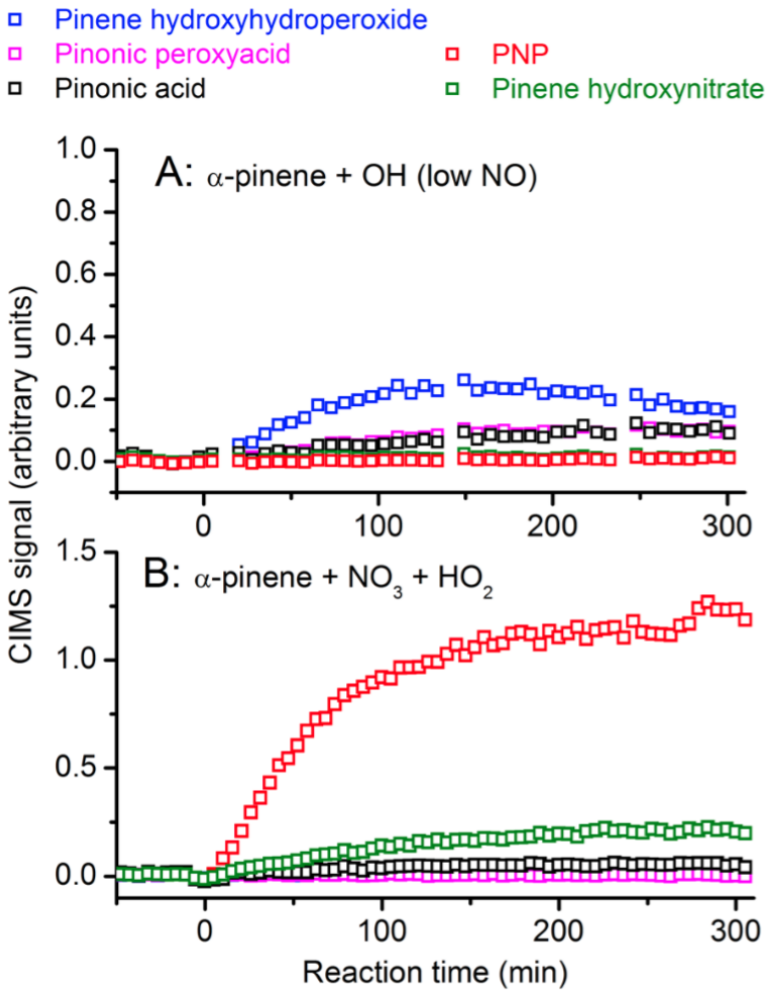

Figure C.13: Ion intensity data (not converted to mixing ratio) from the negative ion mode CIMS during control experiments performed with α-pinene: (A) The pinene nitrooxyhydroperoxide (PNP, red markers) used as a tracer for NO_3 in this work is not formed under the low-NO conditions that were used to photooxidize MPAN; (B) PNP is only formed (and is a major product) when NO_3 is available to oxidize α-pinene (or β-pinene) in the presence of HO_2 radicals (generated from photolysis of HCHO in these experiments). Pinonaldehyde (measured in positive ion mode, not shown) is also a major product in both oxidation experiments.

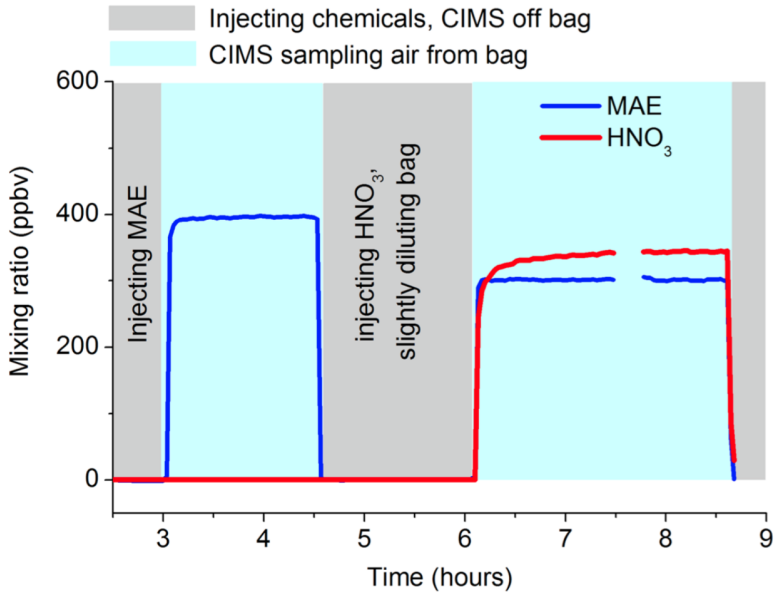

Figure C.14: Monitoring the loss of MAE to the walls of a 1000 L Teflon bag, filled with dry purified ("zero") air (relative humidity < 5% in the bag). MAE did not demonstrate any observable wall loss under these conditions. Injections of nitric acid (~500 ppbv injected, ~300 ppbv observed in the gas phase) did not change the wall loss behavior of MAE over the course of 2.5 hours, after which the instrument was taken off the bag.

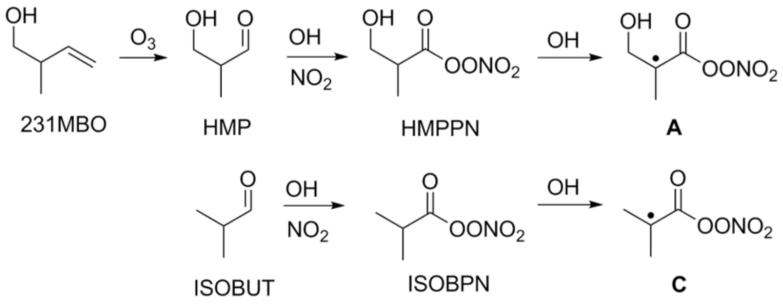

Figure C.15: Gas-phase synthesis of β-alkyl radicals from saturated APNs: hydroxymethylpropanoyl peroxynitrate (HMPPN) and isobutanoyl peroxynitrate (ISOBPN).

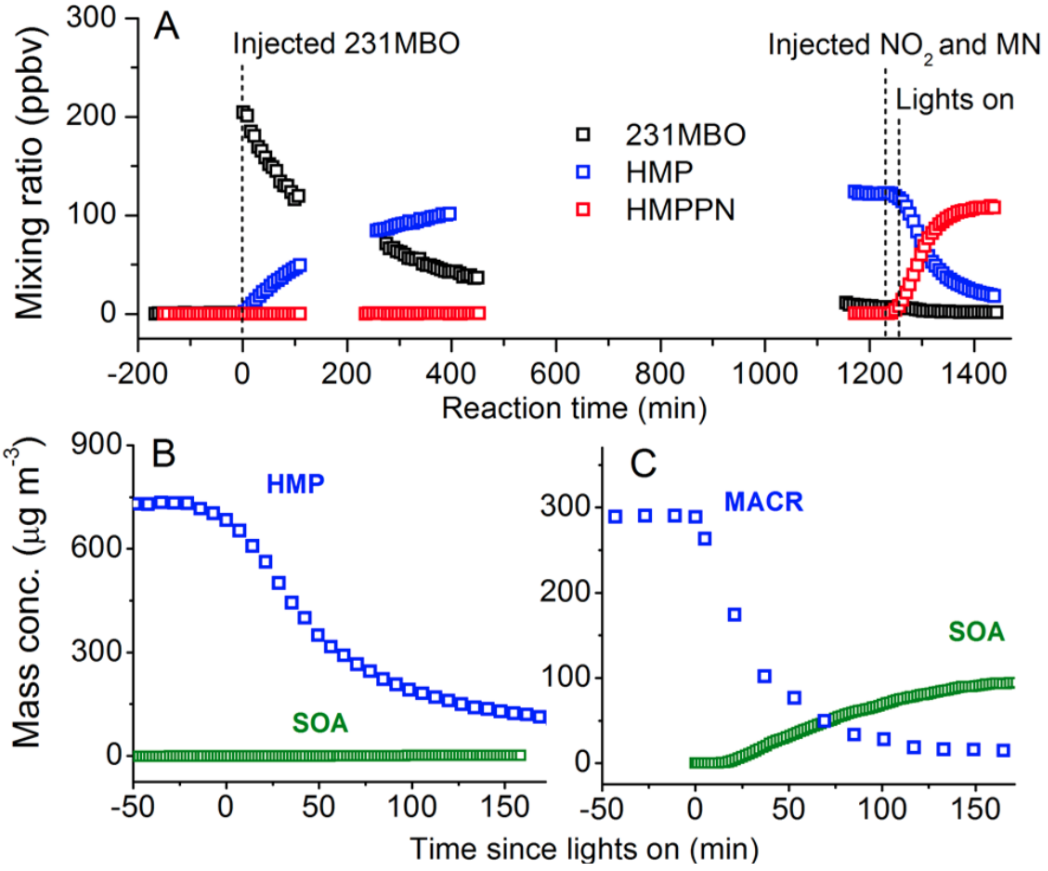

Figure C.16: SOA formation from saturated vs. unsaturated APNs: (A) the results from Expt. 11 where 231MBO is ozonized into its aldehyde HMP, followed by high-NO_2 photooxidation to the APN (HMPPN) with methyl nitrite (MN) as an OH precursor; (B) the reaction shown in panel A where the time axis is renormalized to start when UV lights are switched on and SOA from the dark period is subtracted; (C) similar to panel B but with MACR as the hydrocarbon (Expt. 9). Both vertical axes in panels B and C are with respect to mass. Breaks in data occur when instruments are not sampling from the chamber.

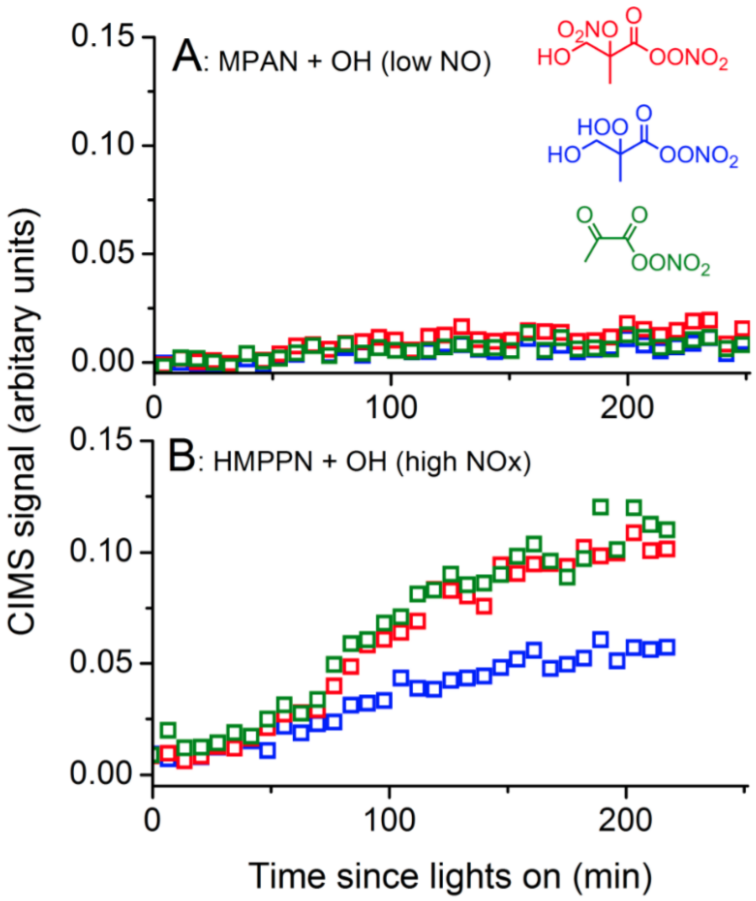

Figure C.17: High-NO and low-NO compounds from alkylperoxyl (RO_2) radical B: the hydroxynitrates (RO_2 + NO $\rightarrow$ $RONO_2$, red), hydroxyhydroperoxides (RO_2 + HO_2 $\rightarrow$ ROOH + O_2, blue), and 2-oxopropanoyl peroxynitrate (2OPN, green) from (A) the MPAN photooxidation and (B) the HMPPN photooxidation. The production of HAC from MPAN (reaching ~0.25 at the 250 min mark) and HMPPN (reaching 1.8 at the 220 min mark), *via* different mechanisms, is greater than the production of the shown compounds.

Appendix D

KINETICS AND PRODUCTS OF THE REACTION OF THE FIRST-GENERATION ISOPRENE HYDROXY HYDROPEROXIDE (ISOPOOH) WITH OH

St. Clair, J. M., J. C. Rivera-Rios, J. D. Crounse, H. C. Knap, K. H. Bates, A. P. Teng, S. Jorgensen, H. G. Kjaergaard, F. N. Keutsch, and P. O. Wennberg (2015). "Kinetics and products of the reaction of the first-generation isoprene hydroxy hydroperoxide (ISOPOOH) with OH". In: *J. Phys. Chem. A* 120.9, pp. 1441–1451. DOI: 10.1021/acs.jpca.5b06532.

Abstract

The atmospheric oxidation of isoprene by the OH radical leads to the formation of several isomers of an unsaturated hydroxy hydroperoxide, ISOPOOH. Oxidation of ISOPOOH by OH produces epoxydiols, IEPOX, which have been shown to contribute mass to secondary organic aerosol (SOA). We present kinetic rate constant measurements for OH + ISOPOOH using synthetic standards of the two major isomers: (1,2)- and (4,3)-ISOPOOH. At 297 K, the total OH rate constant is $7.5 \pm 1.2 \times 10^{-11}$ cm^3 molecule^{-1} s^{-1} for (1,2)-ISOPOOH and $1.18 \pm 0.19 \times 10^{-10}$ cm^3 molecule^{-1} s^{-1} for (4,3)-ISOPOOH. Abstraction of the hydroperoxy hydrogen accounts for approximately 12% and 4% of the reactivity for (1,2)-ISOPOOH and (4,3)-ISOPOOH, respectively. The sum of all H-abstractions account for approximately 15% and 7% of the reactivity for (1,2)-ISOPOOH and (4,3)-ISOPOOH, respectively. The major product observed from both ISOPOOH isomers was IEPOX (*cis*-β and *trans*-β isomers), with a ~2:1 preference for *trans*-β IEPOX and similar total yields from each ISOPOOH isomer (~70-80%). An IEPOX global production rate of more than 100 Tg C each year is estimated from this chemistry using a global 3D chemical transport model, similar to earlier estimates. Finally, following addition of OH to ISOPOOH, approximately 13% of the reactivity proceeds *via* addition of O_2 at 297 K and 745 Torr. In the presence of NO, these peroxy radicals lead to formation of small carbonyl compounds. Under HO_2 dominated chemistry, no products are observed from these channels. We suggest that the major products, highly oxygenated organic peroxides, are lost to the chamber walls. In the atmosphere, formation of these compounds may contribute to organic aerosol mass.

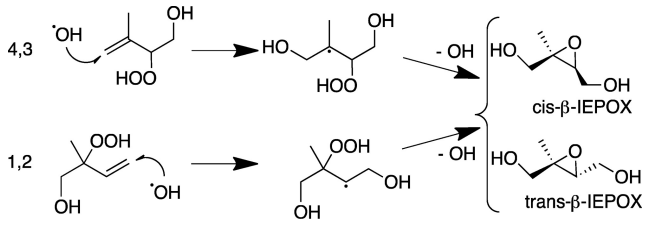

Figure D.1: Mechanism for the formation of *cis*- and *trans*-β-IEPOX from OH addition to (4,3)- and (1,2)-ISOPOOH.

D.1 Introduction

Global emissions of isoprene (2-methyl-1,3-butadiene, C_5H_8, ISOP) are estimated to be ~540 Tg (~470 Tg C) each year (reference year 2000) and are the single largest source of atmospheric nonmethane hydrocarbons (Guenther *et al.*, 2006; Guenther *et al.*, 2012). Emissions from tropical broadleaf trees and other deciduous plants dominate the source (Guenther *et al.*, 2006; Guenther *et al.*, 2012). The oxidation of isoprene and its oxidation products by OH results in the formation of ozone and secondary organic aerosol (SOA), with impacts on human health and climate. The chemical fate of isoprene and its oxidative products also affects the abundance of OH in regions influenced by biological emissions (Archibald *et al.*, 2010; Lelieveld *et al.*, 2008).

Organic peroxy radicals, hereafter RO_2, formed from OH and subsequent O_2 addition to isoprene generally follow one of three reaction pathways: (1) reaction with HO_2 to form hydroperoxides (Crutzen *et al.*, 2000; Paulot *et al.*, 2009b); (2) reaction with NO to form hydroxynitrates or formaldehyde and methyl vinyl ketone (MVK)/methacrolein (MACR) and HO_2 (Paulot *et al.*, 2009a); (3) RO_2 H-shift isomerization of the RO_2 radicals followed by reaction with O_2 to form hydroperoxyenals (HPALDs) and other oxidized products (Crounse *et al.*, 2011; Peeters *et al.*, 2009; Wolfe *et al.*, 2012). The fate of the RO_2 is dependent on the concentrations of HO_2, NO, RO_2, and the temperature. Under HO_2-dominated conditions, the main products are unsaturated hydroperoxides (several isomers, collectively referred to as ISOPOOH):

$ISOP + OH + O_2 \rightarrow ISOPOO\cdot$

$ISOPOO\cdot + HO_2 \rightarrow ISOPOOH$

As illustrated in Figure D.1, a subsequent reaction of ISOPOOH with OH can produce epoxydiols (several isomers, collectively referred to as IEPOX) and recycle OH (Paulot *et al.*, 2009b).

IEPOX was proposed as an SOA precursor (Paulot *et al.*, 2009b; Surratt *et al.*, 2010), and has subsequently been shown to contribute to SOA mass in field (Budisulistiorini *et al.*, 2013; Froyd *et al.*, 2011; Worton *et al.*, 2013) and laboratory (Gaston *et al.*, 2014; Lin *et al.*, 2012; Liu *et al.*, 2015; Nguyen *et al.*, 2014a) measurements. Recent laboratory studies of gas phase oxidation of IEPOX by OH (Bates *et al.*, 2014; Jacobs *et al.*, 2013) and of IEPOX aerosol uptake properties (Gaston *et al.*, 2014; Lin *et al.*, 2012; Liu *et al.*, 2015; Nguyen *et al.*, 2014a) were made possible by the development of synthetic routes to IEPOX (Zhang *et al.*, 2012).

Previously, estimates of the OH + ISOPOOH rate coefficients and products were inferred from OH + isoprene experiments, with limited ability to elucidate the relative role of the different isomers of ISOPOOH (Paulot *et al.*, 2009b). Here, using synthetic ISOPOOH standards (Rivera-Rios *et al.*, 2014), we report kinetic rate constant measurements for the OH + ISOPOOH reaction, relative to OH + propene, for the two main isomers, (1-OH,2-OOH)-ISOPOOH (hereafter (1,2)-ISOPOOH) and (4-OH,3-OOH)-ISOPOOH (hereafter (4,3)-ISOPOOH) (Figure D.1). The products of this chemistry were also determined. The impact of updating the low NO isoprene mechanism on the global production of IEPOX was explored using the GEOS-Chem chemical transport model.

D.2 Experimental Methods

The environmental chamber and techniques used for these experiments have been described previously (Bates *et al.*, 2014; Crounse *et al.*, 2013; Lee *et al.*, 2014), with study-specific details provided below. A gas chromatograph with a flame ionization detector (GC-FID, Hewlett-Packard 5890 series II Plus) was used to measure propene for the relative rate kinetics experiments. Measurements of ISOPOOH and its oxidation products were made using two CF_3O^- chemical ionization mass spectrometers (CIMS), which have been described previously (Crounse *et al.*, 2006; Paulot *et al.*, 2009a; St. Clair *et al.*, 2010). CF_3O^- selectively ionizes analytes to typically form either an ion cluster (*m/z* = analyte mass +85) or a fluoride *trans*fer ion (*m/z* = analyte mass +19). The time-of-flight CIMS (ToF-CIMS) provided 1 Hz unit mass data for *m/z* = 19 to *m/z* = 396. The triple quadrupole CIMS (TQ-CIMS) was operated exclusively in tandem MS mode to differentiate the cluster ion *m/z* = 203 signal from the two isobaric compounds, ISOPOOH and IEPOX (Paulot *et al.*, 2009b). The signal observed at *m/z* = 203 → *m/z* = 63 arises primarily from ISOPOOH while the signal at *m/z* = 203 → *m/z* = 183 is primarily from IEPOX.

expt #	$[ISOPOOH]_0$ (ppbv)	$[propene]_0$ (ppbv)	$[H_2O_2]_0$ (ppmv)	$[NO]_0$ (ppbv)	reaction time (h)
K1	210	61	2.2	515	1.7
K2	108	76	1.9	518	1.7
K3	15	68	1.8	514	2.4
K4	18	66	2.2	513	3.0
K5	23	77	2.1	539	2.0
K6	51	116	2.1	513	2.1
K7	45	161	2.0	515	2.5
K8	41	183	2.2	507	1.7
K9	31	166	2.2	510	1.8

Table D.1: Experimental conditions for OH + ISOPOOH kinetics experiments.

All experiments were conducted in a 0.85 m^3 chamber made of fluorinated ethylene propylene (Teflon-FEP, DuPont) with one port for the introduction of reagents and sampling. During an experiment, approximately 1 std L min^{-1} of sample flow was drawn from the bag *via* a 6.35 mm O.D. PFA tube, with the CIMS instruments subsampling the main tube flow *via* glass orifices. The chamber was at 297 ± 2 K and 745 Torr (99.3 kPa) for all experiments.

The chamber was prepared for each experiment with multiple flushes of dry air from a purge gas generator (Perkin, model 75-52). H_2O_2, the OH source, was added first to the bag by flowing 20 std L min^{-1} of dry air over ~5 μL of 50% H_2O_2 contained in a shallow glass vial for 12 min, resulting in ~2 ppmv in the final mixture. The addition of ISOPOOH followed, with 1-2 min of dry air at 20 std L min^{-1} passed over ISOPOOH in a shallow glass vial. For the HO_2-dominated experiments, the remainder of the bag volume was filled with dry air. For NO-dominated kinetics experiments, propene was added next, with NO added once the bag was nearly full to minimize conversion to NO_2. Propene (Sigma-Aldrich, ≥99%) was prepared for addition by obtaining a ~300 ppmv propene sample in a 500 cm^3 glass flask at room pressure using pure propene and serial dilution. The mixing ratio of the ~300 ppmv propene sample was verified using FT-IR and tabulated propene cross section (Johnson *et al.*, 2002; Sharpe *et al.*, 2004). NO was prepared by adding ~330 Torr of 2000 ppmv NO (Matheson Gas Products) to a 500 cm^3 glass flask. Tables D.1 and D.2 contain the details for each high NO and low NO experiment, respectively.

Kinetics experiments were conducted using four of the eight available UV lights ($J_{NO_2} \approx 1 \times 10^{-3}$ s^{-1}). At least 2/3 of the ISOPOOH was oxidized in each experiment,

expt #	$[ISOPOOH]_0$ (ppbv)	$[H_2O_2]_0$ (ppmv)	% ISOPOOH reacted
Y1	119	2.0	9
Y2	25	1.8	12
Y3	21	1.9	13
Y4	22	2.1	15
Y5	33	2.1	9
Y6	25	2.0	12
Y7	21	1.9	15
Y8	45	2.2	12
Y9	36	2.2	9
Y10	34	2.2	17
Y11	37	2.2	33

Table D.2: Experimental conditions for OH + ISOPOOH product yield experiments.

requiring 1.5-3 h of photo-oxidation. Low NO product yield experiments were run with all available lights, oxidizing only ~10% of the starting ISOPOOH to minimize the secondary loss of products to reaction with OH and to the walls. Before and after the oxidation, GC-ToF-CIMS chromatograms were collected to aid in product identification (Bates *et al.*, 2014). Product yields were determined by dividing the change in the product mixing ratio ($X_{postoxidation}$ - $X_{preoxidation}$) by the change in the ISOPOOH mixing ratio. CF_3O^- CIMS sensitivities used to determine mixing ratios are included in the Supporting Information. Wall loss of ISOPOOH in the presence of H_2O_2 was determined before and after the oxidation during the kinetics experiments and was found to be negligible ($-1 \pm 1\%\ h^{-1}$). Previous work investigated the wall loss of IEPOX and found it to be small ($<-1\%\ h^{-1}$) in the absence of acid (Bates *et al.*, 2014).

The experiments used several different synthetic ISOPOOH batches with differing purities. The ISOPOOH samples used for experiments K8-K9 and Y8-Y11 had fewer impurities than those available for experiments K1-K7 and Y1-Y7. The main impurity was 2-methyl-1-butene-3,4-diol, observed in the CIMS instruments as a CF_3O^- cluster ion with *m/z* = 187, for the (4,3)-ISOPOOH and 3-methyl-1-butene-3,4-diol for the (1,2)-ISOPOOH. In the (4,3)-ISOPOOH samples used for experiments K1-K7 and Y1-Y7, the diol impurity signal was about 10% of the ISOPOOH signal; the impurity in the samples used in the last few experiments was only ~2%. For the (1,2)-ISOPOOH, the impurity signal was always small (1% in initial experiments, 0.5% in later). Other impurities included H_2O_2 and

two compounds that produce signal at *m/z* = 201 and *m/z* = 185, with the latter two assumed to be the same compounds as are produced from the OH oxidation of ISOPOOH (see products of ISOPOOH sections below). The ISOPOOH product yields were corrected for the methylbutenediol oxidation products, as discussed in the Supporting Information.

D.3 Results and Discussion

D.3.1 Kinetics

The kinetic rate coefficient of the ISOPOOH + OH reaction was determined relative to that of OH + propene for both (1,2)-ISOPOOH and (4,3)-ISOPOOH. The propene rate coefficient (2.59×10^{-11} cm^3 molecule^{-1} s^{-1} at 298 K) was obtained using the pressure dependence from the IUPAC recommendation and normalizing the rate constant to the Atkinson and Arey recommended rate constant (Atkinson and Arey, 2003b; Atkinson *et al.*, 2006). For each experiment, a linear regression (York *et al.*, 2004) was performed on $\log_e([\text{propene}]/[\text{propene}]_0)$ vs $\log_e([\text{ISOPOOH}]/[\text{ISOPOOH}]_0)$ data set (Figure D.2), with the ISOPOOH + OH reaction rate coefficient equal to the fitted slope divided by the propene rate constant. Table D.3 contains the rate constants determined for each experiment and the recommended rate constants for the two ISOPOOH isomers. The recommended rate constant was calculated by taking a mean from all the experiments weighted by their respective uncertainties. Uncertainties for all the ISOPOOH+OH rate constants include ±15% from the propene rate constant (Atkinson and Arey, 2003b). The rate constant uncertainty is dominated by the uncertainty in the propene rate constant, with the precision of the GC-FID measurement of propene dominating the fit uncertainty.

Estimates of the hydrogen abstraction rate constants were also obtained, using both the high NO kinetics experiments and the low NO product yield experiments (Tables D.4 and D.5). Both ISOPOOH isomers have labile hydrogens on the hydroperoxy group and α to the hydroxy group. (4,3)-ISOPOOH has, in addition, a hydrogen α to the hydroperoxy group. Removal of the hydroperoxy hydrogen produces the RO_2 that can reform the same ISOPOOH isomer upon reaction with HO_2. Standard chemistry suggests that abstraction of the hydrogen α to the hydroxy group will lead to a C_5-hydroperoxyenal (HPALD, *m/z* = 201) under low NO conditions (Figure D.3). The abstraction of the hydrogen α to the (4,3)-ISOPOOH hydroperoxy group is expected to form a β-C_5-hydroxy carbonyl (HC_5, *m/z* = 185) in a OH-neutral reaction (Figure D.4) (Vereecken *et al.*, 2004).

compound	experiment	rate $\times 10^{11}$ (cm^3 molecule^{-1} s^{-1})
(1,2)-ISOPOOH	K3	7.49 ± 1.61
	K4	7.44 ± 1.31
	K5	7.84 ± 1.85
	K7	7.50 ± 1.36
		weighted mean: 7.5 ± 1.2
(4,3)-ISOPOOH	K1	12.6 ± 3.1
	K2	10.8 ± 2.7
	K6	11.7 ± 2.2
	K8	11.9 ± 2.6
	K9	12.0 ± 2.6
		weighted mean: 11.8 ± 1.9

Table D.3: OH + ISOPOOH kinetic rate coefficients.

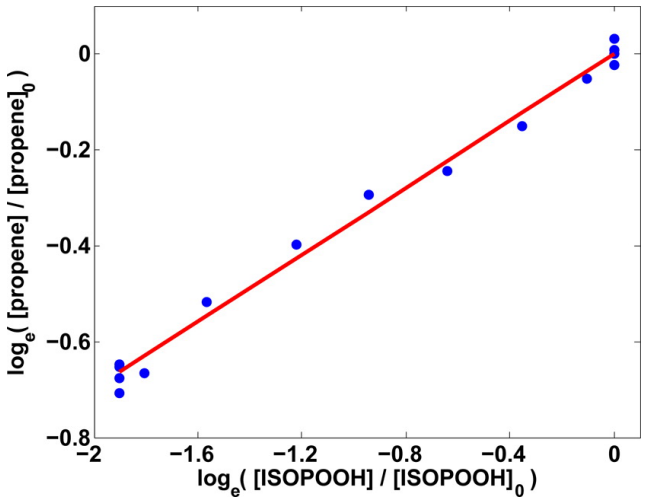

Figure D.2: Fit to the propene vs (1,2)-ISOPOOH decay to determine the ISOPOOH + OH rate relative to propene + OH for experiment K4. The slope in this experiment is 0.349 ± 0.032, with an ISOPOOH + OH rate of 7.44 ± 1.31 × 10^{-11} cm^3 molecule^{-1} s^{-1}.

product	Y1	Y2	Y3	Y4	Y11	mean
hydroxyacetone	3.7	6.3	5.6	4.6	2.0	4.4
m/z = 189	3.3	3.4	3.6	3.5	2.1	3.2
m/z = 201	2.1	2.5	2.5	2.6	1.9	2.3
glycolic acid	1.3	1.6	1.7	2.0	0.6	1.4
m/z = 185	0.9	1.4	1.1	0.9	1.0	1.1
sum of non-IEPOX products	11.3	15.2	14.5	13.6	7.6	12.4

Table D.4: Reaction products from OH + (4,3)-ISOPOOH for HO_2-dominated conditions. Molar yields reported in percent.

product	Y5	Y6	Y7	Y8	Y9	Y10	mean
hydroxyacetone	1.3	1.0	1.5	1.4	1.2	1.5	1.3
m/z = 189	2.8	2.7	3.5	3.7	3.6	3.4	3.4
m/z = 201	1.5	1.7	2.1	2.1	2.2	1.9	2.0
m/z = 93	1.5	2.4	1.3	1.1	1.3	1.0	1.4
m/z = 161	1.1	0.8	1.3	1.1	1.3	0.9	1.1
m/z = 185	2.1	1.6	2.1	2.1	2.1	1.9	2.0
glycolaldehyde	0.7	0.8	1.0	1.2	0.7	0.9	0.9
sum of non-IEPOX products	11.4	11.4	13.2	12.7	12.4	11.5	12.1

Table D.5: Reaction products from OH + (1,2)-ISOPOOH for HO_2-dominated conditions. Yields reported in percent.

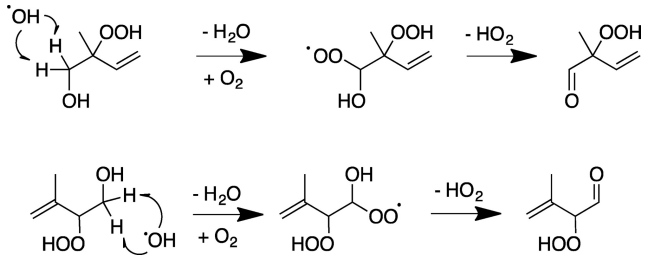

Figure D.3: Mechanism for the formation of HPALD (*m/z* = 201) from (1,2)-ISOPOOH (top) and (4,3)-ISOPOOH (bottom) by H-abstraction.

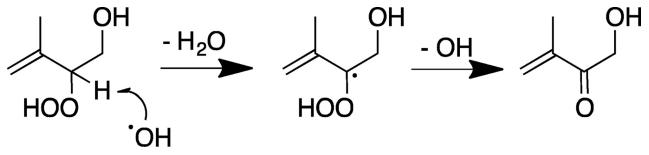

Figure D.4: Mechanism for the formation of a β-HC_5 (*m/z* = 185) from (4,3)-ISOPOOH by H-abstraction.

The yield of *m/z* = 185, presumed to be a β-hydroxy-carbonyl, HC_5, from (4,3)-ISOPOOH was low: ~1%. We also observed a compound at *m/z* = 185 from (1,2)-ISOPOOH with a yield of ~2%. However, because the (1,2)-ISOPOOH lacks a hydrogen α to the hydroperoxy group, it cannot form HC_5 *via* this route. One possibility is an epoxide, shown in Figure D.5. Alternatively, it is possible that HC_5 is formed from an impurity (such as (2,1)-ISOPOOH). Impurities at *m/z* = 185 and *m/z* = 201 were large enough that loss of the initial compound by reaction with OH affected the determination of yields, and consequently H-abstraction rate constants, from OH + ISOPOOH. An approximate correction for the loss by OH was applied using the approach of Atkinson *et al.* (1982). OH rate constants for both compounds

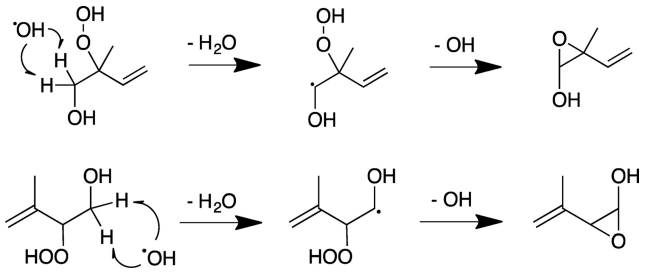

Figure D.5: Mechanism for the formation of an unsaturated hydroxy epoxide (*m/z* = 185) from (1,2)-ISOPOOH (top) and (4,3)-ISOPOOH (bottom) by H-abstraction. This channel is in competition with the chemistry illustrated in Figure D.3.

were assumed to be the same as the ISOPOOH standard.

The abstraction rate coefficient of the hydroperoxy hydrogen was determined using the observed formation of isoprene hydroxy nitrate (ISOPN, *m/z* = 232), which is formed from the product RO_2 under high NO conditions (Figure D.6). ISOPN CIMS sensitivities have been determined previously (Lee *et al.*, 2014; Teng *et al.*, 2015), and a 0.14 yield was used based on a currently unpublished best estimate. The ISOPN data were corrected for loss by OH (Atkinson *et al.*, 1982) and the slope of (ISOPN/Y_{ISOPN}) vs ISOPOOH was multiplied by the total ISOPOOH + OH rate constant to give the hydroperoxy hydrogen abstraction rate constant (Table D.6). We find that this channel is 12% of the overall OH reactivity for the (1,2)-ISOPOOH and 4% for the (4,3)-ISOPOOH, assuming equal Y_{ISOPN} for each isomer. From the sum of the H-abstraction rate constants determined *via* the formation rate of the *m/z* = 185 and *m/z* = 201 products, plus the lower uncertainty hydroperoxy hydrogen abstraction rate constant, we infer that the overall H-abstraction rate constants are 1.2×10^{-11} cm^3 molecule^{-1} s^{-1} for (1,2)-ISOPOOH and 8×10^{-12} cm^3 molecule^{-1} s^{-1} for (4,3)-ISOPOOH.

From the isomer specific rate coefficients determined here, and assuming an ambient ISOPOOH distribution as 67% (1,2)-ISOPOOH, 29% (4,3)-ISOPOOH, and 4% δ-ISOPOOH (Bates *et al.*, 2014), the isomer-averaged OH addition rate constant is 7.8×10^{-11} cm^3 molecule^{-1} s^{-1} and the isomer-averaged H-abstraction rate constant is 1.1×10^{-11} cm^3 molecule^{-1} s^{-1}. This can be compared with the results of Paulot *et al.* (2009b), who estimated the OH addition rate constant to ISOPOOH as 7.0×10^{-11} cm^3 molecule^{-1} s^{-1} and the H-abstraction rate constant as 7×10^{-12} cm^3 molecule^{-1} s^{-1}, both at 298 K.

compound	experiment	rate × 10^{12} (cm^3 $molecule^{-1}$ s^{-1})
(1,2)-ISOPOOH	K3	8.59 ± 1.59
	K4	8.91 ± 1.46
	K5	8.68 ± 1.43
	K7	9.38 ± 1.54
		weighted mean: 9.0 ± 1.4
(4,3)-ISOPOOH	K1	4.30 ± 0.70
	K2	4.01 ± 0.65
	K6	5.34 ± 0.89
	K8	4.23 ± 0.69
	K9	3.89 ± 0.63
		weighted mean: 4.2 ± 0.7

Table D.6: OH + ISOPOOH hydroperoxy H-abstraction rate coefficients.

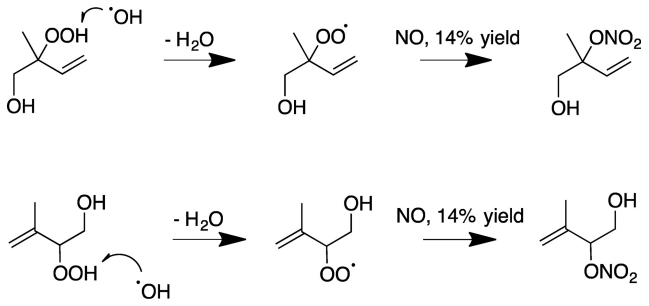

Figure D.6: Mechanism for the formation of isoprene β-hydroxynitrate (m/z = 232) from (1,2)-ISOPOOH (top) and (4,3)-ISOPOOH (bottom) following abstraction of the hydroperoxy hydrogen.

D.3.2 Products of OH Addition to (4,3)-ISOPOOH

OH addition to the internal carbon of the double bond, as well as external OH addition followed by O_2 addition to the alkyl radical, will result in products other than IEPOX. The formation of aldehydes and ketones in the high NO experiments provides a constraint on the amount of ISOPOOH that does not yield IEPOX after OH addition. A summary of these mechanisms is shown in Figures D.7 and D.8.

Following OH addition at C1 and O_2 addition at C2 of (4,3)-ISOPOOH, glycolaldehyde is expected to be produced as the primary product of the reaction of the peroxy radical with NO. Its yield will be matched by hydroxyacetone (Figure D.7). Additionally, a minor yield of five-carbon dihydroxy hydroperoxy nitrate is expected. Experiments K6, K8, and K9 were used for study of (4,3)-ISOPOOH. The glycolaldehyde and hydroxyacetone yields were corrected for production from

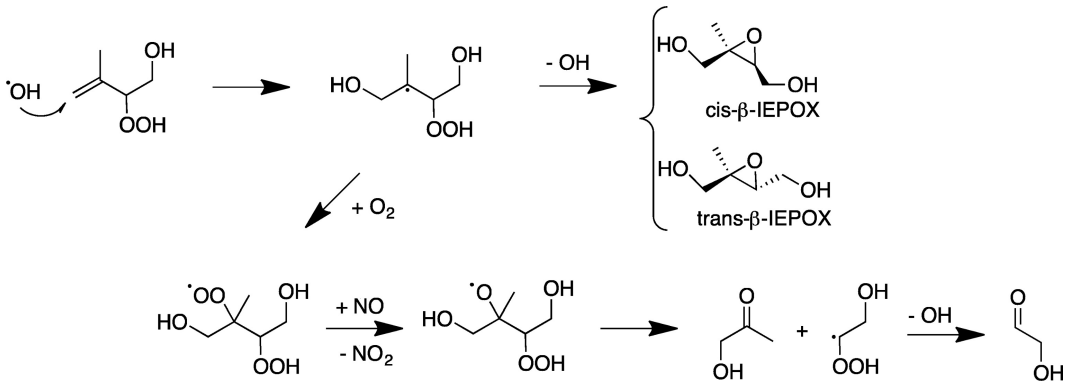

Figure D.7: External OH addition mechanism for (4,3)-ISOPOOH under high [NO]. Owing to the fast H-shift between RO_2 groups, the peroxy radical that reacts with NO may be on C3 rather than C2 as illustrated. Products will, however, be the same.

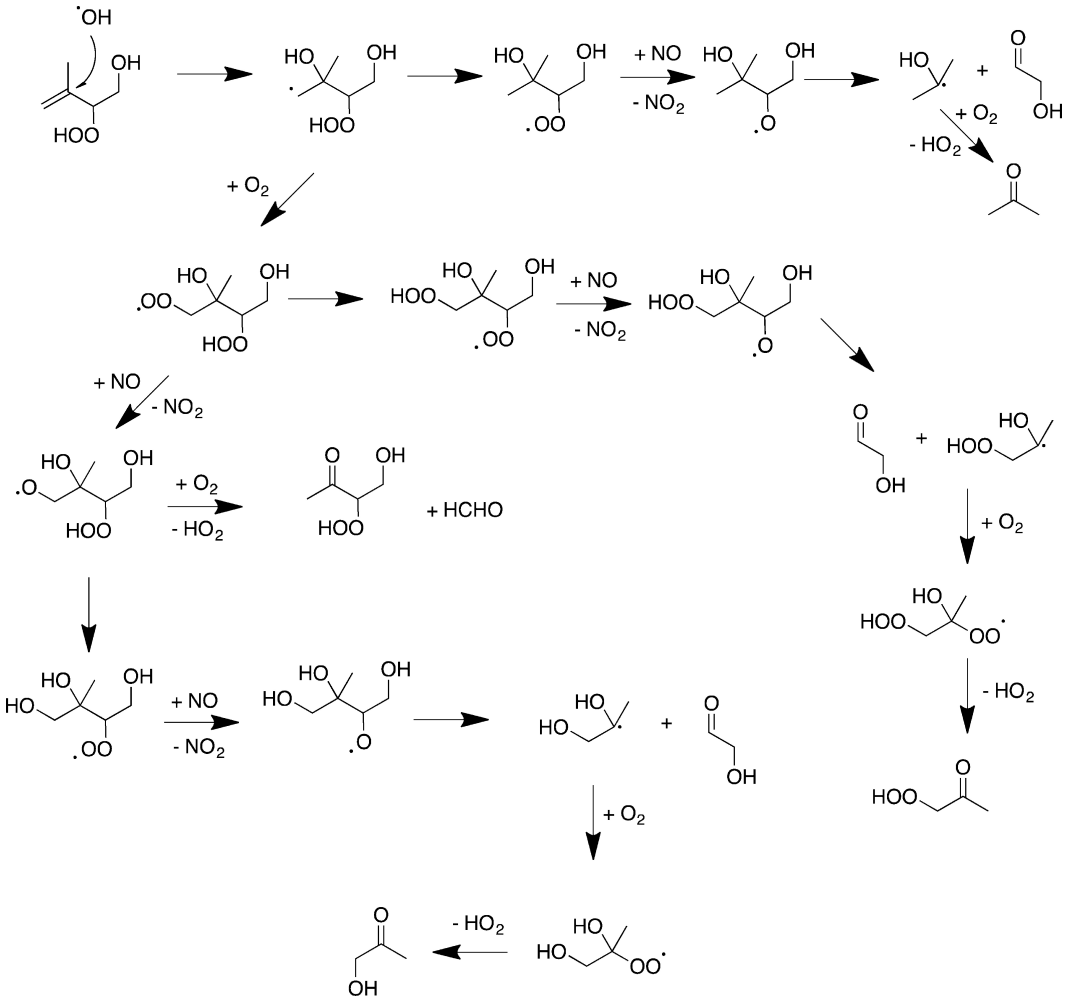

Figure D.8: Internal OH addition mechanism for (4,3)-ISOPOOH under high [NO].

the main sample impurity, the methylbutenediols described above. Synthesized methylbutenediol standards were oxidized in separate experiments under similar conditions to provide a correction factor that was then applied to the ISOPOOH experiments. The correction term was <1% yield for K8 and K9, and ~4% yield for K6. The mean glycolaldehyde yield from the high NO experiments is 14 ± 2%, and was accompanied by a hydroxyacetone yield of 13 ± 2%.

Internal addition to (4,3)-ISOPOOH is expected to be only a small fraction of the reactivity (probably equal to or less than 10% of the external addition). Thus, only a small fraction of the glycolaldehyde yield arises from this channel (Figure D.8). Because of the fast H-shift chemistry between peroxy radicals (Jørgensen *et al.*, 2016), however, this channel may be responsible for the small yield (~2%) of a three carbon hydroperoxy ketone (CF_3O^- cluster *m/z* = 175).

The total (4,3)-ISOPOOH reactivity that yields products other than IEPOX is thus 14% from OH addition and 7% from the sum of all hydrogen abstraction channels. By difference, the IEPOX yield is estimated to be 79%.

The relative amount of *cis*- and *trans*-β-IEPOX was determined using GC-ToF CIMS. The large ISOPOOH peak was removed by scaling the preoxidation chromatogram to match the height of the postoxidation ISOPOOH peak (Figures D.9 and D.10). IEPOX peaks were then fit using Gaussian curves, and the peak areas were scaled by their relative CIMS sensitivities (Bates *et al.*, 2014). The IEPOX yield was determined to be 68 ± 2% *trans*- and 32 ± 2% *cis*-β-IEPOX, assuming equal GC transmission for the two isomers and using our estimate of the relative sensitivity of the CIMS instrument to these two isomers (Bates *et al.*, 2014; Paulot *et al.*, 2009b). Without a direct measurement of the sensitivity, however, the uncertainty in the relative yields is substantially higher (70 ± 20% *trans* and 30 ± 10% *cis*).

D.3.3 Products of OH Addition to (1,2)-ISOPOOH

As was done for the (4,3)-ISOPOOH, the fraction of (1,2)-ISOPOOH that does not form IEPOX following OH addition was determined from the high NO experiments. For (1,2)-ISOPOOH, external OH addition and subsequent O_2 addition in the presence of high NO is expected to produce glycolaldehyde and hydroxyacetone as the major products (Figure D.11). For internal addition of OH (Figure D.12), production of hydroxyacetone can also be accompanied by a two-carbon hydroperoxyaldehyde (CF_3O^- cluster *m/z* = 161) *via* fast H-shift between RO_2 groups. In

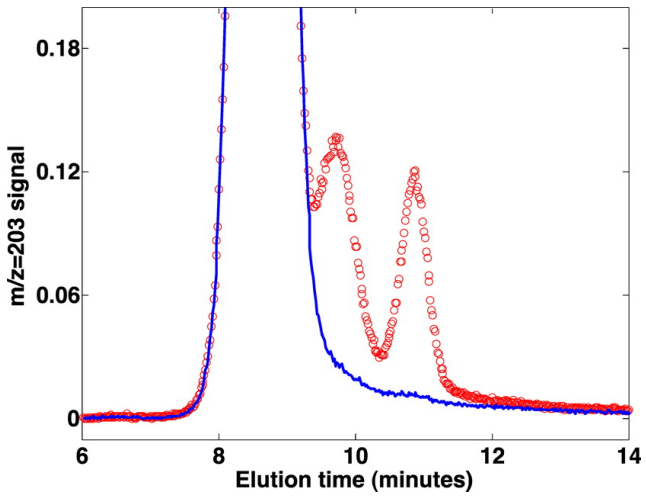

Figure D.9: Removal of the preoxidation (4,3)-ISOPOOH peak (blue line) from the postoxidation m/z = 203 GC-ToF CIMS chromatogram (red circles).

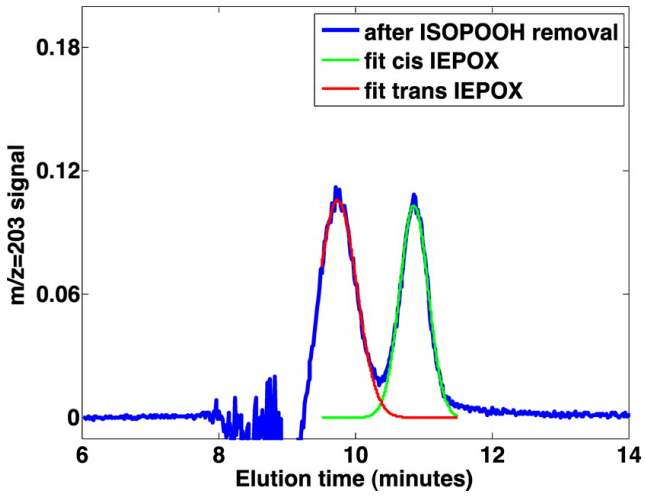

Figure D.10: Fitting the *trans*- and *cis*-β-IEPOX GC-ToF CIMS peaks after ISOPOOH removal. Because of its much higher dipole moment, the CIMS instrument is much more sensitive to the *cis* isomer.

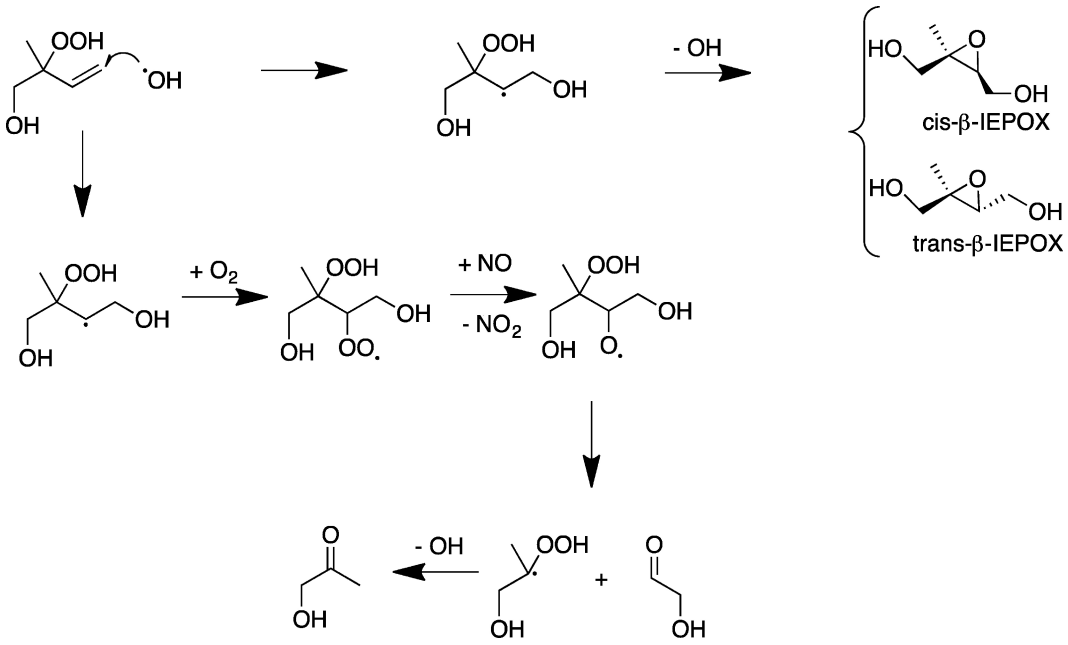

Figure D.11: External OH addition mechanism for (1,2)-ISOPOOH under high [NO]. Owing to the fast H-shift between RO_2 groups, the peroxy radical that reacts with NO may be on C2 rather than C4 as illustrated. Products will, however, be the same.

addition, a small yield of the five carbon dihydroxy hydroperoxy nitrate is expected for both the internal and external OH addition, followed by O_2 addition and NO reaction. From experiments K3, K4, K5, and K7, the hydroxyacetone yield is estimated to be 13 ± 2%. The glycolaldehyde yield is 9 ± 1%. The two-carbon hydroperoxyaldehyde yield is 3 ± 1%. As was done for (4,3)-ISOPOOH, the glycolaldehyde and hydroxyacetone yields were corrected for production from the main sample impurity (no larger than 1% yield correction for all experiments).

By adding the high NO hydroxyacetone yield (13%) to the hydrogen abstraction fraction (16%) we infer (by difference from unity) an IEPOX yield of 71% for the OH oxidation of (1,2)-ISOPOOH. The relative distribution of the two β-IEPOX was determined to be 67 ± 1% *trans* and 33 ± 1% *cis*-IEPOX using GC-ToF CIMS chromatography. The uncertainty is the standard deviation of the measurements and does not include uncertainty in the relative transmission or in the relative sensitivity of the two isomers.

Under low NO conditions, a larger number of products were observed from the oxidation of (1,2)-ISOPOOH than from (4,3)-ISOPOOH. Other than IEPOX, however, no observed product exceeded a 4% yield, and the sum of all observed products

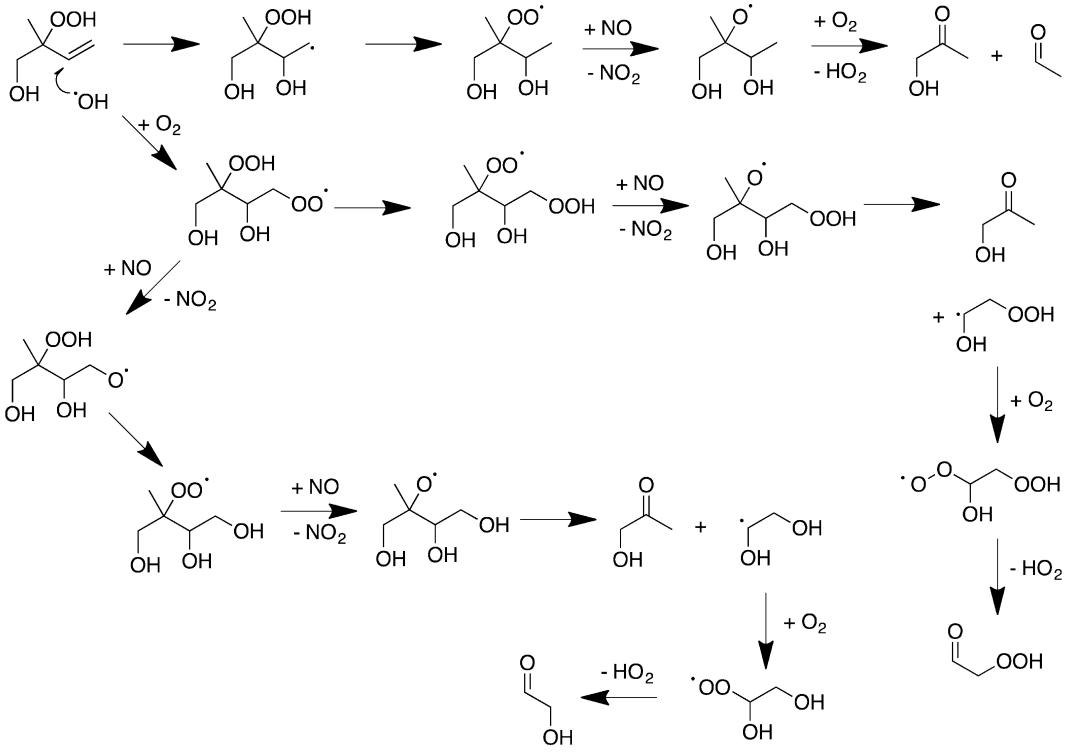

Figure D.12: Internal OH addition mechanism for (1,2)-ISOPOOH under high [NO].

equaled 12% of the ISOPOOH reacted (Table D.5). As with the (4,3)-ISOPOOH, some of the observed products are likely oxidation products of impurities. Tentatively, the *m/z* = 201 (HPALD) is thought to arise from H-abstraction α to the hydroxy, as is *m/z* = 185 (unsaturated epoxide).

Consistent with the observed formation of the C_2 hydroperoxy aldehyde in the high NO experiments, the internal OH addition to (1,2)-ISOPOOH is non-negligible. Under low NO conditions, however, this channel (as well as any non-IEPOX chemistry following addition at C4) likely forms low volatility substituted hydroperoxide products that are lost to the chamber walls and sample tubing. One likely product, a dihydroperoxydiol, would be observed at *m/z* = 253. Alternatively, ketones or aldehydes produced *via* autoxidation of the RO_2 may form. Because of either uptake on the chamber walls or fragmentation in the CF_3O^- ionization, no signal at the expected *m/z* was observed.

D.3.4 Ab Initio Calculations

Both (1,2)-ISOPOOH + OH and (4,3)-ISOPOOH + OH reactions were investigated using ab initio techniques, with the details contained in the Supporting Infor-

pathway	(4,3)-ISOPOOH	(1,2)-ISOPOOH
cis-β-IEPOX	40.1	26.7
trans-β-IEPOX	46.7	19.0
external OH, O_2 addition	8.3	10.2
internal OH, O_2 addition	1.2	29.0
OOH H-abstraction	0.9	7.2
OH H-abstraction	0.0	1.4
CH_2 H-abstraction	0.2	6.5
CH H- abstraction	2.6	N/A

Table D.7: Reaction pathway yields (%) calculated with MESMER modeling.

mation and a brief summary given here. The reactions were assumed to proceed *via* a reactive complex ISOPOOH-OH before forming a transition state and yielding the different products. The energies of the numerous structures between and including the reactants and products were calculated relative to the starting ISOPOOH + OH energy. All calculations were performed using the Gaussian 09 suite (Frisch *et al.*, 2009) with the M06-2X/aug-cc-pVTZ method (Knap *et al.*, 2015). The kinetic rate calculations were carried out using the Master Equation Solver for Multi Energy well Reaction (MESMER) (Glowacki *et al.*, 2012). The Arrhenius pre-exponential factors (A) used in MESMER were selected to best match the experimental overall addition and H- abstraction reaction rate constants for each ISOPOOH isomer. Calculated individual rate constants for each reaction channel provide estimates of product yields, including the IEPOX isomer (*cis* vs *trans*) and the dihydroperoxy diol from O_2 addition.

D.3.5 (4,3)-ISOPOOH

An abstraction rate constant of 7.2×10^{-12} cm^3 molecule^{-1} s^{-1} and an addition rate constant of 9.7×10^{-11} cm^3 molecule^{-1} s^{-1} were determined assuming A = 5.0×10^{-12} cm^3 molecule^{-1} s^{-1} and 1.5×10^{-10} cm^3 molecule^{-1} s^{-1}, for these channels, respectively. The reaction pathway yields are summarized in Table D.7.

External OH addition dominated, with 95% of the total yield, and 87% of the total yield forming IEPOX. The IEPOX yield is similar to the experimental yield, and the *trans* isomer fraction at 54% is slightly below the experimental value of 68 ± 2% but with the same preference for formation of the *trans* isomer. The O_2 addition channels from internal and external addition are calculated to be ∼10%, within the uncertainty of the experimental estimate (13 ± 4%). The hydroperoxy

hydrogen abstraction was calculated as ~1%, which is smaller than the experimental value (4%).

D.3.6 (1,2)-ISOPOOH

An abstraction rate constant of 1.2×10^{-11} cm^3 $molecule^{-1}$ s^{-1} and an addition rate constant of 6.2×10^{-11} cm^3 $molecule^{-1}$ s^{-1} were determined by using A = 1×10^{-11} cm^3 $molecule^{-1}$ s^{-1} and 6×10^{-11} cm^3 $molecule^{-1}$ s^{-1}, for these channels, respectively. The reaction pathway yields are summarized in Table D.7. The abstraction reactions account for 15% (with 7% attributed to abstraction of the hydroperoxy hydrogen) compared to 12% from the experimental data. The addition channels exhibit a bigger difference between the calculated and experimental yields. The calculated yield of IEPOX is 46%. Following either internal or external OH addition, 39% proceeds *via* O_2 addition. Assuming that O_2 addition ultimately yields hydroxyacetone under high NO conditions, the experimental data suggest the O_2 addition channels account for less than half of the calculated yield. The IEPOX isomer yield is notably different for the calculations compared to the experimental data: in the calculations, the *cis* isomer is preferred (58% of total IEPOX) while the experimental results suggest the *trans* isomer is preferred at 67 ± 1% of the total IEPOX.

D.3.7 Atmospheric Implications

The global impact of recent changes to the HO_2-dominated pathway of the isoprene oxidation mechanism were investigated using the GEOS-Chem chemical transport model (Bey *et al.*, 2001). Three sets of simulations were run for the year 2012 with a model spin-up of 1.5 years. All three simulations employed version 9.02 of GEOS-Chem on a 4×5 degree grid, with GEOS5 meteorology and the Rosenbrock Rodas-3 solver.

The first simulation used the isoprene mechanism in the current GEOS-Chem version (v9-02) (Mao *et al.*, 2013), hereafter referred to as "Standard". The second simulation, denoted "Old", restored the HO_2-dominated pathway of the isoprene oxidation mechanism to that of Paulot *et al.* (2009b) The "Standard" and "Old" simulations differed only in their ISOPOOH H-abstraction rate constant and ISOPOO recycling yield, and in their HO_2 + RO_2 rate constant: the "Standard" used k = $2.91 \times 10^{-13} \times e^{(1300/T)} \times [1 - e^{(-0.245 \times n)}]$ (Jenkin *et al.*, 1997; Saunders *et al.*, 2003) and the "Old" used k = $7.4 \times 10^{-13} \times e^{(700/T)}$ (Paulot *et al.*, 2009b). The third simulation updated the mechanism with the results from this study and that of Bates *et al.* (2014)

mechanisms:	old[a]	standard	recommended
ISOPOOH produced (Tg C/y)	129	168	181
IEPOX produced (Tg C/y)	94	122	115

[a] Paulot *et al.* (2009b)

Table D.8: Yearly ISOPOOH and IEPOX production for three GEOS-Chem simulations with differing isoprene oxidation mechanisms. Global isoprene emissions are 454 Tg C each year in all simulations

as well as an ISOPOOH yield of 94% from HO_2 + ISOPOO (Liu *et al.*, 2013) and a speciated ISOPOOH and IEPOX distribution to utilize the isomer-specific reaction rate constants and product yields (see Supporting Information). The third simulation is referred to as "Recommended".

The increase in the $HO_2 + RO_2$ rate constant had the largest effect on the ISOPOOH and IEPOX produced, with the annual production of both species 30% higher in the "Standard" run than the "Old" run (Table D.8). From the "Standard" to the "Recommended" simulation, the ISOPOOH yield from $HO_2 + RO_2$ increased but so did the ISOPOOH + OH rate constant, resulting in a net 8% increase in ISOPOOH. Despite a lower OH + IEPOX rate constant, the IEPOX decreased by 9% due to the lower IEPOX yield from the OH addition to ISOPOOH in the "Recommended" simulation.

isoprene emissions for all simulations were 454 Tg C y^{-1}, resulting in 115 Tg C y^{-1} of IEPOX in the "Recommended" run, about 20 Tg C y^{-1} higher than in the "Old" simulation. The global average distribution for IEPOX in the "Recommended" simulation is shown in Figure D.13 for northern hemisphere summer (JJA) and winter (DJF). The highest IEPOX concentrations for both seasons appear in the Southern Hemisphere (South America and Africa), though in the Northern Hemisphere summer significant IEPOX is produced in the Southeastern United States and in the boreal forests.

D.3.8 isoprene Hydroxynitrates as an IEPOX Source

Two recent laboratory studies have demonstrated a path to IEPOX formation from oxidation of isoprene by OH under NO-dominated conditions, *via* OH addition to isoprene hydroxynitrates (ISOPN) (Jacobs *et al.*, 2014; Lee *et al.*, 2014). Data from both studies are consistent with an IEPOX yield of 12-13% from the (4,3)-ISOPN. From the experiments described by Lee *et al.* (2014) we estimate the combined

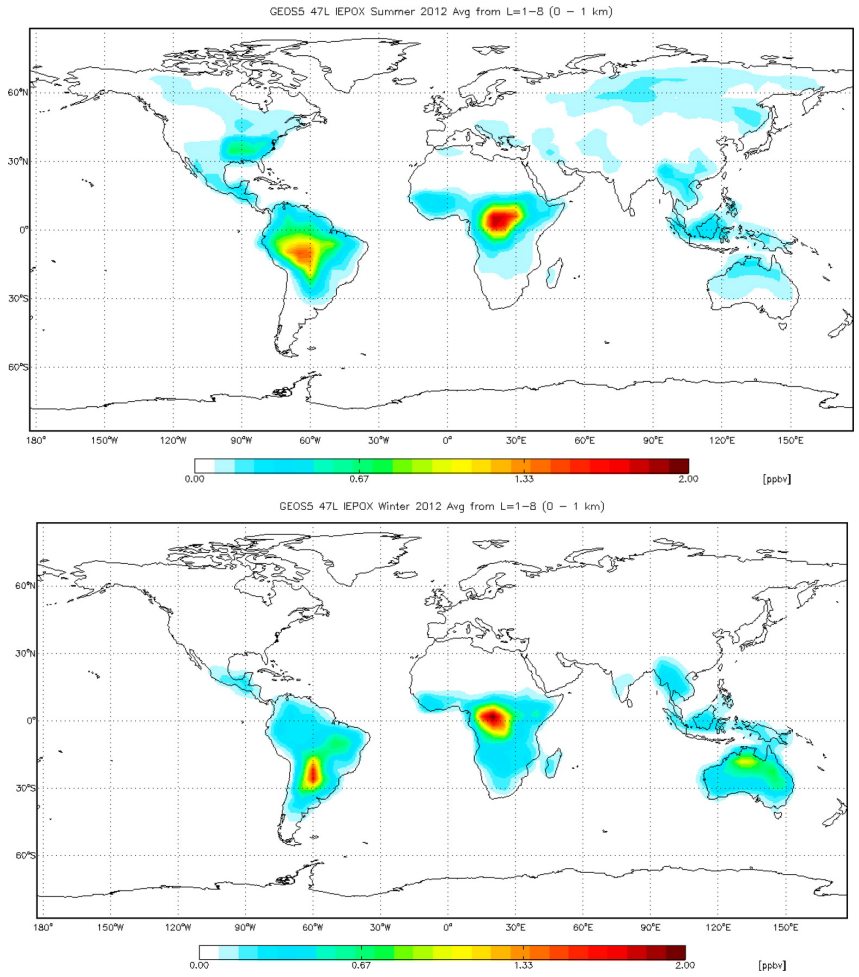

Figure D.13: Average distribution for IEPOX during northern hemisphere summer (top) and winter (bottom) using GEOS-Chem with an updated isoprene mechanism.

yield of IEPOX from the two β ISOPN to be 15 ± 3%. To evaluate the atmospheric importance of this channel to the global IEPOX budget, an upper limit IEPOX yield of 18% was implemented for a GEOS-Chem simulation with all other input identical to the "Recommended" simulation. The global IEPOX production changed from 115 to 116 Tg C y^{-1}, suggesting that the ISOPN channel contributes only ~1% to the total IEPOX production.

D.3.9 Formation of Low Volatility Compounds Other than IEPOX

Following addition of OH to ISOPOOH, our experiments suggest that a number of low volatile products including dihydroperoxydiols, aldehydes, and ketones will form in low NO environments. Assuming these channels together account for ~15% of the products of the OH addition to ISOPOOH, approximately 20 Tg C of low

volatility hydroperoxide compounds are formed each year globally. While these compounds will likely add to the organic aerosol burden, their lifetimes may be short due to photolysis and subsequent fragmentation. Recent laboratory and field observations (Krechmer *et al.*, 2015; Nguyen *et al.*, 2014b) provide evidence for the importance of this chemistry and suggest further study to place the atmospheric mechanistic pathways involved on a more firm footing.

D.4 Conclusions

The photochemistry of ISOPOOH is central to the oxidation of isoprene under HO_2-dominated conditions. Synthetic standards of the two major ISOPOOH isomers, (1,2)-ISOPOOH and (4,3)-ISOPOOH, enabled the direct and isomer-specific measurement of ISOPOOH + OH product yields and reaction rate constants relative to propene. The isomer-averaged OH addition rate coefficient was similar to a previous estimate while the H-abstraction rate coefficient was faster (Paulot *et al.*, 2009b). The rate constants for OH reaction with the two ISOPOOH are sufficiently different that the overall ISOPOOH loss rate to OH will be affected by the relative production rates of the ISOPOOH isomers, which in turn are determined by the isoprene RO_2 distribution.

IEPOX is the major product of this chemistry. The *cis*- and *trans*-β-IEPOX relative product distribution was similar from the two ISOPOOH isomers and was also similar to the previous estimate (Bates *et al.*, 2014). The total IEPOX yield, however, was estimated to differ somewhat between the two ISOPOOH due to the larger importance of internal OH addition to the (1,2)-ISOPOOH.

Because the two IEPOX isomers differ in their OH reaction rates, the unequal isomer distribution affects the overall IEPOX loss rate to OH reaction, with the observed distribution reacting 8% slower than an equal distribution (Bates *et al.*, 2014). Organic aerosol formation studies with synthesized IEPOX standards suggest little or no difference in aerosol formation between the two IEPOX isomers (Nguyen *et al.*, 2014a). Any difference in aerosol formation between the two isomers in the atmosphere would instead be due to the difference in their OH lifetimes causing more *trans*-β-IEPOX to be available for uptake.

Finally, a non-negligible fraction of the ISOPOOH oxidation likely leads to the formation of highly oxidized five carbon peroxy radicals. Under low NO or long RO_2 lifetimes, these channels will likely yield very low vapor pressure compounds that contribute to aerosol formation.

D.5 Supporting Information

D.5.1 CIMS Sensitivities

CIMS sensitivities to the oxidation products were determined in multiple ways. Hydroxyacetone and glycolaldehyde are commercially available and were quantified gravimetrically and by Fourier transform Infrared Spectroscopy (FT-IR) for CIMS calibration (St. Clair *et al.*, 2014). Uncalibrated compounds (glycolic acid and all products identified by *m/z*) were assigned a generic CIMS sensitivity of 2.5×10^{-4} ncts /pptv, and are considered accurate to within a factor of 2. Here, normalized counts (ncts) represent the counts observed at the analyte *m/z* divided by the reagent ion counts. The reagent ion counts are the sum of the signal at *m/z* = 86 ($^{13}CF_3O^-$) and *m/z* = 104 ($^{13}CF_3O^-\cdot H_2O$), as well as *m/z* = 120 ($^{13}CF_3O^-\cdot H_2O_2$) for experiments with H_2O_2 as the OH source.

The sensitivities for ISOPOOH and IEPOX were obtained by matching the output of a box model to a laboratory isoprene + OH oxidation under low NO conditions. The sensitivity is therefore dependent on the box model chemistry, including the yield of ISOPOOH from isoprene (0.94) and the yield of IEPOX from ISOPOOH (0.8). The ISOPOOH yield used was based on a 6% yield of methyl vinyl ketone and methacrolein (Liu *et al.*, 2013), and the IEPOX yield used was 80%, in general agreement with the sum of the nonIEPOX products observed by the CIMS in this study. ToF-CIMS sensitivities for ISOPOOH and IEPOX were 1.6×10^{-4} ncts pptv^{-1} and 1.9×10^{-4} ncts pptv^{-1}, respectively. For the TQ-CIMS, the MSMS sensitivities were 5.1×10^{-6} ncts pptv^{-1} and 3.9×10^{-6} ncts pptv^{-1} for ISOPOOH and IEPOX, respectively. The CIMS sensitivity to ISOPOOH was also verified gravimetrically by completely evaporating a known mass of the pure compound into a known volume of dry air. For the (4,3)-ISOPOOH, the sample evaporated completely and gave a sensitivity of 1.6×10^{-4} ncts pptv^{-1}. The (1,2)-ISOPOOH gave a sensitivity of 1.5×10^{-4} ncts pptv^{-1} but with a slight residual mass, and 1.6×10^{-4} ncts pptv^{-1} was determined appropriate for both isomers.

D.5.2 Impurity Oxidation Products

The main impurities in the ISOPOOH samples, 2-methyl-1-butene-3,4-diol for (4,3)-ISOPOOH and 3-methyl-1-butene-3,4-diol for (1,2)-ISOPOOH, also react with OH to produce some of the same product masses as ISOPOOH. To correct for the impurity oxidation products, both methylbutanediols were synthesized and each was oxidized by OH under similar conditions to the ISOPOOH experiments. The ratio of the product formation to methylbutanediol loss was then used to remove

the methylbutanediol products from the ISOPOOH experiment data.

D.5.3 Ab Initio Calculations

We used the M06-2X/aug-cc-pVTZ method as implemented in the Gaussian 09 program (Frisch *et al.*, 2009). Frequency calculations were done at all stationary points with the same method to ensure that the equilibrium structures (reactants, reactive complexes, products) only have positive vibrational frequencies and the transition states have one imaginary frequency. To ensure that the transition state connects the reactive complex and the product, intrinsic reaction coordinate (IRC) calculations were performed and, if needed, the end product was optimized (Gonzalez and Schlegel, 1989, 1990). None of the M06-2X/aug-ccpVTZ calculations have any significant spin contamination. Single point energy CCSD(T)-F12a/VDZ-F12 [F12] calculations were performed on the M06-2X/aug-ccpVTZ geometries (Adler *et al.*, 2007; Peterson *et al.*, 2008). All the CCSD(T) calculations were carried out with the Molpro2012 program suite using default convergence criteria (Werner *et al.*, 2012). High T1-diagnostic values were observed for H-abstraction from the OH group, and we have therefore used the M06-2X/aug-cc-pVTZ energies for Mesmer modeling. High T1-diagnostic values have been observed previously for H-shift from OH groups (Knap *et al.*, 2015; Peeters and Nguyen, 2012). For OH addition and H-abstraction involving -CH_2 and >CH groups, the M06-2X/aug-cc-pVTZ energies of the reactant complex and the transition state are in good agreement with the CCSD(T)-F12A/VDZF12 energies. The M06-2X/aug-cc-pVTZ (and wb97-XD) method has also previously been found to calculate barrier heights similar to those obtained with the much more computationally expensive CCSD(T)-F12A/VD2-F12 single point calculations on the DFT geometry (Knap *et al.*, 2015). In the following we are therefore using the M06-2X/aug-cc-pVTZ energies for kinetic modeling.

D.5.3.1 The energetics of the reaction between ISOPOOH and OH

We have assumed that the association reaction between OH and ISOPOOH produces a reactive complex (ISOPOOH-OH). The reactive complex can hereafter overcome the transition state and produce the different product complexes and products.

OH + ISOPOOH → ISOPOOH-OH → Products

In Figures D.14 and D.15 the different reaction pathways for (1,2)-ISOPOOH and (4,3)-ISOPOOH are shown, respectively, and the energetics of the reaction pathways are given in Tables D.9 and D.10. The reactant complexes for each of the individual

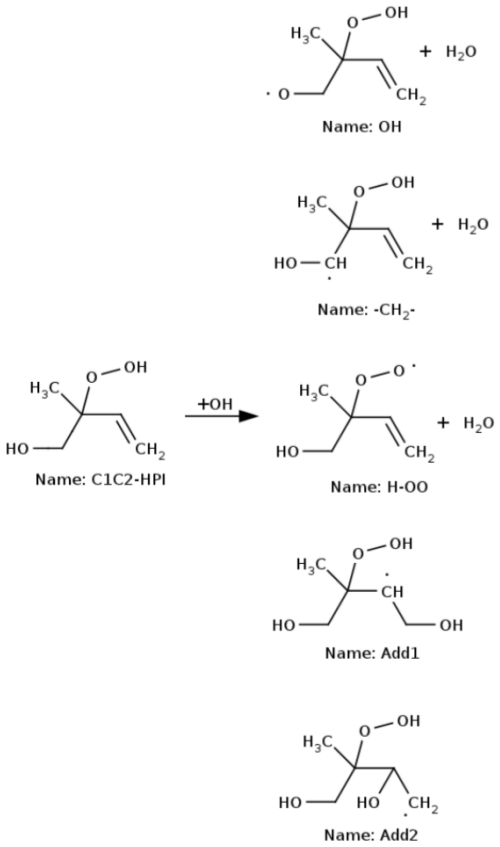

Figure D.14: The different reaction pathways for the reaction between (1,2)-ISOPOOH and the OH radical.

reaction paths are different.

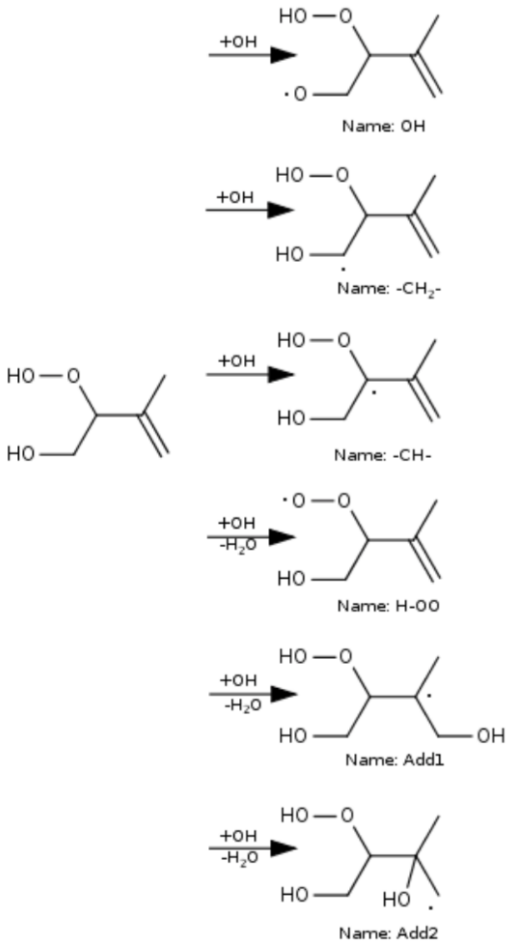

Figure D.15: The different reaction pathways for the reaction between (4,3)-ISOPOOH and the OH radical.

	OH	-CH_2-	H-OO	Add1	Add2
(1,2)-ISOPOOH+OH	0.0	0.0	0.0	0.0	0.0
Reactive Complex	-8.9 (-8.3)	-7.3 (-6.1)	-5.0 (-3.7)	-6.2 (-6.1)	-7.8 (-6.2)
Transition State	-2.2 (-1.0[a])	-4.0 (-3.5)	-3.8 (-3.3)	-5.3 (-5.2)	-5.6 (-5.4)
Product Complex	-21.8 (-20.9)	-34.0 (-33.0)	-40.8 (-40.2)	-	-
Product	-13.8 (-8.7)	-24.2 (-23.5)	-34.7 (-34.4)	-34.4 (-31.1)	-33.4 (-30.0)

Table D.9: The relative energies (kcal mol^{-1}) for the reaction between the (1,2)-ISOPOOH molecule and the OH radical with the M06-2X/aug-cc-pVTZ method and the F12//M06- 2X/aug-cc-pVTZ. The values in () are the F12//M06-2X/aug-cc-pVTZ values. The energies are corrected with zero point vibrational energies. The marked calculation ([a]) has a T1 diagnostic value of 0.078.

	OH	-CH_2-	-CH-	H-OO	Add1	Add2
(4,3)-ISOPOOH+OH	0.0	0.0	0.0	0.0	0.0	0.0
Reactive Complex	-6.2 (-5.3)	-6.8 (-6.2)	-6.4 (-4.9)	-5.7 (-4.4)	-7.7 (-6.5)	-5.8 (-4.3)
Transition State	-0.4 (25.6[a])	-1.7 (-1.3)	-4.8 (-4.5)	-2.8 (-1.5[b])	-7.7 (-7.0)	-2.7 (-5.1)
Product Complex	-19.4 (-18.1)	-30.6 (-29.2)	-43.0 (-41.3)	-36.0 (-35.1)	-	-
Product	-10.8 (-9.7)	-23.2 (-22.5)	-33.9 (-34.2)	-33.4 (-33.2)	-34.9 (-31.7)	-31.2 (-28.7)

Table D.10: The relative energies (kcal mol^{-1}) for the reaction between (4,3)-ISOPOOH and OH with the M06-2X/aug-cc-pVTZ method and the F12//M06-2X/aug-cc-pVTZ. The values in () are the F12//M06-2X/aug-cc-pVTZ values.. The energies are corrected with zero point vibrational energies. Marked calculations have T1 diagnostic values of [a]0.116 and [b]0.058.

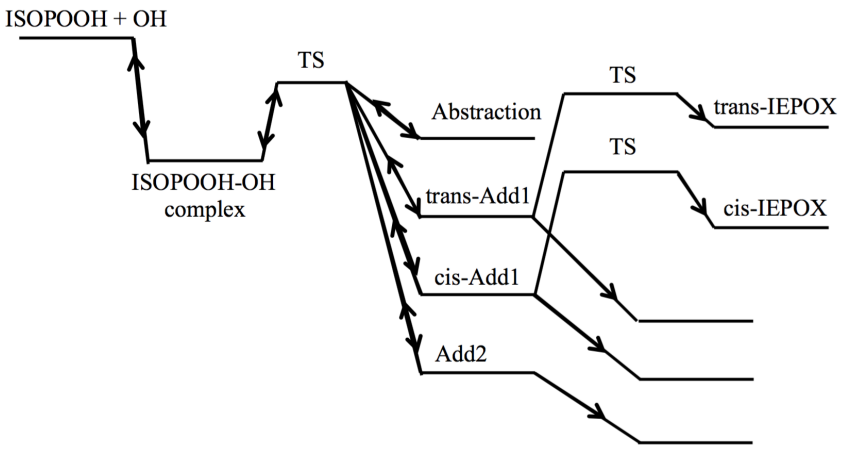

Figure D.16: The reaction scheme as used in the MESMER model (Only an illustration, not the energetically correct picture of the reactions). The ISOPOOH-OH complexes are different for each of the reaction pathways even though they are given with the same energy at this figure.

D.5.3.2 The kinetics of the reaction between ISOPOOH and OH

The kinetic calculations are carried out using the master equation solver for multi energy well reaction, MESMER program (Glowacki *et al.*, 2012). The general reaction scheme is shown in Figure D.16.

In our Mesmer modeling the Lennard-Jones (L-J) parameters of the bath gas were chosen to be a nitrogen gas resembling the atmospheric gas (σ (N_2) = 3.919 Å, ϵ/k_b (N_2) = 91.85 K) whereas the reactive complex (ISOPOOH-OH) is modeled with the L-J parameters of methylcyclohexane (σ (methylcyclohexane) = 7.045 Å, ϵ/k_b (methylcyclohexane) = 379.95 K) (Cuadros *et al.*, 1996). The average collisional activation/deactivation energy transfer of all the molecules is set to 200 cm^{-1} per collision and the grain size of each grain is 50 cm^{-1}. The span of the energy grains is set to 30 kT above the highest stationary point. We have used a pressure of 745 Torr and a temperature of 298 K for all the calculations, similar to the experimental conditions.

We have performed a sensitivity test of Mesmer input parameters. In our sensitivity test we used three collisional activation/deactivation energies of 50, 100 and 200 cm^{-1} and two different grain sizes of 25 and 50 cm^{-1}. We did not observe any significant changes in the reaction rate constants (only changes of a few percent). We have also tested the system with different sizes of grain span, *e.g.*, 10 kT, 20 kT, 30 kT, 40 kT, and 50 kT. If a grain span of 30 kT or higher is used, the reaction rate

constants do not change. We have therefore used a grain size of 30 kT.

The reaction rate constants are sensitive to the choice of the Arrhenius pre-exponential factor (A). Each reaction pathway is a separate Mesmer calculation (See Figures D.17 and D.18 for the individual reaction pathways) – we have not coupled between the reactions in the fitting of the Arrhenius pre-exponential factor (A). We treat the pre-exponential factor as temperature independent and it is varied between 1.0×10^{-12} and 2.0×10^{-10} cm^3 $molecule^{-1}$ s^{-1}. We use nine different Arrhenius pre-exponential factors to calculate the rates. Three of the factors are from the three reactions of n-butane, 3-methyl-3-butene-1-ol and 1-butene with OH (Atkinson and Arey, 2003a; Cometto *et al.*, 2008; Vakhtin *et al.*, 2003). The total reaction rate constants (OH +ISOPOOH $\rightarrow$ Products) of the (1,2)-ISOPOOH and (4,3)-ISOPOOH systems are shown in Table D.11 and Table D.12, respectively.

reaction	A($1\cdot10^{-12}$)[a]	A($2\cdot10^{-12}$)	A($5\cdot10^{-12}$)[b]	A($1\cdot10^{-11}$)	A($3\cdot10^{-11}$)[c]	A($6\cdot10^{-11}$)	A($1\cdot10^{-10}$)	A($1.5\cdot10^{-10}$)	A($2\cdot10^{-10}$)	Mix
OH	$3.3\cdot10^{-13}$ (8.3)	$4.7\cdot10^{-13}$ (6.4)	$6.8\cdot10^{-13}$ (4.2)	$8.2\cdot10^{-13}$ (3.0)	$1.0\cdot10^{-12}$ (1.7)	$1.1\cdot10^{-12}$ (1.2)	$1.2\cdot10^{-12}$ (1.0)	$1.2\cdot10^{-12}$ (0.8)	$1.2\cdot10^{-12}$ (0.8)	$8.2\cdot10^{-13}$ (1.1)
-CH_2-	$8.6\cdot10^{-13}$ (21.8)	$1.6\cdot10^{-12}$ (21.4)	$3.2\cdot10^{-12}$ (20.2)	$5.2\cdot10^{-12}$ (18.7)	$9.2\cdot10^{-12}$ (15.5)	$1.2\cdot10^{-11}$ (13.5)	$1.4\cdot10^{-11}$ (12.1)	$1.6\cdot10^{-11}$ (11.0)	$1.7\cdot10^{-11}$ (10.4)	$5.2\cdot10^{-12}$ (7.0)
H-OO	$9.0\cdot10^{-13}$ (22.8)	$1.7\cdot10^{-12}$ (22.8)	$3.6\cdot10^{-12}$ (22.3)	$5.8\cdot10^{-12}$ (21.2)	$1.1\cdot10^{-11}$ (18.3)	$1.4\cdot10^{-11}$ (16.1)	$1.7\cdot10^{-11}$ (14.3)	$1.9\cdot10^{-11}$ (13.2)	$2.0\cdot10^{-11}$ (12.4)	$5.8\cdot10^{-12}$ (7.9)
Add1 (C1)	$9.8\cdot10^{-13}$ (24.9)	$1.9\cdot10^{-12}$ (26.3)	$4.7\cdot10^{-12}$ (29.3)	$9.0\cdot10^{-12}$ (32.6)	$2.3\cdot10^{-11}$ (39.4)	$4.0\cdot10^{-11}$ (44.3)	$5.6\cdot10^{-11}$ (48.0)	$7.2\cdot10^{-11}$ (50.6)	$8.5\cdot10^{-11}$ (52.4)	$4.0\cdot10^{-11}$ (53.7)
Add2 (C2)	$8.8\cdot10^{-13}$ (22.3)	$1.7\cdot10^{-12}$ (23.0)	$3.8\cdot10^{-12}$ (24.0)	$6.8\cdot10^{-12}$ (24.6)	$1.5\cdot10^{-11}$ (25.1)	$2.2\cdot10^{-11}$ (24.9)	$2.9\cdot10^{-11}$ (24.6)	$3.5\cdot10^{-11}$ (24.3)	$3.9\cdot10^{-11}$ (24.0)	$2.2\cdot10^{-11}$ (30.2)

Table D.11: The reaction rate constants at 298K (in cm^3 $molecules^{-1}$ s^{-1}) for the reaction between the (1,2)-ISOPOOH molecule and the OH radical with the M06-2X/aug-cc-pVTZ method. All the reaction rates are without tunneling correction. In () are the yields in percent. The ratios are calculated as Γ_i=k_i/k_{tot} ×100%, where $k_{tot} = \Sigma k_i$. In the Mix column, the addition and the abstraction reactions use an Arrhenius value of $6\cdot10^{-11}$ and $1\cdot10^{-11}$ cm^3 $molecule^{-1}$ s^{-1}, respectively. Marked preexponential factors are from [a]an OH reaction with n-butane (Abstraction) [3], [b] the reaction of OH with 3-methyl-3-buten-1-ol (Addition and Abstraction)[4], and [c]OH and 1-butene (Addition)[5].

reaction	A($1\cdot10^{-12}$)[a]	A($2\cdot10^{-12}$)	A($5\cdot10^{-12}$)[b]	A($1\cdot10^{-11}$)	A($3\cdot10^{-11}$)[c]	A($6\cdot10^{-11}$)	A($1\cdot10^{-10}$)	A($1.5\cdot10^{-10}$)	A($2\cdot10^{-10}$)	Mix
OH	7.1·10-14 (1.2)	7.7·10-14 (1.2)	8.1·10-14 (0.6)	8.2·10-14 (0.4)	8.4·10-14 (0.2)	8.5·10-14 (0.1)	8.5·10-14 (0.1)	8.5·10-14 (0.1)	8.5·10-14 (0.0)	8.1·10-14 (0.1)
-CH_2-	$3.1\cdot10^{-13}$ (6.8)	$4.2\cdot10^{-13}$ (6.8)	$5.5\cdot10^{-13}$ (4.4)	$6.3\cdot10^{-13}$ (3.0)	$7.2\cdot10^{-13}$ (1.6)	$7.7\cdot10^{-13}$ (1.0)	$7.9\cdot10^{-13}$ (0.7)	$8.0\cdot10^{-13}$ (0.6)	$8.1\cdot10^{-13}$ (0.5)	$5.5\cdot10^{-13}$ (0.5)
-CH-	$9.3\cdot10^{-13}$ (29.3)	$1.8\cdot10^{-12}$ (29.3)	$4.1\cdot10^{-12}$ (33.3)	$7.4\cdot10^{-12}$ (35.7)	$1.7\cdot10^{-11}$ (36.3)	$2.5\cdot10^{-11}$ (33.6)	$3.2\cdot10^{-11}$ (30.3)	$3.9\cdot10^{-11}$ (27.2)	$4.4\cdot10^{-11}$ (24.9)	$4.1\cdot10^{-12}$ (4.0)
H-OO	$7.9\cdot10^{-13}$ (21.8)	$1.3\cdot10^{-12}$ (21.8)	$2.4\cdot10^{-12}$ (19.1)	$3.3\cdot10^{-12}$ (15.9)	$4.8\cdot10^{-12}$ (10.5)	$5.5\cdot10^{-12}$ (7.4)	$6.0\cdot10^{-12}$ (5.6)	$6.3\cdot10^{-12}$ (4.4)	$6.5\cdot10^{-12}$ (3.7)	$2.4\cdot10^{-12}$ (2.3)
Add1 (C1)	$6.9\cdot10^{-13}$ (22.3)	$1.4\cdot10^{-12}$ (22.3)	$3.4\cdot10^{-12}$ (27.4)	$6.8\cdot10^{-12}$ (32.7)	$2.0\cdot10^{-11}$ (44.0)	$3.9\cdot10^{-11}$ (52.7)	$6.4\cdot10^{-11}$ (59.4)	$9.2\cdot10^{-11}$ (64.7)	$1.2\cdot10^{-10}$ (68.3)	$9.2\cdot10^{-11}$ (89.0)
Add2 (C2)	$7.0\cdot10^{-13}$ (18.5)	$1.1\cdot10^{-12}$ (18.5)	$1.9\cdot10^{-12}$ (15.2)	$2.5\cdot10^{-12}$ (12.1)	$3.4\cdot10^{-12}$ (7.5)	$3.8\cdot10^{-12}$ (5.2)	$4.1\cdot10^{-12}$ (3.8)	$4.3\cdot10^{-12}$ (3.0)	$4.4\cdot10^{-12}$ (2.5)	$4.3\cdot10^{-12}$ (4.1)

Table D.12: The absolute reaction rates at 298K in units of cm^3 $molecules^{-1}$ s^{-1} for the OH radical reaction with the (4,3)-ISOPOOH molecule with the M06-2X/aug-cc-pVTZ method. All the reaction rates are without tunneling correction. In () are the ratios of the different OH and (4,3)-ISOPOOH reactions shown. The ratios are calculated as Γ_i=k_i/k_{tot} ×100%, where $k_{tot} = \Sigma k_i$. In the Mix column, the addition and the abstraction reactions use an Arrhenius value of $1.5\cdot10^{-10}$ and $5\cdot10^{-12}$ cm^3 $molecule^{-1}$ s^{-1}, respectively. Marked preexponential factors are from [a]an OH reaction with n-butane (Abstraction) [3], [b] the reaction of OH with 3-methyl-3-buten-1-ol (Addition and Abstraction)[4], and [c]OH and 1-butene (Addition)[5].

D.5.3.3 (1,2)-ISOPOOH

For the (1,2)-ISOPOOH + OH reactions, the absolute rate constants of all the different reaction pathways increase with an increase in the Arrhenius pre-exponential factor, and the relative yields (in %) of the reaction pathways also change. The yield of the two addition reactions increased more compared to yield of the three abstraction reaction pathways with increasing Arrhenius pre-exponential factor. The rate constant is sensitive to the Arrhenius pre-exponential factor since the energy of the transition state is below the energy of the individual reactants. The rate constant for each reaction path is therefore almost identical to the Arrhenius pre-exponential factor.

With an Arrhenius pre-exponential factor of 1×10^{-11} cm^3 molecule^{-1} s^{-1} for the OH abstraction reactions and 6×10^{-11} cm^3 molecule^{-1} s^{-1} for the addition reactions (see Mix column, Table D.11), the yield of the (1,2)-ISOPOOH + OH reactions is OH (1.1), -CH_2- (7.0), H-OO (7.9), Add1 (53.7), and Add2 (30.2). The rate constant for abstraction is 1.2×10^{-11} cm^3 molecule^{-1} s^{-1} and the rate constant for addition is 6.2×10^{-11} cm^3 molecule^{-1} s^{-1}. The sum of the OH addition and OH abstraction rate constants are 7.4×10^{-11} cm^3 molecule^{-1} s^{-1}, and was constrained to mimic the experimentally determined rate.

D.5.3.4 (4,3)-ISOPOOH

With an Arrhenius pre-exponential factor of 5×10^{-12} cm^3 molecule^{-1} s^{-1} for the OH abstraction reactions and 1.5×10^{-10} cm^3 molecule^{-1} s^{-1} for the addition reactions (see Mix column, Table D.12), the yield of the (4,3)-ISOPOOH + OH reactions is OH (0.1), -CH_2- (0.5), -CH- (4.0), H-OO (2.3), Add1 (89.0), and Add2 (4.1). The rate constant for abstraction is 7.2×10^{-12} cm^3 molecule^{-1} s^{-1} and the rate constant for addition is 9.7×10^{-11} cm^3 molecule^{-1} s^{-1}. The sum of these, 1.1×10^{-10} cm^3 molecule^{-1} s^{-1}, was constrained to mimic the experimentally determined rate.

D.5.3.5 IEPOX production

The formation of *cis*-β-IEPOX (*cis*-C_1C_2), the product of the addition to C1 in (1,2)-ISOPOOH, has a rate constant (the "energetically cold" reaction rate constant) which is three times faster than the rate constant for the formation of *trans*-β-IEPOX (trans-C_1C_2). The *trans*-β-IEPOX (trans-C_4C_3) rate is faster than the *cis*-β-IEPOX (*cis*-C_4C_3) production rate in the (4,3)-ISOPOOH+OH reaction. The *trans*-C_4C_3 rate constant is fastest because of a lower transition state barrier. The differences

Species	ΔE forward / (kcal mol^{-1})	k$_{TST}$ / (s^{-1})	k$_{TST\cdot\kappa_{Eckart}}$ / (s^{-1})
cis-C_1C_2	12.8	3.7×10^3	9.2×10^3
trans-C_1C_2	12.8	1.1×10^3	2.8×10^3
cis-C_4C_3	12.4	2.1×10^3	4.9×10^3
trans-C_4C_3	10.6	3.5×10^4	7.4×10^4

Table D.13: The energy barriers, transition state theory (TST) reaction rate constants and the Eckart-corrected TST reaction rate constants for the production of IEPOX. The energies are calculated with the M06-2X/aug-cc-pVTZ method.

between the reaction rate constants of the *cis*/trans-C_1C_2 isomers are due to changes in the vibrational partition functions (Table D.13).

We have used the bimolecular reaction rate constant obtained by Park *et al.* (2004), 2.3×10^{-12} cm^3 molecule^{-1} s^{-1} for the reaction between molecular oxygen and OH-isoprene, to represent the bimolecular reaction between our OH addition products and molecular oxygen. With the Park *et al.* (2004) reaction rate constant and a molecular oxygen concentration of 5.2×10^{18} molecule cm^{-3} the pseudo-first order reaction rate becomes 1.2×10^7 s^{-1}.

The "cold" reaction rate constants are estimated using transition state theory including the quantum tunneling given by

$$k_{TST} = \frac{k_B T}{h} \times \frac{Q_{TS}}{Q_R} \times e^{-\Delta E / k_B T} \tag{D.1}$$

where Q_R and Q_{TS} are the partition functions for the reactant, R, and the transition state, TS, respectively (Henriksen and Hansen, 2008). The rigid rotor and harmonic oscillator approximations have been used to calculate the partition functions. The energy ΔE is the energy difference between the transition state and the reactant. The constants, h and k_B, are the Planck constant and the Boltzmann constant, respectively. Tunneling was done with the Eckart approach (Eckart, 1930). The "cold" TST reaction rate constants are all much slower than the estimated pseudofirst order reaction rate constant of the OH-addition ISOPOOH products and molecular oxygen. With this reaction rate constant the bimolecular reaction dominates over the *cis*/*trans*-β-IEPOX production at atmospheric pressures.

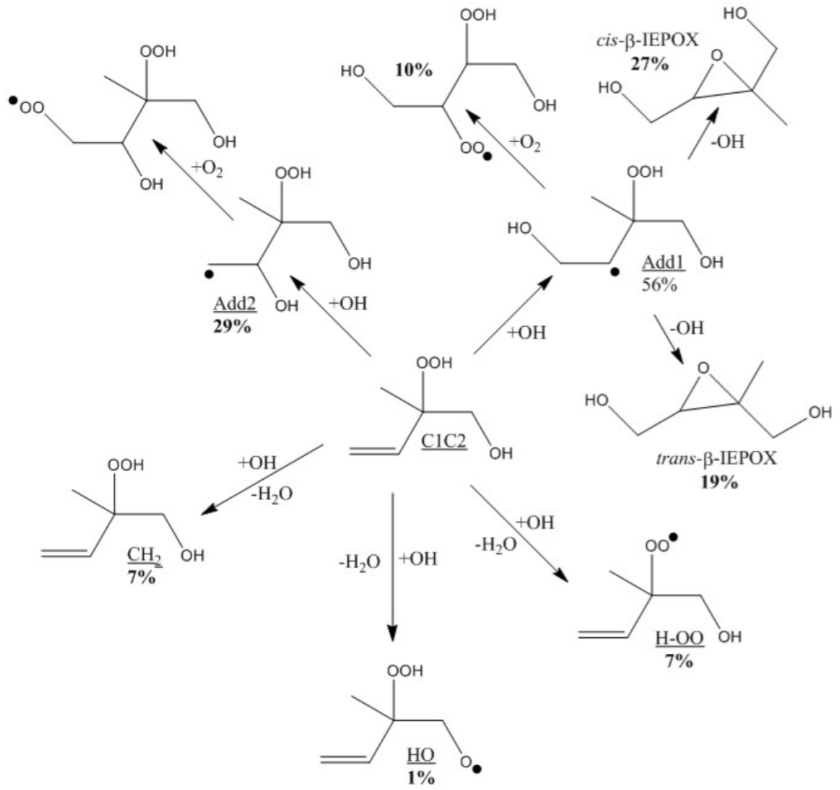

Figure D.17: The reactions of (1,2)-ISOPOOH with OH.

D.5.3.6 Mesmer Modeling

Our MESMER models have all the ISOPOOH+OH reactions along with the *cis*/trans-β-IEPOX production reactions that occur following the OH addition to the outer carbon. All the reactions are shown in Figure D.17 and Figure D.18 for the (1,2)-ISOPOOH and (4,3)-ISOPOOH molecules, respectively. We have used a grain size of 50 cm^{-1} and a grain span in the model of 30 kT (above the ISOPOOH+OH energy stationary point). We used a collisional activation/deactivation energy of 200 cm^{-1} per bath gas (N_2) collision, a temperature of 298.15 K, a pressure of 745 Torr and an OH concentration of 10^6 molecules cm^{-3}.

(1,2)-ISOPOOH+OH. The yields of each component are shown on Figure D.17. The total for the compounds' yields shown in bold add to 100%. Our model suggests that only a minor amount of the ISOPOOH-OH molecules are stabilized in the ISOPOOH-OH well. For the (1,2)-ISOPOOH+OH reaction in Figure D.17, we observe that the two addition reactions (Add1 and Add2) dominate over all the OH abstraction reactions. All OH abstraction reactions have yields that are lower than 7%. The OH addition to the inner carbon of the double bond has a yield of

29% of the total yield. After the inner OH addition, molecular oxygen adds and a hydroperoxydiol peroxy radical is produced.

The H-shift between the hydroperoxy hydrogen and the peroxy radical is calculated to be very fast ($\sim 10^4$ s^{-1}) - much faster than the bimolecular chemistry - so an equilibrium distribution between the two peroxy radicals will result. The calculations suggest that the peroxy radical on C2 will be favored.

The yield of the OH addition to the outer carbon is 56%. After the OH addition, the molecule can either produce *cis*/*trans*-β-IEPOX or a peroxy hydroperoxydiol molecule. Our model shows that the excess energy is high enough to overcome the energy barriers and to produce a high yield of β-IEPOX molecules. The 56% of OH addition to the outer carbon will divide into a production of a total yield of 19% *trans*-β-IEPOX, 27% *cis*-β-IEPOX molecule and 10% will add O_2 yielding a hydroperoxydiol peroxy radical. H-shift between the hydroperoxy hydrogen and the peroxy radical is also calculated to be very fast ($\sim 10^4$ s^{-1}) - much faster than the bimolecular chemistry and so, an equilibrium distribution between the two peroxy radicals will result.

(4,3)-ISOPOOH + OH. The calculated yields of each component are shown in Figure D.18. The total for the yields shown in bold add to 100%. OH addition to the outer carbon in the double bond dominates with a yield of 95% of the total yield. The yield of the OH abstraction reaction of the hydrogen α to the hydroperoxy group is around 3%, and all other reactions have production yields around 1% or lower. Of the 95% yield added to the outer carbon around 40% will produce the *cis*-β-IEPOX, 47% produce *trans*-β-IEPOX and around 8% will produce the hydroxyperoxydiol peroxy radical. The yield of *cis*/*trans*-β-IEPOX is much higher for (4,3)-ISOPOOH+OH compared to (1,2)-ISOPOOH+OH.

D.5.3.7 Further decomposition after the inner OH addition to the (1,2)-ISOPOOH molecule

Following addition of OH to the (1,2)-ISOPOOH *via* add2, we expect O_2 to add (C4OO) rather than formation of a 4 member epoxide-like compound. After O_2 addition, we find a rapid H-shift from the hydroperoxide group to the ROO (C2OO). A reaction scheme is shown in Figure D.19. We have looked at the (R,R)-enantiomer of the molecule and performed preliminary calculations with the M06-2X/aug-cc-pVTZ method. The calculated H-shift barrier height for this reaction is found to be 9.3 kcal mol^{-1}. The product is 0.4 kcal mol^{-1} lower than the reactant. The

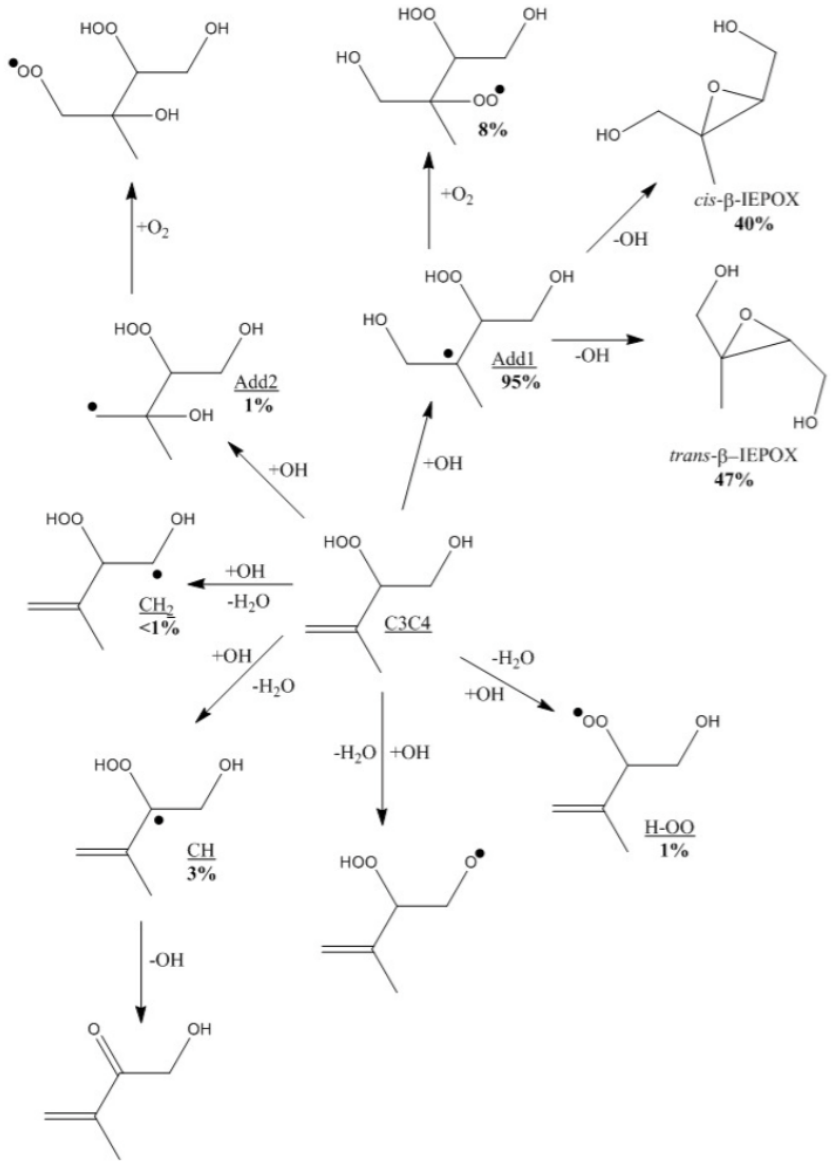

Figure D.18: The reactions of (4,3)-ISOPOOH with OH.

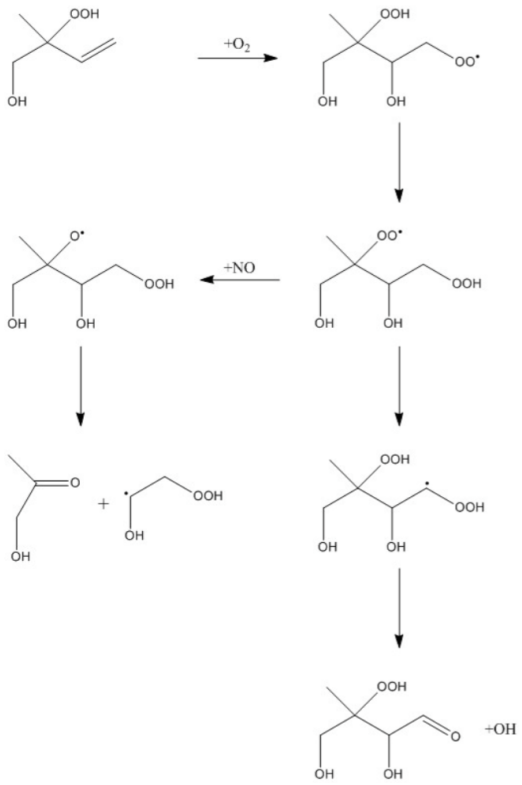

Figure D.19: The two possible H-shift reactions after the internal OH addition ($+O_2$) in the (1,2)-ISOPOOH molecule.

attachment of molecular oxygen releases an energy of 34.4 kcal mol^{-1} compared to the (1,2)-ISOPOOH-OH added product (inner addition), and the energy difference between the (1,2)-ISOPOOH+OH+O_2 and the molecule with the oxygen attached (reactant) is 63.8 kcal mol^{-1}. The "cold" TST reaction rate constants, including the Eckart tunneling correction, are 5.6×10^6 s^{-1} and 5.8×10^6 s^{-1} for the forward and backward H-shift reactions, respectively.

The second H-shift reaction would likely take the terminal hydrogen with the OOH group, and lead to loss of OH. It has a barrier height of 23.1 kcal mol^{-1} and a TST Eckart-corrected reaction rate constant of 1.2×10-4 s^{-1}. The energy of the final aldehyde + OH is almost 50.4 kcal mol^{-1} lower in energy than the transition state. The energetics are shown in Table D.14.

D.5.4 GEOS-Chem Calculations

The chemical mechanisms for the "Standard" and "Old" GEOS-Chem runs were identical except for the differences included in Table D.15. The complete "Standard" mechanism can be obtained at http://wiki.seas.harvard.edu/GEOS-Chem/index.php/

Species	δE+ZPVE (kcal mol^{-1})
(1,2)-ISOPOOH+OH+O_2	0.0
C4OO	-63.8
TS	-53.0
C2OO	-64.2
TS	-41.1
Aldehyde+OH	-91.5

Table D.14: The energetics (in kcal mol^{-1}) of the two H-shift reactions after the inner OH addition (+O_2) to the (1,2)-ISOPOOH molecule calculated with the M06-2X/aug-ccpVTZ method.

	"Standard"	"Old"
HO_2+RO_2 rate coefficient	$2.91\times10^{-13} \times e^{(1300/T)} \times [1\text{-}e^{(-0.245n}]$	$7.4\times10^{-13} \times e^{(700/T)}$
H-abstraction rate coefficient	$4.75\times10^{-12} \times e^{(200/T)}$	$3.8\times10^{-12} \times e^{(200/T)}$
H-abstraction yields	0.387ISOPOO + 0.613OH + 0.613HC_5	0.70ISOPOO + 0.300HC_5 + 0.300OH

Table D.15: Differences between the "Standard" and "Old" GEOS-Chem mechanisms.

New_isoprene_scheme.

The "Recommended" simulation run in GEOS-Chem included an increased ISOPOOH yield of 94% from the reaction of HO_2 with ISOPOO, as well as individually speciated ISOPOOH and IEPOX isomers. Listed below are the rates and products of individual reactions edited and added to the GEOS-Chem mechanism in the "Recommended" simulation to account for the isomers of ISOPOOH and IEPOX. In the GEOS-Chem mechanism, ISOPOOH is referred to as RIP; RIPA, RIPB, and RIPD refer to (1,2), (4,3), and delta (1,4 and 4,1) ISOPOOH respectively, while IEPOXA, IEPOXB, and IEPOXD refer to *trans-*β, *cis-*β, and δ IEPOX respectively. Temperature dependencies of rate constants were kept from the "Standard" GEOS-Chem mechanism.

RIO_2 + HO_2 $\rightarrow$ 0.628RIPA + 0.272RIPB + 0.037RIPD + 0.063(OH + CH_2O + HO_2) + 0.038MVK + 0.025MACR; k = $2.06 \times 10^{-13} \times e^{(1300/T)}$

RIPA + OH $\rightarrow$ 0.750RIO_2 + 0.250HC_5 + 0.125(OH + H_2O); k = $6.13 \times 10^{-12} \times e^{(200/T)}$

RIPA + OH $\rightarrow$ 0.850OH + 0.578IEPOXA + 0.272IEPOXB + 0.150HC_5OO; k = $1.70 \times 10^{-11} \times e^{(390/T)}$

RIPB + OH $\rightarrow$ 0.480RIO_2 + 0.520HC_5 + 0.26(OH + H_2O); k = $4.14 \times 10^{-12} \times e^{(200/T)}$

RIPB + OH $\rightarrow$ 1.000OH + 0.680IEPOXA + 0.320IEPOXB; k = $2.97 \times 10^{-11} \times e^{(390/T)}$

RIPD + OH $\rightarrow$ 0.250RIO_2 + 0.750HC_5 + 0.375(OH + H_2O); k = $5.11 \times 10^{-12} \times e^{(200/T)}$

RIPD + OH $\rightarrow$ 0.500OH + 0.500IEPOXD + 0.500HC_5OO; k = $2.92 \times 10^{-11} \times e^{(390/T)}$

IEPOXA + OH $\rightarrow$ IEPOXOO; k = $3.73 \times 10^{-11} \times e^{(-400/T)}$

IEPOXB + OH $\rightarrow$ IEPOXOO; k = $5.79 \times 10^{-11} \times e^{(-400/T)}$

IEPOXD + OH $\rightarrow$ IEPOXOO; k = $3.20 \times 10^{-11} \times e^{(-400/T)}$

Other reactions involving RIP and IEPOX in the original GEOS-Chem mechanism, including deposition and photolysis, were simply updated to apply to each individual isomer of the two compounds.

Appendix E

ATMOSPHERIC FATES OF CRIEGEE INTERMEDIATES IN THE OZONOLYSIS OF ISOPRENE

Nguyen, T. B., G. S. Tyndall, J. D. Crounse, A. P. Teng, K. H. Bates, R. H. Schwantes, M. M. Coggon, L. Zhang, P. Feiner, D. O. Milller, K. M. Skog, J. C. Rivera-Rios, M. Dorris, K. F. Olson, A. Koss, R. J. Wild, S. S. Brown, A. H. Goldstein, J. A. de Gouw, W. H. Brune, F. N. Keutsch, J. H. Seinfeld, and P. O. Wennberg (2016). "Atmospheric fates of Criegee intermediates in the ozonolysis of isoprene". In: *Phys. Chem. Chem. Phys.* 18.15, pp. 10241–10254. DOI: 10.1039/C6CP00053C.

Abstract

We use a large laboratory, modeling, and field dataset to investigate the isoprene + O_3 reaction, with the goal of better understanding the fates of the C_1 and C_4 Criegee intermediates in the atmosphere. Although ozonolysis can produce several distinct Criegee intermediates, the C_1 stabilized Criegee (CH_2OO, 61 ± 9%) is the only one observed to react bimolecularly. We suggest that the C_4 Criegees have a low stabilization fraction and propose pathways for their decomposition. Both prompt and non-prompt reactions are important in the production of OH (28% ± 5%) and formaldehyde (81% ± 16%). The yields of unimolecular products (OH, formaldehyde, methacrolein (42 ± 6%) and methyl vinyl ketone (18 ± 6%) are fairly insensitive to water, *i.e.*, changes in yields in response to water vapor (≤4% absolute) are within the error of the analysis. We propose a comprehensive reaction mechanism that can be incorporated into atmospheric models, which reproduces laboratory data over a wide range of relative humidities. The mechanism proposes that $CH_2OO + H_2O$ ($k_{(H_2O)} \sim 1 \times 10^{-15}$ cm^3 molec^{-1} s^{-1}) yields 73% hydroxymethyl hydroperoxide (HMHP), 6% formaldehyde + H_2O_2, and 21% formic acid + H_2O; and $CH_2OO + (H_2O)_2$ ($k_{(H_2O)_2} \sim 1 \times 10^{-12}$ cm^3 molec^{-1} s^{-1}) yields 40% HMHP, 6% formaldehyde + H_2O_2, and 54% formic acid + H_2O. Competitive rate determinations ($k_{SO_2}/k_{(H_2O)_{n=1,2}} \sim 2.2\ (\pm 0.3) \times 10^4$) and field observations suggest that water vapor is a sink for greater than 98% of CH_2OO in a Southeastern US forest, even during pollution episodes ($[SO_2] \sim 10$ ppb). The importance of the $CH_2OO + (H_2O)_n$ reaction is demonstrated by high HMHP mixing ratios observed over the forest canopy. We find that CH_2OO does not substantially affect the lifetime of SO_2 or HCOOH in the Southeast US, *e.g.* $CH_2OO + SO_2$ reaction is a minor contribution

(<6%) to sulfate formation. Extrapolating, these results imply that sulfate production by stabilized Criegees is likely unimportant in regions dominated by the reactivity of ozone with isoprene. In contrast, hydroperoxide, organic acid, and formaldehyde formation from isoprene ozonolysis in those areas may be significant.

E.1 Introduction

Ozonolysis is one of the main atmospheric oxidation pathways for volatile alkenes. Reaction with ozone globally removes ~10% of isoprene (C_5H_8), the most abundant alkene in the atmosphere. For monoterpenes ($C_{10}H_{16}$) and sesquiterpenes ($C_{15}H_{24}$), ozonolysis is a substantially larger sink due to their faster rate coefficients with ozone (Atkinson *et al.*, 2006). The first steps of the alkene ozonolysis mechanism are shown in Figure E.1 (Criegee, 1975). Two primary ozonides (POZ) are formed from ozone addition at either double bond of isoprene, decomposing into methacrolein (MACR), methyl vinyl ketone (MVK), formaldehyde (HCHO), and potentially up to nine activated Criegee intermediates (CI, denoted with asterisk). The C_4 Criegees (MACR-OO* and MVK-OO*) can be formed with four conformations each that are *syn* or *anti* to methyl or vinyl groups. The CI can experience a few unimolecular processes – most notably, decomposition into a hydroxyl radical (OH) and a β-oxy alkyl radical (R) and thermalization by atmospheric gases to form the stabilized Criegee intermediate (SCI) (Kroll *et al.*, 2001). In addition, a fraction of SCI has been suggested to be formed through POZ decomposition (Drozd and Donahue, 2011). Most of the OH from isoprene ozonolysis is thought to be produced by the *syn*-methyl MVK-OO conformers (Figure E.1, g and h) *via* the formation of a vinyl hydroperoxide (VHP) intermediate (Aschmann and Atkinson, 1994; Donahue *et al.*, 2011; Gutbrod *et al.*, 1997; Kuwata *et al.*, 2010; Paulson *et al.*, 1992).

The stabilized Criegees (SCIs) may undergo bimolecular reaction with a number of atmospheric species, including water vapor (H_2O), sulfur dioxide (SO_2), formic acid (HCOOH), carbonyls (*e.g.* HCHO and acetaldehyde), NO, NO_2, O_3, RO_2, alkenes, among others (Fenske *et al.*, 2000; Hatakeyama and Akimoto, 1994; Johnson and Marston, 2008; Kjaergaard *et al.*, 2013; Neeb *et al.*, 1998; Vereecken *et al.*, 2012, 2014). Even if a substantial fraction of CIs are stabilized, they may still experience unimolecular losses. The structure, and even conformation, of the SCI dictate their unimolecular and bimolecular reactivities (Gutbrod *et al.*, 1997), with *syn* SCI more susceptible to decomposition. The simplest SCI (CH_2OO) has special importance in atmospheric chemistry as it is produced by all exocyclic alkenes, including isoprene. Unlike other SCIs, however, CH_2OO is non-*syn* (*i.e.*, not facing any

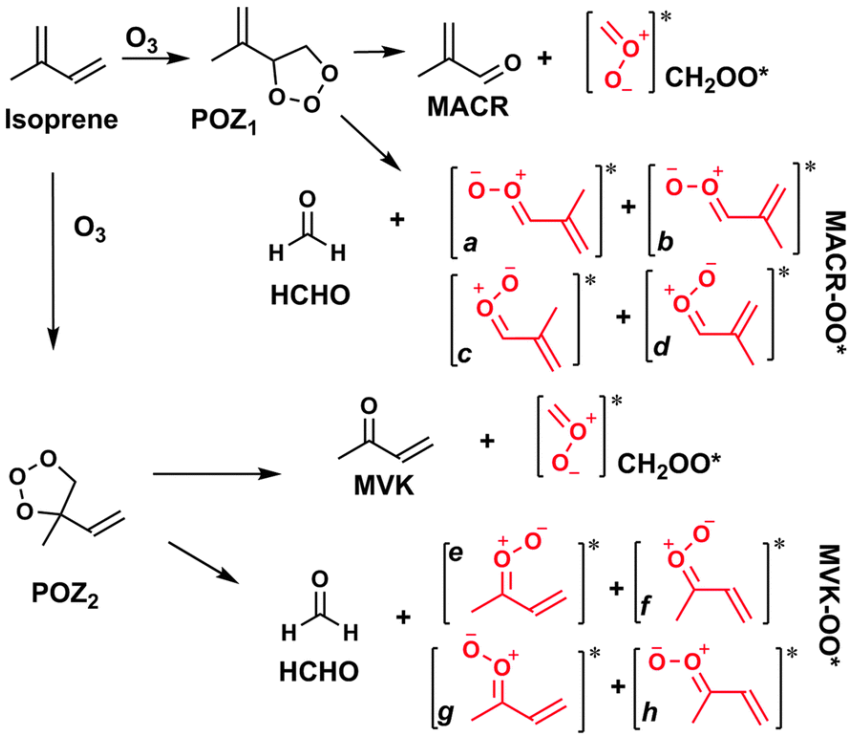

Figure E.1: The first steps of the Criegee mechanism of ozonolysis, shown for isoprene. Criegee intermediates are drawn as zwitterions; however, depending on the chemical structure, they may also have diradical character.

hydrocarbon groups), which greatly reduces its unimolecular reactivity (Anglada *et al.*, 2011).

Figure E.2 shows a simplified reaction scheme between CH_2OO and water (or water clusters) (Berndt *et al.*, 2014; Chao *et al.*, 2015; Ryzhkov and Ariya, 2003, 2006), sulfur dioxide (SO_2), and formic acid (HCOOH). The CH_2OO + $(H_2O)_n$ reaction (where n = 1, 2,...) produces hydroxymethyl hydroperoxide (HMHP), hydrogen peroxide (H_2O_2) + formaldehyde (HCHO), and formic acid (HCOOH) + H_2O as main products (Becker *et al.*, 1993; Gab *et al.*, 1985; Horie *et al.*, 1994a; Huang *et al.*, 2013; Neeb *et al.*, 1995, 1997; Ryzhkov and Ariya, 2004). The CH_2OO + HCOOH reaction produces hydroperoxy methylformate (HPMF) (Neeb *et al.*, 1995, 1997; Thamm *et al.*, 1996). Finally, the CH_2OO + SO_2 reaction produces SO_3, which then reacts with water to form H_2SO_4 (Hatakeyama *et al.*, 1984).

Certain populations of SCIs may produce OH (Novelli *et al.*, 2014), perhaps analogously to the hot Criegee VHP channel, among other products. Decomposition of SCIs is rarely discussed within the scope of the atmospheric fates; however, it is an

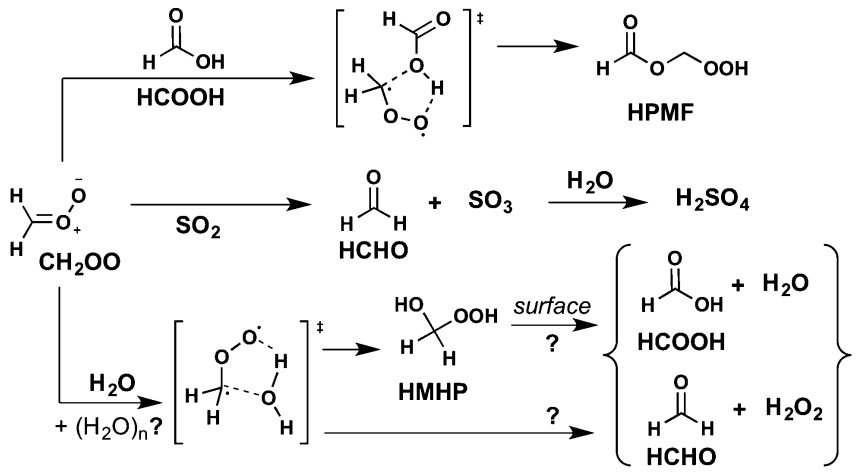

Figure E.2: The reaction of CH_2OO with HCOOH, SO_2, and H_2O (and possibly water clusters). The production of HCOOH + H_2O and HCHO + H_2O_2 from the water reaction has been suggested to (at least partially) result from surface-mediated decomposition of HMHP (Neeb *et al.*, 1997); however, it is not clear if there are direct routes to these products from CH_2OO + H_2O.

important consideration in understanding their total reactivity. Previously published unimolecular decomposition rates for larger Criegees have high uncertainty, so the following is only a qualitative discussion. SCI decomposition rates has been shown to increase with size (Fenske *et al.*, 2000; Newland *et al.*, 2015). For example, even though the thermalized acetone oxide ($(CH_3)_2COO$) has been recently reported to undergo a diffusion-limited reaction with SO_2 (Huang *et al.*, 2015), its short unimolecular lifetime due to its all-*syn* conformation, *i.e.*, both sides facing methyl groups, severely limits the atmospheric relevance of its bimolecular reactions (τ_{uni} = 0.001–0.004 s) (Huang *et al.*, 2015; Newland *et al.*, 2015; Olzmann *et al.*, 1997). It should be noted that experimental determinations of unimolecular lifetimes (*e.g.* 0.002 s) may have some contribution from Criegee self-reaction (Huang *et al.*, 2015); thus, τ_{uni} may be closer to the higher end of the reported range. The ratio k_{decomp}/k_{SO_2} for *syn*-CH_3CHOO and $(CH_3)_2COO$ have been measured to be 1 and 2 orders of magnitude higher than that for CH_2OO, respectively (Newland *et al.*, 2015). Thus, even in a polluted atmosphere (~10 ppb SO_2 and 50% RH at room temperature), decomposition using the Olzmann *et al.* (1997) lower-limit rate coefficient accounts for the majority (~76%) of the acetone oxide fate, while the reaction with SO_2 is minor (~8%). The Newland *et al.* (2015) relative rate coefficient (using k_{SO_2} of Huang *et al.*, 2015) predicts an even higher decomposition fraction.

The present work focuses on understanding the bimolecular reactive channels of CH_2OO and, more generally, the mechanism of isoprene ozonolysis in the atmosphere. We neglect the unimolecular reactions for CH_2OO, as it has a long lifetime with respect to decomposition at 298 K and 1 atm (~3 s) (Olzmann *et al.*, 1997). Furthermore, we provide suggestions for a unifying reaction scheme that may be incorporated into atmospheric models.

E.2 Experimental Methods

E.2.1 Chamber Methods

Experiments were conducted in the Caltech dual 24 m^3 Teflon environmental chambers at ~295 K and ~1 atm. A subset of the work was performed as part of the FIXCIT campaign and the overview manuscript (Nguyen *et al.*, 2014b) provides an in-depth description of the chamber and relevant experiments. Product yield studies were investigated with isoprene and ozone mixing ratios of ~100 and 600 ppb, respectively, and relative humidity (RH) in the approximate range of <4 – 76%. The production of OH was investigated in the absence of a chemical scavenger, but all other studies were performed with excess cyclohexane (50 ppm) to scavenge OH. Although excess cyclohexane is used, a minor fraction of the products will result from OH chemistry. Relative rate experiments were used to investigate the competition between SO_2 and H_2O at lower isoprene and ozone mixing ratios (~25 ppb and 100 ppb, respectively) and 10 ppm cyclohexane.

RH inside the reaction chambers was adjusted to the desired level at the beginning of each experiment with a Nafion membrane humidifier (Permapure, LLC) and recirculating ultra-purified water (Millipore Milli-Q, 18 MΩ, <3 ppb TOC). The RH was stable throughout each experiment, as verified by a Vaisala HMT221 probe that was calibrated in the range of 11–95% with saturated salt solutions. Water vapor in the range of RH < 10% was measured by chemical ionization mass spectrometry (CIMS, see Section E.2.2). However, the accuracy of RH measurements degrades in the lower range due to the difficulty in determining small mixing ratios of H_2O; thus we quote "dry" RH as "<4%". Although RH in dry conditions is quoted as an upper bound, we estimate the actual RH in the chamber is closer to 1%. Ozone was introduced into the chamber by flowing air through a commercial UV ozone generator. Reagents, *e.g.* isoprene (Aldrich, ≥99%) and cyclohexane (CHX, Aldrich >99%), were introduced into the chamber by volumetric injection of liquid material using Hamilton gas-tight syringes. In general, the order of introduction was water vapor, ozone, cyclohexane, and then isoprene. For relative rate studies, gaseous SO_2

(standard mixture 10 ppm in N_2, Scott Specialty Gases) was introduced into the chamber using a calibrated mass flow controller. After injection of isoprene, several short high-pressure pulses of air were introduced into the chamber to homogenize the contents of the chamber so that the reaction can start immediately and uniformly. We verified that injected gases were well-mixed in <5 minutes using this method. The duration of a typical experiment was 5–7 hours.

E.2.2 Analytical Quantification

isoprene, methacrolein (MACR), methyl vinyl ketone (MVK), and cyclohexane (CHX) were quantified by gas chromatography with a flame ionization detector (GC-FID). The GC-FID was calibrated with commercial standards (Aldrich) in the range of 20–200 ppb by use of volumetric gas-tight syringes and a calibrated mass flow of N_2 into a 100L Teflon calibration bag. Additionally, the absolute quantities of ISOP, MACR, and MVK was cross calibrated using Fourier transform infrared spectroscopy (FT-IR) in the range of 1–20 ppm *via* a similar method. The ppm-level calibration bags were quantified with FT-IR using tabulated absorption cross sections (Sharpe *et al.*, 2002) before sampling with GC-FID. The mixing ratio of ozone was quantified by a calibrated ozone absorption monitor (Horiba APOA-360). The mixing ratios of NO and NO_2 were quantified with a commercial NOx monitor (Teledyne T200). NO was observed at baseline level (limit of detection 0.5 ppb) and NO_2 remained below 5 ppb during ozonolysis experiments. Sulfuric acid aerosols were measured using a time-of-flight aerosol mass spectrometer (AMS, Aerodyne) and data processing was performed using the Pika 1.14D analysis module in Igor Pro (Drewnick *et al.*, 2005). The instrumental ionization efficiency was calibrated with 350 nm ammonium nitrate particles.

Formaldehyde and HO_x (OH and HO_2) were measured in situ by two laser-induced fluorescence (LIF) instruments during the FIXCIT campaign. The University of Wisconsin (UW) LIF instrument (DiGangi *et al.*, 2011; Hottle *et al.*, 2009) quantified formaldehyde from the difference between its online (353 nm) and offline signal. The Pennsylvania State University (PSU) Ground-based Tropospheric Hydrogen Oxides Sensor (GTHOS (Brune *et al.*, 1995)) measured OH and HO_2 by the fluorescent assay by gas expansion (FAGE) technique. OH was quantified spectroscopically (near 308 nm) and the zero background is determined using hexafluoropropene (C_3F_6) as an OH scrubber in the instrument inlet. HO_2 was measured after its chemical conversion in the instrument inlet to OH using pure NO ($HO_2 + NO \rightarrow OH + NO_2$). The known interference of HO_2 measurement by RO_2 radicals (Fuchs

et al., 2011) was corrected in the following manner: the NO addition to GTHOS was modified to reduce the reaction time and the amount of NO added. Although the conversion of HO_2 to OH was decreased from ~90% to less than 10%, the conversion of RO_2 to OH was reduced to less than 1%, so that more than 95% of the signal was due to converted HO_2 and only a few percent was due to RO_2 (Fuchs *et al.*, 2011). These conversion rates were measured with GTHOS in the Brune laboratory at PSU and are similar to those determined by Fuchs *et al.* (2011).

Gas-phase hydroperoxides (H_2O_2, HMHP, MHP, *etc.*), acidic compounds (SO_2, HCOOH, *etc.*), and other volatiles with more than one polar functional group (*e.g.* hydroxy carbonyls) are quantified with a triple-quadrupole chemical ionization mass spectrometer (CIMS) using CF_3O^- as an ionization reagent (Crounse *et al.*, 2006; St. Clair *et al.*, 2010). The sample flow from the chamber was diluted by a factor of 12 with dry N_2 before mass spectrometry analysis. The dry (RH < 4%) sensitivity of triple-quadrupole CF_3O^- CIMS to different analytes was cross-calibrated with a CF_3O^- time-of-flight (ToF) CIMS during the FIXCIT campaign. The ToF CIMS was calibrated for a variety of compounds (H_2O_2, HMHP, HCOOH, SO_2, peracetic acid (PAA), acetic acid (AA), hydroxyacetone (HAC), *etc.*) with commercial or *syn*thesized standards based on gravimetric or spectrometric techniques (see Section S3 of Nguyen *et al.* (2015a) for more information). Table E.2 in the Supporting Information provides more information about CIMS detection of the major compounds discussed in this work. The CIMS measurement uncertainties are approximately 20–30% for calibrated compounds (*e.g.* HCOOH) and -50% for uncalibrated compounds (*e.g.* HPMF).

In addition to the dry sensitivity, the dependence of the ion chemistry on water vapor is unique to each CIMS instrument and is critical for the accurate interpretation of RH-dependent yields. We obtained the water-dependent calibration curves in the experimental RH range by introducing a sample stream (containing a stable gaseous source of each compound) and a dilution stream that has tunable water vapor content to the CIMS flow tube region. The water vapor mixing ratio of the dilution stream was achieved by mixing flow-controlled quantities of a humid air stream ([H_2O] ~ 3%, quantified by FT-IR) and a dry N_2 stream ([H_2O] < 100 ppm). A stable source of HMHP, for which a commercial standard is unavailable, was *syn*thesized in the Teflon chamber using the HCHO + HO_2 reaction (Niki *et al.*, 1980), which produces a low yield of HMHP. The photolysis of HCHO (~2 ppm) generates the HO_2 that is needed to react with HCHO. The UV lights were turned off after approximately

1 hour, and the ~6 ppb HMHP formed during the photolytic period was stable in the dark indefinitely. A typical water-dependent calibration alternates a dry data point with several humid points and zeros (where sample flow is shut off), after each period is allowed to stabilize (Figure E.9 in the Supporting Information). Water curves were obtained for HCOOH, H_2O_2, and SO_2 using commercial standards as the sample source, in an identical manner. The sensitivity of the CIMS toward HPMF was not measured, but was assumed to be similar to HMHP based on the molecular characteristics of these two compounds (Su and Chesnavich, 1982).

E.2.3 Wall loss Corrections

α-hydroxy hydroperoxides like HMHP have a propensity to participate in heterogeneous reactions on humid surfaces (Neeb *et al.*, 1997). Thus, we measured wall loss rates for HMHP, HCOOH, and H_2O_2 as a function of RH to correct for this effect. HMHP was synthesized *via* an alternative method to the one described in Section E.2.2: a gaseous mixture of formaldehyde/N_2 (produced by flowing dry N_2 past heated paraformaldehyde solid) was bubbled into an aqueous H_2O_2 solution (50% v/v). The outflow of the bubbler (containing HCHO, HMHP, HCOOH, and H_2O_2) was introduced into the chamber until the signal of HMHP in CIMS was adequate, after which the flow was stopped and the wall loss was monitored for 8–10 hours. The production of HCOOH from HMHP conversion may obscure the HCOOH wall loss to a degree. However, by virtue of the synthesis method (high water content in the H_2O_2 bubbler), the HCOOH mixing ratio in the chamber was more abundant than HMHP by a factor of 100, so that even if all of the HMHP were converted to HCOOH, the production yield signal would impact k_{wall} of HCOOH by only 1%. We did not observe noticeable wall loss of HMHP, HCOOH, or H_2O_2 under dry conditions (Figure E.10 in the Supporting Information); however, the wall loss rates become non-negligible at the highest RH investigated (72%), where HMHP was removed at a rate of approximately 0.1% per minute. The humidity-dependent wall loss rates ($k_{wall,HMHP} = -1.4 \times 10^{-5} \times \text{RH min}^{-1}$, $k_{wall,H_2O_2} = -9.6 \times 10^{-6} \times \text{RH min}^{-1}$, and $k_{wall,HCOOH} = -2.2 \times 10^{-6} \times \text{RH min}^{-1}$) were used to correct the CIMS data.

E.3 Results and Discussion

E.3.1 Humidity-Dependent Product Yields

The molar yields of products from the isoprene ozonolysis in the RH range of <4–76% are reported in Table E.1. Figure E.3 shows the trends in yields of select gas-

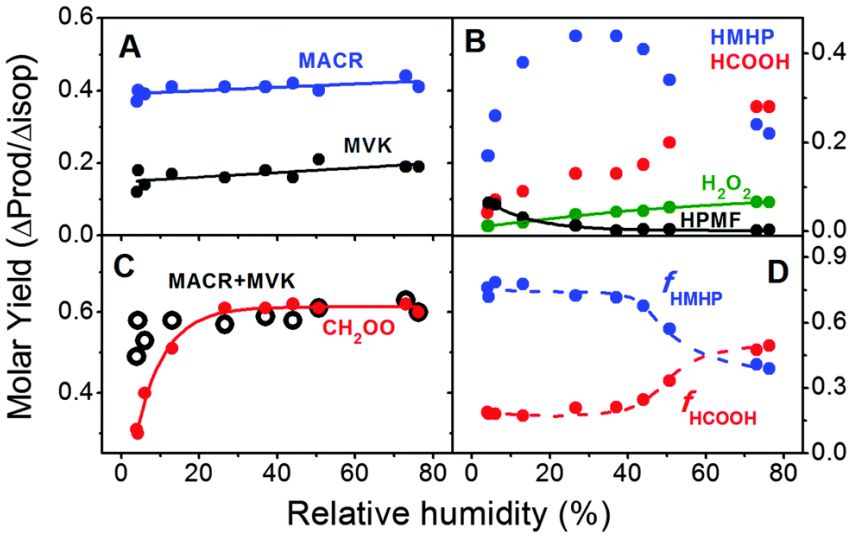

Figure E.3: Molar yields of the isoprene + O_3 reaction products (A–C) at several RH conditions. The CH_2OO yield in panel C is inferred from the sum of the scavenged products of CH_2OO with water vapor and formic acid. Panel D shows the fraction of water-scavenged CH_2OO that is observed as HMHP (f_{HMHP}) and HCOOH (f_{HCOOH}). Solid lines indicate least-squares fits, when applicable, and dashed lines only serve to guide the eyes. HMHP and HCOOH in panel B can each be fit by two exponential curves delineated at RH ~40%, but no singular relationship.

phase organic products measured by GC-FID and CIMS. As expected, the "prompt" products, *i.e.*, those formed primarily from the decomposition of primary ozonides (POZ) such as HCHO, MACR, and MVK, do not exhibit a strong dependence on water vapor (Figure E.3a and Table E.1). This is also true for yields of OH radicals, which are produced from decomposition channels. The observation that OH yields from isoprene ozonolysis are independent of humidity has been reported in other works (Hasson *et al.*, 2003; Kuwata *et al.*, 2010). Further insights on the sources of OH and HCHO yields are obtained by model simulations (see Section E.3.2). The yields of carbonyls and OH from this work are not significantly different from those reported elsewhere (Aschmann and Atkinson, 1994; Atkinson *et al.*, 1992; Grosjean *et al.*, 1993b; Gutbrod *et al.*, 1997; Hasson *et al.*, 2001a; Sauer *et al.*, 1999). The trends in yields for carbonyls are slightly positive with humidity, possibly supporting a minor production from SCI + $(H_2O)_n$ reaction (H_2O_2 as coproduct). However, the measurement uncertainties are significant (10-30%) and, thus, this channel was treated as minor in the development of our mechanism.

Stabilized CH_2OO yields obtained by a chemical scavenging method were similar whether H_2O or SO_2 was used as the Criegee scavenger (Table E.1, Y_{SCI} ~0.60

expt.	type	SO_2 (ppb)	RH (%)	Y_{CH_2OO}	Y_{MACR}	Y_{MVK}	Y_{OH}	Y_{HCHO}	Y_{HCO_2H}	$Y_{H_2O_2}$	Y_{HMHP}	Y_{HPMF}
1	A	0	<4	0.30	0.39	0.15	—	0.79	0.05	0.012	0.17	0.064
2	A	0	6	0.40	0.39	0.14	—	—	0.07	0.014	0.26	0.060
3	A	0	13	0.51	0.41	0.17	—	—	0.09	0.019	0.38	0.030
4	A	0	27	0.61	0.41	0.16	—	—	0.13	0.038	0.44	0.013
5	A	0	37	0.61	0.41	0.18	—	0.83	0.13	0.044	0.44	0.001
6	A	0	44	0.62	0.42	0.16	—	— 0.15	0.046	0.41	0.005	
7	A	0	51	0.61	0.40	0.21	—	—	0.20	0.054	0.34	0.004
8	A	0	73	0.62	0.44	0.19	—	—	0.28	0.066	0.24	0.002
9	A	0	76	0.60	0.41	0.19	—	—	0.28	0.065	0.22	0.003
10	B	0	4	—	—	—	0.28	—	—	—	—	—
11	B	0	52	—	—	—	0.28	—	—	—	—	—
12	C	15	20	0.60	BDL	BDL	—	—	—	—	-	—
13	C	15	3	0.65	BDL	BDL	—	—	—	—	—	—
14	C	75	3	0.66	BDL	BDL	—	—	—	—	—	—

Table E.1: Molar yields (Y) of major products for different RH and SO_2 conditions. Experiment types are (A) product yields with OH scavenger ([ISO] ~100 ppb, [O_3] ~600 ppb, [CHX] ~50 ppm), (B) product yields without OH scavenger (same initial conditions as A but without CHX), and (C) relative rates ([ISO] ~25 ppb, [O_3] ~120 ppb, [CHX] ~10 ppm). CH_2OO yields for A are obtained by summing the yields of CH_2OO + $(H_2O)_n$ and CH_2OO + HCOOH products measured using CIMS. In C, CH_2OO yield determinations include the measurement of H_2SO_4 aerosol using AMS. All experiments were performed at 295 K. See Table E.2 in the Supporting Information for details on quantification with CIMS. Missing entries indicate unavailability of instruments or irrelevancy of data. Measurement uncertainties are: SO_2 (±20%), CH_2OO (±15 AMS, ±30% CIMS), MACR (±15%), MVK (±33%), OH (±25%), HCHO (±20%), HCOOH (±10%), H_2O_2 (±20%), HMHP (±20%), HPMF (±50%). BDL = below detection limit for GC-FID.

using CIMS, and ~0.64 using AMS). As the detection of scavenged products utilized two independently-calibrated instruments, their agreement lends further confidence to the yield results. Our CH_2OO determination is consistent, within uncertainties, with those reported recently (0.56–0.60) (Newland *et al.*, 2015; Sipilä *et al.*, 2014). However, it is in poor agreement with the 0.27 yield determined by Hasson *et al.* (2001a). We believe the discrepancy is due to the fact that HCOOH and H_2O_2 were not counted as $CH_2OO + (H_2O)_n$ products in the Hasson *et al.* (2001a) work, and the offline HMHP determination may have experienced aqueous losses. The CH_2OO yield reported here is supported by independent observations of its co-products, MVK and MACR (Figure E.1). Figure E.3c shows that the CH_2OO yield determined here is in good agreement with the C_4 carbonyl sum at high water vapor mixing ratios where CH_2OO is fully scavenged. The inferred CH_2OO yield in our work does not include formaldehyde as a product due to limited data. Formaldehyde formation becomes important at low RH because of competing reactions such as $CH_2OO + O_3$; thus, a significant deviation in the inferred CH_2OO yield compared to the C_4 carbonyl sum occurs in the low RH range.

The products derived from CH_2OO bimolecular reactions have a strong relationship with water vapor mixing ratio due to competition from the $CH_2OO + (H_2O)_n$ reaction (Figure E.3b). Hydroperoxy methylformate (HPMF), seemingly the sole product of the CH_2OO + HCOOH reaction (Figure E.11 in the Supporting Information), is observed only under very dry conditions in accordance with previous reports (Hasson *et al.*, 2001b; Neeb *et al.*, 1997). This is because formic acid in ozonolysis experiments is rarely present at the levels needed to compete with water vapor. In addition to compounds reported in Table E.1, RH-dependent yields of minor species like acetic acid were also observed (<0.06). Representative CIMS mass spectra showing all products are given in Figure E.12 in the Supporting Information. Acetic acid has not been identified in past isoprene ozonolysis studies, but serves as an important clue in deducing the fragmentation patterns of C_4 Criegees.

HMHP is the most abundant $CH_2OO + (H_2O)_n$ product, followed by formic acid, then H_2O_2 (+ HCHO). The maximum HMHP yield is determined to be ~44% from isoprene (~73% from CH_2OO), somewhat higher than other values reported in the literature. Insightful comparisons with literature values prove challenging, however, due to the poor agreement in $CH_2OO + (H_2O)_n$ product yields. For example, single-point "humid" HMHP and H_2O_2 yields are reported to be 0.09–0.30 and 0.01–0.12, respectively (Becker *et al.*, 1990; Hasson *et al.*, 2001a; Neeb *et al.*, 1997; Sauer *et al.*,

1999; Simonaitis *et al.*, 1991). Some of the inconsistencies in past experiments have been attributed to the challenge of quantifying hydroperoxides with offline aqueous methods (*e.g.* high-performance liquid chromatography, HPLC).

Interestingly, we find HMHP yields decrease above RH ~40% (Figure E.3b). The reduction in yield for HMHP at high humidity is almost fully compensated by an increase in yield for HCOOH (Figure E.3d). Although wall-mediated reaction is a convenient explanation, our RH-dependent corrections for wall loss using authentic compounds should account for this chemistry (Figure E.10 in the Supporting Information). Instead, model simulation results in Section E.3.2 support the idea that the RH-dependent yields of HMHP and HCOOH are controlled by reactions of both the water monomer and dimer. The dimer becomes exceedingly more abundant at higher RH. As the model simulations fit concentration data that have been wall-loss corrected, the heterogeneous reaction is not included in the mechanism. The atmospherically-relevant reaction of water dimer with CH_2OO was first suggested by Ryzhkov and Ariya (Ryzhkov and Ariya, 2003, 2004, 2006) and later confirmed by experimental works (Berndt *et al.*, 2014; Chao *et al.*, 2015). Ryzhkov and Ariya suggested the decomposition products to be H_2O_2 and HCHO; however, our data are more consistent with HCOOH as the major product from this reaction.

Past studies explored a large range in water vapor mixing ratio (9000–20,000 ppm, RH ~ 28–63% at 298 K) while reporting only a single 'humid' yield for products. Thus, it is possible that poor literature agreement may be due to snapshot observations along different humidity points in the HMHP yield curve. These disagreements are likely exacerbated by the absence of wall loss corrections, which depend on the reaction vessel. To our knowledge, only two other HMHP yield studies have been performed at multiple RH conditions (Hasson *et al.*, 2001a; Huang *et al.*, 2013). Hasson *et al.* (2001a) and Huang *et al.* (2013) did not report yield trends similar to this work, *i.e.*, their data reported a rise-to-maximum relationship of HMHP with RH (maximum yields of 16% and 25%, respectively). Yet, despite the fitting function used by Hasson *et al.* (2001a), their data show that the average HMHP yield at RH ~80% (~0.12 ± 0.03) is lower than its yield at RH ~40% (~0.16 ± 0.04) for isoprene – congruent with our observed trends.

We are unsure of the reasons for discrepancies with the Huang *et al.* (2013) work. In addition to the plateauing HMHP yield, Huang *et al.* (2013) reported a declining yield of HCOOH with humidity (*e.g.* 40% yield of HCOOH at RH 5% that decreases to 30% yield at RH 90%). It is difficult to understand how HCOOH can

be produced in higher yields under dry conditions when HCOOH formation from Criegee isomerization is minor compared to the major channel of $CH_2OO + (H_2O)_n$ (Herron and Huie, 1977; Su *et al.*, 1980). Again, given the lower HMHP yields reported by studies using offline analysis techniques, it is possible that aqueous losses may have occurred and direct comparisons are not possible. Furthermore, the bis-hydroxymethyl peroxide (BHMP) reported in Huang *et al.* (2013) (and absent in this work) may hint at side reactions that are symptomatic of the high reagent concentrations (ppm level) used in that work or condensed-phase chemistry of H_2O_2 and HCHO.

E.3.2 Toward a Unifying Mechanism

Major atmospheric models either do not represent ozonolysis chemistry or provide a significantly abridged version that generally neglects the formation of major compounds such as HMHP (Bey *et al.*, 2001; Saunders *et al.*, 2003). Here, we describe a detailed chemical mechanism based on the new data presented in this work and those available in the literature. The *in situ* observations of oxygenated volatile organic compounds and HO_x enable us to place new constraints on many aspects of the mechanism. Mechanism simulations of HCHO assumes that are no observational interferences from ROOH or other compounds, which is currently unverified for the LIF instrument used here but has been identified for proton-transfer-reaction (PTR-) and GC-based instruments (Rivera-Rios *et al.*, 2014). The proposed mechanism provides enough chemical specificity to capture the RH-dependent yields of OH, carbonyls (HCHO, MACR, MVK), and major products of $CH_2OO + (H_2O)_n$ chemistry. Although uncertainties persist along several channels in the ozonolysis chemistry, especially in the fate of the C_4 Criegees, the proposed scheme is a good starting point for further development and use in atmospheric models.

E.3.2.1 POZ and C_4 Criegee Reactions

Figure E.4 shows the proposed reaction scheme for isoprene ozonolysis. Compounds observed in this work are shown in red. The chemical structures of some of the minor oxygenated species may not be unique, as this CIMS technique cannot distinguish isobaric species. We used the branching ratios for POZ formation that was suggested by Aschmann and Atkinson (Aschmann and Atkinson, 1994), which implies that the lower steric hindrance from the 3,4-addition of ozone is more important than the effect of the electron-donating CH_3 group in the 1,2-addition (Zhang and Zhang, 2002). It is assumed that there is negligible conformational intercon-

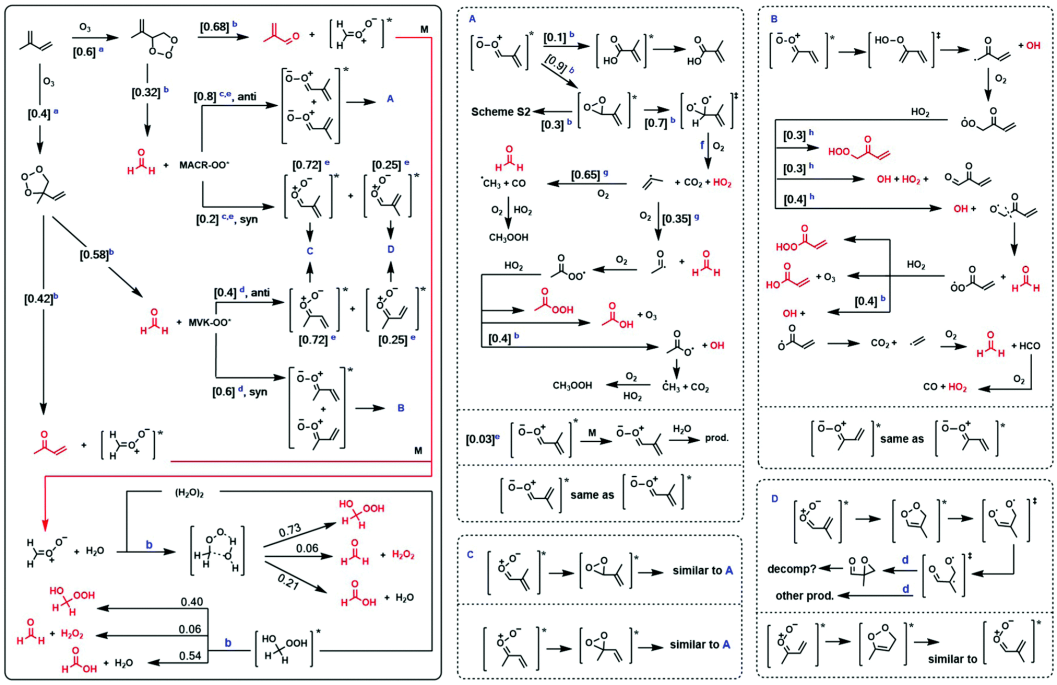

Figure E.4: Overall scheme of isoprene ozonolysis and reactions of Criegee intermediates, with proposed isomerization and decomposition pathways of C_4 Criegees. Observed product species are shown in red. The reaction of CH_2OO with O_3 and isoprene, although present in the model mechanism, are not shown in the figure. Literature values: [a] Aschmann and Atkinson (1994), [b] this work, [c] Zhang and Zhang (2002), [d] Kuwata and Valin (2008), [e] Kuwata *et al.* (2010), [f] Horie *et al.* (1994b) and Nguyen *et al.* (2009a,b), [g] Orlando *et al.* (1999), [h] Praske *et al.* (2015).

version between Criegees due to their zwitterionic character (Hull, 1978; Taatjes *et al.*, 2013), *i.e.*, the barrier to interconversion is expected to be large (Anglada *et al.*, 1996). We note that data available for Criegees with allylic groups, which would presumably facilitate interconversion, is still scarce. Thus, the assumptions and reaction channels discussed here may need to be re-evaluated in future work.

Evidence of bimolecular reactions of the C_4 SCI is not significant. For example, the signals of C_4 α-hydroxyalkyl hydroperoxides that are analogous to HMHP, *e.g.* from the reaction of *anti* MACROO + $(H_2O)_n$, were not observed here. Furthermore, MACR + MVK yields did not significantly increase following SO_2 addition, *e.g.* as would be expected from the MACROO + SO_2 $\rightarrow$ MACR + SO_3 reaction. The insignificant production of MACR from the MACROO + SO_2 reaction and the fast *anti*-SCI + H_2O rate coefficient determined recently (2.4×10^{-14} cm^3 molec^{-1} s^{-1}) (Sheps *et al.*, 2014) favor the hypothesis that the stabilization fraction of the

C_4 Criegees is small, as opposed a larger population of SCI where bimolecular reactions are non-competitive. Thus, we assumed a Criegee stabilization fraction of 0.03 as suggested by Kuwata and Valin (2008). However, accessible unimolecular pathways of CIs and SCIs are often identical, so it is not possible for this study to fully distinguish the two fates. An SCI unimolecular rate constant of ~250 s^{-1} would also be consistent with observations. The 0.03 "stabilization fraction" can be viewed as an effective fraction of Criegees that react bimolecularly under H_2O-dominated conditions. Extensive C_4 Criegee decomposition (hot or thermalized) is consistent with the high yields (>80%) of HCHO that are observed in this work and elsewhere (Grosjean *et al.*, 1993b). The production of HCHO from the prompt POZ decomposition is constrained by MVK + MACR yields to be approximately ~40% by mole with respect to isoprene loss. CH_2OO is fully scavenged by water in most of our experiments, so little additional HCHO can originate from side reactions of CH_2OO at atmospherically-relevant RH.

After the POZ decomposition, the distribution of the *syn*/*anti* conformers of the C_4 Criegees is thought to be asymmetric. We used the branching ratios suggested by Kuwata and coworkers (Kuwata *et al.*, 2010; Kuwata and Valin, 2008), with the caveat that the MVK-OO* conformer distribution is loosely based on the hot acetaldehyde oxide, for lack of direct information. Unimolecular reactions of the C_4 Criegees have been suggested to occur *via* 5-member dioxole or 3-member dioxirane intermediates (Kuwata *et al.*, 2010; Kuwata and Valin, 2008; Vereecken *et al.*, 2012). The model mechanism allows C_4 Criegees that are *syn* and *anti* to vinyl groups to form dioxole and dioxirane intermediates, respectively, using the theoretically-predicted dioxole/dioxirane branching ratios (Kuwata and Valin, 2008). Dioxoles have been suggested to isomerize into products containing carbonyl and epoxide functional groups, which may further decompose (Kuwata *et al.*, 2010); however, the CIMS technique used in this work is likely not sensitive to these specific compounds. The dioxole products were not traced in the model because they represent an insignificant fraction of the carbon in the mechanism (~3%) and are not thought to impact OH or HCHO yields. A minor fraction of the *anti* MACROO* is allocated toward hot acid formation, yielding methacrylic acid (which may also occur *via* a dioxirane intermediate) (Cremer *et al.*, 1998). The dioxirane channels represent a larger fraction of the carbon in the ozonolysis. We followed the recommendations of Peeters, Vereecken, and coworkers (Nguyen *et al.*, 2009a,b), in conjunction with observations derived from acetaldehyde oxide (Horie *et al.*, 1994b), to assign the majority of the dioxirane fate to the decarboxylation pathway

(products CO_2 + HO_2 + alkyl radical for dioxiranes in the primary position). A decarboxylation branching ratio of ~0.7 gave good agreement with observations. As these dioxiranes have allylic functionality, we assign the balance of the carbon to a proposed isomerization pathway (Figure E.13 in the Supporting Information) that may form a stable product. The alkyl radical that is produced in the decarboxylation step in Route A is the methylvinyl radical, which is known to generate HCHO + peroxyacetyl radical (~0.35) or HCHO + methylperoxyl radical + CO (~0.65) in the presence of oxygen (Orlando *et al.*, 1999). It is probable that the observed acetic acid (0.02–0.06 from dry to humid) is produced from the reaction of peroxyacetyl radicals with HO_2 or RO_2 (Crawford *et al.*, 1999; Hasson *et al.*, 2004; Horie and Moortgat, 1992; Madronich and Calvert, 1990). We speculate that the higher acetic acid yield under more humid conditions may be due to unidentified wall reactions. The methylperoxyl radical is a precursor to methyl hydroperoxide under HO_2-dominant conditions. Methyl hydroperoxide has been identified in previous works (Gäb *et al.*, 1995; Sauer *et al.*, 1999), but without complete mechanistic knowledge of its chemical source.

The *syn* MVKOO* will decompose to OH and a β-oxy alkyl radical *via* a vinylhydroperoxide intermediate (B route). The further reactions of the β-oxy alkylperoxyl radical (RO_2) are much more uncertain. In the mechanism suggested here, this chemistry is proposed to proceed similarly to the RO_2 radicals found in MVK + OH chemistry that have analogous functionality (Praske *et al.*, 2015). We followed the recommendations in Praske *et al.* (2015) for the branching ratios of the three product channels with HO_2: β-oxy hydroperoxide, 1,2-dicarbonyl + OH + HO_2, and alkoxyl radical (RO) + OH + O_2. The RO radical fragments to formaldehyde and an acyl radical and promptly reacts with O_2 to produce an acylperoxyl (RC(O)OO) radical. The acylperoxyl radical may undergo three fates upon reaction with HO_2 (Figure E.4B), modeled after reactions of peroxyacetyl (Moortgat *et al.*, 1989; Tomas *et al.*, 2001). These data suggest that decarboxylation is an important fate for this particular acylperoxyl radical, which affects both OH and formaldehyde in the process (*via* the chemistry of the vinyl radical) (Knyazev and Slagle, 1995).

E.3.2.2 C_1 Criegee + Water Reaction

The mechanism illustrated in Figure E.4 was integrated into a kinetic model. Most of the rates and branching ratios available in the literature were imported for use in the model mechanism and assumed to be accurate. The product yields and rate

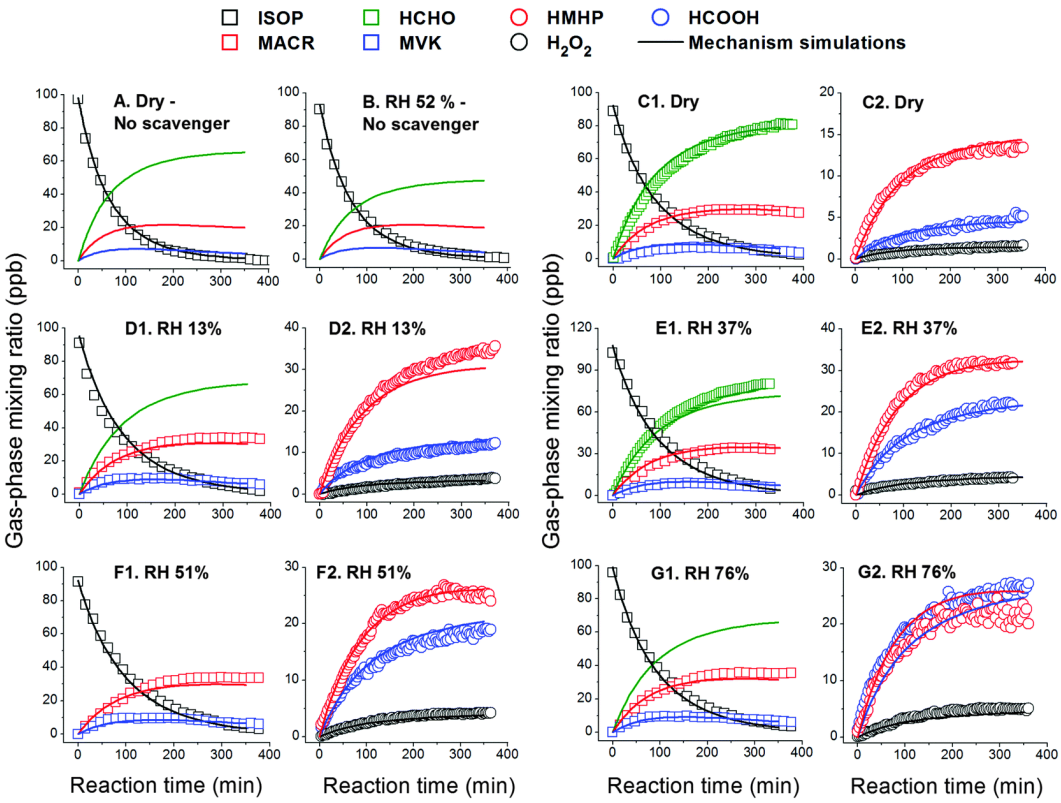

Figure E.5: Panels A–G show the comparison between gas-phase observations from different experiments (various markers) and results from model mechanism simulations based on Figure E.4 (solid lines). Subpanels show the mixing ratios of (1) isoprene and carbonyls and (2) CH_2OO + $(H_2O)_n$ products, when applicable. Simulations under "Dry" conditions used RH = 1.2%. The displayed mixing ratios of HMHP and HCOOH have been corrected for first-order wall loss (Figure E.10 in the Supporting Information). The model inputs are shown in the Supporting Information. Experimental conditions for the measured data are found in Table E.1.

coefficients of Criegee reactions labeled [b] in Figure E.4 were empirically tuned to provide satisfactory agreement with observational data within the full RH range, as shown in Figure E.5. The reaction inputs into the kinetic model are shown in the Supporting Information. We find that variations in the molar yields of HMHP, HCOOH, HCHO and H_2O_2 with RH can only be simulated if the reaction with water dimer is included in the mechanism. The mixing ratio of water dimers was calculated based on their equilibrium thermodynamics at 295 K (Figure E.14 in the Supporting Information) (Owicki *et al.*, 1975).

Some of the observed H_2O_2 in the ozonolysis experiments (Table E.1) originates from the HO_2 + HO_2 → H_2O_2 + O_2 reaction (Figure E.15 in the Supporting Information). Using published rate constants and HO_2 observations we estimate the

HO_2 self-reaction accounts for ~50% of the observed H_2O_2. However, considering the uncertainties in the HO_2 and H_2O_2 observations we cannot exclude the possibility that the HO_2 self-reaction explains the entirety of the observed H_2O_2, and thus, that the $CH_2OO + (H_2O)_n \rightarrow H_2O_2 + HCHO$ channel has zero yield (see error bounds in Figure E.15 in the Supporting Information). We adjusted the product branching ratios for the $CH_2OO + (H_2O)_n$ reactions to remove the average contribution from HO_x chemistry, and this is shown in the left-most panel of Figure E.4. The product branching in the dimer reaction favors formic acid formation over HMHP formation, which is consistent with the suggestion that the reaction of CH_2OO with water dimer to form HMHP is exothermic, and some of the excited HMHP produced by that pathway may further decompose (in this case to formic acid + H_2O) with water acting as a catalyst (Ryzhkov and Ariya, 2004).

We used the following rate coefficients for the reaction of CH_2OO with water in the model mechanism: $k_{H_2O} = 9 \times 10^{-16}$ cm^3 molec^{-1} s^{-1} and $k_{(H_2O)_2} = 8 \times 10^{-13}$ cm^3 molec^{-1} s^{-1}. The water monomer reaction rate coefficient falls within the upper limit determined by Welz *et al.* (2012) and by other works ($<4 \times 10^{-15}$ cm^3 molec^{-1} s^{-1}). The dry (RH ~1%) observations provided constraints for the monomer rate coefficient, and the dimer rate coefficient was adjusted until model results satisfactorily reproduces measurements. We found that a dimer reaction coefficient faster than that of the monomer reaction, but slower than the coefficient suggested by some studies (4–6.5 $\times 10^{-12}$ cm^3 molec^{-1} s^{-1}; Berndt *et al.*, 2014; Chao *et al.*, 2015; Lewis *et al.*, 2015), gave the best fit with the observational results across all RH conditions.

Figure E.16 in the Supporting Information shows results of a sensitivity study of the water rate coefficients in the model, which concludes that the rate coefficient of Chao *et al.* (2015) is too large to simulate the data in this work. Our suggested dimer rate coefficient of $k_{(H_2O)_2} = 8 \times 10^{-13}$ cm^3 molecule^{-1} s^{-1} is consistent with those of Newland *et al.* (2015), who found that 5.6 ($\pm$7.0) $\times 10^{-13}$ cm^3 molec^{-1} s^{-1} best describe their chamber data. Leather *et al.* (2012) also found the rate coefficient of CH_2OO with "water" to be in the range of ~1×10^{-15} - 1×10^{-12} cm^3 molec^{-1} s^{-1} when measuring HCOOH. HCOOH is the product of both the water monomer and dimer reaction with CH_2OO, so the observed range is in agreement with this work. The difference between reported CH_2OO + water dimer rate coefficients in the literature is striking, but the source of the disagreement is unclear.

The reaction timescales, Criegee generation methods, reaction vessel character-

istics, and Criegee concentrations in literature works are different – all of which may play a role in the discrepancy. Furthermore, if water vapor may intercept the hot Criegee directly during ozonolysis reactions, in a manner analogous to the interception of excited alkyl radicals by O_2 (Glowacki *et al.*, 2012), then there may be significant deviations between chamber and direct kinetic determinations as direct determinations produce and investigate SCI preferentially. The result is a promotion of the H_2O reaction over the $(H_2O)_2$ reaction during ozonolysis. Assuming CI interception occurs to a non-negligible extent, observations from chamber studies would be more immediately relevant for atmospheric modeling than current data from direct determinations.

Figure E.14c in the Supporting Information shows the relative contribution of each reaction using the aforementioned rate coefficients, where the dimer reaction can contribute up to ~65% as the humidity approaches 100%. However, the water monomer reaction is an important sink for CH_2OO under all atmospherically-relevant RH.

E.3.2.3 OH and HO_2 formation

The production of OH can be visualized from the decay of isoprene in the experiments where an OH scavenger was not present (Figure E.5 a and b). OH was directly measured by LIF; however, the high dilution ratio used in the laboratory to conserve chamber volume degraded the signal-to-noise of the instrument. In addition, the experimental conditions in the reaction (including high peroxide mixing ratios) and unknown interferences that may be related to unsaturated hydrocarbon + ozone chemistry resulted in uncertainty bounds in the direct OH determination that were too high to constrain yields (Mao *et al.*, 2012; Nguyen *et al.*, 2014b). Thus, a combination of modeling and isoprene decay measurements was used to estimate [OH]. Estimations of OH sources in the model mechanism relied on constraints provided by other products. An overall OH yield of approximately 28(±5)% gives good agreement with observations under both dry and humid conditions, *e.g.* the comparison between observed and simulated isoprene decays produced least-squares slope = 1.023, R^2 = 0.999 at RH < 4% and slope = 1.015, R^2 = 0.998 at RH 52%, and is consistent with the recommended value by IUPAC (25%) (Atkinson *et al.*, 2006). It should be noted that not all of this OH is produced from the prompt VHP channel. This would necessitate almost 100% *syn* branching for MVKOO* and for the following radical chemistry to be OH neutral. Instead, the constraints placed by

closed-shell products in the mechanism predict that prompt decomposition (from *syn*-MVKOO*) accounts for a 14% yield of OH, with respect to the reaction of isoprene, and further chemistry of the β-oxy alkyl radical generates another 12%. The remaining minor fraction arises from unimolecular reactions of the C_4 Criegees. Neither the POZ decomposition nor the following RO_2 chemistry is expected to be sensitive to water vapor, in good agreement with the stable OH yields between dry and humid conditions. Our OH source contribution results are fairly consistent with those using a statistical-dynamical master equation and transition state theory, which predicts an OH prompt production yield of 11% for a total yield of 25% (Zhang and Zhang, 2002).

HO_2 is generated and consumed along various reaction channels in ozonolysis (Figure E.4). The HO_x cycling of OH and HO_2 also occurs in conjunction with ozonolysis in the model mechanism (Supporting Information). Major sources of HO_2 from ozonolysis include decarboxylation of primary dioxiranes (Route A) and the further chemistry of the β-oxy alkyl radical (Route B). A major sink of HO_2 in this work is the reaction with the RO_2 radical produced from cyclohexane (OH scavenger). As a result, the usage of other OH scavengers may change the HO_2 concentrations during similar experiments. Figure E.17 in the Supporting Information shows that HO_2 simulated using the kinetic model shown in the Supporting Information agrees fairly well with the measured values under dry and humid conditions at the start of the reaction (~40 ppt). As the reaction progresses, however, the agreement worsens (simulated HO_2 is lower than measured.) We believe this is because the simulated scheme does not trace second generation products, which appear to produce a significant quantity of HO_2.

E.3.2.4 HCHO Formation

The difference in observed HCHO between the dry (RH ~1% in the simulation) and RH 37% experiments provides unique insights into the bimolecular reaction of CH_2OO (Figure E.5, Panels c1 and e1). The model predicts that a non-negligible fraction of HCHO can be produced from the CH_2OO reaction with ozone (Kjaergaard *et al.*, 2013; Wei *et al.*, 2014), the second most abundant reaction partner for CH_2OO in our experiments, when the reaction conditions are dry. For $k_{CH_2OO+O_3}$ $\sim 1 \times 10^{-12}$ cm^3 molec^{-1} s^{-1}, as has been previously suggested (Vereecken *et al.*, 2014), the best fit with observations is achieved by assuming a formaldehyde yield of 0.7 (while conserving a faster rate), instead of the recommended value of 1. While

it is possible that unknown pathways for the $CH_2OO + O_3$ reaction exist, we believe it more likely that the model mechanism is missing a Criegee sink that is ~30% of the effective $CH_2OO + O_3$ reaction, but does not produce HCHO, when the reaction is performed dry. If a missing sink exists, it is not the Criegee self-reaction, as including even the fastest experimentally-determined rate coefficient did not alter the simulations (Su *et al.*, 2014). All side reactions of CH_2OO become negligible when RH reaches atmospherically relevant levels. Of the HCHO sources discussed in this work that are important under atmospherically relevant conditions, the initial POZ decomposition comprises the majority production pathway (~60%). The model simulations predict that unimolecular reactions of C_4 Criegees to contribute another relative ~35% and the reaction of $CH_2OO + (H_2O)_n$ is a relatively small (~5%) source of formaldehyde. As we noted above, the yield of HCHO and H_2O_2 from this channel could be zero within uncertainties.

E.3.2.5 Other Reactions of the C_1 Criegee

Finally, we use the $RO_2 + CH_2OO$ rate coefficient of Vereecken *et al.* (2012) ($k \sim 5 \times 10^{-12}$ cm^3 molec^{-1} s^{-1}) and the OH reaction kinetics for cyclohexane (Atkinson *et al.*, 2006) to examine whether the 50 ppm of OH scrubber produces enough RO_2 to impact CH_2OO yields in the ozonolysis reaction. The model results suggest that cyclohexane RO_2 radicals were not competitive with water as a Criegee scavenger during the experiments in this work. In addition, inserting the reaction of isoprene + CH_2OO into the model mechanism ($k = 1.78 \times 10^{-13}$ cm^3 molec^{-1} s^{-1}), as suggested by Vereecken *et al.* (2014), did not significantly perturb the model simulation results. However, in studies where initial isoprene and ozone are present at ppm levels, the CH_2OO + alkene reaction may play a bigger role. These newly-identified reactions may be one source of discrepancy in literature yield data, underscoring the importance of using atmospherically-relevant mixing ratios of reactants or verifying that secondary chemistry is not affecting laboratory results.

E.3.3 Competitive Rates of $CH_2OO + (H_2O)_n$ and $CH_2OO + SO_2$

Although water reactions are thought to dominate the fate of CH_2OO in the atmosphere (Berndt *et al.*, 2014; Chao *et al.*, 2015; Fenske *et al.*, 2000; Newland *et al.*, 2015; Ryzhkov and Ariya, 2004), it has been suggested that the reaction of SCI with SO_2 may be important from the perspective of H_2SO_4 production and, thus, particle formation (Mauldin *et al.*, 2012). Here, we measure the competitive

rates of the reaction of isoprene SCIs with H_2O and SO_2, using isoprene mixing ratios that approach atmospheric levels (~20 ppb) and realistic concentrations of SO_2. This measurement is sensitive to the combined effects of CH_2OO and the C_4 SCIs of isoprene. However, it is clear that the dominant fraction of the bimolecular reactivity originates from CH_2OO, illustrated by the similar SCI yields when using SO_2 as a scavenger compared to H_2O (Table E.1). Notably, the orders of magnitude uncertainties that exist in the absolute rate coefficients for CH_2OO bimolecular reactions become immaterial when determining relative rates (Anglada *et al.*, 2011; Atkinson and Lloyd, 1984; Herron *et al.*, 1982; Kurtén *et al.*, 2011; Kuwata and Valin, 2008; Ryzhkov and Ariya, 2004; Stone *et al.*, 2014; Welz *et al.*, 2012).

Figure E.6 shows the reaction progress for three relative rate experiments between H_2O and SO_2 during an isoprene ozonolysis performed with an OH scavenger. At 15 ppb of SO_2 and 20% RH, representative of a dry and polluted day, greater than 90% of CH_2OO reacted with water as evidenced by the large abundance of HMHP and HCOOH as compared to H_2SO_4 (Figure E.6a). Only under the driest conditions (RH < 4%) does CH_2OO appreciably oxidize SO_2 at initial levels of ~15 ppb (Figure E.6b). Although under these conditions, the water reaction is still the major reaction pathway for CH_2OO. Here, we start to witness decreasing mixing ratios of HMHP with time, which is due to heterogeneous loss on acidic surfaces from the H_2SO_4 production and is uncorrected in Figure E.6. Only under exceptionally dry (RH < 4%) and exceptionally high $[SO_2]_0$ (~75 ppb) conditions does SO_2 oxidation become the dominant fate of CH_2OO (Figure E.6c), although these specific conditions are rarely found on Earth.

The relative rate of $k_{SO_2}/k_{(H_2O)_n} = 2.2\ (\pm 0.3) \times 10^4$ determined from the data is in good agreement with the $k_{SO_2}/k_{(H_2O)_n}$ range of (1-3) $\times 10^4$ reported in other studies (Atkinson and Lloyd, 1984; Newland *et al.*, 2015; Welz *et al.*, 2012). However, these results are considerably different than those of Stone *et al.* (2014), who measured a lower limit of $k_{SO_2}/k_{(H_2O)_n} > 4 \times 10^5$. Although the source of the discrepancy is not clear, the experiments of Stone *et al.* (2014) were performed differently compared to this work. Stone *et al.* (2014) quantified CH_2OO decay *via* chemical scavenging to form HCHO and made the assumption that HCHO production is proportional to CH_2I (Criegee precursor) concentrations. Like other studies that measure CH_2OO decay (Taatjes *et al.*, 2008), Stone *et al.* (2014) provides lower limits on $k_{SO_2}/k_{(H_2O)_n}$ due to unknown processes that affect the first-order SCI decay when H_2O is added. As this work captures at least one co-product of each branch in the $CH_2OO + (H_2O)_n$

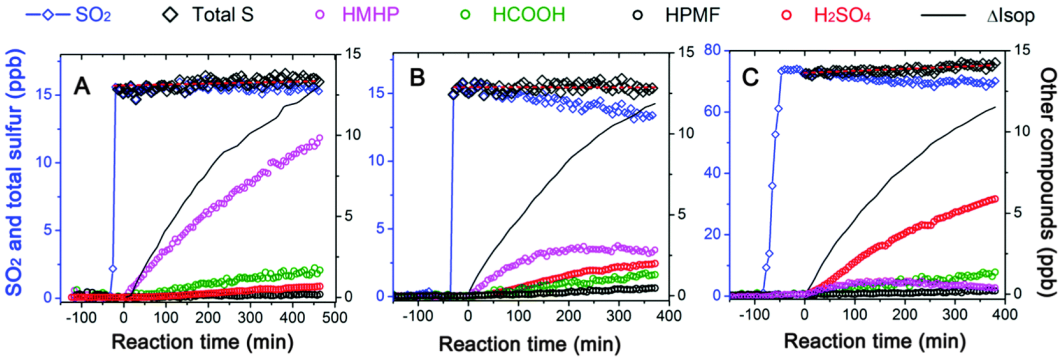

Figure E.6: Relative rate experiments of H_2O and SO_2 as scavengers for CH_2OO, produced by the ozonolysis of ~20 ppbv of isoprene at 298 K, under the following conditions: (A) 15 ppbv of SO_2 and 20% RH, (B) 15 ppbv of SO_2 and <4% RH, and (C) 75 ppbv of SO_2 and <4% RH. Total sulfur (black diamonds) represents the sum of SO_2 and H_2SO_4.

reaction, our measurement can be considered absolute. However, it must be noted that challenges in quantifying low [H_2O] and complex reaction products also give rise to significant uncertainties in this work – a limitation that likely permeates all studies of SCI + $(H_2O)_n$ reactions.

E.3.4 Fates of CH_2OO in the Atmosphere: A Case Study from SOAS

To put the competition between the reaction of H_2O and SO_2 with CH_2OO into perspective, it would require 500 ppb of SO_2 to have equal reactivity with H_2O at an average RH of 30% (T = 295 K, P = 1 atm). Many areas of the world are more humid than this RH level, especially in forested areas where biogenic emissions are high. At RH > 50%, the amount of SO_2 needed for equal reactivity would be found only in a power plant or volcanic plume. Here, we examine the fates of CH_2OO and molecular contributors to SO_2 oxidation in a typical Southeastern United States forest that emits predominantly isoprene during summer. The comprehensive datasets were obtained by multiple investigators as part of the Southern Oxidant and Aerosol Study in Brent, AL during June of 2013 (https://SOAS2013.rutgers.edu/). A time-of-flight CF_3O^- CIMS provided measurements of SO_2, H_2O_2, and oxidized organic compounds and a commercial weather station (Coastal Environmental Systems model Zeno 3200) provided measurements of T, P, and RH needed to calculate water vapor mixing ratio. The measurement site was occasionally impacted by SO_2 pollution from nearby power plants.

Figure E.7 shows the measured CH_2OO + $(H_2O)_n$ products and the CH_2OO +

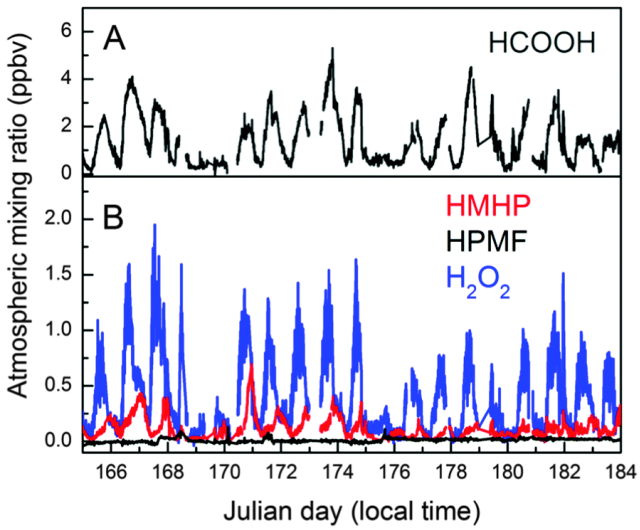

Figure E.7: Measurements of compounds that are formed *via* CH_2OO bimolecular reactions during the SOAS 2013 campaign (A) formic acid, and (B) HMHP, HPMF, and H_2O_2. HCOOH and H_2O_2, in particular, have multiple photochemical sources.

HCOOH product for the duration of the SOAS study. While HCOOH and H_2O_2, two compounds with multiple photochemical sources, are known to have high concentrations at the Earth's surface, the presence of large abundances of HMHP produced from biogenic ozonolysis chemistry has previously not been fully appreciated. The mixing ratio of HMHP reaches 600 ppt during some events at this site (Figure E.7b). Other limited observations of HMHP report even higher mixing ratios (Lee *et al.*, 1993a). Concentrations of HMHP are comparable to the sum of two major products of the isoprene + OH oxidation under HO_2-dominated conditions (ISOPOOH + IEPOX) during the SOAS campaign (Nguyen *et al.*, 2015a). We note, however, that the interpretation of the ambient surface mixing ratio of HMHP is challenging as it is affected by poorly-constrained oxidative and photolytic loss processes. Additionally, the nocturnal peak concentrations of HMHP reflect both chemical production and nighttime boundary layer dynamics.

The persistently humid (2–3 vol% H_2O) and occasionally polluted atmosphere at SOAS provides a useful case study to examine the reactions of CH_2OO (Figure E.18 in the Supporting Information). Despite plumes that approached 10 ppb, SO_2 only negligibly impacted the CH_2OO fate. Using laboratory-derived relative rate results (Section E.3.3), CH_2OO loss in the gas phase was almost entirely controlled by the H_2O reactions (>98%) for every day of the SOAS study (Figure E.19a in the Supporting Information). At peak SO_2 mixing ratios, the fraction of CH_2OO

that was oxidized by SO_2 was below 1%. In comparison, the effective reaction with HCOOH is slightly more efficient at 1–2% of the total CH_2OO fate due to high HCOOH mixing ratios (~4 ppb, Figure E.7a) and a faster rate coefficient ($k_{HCOOH}/k_{SO_2} \sim 2.8$; Sipilä *et al.*, 2014). Still, the product of the CH_2OO + HCOOH reaction, HPMF, was not present at quantifiable concentrations during the majority of the month-long study (Figure E.7b). Using peak SO_2 and HCOOH mixing ratios observed during the SOAS campaign, we find that the water reaction is dominant at all atmospherically-relevant RH (Figure E.19b in the Supporting Information).

Given the ubiquity of water in the troposphere, it is more informative to explore the CH_2OO reactions from the point of view of SO_2 and HCOOH oxidation. We use the observed mixing ratios of ozone, abundant exocyclic alkenes (isoprene and β-pinene), and water vapor to estimate the steady-state concentrations of CH_2OO at this site (~2×10^3 molec cm^3 in the daytime) for the month-long study (Figure E.17 in the Supporting Information). The production term was calculated from the ozonolysis reaction, using respective SCI yields of 0.6 for isoprene (this work) and 0.3 for β-pinene (assuming that the scavenged SCI are mostly CH_2OO; Hasson *et al.*, 2001a). The loss term assumes H_2O and $(H_2O)_2$ are the only sinks for CH_2OO at this site (Figure E.19b in the Supporting Information). α-Pinene is the second most abundant alkene in this forest but its ozonolysis is not thought to produce CH_2OO. The rate coefficients of relevant reactions (Atkinson *et al.*, 2006; Khamaganov and Hites, 2001) were calculated using measured temperature inputs (292–306 K) during SOAS: k_{ISO+O_3} (~1×10^{-17} cm^3 molec^{-1} s^{-1}), $k_{\beta-PIN+O_3}$ (~2×10^{-17} cm^3 molec^{-1} s^{-1}), k_{OH+SO_2} (~1×10^{-12} cm^3 molec^{-1} s^{-1}), and $k_{OH+HCOOH}$ (~4.5×10^{-13} cm^3 molec^{-1} s^{-1}). The average OH concentration used in the calculation was 1×10^6 molec cm^{-3}. For CH_2OO reaction coefficients, we used $k_{SO_2}/k_{(H_2O)_n}$ ~2.2×10^4 (where n = 1, 2; this work), absolute rate coefficients as reported in Section E.3.2.2, and two different relative rate determinations for HCOOH reactions that are notably different: k_{HCOOH}/k_{SO_2} ~2.8 ("k_{HCOOH1}", Sipilä *et al.* (2014)) and $k_{HCOOH}/k(H_2O)$ ~1.4×10^4 ("k_{HCOOH2}", Neeb *et al.* (1997)). Using $k_{SO_2}/k_{(H_2O)_n}$ and $k(H_2O)$ in this work, $k_{HCOOH1} \approx 5.5 \times 10^{-11}$ cm^3 molec^{-1} s^{-1} and $k_{HCOOH2} \approx 2.0 \times 10^{-11}$ cm^3 molec^{-1} s^{-1}.

Figure E.8a shows that CH_2OO accounts for <6% of the gas-phase SO_2 oxidation at the SOAS site. This is in stark contrast to the proposed 50% contribution of "compound X" (suggested to be related to Criegee chemistry) to the oxidation of SO_2 in a Finnish boreal forest (Mauldin *et al.*, 2012). The discrepancy has

been suggested to be due to the different distribution of volatile alkenes in boreal forests, *i.e.*, that the SCI from α-pinene may have a higher relative contribution to SO_2 oxidation. However, given the large OH yields from α-pinene ozonolysis (0.70–0.91) (Atkinson and Aschmann, 1993; Chew and Atkinson, 1996; Paulson *et al.*, 1998; Rickard *et al.*, 1999; Siese *et al.*, 2001), and the fast decomposition rates of larger Criegees (this work and elsewhere), the population of SCIs that are available for bimolecular reaction from α-pinene is expected to be small and their contribution to sulfate formation, thus, an open question. In cleaner environments, a significant pathway toward new particle formation may be the production of extremely low volatility compounds from α-pinene ozonolysis (Ehn *et al.*, 2014; Jokinen *et al.*, 2014), through the VHP channel and subsequent autoxidation reactions (Crounse *et al.*, 2012) of the RO_2. In comparison, CH_2OO may oxidize a larger amount (<35%) of HCOOH, as its CH_2OO reaction is faster and its OH reaction is slower than the analogous reactions for SO_2. However, depositional losses, instead of oxidation, is thought to dominate the atmospheric fate of HCOOH ($\tau_{dep} \sim$ 20–40 h (at 1.5 km PBL height), $\tau_{OH} \sim$ 620 h, $\tau_{SCI} \sim$ 1800 h) (Nguyen *et al.*, 2015a). Finally, we conclude that CH_2OO does not significantly affect the atmospheric lifetime of SO_2 or HCOOH.

E.4 Atmospheric Implications

This work provides new insights into the reactions of isoprene-derived Criegee intermediates, especially for the decomposition pathways of the excited C_4 Criegees where scarce experimental data are available. The model mechanism in this work suggests that C_4 Criegees decompose to OH, HCHO, and other products in the atmosphere without significantly producing SCI that participate in bimolecular reactions. Some existing atmospheric models, such as the Master Chemical Mechanism (MCM), assume the C_4 Criegees lose $O(^3P)$ to form MVK and MACR, although this is not supported by our observations. A significant portion of the OH and HCHO yields is secondary. One reaction, subset $CH_2OO + (H_2O)_n$, accounts for almost all of the SCI bimolecular reactions in isoprene ozonolysis under typical atmospheric conditions. This implies that isoprene-derived SCIs are a negligible contributor to H_2SO_4 production in the atmosphere. If stabilized Criegees indeed play a role in new particle formation, the events will be localized to regions that are not dominated by the reactivity of ozone with isoprene. Those areas may instead be abundant in the small hydroperoxides that are quickly deposited to plant canopies (Nguyen *et al.*, 2015a). Our data are consistent with the suggestion that isoprene emissions

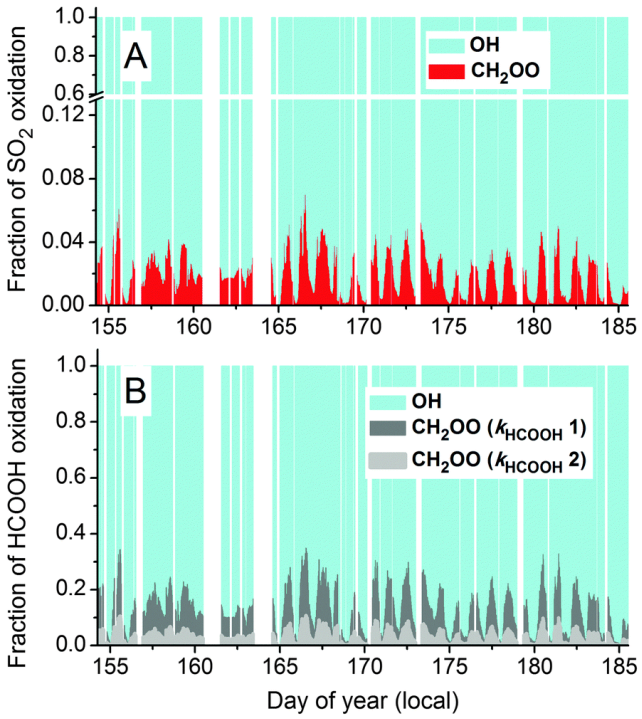

Figure E.8: Significance of CH_2OO as an oxidant for (A) SO_2 and (B) HCOOH. In panel B, relative rate determinations by (1) Sipilä *et al.* (2014) and (2) Neeb *et al.* (1997) were used.

can suppress new particle formation (Kiendler-Scharr *et al.*, 2009), although the specific inhibition mechanism is still unclear, while these events readily occur in boreal forests (Mäkelä *et al.*, 1997). Discussions of whether monoterpene SCI in Boreal forests may appreciably oxidize SO_2 will hinge on the understanding of their unimolecular lifetimes and $(H_2O)_n$ reactivity. Lastly, due to the structurally-specific reactivities of SCI, model simulations of ozonolysis chemistry should explicitly speciate alkenes and incorporate a conformationally-dependent reaction scheme. Incorporation of the isoprene ozonolysis mechanism (Figure E.4 and Supporting Information) into atmospheric models will likely improve the accuracy of OH, HO_2, and trace gas simulations in the atmosphere.

E.5 Supporting Information

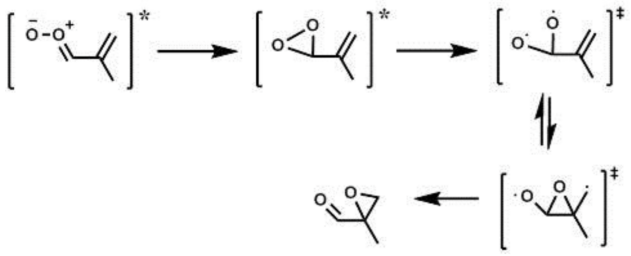

Figure E.9: (A) Partial calibration of the humidity dependence of HMHP ion sensitivity in CIMS. The HO_2 + HCHO reaction (from the photolysis of 4ppmv of formaldehyde, yellow shaded region) was used to produce approximately 5.7 ppbv of HMHP in the atmospheric chamber at 298K and 1 atm. The HMHP mixing ratio was allowed to stabilize for 1 hour before water-dependent calibration started. The stabilized HMHP mixing ratio from the chamber was sampled in the dark by CIMS, with nitrogen dilution streams that contained various mixing ratios of water: Gray regions denote 147 sccm of chamber air (dry) mixed with 1600 sccm of a dry ([H_2O] < 100 ppmv) nitrogen flow (similar to standard operation), blue regions denote 147 sccm of chamber air mixed with 1600 sccm of a humid ([H_2O] up to 4000 ppmv) nitrogen flow, and white regions denote a break in sampling or sampling of 147 sccm of clean air mixed with 1600 sccm of a dry nitrogen flow. Data from the gray regions were used to confirm that the mixing ratio of HMHP in the chamber did not change significantly throughout the calibration period. Data from the white regions were used to confirm that the background (free of HMHP) did not shift throughout the calibration period. (B) The complete relationship of CIMS ion sensitivity vs. water vapor in the CIMS flow region for H_2O_2, HCOOH, and HMHP for the instrument used in this study.

chemical name (abbrev.)	chemical formula	MS stage	Ion *m/z*	ionic composition	quantification method	water dependence
water vapor	H_2O	1	104	$^{13}CF_3O\cdot(H_2O)^-$	FT-IR	v. strong
		1	121	$CF_3O\cdot(H_2O)_2^-$	FT-IR	v. strong
acetic acid (AA)	$CH_3C(O)OH$	1	79	$HF\cdot[O(O)CCH_3]^-$	gravimetric	strong
		2	145 → 79	$CF_3O\cdot[AA]^- \rightarrow HF[O(O)CCH_3]^-$	gravimetric	strong
formic acid	$HC(O)OH$	1	65	$HF\cdot(O(O)CH)^-$	gravimetric	strong
nitric acid	HNO_3	1	82	$HF\cdot(ONO_2)^-$	gravimetric	weak
peracetic acid (PAA)	$CH_3C(O)OOH$	1	161	$CF_3O\cdot(PAA)^-$	colorimetric (UV-Vis)	moderate
hydrogen peroxide	HOOH	1	119	$CF_3O\cdot(HOOH)^-$	colorimetric (UV-Vis)	strong
		2	119 → 85	$CF_3O\cdot(HOOH) \rightarrow CF_3O^-$	colorimetric (UV-Vis)	strong
methyl hydroperoxide (MHP)	CH_3OOH	2	133 → 85	$CF_3O\cdot(CH_3OOH)^-$	colorimetric (UV-Vis)	strong
hydroxymethyl hydroperoxide (HMHP)	$HOCH_2OOH$	1	149	$CF_3O\cdot(HMHP)^-$	FT-IR	weak
hydroxy-acetone (HAC)	$HOCH_2C(O)CH_3$	1	159	$CF_3O\cdot(HAC)^-$	gravimetric	weak
glycolaldehyde (GLYC)	$HOCH_2C(O)H$	2	145 → 85	$CF_3O\cdot(GLYC)^- \rightarrow CF_3O^-$	FT-IR	weak

Table E.2: Detection and quantification of compounds using negative-ion CF_3O^- CIMS.

Scheme S1: Model mechanism at T = 295 K and P = 1 atm, based on a condensed version of Figure E.4 in the main text. The OH chemistry of cyclohexane (CHX) is monitored as it produces RO_2 and consumes HO_2. Standard background chemistry (*e.g.* HO_x, NO_y reactions, not shown) is also incorporated. Minor oxygenated organics (*e.g.* 1-hydroperoxy-2-oxybut-3-ene) are all lumped as a generic "product" compound. Rate coefficients for the background reactions are based off IUPAC recommendations except where noted.

Ozonolysis Mechanism

```
x34POZ = 0.6;
x12POZ = 0.4;
xMACR = 0.68;
xMACROO = 1-xMACR;
xsynMACROO = 0.2;
xantiMACROO = 0.8;
xMVK = 0.42;
xMVKOO = 1-xMVK;
xsynMVKOO = 0.6;
xantiMVKOO = 0.4;
xdioxole = 0.25;
xdioxirane = 0.72;
xstable = 0.03;
xdecarbox = 0.7;
xPA_CH3CH2 = 0.35;
xHP = 0.3;
xDC = 0.3;
xRO = 0.4;

xOH = x12POZ.*xMVKOO.*xsynMVKOO;
yOH = xOH ...
        + xOH.*xRO + xOH.*xDC + xOH.*xRO.*xRO...
        + x34POZ.*xMACROO.*xantiMACROO.*xdioxirane...
        .*xdecarbox.*xRO.*xPA_CH3CH2...
        + x34POZ.*xMACROO.*xsynMACROO.*xdioxirane...
        .*xdecarbox.*xRO.*xPA_CH3CH2...
        + x12POZ.*xMVKOO.*xantiMVKOO.*xdioxirane...
        .*xdecarbox.*xRO.*xPA_CH3CH2;
yform = (x34POZ.*xMACROO + x12POZ.*xMVKOO)...
        + xOH.*xRO + xOH.*xRO.*xRO ...
        + x34POZ.*xMACROO.*xantiMACROO.*xdioxirane.*xdecarbox...
        + x34POZ.*xMACROO.*xsynMACROO.*xdioxirane.*xdecarbox ...
        + x12POZ.*xMVKOO.*xantiMVKOO.*xdioxirane.*xdecarbox;

yHO2 = xOH.*xDC + xOH.*xRO.*xRO ...
        + x34POZ.*xMACROO.*xantiMACROO.*xdioxirane.*xdecarbox...
```

```
        + x34POZ.*xMACROO.*xsynMACROO.*xdioxirane.*xdecarbox;

ymacr = x34POZ.*xMACR;
ymvk = x12POZ.*xMVK;

Isop + O3;
k = 1.3e-17;
Y(MACR) = ymacr;
Y(MVK) = ymvk;
Y(HCHO) = yform;
Y(CH2OO_SCI) = ymacr + ymvk;
Y(MACROO_SCI) = x34POZ.*xMACROO.*xstable;
Y(MVKOO_SCI) = x12POZ.*xMVKOO.*xstable;
Y(OH) = yOH;
Y(HO2) = yHO2;
Y(products) = xOH*xHP + xOH.*xDC + xOH.*xRO...
        + x34POZ.*xMACROO.*xantiMACROO.*xdioxole...
        + x12POZ.*xMVKOO.*xantiMVKOO.*xdioxole;

MACR + O3;
k = 1.8e-18;
Y(products) = 1;

MVK + O3;
k = 4.8e-18;
Y(products) = 1;

Isop + OH;
k = 1e-10;
Y(products) = 1;

MACR + OH;
k = 3.4e-11;
Y(products) = 1;

MACR + OH;
k = 1.9e-11;
Y(products) = 1;

CHX + OH;
k = 7.3e-12;
Y(CHX_RO2) = 1;

CHX_RO2 + CHX_RO2;
k = 5.7e-12;
Y(cyclohexanone) = 0.5;
Y(cyclohexanol) = 0.5;
```

CHX_RO2 + HO2;
k = 1.612e-11;
Y(cyclohexane hydroperoxide) = 1;

CHX_RO2 + SCI;
k = 5e-12;
Y(products) = 1;

CH2OO_SCI + H2O;
k = 0.9e-15;
Y(HMHP) = 0.73;
Y(H2O2) = 0.06;
Y(HCHO) = 0.06;
Y(HCOOH) = 0.21;

CH2OO_SCI + (H2O)2;
k = 0.8e-12;
Y(HMHP) = 0.40;
Y(H2O2) = 0.06;
Y(HCHO) = 0.06;
Y(HCOOH) = 0.54;

CH2OO_SCI + Isop;
k = 1.78e-13;
Y(products) = 1;

CH2OO_SCI + O3;
k = 1e-12;
Y(HCHO) = 0.7;

MACROO_SCI + H2O;
k = 1.8e-15;
Y(products) = 1;

MACROO_SCI;
k = 250;
Y(products) = 1;

MVKOO_SCI + H2O;
k = 1.8e-15;
Y(products) = 1;

MVKOO_SCI;
k = 250;
Y(products) = 1;

Background Mechanism

HO2 + HO2; % water dependent, k based on Stone and Rowley PCCP 2005
k = 1.8e-14.*exp(1500/T)*(1+1e-25.*fH2O.*M.*exp(4670/T));
Y(H2O2) = 1;
Y(O2) = 1;

OH + H2O2;
k = 1.69e-12;
Y(H2O) = 1;
Y(HO2) = 1;

OH + HO2;
k = 1e-10;
Y(H2O) = 1;
Y(O2) = 1;

OH + OH;
k0 = 7.0e-31.*(T./300).^(-1);
kinf = 2.6e-11.*(T./300).^(-0);
Fc = 0.6;
k = (k0.*M)./(1+(k0.*M./kinf)).*Fc.^((1+(log10(k0.*M./kinf)).^2).^(-1));
Y(H2O2) = 1;

OH + HONO;
k0 = 7.0e-31.*(T./300).^(-1);
kinf = 2.6e-11.*(T./300).^(-0);
Fc = 0.6;
k = (k0.*M)./(1+(k0.*M./kinf)).*Fc.^((1+(log10(k0.*M./kinf)).^2).^(-1));
Y(H2O) = 1;
Y(H2O2) = 1;

OH + HNO3;
k0 = 2.4e-14*exp(460/T);
k2 = 2.7e-17*exp(2199/T);
k3 = 6.5e-34*exp(1335/T);
k = k0+k3.*M./(1+k3.*M./k2);
Y(H2O) = 1;
Y(NO3) = 1;

OH + NO;
k0 = 7.0e-31.*(T./300).^(-2.6);
kinf = 3.6e-11.*(T./300).^(-0.1);
k = k0.*M./(1+(k0.*M./kinf)).*0.6.^((1+(log10(k0.*M./kinf)).^2).^(-1));
Y(HONO) = 1;

OH + NO2;
k0 = 1.51e-30.*(T./300).^(-3.0); % Updated to Mollner, Science, 2010
kinf = 2.58e-11.*(T./300).^(-0.0);
k = k0.*M./(1+(k0.*M./kinf)).*0.6.^((1+(log10(k0.*M./kinf)).^2).^(-1));

Y(HNO3) = 1;

OH + NO2;
k0 = 6.2e-32.*(T./300).^(-3.9);
kinf = 8.1e-11.*(T./300).^(-0.5);
k = k0.*M./(1+(k0.*M./kinf)).*0.6.^((1+(log10(k0.*M./kinf)).^2).^(-1));
Y(HOONO) = 1;

HOONO;
eq = 3.9e-27.*exp(10125./T);
k0 = 6.2e-32.*(T./300).^(-3.9);
kinf = 8.1e-11.*(T./300).^(-0.5);
kf = k0.*M./(1+(k0.*M./kinf)).*0.6.^((1+(log10(k0.*M./kinf)).^2).^(-1));
k = kf/eq;
Y(HO) = 1;
Y(NO2) = 1;

HO2 + NO;
k = 8.17E-12;
Y(OH) = 1;
Y(NO2) = 1;

O(3P) + HO2;
k = 5.9e-11;
Y(OH) = 1;
Y(O2) = 1;

O(3P) + O2;
k = 6.0e-34*(T/300).^(-2.4)*M;
Y(O3) = 1;

O3 + HO2;
k = 1.9e-15;
Y(OH) = 1;
Y(O2) = 2;

O3+OH;
k = 7e-14;
Y(HO2) = 1;
Y(O2) = 1;

O(1D) + H2O;
k = 2e-10;
Y(OH) = 2;

O(1D);
k = 3.2e-11*exp(67/T)*M;
Y(O3P) = 1;

O(3P) + NO;
k0 = 9.0e-32.*(T./300).^(-1.5);
kinf = 3.0e-11.*(T./300).^(-0.0);
k = k0.*M./(1+(k0.*M./kinf)).*0.6.^((1+(log10(k0.*M./kinf)).^2).^(-1));
Y(NO2) = 1;

O(3P) + NO2;
k = 1.04e-11;
Y(NO) = 1;
Y(O2) = 1;

O(3P) + NO2;
k0 = 2.5e-31.*(T./300).^(-1.8);
kinf = 2.2e-11.*(T./300).^(-0.7);
k = k0.*M./(1+(k0.*M./kinf)).*0.6.^((1+(log10(k0.*M./kinf)).^2).^(-1));
Y(NO3) = 1;

O3 + NO;
k = 1.86e-14;
Y(NO2) = 1;
Y(O2) = 1;

O3+NO+NO;
k = 2e-38.*cO2;
Y(NO) = 1;
Y(NO3) = 1;

O3 + NO2;
k = 3.46e-11;
Y(NO3) = 1;
Y(O2) = 1;

NO3 + NO2;
k0 = 2.7e-27.*(T./300).^(-4.4);
kinf = 1.4e-12.*(T./300).^(-0.7);
k = k0.*M./(1+(k0.*M./kinf)).*0.6.^((1+(log10(k0.*M./kinf)).^2).^(-1));
Y(N2O5) = 1;

N2O5 + H2O;
k = 2.5e-22;
Y(HNO3) = 2;

N2O5 + H2O + H2O;
k = 1.8E-39*fH2O*M;
Y(HNO3) = 2;
Y(H2O) = 1;

N2O5;
eq = 2.7e-27.*exp(11000./T);
k0 = 9.0e-29.*(T./300).^(-4.4);
kinf = 1.4e-12.*(T./300).^(-0.7);
kf = k0.*M./(1+(k0.*M./kinf)).*0.6.^((1+(log10(k0.*M./kinf)).^2).^(-1));
k = kf/eq;
Y(NO3) = 1;
Y(NO2) = 1;

NO3 + NO;
k = 2.27e-11;
Y(NO2) = 2;

NO3 + NO3;
k = 2.1e-16;
Y(NO2) = 2;
Y(O2) = 1;

NO3 + HO2;
k = 3.5e-12;
Y(NO2) = 1;
Y(O2) = 1;
Y(OH) = 1;

HO2 + NO2;
k0 = 2.0e-31.*(T./300).^(-3.4);
kinf = 2.9e-12.*(T./300).^(-1.1);
k = k0.*M./(1+(k0.*M./kinf)).*0.6.^((1+(log10(k0.*M./kinf)).^2).^(-1));
Y(HO2NO2) = 1;

HO2NO2;
eq = 2.1e-27.*exp(10900/T);
k0 = 2.0e-31.*(T./300).^(-3.4);
kinf = 2.9e-12.*(T./300).^(-1.1);
kf = k0.*M./(1+(k0.*M./kinf)).*0.6.^((1+(log10(k0.*M./kinf)).^2).^(-1));
k = kf./eq;
Y(HO2) = 1;
Y(NO2) = 1;

OH + HO2NO2;
k = 4.71e-12;
Y(HO2) = 1;
Y(NO2) = 1;

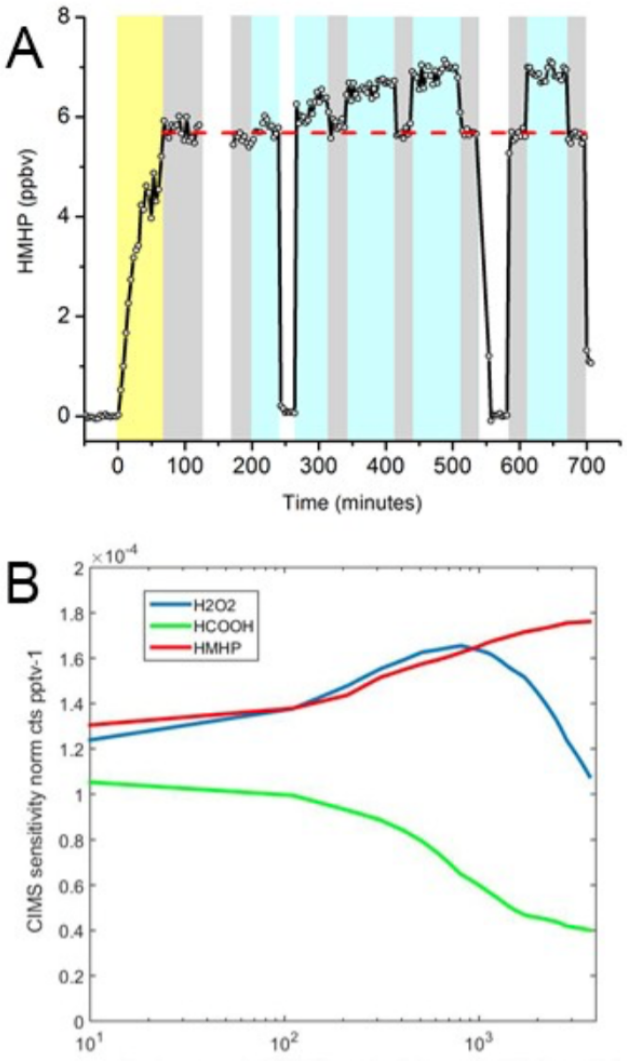

Figure E.10: Wall loss rates of HMHP, HCOOH, and H_2O_2 at two representative relative humidity conditions.

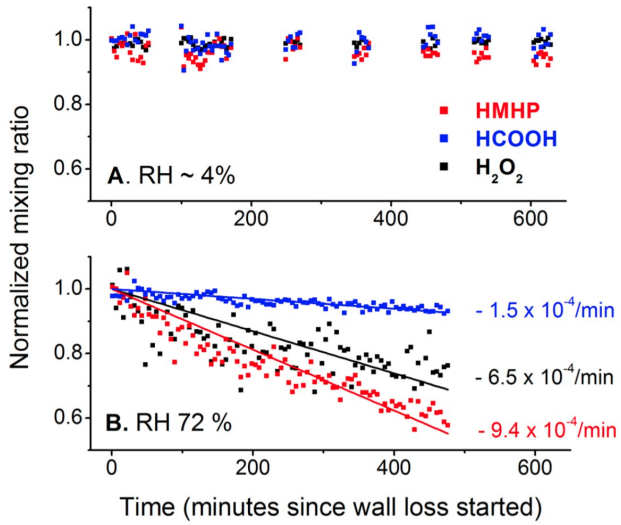

Figure E.11: An ozonolysis experiment, where formic acid was injected halfway through the experiment. The signal for HPMF was the only one (besides formic acid) that increased due to the reaction of CH_2OO + HCOOH.

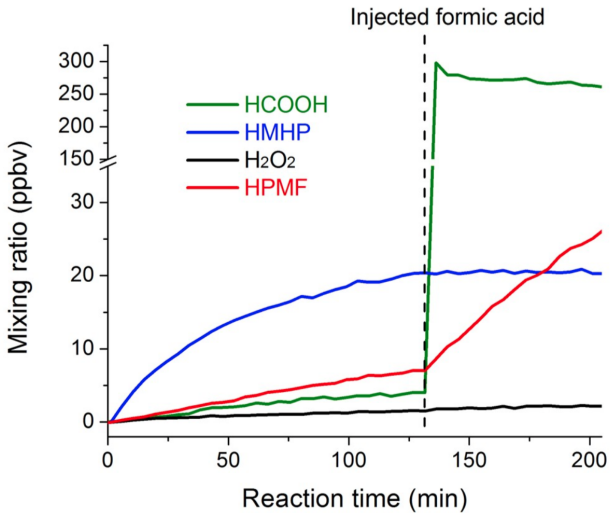

Figure E.12: CF_3O^- CIMS mass spectra shown for three RH experiments. In general acidic compounds are quantified by their fluoride transfer ($M + F^-$) ion and most other compounds by the cluster ion ($M + CF_3O^-$). Each compound has a water-dependent calibration that has not been applied to the figure, so the ion signals should be interpreted qualitatively. The peak labels correspond to: (a) HCOOH – *m/z* 65 (transfer) and *m/z* 131 (cluster), (b) H_2O_2 – *m/z* 119 (cluster), (c) Glycolaldehyde or isobaric compound – *m/z* 145 (cluster), (d) HMHP – *m/z* 149 (cluster), (e) Hydroxyacetone or methylvinylhydroperoxide – *m/z* 159 (cluster), (f) Unidentified – *m/z* 171, (g) HPMF – *m/z* 177 (cluster), (h) Unidentified – *m/z* 191, (i) Unidentified – *m/z* 217, (j) Acetic acid – *m/z* 79 (transfer) and *m/z* 145 (cluster), (k) Methyl hydroperoxide - *m/z* 133 (cluster). Peaks from CF_3O reagent have been subtracted and suspected impurities are not labelled. Glycolaldehyde and acetic acid cluster (*m/z* 145) are isobaric; however, the *m/z* 145 signal is mainly due to glycolaldehyde at low RH and acetic acid at higher RH (confirmed by a corresponding transfer ion).

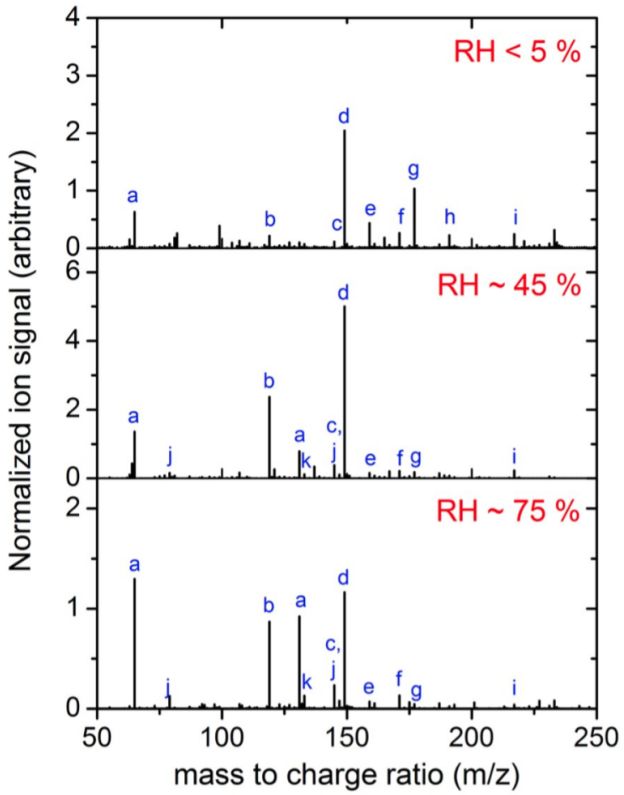

Figure E.13: Possible rearrangement of dioxiranes with allylic functionality.

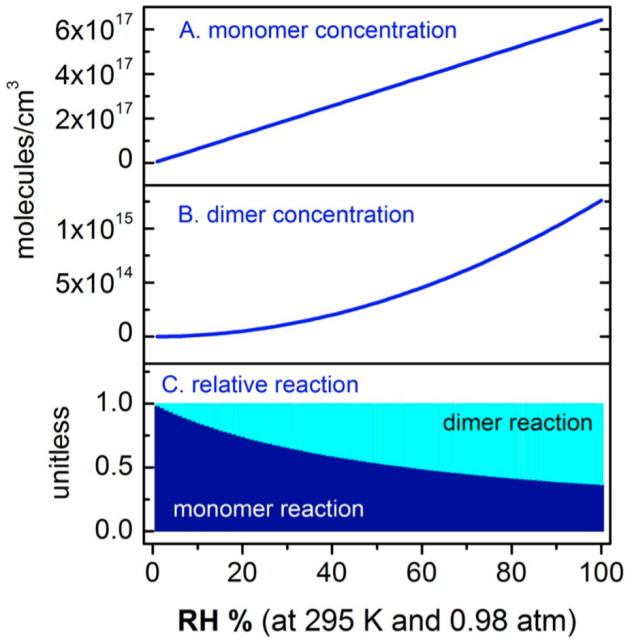

Figure E.14: The population of (A) water monomer molecules and (B) water dimer molecules as a function of RH, based on cluster association equilibrium thermodynamic functions reported in Owicki *et al.* (1975). The fraction of each reaction, using rate coefficients reported in the main text and in the Supporting Information, is shown in panel C.

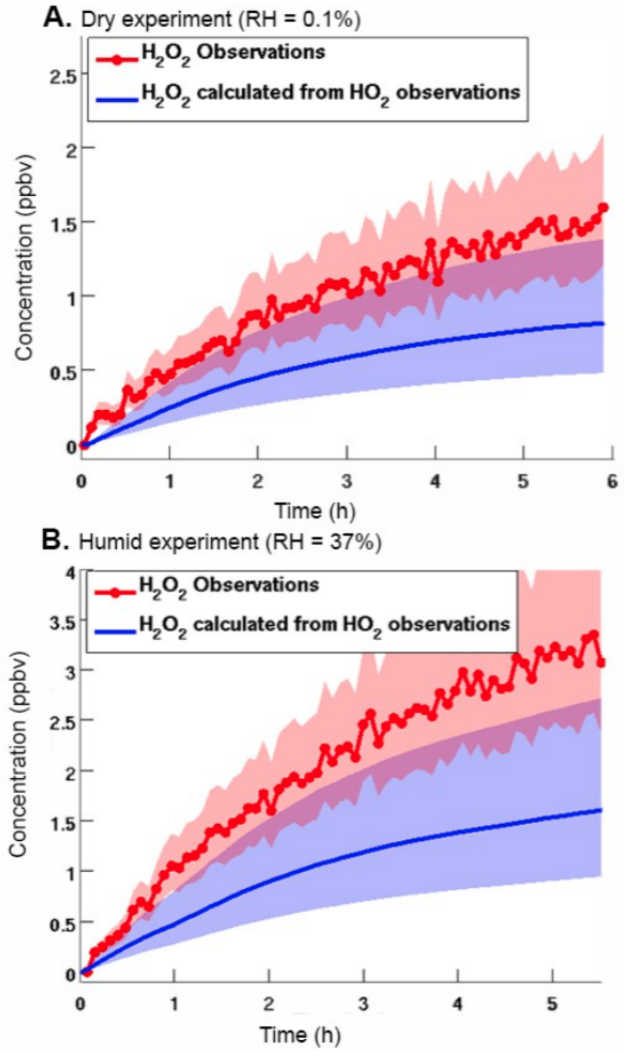

Figure E.15: Comparison between H_2O_2 observed by CIMS (filled markers) and calculated H_2O_2 using observed HO_2 data from GTHOS (Figure E.17, lines) for (A) dry conditions, $k_{HO_2+HO_2,295K}$ = 2.92 × 10^{-12} cm^3 $molec^{-1}$ s^{-1} and (B) RH 37% conditions, $k_{HO_2+HO_2,295K}$ = 3.53 × 10^{-12} cm^3 $molec^{-1}$ s^{-1}. Uncertainty bounds are used as reported in the main text. Rate coefficients are derived from the temperature and RH dependence reported by Stone and Rowley (2005).

Rate coefficients used	***RH = 51%***	***RH = 1.3%***
CASE 1 *The rates used in our model* $k_{H2O} = 0.1 \times 10^{-15}$ $k_{(H2O)2} = 0.8 \times 10^{-12}$	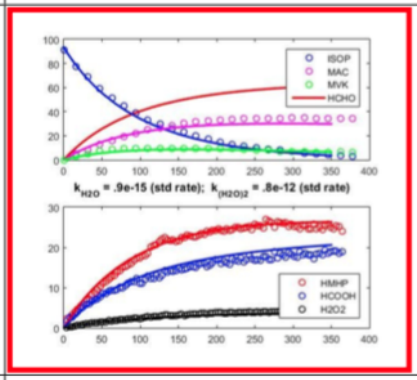	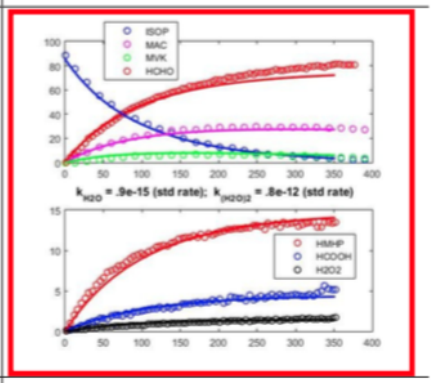
CASE 2 *Our monomer rate + Chao et al dimer rate* $k_{H2O} = 0.9 \times 10^{-15}$ $k_{(H2O)2} = 6.5 \times 10^{-12}$	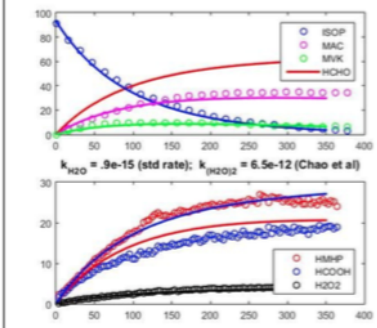	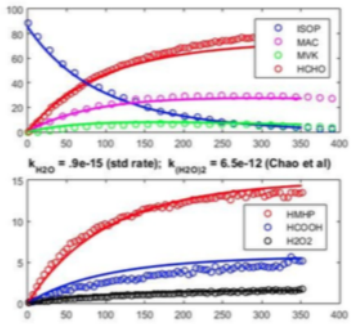
CASE 3 *Low monomer rate + Chao et al dimer rate* $k_{H2O} = 0.1 \times 10^{-15}$ $k_{(H2O)2} = 6.5 \times 10^{-12}$	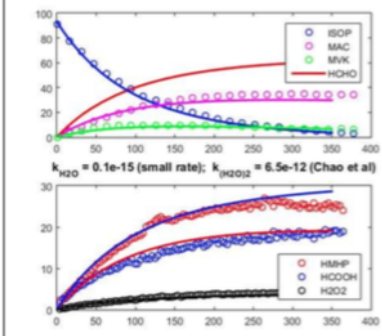	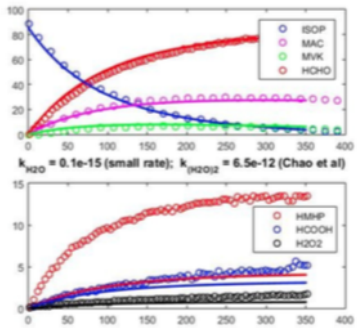

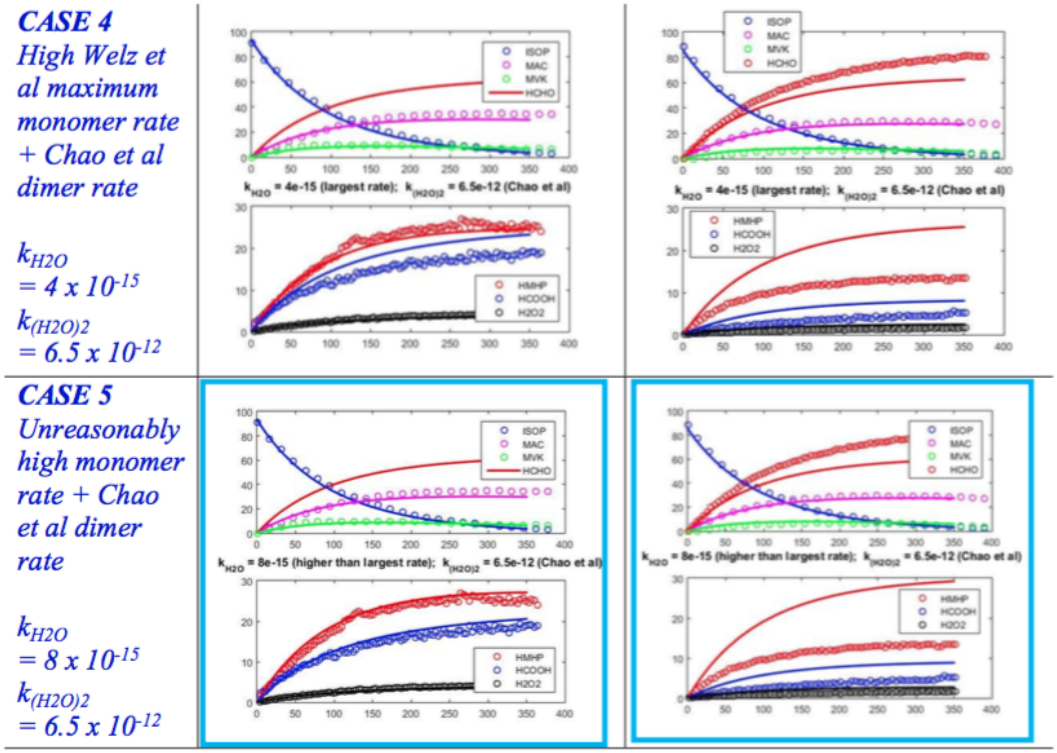

Figure E.16: Model sensitivity study using two RH conditions (RH = 51%, where the water dimer and water monomer rate are both important, and RH = 1.2%, where only the water monomer rate is important). Results from 5 sensitivity cases, using different monomer and dimer rate coefficients, are shown. Case 1, shown in the red border, successfully reproduces all data reported in this work (Figure E.5 in the manuscript). Cases 2-5 explored the dimer rate coefficient of Chao *et al.* (2015). For the Chao *et al.* (2015) dimer rate coefficient to reproduce the RH = 51% results, the monomer rate coefficient would need to be adjusted to be higher than the upper bound reported by Welz *et al.* (2012) – shown in the blue border, Case 5. The high monomer rate in Case 5 now over predicts CH_2OO water products in the dry case.

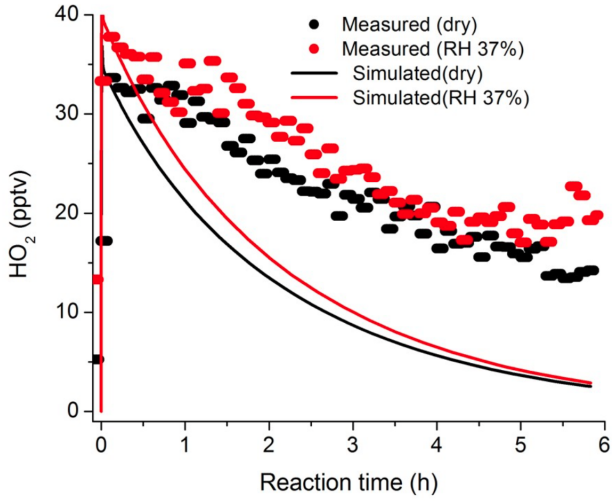

Figure E.17: Simulated and measured HO_2 mixing ratios at two RH conditions during the FIXCIT campaign. The model mechanism does not yet include second-generation sources of HO_2.

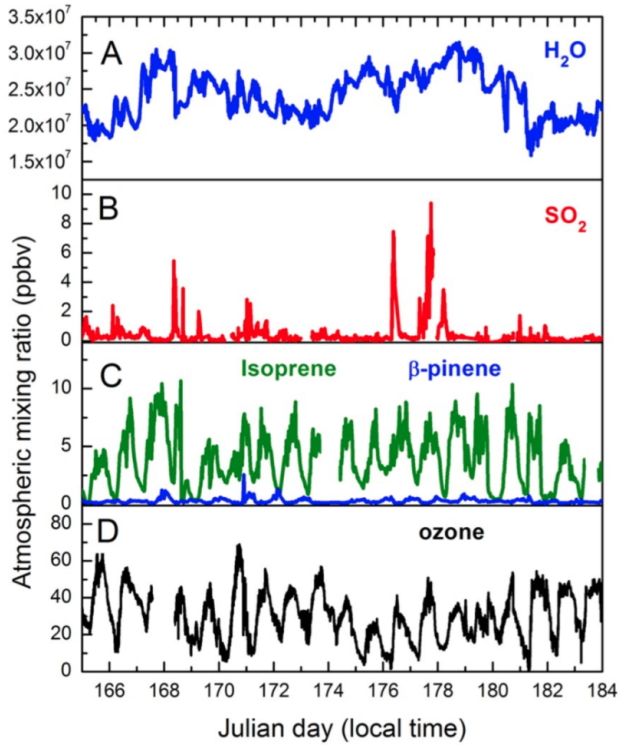

Figure E.18: Atmospheric mixing ratios of (A) water vapor, (B) sulfur dioxide, (C) exocyclic VOCs isoprene and β-pinene, and (D) ozone during the measurement period of the SOAS campaign.

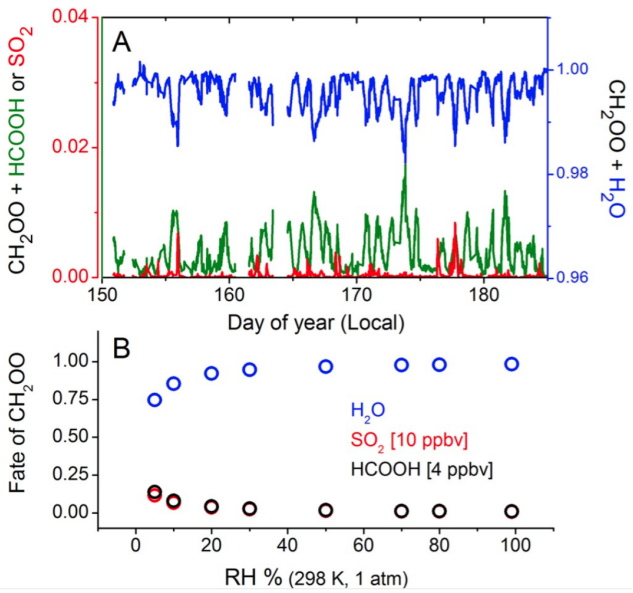

Figure E.19: (A) Fraction of CH_2OO that reacts with H_2O, SO_2 and HCOOH during the SOAS campaign. (B) Given high SO_2 and HCOOH mixing ratios, the fate of CH_2OO varies with RH; however, the H_2O reaction dominates at all realistic atmospheric humidities.

Appendix F

TIME-RESOLVED MOLECULAR CHARACTERIZATION OF ORGANIC AEROSOLS BY PILS + UPLC/ESI-Q-TOFMS

Zhang, X., N. Dalleska, D. Huang, K. Bates, A. Sorooshian, R. Flagan, and J. Seinfeld (2016). "Time-resolved molecular characterization of organic aerosols by PILS + UPLC/ESI-Q-TOFMS". In: *Atmos. Environ.* 130, pp. 180–189. DOI: http://doi.org/10.1016/j.atmosenv.2015.08.049.

Abstract

Real-time and quantitative measurement of particulate matter chemical composition represents one of the most challenging problems in the field of atmospheric chemistry. In the present study, we integrate the Particle-into-Liquid Sampler (PILS) with Ultra Performance Liquid Chromatography/Electrospray ionization Quadrupole Time-of-Flight High-Resolution/Mass Spectrometry (UPLC/ESI-Q-TOFMS) for the time-resolved molecular speciation of chamber-derived secondary organic aerosol (SOA). The unique aspect of the combination of these two well-proven techniques is to provide quantifiable molecular-level information of particle-phase organic compounds on timescales of minutes. We demonstrate that the application of the PILS + UPLC/ESI-Q-TOFMS method is not limited to water-soluble inorganic ions and organic carbon, but is extended to slightly water-soluble species through collection efficiency calibration together with sensitivity and linearity tests. By correlating the water solubility of individual species with their O:C ratio, a parameter that is available for aerosol ensembles as well, we define an average aerosol O:C ratio threshold of 0.3, above which the PILS overall particulate mass collection efficiency approaches ~0.7. The PILS + UPLC/ESI-Q-TOFMS method can be potentially applied to probe the formation and evolution mechanism of a variety of biogenic and anthropogenic SOA systems in laboratory chamber experiments. We illustrate the application of this method to the reactive uptake of isoprene epoxydiols (IEPOX) on hydrated and acidic ammonium sulfate aerosols.

F.1 Introduction

Chemical characterization of particulate organic compounds is crucial to understand the formation and evolution of secondary organic aerosol (SOA). The

conventional method for particle-phase molecular speciation is to collect aerosols on a filter substrate, followed by extraction and preconcentration. Analysis of filter extracts is commonly performed by liquid chromatography (LC) and gas chromatography (GC), coupled to mass spectrometry with the use of electron ionization (EI), chemical ionization (CI), electrospray ionization (ESI), and atmospheric pressure chemical ionization (APCI) (Dye and Yttri, 2005; Lavrich and Hays, 2007; Lin *et al.*, 2012; Simpson *et al.*, 2005; Surratt *et al.*, 2007a; Surratt *et al.*, 2007b; Surratt *et al.*, 2006; Szmigielski *et al.*, 2007). Major organic classes in SOA that have been identified from filter-based analysis include (nitrooxy)-organosulfates (Chan *et al.*, 2011; Iinuma *et al.*, 2007; Surratt *et al.*, 2007a; Surratt *et al.*, 2008, 2007b), dimers, trimers, and oligomers (Gao *et al.*, 2004; Jang *et al.*, 2002; Kalberer *et al.*, 2004; Limbeck *et al.*, 2003; Schilling Fahnestock *et al.*, 2015), and humic-like substances (Gelencser *et al.*, 2002; Graham *et al.*, 2002). A limitation of filter-based analysis is low time resolution and, consequently, the inability to track particle-phase kinetics. In addition, filter artifacts, such as adsorption of ambient vapors and evaporation of semi-volatile compounds from the filter surface, lead to uncertainties in the quantification of particle-phase components (Dzepina *et al.*, 2007; Schauer *et al.*, 2003; Turpin *et al.*, 2000).

Powerful, on-line techniques have been developed for chemical speciation of organic aerosols, with rapid time response and minimum sample handling. The general principle is to vaporize airborne aerosols by thermal or laser desorption, followed by ionization and mass spectrometric detection (Canagaratna *et al.*, 2007; Sullivan and Prather, 2005). The Aerodyne Aerosol Mass Spectrometer (AMS), which is now a routine component of ambient and chamber studies, enables measurement of organic fragments and derivation of the atomic O:C and H:C ratios (Aiken *et al.*, 2007; Aiken *et al.*, 2008; Jimenez *et al.*, 2003). Identification of individual species by AMS is not available due to the high evaporation temperature (600 °C) and EI energy (70 eV), which result in significant molecular fragmentation. Moreover, all thermal/laser desorption methods are susceptible to fragmentation of non-refractory compounds. To achieve unambiguous molecular identification of particulate organic compounds, extensive fragmentation is avoided by employing soft ionization techniques such as chemical ionization (Aljawhary *et al.*, 2013; Hearn and Smith, 2004; Hellen *et al.*, 2008; Hoffmann *et al.*, 1998; Lopez-Hilfiker *et al.*, 2014; Smith *et al.*, 2005; Yatavelli and Thornton, 2010), photoelectron resonance capture ionization (LaFranchi and Petrucci, 2006; Zahardis *et al.*, 2006), and vacuum ultraviolet single photon ionization (Ferge *et al.*, 2005; Isaacman *et al.*, 2012; Northway *et al.*, 2007;

Oktem *et al.*, 2004). Full-scale implementation of these methods into routine measurements requires achieving short measurement cycles, resolving quantification capability, interpreting the mass spectral complexity, and comparing data recovery with conventional methods.

The Particle-into-Liquid Sampler (PILS), first developed by Weber *et al.* (2001), grows aerosols by supersaturated water vapor condensation, producing droplets sufficiently large for collection by inertial impaction. The resulting liquid samples can be analyzed by ion chromatography (IC) for water-soluble inorganic ions and small dicarboxylic acids (Ma *et al.*, 2004; Oakes *et al.*, 2010; Orsini *et al.*, 2003; Rastogi *et al.*, 2009; Sorooshian *et al.*, 2008; Sorooshian *et al.*, 2007), or by a total organic carbon analyzer (TOC) for the total water soluble organic carbon (WSOC) (Peltier *et al.*, 2007; Sullivan *et al.*, 2006). PILS coupled with mass spectrometry has also been deployed for the analysis of WSOC in field and chamber measurements. Bateman *et al.* (2010) compared the off-line mass spectra of limonene + O_3 derived SOA samples collected by PILS with those collected on filter substrates and found that the peak abundance, organic mass to organic carbon ratios, and the average O:C ratio are essentially identical. Parshintsev *et al.* (2010) integrated PILS on-line with a solid-phase extraction chromatographic system for the characterization of organic acids. Using a similar concept, Clark *et al.* (2013) directly injected PILS samples into the ionization source of the mass spectrometer and validated the PILS-ToF-MS system against other particle measurement methods in terms of total ion abundance and average O:C ratios of isoprene and α-pinene derived SOA.

A primary challenge in the deployment of PILS as an effective particle collection device lies in the determination of the overall mass collection efficiency. Ambient and chamber derived organic aerosols usually comprise of thousands of species with various physicochemical properties. Since PILS was originally designed to use water steam as the growing agent, one expects that particles with an extreme hydrophobic surface would be difficult to collect. Therefore, a guideline needs to be developed for the reference of PILS selectivity to certain types of aerosols. This is one main focus of the present study.

Here we combine PILS with Ultra Performance Liquid Chromatography/ Electrospray Ionization Quadrupole Time-of-Flight High-Resolution Mass Spectrometry (UPLC/ESI-Q-TOFMS), for time-revolved molecular-level characterization of SOA during chamber experiments. This technique is particularly suited to polar or water-soluble organic molecules, and potentially high molecular weight species, such

as organosulfates. Advantages of this technique include: 1) No need for sample preparation; 2) Molecular-level information can be inferred from the electrospray ionization process, in which ions are, in general, observed as those of the parent molecule with the addition of an H atom (positive mode) or removal of an H atom (negative mode); 3) Temporal profiles of particle composition can be obtained on a time scale consistent with that of SOA evolution; and 4) Chromatographic separation of organic compounds with different polarities avoids the analyte signal suppression that occurs during the electrospray process of organic mixtures, leading to molecular-level quantification of particle-phase constituents. We demonstrate that the PILS + UPLC/ESI-Q-TOFMS method is suitable to measure water-soluble organic carbon (WSOC), as well as less hydrophilic or slightly water-soluble compounds. A collection efficiency of >0.6 can be achieved for chamber-derived SOA systems with average O:C ratios >0.3. We illustrate the application of this technique to the reactive uptake of isoprene epoxydiols (IEPOX) on hydrated and acidic ammonium sulfate aerosols.

F.2 Experimental Methods

F.2.1 Pure Component Organic Aerosols

Table F.1 gives the chemical properties of organic standards (purchased from Sigma Aldrich) that were used to generate pure component organic aerosols. These standards include carboxylic acids, amines, and polyols that span a broad range in water solubility from miscible to insoluble, and vapor pressure from intermediate to low volatility. Each standard was dissolved in water or isopropanol to produce a concentrated solution. Aerosols with known chemical composition were produced by atomizing each single concentrated solution followed by desolvation. Two diffusion denuders filled with silica gel and activated carbon were used to remove the solvent prior to injection into the Caltech 24 m^3 Teflon chamber. Relative humidity (RH) and temperature in the chamber were maintained at <5% and 25 °C, respectively. The size distribution and number concentration of the pure component organic aerosols were measured continuously using a custom-built scanning mobility particle sizer (SMPS) consisting of a differential mobility analyzer (DMA, TSI, 3081) coupled with a condensation particle counter (CPC, TSI, 3010). More details of the SMPS operation can be found in Loza *et al.* (2014), Zhang *et al.* (2014a), and Zhang *et al.* (2014b).

compound	chemical formula	exact mass	*m/z* (error/mDa)	water solubility at 20 °C	vapor pressure (atm at 298 K)
Adenine	$C_5H_5N_5$	135.0545	$[M+H]^+$ (1.6)	0.103 g L^{-1}	8.117×10^{-5}
Adonitol	$C_5H_{12}O_5$	152.0685	$[M-H]^-$ (4.8)	50.0 g L^{-1}	7.711×10^{-12}
Adipic acid	$C_6H_{10}O_4$	146.0579	$[M-H]^-$ (0.6)	0.25 g L^{-1}	3.292×10^{-9}
d-Sorbitol	$C_6H_{14}O_6$	180.0634	$[M-H]^-$ (2.5)	182.0 g L^{-1}	2.424×10^{-14}
Diethylmalonic acid	$C_7H_{12}O_4$	160.0736	$[M-CO_2-H]^-$ (0.1)	25.0 g L^{-1}	2.696×10^{-9}
Vanillic acid	$C_8H_8O_4$	168.0423	$[M-H]^-$ (-1.8)	1.5 g L^{-1}	7.940×10^{-10}
Azelaic acid	$C_9H_{16}O_4$	188.1049	$[M-H]^-$ (-4.2)	2.14 g L^{-1}	1.151×10^{-10}
cis-Pinonic acid	$C_{10}H_{16}O_3$	184.1099	$[M-H]^-$ (1.9)	7.8 g L^{-1}	1.485×10^{-7}
Myristic acid	$C_{14}H_{28}O_2$	228.2089	$[M-H]^-$ (0.7)	20.0 mg L^{-1}	6.711×10^{-9}
Palmitic acid	$C_{16}H_{32}O_2$	256.2402	$[M-H]^-$ (1.3)	7.2 mg L^{-1}	7.175×10^{-10}

Table F.1: Compounds used for method development. Water solubility data are from Yaws (2003), and vapor pressure is estimated by taking the average of predictions from the 'Evaporation' (Compernolle *et al.*, 2011) and 'SIMPOL.1' (Pankow and Asher, 2008) models.

F.2.2 Particle-into-Liquid Sampler (PILS)

Detailed characterization of the Caltech PILS, which is based on a modification of the original design of Weber *et al.* (2001), is described by Sorooshian *et al.* (2006). The chamber aerosol is sampled through a 1 μm cut size impactor with a flow rate of 12.5 L min^{-1}, and passed successively through individual acid and base gas denuders and an organic carbon denuder to remove inorganic and organic vapors. A steam flow generated at 100 °C is adiabatically mixed with the cooler sampled air in a condensation chamber, creating a high water supersaturation environment in which particles grow sufficiently large (D_p > 1 μm) for collection by inertial impaction onto a quartz plate. Impacted particles are transported to a debubbler by a washing flow (0.15 mL min^{-1}) comprising 50% water and 50% isopropanol. The sampled liquid is delivered into vials held on a rotating carousel. This design is especially beneficial for the application of liquid chromatography for organic compound separation and selection, which generally requires a longer time than the PILS collection cycle. Under the current configuration, a 5 min time resolution can be achieved for the characterization of particle-phase dynamics.

F.2.3 UPLC/ESI-Q-TOFMS

The PILS collected samples are stored at 4 °C and analyzed by UPLC/ESI-Q-TOFMS within 24 h without further pretreatment. A WATERS ACQUITY UPLC I-Class System, coupled with a Quadrupole Time-of-flight Mass Spectrometer (Xevo G2-S QToF) and equipped with an electrospray ionization (ESI) source, was used to identify and quantify the PILS collected samples, including organic aerosol

standards and chamber generated SOA. An ACUITY BEH C_{18} column (2.1 × 50 mm) was used to separate relatively nonpolar species, including vanillic acid, azelaic acid, *cis*-pinonic acid, myristic acid, palmitic acid, and IEPOX-derived SOA. The eluent program is: 0-3.2 min: 100% A (0.1% formic acid in water); 3.2-3.5 min: 10% A and 90% B (acetonitrile); 3.5-5 min: 100% A. The total flow rate is 0.5 mL min^{-1} and the injection volume is 5 μL. For extremely polar or water soluble compounds, including adenine, adonitol, adipic acid, d-sorbitol and diethylmalonic acid, an ACUITY BEH Amide column (2.1 × 150 mm) was used for species separation. The eluent program is: 0-3 min: 5% A (10 mM ammonium formate in water at pH = 9) and 95% B (acetonitrile); 3-3.01 min: 45% A and 55% B; 3.01-8 min: 5% A and 95% B. The total flow rate is 0.6 mL min^{-1} and the injection volume is 4 μL. Note that the eluent program used here is customized for the characterization of test aerosols that are composed of a single chemical standard. For chamber-derived SOA samples that might contain thousands of species with a variety of polarities, key parameters of the eluent program, such as the type and ratio of polar vs. nonpolar solvents, the additives and pH range in the mobile phase, and the overall elution duration, need to be optimized to achieve compound specificity. The choice of separation modes is also very important. For extremely polar compounds, hydrophilic-interaction chromatography is a more suitable approach, compared with reverse-phase chromatography, which has been, though, widely used in particle-phase speciation in previous studies. Optimum electrospray conditions are: 2.0 kV capillary voltage, 40 V sampling cone, 30 V source offset, 120 °C source temperature, 350 °C desolvation temperature, 30 L h^{-1} cone gas, and 650 L h^{-1} desolvation gas. MS/MS spectra were obtained by applying a collision energy ramping program starting from 15 eV to 50 eV over one MS scan in the collision cell. Accurate masses were corrected by a lock spray of leucine encephalin (*m/z* 556.2771 $[M+H]^+$). Data were acquired and processed using the MassLynx v4.1 software.

F.3 Method evaluation

F.3.1 Simulation of Hygroscopic Growth of Organic Aerosols

The operational principle of the PILS is to grow particles in the presence of supersaturated water vapor to the size of micro-droplets that can be collected by inertial impaction. A key parameter that governs the extent of particle growth is the water accommodation coefficient (α_w), which is defined as the fraction of water molecules that are taken up by the particles upon collision with the surface. Here we

investigate numerically the influence of α_w on the predicted final size of the droplets by condensational growth of particles.

The growth of a particle of diameter D_p in the presence of supersaturated water vapor is governed by (Seinfeld and Pandis, 2006):

$$\frac{dD_p}{dt} = \frac{4 \cdot D_w \cdot M_w}{R \cdot T \cdot D_p \cdot \rho_p} \left[p_w^{\infty} - p_w^s(D_p, T_s) \right] \cdot f(Kn, \alpha_w) \tag{F.1}$$

where D_w is the water vapor diffusivity, M_w is the water molecular weight, R is the gas constant, T is the temperature, ρ_p is the particle density, Kn (=$2\lambda/D_p$) is the Knudsen number, $f(Kn, \alpha_w)$ is the correction factor for noncontinuum conditions and imperfect accommodation, p_w^{∞} is the water saturation vapor pressure far from the particle, and $p_w^s(D_p, T_s)$ is the water vapor pressure over the particle surface. Taking into account the vapor pressure variation due to the Kelvin effect, $p_w^s(D_p, T_s)$ becomes:

$$p_w^s(D_p, T_s) = p_w^0(T_s) \cdot \chi_w \cdot \gamma_w \cdot exp\left(\frac{4 \cdot \sigma \cdot \nu_l}{R \cdot T \cdot D_p} \right) \tag{F.2}$$

where $p_w^0(T_s)$ is the water saturation vapor pressure at the particle temperature T_s, χ_w is the mole fraction of water in the particle phase, σ is the water surface tension, ν_l is the water molar volume, and γ_w is the water activity coefficient, which is assumed to be unity here. Note that particles in the PILS condensation chamber are assumed to behave as a dilute solution so that γ_w approaches its infinite dilution limit $\gamma_w \rightarrow 1$. This is reasonable considering that the water volume fraction exceeds 0.93 in particles after 0.1 s of hygroscopic growth. The water activity coefficient deviates from unity (<1) in non-ideal organic-salt-water mixtures (Zuend *et al.*, 2008, 2010), which is the case during the initial particle growth stage in the PILS condensation chamber. This leads to an overestimate of the water vapor partial pressure over the particle surface, and consequently, slower simulated particle growth rate due to water condensation. In other words, the actual particle hydroscopic growth rate in the PILS condensation chamber should be faster than the model simulations.

The particle surface temperature is determined by an energy balance on the particle (Seinfeld and Pandis, 2006):

$$\Delta T = \frac{\Delta H_v \cdot D_w \cdot \rho_w}{k_a' \cdot T_{\infty}} \cdot \left[S_{w,\infty} - exp\left(\frac{\Delta H_v \cdot M_w}{R \cdot T_{\infty}} \cdot \frac{\Delta T}{1 + \Delta T} + \frac{4 \cdot \sigma \cdot \nu_l}{R \cdot T \cdot D_p} \right) \right] \cdot f(Kn, \alpha) \tag{F.3}$$

where $\Delta T = (T_s - T_{\infty})/T_{\infty}$, ΔH_v is the latent heat of vaporization of water, ρ_w is the density of water steam, k_a' is the effective thermal conductivity of air corrected

for noncontinuum effects, and $S_{w,\infty} = p_w^{\infty}/p_w^0(T_\infty)$ is the environmental saturation ratio. Equation F.3 needs to be solved numerically to determine the particle surface temperature that is required in the calculation of the particle growth rate.

Figure F.1 shows the predicted hygroscopic growth of particles, with initial diameters ranging from 20 nm to 800 nm, as a function of water accommodation coefficient (α_w). Particles with highly hydrophilic surface composition ($\alpha_w \rightarrow 1$) can grow sufficiently large ($D_p > 1$ μm) to be collected by inertial impaction within 1 s, the particle residence time in the PILS condensation chamber. Water vapor mass transfer to less hydrophilic particles ($\alpha_w \leq 10^{-2}$) is still sufficiently rapid to grow particles to droplets >1 μm size. Significant kinetic reductions in water uptake result when the particle-phase constituents are strongly hydrophobic ($\alpha_w \leq 10^{-3}$). The effect of initial relative humidity (RH) in aerosol sampling flow on the ultimate droplet size becomes critical when α_w is $\sim 10^{-3}$. The simulations suggest that PILS can potentially collect particles with a wide range of water solubility, due to the substantial imbalance in water vapor abundance far from and over the particle surface. As discussed earlier, the assumption of ideal water-ion-organic interactions leads to the underestimation of particle hygroscopic growth rate. As a result, the specification of α_w in the order of $\sim 10^{-3}$ as a criterion for "hydrophobic" particles that fail to grow over 1 μm diameter might be a bit conservative.

F.3.2 Collection Efficiency

The PILS collection efficiency may deviate from unity owing to three processes: 1) particle losses due to gravitational settling, diffusion, and inertial deposition during transport in the PILS plumbing system and condensation chamber, 2) evaporation of semi-volatile components during adiabatic mixing with steam, and 3) imperfect accommodation of water vapor on particles, if hydrophobic (Orsini *et al.*, 2003; Sorooshian *et al.*, 2006; Weber *et al.*, 2001). In the present study, we characterize the PILS collection efficiency by varying the particle chemical composition (*i.e.*, polarity and volatility) and size distribution. The overall mass collection efficiency (CE_{PILS}) can be obtained by comparing the mass concentration measured by the UPLC/ESI-Q-TOFMS and that derived from the DMA measured particle volume distribution, assuming particle sphericity (Sorooshian *et al.*, 2006):

$$CE_{PILS} = \frac{1000 \cdot m \cdot Q_l \cdot DF \cdot \rho_l}{Q_g \cdot \rho_p \cdot V_p} \tag{F.4}$$

where 1000 is the unit conversion factor, m is the UPLC/ESI-Q-TOFMS measured organic standard mixing ratio (ppm), Q_l is the liquid sampling flow rate (1.5 mL

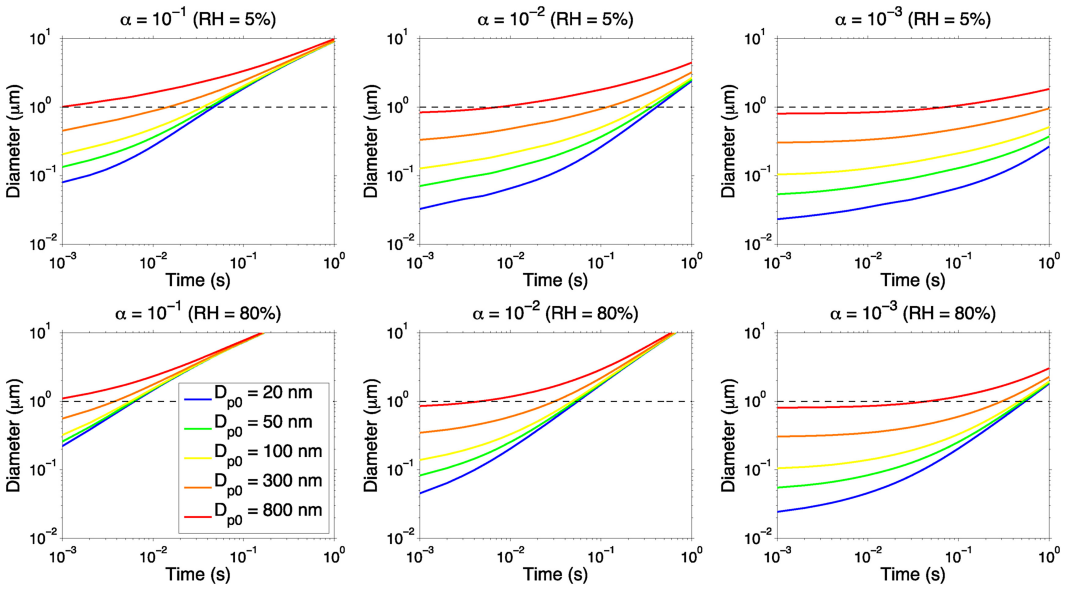

Figure F.1: Simulations of particle condensational growth over an initial size range of 20-800 nm diameter in the presence of supersaturated water vapor for different assumed water accommodation coefficients (α_w = 10^{-3}, 10^{-2}, and 10^{-1}) at initial relative humidities (RH) of 5% (upper panel) and 80% (lower panel) in the chamber. The black dashed line denotes the threshold value (1 μm in diameter) of particle size for effective PILS collection.

min^{-1}), DF is the dilution factor that accounts for the water vapor condensation on the impactor wall and air bubbles during the filling of vials, ρ_l is the density of collected liquid, which is assumed as the density of the washing flow (0.893 g cm^{-3}), Q_g is the gas sampling flow rate (12.5 L min^{-1}), V_p is the particle total volume concentration (μm^3 cm-3) derived from the DMA measured number distribution, and ρ_p is the particle density (g cm^{-3}). Note that ρ_p here is assumed as the density of corresponding chemical standards that are used to generate test aerosols. For chamber-derived SOA, ρ_p can be derived from the AMS measured O:C and H:C ratios (Kuwata *et al.*, 2012). A 5 min offset in the PILS measurement is taken into account to retrieve the particle concentration at the moment of entry into the PILS inlet.

Figure F.2 shows the measured PILS mass collection efficiency (CE_{PILS}) as a function of particle water solubility and volatility. Consistent with the model prediction, the high collection efficiency in the PILS is achieved not only for highly water soluble and non-volatile aerosols such as sorbitol, but also for slightly water soluble and intermediate/semi-volatile aerosols such as pinonic acid. The water solubility of particle-phase constituents clearly governs CE_{PILS}. The effect of

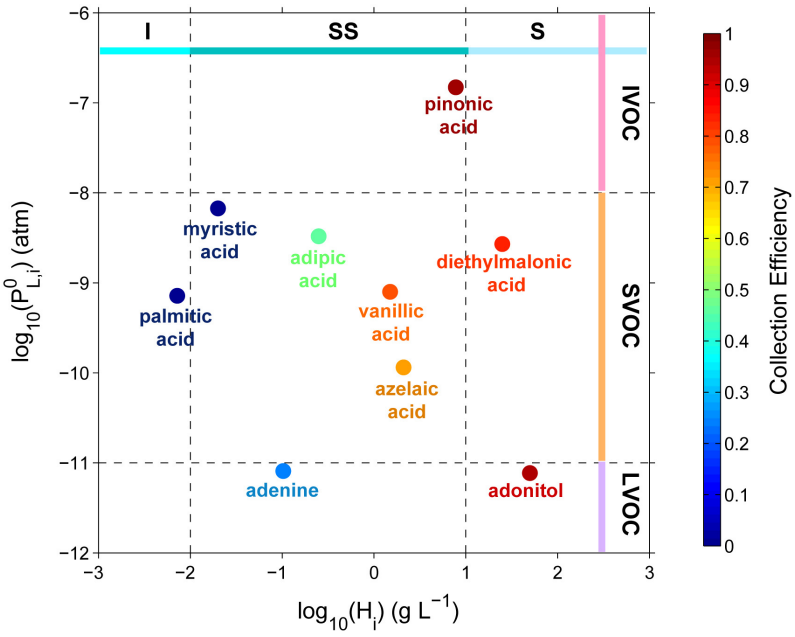

Figure F.2: Measured PILS overall mass collection efficiency for the test organic aerosols as a function of volatility, which is defined as the vapor pressure of compound i as pure liquid at 20 °C on the logarithm scale ($\log_{10}P^0_{L,i}$, atm), and water solubility, which is defined here as the maximum amount of the compound i that will dissolve in pure water at 20 °C on the logarithm scale ($\log_{10}H_i$, g L^{-1}). Compound volatility is categorized according to intermediate volatility organic compound (IVOC), semi-volatile organic compound (SVOC), and low volatility organic compound (LVOC). Water solubility is categorized broadly as insoluble (I), slightly soluble (SS), and soluble (S).

volatility on CE_{PILS}, however, is not discernable, indicating that the evaporation of semi-volatiles from particles during adiabatic mixing with steam is negligible for compounds with vapor pressure $<10^{-6}$ atm. We define the particle water solubility threshold of 1 g L^{-1} above which >0.6 mass collection efficiency can be achieved. Considering that SOA water solubility data are generally unavailable, this quantity can be related to the average particle O:C ratio, which is relatively well constrained by the AMS measurement.

Figure F.3 shows the water solubilities (the maximum amount of the compound i that will dissolve in pure water at 20 °C on the logarithm scale, $\log_{10}H_i$/g L^{-1}) of a variety of organic compounds, including carboxylic acids, alcohols, carbonyls, esters, and ethers, as a function of their O:C ratios. Regardless of the nature of functionalities in the molecule, the water solubility increases with the O:C ratio and eventually reaches a plateau, a miscible state with water. The O:C ratio correspond-

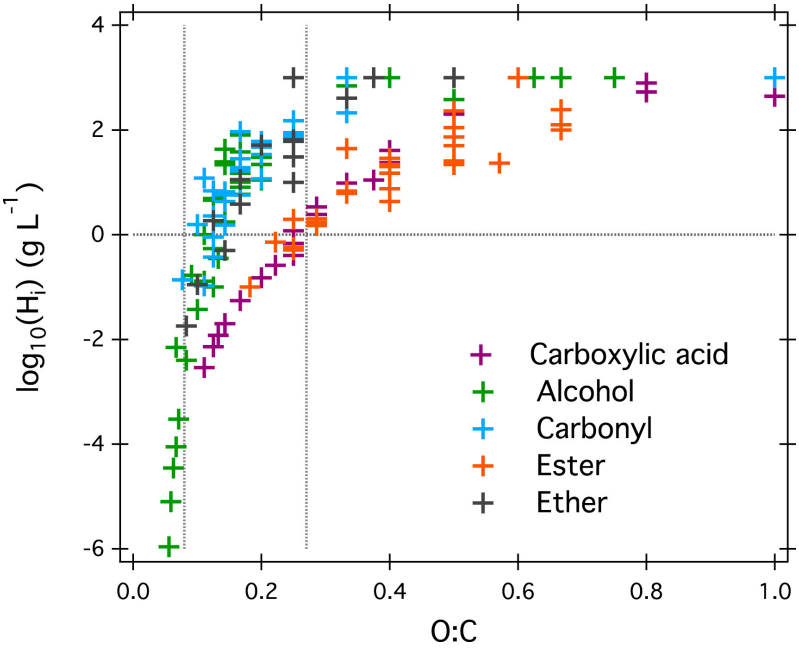

Figure F.3: Water solubility of carboxylic acid, alcohol, carbonyl, ester, and ether standards at 20 °C as a function of their O:C ratios. Each data point represents an individual compound with certain functionalities. The horizontal gray line represents the water solubility threshold (1 g L^{-1}) at which the PILS collection efficiency of ~0.6 will be achieved. The two vertical gray lines define a region of average particle O:C ratios that correspond to the water solubility threshold. Data source: Yaws (2003).

ing to the water solubility threshold of 1 g L^{-1} varies with functionalities, ranging from 0.07 to 0.26. Considering that SOA is generally a mixture of species that might contain all the functional groups above, we suggest that the upper limit of the O:C ratio, 0.26, represents a criterion to constrain an effective PILS mass collection efficiency. The AMS measured O:C ratios for SOA produced from isoprene + OH, α-pinene + O_3/OH, aromatics + OH, and C_{12}-alkane + OH in the Caltech Environmental Chamber have been summarized previously (Chhabra *et al.*, 2010, 2011; Loza *et al.*, 2014; Zhang and Seinfeld, 2013). Among all the systems investigated, long-chain alkane derived SOA exhibits the lowest O:C ratio, ranging from ~0.2 to ~0.3, over the course of 3-36 h experiments ([OH] exposure = 2-8 molecules cm^{-3} h). The average O:C ratios measured from other SOA systems, on the other hand, exceed the threshold, 0.26, at which >0.6 mass collection efficiency by PILS can be achieved. Thus, PILS is a candidate as a high efficiency, time-resolved particle collection method for a majority of SOA systems.

Particles are subject to gravitational settling, diffusion, and inertial deposition in

the PILS plumbing system and condensation chamber. The largest losses occur for small (D_p < 10 nm) and large particles (D_p > 1000 nm), as predicted to be 2.2% and 8.6%, respectively (Sorooshian *et al.*, 2006). Considering that the PILS transmission efficiency (defined as the fraction of particles of a certain size that are transported through the PILS plumbing system and condensation chamber) depends strongly on the particle size, the impact of variations in the particle size distribution on the PILS overall mass collection efficiency (CEPILS) is at issue. For a typical SOA chamber experiment, the initial size distribution of seed particles spans from ~20 nm to ~600 nm, with a median diameter of ~60-70 nm. Growth driven by gas-phase photochemistry and gas-particle partitioning occurs primarily on large particles and, as a result, the number median diameter shifts to ~200 nm after ~20 h of irradiation. To mimic the progression of the particle size distribution during SOA formation, test particles were initially generated by atomizing concentrated pinonic acid solution into the chamber. An external flow pulse creates intense turbulent mixing in the chamber. As a result, the median diameter of the *cis*-pinonic acid particles shifted from ~90 nm to ~200 nm during the 3.5 h experiment, due to rapid deposition of the smaller particles onto the chamber wall (see Figure F.4). The overall PILS mass collection efficiency, on the other hand, remains consistently close to unity, within ~8% uncertainty. This test demonstrates that change in particle size distribution during SOA formation and evolution under typical chamber experimental conditions does not significantly impact the PILS collection efficiency.

F.3.3 Sensitivity, Detection Limit, and Uncertainties

The extent of linearity of UPLC/ESI-Q-TOFMS detected signals for PILS collected organic aerosols was examined in response to changes in particle mass loadings. Sorbitol, azelaic acid, pinonic acid, and adipic acid aerosols, with mass concentrations ranging from 20 to 300 μg m^{-3}, were generated by varying the atomization and dilution duration. Mass concentrations of these four organic aerosol standards were derived from the SMPS measured particle volume distribution. The UPLC/ESI-Q-TOFMS signals for sorbitol, azelaic acid, and pinonic acid, as shown in Figure F.5, exhibit linearity (R^2 = 0.99) with organic mass loadings. The sensitivity for adipic acid, however, is drifting low when particle concentrations are diluted, and as a result, there is a strong negative offset in the linear fitting curve. The low sensitivity for adipic acid might be attributed to the slight solubility of adipic acid dimer, which is the dominant particle-phase form of adipic acid (Wolfs and Desseyn, 1996).

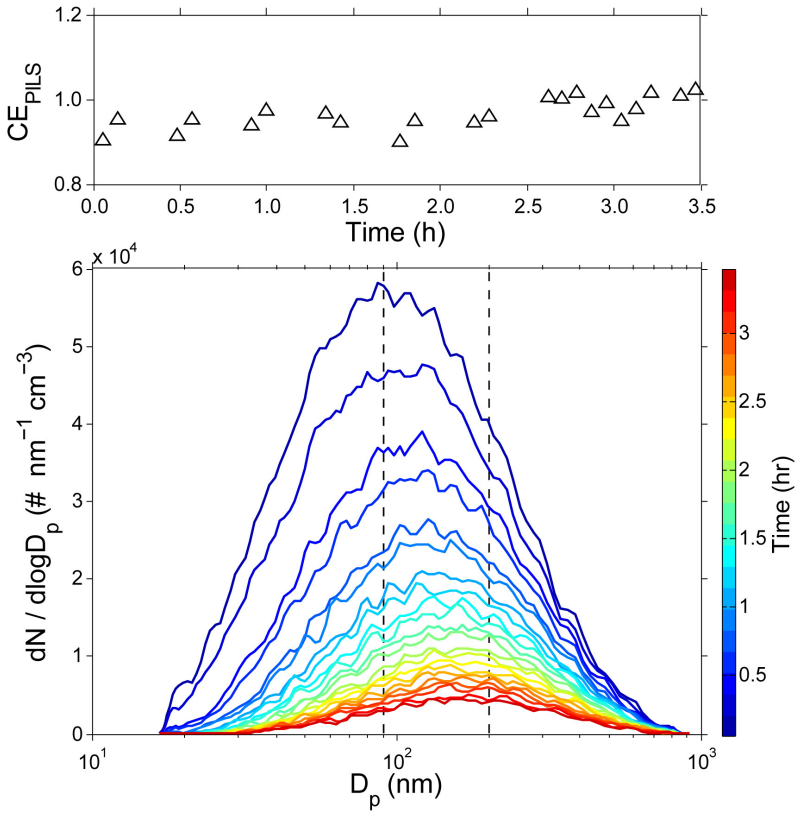

Figure F.4: PILS overall mass collection efficiency (upper panel) for *cis*-pinonic acid aerosols as a function of particle number distribution (lower panel). Over ~3 h, aerosol wall deposition from intense turbulent mixing in the chamber caused the number median aerosol diameter to shift from 90 nm to 200 nm.

The detection limit of the PILS + UPLC/ESI-Q-TOFMS system can be estimated from the expected UPLC/ESI-Q-TOFMS sensitivity and measured flow rates of sampling air and liquid washing stream. The UPLC/ESI-Q-TOFMS detection limit (LOD) was calculated according to the expression:

$$\frac{S}{N} = \frac{k_i \cdot LOD}{\sigma} \tag{F.5}$$

where S/N is the signal-to-noise ratio, k_i is the response factor or the sensitivity of UPLC/ESI-Q-TOFMS for species i, and σ is the standard deviation of the response. Using a signal-to-noise ratio of 2, LOD of 0.68 ppb is obtained for *cis*-pinonic acid as an example. With a gas flow rate of 12.5 L min^{-1}, and a washing flow rate of 0.15 mL min^{-1}, the PILS + UPLC/ESI-Q-TOFMS system is estimated to have a detection limit of 19.02 ng m^{-3} for *cis*-pinonic acid in the particle phase. By analogy with other compounds that are selected by UPLC, the sensitivity of the Q-TOFMS technology can be practically achieved as low as ~ ppb level. Thus

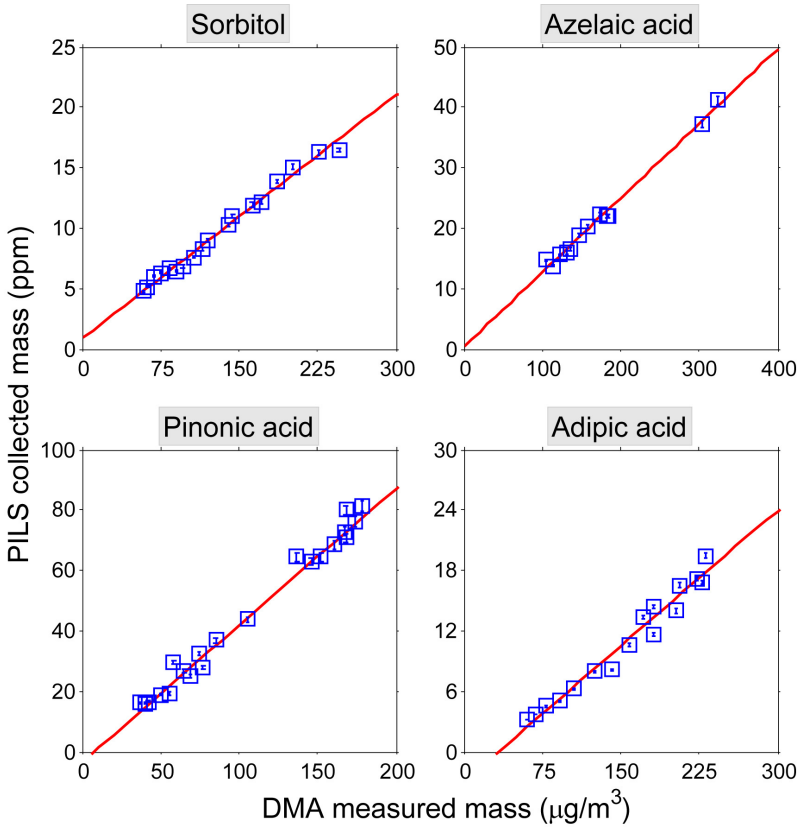

Figure F.5: UPLC/ESI-Q-TOFMS measured mass concentration of sorbitol, azelaic acid, pinonic acid, and adipic acid in PILS samples versus the DMA-measured total particle mass. Linear fits to the data are shown with the mean R^2 = 0.99.

we expect the detection limit of PILS + UPLC/ESI-Q-TOFMS measurement of the mass of particle components in the range of tens of ng m^{-3} to a few μg m^{-3}.

Uncertainties in the PILS + UPLC/ESI-Q-TOFMS measurement arise mainly from variation of the collected liquid volume due to the existence of air bubbles. Specifically, the washing flow carries the impacted droplets *via* a stainless steel mesh wick on the perimeter of the impactor to a 'T-shape' debubbler. Air bubbles are vacuumed out of the system by a peristaltic pump. The liquids are delivered into the injection needle that is inserted into individual vials by two syringe pumps. Perfect debubbling cannot always be achieved and as a result, the collected liquid volumes in some vials can drift low. The measurement uncertainties due to the existence of air bubbles in the liquid samples are estimated to be <11% by weighing a batch of vials over one carousel running cycle (72 vials). Repeatability in the detected yield of ions from the electrospray ionization of the analyte is another potential origin of measurement uncertainties. This was estimated to be <3% by

repeating injection of 4 μL standard organic samples into the electrospray source. The effect of ESI-MS sensitivity drift on the measurement accuracy is accounted for by regularly performing the repeatability of organic standards (one standard every ten samples) during routine sample analysis.

While the PILS + UPLC/ESI-Q-TOFMS system is demonstrated to achieve time-resolved molecular speciation of secondary organic aerosols, we acknowledge the potential artifacts and uncertainties arising from aerosol sampling and analysis procedures. First, the hydrolysis of labile functionalities, mainly including organic nitrates, carbonyls, and epoxides, upon solvation is inevitable in any aerosol collection, pretreatment and analysis procedures using water as the solvent. Second, water steam (100 ± 2 °C) is mixed with aerosol sample flow (25 ± 5 °C) in the PILS condensation chamber, with temperature eventually stabilized as ~36 °C. During mixing, organic aerosol constituents are subjected to evaporation and thermal decomposition. We have demonstrated earlier that the evaporation of semivolatile organic compounds is not significant during adiabatic mixing (Figure F.2). Steady decomposition of thermally labile compounds in neutral solution, such as organic peroxides, requires a temperature higher than ~80 °C (Hart, 1949). Considering that the residence time of the PILS condensation chamber is only 1 s, it is expected that the original structure of thermally labile organic molecules should be mostly intact in such a short timescale.

F.4 Method Application: IEPOX Uptake onto Acidified and Hydrated Ammonium Sulfate Particles

The heterogeneous chemistry of isoprene epoxydiols (IEPOX), a second generation product formed from isoprene photochemistry in the absence of NO, contributes significantly to the SOA formation (Lin *et al.*, 2014, 2012; Nguyen *et al.*, 2014a; Paulot *et al.*, 2009b; Surratt *et al.*, 2010). Proposed mechanisms leading to SOA production involve the ring opening of the epoxide group, followed by the addition of available nucleophiles in the condensed phase, *e.g.*, tetrol production *via* the addition of water and organosulfate production *via* the addition of sulfate (Eddingsaas *et al.*, 2010; Nguyen *et al.*, 2014a; Surratt *et al.*, 2010). The PILS + UPLC/ESI-Q-TOFMS method was employed to characterize the SOA formation and evolution *via* the reactive uptake of IEPOX onto hydrated and acidified ammonium sulfate particles. The IEPOX-derived SOA is a well-established system to test the performance of the PILS + UPLC/ESI-Q-TOFMS technique.

F.4.1 Chamber experiment and instrument operation protocols

The experiment was conducted in the Caltech 24 m^3 Environmental Chamber maintained at 20 °C. Detailed experimental protocols are presented in an earlier study (Nguyen *et al.*, 2014a). The general experimental procedure is as follows: 1) flushing the chamber with purified dry air for 24 h prior to the experiment; 2) humidifying the chamber to ~78% RH by passing purified air through a Nafion membrane humidifier (FC200, Permapure LLC) that is kept wet by recirculation of 27 °C ultra-pure water (18 MΩ, Millipore Milli-Q); 3) Injecting inorganic seed aerosols by atomizing an acidified ammonium sulfate aqueous solution (0.06 M $(NH_4)_2SO_4$ + 0.06 M H_2SO_4) followed by a custom-built wet-wall denuder; and 4) injecting the gas-phase trans β-IEPOX isomer by evaporating several droplets in a glass bulb with 6 L min^{-1} of purified and heated dry air (60 °C) for ~ 100 min.

The gas-phase IEPOX mixing ratio was monitored using a custom-modified Varian 1200 triple-quadrupole chemical ionization mass spectrometer (CIMS). In negative mode operation, CF_3O^- was used as the reagent ion to cluster with the analyte [R], producing $[R{\cdot}CF_3O]^-$ or *m/z* $[M+85]^-$, where M is the molecular weight of the analyte. More details on the CIMS operation and data analysis are given by Zhang *et al.* (2015). Real-time particle mass spectra were collected continuously by an Aerodyne High Resolution Time-of-Flight Aerosol Mass Spectrometer (HR-AMS). The AMS switched once every minute between the high resolution 'W-mode' and the lower resolution, higher sensitivity 'V-mode'. The V-mode was utilized for quantification, as the higher *m/z* values exhibit a more favorable signal-to-noise ratio. The W-mode was used for ion identification and clarification. More details on AMS operation and data analysis are given by Nguyen *et al.* (2014a).

F.4.2 Results and Discussions

Shown in Figure F.6 (upper panel) are the CIMS signals at *m/z* (-) 203, which represents the fluoride cluster product of IEPOX ($C_5H_{10}O_3{\cdot}CF_3O^-$), and organic particulate mass concentrations measured by the HR-AMS. Dominant ions observed in the HR-AMS spectra include *m/z* 29, *m/z* 43, *m/z* 53 (mostly $C_4H_5^+$) and *m/z* 82 (mostly $C_5H_6O^+$). The latter two are considered as the tracers for IEPOX derived organic aerosols (Budisulistiorini *et al.*, 2013; Lin *et al.*, 2012). The time-dependent trend of gas-phase IEPOX measured by CIMS during the injection period (0-100 min) is almost identical to the AMS measured total particulate organics, indicating the uptake of IEPOX and the subsequent reactions are essentially instantaneous. Gas-particle equilibrium is rapidly established after the IEPOX injection. Over the

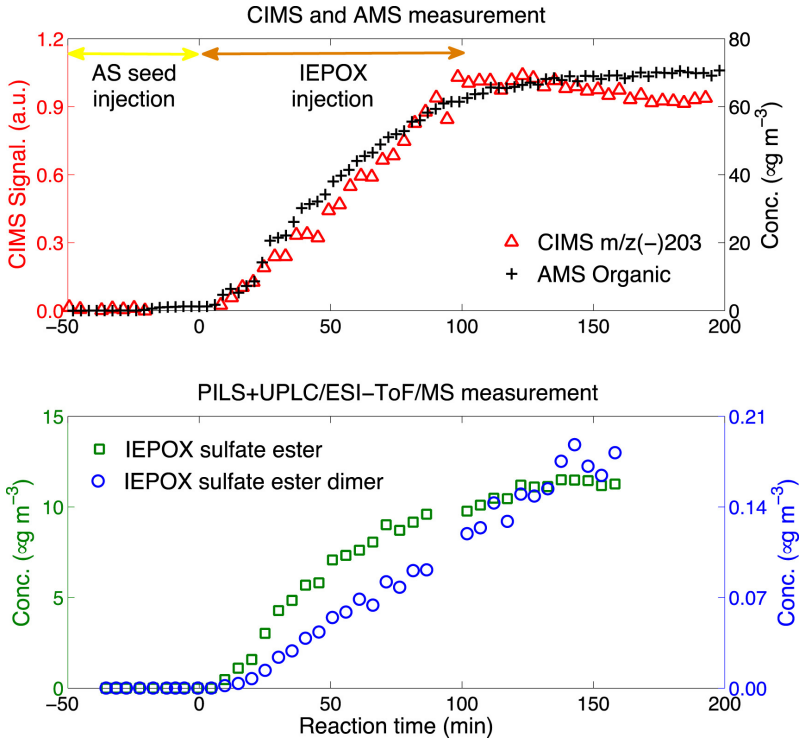

Figure F.6: Temporal profiles of normalized CIMS signals at *m/z* (-) 203, which represents the fluoride cluster product of IEPOX ($C_5H_{10}O3{\cdot}CF_3O^-$), and AMS measured total organic (upper panel), as well as IEPOX-derived sulfate ester and dimer measured by the PILS + UPLC/ESI-Q-TOFMS technique (lower panel).

remaining 100 min of the experiment, AMS measured total organic mass is at a steady state, whereas the CIMS signal at *m/z* (-) 203 exhibits a slow decay, which is likely a result of vapor wall losses of epoxide at high RH in the chamber.

For the PILS collected samples, the dominant ion observed in the UPLC/ESI-Q-TOFMS mass spectra in the negative mode is $C_5H_{11}SO_7^-$, which corresponds to the IEPOX-derived hydroxyl sulfate ester. The hydroxyl sulfate ester dimer $C_{10}H_{22}SO_{10}^-$ is also observed in the form of $[M\text{-}H]^-$. Corresponding normalized mass spectra and temporal profiles of these two products are shown in Figure F.7 and the lower panel of Figure F.6, respectively. Prompt formation of sulfate ester was observed at the onset of IEPOX injection, and the time-dependent trend agrees with the AMS measured organic aerosol growth curve. The sulfate ester dimer, on the other hand, exhibits a 20 min induction period and creeps up over the course of the experiment. As authentic standards for IEPOX-derived organosulfates are not commercially available, the UPLC/ESI-Q-TOFMS was externally calibrated with a surrogate quantification standard, d-galactone 6-sulfate sodium salt (Sigma Aldrich

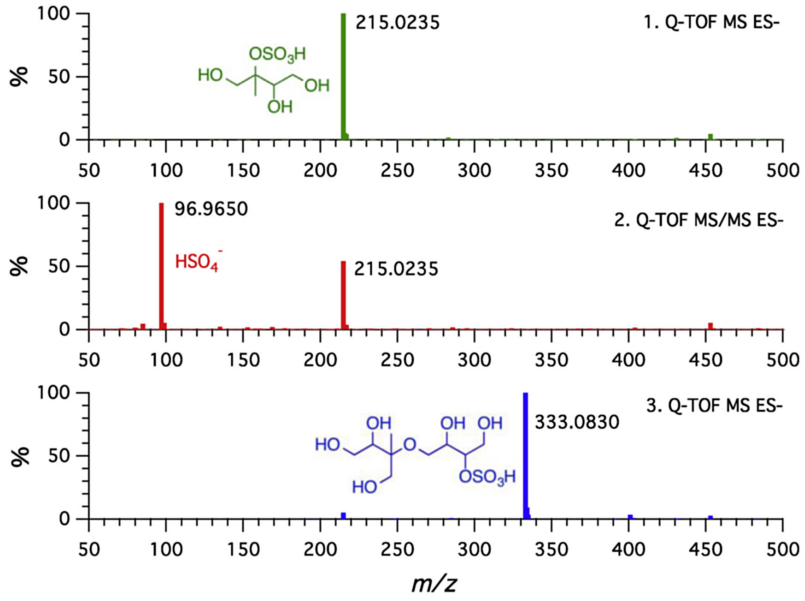

Figure F.7: (Panel 1) Mass spectrum for the IEPOX-derived hydroxyl sulfate ester, detected as *m/z* = 215 in the form of $C_5H_{11}SO_7^-$ ($[M\text{-}H]^-$). (Panel 2) The MS/MS fragmentation confirms the organosulfate with the *m/z* 97 (HSO_4^-) daughter ion. (Panel 3) Mass spectrum for the IEPOX-derived hydroxyl sulfate ester dimer, detected as *m/z* = 333 in the form of $C_{10}H_{20}SO_6^-$ ($[M\text{-}H]^-$).

> 98%), the elemental composition and functionality of which most closely resemble that of the IEPOX-derived organosulfates. An ESI/MS response factor of 1.56×10^{-5} ppm/area, is obtained for the d-galactone 6-sulfate anion ($C_6H_{11}SO_9^-$) at *m/z* 259 and applied to quantify the IEPOX-derived organosulfate ester and dimer. This sensitivity gives the overall equilibrium particle-phase organosulfate concentration of ~12 μg m^{-3}, which accounts for 17% of the AMS measured total organic masses. Note that although both belong to the organosulfate family and readily fragment to bisulfate anion (HSO_4^-) in the MS/MS analysis, the molecular properties of d-galactone 6-sulfate ($C_6H_{11}SO_9^-$) and IEPOX-derived sulfate ($C_5H_{11}SO_7^-$) that affect the ESI ionization efficiency, such as pK_a value, hydrophobicity, surface activity, *etc.*, are not exactly the same. One should expect that the ESI-MS responses for these two organosulfates differ even under identical instrument operation conditions, and as a result, the conclusion that IEPOX-derived organosulfates account for 17% of the AMS measured total organic masses has a degree of uncertainty.

F.5 Conclusions

We introduce here the combination of two well-established analytical techniques, PILS and UPLC/ESI-Q-TOFMS, for time-resolved and quantitative measurement of

chamber-generated organic aerosol chemical composition. The PILS + UPLC/ESI-Q-TOFMS system shows its promising utility, including relatively high-time resolution that allows for the investigation of aerosol dynamics and soft ionization to identify the integral molecular structure of particle-phase components. Additionally, the incorporation of liquid chromatography allows the pre-separation of species prior to the electrospray ionization, thus making the quantification of individual compounds plausible.

The PILS collection efficiency (CEPILS) towards a population of sub-micron particles composed of pure chemical standards, including carboxylic acids, polyols, and amines, is estimated by simultaneously comparing the DMA vs. UPLC/ESI-Q-TOFMS measured total organic mass concentrations. The overall mass collection efficiency exceeds 0.6 for particles with water solubility of >1 g L^{-1}, which corresponds to an average O:C ratio of >0.26. The AMS measured O:C ratios for SOA produced from photooxidation of a variety of VOCs (*e.g.*, isoprene, toluene, m-xylene, α-pinene, and naphthalene) in chamber experiments exceed 0.3, for which it is possible to characterize time-resolved chemical composition of these SOA systems at the molecular level. Instrument sensitivity and linearity were tested using single component organic aerosols generated from sorbitol, azelaic acid, pinonic acid, and adipic acid.

The PILS + UPLC/ESI-Q-TOFMS method is then applied to study the SOA formation driven by reactive IEPOX uptake onto hydrated and acidic ammonium sulfate particles. For the first time, time-resolved traces of IEPOX-derived organosulfate ester and dimer are observed. The temporal profile of the organosulfate ester is essentially identical to the AMS observed organic growth curve. The equilibrium organosulfate concentration potentially accounts for a significant fraction of the overall organic aerosol mass resulting from reactive IEPOX uptake. The combination of PILS collection with UPLC/ESI-Q-TOFMS analysis offers a new approach for time-resolved and quantitative characterization of aerosol constituents at molecular level.

Appendix G

ISOPRENE PHOTOCHEMISTRY OVER THE AMAZON RAINFOREST

Liu, Y., J. Brito, M. R. Dorris, J. C. Rivera-Rios, R. Seco, K. H. Bates, P. Artaxo, S. Duvoisin, F. N. Keutsch, S. Kim, A. H. Goldstein, A. B. Guenther, A. O. Manzi, R. A. F. Souza, S. R. Springston, T. B. Watson, K. A. McKinney, and S. T. Martin (2016). "Isoprene photochemistry over the Amazon rainforest". In: *Proc. Nat'l. Acad. Sci.* 113.22, pp. 6125–6130. DOI: 10.1073/pnas.1524136113.

Abstract

isoprene photooxidation is a major driver of atmospheric chemistry over forested regions. Isoprene reacts with hydroxyl radicals (OH) and molecular oxygen to produce isoprene peroxy radicals (ISOPOO). These radicals can react with hydroperoxyl radicals (HO_2) to dominantly produce hydroxyhydroperoxides (ISOPOOH). They can also react with nitric oxide (NO) to largely produce methyl vinyl ketone (MVK) and methacrolein (MACR). Unimolecular isomerization and bimolecular reactions with organic peroxy radicals are also possible. There is uncertainty about the relative importance of each of these pathways in the atmosphere and possible changes because of anthropogenic pollution. Herein, measurements of ISOPOOH and MVK + MACR concentrations are reported over the central region of the Amazon basin during the wet season. The research site, downwind of an urban region, intercepted both background and polluted air masses during the GOAmazon2014/5 Experiment. Under background conditions, the confidence interval for the ratio of the ISOPOOH concentration to that of MVK + MACR spanned 0.4 to 0.6. This result implies a ratio of the reaction rate of ISOPOO with HO_2 to that with NO of approximately unity. A value of unity is significantly smaller than simulated at present by global chemical transport models for this important, nominally "low-NO", forested region of Earth. Under polluted conditions, when NO concentrations were high (>1 ppb), ISOPOOH concentrations dropped below the instrumental detection limit (<60 ppt). This abrupt shift in isoprene photooxidation, sparked by human activities, speaks to ongoing and possible future changes in the photochemistry active over the Amazon rain forest.

G.1 Statement of Significance

For isolated regions of the planet, organic peroxy radicals produced as intermediates of atmospheric photochemistry have been expected to follow HO_2 rather than NO pathways. Observational evidence, however, has been lacking. An accurate understanding of the relative roles of the two pathways is needed for quantitative predictions of the concentrations of particulate matter, oxidation capacity, and consequent environmental and climate impacts. The results herein, based on measurements, find that the ratio of the ISOPOO reaction rate with HO_2 to that with NO is about unity for background conditions of Amazonia. The implication is that sufficient NO emissions are maintained by natural processes of the forest such that both HO_2 and NO pathways are important, even in this nominally "low-NO" region.

G.2 Introduction

isoprene (ISOP; C_5H_8) accounts for approximately half of the global flux of non-methane biogenic volatile organic compounds (BVOCs) to the atmosphere (Guenther *et al.*, 2012). The reactive chemistry of isoprene influences the oxidative capacity of the troposphere and the associated chemical cycles of atmospheric trace gases (Chameides *et al.*, 1988; Lelieveld *et al.*, 2008). Isoprene photo-oxidation products are also important sources of atmospheric organic particulate matter (Claeys *et al.*, 2004; Paulot *et al.*, 2009b; Surratt *et al.*, 2010). Isoprene is mostly oxidized in the atmospheric mixed layer, although entrainment and reaction in the free troposphere can also be important (Karl *et al.*, 2007; Kuhn *et al.*, 2007).

isoprene oxidation is mostly initiated by an addition reaction of a photochemically produced hydroxyl radical (OH) across the double bond, followed by the rapid addition of molecular oxygen (O_2) to the primary radical (Jenkin *et al.*, 2015). A population of isoprene peroxyl radicals (ISOPOO) is thereby produced. The subsequent chemistry of ISOPOO radicals proceeds along several competing pathways (Jenkin *et al.*, 2015). Reaction of ISOPOO with nitric oxide (NO) dominates in polluted regions of the planet. The major products are methyl vinyl ketone (MVK, C_4H_6O) and methacrolein (MACR, C_4H_6O).

The fate of ISOPOO radicals over unpolluted regions of the planet remains unclear. For many isoprene source regions, reaction of ISOPOO with hydroperoxyl radicals (HO_2) has been taken as the dominant pathway (Chen *et al.*, 2015; Crounse *et al.*, 2011; Liu *et al.*, 2013; Paulot *et al.*, 2009b; Rivera-Rios *et al.*, 2014), including over remote tropical forests like Amazonia where there are few anthropogenic NO

sources. The major products of the HO_2 pathway are an isomeric family of hydroxyl hydroperoxides (ISOPOOH; $C_5H_{10}O_3$). In addition, isomerization and bimolecular reactions with other organic peroxyl radicals (RO_2) can also be important (Crounse *et al.*, 2011; Jenkin *et al.*, 1998; Peeters *et al.*, 2014). Measurements of HO_2, RO_2, and NO, if available, could help to constrain these pathways for unpolluted regions, but each of these measurements is challenging in its own way (Fuchs *et al.*, 2011; Hoell *et al.*, 1987) and available data sets are sparse (Hewitt *et al.*, 2010; Lelieveld *et al.*, 2008). Unimolecular ISOPOO isomerization, for its part, remains in the early stages of study (Crounse *et al.*, 2011; Peeters *et al.*, 2014). As a result, the relative contribution of each pathway to the fate of atmospheric ISOPOO radicals remains uncertain for unpolluted regions of Earth (Wennberg, 2013).

The uncertainty in ISOPOO reaction pathways, in particular the uncertainties of the contributions of NO and HO_2 pathways, hinders accurate prediction of the environmental and climate impacts of isoprene chemistry. The HO_2 reaction pathway is important for the production of particulate matter through second-generation epoxydiol products (Paulot *et al.*, 2009b; Surratt *et al.*, 2010). The NO pathway contributes to the transport of nitrogen beyond the isoprene source region through the formation of stable organic nitrogen compounds (Perring *et al.*, 2013). The two pathways to different extents help to maintain the atmospheric oxidation cycle, including feedbacks on OH and O_3 concentrations (Chameides *et al.*, 1988; Liu *et al.*, 2013; Paulot *et al.*, 2009b).

Accurate ambient measurements of the molecular identities and concentrations of isoprene oxidation products are a first-order requirement for testing concepts of the reaction pathways of isoprene and the associated predictions of chemical transport models (CTMs). The products MVK and MACR have been studied in many atmospheric environments both by proton-transfer-reaction mass spectrometry (PTR-MS) and gas chromatography (GC) (Gouw and Warneke, 2007). Large data sets are available (Gouw and Warneke, 2007; Karl *et al.*, 2009, 2007; Kuhn *et al.*, 2007). By comparison, ambient measurements of ISOPOOH isomers are sparse, and available data sets are limited to temperate regions (Worton *et al.*, 2013; Xiong *et al.*, 2015).

An additional issue is that the utility of existing data sets of MVK and MACR concentrations to test and constrain models of isoprene chemistry is challenged by recent laboratory studies that have shown that both PTR-MS and GC techniques can have a contribution from ISOPOOH species in the nominal detection of MVK

and MACR (Liu *et al.*, 2013; Rivera-Rios *et al.*, 2014). For the usual operating conditions of PTR-MS and GC instrumentation, the two main ISOPOOH isomers (specifically, (1-OH, 2-OOH)-ISOPOOH, hereafter (1,2)-ISOPOOH, and (4-OH, 3-OOH)-ISOPOOH, hereafter (4,3)-ISOPOOH) decompose on the hot metal surfaces inside both types of instruments (Rivera-Rios *et al.*, 2014). (1,2)-ISOPOOH and (4,3)-ISOPOOH decompose to MVK and MACR, respectively. In this case, MVK and MACR concentrations reported in the literature can be expected to be upper limits, rather than best estimates, for regions of Earth where the HO_2 pathway is important for the fate of ISOPOO radicals. On a planetary scale, the contribution of the HO_2 pathway has been modeled as 60% larger than that of the NO pathway (Crounse *et al.*, 2011). The need for corrections to MVK and MACR data sets could be widespread.

In light of these issues, the present study was undertaken to measure the sum of (1,2)-ISOPOOH and (4,3)-ISOPOOH concentrations (hereafter, "ISOPOOH concentration"), in comparison to the sum of MVK and MACR concentrations. The measurements took place in the central region of the Amazon basin during the wet season of 2014. The measurements were made as part of the Observations and Modeling of the Green Ocean Amazon (GOAmazon2014/5) Experiment (Martin *et al.*, 2016). A major concept of the experiment was to locate a research site ("T3") several hours downwind of an urban region (specifically, 70 km west of Manaus, Amazonas, Brazil, a city of two million people). Local winds at different times swept either the pollution plume of Manaus or background air of the Amazon basin across the research site. As a result, the species observed at T3 were at times produced upwind under background conditions whereas at other times they were significantly affected by pollution. Based on back trajectories, the most probable transport time from the city to the measurement site was between 4 and 5 h. By comparison, (4,3)-ISOPOOH, ISOP, (1,2)-ISOPOOH, MACR, and MVK have characteristic lifetimes to OH loss of approximately 2, 3, 4, 10, and 14 h, respectively, for a reference OH concentration of 10^6 cm^{-3} typical of many environments. Deposition and entrainment can also be important loss mechanisms (Karl *et al.*, 2013; Nguyen *et al.*, 2015a). Background air, meaning the Amazon basin in the nominal absence of the pollution plume of Manaus, had significant variability associated with it, especially with respect to effective photochemical age. Background variability arose from variations of in-basin emissions and transformations integrated across several days of meteorology as well as, at times, from significant out-of-basin influences and variability tied to transport from the Atlantic Ocean and Africa (Chen *et al.*, 2009;

Martin *et al.*, 2010). Even so, the effect of the plume, when present, dominated over this background variability for the measured quantities of the present study. Measurements of the ratio of ISOPOOH to MVK + MACR concentrations, reported herein, are used to assess how different amounts of pollution, including background conditions in absence of anthropogenic influence (*i.e.*, "low NO"), regulate the relative importance of isoprene photooxidation pathways in the tropical forest of central Amazonia.

G.3 Materials and Methods

G.3.1 Measurements

Measurements were made at the T3 site of the GOAmazon2014/5 Experiment (Martin *et al.*, 2016). The site T3 was located in a pasture area of 2.5 km × 2 km (-3.2133°, -60.5987°). Pasture regions have low emissions of isoprene (Guenther *et al.*, 2006), and the isoprene observed at T3 originated predominantly from the upwind forest. The fetch of the T3 site oscillated between the extremes of a background atmosphere and influences of Manaus pollution depending on the deflection of trade winds slightly to the north or south with daily weather. At T3, a research container, part of the Mobile Aerosol Observing System (MAOS) of the USA Department of Energy, housed instrumentation (www.arm.gov). The main trace-gas inlet (12.7 mm PFA; 13 sLpm) was 10 m above the ground.

A proton-transfer-reaction time-of-flight mass spectrometer (PTR-ToF-MS, Ionicon Analytik GmbH, Austria; Jordan *et al.*, 2009) was employed to measure ISOPOOH and MVK + MACR concentrations (Section G.3.2.1). Intensities are reported herein in normalized count per second (ncps), calculated as the signal of the $C_4H_7O^+$ ion (cps) normalized to the total ion signal of H_3O^+ and $H_5O_2^+$, corrected for transmission. A cold trap was deployed upstream of the PTR-ToF-MS to selectively remove ISOPOOH isomers (Liu *et al.*, 2013). The approach was to collect data for a period of time with the trap in line followed by a period of time in bypass. A difference signal $\Delta C_4H_7O^+$ measured with and without the trap can be defined (Section G.3.3.1). Synthesized (1,2)-ISOPOOH was used to perform an on-site calibration of the PTR-ToF-MS for both bypass and trap (Section G.3.2.2). An on-site MVK standard showed that the sensitivity (ncps ppb 1) of the signal intensity for $C_4H_7O^+$ to the MVK concentration was the same through the bypass as through the trap. Detection limits of ISOPOOH and MVK + MACR were 60 ppt and 8 ppt, respectively for a 1 minute measurement. Uncertainty estimates were based on calibration with authentic standards and obtained by a Monte Carlo method of

sampling from the uncertainties in the $C_4H_7O^+$ signals and calibration parameters (Section G.3.3.2).

A trap experiment lasted for 15 min, alternating with 15 min in bypass. The first four and the last one of the 1-minute data points in each mode were deleted from the analysis to exclude the transition periods between trap and bypass, resulting in a total of 2810 trap-mode data points for analysis. Of these, 91% of the measurements, which required the presence of an operator for trap maintenance when power failures occurred, were made during daytime (Figure G.9 in the Supporting Information). Atmospheric oxidation of isoprene is most active during the daytime.

Instrumentation for measuring NO, NO_x, and NO_y concentrations was part of the MAOS package. The NO and NO_y data streams were obtained from the ARM data archive (http://www.arm.gov/campaigns/amf2014GOAmazon). NO_x data were not available during IOP1 due to lamp failure of the photolytic converter. The operational detection limits of NO and NO_y were 70 ppt and 100 ppt, respectively. The NO_y concentrations were smoothed by applying a 30-min median filter to minimize the contribution of any local emissions.

G.3.2 Experiments

G.3.2.1 PTR Instrumentation

The PTR-ToF-MS instrument was operated at a drift tube temperature of 80 °C and a drift tube pressure of 220 Pa (2.2 mbar). The drift tube voltage was set to 550 V, resulting in an E/N of 132 Td (E, electric field strength; N, number density of air in the drift tube; unit, Townsend, Td; 1 Td = 10^{-21} V m^2).

The inlet system of the PTR-ToF-MS (Figure G.10 in the Supporting Information) subsampled from the main trace-gas sampling line. The system had flow lines for calibration and measurement. Three-way valves having contact surfaces of PTFE Teflon (NResearch 225T031) were used to switch between the calibration and measurement modes. The valves were controlled by analog outputs of the PTR-ToF-MS. Metal-sealed mass flow controllers (MFC; MKS 1479A) without Viton O-rings were used for calibration flow to avoid artifacts of ketone reactions. The inlet system inside the container was maintained above 27 °C to prevent condensation. As a comparison point, the 97.7-percentile of the distribution in dew point temperature of the atmosphere during IOP1 was 26.5 °C.

The instrument background was determined a few times per day using a zero air

generator (Parker Balston 75-83NA) in the MAOS container. Laboratory tests prior to deployment indicated that concentrations of target compounds in the outflow of the zero air generator were as low as in ultra-high-purity zero air (Airgas). Instrument sensitivity during IOP1 was determined daily by standard addition (5.14 ppm isoprene and 5.14 ppm MVK in nitrogen; Air Liquide) to ambient air. Background and calibration measurements were carried out at ambient humidity to compensate for possible changes in the instrument response with humidity.

The subsample flow passed either through a cold-trap or along a bypass before being sampled by the PTR-ToF-MS. The trap consisted of a cylindrical glass bottle (ChemGlass CG-1140; 35 × 100 mm) and a 6.4-mm (OD) PFA coil in series, both immersed in a cold bath (Lauda ECO RE 1050) at -40 °C. Compared to the implementation described in Liu *et al.* (2013), the inclusion of the glass bottle was new. The glass bottle having a large cross section served to remove much of the water vapor upstream of the PFA Teflon tubing so as to avoid clogging. Ice was removed once per day from the bottle. A constant purge flow of 0.1 sLpm through the trap was maintained during bypass to reduce the equilibration time for switching from bypass to trap measurement. Onsite measurements using an MVK standard showed that the sensitivity (ncps ppb 1) of the signal intensity for $C_4H_7O^+$ to the MVK concentration was the same along the bypass as through the trap.

PTR-ToF-MS spectra were collected at a time resolution of 60 s using ToF-DAQ recorder (v. 1.2.92; TOFWERKS). Analog outputs of the PTR-ToF-MS (*i.e.*, determining valve status) were recorded simultaneously. The ToF-DAQ recorder was set to perform automatic mass calibrations every 6 min using peaks at *m/z* 39.0327 ($H_5O(^{18}O)^+$), *m/z* 59.0491 ($C_3H_7O^+$), and *m/z* 123.9454 ($FeH_4O_4^+$). Time series of integrated ion signals for isoprene ($C_5H_9^+$; *m/z* 69.0699) and MVK/MACR/ISOPOOH ($C_4H_7O^+$; *m/z* 71.0492) in counts per second (cps) were generated using the ToF-DAQ viewer software (v 1.2.92 TOFWERK, Switzerland).

G.3.2.2 Calibration Using Authentic ISOPOOH Compounds

(1,2)-ISOPOOH was synthesized (Nguyen *et al.*, 2015a) and used to perform an RH-dependent calibration at T3 of the PTR-ToF-MS for both bypass and trap modes. Further calibration was undertaken later in the laboratory using both (1,2)-ISOPOOH and (4,3)-ISOPOOH standards. For calibration at T3, (1,2)-ISOPOOH was synthesized at laboratories in Manaus, and analytical tools were not available to determine purity. The purity was inferred based on the instrument response of

(1,2)-ISOPOOH later characterized in the laboratory (vide infra). For calibration, the (1,2)-ISOPOOH standard was nebulized and flowed into a mixing flask (Bates *et al.*, 2014). The dilution flow to the mixing flask was humidified to controlled RH values using a bubbler.

For bypass mode, laboratory experiments using standards of known purity suggested that the conversion efficiency of (1,2)-ISOPOOH to MVK in PTR-ToF-MS was close to unity. The measured sensitivity of (1,2)-ISOPOOH at $C_4H_7O^+$ was (95 ± 5)% of the sensitivity of MVK. The $C_4H_7O^+$ was the dominant peak on the mass spectra measured by PTR-ToF-MS for (1,2)-ISOPOOH. In addition, after passing the (1,2)-ISOPOOH-containing flow through a heated stainless steel tube at 80-90 °C to convert (1,2)-ISOPOOH to MVK prior to PTR-MS, the measured signal intensity of $C_4H_7O^+$ ion increased by less than 10%. Experiments using (4,3)-ISOPOOH also suggested almost complete conversion to MACR in PTR-ToF-MS.

Under the assumption that a conversion efficiency of (95 ± 5)% from (1,2)-ISOPOOH and (4,3)-ISOPOOH to MVK and MACR can be applied to bypass measurements at T3 site, the inferred purity of (1,2)-ISOPOOH standards synthesized in Manaus (52%) fell in the typical purity range of (1,2)-ISOPOOH standards (50-65%) synthesized using the same method.

For (1,2)-ISOPOOH calibration at trap mode, both lab and field experiments showed that the $C_4H_7O^+$ ion signal did not drop completely to background levels when the trap was in place. Figure G.11 in the Supporting Information shows the dependence of trap $C_4H_7O^+$ signal on the concentration of ISOPOOH and the humidity of the sample based on on-site calibration using (1,2)-ISOPOOH. At fixed concentration, the trap $C_4H_7O^+$ signal was proportional to humidity. At fixed humidity, the trap signal intensity can be fitted using a second degree polynomial of the concentration. The dependence of trap $C_4H_7O^+$ signal intensity $I_{C_4H_7O^+,ISOPOOH,trap}$ on ISOPOOH concentration and humidity can hence be described using the following equation:

$$I_{C_4H_7O^+,ISOPOOH,trap} = a \cdot \Gamma_{C_4H_7O^+,MVK} \cdot C_{ISOPOOH} \cdot (C_{ISOPOOH} + b) \cdot (AH + c) \quad \text{(G.1)}$$

where $C_{ISOPOOH}$ is the concentration of (1,2)-ISOPOOH in the sample flow in ppb; $\Gamma_{C_4H_7O^+,MVK}$ is the sensitivity of MVK at $C_4H_7O^+$; AH is the absolute humidity of the sample flow in hPa; and a, b, and c are fitting parameters. Figures G.11a and G.11b in the Supporting Information show the comparison of measured and fitted data of all the calibrations.

The detection of considerable $C_4H_7O^+$ signal for (1,2)-ISOPOOH through the trap suggested that processes other than condensation of ISOPOOH isomers took place in the trap to produce $C_4H_7O^+$ ions. One possibility was that volatile impurities contained in the synthesized standard gave rise to $C_4H_7O^+$ ions. This possibility was not supported, however, by the observation that the $C_4H_7O^+$ signal intensity dropped to close to background level at low humidity and the $C_4H_7O^+$ signal intensity was not linearly proportional to the concentration of (1,2)-ISOPOOH at fixed humidity (Figure G.11b in the Supporting Information). Another possibility was that (1,2)-ISOPOOH was insufficiently removed by the trap due to competition of the condensation of water vapor. This possibility was excluded based on experiments of increasing the residence time of the calibration flow in the trap, in which case the $C_4H_7O^+$ signal intensity slightly increased instead of decreased (results not shown here).

One plausible possibility is that certain reactions of (1,2)-ISOPOOH in the trap led to MVK. This possibility was consistent with the small increase of trap signal intensity with the increase of residence time (*i.e.*, reaction time). Water vapor or water in another form should be involved in the reaction because the trap $C_4H_7O^+$ signal intensity was proportional to humidity (Figure G.11a in the Supporting Information). The reactions might have taken place in the upper part of trap, where the temperature transited from ambient of above 27 °C down to −40 °C, and water vapor partly condensed in liquid form. The amount of condensed liquid water should relate to absolute humidity given the temperature gradient. Further studies are needed to understand the reaction mechanism, the role of water, and possible designs to eliminate the need to use a complex calibration like Equation G.1.

Figure G.11b in the Supporting Information shows that at ambient humidity the $C_4H_7O^+$ signal during trap measurements of (1,2)-ISOPOOH was smaller than that of the bypass signal. As a result, through use of Equation G.1 the ISOPOOH concentration in the ambient air was obtained based on the difference signal for $C_4H_7O^+$. The measured signal intensities $I_{C_4H_7O^+,ambient,bypass}$ of $C_4H_7O^+$ ion when bypassing the cold trap and $I_{C_4H_7O^+,ambient,trap}$ when passing through the trap are given as follows:

$$\begin{aligned} I_{C_4H_7O^+,ambient,bypass} = & I_{C_4H_7O^+,bg} + \Gamma_{C_4H_7O^+,MVK/MACR} \cdot C_{MVK+MACR} \\ & + \Gamma_{C_4H_7O^+,ISOPOOH} \cdot C_{ISOPOOH} \end{aligned} \tag{G.2}$$

$$\begin{aligned} I_{C_4H_7O^+,ambient,trap} = & I_{C_4H_7O^+,bg} + \Gamma_{C_4H_7O^+,MVK/MACR} \cdot C_{MVK+MACR} \\ & + I_{C_4H_7O^+,ISOPOOH,trap} \end{aligned} \tag{G.3}$$

where $I_{C_4H_7O^+,bg}$ is the background signal intensity of $C_4H_7O^+$ ion in ncps; $\Gamma_{C_4H_7O^+,MVK/MACR}$ is the combined sensitivity of MVK and MACR; $C_{MVK+MACR}$ is the sum concentration of MVK an MACR; $C_{ISOPOOH}$ is the sum concentration of (1,2)-ISOPOOH and (4,3)-ISOPOOH, both detected as $C_4H_7O^+$ ion in PTR-ToF-MS; $\Gamma_{C_4H_7O^+,ISOPOOH}$ is the combined sensitivity of (1,2)-ISOPOOH and (4,3)-ISOPOOH; and $I_{C_4H_7O^+,ISOPOOH,trap}$ is trap signal intensity of the $C_4H_7O^+$ ion as a function of CISOPOOH and absolute humidity (AH).

For use of Equations G.2 and G.3, $I_{C_4H_7O^+,ambient,bypass}$ and $I_{C_4H_7O^+,ambient,trap}$ were obtained from ambient measurements. $\Gamma_{C_4H_7O^+,MVK/MACR}$ and $I_{C_4H_7O^+,bg}$ were determined by using MVK/MACR standards and pure air generator. For both of the two parameters, there was insignificant difference between trap and bypass measurements. Further studies carried out in laboratory suggested that the bypass sensitivity and the trap response of (4,3)-ISOPOOH were similar with those of (1,2)-ISOPOOH. $\Gamma_{C_4H_7O^+,ISOPOOH}$ and $I_{C_4H_7O^+,ambient,trap}$ were equivalent to those derived for (1,2)-ISOPOOH. By solving Equations G.2 and G.3, $_{CMVK+MACR}$ and $C_{ISOPOOH}$ were determined. More directly, combining Equations G.2 and G.3, the signal difference $\Delta C_4H_7O^+$ of bypass and trap measurement is obtained, giving CISOPOOH in implicit form:

$$\begin{aligned}\Delta C_4H_7O^+ &= I_{C_4H_7O^+,ambient,bypass} - I_{C_4H_7O^+,ambient,trap} \\ &= 0.95 \cdot \Gamma_{C_4H_7O^+,MVK} \cdot C_{ISOPOOH} \\ &- a \cdot \Gamma_{C_4H_7O^+,MVK} \cdot C_{ISOPOOH} \cdot (C_{ISOPOOH} + b) \cdot (AH + c)\end{aligned} \tag{G.4}$$

G.3.3 Data Analysis

G.3.3.1 Determination and Compound Assignment of $\Delta C_4H_7O^+$

The bypass intensities at the time points of the trap measurements were obtained by applying linear interpolation and low-pass filtering to the bypass measurements before and after each trap experiment. Figure G.12 in the Supporting Information shows the interpolated bypass signals of $C_4H_7O^+$ and the signal difference $\Delta C_4H_7O^+$ on March 14 and 30, 2014. Interpolation of the bypass signals to the times of the trap measurements can introduce some error in the signal difference, particularly when concentrations are changing rapidly with time, resulting in a large variance in $\Delta C_4H_7O^+$. A histogram of all the $\Delta C_4H_7O^+$ values is shown in Figure G.13 in the Supporting Information. Despite the large variance in the $\Delta C_4H_7O^+$ data, the median value is significantly greater than zero, indicating net removal of low-volatility compounds by the trap.

The possibility of significant contributions to $\Delta C_4H_7O^+$ by compounds other than ISOPOOH was considered. Pinonaldehyde ($C_{10}H_{16}O_2$) and isoprene epoxydiols (IEPOX; $C_5H_{10}O_3$) fragment to the $C_4H_7O^+$ ion and can be removed at low temperature (Praske *et al.*, 2015). Nevertheless, for the study conditions the following lines of evidence appear to rule out these species as substantial contributors to the observed $\Delta C_4H_7O^+$ values. For pinonaldehyde, $C_4H_7O^+$ is a minor fragment ion, and its intensity is about one third of the major fragment ion $C_{10}H_{15}O^+$ (Wisthaler *et al.*, 2001). The observed intensity of $C_{10}H_{15}O^+$ ion was less than 15% of $\Delta C_4H_7O^+$ under background conditions, suggesting that the possible contribution of pinonaldehyde to $\Delta C_4H_7O^+$ was less than 5%. Additional evidence is that the concentration of pinonaldehyde, represented by the signal intensity of $C_{10}H_{15}O^+$, did not increase during times of background conditions. The other possibility, IEPOX compounds, was evaluated by sampling authentic IEPOX standards. The results show that the $C_4H_7O^+$ ion was a minor fragment for the standards, corresponding to less than 10% of the main product ion ($C_5H_7O^+$), at least for the employed PTR-ToF-MS operating conditions. Based on the signal intensity of $C_5H_7O^+$ observed for background air masses and changes with the trap in place, the IEPOX contribution accounted for no more than 5% of the observed $\Delta C_4H_7O^+$.

G.3.3.2 Uncertainty Estimate of the ISOPOOH Concentration and Concentration Ratio ξ

The central value of the concentrations of ISOPOOH and MVK+MACR of each data subset were estimated for the median $\Delta C_4H_7O^+$ and median $I_{C_4H_7O^+,ambient,trap}$. The central value of the ratio ξ of concentrations was then determined. Confidence intervals (75%) were obtained by a Monte Carlo method of sampling from the uncertainties in fit parameters in Equation G.1 (*i.e.*, a, b, and c), the absolute humidity, the bypass sensitivities of ISOPOOH and MVK at $C_4H_7O^+$, the median $\Delta C_4H_7O^+$, and the median $I_{C_4H_7O^+,ambient,trap}$.

G.3.4 Modeling

Three models were used to aid in the interpretation of the measurements. (1) An analytical model was used to infer production ratio χ from observed concentration ratio ξ. (2) A measurement-constrained box model of the chemistry in the planetary boundary layer was used to simulate daytime HO_2 and RO_2 concentrations for variable NO concentration (1 to 400 ppt). The model was used to determine the corresponding fractional loss of ISOPOO *via* each reaction pathway and hence

the production ratio χ. (3) Simulation results using GEOS-Chem, a global three-dimensional chemical transport model, were compared with observations.

For the box model, the chemistry component consisted of the Master Chemical Mechanism (MCM; version 3.3.1; Jenkin *et al.*, 2015). In addition, some recent experimental results on the chemical production and fate of MVK, MACR, and ISOPOOH were incorporated (Liu *et al.*, 2013; St. Clair *et al.*, 2015). A basic representation of deposition and entrainment was implemented (Section G.3.4.2). The model was configured to simulate daytime chemistry (10:00-17:00 local time (LT); 14:00-21:00 UTC). Most trap measurements were made during this time period (Figure G.9 in the Supporting Information), and the concentrations of isoprene and its oxidation products were relatively stable (Figure G.7 in the Supporting Information). Irradiance levels were held constant, corresponding to the solar zenith angle at 14:30 LT, with no diel cycle for photolysis (Section G.3.4.3). The temperature was set at 298 K. The simulation was constrained by constant concentrations of isoprene (1.7 ppb), monoterpenes (0.17 ppb), methane (1.85 ppm), and carbon monoxide (110 ppb) at the observed daytime mean values. The hydroxyl radical concentration was fixed at 5×10^5 cm^{-3}. The concentrations of HO_2 and RO_2 (Section G.3.4.4), fractional loss of ISOPOO by reaction with NO, HO_2, RO_2, and isomerization, and production ratio χ were obtained at steady state.

For the CTM, the simulations were run in GEOS-Chem (Bey *et al.*, 2001) for the year 2012 on a $4^\circ \times 5^\circ$ grid with a model spin-up of 1.5 years. The GEOS5 meteorology and the Rosenbrock Rodas-3 solver was used. The chemical mechanism was largely as described in Mao *et al.* (2013) but included several updates of the isoprene chemistry based on recent laboratory results (Bates *et al.*, 2014, 2016; Nguyen *et al.*, 2015a; Praske *et al.*, 2015; St. Clair *et al.*, 2015). Information obtained from the simulations included the daytime average values of the concentration ratio ξ, the NO concentration, the NO_y concentration, and the fractional loss of ISOPOO radicals to individual pathways. This information was obtained for February and March over the grid box encompassing the observation site (<1000 m height). In addition to the simulation using default settings, simulations that increased above-canopy NO emissions by factors of 10 and 30 were carried out. Further information is provided in Section G.3.4.5.

G.3.4.1 Analytical Model to Estimate of χ from ξ

The time course of concentration C_i of species i, where i is one of (1,2)-ISOPOOH, (4,3)-ISOPOOH, MVK, or MACR, is governed by the following equation:

$$\frac{dC_i}{dt} = S_i - k_i C_i \tag{G.5}$$

where S_i is the production rate *via* the reaction of isoprene with OH and k_i is the first-order loss coefficient. For constant S_i and k_i, the solution to Equation G.5 is as follows:

$$C_i(t) = \frac{S_i}{k_i}(1 - e^{-k_i t}) + C_i(0)e^{-k_i t} \tag{G.6}$$

Before sunrise (*i.e.*, taken as time zero), the concentrations of MVK, MACR, and ISOPOOH approach zero (Figure G.7 in the Supporting Information). For $C_i(0) = 0$, the following equation is obtained:

$$\begin{aligned}
\zeta = \frac{C_{ISOPOOH}}{C_{MVK+MACR}} &= \frac{\frac{S_1}{k_1}(1 - e^{-k_1 t}) + \frac{S_2}{k_2}(1 - e^{-k_2 t})}{\frac{S_3}{k_3}(1 - e^{-k_3 t}) + \frac{S_4}{k_4}(1 - e^{-k_4 t})} \\
&= \frac{\frac{f^1_{1+2} S_{1+2}}{k_1}(1 - e^{-k_1 t}) + \frac{f^2_{1+2} S_{1+2}}{k_2}(1 - e^{-k_2 t})}{\frac{f^3_{3+4} S_{3+4}}{k_3}(1 - e^{-k_3 t}) + \frac{f^4_{3+4} S_{3+4}}{k_4}(1 - e^{-k_4 t})} \\
&= \frac{(0.6/k_1)(1 - e^{-k_1 t}) + (0.4/k_2)(1 - e^{-k_2 t})}{(0.6/k_3)(1 - e^{-k_3 t}) + (0.4/k_4)(1 - e^{-k_4 t})}
\end{aligned} \tag{G.7}$$

where the indices 1-4 represent (1,2)-ISOPOOH, (4,3)-ISOPOOH, MVK, and MACR, respectively; f^1_{1+2}, f^2_{1+2}, f^3_{3+4}, and f^4_{3+4} are the respective fractions of the total production rates S_{1+2} and S_{3+4} (*e.g.*, $S_{1+2} = S_1 + S_2$ and $f^1_{1+2} = S_1/S_{1+2}$); and $\chi = S_{1+2}/S_{3+4}$. The fractions f^1_{1+2}, f^2_{1+2}, f^3_{3+4}, and f^4_{3+4} are independent of S_{1+2} and S_{3+4} and are ultimately determined by the branching ratio of isoprene to the respective precursor peroxy radicals. MVK and (1,2)-ISOPOOH originate from the same isoprene peroxy radical. MACR and (4,3)-ISOPOOH likewise originate from the same radical. Values $f^1_{1+2} = f^3_{3+4} = 0.6$ and $f^2_{1+2} = f^4_{3+4} = 0.4$ are used based on the reported ratio of product yields of MVK and MACR *via* the NO pathway (4). For a given reaction time, χ is directly proportional to ξ.

Loss coefficients k_i of MVK, MACR, and ISOPOOH and an effective reaction time are needed in order to calculate the proportionality coefficient of χ to ξ using Equation G.7. The loss coefficient is given by $k_i = k_{i,OH}[\mathrm{OH}] + k_{i,en} + k_{i,d}$ for rate coefficients of reaction (OH), entrainment (en), and deposition (d). Parameter values are listed in Table G.1. The entrainment process of these species is less well

understood compared to deposition as well to OH oxidation. The sensitivity of the proportionality coefficient χ/ξ to k_{en} is investigated. Values of k_{en} used for the sensitivity study are 0, 1, and 2×10^5 s^{-1}, where 1×10^5 s^{-1} is the best estimate based on current knowledge (Table G.1). As shown in Figure G.14 in the Supporting Information, the proportionality factor for an effective reaction time of 5 h changed by less than 2% for a change in the entrainment coefficient from 1×10^5 s^{-1} to 0 or 2×10^5 s^{-1}. The production ratio χ inferred from the concentration ratio ξ is therefore considered insensitive to the coefficient k_{en} of entrainment.

As a test of the accuracy of the effective photochemical reaction time (*i.e.*, 5×10^5 OH cm^{-3} across 5 h), the ratio C_{total}/C_{ISOP} of the total concentration of measured reaction products (*i.e.*, the sum of MVK, MACR, and ISOPOOH) to the isoprene concentration was calculated using the following equation:

$$\begin{aligned}\frac{C_{total}}{C_{ISOP}} &= \frac{S_{total}}{C_{ISOP}} \cdot \frac{\chi}{1+\chi} \cdot \left(\frac{0.6}{k_1}(1-e^{-k_1 t_{eff}}) + \frac{0.4}{k_2}(1-e^{-k_2 t_{eff}})\right. \\ &\left. + \frac{0.6}{k_3}(1-e^{-k_3 t_{eff}}) + \frac{0.4}{k_4}(1-e^{-k_4 t_{eff}})\right) \\ &= 0.65 \cdot k_{ISOP,OH} \cdot [\mathrm{OH}] \cdot \frac{\chi}{1+\chi} \cdot \left(\frac{0.6}{k_1}(1-e^{-k_1 t_{eff}}) + \frac{0.4}{k_2}(1-e^{-k_2 t_{eff}})\right. \\ &\left. + \frac{0.6}{k_3}(1-e^{-k_3 t_{eff}}) + \frac{0.4}{k_4}(1-e^{-k_4 t_{eff}})\right)\end{aligned} \tag{G.8}$$

where the variables k_i and χ are the same as in Equation G.7 and S_{total} is the total production rate of MVK, MACR, and ISOPOOH. The term S_{total} is equal to 0.65 $k_{ISOP,OH} C_{ISOP}$[OH] based on MCM v3.3.1 for background conditions. Other values include t_{eff} = 5 h and [OH] = 5×10^5 cm^{-3}. For χ ranging from 0.61 to 0.93 for background conditions, the calculated C_{total}/C_{ISOP} ranges from 0.41 to 0.43. This value is in good agreement with the median of the observations of 0.4 for background condition, as illustrated in Figure G.6 in the Supporting Information.

One approximation of the foregoing analysis is the use of production rates S_i and loss coefficients k_i that are constant throughout the day, thereby corresponding to average or effective daily values. One critical simplification in this treatment is the entrainment processes. Whereas it is reasonable to assume that cleaner air is entrained from upper troposphere into the boundary layer for afternoon hours, entrainment of air from the residual layer, which might contain some MVK and MACR due to their longer lifetime, can occur in the morning. In this case, entrainment in the morning can be a source or neutral instead of a sink. Possible

Species (i)	$k_{i,OH}$ (10^{-5} s^{-1})^a	$k_{i,d}$ (10^{-5} s^{-1})^b	$k_{i,en}$ (10^{-5} s^{-1})^c	k_i (10^{-5} s^{-1})^d
(1,2)-ISOPOOH	3.7	2.0	1.0	6.7
(4,3)-ISOPOOH	5.9	2.0	1.0	8.9
MVK	1.0	0.2	1.0	2.2
MACR	1.4	0.2	1.0	2.6

Table G.1: Loss rate coefficients for species in Equation G.9 for background conditions. A 1000-m deep, well mixed planetary boundary layer (PBL) is assumed. A temperature of 298 K is used. $^{(a)}$For reactions with OH, the rate coefficients were taken from IUPAC recommendation for MVK and MACR (Atkinson *et al.*, 2006) and from St. Clair *et al.* (2015) for (1,2)-ISOPOOH and (4,3)-ISOPOOH (6). A daytime (10:00-17:00 LT) background OH concentration of 5×10^5 cm^{-3} was used, as measured by a chemical ionization mass spectrometer at T3 (Vilà-Guerau de Arellano *et al.*, 2009). These values hold for background conditions. Oxidation can be faster inside the pollution plume. $^{(b)}$A deposition velocity of 2.0 cm s^{-1} was used for ISOPOOH isomers, as recommended recently by Nguyen *et al.* (2015a) based on measurements over a temperate forest. For MVK and MACR, the deposition rate was assumed to be one magnitude lower (*i.e.*, 0.2 cm s^{-1}) considering its lower water solubility and reactivity. $^{(c)}$An entrainment rate coefficient was determined by considering the entrainment velocity and concentration gradient between PBL and cloud layer. An entrainment velocity of 2.0 cm s^{-1} was taken based on the simulated evolution of PBL height over a tropical forest during daytime (10:00-17:00 LT) (Kuhn *et al.*, 2007). Based on reported vertical profiles of isoprene concentration and the ratio of the concentration of (MVK+MACR+ISOPOOH) to that of isoprene over central Amazonia (Karl *et al.*, 2007; Kuhn *et al.*, 2007), the concentration jump of MVK, MACR, and ISOPOOH between the PBL and the cloud layer is approximated by half of PBL concentration. Compared with a concentration jump of isoprene of one order of magnitude, the concentration jump of MVK, MACR, and ISOPOOH is smaller because of enhanced oxidation in the cloud layer (Karl *et al.*, 2007; Kuhn *et al.*, 2007). The uncertainty of the current parameterization of entrainment rate can be a factor of two due to limited understanding of entrainment processes of these species. Sensitivity of model results to entrainment rate was examined (Section G.3.3.1). $^{(d)}$The first-order loss coefficient is given by $k_i = k_{i,OH}[\mathrm{OH}] + k_{i,en} + k_{i,d}$.

entrainment from the residual layer to the boundary layer in the morning can be viewed as a small but nonzero initial concentration of MVK and MACR in the model. In this case, concentration ratio ξ(t) can be calculated given production ratio χ and $C_{MVK+MACR}(0)$, but χ cannot be retrieved just based on ξ(t). As a sensitivity test on $C_{MVK+MACR}(0)$, ξ(t) is plotted for $C_{MVK+MACR}(0)$ = 0 and 0.1 ppb in Figure G.15 in the Supporting Information. The value of χ is fixed at 0.75, which is the estimated median value for the background condition (Figure G.3). For t <2 h, the concentration ratio ξ varies strongly with $C_{MVK+MACR}(0)$. As t increases, ξ(t) for different $C_{MVK+MACR}(0)$ converge. For an effective reaction time of 5 h, ξ values for $C_{MVK+MACR}(0)$ of 0.1 ppb is 12% lower than that for $C_{MVK+MACR}(0)$ of 0 ppb. The conclusion is that the afternoon concentration ratio ξ is not sensitive to possible morning entrainment of MVK and MACR from residual layer, and the simplified treatment of entrainment used here is acceptable.

G.3.4.2 Box Model: Deposition and Entrainment

Deposition and entrainment rate coefficients of ISOPOOH, MVK, and MACR are set as the same values as in the analytical model (Table G.1). In addition, deposition of O_3, H_2O_2, HNO_3, and PAN was also considered, with deposition velocities of 5, 3, 2 cm s^{-1}, respectively (Fan *et al.*, 1990; Nguyen *et al.*, 2015a). The effective entrainment loss coefficient of 1.0×10^{-5} s^{-1} for MVK, MACR, and ISOPOOH (Table G.1) was also applied to all the other oxygenated oxidation products.

G.3.4.3 Box Model: Photolysis

The parameterization for photolysis frequencies in Master Chemical Mechanism (MCM) was historically calibrated for clear sky condition using a radiation transfer model (Jenkin *et al.*, 1997). The parameterization (photolysis frequency as a function of solar zenith angle) represents clear sky conditions at a latitude of 45 °N at summertime. Site T3 was located near the equator with a different column air mass. For inorganics included in MCM, the noon-time photolysis frequencies at T3 site calculated using the MCM parameterization were on average 18% lower than those simulated by us in a test using the Tropospheric Ultraviolet and Visible (TUV) model (https://www2.acom.ucar.edu/modeling/tropospheric-ultraviolet-and-visible-tuv-radiation-model). A scaling factor of 1.2 was, therefore, applied in the model treatment herein to the photolysis frequencies simulated by MCM for clear sky conditions. A further factor was incorporated for all sky conditions. A sky

radiometer at T3 measured the shortwave broadband total downwelling irradiance (SKYRAD). For the days and hours of trap measurements, the average irradiance level for all skies was estimated as 76% of clear skies. Scaling factors of 1.2 and 0.76 represented a net 0.91 factor applied to the MCM photolysis frequencies for the modeling activities carried out in the present study.

G.3.4.4 Box Model: Simulated HO_2 and RO_2 Concentrations

The simulated HO_2 and RO_2 concentrations using the box model are in the range of measurement values for in tropical forests, as reported in the literature, both in terms of magnitude and ratio. Lelieveld *et al.* (2008) reported a mean HO_2 concentration of $(11 \pm 3) \times 10^8$ cm^{-3} for a mean NO concentration of 0.02 ± 0.02 ppb over coastal Amazonia during the GABRIEL aircraft campaign. The HO_2 measurement technique was later found to have a significant interference from RO_2 radicals produced from OH reaction with alkene- and aromatic-precursors including isoprene, which contribute to the nominal detection of HO_2 radicals by a conversion efficiency of greater than 80% (Fuchs *et al.*, 2011). As shown in Figure G.16 in the Supporting Information, although the simulated HO_2 concentration is below 4×10^8 cm^{-3}, the total concentration of HO_2 and RO_2 is 8×10^8 cm^{-3} for 0.02 ppb NO. This simulated range is close to the observation of Lelieveld *et al.* (2008) with correction for the measurement interference. Observations over southeast Asia in the OP3 Experiment found a mean mid-day total concentration of HO_2 and RO_2 of $(9 \pm 2) \times 10^8$ cm^{-3} for a mean NO concentration of 0.04 ppb (Hewitt *et al.*, 2010). By comparison, in the present study, the simulated concentration of HO_2 + RO_2 is 7×10^8 cm^{-3} for 0.04 ppb NO. As shown in Figure G.16 in the Supporting Information, the simulated concentration of RO_2 is several times higher than that of HO_2 at lower NO concentrations. The HO_2 and RO_2 become similar at higher NO concentrations. This trend is quantitatively consistent with the field observations by Fleming *et al.* (2006). In that study, the fraction of HO_2 in the total concentration of HO_2 and RO_2 was 0.2 for lower NO_x and 0.4 to 0.6 for higher NO_x. Although the concentrations of HO_2 and RO_2 are often assumed to be equal (Barket *et al.*, 2004), the simulation here as well as the cited observations suggest that the concentration ratio of HO_2 to RO_2 decreases below unity for low NO concentration.

G.3.4.5 GEOS-Chem Simulation: Sensitivity to Soil NO Emissions

There have been only a few field studies of soil NO emission in the Amazon rainforests in the wet season (Bakwin *et al.*, 1990a; Garcia-Montiel *et al.*, 2001; Verchot *et al.*, 1999). The reported soil NO emission rates are in the range of 0.6 to 1.4×10^{10} molec cm^{-2} s^{-1}. For dry season, the reported soil NO emission can be higher (Garcia-Montiel *et al.*, 2001; Kaplan *et al.*, 1988; Verchot *et al.*, 1999). One must keep in mind the wide range of soils and forest types throughout Amazonia, so that these measurements reported in the literature cannot be readily generalized; even so, they are the measurements that we do have at this time, and they do represent what models are based on. Furthermore, not all the NO emitted from forest soil is exported to the atmosphere above the canopy due to NO oxidation by ozone forming NO_2 and subsequent NO_2 deposition within the canopy. There is large uncertainty in the canopy reduction factor, defined as the ratio of above-canopy NO_x emission to above-soil NO emission (Ganzeveld *et al.*, 2002). For tropical forests, earlier study by Jacob and Bakwin suggested a canopy reduction factor of around 0.2 (Jacob and Bakwin, 1991), whereas later study by Ganzeveld *et al.* (2002) suggested a value of 0.4-0.5. Based on these studies, the above-canopy NO_x emission can be in the range of 1.2 to 7.0×10^9 molec cm^{-2} s^{-1}.

Soil NO emission in GEOS-Chem is based on parameterization by Hudman *et al.* (2012), and canopy reduction is implemented following Jacob and Bakwin (1991) (*c.f.* http://wiki.seas.harvard.edu/geos-chem/index.php/Hudman_et_al_2012_soil_NOx_emissions_algorithm). For the grid square encompassing the measurement site, the modeled above-canopy NO_x emission is 2.0×10^8 molec cm^{-2} s^{-1} in the wet season. The value is one order of magnitude lower than the range suggested by the field observations. In this light, we reran the model with increased soil NO emissions by factors of 10 and 30 and kept the canopy reduction unchanged. The simulation results are presented in Table G.4. The resultant above-canopy NO_x emissions are 2.0 to 6.0×10^9 molec cm^{-2} s^{-1}, respectively. The modeled daytime ratio of ISOPOOH concentration to MVK + MACR concentration is 1.0, 0.93, and 0.76 for default, 10 × default, and 30 × default soil NO emission scenarios, respectively, in the wet season in the grid square where measurement site is located. The simulated concentration ratios with increased NO_x emissions, especially in the case of NO emission that are 30 times higher, get closer to the confidence interval of the observed ratio of 0.4-0.6 reported in the present study.

G.4 Results and Discussion

G.4.1 Observations

Data sets were collected at the T3 site of GOAmazon2014/5 in the wet season during an eight-week Intensive Operating Period ("IOP1") (*c.f.* Materials and Methods, Section G.3). Concentrations of ISOPOOH and MVK + MACR were measured using a proton-transfer-reaction time-of-flight mass spectrometer (PTR-ToF-MS). ISOPOOH and MVK + MACR, both detected as the $C_4H_7O^+$ ion by the PTR-ToF-MS, were discriminated by use of an upstream cold trap. ISOPOOH, having a lower volatility than does MVK or MACR, was selectively removed by the cold trap (Liu *et al.*, 2013; Nguyen *et al.*, 2014b).

Figure G.1 shows the time series of trap and bypass signal intensities of the $C_4H_7O^+$ ion for two contrasting afternoons. The time series of the concentrations of reactive nitrogen compounds (NO_y), ozone (O_3), and carbon monoxide (CO) show that the left and right panels of Figure G.1 correspond, respectively, to time periods when the pollution plume or background air passed over T3. The NO_y concentration is defined as the sum concentration of NO, NO_2, and compounds produced from them. NO_y favors NO and NO_2 near source regions and remains a semi-conserved quantity downwind as NO and NO_2 are incorporated into product molecules. The instantaneous concentrations of NO at T3 are often below detection limit (70 ppt) because of the rapid titration of this species by peroxy radicals and ozone, even as it remains an important reactant. For these reasons, NO_y concentration is used in this study as a surrogate variable for the integrated effects of NO on the chemistry that took place during transport to T3. As a reference point, background air in the boundary layer of the central Amazon basin in the wet season is characterized by 0.5 ± 0.3 ppb of NO_y (Bakwin *et al.*, 1990a).

On the afternoon affected by pollution, the NO_y concentrations measured at T3 were regularly above 1 ppb (blue line, Figure G.1a). The concentrations of O_3 and CO were also elevated (orange and gray lines). Back-trajectories from T3 show that the air came from Manaus (Figure G.5a in the Supporting Information). Under the influence of this pollution, the trap and bypass intensities for the $C_4H_7O^+$ ion followed each other closely (lower panel, Figure G.1a), without any statistically significant differences. The conclusions for this polluted afternoon are that the NO pathway dominated over the HO_2 pathway for the fate of ISOPOO radicals and that the $C_4H_7O^+$ intensity predominantly arose from MVK and MACR, without any contribution by ISOPOOH.

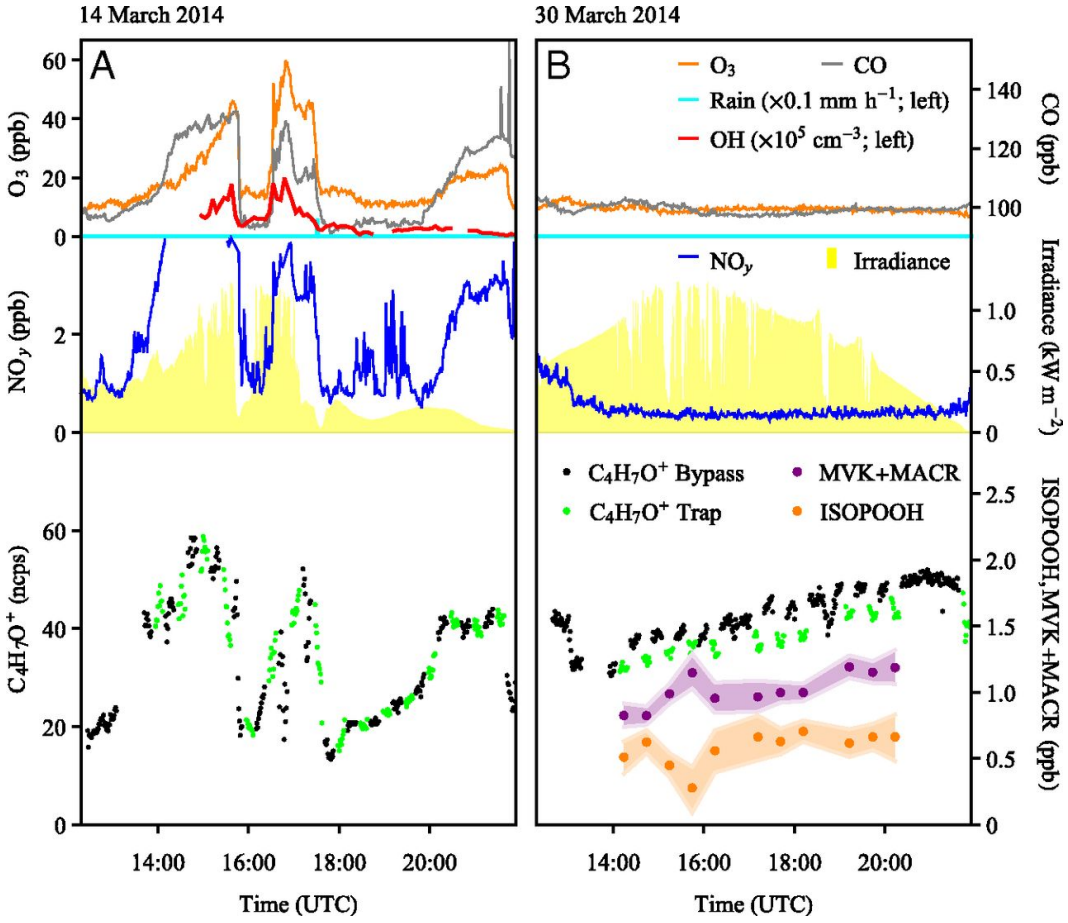

Figure G.1: Representative afternoon time series of (top) CO concentrations, O_3 concentrations, OH concentrations, and rain amount, (middle) NO_y concentrations and shortwave broadband total downwelling irradiance, and (bottom) signal intensities of $C_4H_7O^+$ ions and concentrations of MVK+MACR and ISOPOOH. Lifetimes of CO, O_3, and OH are many days, many hours, and less than one second over the tropical forest in Amazonia. (a) The left panels of this figure represent polluted conditions (14 March 2014). The weather was partly cloudy with scattered showers. (b) The right panels represent background conditions (30 March 2014). The weather was sunny, and there was no rainfall. Local noon is at 16:00 UTC. The green and black points for the $C_4H_7O^+$ ions represent intensities with and without the cold trap in place, respectively. Intensities are given in normalized counts per second (ncps) (*c.f.* Materials and Methods). For concentrations of MVK + MACR and ISOPOOH, the light shadings represent 75% confidence intervals. Measurements of OH concentrations are not available for 30 March 2014.

Fluctuations are apparent in the data sets of Figure G.1a at several time points throughout the day. The fluctuations at 16:00 arose from a 45-min shift in the local winds from polluted easterlies to background southerlies associated with a local convective cell (Figure G.6 in the Supporting Information). Atmospheric concentrations of the measured species decreased because of a combination of wet deposition and convective mixing with clean air. The precipitous drops in the data sets at 17:45 were associated with rainfall. At other times, small fluctuations reflected variations in the amounts of Manaus pollution that reached the measurement site during the course of the observations. The $C_4H_7O^+$ intensity fluctuated in correlation with the NO_y concentration (middle compared to bottom panel, Figure G.1a). MVK and MACR were produced more rapidly in air masses having higher NO_y concentrations because the atmospheric oxidation cycle was accelerated (Valin *et al.*, 2013). As an example of this acceleration, the instantaneous OH concentration increased markedly when pollution and sunlight were simultaneously present (red line, Figure G.1a).

During the afternoon of background conditions, the NO_y concentration at T3 varied little from 0.4 ppb throughout the day (blue line, Figure G.1b). Ozone and carbon monoxide had concentrations typical of background air masses in the wet season (orange and gray lines, Figure G.1b) (Martin *et al.*, 2010). Back-trajectories launched from T3 showed that the air did not intersect Manaus. The air instead came from remote regions of the Amazon basin (Figure G.5b in the Supporting Information). Under these conditions, the HO_2 pathway played an important role in the fate of ISOPOO radicals, and on this afternoon the $C_4H_7O^+$ intensity with the cold trap in place was lower than in its absence (bottom panel, Figure G.1b).

A difference signal $\Delta C_4H_7O^+$ measured with and without the trap can be defined. A nonzero $\Delta C_4H_7O^+$ is attributed to the presence of ISOPOOH (Liu *et al.*, 2013). The possibility of significant contributions by other compounds to $\Delta C_4H_7O^+$, such as pinonaldehyde and isoprene epoxydiols (IEPOX), was considered but ruled out. The difference signal $\Delta C_4H_7O^+$ was converted to ISOPOOH concentration based on calibrations using synthesized standards of ISOPOOH isomers. The MVK+MACR concentration was subsequently determined. For the afternoon of background conditions, the ISOPOOH concentration was approximately 0.6 ppb throughout the day (bottom panel, Figure G.1b). The MVK + MACR concentration increased from 0.9 to 1.2 ppb. For comparison, daytime ISOPOOH concentrations in the western United States (USA) of up to 1 ppb were reported using CF_3O^- as the ionization

agent in a chemical ionization mass spectrometer, although authentic standards were not available for instrument calibration (Worton *et al.*, 2013). A similar instrument, but with calibration, subsequently measured 0.4 ppb as the daytime ISOPOOH + IEPOX concentration in the southeastern USA (Xiong *et al.*, 2015).

Twenty-three days of daytime trap data were obtained during the measurement period, and a statistical analysis was carried out (Figure G.2). The $\Delta C_4H_7O^+$ values were grouped by NO_y concentration such that each of the six data subsets had an equal number of data points. Quartile and median values of $\Delta C_4H_7O^+$ intensity and NO_y concentration were calculated for each subset. Results are plotted in Figure G.2a. For subsets of NO_y >1 ppb, indicating the influence of the Manaus pollution plume, the medians were approximately zero (Figure G.2a), meaning that no ISOPOOH was detected for these conditions. By comparison, for subsets having NO_y <1 ppb, indicating the sampling of background air, the medians increased for decreasing NO_y concentration. The implication is that ISOPOOH concentrations increased with lower NO_y concentrations.

The central values of the ISOPOOH concentrations derived from the median values of the $\Delta C_4H_7O^+$ measurements are represented on the right axis of Figure G.2a. The bar represents 75% confidence interval around the central value of the obtained ISOPOOH concentration. Medians of $\Delta C_4H_7O^+$ (left axis) and central values of ISOPOOH concentrations (right axis) are slightly offset from one another because of nonlinearity in the ISOPOOH calibration, including a dependence on humidity. For the bin of lowest NO_y concentration, which corresponds to 0.5 ppb as a median value, the central value of the ISOPOOH concentration was 0.5 ppb. This NO_y bin is coincident with the envelope of 0.5 ± 0.3 ppb characteristic of background conditions in the wet season of Amazonia (Bakwin *et al.*, 1990a).

The concentration of ISOPOOH compared to that of MVK + MACR, represented as a ratio quantity ξ, was calculated and its relationship to NO_y was analyzed. Figure G.2b plots the central value of ξ and its 75% confidence interval (bar length) for each NO_y bin. The ratio ξ decreases for increasing NO_y concentration, approaching zero for NO_y >1 ppb. For the lowest NO_y concentration, characteristic of background conditions, the central value of ξ was 0.5 (0.4 to 0.6 with uncertainty).

From a technical perspective, ξ can indicate the possible quantitative error in the historical assumption that the $C_4H_7O^+$ signal arose exclusively from MVK and MACR. Figure G.2b shows that ξ changed with NO_y concentration for NO_y <1 ppb but was close to zero for NO_y >1 ppb. A criterion of NO_y >1 ppb is, therefore,

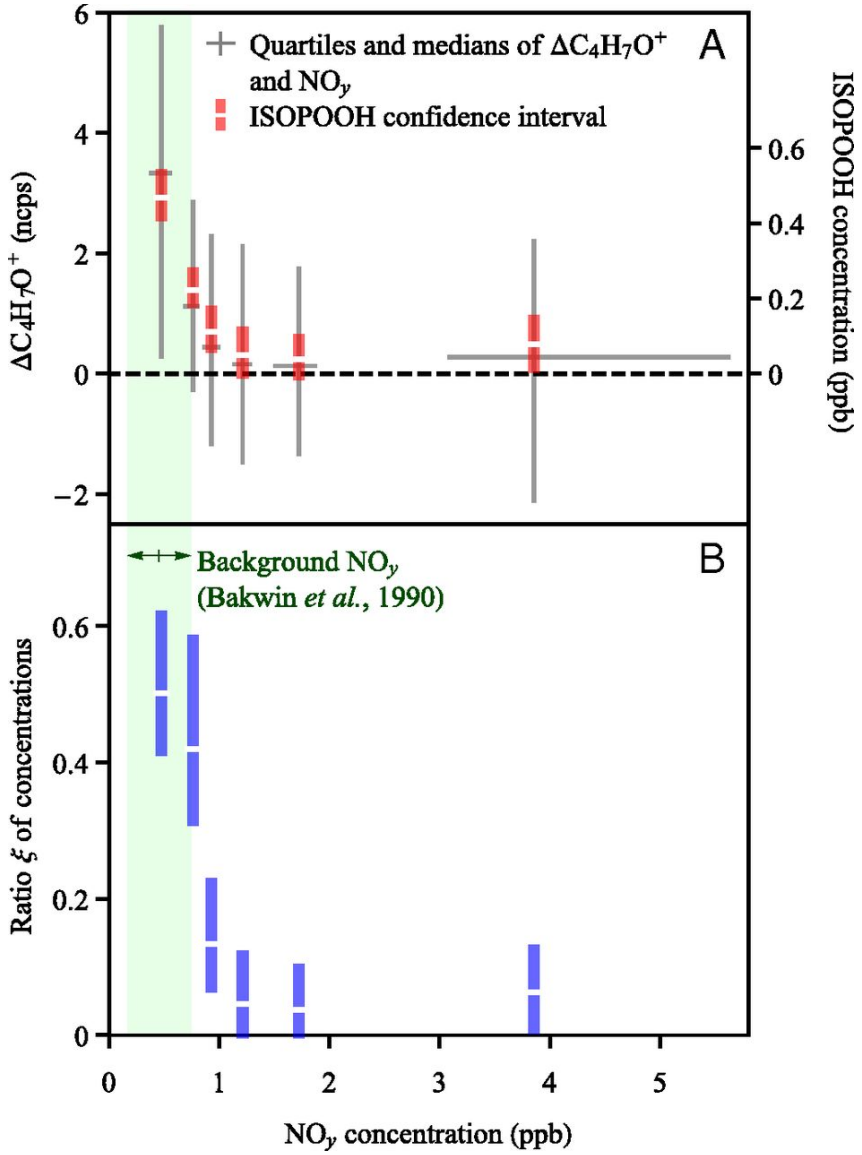

Figure G.2: Dependence of observations on NO_y concentration. (a) Quartiles and median of $\Delta C_4H_7O^+$ measurements. The panel also shows the central value of the ISOPOOH concentration corresponding to the median of the $\Delta C_4H_7O^+$ measurements. The bar represents 75% confidence interval around the central value of the obtained ISOPOOH concentration. (b) Ratio ξ of ISOPOOH concentration to that of MVK + MACR. The central value of the ratio is based on the median of the $\Delta C_4H_7O^+$ measurements. The bar represents 75% confidence interval around the central value of the obtained ratio. Light green shading represents NO_y concentrations of background air masses in the central Amazon basin in the wet season (Bakwin *et al.*, 1990a).

suggested as a simple heuristic check before attributing the $C_4H_7O^+$ signal in future studies exclusively to MVK and MACR concentrations. This heuristic applies assuming that the dependence observed in the wet season of the central Amazon basin also applies to other environments. More generally, a confidence interval of 0.4 to 0.6 for ξ under background conditions in central Amazonia suggests that the nominal MVK and MACR concentrations reported in the literature for remote locations are in need of correction for ISOPOOH contributions when PTR-MS, GC, or other methods having hot metal surfaces were employed for the measurements.

G.4.2 Modeling

The observed concentration ratio ξ can be used in an analytical model to estimate the ratio χ of the production rate of ISOPOOH to that of MVK + MACR. This ratio corresponds to $(S_1 + S_2)/(S_3 + S_4)$ for production rates S_i (molec cm^{-3} s^{-1}) of species i. Species 1 to 4 correspond to (1,2)-ISOPOOH, (4,3)-ISOPOOH, MVK, and MACR, respectively. Quantities ξ and χ differ from one another because of the different atmospheric lifetimes of species i. For initial concentrations of zero and for production rates S_i and loss coefficients k_i (s^{-1}) that are constant, the following result can be obtained to relate χ to ξ for a reaction time t (*c.f.* Supporting Information, Section G.6):

$$\chi = \frac{(0.6/k_3)(1 - e^{-k_3 t}) + (0.4/k_4)(1 - e^{-k_4 t})}{(0.6/k_1)(1 - e^{-k_1 t}) + (0.4/k_2)(1 - e^{-k_2 t})} \times \zeta \tag{G.9}$$

Composite, pseudo-first order loss coefficients k_i are given by $k_i = k_{i,OH}[\mathrm{OH}] + k_{i,en} + k_{i,d}$ for bimolecular reactions with OH, atmospheric entrainment (en), and surface deposition (d). On-site measurements of OH concentrations by chemical ionization mass spectrometry (Kim *et al.*, 2013), recent advances in the understanding of the deposition processes of ISOPOOH (Nguyen *et al.*, 2015a), and an approximate description of the boundary layer dynamics over the Amazonia (Vilà-Guerau de Arellano *et al.*, 2009) allow reasonable estimates of the loss coefficents k_i (Table G.1).

The model derivation relies on the accuracy of two approximations. (1) Species concentrations are taken as zero at sunrise, which then represents time zero. This approximation is well supported by measured concentrations, which at sunrise were <5% of the maximum measured daily concentrations (Figure G.7 in the Supporting Information). (2) Production rates S_i and loss coefficients k_i are approximated as constant throughout the day, thereby corresponding to average or effective daily

values. The sensitivity of the results to this approximation is examined in Section G.6, and the approximation is found to be acceptable.

Equation G.9 shows that the production ratio χ is proportional to the concentration ratio ξ for any fixed reaction time. For the actual values of k_i, the proportionality coefficient was greater than unity for any reaction time t because of the longer lifetimes of MVK and MACR compared to those of (1,2)-ISOPOOH and (4,3)-ISOPOOH. The implication is $\chi > \xi$. Plots of Equation G.9 in Figure G.3 show the dependence of χ on ξ for different reaction times ranging from 0 to 10 h. Figure G.3 is drawn for an average daytime OH concentration of 5×10^5 cm^{-3} for background conditions (Kim *et al.*, 2013). The proportionality coefficient relating χ to ξ increases for greater reaction times. For an assumed effective reaction time of 5 h representing daybreak to midafternoon (green line, Figure G.3), the slope is 1.5. The confidence interval of 0.4 to 0.6 for ξ under background conditions (Figure G.2b) implies a range of 0.6 to 0.9 for χ. One test of the accuracy of the effective photochemical reaction time (*i.e.*, 5×10^5 OH cm^{-3} for 5 h) is to compare the predicted and measured ratios given by the total concentration of reaction products (*i.e.*, sum of MVK, MACR, and ISOPOOH) divided by the isoprene concentration. The predicted ratio was in agreement with the median of the measured ratios for background conditions, supporting the appropriateness of the effective reaction time. As an aside, the observed ratio shifted from 0.4 under background conditions to around 2 under polluted conditions for the data of Figure G.1 (and Figure G.6 in the Supporting Information), as is consistent with the accelerated oxidation cycle in the pollution plume.

The preceding product-focused methodology to determine χ was complemented by a source-based analysis. Reactions of ISOPOO serve as the sources of ISOPOOH and MVK + MACR. In a source-based analysis, the production ratio χ is expressed as follows:

$$\chi = \frac{Y_{ISOPOOH,HO_2} f_{HO_2}}{\sum\limits_{j \in (HO_2, NO, RO_2, ISOM)} Y_{MVK+MACR,j} \times f_j} \tag{G.10}$$

The fractional yield of ISOPOOH in the reaction of ISOPOO with HO_2 is represented by the term $Y_{ISOPOOH,HO_2}$, which has an estimated value of 0.90 (St. Clair *et al.*, 2015). By comparison, ISOPOOH is believed to be produced neither from the reactions of ISOPOO with NO and RO_2 nor by isomerization. The fractional yields of MVK + MACR in the reactions of ISOPOO with NO, HO_2, RO_2, and isomerization are represented by the terms $Y_{MVK+MACR,HO_2}$, $Y_{MVK+MACR,NO}$, $Y_{MVK+MACR,RO_2}$, and

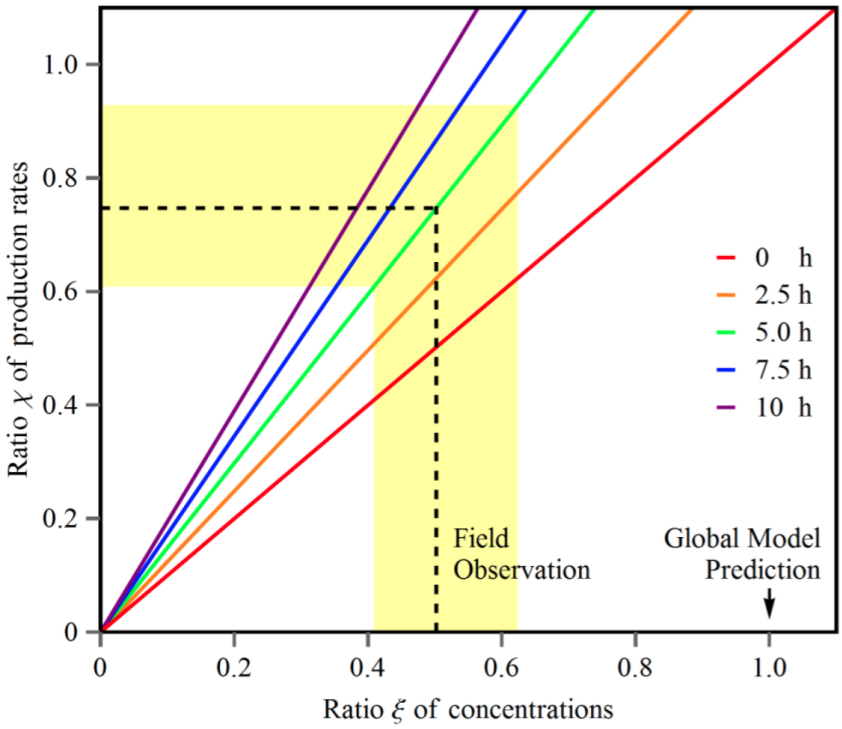

Figure G.3: Modeled dependence of the production ratio χ on the measured concentration ratio ξ for different reaction times (Equation G.9). The dashed line projects the central value of ξ measured during background conditions onto the inferred production ratio χ when assuming 5 h of reaction time. The yellow region shows the same when taking into account the confidence interval in ξ. Figure is drawn for 5×10^5 OH cm^{-3}, corresponding to daytime background conditions. The black arrow points to daytime ξ value simulated using a global chemical transport model for this region in a typical wet season.

$Y_{MVK+MACR,ISOM}$, respectively. The best-estimate values are 0.06, 0.71, 0.75, and 0.10, respectively (Table G.2 and references therein).

Terms f_{HO_2}, f_{NO}, f_{RO_2}, and f_{ISOM} of Equation G.10 are the fractional contributions of reactions with HO_2, NO, RO_2, and isomerization to ISOPOO loss. These fractions sum to unity. The fractions were obtained for NO concentrations ranging from background to polluted conditions using a box model based on the Master Chemical Mechanism (MCM; version 3.3.1) and supplemented by recent experimental results (Jenkin *et al.*, 2015; Liu *et al.*, 2013; St. Clair *et al.*, 2015). The model is further described in Materials and Methods. For straightforwardness, the OH concentration was held constant, although in reality it increased under polluted conditions (Figure G.1a). Figure G.4a shows the simulated dependence of f_{HO_2}, f_{NO}, f_{RO_2}, and f_{ISOM} on NO concentration. Under polluted conditions of greater

	$Y_{MVK+MACR}$	$Y_{ISOPOOH}$
HO_2 Pathway	6.3%[a]	90%[d]
NO Pathway	71%[a]	0
RO_2 Pathway	75%[b]	0
ISOM Pathway	10%[c]	0

Table G.2: Reported production yields of MVK + MACR and ISOPOOH *via* individual pathways. For measurement-based values, the reference is included. [(a)]From Liu *et al.* (2013). [(b)]Although the MVK and MACR yields were reported for several "low-NO" experiments, the contribution of RO_2 pathway is not clear. The value adopted here is based on MCM v3.1.1 Jenkin *et al.* (2015). [(b)]Theoretical prediction by Peeters *et al.* (2014). There is no direct laboratory evidence that MVK and MACR can be produced *via* the isomerization pathway. [(d)]From St. Clair *et al.* (2015).

than several hundred ppt of NO, ISOPOO loss is dominated by reaction with NO (*e.g.*, 90% for 400 ppt NO). Under less polluted conditions, the other three reaction pathways become important.

Figure G.4b shows the simulated dependence of production ratio χ on NO concentration and allows an inference of an effective NO concentration associated with the confidence interval 0.6 to 0.9 for χ. As a point of reference, background NO mixing ratios of 15 to 60 ppt (Torres and Buchan, 1988), 10 to 30 ppt (Levine *et al.*, 2015), 20 to 80 ppt (Bakwin *et al.*, 1990a), and 35 ppt (mean value of GOAmazon 2014/5 aircraft measurement; Figure G.8 in the Supporting Information) have been measured for the central region of the Amazon basin for studies from 1985 through 2014. These ranges are represented by the brown arrows in Figure G.4b. According to Figure G.4b, the effective NO concentration associated with the confidence interval of χ ranged from 16 to 30 ppt (yellow shading, Figure G.4). This effective value represents the net chemistry across the history of the air parcel. The good agreement between the effective NO concentration inferred in this way and the range of measured ambient concentrations for background conditions lends confidence to the accuracy of the overall model framework of the present study. Across the range of effective NO concentrations the following fractional contributions to ISOPOO reaction are obtained: $0.31 < f_{HO_2} < 0.39$, $0.27 < f_{NO} < 0.40$, $0.03 < f_{RO_2} < 0.05$, and $0.25 < f_{ISOM} < 0.30$ (yellow shading, Figure G.4a). Notably, compared with the wide range of NO concentrations reported (gray shading, Figure G.4a), the effective NO concentrations based on our observation provide a tighter constraint to ISOPOO reaction under background conditions. Specifically, the confidence interval of the

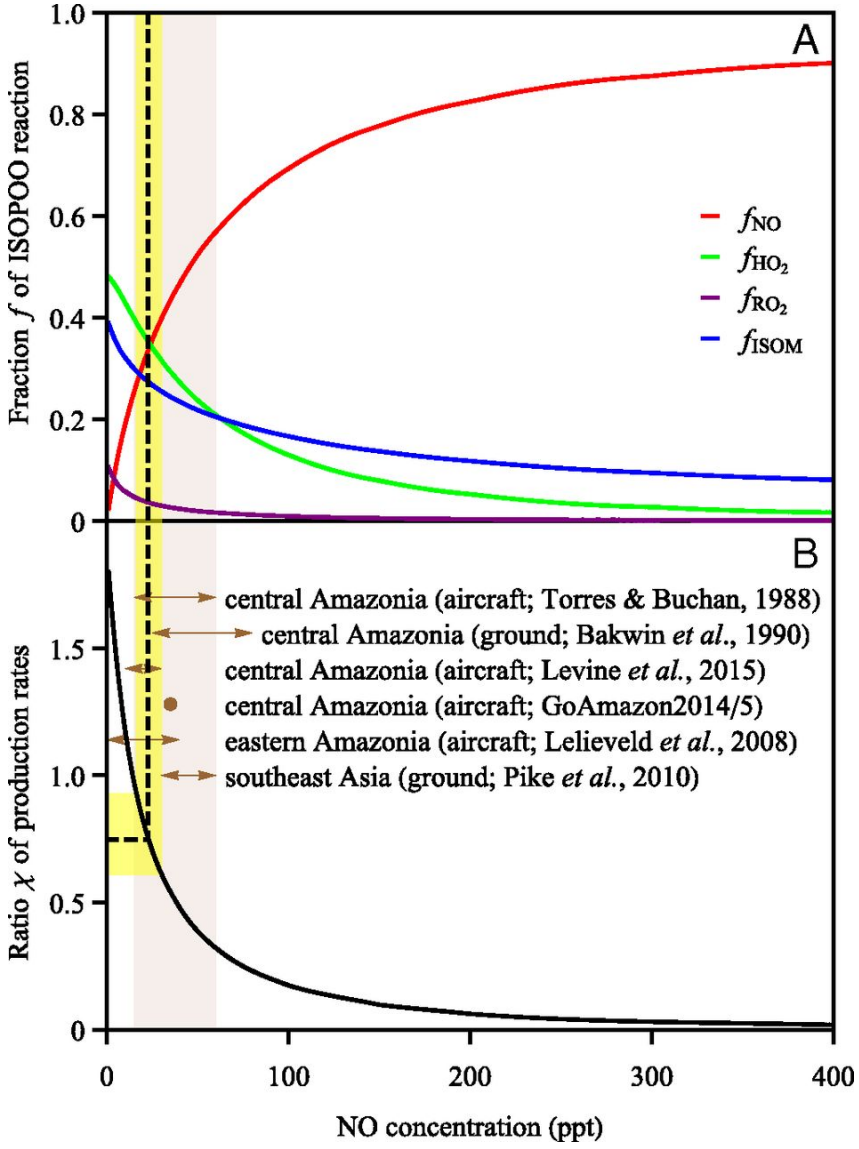

Figure G.4: Modeled dependence on NO concentration of (a) fractional contributions f_{HO_2}, f_{NO}, f_{RO_2}, and f_{ISOM} to ISOPOO reactive loss and (b) the ratio χ of the production rate of ISOPOOH to that of MVK + MACR. The brown arrows represent the reported ranges of NO concentration for central Amazonia, eastern Amazonia, and southeast Asia under background conditions (Bakwin *et al.*, 1990a; Lelieveld *et al.*, 2008; Levine *et al.*, 2015; Pöschl *et al.*, 2010; Torres and Buchan, 1988). The gray region represents NO concentrations reported by Torres and Buchan (1988) for measurements in 1985. The dashed line projects the central value of χ for background conditions onto the effective NO concentration, illustrating the possible relative contributions of different reaction pathways of ISOPOO. The yellow region shows the same as the dashed line but for confidence interval in χ.

	MCM 3.3.1 + updates[a,b]	MCM 3.3.1	MCM 3.2 + updates[b,c]	MCM 3.2
NO (ppt)	16-30	19-33	19-36	22-40
f_{HO_2}	0.31-0.39	0.29-0.36	0.39-0.51	0.37-0.48
f_{NO}	0.27-0.40	0.30-0.42	0.40-0.55	0.44-0.58
f_{RO_2}	0.03-0.05	0.03-0.04	0.05-0.09	0.05-0.08
f_{ISOM}	0.25-0.30	0.26-0.30	0	0
f_{HO_2}:f_{NO}	0.8-1.4	0.7-1.2	0.7-1.3	0.6-1.1

Table G.3: Simulation results using a box model with different chemical mechanisms. Inferred range of NO concentrations and fractional contribution to ISOPOO reaction from observation-constraint χ range of 0.61-0.93 using four sets of chemical mechanisms. [(a)]Mechanism used in the main text (Figure G.4). [(b)]Updates include measured production yields of MVK and MACR *via* the HO_2 pathway (Liu *et al.*, 2013) and measured reaction rate coefficients of (1,2)-ISOPOOH and (4,3)-ISOPOOH with OH (St. Clair *et al.*, 2015). [(c)]Compared with MCM 3.3.1, MCM 3.2 does not include isomerization pathway of ISOPOO reaction. The simulated dependence of χ and f on NO using MCM 3.2 + updates is presented in Figure G.17 in the Supporting Information.

f_{HO_2}-to-f_{NO} ratio spans 0.8 to 1.4. This result is robust with respect to the inclusion or not of the isomerization pathway (Table G.3). An important point to emphasize is that the modeling analysis leading to this ratio for background conditions is ultimately constrained by the measured concentrations of ISOPOOH, MVK + MACR, and NO_y.

G.5 Atmospheric Implications

The ranges in f_{HO_2}, f_{NO}, f_{RO_2}, and f_{ISOM} for the yellow region of Figure G.4a imply that the HO_2 pathway accounted for 31% to 39% of the reactive loss of ISOPOO under the "low-NO" conditions of the wet season in the central Amazon basin. Conversely, reactions with NO under "low NO" conditions accounted for 27% to 40% of ISOPOO loss. For comparison to these values, a state-of-the-art chemical transport model (CTM) predicted that the HO_2 pathway contributed 59% of the reactive loss of ISOPOO radicals for the grid box of $4^\circ \times 5^\circ$ encompassing the measurement site and that the contribution of the NO pathway to reactive loss was 14% for a typical wet season (Table G.4). An overestimate in models of the importance of the HO_2 pathway for ISOPOO reactive loss has important implications for predicted concentrations of organic particulate matter (Paulot *et al.*, 2009b) and consequent connections among flora, oxidative capacity, aerosol particles, cloud condensation nuclei, clouds, and rainfall over this vast tropical forest (Pöschl *et al.*,

Model settings Soil NO_x emission[a]	default	default × 10	default × 30
Simulation results			
Above-canopy NO_x emissions[b]	2.0×10^8	2.0×10^9	6.0×10^9
Daytime NO concentration[c]	0.0075	0.010	0.015
Daytime NO_y concentration[c]	0.11	0.18	0.36
Daytime ISOPOOH concentration[c]	0.65	0.62	0.52
Daytime MVK+MACR concentration[c]	0.62	0.67	0.68
Concentration ratio ξ	1.0	0.93	0.76
f_{HO_2}	0.59	0.55	0.49
f_{NO}	0.14	0.22	0.34
f_{RO_2}	0.06	0.06	0.05
f_{ISOM}	0.21	0.16	0.13
f_{HO_2}:f_{NO}	4.3	2.5	1.4

Table G.4: Simulation results using GEOS-Chem for central Amazonia. Simulation results are for the grid square (0° - 4° S, 57.5 ° - 62.5° W) where the measurement site is located during February and March in 2012. [(a)]Justification of increasing soil NO_x emission by a factor of 10 and 30 is provided in Section G.3.4.5. [(b)]In units of (molec m^{-2} s^{-1}). [c]In units of ppb.

2010). An underestimate of the NO pathway in central Amazonia can have profound impacts on the predicted concentrations of isoprene nitrates transported to adjacent regions, influencing NO_x concentrations and photochemistry in those regions (Ito *et al.*, 2007). In addition, given the importance of this geographical region in the global isoprene budget (Guenther *et al.*, 2012), previous estimates of the fraction of ISOPOO reacting *via* the HO_2 pathway on a global basis by CTMs might also be too high (Crounse *et al.*, 2011). Future studies are needed to better constrain the fraction of ISOPOO reactive loss *via* the HO_2 pathway in other locations having high isoprene concentrations and low anthropogenic NO_x emissions.

One possible reason, among others, for the gap between observations and the CTM model predictions is an underprediction of NO concentrations and hence an underestimate of the importance of the NO reaction pathway in the model. The modeled daytime average concentration of NO was 0.008 ppb for the grid box in which the measurement site was located. This value is much lower than the range of NO concentrations measured in central Amazonia (Figure G.4). Furthermore, the modeled daytime concentration of NO_y was 0.1 ppb, which is 80% lower than the observed background NO_y concentrations in central Amazonia (Bakwin *et al.*, 1990a). Underpredicted NO and NO_y concentrations in the model might in turn be related to underestimated NO emissions from tropical forests. Flux measurements have shown that soils have high emissions of NO_x in the forested regions of both

central Amazonia (Bakwin *et al.*, 1990b; Garcia-Montiel *et al.*, 2001; Kaplan *et al.*, 1988; Verchot *et al.*, 1999) and southeast Asia (Hewitt *et al.*, 2009). The above-soil NO_x emission modeled in the CTM for the wet season of central Amazonia was ten times lower than the observations reported in the literature. Ganzeveld *et al.* (2002) additionally suggest that CTMs might underestimate the fraction of soil-emitted NO_x that survives transport through tropical forest layers and is ultimately emitted to the overlying atmosphere. Herein, additional model runs were performed as a sensitivity study to establish that increasing NO_x emissions above canopy by a factor of 30 can bring the modeled ratio ξ closer to its observed range. Any change made to model emissions on this basis must, however, also assess possible perturbations of other modeled quantities, such as ozone or hydroxyl radical concentrations, compared to measured values (Jacob and Wofsy, 1988; Lelieveld *et al.*, 2008).

In outlook, current trends in human activities, including ongoing land use changes for agricultural activities as well as growing urbanization, are associated with the continual reduction of forest coverage in the Amazon basin (Davidson *et al.*, 2012). These trends in turn lead to increased demand for electricity and transport, which with current technologies increases NO_x emissions (Hewitt *et al.*, 2009). With respect to the atmospheric chemistry of the region, the concentration ratio ξ and its complement of the production ratio χ serve as surrogates of the qualitative characteristics of isoprene chemistry, with associated effects that are of concern to humans, such as production of ozone and organic particulate matter and changes in visibility and rainfall, among others (Chameides *et al.*, 1988; Pike *et al.*, 2010). Under background conditions, expressed as 75% confidence intervals, the ratio of the fractional contribution by HO_2 to the reactive loss of ISOPOO to that by NO ranges from 0.8 to 1.4, the ratio of the production rate χ of ISOPOOH to that of MVK + MACR ranges from 0.6 to 0.9, and the ratio ξ of the concentration of ISOPOOH to that of MVK + MACR ranges from 0.4 to 0.6. In this regard, the data (Figure G.2; ξ) and the model (Figure G.4; χ) show that the oxidant cycle is highly sensitive to changes from background to polluted conditions. The implication is that small increases in NO concentration above the background level can lead to a large change in the aforementioned endpoints of air quality and climate. In particular, the abrupt drop in ISOPOOH concentration associated with pollution speaks to the extent of human-induced changes in photochemical cycles over the rain forest, both at present during times of widespread biomass burning in the dry season and possibly in the future during all seasons as a consequence of economic development and increasing pollution throughout the Amazon basin.

G.6 Supporting Information

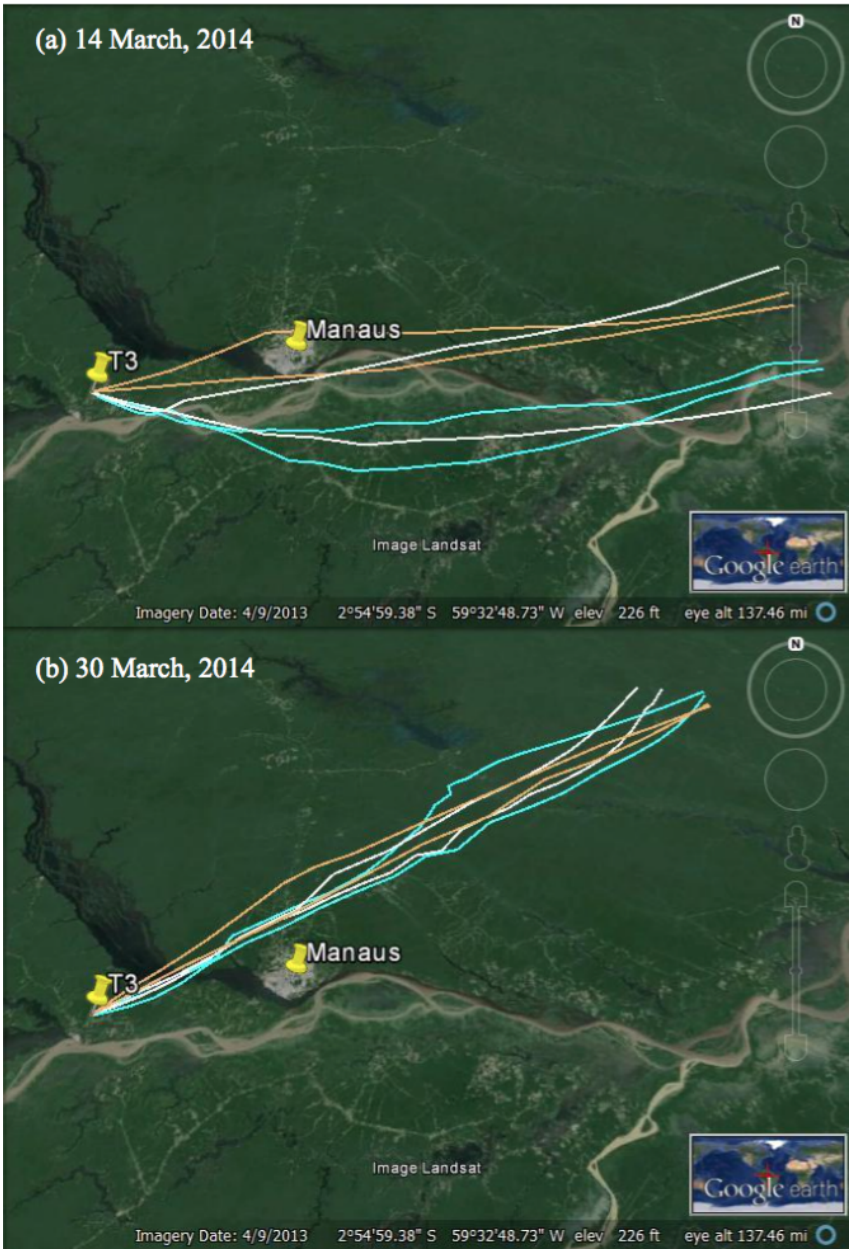

Figure G.5: Back-trajectories launched at T3 on (a) 14 March 2014 and (b) 30 March 2014. The back-trajectories start at 12 and 18 h (UTC). Colors differentiate back-trajectories launched at height 660 m (orange), 270 m (white) and 90 m (cyan).

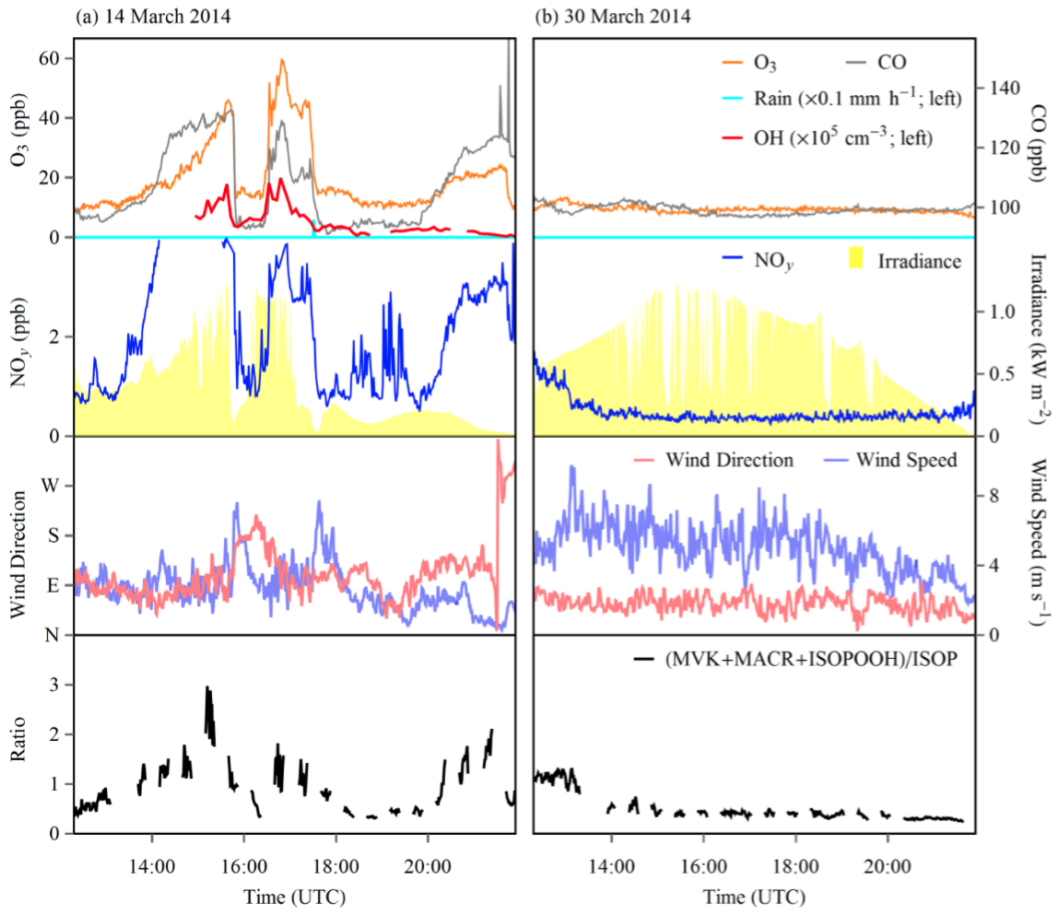

Figure G.6: Representative afternoon time series (top to bottom) of (1) CO concentrations, O_3 concentrations, OH concentrations, and rain amount, (2) NO_y concentrations and shortwave broadband total downwelling irradiance, (3) wind direction and wind speed, and (4) ratio of total concentration of MVK, MACR and ISOPOOH to isoprene concentration. (a) The left panels of this figure represent polluted conditions (14 March 2014). (b) The right panels represent background conditions (30 March 2014). Local noon is at 16:00 UTC. This figure is a supplement of Figure G.1.

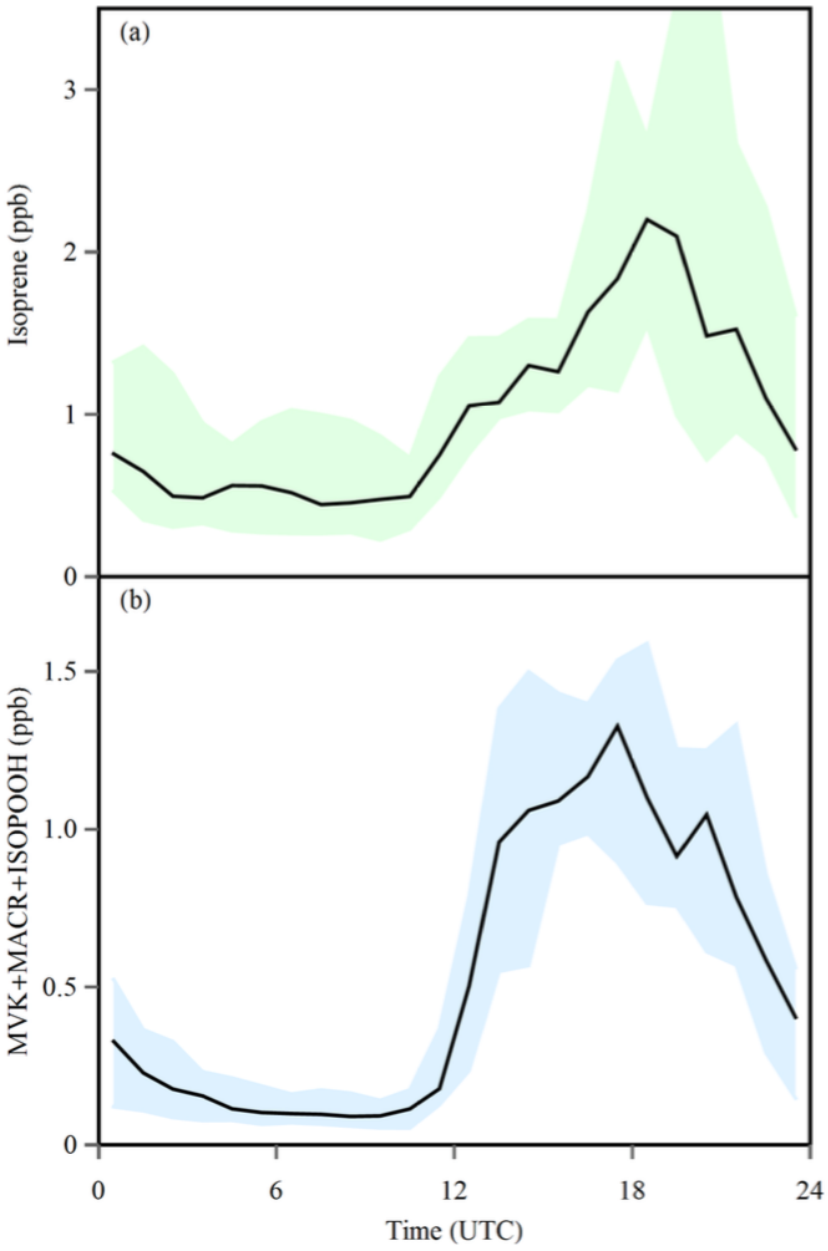

Figure G.7: Diel variation for trap-measurement days of (a) isoprene concentration and (b) the total concentration of MVK, MACR, and ISOPOOH. The solid line and shaded regions respectively represent the median and interquartile ranges of each hour of the day.

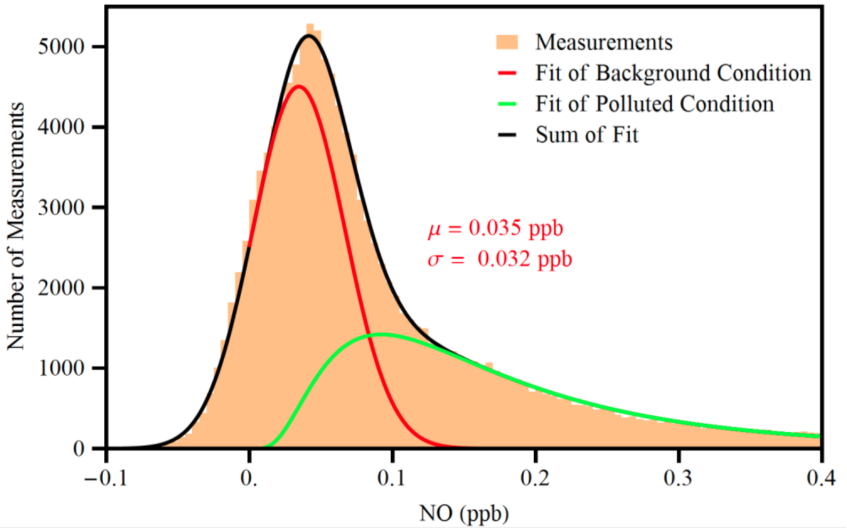

Figure G.8: Histogram of NO concentrations measured by the G1 aircraft in the environs of Manaus during GOAmazon 2014/5. Data are collected at flight heights of 200 to 1000 m. The measured histogram can be fitted as the sum of the histograms under background and polluted conditions, which follow normal and lognormal distribution, respectively. The fitted mean and standard deviation of the normal distribution for background condition is noted in the figure. The large variance of measured NO concentration under background condition (and also the existence of negative values) is largely due to large variation of instrumental background level. The mean value of the normal distribution can represent mean background NO concentration, but its standard deviation can be much larger than the variation of NO concentration.

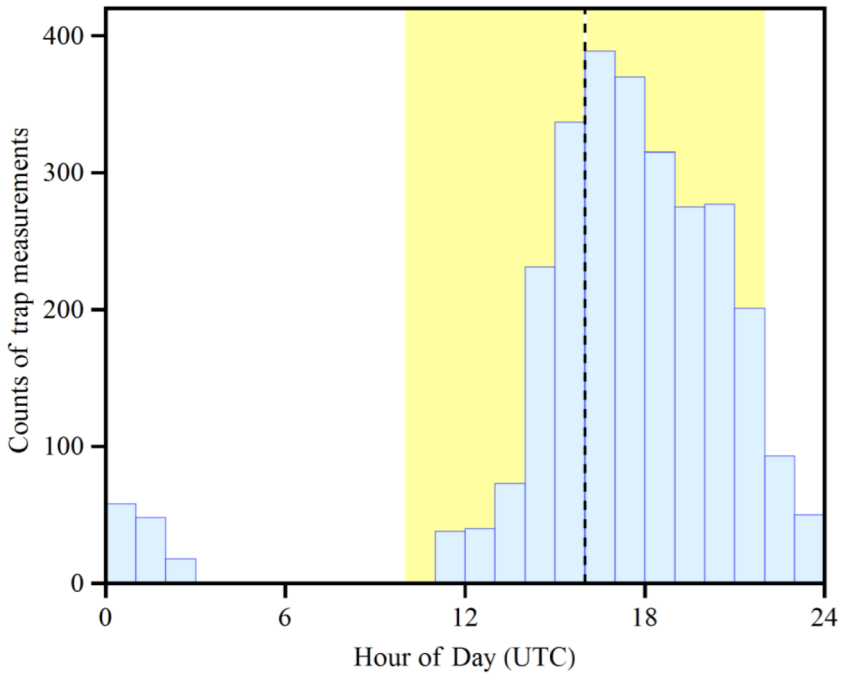

Figure G.9: Histogram of trap measurements in UTC. The yellow region represents local daytime, and the dashed line represents local noon.

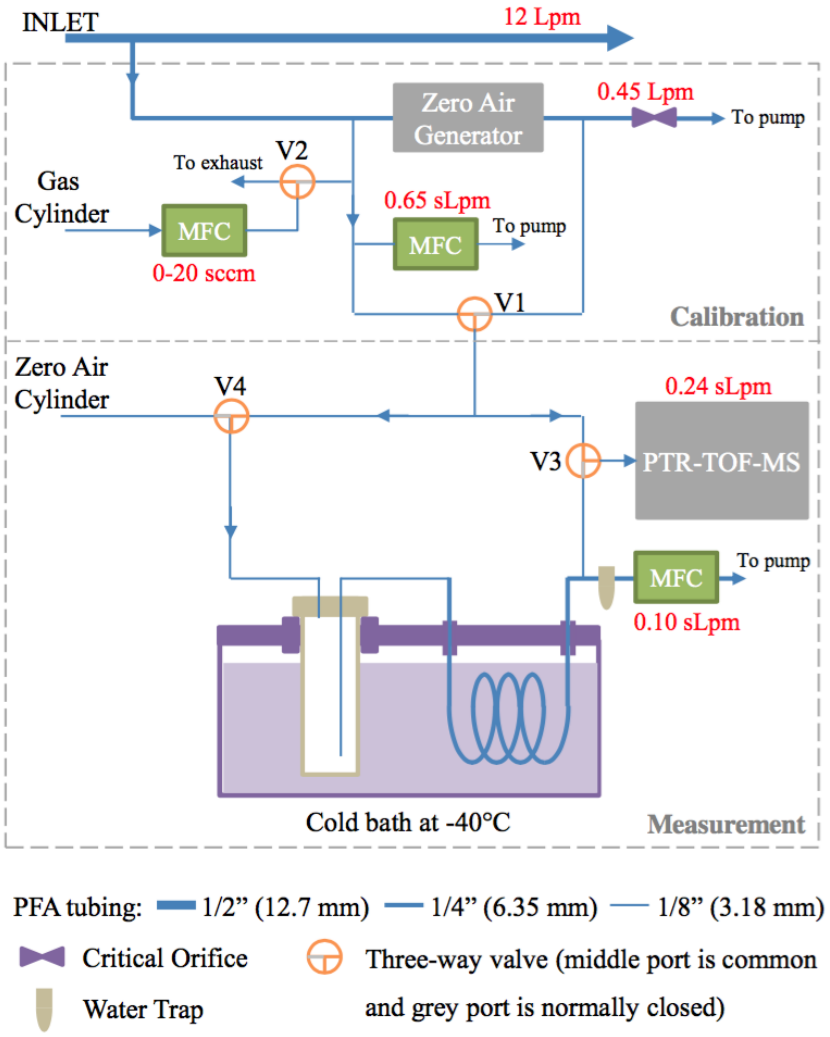

Figure G.10: Schematic diagram of the gas inlet system for the PTR-ToF-MS. The top and bottom sections represent calibration and measurement set-ups, respectively.

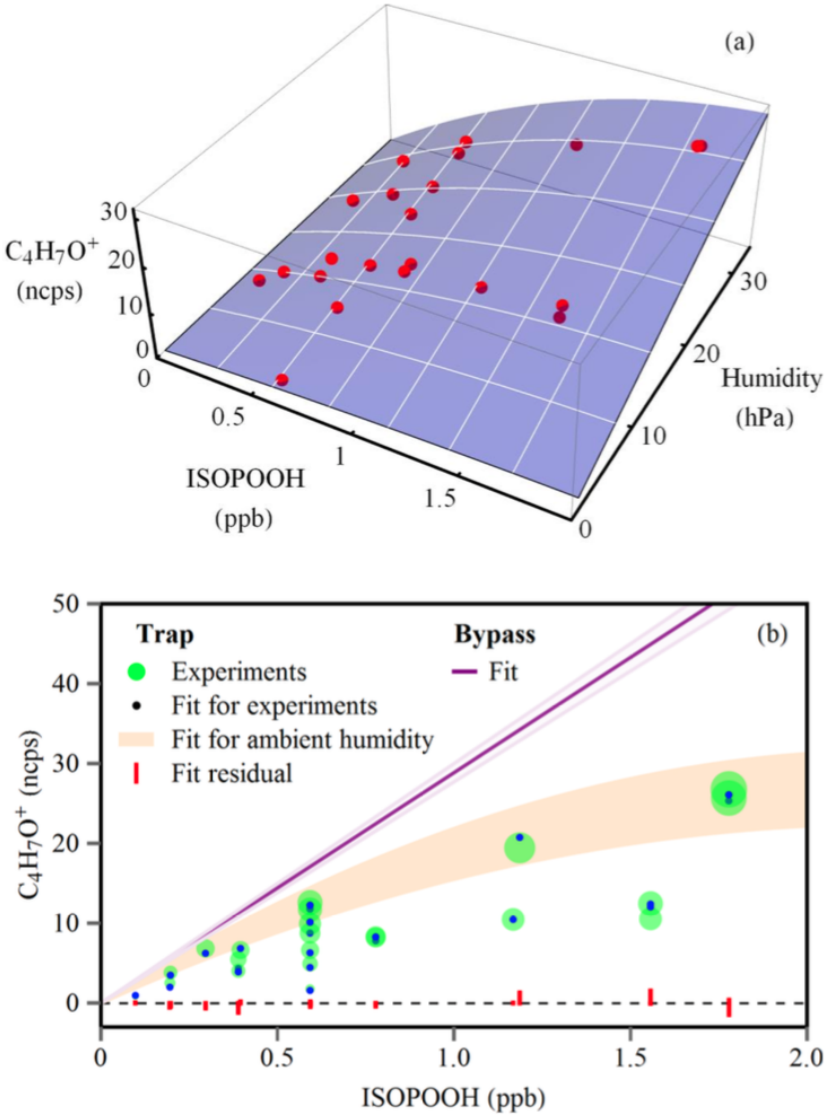

Figure G.11: Calibration curve. (a) Comparison of measured and fitted data in a three-dimensional plot. (b) Comparison and fitting residuals. Point size is scaled by the absolute humidity. The signal intensities of the $C_4H_7O^+$ ion shown in the figures are background-corrected.

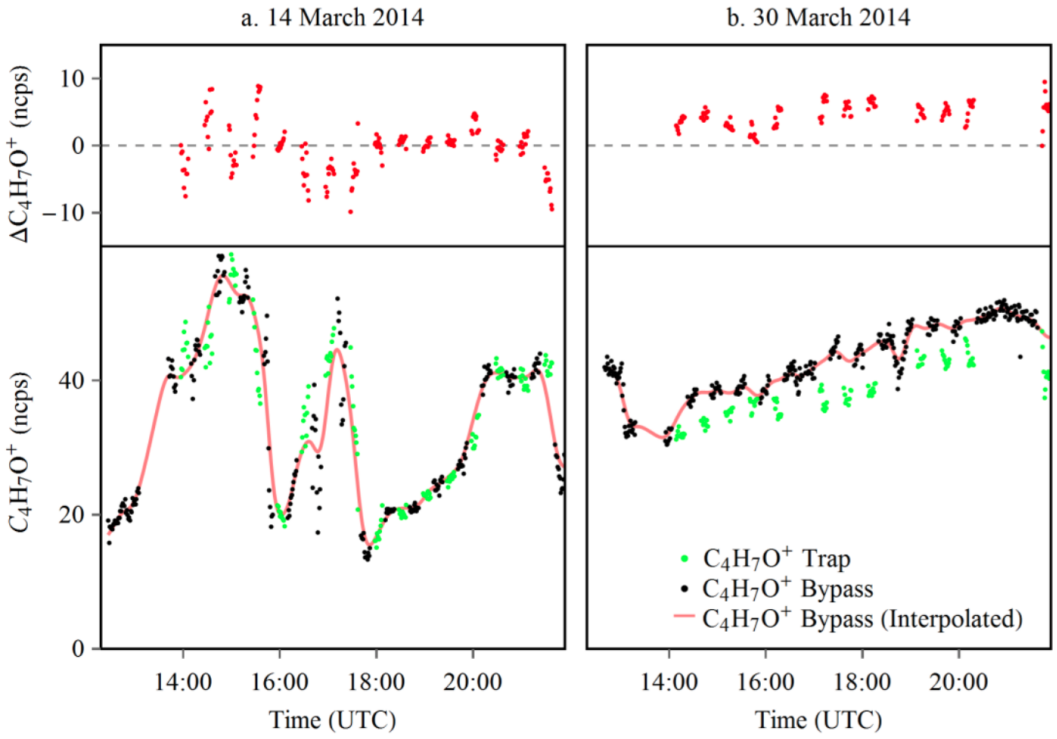

Figure G.12: Example time series of (top) $\Delta C_4H_7O^+$ and (btm) $C_4H_7O^+$ signal on (a) 14 March 2014 and (b) 30 March 2014, representing polluted and background conditions, respectively. The black and green points in the bottom panels show the $C_4H_7O^+$ signal intensities measured through the cold trap and along the bypass, respectively. Red lines show the interpolated intensities for the $C_4H_7O^+$ ions measured with the bypass in place.

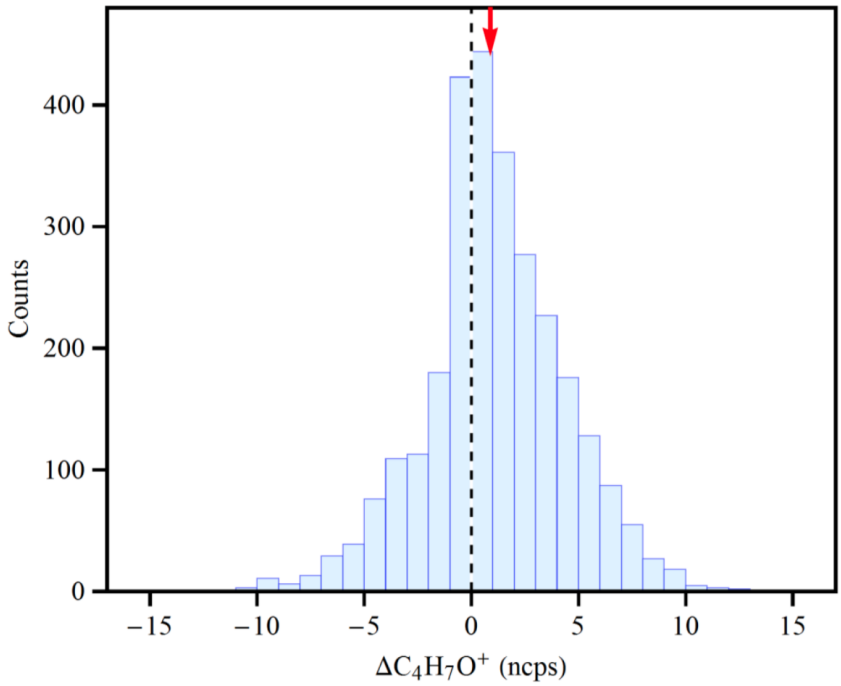

Figure G.13: Histogram of intensity difference $\Delta C_4H_7O^+$, defined as the intensity of the $C_4H_7O^+$ ion signal recorded through compared to in-bypass of the cold trap. The red arrow shows the mean value of $\Delta C_4H_7O^+$.

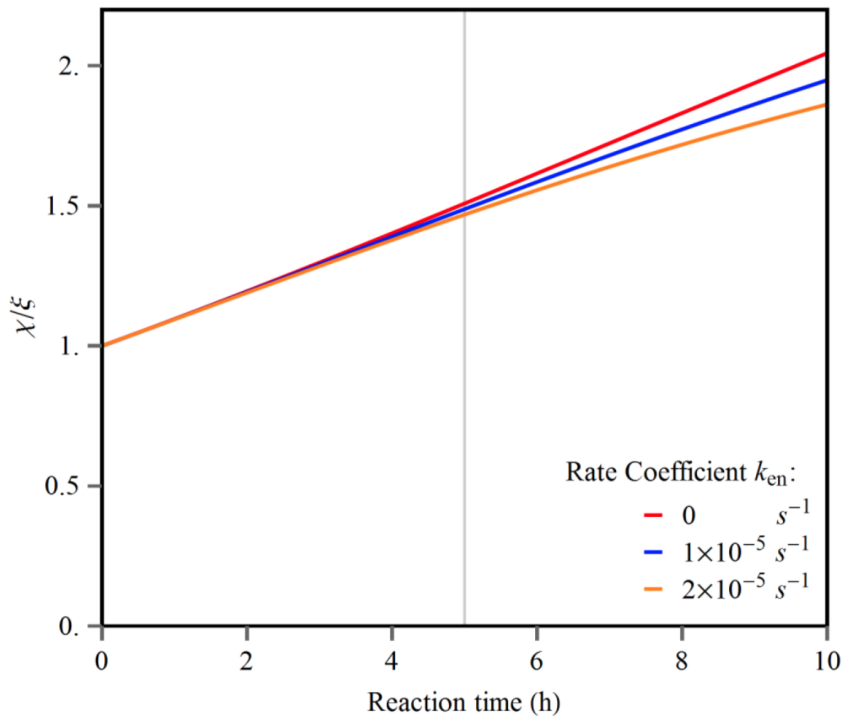

Figure G.14: The proportionality coefficient, represented by χ/ξ, as a function of reaction time. The loss rate coefficient k_{en} due to entrainment is set to 0, 1, or 2×10^5 s^{-1}.

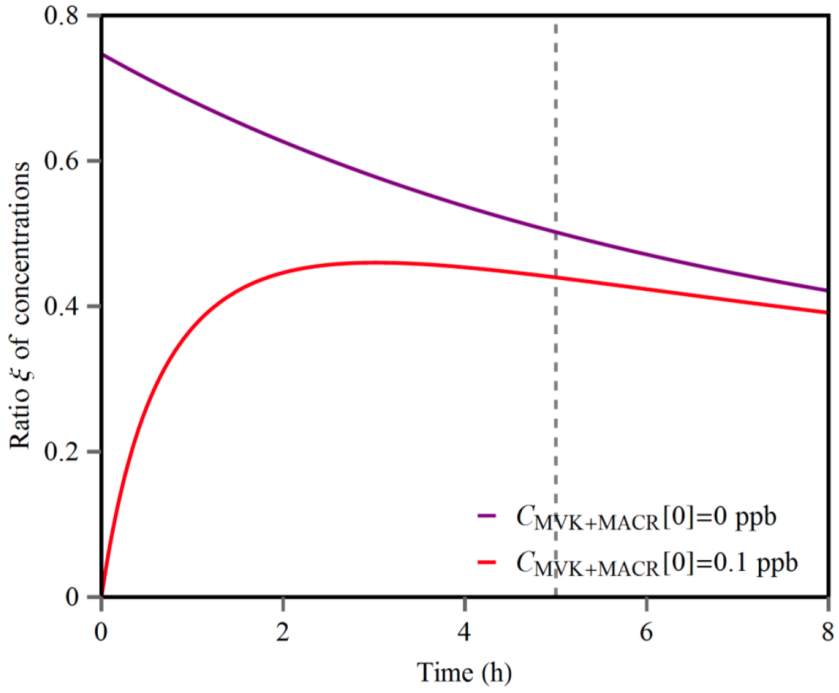

Figure G.15: Ratio ξ of concentrations as a function of reaction time for initial concentration of MVK+MACR of 0 and 0.1 ppb. The production ratio χ was set to 0.75, which is the central value inferred from observations for background condition assuming zero initial concentration of MVK and MACR (Figure G.3). The dashed line shows a reaction time of 5 h. The value of ξ is calculated using Equation G.7 for zero initial concentration and a similar equation for non-zero initial concentration.

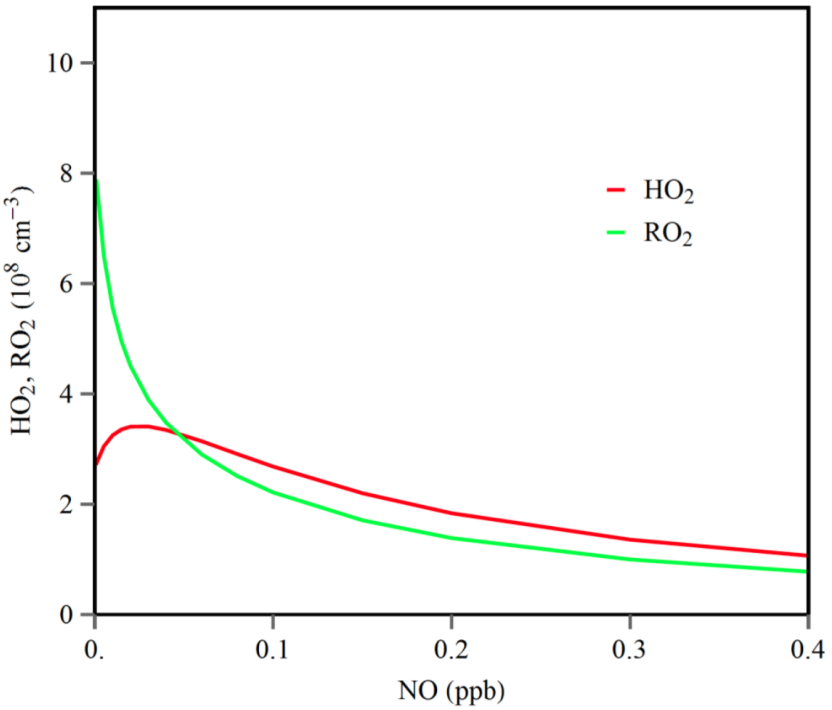

Figure G.16: Simulated steady-state HO_2 and RO_2 concentrations as a function of NO using the MCM 3.3.1 supplemented with recent experimental results at an OH concentration of 5×10^5 cm^{-3}.

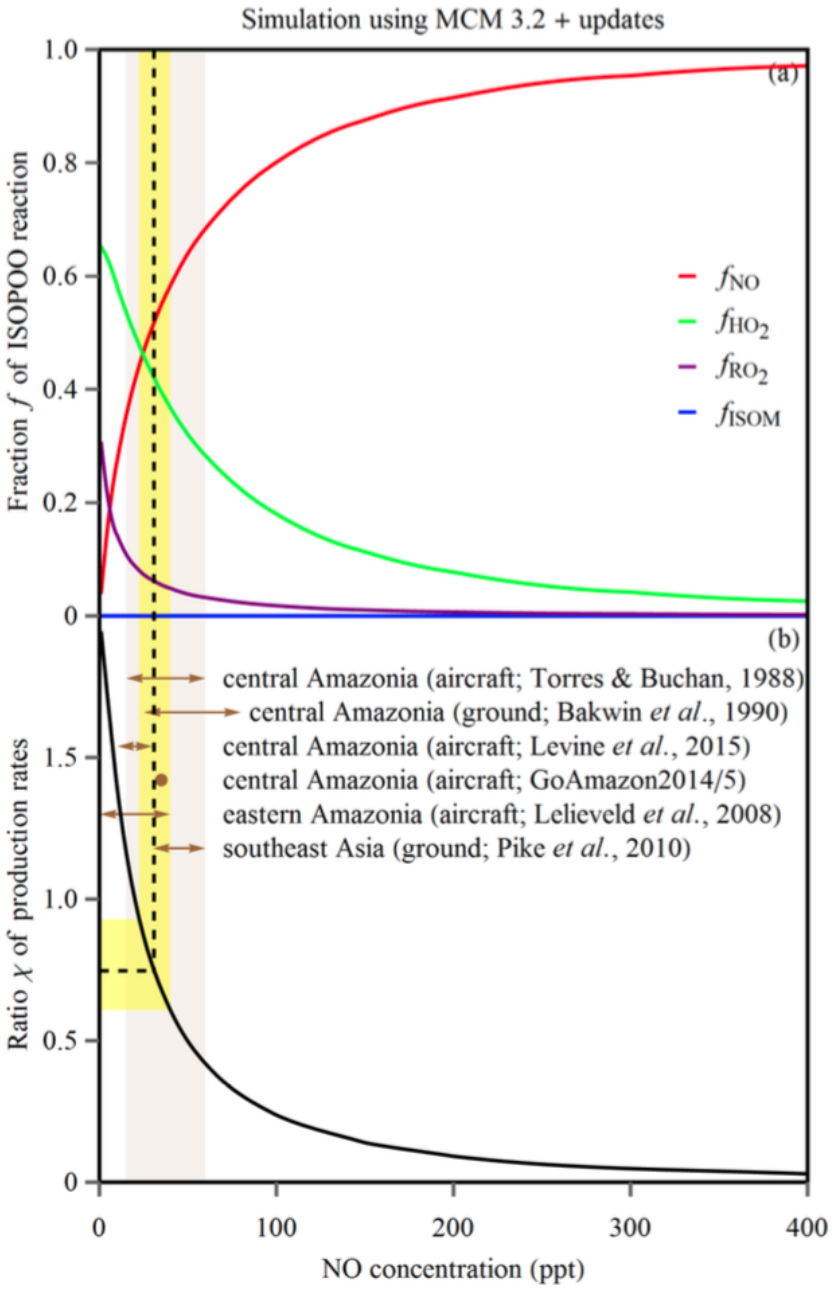

Figure G.17: Modeled dependence on NO concentration of (a) the fractional contributions f_{HO_2}, f_{NO}, f_{RO_2}, and f_{ISOM} to ISOPOO reactive loss and (b) the ratio χ of ISOPOOH to MVK + MACR production rates using MCM 3.2 supplemented with recent experimental results. By comparison, Figure G.4 presents the dependence simulated using MCM 3.3.1 supplemented with recent experimental results (Table G.3).

Appendix H

CONTRASTING CLOUD COMPOSITION BETWEEN COUPLED AND DECOUPLED MARINE BOUNDARY LAYER CLOUDS

Wang, Z., M. Mora Ramirez, H. Dadashazar, A. B. MacDonald, E. Crosbie, K. H. Bates, M. M. Coggon, J. S. Craven, P. Lynch, J. R. Campbell, M. Azadi Aghdam, R. K. Woods, H. Jonsson, R. C. Flagan, J. H. Seinfeld, and A. Sorooshian (2016). "Contrasting cloud composition between coupled and decoupled marine boundary layer clouds". In: *J. Geophys. Res. - Atmos.* 121.19, pp. 11679–11691. DOI: 10.1002/2016JD025695.

Abstract

Marine stratocumulus clouds often become decoupled from the vertical layer immediately above the ocean surface. This study contrasts cloud chemical composition between coupled and decoupled marine stratocumulus clouds for dissolved nonwater substances. Cloud water and droplet residual particle composition were measured in clouds off the California coast during three airborne experiments in July–August of separate years (Eastern Pacific Emitted Aerosol Cloud Experiment 2011, Nucleation in California Experiment 2013, and Biological and Oceanic Atmospheric Study 2015). Decoupled clouds exhibited significantly lower air-equivalent mass concentrations in both cloud water and droplet residual particles, consistent with reduced cloud droplet number concentration and subcloud aerosol(D_p > 100 nm) number concentration, owing to detachment from surface sources. Nonrefractory submicrometer aerosol measurements show that coupled clouds exhibit higher sulfate mass fractions in droplet residual particles, owing to more abundant precursor emissions from the ocean and ships. Consequently, decoupled clouds exhibited higher mass fractions of organics, nitrate, and ammonium in droplet residual particles, owing to effects of long-range transport from more distant sources. Sodium and chloride dominated in terms of air-equivalent concentration in cloud water for coupled clouds, and their mass fractions and concentrations exceeded those in decoupled clouds. Conversely, with the exception of sea-salt constituents (*e.g.*, Cl, Na, Mg, and K), cloud water mass fractions of all species examined were higher in decoupled clouds relative to coupled clouds. Satellite and Navy Aerosol Analysis and Prediction System-based reanalysis data are compared with each other, and the airborne data to conclude that limitations in resolving boundary layer processes in

a global model prevent it from accurately quantifying observed differences between coupled and decoupled cloud composition.

H.1 Introduction

The composition of gases, particles, and droplets in and around clouds impacts cloud properties, radiative forcing, the water cycle, and geochemical cycling of nutrients. The degree of coupling between the cloud and the surface layer in a given region is a fundamental property of the cloud system that is expected to impact its composition. Quantifying the effect of coupling on composition is particularly important for marine stratocumulus clouds, which are the dominant cloud type by global area (*e.g.*, Warren *et al.*, 1986), exerting a strong negative net radiative effect (*e.g.*, Stephens and Greenwald, 1991). Stratocumulus-topped boundary layers are often capped by a strong temperature inversion and are well mixed due to longwave radiative and evaporative cooling at cloud top (*e.g.*, Wood, 2012). When the negative buoyancy generated at cloud top is not sufficiently strong, the cloud layer can become decoupled from the layer immediately above the ocean (*e.g.*, Nicholls, 1984).

The goal of this study is to determine how the degree of coupling of clouds to the surface layer affects mass concentrations and chemical ratios in cloud water and droplet residual particles for dissolved nonwater substances. While numerous past studies have examined either cloud microphysical properties of stratocumulus clouds in our study region over the eastern Pacific Ocean off the Califonia coast (*e.g.*, Coakley *et al.*, 2000; Durkee *et al.*, 2000; Ferek *et al.*, 2000; Gerber *et al.*, 2005; Lu *et al.*, 2009; Mechem and Kogan, 2003; Modini *et al.*, 2015; Noone *et al.*, 2000; Painemal and Minnis, 2012; Sanchez *et al.*, 2016; Sharon *et al.*, 2006; Stevens *et al.*, 2003; Wang *et al.*, 2008a) or the nature of decoupled marine clouds versus coupled clouds (*e.g.*, Berner *et al.*, 2011; Bretherton *et al.*, 2010a; Bretherton and Wyant, 1997; Bretherton *et al.*, 2010b; Burleyson *et al.*, 2013; Considine, 1997; Crosbie *et al.*, 2015; Dong *et al.*, 2015; Garreaud *et al.*, 2001; Glantz *et al.*, 2003; Jones *et al.*, 2011; Nicholls and Leighton, 1986; O'Dowd *et al.*, 2000; Terai *et al.*, 2014), none to our knowledge have focused on contrasting composition between coupled and decoupled clouds. It is hypothesized that clouds more strongly coupled to the surface will be more influenced by ocean and ship emissions and less so by continental emissions. Our observations are compared with satellite data and reanalysis data based on the Navy Aerosol Analysis and Prediction System (NAAPS) model to assess the extent to which the model can capture the chemical signature of the two cloud types. The results are intended to motivate more attention to the

extent to which clouds are coupled to the surface layer in future studies of cloud composition and aerosol-cloud interactions.

H.2 Experimental Methods

H.2.1 Airborne Measurements

Data are analyzed from three flight campaigns using the Center for Interdisciplinary Remotely-Piloted Aircraft Studies Twin Otter based in Marina, CA. The Eastern Pacific Emitted Aerosol Cloud Experiment (E-PEACE) (Russell *et al.*, 2013) included 30 flights between July and August in 2011, the Nucleation in California Experiment (NiCE) (Coggon *et al.*, 2014) included 23 flights between July and August in 2013, and the Biological and Oceanic Atmospheric Study (BOAS) comprised 15 flights in July 2015.

Cloud water was collected with a Mohnen slotted-rod collector (Hegg and Hobbs, 1987). Details about the collection, storage, and chemical analyses during the three field campaigns are provided elsewhere (Wang *et al.*, 2014). Briefly, samples were collected over a ~10–30 min duration in high-density polyethylene bottles, with 87, 119, and 29 samples collected in E-PEACE, NiCE, and BOAS, respectively. Samples were tested for pH (Oakton Model 110 pH meter calibrated with pH 4.01 and pH 7.00 buffer solutions), water-soluble composition (Ion Chromatography, IC; Thermo Scientific Dionex ICS-2100 system), and elemental composition (inductively coupled plasma mass spectrometry, ICP-MS; Agilent 7900 Series). The non-sea-salt (NSS) fractions of sulfate and calcium in cloud water were calculated using the relative abundance of sodium to other constituents of sea salt (Seinfeld and Pandis, 2006). Sodium data presented are from ICP-MS (Na), owing to improved data quality, rather than from IC (Na^+); it is assumed that most all of Na is in the form of sea salt. Liquid-phase concentrations of dissolved nonwater cloud water species were converted to air-equivalent concentrations based on the average cloud liquid water content (LWC), as measured by a PVM-100 probe (Gerber *et al.*, 1994). A threshold LWC value of 0.02 g m^{-3} was used to distinguish between cloud and cloud-free air, as has been done in past work in the study region (Prabhakar *et al.*, 2014; Wang *et al.*, 2014).

Droplet residual particle composition data were collected using a compact time-of-flight aerosol mass spectrometer (C-ToF-AMS; Aerodyne) (Drewnick *et al.*, 2005) downstream of a counterflow virtual impactor (CVI; Brechtel Manufacturing Inc.) (Shingler *et al.*, 2012). The C-ToF-AMS measured nonrefractory aerosol composi-

tions (organics, sulfate, nitrate, and ammonium) for submicrometer aerosol. During the three field experiments,the CVI exhibited a $D_{p,50}$ cutsize of 11 μm, with a decreasing transmission efficiency as a function of increasing drop size inside the inlet mainly owing to inertial deposition. As already reported by Shingler *et al.* (2012) for the study region, the $D_{p,50}$ of the CVI was sufficiently low to sample the majority of the drop distribution during flights in the study region, with the exception of periods near cloud base, especially when influenced by ship plumes. In cloud-free air, particles were sampled through a subisokinetic aerosol inlet (Hegg *et al.*, 2005).

Size-resolved particle number concentrations were measured with a condensation particle counter (CPC3010; TSI Inc.; D_p > 10 nm) and a passive cavity aerosol spectrometer probe (PCASP; $D_p \sim$ 0.1-2.6 μm); subcloud sampling data are used in this study as the precloud aerosol. Cloud drop number concentration data were obtained with a cloud aerosol spectrometer (CAS; $D_p \sim$ 0.6-60 μm) and a forward scattering spectrometer probe (FSSP; $D_p \sim$2-46 μm). CAS data are used for E-PEACE and NiCE, while FSSP data are used for BOAS. Standard meteorological data were also measured, including temperature, winds, and humidity (*e.g.*, Crosbie *et al.*, 2015).

Differentiating between coupled and decoupled clouds requires criteria involving thermodynamic vertical profile data, including quantification of moisture and temperature decoupling metrics and calculating the difference between the lifting condensation level and cloud base height (*e.g.*, Dong *et al.*, 2015; Jones *et al.*, 2011; Terai *et al.*, 2014). Decoupling was initially identified based on observed discontinuities in vertical profiles of thermodynamic properties (potential temperature and water vapor mixing ratio) and aerosol number concentration as measured by the PCASP. When contrasting these clouds to all others, the criteria that emerged for decoupled clouds were that the difference between the bottom and top of the subcloud layer of potential temperature and water vapor mixing ratio had to exceed 1.0 K and 0.6 g kg^{-1}, respectively. All other clouds are considered coupled. In total, we analyzed 13 and 80 decoupled and coupled clouds, respectively. Figure H.1 illustrates an example of both a decoupled and coupled cloud based on the aforementioned criteria.

H.2.2 Vertical Profiles of Particulate Constituents

In order to supplement data from the three aircraft experiments, average vertical profiles of different aerosol constituents were obtained from both the Cloud-Aerosol

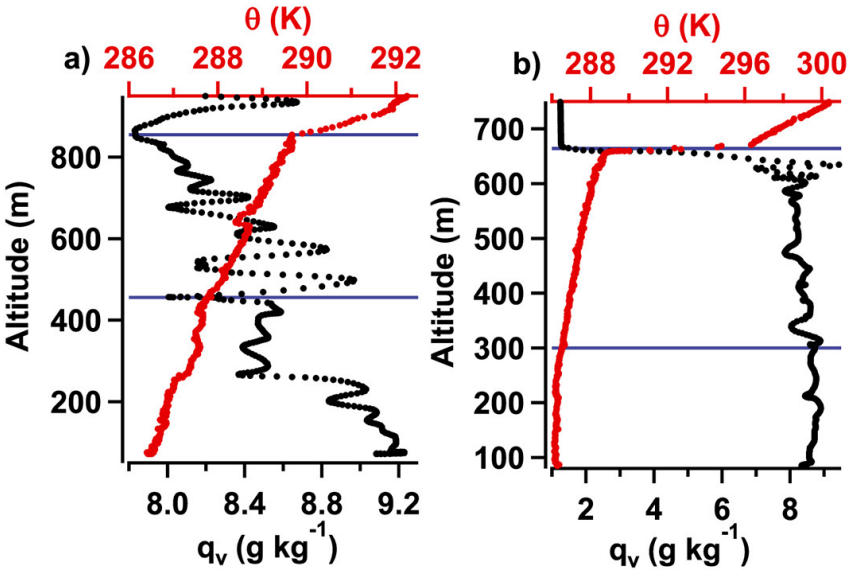

Figure H.1: Example of a cloud (a) decoupled from the surface layer and (b) coupled to the surface layer based on vertical profiles of potential temperature and water vapor mixing ratio.

Lidar with Orthogonal Polarization (CALIOP) and an aerosol reanalysis product, which combines observations with a forecasting model to produce gridded data of atmospheric parameters at a temporal resolution of a few hours. For CALIOP, monthly averaged climatological profile values are used for total and speciated 532 nm aerosol extinction coefficient (km^{-1}) derived at $5° \times 5°$ resolution centered at 37.5 °N and -122.5 °W; the methods used to solve these profiles from available quality-assured Version 3 Level 2 Aerosol Profile products are described in Campbell *et al.* (2012). We specifically report climatological profile data derived between 2006 and 2015 for the months of July and August. Version 3 Level 2 CALIOP aerosol species include "clean marine" (CAL-CM), "dust" (CAL-D), "polluted continental" (CAL-PC), "clean continental" (CAL-CC), "polluted dust" (CAL-PD), and "smoke" (CAL-S) (Omar *et al.*, 2005). The sum of these species is denoted as "All."

A decade-long global $1° \times 1°$ and 6-hourly 550 nm aerosol optical thickness (AOT) reanalysis product was recently developed and validated at the Naval Research Laboratory (Lynch *et al.*, 2016). This reanalysis utilizes a modified version of the Navy Aerosol Analysis and Prediction System (NAAPS) as its core and assimilates quality-controlled retrievals of AOT from Moderate Resolution Imaging Spectroradiometer on Terra and Aqua and the Multiangle Imaging Spectroradiometer on Terra (Hyer *et al.*, 2011; Shi *et al.*, 2014; Zhang and Reid, 2006). NAAPS

characterizes anthropogenic and biogenic fine (ABF, including sulfate and primary and secondary organic aerosols) aerosols, dust, biomass burning smoke, and sea-salt aerosols, the sum of which is denoted as All. The reanalyzed fine (*i.e.*, ABF + smoke) and coarse mode (*i.e.*, sea salt + dust) AOTs at 550 nm are shown to have good agreement with the ground-based global-scale Sun photometer network Aerosol Robotic Network AOTs (Holben *et al.*, 1998). The three-dimensional NAAPS concentration and extinction data here are extracted from the same NAAPS reanalysis run. Data represent the region encompassed by the following: 125.5 to 122.5 °W; 35.5 to 40.5 °N.

H.2.3 Air Back-Trajectory Modeling

Air mass source origins for cloud water samples were identified based on 72 h back trajectories from the NOAA Hybrid Single-Particle Lagrangian Integrated Trajectory (HYSPLIT) model (Stein *et al.*, 2015) ending at the location and altitude of the average point for each sample. HYSPLIT was run using the Global Data Assimilation System data with the "Model vertical velocity" method.

H.3 Airborne Data Category Definitions

To compare decoupled and coupled clouds, six categories are defined to include cases with similar cloud base heights and air mass influences. Following the criteria previously used by Wang *et al.* (2014), three air mass categories are as follows: (i) "Ship" = maximum subcloud aerosol concentration as measured by a CPC concentration > 14000 cm^{-3}; (ii) "Marine Reference" = maximum subcloud aerosol concentration as measured by a CPC concentration < 1000 cm^{-3}; and (iii) "Land" = 72 h back-trajectory contacted land. The first two categories are characterized by an oceanic air source origin, with the primary distinction that the Marine Reference category has an absence of fresh ship emissions. The Land category is associated with continental emissions that impact marine clouds with sources including biogenic emissions, wildfires, and crustal emissions (Coggon *et al.*, 2014; Maudlin *et al.*, 2015; Prabhakar *et al.*, 2014; Sorooshian *et al.*, 2015; Youn *et al.*, 2015). Each of these three categories is further subdivided into two categories based on cloud base height, resulting in the six categories shown in Table H.1. The following cloud base heights were identified as threshold values below and above which cases were categorized as having low base or high base heights, respectively, to maintain a combination of similar numbers of data points and a reasonable separation in height: 250 m (Ship), 600 m (Marine Reference), and 700 m (Land). Cloud base heights

for low or high base categories differ between the three air mass categories due to the limited number of decoupled clouds encountered in these campaigns (Table H.1); the comparison between coupled and decoupled clouds at each base height condition within each category is now addressed.

H.4 Results and Discussion

H.4.1 Vertical Chemical Profiles From CALIOP

Vertical aerosol extinction profiles from CALIOP are first presented for major aerosol types to provide context for the aircraft data that are for more detailed chemical species (Figure H.2). The data begin at a starting altitude of 0.2 km, where the CAL-CM aerosol type dominates the total aerosol extinction coefficient up to between 0.4 and 0.5 km, at which point CAL-PD dominates up to approximately 2.5 km, which surpasses the altitude of the flight data. Most aerosol types decreased in extinction with altitude except for CAL-D (increased up to 0.7 km) and CAL-S (increased up to 1.8 km), indicative of their presence in the free troposphere from continental sources. CAL-CM decreased at the fastest rate above the surface owing to the surface source of sea salt and effective scavenging at low altitudes. Since the typical boundary layer height in these aircraft campaigns was < 1 km in altitude, it is expected that sea salt is the major component in cloud water; however, a decoupled cloud below 1 km will presumably exhibit a chemical signature impacted more by continental pollution (*e.g.*, dust,smoke, and anthropogenic and biogenic emissions). The CALIOP results are more readily related to cloud water composition (Section H.4.4) than to droplet residual particle composition data, as the latter data from the C-ToF-AMS represent only nonrefractory species (*i.e.*, excludes sea salt, smoke, and dust).

H.4.2 Environmental Characteristics

Three-day back-trajectory analysis for the sampled air masses revealed similar pathways generally moving southwards off the western United States coast (Figure H.3). Back trajectories for some samples included transects over land usually to the north of San Francisco. Overall, the HYSPLIT results suggest that the studied clouds were impacted by similar air masses.

Environmental characteristics for decoupled and coupled clouds in each of the six categories are summarized in Table H.1. Category averages for cloud base height and cloud depth ranged from 122 to 808 m and 167 to 414 m, respectively. Cloud drop number concentration (N_d) and subcloud number concentration, as

category	characteristics	base height (m)		cloud depth (m)		in-cloud N_d(cm^{-3})		subcloud CPC (cm^{-3})		subcloud PCASP (cm^{-3})	
		DC	C	DC	C	DC	C	DC	C	DC	C
A	Ship, low base	122	136	285	414	42	175	3164	1881	79	304
B	Ship, high base	338	285	320	319	135	240	865	1269	191	360
C	Marine, low base	427	335	400	270	69	149	180	433	98	257
D	Marine, high base	794	766	279	174	82	164	209	343	109	194
E	Land, low base	574	430	343	294	128	163	305	469	91	236
F	Land, high base	808	789	167	244	28	197	369	400	64	224

Table H.1: Summary of average environmental properties associated With the decoupled (DC) and coupled (C) clouds for six different categories defined based on air mass influence and cloud base height. The number of data points in each category is as follows (coupled/decoupled): A = 12/2; B = 8/1; C = 26/4; D = 14/2; E = 17/3; and F = 3/1.

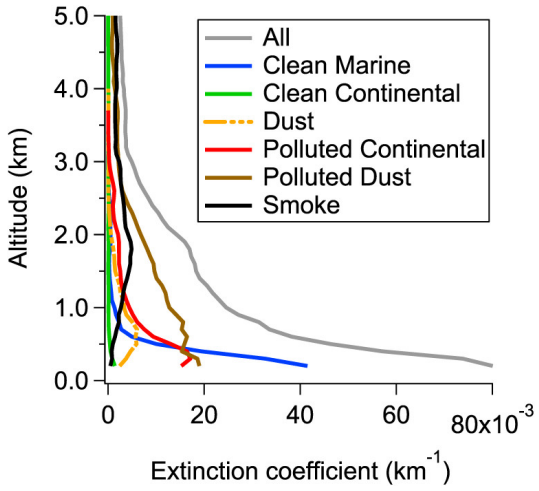

Figure H.2: Vertical profiles of aerosol extinction coefficient from CALIOP climatological data for July–August between 2006 and 2015 in the study region.

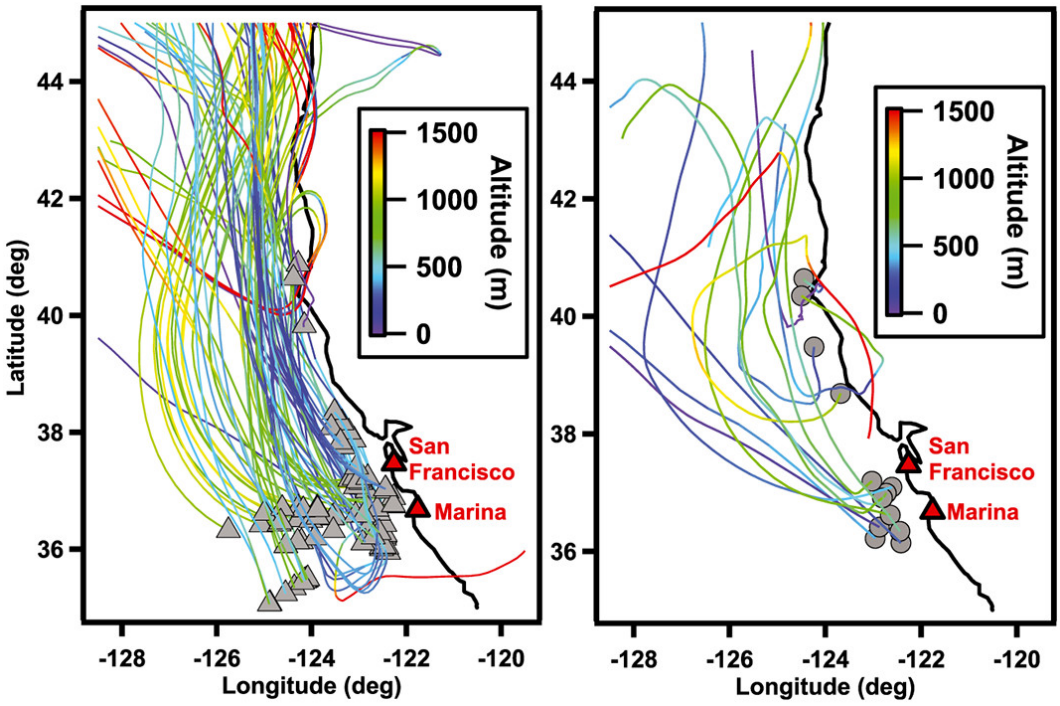

Figure H.3: Spatial map of where the cloud water and droplet residual samples were collected in (left) coupled clouds (n = 80) (triangles) and (right) decoupled clouds (n = 13) (circles) with HYSPLIT 72 h back-trajectories ending at the point of sample collection.

measured by the PCASP (D_p > 100 nm), were both higher in coupled clouds for all categories owing most likely to influence from ocean and shipping emissions. Another contributing factor to higher N_d in coupled clouds could be higher updraft velocities. One indication that updraft velocity was not the prime driver of the difference in N_d between coupled and decoupled clouds is that the mean vertical wind was lower for coupled clouds in some categories. Coupled stratocumuli over the Azores have also been shown to exhibit higher N_d and surface cloud condensation nucleus concentrations as compared to decoupled stratocumuli (Dong *et al.*, 2015); that study did not examine updraft velocities though to determine how influential that factor was in governing N_d values. Subcloud number concentrations, as measured by the CPC (D_p > 10 nm), were higher for decoupled versus coupled clouds for only one category (Ship-low base) due, most likely, to secondary, organic-rich particles that are formed *via* gas-to-particle conversion in the free troposphere that tend to have diameters < 100 nm (*e.g.*, Coggon *et al.*, 2014; Hersey *et al.*, 2009). As larger particles have a greater chance to activate into drops, N_d is better related to subcloud number concentrations measured by the PCASP (D_p > 100 nm) as compared to those measured by the CPC (D_p > 10 nm).

H.4.3 Droplet Residual Particle Composition

The focus of the drop residual particle chemical analysis is on chemical ratios (Table H.2 and Figure H.4) and not absolute mass concentrations owing to uncertainty in their quantification using CVI inlets (Shingler *et al.*, 2012). CVI data are not available for decoupled clouds in category F.

For decoupled clouds, organics were usually the dominant component, with a cumulative mass fraction average of 0.55 and a category range of 0.32 to 0.88. Aside from having the highest mass fraction in category C (Marine Reference-low base), sulfate was the second most abundant component for category E (mass fraction = 0.06), which consisted of samples obtained farther to the north of the San Francisco area. For categories A/B/D, ammonium was the next most abundant component (mass fraction range: 0.26–0.30). Nitrate was the least abundant component, with a mass fraction maximum of only 0.05 in category E. Nitrate is prone to volatilization in the CVI inlet, and it is present in coarse and/or refractory particles that are undetectable by the C-ToF-AMS (*e.g.*, Prabhakar *et al.*, 2014), and thus, its reported values most likely represent a lower bound.

For coupled clouds, organics are the dominant contributor to droplet residual

		decoupled	coupled	ratio
Droplet residual particles	Organic	54.5%	44.7%	1.22
	SO_4^{2-}	23.6%	39.4%	0.60
	NH_4^+	17.9%	13.0%	1.37
	NO_3^-	4.0%	2.9%	1.38
Cloud water	Cl^-	27.9%	42.6%	0.65
	Na	9.8%	18.6%	0.53
	NO_3^-	19.8%	12.7%	1.55
	NSS SO_4^{2-}	14.5%	12.1%	1.20
	Mg	1.7%	2.7%	0.61
	Glyoxylate	1.5%	0.4%	4.15
	K	0.5%	0.7%	0.71
	MSA	1.7%	1.6%	1.06
	Oxalate	3.4%	1.3%	2.51
	Acetate	3.9%	1.5%	2.69
	Si	7.4%	1.2%	6.32
	Formate	4.1%	1.1%	3.70
	NSS Ca	0.6%	0.3%	2.06
	NO_2^-	1.4%	0.6%	2.30
	Maleate	0.5%	0.4%	1.30

Table H.2: Summary of constituent mass fractions (in percentage) in droplet residual particles (as measured by the C-ToF-AMS downstream of a CVI) and cloud water in decoupled and coupled clouds, based on cumulative data for all six categories in Table H.1. It is noted that C-ToF-AMS data represent only nonrefractory speciesand exclude sea salt. "Ratio" = decoupled:coupled mass fraction. Cloudwater species in italics were examined using IC, while the rest wereexamined using ICP-MS.

particle mass for three of six categories (D–F), with a cumulative mass fraction average of 0.45 and category range of 0.38 to 0.57. The main difference between coupled and decoupled clouds can be distinguished by the sulfate mass fraction, which is generally higher for coupled clouds (0.39 versus 0.24) with lower relative amounts of the other constituents. Sulfate stems from precursor emissions emitted at the ocean surface, including dimethylsulfide (DMS) and SO_2 from shipping. Consequently, sulfate exhibited a higher mass fraction than organics for the two ship categories (A and B). As in decoupled clouds, nitrate was the least abundant constituent of droplet residual particles (mass fraction average = 0.03) based on C-ToF-AMS data.

Previous work in the study region has shown that aerosol particles above cloud top generally have a higher organic:sulfate ratio versus that below and in clouds (*e.g.*, Coggon *et al.*, 2012; Sorooshian *et al.*, 2007). The source of organics aloft includes biogenic and wildfire emissions from the northwestern United States (Coggon *et al.*,

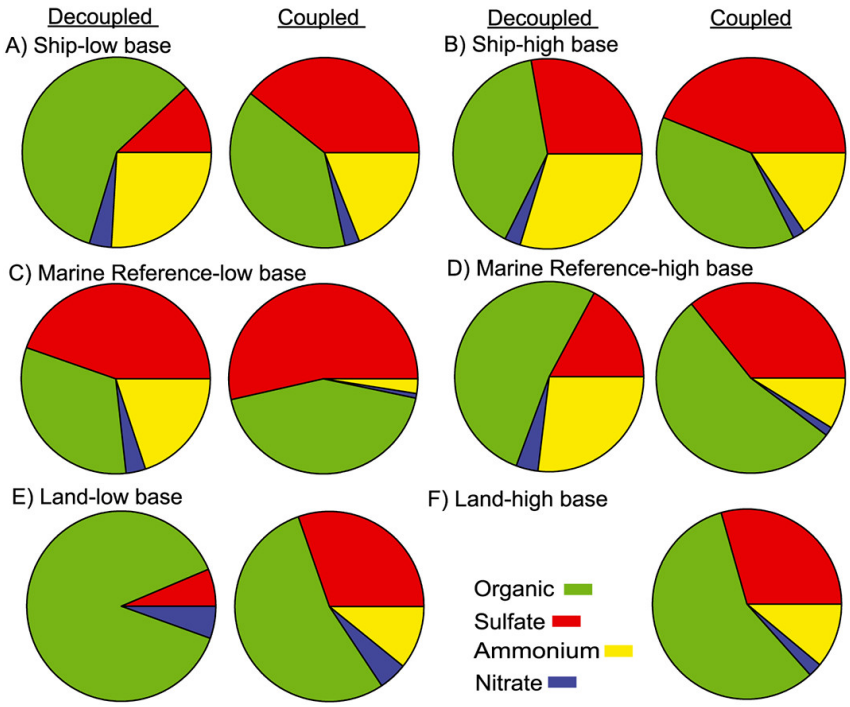

Figure H.4: Comparison of droplet residual particle chemical mass fractions, as measured by a C-ToF-AMS downstream of a CVI, for decoupled versus coupled clouds in the six categories (A–F) defined in Table H.1. CVI data were not available for decoupled clouds in category F.

2014, 2012). The average organic:sulfate mass concentration ratio for decoupled clouds (116.1) was approximately 10 times larger than that in coupled clouds (11.7). The high value for decoupled clouds was driven by two individual samples with values of 422.5 and 547.4; when omitting those two samples, the decoupled ratio becomes 23.8, which still is more than twice that of coupled clouds. Particles in the study region with higher organic:sulfate ratios are less hygroscopic, as has previously been shown by comparisons of aerosol particles above coupled cloud tops versus below bases both in the subsaturated (Hersey *et al.*, 2009) and supersaturated regime (Crosbie *et al.*, 2015). Thus, the extent to which clouds are decoupled from the surface layer has implications for hygroscopic, and thus radiative, properties of particles in and around clouds.

H.4.4 Cloud Water Composition

H.4.4.1 Cumulative Concentration Data

Tables H.2 and H.3 summarize mass fractions and air-equivalent mass concentrations, respectively, of cloud water constituents for decoupled and coupled clouds.

Total cloud water mass concentration is calculated as the sum of the following species: (from IC) NSS SO_4^{2-},NO_3^-,Cl^-,NO_2^-, glyoxylate, acetate, formate, methane sulfonate (MSA), pyruvate, maleate, oxalate, fluoride, and lactate and (from ICP-MS) Na, Mg, Al, Si, K, NSS Ca, Ti, V, Cr, Mn, Fe, Co, Ni, Cu, Zn, As, Se, Br, Rb, Sr, Cd, I, and Pb. Total cloud water air-equivalent mass concentration was significantly higher for coupled versus decoupled clouds, exceeding a factor of 5 based on cumulative data (13.38 versus 2.47 μg m^{-3}, respectively).

Due to sea-salt emissions, chloride, followed by sodium, contributed the most to cloud water mass for coupled clouds, each being nearly an order of magnitude higher in concentration than in decoupled clouds. This result is consistent with the vertical profiles of aerosol extinction from CALIOP (Figure H.2), which show the dominance of the CAL-CM aerosol type in the first few hundred meters above the surface in the region where the coupled cloud measurements were conducted. The combined mass fraction of chloride and sodium relative to total mass is 0.61 and 0.38 for coupled and decoupled clouds, respectively. There is no significant difference in the Cl:Na molar ratio, with values of 1.15 and 1.13 for the coupled and decoupled clouds, respectively. These values are close to those characteristic of natural sea salt, 1.17, and thus, there is no obvious evidence of significant chloride depletion owing to acidic constituents, even though cloud water pH was 4.26 and 4.48 for coupled and decoupled cloud samples, respectively. Furthermore, the similarity in the ratios is suggestive of sea salt having been lofted above the surface layer (*e.g.*, Hara *et al.*, 2014; Lewis and Schwartz, 2004) in decoupled clouds at some earlier point.

Nitrate and NSS sulfate are the third and fourth most abundant components in coupled clouds, respectively. Regional sources of nitrate include ship exhaust, ocean sea spray and biogenic emissions, and wildfires (Prabhakar *et al.*, 2014). Nitrate is more abundant than NSS sulfate in cloud water, in contrast to droplet residual particle measurements, likely as a result of a combination of dissolution of HNO_3^-, activation of coarse and/or refractory particles undetectable by the C-ToF-AMS, and the absence of volatilization effects that are associated with heating in the CVI inlet (Prabhakar *et al.*, 2014).

A few of the less abundant species in Table H.3 are more than 5 times enhanced in coupled clouds relative to decoupled clouds, including K, Sr, Br, and Mg. These species have a mix of natural and anthropogenic sources in the study region (Wang *et al.*, 2014). MSA was more than 3 times higher in concentration in coupled clouds

presumably due to DMS emissions from the ocean surface. With the exception of acetate and formate, organic acids in Table H.3 (glyoxylate, oxalate, maleate, and pyruvate) were higher in concentration in coupled clouds, particularly maleate (by over a factor of 3.5) that forms from aromatic hydrocarbon oxidation (Rogge *et al.*, 1993), sources of which in the study region include diesel and gasoline engines. Maleate is a precursor to glyoxylate, the chief aqueous precursor to oxalate (*e.g.*, Sorooshian *et al.*, 2013), the latter two of which are ~2.6 and ~1.5 times higher in concentration, respectively, in coupled clouds than in decoupled ones.

In decoupled clouds, species enhanced in concentration relative to coupled clouds include formate, Si, Co, Mn, nitrite, Al, Cr, and acetate by factors reaching as high as 1.66, with the difference in mean concentration being statistically significant (t test with a two-tailed p value threshold of 0.05) for the first four species. These species are influenced from continental sources near the study region such as crustal matter, which is the likely source of Si (Coggon *et al.*, 2014; Wang *et al.*, 2014). Continental air masses almost certainly influence the composition of decoupled clouds owing to their general presence in the free troposphere of the region (*e.g.*, Coggon *et al.*, 2014). As air masses impacting the study region were transported southward along the coast (Figure H.3), forest emissions likely influenced their compositions, especially north of central CA (Coggon *et al.*, 2014). Formate is one of the most enhanced species in decoupled clouds versus coupled ones (factor of 1.52). Formate originates from formic acid, 90% of which is biogenic in origin, especially from boreal forests (Stavrakou *et al.*, 2012). CALIOP data also show that above approximately 0.4–0.5 km, CAL-D, CAL-PD, and CAL-PC aerosol types exceed CAL-CM aerosol in terms of extinction coefficient, confirming that clouds impacted by free tropospheric air in the region exhibit greater influence from continental air than by sea salt. In summary, the results in Table H.3 indicate that the decoupled clouds have much smaller air-equivalent mass concentrations of the species studied, except for a few species with likely continental sources, owing to the large size of sea-salt particles driving mass concentrations much higher in coupled clouds.

H.4.4.2 Cumulative Mass Fraction Data

Because microphysical properties, such as aerosol hygroscopicity, depend on relative concentrations of chemical constituents, differences in mass fractions in cloud water are discussed here (Table H.2) with a focus on those species accounting for

	units	decoupled	coupled	ratio
Total		2.47	13.38	0.18
Cl^-		0.76	7.06	0.11
Na		0.36	3.24	0.11
NO_3^-		0.45	0.87	0.52
NSS SO_4^{2-}		0.30	0.85	0.35
Mg		0.06	0.46	0.13
Glyoxylate	μg m^{-3}	0.11	0.27	0.39
K		0.02	0.13	0.17
MSA		0.04	0.12	0.32
Oxalate		0.07	0.11	0.65
Acetate		0.11	0.10	1.10
Si		0.16	0.10	1.66
Formate		0.12	0.08	1.52
NSS Ca		0.02	0.04	0.57
NO_2^-		0.03	0.03	1.06
Maleate		8.63	30.53	0.28
Fluoride		8.89	23.92	0.37
Pyruvate		7.89	15.09	0.52
Br		2.17	14.36	0.15
I		7.79	9.85	0.79
Fe		5.68	5.70	1.00
Al		5.42	4.97	1.09
Cd		2.80	3.83	0.73
Sr		0.67	3.39	0.20
Cu		1.03	1.61	0.64
Mn	ng m^{-3}	2.25	1.40	1.61
Zn		0.81	1.33	0.61
V		0.25	0.63	0.40
Se		0.17	0.33	0.50
Ni		0.12	0.13	0.93
Ti		0.12	0.12	0.98
Pb		0.03	0.09	0.30
Cr		0.08	0.08	1.01
As		0.02	0.06	0.41
Rb		0.01	0.05	0.29
Co		0.02	0.02	1.55

Table H.3: Cumulative average cloud water mass concentration summary of species measured in decoupled and coupled clouds. Ratio = decoupled:coupled concentration. Species in italics were examined using IC, while the rest were examined using ICP-MS. Species are listed in decreasing order of value for the coupled category.

most of the total mass. In decoupled clouds, mass fractions of sodium and chloride are reduced relative to coupled clouds by factors of ~1.9 and ~1.5, respectively. As these two species dominate the mass concentration in coupled clouds, the mass fractions of all species except for Mg and K in Table H.2 are higher for decoupled clouds. Mg and K are the fourth and sixth most abundant components of natural sea salt by mass after chloride, sodium, and sulfate (*e.g.*, Seinfeld and Pandis, 2006). Thus, they are expected to preferentially impact coupled clouds. The greatest enhancements in the mass fraction in decoupled versus coupled clouds are for carboxylic acids (glyoxylate, formate, oxalate, and acetate), nitrite, Si, and NSS Ca with enhancement factors ranging from 2.06 to 6.32.

H.4.4.3 Categorical Chemical Differences

Figure H.5 contrasts cloud water chemical data for coupled and decoupled clouds for each of the six categories of Table H.1, with statistically significant (t test with a two-tailed p value threshold of 0.05) differences in mean values highlighted on each x axis. Although many differences are not statistically significant owing largely to limited data points in the decoupled categories, relative differences are still of importance to discuss. Total mass concentrations are highest in coupled clouds in categories E to F (Land-low base and Land-high base), and highest in categories C/E (Marine Reference-low base; Land-low base) for decoupled clouds. Analysis of the various constituents in Figure H.5 explains this result. For coupled clouds, chloride is highest in concentration for categories E and F, thus driving the total mass concentration to maximum levels. Nitrate is also highest in category F owing to its association with sea salt in the study region (Prabhakar *et al.*, 2014). MSA levels are also highest in categories E and F, suggesting that biogenic emissions contribute in addition to direct emission of sea spray. While ship emissions are shown to be less influential to cloud water mass concentrations relative to ocean emissions (*e.g.*, sea salt), it is worth noting that the ship exhaust tracer, V, was most enhanced in categories A and B (Ship-low base and Ship-high base) as expected for coupled clouds. NSS sulfate is highest in category B due to the contribution from ship-derived SO_2.

For decoupled clouds, the largest contributors to the peak total mass in category C are chloride, followed by nitrate, while the order of these two species is reversed for category E. Representative tracer species for continental crustal matter, namely, Si and NSS Ca (not shown in Figure H.5) (Wang *et al.*, 2014), clearly exhibit a

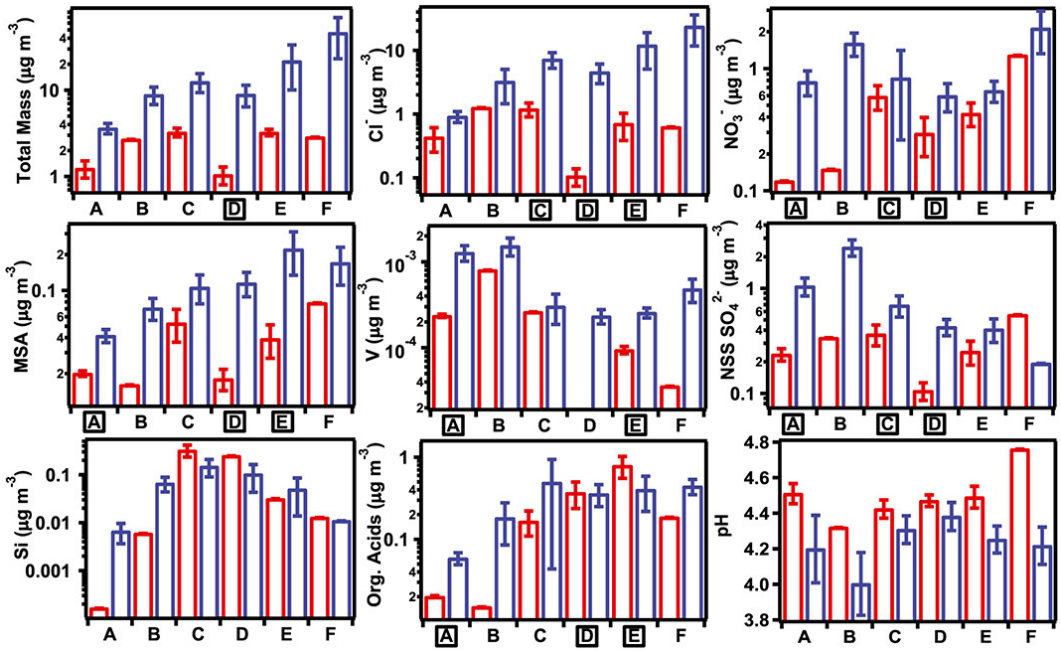

Figure H.5: Comparison of cloud water parameters between coupled (blue) and decoupled (red) clouds for the six categories (A–F) defined in Table H.1. Category labels with a box around them indicate that the difference between the two means of that category is statistically significant (two-sample t test with a two-tailed p value threshold of 0.05).

peak concentration in category C. Interestingly, the coupled clouds also show the highest Si concentration in the same categories as the decoupled clouds, albeit at lower concentrations, indicative of the influence of continental air for coupled clouds near the coast; CALIOP profiles showing enhanced levels of CAL-PD and CAL-PC aerosol types in the first few hundred meters above the surface support this inference. The total concentration peak in category E for decoupled clouds appears to be influenced by different sources when compared to category C. More specifically, while crustal matter tracer species are much lower in category E,concentrations of organic acids are much higher. The cumulative concentration of acetate, formate, pyruvate, glyoxylate, oxalate, and maleate was 0.79 μg m^{-3}, exceeding by more than a factor of 2 the concentration of any other category for decoupled clouds. Formate and acetate were the two most abundant organic acids in category E, with their source likely being biogenic emissions from upwind continental areas as noted in previous work (Coggon *et al.*, 2014).

Cloud water pH is higher in decoupled clouds than coupled ones for all six categories, owing presumably to a lower impact of acidic compounds from shipping

combined with increased contributions of basic com-pounds coming upwind from the continent. The lowest pH (4.0) occurred for coupled clouds in category B (Ship-high base), which exhibits the highest V concentration and thus shipping influence. The highest pH (4.76) occurred for decoupled clouds in category F (Land-high base), consistent with past work showing that cloud water pH is higher when influenced by continental air masses enriched with crustal species, especially Si, in the study region (Wang and Laskin, 2014).

H.4.5 Reanalysis Data

It is of interest to contrast vertically resolved chemical profiles from the NAAPS-based reanalysis product for the same time periods of the decoupled and coupled clouds. NAAPS can resolve aerosol vertical profiles on atemporal/spatial scales consistent with the flights described. CALIOP observations cannot be used in this capacity as they are dependent on orbital configurations and cannot provide measurements near the flights. The NAAPS reanalysis was specifically designed as an aerosol optical depth product, with little tuning done vertically to ensure vertical profiling skill explicitly (Lynch *et al.*, 2016). Fortunately, Figure H.6a demonstrates that the reanalysis data, when averaged for July–August for the three experiment years (2011, 2013, and 2015), generally agree with the climatological CALIOP profiles. Similar to CALIOP observations, the reanalysis data show that the maximum total extinction coefficient (denoted as All) is ~0.08 km^{-1} near the surface. Sea salt accounts for most extinction below about 0.5 km, above which other constituents dominate, mainly fine mode components (smoke, ABF).

Figures H.6b and H.6c show mass concentration vertical profiles for the same time as when coupled and decoupled cloud measurements, respectively, were conducted. Rather than extinction coefficients, mass concentrations are shown for a direct comparison with the cloud water measurements. The relative concentration variations with altitude are nearly identical between the composite profiles for coupled and decoupled clouds. Perhaps,the most significant difference is the much higher sea-salt concentrations (by up to a factor of 1.8) in the lowest few hundred meters for the coupled composite profile owing to stronger surface winds (at 10 m) as predicted by the model. The average near-surface (<100 m) wind speeds coinciding with measurements of the coupled and decoupled clouds were 4.8 and 4.6 m s^{-1}, respectively, indicating that at least in the spatial range of where the aircraft flew, there was no significant difference in wind speed unlike in the model.

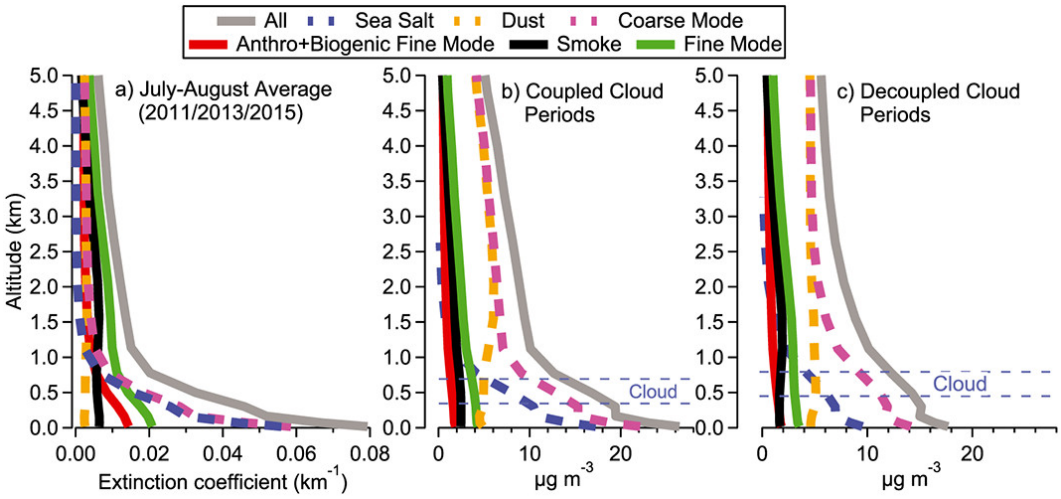

Figure H.6: Vertical profile of aerosol constituents from the NAAPS-based reanalysis product. (a) Profiles of aerosol extinction coefficient for July and August for the three summers that field campaign data were analyzed. (b) Profile of aerosol mass concentrations for the times coinciding with the coupled clouds examined. (c) Profile of aerosol mass concentrations for the times coinciding with the decoupled clouds examined. The horizontal bars in Figures 6b and 6c correspond to the average cloud base and top heights for coupled and decoupled clouds.

To compare the composite profiles to the cloud composition data, the mass fractions of the four main components (ABF, sea salt, dust, and smoke) are compared between coupled and decoupled composite profiles at cloud-relevant altitudes for each category. In contrast to the measurements (Table H.2), the reanalysis mass fractions are nearly identical for the two cloud types (coupled/decoupled): ABF = 0.10/0.10, sea salt = 0.40/0.41, dust = 0.34/0.37, and smoke = 0.16/0.12. As sea salt is the most abundant cloud water constituent, its modeled and observed mass concentrations at cloud-relevant altitudes for coupled and decoupled clouds are as follows (modeled/observed): 6.1/10.3 μg m^{-3} for coupled and 5.8/1.1 μg m^{-3} for decoupled clouds,where the observed value is calculated as the sum of Na and Cl. While the modeled and measured concentrations are within an order of magnitude, the remaining discrepancy is indicative of the current limitations of the resolution of a global model for boundary layer processes, leading to the observed difference in coupled and decoupled composition.

H.5 Conclusions

Aircraft measurements of cloud water and droplet residual particle composition over the eastern Pacific Ocean off the California coast between July and August of 3

years (2011, 2013, and 2015) are examined in this work for clouds decoupled from and coupled to the surface layer. While differences are expected between these two cloud conditions, this work provides quantitative data. The main findings of this work are as follows:

1. Total mass concentration of measured constituents in droplet residual particles and cloud water was significantly enhanced in coupled clouds, coincident with higher N_d and subcloud number concentrations as measured by the PCASP (D_p > 100 nm). This can be explained by the stronger influence on coupled clouds by ocean and shipping emissions.

2. Organics and sulfate were the most abundant components in droplet residual particles, with sulfate mass fraction generally being higher in coupled versus decoupled clouds (0.39 versus 0.24), unlike organics, ammonium, and nitrate. Consequently, organic:sulfate ratios are much larger in decoupled clouds, resulting in less hygroscopic aerosol particles.

3. Of the 35 cloud water constituents analyzed, 27 were higher in concentration in coupled clouds, with chloride, followed by sodium, being the most abundant owing to sea-salt emissions. The remaining eight constituents (acetate, formate, Si, nitrite, Al, Mn, Cr, and Co) that were more enhanced in decoupled clouds are consistent with the influence of continental air masses in the free troposphere of the region.

4. With exception of components associated with sea salt (*e.g.*, Cl, Na, Mg, and K), cloud water mass fractions of all species examined were higher in decoupled clouds relative to coupled clouds. Species with the largest enhancement in mass fraction in decoupled clouds included numerous carboxylic acids (glyoxylate, formate, oxalate, and acetate), nitrite, Si, and NSS Ca. Cloud water pH was also higher in decoupled clouds, which has implications for heterogeneous chemistry such as affecting sulfur oxidation rates (*e.g.*, Collett *et al.*, 1994).

5. Limitations in resolving boundary layer processes in a global model, based on NAAPS-based reanalysis data, prevent it from accurately quantifying observed differences between coupled and decoupled cloud composition.

Clouds detached from the surface layer are shown here to have significantly different cloud composition, which, in turn, impacts the nature of the chemical processing that takes place in those clouds, microphysical cloud properties, and the physicochemical properties of aerosol particles after cloud drop evaporation.

A p p e n d i x I

COMPOUNDS AND REACTIONS IN THE EXPLICIT ISOPRENE MECHANISM

functional group	abbreviation
carbonyl	CO
nitrate	N
hydroxy	OH
hydroperoxy	OOH
epoxide	##O[a]
alkyl radical	R
alkoxy radical	O
peroxy radical	OO
double bond	##[b]

Table I.1: Abbreviations for functional groups used in the naming of compounds in the explicit isoprene mechanism. [a]## are the two carbon numbers the epoxide is attached to; [b]## are the two carbon numbers the double bond is attached to.

Table I.2: Names used for compounds in the explicit isoprene mechanism. Italics denote radical species; bold font denotes species with no further chemistry in the model.

common / IUPAC name	our name	MCM name
Isoprene	ISOP	C5H8
cis-OH-isoprene-adduct 1 addition	*ISOP1OHc*	CISOPA
trans-OH-isoprene-adduct 1 addition	*ISOP1OHt*	TISOPA
cis-OH-isoprene-adduct 4 addition	*ISOP4OHc*	CISOPC
trans-OH-isoprene-adduct 1 addition	*ISOP4OHt*	TISOPC
E-(4,1)-ISOPOO	*ISOP1OO4OHt*	ISOPCO2
Z-(4,1)-ISOPOO	*ISOP1OO4OHc*	CISOPCO2
Z-(1,4)-ISOPOO	*ISOP1OH4OOc*	CISOPAO2
E-(1,4)-ISOPOO	*ISOP1OH4OOt*	ISOPAO2
(1,2)-ISOPOO	ISOP1OH2OO	*ISOPBO2*
(4,3)-ISOPOO	ISOP3OO4OH	*ISOPDO2*
peroxy radical from ISOP1OH4OO + NO (major)	*ISOP1CO2OO3OOH4OH*	C526O2
peroxy radical from ISOP1OH4OO + NO (minor)	*ISOP1CO2OOH3OO4OH*	-
peroxy radical from ISOP1OH4OO + NO (major)	*ISOP1OH2OO3OOH4CO*	-
peroxy radical from ISOP1OO4OH + NO (minor)	*ISOP1OH2OOH3OO4CO*	C527O2
RO_2 + RO_2 PRODUCTS		
(1,2)-isoprene diol	**ISOP1OH2OH**	ISOPBOH
(3,4)-isoprene diol	**ISOP3OH4OH**	ISOPDOH
(1,4)-isoprene diol	**ISOP1OH4OH**	ISOPAOH
1-hydroxy-3-methylbut-3-en-2-one	ISOP3CO4OH	HCOC5
4-hydroxy-2-methylbute-2-en-1-al	ISOP1CO4OH	HC4CCHO
4-hydroxy-3-methylbute-2-en-1-al	ISOP1OH4CO	HC4ACHO
peroxy radical from ISOP3CO4OH	*ISOP1OH2OO3CO4OH*	C59O2
3-hydroperoxy-1,4-dihydroxy-3-methylbutan-2-one	**ISOP1OH2OOH3CO4OH**	C59OOH
1,4-dihydroxy-3-methyl-3-nitrooxybutan-2-one	**ISOP1OH2N3CO4OH**	-
ISOPOOH		
(1,2)-ISOPOOH	ISOP1OH2OOH	ISOPBOOH

continued on next page

continued from previous page

common / IUPAC name	our name	MCM name
(4,3)-ISOPOOH	ISOP3OOH4OH	ISOPDOOH
(1,4)-ISOPOOH	ISOP1OOH4OH	ISOPCOOH
(4,1)-ISOPOOH	ISOP1OH4OOH	ISOPAOOH
alkoxy radical from (1,2)-ISOPOOH + OH	*ISOP1OH2OOH3R4OH*	-
alkoxy radical from (4,3)-ISOPOOH + OH	*ISOP1OH2R3OOH4OH*	-
peroxy radical from (1,2)-ISOPOOH + OH (major)	*ISOP1OH2OOH3OO4OH*	-
peroxy radical from (1,2)-ISOPOOH + OH (minor)	*ISOP1OH2OOH3OH4OO*	-
peroxy radical from (1,2)-ISOPOOH + OH (minor)	*ISOP1OH2OO3OH4OOH*	-
peroxy radical from (4,3)-ISOPOOH + OH (major)	*ISOP1OH2OO3OOH4OH*	-
peroxy radical from (4,3)-ISOPOOH + OH (minor)	*ISOP1OO2OH3OOH4OH*	-
peroxy radical from (4,3)-ISOPOOH + OH (minor)	*ISOP1OOH2OH3OO4OH*	-
isoprene 2,4-diperoxy-1,3-diol; $ISOP(OOH)_2$	**ISOP1OH2OOH3OH4OOH**	-
isoprene 1,3-diperoxy-2,4-diol; $ISOP(OOH)_2$	**ISOP1OOH2OH3OOH4OH**	-
isoprene 2,3-diperoxy-1,4-diol; $ISOP(OOH)_2$	**ISOP1OH2OOH3OOH4OH**	-
3-hydroperoxy-2,4-hydroxy-3-methylbutanal	**ISOP1OH2OOH3OH4CO**	C58OOH
2-hydroperoxy-3-methyl-4-nitrooxybutane-1,3-diol	**ISOP1N2OH3OOH4OH**	INCOOH
2-hydroperoxy-2-methyl-4-nitrooxybutane-1,3-diol	**ISOP1OH2OOH3OH4N**	INAOOH
4-hydroperoxy-2-methyl-2-nitrooxybutane-1,3-diol	**ISOP1OH2N3OH4OOH**	INB2OOH
4-hydroperoxy-3-methyl-2-nitrooxybutane-1,3-diol	**ISOP1OOH2OH3N4OH**	-
2-hydroperoxy-2-methyl-3-nitrooxybutane-1,4-diol	**ISOP1OH2OOH3N4OH**	INDOOH
3-hydroperoxy-2-methyl-2-nitrooxybutane-1,4-diol	**ISOP1OH2N3OOH4OH**	INB1OOH
IEPOX AND OTHER EPOXIDES		
trans-β-IEPOX	ISOP1OH23O4OHt	IEPOXB
cis-β-IEPOX	ISOP1OH23O4OHc	IEPOXB
δ1-IEPOX	ISOP1OH2OH34O	IEPOXA
δ4-IEPOX	ISOP12O3OH4OH	IEPOXC
1,2-epoxy-3-hydroperoxy-2-methylbutane-1,4-diol	**ISOP1OH12O3OOH4OH**	-
1,2-epoxy-3-hydroperoxy-3-methylbutane-1,4-diol	**ISOP1OH2OOH34O4OH**	-
2,3-epoxy-3-methyl-4-nitrooxybutan-1-ol	ISOP1N23O4OH	-
2,3-epoxy-2-methyl-4-nitrooxybutan-1-ol	ISOP1OH23O4N	-
3,4-epoxy-2-methyl-1-nitrooxybutan-2-ol	ISOP1N2OH34O	-
3,4-epoxy-3-methyl-1-nitrooxybutan-2-ol	ISOP12O3OH4N	-
3,4-epoxy-1-hydroperoxy-3-methylbutan-2-ol	**ISOP12O3OH4OOH**	-

continued on next page

continued from previous page

common / IUPAC name	our name	MCM name
3,4-epoxy-1-hydroperoxy-2-methylbutan-2-ol	**ISOP1OOH2OH34O**	-
2,3-epoxy-4-hydroxy-3-methylbutanal	**ISOP1OH23O4CO**	IEB4CHO
2,3-epoxy-4-hydroxy-2-methylbutanal	**ISOP1CO23O4OH**	IEB1CHO
3,4-epoxy-2-hydroxy-3-methylbutanal	**ISOP12O3OH4CO**	IECCHO
3,4-epoxy-1-hydroxy-3-methylbutan-2-one	**ISOP12O3CO4OH**	-
3,4-epoxy-2-hydroxy-2-methylbutanal	**ISOP1CO2OH34O**	IEACHO
2,3-epoxy-3-methyl-4-nitrooxybutanal	**ISOP1N23O4CO**	-
2,3-epoxy-2-methyl-4-nitrooxybutanal	**ISOP1CO23O4N**	-
1,2-epoxy-2-methylbut-3-en-1-ol	**ISOP1OH12O**	-
3,4-epoxy-2-methylbut-1-en-1-al	**ISOP121CO34O**	-
3,4-epoxy-3-methylbut-1-en-1-al	**ISOP12O344CO**	-
alkyl radical from *cis*-β-IEPOX (major)	*ISOP1OH1R23O4OHc*	-
alkyl radical from *cis*-β-IEPOX (minor)	*ISOP1OH23O4R4OHc*	-
alkyl radical from *trans*-β-IEPOX (major)	*ISOP1OH1R23O4OHt*	-
alkyl radical from *trans*-β-IEPOX (minor)	*ISOP1OH23O4R4OHt*	-
alkyl radical from δ4-IEPOX	*ISOP12O3OH3R4OH*	-
alkyl radical from β-INHE (major)	*ISOP1OH1R23O4N*	-
alkyl radical from β-INHE (minor)	*ISOP1N23O4OH4R*	-
alkyl radical from δ4-INHE	*ISOP12O3OH3R4N*	-
2,4-dihydroxy-3-methylbutanal	**ISOP1OH3OH4CO**	-
ISOPOO ISOMERIZATION AND HPALD		
HPALD1 (from *Z*-(1,4)-ISOPOO)	ISOP1CO4OOHc	C5HPALD1
HPALD2 (from *Z*-(4,1)-ISOPOO)	ISOP1OOH4COc	C5HPALD2
HPALD from (1,2)-ISOPOOH	**ISOP1CO2OOH**	-
HPALD from (4,3)-ISOPOOH	**ISOP3OOH4CO**	-
alkyl radical from HPALD1 + OH addition	*ISOP1CO2OH3R4OOH*	-
alkyl radical from HPALD1 + OH abstraction	*ISOP1CO3R4OOH*	-
alkyl radical from HPALD2 + OH addition	*ISOP1OOH2R3OH4CO*	-
alkyl radical from HPALD2 + OH abstraction	*ISOP1OOH2R4CO*	-
peroxy radical from HPALD1 + OH abstraction	*ISOP1CO4OOc*	-
peroxy radical from HPALD1 + OH abstraction	*ISOP1CO2OO*	-
peroxy radical from HPALD1 + OH addition (major)	*ISOP1CO2OO3OH4OOH*	-
peroxy radical from HPALD1 + OH addition (minor)	*ISOP1CO2OH3OO4OOH*	-

continued on next page

continued from previous page

common / IUPAC name	our name	MCM name
peroxy radical from HPALD2 + OH abstraction	*ISOP1OO4COc*	-
peroxy radical from HPALD2 + OH abstraction	*ISOP3OO4CO*	-
peroxy radical from HPALD2 + OH addition (major)	*ISOP1OOH2OO3OH4CO* -	HPC52O2
peroxy radical from HPALD2 + OH addition (minor)	*ISOP1OOH2OH3OO4CO*	-
peroxy radical from 1,6 H-shift of ISOP1OH4OOc	*ISOP1CO2OO3OOH4OOH*	C536O2
peroxy radical from 1,6 H-shift of ISOP1OH4OOc	*ISOP1CO2OOH3OO4OOH*	-
peroxy radical from 1,6 H-shift of ISOP1OH4OOc	*ISOP1CO2OOH3OOH4OO*	-
peroxy radical from 1,6 H-shift of ISOP1OO4OHc	*ISOP1OOH2OOH3OO4CO*	C537O2
peroxy radical from 1,6 H-shift of ISOP1OO4OHc	*ISOP1OOH2OO3OOH4CO*	-
peroxy radical from 1,6 H-shift of ISOP1OO4OHc	*ISOP1OO2OOH3OOH4CO*	-
C_5 peroxy acid aldehyde (PACALD) from HPALD1	**ISOP1CO1OOH4CO**	C5PACALD1
C_5 peroxy acid aldehyde (PACALD) from HPALD2	**ISOP1CO4CO4OOH**	C5PACALD2
C_5 ketene peroxy radical from HPALD1	*ISOP121CO3OO4OOH*	-
C_5 ketene peroxy radical from HPALD2	*ISOP1OOH2OO344CO*	-
C_4 hydroxy vinyl peroxy radical from HPALD1	C4HVP1	-
C_4 hydroxy vinyl peroxy radical from HPALD2	C4HVP2	-
2-methylbut-2-ene-1,4-dial	**ISOP1CO4CO**	C4MDIAL
3,4-dihydroperoxy-2-methyl-2-nitrooxybutanal	**ISOP1CO2N3OOH4OOH**	-
2,4-dihydroperoxy-2-methyl-3-nitrooxybutanal	**ISOP1CO2OOH3N4OOH**	-
2,3-dihydroperoxy-2-methyl-4-nitrooxybutanal	**ISOP1CO2OOH3OOH4N**	-
3,4-dihydroperoxy-3-methyl-2-nitrooxybutanal	**ISOP1OOH2OOH3N4CO**	-
2,4-dihydroperoxy-3-methyl-3-nitrooxybutanal	**ISOP1OOH2N3OOH4CO**	-
2,3-dihydroperoxy-3-methyl-4-nitrooxybutanal	**ISOP1N2OOH3OOH4CO**	-
2,3,4-trihydroperoxy-2-methylbutanal	**ISOP1CO2OOH3OOH4OOH**	C536OOH
2,3,4-trihydroperoxy-3-methylbutanal	**ISOP1OOH2OOH3OOH4CO**	C537OOH
DAYTIME NITRATES		
(1,2) β isoprene hydroxy nitrate (IHN)	ISOP1OH2N	ISOPBNO3
(4,3) β isoprene hydroxy nitrate (IHN)	ISOP3N4OH	ISOPDNO3
Z-δ (1,4) isoprene hydroxy nitrate (IHN)	ISOP1OH4Nc	ISOPANO3
E-δ (1,4) isoprene hydroxy nitrate (IHN)	ISOP1OH4Nt	ISOPANO3
Z-δ (4,1) isoprene hydroxy nitrate (IHN)	ISOP1N4OHc	ISOPCNO3
E-δ (4,1) isoprene hydroxy nitrate (IHN)	ISOP1N4OHt	ISOPCNO3
alkyl radical from (1,2)-IHN + OH	*ISOP1OH2N3R4OH*	-

continued on next page

continued from previous page

common / IUPAC name	our name	MCM name
alkyl radical from (4,3)-IHN + OH	*ISOP1OH2R3N4OH*	-
peroxy radical from (1,2)-IHN + OH	*ISOP1OH2N3OO4OH*	INB1O2
peroxy radical from (1,2)-IHN + OH	*ISOP1OH2N3OH4OO*	INB2O2
peroxy radical from (4,3)-IHN + OH	*ISOP1OH2OO3N4OH*	INDO2
peroxy radical from (4,3)-IHN + OH	*ISOP1OO2OH3N4OH*	-
3-hydroperoxy-4-hydroxy-3-methyl-2-nitrooxybutanal	**ISOP1OH2OOH3N4CO**	C527NO3
3-hydroperoxy-4-hydroxy-2-methyl-2-nitrooxybutanal	**ISOP1CO2N3OOH4OH**	C526NO3
2-hydroperoxy-4-hydroxy-2-methyl-3-nitrooxybutanal	**ISOP1CO2OOH3N4OH**	INDHPCHO
2-hydroperoxy-4-hydroxy-3-methyl-3-nitrooxybutanal	**ISOP1OH2N3OOH4CO**	INB1HPCHO
4-hydroperoxy-3-hydroxy-2-methyl-2-nitrooxybutanal	**ISOP1CO2N3OH4OOH**	-
4-hydroperoxy-3-hydroxy-3-methyl-2-nitrooxybutanal	**ISOP1OOH2OH3N4CO**	-
2-methyl-2,3-dinitrooxybutane-1,4-diol	**ISOP1OH2N3N4OH**	INB1NO3
2-methyl-2,4-dinitrooxybutane-1,3-diol	**ISOP1OH2N3OH4N**	INANO3
3-methyl-2,4-dinitrooxybutane-1,3-diol	**ISOP1N2OH3N4OH**	INCNO3
2,3-dihydroperoxy-4-hydroxy-2-methylbutanal	**ISOP1CO2OOH3OOH4OH**	C526OOH
2,3-dihydroperoxy-4-hydroxy-3-methylbutanal	**ISOP1OH2OOH3OOH4CO**	C527OOH
NIGHTTIME NITRATES		
peroxy radical from isoprene + NO_3	*ISOP1N2OO*	-
peroxy radical from isoprene + NO_3	*ISOP1N4OO*	NISOPO2
peroxy radical from isoprene + NO_3	*ISOP3OO4N*	-
peroxy radical from isoprene + NO_3	*ISOP1OO4N*	-
alkoxy radical from ISOP1N4OO	*ISOP1N4O*	NISOPO
alkoxy radical from ISOP1OO4N	*ISOP1O4N*	-
(2,1) isoprene hydroperoxy nitrate (IPN)	ISOP1N2OOH	-
(4,1) isoprene hydroperoxy nitrate (IPN)	ISOP1N4OOH	NISOPOOH
(3,4) isoprene hydroperoxy nitrate (IPN)	ISOP3OOH4N	-
(1,4) isoprene hydroperoxy nitrate (IPN)	ISOP1OOH4N	-
(2,1) isoprene hydroxy nitrate (IHN)	ISOP1N2OH	-
(3,4) isoprene hydroxy nitrate (IHN)	ISOP3OH4N	ISOP34NO3
(4,1) isoprene carbonyl nitrate (ICN)	ISOP1N4CO	NC4CHO
(1,4) isoprene carbonyl nitrate (ICN)	ISOP1CO4N	-
(3,4) isoprene carbonyl nitrate (ICN)	ISOP3CO4N	-
(1,2) isoprene dinitrate	**ISOP1N2N**	-

continued on next page

continued from previous page

common / IUPAC name	our name	MCM name
(1,4) isoprene dinitrate	**ISOP1N4N**	NISOPNO3
(3,4) isoprene dinitrate	**ISOP3N4N**	-
alkyl radical from (1,4)-IHN + OH	*ISOP1OH2OH3R4N*	-
alkyl radical from (4,1)-IHN + OH	*ISOP1N2R3OH4OH*	-
alkyl radical from (2,1)-IPN + OH	*ISOP1N2OOH3R4OH*	-
alkyl radical from (4,1)-IPN + OH (major)	*ISOP1N2OH3R4OOH*	-
alkyl radical from (4,1)-IPN + OH (minor)	*ISOP1N2R3OH4OOH*	-
alkyl radical from (3,4)-IPN + OH	*ISOP1OH2R3OOH4N*	-
alkyl radical from (1,4)-IPN + OH (major)	*ISOP1OOH2R3OH4N*	-
alkyl radical from (1,4)-IPN + OH (minor)	*ISOP1OOH2OH3R4N*	-
alkyl radical from (4,1)-ICN + OH	*ISOP1N2R3OH4CO*	-
alkyl radical from (1,4)-ICN + OH	*ISOP1CO2OH3R4N*	-
alkyl radical from (4,1)-ICN + OH	*ISOP1N4R4CO*	-
alkyl radical from (1,4)-ICN + OH	*ISOP1CO1R4N*	-
peroxy radical from (4,1)-IHN + OH (major)	*ISOP1N2OO3OH4OH*	-
peroxy radical from (4,1)-IHN + OH (minor)	*ISOP1N2OH3OO4OH*	INCO2
peroxy radical from (1,4)-IHN + OH (major)	*ISOP1OH2OO3OH4N*	INAO2
peroxy radical from (1,4)-IHN + OH (minor)	*ISOP1OH2OH3OO4N*	-
peroxy radical from (3,4)-IHN + OH	*ISOP1OO2OH3OH4N*	-
peroxy radical from (2,1)-IHN + OH	*ISOP1N2OH3OH4OO*	-
peroxy radical from (2,1)-IPN + OH (major)	*ISOP1N2OO3OOH4OH*	-
peroxy radical from (2,1)-IPN + OH (minor)	*ISOP1N2OOH3OO4OH*	-
peroxy radical from (2,1)-IPN + OH (minor)	*ISOP1N2OOH3OH4OO*	-
peroxy radical from (4,1)-IPN + OH (major)	*ISOP1N2OO3OH4OOH*	-
peroxy radical from (4,1)-IPN + OH (minor)	*ISOP1N2OH3OO4OOH*	-
peroxy radical from (4,1)-IPN + OH (minor)	*ISOP1N2OH3OOH4OO*	-
peroxy radical from (3,4)-IPN + OH (major)	*ISOP1OH2OO3OOH4N*	-
peroxy radical from (3,4)-IPN + OH (minor)	*ISOP1OH2OOH3OO4N*	-
peroxy radical from (3,4)-IPN + OH (minor)	*ISOP1OO2OH3OOH4N*	-
peroxy radical from (1,4)-IPN + OH (major)	*ISOP1OOH2OO3OH4N*	-
peroxy radical from (1,4)-IPN + OH (minor)	*ISOP1OOH2OH3OO4N*	-
peroxy radical from (1,4)-IPN + OH (minor)	*ISOP1OO2OOH3OH4N*	-
peroxy radical from (4,1)-ICN + OH (major)	*ISOP1N2OO3OH4CO*	C510O2

continued on next page

continued from previous page

common / IUPAC name	our name	MCM name
peroxy radical from (4,1)-ICN + OH (minor)	*ISOP1N2OH3OO4CO*	-
peroxy radical from (4,1)-ICN + OH (minor)	*ISOP1N2OO344CO*	-
peroxy radical from (4,1)-ICN + OH (minor)	*ISOP1N4CO4OO*	NC4CO3
peroxy radical from (1,4)-ICN + OH (major)	*ISOP1CO2OO3OH4N*	-
peroxy radical from (1,4)-ICN + OH (minor)	*ISOP1CO2OH3OO4N*	-
peroxy radical from (1,4)-ICN + OH (minor)	*ISOP121CO3OO4N*	-
peroxy radical from (1,4)-ICN + OH (minor)	*ISOP1CO1OO4N*	-
peroxy radical from (1,4)-INHE + OH	*ISOP1OH2OO3CO4N*	-
peroxy radical from (4,1)-INHE + OH	*ISOP1N2OO3CO4OH*	-
C_4 nitrooxy vinyl peroxy radical from (1,4)-ICN	*C4NVP1*	-
C_4 nitrooxy vinyl peroxy radical from (4,1)-ICN	*C4NVP2*	-
3-methyl-3,4-dinitrooxybutane-1,2-diol	**ISOP1N2N3OH4OH**	-
2-methyl-3,4-dinitrooxybutane-1,2-diol	**ISOP1OH2OH3N4N**	-
2-methyl-1,4-dinitrooxybutane-2,3-diol	**ISOP1N2OH3OH4N**	-
3-hydroperoxy-3-methyl-4-nitrooxybutane-1,2-diol	**ISOP1N2OOH3OH4OH**	-
4-hydroperoxy-2-methyl-4-nitrooxybutane-1,2-diol	**ISOP1OH2OH3OOH4N**	-
4-hydroperoxy-2-methyl-1-nitrooxybutane-2,3-diol	**ISOP1N2OH3OH4OOH**	-
1-hydroperoxy-2-methyl-4-nitrooxybutane-2,3-diol	**ISOP1OOH2OH3OH4N**	-
3-hydroperoxy-3-methyl-2,4-dinitrooxybutan-1-ol	**ISOP1N2OOH3N4OH**	-
3-hydroperoxy-3-methyl-1,4-dinitrooxybutan-2-ol	**ISOP1N2OOH3OH4N**	-
4-hydroperoxy-2-methyl-1,3-dinitrooxybutan-2-ol	**ISOP1N2OH3N4OOH**	-
1-hydroperoxy-3-methyl-3,4-dinitrooxybutan-2-ol	**ISOP1N2N3OH4OOH**	-
3-hydroperoxy-2-methyl-2,4-dinitrooxybutan-1-ol	**ISOP1OH2N3OOH4N**	-
3-hydroperoxy-2-methyl-1,4-dinitrooxybutan-2-ol	**ISOP1N2OH3OOH4N**	-
4-hydroperoxy-3-methyl-1,3-dinitrooxybutan-2-ol	**ISOP1OOH2N3OH4N**	-
1-hydroperoxy-2-methyl-3,4-dinitrooxybutan-2-ol	**ISOP1OOH2OH3N4N**	-
2-hydroperoxy-3-methyl-3,4-dinitrooxybutan-1-ol	**ISOP1N2N3OOH4OH**	-
2-hydroperoxy-2-methyl-3,4-dinitrooxybutan-1-ol	**ISOP1OH2OOH3N4N**	-
3-methyl-3,4-dinitrooxybut-1-enal	**ISOP1N2N344CO**	-
2-methyl-3,4-dinitrooxybut-1-enal	**ISOP121CO3N4N**	-
1,3-dihydroperoxy-2-methyl-4-nitrooxybutan-2-ol	**ISOP1OOH2OH3OOH4N**	-
3,4-dihydroperoxy-3-methyl-1-nitrooxybutan-2-ol	**ISOP1OOH2OOH3OH4N**	-
2,3-dihydroperoxy-2-methyl-4-nitrooxybutan-1-ol	**ISOP1OH2OOH3OOH4N**	-

continued on next page

continued from previous page

common / IUPAC name	our name	MCM name
1,3-dihydroperoxy-3-methyl-4-nitrooxybutan-2-ol	**ISOP1N2OOH3OH4OOH**	-
3,4-dihydroperoxy-2-methyl-1-nitrooxybutan-2-ol	**ISOP1N2OH3OOH4OOH**	-
2,3-dihydroperoxy-3-methyl-4-nitrooxybutan-1-ol	**ISOP1N2OOH3OOH4OH**	-
2-hydroperoxy-3-hydroxy-2-methyl-4-nitrooxybutanal	**ISOP1CO2OOH3OH4N**	INAHPCHO
2-hydroperoxy-3-hydroxy-3-methyl-4-nitrooxybutanal	**ISOP1N2OH3OOH4CO**	-
3-hydroperoxy-4-hydroxy-3-methyl-1-nitrooxybutan-2-one	**ISOP1OH2OOH3CO4N**	-
3-hydroperoxy-1-hydroxy-3-methyl-4-nitrooxybutan-2-one	**ISOP1N2OOH3CO4OH**	-
3-methyl-4-nitrooxybut-1-enoic acid	**ISOP1N4CO4OH**	NC4CO2H
2-methyl-4-nitrooxybut-1-enoic acid	**ISOP1CO1OH4N**	-
3-methyl-4-nitrooxybut-1-enoic peracid	**ISOP1N4CO4OOH**	-
2-methyl-4-nitrooxybut-1-enoic peracid	**ISOP1CO1OOH4N**	-
3-hydroperoxy-3-methyl-4-nitrooxybut-1-enal	**ISOP1N2OOH344CO**	-
3-hydroperoxy-2-methyl-4-nitrooxybut-1-enal	**ISOP121CO3OOH4N**	-
3-hydroxy-2-methyl-2,4-dinitrooxybutanal	**ISOP1CO2N3OH4N**	INANCHO
3-hydroxy-3-methyl-2,4-dinitrooxybutanal	**ISOP1N2OH3N4CO**	INCNCHO
4-hydroxy-3-methyl-1,3-dinitrooxybutan-2-one	**ISOP1OH2N3CO4N**	INANCO
1-hydroxy-3-methyl-3,4-dinitrooxybutan-2-one	**ISOP1N2N3CO4OH**	INANCO
peroxyacyl nitrate from (4,1)-ICN	ISOP1N4PAN	-
peroxyacyl nitrate from (1,4)-ICN	ISOP1PAN4N	-
ROOR from ISOP1N2OO + ISOP1N4OO	**ISOP1N2OOISOP1N4**	-
ROOR from ISOP1N4OO + ISOP1N4OO	**ISOP1N4OOISOP1N4**	-
ROOR from ISOP3OO4N + ISOP1N4OO	**ISOP3OO4NISOP1N4**	-
ROOR from ISOP1OO4N + ISOP1N4OO	**ISOP1OO4NISOP1N4**	-
ROOR from ISOP1N2OO + ISOP1N2OO	**ISOP1N2OOISOP1N2**	-
ROOR from ISOP3OO4N + ISOP1N2OO	**ISOP3OO4NISOP1N2**	-
ROOR from ISOP1OO4N + ISOP1N2OO	**ISOP1OO4NISOP1N2**	-
peroxy radical from ISOP1N4O isomerization	*ISOP1N25_3OO4OH*	-
alkoxy radical from ISOP1N25_3OO4OH	*ISOP1N25_3O4OH*	-
3-hydroperoxy-4-hydroxy-2-nitrooxymethylbut-1-ene	**ISOP1N25_3OOH4OH**	-
3,4-dihydroxy-2-nitrooxymethylbut-1-ene	**ISOP1N25_3OH4OH**	-
1-hydroxy-3-nitrooxymethylbut-3-en-2-one	**ISOP1N25_3CO4OH**	-
4-hydroxy-3-nitrooxy-2-nitrooxymethylbut-1-ene	**ISOP1N25_3N4OH**	-
ROOR from ISOP1N25_3OO4OH + ISOP1N4OO	**ISOP1N25_3OO4OHISOP1N4**	-

continued on next page

continued from previous page

common / IUPAC name	our name	MCM name
ROOR from ISOP1N25_3OO4OH + ISOP1N2OO	**ISOP1N25_3OO4OHISOP1N2**	-
MPAN		
Methacryloyl peroxynitrate	MPAN	MPAN
energetically hot alkyl radical of MPAN	*MPAN1OHx*	-
stabilized alkyl radical of MPAN	*MPAN1OH*	-
peroxy radical from MPAN1OH	*MPAN1OH2OO*	-
alkoxy radical from MPAN1OH2OO	*MPAN1OH2O*	-
MPAN hydroperoxynitrate	**MPAN1OH2OOH**	-
Energetically hot HMML	HMMLx	-
Hydroxymethyl methyl-α-lactone	**HMML**	HMML
2-oxopropanoyl peroxynitrate	**CH3COCOON**	CH3COPAN
OZONE CHEMISTRY		
C1 Stabilized Criegee	ciCH2OO	CH2OOE
C4 Stabilized Criegee, structure MACR	ciMACROO	MACROOA
C4 Stabilized Criegee, structure MVK	ciMVKOO	MVKOOA
Hydroxymethyl hydroperoxide	HMHP	-
Hydroperoxy methyl formate	HPMF	CHOOCH2OOH
Formic anhydride	FAH	CHOOCHO
Water dimer	H2Od	-
METHACROLEIN DERIVATIVES		
Methacrolein	MACR	MACR
peroxy radical from MACR + OH (major)	*MACR2OO3OH*	MACRO2
peroxy radical from MACR + OH (minor)	*MACR2OH3OO*	MACROHO2
peroxy radical from MACR + OH (abstraction)	*MACR1OO*	MACO3
2-hydroperoxy-3-hydroxy-2-methylpropanal	**MACR2OOH3OH**	MACROOH
3-hydroperoxy-2-hydroxy-2-methylpropanal	**MACR2OH3OOH**	MACROHOOH
Methacrylic acid	**MACR1OH**	MACO2H
Methacrylic peracid	**MACR1OOH**	MACO3H
2-nitrooxymethylacrolein	**MACR3N**	-
peroxy radical from C4NVP2	*MACR2OO3N*	-
2,3-dinitrooxy-2-methylpropanal	**MACR2N3N**	-
3-hydroxy-2-methyl-2-nitrooxypropanal	**MACR2N3OH**	MACRNO3

continued on next page

continued from previous page

common / IUPAC name	our name	MCM name
2-hydroxy-2-methyl-3-nitrooxypropanal	**MACR2OH3N**	MACRNB
2-hydroperoxy-2-methyl-3-nitrooxypropanal	**MACR2OOH3N**	-
2,3-dihydroperoxy-2-methylpropanal	**MACR2OOH3OOH**	DHPMPAL
2,3-dihydroxy-2-methylpropanal	MACR2OH3OH	MACROH
2-hydroxy-2-methylpropane-1,3-dial	MACR2OH3CO	C3MDIALOH
1-Hydroperoxy-2-methyl-2-propen-1-ol	**MACR3OH3OOH**	-
2-hydroperoxy-2-methylpropane-1,3-dial	MACR2OOH3CO	C3MDIALOOH
3-hydroxy-2-methylprop-2-enal	MACRENOL	HMAC
2-methylpropene-1,3-dial	MACR3CO	-
MVK DERIVATIVES		
Methyl vinyl ketone	MVK	MVK
peroxy radical from MVK + OH (major)	*MVK3OO4OH*	HMVKBO2
peroxy radical from MVK + OH (minor)	*MVK3OH4OO*	HMVKAO2
3,4-dihydroperoxybutan-2-one	**MVK3OOH4OOH**	DHPMEK
3-hydroperoxy-4-hydroxybutan-2-one	MVK3OOH4OH	HMVKBOOH
4-hydroperoxy-3-hydroxybutan-2-one	**MVK3OH4OOH**	HMVKAOOH
2-Hydroperoxy-3-buten-2-ol	**MVK3OH3OOH**	-
3-hydroxy-4-nitrooxybutan-2-one	MVK3OH4N	HMVKANO3
4-hydroxy-3-nitrooxybutan-2-one	MVK3N4OH	MVKNO3
3-hydroperoxy-4-nitrooxybutan-2-one	**MVK3OOH4N**	-
3,4-dihydroxybutan-2-one	MVK3OH4OH	HO12CO3C4
1-hydroxybutane-2,3-dione	MVK3CO4OH	BIACETOH
1-nitrooxybutane-2,3-dione	**MVK3CO4N**	CO2C4NO3
peroxy radical from C4NVP1	*MVK3OO4N*	-
3,4-dinitrooxybutan-2-one	**MVK3N4N**	-
2-hydroxy-3-oxobutanal	MVK3OH4CO	CO2H3CHO
2-hydroperoxy-3-oxobutanal	MVK3OOH4CO	C4CO2OOH
4-hydroxybut-3-en-2-one	MVKENOL	HVMK
peroxy radical from MVKENOL + OH	*MVK3OO4OH4OH*	-
3-oxobut-1-enal	MVK4CO	-
peroxy radical from MVK4CO	*MVK3OO4CO4OH*	-
SMALL PRODUCTS		

continued on next page

continued from previous page

common / IUPAC name	our name	MCM name
Formaldehyde	**HCHO**	HCHO
Glycolaldehyde	**GLYC**	HOCH2CHO
Methylglyoxal	**MGLY**	MGLYOX
Peroxyacetyl radical (PA)	***CH3CO3***	CH3CO3
Hydroxyperacetyl radical	***HPA***	HOCH2CO3
Nitrooxyperacetyl radical	***NPA***	NO3CH2CO3
Hydroxyacetone	**HAC**	ACETOL
Glyoxal	**GLYX**	GLYOX
Hydroperoxyacetone	**HPAC**	HYPERACET
Hydroperoxyethanal	**HPETHNL**	HCOCH2OOH
Methyl peroxy radical	*CH3OO*	CH3O2
Methoxy radical	***CH3O***	CH3O
Methanol	**CH3OH**	CH3OH
Formic acid	HCOOH	HCOOH
Ethanal nitrate	**ETHLN**	NO3CH2CHO
Propanone nitrate	**PROPNN**	NOA
2-peroxypropene radical	***CH3COOCH2***	CH3C2H2O2
Pyruvic acid	PYRAC	**CH3COCO2H**
1,1-dihydroxyacetone	DHA	-

Table I.3: Reactions included in the explicit isoprene mechanism, written in a syntax readable by the Kinetic PreProcessor (KPP). Each line is written "REACTANT + REACTANT = PRODUCTS : RATE COEFFICIENT ;\". Product and reactant names are given in Table I.2; rates coefficients are written in standard Arrhenius form unless they fall into one of the four alternative rate categories detailed in Chapter 4. Lines in bold denote section headings, while lines in italics denote epoxide formation reactions, for which alternate formulations can be found in Table I.4.

//OH Oxidation of Isoprene
ISOP + OH = ISOP1OHc : 2.7e-11*exp(390/T)*0.64*0.5;\
ISOP + OH = ISOP1OHt : 2.7e-11*exp(390/T)*0.64*0.5;\
ISOP + OH = ISOP4OHc : 2.7e-11*exp(390/T)*0.36*0.7;\
ISOP + OH = ISOP4OHt : 2.7e-11*exp(390/T)*0.36*0.3;\
//Reversible Addition of O2
ISOP4OHt + O2 = ISOP1OO4OHt : 5.3e-13;\
ISOP4OHt + O2 = ISOP3OO4OH : 7.1e-13;\
ISOP4OHc + O2 = ISOP1OO4OHc : 2.3e-13;\
ISOP4OHc + O2 = ISOP3OO4OH : 7.1e-13;\
ISOP1OHc + O2 = ISOP1OH4OOc : 1.4e-13;\
ISOP1OHc + O2 = ISOP1OH2OO : 7.8e-13;\
ISOP1OHt + O2 = ISOP1OH4OOt : 3.7e-13;\
ISOP1OHt + O2 = ISOP1OH2OO : 7.8e-13;\
ISOP1OO4OHt = ISOP4OHt : 2.08e14*exp(-9400/T);\
ISOP3OO4OH = ISOP4OHt : 2.49e15*exp(-10890/T);\
ISOP1OO4OHc = ISOP4OHc : 1.75e14*exp(-9054/T);\
ISOP3OO4OH = ISOP4OHc : 2.49e15*exp(-11112/T);\
ISOP1OH4OOc = ISOP1OHc : 1.79e14*exp(-8830/T);\
ISOP1OH2OO = ISOP1OHc : 2.22e15*exp(-10355/T);\
ISOP1OH4OOt = ISOP1OHt : 1.83e14*exp(-8930/T);\
ISOP1OH2OO = ISOP1OHt : 2.24e15*exp(-10865/T);\
// RO2 + NO
ISOP1OH2OO + NO = NO2 + MVK + HO2 + HCHO : k_alkoxy[2.7,350,1.190,6];\
ISOP1OH2OO + NO = ISOP1OH2N : k_nitrate[2.7,350,1.190,6];\
ISOP1OH4OOc + NO = NO2 + HO2 + ISOP1CO4OH : k_alkoxy[1.08,350,1.421,6];\
ISOP1OH4OOc + NO = NO2 + ISOP1CO2OO3OOH4OH : k_alkoxy[1.62,350,1.421,6];\
ISOP1OH4OOc + NO = ISOP1OH4Nc : k_nitrate[2.7,350,1.421,6];\
ISOP1OH4OOt + NO = NO2 + HO2 + ISOP1CO4OH : k_alkoxy[1.08,350,1.421,6];\
ISOP1OH4OOt + NO = NO2 + ISOP1CO2OO3OOH4OH : k_alkoxy[1.62,350,1.421,6];\
ISOP1OH4OOt + NO = ISOP1OH4Nt : k_nitrate[2.7,350,1.421,6];\
ISOP1CO2OO3OOH4OH = ISOP1CO2OOH3OO4OH: 3e6;\
ISOP1CO2OOH3OO4OH = ISOP1CO2OO3OOH4OH : 4e6;\
ISOP1CO2OO3OOH4OH + NO = NO2 + MGLY + GLYC + OH : k_alkoxy[2.7,350,22.270,9];\
ISOP1CO2OO3OOH4OH + NO = ISOP1CO2N3OOH4OH : k_nitrate[2.7,350,22.270,9];\
ISOP1CO2OO3OOH4OH = MVK3OOH4OH + CO + OH : 1e7*exp(-5000/T);\
ISOP1CO2OO3OOH4OH + HO2 = ISOP1CO2OOH3OOH4OH : 2.47e-13*exp(1300/T);\
ISOP1CO2OOH3OO4OH + NO = NO2 + MGLY + GLYC + OH : k_alkoxy[2.7,350,4.457,9];\
ISOP1CO2OOH3OO4OH + NO = ISOP1CO2OOH3N4OH : k_nitrate[2.7,350,4.457,9];\
ISOP1CO2OOH3OO4OH = MVK3OOH4OH + CO + OH : 4e8*exp(-5000/T);\
ISOP1CO2OOH3OO4OH + HO2 = ISOP1CO2OOH3OOH4OH : 2.47e-13*exp(1300/T);\
ISOP3OO4OH + NO = NO2 + MACR + HO2 + HCHO : k_alkoxy[2.7,350,1.297,6];\
ISOP3OO4OH + NO = ISOP3N4OH : k_nitrate[2.7,350,1.297,6];\
ISOP1OO4OHc + NO = NO2 + HO2 + ISOP1OH4CO : k_alkoxy[1.08,350,1.421,6];\
ISOP1OO4OHc + NO = NO2 + ISOP1OH2OOH3OO4CO : k_alkoxy[1.62,350,1.421,6];\
ISOP1OO4OHc + NO = ISOP1N4OHc : k_nitrate[2.7,350,1.421,6];\
ISOP1OO4OHt + NO = NO2 + HO2 + ISOP1OH4CO : k_alkoxy[1.08,350,1.421,6];\
ISOP1OO4OHt + NO = NO2 + ISOP1OH2OOH3OO4CO : k_alkoxy[1.62,350,1.421,6];\
ISOP1OO4OHt + NO = ISOP1N4OHt : k_nitrate[2.7,350,1.421,6];\
ISOP1OH2OOH3OO4CO = ISOP1OH2OO3OOH4CO : 4e6;\
ISOP1OH2OO3OOH4CO = ISOP1OH2OOH3OO4CO : 3e6;\
ISOP1OH2OOH3OO4CO + NO = NO2 + GLYX + HAC + OH : k_alkoxy[2.7,350,33.606,9];\
ISOP1OH2OOH3OO4CO + NO = ISOP1OH2OOH3N4CO : k_nitrate[2.7,350,33.606,9];\
ISOP1OH2OOH3OO4CO = MACR2OOH3OH + CO + OH : 1e7*exp(-5000/T);\
ISOP1OH2OOH3OO4CO + HO2 = ISOP1OH2OOH3OOH4CO : 2.47e-13*exp(1300/T);\
ISOP1OH2OO3OOH4CO + NO = NO2 + GLYX + HAC + OH : k_alkoxy[2.7,350,2.838,9];\

ISOP1OH2OO3OOH4CO + NO = ISOP1OH2N3OOH4CO : k_nitrate[2.7,350,2.838,9];\
ISOP1OH2OO3OOH4CO = MACR2OOH3OH + CO + OH : 4e8*exp(-5000/T);\
ISOP1OH2OO3OOH4CO + HO2 = ISOP1OH2OOH3OOH4CO : 2.47e-13*exp(1300/T);\
ISOP1CO4OH + OH = MVK3OH4OH + CO + OH : 2.7e-11*exp(390/T);\
ISOP1OH4CO + OH = MACR2OOH3OH + HO2 + CO : 2.7e-11*exp(390/T);\
ISOP3CO4OH + OH = ISOP1OH2OO3CO4OH : 2.7e-11*exp(390/T);\
ISOP1OH2OO3CO4OH + HO2 = ISOP1OH2OOH3CO4OH : 2.38e-13*exp(1300/T);\
ISOP1OH2OO3CO4OH + NO = ISOP1OH2N3CO4OH : k_nitrate[2.7,350,13.338,8];\
ISOP1OH2OO3CO4OH + NO = NO2 + HAC + HPA : k_alkoxy[2.7,350,13.338,8];\
//RO2 + Peroxy Radical
ISOP1OH2OO + ISOP1OH2OO = MVK + MVK + HO2 + HO2 + HCHO + HCHO : 6.92e-14;\
ISOP3OO4OH + ISOP3OO4OH = MACR + MACR + HO2 + HO2 + HCHO + HCHO : 5.74e-12*0.8;\
ISOP3OO4OH + ISOP3OO4OH = ISOP3CO4OH + ISOP3OH4OH : 5.74e-12*0.2;\
ISOP1OH2OO + ISOP3OO4OH = MVK + MACR + HO2 + HO2 + HCHO + HCHO : 3.08e-12*0.9;\
ISOP1OH2OO + ISOP3OO4OH = ISOP1OH2OH + ISOP3CO4OH : 3.08e-12*0.1;\
ISOP1OH2OO + ISOP1OO4OHc = MVK + HO2 + HCHO + HO2 + ISOP1OH4CO : 2.49e-12*0.805*0.4;\
ISOP1OH2OO + ISOP1OO4OHc = MVK + HO2 + HCHO + ISOP1OH2OOH3OO4CO : 2.49e-12*0.805*0.6;\
ISOP1OH2OO + ISOP1OO4OHc = ISOP1OH2OH + ISOP1CO4OH : 2.49e-12*(1-0.805);\
ISOP1OH2OO + ISOP1OO4OHt = MVK + HO2 + HCHO + HO2 + ISOP1OH4CO : 2.49e-12*0.805*0.4;\
ISOP1OH2OO + ISOP1OO4OHt = MVK + HO2 + HCHO + ISOP1OH2OOH3OO4CO : 2.49e-12*0.805*0.6;\
ISOP1OH2OO + ISOP1OO4OHt = ISOP1OH2OH + ISOP1CO4OH : 2.49e-12*(1-0.805);\
ISOP1OH2OO + ISOP1OH4OOc = MVK + HO2 + HCHO + HO2 + ISOP1CO4OH : 2.49e-12*0.805*0.4;\
ISOP1OH2OO + ISOP1OH4OOc = MVK + HO2 + HCHO + ISOP1CO2OO3OOH4OH : 2.49e-12*0.805*0.6;\
ISOP1OH2OO + ISOP1OH4OOc = ISOP1OH2OH + ISOP1OH4CO : 2.49e-12*(1-0.805);\
ISOP1OH2OO + ISOP1OH4OOt = MVK + HO2 + HCHO + HO2 + ISOP1CO4OH : 2.49e-12*0.805*0.4;\
ISOP1OH2OO + ISOP1OH4OOt = MVK + HO2 + HCHO + ISOP1CO2OO3OOH4OH : 2.49e-12*0.805*0.6;\
ISOP1OH2OO + ISOP1OH4OOt = ISOP1OH2OH + ISOP1OH4CO : 2.49e-12*(1-0.805);\
ISOP3OO4OH + ISOP1OO4OHc = MACR + HO2 + HCHO + HO2 + ISOP1OH4CO : 3.94e-12*0.705*0.4;\
ISOP3OO4OH + ISOP1OO4OHc = MACR + HO2 + HCHO + ISOP1OH2OOH3OO4CO : 3.94e-12*0.705*0.6;\
ISOP3OO4OH + ISOP1OO4OHc = ISOP3OH4OH + ISOP1CO4OH : 3.94e-12*(1-0.705)*0.5;\
ISOP3OO4OH + ISOP1OO4OHc = ISOP1OH4OH + ISOP3CO4OH : 3.94e-12*(1-0.705)*0.5;\
ISOP3OO4OH + ISOP1OO4OHt = MACR + HO2 + HCHO + HO2 + ISOP1OH4CO : 3.94e-12*0.705*0.4;\
ISOP3OO4OH + ISOP1OO4OHt = MACR + HO2 + HCHO + ISOP1OH2OOH3OO4CO : 3.94e-12*0.705*0.6;\
ISOP3OO4OH + ISOP1OO4OHt = ISOP3OH4OH + ISOP1CO4OH : 3.94e-12*(1-0.705)*0.5;\
ISOP3OO4OH + ISOP1OO4OHt = ISOP1OH4OH + ISOP3CO4OH : 3.94e-12*(1-0.705)*0.5;\
ISOP3OO4OH + ISOP1OH4OOc = MACR + HO2 + HCHO + HO2 + ISOP1CO4OH : 3.94e-12*0.705*0.4;\
ISOP3OO4OH + ISOP1OH4OOc = MACR + HO2 + HCHO + ISOP1CO2OO3OOH4OH : 3.94e-12*0.705*0.6;\
ISOP3OO4OH + ISOP1OH4OOc = ISOP3OH4OH + ISOP1OH4CO : 3.94e-12*(1-0.705)*0.5;\
ISOP3OO4OH + ISOP1OH4OOc = ISOP1OH4OH + ISOP3CO4OH : 3.94e-12*(1-0.705)*0.5;\
ISOP3OO4OH + ISOP1OH4OOt = MACR + HO2 + HCHO + HO2 + ISOP1CO4OH : 3.94e-12*0.705*0.4;\
ISOP3OO4OH + ISOP1OH4OOt = MACR + HO2 + HCHO + ISOP1CO2OO3OOH4OH : 3.94e-12*0.705*0.6;\
ISOP3OO4OH + ISOP1OH4OOt = ISOP3OH4OH + ISOP1OH4CO : 3.94e-12*(1-0.705)*0.5;\
ISOP3OO4OH + ISOP1OH4OOt = ISOP1OH4OH + ISOP3CO4OH : 3.94e-12*(1-0.705)*0.5;\
ISOP1OH2OO + CH3OO = MVK + CH3O + HO2 + HCHO : 2.00e-12*0.5;\
ISOP1OH2OO + CH3OO = ISOP1OH2OH + HCHO : 2.00e-12*0.5;\
ISOP3OO4OH + CH3OO = MACR + CH3O + HO2 + HCHO : 2.00e-12*0.5;\
ISOP3OO4OH + CH3OO = ISOP3OH4OH + HCHO : 2.00e-12*0.25;\
ISOP3OO4OH + CH3OO = ISOP3CO4OH + CH3OH : 2.00e-12*0.25;\
//RO2 + HO2 Radical
HO2 + ISOP1OH2OO = ISOP1OH2OOH + O2 : 2.12e-13*exp(1300/T)*0.937;\
HO2 + ISOP1OH2OO = MVK + OH + HO2 + HCHO : 2.12e-13*exp(1300/T)*0.063;\
HO2 + ISOP3OO4OH = ISOP3OOH4OH + O2 : 2.12e-13*exp(1300/T)*0.937;\
HO2 + ISOP3OO4OH = MACR + OH + HO2 + HCHO : 2.12e-13*exp(1300/T)*0.063;\
HO2 + ISOP1OO4OHc = ISOP1OOH4OH + O2 : 2.12e-13*exp(1300/T);\
HO2 + ISOP1OO4OHt = ISOP1OOH4OH + O2 : 2.12e-13*exp(1300/T);\
HO2 + ISOP1OH4OOc = ISOP1OH4OOH + O2 : 2.12e-13*exp(1300/T);\
HO2 + ISOP1OH4OOt = ISOP1OH4OOH + O2 : 2.12e-13*exp(1300/T);\
//Peroxy Isomerization
ISOP1OH4OOc = ISOP1CO4OOHc + HO2 : 0.34*k_tunneling[5.47e15,-12200,1e8];\
ISOP1OH4OOc = ISOP1CO2OO3OOH4OOH : 0.66*k_tunneling[5.47e15,-12200,1e8];\
ISOP1CO2OO3OOH4OOH = ISOP1CO2OOH3OO4OOH : 3e6;\
ISOP1CO2OO3OOH4OOH = ISOP1CO2OOH3OOH4OO : 2e6;\
ISOP1CO2OOH3OO4OOH = ISOP1CO2OO3OOH4OOH : 4e6;\
ISOP1CO2OOH3OO4OOH = ISOP1CO2OOH3OOH4OO : 2e6;\
ISOP1CO2OOH3OOH4OO = ISOP1CO2OO3OOH4OOH : 4e6;\
ISOP1CO2OOH3OOH4OO = ISOP1CO2OOH3OO4OOH : 3e6;\
ISOP1CO2OO3OOH4OOH = MVK3OOH4OOH + OH + CO : 1e7*exp(-5000/T);\
ISOP1CO2OOH3OO4OOH = MVK3OOH4OOH + OH + CO : 4e8*exp(-5000/T);\
ISOP1CO2OOH3OOH4OO = MVK3OOH4OOH + OH + CO : 1e8*exp(-5000/T);\
ISOP1CO2OO3OOH4OOH + NO = ISOP1CO2N3OOH4OOH : k_nitrate[2.7,350,20.511,10];\
ISOP1CO2OO3OOH4OOH + NO = NO2 + CO + HO2 + MVK3OOH4OOH : k_alkoxy[0.54,350,20.511,10];\
ISOP1CO2OO3OOH4OOH + NO = NO2 + OH + MGLY + HPETHNL : k_alkoxy[2.16,350,20.511,10];\
ISOP1CO2OO3OOH4OOH + HO2 = OH + OH + MGLY + HPETHNL : 0.58*2.54e-13*exp(1300/T);\

ISOP1CO2OO3OOH4OOH + HO2 = OH + CO + HO2 + MVK3OOH4OOH : 0.15*2.54e-13*exp(1300/T);\
ISOP1CO2OO3OOH4OOH + HO2 = ISOP1CO2OOH3OOH4OOH : 0.27*2.54e-13*exp(1300/T);\
ISOP1CO2OOH3OO4OOH + NO = ISOP1CO2OOH3N4OOH : k_nitrate[2.7,350,7.425,10];\
ISOP1CO2OOH3OO4OOH + NO = NO2 + CO + HO2 + MVK3OOH4OOH : k_alkoxy[0.54,350,7.425,10];\
ISOP1CO2OOH3OO4OOH + NO = NO2 + OH + MGLY + HPETHNL : k_alkoxy[2.16,350,7.425,10];\
ISOP1CO2OOH3OO4OOH + HO2 = OH + OH + MGLY + HPETHNL : 0.58*2.54e-13*exp(1300/T);\
ISOP1CO2OOH3OO4OOH + HO2 = OH + CO + HO2 + MVK3OOH4OOH : 0.15*2.54e-13*exp(1300/T);\
ISOP1CO2OOH3OO4OOH + HO2 = ISOP1CO2OOH3OOH4OOH : 0.27*2.54e-13*exp(1300/T);\
ISOP1CO2OOH3OOH4OO + NO = ISOP1CO2OOH3OOH4N : k_nitrate[2.7,350,5.854,10];\
ISOP1CO2OOH3OOH4OO + NO = OH + NO2 + CH2O + MACR2OOH3CO : k_alkoxy[2.7,350,5.854,10];\
ISOP1CO2OOH3OOH4OO + HO2 = ISOP1CO2OOH3OOH4OOH : 2.54e-13*exp(1300/T);\
ISOP1OO4OHc = ISOP1OOH4COc + HO2 : 0.34*k_tunneling[2.40e9,-7160,1e8];\
ISOP1OO4OHc = ISOP1OOH2OOH3OO4CO : 0.66*k_tunneling[2.40e9,-7160,1e8];\
ISOP1OOH2OOH3OO4CO = ISOP1OOH2OO3OOH4CO : 4e6;\
ISOP1OOH2OOH3OO4CO = ISOP1OO2OOH3OOH4CO : 2e6;\
ISOP1OOH2OO3OOH4CO = ISOP1OOH2OOH3OO4CO : 3e6;\
ISOP1OOH2OO3OOH4CO = ISOP1OO2OOH3OOH4CO : 2e6;\
ISOP1OO2OOH3OOH4CO = ISOP1OOH2OOH3OO4CO : 3e6;\
ISOP1OO2OOH3OOH4CO = ISOP1OOH2OO3OOH4CO : 4e6;\
ISOP1OOH2OOH3OO4CO = MACR2OOH3OOH + OH + CO : 1e7*exp(-5000/T);\
ISOP1OOH2OO3OOH4CO = MACR2OOH3OOH + OH + CO : 4e8*exp(-5000/T);\
ISOP1OO2OOH3OOH4CO = MACR2OOH3OOH + OH + CO : 1e8*exp(-5000/T);\
ISOP1OOH2OOH3OO4CO + NO = ISOP1OOH2OOH3N4CO : k_nitrate[2.7,350,30.981,10];\
ISOP1OOH2OOH3OO4CO + NO = NO2 + CO + HO2 + MACR2OOH3OOH : k_alkoxy[0.54,350,30.981,10];\
ISOP1OOH2OOH3OO4CO + NO = NO2 + OH + GLYX + HPAC : k_alkoxy[2.16,350,30.981,10];\
ISOP1OOH2OOH3OO4CO + HO2 = HO2 + OH + GLYX + HPAC : 0.58*2.54e-13*exp(1300/T);\
ISOP1OOH2OOH3OO4CO + HO2 = HO2 + CO + HO2 + MACR2OOH3OOH : 0.15*2.54e-13*exp(1300/T);\
ISOP1OOH2OOH3OO4CO + HO2 = ISOP1OOH2OOH3OOH4CO : 0.27*2.54e-13*exp(1300/T);\
ISOP1OOH2OO3OOH4CO + NO = ISOP1OOH2N3OOH4CO : k_nitrate[2.7,350,4.808,10];\
ISOP1OOH2OO3OOH4CO + NO = NO2 + CO + HO2 + MACR2OOH3OOH : k_alkoxy[0.54,350,4.808,10];\
ISOP1OOH2OO3OOH4CO + NO = NO2 + OH + GLYX + HPAC : k_alkoxy[2.16,350,4.808,10];\
ISOP1OOH2OO3OOH4CO + HO2 = HO2 + OH + GLYX + HPAC : 0.58*2.54e-13*exp(1300/T);\
ISOP1OOH2OO3OOH4CO + HO2 = HO2 + CO + HO2 + MACR2OOH3OOH : 0.15*2.54e-13*exp(1300/T);\
ISOP1OOH2OO3OOH4CO + HO2 = ISOP1OOH2OOH3OOH4CO : 0.27*2.54e-13*exp(1300/T);\
ISOP1OO2OOH3OOH4CO + NO = ISOP1N2OOH3OOH4CO : k_nitrate[2.7,350,5.854,10];\
ISOP1OO2OOH3OOH4CO + NO = NO2 + OH + CH2O + MVK3OOH4CO : k_alkoxy[2.7,350,5.854,10];\
ISOP1OO2OOH3OOH4CO + HO2 = ISOP1OOH2OOH3OOH4CO : 2.54e-13*exp(1300/T);\
ISOP1OH2OO = HCHO + OH + MVK : 1.04e11*exp(-9746/T);\
ISOP3OO4OH = MACR + OH + HCHO : 1.88e11*exp(-9752/T);\
//MVK
MVK + OH = MVK3OO4OH : 2.6e-12*exp(610/T)*0.76;\
MVK + OH = MVK3OH4OO : 2.6e-12*exp(610/T)*0.24;\
MVK3OO4OH + HO2 = CH3CO3 + GLYC + OH: 2.12e-13*exp(1300/T)*0.48;\
MVK3OO4OH + HO2 = MVK3CO4OH + OH + HO2: 2.12e-13*exp(1300/T)*0.34;\
MVK3OO4OH + HO2 = MVK3OOH4OH: 2.12e-13*exp(1300/T)*0.18;\
MVK3OH4OO + HO2 = MVK3OH4OOH: 2.12e-13*exp(1300/T)*0.83;\
MVK3OH4OO + HO2 = MGLY + HCHO + OH + HO2 : 2.12e-13*exp(1300/T)*0.17;\
MVK3OOH4OH = CH3CO3 + GLYC + OH : SUN*3e-5;\
MVK3OO4OH + NO = CH3CO3 + GLYC + NO2: k_alkoxy[2.7,350,6.161,6];\
MVK3OO4OH + NO = MVK3N4OH : k_nitrate[2.7,350,6.161,6];\
MVK3OH4OO + NO = MGLY + HCHO + HO2 + NO2: k_alkoxy[2.7,350,2.531,6];\
MVK3OH4OO + NO = MVK3OH4N: k_nitrate[2.7,350,2.531,6];\
MVK3N4OH = CH3CO3 + GLYC + NO2 : SUN*6.46e-5;\
MVK3OH4N = CH3CO3 + ETHLN + HO2 : SUN*4.21e-5;\
//MACR
MACR + OH = MACR2OO3OH : 8.0e-12*exp(380/T)*0.53;\
MACR + OH = MACR2OH3OO : 8.0e-12*exp(380/T)*0.02;\
MACR + OH = MACR1OO : 2.7e-12*exp(470/T);\
MACR2OO3OH + HO2 = MACR2OOH3OH : 2.12e-13*exp(1300/T)*0.41;\
MACR2OO3OH + HO2 = HAC + CO + HO2 + OH + O2 : 2.12e-13*exp(1300/T)*0.59*0.86;\
MACR2OO3OH + HO2 = MGLY + HCHO + OH + O2 : 2.12e-13*exp(1300/T)*0.59*0.14;\
MACR2OH3OO + HO2 = MACR2OH3OOH : 2.12e-13*exp(1300/T)*0.83;\
MACR2OH3OO + HO2 = MGLY + HCHO + HO2 + OH + O2 : 2.12e-13*exp(1300/T)*0.17;\
MACR1OO + HO2 = MACR1OOH : 1.93e-13*exp(1300/T)*0.40;\
MACR1OO + HO2 = CH3COOCH2 + O2 + CO2 + OH : 1.93e-13*exp(1300/T)*0.40;\
MACR1OO + HO2 = MACR1OH + O3 : 1.93e-13*exp(1300/T)*0.20;\
MACR2OO3OH + NO = HAC + CO + HO2 + NO2 : k_alkoxy[2.322,350,2.985,6];\
MACR2OO3OH + NO = MGLY + HCHO + NO2 : k_alkoxy[0.378,350,2.985,6];\
MACR2OO3OH + NO = MACR2N3OH : k_nitrate[2.7,350,2.985,6];\
MACR2OH3OO + NO = MGLY + HCHO + HO2 + NO2 : k_alkoxy[2.7,350,2.985,6];\
MACR2OH3OO + NO = MACR2OH3N : k_nitrate[2.7,350,2.985,6];\
MACR1OO + NO = CH3COOCH2 + CO2 + NO2 : 8.7e-12*exp(290/T);\
MACR1OO + NO2 + M = MPAN + M : k_troe[k_0 = 2.133e-28*(T/300)^(-7.1), k_inf= 1.2e-11*(T/300)^(-0.9), Fc = 0.3];\

MPAN + M = MACR1OO + NO2 + M : k_troe[k_0 = 3.871e-3*exp(-12100/T), k_inf = 5.4e16*exp(-13830/T), Fc = 0.3];\
MACR2OO3OH = HAC + CO + OH : 2.9e7*exp(-5297/T);\
MACR2OH3OO = HPAC + CO + HO2 : 4e8*exp(-5000/T);\
//MPAN
MPAN + OH = MPAN1OHx : 2.9e-11;\
MPAN1OHx = MPAN1OH2OO : 1e7;\
MPAN1OHx = HMMLx : 4e9;\
MPAN1OHx = MPAN1OH: 8.18e7;\
MPAN1OH = HMMLx: 1e3;\
MPAN1OH = MPAN1OH2OO : 1e7;\
HMMLx = HMML + NO3 : 1E8*0.75;\
HMMLx = HAC + CO + NO3 : 1E8*0.25;\
MPAN1OH2OO + NO = MPAN1OH2O + NO2: 2.7E-12*exp(350/T);\
MPAN1OH2OO + HO2 = MPAN1OH2OOH : 2.6e-13*exp(1300/T)*0.1;\
MPAN1OH2OO + HO2 = MPAN1OH2O + OH : 2.6e-13*exp(1300/T)*0.9;\
MPAN1OH2O = HAC + CO2 + NO3 : 1E8*0.4;\
MPAN1OH2O = HO2 + HCHO + CH3COCOON : 1E8*0.6;\
//ISOPOOH
*ISOP1OH2OOH + OH = ISOP1OH2OOH3R4OH : 1.7e-11*exp(390/T)*0.95*;\
ISOP1OH2OOH3R4OH + O2 = ISOP1OH2OOH3OO4OH: 1e-14;\
*ISOP1OH2OOH3R4OH = ISOP1OH23O4OHt: 4.4e5*0.67*;\
*ISOP1OH2OOH3R4OH = ISOP1OH23O4OHc: 4.4e5*0.33*;\
*ISOP3OOH4OH + OH = ISOP1OH2R3OOH4OH : 3.0e-11*exp(390/T)*0.95*;\
ISOP1OH2R3OOH4OH + O2 = ISOP1OH2OO3OOH4OH: 1e-14;\
*ISOP1OH2R3OOH4OH = ISOP1OH23O4OHt: 4.4e5*0.68*;\
*ISOP1OH2R3OOH4OH = ISOP1OH23O4OHc: 4.4e5*0.32*;\
ISOP1OOH4OH + OH = ISOP12O3OH4OH + OH : 2.9e-11*exp(390/T);\
ISOP1OH4OOH + OH = ISOP1OH2OOH3OH4CO + OH : 2.9e-11*exp(390/T);\
ISOP1OH2OOH + OH = ISOP1OH2OOH3OH4OO : 1.7e-11*exp(390/T)*0.05;\
ISOP1OH2OOH3OH4OO = ISOP1OH2OO3OH4OOH : 3e6;\
ISOP1OH2OO3OH4OOH = ISOP1OH2OOH3OH4OO : 7e6;\
ISOP1OH2OOH3OH4OO + NO = GLYC + HAC + NO2 + OH : k_alkoxy[2.7,350,3.485,9];\
ISOP1OH2OOH3OH4OO + NO = ISOP1OH2OOH3OH4N : k_nitrate[2.7,350,3.485,9];\
ISOP1OH2OO3OH4OOH + NO = HPETHNL + HAC + NO2 + HO2 : k_alkoxy[2.7,350,1.450,9];\
ISOP1OH2OO3OH4OOH + NO = ISOP1OH2N3OH4OOH : k_nitrate[2.7,350,1.450,9];\
ISOP1OH2OOH3OH4OO + HO2 = ISOP1OH2OOH3OH4OOH : 2.47e-13*exp(1300/T);\
ISOP1OH2OO3OH4OOH + HO2 = ISOP1OH2OOH3OH4OOH : 2.47e-13*exp(1300/T);\
ISOP1OH2OO3OH4OOH = ISOP1OH2OOH3OH4CO : 3.75e13*exp(-10000/T);\
ISOP3OOH4OH + OH = ISOP1OO2OH3OOH4OH : 3.0e-11*exp(390/T)*0.05;\
ISOP1OO2OH3OOH4OH = ISOP1OOH2OH3OO4OH : 3e6;\
ISOP1OOH2OH3OO4OH = ISOP1OO2OH3OOH4OH : 7e6;\
ISOP1OO2OH3OOH4OH + NO = HAC + GLYC + NO2 + OH : k_alkoxy[1.89,350,3.485,9];\
ISOP1OO2OH3OOH4OH + NO = ISOP1N2OH3OOH4OH : k_nitrate[1.89,350,3.485,9];\
ISOP1OOH2OH3OO4OH + NO = HPAC + GLYC + NO2 + HO2 : k_alkoxy[0.81,350,2.375,9];\
ISOP1OOH2OH3OO4OH + NO = ISOP1OOH2OH3N4OH : k_nitrate[0.81,350,2.375,9];\
ISOP1OO2OH3OOH4OH + HO2 = ISOP1OOH2OH3OOH4OH : 2.47e-13*exp(1300/T);\
ISOP1OOH2OH3OO4OH + HO2 = ISOP1OOH2OH3OOH4OH : 2.47e-13*exp(1300/T);\
ISOP1OOH2OH3OO4OH = ISOP1CO2OH3OOH4OH : 3.75e13*exp(-10000/T);\
ISOP1OH2OOH3OO4OH = ISOP1OH2OO3OOH4OH : 4e6;\
ISOP1OH2OO3OOH4OH = ISOP1OH2OOH3OO4OH : 3e6;\
ISOP1OH2OOH3OO4OH + NO = ISOP1OH2OOH3N4OH : k_nitrate[2.7,350,4.457,9];\
ISOP1OH2OOH3OO4OH + NO = GLYC + HAC + NO2 + OH : k_alkoxy[2.7,350,4.457,9];\
ISOP1OH2OOH3OO4OH + HO2 = ISOP1OH2OOH3OOH4OH : 2.47e-13*exp(1300/T);\
ISOP1OH2OOH3OO4OH = ISOP1OH12O3OOH4OH : 1e14*exp(-10000/T);\
ISOP1OH2OO3OOH4OH + NO = ISOP1OH2N3OOH4OH : k_nitrate[2.7,350,2.838,9];\
ISOP1OH2OO3OOH4OH + NO = HAC + GLYC + NO2 + OH : k_alkoxy[2.7,350,2.838,9];\
ISOP1OH2OO3OOH4OH + HO2 = ISOP1OH2OOH3OOH4OH : 2.47e-13*exp(1300/T);\
ISOP1OH2OO3OOH4OH = ISOP1OH2OOH34O4OH : 1e14*exp(-10000/T);\
ISOP1OH2OOH + OH = ISOP1OH2OO : 4.6e-12*exp(200/T);\
ISOP1OH2OOH + OH = ISOP1CO2OOH + HO2 : 1.5e-12*exp(200/T)*0.5;\
ISOP1OH2OOH + OH = ISO1OH12O + OH : 1.5e-12*exp(200/T)*0.5;\
ISOP3OOH4OH + OH = ISOP3OO4OH : 2.1e-12*exp(200/T);\
ISOP3OOH4OH + OH = ISOP3CO4OH + OH : 2.0e-12*exp(200/T)*0.32;\
ISOP3OOH4OH + OH = ISOP3OOH4CO + HO2 : 2.0e-12*exp(200/T)*0.68;\
ISOP1OH2OOH = MVK + HCHO + HO2 + OH : SUN*6.5e-6;\
ISOP3OOH4OH = MACR + HCHO + HO2 + OH : SUN*6.5e-6;\
//IEPOX
*ISOP1OH23O4OHc + OH = ISOP1OH23O4R4OHc : 0.168*5.82e-11*exp(-400/T)*;\
ISOP1OH23O4R4OHc + O2 = ISOP1OH23O4CO + H2O + HO2 : 1e-14;\
*ISOP1OH23O4R4OHc = HAC + GLYX + OH : 0.63*0.168*1.752e5*;\
*ISOP1OH23O4R4OHc = MACR2OH3OH + OH + CO : 0.37*0.168*1.752e5*;\
*ISOP1OH23O4OHc + OH = ISOP1OH1R23O4OHc : 0.752*5.82e-11*exp(-400/T)*;\
ISOP1OH1R23O4OHc + O2 = ISOP1CO23O4OH + H2O + HO2: 1e-14;\

*ISOP1OH1R23O4OHc = GLYC + MGLY + OH: 0.287*0.752*1.752e5*;\
*ISOP1OH1R23O4OHc = MVK3OH4OH + OH + CO: 0.713*0.752*1.752e5*;\
ISOP1OH23O4OHc + OH = MVK3CO4OH + OH + HCHO: 0.08*5.82e-11*exp(-400/T);\
*ISOP1OH23O4OHt + OH = ISOP1OH23O4R4OHt : 0.31*3.75e-11*exp(-400/T)*;\
ISOP1OH23O4R4OHt + O2 = ISOP1OH23O4CO + H2O + HO2: 1e-14;\
*ISOP1OH23O4R4OHt = HAC + GLYX + OH: 0.63*0.31*2.15e5*;\
*ISOP1OH23O4R4OHt = MACR2OH3OH + OH + CO: 0.37*0.31*2.15e5*;\
*ISOP1OH23O4OHt + OH = ISOP1OH1R23O4OHt : 0.62*3.75e-11*exp(-400/T)*;\
ISOP1OH1R23O4OHt + O2 = ISOP1CO23O4OH + H2O + HO2: 1e-14;\
*ISOP1OH1R23O4OHt = GLYC + MGLY + OH: 0.287*0.62*2.15e5*;\
*ISOP1OH1R23O4OHt = MVK3OH4OH + OH + CO: 0.713*0.62*2.15e5*;\
ISOP1OH23O4OHt + OH = MVK3CO4OH + OH + HCHO: 0.07*3.75e-11*exp(-400/T);\
ISOP1OH2OH34O + OH = ISOP1CO2OH34O + HO2 : 3.22e-11*exp(-400/T);\
ISOP12O3OH4OH + OH = ISOP12O3OH4CO + HO2 : 0.2*3.22e-11*exp(-400/T);\
*ISOP12O3OH4OH + OH = ISOP12O3OH3R4OH : 0.8*3.22e-11*exp(-400/T)*;\
*ISOP12O3OH3R4OH + O2 = ISOP12O3CO4OH + HO2 : 0.33*1e-14*;\
*ISOP12O3OH3R4OH + O2 = ISOP1OH3OH4CO + HO2 : 0.67*1e-14*;\
ISOP12O3OH3R4OH = ISOP1OH2OO3CO4OH : 3.45e4;\
//C4 dihydroxycarbonyls\
MVK3OH4OH + OH = MVK3OH4CO + HO2 : 0.4*8.7e-12*exp(70/T);\
MVK3OH4OH + OH = MVK3CO4OH + HO2 : 0.6*8.7e-12*exp(70/T);\
MVK3OH4CO + OH = OH + MGLY + CO2 : 5e-12*exp(470/T);\
MVK3OH4CO = CO + HO2 + HO2 + MGLY : 0.5*2.5e-4*SUN;\
MVK3OH4CO = GLYX + HO2 + CH3CO3 : 0.5*2.5e-4*SUN;\
MVK3CO4OH + OH = CO + CO + HO2 + CH3CO3 : 2e-12*exp(70/T);\
MVK3CO4OH = CO + HO2 + CH2O + CH3CO3 : 2.5e-4*SUN;\
MACR2OH3OH + OH = MACR2OH3CO + HO2 : 0.16*2.4e-11*exp(70/T);\
MACR2OH3OH + OH = HAC + OH + CO2 : 0.84*2.4e-11*exp(70/T);\
MACR2OH3CO + OH = CO2 + OH + MGLY: 5e-12*exp(470/T);\
//HPALD\
ISOP1CO4OOHc = MVKENOL + OH + OH + CO : 0.552*0.58*SUN*4e-4;\
ISOP1CO4OOHc = C4HVP1 + OH + CO: 0.224*0.58*SUN*4e-4;\
ISOP1CO4OOHc = ISOP1CO4CO + HO2 + OH : 0.112*0.58*SUN*4e-4;\
ISOP1CO4OOHc = MACR2OOH3CO + OH + OH + CO : 0.019*0.58*SUN*4e-4;\
ISOP1CO4OOHc = MVK3OOH4CO + OH + OH + CO : 0.093*0.58*SUN*4e-4;\
ISOP1OOH4COc = MACRENOL + OH + OH + CO : 0.455*0.55*SUN*4e-4;\
ISOP1OOH4COc = C4HVP2 + OH + CO : 0.182*0.55*SUN*4e-4;\
ISOP1OOH4COc = ISOP1CO4CO + HO2 + OH : 0.182*0.55*SUN*4e-4;\
ISOP1OOH4COc = MACR2OOH3CO + OH + OH + CO : 0.031*0.55*SUN*4e-4;\
ISOP1OOH4COc = MVK3OOH4CO + OH + OH + CO : 0.151*0.55*SUN*4e-4;\
MVKENOL + OH = HO2 + MVK3OH4CO : 0.3*3.35e-12*exp(983/T);\
MVKENOL + OH = MVK3OO4OH4OH : 0.7*3.35e-12*exp(983/T);\
MVKENOL = CH3CO3 + GLYX + OH : 0.5*2.5e-4*SUN;\
MVKENOL = MGLY + HO2 + CO + OH : 0.5*2.5e-4*SUN;\
MVK3OO4OH4OH + NO = NO2 + HO2 + HCOOH + MGLY : 2.7E-12*exp(350/T);\
MVK3OO4OH4OH + HO2 = OH + HO2 + HCOOH + MGLY : 2.26e-13*exp(1300/T);\
MACRENOL + OH = DHA + CO + OH : 3.35e-12*exp(983/T);\
DHA + OH = HO2 + PYRAC : 8e-12*exp(70/T);\
MACRENOL = MACR3CO + OH + OH : 2.5e-4*SUN;\
MACR3CO + OH = PYRAC + OH + CO: 2.7e-11*exp(390/T);\
C4HVP1 + NO = NO2 + MVK3OO4OH : 2.7E-12*exp(350/T);\
C4HVP1 + HO2 = OH + MVK3OO4OH : 1.93e-13*exp(1300/T);\
C4HVP1 + NO2 = MVK3N4OH : 9e-12;\
C4HVP2 + NO = NO2 + MACR2OO3OH : 2.7E-12*exp(350/T);\
C4HVP2 + HO2 = OH + MACR2OO3OH : 1.93e-13*exp(1300/T);\
C4HVP2 + NO2 = MACR2N3OH : 9e-12;\
MACR2OOH3CO = OH + MGLY + HO2 + CO : 2.5e-4*SUN;\
MVK3OOH4CO = OH + GLYX + CH3CO3 : 2.5e-4*SUN;\
ISOP1CO4OOHc + OH = ISOP1CO4CO + OH : 7.5e-12*exp(20/T);\
ISOP1CO4OOHc + OH = ISOP1CO4OOc : 2.0e-12*exp(200/T);\
ISOP1CO4OOHc + OH = ISOP1CO2OO3OH4OOH : 2.0e-12*exp(650/T);\
*ISOP1CO4OOHc + OH = ISOP1CO2OH3R4OOH : 1.0e-12*exp(650/T)*;\
ISOP1CO2OH3R4OOH + O2 = ISOP1CO2OH3OO4OOH : 1e-14;\
ISOP1CO2OH3R4OOH = ISOP1CO2OH34O : 5.2e4;\
*ISOP1CO4OOHc + OH = ISOP1CO3R4OOH : 3.8e-12*exp(400/T)*;\
*ISOP1CO3R4OOH + O2 = ISOP1CO1OOH4CO : 1e-14*0.125*;\
*ISOP1CO3R4OOH + O2 = ISOP121CO3OO4OOH : 1e-14*0.875*;\
ISOP1CO3R4OOH = ISOP121CO34O : 1.3e4;\
ISOP1CO2OH3OO4OOH = MVK3OOH4OOH + CO2 + HO2 : 4e8*exp(-5000/T);\
ISOP1CO2OH3OOH4OO = MVK3OOH4OOH + CO2 + HO2 : 1e8*exp(-5000/T);\
ISOP1CO2OH3OO4OOH = ISOP1CO2OH3OOH4OO : 2e6;\
ISOP1CO2OH3OOH4OO = ISOP1CO2OH3OO4OOH : 3e6;\
ISOP1CO2OO3OH4OOH = MVK3OH4OOH + CO + OH : 1e7*exp(-5000/T);\

ISOP1CO2OOH3OH4OO = MVK3OH4OOH + CO + OH : 1e8*exp(-5000/T);\
ISOP1CO2OO3OH4OOH = ISOP1CO2OOH3OH4OO : 2e6;\
ISOP1CO2OOH3OH4OO = ISOP1CO2OO3OH4OOH : 4e6;\
ISOP1CO4OOc = ISOP1CO2OO : 10;\
ISOP1CO2OO = MVK + OH + CO : 1e7*exp(-5000/T);\
ISOP1CO4OOc = ISOP1CO3R4OOH : 10;\
ISOP121CO3OO4OOH + NO = OH + CH2O + NO2 + MACR3CO : 2.7E-12*exp(350/T);\
ISOP121CO3OO4OOH + HO2 = OH + OH + CH2O + MACR3CO : 2.38e-12*exp(1300/T);\
ISOP1OOH4COc + OH = ISOP1CO4CO + OH : 7.5e-12*exp(20/T);\
ISOP1OOH4COc + OH = ISOP1OO4COc : 2.0e-12*exp(200/T);\
ISOP1OOH4COc + OH = ISOP1OOH2OH3OO4CO : 1.0e-12*exp(650/T);\
*ISOP1OOH4COc + OH = ISOP1OOH2R3OH4CO : 2.0e-12*exp(650/T)*;\
ISOP1OOH2R3OH4CO + O2 = ISOP1OOH2OO3OH4CO : 1e-14;\
ISOP1OOH2R3OH4CO = ISOP12O3OH4CO : 5.2e4;\
*ISOP1OOH4COc + OH = ISOP1OOH2R4CO : 3.8e-12*exp(400/T)*;\
*ISOP1OOH2R4CO + O2 = ISOP1OOH2OO344CO : 1e-14*0.875*;\
*ISOP1OOH2R4CO + O2 = ISOP1CO4CO4OOH : 1e-14*0.125*;\
ISOP1OOH2R4CO = ISOP12O344CO : 1.3e4;\
ISOP1OOH2OH3OO4CO = MACR2OH3OOH + OH + CO : 1e7*exp(-5000/T);\
ISOP1OO2OH3OOH4CO = MACR2OH3OOH + OH + CO : 1e8*exp(-5000/T);\
ISOP1OOH2OH3OO4CO = ISOP1OO2OH3OOH4CO : 2e6;\
ISOP1OO2OH3OOH4CO = ISOP1OOH2OH3OO4CO : 3e6;\
ISOP1OOH2OO3OH4CO = MACR2OOH3OOH + CO + HO2 : 4e8*exp(-5000/T);\
ISOP1OO2OOH3OH4CO = MACR2OOH3OOH + CO + HO2 : 1e8*exp(-5000/T);\
ISOP1OOH2OO3OH4CO = ISOP1OO2OOH3OH4CO : 2e6;\
ISOP1OO2OOH3OH4CO = ISOP1OOH2OO3OH4CO : 4e6;\
ISOP1OO4COc = ISOP3OO4CO : 10;\
ISOP3OO4CO = MACR + CO + OH : 2.9e7*exp(-5297/T);\
ISOP1OO4COc = ISOP1OOH2R4CO : 10;\
ISOP1OOH2OO344CO + NO = OH + OH + CH2O + MVK4CO : 2.7E-12*exp(350/T);\
ISOP1OOH2OO344CO + HO2 = OH + OH + CH2O + MVK4CO : 2.38e-12*exp(1300/T);\
MVK4CO + OH = MVK3OO4CO4OH : 2.7e-11*exp(390/T);\
MVK3OO4CO4OH + NO = NO2 + CO2 + HO2 + MGLY : 2.7E-12*exp(350/T);\
MVK3OO4CO4OH + HO2 = OH + CO2 + HO2 + MGLY : 2.26e-12*exp(1300/T);\
//Daytime Hydroxynitrates\
*ISOP1OH2N + OH = ISOP1OH2N3R4OH: 0.75*8.4e-12*exp(390/T)*;\
ISOP1OH2N3R4OH + O2 = ISOP1OH2N3OO4OH: 1e-14;\
*ISOP1OH2N3R4OH = ISOP1OH23O4OHt: 1.3e4*0.67*;\
ISOP1OH2N3R4OH = ISOP1OH23O4OHc: 1.3e4.33*;\
ISOP1OH2N + OH = ISOP1OH2N3OH4OO: 0.25*8.4e-12*exp(390/T);\
ISOP1OH2N3OH4OO + NO = ISOP1OH2N3OH4N: k_nitrate[2.7,350,2.849,11];\
ISOP1OH2N3OH4OO + NO = MACR2N3OH + HO2 + HCHO + NO2: k_alkoxy[2.7,350,2.849,11];\
ISOP1OH2N3OO4OH + NO = ISOP1OH2N3N4OH: k_nitrate[2.7,350,16.019,11];\
ISOP1OH2N3OO4OH + NO = GLYC + NO2 + NO2 + HAC: k_alkoxy[2.7,350,16.019,11];\
ISOP1OH2N3OO4OH = ISOP1CO2N3OOH4OH + HO2 : 3.75e13*exp(-10000/T);\
ISOP1OH2N3OH4OO = ISOP1CO2N3OH4OOH + HO2 : 3.75e12*exp(-10000/T);\
ISOP1OH2N3OH4OO + HO2 = ISOP1OH2N3OH4OOH: 2.6e-13*exp(1300/T);\
ISOP1OH2N3OO4OH + HO2 = ISOP1OH2N3OOH4OH: 0.15*2.6e-13*exp(1300/T);\
ISOP1OH2N3OO4OH + HO2 = GLYC + HAC + OH + NO2: 0.85*2.6e-13*exp(1300/T);\
*ISOP3N4OH + OH = ISOP1OH2R3N4OH: 0.9*1.17e-11*exp(390/T)*;\
ISOP1OH2R3N4OH + O2 = ISOP1OH2OO3N4OH: 1e-14;\
*ISOP1OH2R3N4OH = ISOP1OH23O4OHt: 0.67*8.42e3*;\
*ISOP1OH2R3N4OH = ISOP1OH23O4OHc: 0.33*8.42e3*;\
ISOP3N4OH + OH = ISOP1OO2OH3N4OH: 0.1*1.17e-11*exp(390/T);\
ISOP1OH2OO3N4OH + NO = MVK3N4OH + HO2 + NO2 + HCHO: 0.76*2.7E-12*exp(350/T);\
ISOP1OH2OO3N4OH + NO = ISOP1OH2N3N4OH: k_nitrate[2.7,350,10.532,11];\
ISOP1OH2OO3N4OH + NO = GLYC + NO2 + NO2 + HAC: k_alkoxy[2.7,350,10.532,11];\
ISOP1OO2OH3N4OH + NO = ISOP1N2OH3N4OH: k_nitrate[2.7,350,2.849,11];\
ISOP1OO2OH3N4OH + NO = MVK3N4OH + HO2 + NO2 + HCHO: k_alkoxy[2.7,350,2.849,11];\
ISOP1OO2OH3N4OH = ISOP1OOH2OH3N4CO + HO2: 3.75e12*exp(-10000/T);\
ISOP1OH2OO3N4OH = ISOP1OH2OOH3N4CO + HO2: 3.75e13*exp(-10000/T);\
ISOP1OH2OO3N4OH + HO2 = MVK3N4OH + HO2 + OH + O2 + HCHO: 0.74*2.6e-13*exp(1300/T);\
ISOP1OH2OO3N4OH + HO2 = ISOP1OH2OOH3N4OH: 0.15*2.6e-13*exp(1300/T);\
ISOP1OH2OO3N4OH + HO2 = GLYC + HAC + OH + NO2: 0.11*2.6e-13*exp(1300/T);\
ISOP1OO2OH3N4OH + HO2 = ISOP1OOH2OH3N4OH: 2.6e-13*exp(1300/T);\
//Ozonolysis\
ISOP + O3 = MACR + ciCH2OO : 1.1e-14*exp(-2000/T)*(0.41);\
ISOP + O3 = MVK + ciCH2OO : 1.1e-14*exp(-2000/T)*(0.17);\
ISOP + O3 = OH : 1.1e-14*exp(-2000/T)*(0.28);\
ISOP + O3 = ciMVKOO : 1.1e-14*exp(-2000/T)*(0.007);\
ISOP + O3 = ciMACROO : 1.1e-14*exp(-2000/T)*(0.006);\
ISOP + O3 = HO2 : 1.1e-14*exp(-2000/T)*(0.16);\
ISOP + O3 = HCHO + CO2 + HCHO + CO + CH3OO : 1.1e-14*exp(-2000/T)*0.407;\

//Reactions of SCI
ciCH2OO + SO2 = H2SO4 : 2e-11;\
ciCH2OO + HCOOH = HPMF : 5.6e-11;\
ciCH2OO + H2O = HMHP : 0.9e-15*(0.73);\
ciCH2OO + H2O = HCOOH : 0.9e-15*(0.21);\
ciCH2OO + H2O = HCHO : 0.9e-15*(0.06);\
ciCH2OO + H2O = H2O2 : 0.9e-15*(0.06);\
ciCH2OO + H2Od = HMHP : 0.8e-12*(0.4);\
ciCH2OO + H2Od = HCOOH : 0.8e-12*(0.54);\
ciCH2OO + H2Od = HCHO : 0.8e-12*(0.06);\
ciCH2OO + H2Od = H2O2 : 0.8e-12*(0.06);\
ciCH2OO + O3 = HCHO : 1.0e-12*(0.7);\
ciMACROO + H2O = MACR3OH3OOH : 1e-15;\
ciMVKOO + H2O = MVK3OH3OOH : 1e-15;\
HMHP + OH = HCHO + HO2 : 4.3e-12*exp(190/T)*0.5;\
HMHP + OH = HCOOH + OH : 4.3e-12*exp(190/T)*0.5;\
HPMF + OH = HO2 + FAH : 4.31e-12;\
FAH + OH = CO + HO2 + CO2 : 1.80e-13;\
//NO3 Oxidation of Isoprene
//Isoprene + NO3
ISOP + NO3 = ISOP1N2OO : 2.95E-12*exp(-450/T)*0.42;\
ISOP + NO3 = ISOP3OO4N : 2.95E-12*exp(-450/T)*0.045;\
ISOP + NO3 = ISOP1N4OO : 2.95E-12*exp(-450/T)*0.45;\
ISOP + NO3 = ISOP1OO4N : 2.95E-12*exp(-450/T)*0.085;\
//RO2 + HO2
ISOP1N2OO + HO2 = ISOP1N2OOH : 2.47e-13*exp(1300/T)*0.47;\
ISOP1N2OO + HO2 = MVK + OH + HCHO + NO2 : 2.47e-13*exp(1300/T)*0.53;\
ISOP1N4OO + HO2 = ISOP1N4OOH : 2.47e-13*exp(1300/T);\
ISOP3OO4N + HO2 = ISOP3OOH4N : 2.47e-13*exp(1300/T)*0.735;\
ISOP3OO4N + HO2 = MACR + OH + HCHO + NO2 : 2.47e-13*exp(1300/T)*0.265;\
ISOP1OO4N + HO2 = ISOP1OOH4N : 2.47e-13*exp(1300/T);\
//RO2 + Dominant RO2
ISOP1N2OO + ISOP1N2OO = MVK + HCHO + NO2 + MVK + HCHO + NO2 : 6.92e-14*0.965;\
ISOP1N2OO + ISOP1N2OO = ISOP1N2OOISOP1N2 : 6.92e-14*0.035;\
ISOP1N2OO + ISOP3OO4N = ISOP1N2OH + ISOP3CO4N : 3.08e-12*0.77*0.5 ;\
ISOP1N2OO + ISOP3OO4N = MVK + MACR + HCHO + HCHO + NO2 + NO2 : 3.08e-12*0.58 ;\
ISOP1N2OO + ISOP3OO4N = ISOP3OO4NISOP1N2 : 3.08e-12*0.035 ;\
ISOP1N2OO + ISOP1OO4N = ISOP1N2OH + ISOP1CO4N : 2.49e-12*0.77*0.5 ;\
ISOP1N2OO + ISOP1OO4N = MVK + HCHO + NO2 + ISOP1O4N : 2.49e-12*0.58 ;\
ISOP1N2OO + ISOP1OO4N = ISOP1OO4NISOP1N2: 2.49e-12*0.035 ;\
ISOP1N2OO + ISOP1N4OO = ISOP1N4CO + ISOP1N2OH : 2.49E-12*0.77*0.5;\
ISOP1N2OO + ISOP1N4OO = MVK + HCHO + NO2 + ISOP1N4O : 2.49E-12*0.58;\
ISOP1N2OO + ISOP1N4OO = ISOP1N2OOISOP1N4 : 2.49E-12*0.035;\
ISOP1N4OO + ISOP1N4OO = ISOP1N4CO + ISOP1N4OHc : 3.9E-12*0.77*0.5;\
ISOP1N4OO + ISOP1N4OO = ISOP1N4CO + ISOP1N4OHt : 3.9E-12*0.77*0.5;\
ISOP1N4OO + ISOP1N4OO = ISOP1N4O + ISOP1N4O : 3.9E-12*0.195;\
ISOP1N4OO + ISOP1N4OO = ISOP1N4OOISOP1N4 : 3.9E-12*0.035;\
ISOP3OO4N + ISOP1N4OO = ISOP3OH4N + ISOP1N4CO : 3.94E-12*0.77*0.5;\
ISOP3OO4N + ISOP1N4OO = ISOP3CO4N + ISOP1N4OHc : 3.94E-12*0.77*0.5*0.5;\
ISOP3OO4N + ISOP1N4OO = ISOP3CO4N + ISOP1N4OHt : 3.94E-12*0.77*0.5*0.5;\
ISOP3OO4N + ISOP1N4OO = MACR + HCHO + NO2 + ISOP1N4O : 3.94E-12*0.195;\
ISOP3OO4N + ISOP1N4OO = ISOP3OO4NISOP1N4 : 3.94E-12*0.035;\
ISOP1OO4N + ISOP1N4OO = ISOP1CO4N + ISOP1N4OHc : 3.29E-12*0.77*0.5*0.5;\
ISOP1OO4N + ISOP1N4OO = ISOP1CO4N + ISOP1N4OHt : 3.29E-12*0.77*0.5*0.5;\
ISOP1OO4N + ISOP1N4OO = ISOP1OH4Nc + ISOP1N4CO : 3.29E-12*0.77*0.5*0.5;\
ISOP1OO4N + ISOP1N4OO = ISOP1OH4Nt + ISOP1N4CO : 3.29E-12*0.77*0.5*0.5;\
ISOP1OO4N + ISOP1N4OO = ISOP1O4N + ISOP1N4O : 3.29E-12*0.195;\
ISOP1OO4N + ISOP1N4OO = ISOP1OO4NISOP1N4 : 3.29E-12*0.035;\
ISOP1N2OO + CH3OO = HCHO + ISOP1N2OH : 1.6E-13*0.71*0.5;\
ISOP1N2OO + CH3OO = MVK + HCHO + NO2 + CH3O : 1.6E-13*0.645;\
ISOP1N4OO + CH3OO = ISOP1N4CO + CH3OH : 1.2E-12*0.71*0.5;\
ISOP1N4OO + CH3OO = ISOP1N4OHc + HCHO : 1.2E-12*0.71*0.5*0.5;\
ISOP1N4OO + CH3OO = ISOP1N4OHt + HCHO : 1.2E-12*0.71*0.5*0.5;\
ISOP1N4OO + CH3OO = ISOP1N4O + CH3O : 1.2E-12*0.29;\
ISOP3OO4N + CH3OO = ISOP3OH4N + HCHO : 1.4E-12*0.71*0.5;\
ISOP3OO4N + CH3OO = ISOP3CO4N + CH3OH : 1.4E-12*0.71*0.5;\
ISOP3OO4N + CH3OO = MACR + HCHO + NO2 + CH3O : 1.4E-12*0.29;\
ISOP1OO4N + CH3OO = ISOP1CO4N + CH3OH : 9.8E-13*0.71*0.5;\
ISOP1OO4N + CH3OO = ISOP1OH4Nc + HCHO : 9.8E-13*0.71*0.5*0.5;\
ISOP1OO4N + CH3OO = ISOP1OH4Nt + HCHO : 9.8E-13*0.71*0.5*0.5;\
ISOP1OO4N + CH3OO = ISOP1O4N + CH3O : 9.8E-13*0.29;\
//RO2 + NO
ISOP1N2OO + NO = MVK + HCHO + NO2 + NO2 : k_alkoxy[2.7,350,8.667,9];\

ISOP1N2OO + NO = ISOP1N2N : k_nitrate[2.7,350,8.667,9];\
ISOP1N4OO + NO = ISOP1N4O + NO2 : k_alkoxy[2.7,350,2.319,9];\
ISOP1N4OO + NO = ISOP1N4N : k_nitrate[2.7,350,2.319,9];\
ISOP3OO4N + NO = MACR + HCHO + NO2 + NO2 : k_alkoxy[2.7,350,13.202,9];\
ISOP3OO4N + NO = ISOP3N4N : k_nitrate[2.7,350,13.202,9];\
ISOP1OO4N + NO = ISOP1O4N + NO2 : k_alkoxy[2.7,350,2.319,9];\
ISOP1OO4N + NO = ISOP1N4N : k_nitrate[2.7,350,2.319,9];\
ISOP1N4O + O2 = ISOP1N4CO + HO2 : 2.5E-14*exp(-300/T);\
ISOP1O4N + O2 = ISOP1CO4N + HO2 : 2.5E-14*exp(-300/T);\
//RO2 + NO3
ISOP1N2OO + NO3 = MVK + HCHO + NO2 + NO2 : 2.3E-12;\
ISOP1N4OO + NO3 = ISOP1N4O + NO2 : 2.3E-12;\
ISOP3OO4N + NO3 = MACR + HCHO + NO2 + NO2 : 2.3E-12;\
ISOP1OO4N + NO3 = ISOP1O4N + NO2 : 2.3E-12;\
//1,5 H-shift
ISOP1N4O = ISOP1N25_3OO4OH : 1e20*exp(-10000/T);\
ISOP1N25_3OO4OH + NO3 = ISOP1N25_3O4OH + NO2 : 2.3E-12;\
ISOP1N25_3OO4OH + NO = ISOP1N25_3O4OH + NO2 : k_alkoxy[2.7,350,1.368,10];\
ISOP1N25_3OO4OH + NO = ISOP1N25_3N4OH + NO2 : k_nitrate[2.7,350,1.368,10];\
ISOP1N25_3O4OH + O2 = MACR3N + HCHO + HO2 : 2.5E-14*exp(-300/T);\
ISOP1N25_3OO4OH + HO2 = ISOP1N25_3OOH4OH : 2.54e-13*exp(1300/T);\
ISOP1N25_3OO4OH + ISOP1N4OO = ISOP1N25_3CO4OH + ISOP1N4OHc : 3.94E-12*0.77*0.5*0.5;\
ISOP1N25_3OO4OH + ISOP1N4OO = ISOP1N25_3CO4OH + ISOP1N4OHt : 3.94E-12*0.77*0.5*0.5;\
ISOP1N25_3OO4OH + ISOP1N4OO = ISOP1N25_3OH4OH + ISOP1N4CO : 3.94E-12*0.77*0.5;\
ISOP1N25_3OO4OH + ISOP1N4OO = ISOP1N25_3O4OH + ISOP1N4O : 3.94E-12*0.195;\
ISOP1N25_3OO4OH + ISOP1N4OO = ISOP1N25_3OO4OHISOP1N4 : 3.94E-12*0.035;\
ISOP1N25_3OO4OH + ISOP1N2OO = MVK + HCHO + NO2 + ISOP1N25_3O4OH : 3.08e-12*0.58;\
ISOP1N25_3OO4OH + ISOP1N2OO = ISOP1N2OH + ISOP1N25_3CO4OH : 3.08e-12*0.77*0.5;\
ISOP1N25_3OO4OH + ISOP1N2OO = ISOP1N25_3OO4OHISOP1N2 : 3.08e-12*0.035;\
ISOP1N25_3OO4OH + CH3OO = ISOP1N25_3OH4OH + HCHO : 1.4E-12*0.71*0.5;\
ISOP1N25_3OO4OH + CH3OO = ISOP1N25_3CO4OH + CH3OH : 1.4E-12*0.71*0.5;\
ISOP1N25_3OO4OH + CH3OO = ISOP1N25_3O4OH + CH3O : 1.4E-12*0.29;\
//INP
*ISOP1N2OOH + OH = ISOP1N2OOH3R4OH : 8.38e-12*exp(390/T)*0.76*;\
ISOP1N2OOH3R4OH + O2 = ISOP1N2OOH3OO4OH : 1e-14;\
ISOP1N2OOH3R4OH = ISOP1N23O4OH + OH: 9.2e4;\
ISOP1N2OOH + OH = ISOP1N2OOH3OH4OO : 8.38e-12*exp(390/T)*0.24;\
*ISOP1N4OOH + OH = ISOP1N2OH3R4OOH : 2.24e-11*exp(390/T)*0.31*;\
ISOP1N2OH3R4OOH + O2 = ISOP1N2OH3OO4OOH : 1e-14;\
ISOP1N2OH3R4OOH = ISOP1N2OH34O + OH : 9.61e4;\
*ISOP1N4OOH + OH = ISOP1N2R3OH4OOH : 2.24e-11*exp(390/T)*0.69*;\
ISOP1N2R3OH4OOH + O2 = ISOP1N2OO3OH4OOH : 1e-14;\
ISOP1N2R3OH4OOH = ISOP12O3OH4OOH + NO2 : 7.73e3;\
*ISOP3OOH4N + OH = ISOP1OH2R3OOH4N : 1.17e-11*exp(390/T)*0.965*;\
ISOP1OH2R3OOH4N + O2 = ISOP1OH2OO3OOH4N: 1e-14;\
ISOP1OH2R3OOH4N = ISOP1OH23O4N + OH : 9.2e4;\
ISOP3OOH4N + OH = ISOP1OO2OH3OOH4N : 1.17e-11*exp(390/T)*0.035;\
*ISOP1OOH4N + OH = ISOP1OOH2R3OH4N : 3.07e-11*exp(390/T)*0.69*;\
ISOP1OOH2R3OH4N + O2 = ISOP1OOH2OO3OH4N : 1e-14;\
ISOP1OOH2R3OH4N = ISOP12O3OH4N + OH : 9.61e4;\
*ISOP1OOH4N + OH = ISOP1OOH2OH3R4N : 3.07e-11*exp(390/T)*0.31*;\
ISOP1OOH2OH3R4N + O2 = ISOP1OOH2OH3OO4N : 1e-14;\
ISOP1OOH2OH3R4N = ISOP1OOH2OH34O + NO2 : 7.73e3;\
ISOP1N2OOH + OH = ISOP1N2OO + H2O : 3.4E-12*exp(200/T);\
ISOP1N4OOH + OH = ISOP1N4OO + H2O : 3.4E-12*exp(200/T);\
ISOP3OOH4N + OH = ISOP3OO4N + H2O : 3.4E-12*exp(200/T);\
ISOP1OOH4N + OH = ISOP1OO4N + H2O : 3.4E-12*exp(200/T);\
//ISOPNOOHOHOO
ISOP1N2OOH3OO4OH + NO = ISOP1N2OOH3N4OH : k_nitrate[2.7,350,3.322,12];\
ISOP1N2OOH3OO4OH + NO = NO2 + PROPNN + GLYC + OH : k_alkoxy[2.1375,350,3.322,12];\
ISOP1N2OOH3OO4OH + NO = NO2 + HO2 + HCHO + MACR2OOH3N : k_alkoxy[0.5625,350,3.322,12];\
ISOP1N2OOH3OO4OH + HO2 = NO2 + HO2 + HCHO + MACR2OOH3N : 0.15*2.64e-13*exp(1300/T);\
ISOP1N2OOH3OO4OH + HO2 = OH + PROPNN + GLYC + OH : 0.58*2.64e-13*exp(1300/T);\
ISOP1N2OOH3OO4OH + HO2 = ISOP1N2OOH3OOH4OH : 0.27*2.64e-13*exp(1300/T);\
ISOP1N2OOH3OH4OO + NO = ISOP1N2OOH3OH4N : k_nitrate[2.7,350,2.567,12];\
ISOP1N2OOH3OH4OO + NO = NO2 + HO2 + HCHO + MACR2OOH3N : k_alkoxy[2.7,350,2.567,12];\
ISOP1N2OOH3OH4OO + HO2 = ISOP1N2OOH3OH4OOH : 2.64e-13*exp(1300/T);\
ISOP1N2OH3OO4OOH + NO = ISOP1N2OH3N4OOH : k_nitrate[2.7,350,3.322,12];\
ISOP1N2OH3OO4OOH + NO = NO2 + MACR2OH3N + HCHO + OH : k_alkoxy[0.5625,350,3.322,12];\
ISOP1N2OH3OO4OOH + NO = NO2 + PROPNN + HPETHNL + HO2 : k_alkoxy[2.1375,350,3.322,12];\
ISOP1N2OH3OO4OOH + HO2 = OH + PROPNN + HPETHNL + HO2 : 0.58*2.64e-13*exp(1300/T);\
ISOP1N2OH3OO4OOH + HO2 = OH + MACR2OH3N + HCHO + OH : 0.15*2.64e-13*exp(1300/T);\
ISOP1N2OH3OO4OOH + HO2 = ISOP1N2OH3OOH4OOH : 0.27*2.64e-13*exp(1300/T);\

ISOP1N2OO3OH4OOH + NO = ISOP1N2N3OH4OOH : k_nitrate[2.7,350,9.617,12];\
ISOP1N2OO3OH4OOH + NO = NO2 + PROPNN + HPETHNL + HO2 : k_alkoxy[2.7,350,9.617,12];\
ISOP1N2OO3OH4OOH + HO2 = OH + PROPNN + HPETHNL + HO2 : 0.73*2.64e-13*exp(1300/T);\
ISOP1N2OO3OH4OOH + HO2 = ISOP1N2OOH3OH4OOH : 0.27*2.64e-13*exp(1300/T);\
ISOP1OH2OO3OOH4N + NO = ISOP1OH2N3OOH4N : k_nitrate[2.7,350,2.063,12];\
ISOP1OH2OO3OOH4N + NO = NO2 + HO2 + HCHO + MVK3OOH4N : k_alkoxy[0.5625,350,2.063,12];\
ISOP1OH2OO3OOH4N + NO = NO2 + HAC + ETHLN + OH : k_alkoxy[2.1375,350,2.063,12];\
ISOP1OH2OO3OOH4N + HO2 = OH + HAC + ETHLN + OH : 0.58*2.64e-13*exp(1300/T);\
ISOP1OH2OO3OOH4N + HO2 = OH + HO2 + HCHO + MVK3OOH4N : 0.15*2.64e-13*exp(1300/T);\
ISOP1OH2OO3OOH4N + HO2 = ISOP1OH2OOH3OOH4N : 0.27*2.64e-13*exp(1300/T);\
ISOP1OO2OH3OOH4N + NO = ISOP1N2OH3OOH4N : k_nitrate[2.7,350,2.567,12];\
ISOP1OO2OH3OOH4N + NO = HO2 + HO2 + HCHO + MVK3OOH4N : k_alkoxy[2.7,350,2.567,12];\
ISOP1OO2OH3OOH4N + HO2 = ISOP1OOH2OH3OOH4N : 2.64e-13*exp(1300/T);\
ISOP1OOH2OO3OH4N + NO = ISOP1OOH2N3OH4N : k_nitrate[2.7,350,2.063,12];\
ISOP1OOH2OO3OH4N + NO = NO2 + HPAC + ETHLN + HO2 : k_alkoxy[2.1375,350,2.063,12];\
ISOP1OOH2OO3OH4N + NO = NO2 + MVK3OH4N + HCHO + OH : k_alkoxy[0.5625,350,2.063,12];\
ISOP1OOH2OO3OH4N + HO2 = OH + MVK3OH4N + HCHO + OH : 0.15*2.64e-13*exp(1300/T);\
ISOP1OOH2OO3OH4N + HO2 = OH + HPAC + ETHLN + HO2 : 0.58*2.64e-13*exp(1300/T);\
ISOP1OOH2OO3OH4N + HO2 = ISOP1OOH2OOH3OH4N : 0.27*2.64e-13*exp(1300/T);\
ISOP1OOH2OH3OO4N + NO = ISOP1OOH2OH3N4N : k_nitrate[2.7,350,14.652,12];\
ISOP1OOH2OH3OO4N + NO = NO2 + HPAC + ETHLN + HO2 : k_alkoxy[2.7,350,14.652,12];\
ISOP1OOH2OH3OO4N + HO2 = OH + HPAC + ETHLN + HO2 : 0.73*2.64e-13*exp(1300/T);\
ISOP1OOH2OH3OO4N + HO2 = ISOP1OOH2OH3OOH4N : 0.27*2.64e-13*exp(1300/T);\
ISOP1N2OOH3OO4OH = ISOP1N2OO3OOH4OH : 4e6;\
ISOP1N2OOH3OH4OO = ISOP1N2OO3OH4OOH : 4e6;\
ISOP1N2OH3OO4OOH = ISOP1N2OH3OOH4OO : 2e6;\
ISOP1N2OO3OH4OOH = ISOP1N2OOH3OH4OO : 2e6;\
ISOP1OH2OO3OOH4N = ISOP1OH2OOH3OO4N : 3e6;\
ISOP1OO2OH3OOH4N = ISOP1OOH2OH3OO4N : 3e6;\
ISOP1OOH2OO3OH4N = ISOP1OO2OOH3OH4N : 2e6;\
ISOP1OOH2OH3OO4N = ISOP1OO2OH3OOH4N : 2e6;\
ISOP1N2OO3OOH4OH = ISOP1N2OOH3OO4OH : 3e6;\
ISOP1N2OH3OOH4OO = ISOP1N2OH3OO4OOH : 3e6;\
ISOP1OH2OOH3OO4N = ISOP1OH2OO3OOH4N : 4e6;\
ISOP1OO2OOH3OH4N = ISOP1OOH2OO3OH4N : 4e6;\
ISOP1N2OO3OOH4OH + HO2 = ISOP1N2OOH3OOH4OH : 0.27*2.64e-13*exp(1300/T);\
ISOP1N2OO3OOH4OH + HO2 = MVK3OOH4OH + NO2 + CH2O + OH : 0.15*2.64e-13*exp(1300/T);\
ISOP1N2OO3OOH4OH + HO2 = OH + OH + GLYC + PROPNN : 0.58*2.64e-13*exp(1300/T);\
ISOP1N2OO3OOH4OH + NO = ISOP1N2N3OOH4OH : k_nitrate[2.7,350,17.17,12];\
ISOP1N2OO3OOH4OH + NO = MVK3OOH4OH + NO2 + CH2O : k_alkoxy[0.5625,350,17.17,12];\
ISOP1N2OO3OOH4OH + NO = NO2 + OH + GLYC + PROPNN : k_alkoxy[2.1375,350,17.17,12];\
ISOP1N2OH3OOH4OO + HO2 = ISOP1N2OH3OOH4OOH : 2.64e-13*exp(1300/T);\
ISOP1N2OH3OOH4OO + NO = ISOP1N2OH3OOH4N : k_nitrate[2.7,350,4.833,12];\
ISOP1N2OH3OOH4OO + NO = MACR2OH3N + OH + NO2 + CH2O : k_alkoxy[2.7,350,4.833,12];\
ISOP1OH2OOH3OO4N + HO2 = ISOP1OH2OOH3OOH4N : 0.27*2.64e-13*exp(1300/T);\
ISOP1OH2OOH3OO4N + HO2 = MACR2OOH3OH + OH + NO2 + CH2O : 0.15*2.64e-13*exp(1300/T);\
ISOP1OH2OOH3OO4N + HO2 = HAC + ETHLN + OH + OH : 0.58*2.64e-13*exp(1300/T);\
ISOP1OH2OOH3OO4N + NO = ISOP1OH2OOH3N4N : k_nitrate[2.7,350,25.983,12];\
ISOP1OH2OOH3OO4N + NO = MACR2OOH3OH + NO2 + NO2 + CH2O : k_alkoxy[0.5625,350,25.983,12];\
ISOP1OH2OOH3OO4N + NO = HAC + ETHLN + OH + NO2 : k_alkoxy[2.1375,350,25.983,12];\
ISOP1OO2OOH3OH4N + HO2 = ISOP1OOH2OOH3OH4N : 2.64e-13*exp(1300/T);\
ISOP1OO2OOH3OH4N + NO = ISOP1N2OOH3OH4N : k_nitrate[2.7,350,4.833,12];\
ISOP1OO2OOH3OH4N + NO = MVK3OH4N + OH + NO2 + CH2O : k_alkoxy[2.7,350,4.833,12];\
//INHE\
ISOP1N23O4OH + OH = NO2 + ISOP1CO23O4OH : 4.78e-11*exp(-400/T)*0.69;\
ISOP1N23O4OH + OH = ISOP1N2OO3CO4OH : 4.78e-11*exp(-400/T)*0.07;\
*ISOP1N23O4OH + OH = ISOP1N23O4OH4R : 4.78e-11*exp(-400/T)*0.24*;\
ISOP1N23O4OH4R + O2 = ISOP1N23O4CO + HO2 : 1e-14;\
*ISOP1N23O4OH4R = CH2O + NO2 + MVKENOL : 0.5*2.07e5*;\
*ISOP1N23O4OH4R = ISOP1N2OH3OO4CO : 0.5*2.07e5*;\
ISOP1OH23O4N + OH = ISOP1OH23O4CO + NO2 : 4.78e-11*exp(-400/T)*0.24;\
ISOP1OH23O4N + OH = ISOP1OH2OO3CO4N : 4.78e-11*exp(-400/T)*0.07;\
*ISOP1OH23O4N + OH = ISOP1OH1R23O4N : 4.78e-11*exp(-400/T)*0.69*;\
ISOP1OH1R23O4N + O2 = ISOP1CO23O4N + HO2 : 1e-14;\
*ISOP1OH1R23O4N = CH2O + NO2 + MCRENOL : 0.5*2.07e5*;\
*ISOP1OH1R23O4N = ISOP1CO2OO3OH4N : 0.5*2.07e5*;\
ISOP1N2OH34O + OH = NO2 + ISOP1CO2OH34O : 3.22e-11*exp(-400/T);\
ISOP12O3OH4N + OH = ISOP12O3OH4CO + NO2 : 0.2*3.22e-11*exp(-400/T);\
*ISOP12O3OH4N + OH = ISOP12O3OH3R4N : 0.8*3.22e-11*exp(-400/T)*;\
*ISOP12O3OH3R4N + O2 = ISOP12O3CO4N + HO2 : 0.33*1e-14*;\
*ISOP12O3OH3R4N + O2 = ISOP1OH3OH4CO + NO2 : 0.67*1e-14*;\
ISOP12O3OH3R4N = ISOP1OH2OO3CO4N : 3.45e4;\
//ICN\

ISOP3CO4N + OH = ISOP1OH2OO3CO4N : 1.17e-11*exp(390/T);\
ISOP1OH2OO3CO4N + HO2 = ISOP1OH2OOH3CO4N : 2.6e-13*exp(1300/T)*0.27;\
ISOP1OH2OO3CO4N + HO2 = HAC + OH + NPA : 2.6e-13*exp(1300/T)*0.58;\
ISOP1OH2OO3CO4N + HO2 = MVK3CO4N + HO2 + OH + CH2O : 2.6e-13*exp(1300/T)*0.15;\
ISOP1OH2OO3CO4N + NO = MVK3CO4N + NO2 + HO2 + CH2O: k_alkoxy[0.5625,350,7.239,11];\
ISOP1OH2OO3CO4N + NO = ISOP1OH2N3CO4N : k_nitrate[2.7,350,7.239,11];\
ISOP1OH2OO3CO4N + NO = HAC + NO2 + NPA : k_alkoxy[2.1375,350,7.239,11];\
ISOP1N2OO3CO4OH + NO = ISOP1N2N3CO4OH: k_nitrate[2.7,350,76.383,11];\
ISOP1N2OO3CO4OH + NO = MVK3CO4OH + CH2O + NO2 + NO2: k_alkoxy[0.5625,350,76.383,11];\
ISOP1N2OO3CO4OH + NO = NO2 + PROPNN + CH3CO3: k_alkoxy[2.1375,350,76.383,11];\
ISOP1N2OO3CO4OH + HO2 = OH + PROPNN + CH3CO3 : 2.6e-13*exp(1300/T)*0.58;\
ISOP1N2OO3CO4OH + HO2 = MVK3CO4OH + CH2O + NO2 + OH : 2.6e-13*exp(1300/T)*0.15;\
ISOP1N2OO3CO4OH + HO2 = ISOP1N2OOH3CO4OH : 2.6e-13*exp(1300/T)*0.27;\
*ISOP1N4CO + OH = ISOP1N4R4CO : 4.13e-12*exp(470/T)*;\
ISOP1N4R4CO = NO2 + ISOP12O344CO : 1.294e4;\
*ISOP1N4R4CO + O2 = ISOP1N2OO344CO : 0.875*1e-14*;\
*ISOP1N4R4CO + O2 = ISOP1N4CO4OO : 0.125*1e-14*;\
ISOP1N2OO344CO + NO = ISOP1N2N344CO : k_nitrate[2.7,350,7.948,10];\
ISOP1N2OO344CO + NO = NO2 + NO2 + CH2O + MVK4CO : k_alkoxy[2.7,350,7.948,10];\
ISOP1N2OO344CO + HO2 = OH + NO2 + CH2O + MVK4CO : 2.54e-13*exp(1300/T)*0.54;\
ISOP1N2OO344CO + HO2 = ISOP1N2OOH344CO : 2.54e-13*exp(1300/T)*0.47;\
ISOP1N4CO4OO + NO2 + M = ISOP1N4PAN + M : k_troe[k_0 = 2.133e-28*(T/300)^(-7.1), k_inf= 1.2e-11*(T/300)^(-0.9), Fc = 0.3];\
ISOP1N4CO4OO + NO = NO2 + CO2 + C4NVP2 : 2.7E-12*exp(350/T);\
ISOP1N4CO4OO + HO2 = ISOP1N4CO4OOH : 2.54e-13*exp(1300/T)*0.4;\
ISOP1N4CO4OO + HO2 = O3 + ISOP1N4CO4OH : 2.54e-13*exp(1300/T)*0.2;\
ISOP1N4CO4OO + HO2 = OH + CO2 + C4NVP2 : 2.54e-13*exp(1300/T)*0.4;\
C4NVP2 + NO = NO2 + MACR2OO3N : 2.7E-12*exp(350/T);\
C4NVP2 + HO2 = OH + MACR2OO3N : 2.38e-13*exp(1300/T);\
C4NVP2 + NO2 = MACR2N3N : 9e-12;\
MACR2OO3N + NO = NO2 + HO2 + CO + PROPNN : 2.7E-12*exp(350/T);\
MACR2OO3N + HO2 = OH + HO2 + CO + PROPNN : 2.47e-13*exp(1300/T);\
ISOP1N4PAN + M = ISOP1N4CO4OO + NO2 + M : k_troe[k_0 = 3.871e-3*exp(-12100/T), k_inf = 5.4e16*exp(-13830/T), Fc = 0.3];\
*ISOP1CO4N + OH = ISOP1CO1R4N : 4.13e-12*exp(470/T)*;\
ISOP1CO1R4N = NO2 + ISOP121CO34O : 1.294e4;\
*ISOP1CO1R4N + O2 = ISOP121CO3OO4N : 0.875*1e-14*;\
*ISOP1CO1R4N + O2 = ISOP1CO1OO4N : 0.125*1e-14*;\
ISOP121CO3OO4N + NO = ISOP121CO3N4N : k_nitrate[2.7,350,12.136,10];\
ISOP121CO3OO4N + NO = NO2 + NO2 + CH2O + MACR3CO : k_alkoxy[2.7,350,12.136,10];\
ISOP121CO3OO4N + HO2 = OH + NO2 + CH2O + MACR3CO : 2.54e-13*exp(1300/T)*0.26;\
ISOP121CO3OO4N + HO2 = ISOP121CO3OOH4N : 2.54e-13*exp(1300/T)*0.74;\
ISOP1CO1OO4N + NO2 + M = ISOP1PAN4N + M : k_troe[k_0 = 2.133e-28*(T/300)^(-7.1), k_inf= 1.2e-11*(T/300)^(-0.9), Fc = 0.3];\
ISOP1CO1OO4N + NO = NO2 + CO2 + C4NVP1 : 2.7E-12*exp(350/T);\
ISOP1CO1OO4N + HO2 = ISOP1CO1OOH4N : 2.54e-13*exp(1300/T)*0.4;\
ISOP1CO1OO4N + HO2 = O3 + ISOP1CO1OH4N : 2.54e-13*exp(1300/T)*0.2;\
ISOP1CO1OO4N + HO2 = OH + CO2 + C4NVP1 : 2.54e-13*exp(1300/T)*0.4;\
C4NVP1 + NO = NO2 + MVK3OO4N : 2.7E-12*exp(350/T);\
C4NVP1 + HO2 = OH + MVK3OO4N : 2.38e-13*exp(1300/T);\
C4NVP1 + NO2 = MVK3N4N : 9e-12;\
MVK3OO4N + NO = NO2 + ETHLN + CH3CO3 : 2.7E-12*exp(350/T);\
MVK3OO4N + HO2 = OH + ETHLN + CH3CO3 : 2.47e-13*exp(1300/T);\
ISOP1PAN4N + M = ISOP1N4CO4OO + NO2 + M : k_troe[k_0 = 3.871e-3*exp(-12100/T), k_inf = 5.4e16*exp(-13830/T), Fc = 0.3];\
*ISOP1N4CO + OH = ISOP1N2R3OH4CO: 2.24e-11*exp(390/T)*0.69*;\
ISOP1N2R3OH4CO + O2 = ISOP1N2OO3OH4CO : 1e-14;\
ISOP1N2R3OH4CO = ISOP12O3OH4CO + NO2 : 7.73e3;\
ISOP1N4CO + OH = ISOP1N2OH3OO4CO : 2.24e-11*exp(390/T)*0.31;\
*ISOP1CO4N + OH = ISOP1CO2OH3R4N : 3.07e-11*exp(390/T)*0.31*;\
ISOP1CO2OH3R4N + O2 = ISOP1CO2OH3OO4N : 1e-14;\
ISOP1CO2OH3R4N = ISOP1CO2OH34O + NO2 : 7.73e3;\
ISOP1CO4N + OH = ISOP1CO2OO3OH4N : 3.07e-11*exp(390/T)*0.69;\
ISOP1N2OO3OH4CO = MACR2OOH3N + CO + HO2 : 4e8*exp(-5000/T);\
ISOP1CO2OH3OO4N = MVK3OOH4N + CO + HO2 : 4e8*exp(-5000/T);\
ISOP1N2OH3OO4CO = MACR2OH3N + CO + OH : 1e7*exp(-5000/T);\
ISOP1N2OH3OO4CO + HO2 = ISOP1N2OH3OOH4CO :2.6e-13*exp(1300/T)*0.27;\
ISOP1N2OH3OO4CO + HO2 = MACR2OH3N + OH + HO2 + CO : 2.6e-13*exp(1300/T)*0.15;\
ISOP1N2OH3OO4CO + HO2 = OH + HO2 + PROPNN + GLYX : 2.6e-13*exp(1300/T)*0.58;\
ISOP1N2OH3OO4CO + NO = ISOP1N2OH3N4CO : k_nitrate[2.7,350,16.019,11];\
ISOP1N2OH3OO4CO + NO = MACR2OH3N + NO2 + HO2 + CO : k_alkoxy[0.5625,350,16.019,11];\
ISOP1N2OH3OO4CO + NO = NO2 + HO2 + PROPNN + GLYX : k_alkoxy[2.1375,350,16.019,11];\
ISOP1CO2OO3OH4N = MVK3OH4N + CO + OH : 1e7*exp(-5000/T);\
ISOP1CO2OO3OH4N + HO2 = MVK3OH4N + OH + HO2 + CO : 2.6e-13*exp(1300/T)*0.15;\
ISOP1CO2OO3OH4N + HO2 = OH + HO2 + MGLY + ETHLN : 2.6e-13*exp(1300/T)*0.58;\
ISOP1CO2OO3OH4N + HO2 = ISOP1CO2OOH3OH4N : 2.6e-13*exp(1300/T)*0.27;\
ISOP1CO2OO3OH4N + NO = MVK3OH4N + NO2 + HO2 + CO : k_alkoxy[0.5625,350,10.532,11];\

ISOP1CO2OO3OH4N + NO = NO2 + HO2 + MGLY + ETHLN : k_alkoxy[2.1375,350,10.532,11];\
ISOP1CO2OO3OH4N + NO = ISOP1CO2N3OH4N : k_nitrate[2.7,350,10.532,11];\
//IHN\
ISOP1N2OH + OH = ISOP1N2OH3OO4OH : 8.38e-12*exp(390/T)*0.76;\
ISOP1N2OH + OH = ISOP1N2OH3OH4OO : 8.38e-12*exp(390/T)*0.24;\
*ISOP1N4OHc + OH = ISOP1N2R3OH4OH : 2.24e-11*exp(390/T)*0.69*;\
*ISOP1N4OHt + OH = ISOP1N2R3OH4OH : 2.24e-11*exp(390/T)*0.69*;\
ISOP1N2R3OH4OH + O2 = ISOP1N2OO3OH4OH : 1e-14;\
ISOP1N2R3OH4OH = ISOP12O3OH4OH : 7.73e3;\
ISOP1N4OHc + OH = ISOP1N2OH3OO4OH : 2.24e-11*exp(390/T)*0.31;\
ISOP1N4OHt + OH = ISOP1N2OH3OO4OH : 2.24e-11*exp(390/T)*0.31;\
ISOP3OH4N + OH = ISOP1OH2OO3OH4N : 1.17e-11*exp(390/T)*0.965;\
ISOP3OH4N + OH = ISOP1OO2OH3OH4N : 1.17e-11*exp(390/T)*0.035;\
*ISOP1OH4Nc + OH = ISOP1OH2OH3R4N : 3.07e-11*exp(390/T)*0.31*;\
*ISOP1OH4Nt + OH = ISOP1OH2OH3R4N : 3.07e-11*exp(390/T)*0.31*;\
ISOP1OH2OH3R4N + O2 = ISOP1OH2OH3OO4N : 1e-14;\
ISOP1OH2OH3R4N = ISOP1OH2OH34O : 7.73e3;\
ISOP1OH4Nc + OH = ISOP1OH2OO3OH4N : 3.07e-11*exp(390/T)*0.69;\
ISOP1OH4Nt + OH = ISOP1OH2OO3OH4N : 3.07e-11*exp(390/T)*0.69;\
ISOP1N2OO3OH4OH + HO2 = ISOP1N2OOH3OH4OH : 2.6e-13*exp(1300/T)*0.27;\
ISOP1N2OO3OH4OH + HO2 = OH + HO2 + PROPNN + GLYC : 2.6e-13*exp(1300/T)*0.73;\
ISOP1N2OH3OO4OH + HO2 = ISOP1N2OH3OOH4OH : 2.6e-13*exp(1300/T)*0.27;\
ISOP1N2OH3OO4OH + HO2 = MACR2OH3N + HCHO + HO2 + OH : 2.6e-13*exp(1300/T)*0.73*0.21;\
ISOP1N2OH3OO4OH + HO2 = OH + HO2 + PROPNN + GLYC : 2.6e-13*exp(1300/T)*0.73*0.79;\
ISOP1OH2OH3OO4N + HO2 = ISOP1OH2OH3OOH4N : 2.6e-13*exp(1300/T)*0.27;\
ISOP1OH2OH3OO4N + HO2 = OH + HO2 + HAC + ETHLN : 2.6e-13*exp(1300/T)*0.73;\
ISOP1OH2OO3OH4N + HO2 = ISOP1OH2OOH3OH4N : 2.6e-13*exp(1300/T)*0.27;\
ISOP1OH2OO3OH4N + HO2 = MVK3OH4N + HCHO + HO2 + OH : 2.6e-13*exp(1300/T)*0.73*0.21;\
ISOP1OH2OO3OH4N + HO2 = OH + HO2 + HAC + ETHLN : 2.6e-13*exp(1300/T)*0.73*0.79;\
ISOP1N2OO3OH4OH + NO = ISOP1N2N3OH4OH : k_nitrate[2.7,350,10.532,11];\
ISOP1N2OO3OH4OH + NO = NO2 + HO2 + PROPNN + GLYC : k_alkoxy[2.7,350,10.532,11];\
ISOP1N2OH3OO4OH + NO = ISOP1N2OH3N4OH : k_nitrate[2.7,350,1.908,11];\
ISOP1N2OH3OO4OH + NO = MACR2OH3N + HCHO + HO2 + NO2 : k_alkoxy[0.567,350,1.908,11];\
ISOP1N2OH3OO4OH + NO = NO2 + HO2 + PROPNN + GLYC : k_alkoxy[2.133,350,1.908,11];\
ISOP1OH2OH3OO4N + NO = ISOP1OH2OH3N4N : k_nitrate[2.7,350,16.019,11];\
ISOP1OH2OH3OO4N + NO = NO2 + HO2 + HAC + ETHLN : k_alkoxy[2.7,350,16.019,11];\
ISOP1OH2OO3OH4N + NO = ISOP1OH2N3OH4N : k_nitrate[2.7,350,1.124,11];\
ISOP1OH2OO3OH4N + NO = MVK3OH4N + HCHO + HO2 + NO2 : k_alkoxy[0.567,350,1.124,11];\
ISOP1OH2OO3OH4N + NO = NO2 + HO2 + HAC + ETHLN : k_alkoxy[2.133,350,1.124,11];\
ISOP1N2OH3OH4OO + HO2 = ISOP1N2OH3OH4OOH : 2.6e-13*exp(1300/T);\
ISOP1OO2OH3OH4N + HO2 = ISOP1OOH2OH3OH4N : 2.6e-13*exp(1300/T);\
ISOP1N2OH3OH4OO + NO = ISOP1N2OH3OH4N : k_nitrate[2.7,350,2.849,11];\
ISOP1N2OH3OH4OO + NO = HO2 + NO2 + CH2O + MACR2OH3N : k_alkoxy[2.7,350,2.849,11];\
ISOP1OO2OH3OH4N + NO = ISOP1N2OH3OH4N : k_nitrate[2.7,350,2.849,11];\
ISOP1OO2OH3OH4N + NO = HO2 + NO2 + CH2O + MVK3OH4N : k_alkoxy[2.7,350,2.849,11];\

Table I.4: Alternate formulations of epoxide formation reactions for the explicit isoprene mechanism. These reactions replace the italicized reactions found in Table I.3.

```
ISOP1OH2OOH + OH = ISOP1OH2OOH3OO4OH : 1.7e-11*exp(390/T)*0.95*0.10;\
ISOP1OH2OOH + OH = ISOP1OH23O4OHt : 1.7e-11*exp(390/T)*0.95*0.67*[1/(4.77e-21*[M]+1)];\
ISOP1OH2OOH + OH = ISOP1OH23O4OHc : 1.7e-11*exp(390/T)*0.95*0.33*[1/(4.77e-21*[M]+1)];\
ISOP3OOH4OH + OH = ISOP1OH2OO3OOH4OH : 3.0e-11*exp(390/T)*0.95*0.10;\
ISOP3OOH4OH + OH = ISOP1OH23O4OHt : 3.0e-11*exp(390/T)*0.95*0.68*[1/(4.77e-21*[M]+1)];\
ISOP3OOH4OH + OH = ISOP1OH23O4OHc : 3.0e-11*exp(390/T)*0.95*0.32*[1/(4.77e-21*[M]+1)];\
ISOP1OH23O4OHc + OH = ISOP1OH23O4CO + H2O + HO2 : 0.168*0.228*5.82e-11*exp(-400/T);\
ISOP1OH23O4OHc + OH = HAC + GLYX + OH : 0.168*0.63*5.82e-11*exp(-400/T)*[1/(1.20e-20*[M]+1)];\
ISOP1OH23O4OHc + OH = MACR2OH3OH + OH + CO : 0.168*0.37*5.82e-11*exp(-400/T)*[1/(1.20e-20*[M]+1)];\
ISOP1OH23O4OHc + OH = ISOP1CO23O4OH + H2O + HO2: 0.752*0.228*5.82e-11*exp(-400/T);\
ISOP1OH23O4OHc + OH = GLYC + MGLY + OH: 0.752*0.287*5.82e-11*exp(-400/T)*[1/(1.20e-20*[M]+1)];\
ISOP1OH23O4OHc + OH = MVK3OH4OH + OH + CO: 0.752*0.713*5.82e-11*exp(-400/T)*[1/(1.20e-20*[M]+1)];\
ISOP1OH23O4OHt + OH = ISOP1OH23O4CO + H2O + HO2: 0.31*0.194*3.75e-11*exp(-400/T);\
ISOP1OH23O4OHt + OH = HAC + GLYX + OH: 0.31*0.63*3.75e-11*exp(-400/T)*[1/(9.77e-21*[M]+1)];\
ISOP1OH23O4OHt + OH = MACR2OH3OH + OH + CO: 0.31*0.37*3.75e-11*exp(-400/T)*[1/(9.77e-21*[M]+1)];\
ISOP1OH23O4OHt + OH = ISOP1CO23O4OH + H2O + HO2: 0.62*0.194*3.75e-11*exp(-400/T);\
ISOP1OH23O4OHt + OH = GLYC + MGLY + OH: 0.62*0.287*3.75e-11*exp(-400/T)*[1/(9.77e-21*[M]+1)];\
ISOP1OH23O4OHt + OH = MVK3OH4OH + OH + CO: 0.62*0.713*3.75e-11*exp(-400/T)*[1/(9.77e-21*[M]+1)];\
ISOP12O3OH4OH + OH = ISOP12O3CO4OH + HO2 : 0.8*0.2*3.22e-11*exp(-400/T);\
ISOP12O3OH4OH + OH = ISOP1OH3OH4CO + HO2 : 0.8*0.4*3.22e-11*exp(-400/T);\
ISOP12O3OH4OH + OH = ISOP1OH2OO3CO4OH : 0.8*3.22e-11*exp(-400/T)*[1/(6.09e-20*[M]+1)];\
ISOP1CO4OOHc + OH = ISOP1CO2OH3OO4OOH : 5.0e-13*exp(650/T);\
ISOP1CO4OOHc + OH = ISOP1CO2OH34O : 1.0e-12*exp(650/T)*[1/(4.058e-20*[M]+1)];\
ISOP1CO4OOHc + OH = ISOP1CO1OOH4CO : 3.8e-12*exp(400/T)*0.1;\
ISOP1CO4OOHc + OH = ISOP121CO3OO4OOH : 3.8e-12*exp(400/T)*0.7;\
ISOP1CO4OOHc + OH = ISOP121CO34O : 3.8e-12*exp(400/T)*[1/(1.623e-19*[M]+1)];\
ISOP1CO4OOc = ISOP1CO1OOH4CO : 10*0.1;\
ISOP1CO4OOc = ISOP121CO3OO4OOH : 10*0.7;\
ISOP1CO4OOc = ISOP121CO34O : 10*[1/(1.623e-19*[M]+1)];\
ISOP1OOH4COc + OH = ISOP1OOH2OO3OH4CO : 1.0e-12*exp(650/T);\
ISOP1OOH4COc + OH = ISOP12O3OH4CO : 2.0e-12*exp(650/T)*[1/(4.058e-20*[M]+1)];\
ISOP1OOH4COc + OH = ISOP1OOH2OO344CO : 3.8e-12*exp(400/T)*0.7;\
ISOP1OOH4COc + OH = ISOP1CO4CO4OOH : 3.8e-12*exp(400/T)*0.1;\
ISOP1OOH4COc + OH = ISOP12O344CO : 3.8e-12*exp(400/T)*[1/(1.623e-19*[M]+1)];\
ISOP1OO4COc = ISOP1OOH2OO344CO : 10*0.7;\
ISOP1OO4COc = ISOP1CO4CO4OOH :10*0.1;\
ISOP1OO4COc = ISOP12O344CO : 10*[1/(1.623e-19*[M]+1)];\
ISOP1OH2N + OH = ISOP1OH2N3OO4OH: 0.75*0.8*8.4e-12*exp(390/T);\
ISOP1OH2N + OH = ISOP1OH23O4OHt: 0.75*0.67*8.4e-12*exp(390/T)*[1/(1.62e-19*[M]+1)];\
ISOP1OH2N + OH = ISOP1OH23O4OHc: 0.75*0.33*8.4e-12*exp(390/T)*[1/(1.62e-19*[M]+1)];\
ISOP3N4OH + OH = ISOP1OH2OO3N4OH: 0.9*0.86*1.17e-11*exp(390/T);\
ISOP3N4OH + OH = ISOP1OH23O4OHt: 0.9*0.67*1.17e-11*exp(390/T)*[1/(2.49e-19*[M]+1)];\
ISOP3N4OH + OH = ISOP1OH23O4OHc: 0.9*0.33*1.17e-11*exp(390/T)*[1/(2.49e-19*[M]+1)];\
ISOP1N2OOH + OH = ISOP1N23O4OH + OH : 8.38e-12*exp(390/T)*0.76*[1/(2.28e-20*[M]+1)];\
ISOP1N2OOH + OH = ISOP1N2OOH3OO4OH : 8.38e-12*exp(390/T)*0.276;\
SOP1N4OOH + OH = ISOP1N2OH34O + OH : 2.24e-11*exp(390/T)*0.31*[1/(2.185e-20*[M]+1)];\
ISOP1N4OOH + OH = ISOP1N2OH3OO4OOH : 2.24e-11*exp(390/T)*0.109;\
IISOP1N4OOH + OH = ISOP1N2OO3OH4OOH : 2.24e-11*exp(390/T)*0.6;\
ISOP1N4OOH + OH = ISOP12O3OH4OOH + NO2 : 2.24e-11*exp(390/T)*0.69*[1/(2.715e-19*[M]+1)];\
ISOP3OOH4N + OH = ISOP1OH23O4N + OH : 1.17e-11*exp(390/T)*0.965*[1/(2.28e-20*[M]+1)];\
ISOP3OOH4N + OH = ISOP1OH2OO3OOH4N : 1.17e-11*exp(390/T)*0.35;\
ISOP1OOH4N + OH = ISOP12O3OH4N + OH : 3.07e-11*exp(390/T)*0.69*[1/(2.185e-20*[M]+1)];\
ISOP1OOH4N + OH = ISOP1OOH2OO3OH4N : 3.07e-11*exp(390/T)*0.243;\
ISOP1OOH4N + OH = ISOP1OOH2OH3OO4N : 3.07e-11*exp(390/T)*0.27;\
ISOP1OOH4N + OH = ISOP1OOH2OH34O + NO2 : 3.07e-11*exp(390/T)*0.31*[1/(2.715e-19*[M]+1)];\
ISOP1N23O4OH + OH = ISOP1N23O4CO + HO2 : 4.78e-11*exp(-400/T)*0.24*0.2;\
ISOP1N23O4OH + OH = CH2O + NO2 + MVKENOL : 4.78e-11*exp(-400/T)*0.24*0.5*[1/(1.014e-20*[M]+1)];\
ISOP1N23O4OH + OH = ISOP1N2OH3OO4CO : 4.78e-11*exp(-400/T)*0.24*0.5*[1/(1.014e-20*[M]+1)];\
ISOP1OH23O4N + OH = ISOP1CO23O4N + HO2 : 4.78e-11*exp(-400/T)*0.24*0.2;\
ISOP1OH23O4N + OH = CH2O + NO2 + MCRENOL : 4.78e-11*exp(-400/T)*0.24*0.5*[1/(1.014e-20*[M]+1)];\
ISOP1OH23O4N + OH = ISOP1CO2OO3OH4N : 4.78e-11*exp(-400/T)*0.24*0.5*[1/(1.014e-20*[M]+1)];\
ISOP12O3OH4N + OH = ISOP12O3CO4N + HO2 : 0.8*0.2*3.22e-11*exp(-400/T);\
ISOP12O3OH4N + OH = ISOP1OH3OH4CO + NO2 : 0.8*0.4*3.22e-11*exp(-400/T);\
ISOP12O3OH4N + OH = ISOP1OH2OO3CO4N : 0.8*3.22e-11*exp(-400/T)*[1/(6.09e-20*[M]+1)];\
```

```
ISOP1N4CO + OH = NO2 + ISOP12O344CO : 4.13e-12*exp(470/T)*[1/(1.623e-19*[M]+1)];\
ISOP1N4CO + OH = ISOP1N2OO344CO : 0.7*4.13e-12*exp(470/T);\
ISOP1N4CO + OH = ISOP1N4CO4OO : 0.1*4.13e-12*exp(470/T);\
ISOP1CO4N + OH = NO2 + ISOP121CO34O : 4.13e-12*exp(470/T)*[1/(1.623e-19*[M]+1)];\
ISOP1CO4N + OH = ISOP121CO3OO4N : 0.7*4.13e-12*exp(470/T);\
ISOP1CO4N + OH = ISOP1CO1OO4N : 0.1*4.13e-12*exp(470/T);\
ISOP1N4CO + OH = ISOP1N2OO3OH4CO : 2.24e-11*exp(390/T)*0.6;\
ISOP1N4CO + OH = ISOP12O3OH4CO + NO2 :  2.24e-11*exp(390/T)*0.69*[1/(2.715e-19*[M]+1)];\
ISOP1CO4N + OH = ISOP1CO2OH34O + NO2 :  3.07e-11*exp(390/T)*0.31*[1/(2.715e-19*[M]+1)];\
ISOP1CO4N + OH = ISOP1CO2OH3OO4N : 3.07e-11*exp(390/T)*0.27;\
ISOP1N4OHc + OH = ISOP12O3OH4OH : 2.24e-11*exp(390/T)*0.69*[1/(2.715e-19*[M]+1)];\
ISOP1N4OHc + OH = ISOP1N2OO3OH4OH : 2.24e-11*exp(390/T)*0.69*0.87;\
ISOP1N4OHt + OH = ISOP12O3OH4OH : 2.24e-11*exp(390/T)*0.69*[1/(2.715e-19*[M]+1)];\
ISOP1N4OHt + OH = ISOP1N2OO3OH4OH : 2.24e-11*exp(390/T)*0.69*0.87;\
ISOP1OH4Nc + OH = ISOP1OH2OH34O : 3.07e-11*exp(390/T)*0.31*[1/(2.715e-19*[M]+1)];\
ISOP1OH4Nc + OH = ISOP1OH2OH3OO4N : 3.07e-11*exp(390/T)*0.31*0.87;\
ISOP1OH4Nt + OH = ISOP1OH2OH34O : 3.07e-11*exp(390/T)*0.31*[1/(2.715e-19*[M]+1)];\
ISOP1OH4Nt + OH = ISOP1OH2OH3OO4N : 3.07e-11*exp(390/T)*0.31*0.87;\
```

INDEX

L

M

ABOUT THE AUTHOR

Kelvin Hamilton Bates was born on January 9, 1990, in Seattle, Washington, to Tim Bates, an oceanographer, and Susan Hamilton, a biochemist. His parents' scientific backgrounds did not lead them to name their son after a unit of temperature – Kelvin was, instead, named after his grandfather – but did inspire them to invest heavily in his education. Kelvin's early schooling emphasized immersive cultural experiences, including travels to Japan, Vietnam, and the Dominican Republic, and instilled in him a profound love of learning. That passion helped him to thrive at Lakeside High School, where he first discovered his interests in organic chemistry and theater. In his eighteen years of childhood in the Pacific Northwest, Kelvin also gained an abiding appreciation for the splendor of the natural world.

In 2008 Kelvin matriculated at Davidson College, where he enjoyed the diversity of a liberal arts education and struggled to pick a major. He eventually settled on economics and chemistry, but not before taking a semester to study international politics in Geneva, Switzerland. While attending college, Kelvin spent two summers conducting biochemical research at pharmaceutical companies before being awarded a NOAA Hollings Scholarship, which led him to a summer research project with Dr. Chuck Brock at NOAA's facility in Boulder, CO, programming and calibrating an SMPS. Hooked on atmospheric research, he spent the following summer as an intern with NASA's Student Airborne Research Program, where he got his first taste of fieldwork under Prof. Don Blake at UC Irvine, investigating hydrocarbon emissions from California oil and gas infrastructure.

After graduating Summa cum Laude from Davidson, Kelvin came to Caltech on a Sharp Fellowship (and later an NSF Graduate Fellowship). As a graduate student in chemistry, Kelvin worked in a uniquely interdisciplinary collaboration between the labs of Profs. Brian Stoltz, Paul Wennberg, and John Seinfeld. While his main focus was to synthesize isoprene oxidation products and study their atmospheric fate in environmental chamber experiments, he also participated in a number of fieldwork and modeling projects. Kelvin will continue his studies in atmospheric chemistry at Harvard as a Harvard University Center for the Environment and NOAA Climate and Global Change postdoctoral fellow, in another collaboration between Profs. Daniel Jacob and Frank Keutsch.